PROCEEDINGS

SPIE—The International Society for Optical Engineering

GOES-8 and Beyond

Edward R. Washwell
Chair/Editor

7–9 August 1996
Denver, Colorado

Volume 2812

PROCEEDINGS
SPIE—The International Society for Optical Engineering

TL
798
.M4
G647
1996

GOES-8 and Beyond

Edward R. Washwell
Chair/Editor

LIBRARY
JAN 7 1997

7–9 August 1996
Denver, Colorado

Sponsored and Published by
SPIE—The International Society for Optical Engineering

Cooperating Organizations
NARSIA—North American Remote Sensing Industries Association
ASPRS—American Society for Photogrammetry and Remote Sensing

Volume 2812

SPIE is an international technical society dedicated to advancing engineering and scientific applications of optical, photonic, imaging, electronic, and optoelectronic technologies.

National Oceanic and Atmospheric Administration
TIROS Satellites and Satellite Meteorology

ERRATA NOTICE

One or more conditions of the original document may affect the quality of the image, such as:

Discolored pages
Faded or light ink
Binding intrudes into the text

This has been a co-operative project between the NOAA Central Library and the Climate Database Modernization Program, National Climate Data Center (NCDC). To view the original document contact the NOAA Central Library in Silver Spring, MD at (301) 713-2607 x124 or Library.Reference@noaa.gov.

HOV Services
Imaging Contractor
12200 Kiln Court
Beltsville, MD 20704-1387
January 26, 2009

The papers appearing in this book comprise the proceedings of the meeting mentioned on the cover and title page. They reflect the authors' opinions and are published as presented and without change, in the interests of timely dissemination. Their inclusion in this publication does not necessarily constitute endorsement by the editors or by SPIE.

Please use the following format to cite material from this book:
Author(s), "Title of paper," in *GOES-8 and Beyond,* Edward R. Washwell, Editor, Proc. SPIE 2812, page numbers (1996).

Library of Congress Catalog Card No. 96-68310
ISBN 0-8194-2200-2

Published by
SPIE—The International Society for Optical Engineering
P.O. Box 10, Bellingham, Washington 98227-0010 USA
Telephone 360/676-3290 (Pacific Time) • Fax 360/647-1445

Copyright ©1996, The Society of Photo-Optical Instrumentation Engineers.

Copying of material in this book for internal or personal use, or for the internal or personal use of specific clients, beyond the fair use provisions granted by the U.S. Copyright Law is authorized by SPIE subject to payment of copying fees. The Transactional Reporting Service base fee for this volume is $6.00 per article (or portion thereof), which should be paid directly to the Copyright Clearance Center (CCC), 222 Rosewood Drive, Danvers, MA 01923. Payment may also be made electronically through CCC Online at http://www.directory.net/copyright/. Other copying for republication, resale, advertising or promotion, or any form of systematic or multiple reproduction of any material in this book is prohibited except with permission in writing from the publisher. The CCC fee code is 0-8194-2200-2/96/$6.00.

Printed in the United States of America.

Contents

ix *Conference Committee*
xi *Introduction*

SESSION 1 GOES PROGRAM OVERVIEW

2 **Impact of GOES satellites on the National Weather Service (Keynote Address)** [2812-01]
E. W. Friday, National Weather Service

11 **GOES program status** [2812-02]
G. J. Dittberner, National Environmental Satellite Data and Information Service/NOAA

20 **NOAA's future GOES satellite program** [2812-03]
E. Howard, R. Heymann, G. J. Dittberner, S. Kirkner, U.S. Dept. of Commerce/NOAA

30 **GATES: a small, agile imaging satellite prototype for GOES-R** [2812-04]
D. Chesters, D. T. Jenstrom, NASA Goddard Space Flight Ctr.

40 **GOES-8 and -9 launch and mission operations support overview** [2812-05]
C. Bengston, Computer Sciences Corp.; D. McCuistion, NASA Goddard Space Flight Ctr.

SESSION 2 WEATHER SCIENCE AND WEATHER PRODUCTS

50 **Monitoring biomass burning and aerosol loading and transport using multispectral GOES data** [2812-06]
W. P. Menzel, National Environmental Satellite Data and Information Service/NOAA;
E. M. Prins, Cooperative Institute for Meteorological Satellite Studies

60 **Automated cloud-motion winds from GOES-8 and -9** [2812-07]
S. J. Nieman, Cooperative Institute for Meteorological Satellite Studies; W. P. Menzel, National Environmental Satellite Data and Information Service/NOAA; C. S. Velden, S. Wanzong, Cooperative Institute for Meteorological Satellite Studies

68 ***Variability of marine stratiform clouds derived from* GOES-8 imagery** [2812-08]
G. I. Molnar, D. Chesters, NASA Goddard Space Flight Ctr.

80 **High-performance animation of GOES weather images** [2812-09]
A. F. Hasler, D. Chesters, M. Jentoft-Nilsen, K. Palaniappan, NASA Goddard Space Flight Ctr.

84 **Impact of the new-generation GOES on the determination of sea surface temperature** [2812-10]
X. Wu, W. P. Menzel, W. L. Smith, Cooperative Institute for Meteorological Satellite Studies

95 **Asynchronous stereo height and motion estimation from multiple satellite images** [2812-11]
G. G. Campbell, Colorado State Univ. ; J. F. W. Purdom, Colorado State Univ. and National Environmental Satellite Data and Information Service/NOAA; C. Vaughn, Colorado State Univ.

111 **Meteorological features from principal component image transformation of GOES imagery** [2812-12]
D. W. Hillger, National Environmental Satellite Data and Information Service/NOAA and Colorado State Univ

122 **Automated cloud-drift winds from GOES images** [2812-13]
C. Kambhamettu, K. Palaniappan, A. F. Hasler, NASA Goddard Space Flight Ctr.

134 **Enhancement and quality control of GOES images** [2812-14]
M. Jentoft-Nilsen, K. Palaniappan, Science Systems Applications Inc. and NASA Goddard Space Flight Ctr.; A. F. Hasler, D. Chesters, NASA Goddard Space Flight Ctr.

146 **GOES-8 and -9 data ingest and public file service at NASA-GSFC** [2812-15]
D. Chesters, O. Sharma, A. F. Hasler, NASA Goddard Space Flight Ctr.; T. Nielsen, Univ. of Hawaii/Honolulu

SESSION 3 IMAGER AND SOUNDER

160 **GOES imager: overview and evolutionary development** [2812-16]
K. A. Hursen, McDonnell Douglas Aerospace; R. W. Ross, NASA Goddard Space Flight Ctr.

174 **GOES sounder overview** [2812-17]
J. E. Murphy, S. W. Hinkal, NASA Goddard Space Flight Ctr.

182 **Polarization contributions from optical components on infrared sounding instruments** [2812-18]
J. B. Heaney, K. P. Stewart, NASA Goddard Space Flight Ctr.; S. E. Bradley, Orbital Sciences Corp.; P. W. Alley, SUNY/Geneseo

199 **Improved pointing accuracy using high-precision theodolite measurements** [2812-19]
R. Krishna, ITT Defense & Electronics, Inc.

210 **On-orbit determination of focal plane detector positions** [2812-20]
J. J. Shea, Swales and Associates, Inc.

221 **On-orbit MTF measurements** [2812-21]
J. J. Shea, Swales and Associates, Inc.

231 **GOES-8 imager and sounder radiometric performance models: methodology and application** [2812-22]
P. McDonald, Lockheed Martin IR Imaging Systems

251 **Solar intrusion thermal analysis** [2812-23]
B. Ghaffarian, K. Sprunger, ITT Defense & Electronics, Inc.

260 **Comparison between subsystem and system optical MTF for GOES imager** [2812-24]
F. L. Williams, J. C. Ehlert, D. R. Wickholm, ITT Defense & Electronics, Inc.

SESSION 4 SPACE ENVIRONMENT MONITORING

274 **NOAA Space Environment Center mission and the GOES space environment monitoring subsystem** [2812-25]
G. Heckman, D. Speich, J. W. Hirman, T. DeFoor, Space Environment Ctr./NOAA

281 **Operational uses of the GOES energetic particle detectors** [2812-26]
T. G. Onsager, R. N. Grubb, J. Kunches, L. Matheson, D. Speich, R. W. Zwickl, Space Environment Ctr./NOAA; H. Sauer, Space Environment Ctr./NOAA and Univ. of Colorado/Boulder

291 **GOES x-ray sensor and its use in predicting solar-terrestrial disturbances** [2812-27]
P. L. Bornmann, D. Speich, J. W. Hirman, L. Matheson, R. N. Grubb, H. A. Garcia, R. Viereck, Space Environment Ctr./NOAA

299 ***Monitoring* space weather with the GOES magnetometers** [2812-28]
H. J. Singer, L. Matheson, R. N. Grubb, A. Newman, Space Environment Ctr./NOAA; S. D. Bouwer, Space Environment Ctr./NOAA and Univ. of Colorado/Boulder

309 **GOES solar x-ray imager: overview and operational goals** [2812-29]
P. L. Bornmann, D. Speich, J. W. Hirman, V. J. Pizzo, R. N. Grubb, C. Balch, G. Heckman, Space Environment Ctr./NOAA

320 **Space environment monitoring mission beyond GOES-M** [2812-30]
R. N. Grubb, P. L. Bornmann, G. Heckman, T. G. Onsager, H. J. Singer, R. Viereck, Space Environment Ctr./NOAA

329 **Compensating GOES-8 and -9 magnetometer data for spacecraft-induced errors** [2812-31]
F. Zimmermann, Space Systems/Loral; S. Cauffman, NASA Goddard Space Flight Ctr.; W. H. Farthing, Swales and Associates, Inc.; R. Hooker, NOAA

344 **Design and calibration of the GOES-8 solar x-ray sensor: the XRS** [2812-32]
F. A. Hanser, F. B. Sellers, Panametrics, Inc.

353 **Design and calibration of the GOES-8 particle sensors: the EPS and HEPAD** [2812-33]
F. B. Sellers, F. A. Hanser, Panametrics, Inc.

365 **Design and performance of the GOES-8 high-resolution magnetometer** [2812-34]
W. D. Dunham, S. A. Macintyre, C. R. Upton, Macintyre Electronic Design Associates, Inc.

SESSION 5 ADVANCED TECHNOLOGIES AND INSTRUMENTS

376 **GOES imager upgrade design for minimum system impact** [2812-35]
D. Cousins, M. S. Cafferty, L. M. Candell, MIT Lincoln Lab.; J. Kimchi, EG&G Judson Inc.

389 **Overview of GOES high-resolution interferometer sounder brassboard development and test program** [2812-36]
W. E. Bicknell, MIT Lincoln Lab.

409 **GOES advanced sounder design study** [2812-37]
W. E. Bicknell, J. P. Kerekes, D. P. Ryan-Howard, MIT Lincoln Lab.

426 **Advanced imager concept for GOES-R** [2812-38]
D. E. Lencioni, D. R. Hearn, MIT Lincoln Lab.

437 **GOES high-resolution interferometer sounder retrieval performance simulations** [2812-40]
J. P. Kerekes, H. R. Finkle, MIT Lincoln Lab.

446 **Electronics considerations for a geostationary interferometer sounder** [2812-41]
L. M. Candell, D. M. Weitz, MIT Lincoln Lab.

453 **GHIS optical design** [2812-42]
D. P. Ryan-Howard, MIT Lincoln Lab.

462 **Assembly, alignment, and testing of a GHIS brassboard instrument** [2812-43]
A. B. Plaut, D. P. Ryan-Howard, A. C. Parker, D. M. Weitz, MIT Lincoln Lab.

472 **Comparative performance analyses of passive microwave systems for tropospheric sounding of temperature and water vapor profiles** [2812-78]
W. J. Blackwell, D. H. Staelin, Massachusetts Institute of Technology

479 **Mechanical design of GHIS brassboard** [2812-79]
D. E. Weidler, MIT Lincoln Lab.

SESSION 6 DETECTOR TECHNOLOGIES AND MODELING

490 **High-performance HgCdTe infrared detectors for the GOES long-wave sounder** [2812-44]
R. J. Martineau, NASA Goddard Space Flight Ctr.; K. Hu, Hughes STX Corp.; S. Manthripragada, NASA Goddard Space Flight Ctr.; J. Shi, Hughes STX Corp.; C. A. Kotecki, F. A. Peters, A. S. Burgess, D. J. Krebs, R. Johnson, D. B. Mott, P. K. Shu, NASA Goddard Space Flight Ctr.

501 **Photovoltaic HgCdTe detectors for advanced GOES instruments** [2812-45]
M. B. Reine, E. E. Krueger, P. O'Dette, C. L. Terzis, Lockheed Martin IR Imaging Systems

518 **Photoconductive HgCdTe detector assemblies for the GOES imager and sounder instruments** [2812-46]
J. M. Hartley, M. B. Reine, C. L. Terzis, A. J. Verrilli, R. T. Hassler, E. P. Lesondak, Lockheed Martin IR Imaging Systems

528 **High-performance HgCdTe photoconductive detector assemblies for space applications** [2812-47]
J. R. Frederick, J. Kimchi, T. T. S. Wong, EG&G Judson Inc.

540 **Low-frequency noise in photoconductive HgCdTe detectors** [2812-48]
J. Kimchi, J. R. Frederick, T. T. S. Wong, EG&G Judson Inc.

552 **Improving the performance of the GOES solar x-ray imager with a back-illuminated x-ray sensitive CCD** [2812-49]
G. D. Berthiaume, B. E. Burke, J. A. Gregory, MIT Lincoln Lab.; P. L. Bornmann, Space Environment Ctr./NOAA

559 **Impact of the visible detector design on GOES imager and sounder MTF** [2812-50]
F. L. Williams, D. R. Wickholm, J. C. Ehlert, ITT Defense & Electronics, Inc.

SESSION 7 CALIBRATION

572 **Real-world calibration of GOES-8 and -9 sensors** [2812-52]
M. P. Weinreb, National Environmental Satellite Data and Information Service/NOAA

587 **Characteristics of E/W stripes in infrared images from the GOES-8 imager** [2812-53]
J. G. Baucom, Swales and Associates, Inc.; M. P. Weinreb, National Environmental Satellite Data and Information Service/NOAA

596 **GOES-8 imager midnight effects and slope correction** [2812-54]
R. X. Johnson, Integral Systems, Inc.; M. P. Weinreb, National Environmental Satellite Data and Information Service/NOAA

608 **Simulation of GOES-8 imager IR striping due to 1/f noise** [2812-55]
E. C. Wack, L. M. Candell, MIT Lincoln Lab.

614 **Statistical properties of intercalibration techniques that use empirical distribution functions** [2812-56]
D. S. Crosby, National Environmental Satellite Data and Information Service/NOAA; E. Randou, American Univ.

618 ***Technique* for visible calibration of future GOES sensors by solar viewing through a perforated screen** [2812-57]
J. C. Bremer, G. Si, Swales and Associates, Inc.

630 **Sounder bias correction of the east-west radiance gradient** [2812-58]
T. J. Schmit, National Satellite Data and Information Service/NOAA

638 **Solar x-ray imager (SXI) detector calibration and characterization** [2812-59]
K. Russell, J. Briscoe, E. L. Corder, S. Wallace, NASA Marshall Space Flight Ctr.; J. H. Chappell, New England Advanced Research Labs.

SESSION 8 ATTITUDE CONTROL

652 **GOES orbit and attitude determination: theory, implementation, and recent results** [2812-60]
K. M. Ong, S. D. Lutz, Space Systems/Loral

664 **On-orbit jitter performance of the GOES spacecraft and instruments** [2812-61]
J. Sudey, Jr., W. Dellinger, Swales and Associates, Inc.; M. Hagopian, NASA Goddard Space Flight Ctr.

677 **Effect of the magnetometer boom shadow on the attitude pointing and control of the GOES-8 and GOES-9 spacecraft** [2812-62]
A. Dress, Computer Sciences Corp.; K. Chevray, Space Systems/Loral

685 **Improved GOES earth sensor performance** [2812-63]
E. R. Washwell, K. Chevray, A. A. Kamel, Space Systems/Loral; A. Dress, Computer Sciences Corp.; T. Walsh, NOAA

697 **Understanding GOES-8 dynamics** [2812-64]
S. S. K. Tadikonda, McDonnell Douglas Aerospace; S. Cauffman, NASA Goddard Space Flight Ctr.

709 **Long-term stability of GOES-8 and -9 attitude control** [2812-65]
J. L. Carr, Carr Astronautics Corp.

721 **Evaluating the GOES-8 and -9 earth IR horizon sensor error response using the GOES-9 sounder IR channel 1 through 4 data** [2812-66]
M. C. Phenneger, Computer Sciences Corp.; W. C. Bryant, Jr., J. G. Baucom, Swales and Associates, Inc.; K. Woodham, McDonnell Douglas Aerospace

732 **Numerical filter equalization of spacecraft parameters telemetered in disparate bandwidths** [2812-67]
W. H. Farthing, Swales and Associates, Inc.; S. Cauffman, NASA Goddard Space Flight Ctr.; E. G. Chipman, Computer Sciences Corp.

741 **Performance analysis of the GOES trim tab solar pressure torque angular momentum control** [2812-68]
E. Harvie, III, J. Rowe, Computer Sciences Corp.; Y.-K. J. Tsui, Lockheed Martin Corp.

753 **Using the sun analog sensor (SAS) data to investigate solar array yoke motion on the GOES-8 and -9 spacecraft** [2812-69]
M. C. Phenneger, J. L. Knack, Computer Sciences Corp.

SESSION 9 IMAGE NAVIGATION AND REGISTRATION

766 **GOES image navigation and registration system** [2812-70]
A. A. Kamel, Space Systems/Loral

777 **GOES-8 and -9 image navigation and registration operations** [2812-71]
K. A. Kelly, J. F. Hudson, National Environmental Satellite Data and Information Service/NOAA; N. Pinkine, Lockheed Martin Corp.

789 **GOES landmark positioning system** [2812-72]
W. G. Eppler, D. W. Paglieroni, M. Louie, J. Hanson, Lockheed Martin Western Development Labs.

805 **GOES image navigation and registration on-orbit performance** [2812-73]
W. C. Bryant, Jr., S. Ashton, G. J. Comeyne III, D. A. Ditillo, Swales and Associates, Inc.

SESSION 10 STAR TRACKERS

824 **Attitude determination designs for the GOES spacecraft** [2812-74]
J. L. Crassidis, F. L. Markley, A. M. Kyle, NASA Goddard Space Flight Ctr.; K. Blackman, Orbital Sciences Corp.

836 **Image navigation improvement using star trackers** [2812-75]
S. H. Hur-Diaz, A. A. Kamel, Space Systems/Loral

847 **Autonomous star trackers for geostationary satellites** [2812-76]
R. W. H. van Bezooijen, Lockheed Martin Palo Alto Advanced Technology Ctr.

859 **Stellar attitude determination for geosynchronous missions** [2812-77]
D. J. Flynn, L. W. Cassidy, Hughes Danbury Optical Systems, Inc.

874 *Addendum*
875 *Author Index*

Conference Committee

Conference Chair

Edward R. Washwell, Space Systems/Loral

Cochairs

Martin A. Davis, NASA Goddard Space Flight Center
Gerald J. Dittberner, U.S. Department of Commerce/NOAA
Steven Kirkner, U.S. Department of Commerce/NOAA

Program Committee

William M. Brown, MIT Lincoln Laboratory
Winfield H. Farthing, Swales and Associates, Inc.
Frederick A. Hanser, Panametrics, Inc.
James B. Heaney, NASA Goddard Space Flight Center
Ahmed A. Kamel, Space Systems/Loral
W. Paul Menzel, National Environmental Satellite Data and Information Service/NOAA
James F. W. Purdom, Colorado State University
Michael P. Weinreb, National Environmental Satellite Data and Information Service/NOAA

Session Chairs

1 GOES Program Overview
Gerald J. Dittberner, U.S. Department of Commerce/NOAA
Steven Kirkner, U.S. Department of Commerce/NOAA

2 Weather Science and Weather Products
W. Paul Menzel, National Environmental Satellite Data and Information Service/NOAA
James F. W. Purdom, Colorado State University

3 Imager and Sounder
Martin A. Davis, NASA Goddard Space Flight Center

4 Space Environment Monitoring
Frederick A. Hanser, Panametrics, Inc.

5 Advanced Technologies and Instruments
William M. Brown, MIT Lincoln Laboratory

6 Detector Technologies and Modeling
Edward R. Washwell, Space Systems/Loral

7 Calibration
Michael P. Weinreb, National Environmental Satellite Data and Information Service/NOAA

8 Attitude Control
Ahmed A. Kamel, Space Systems/Loral

9 Image Navigation and Registration
Pam Sullivan, NASA Goddard Space Flight Center

10 Star Trackers
Edward R. Washwell, Space Systems/Loral

Introduction

The GOES I–M series of operational satellites (renamed GOES 8–12 once in orbit) represents a significant advance in data products for weather forecasting and storm warnings from the previous series of geostationary satellites. Independent imaging and sounding instruments on GOES I–M provide improved performance, coverage, flexibility, and spectral bands with improved resolution to meet the meteorological science and weather forecasting communities' needs. These satellites are also equipped with instruments designed to provide real-time measurements of solar activity, the charged particle environment, and the Earth's magnetic field at synchronous orbit. In addition, the satellites can relay distress signals from people, aircraft, or ships to search and rescue ground stations of the Search and Rescue Satellite Aided Tracking system. The GOES I–M series enhances service to the data collection system for receiving meteorological data from earth-based data collection platforms and relaying the data to end users.

This conference provides a detailed look into the products provided by the GOES-8 and -9 satellites, a description of the principal payloads and their performance characteristics, and technologies and instruments that have potential application to the next generation of these satellites.

Edward R. Washwell

SESSION 1

GOES Program Overview

Impact of GOES satellites on the National Weather Service

Elbert W. Friday

National Weather Service
Silver Spring, MD 20910

ABSTRACT

The geostationary weather satellites are a critical component of the National Weather Service operations and on going nation wide modernization program. Geostationary satellites, because of their ability to constantly image the Earth, are important tools for observing severe weather such as hurricanes, severe thunderstorms, flash floods and winter storms. When satellite data are combined with other observing technologies such as weather radars, the operational forecaster has significantly increased their capabilities to produce timely, specific and very accurate short-term forecasts. The new generation of geostationary weather satellites are producing new products such as more frequent images over the United States, high density wind fields in the vicinity of hurricanes, a more comprehensive look at the phenomenon known as the Lake Effect Snow Storm, and the formation and dissipation of local fog areas. Atmospheric temperature and moisture profiles are now possible operationally with independent imager and sounder instruments. The sounder instrument is providing important information on the flow of low-level moisture from the Gulf of Mexico, an important source of energy for severe weather over the eastern part of the country.

Keywords: geostationary satellites, severe weather, hurricanes, thunderstorms, flash floods, atmospheric profiles, instruments, weather radar, weather observations

1. The National Weather Service Key Focus

The mission of the National Weather Service (NWS) is to provide Weather and Flood Warnings, Public Forecasts and Advisories for all of the United States, its territories, adjacent waters and ocean areas, primarily for the protection of life and property.

On an annual basis, the United States encounters more severe weather than any other nation. For example, 10,000 severe thunderstorms strike the United States during an average year. The 1995 Atlantic Hurricane season was the second busiest season since 1871. In 1994 Tropical Storm Alberto caused 32 deaths and damages of approximately $1 billion dollars. During the first half of 1996 several severe weather events have occurred, flooding in the Pacific Northwest and in the Mid-West/Ohio Valley, major outbreaks of Tornadoes in Kentucky, Illinois/Indiana, Alabama, and Arkansas, the east coast Blizzard

 0-8194-2200-2/96/$6.00

in January and related flooding in the northeast.

There are two major factors contributing to the severe weather problem impacting this country. First, there is a continuous source of low level moisture from the Gulf of Mexico and the Gulf Stream. This source of energy is, in part, responsible for the development of tornadoes and flash floods in the south and mid west parts of the country. This source of moisture is also necessary for the formation of large winter storms tracking northward along the east coast and helps hurricanes maintain their intensity as they approach the coastal regions. The second contributor is the lack of any large east-west mountain chain to inhibit the interaction of cold, dry canadian air with warm, moist air from the tropics. This clash of air masses in the early spring is another major contributor to the formation of tornadoes over the mid-west part of the country.

2. CURRENT OPERATIONS AND ORGANIZATION

The forecast process consists of five major elements. This includes: 1) the collection of observations, 2) data assimilation, 3) weather forecasts at all scales, 4) production of watches and warnings, 5) dissemination of products and services. Ultimately the "litmus" test for the NWS is that people will react to a forecast and take the necessary actions to minimize their risks from severe weather.

The current NWS organizational structure consists of over 250 offices nation-wide, 13 river forecast centers and 9 national centers for numerical processing and forecasting [1]. Forecast guidance products are generated on large computer systems at each of the national centers. This guidance is then communicated to each local forecast office. The local forecast office produces the local daily forecasts as well as all severe weather warnings. Severe weather warnings are only issued by local NWS offices. The NWS operates a National Oceanic and Atmospheric Administration (NOAA) Weather Radio system which broadcasts NWS forecasts, warnings and more, 24-hours a day. This low-cost system has proven to be very effective in broadcasting emergency information during severe weather events. These warnings can also be broadcast by radio and television companies.

The relationship between the private sector weather companies and the NWS has grown closer, almost seamless, in the past 50 years. This existing partnership has contributed to a $200M a year industry. Weather information used by weather broadcasters on television is almost exclusively produced by the private sector. The NWS collects, processes data, generates numerical analysis and guidance products, broadcasts warnings and makes NWS products and services readily accessible by weather

companies. The private weather companies tailor NWS products, except warnings, to meet the specific requirements of industry clients. Many weather companies have their own direct read-out stations to directly access the real-time weather satellite data. Users of weather information include agriculture, aviation, transportation, media, shipping/fishing, and the university community.

3. MODERNIZATION

3.1 Overview

The goal of the NWS modernization program is to implement the advances in science and technology over the past 20 to 30 years to improve warning services and operations. NWS modernization will provide the following benefits: 1) increased timeliness and accuracy of warnings, 2) improve professional forecasting skills, 3) a uniform level of improved service across the country, 4) replace obsolete systems, and 5) achieve productivity improvements [2]. In this era of tight federal budgets, the economic Benefit-Cost Ratio of the NWS modernization is 8 to 1, compared to the 5 to 1 ratio of the old systems [3].

The NWS modernization has two major elements, the integration of new observing and forecast technologies and the training of NWS personnel to take advantage of their new capabilities in order to produce improved products and services. The new technologies currently being installed nation wide include, the new series of geostationary weather satellites, a network of advanced Doppler radars and automated weather observing systems, advanced computers/workstations and a telecommunications system, and the next generation of super computers. The forecasters will need to be trained on how to use these new technologies. Computer Based Learning modules have been developed and delivered to forecast offices. This will enable the meteorologist to learn at his forecast office, reducing the need for centralized training.

3.2 Geostationary Weather Satellites

The Geostationary Operational Environmental Satellite (GOES) is a major contributor in supporting current NWS operations and new products and services associated with the nation wide modernization program. The GOES-8/9 spacecraft were successfully launched in April 1994 and May 1995 respectively. The new GOES system offers many new capabilities for the user community [4]. The major new capabilities of specific interest to the NWS are the independent imager and sounder instruments, improved Earth location, new imager channels, and increased temporal resolution of the imager. These new capabilities will produce new and

improved products directly impacting current operations especially during severe weather events. The NWS is currently conducting an assessment of the GOES products and documenting their impacts to specific NWS forecast products and operations [5].

The GOES spacecraft has demonstrated a very exciting, new capability, one-minute imagery [6]. The satellite is in a 3-axis stabilized orbit, allowing the instruments to almost always point towards the Earth. The imager can take very rapid, one to three minute intervals, observations over very small areas. Although this is not a current NWS operational requirement, it does offer the potential of dramatically altering the future capabilities of local forecast operations. Several videos showing rapid-scan data sets have been produced with spectacular results. Meteorologists can monitor the rapid development of severe thunderstorms and the central features of a hurricane. High resolution imagery shows the atmosphere responding to the fundamental principles of fluid dynamics.

Derived Product Imagery (DPI) is a method of displaying quantitative hydrometeorological data and information from the GOES sounder instrument. Animated sequences showing total precipitable water, lifted index, and surface skin temperature are important parameters for the development of severe weather. This capability was demonstrated by Chesters [7]. The GOES imager is capable of observing fires with the 3.9 micron channel [8]. Fire weather meteorologists can use the imagery to detect the existence of a fire and track its history with the standard 15 minute image cycles over the United States. Early successful results were first demonstrated during the Pingree Park, Colorado forest fire, July 1994.

Preliminary assessment results from the local NWS field offices have identified three new products making an impact upon three local forecast operations. 1) The Lake Effect Snow (LES) Study is investigating the use of satellite data with local radar data to improve the detection and forecast of these localized, low-level events. During study, the local meteorologists used GOES data to extend, cancel or adjust Winter Storm Watches based on features observed in the GOES images. 2) Forecasting the onset, dissipation and local of local pockets of fog is important to the aviation and transportation industries. Combining two of the GOES-Imager channels allows the forecaster to detect fog areas previously not seen from the older generation GOES. Several techniques are under evaluation by forecast offices to determine which algorithm best meets their needs. 3) Rapid scan imagery, small sectors every 7.5 minutes, is a very useful in detecting and monitoring

very small weather events. Mature and dissipating thunderstorms can produce a feature known as an "arc" cloud line originating from the main part of the thunderstorm. The "arc" line can cause new thunderstorm development if it intersects with another "arc" cloud line or it can cause gusty winds when it passes over an area.

The use of GOES digital data from the sounder instrument is expected to make major improvements in NWS numerical weather prediction models. The sounder instrument is producing atmospheric profiles of temperature and moisture, mainly over the data sparse ocean areas. Preliminary findings have demonstrated a positive impact in defining the changes to the moisture fields surrounding major synoptic storms. High density wind fields, from both the imager and sounder, are important to hurricane forecasters in determining the future track, 24-72 hours, of these large tropical storms. Local emergency officials use track prediction information when trying to evacuate the public from low coastal areas prone to flooding during an approaching hurricane. The 1995 Atlantic hurricane season, second busiest in history, provided many examples to determine the positive impact GOES data made on hurricane forecasting operations.

3.3 Weather Radars

The Doppler weather surveillance radar (WSR-88D) is a major scientific and technological milestone in the modernization of the NWS. The WSR-88D program, also known as NEXRAD (Next Generation Weather Radar), is a joint venture of three United States Government agencies. This Tri-agency consists of the Department of Commerce's NWS, Department of Transportation's Federal Aviation Administration (FAA), and the Department of Defense (DOD). Each agency owns and operates specific radar units however, each agency has full access to each radar's data within the Continental United States (CONUS), in Alaska, Hawaii, and the Caribbean.

Installation of WSR-88D's began at NWS sites in early 1992 with a total of twelve installations completed by the end of 1992. The pace of installation grew in 1993 with the bulk of radars being deployed in 1994 and 1995. Installations will be nearly completed in the fall 1996.

Early results from six of the first Weather Forecast Offices (WFOs) using the WSR-88D showed marked improvement in their severe storm warning performances. This was documented in the verification statistics compiled for Dodge City, Kansas: Norman, Oklahoma; Houston, Texas; St. Louis, Missouri; Sterling, Virginia; and Melbourne, Florida. This improving trend has continued throughout the NWS as the modernization continued and

more WSR-88D's were installed and put into use. NWS nationwide verification statistics show that average lead times for tornado warnings have increased from 4.7 minutes to 8.3 minutes from 1989 to 1995. During this same time frame, Probability of Detection (POD) of severe thunderstorms and tornadoes have improved from 66 percent to 79 percent, while the False Alarm Ratios (FAR) has decrease from 54 percent to 44 percent. The WSR-88D has been equally effective in flash flood and flood situations, and has provided improved capabilities in winter weather conditions.

Using Doppler radar technology, forecasters are able to observe the presence of precursor conditions that favor the formation of severe weather elements such as tornadoes and violent thunderstorms. Velocity information enables forecasters to pinpoint areas of damaging winds from downbursts, gust fronts, tropical storms and hurricanes. The WSR-88D provides quantitative estimates of area precipitation that is a critical element in hydrologic forecasting of potential flooding and water resource management, and more clearly delineates precipitation types from winter storm systems.

Research efforts are ongoing to enhance WSR-88D capabilities through the development of improved algorithms. There are many areas were development work continues but some of the more significant include, snowfall estimation, quantitative precipitation estimation, determination of wind fields and precipitation distributions in tropical cyclones, and various severe weather phenomena.

3.4 Automated Weather Observing Systems

New Automated Surface Observing Systems (ASOS) are currently being installed at over 850 locations throughout the U.S. The ASOS program is a joint effort of the NWS, the FAA, and the DOD. When fully deployed in 1997, the ASOS systems will serve as the nation's primary surface weather observing network. ASOS is designed to support weather forecast activities and aviation operations and, at the same time, support the needs of the meteorological, hydrological, and climatological research communities.

With the largest and most modern complement of weather sensors, ASOS will significantly expand the information available to forecasters and the aviation community. The ASOS network will more than double the number of full-time surface weather observing locations. The ASOS sensors measure cloud height, visibility, precipitation, pressure, temperature/dewpoint, wind direction/speed, and precipitation accumulation. ASOS works non-stop, updating observations every minute, 24 hours daily.

Getting more information on the atmosphere, more frequently and from more locations, is the key to improving forecasts and warnings. Thus, ASOS information will help the NWS to increase the accuracy and timeliness of its forecasts and warnings-the overriding goal of the NWS modernization.

The primary concern of the aviation community is safety, and weather conditions often threaten that safety. A basic strength of ASOS is that critical aviation weather parameters are measured where they are needed most: airport runway touchdown zone(s). ASOS detects significant changes, disseminating hourly and special observations via the NWS and FAA communications networks. Additionally, ASOS will routinely and automatically provide computer-generated voice observations directly to aircraft in the vicinity of airports, using FAA ground-to-air radio. These messages will also be available via a telephone dial-in port at the ASOS.

The current ASOS system was not designed to detect cloud information, cloud amounts and heights, above 12,000 feet. A new GOES product is providing cloud information, cloud amounts and cloud tops, above 12,000 feet and merged with the ASOS cloud products. This integrated product provides the forecaster with a more complete description of the clouds surrounding the local forecast office.

The NWS modernization technologies are being delivered and becoming operational almost on a daily basis. The challenge ahead is to integrate data and information from these new technologies in order to produce more accurate, detailed forecasts at all scales. For example, the NWS now has the ability to estimate precipitation from GOES and WSR-88D radars. Combining measurements from these two technologies will lead to more site specific, and timely flash flood watches and warnings. Predictions of coastal flooding before hurricane landfall can be anticipated with new information from satellites and radars. Frequent atmospheric profiles of temperature and moisture from the GOES spacecraft stationed over the Pacific Ocean is expected to make dramatic improvements in the five day forecast over the United States.

5. Summary

The new GOES spacecraft are making major contributions in improving the NWS current forecast products and services. Clearly the GOES spacecraft observes significant weather events in ways no other NWS observing technology can provide. The major challenge remains in integrating the various digital data streams into a single presentation, giving the operational forecaster a better picture of the atmosphere and how it is changing.

Providing real-time digital satellite data, and the ability to manipulate the data, to all forecasters at the national centers and at the local forecast offices is a critical element in improving the forecast services to this country. When the NWS modernization is completed, the NWS will operate the most sophisticated, advanced hydrometeorological warning and forecast system in the world [9]. We will be closer to achieving a long standing NWS goal, providing more accurate short-range forecasts, improving the predictability for all weather events, and to make this information readily accessible to industry and the american public.

6. REFERENCES

1. E. W. Friday, "The Modernization and Associated Restructuring of the National Weather Service: An Overview," Bulletin of the American Meteorological Society, Vol. 75, No.1, January 1994.

2. L. J. Boezi, "The "Bottom Line" of Weather Service Modernization," American Meteorological Society annual meeting, January, 1995.

3. R. E. Chapman, "Benefit-cost analysis for the modernization and associated restructuring of the National Weather Service," National Institute of Standards, NISTR 4867, U.S. Department of Commerce, July 1992.

4. W.P. Menzel and J.F. Purdom, "Introducing GOES-I: The First of a New Generation of Geostationary Operational Environmental Satellites," Bulletin of the American Meteorological Society, Vol. 75, No.5, May 1994.

5. J.J. Gurka, R.S. Gird, and A. Mostek, "The National Weather Service GOES Assessment Project," 8th Conference on Satellite Meteorology and Oceanography, American Meteorological Society, January 1996.

6. J.F. Purdom, "One-minute interval imagery of atmospheric phenomena using NOAA's new generation of geostationary satellites," 8th Conference of Satellite Meteorology and Oceanography, American Meteorological Society, January 1996.

7. D. Chesters, A. Mostek, and D.A. Keyser, "VAS sounding images of atmospheric stability," AMS Weather Forecasting, Vol. 1, 1986.

8. J.F. Weaver, J.F. Purdom, and T.L. Schneider, "Observing Forest Fires with the GOES-8, 3.9-micron Imaging Channel," AMS Weather and Forecasting, Vol. 10, No. 4, December 1994.

9. L. W. Uccellini, "Office of Meteorology 1996-2005 Strategic Operating Plan," NWS, April 1996

GOES program status

Gerald J. Dittberner

National Environmental Satellite, Data, and Information Service
Suitland, MD 20746

ABSTRACT

Two successful launches of NOAA's Geostationary Operational Environmental Satellites (GOES) provide continuous images and atmospheric soundings from positions over the Pacific Ocean and the Atlantic Ocean. GOES-8, launched April 13, 1994 and GOES-9, launched on May 23, 1995 are the first three axis stabilized meteorological satellites ever placed in orbit. Their unique capabilities have provided over two years of opportunities for observing the atmosphere with 1 km resolution visible and 4 and 8 km infrared channels at 3.9, 6.7, 10.7, and 12.0 micrometers. In addition, the 19-channel atmospheric sounders provide soundings throughout the atmosphere over vast portions of the two oceans. This paper describes the status of current GOES satellites and provides a look into the future for coming spacecraft and instruments.

Keywords: geostationary satellites, meteorological satellites, weather satellites, remote sensing, space environment, atmospheric sounding, cloud pictures, satellite data, images, satellites.

1. Introduction

The GOES mission is to maintain two reliable operational, environmental, and storm warning systems to protect life and property; to monitor Earth's surface, atmosphere, and space environmental conditions; to introduce improved atmospheric and oceanic observations and data dissemination capabilities; and to develop new and improved applications and products for a wide range of federal agencies, state and local governments, and private users.

2. Current GOES satellites

At present, there are two operational GOES satellites. GOES-8 and GOES-9. GOES-7, being nearly out of station-keeping fuel, is in standby over the central United States. Two older satellites, GOES-2 and GOES-3, are in use for their remaining communications functions.

GOES-8 and GOES-9 coverage is presented in Figure 1. It is clear that two GOES satellites are required, because one satellite cannot see around the curvature of the Earth to the observe two oceans.

0-8194-2200-2/96/$6.00

2.1 GOES-8

GOES-8 was launched from Cape Canaveral on April 13, 1994 and became operational on June 1, 1995. It is the GOES-East satellite at 75 degrees West longitude (75°W). Instrumentation includes an Imager, Sounder, and a suite of Space Environment Monitor (SEM) instruments[1]. Four instruments make up the SEM. An Energetic Particle Sensor (EPS) and a High Energy Proton and Alpha Detector (HEPAD) monitor incident flux density of protons, alpha particles, and electrons over an extensive range of energy levels. Solar output is measured by an X-Ray Sensor (XRS). Two three axis magnetometers mounted on a three meter boom monitor the Earth's geomagnetic field strength at the spacecraft.

GOES-8 also has a Data Collection System (DCS), Search and Rescue (SAR) receivers and transmitters, and provides broadcasts using a Processed Data Relay (PDR) and weather facsimile (WEFAX) transponders. The spacecraft was manufactured by Space Systems/Loral (SS/L) in Palo Alto, California.

2.1.1 GOES-8 Imager

The Imager and Sounder instruments were manufactured by the Aerospace/Communications Division of ITT in Fort Wayne, Indiana. The Imager has eight visible detector of 1 km resolution each, that sweep across the Earth's disk in an East-West motion to sense reflected radiation in eight 1 km wide swaths[1]. A number of these swaths make up an image of the complete Earth disk. Of the four infrared (IR) channels, the 3.9, 10.7, and 12.0 micrometer bands have 4 km resolution. There are two 4 km detectors mounted such that they that sweep out an eight km swath. The 6.7 micrometer channel is has 8 km resolution. One sweep of the instrument across the Earth disk produces eight visible lines, two IR lines (3.9, 10.7, and 12.0 micrometers), and one line at 6.7 micrometer wavelength.

Radiation from the visible channel senses reflected sunlight to detect clouds. A more complete description of channels and their uses is described in the 1994 article by Menzel and Purdom[2]. The IR channels measure radiation emitted by the atmosphere's constituents. The 3.9 micrometer channel is used for nighttime fog, the 6.7 channel for water vapor and water vapor winds, the 10.7 "window" channel measures cloud top and surface temperatures, and the 12.0 "split window" measures surface temperature, but includes the added benefit of low level water vapor for estimating precipitable water.

The GOES-8 Imager currently covers the region in Figure 2. There are two modes of operation, normal and rapid scan mode. In normal scan mode, one full disk is sensed every three hours, an extended Northern hemisphere, and Eastern Continental U.S., and a Southern hemisphere sector. The United States is covered once each fifteen minutes in this mode. The cycle then repeats itself every three hours. Rapid scan mode is invoked whenever the

threat of severe weather events requires additional scan frequency. In rapid scan mode, one full disk is still sensed every three hours, but reduced extent areas are covered at seven and a half minute intervals until the next three hourly full disk or a return to normal scan mode.

Imager based products include wind vectors at several levels in the atmosphere, low level moisture, Sea Surface Temperature, volcanic activity hazard detection, and fog product at night.

2.1.2 GOES-8 Sounder

The Sounder instrument is designed to measure radiation emitted from various levels within the atmosphere. It has a nineteen-channel filter wheel arrangement which measures IR energy with several detectors in the shortwave, midwave, and longwave IR wavelengths. To measure the radiation, it must stare at a particular spot long enough to produce a meaningful signal to noise ratio, since IR radiation levels in many of the channels are very low compared with energy in the visible. This is the main purpose for having a three axis stabilized spacecraft - to allow this staring mode. Sounder coverage is shown in Figure 3. The particular box covered depends on weather events occurring at the time.

Sounder products include temperature and moisture profiles from the surface to the uppermost extent of the atmosphere, precipitable water, sounder-based winds, upper level cloud amount to supplement the Automated Surface Observing Stations (ASOS), and derived products such as lifted index, and atmospheric stability. A number of assessments are underway to determine the impact of sounder products on numerical weather forecast models. To date results are very encouraging.

The GOES-8 sounder is constructed with two windings in its East-West servo motor. One winding acts to backup the other in case of failure. In August 1994, one GOES-8 sounder motor winding failed, leaving operations intact, but eliminating the backup winding. In this sense, it has a single point of failure. This is a failure similar to one which occurred in the GOES-9 Imager in April 1996. In addition, one of two Attitude and Orbit Control Electronics (AOCE) memory chips on GOES-8 suffered permanent damage due to an Electrostatic Discharge (ESD) event. Part of one AOCE's memory is no longer available. ESD shielding was added to GOES-9 before launch, and GOES-9 has had no ESD events to date.

2.2 GOES-9

GOES-9 was launched for Cape Canaveral on May 23, 1995 and is the GOES-West satellite at 135°W. It has the same instrumentation as GOES-8: Imager, Sounder, SEM package, DCS, SAR, and WEFAX. Current coverage is shown in Figures 4 and 5.

The GOES-9 Imager has the same arrangement of motor windings for the East-West servo motor. One of its two redundant windings failed in April 1996, leaving one winding intact. With essentially identical failures on both GOES-8 and GOES-9, efforts are underway to redesign the motor for GOES-K and remaining spacecraft instruments.

2.3 GOES-7

GOES-7 was launched on February 26, 1987 and was the last of the spin stabilized GOES satellites. Its Visible Infrared Spin Scan Radiometer and Sounder (VAS) instrument has not failed, however, station-keeping fuel has nearly run out after almost nine years of continuous, faithful service. After the last image was taken on January 11, 1996, GOES-7 as placed in standby mode and moved to 95°W over the central U.S. where it remains at this writing.

3. Future GOES Satellites

The next satellite, GOES-K, is being readied for a launch planing date of April 1997. It is being considered for a launch into a store on orbit mode whereby it will be ready to replace GOES-8 or GOES-9 should either fail. GOES-K will have the same instrumentation as GOES-8 and GOES-9. While in standby mode, no data will be taken.

GOES-M is to be completed before GOES-L because it is the only GOES spacecraft being manufactured with special accommodations for a new instrument, the Solar X-Ray Imager (SXI). Plans are to launch GOES-M in the 2000 time frame to gather as much data as possible during the solar maximum period, expected to peak near 2000. This instrument will stare at the Sun continuously and provide images in up to eight X-Ray energy bands. All other instrumentation is the same as GOES-K.

GOES-L will be the fifth spacecraft manufactured, with a planning launch date near 2002. GOES-L will have the same instrumentation as GOES-K. It will not have an SXI instrument. One important change to GOES-L will be in the Imager channels. The channel at 12.0 micrometers will be replaced with one at 13.3 micrometers in order to better establish the level of steering winds for hurricanes and other severe weather events. In addition, the horizontal resolution of the 6.7 micrometer water vapor channel will be improved from 8 km to 4 km.

4. Future Instruments

Concept studies are presently underway to examine the practicality of an interferometer sounder to sense temperature and moisture in layers as thin as 1 km with accuracies near 1 Celsius degree. Potential imager improvements as also being considered, including the possibility of increasing the number of channels from five to eight, and scanning the Earth at double the

present scan rate for each image. Both these studies are in the early stages and, if affordable, would be implemented after the GOES-I-M series.

Longer term studies are in the works to examine the possibility of GOES-based lightning mappers and microwave sounders.

5. Summary

The GOES satellite program is an important part of the National Weather Service Modernization effort. Two operational GOES satellites now in operation are providing data required for improving severe weather warning and forecasting. However, the new data also are stimulating development and experimentation with potential new operational products that were not yet in meteorologists' minds when the GOES I-M series was conceived around 1980. As these data and products are used more and more, new insights will generate new products and, hopefully, improved forecasts.

6. References

1. Space Systems/Loral, "GOES-I-M databook", DRL 101-08, Prepared for National Aeronautics and Space Administration, Goddard Space Flight Center, Greenbelt, Maryland, 20771, 1990.

2. P. Menzel and J. Purdom, "Introducing GOES-I: The first of a new generation of geostationary operational environmental satellites", Bulletin of the American Meteorological Society, Vol. 75, No. 5, May 1994.

OPERATIONAL GLOBAL GEOSTATIONARY COVERAGE

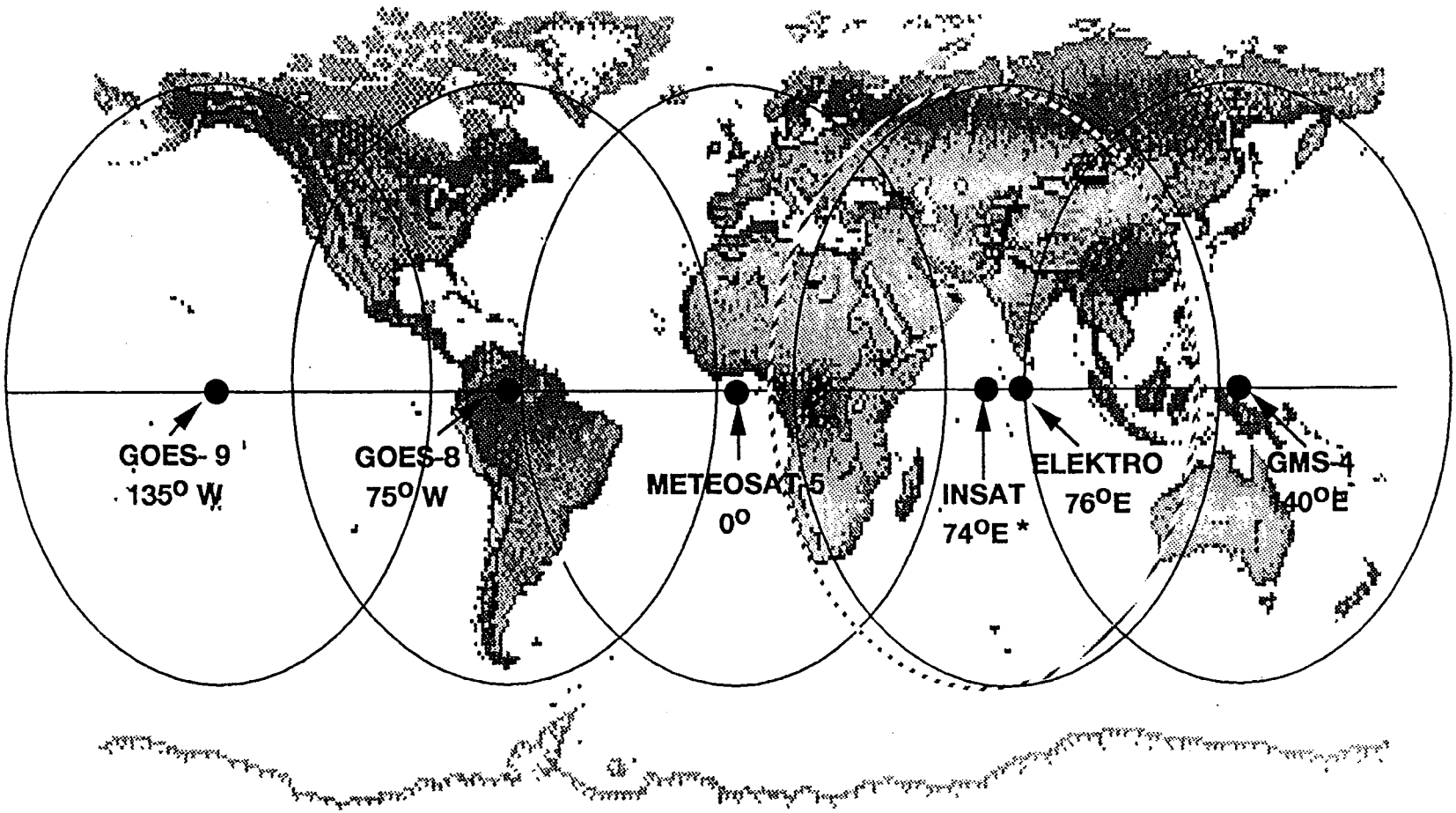

* INSAT not openly broadcast

Figure 1.

AS OF FEBRUARY 1996

Routine Mode - GOES-8 at 75°W

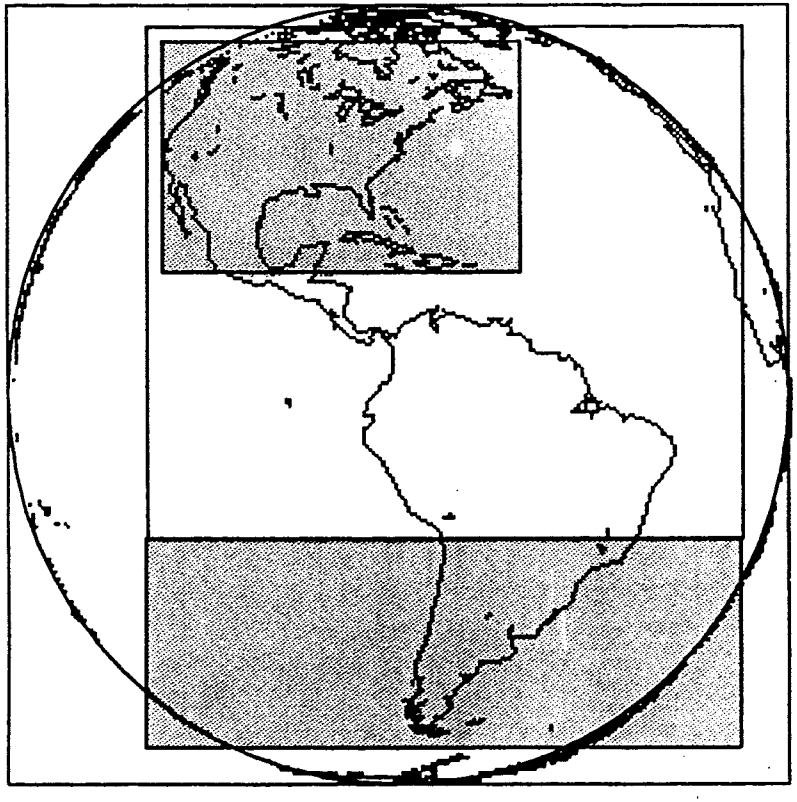

- Full Disk every three hours
- Five half-hourly cycles:
  - Extended northern hemisphere
  - Eastern CONUS
  - Southern hemispheric sector
- Yields 4 US views per hour

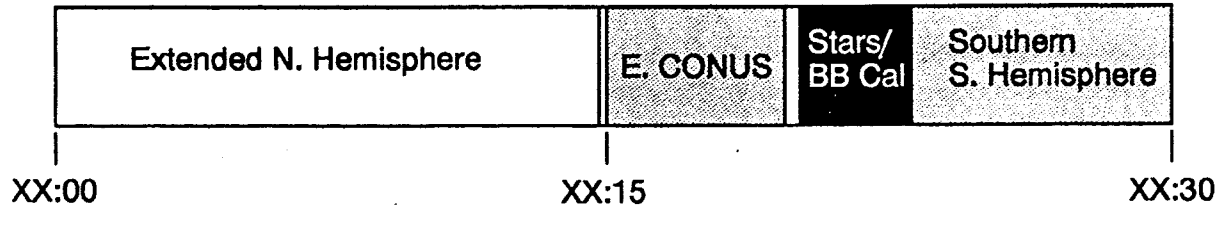

Figure 2.

GOES-East Operational Sounder Coverage

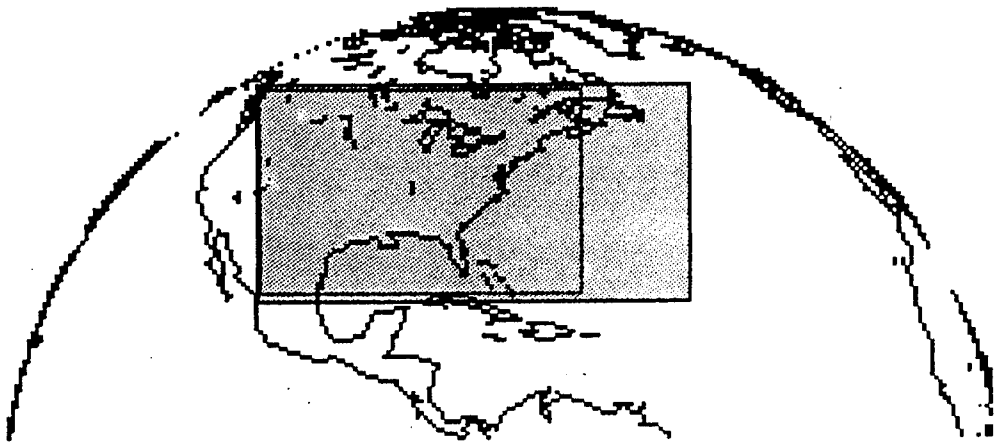

Figure 3.

GOES-West Operational Sounder Coverage

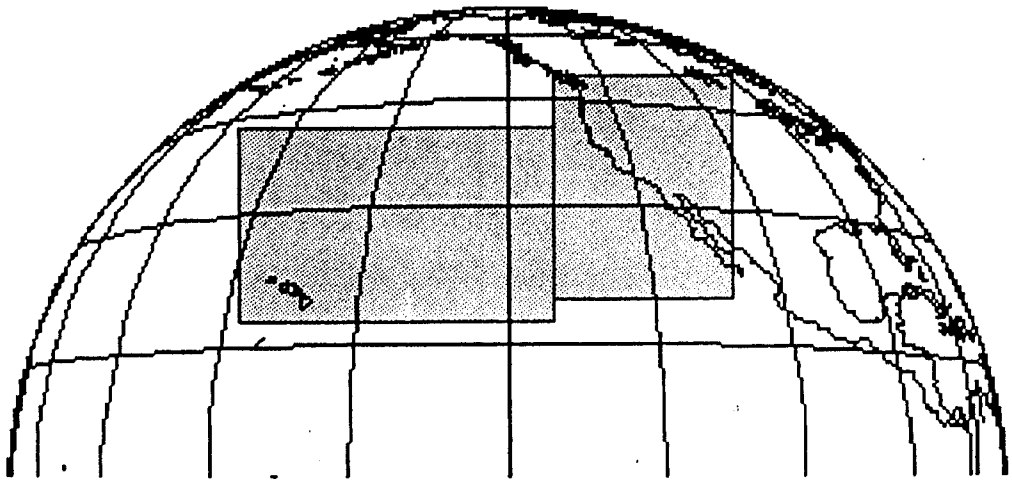

Figure 5.

Routine Mode - GOES-9 at 135°W

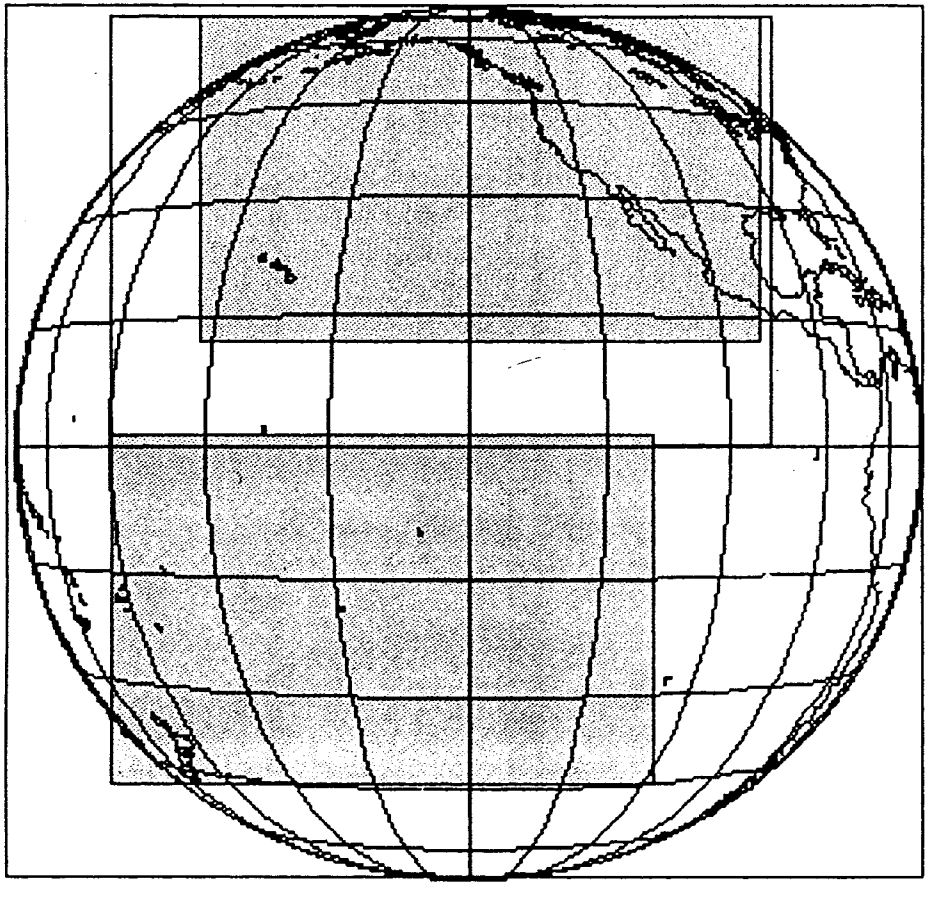

- Full Disk every three hours
- Five half-hourly cycles:
  - Northern hemisphere
  - Pacific-U.S. (PACUS)
  - Southern hemisphere
- **Provides 4 views per hour** over Western, Alaska, & Hawaii Regional areas

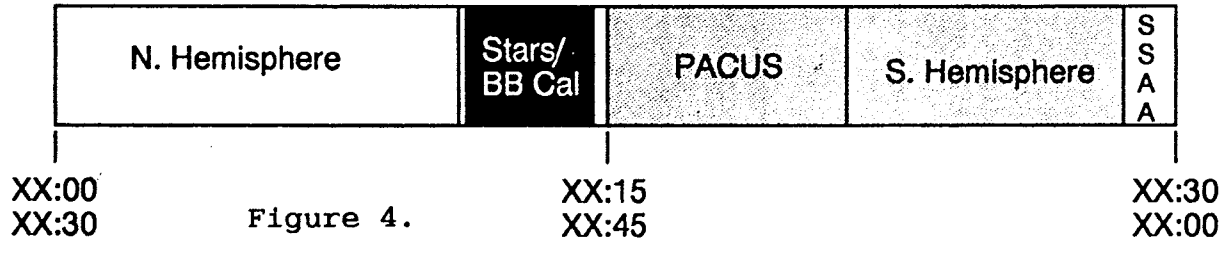

Figure 4.

NOAA'S FUTURE GOES SATELLITE PROGRAM

Edward Howard
Roger Heymann
Gerald Dittberner
Steven Kirkner

U.S. Dept. of Commerce/NOAA
Washington, D.C. 20233

ABSTRACT

Future weather satellites for NOAA at geosynchronous orbit may be smaller, less costly, and developed by a different process than is currently done. This path is sometimes called the "smaller, cheaper and faster" process being pursued by NASA. We believe in the future there will be less money, a focus on using the right technology and the desire to get the most value for the resources invested in space missions. In this paper we give an update on our progress to define future GOES. It will include our efforts to trade on user requirements early, to use evolutionary technology, and to consider new cost reduction and program management techniques.

Keywords: NOAA, GOES satellites, future requirements, satellite development, technology infusion, program management, trade on requirements, New Millennium Program.

1.0 INTRODUCTION

In an earlier paper last year, we reported on progress being made to look at future GOES requirements into the next decade.[13] Our approach was to form small expert teams to consider both needs and possibilities. These 10 groups with about 6 members each identified the need for enhanced capabilities to meet NWS and NOAA missions. For example, these early study teams considered the addition of several new instruments to GOES. These included: passive microwave, ocean color, advanced solar, and lightning mapping. It was considered, too, that the present imager and sounder instruments could be redesigned with new focal plane technology to allow faster response and better spatial and spectral resolution. Please refer to the earlier paper for a summary of those results.[13]

Here we wish to move ahead and indicate progress in the last year. We found a greater need to study the introduction of technology. Instead of block changes to a new generation of satellites, we have considered evolutionary technology which may require that we infuse technology first into the spacecraft, then into instruments and then into ground systems.[5] We want to place emphasis on design-to-cost. And we will give specific examples of trading on requirements early.

0-8194-2200-2/96/$6.00

2.0 TRADING ON REQUIREMENTS EARLY

Because of funding constraints it has not been possible to contract outside of NOAA for traditional Phase A studies that would consider requirements and possible new instruments. But we have made some progress in two areas to be described next: Early studies of a possible passive microwave instrument, and design levels to incorporate an imager on a potential small satellite that could support future weather measurements. Indeed, the continued use of small expert teams is an effective method to explore design to cost. i.e. different levels of performance are sought that will permit valuable measurements but at lower costs.

2.1 GOES Special Imager for a Small Satellite

We know that the imager on our present GOES satellite can be improved for new products and services to the nation.[2] As mentioned earlier our small expert teams have identified such exciting paths. However, rather than going directly to the highest performance option of design, however, we might ask our team to determine four options as shown in Table 1.

Table 1: GOES Imager (Storm Sat) Design Options

Option	Description
1	2 Channels VIS at 0.51 - 0.71 um IR at 10.2 - 11.2 um
2	5 Channels (ADD) IR at 3.7 - 4.1 um IR at 6.9 - 7.9 um IR at 11.5 - 12.8 um Above still at 1 km spatial resolution, VIS 4 km spatial resolution, IR
3	5 Channels above (PLUS) 0.5 km VIS spatial resolution 2.0 km IR spatial resolution CONUS scan coverage @ 5 min.
4	All of the above in 3 plus: Add IR chanel at 5.4 - 7.2 um NEdT of 0.1 C at scene temp. Bit depth of 12 Dynamic Range of Tmax of 320K Tmax of 345K SWIR CONUS coverage @ 30 sec. Encircled energy 89% from 1.5 FOV dia. User data access via digital TV reception

Table 1 is an example of early discussions by NOAA and with key inputs from JPL (The Jet Propulsion Lab) in Pasadena, CA, who have extensive experience with small satellites and future space technologies. We acknowledge, also, NOAA inputs from Dr. Paul Menzel and Dr. James Purdom for future NOAA satellite planning.

Option 1 is a "bare bones" option that pegs the lowest cost for a new imager design. It may not be a productive path, and it requires more study. Option 2 adds more IR channels and appears to give much increased measurement performance, but adds design complexity and costs. Option 3 increases temporal and spatial resolution performance, but the design parameters may be very costly. Finally option 4 is the highest performance option that might be envisioned but at a much higher cost.

Our first point is that there are design to cost options and low cost options that need to be explored in early stages of a new space program to satisfy, if not to optimize, performance. Lower cost may have to prevail over optimal performance and small teams have the flexibility to look at many early design approaches.

Our second point is that we have envisioned a new configuration or mode of operation for our weather satellites that may require a small satellite. Or the small satellite may not give us much advantage over the larger ones with multiple instruments? We don't know yet. But we pick the imager as our key instrument and try to determine its performance on a small satellite. By allowing 4 levels of design, we give ourselves broader design trade space.

2.2 Ongoing Studies of a Passive Microwave Instrument for GOES

One of the more exciting new options for GOES could be a passive microwave instrument.[8] In the past 8 months Prof. Staelin of MIT/LL has chaired a small expert team to find a lower cost, workable design for microwave measurements.[7] Earlier work is of strong value, also, and resulted in a thorough analysis of single point designs.[16,17] Microwaves can penetrate non-raining clouds and explore interesting storm regions along with visual and IR sounder measurements. Currently IR and visual sensors do not see through clouds, but measure cloud top temperatures and get temperature and moisture readings in clear air near clouds.

Table 2 shows some of the converging features of a modest microwave instrument that would be far less costly than a lower frequency design.[7] If we were to start with a clean design sheet and adequate funding, we might wish measurements for soil moisture and surface features. While this would be exciting input, it would involve frequencies below 100 GHz, and would necessitate a very large antenna, perhaps over 25 meters. We know such an antenna is not likely to fly at low cost and on a smaller satellite, so a 2-meter antenna was chosen. The team was asked what significant measurements can be done at that design level? The answer is that much can be done in both storm investigations near clouds and to provide inputs to numerical weather prediction models at NOAA.

Table 2: GOES Passive Microwave Early Design Concepts

Antenna Size	2 meters
Ground Resolution	66 km at 118 GHz 42 km at 183 GHz 19 km at 400 GHz
Scan 5000 km square in	3 hours
Instrument Noise	0.05 K at 118 GHz 0.30 K at 400 GHz
Moving Antenna Issue	0.14 degree/sec
Future Use	Stated Below

In order to converge on a cost effective design for a microwave instrument, a lot of system trade-offs need to be done. Some have been accomplished in the small expert team, others remain to be completed in the future. Some of the system issues studied include:[7]

- low noise receivers at 50-430 GHz
- types of 2 meter dish and RMS tolerances available
- cost models developed for array, bands, electronics, and antenna. What does cooling add?
- torque on dish scanning?
- pointing and momentum compensation control
- borrowed technology from NASA New Millennium Program?

Two other investigations are a key to getting microwave instrumentation on future GOES: Delineation of microwave data products and user needs. The small study team under Prof. Staelin's leadership has made progress in both areas. Since work is still in progress we only summaries a few critical areas here.[7]

Microwave measurements at a spatial resolution of 20 km would be very desirable for mesoscale numerical modeling. Other larger resolutions will be useful if they are in a critical area to a forecast. Microwave data will help with precipitation measurement and flash flood warning and may measure the warm cores of hurricanes to aid in tracking and analyses. The team is still looking at the quality and uniqueness of data products at the various observing frequencies. Some microwave channels are blinded

by heavy water vapor and some channels see light rain well and are sensitive to the particle size distribution.

3.0 GOES TECHNOLOGY INFUSION

Up until the early 1980's NOAA and NASA had an effective program called OSIP (Operational Satellite Improvement Program) It was an agreeement whereby NASA developed new technology and sensors related to weather satellites. After successful flight, the technology/sensors would be adopted by NOAA for operational satellites. OSIP was a victim of budget constraints.

In recent months there have been study groups by NASA and NOAA to look for ways to fund OSIP-like technology development programs. We discuss this recent activity and other cooperative efforts with NASA in their New Millennium Program.

3.1 GOES Technology Upgrades Studied

A recent GEOS technology infusion plan suggests that efforts might be delineated on the basis of short term vs long term.[5] NOAA is working closely with NASA, Goddard to consider both technology infusion to the spacecraft and to instruments.

Several results may be forthcoming, but budgets may not permit implementation in the short term. It may be necessary to upgrade the attitude and orbital control system. The AOCS would benefit greatly, we believe, by adding two star trackers instead of our current Earth limb sensors. The benefits would be improved attitude knowledge and hence, intrinsic image registration. It is important to know accurately where an image pixel is centered on the earth and to have accurate pixel to pixel repeatability between image frames.

Studies are also in progress to consider the costs and benefits of upgrading the current imager to give rates double the present ones, i.e., by using more detectors, more ground area can be measured in less time. Detectors might be added in either visual or IR or in both. The increased data rates could exceed the present ground system capabilities, however, and data compression is being explored. Also, the present sounder could be increased significantly by substitution of an interferometer in place of the existing filter wheel instrument. Spectral resolution would be much improved giving more accurate temperature and moisture sounding locations. Firm decisions have not been made, yet.

3.2 Technology Teamwork with NASA's New Millennium Program

One of our steps in evolutionary technology has been to work with NASA in their New Millennium Program. NMP seeks to space validate critical technologies for the next generation of space missions. In developing the technologies, costs will be lowered for operational use later, and the risk of their use will be lowered. Excellent reviews of NMP are available.[1]

Members of NOAA have served on IPDT's (Integrated Product Development Teams) of NMP--primarily in advanced Instrumentation. However, other NMP teams include: Autonomy, Microelectronics, in situ instruments and MEMS (MicroElectronic Measurement Systems), Communications, Modular and Multifunctional Systems, and Architectures. Future technology roadmaps have been developed by NMP program at JPL and deserve more study.[1]

NOAA has worked closely with NASA on various NMP teams and workshops. We have provided to NASA a list of some of our perceived evolutionary technology needs for geostationary satellites of the future.[3] Table 3 shows such information divided into three categories: instruments, spacecraft and operations. It is not clear, yet, how many of these technologies will be validated in space. We at NOAA continue to encourage NMP goals and work toward the sharing of technology development.

Table 3: GOES Technology Needs Shared With NASA's New Millennium Program

Instruments	Technology
o	Microwave Radiometers
o	Advanced Imager or Sounder
o	Lightning Mapper
o	Ocean Color Imager
o	Advanced Solar Instruments
Spacecraft	**Technology**
o	Advanced Solar Cells
o	Stability and Control Systems
o	Advanced Thermal Designs
o	Greater On-Board Calibration
o	Multiplex of High Data Sensors
o	Data Compression
Operations	**Technology**
o	SEP (Solar Electric Propulsion) for Transit to GEO/Station Keeping
o	Limitations on Sun Angles for Ops.
o	Data Fusion Techniques
o	Configuration Flying
o	Constellation Flying
o	Cross-Calibration of Sensors on Different Spacecraft

Table 3 indicates at a high level some of the directions we wish to move in with regard to new instruments, spacecraft subsystems and ground operations. More detail is available in other references. Keep in mind, this table stressed flight demonstration of technology important to do in geosyn orbit. We have developed other references with NMP that list technology

validation that would be desirable to do in geo orbit, and technology that could be shared in lower earth orbits.[14]

4.0 SPACE PROGRAM DEVELOPMENT AND COST REDUCTION

In the Section 3.2, we referenced the fact that NASA's New Millennium Program seeks to space validate technology. Another element of NMP is Process Millennia where Dr. Ed Crawley and team at MIT have envisioned a better process for the conception, design, development, test and operation of future space systems.[11]

4.1 NASA's Process Millennia

Dr. Crawley describes a useful analogy between preparing a better meal and developing a better space mission.[11] The real food may be the technologies we use in spacecraft including hardware and software. The kitchen is the spacecraft design environment. Appliances are the tools we use. And recipes are the process we use in spacecraft development. Process Millennia seeks to change the process via:

- computer assisted environment
- state of the art tools
- smaller virtual design teams
- standardized practices
- modular components
- design to cost
- better technology, and
- seamless interfaces on the project.

The Process Millennia part of NMP is trying to solve three problems related to program development in more efficient ways: solving coupled issues faster; accelerating sequential tasks; and coordinating parallel activities.[11] Imagine a complex design process with many hundreds of work modes in which the three problems above could be improved. The result would be more work done, much faster, and with less resources.

Finally, the NMP and other effective technical groups practice concurrent engineering with several key ingredients:[11]

- get an early start on production from design
- resolve conflicts fast by mutual understanding
- use high communication skills/tools
- keep teams small at no more than 5 to 20 people
- use virtual teams via computer tools
- seek integration among sub-problems, and
- decompose large complex tasks into small simple ones

4.2 Lowering Space Program Costs

The final section of our Future GOES paper is devoted to lowering program costs.[12,9,4] We first state our conclusions up front and then offer some additional guidelines that will help to lower costs for large technical programs like building future spacecraft.

4.2.1 Cost Reduction is a Question of Correct Balance

It is possible to lower costs in many different ways--some ways work for some groups, some for others. There is no one best formula for cost reduction. For example, some groups believe in a highly structured approach to design, others prefer small, unconstrained teams. Some groups insist on doing most of the work in house with highly specialized teams. Others much prefer the virtual approach with nearly all subsystems contracted out.

We suggest that each program be examined closely for its unique requirements, workers, resources, and timing/delivery needs. We believe the government can learn from virtual organization principles--especially virtual information technology to make faster, smoother decisions with less controls. However, government needs the ability to set goals, to ensure long term continuity of service, to settle conflicts early, and to coordinate complex or systematic innovation/technology.[6] Some of these latter needs require elements of centralization which are at opposite ends to a virtual company.

4.2.2 Some Guidelines for Reducing Program Costs

A lot of effort has gone into methods and proceedures for reducing space mission costs.[4,12,10] A recent book by Jim Wertz and Wiley Larson is excellent for providing many guidelines in this regard.[9]

In the above text the authors provide helpful discussion, case studies and many guideline lists of points that can be used directly in advanced mission designs. For example in Chapter 10, Dr. Wertz suggest action the government can take to create an environment that reduces costs.[9] Five of our favorites are: force trading on requirements, strong mission engineering, rewarding low costs, decentralize or streamline procurement, and sponsor technology infusion or R&D to reduce future mission costs. In the main body of this paper we have stressed several of these elements--especially trade on requirements, technology and lower costs.

5.0 SUMMARY

We suspect the traditional way of developing spacecraft by division into Phase's A,B,C,D, & E via NASA's Systems Engineering Handbook needs changing for the future.[15] There are good methods in the handbook, but the new orders are: "smaller, cheaper and faster." If money is tight and much more must be done with less

resources, then new ways need to be found for championing complex technology programs--including spacecraft start, design, and implementation. We are still adjusting to the changes ahead. However, this paper has summarized some of our recent progress. We have tried the following actions:

- Keep the user requirements open much longer and wider than you might be tempted to do. Don't think in terms of a block change to satellites, but to incremental changes including technology.

- Go ahead and study those new sensors that will be used at some time in the future--like new microwave and faster imaging needs.

- Look at new ways of doing the missions--including small satellites or even constellations of satellites, for different purposes.

- Use the infusion of technology in an incremental fashion, not an aggressive one. Technology might be added first in satellite, next in instruments, and finally in ground systems.

- Cooperate with others in the use of technology and their knowledge of success in program development. NOAA is working with NASA on their New Millennium Program.

- Finally, keep the lowering of costs a priority from the beginning of a program. Permit real incentives for generating effective systems at lower costs. The system may not be the highest of attainable performance, or even optimum cost performance, but it can be very effective at an appropriate design to cost.

6.0 REFERENCES

1. Casani, E. Kane and Wilson, Barbara, "The New Millennium Program: Technology Development for the 21st Century," AIAA, Reno Meeting papers, Jan. 17, 1996.

2. Howard, Edward and Gunson, Mike, New Millennium Program Instrument Technology Workshops, GOES Program, Presentation Material, Nov. 7, 1995, JPL.

3. Howard, Edward, Letter to Dr. Chris Stevens at JPL, Technology for GOES Program and Cooperation with NMP March 12, 1996, NOAA.

4. Grawford, L.J. et. al., "Cost Estimation and Modeling for Space Missions at APL/JHU," 2nd IAA International Conference on Low-Cost Planetary Missions, April 16-19, 1996, Preprints.

5. Kirkner, Steve et. al., GOES Technology Infusion Plan, Working Papers, April 29, 1996, NOAA and NASA/Goddard.

6. Mintzberg, Henry, "Managing Government, Governing Management," Harvard Business Review, May-Jun, 1966 pp. 79-83.

7. Staelin, David and Kerekes, John, "Minutes of the GMSWG (Geosynchronous Microwave Sounder Working Group), May 28, 1996 and earlier minutes by MIT/LL for NOAA.

8. Savage, Richard, C. et. al., "Concepts for a Geo-Stationary Microwave Imager Sounder (GeoMIS)," IEEE, Paper 0-7803-2567, Feb., 1995, pp. 652-654.

9. Wertz, James and Larson, Wiley, eds. Reducing Space Mission Cost, Microcosm and Kluwer Publishers, Torrance, CA, May, 1966. From Athena Edu. Group, 310 539-9444.

10. Wertz, James and Larson, Wiley, eds. Space Mission Analysis and Design, 2nd ed. Kluwer Pubs. 1995.

11. Crawley, Ed et. al., "Process Millennia," MIT Space Engineering Research Center, Work for NMP, Jan., 1996.

12. Glackin, David et. al., "Small Satellites: Cost Methodologies and Remote Sensing Issues," SPIE, Vol. 2583, Paper 0-8194-1947, Aug., 1995.

13. Dittberner, Gerald et. al., "NOAA's Future Earth Observations From Advanced GOES Satellites," AIAA and IAF, Paper 95-B.2.01, 46th IAF Congress, Olso, Norway, Oct. 2-6, 1996.

14. Howard, Edward et. al., Early Cooperation of NOAA with NASA in the New Millennium Program, SPIE, Paper 2810A-07, Denver, CO, Aug. 6-9, 1996.

15. Shishko, Robert, NASA's Systems Engineering Handbook, SP-6105, June, 1995.

16. Staelin, David and Rosenkranz, Phillip, High Resolution Passive Satellites, N 81-71117, April, 1978.

17. Wilson, William J., Geostationary Microwave Precipitation Radiometer, JPL, D-8136, January, 1991.

GATES - a small, agile imaging satellite prototype for GOES-R

Dennis Chesters and Del Jenstrom

NASA-GSFC, Greenbelt, MD 20771

ABSTRACT

By using current technology, it appears possible to build and launch a prototype for an advanced geosynchronous imager on a small satellite within a few years. This could be done independently of upgrading the other GOES mission functions of atmospheric sounding, communications, and space- and solar-monitoring.

At NASA-GSFC, we are engaged in a feasibility study for a Geosynchronous Advanced Technology Environmental System (GATES). GATES is envisioned as a high performance imager on a small dedicated satellite with a complete ground system. GATES could fly in the era of the Earth Observing System (EOS, circa 1999-2004 AD) and serve as a prototype for NOAA's next generation of operational satellites (GOES-R, circa 2008 AD). In addition to carrying all the channels identified for NOAA's GOES-R Imager, GATES is being designed to carry all the broadband channels specified for NASA's Moderate-resolution Imaging Spectro-radiometer (MODIS) instrument on the EOS platforms. This channel complement gives GATES the capability to fill in the space-time gaps in cloud observations from polar-orbiting satellites and to serve as a cross-reference between polar radiometers.

Multispectral rapid-imaging requirements are met by using several recently developed technologies -- large detector arrays with active cooling, star-tracking and gyroscopic attitude-determination, a small and rigid spacecraft, a heat-resistant telescope, a phased-array Ka-band downlink, realtime digital image rectification, and Internet data distribution on the ground. The GATES design is so small and agile that it could use the momentum wheels to scan the entire spacecraft back-and-forth across the Earth.

Keywords: spacecraft, imaging, GOES, GATES

1. INTRODUCTION

Global weather and climate operations and research benefit from the national observatories in geosynchronous orbit, such as the USA's GOES-8 and GOES-9 spacecraft. Both NASA and NOAA benefit from the ability to monitor rapidly changing cloud and moisture fields in the western hemisphere. NOAA has identified the need to improve on the GOES weather monitoring capabilities in their weather observing requirements for a next-generation GOES-R[1] Imager (circa 2008 AD). These requirements call for roughly doubling the capabilities (channels, resolution, and coverage rate) of the current GOES-8 Imager. Climate research could also benefit from an improved geosynchronous observing platform by observing the diurnal cycle with greater precision and with spectral bands tailored to climate studies.

We believe the technology now exists to develop an imaging system that can meet both weather and climate needs. However, due to the level of technological challenge and risk involved, developing such an imager as part of the operational GOES program could be a significant gamble, risking program schedule, cost, and continuity of data delivery. For example, there were serious programmatic and engineering difficulties experienced with GOES-I in the early 1990's, when trying to convert the AVHRR heritage to fly on a 3-axis semi-stabilized satellite. GOES-8, the first satellite in the current operational series, required over one year of on-orbit characterization and software corrections to develop adequate pointing and radiometric performance. That experience made it clear that the next generation geo-imager should be first prototyped with a flight model to minimize risk and expense to an operational series. A prototype

 0-8194-2200-2/96/$6.00

provides the opportunity to correct any shortcomings which are discovered in orbit, before flying the operational model.

To meet this need, we propose a synergistic design for a complete geostationary atmospheric imager with state-of-the-art radiometric qualities. This imager is envisioned to fly on a small dedicated satellite in the era of the Earth Observing System (EOS, circa 1999-2004 AD) with its own complete ground station, and serve as a prototype for NOAA's next generation of operational satellites.

The advanced geo-imager is distinct from NOAA's entire GOES program, and so it is called the "Geosynchronous Advanced Technology Environmental System" (GATES). The word "System" is used because GATES is more than just an instrument -- it is an autonomous satellite that also includes a ground system for command-and-control and for data processing-and-delivery to scientific users. GATES will act as a proving ground on which NASA can wrestle with the technological difficulties of meeting the science and operational requirements using the latest available technologies without the fear and consequent expense of jeopardizing the operational GOES system. In addition, while on orbit, GATES will be a state-of-the-art national geo-observatory, capable of providing unsurpassed weather and climate data.

2. CONCEPT DEVELOPMENT

2.1 New Millennium Technologies

In 1995, NASA reviewed the latest high technology items for its New Millennium program. That review identified a number of enabling technologies that are now available for purchase, including:

- mechanical cooling of optics and detectors
- large focal plane arrays
- sun- and heat-resistant optics
- precise star-trackers and gyros
- high-speed data handling and mass storage on-orbit
- lossless data compression
- Ka-band downlinks for high data rates
- efficient solar arrays and batteries
- autonomous spacecraft
- a selection of geosynchronous launchers
- efficient command-and-control rooms
- realtime image data processing
- fast client-server data access systems on a national and global scale

So many enabling technologies inspired a concept study for an advanced geo-imager.

2.2 Goals for an Advanced Geo-Imager

The most important scientific and operational goals are to capture the rapidly changing weather and the diurnal climate patterns:

- clouds: location, height, amount, and phase
- water vapor: high and low amounts and motion in the troposphere
- surface conditions: temperature, vegetation and soil moisture
- transient events like fires and volcanoes
- survey the entire hemisphere several times per hour
- observe severe storms many times per hour
- operate 24 hours per day, despite eclipses and solar loading near midnight
- design life of 5 to 7 years

2.3 Design Objectives for an Advanced Geo-Imager

Geosynchronous and polar orbits can be complementary in their coverage of the Earth. In particular, a geo-imager equipped with the proper spectral bands can fill in the gaps of the space-time coverage by the polar orbiting imagers, thus providing direct measurement of the rapid variations in water vapor and cloud cover that polar imagers would otherwise miss. A geo-imager can also serve as a cross-reference between polar imagers providing continuity of calibration.

It is important to recognize, however, the challenges of geosynchronous orbit, which is approximately 50 times farther from the Earth's surface than the polar-orbiting weather and climate satellites. At that distance, pointing and horizontal resolution is 50 time more difficult, and the radiant flux is 2500 times less than in low-earth orbit. These factors constrain a fast geosynchronous radiometer to use relatively broadband channels in order to gather enough light, and to use accurate knowledge of orbit and attitude to earth-locate images. In addition, every 24 hours, the sun appears in or near the field-of-view of a geosynchronous Earth-pointing instrument, causing very significant optical and radiometric difficulties.

Keeping these issues in mind, an advanced geo-imager should:

- be simple, reliable, and unaffected by diurnal solar loading
- complement the polar orbiting systems
- use broadband spectral channels to gather sufficient flux
- have many detectors with high signal-to-noise and low drift rates
- have an accurate calibration scheme
- use a fast, dedicated downlink
- use precise knowledge for pointing and registration
- register and geo-locate every pixel in realtime
- perform realtime data processing and distribution to weather forecasters
- scan the earth frequently enough to track the local diurnal cycles over the hemisphere
- archive data to mass storage for climate re-analysis
- fly an operational prototype for at least one year to test diurnal and seasonal behavior

3. IMAGING REQUIREMENTS

The design of an advanced satellite imager is driven by requirements for multiple bandpasses with good signal-to-noise at high spatial and spectral resolution. For time-lapse animation of weather events, one needs wide area coverage with frequent updates remapped to earth-coordinates. For realtime forecasts, high speed data processing and distribution is required.

3.1 Space-Time Requirements

NOAA's space-time requirements (draft) for GOES-R[1] are listed in Figure 1. The resolution and refresh rates required by GOES-R imply data rates more than an order-of-magnitude larger than the current low-frequency S-band downlinks from GOES-8, especially since the datarates in colmn 3 add together.

Region, NS x EW km x km	Duration min	Data rate, vis. Mbits/sec	Purpose	Refresh frequency scenes/hour
1000 x 1000	<1	>3	mesoscale (storm)	>60
3000 x 5000	<5	>8	regional (USA)	>12
12000 x 12000	<15	>25	hemisphere	>4

Figure 1: NOAA's space-time requirements for GOES-R imaging (1994 draft).

In addition, NOAA requires operational robustness:

- independent mesoscale and hemispheric imaging
- ±1 km navigation and registration
- 24-hour service, through eclipse
- minimal outages for maneuvers and housekeeping

3.2 Radiometric Requirements

If we combine NOAA's draft of its imaging radiometric requirements for the GOES-R[1] era (2008 AD) with the most effective Imager and Sounder channels on GOES-8, and then add the NASA-NOAA specifications for the MODIS[2] broadband channels, we arrive at the list of bandpasses, signal/noise and horizontal resolution requirements shown in Figure 5. The radiometric specifications and main data products from each band have been established by a myriad of previous GOES, POES, GEO and EOS committees.

Figure 6 presents the GOES-8, GOES-R and GATES bandpass specifications graphically. The bands are compared to a sketch of the Earth's transmittance spectrum from the solar shortwave to the thermal longwave bands. The GATES bands occupy all of the atmospheric windows, splitting them where differential radiances are a reliable measure of the total column property of that atmosphere. The cluster of absorption bands in the 6 to 8 micron spectrum is planned for tracking water vapor as a function of height.

The many additional MODIS bands shown in Figure 5 and Figure 6 are not a significant burden on top of the GOES-R bands because the optics and focal planes required for the GOES-R bands are already in place. Only the detector population occupying the optical-mechanical design doubles, not the design itself.

In addition to the union of the GOES-I, GOES-R and MODIS channels, it would be very useful to add a blue channel between 0.45 and 0.50 microns to monitor dust and haze, since it is now recognized that aerosols are as important in controlling the radiation budget as carbon dioxide, water vapor, and clouds. This blue channel could be accommodated with little effort in the visible focal plane. The blue channel is included in Figure 6, indicating that the conceptual design of GATES is still open to modification.

4. CONCEPTUAL DESIGN

To achieve high spatial resolution over the western hemisphere in a short time, we require many detectors spanning a wide field-of-view. Global coverage can be achieved by scanning "tall" pushbrooms of detectors having N-S nadir projections of 1000 km in height. At geosynchronous altitude, this corresponds to a full-height field-of-view of 1.6 degrees, comparable to MODIS. Using this tall pushbroom, one can scan the entire Earth in twelve back-and-forth east-west sweeps, or scan a local storm in a single east-west sweep. Finally, global and local scans can be interlaced to achieve simultaneous synoptic and mesoscale coverage, as desired by the National Weather Service (NWS). Some of these scan strategies are illustrated in Figure 2.

Because GATES is a small, agile dedicated satellite, it is possible to execute the pushbroom scans by slewing the entire satellite, thus eliminating the more traditional scan mirror. This requires a rigid design, probably with stationary solar arrays. Initial analysis shows that the satellite scanning motion can be performed using available wheel technology.

The effects of solar intrusion are minimized by doing away with the traditional exposed scan mirror, and by using a easily baffled off-axis telescope. The telescope can be made of silicon carbide or composites for low thermal expansion and good resistance to solar heating, and can be well monitored with thermistors to characterize and correct radiometric calibration variations over the course of the diurnal cycle.

Low noise performance will be achieved using a mechanical cooler for the thermal bands. It is expected that a temperature on the order of 65K will be targeted.

Figure 2: Some scan strategies available for synoptic and mesoscale coverage using a tall pushbroom scanner at geosynchronous station.

Radiometric calibration is always a difficult issue for a radiometer that has both shortwave (solar) and longwave (thermal) bands. Consequently, we aim to have more than one calibration strategy:

- on-board thermal absolute and relative calibration
- absolute and relative calibration using the sun through a pinhole array
- relative calibration using the moon
- surrogate calibration with respect to the polar orbiters

Lunar and solar calibration are possible because GATES is a small, agile dedicated satellite that can be pointed anywhere in the sky using momentum wheels.

The large number of bands and the high ground coverage rate will require the use of fast on-board data buffering and data handling, lossless data compression, and a high-frequency Ka-band downlink to move the pixel stream to the ground.

5. SCIENCE CAPABILITIES

Only geosynchronous orbits provide a way to directly measure the rapid changes in cloud and surface conditions which occur every day. Figure 3 compares the data products available from a simple 3-channel "stormsat" like GOES-7, to GOES-R and to GATES. GATES shows a distinct advantage for monitoring climate and land processes, which NOAA can expect to have under its stewardship when the US Global Change monitoring program becomes operational early in the next century. Because GATES is still in the conceptual phase, the list in Figure 3 is only an outline of a science plan. Fortunately, the GOES-R and MODIS science teams have done their homework, and they will be in place when and if GATES flies.

WEATHER		
3-CHANNEL STORMSAT	**8-CHANNEL GOES-R**	**17-CHANNEL GATES**
High res. clouds, Cloud-track winds, 300 mb water vapor, High-level winds, Cloud top temp., Convective vigor	High res. clouds, Cloud-track winds, 300 mb water vapor, High-level winds, Cloud top temp., Convective vigor, Cloud/snow diff., Winds in winter, Surface/fog diff., Aviation weather, 500 mb water vapor, mid-level winds, Split window (H2O), total water vapor, CO2-sliced cloud top, ASOS supplement	High res. clouds, Cloud-track winds, 300 mb water vapor, High-level winds, Cloud top temp., Convective vigor, Cloud/snow diff., Winds in winter, Surface/fog diff., Aviation weather, 500 mb water vapor, mid-level winds, Split window (H2O), total water vapor, CO2-sliced cloud top, ASOS supplement, water/ice cloud top, cloud phase processes, Split window (N2), Boundary layer temp., 700 mb water vapor, low level winds
CLIMATE AND LAND		
3-CHANNEL STORMSAT	**8-CHANNEL GOES-R**	**17-CHANNEL GATES**
	• Split window (H2O), Total water vapor, fires	• Split window (H2O), Total water vapor, water/ice cloud top, cloud phase processes, Split window (N2), Boundary layer temp., 700 mb water vapor, low level winds, Vegetation, bio-status Americas, Cirrus, Greenhouse process, Split window (H2O), fires, Total Ozone

Figure 4: Comparison of the kind of data products from some proposed geosynchronous Imagers.

6. DATA PROCESSING AND DELIVERY

GATES can generate a firehose of data, comparable to MODIS, for the same reasons. We expect that the Ka-band downlink form GATES would go to a central processing system that would calibrate and rectify the multi-channel imagery. We expect to distribute the imagery and selected data products using high speed land lines and protocols, as sketched in Figure 4.

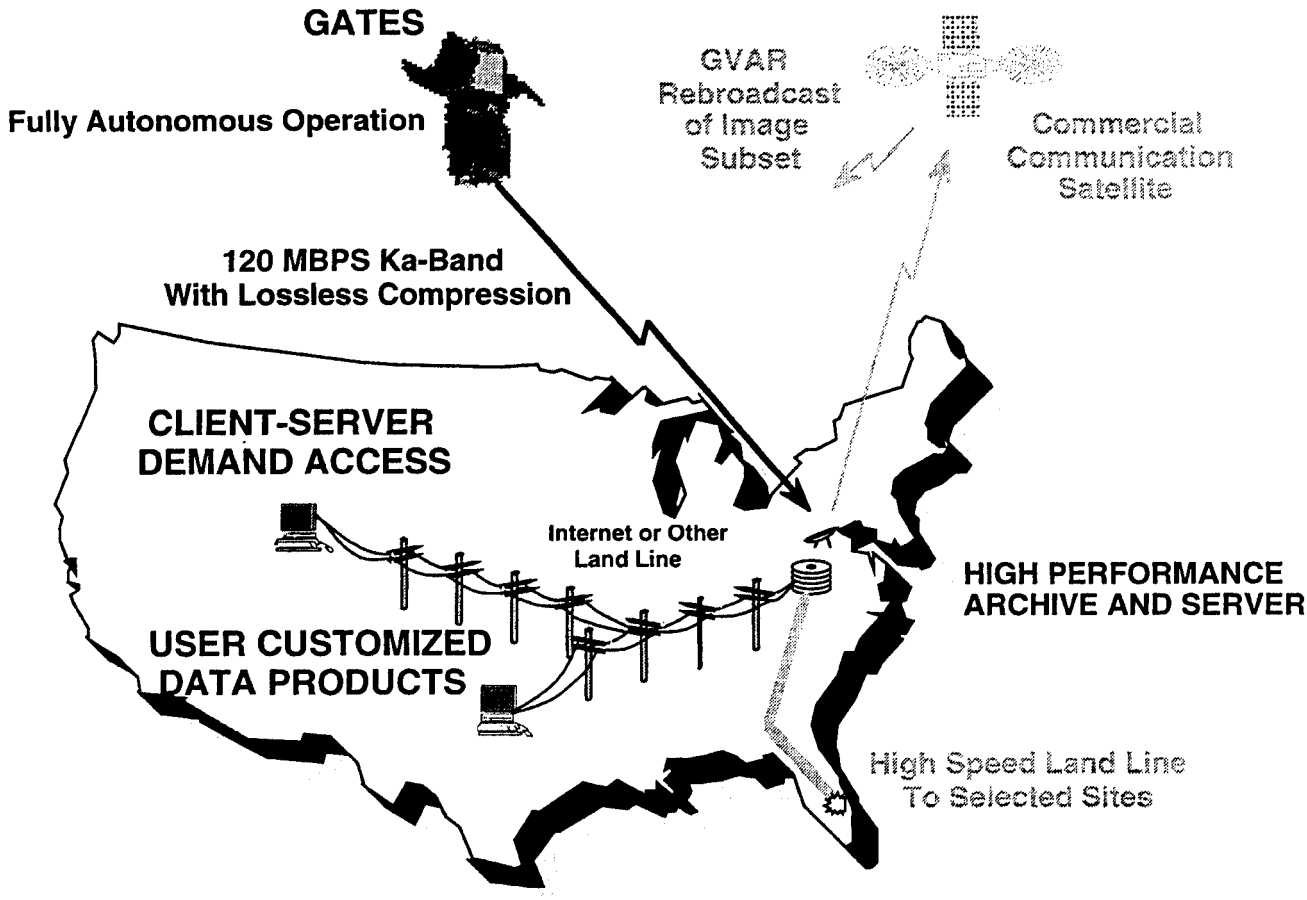

Figure 4: Ka-band downlink and landline data distribution concept for GATES.

Client-server architecture and predefined custom products will deliver timely images to remote weather forecasting sites, using the high-speed national ATM network that should be in place by the turn of the century. In addition, we could re-create the GOES-8 GVAR data format for broadcasting 5-channel imagery through old GOES or through commercial satellites to operational NOAA and private users during the GATES demonstration

7. SUMMARY

GATES could meet or exceed NOAA's draft GOES-R imaging requirements
- 17 channels merging GOES and EOS science
- excellent S/N and NEDT performance
- 0.5 km vis, 1 & 2 km IR effective ground patch sizes
- ground registration to 1 km
- operate through local midnight and eclipse
- full disk in ≤ 10 minutes
- full disk in ≤ 15 minutes with simultaneous 1 minute storm coverage

Compared to the GOES-I/M Imager
- 3x number of channels
- 5x faster coverage
- 2x higher spatial resolution
- up to 2x lower noise

8. ACKNOWLEDGMENTS

The GATES conceptual design was the result of design teamwork at NASA-GSFC, sponsored by Al Sherman, Director of Engineering, managed by Don Krueger and Jim Mason, and supported by many subsystem engineers in the GSFC Engineering Directorate. Northrop-Grumman provided design assistance and estimates of detector performance.

9. REFERENCES

1) National Weather Service observational requirements for the evolution of future NOAA operational geostationary satellites, NOAA-NWS draft copy, 1994.
2) The Geostationary Earth Observatory (GEO), NASA-MSFC draft copy, 1994.
3) MTPE EOS Reference Handbook, Ed. Asrar and Greenstone, NASA publication NP-215, 1995.

Band	Wavel. μm	Width μm	Noise	FOV km	Purpose	GATES 1999	GOES-R 2008	GOES-I 1994	POES now	MODIS 1998	Landsat 1998
VIS											
1	0.6	0.2	250/1	0.5	cloud albedo	x	x	x	x	x	x
NIR											
2	0.8	0.2	200/1	0.5	vegetation	x			x	x	x
SWIR											
3	1.37	0.02	150/1	1	cirrus	x				x	
4	1.65	0.2	250/1	1	cloud water, snow	x	x		x	x	x
5	2.2	0.2	200/1	1	cloud ice	x				x	x
MWIR											
6	3.60	0.4	0.1 K	1	low water vapor	x		S		x	
7	3.95	0.2	0.1 K	1	sfc & cloud temp.	x	x	x	x	x	
8	4.15	0.1	0.2 K	1	low air temp.	x		S			
mLWIR											
9	5.5	1.0	0.2 K	2	mid water vapor	x	x				
10	6.5	0.4	0.2 K	2	high water vapor	x		S		x	
11	7.0	0.4	0.2 K	2	mid water vapor	x	x	x	x	x	
12	7.5	0.4	0.2 K	2	low water vapor	x		S		x	
LWIR											
13	8.5	1.0	0.2 K	2	total water vapor	x			x	x	
14	9.7	0.2	1.0 K	2	ozone	x		S	x	x	
15	11.0	1.4	0.2 K	2	sfc & cloud temp.	x	x	x	x	x	x
vLWIR											
16	12.4	0.9	0.3 K	2	total water vapor	x	x	x	x		
17	13.3	0.4	0.5 K	2	high cloud cover	x	x	S	x	x	

Figure 5: Listing of the broadband channels proposed for GATES, the union of the GOES-R and MODIS channels. A few of the GOES-I Sounder (S) broadband channels are included that are useful for multispectral imagery, as well as the current POES complement of AVHRR and HIRS channels that are useful for monitoring clouds and water vapor.

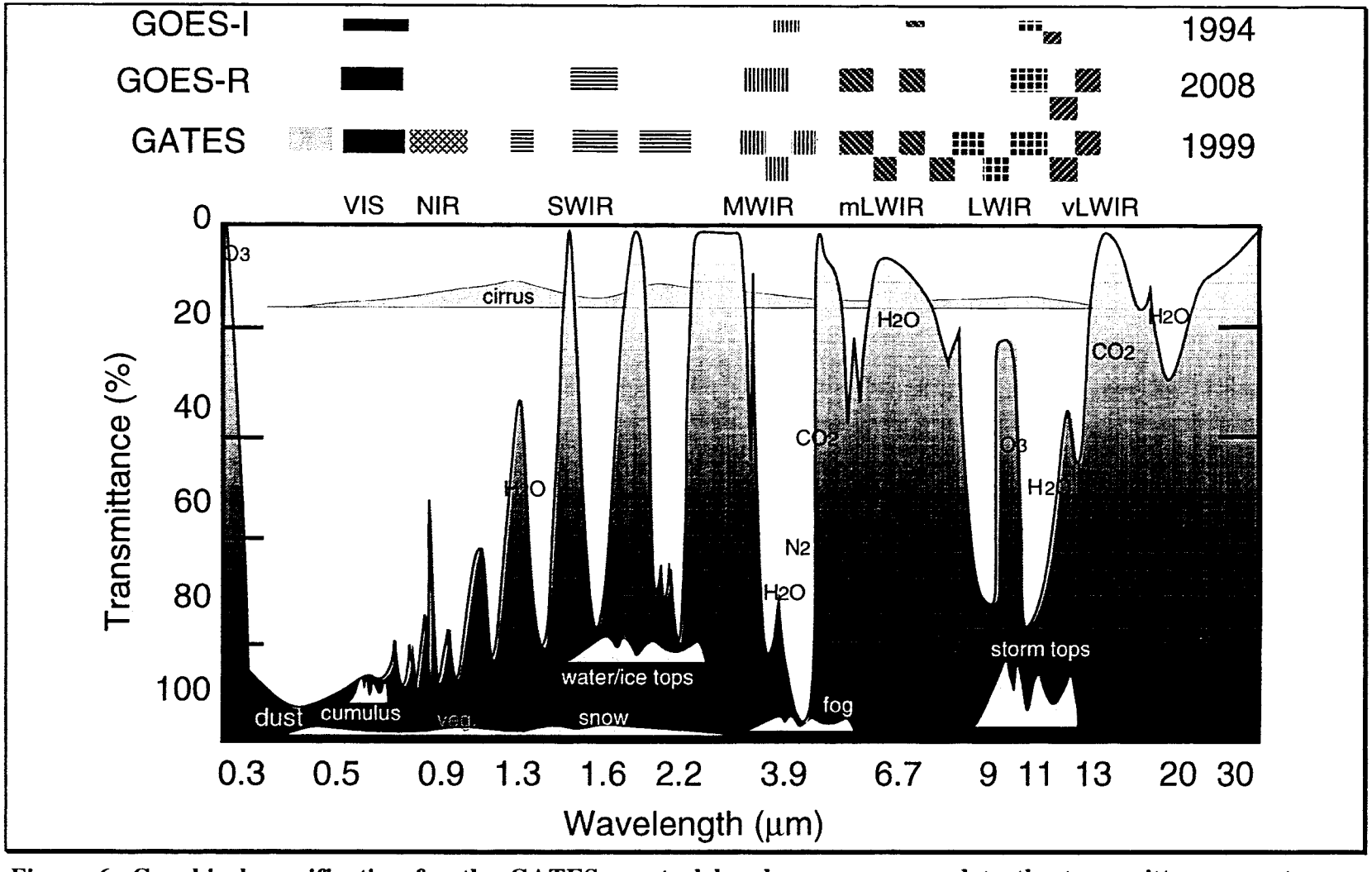

Figure 6: Graphical specification for the GATES spectral bandpasses compared to the transmittance spectrum of the Earth's atmosphere. The bandpasses for GOES-I and GOES-R are compared to GATES.

GOES-8 and -9 launch and mission operations support overview

C. Bengston

Computer Science Corp. 7404 Executive Place, Seabrook, MD 20706

D. McCuistion

NASA Goddard Spacflight Center /Code 415 Greenbelt MD 20771

ABSTRACT

The new series GOES-8 and -9 launched in 1994 and 1995 provide more flexible instrument coverage and higher resolution than previous GOES spinners. This added flexibility and the 3-axis stabilized operating mode however resulted in a more complex satellite system with independent Imager and Sounder, and on-board image navigation systems requiring more daily commanding. Nearly 5000 realtime commands are currently sent each day to each GOES-8 and 9 spacecraft compared to 200 commands per day for GOES-7. These new technological advancements in spacecraft design presented new challenges for the NASA operations support personnel. In order to prepare for launch, post-launch test, and on-orbit operations, a rigorous mission planning scheme was developed to assure safe commanding of the flight system and monitoring of its state of health. This paper overviews the key mission operations approaches and philosophies developed for the GOES I-M missions and key operations tools that were developed to aid operations personnel in performing complex routine and special operations tasks.

Keywords: GOES, Mission Operations, Command Procedures, Telemetry Processing, Post-launch Testing, End-to-end Testing

1. GOES MISSION: AN INTRODUCTION

The primary objective of the Geosynchronous Operational Environmental Satellite (GOES) Mission Operations Team is rather unique in that, unlike most other programs, providing an on-orbit asset or capability to the parent organization is not the primary goal. In fact, the primary objective is more indicative of commercial spacecraft production than a typical government agency's approach to satellite operations: that is to provide a meteorological satellite in geosynchronous orbit to another organization (government agency, in this case) for its exclusive use. Acting as the technical acquisition experts for the National Oceanic and Atmospheric Administration (NOAA), NASA has responsibility for designing, developing, testing, launching and delivering on-orbit, a fully operational spacecraft system for generation of state of the art weather products for the United States. With the technological obsolescence of the GOES-7 series spinners and introduction of the 3-axis stabilized GOES I-M series with dedicated imaging and sounding instruments, the ability to meet the requirement of delivering a turn-key system on-orbit was jeopardized under the previous Operations Team approach. In addition, due to the technological leap from GOES 1-7 to GOES I-M, continuous engineering support for NOAA was mandatory after handover to minimize or eliminate interruptions in operational product generation. Considering the problems that had plagued the GOES program in the late 1980s and early '90s, a derived requirement of the NASA/GOES Project, and NASA Operations, was to re-establish a 2-observatory constellation as quickly as possible (GOES operated with a 1-satellite system approximately 2.5 years after the loss of GOES-6 at launch) while concurrently testing and comprehending an entirely new state-of-the-art meteorological satellite, two rather conflicting yet daunting requirements.

0-8194-2200-2/96/$6.00

2. NASA's MISSION OPERATIONS APPROACH

With these requirements, the time constraints imposed, the technological advancement, growth in complexity, and the need for continued engineering support from the developer (NASA), four core principles to re-engineer NASA/GOES Operations evolved. These approaches and principles were rudimentarily formed during the GOES-8 launch campaign, but came to full fruition, and a permanent part of GOES, for GOES-9.

The first principle was establishment of a single authoritative Project Office Lead for the Operations function, the GOES Operations Manager (GOM). This position has traditionally been a non-Project Mission Operations Manager (MOM) co-located with the Project, from NASA/GSFC's Mission Operations and Data Systems Directorate (MO&DSD). The emphasis under MOMs had been launch-to-orbit operations, but with the GOES I-M series and establishment of a Project GOM, and only mission support provided by the MO&DSD, the fundamental emphasis shifted from simply raising and establishment on orbit to spacecraft engineering and total mission support to NOAA. This sea of change also provided a consistent, dedicated interface for NOAA for the life of the mission, and a direct link to development activities at NASA.

The second core principle was establishment of a self-contained Operations Team for launch and post launch test. This Team must consist of experts in the hardware/software systems of the spacecraft, with a strong operational overtone, thus requiring a multi-organizational approach to Team construction. Team composition was targeted to each particular mission phase as well. Satellite expertise in every subsystem was acquired for the critical launch-to-orbit and activation phases of the mission. A core contractor Team was selected to lead the effort (Computer Systems Corporation and Swales and Associates), bringing solid subsystems experience and operational experience to the Project. This core Team was heavily augmented by the spacecraft and instrument contractor's engineers (Space Systems Loral and ITT) to provide in-depth hardware knowledge to round out launch Team composition. The Team was led real-time by NASA-assigned personnel in the critical leadership roles of Mission Director and Contingency Manager. These positions were solely responsible for mission conduct, and had complete authority of the GOM and Project office. Training was a major component of developing the Team's synergy and efficiency. Six mission simulations and at least 2 launch simulations are conducted in the 6 months prior to launch of each GOES I-M satellite, each lasting up to 96 continuous hours and covering both nominal and contingency operations. For GOES -8 and -9, simulation realism wasrequired to flush out numerous personality conflicts, positional mismatches, and other flaws in the initial Team structures that would have significantly degraded effectiveness if Team refinements had not been made prior to launch. The end result was a strong, well balanced Team that effortlessly handled adverse situations, e.g. aborting of the first apogee motor firing on GOES-8 and complete replan of the mission profile, while concurrently dealing with repetitive Electro-Static Discharge events during the delay in transfer orbit.

The third principle was to thoroughly test the spacecraft prior to launch to ensure a strong knowledge base for the primary NASA Operations Team. An extensive test program evolved encompassing both ground-based testing of each spacecraft by the Operations Team from the Satellite Operations Control Center (SOCC), and comprehensive on-orbit testing. Significant issues were routinely uncovered in the pre-launch End-To-End (ETE) test program, thus the program evolved into a series of ever-more complex ETEs including complete archiving of test data at SOCC for future reference, data trending test-to-test, and troubleshooting of anomalies both real-time and through additional testing. The program has now been adopted as a baseline for the GOES program in the future, is being standardized, verification matrices established, and the program placed under configuration control. The second portion of this test philosophy is comprehensive Post Launch Test program (PLT). Two phases developed consisting of an Activation phase (ACT) and a System Performance and Operational Test phase (SPOT). ACT is a typical series of functional tests and deployments of operational subsystems, and basic characterization of performance. The SPOT phase is significantly more elaborate and complex, including establishment of critical Image Navigation and Registration (INR) functionality. ACT and SPOT combined constitute a total of approximately 350 tests of the instruments, spacecraft bus and ground system.

The final principle was to develop operations tools that enhanced the GOES ground systems ability to aid launch, PLT, and on-orbit operations personnel in real-time spacecraft command execution, telemetry monitoring, and non-real-time telemetry evaluation. Perhaps the most critical and complex set of tools developed were Command Procedures (CPs). Because of the added operational complexity of the GOES I-M series over the previous GOES, the NASA operations group developed standalone CPs, over 800 per spacecraft, that systematically execute spacecraft command functions. These CPs utilize safety checks contained in the command database and pre-programmed logic constructs built to provide automated real-time pre-command and post-command checking and reporting. CPs were developed to provide a multi-layer safety checking approach to ensure that no commands were erroneously executed out of sequence at anytime during the mission. A secondary benefit of CPs is to provide a means of retaining engineering knowledge. As is typical with many multi-spacecraft series, retention of knowledge is very difficult to maintain over the entire spacecraft series due to personnel attrition. Because of strict configuration control required for commands, CPs provided an excellent means for retaining this engineering knowledge derived from experienced gained through testing, and collaboration with the initial spacecraft developers. Another significant ground system enhancement was the development of complex telemetry processing algorithms (PSEUDO-B points) that are used to provide additional information to the spacecraft operator on the overall health of the spacecraft. Many of these PSEUDO-B algorithms are also used to detect and alert the operator when mission threaten conditions exist. For this reason safety monitor alarms were developed to provide additional alarm capabilities over the standard database Red/Yellow High/Low telemetry alarms. NASA working closely with NOAA developed the GOES Engineering Analysis System (GEAS) to provide enhanced offline telemetry analysis capabilities. The GEAS was developed to handle the extremely large engineering analysis needs for all mission operations elements, provide engineers quick data access, produce plots and reports for large volumes of data, and provide autonomous output of routine trending plots.

3. END-TO-END TEST PROGRAM

The ETE test program is the focal point of ground based testing performed by the NASA operations team at the SOCC. These tests have been proven to be an invaluable and necessary tool for ensuring that the ground system, operations team, and spacecraft are fully prepared to support launch, PLT, and on-orbit operations. The primary test goals of these tests are to:

- Fully demonstrate the SOCC ground systems capability to send all commands to the GOES spacecraft in each command mode and receive and accurately process housekeeping telemetry and wideband data.
- Validate spacecraft CPs grouped in logical operational sequences identical to actual sequences performed during nominal and contingency orbit raising, PLT, and on-orbit operations.
- Demonstrate a closed-loop, end-to-end utilization of the GOES primary ground system elements including the validating the ground systems ability to determine the Attitude and Orbit Control Electronics (AOCE) interaction with the Payload instruments, perform flight software reprogrammability, and accurately process Wideband data.
- Provide an accessible archive for aiding operations personnel in troubleshooting on-orbit anomalies.

These goals are achieved through a series of 6 separate ETE tests for each spacecraft. Four ETE tests are performed while the spacecraft is in the clean room in Palo Alto, one while in the Thermal Vacuum chamber, and a final test while in the launch payload processing facility near the NASA Cape Canaveral launch site. In addition, the NASA operations personnel are able to monitor all thermal vacuum testing activities and launch pad activities through archived telemetry data at the SOCC during periods when the spacecraft is powered on. The ETE test team is composed in a similar manner to the multi-organizational launch team. Development of the test plans and detailed test scripts are performed by NASA operations team, and reviewed and approved by SS/L

and ITT Integration and Test personnel. ETE test execution is lead from the SOCC and coordinated through GSFC voice line with the SS/L and ITT team members.

4. LAUNCH AND EARLY ORBIT PROGRAM

GOES orbit raising command sequences present challenges to the NASA operations team, in that all commanding activities are initiated in real-time from the ground. There are no pre-stored command capabilities on-board the spacecraft so all elements in the ground system and network must be fully operational during several time critical maneuvers and deployments required early after launch. The orbit raising network for GOES is made up of the Deep Space Network (DSN) operated out of the Jet Propulsion Laboratory (JPL), the Air Force Space Network (AFSCN) operated out of Onizuka Air Force Base, and GSFC operated NASA Wallops and Bermuda stations. The spacecraft is injected into a highly elliptical orbit following separation from the launch vehicle with the perigee radius approximately 6550 km and the apogee radius approximately 6500 km above geosynchronous altitude (42,164 km). The supersychronous apogee is desired to conserve spacecraft on-board fuel that will increase spacecraft lifetime. Following separation from the Atlas/Centaur, the NASA operations team begins a systematic turn-on of spacecraft bus components. With the exception of telemetry transmitters and command receivers, most spacecraft components are off at first contact, including all attitude sensors. Upon first contact at the Air Force Indian Ocean Station, an initial separation spacecraft spin rate is determined by measuring the duration of telemetry outages caused by the spacecraft spinning through a T&C antenna null. Following the critical first solar array panel deployment, the NASA operations team performs a series of orbit raising maneuvers over the next 14 days using the restartable bi-propellent Main Satellite Thruster to boost the spacecraft into a circular geosynchronous orbit.

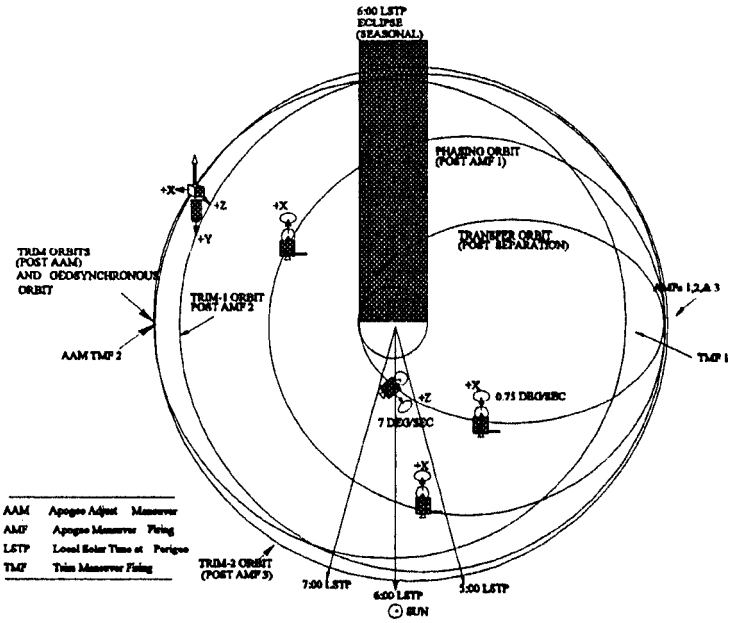

Figure 1. Orbit Raising geometry

The first three maneuvers are used to raise perigee and the fourth to circularize the orbit by lowering the apogee to a geosynchronous altitude. The operations team completes the orbit raising activities by deploying the magnetometer boom, final solar array panel, Solar Sail and spinning momentum wheel up to normal on-orbit operating speeds.

NASA operations team members work in a three shift rotation supplemented with a special events crew during all deployments and orbit maneuvers. As with other GSFC programs, all nominal command sequences are

scripted with branch points to Contingency Operations Procedures (COPs) in the event of a contingency. Over 100 detailed COPs are available to the launch team during orbit raising and Post-Launch Test activities. During all commanding situations (nominal and contingency) CPs are used to ensure proper command sequence execution.

5. POST LAUNCH TEST PROGRAM

The 2 phased PLT program evolved from a combination of other NASA and SS/L program's on-orbit test experience, and the complexity of the first new-generation GOES spacecraft. The need to fully characterize the spacecraft, instruments and especially the Image Navigation and Registration (INR) system was an over-riding factor in the extensiveness of the GOES-8 test program. Testing is performed in a logical, systematic manner, similar to most other project's test programs. A PLT plan is developed, approved, and under configuration control months prior to launch. During PLT only the Mission Director or GOM have the authority to modify the test program, or any individual test within the program, thus providing pre-planned operations so that product users can receive and process data as early as possible in a pre-defined, logical sequence. All functional testing is completed first in the ACT phase (approximately 45 days after establishment on orbit) with methodical turn-on and characterization of each subsystem by the applicable engineers from the NASA/Contractor Team. NASA delivers the spacecraft's health and safety responsibilities to NOAA at the completion of ACT, and NOAA fulfils console operator and other routine operation positions at this time. Calibration is the next sequence, to understand and normalize each channel's performance, followed by specification compliance testing.

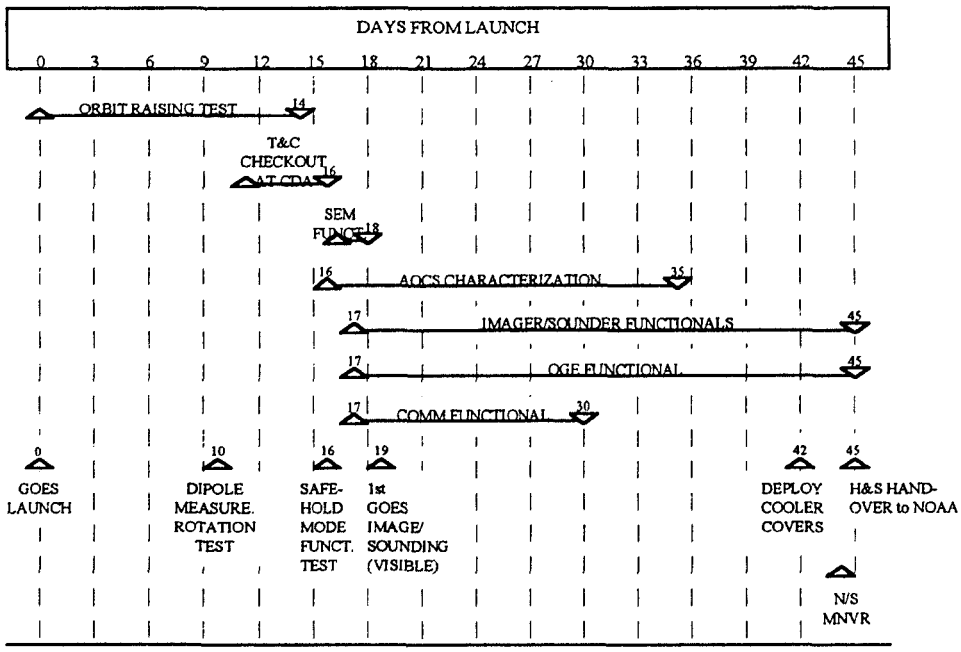

Figure 2. Typical time line for GOES Post Launch Test ACT phase

The SPOT phase for GOES-8 spanned approximately 135 days after the completion of ACT. INR startup occurs at the beginning of the SPOT phase, when most of the functional and calibration activities are complete. INR startup includes the first landmarking and star sensing operations, and testing of various motion compensation routines. SPOT concentrates on specification testing, and routine operations schedules are introduced at this point. These schedules allow the end weather service users to begin collecting and analyzing the new spacecraft's products while concurrently accomplishing test requirements and establishment of spec-performance. At the

completion of SPOT the spacecraft is under full operational purview of NOAA, and NASA's launch and PLT job is complete. National Weather Service priorities and products become the only focus.

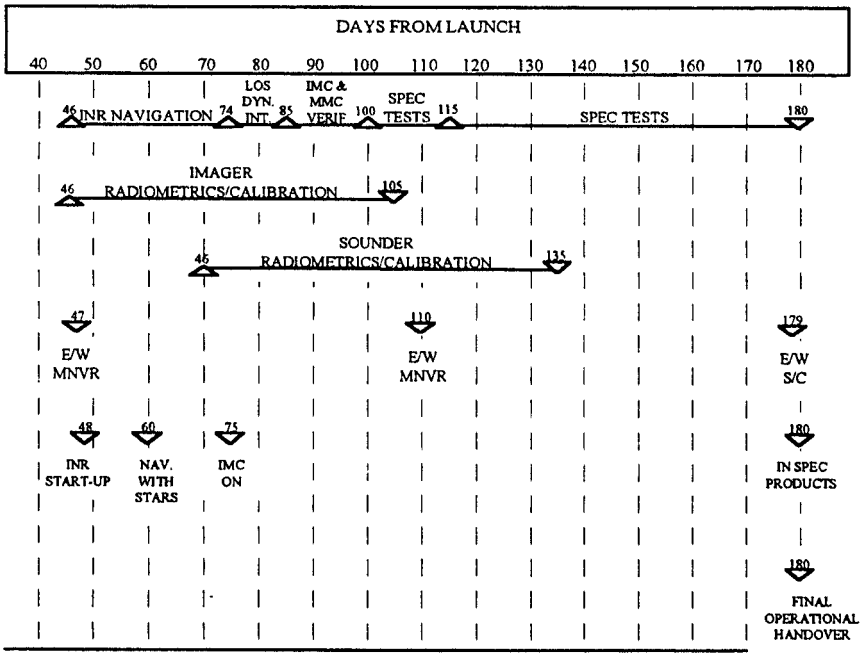

Figure 3 Typical Time line for GOES SPOT Phase

The SPOT phase has seen significant streamlining from GOES-8 to GOES-9, and will see another significant improvement in GOES-K concentrating less on individual tests and more on quickly transitioning into "routine" operations with off-line data analysis for system performance measurement. Streamlining from GOES-8 to -9 resulted in a net reduction in spacecraft and instrument testing from approximately 291 for GOES-8, to 177 on GOES-9, entirely due to efficiencies from improved system knowledge. Future GOES SPOT reductions are planned, to both reduce the complexity and number of dedicated tests, provide more routine operations for more realistic products sooner in test, and to reduce the 135 day SPOT test period to allow progression into operations as soon as possible for the NWS.

5. ON-ORBIT OPERATIONS

Complexity of operations, compared to GOES 1-7, is significant and requires diligence from the NOAA operations teams, with continued anomaly and trending support from the NASA Operations and development Team. With the number of required routine commands sent to the spacecraft an order of magnitude greater than GOES 1-7, the NOAA operations team is presented with challenges to ensure command schedules are built properly and executed correctly and on time. During the on-orbit phase, NASA continues to provide support to NOAA by maintaining CPs and On-orbit COPs required by NOAA operations personnel.

Figure 4. Example of the significantly increased complexity of operations from the GOES 1-7 to the GOES I-M series spacecraft

	GOES-7	GOES-8/-9
Number of Discrete Commands	260	800

Number of Commands Daily	200	5000
Number of Schedule Lines Daily	250	14-18,000
Number of Image Frames Daily Full Disk Routine Rapid Scan	 48 88 --	 48 124 200
Number of Soundings	1400 daily	2500 hourly
Total Lines of Ground Systems Code	120,000	850,000

NOAA schedulers use CPs as building blocks in the development of routine 24 hours command schedules that are initiated by NOAA operations personnel and autonomously executed by the ground system. NOAA on-line operations personnel monitor the execution of the command schedules to verify command activities successfully complete. If a command schedule suspends at any time during the execution, due to a command execution failure or a failed CP logic check, a message to the operator is displayed on screen indicating the severity of the failed command check, the subsystem affected, and pointer to a detailed message text providing the operator with instructions on how to rectify the problem. In the case of high severity levels, indicating potential mission critical situation, message texts may point the operator to detailed COPs in order to safe the spacecraft. Over 1500 message text exist for GOES 8 and 9 spacecraft.

COPs supplied to NOAA for on-orbit operations are formatted differently than orbit raising COPs. On-orbit COPs have been streamlined to allow easier contingency identification and a more straightforward approach to safing the spacecraft since NOAA on-line operations personnel do not have the advantage of having all the engineering support provided during launch. It was therefore the goal to provide NOAA on-line operations personnel with COPs in pre-canned script format that systematically walk the operator through the steps in determining the type of anomaly and command activities required for safing the spacecraft.

6. CONCLUSION

The approach to Mission Operations for this new GOES series requires more manpower, more monitoring, and more commanding than some of the new easy-cheap-autonomous commercial and governmental trends in satellite design and mission operations. However, the United States' meteorological community relies extensively on the products from GOES for hourly and daily forecasting. The national asset status of GOES and the vast user community across the nation (in excess of 10,000 users) demands a methodical, evolutionary approach to change, especially from one spacecraft block change to the next. With the significant leap in technology, related escalation in complexity, and increase in data and products, our methodology for GOES I-M had to be centered on making no immediate, radical change in SOCC operations or data distribution. This methodology, therefore, required significant levels of compatibility with existing data and product processing and distribution systems, and a gradual phase in of ground systems autonomy (begun with the logic-systems of the CPs in a format familiar to the existing operations personnel). With the re-establishment of the GOES constellation we have begun investigating and implementing spacecraft and ground system improvements. While gradual improvements are being brought on line for GOES I-M, visions of the future GOES ground system are being formed. It may never be as evolutionary, or revolutionary, as

some of its contemporary scientific and commercial mission's systems, but the path to increased autonomy and reduced cost is being mapped and pursued for the next generation of GOES.

Blank page retained for pagination

SESSION 2

Weather Science and Weather Products

Monitoring biomass burning and aerosol loading and transport using multispectral GOES data

W. Paul Menzel

NOAA National Environmental Satellite Data and Information Service
1225 West Dayton St., Madison, WI 53706

Elaine M. Prins

Cooperative Institute for Meteorological Satellite Studies
1225 West Dayton St., Madison, WI 53706

ABSTRACT

The successful launch of GOES-8 in 1994 introduced an enhanced capability [1] for diurnal monitoring of subpixel fire activity and aerosol transport in the Western Hemisphere. The higher spatial and temporal resolution, greater radiometric sensitivity, and improved navigation of GOES-8 offer many advantages for monitoring fires and smoke in North, Central, and South America. In South America the GOES-8 Automated Biomass Burning Algorithm (ABBA) is being used to continue monitoring trends in biomass burning associated with agricultural practices and deforestation activities as well as documenting the extent and transport of associated aerosols. GOES-8 ABBA results obtained during the 1995 biomass burning season (June-October) indicate a strong diurnal cycle in fire activity and associated aerosol transport regimes extending over millions of km^2. Examples of GOES-8 diurnal monitoring of fire intensity and size in the United States, Canada, Mexico, Guatemala and Belize show the utility of using GOES-8 as an early warning mechanism for identifying and monitoring wildfires in these regions. The success of the GOES-8 ABBA in the Western Hemisphere suggests the utility of initiating a global geostationary fire monitoring effort.

Keywords: geostationary, infrared, remote sensing, biomass burning, aerosol transport, fire detection

2. GOES-8/9 CHARACTERISTICS FOR OBSERVING FIRES AND ASSOCIATED AEROSOLS

During the past decade the utility of geostationary remote sensing to monitor trends in biomass burning in South America has been demonstrated with the Visible Infrared Spin Scan Radiometer Atmospheric Sounder (VAS) on board GOES 4 through 7. The GOES Automated Biomass Burning Algorithm (ABBA), developed at CIMSS, is a dynamic multispectral thresholding algorithm which uses the shortwave infrared window (SIRW near 4 μm) and longwave infrared window (LIRW near 11 μm) bands to locate fire pixels [2,3]. The algorithm is based on the sensitivity of the SIRW band to high temperature subpixel anomalies and is derived from a technique originally developed by Matson and Dozier [4] for NOAA AVHRR. Once the GOES ABBA locates a fire pixel, it incorporates ancillary data to correct for water vapor attenuation, surface emissivity and solar reflectivity and subsequently provides estimates of subpixel fire size and mean fire temperature. The GOES application is described in more detail in Prins and Menzel [2,3].

GOES is also being used to identify smoke/aerosols associated with biomass burning and to distinguish it from multi-level clouds and low-level moisture. The algorithm, still under development, uses

0-8194-2200-2/96/$6.00

the visible band (VIS near .65 μm), SIRW, LIRW, and moisture sensitive longwave infrared window (often called the dirty window, DIRW near 12 μm) in an automated multispectral thresholding scheme to map smoke/aerosols [5]. The VIS is used to identify haze, the SIRW and LIRW screen out opaque, cirrus, and stratus clouds, and the DIRW indicates low level moisture.

The GOES-8/9 imager detection of burning and associated aerosols is greatly improved over the previous GOES-VAS capability. Table 1 indicates the comparison. The GOES-8/9 shortwave and longwave infrared window bands used for fire detection are more sensitive at higher resolution than GOES-VAS. The SIRW has four times the spatial resolution; the LIRW has twice the spatial resolution. Signal to noise has been maintained and in some cases even improved (e.g. GOES-9 SIRW NEDT and GOES-8/9 DIRW NEDT). Most importantly, the saturation temperature (Tmax) in the SIRW has been set at 338 K for GOES-8 (18 K higher), enabling GOES-8 to measure the characteristics of more fires than GOES-9. Over 80% of the GOES-8 fire pixels observed in South America have a brightness temperature greater than 320K in the SIRW band; these would be saturated pixels if observed by GOES-9. Only 10% of the GOES-8 fire pixels indicate brightness temperatures in excess of 338 (they are saturated); thus GOES-8 is able to diagnose 90% of the detectable fires. The improved performance is also notable in the GOES-8/9 visible band, where 10 bit data from silicon detectors shows much improved low light sensitivity and detector to detector consistency in comparison to the GOES-VAS 6 bit data from photomultiplier tubes.

The GOES-8/9 instrument receives about 70% of the LIRW energy from a circle of one field of view (FOV) diameter; 84% from a circle of 1.5 FOV diameter. For the SIRW this becomes 85 and 92% respectively. This suggests that the fraction of the pixel that is on fire is about 10% smaller for the LIRW band than the SIRW band. This adjustment to the algorithm has not been performed for GOES-8; tests with GOES-7 indicated that the effect on the algorithm was minimal.

Finally, the 30 cm GOES-8/9 mirror resolves point sources (e.g. fires) separated by about 1 km in the LIRW and .5 km in the SIRW.

Table 1: Comparison of the GOES-8/9 and GOES-7 visible and infrared window channels. Tmax represents the maximum scene brightness temperature that can be detected without saturation of the detector. S/N represents the signal to noise ratio of the visible band. NEDT is the noise equivalent temperature referenced to a target of 300 K.

Band	Resolution	Oversampling	Tmax	S/N or NEDT
	G9 /G8 /G7	G9 /G8 /G7	G9 /G8 /G7	G9 /G8 /G7
Visible (0.52-0.75 μm)	1 / 1 / 1 km	1.75/ 1.75/ 1 EW	N/A	300 / 300 / 100 (counts)
SIRW (3.83-4.03 μm)	4 / 4 / 16 km	1.75/ 1.75/ 4 EW	320/ 338/ 321 K	.12/ .23/ .25 K
LIRW (10.2-11.2 μm)	4 / 4 / 8 km	1.75/ 1.75/ 2 EW	320/ 320/ 319 K	.09/ .14/ .15 K
DIRW (11.5-12.5 μm)	4 / 4 / 16 km	1.75/ 1.75/ 4 EW	320/ 320/ 319 K	.19/ .26/ .40 K

The spatial resolution of the SIRW on previous GOES platforms was the primary limiting factor in fire detection. The noise of the GOES-7 VAS sensor in a typical scene (0.25 C in the SIRW and .15 C in

the LIRW) implied that a FOV containing a fire of area .03 km^2 with a mean temperature of 450 K would give a signal that differs from a fire free FOV by the instrument noise. In South America the smallest fires detected with the GOES-7 ABBA were about .1 km^2. For GOES-8, with roughly the same noise constraints, the minimal detectable fire burning at 450 K is .002 km^2. For the 1995 biomass burning season in South America fires as small as .01 km^2 were detected. The enhanced capabilities of the GOES-8 imager make it much more useful for detecting and characterizing biomass burning not only in the Amazon Basin of South America, but also in the temperate and boreal forests of the United States and Canada [6,7].

3. ENHANCED CAPABILITIES FOR GOES-8

The improved capability to detect individual fires with GOES-8 is demonstrated in Figure 1. Figure 1a shows a GOES-8 SIRW image covering Rondonia in Southwest Brazil and a portion of Bolivia at 1745 UTC on 25 August 1995. Hundreds of individual fires are evident as dark hot spots. Although a direct comparison of GOES-8 and GOES-7 in South America during the 1995 burning season was not possible due to the westerly location of the GOES-7 platform, Figure 1b shows similar data from GOES-7 for 29 August 1988. It is possible to see much more detail in the GOES-8 data, including land features and localized fire activity.

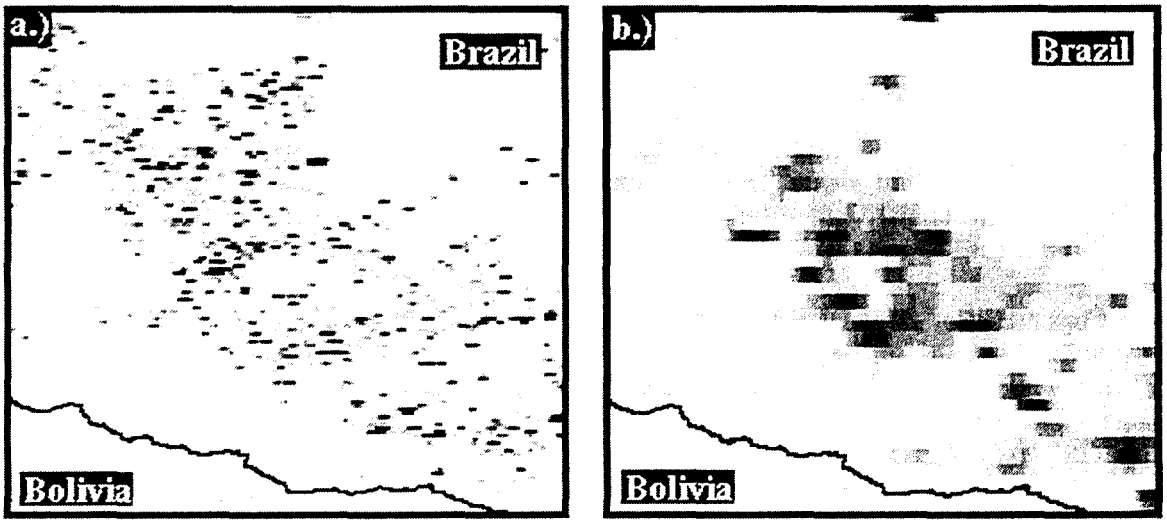

Figure 1. GOES-8 (a) and GOES-7 (b) 4 μm imagery of a section (550 km by 350 km) of the state of Rondonia, Brazil along the Bolivian border on 25 August 1995 and 29 August 1988, respectively. The dark hot spots in both images indicate subpixel burning. The improved resolution of the GOES-8 imager provides more detailed information on localized fire activity.

Validation of the ABBA was attempted with several prescribed burns initiated on 21 September 1994 in Washington in association with the Smoke Clouds and Radiation (SCAR-C) experiment based in the Pacific Northwest. One of those fires at Quinault (48 acres, 47:19°N, 124:16°W) is an illustrative example; it consisted of approximately 5000 tons of red cedar debris ignited by the US Forest Service (USFS) at approximately 1810 UTC. Table 2 shows the GOES-8 and ground esumates of the burning. Over 21 acres were flaming at 1830 UTC; approximately 30 acres remained in the smoldering phase at 2015 UTC; and less than 10 acres were smoldering at 2200 UTC [8]. The first available GOES-8 SIRW image at 1945 UTC clearly shows burning at Quinault. At 2015 UTC the GOES-8 did not detect elevated

SIRW brightness temperatures; however at 2045 UTC the fire reappears in the GOES-8 image and remains until 2215 UTC. The GOES-8 ABBA estimates of area burning and average fire temperature were compared with the ground estimates of flaming and smoldering acres; the estimate of the size of the fires is within 20% on the average at any given time and the temperature of flaming and smoldering fires was estimated by GOES to be near 600 K. Since the ABBA infers uniform background radiance from neighboring clear sky pixels, these estimates are somewhat hindered by the coastal location of Quinault, where background radiation for each GOES-8 fire pixel comes from a combination of ocean and land [3]. The relatively good agreement between GOES-8 and ground truth estimates is very encouraging. The GOES-8 enhanced capability was most evident when GOES-7 did not detect the fire after 2045 UTC.

Table 2. GOES-8 and ground estimates of the intensity and extent of the Quinault, WA controlled burn on 21 September 1994. One acre equals .004 km^2. Ground data is courtesy of Roger Ottmar of the U. S. Forest Service Seattle Forestry Science Laboratory .

	Ground Observations		GOES-8 Estimates	
Times	Flaming	Smoldering	Total Area	Temperature
(UTC)	(Acres)	(Acres)	(Acres)	(°K)
1800	0	0	NA	NA
1815	2	0	NA	NA
1830	21	0	NA	NA
1845	23	7	NA	NA
1900	22	12	NA	NA
1915	21	21	NA	NA
1930	15	24	NA	NA
1945	15	21	40	602
2000	7	26	NA	NA
2015		29	No elevated signal in G-8 data	
2030		23	NA	NA
2045		20	27	626
2100		18	NA	NA
2115		18	16	597
2130		13	17	586
2145		11	NA	NA
2200		10	NA	NA
2215		8	Fire barely detectable in G-8 data	
2230		7	NA	NA
2245		6	Fire not detected in G-8 data	
2300		5	Fire not detected in G-8 data	

NA indicates GOES-8 data was not available

For the first time, the GOES-8 imager makes it possible to monitor diurnal variability in fire intensity by providing SIRW imagery every 15 minutes over the continental United States and half-hourly elsewhere. An example of the GOES-8 diurnal monitoring capability has been indicated in Table 2. The importance of monitoring the diurnal changes in biomass burning is further illustrated in Figure 2; it provides an example of GOES-8 ABBA diurnal fire monitoring on one of the peak burning days during the 1995 biomass burning season. The black markers in Figure 2a-d represent fire pixels detected by the GOES-8 ABBA every three hours from 1145 to 2045 UTC. The algorithm observed 148 fire pixels at 1145 UTC, 1282 at 1445 UTC, 3946 at 1745 UTC, and 1533 at 2045 UTC. The number of fire pixels detected at 1745 UTC is on average 3 times greater than that observed 3 hours earlier or later and 20 times greater than that observed at 1145 UTC; the diurnal variability in detected fires is large [9].

4. DETECTION OF 1995 BIOMASS BURNING WITH GOES-8

Fire monitoring efforts in South America started with GOES-VAS [3] are continuing with the new generation of geostationary satellites [6]. The GOES-8 ABBA was operational for the 1995 biomass burning season (June through October) providing diurnal (3-hourly) information on the location, size, and mean temperature of subpixel fires as well as smoke transport. Figure 3 shows the GOES-8 estimates of the burning area for 15 August to 15 September 1995 within the region 0 to 40 S and 40 to 70 W; the Smoke Cloud and Radiation experiment in Brazil (SCAR-B) was conducting ground and aircraft measurements of the burning and aerosols during this time period. The peak burning occurs at 1745 UTC as expected; the burned area exceeded 1000 square kilometers (km^2) on most days peaking near 2000 km^2 on 6 September 1995. As many as 4000 pixels were estimated to have sub-pixel fire activity at a given time. The majority of the fire activity is concentrated along the perimeter of the Amazon in the Brazilian states of Para, Mato Grosso, Amazonas, and Rondonia. There is also considerable activity in Bolivia, Paraguay and Northern Argentina. The burning pattern is similar to that observed with the GOES VAS ABBA in 1988, but GOES-8 provides much greater detail concerning individual fire activity and other surface features.

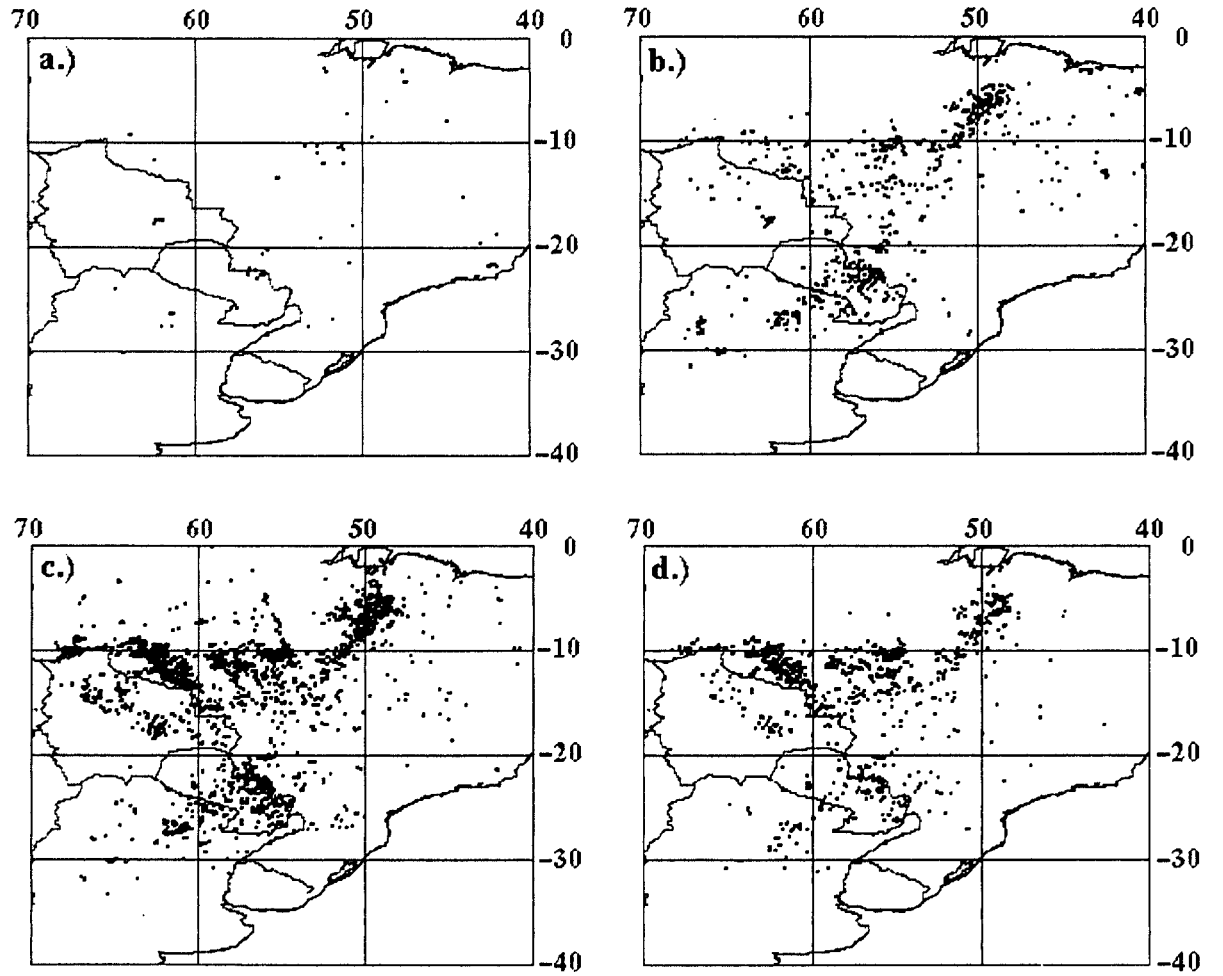

Figure 2. The black locators indicate fires detected by the GOES-8 ABBA on 24 August 1995 at (a) 1145 UTC. (b) 1445 UTC. (c) 1745 UTC. and (d) 2045 UTC.

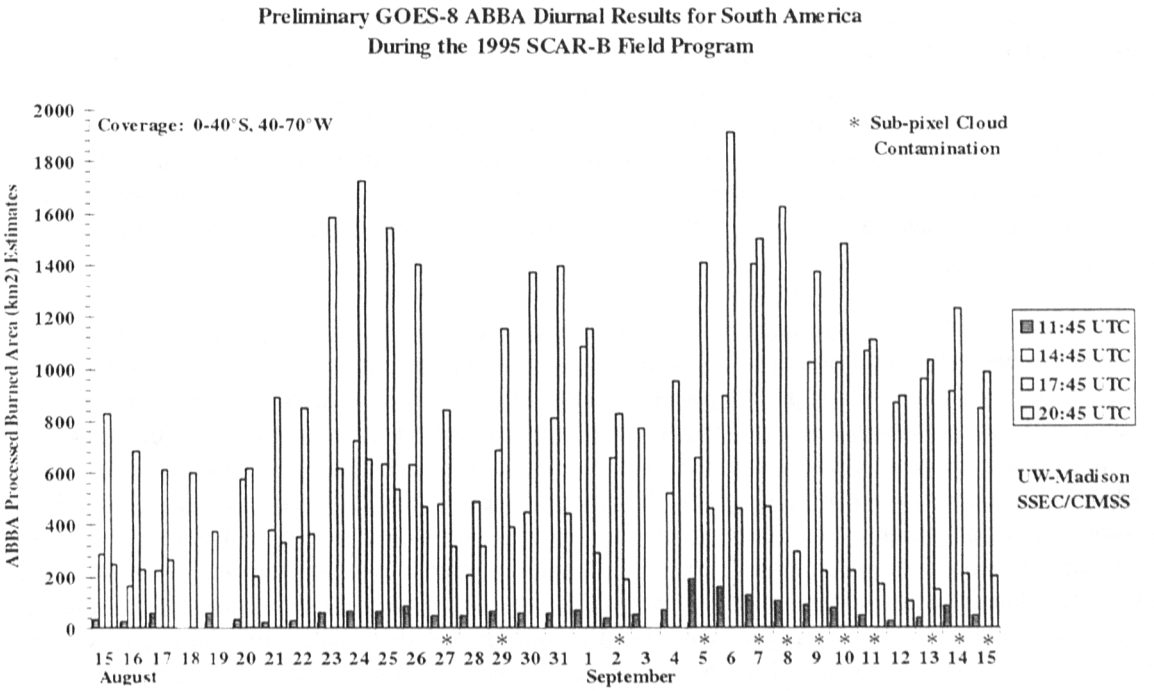

Figure 3. GOES-8 estimates of the burning area (in square kilometers) for 15 August to 15 September 1995 within the region 0 to 40 S and 40 to 70 W. Estimates are made with GOES-8 measurements at 1145, 1445, 1745, and 2045 UTC. Peak burning occurs at 1745 UTC on all days.

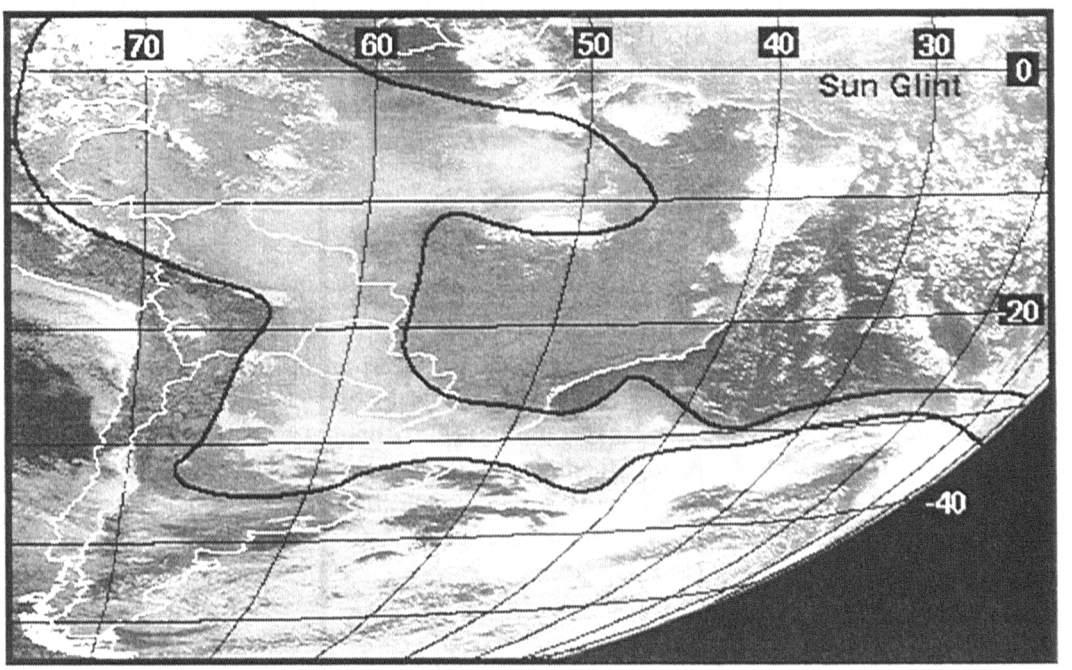

Figure 4. A large smoke pall (outlined in black) was observed in this GOES-8 visible image at 1145 UTC on the morning of 28 August 1995. The smoke extends over 6 million km^2. Once it exits the continent, a narrow band of smoke continues over the Atlantic Ocean extending to the prime meridian.

As in previous years, large smoke palls were identified in the GOES-8 visible imagery in August and September of 1995. Figure 4 shows a visible image of South America at 1145 UTC on the morning of 28 August, 1995. The smoke pall is outlined in black. It represents a combination of fresh and aged emissions from intense burning during the previous week associated with deforestation and agricultural applications. It covers over 6 million km^2. At the southern boundary it extends over the Atlantic Ocean to the edge of the satellite image. The burning practices and meteorological conditions which contributed to this episode are nearly identical to ones which resulted in a similar smoke pall observed during the last week of August 1988 [2].

A review of GOES visible and infrared satellite imagery over South America during previous burning seasons revealed several predominant examples of aerosol transport (see Figure 5) [5]. Anticyclonic flow exists throughout the Amazon Basin where easterly winds in the northern portion of the Amazon Basin transport the aerosols westward, and the Andes Mountains deflect the smoke to the south-southeast. Typically the smoke pall is limited to within the continent east of the Andes by a synoptic disturbance over the South Atlantic Ocean which extends along the eastern coast of South America (Figure 5, track a). Other examples of anticyclonic flow throughout the Amazon Basin resulted in transport out over the Atlantic Ocean near 30°S (Figure 5, track b). This transport regime is often associated with a stalled frontal boundary located south of the Amazon Basin which extends out over the ocean and acts as a barrier at the southern extent of the smoke pall allowing for aerosol transport over the ocean. Additionally, it has been observed that the smoke continued southward along the Andes Mountains into Bolivia, Paraguay, and Argentina instead of being channeled east toward the Atlantic Ocean (Figure 5, track c). In 1991 this was characterized by a lack of cyclonic activity off the coast of Argentina that might otherwise act to channel the emissions east. On several occasions the smoke plume extended south along the front range of the Andes into the southern half of Argentina at 40-50 °S. Lastly, in all years flow is observed from the Amazon Basin into the selva regions in the northwestern portion of the Brazilian Amazon and extending into Peru and Colombia (Figure 5, track d). This is often accompanied by a large scale convective complex associated with a frontal boundary extending from the front range of the Andes Mountains and across the southern and eastern sections of the Amazon Basin.

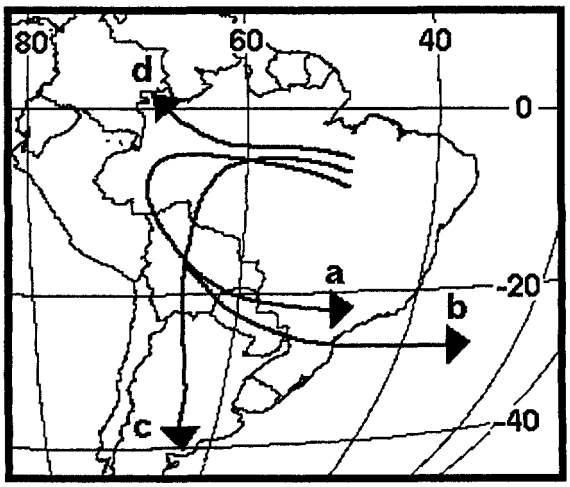

Figure 5. The four labeled trajectories (a, b, c, and d) represent the most common smoke/aerosol transport regimes observed in GOES satellite imagery during six biomass burning seasons (1983, 1988, 1989, 1991, 1994, and 1995).

In order to quantitatively document the extent of smoke/aerosols associated with biomass burning using satellite imagery, it is necessary to be able to distinguish between multi-level clouds, low-level moisture and smoke. Recent work [5] has shown the feasibility of using GOES VIS, SIRW, LIRW, and DIRW data in an automated multispectral thresholding scheme to distinguish smoke/aerosols from other multi-level clouds and low-level moisture (see Table 3). In visible imagery smoke often appears as a milky gray haze, but cirrus, low-level moisture, fog and other multi-level clouds can display the same signature. Some of these clouds can be distinguished from smoke/aerosol in the SIRW and LIRW bands by investigating brightness temperature limits in both bands and considering the SIRW minus LIRW difference. Since the best conditions for monitoring smoke/aerosols in South America are coincident with a low solar zenith angle, the effect of reflected solar radiation in the SIRW region is minimized. A large positive SIRW minus LIRW brightness temperature difference is often indicative of cirrus and a negative difference on the order of 4 °C can indicate stratus. The split window (LIRW and DIRW) bands offer additional help in detecting low-level moisture and the presence of clouds. They were designed to use differential water vapor absorption across this part of the spectrum to estimate the amount of water vapor in the lower atmosphere; the DIRW is more sensitive to water vapor absorption than the LIRW. For low visible brightness reflectance values and surface emissivity corrected brightness temperature differences greater than 5 °C, one can assume substantial amounts of low-level moisture. Semi-transparent cirrus which looks very similar to haze in the visible imagery often displays a relatively cold LIRW brightness temperature and can display a large LIRW minus DIRW brightness temperature difference due to the cirrus effective emissivity differences in the DIRW and LIRW spectral regions [10].

Table 3. GOES Multispectral Smoke/Aerosol Detection Algorithm

Test	VIS Counts	SIRW Temp (K)	LIRW Temp (K)	DIRW Temp (K)	SIRW-LIRW Temp (K)	LIRW-DIRW Temp (K)	Comments
1	60 ↔ 100						Limits the brightness count range to values indicative of haze
2		>285	>285		-4 ↔ +20		Screens for opaque clouds, cirrus, and stratus
3			>285	>280		-4 ↔ +6	Screens for low-level moisture, opaque clouds, and semi-transparent cirrus

This algorithm is still being tuned for applications to the 1995 GOES-8 data in South America. Preliminary delineation of smoke coverage during SCAR-B from visual inspection of the GOES-8 visible and multispectral infrared data is plotted in Figure 6. Smoke coverage between 5 and 7 million square kilometers is observed for the last week of August and the first week of September 1995; transport over the Atlantic was associated with many of those days.

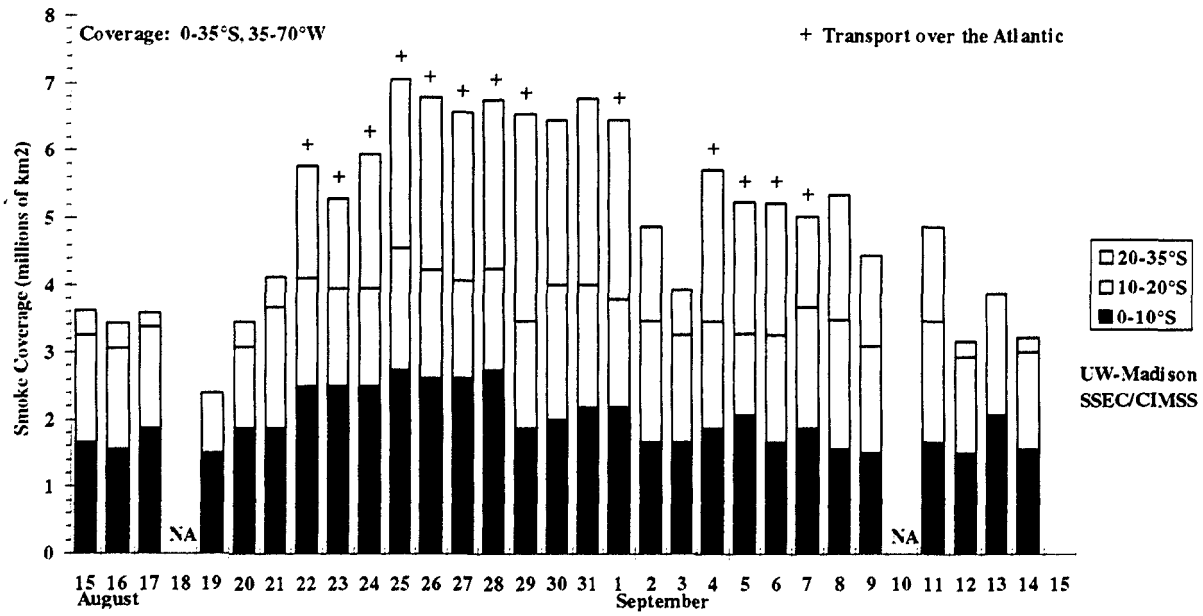

Figure 6. Estimates of daily smoke coverage from 0 to 35 S and 35 to 70 W observed in GOES-8 visible images during SCAR-B. Transport over the Atlantic Ocean is indicated by the symbol +. Smoke coverage in three latitudinal bands (0-10. 10-20. and 20-35 S) is also indicated.

5. CONCLUSIONS

GOES-8 is demonstrating enhanced capability to detect fires with infrared window data at 4 km resolution with .2 C noise. GOES-8 is detecting smaller fires and more of them than GOES-7; GOES-8 has already detected fires smaller than five acres. The GOES-8 operational schedule enables more frequent observations; routine imager coverage (in all five spectral bands) is scheduled every 30 minutes over South America and every 15 minutes over the continental United States. This enhanced capability can be used to assist with early detection of fires in remote regions of North and South America.

Estimation of the areal extent and temperature of a fire with the automated biomass burning algorithm (ABBA) shows good early results in comparison to controlled burns of known characteristics in North America. With the ABBA, GOES-8 continues to indicate a strong variation in the burning as a function of the time of day in South America; a preference for burning between 1500 and 1800 UTC indicated by GOES-7 over ten years is found again in 1995.

GOES-8 appears to be well suited to continue and improve the geostationary remote sensing capability that provides information on the diurnal signature in biomass burning, investigates aerosol transport, and monitors trends in biomass burning for the next decade throughout the Western Hemisphere.

6. REFERENCES

1. Menzel, W. P. and J. F. W. Purdom, "Introducing GOES-I: The first of a new generation of Geostationary Operational Environmental Satellites," Bull. Amer. Meteor. Soc., Vol. 75, No. 5, 757-781, 1994.

2. Prins, E. M., and W. P. Menzel, "Geostationary satellite detection of biomass burning in South America," Int. J. of Rem. Sensing, 13, 2783-2799, 1992.

3. Prins, E. M. and W. P. Menzel, "Trends in South American biomass burning detected with the GOES-VAS from 1983-1991," Jour. Geo. Rev., Vol. 99, No. D8, 16719-16735, 1994.

4. Matson, M., and J. Dozier, "Identification of subresolution high temperature sources using a thermal IR sensor," Photo. Engr. and Rem. Sens., 47, 1311-1318, 1981.

5. Prins, E. M., and W. P. Menzel, "Investigation of biomass burning and aerosol loading and transport utilizing geostationary satellite data," Accepted for publication in Biomass Burning and Global Change, edited by J. S. Levine, The MIT Press, Cambridge, MA, 1995.

6. Menzel, W. P., and E. M. Prins, "Monitoring biomass burning with the new generation of geostationary satellites," Accepted for publication in Biomass Burning and Global Change, edited by J.S. Levine, The MIT Press, Cambridge, MA, 1995.

7. Weaver, J., J. F. W. Purdom, and T. Schneider, "Observing forest fires with the GOES-8 3.9 μm imaging channel," Weather and Forecasting, 10, 803-808, 1995.

8. Ottmar, R., Personal Communication, United States Forest Service, Seattle Forestry Science Laboratory, Pacific Northwest Research Station, Seattle, Washington, 1995.

9. Prins, E. M. and W. P. Menzel, "Monitoring biomass burning and aerosol loading and transport from a geostationary perspective," Presented at the Seventh Symposium on Global Change Studies, Atlanta, GA, Jan. 28 - Feb. 2, 1996, pp. 160-166, 1996.

10. Inoue, T., "On the temperature and effective emissivity determination of semitransparent cirrus clouds by bi-spectral measurements in the 10 micron window region," J. Met. Soc. Japan., 63, 88-99, 1985.

Automated cloud-motion winds from GOES-8/9

Steve Nieman [1], W. Paul Menzel [2],
Christopher S. Velden [1] and Steve Wanzong [1]

[1] - Cooperative Institute for Meteorological Satellite Studies
Madison, Wisconsin

[2] - NOAA/NESDIS
Madison, Wisconsin

ABSTRACT

Automated procedures for deriving cloud-motion vectors (CMVs) from a series of geostationary images have been developed by the Cooperative Institute for Meteorological Satellite Studies (CIMSS) and have been operational in NOAA since 1993 [8]. Since that time, CIMSS has continued work to improve the processing techniques, upgrade the quality of the product, and add further capabilities. Scientific improvements include the addition of the water-vapor intercept technique for assigning heights to semi-transparent clouds, a new version of the automated quality control algorithm which reduces the large mean slow bias observed in the initial system, and improved selection of suitable tracers. These improvements have been successfully applied to the "Day 1" GOES-8/9 operational winds system in NOAA.

Research has already begun to define "Day 2" operations. Improved resolution and signal of the GOES-8/9 imager has made automated water-vapor motion vector (WVMV) production possible for the first time, enabling the measurement of wind velocities in clear air. Work has begun on an automated algorithm for imagery registration quality control and the optimal density for wind products as a function of coverage and computing power is being investigated.

keywords: GOES-8, GOES-9, cloud-drift, winds

2. EXAMPLE GOES-8/9 WINDS

NESDIS currently produces CMV and WVMV products in fully automated fashion at 0000, 0600, 1200 and 1800 UTC each day. An example of the resulting coverage is shown in figure 1. The combination of faster architecture and exclusive CPU access has led to an amazing increase in the amount of winds that can be produced, and NESDIS plans to increase the targeting density within operational processing tenfold by the end of 1996. Since full disk imagery is not available at a time interval conducive to feature tracking, wind products for each satellite must be done in 2 separate pieces which can be obtained half-hourly. The water vapor absorption band of the GOES-8/9 imager does not show features below about 500 hPa, so no low-level WVMVs are possible. However, the WVMVs do provide good information in clear regions where no clouds exist for tracking.

These products benefit from algorithm changes which have occurred over the last several years [9]. Improved tracer selection techniques for CMVs filter out regions of mixed-layer cloudiness and areas that are overly coherent (i.e. surface features), thereby saving computer time and allowing greater targeting density in regions of interest. CMV height assignment for semi-transparent clouds underwent a major overhaul due to the absence of a CO_2-absorption channel on the GOES-8/9 imager. H_2O-Intercept height assignment methodology, as initially used with Meteosat data, serves as an adequate replacement.

 0-8194-2200-2/96/$6.00

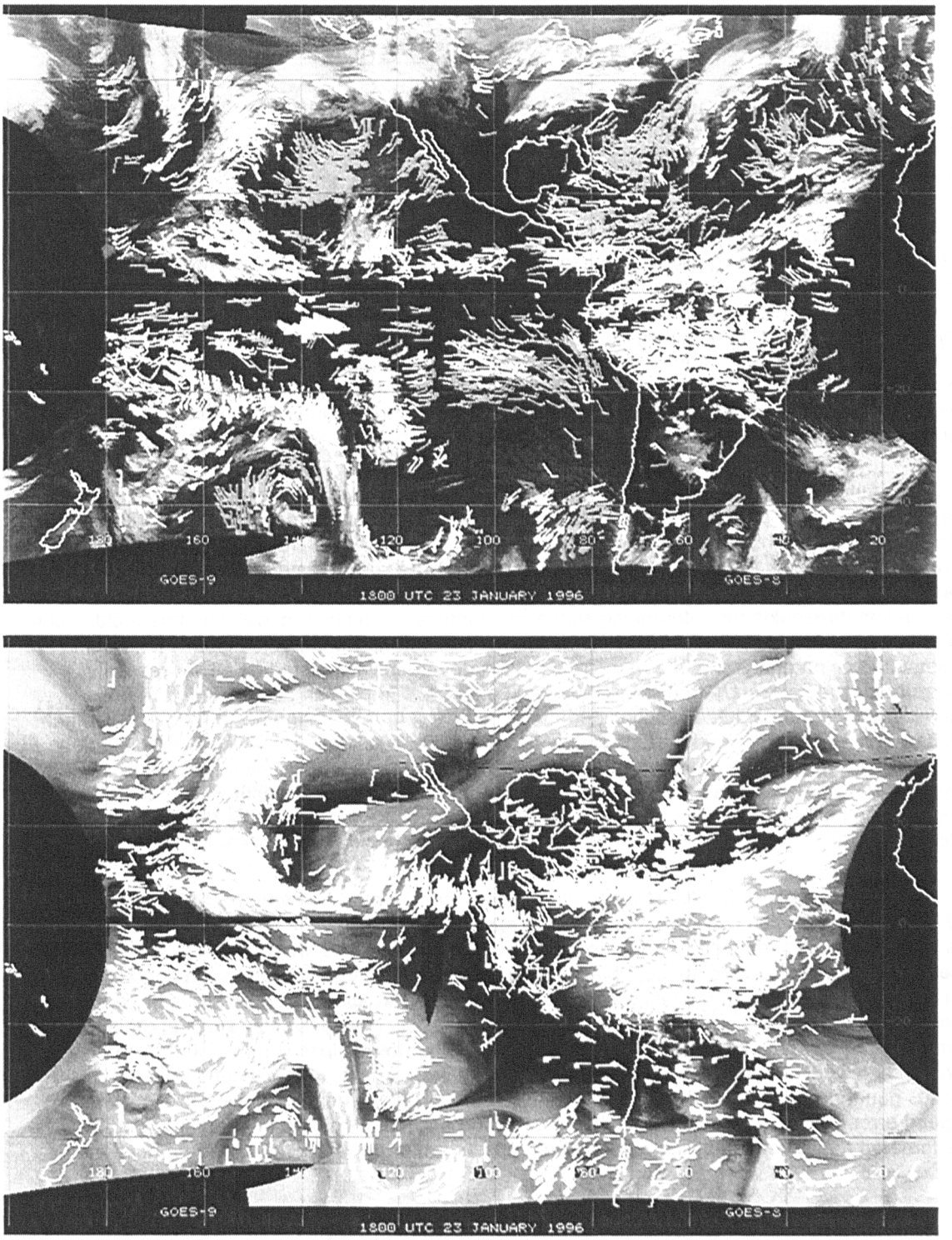

Figure 1. Example coverage available for GOES-8/9 CMV (top) and WVMV (bottom) products. High-level winds (100-699 hPa) are white. Low-level winds (700-950 hPa) are gray. Each image is a composite of the 4 separate pieces which are available for wind production.

3. IMAGERY REGISTRATION

Registration is a measure of the consistency of navigation between successive images. Features such as coastlines must remain stationary from image to image within a certain tolerance [7]. The winds production process is much more sensitive to changes in registration, than to errors in absolute Earth location (i.e. navigation).

The advent of a 3-axis stabilized system with GOES-8/9 has made navigation more challenging. Non-rotating satellites are subject to differential heating, especially near local-midnight, and the result is a reduced ability to consistently navigate the imagery. Local midnight for both GOES-8 (0600 UTC) and GOES-9 (1200 UTC) falls within operational wind production cycles. Furthermore, these navigation problems around local-midnight are worsened during the periods just before and just after the eclipse, which occur twice a year near the time of Solar Equinox. The effects on registration quality were apparent in early non-operational GOES-8/9 winds processing, prompting NESDIS to perform manual registration corrections. These corrections have been necessary for approximately 5-10 percent of all winds generation cycles.

Automated registration quality control relieves the burden of manual intervention by applying the same pattern matching techniques used in the automated tracking algorithm [8] to potential land features. Hundreds of initial landmark locations are screened for obvious cloud contamination using a spatial coherence analysis [1] of the surrounding imagery. Each resulting landmark is sought in subsequent imagery within a small spatial tolerance using extremely tight correlation thresholds for determining successful matches. The tight correlation thresholds act to further screen landmarks with cloud contamination. Potentially undetected cloudy landmarks are eliminated by an analysis of the mean registration deviations suggested by all successfully correlated landmarks. Up to one fourth of this landmark sample can be eliminated if gross differences from the originally suggested mean deviation in registration occur, and a new mean is derived from the remainder. This check also guards against cases in which the registration exhibits varying shifts in different regions of the image. If more than one fourth of the landmarks show a large amount of scatter, less than five landmarks remain, or the diagnosed registration deviations are less than a pre-determined tolerance, the process fails and nothing is done.

An example of the registration adjustments made by this software for all successful 0600 UTC winds generation cycles during the early part of 1996 is shown in figure 1. Since 0600 UTC is the closest winds generation cycle to local midnight for GOES-8, there is a loss of data in the center of the series due to imagery blackout periods during eclipse. Registration specifications around local midnight for images which are 30 minutes apart are about 2.25 km in the north-south direction and 3.1 km in the east-west direction [7]. Several days show shifts in registration which are beyond the specifications, but the period right after eclipse is most interesting. For well over a week, the imagery skipped to the west at least 3.5 km in the second image of the winds generation loop every day. Registration errors of this magnitude would lead to a wind speed error of approximately 2 meters/sec using the normal 30 minute imagery interval, thus the automated registration quality control algorithm is an important addition to wind production.

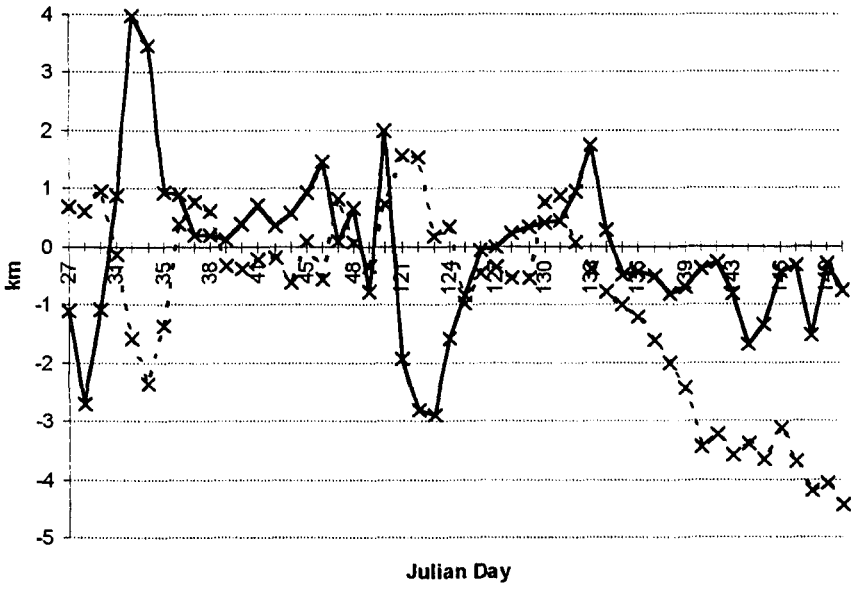

Figure 2. Daily registration shifts (km) between the 0415 and 0445 UTC Northern Hemisphere GOES-8 images as diagnosed by the automated registration quality control software. The solid line represents shifts in the NS direction. The dashed line represents shifts in the EW direction.

During research and development, only 400x400 pixel infra-red window images centered over the Baja Peninsula for GOES-8 and GOES-9 are obtained. Even with this strict limitation, the software is successful in diagnosing the quality of the imagery registration during winds generation cycles about 90 percent of the time, and corrections are suggested 5-10 percent of the time. The success rate varies depending on the time of day. Operational implementation by the Forecast Products Development Team of NESDIS will utilize a global landmark set, and it is expected that the success rate will then near 100 percent.

4. QUALITY CONTROL

An important improvement to the automated wind production system came with the new version of the automated quality control algorithm. The automated procedure for quality control and editing of the data has been well documented [2,4,5].

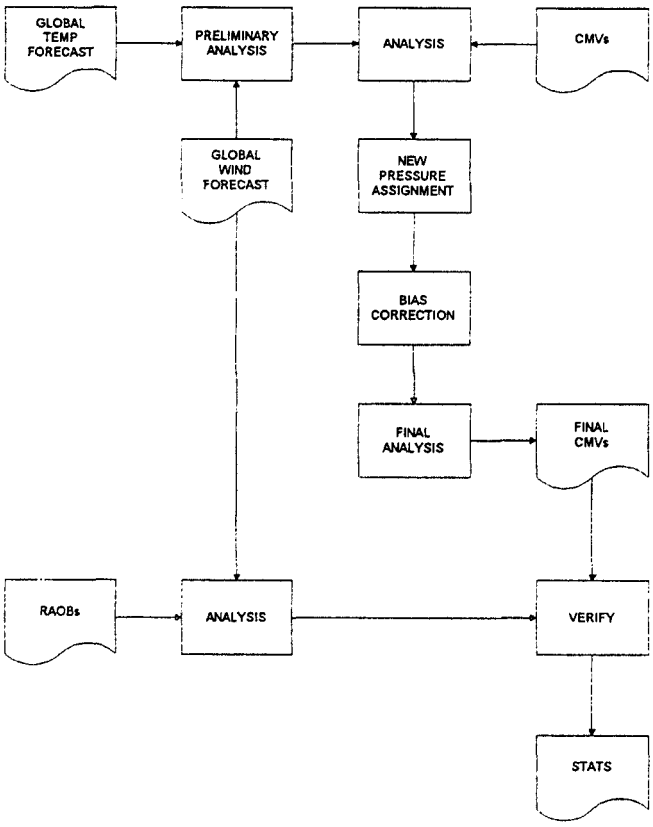

Figure 3. The automated editing system.

In practice, the automated editing algorithm is quite complicated (figure 2), but the methodology can be summarized in 4 main steps. A 3D recursive filter analysis [3] is performed on the available numerical forecast data. Satellite derived winds are incorporated into the analysis via a second pass of the recursive filter, and wind data which differs greatly from the preliminary analysis is eliminated. A penalty function defined by

$$B_{m,k} = \left(\frac{V_m - V_{i,j,k}}{F_v}\right)^2 + \left(\frac{T_m - T_{i,j,k}}{F_t}\right)^2 + \left(\frac{P_m - P_{i,j,k}}{F_p}\right)^2 + \left(\frac{dd_m - dd_{i,j,k}}{F_{dd}}\right)^2 + \left(\frac{s_m - s_{i,j,k}}{F_s}\right)^2 , \quad (2)$$

$V = velocity,\ T = temperature,\ P = pressure,\ dd = direction,\ s = speed$

is applied to the wind data and this second analysis for the purpose or re-assigning the height the heights of the winds to their level of best fit. In this equation, F represents the relative weight applied to each of the quantities shown, the subscripts (i,j,k) identify values from the analysis, and values subscripted by (m) refer to the wind measurements. Finally, another pass of the recursive filter is performed to assess the quality of the height re-assignments within the analyses, and quantitative estimates of the quality of each satellite derived wind are output.

Numerous suggestions from the operational community have found their way into the latest version. The pressure reassignment is now constrained to 150 hPa by the algorithm. A small percentage of the vectors (< 5 percent) are eliminated by this added constraint. Also, the revised editor has tightened the tropopause check to a threshold lapse rate of less than 0.5 K per

25 hPa above 300 hPa in hopes that it will be less likely to re-assign heights to some stratospheric value.

The revised editor contains an adjustment for the well documented slow bias of CMVs. The quarterly statistical summaries of the ECMWF routinely show this feature, with respect to both wind measurements and coincident speeds of the ECMWF forecast. For GOES-7 winds produced with the old automated system, the bias could reach -5 ms^{-1} at higher wind speeds. The bias is also present in comparisons with the NMC aviation forecasts, which are used in the derivation and quality control of GOES CMVs. To mitigate this slow bias, the revised editing procedure now increments each vector with seven percent of the speed of the forecast, interpolated to its reassigned level, provided that the forecast wind speed is greater than 10 ms^{-1}. Philosophically, this is no different from the bias corrections routinely applied to radiance measurements to achieve agreement with forward calculations.

The basic tool of the objective editor remains the 3-dimensional recursive filter objective analysis. This system has undergone an extensive upgrade with attention to improving quality control, especially the recursive-filter-flag (RFF), which is appended to each datum following the analysis. Differences in vector root-mean square error [6] with respect to rawinsonde observations throughout the range of acceptable RFF flags amounted to 0.5 ms^{-1} in the old algorithm. The new configuration shows an expanded range from the lowest acceptable RFF values to the highest (Table 1).

The RFF is a reflection of vector fit of each wind to the analysis of forecast data and the winds themselves. It is influenced by other nearby reports (i.e. neighbor vectors) and the background forecast. In areas of high vector density and reasonable forecast quality the RFF can be considered a reliable indicator of vector quality. However, in meteorolological situations leading to poor model forecasts (e.g. hurricanes, deepening extratropical storms), the RFF should not be considered a pure indicator of vector quality, or as a linear weighting factor in data assimilation. More research is planned to understand the use of RFF in such areas.

Table 1. GOES-8/9 operational CMV and WVMV comparison with rawinsondes for March-May 1996. SMVD is the mean vector difference, SRMSE is the root mean square difference, and SPD is rawinsonde mean speed.

PRODUCT	QC FLAG (RFF)	NUM	SMVD	SRMSE	SPD
GOES-8 CMV	50-60	1368	6.36	7.61	19.86
	60-70	1684	5.35	6.60	17.85
	70-80	1167	4.89	6.15	17.03
GOES-9 CMV	50-60	725	6.44	7.66	19.73
	60-70	950	5.17	6.31	17.72
	70-80	626	4.96	5.99	17.32
GOES-8 WVMV	50-60	4894	7.03	8.38	21.96
	60-70	5816	6.01	7.40	21.37
	70-80	3436	5.57	7.07	20.48
GOES-9 WVMV	50-60	2455	6.75	7.99	21.95
	60-70	2985	5.89	7.02	20.98
	70-80	1763	5.43	6.68	19.93

5. WINDS PERFORMANCE SINCE 1992

A useful verification source comes from the European Center for Medium Range Weather Forecasting (ECMWF), which produces statistics of wind comparisons to their model for not only operational METEOSAT wind products, but all the major operational wind products, including GOES, GMS and INSAT. Verification statistics for the GOES-7/8 cloud drift winds over the last 4 years as reported quarterly by ECMWF are shown in figure 3. NESDIS stopped doing operational GOES-7 winds in January 1996 when the data availability ended. Thus, the last two quarters shown in the graph reflect GOES-8 wind accuracy. As of January, ECMWF has also begun evaluating GOES-9 winds (not shown). Mean Vector RMS difference [6] and bias are shown for low, mid and high level winds. Verification statistics are somewhat better than average during each warm season due to reduced mean wind speed.

The quality of NESDIS operational high- and mid-level cloud-drift winds has improved every year for the past 4 years, despite a gradual increase in automation over the period. In the fall of 1994 the winds production process was ported from the IBM mainframe to workstations. At this time, the upgraded automated quality control algorithm [3] became operational, and operators at the Satellite Analysis Branch (SAB) lost the ability to manually augment the product in limited areas. Throughout GOES-7 production, SAB continued to perform manual quality control after automated production was finished, deleting about one third of available vectors. This practice has now ended due to the large volume of data that now needs to be processed. The operational GOES-8 cloud-drift wind products are fully automated, with no loss of product quality and, in fact, an increased number of vectors.

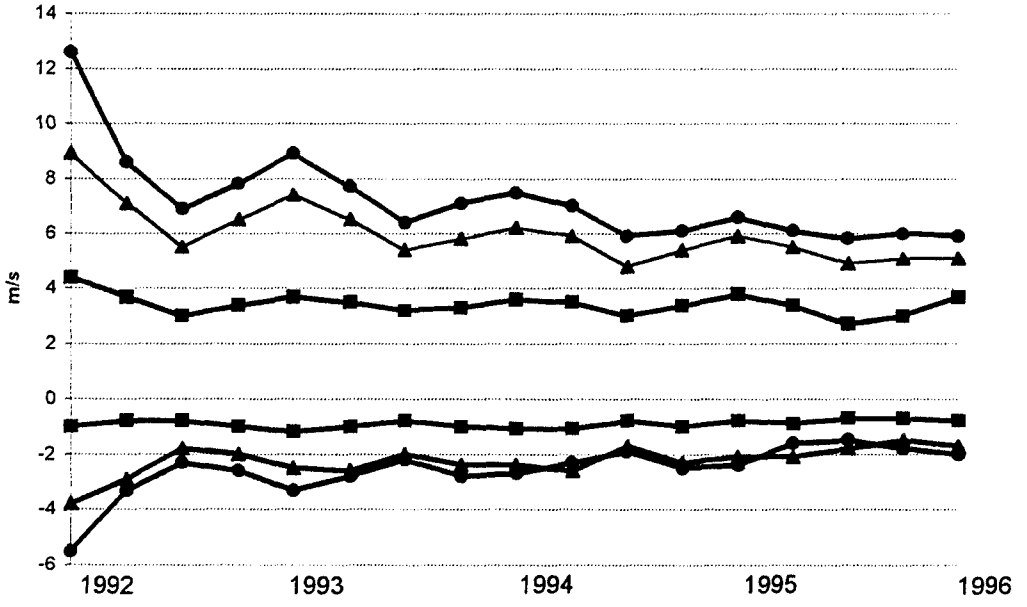

Figure 3. **GOES-7/8 verification statistics with respect to ECMWF model analyses within the Northern Hemisphere extratropical regions as reported by ECMWF. The top three curves represent mean vector RMS differences for high (circle), mid (triangle) and low (square) cloud-drift winds. The bottom three curves are labeled similarly and represent mean bias.**

6. CONCLUSIONS

The GOES-8 automated cloud motion vectors are significantly improved. Operational automated cloud motion vectors are now equal or superior in quality to those which had the benefit of manual quality control a few years ago. The single most important factor in this improvement has been the upgraded auto-editor. Improved tracer selection procedures eliminate targets in difficult regions and allow a higher target density and therefore enhanced coverage in areas of interest. The incorporation of the H2O-intercept height assignment method allows an adequate representation of the heights of semi-transparent clouds in the absence of a CO2-absorption channel. GOES-8 water-vapor motion winds resulting from the automated system are superior to any done previously by NESDIS and should now be considered as an operational product.

7. REFERENCES

1. Coakley,J. and F. Bretherton, 1982: Cloud cover from high resolution scanner data; detecting and allowing for partially filled fields of view. *J. Geophys. Res.*, **87**, C7, 4917-4932.

2. Hayden,C.M. and S.J. Nieman, 1996: A primer for tuning the automated quality control system and for verifying satellite-measured drift winds. *Submitted as a NOAA Tech memo.*

3. Hayden,C.M. and R.J. Purser, 1995: Recursive filter objective analysis of meteorological fields, applications to NESDIS operational processing., *J. Appl. Meteor.*, **34**, 3-15.

4. Hayden,C.M., 1993: Recent research in the automated quality control of cloud motion vectors at CIMSS/NESDIS. *Proceedings of the Second International Winds Workshop*, Tokyo, Japan. December 13-16. 219-226.

5 Hayden,C.M. and C.S. Velden, 1991: Quality control and assimilation experiments with satellite derived wind estimates. *9th Conf. Num. Wea. Pred.*, Denver, CO, Amer. Meteor. Soc., 19-23.

6. Menzel,W.P., Hayden,C.M., Nieman,S.J., Wanzong,S. and C.S. Velden, 1996: Improvements in the quality assessment of automated satellite-motion winds. *Third Int. Wind Workshop*. Monte-Verita-Ascona, Switzerland. 10-12 June.

7. Menzel,W.P. and J.F.W. Purdom, 1994: Introducing GOES-I:The first of a new generation of geostationary operational environmental satellites. *Bull. Amer. Met. Soc.*, **75**, 757-781.

8. Merrill,R., W.P. Menzel, W. Baker, J. Lynch and E. Legg, 1991: A report on the recent demonstration of NOAA's upgraded capability to derive cloud motion satellite winds. *Bull. Amer. Meteor. Soc.*, 72, 372-376.

9. Nieman,S.J., Menzel,W.P., Hayden,C.M., Wanzong,S. and C. S. Velden, 1996: Upgrades to the NOAA/NESDIS automated cloud-motion vector system. *Eig. Conf on Sat. Met. and Ocean.*, Atlanta, GA, AMS, 1-4.

10. Nieman,S.J., Menzel,W.P., Hayden,C.M., Gray,D.,Wanzong,S.T., Velden,C.S. and J. Daniels, 1997: Fully automated cloud-drift winds in the operational environment. *Submitted to Bull. Amer, Met. Soc.,* July, 1996.

Variability of marine stratiform clouds derived from GOES-8 imagery

Gyula I. Molnar

Universities Space Research Association, NASA-GSFC, Code 913, Greenbelt, Maryland 20771

Dennis Chesters

Climate and Radiation Branch, NASA-GSFC, Code 913, Greenbelt, Maryland 20771

ABSTRACT

Marine stratiform clouds (MSC) cover large areas of the globe that are visible to GOES. The operational satellite cloud retrieval algorithms are prone to biases when analyzing MSC, due to the often sub-pixel size cloud elements and radiative temperatures close to that of the underlying ocean. For example, the relatively large pixel size and calibration drifts in GOES-7 imagery have made it difficult to extract unbiased MSC properties using thermal threshold techniques.

Here, we apply a novel retrieval approach to the two important MSC regimes which can be monitored well from the GOES-8 satellite: the Pacific Ocean just west of California/Baja and Peru/Chile. MSC cloud parameters for these areas are retrieved together with surface temperature and column water vapor in a temporally and spatially consistent manner that is insensitive to sensor resolution and calibration errors.

Semi-operational analysis of GOES-8 imagery began in December 1995. So, the main focus is on assessing the diurnal variability of MSC. Following a brief description of the retrieval technique, we present initial results describing the full diurnal cycle of MSC fractional cloud cover and cloud top temperature, monitored using the single-channel (infrared-window) version of the algorithm. In addition, we address the daytime variability of other important cloud parameters (cloud visible optical thickness/albedo, infrared emissivity) using a bispectral extension of the retrieval scheme. The results are also compared with other pertinent MSC analyses.

KEYWORDS: clouds, stratiform, retrieval, climate, goes

1. INTRODUCTION

It is difficult to reliably assess the role of clouds from long-term satellite analyses because the current operational cloud retrieval algorithms are sensitive to sensor resolution and uneven calibration. Limited spatial resolution results in sub-pixel size cloud elements, which are a particularly common for low level **M**arine **S**tratiform **C**loudiness (**MSC**). This may seriously hinder climate predictions, because cloud radiative forcing is the largest for boundary layer clouds[1,2,3]. Previous climatologies of MSC employed threshold (TH) techniques, which assume that the pixels are *fully cloudy or completely clear.* TH methods are sensitive to both sensor resolution and uneven calibration, mainly because they do not account for partially cloudy pixels[4,5,6] (PCPs). In the meantime, according to general circulation model (GCM) simulations, the proper assessment of MSC's role during climate changes requires an approximately 1% accuracy in the absolute cloud amount[7]. Unfortunately, boundary layer clouds such as MSC are poorly represented in GCMs[8].

In this study we provide a multispectral GOES-8 imagery based climatology of important MSC properties, and simultaneously retrieved sea surface temperature (SST) as well as columnar water vapor amount (CWV) on the GCM grid (regional) scale, with future, useful GCM parameterizations in mind. Unlike previous climatologies, we allow for the presence of PCPs. The significance of accounting for PCPs is particularly high when applying *multispectral* analyses to infer cloud optical properties in addition to fractional cloud cover and cloud top height information. For example, Ref. 9 shows the following case: a visible reflectivity of 0.23 could be interpreted as a cloud optical thickness, $\tau = 5$, assuming $A_C = 1.00$. The same reflectivity, however, could be due to reflection from a broken cloud system with $A_C = 0.34$ and $\tau =$

0-8194-2200-2/96/$6.00

30. Comparing high resolution (LANDSAT with nominal resolution of ~1/16 km) and nominal ISCCP resolution (~8 km) analyses, Harshvardhan *et al.*[10] have found that the coarser resolution analysis overestimates cloud fraction except for scenes with small amounts of scattered clouds. For such cases, the low resolution results in the (much larger) pixels being classified as clear. Moreover, the coarse resolution analysis underestimates the optical depth for partly cloudy scenes, and this underestimate can be substantial. Surprisingly, despite significant efforts to better understand MSC behavior (*e. g.*, **FIRE** and **ASTEX** campaigns), *there are no large-scale bispectral (e. g., visible/IR window) MSC analyses performed so far which allow for partially cloudy pixels {PCPs}.*

Our analysis eventually will span a full year and will include about *80-times larger* sample than the largest of the previous studies which also allowed for PCPs[11]. The Ref. 4 and Ref. 11 studies indicate that cloud *semitransparency* often occurs not only for cirrus but even for MSC, *i. e.*, infrared (IR) emissivity (ε) is not always close to unity, especially near cloud edges. Our method also allows for semitransparency besides PCPs. An important aspect of the GOES data usage is that it will improve MSC parameterizations by allowing to assess the often significant diurnal cycle of MSC properties.

2. INPUT DATA

Our data source is the GOES-8 imagery data stream, received locally. Because the data are saved for only a few days, a semi-operational approach is used; our first-pass analysis is performed on the pixel-by-pixel scale, but only the summary results representing 64 x 64 IR pixels (*i. e.*, a 'regional', about 250 km x 250 km scale, referred to as *frames*) are saved for future, second-pass analysis. Besides the diurnal cycle, MSC parameters show strong variability and interdependence with large scale climatic parameters on the seasonal scale as well. However, only the boreal winter and spring months data have been subjected to first-pass analyses so far, so our second-pass analyses will focus on the diurnal cycle.

The areas of study are depicted on Figures 1-2. There are 4, 9, 16 and 36 64x64 IR pixel size frames in the off CA/Baja Upper/Lower-, and in the off Peru/Chile Upper/Lower-regions, respectively. The time period of the full study spans from December 1995 till Nov. 1997. Diurnal sampling for these areas is every 3 hours, except when satellite eclipse restricts us to 7 samplings a day. It occurs approximately at 600 UTC, affecting late winter and early spring imagery. A simple quality control is also performed; beside eclipse, the other major problem with images is striping. To assure that it does not affect our analysis, we visually inspect all of the images for all of the spectral channels used, and also perform objective striping amount assessments/corrections. This latter numerical check discards scenes where there were more than four consecutive scan lines missing, or the total area of missing lines was more than 5% of the scene. In all other cases the missing scanline pixels are replaced by linearly interpolated values from the 2 nearest neighbor pixels. In addition, no scenes affected by sun-glint are processed either. Note that only ~6% of the scenes had to discarded due to the above-mentioned problems so far.

3. RETRIEVAL APPROACH

We *combine* the "Triangle Technique" or **TT**[12,13,14] with the Visible/IR retrieval scheme, suggested by Platt[15] for application to geostationary satellite imagery. Fig. 3 shows an illustration of the **TT** for a 64 x 64 pixel size "scene" of simulated 11 μm radiances, created using ***2X1*** pixel arrays for the Local Standard Deviation*vs.* Local Mean Radiance plot [*cf.*, Ref. 16]. The subresolution pixels have randomly varying cloud fractions in the range [0;1].

The appearance of a triangle shape envelope is rather striking, and intersections of this envelope with the X axis are the radiances of the cloud layer (I_C) and the surface (I_S) for single-layered cloud systems. Thus, allowing for PCPs (but assuming opaque clouds), we obtain the same expression for the fractional MSC cover as the Spatial Coherence Method (SCM) of Coakley and Bretherton[16]:

$$A_C = [I_{av} - I_S]/[I_C - I_S], \qquad (1)$$

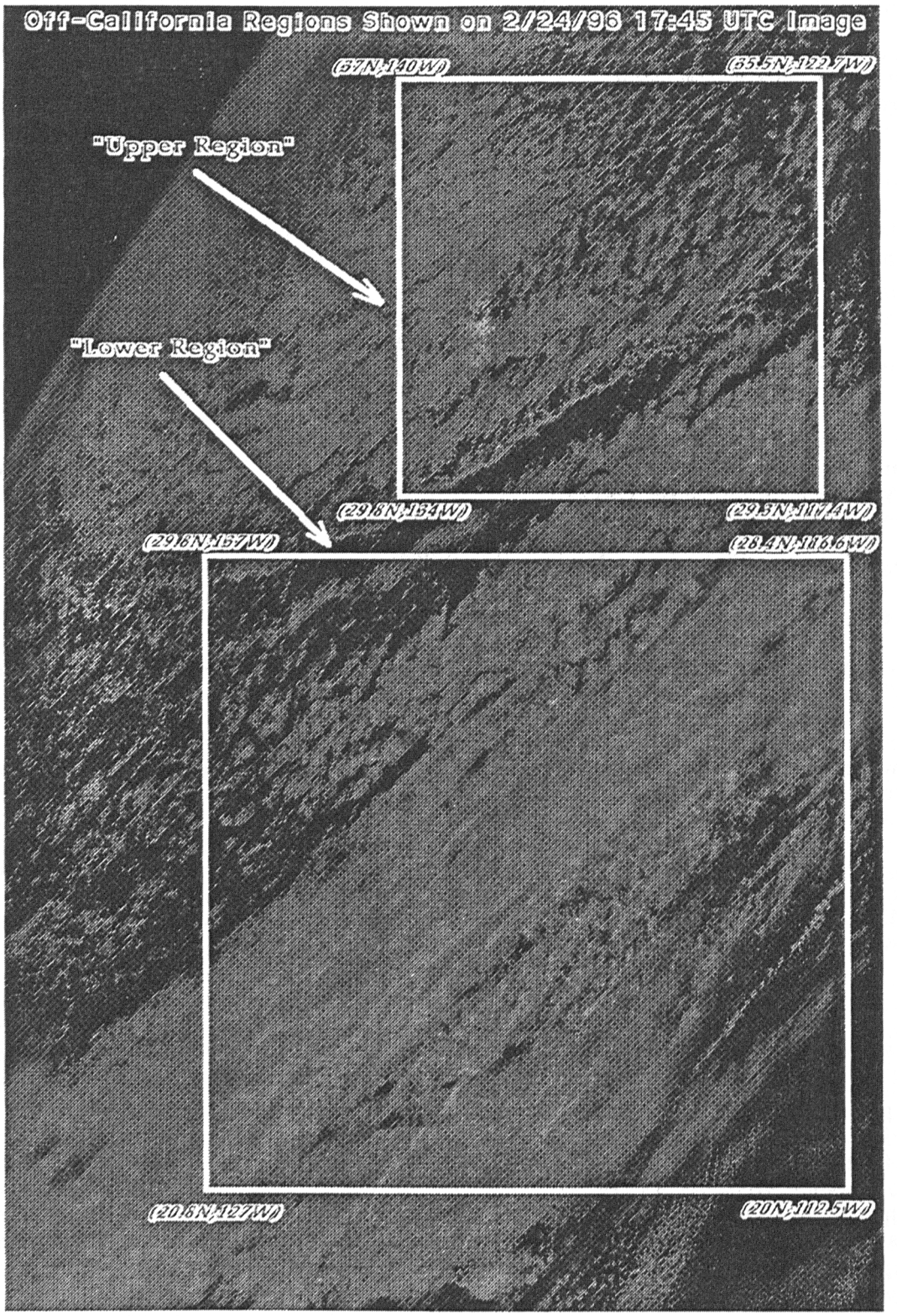

Figure 1: Illustration of the Analysis Regions West of CA/Baja

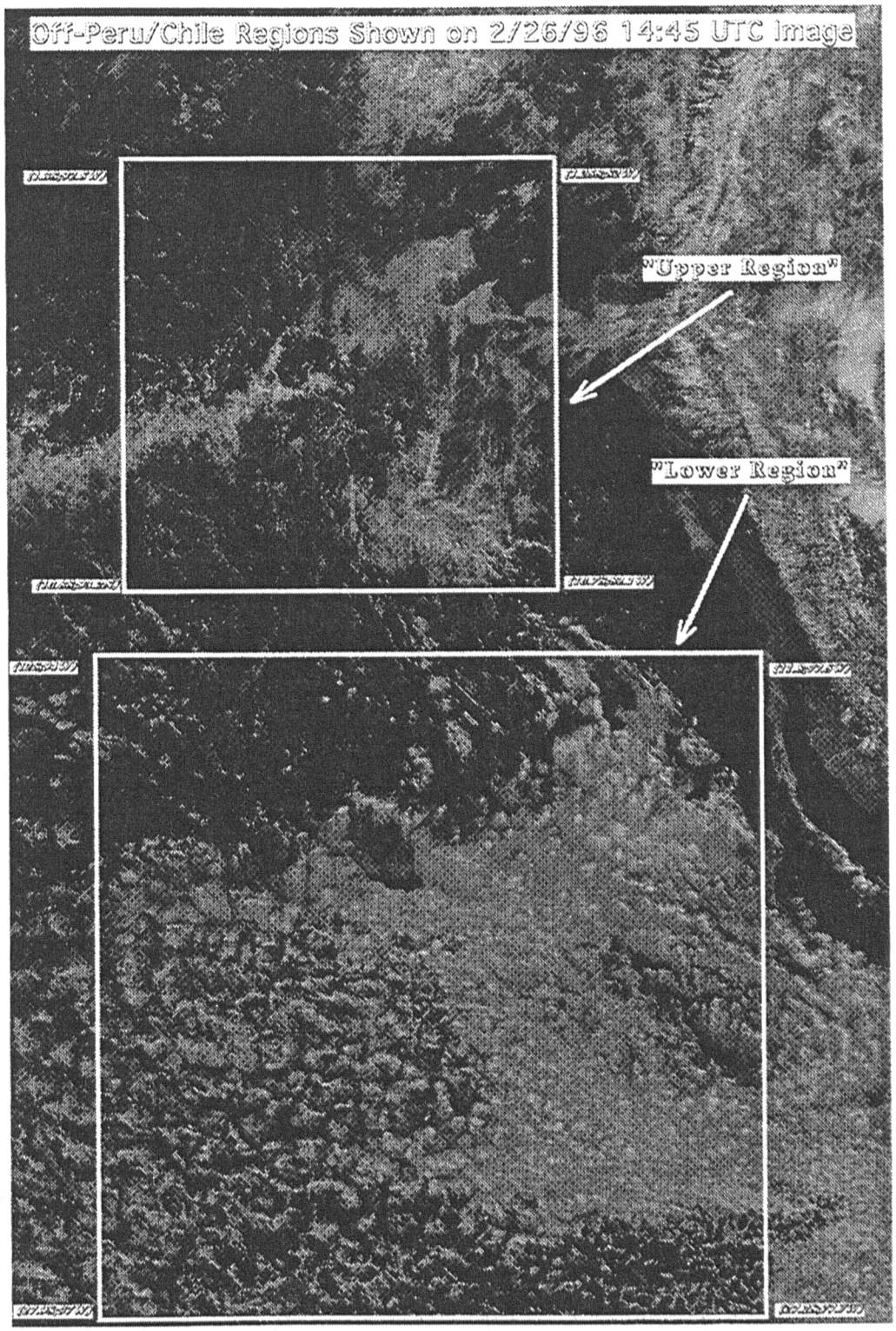

Figure 2: Illustration of the Analysis Regions West of Peru/Chile

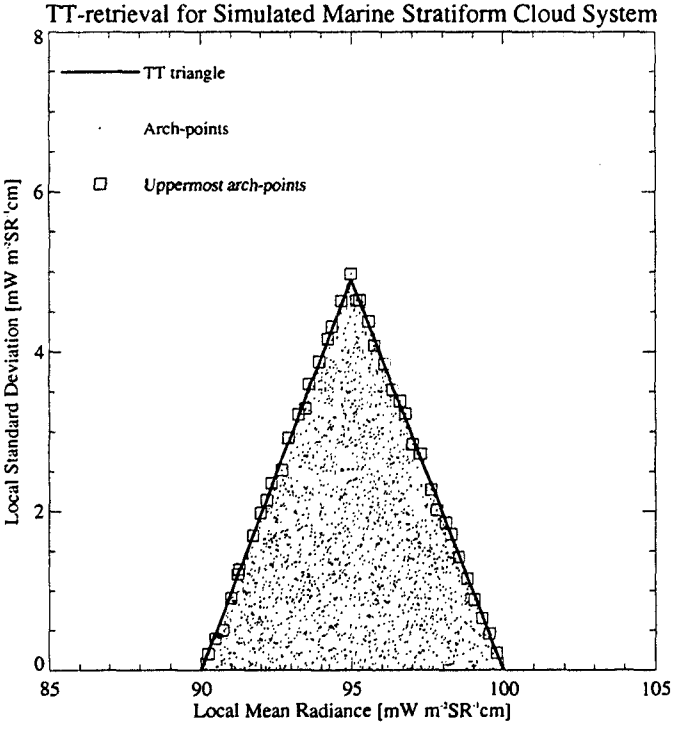

Figure 3: Illustration of the Triangle Technique

where I_{av} is the radiance measured by the satellite. In general, however, clouds can be semitransparent. Recent investigations[4,11] indicate that for MSC, infrared window absorption emittance, ε is often less than unity, most likely near cloud edges. Better understanding of MSC variability, necessary for improved model parameterizations and global climate change predictions, would require the separate monitoring of MSC fractional cover, ε, as well as albedo/reflectivity, particle size and optical thickness. In the following we discuss how a major part of this task can be achieved by combining the IR window TT results with radiance information from a visible channel. This retrieval method will be referred to as the bispectral scheme or **BS** for short.

In an IR window channel (around 11 μm), the pixel-radiance can be written as:

$$I_{av} = \varepsilon A_c I_c + (1-\varepsilon)A_c I_s + (1-A_c)I_s. \qquad (2)$$

Note that we neglect atmospheric attenuation in the IR window for the sake of simplicity. Obviously, additional information is needed to determine the cloud cover and emissivity separately. In this study we elected to use visible channel information, in part because there were previous efforts which we could implement in our scheme, and because we wanted to make comparisons with the Luo *et al.*[11] results, which used an IR-only technique[17] to determine these parameters for MSC off the Peruvian coast.

Assuming an isotropically reflecting cloud, the reflected radiance (assumed constant with the nadir angle ξ of the cloud at the satellite, and the azimuth angle ϕ between the solar and satellite directions) measured in a given pixel can be expressed as[15]:

$$R(\theta) = S\pi^{-1}\{A_c\alpha_c + (1-A_c\alpha_d)^2\alpha_s/(1-\alpha_d\alpha_s)\}, \quad (3)$$

where θ is the solar zenith angle, S is the incoming shortwave spectral solar flux {centered at ~0.65 μm for the GOES-8 visible channel); α_c is the (θ-dependent) cloud albedo to direct solar radiation; α_s is the surface albedo and α_d is the diffuse albedo. The derivation of the above equation includes multiple (diffuse) reflections between the cloud and the surface. The effects of Rayleigh scattering neglected. Following Platt[15], for the sake of simplicity, we neglect other atmospheric constituents (*e. g.*, aerosols) affecting the reflectivity. Note that according to the careful error analysis presented by Platnick and Valero[18], other types of relatively large errors inherent in similar bispectral retrieval methods make this simplification justified. The absorption emittance is given as[19]:

$$\varepsilon(\xi) = 1 - \exp(-\tau_c g^{-1}\sec\xi), \quad (4)$$

where the g factor is the ratio of visible optical depth to the IR absorption optical depth. For water clouds and for boundary layer clouds in particular, the value of g ~2.5[15,20]. There are more unknowns than equations, but we can use the fact that the α_c and ε quantities are linked through the basic scattering and absorption properties of the cloud particles. We adopted the Platt[15] computations of the α_c vs. $\varepsilon(\xi)$ as well as the ε vs. α_d relationships ("look-up tables" for various θ values). We assumed a fixed Lambertian open ocean albedo of 0.06, following Refs. 18 and 21.

We have also added a "water vapor correction scheme", which, over oceans provides an estimate of the CWV as well as SST, using both far IR window channels of the GOES imager. For the former we use the Stephens[22] formula, which provides CWV as a function of SST. It has been shown to be quite accurate over most oceanic areas[23]. Jackson and Stephens[24] further investigated this SST-CWV correlation, and has found that over the MSC regions even the *local* correlations are high. For the latter, we adopted the 2-channel CPSST algorithm[25], because of the similarity of the AVHRR and GOES-8 11 μm and 12 μm IR window channels. Since water vapor is the most important absorber over the tropical/subtropical oceans in this spectral region[26], SST is expected to be determined rather accurately even for areas covered overwhelmingly by PCPs. In summary, *simultaneous* SST, water vapor column amount and cloud properties could be retrieved, and even if *absolute* SSTs (or cloud optical properties) may not be attained with operational quality, the *variability* of these climatically important parameters as well as their *interdependency* could be well explored.

During the actual first-pass analysis procedure, we perform trispectral [visible & split window channels] daytime-, as well as bispectral [split window channels] nighttime-analyses and create summary diagnostics on regional {~250km X 250km} scales for the second-pass analyses. The Split Window Channels allow for SST and CWV retrievals over the full diurnal cycle. According to recent studies[4,11], the IR-only cloud fractions are biased due to commonly occurring MSC semitransparency. Furthermore, our BS method can provide MSC emissivity values only at daytime. In order to assess the full diurnal cycle of these parameters, we correct the IR-only cloud fractions, and also compute nighttime emissivities based on the BS analyses. This is achieved by performing linear regressions between bispectral and IR-only MSC cloud fractions as well as between MSC emissivities and IR-only cloud fractions on the regional scale for each month. The scatterplots on Fig. 4 show typical examples.

The correlation coefficients are particularly high for the BS versus IR-only cloud fraction regressions, whilst they are somewhat lower for the emissivity versus IR-only cloud fractions. These regression coefficients are then used to obtain the full diurnal cycle of MSC (bispectrally-corrected) fraction and IR emissivity.

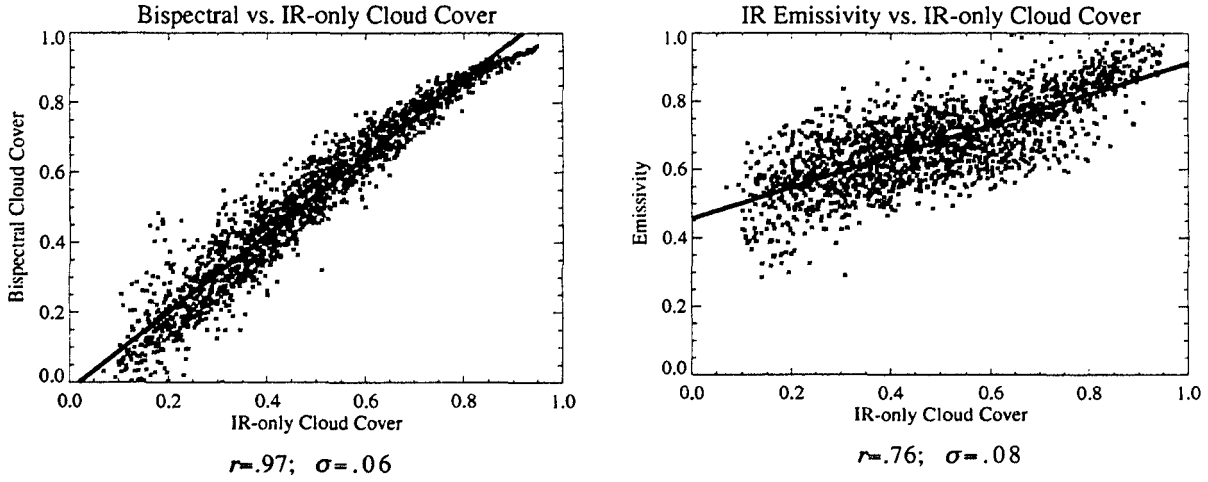

Figure 4: Linear regressions for determining the full diurnal cycle of fractional cloud cover and emissivity for February, 1996 (off-Peru/Chile Lower Region)

It is interesting note that the rather high correlations between *regional scale* MSC cloud fractions and emissivities obtained by us as well as by Luo *et al.*[11] seem to contradict the Harshvardhan *et al.*[10] finding that there is practically no correction between MSC cloud fraction and optical thickness. The latter finding appears to be unexpected in view of their direct relationship [see Eq. (4)] on the *pixel scale*. Thus, to clarify the picture, we also correlated the regional scale cloud fraction with optical thickness; there were no appreciable correlations in any month (most of the correlation coefficients were under 0.15, the largest being 0.28).

Apparently, most of the pixel scale optical thickness variability occurs in the emissivity regime where it changes little even for large optical depth variations, due to the strong non-linearity of Eq. (4). Consequently, the regional scale average (over thousands of pixels) optical depth will loose correlation with emissivity, thus with cloud fraction, *i. e.,* all of the studies are right.

4. RESULTS

Since we are focusing only on MSC, no frames with middle- and high-level cloud 'contamination' were considered. MSC was allowed to have cloud tops up to 3 km (assuming a standard, 6.5 K/km lapse rate) in this study. Overall, about 35% of frames had to be discarded due to this selection criterion, and this number was highly variable depending on location and season. For example, almost 70% of off-CA/Baja frames had to be omitted in the winter. Although, for the sake of preliminary intercomparisons, we will present monthly and/or seasonal analysis results, due to the essentially uncalibrated nature of the GOES-8 visible channel, our emphasis will be on the diurnal variability of MSC properties. Fig. 5 illustrates the typical summertime daytime behavior of MSC off the South-American coast: near sunrise the MSC reflectivity and fractional cloud cover are at maximum; as the solar insolation increases the reflectivity around the "bright spots" (areas of substantial boundary layer cumulus convection) decreases, and near sunset even the areas of thin stratocumulus (areas between the bright spots) break up, leading to a substantial fractional cloud cover decrease. Similar behavior was described, for example, by Klein *et al.*,[27] and Rozendaal *et al.*[28], consistent with the control of the diurnal cloud cover cycle by the diurnal cycle of solar insolation [*e. g.*, Turton and Nicholls[29]]. Conversely, less diurnal variability can be seen on similar image series (not shown) in the off CA/Baja MSC at the same time (*i. e.,* in winter). These observations are quantitatively illustrated in Figs. 6-10, depicting the full diurnal cycle of cloud fraction, cloud emissivity, and cloud top temperatures.

The Figures clearly underline the significant role of diurnal solar radiation forcing in the MSC diurnal development-dissipation cycle. For example the off-CA/Baja regions exhibit significantly less diurnal variability, apparently due to the smaller Northern Hemispheric insolation for the period analyzed so far.

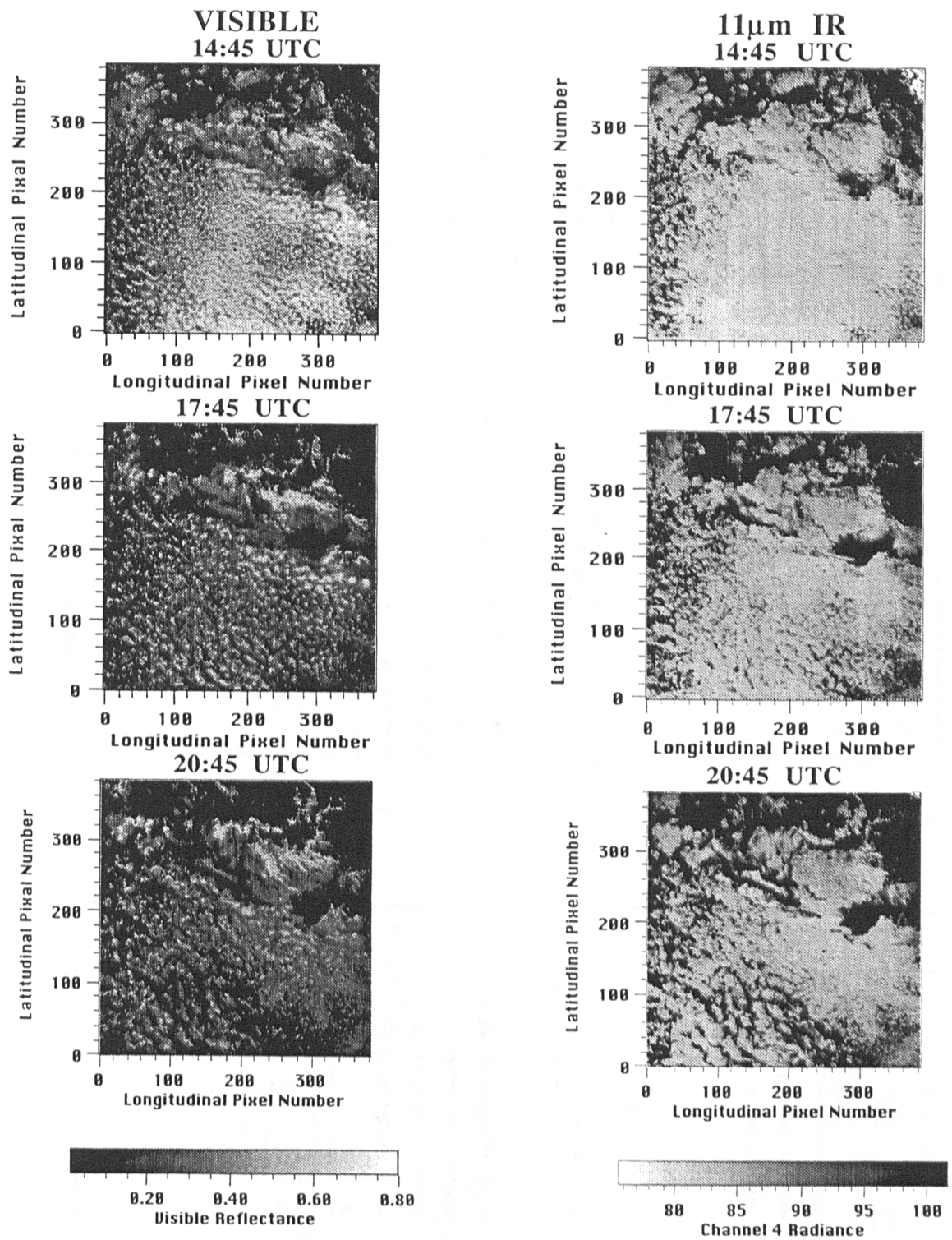

Figure 5: GOES-8 2/24/96 off Peru/Chile "Lower Region" Time Series, Illustrating Diurnal Changes

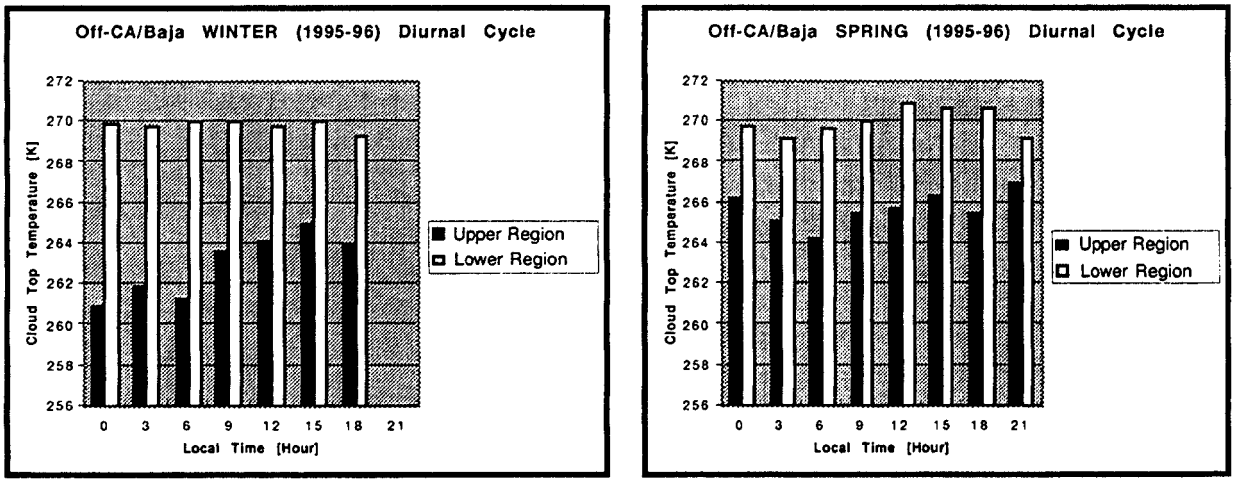

Figure 6: Off CA/Baja Diurnal Cloud Temperature Variability

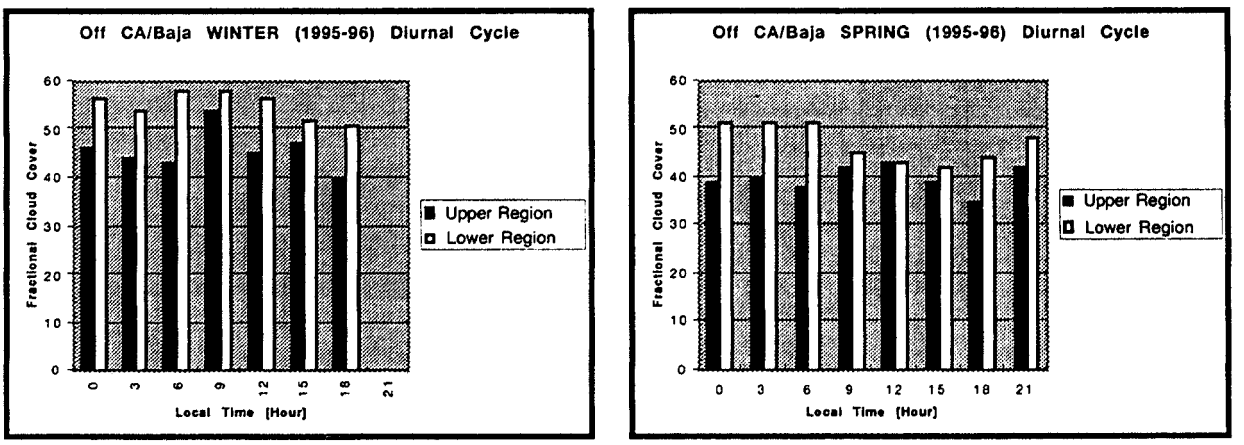

Figure 7: Off CA/Baja Diurnal Cloud Fraction Variability

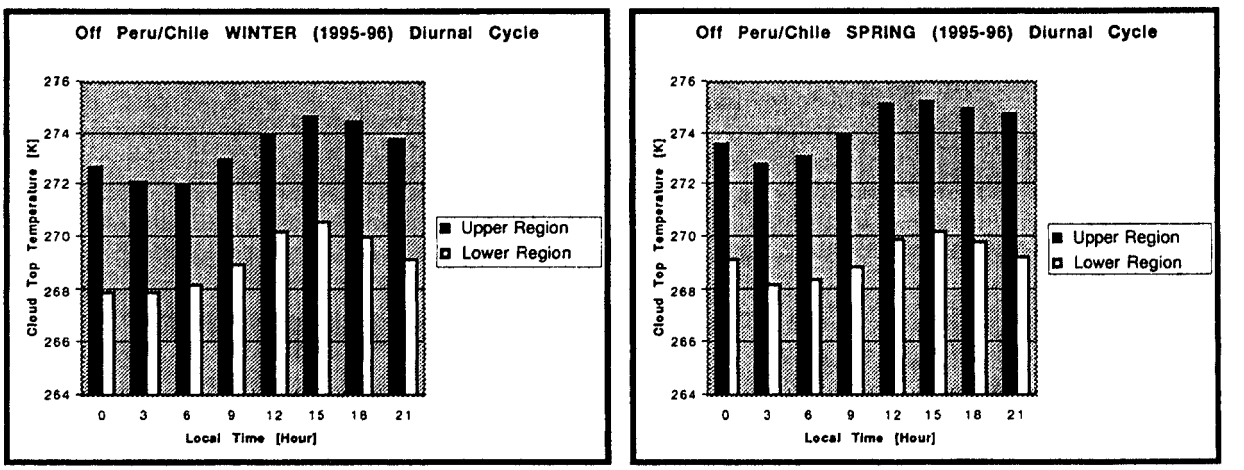

Figure 8: Off Peru/Chile Diurnal Cloud Temperature Variability

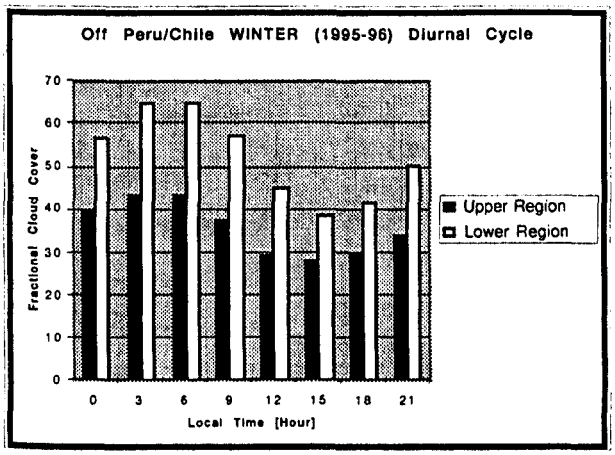

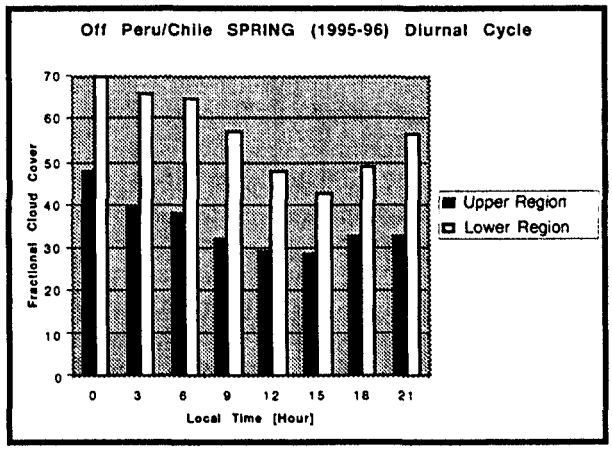

Figure 9: Off Peru/Chile Diurnal Cloud Fraction Variability

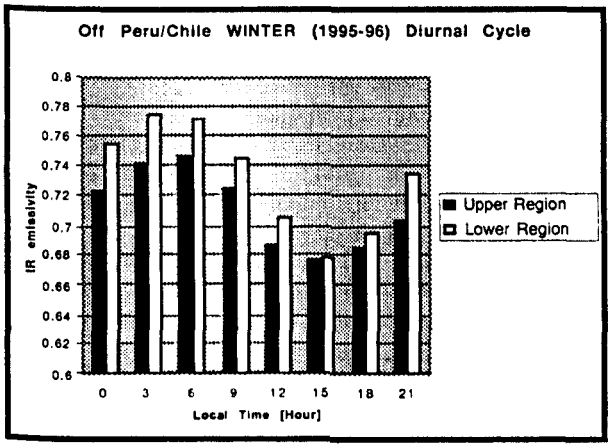

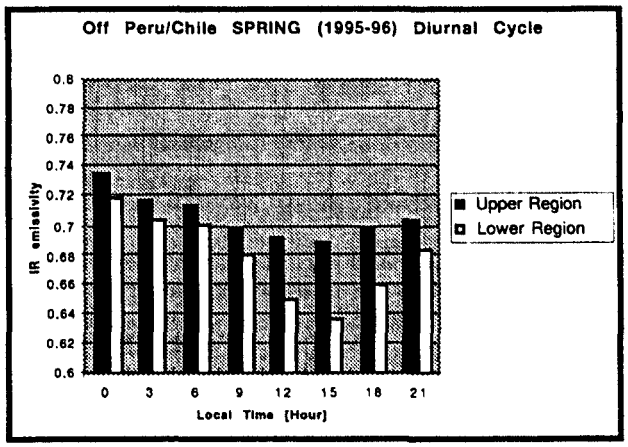

Figure 10: Off Peru/Chile Diurnal Cloud Emissivity Variability

5. DISCUSSION

Semitransparency of MSC is relevant to warrant correction of the IR-only fractional cover; the average SCM correction was found to be 0.155 for March-July 1985[11]. However, we find that the TT cloud fraction has to be corrected only by 0.04 for same area (only for March-May 96 for now).

For the above-mentioned two periods, our MSC emissivities as well as daytime/nighttime emissivity contrasts are quite consistent with the Luo *et al.*[11] results; theirs varies between 0.70-0.76 for March-July, 1985, whilst our range is [0.67-0.73] for March-May, 1996. Our average cloud fraction is 0.56 with a substantial, 0.26 daily amplitude, whist theirs is 0.61 with only a 0.03 night/day contrast. Furthermore, Luo *et al.*[11] finds a negligible day/night cloud top temperature difference, whilst our diurnal amplitude is ~2.5 K. Note that the Minnis and Harrison[30] GOES-East based cloud fraction as well as cloud top temperature diurnal amplitudes (~.30 and ~2.4 K, respectively) are fully consistent with our results.

Thus the *inadequacy of polar orbiters* to assess the substantial diurnal variability of the climatically important MSC is quite apparent; improved geostationary platforms appear to be an absolute necessity even in the EOS satellite era.

Preliminary intercomparisons regarding MSC cloud fraction, emissivity and cloud top temperature variabilities show a general agreement with previous satellite studies[11,29,30,31], as well as surface observations based analyses[29,32]. Published cloud albedo assessments did not overlap temporally as yet with our analyses. Note that our retrieved SSTs are in much better agreement with observations than that obtained using TH methods. For example, the Minnis *et al.*[33] SSTs for the off Peru/Chile Upper Region are 4-9 K less than the corresponding climatological SSTs, whilst our retrievals are within 1 K. Not surprisingly the CWV values are in good agreement with the observations[24] as well. A comprehensive evaluation of the SST and CWV products will be carried out after a full year worth of data will be analyzed.

In the near future, first of all, we plan to complete a full year's worth of analyses, and compare the results with previous works in a more consistent manner. We also plan to further assess the variability of MSC characteristics as well as their relationships over the diurnal and seasonal cycles. Next, we will look for relationships over the seasonal cycle of MSC properties and SST as well as CWV and/or between their anomalies (after subtracting the seasonal cycle). For example, following Tselioudis and Rossow[34], we will correlate variations of MSC optical depth to cloud top temperature, once a full year's worth of analyses were completed. Finally, we plan to evaluate, how our results may improve MSC-regime parameterizations in numerical models.

6. ACKNOWLEDGMENTS

The authors are grateful to W. Ridgeway for help in writing a data conversion script.

7. REFERENCES

1. Randall, D. A., J. A. Coakley, Jr., C. W. Fairall, R. A. Kropfli, and D. H. Lenschow, "Outlook for research on subtropical marine stratiform clouds," *Bull. Am. Meteorol. Soc.*, **65,** 1290-1300, 1984
2. Hartmann, D. L., M. E. Ocker-Bell, and M. L. Michelsen, "The effect of cloud type on the earth's energy balance," *J. Climate,* **5**, 1281-1304, 1992
3. Klein, S. A., and D. L. Hartmann, "The seasonal cycle of low stratiform clouds," *J. Clim.*, **6**, 1587-1606, 1995.
4. Wielicki, B. A., and L. Parker, "On the Determination of Cloud Cover From Satellite Sensors: The Effect of Sensor Spatial Resolution," *J. Geophy. Res.*, **97**, 12799-12823, 1992.
5. Chang, F.-L. and J. A. Coakley, Jr., "Estimating Errors in Fractional Cloud Cover Obtained With Infrared Threshold Methods," *J. Geophys. Res.*, **98**, 8825-8839, 1993.
6. Pincus, R., M. Szczodrak, J. Gu, and P.Austin, "Uncertainty in Cloud Optical Depth Estimates Made from Satellite Radiance Measurements," *J. Climate*, **8**, 1453-1462, 1995.
7. Slingo, A., "Sensitivity of the Earth's radiation budget to changes in low clouds," *Nature*, **343**, 49-51, 1990.
8. Cess, R. D., *et al.*, "Interpretation of Seasonal Cloud-Climate Feedback as Produced by 14 Atmospheric General Circulation Models," *J. Geophys. Res.*, **97**, 7613-7617, 1992.
9. Han, Q., W. B. Rossow, and A. A. Lacis, "Near-Global Survey of Effective Droplet Radii in Liquid water Clouds Using ISCCP Data," *J. Climate,* **7**, 465-497, 1994.
10. Harshvardhan, B. A. Wielicki, and K. M. Ginger, "The Interpretation of Remotely Sensed Cloud Properties from a Model Parameterization Perspective" *J. Clim.*, **7**, 1987-1998, 1994.
11. Luo, G., X. Lin, and J. A. Coakley, Jr., "11-μm emissivities and droplet radii for marine stratocumulus," *J. Geophys. Res.*, **99**, 3685-3698, 1994
12. Molnar, G., "Application of the spatial coherence method for the treatment of subresolution and cirrus clouds," *Preprint Volume: Fifth Conference on Atmospheric Radiation*, Oct. 31-Nov. 4, 1983, Baltimore, MD. AMS Publication, pp. 276-279, 1983.
13. Molnar, G., "Satellite Retrievals of Marine Stratiform Cloud Systems," In *Preprints, Sixth Conference on Satellite Meteorology and Oceanography,* Jan. 5-10, Atlanta, GA, *AMS, Boston,* pp. 7-10, 1992.
14. Molnar, G., and D. Chesters, "Cloud Retrievals from Satellite Imagery Using the Triangle Technique. Part I.: Application for Marine Stratiform Cloud Systems," Submitted to *J. Appl. Met.*, 1996.

15. Platt, C. M. R., "On the bispectral method for cloud parameter determination from satellite VISSR data: Separating broken cloud and semitransparent cloud," *J. Clim. Appl. Meteorol.*, **22**, 429-439, 1983.
16. Coakley, J. A., Jr., and F. P. Bretherton, "Cloud cover from high-resolution scanner data: Detecting and allowing for partially filled fields of view," *J. Geophys. Res.*, **87**, 4917-4932, 1982.
17. Lin, X., and J. A. Coakley, Jr., "Retrieval of Properties of Semitransparent Clouds From Multispectral Infrared Imagery Data," *J. Geophys. Res.* **98**, 18501-18514, 1993.
18. Platnick, S., and F. P. J. Valero, "A Validation of a Satellite Cloud Retrieval during ASTEX," *J. Atmos. Sci.*, **52**, 2985-3001, 1995.
19. Platt, C. M. R., and G. L. Stephens, "Interpretation of remotely sensed high cloud emittances," *J. Atmos. Sci.*, **37**, 2314-2322, 1980.
20. Minnis, P., P. W. Heck, D. F. Young, C. W. Fairall, and J. B. Snider, "Stratocumulus Cloud Properties Derived from Simultaneous Satellite and Island-based Instrumentation during FIRE," *J. Appl. Met.*, **31**, 317-339, 1992.
21. Fairall, C. W., J. E. Hare, and J. B. Snider, "An Eight-Month Sample of Marine Stratocumulus Cloud Fraction, Albedo and Integrated Liquid Water," *J. Climate* **3**, 847-864, 1992.
22. Stephens, G. L., "On the relationship between water vapor over the oceans and sea surface temperature," *J. Climate*, **3**, 634-645, 1990.
23. Schmetz, J., and L. Van De Berg, "Estimation of Precipitable Water from METEOSATInfrared Window Radiances over Sea," *Beitr. Phys. Atmosph.* **64,** 93-102, 1991.
24. Jackson, D. L., and G. L. Stephens, "A Study of SSM/I-Derived Water Vapor over the Global Oceans," *J. Climate*, **8**, 2025-2038, 1995.
25. Walton, C. C., "Nonlinear Multichannel Algorithms for Estimating Sea Surface Temperature with AVHRR Satellite Data," *J. Appl. Met.*, *27*, 115-124, 1988.
26. Saunders, R. W., and D. P. Edwards, "Atmospheric transmittances for the AVHRR channels," *Appl. Optics*, **19**, 4154-4160, 1989.
27. Klein, S. A., and D. L. Hartmann, "The seasonal cycle of low stratiform clouds.," *J. Clim.*, **6**, 1587-1606, 1995.
28. Rozendaal, M. A., C. Leovy, and S. A. Klein, "An Observational Study of Diurnal Variations of Marine Stratiform Cloud," *J. Climate*, **8**, 1795-1809, 1995.
29. Turton, J. D., and S. Nicholls, "A study of the diurnal variation of stratocumulus using a multiple mixed layer model," *Quart. J. Roy. Meteor. Soc.*, **113**, 969-1009, 1987.
30. Minnis, P., and E. F. Harrison, "Diurnal variability of regional cloud and clear-sky radiative parameters derived from GOES data. Part I: Analysis Method," *J. Clim. Appl. Meteorol.*, **23**, 993-1011, 1984.
31. Oreopoulos, L., and R. Davies, "Statistical Dependence of Albedo and Cloud Cover on Sea Surface Temperature for Two Tropical Marine Stratocumulus Regions," *J. Climate*, **6**, 2434-2447, 1994.
32. Klein, S. A., and D. L. Hartmann, and J. R. Norris, "On the Relationships among Low-Cloud Structure, Sea Surface Temperature, and Atmospheric Circulation in the Summertime Northeast Pacific," *J. Climate*, **8**, 1140-1155, 1993.
33. Minnis, P., E. F. Harrison, and G. G. Gibson, "Cloud Cover Over the Equatorial Eastern Pacific Derived From July 1983 ISCCP Data Using a Hybrid Bispectral Threshold Method" *J. Geophys. Res.*, **92**, 4051-4073, 1987.
34. Tselioudis, G., and W. B. Rossow, "Global, multiyear variations of optical thickness with temperature in low and cirrus clouds," *Geophys. Res. Lett.* **21**, 2211-2214, 1994.

High performance animation of GOES weather images

Fritz Hasler, Dennis Chesters, Marit Jentoft-Nilsen, Kannappan Palaniappan

Laboratory for Atmospheres, NASA-GSFC, Greenbelt, MD 20771

ABSTRACT

Geostationary orbit provides a wonderful viewpoint for collecting movies of meteorological processes. Because GOES-8 images are large and frequent, high-performance workstations and user-friendly software are required to review the current pools of GOES weather imagery at full resolution.

During the post-launch checkouts, the GOES-8 and GOES-9 satellites were exercised in rapid-scan imaging modes that challenge most display systems. At NASA-GSFC, the Interactive Imaging Spread Sheet (IISS) software/hardware was used to roam and zoom through gigabytes of GOES image data collected in 1994-95. We use the IISS to examine exciting meteorological features within the hurricanes of 1995 and during typical episodes of severe weather that occur somewhere over the United States every day.

The IISS demonstration shows how weather forecasters could make good use of the full resolution and depth of GOES-8 imagery, adapting to the meteorological event as it develops, especially when synchronized with corresponding weather radar.

Keywords: image, weather, animation, GOES

1. INTRODUCTION

At NASA-GSFC, the Interactive Imaging Spread Sheet (IISS)[1] software/hardware tool is heavily used for examination of GOES-8 and GOES-9 data during post-launch checkouts. The IISS is able to pan and zoom through 400 Mbytes of in-core images, loading a megapixel of full color images to the monitor and to S-video output at video rates (30 frames per second). Not only single frames can be roamed, zoomed and animated, but different channels in separate cells can be grouped together and examined in a coordinated, interactive session. For full use of the 10-bit precision in the GOES Imager data, the IISS software was enhanced to operate on 16-bit integers.

Because animations cannot be printed, this manuscript will just present a few still examples of the animations presented at the conference. Miniaturized versions of some animations are available on the Internet[2] as Quicktime and/or MPEG movies.

0-8194-2200-2/96/$6.00

2. IISS EXAMPLE

Figure 1 shows a GOES session on the IISS, simultaneously probing the relative values of GOES-8 and GOES-9 pictures of Hurricane Luis in side-by-side stereo, and top-to-bottom zooms.

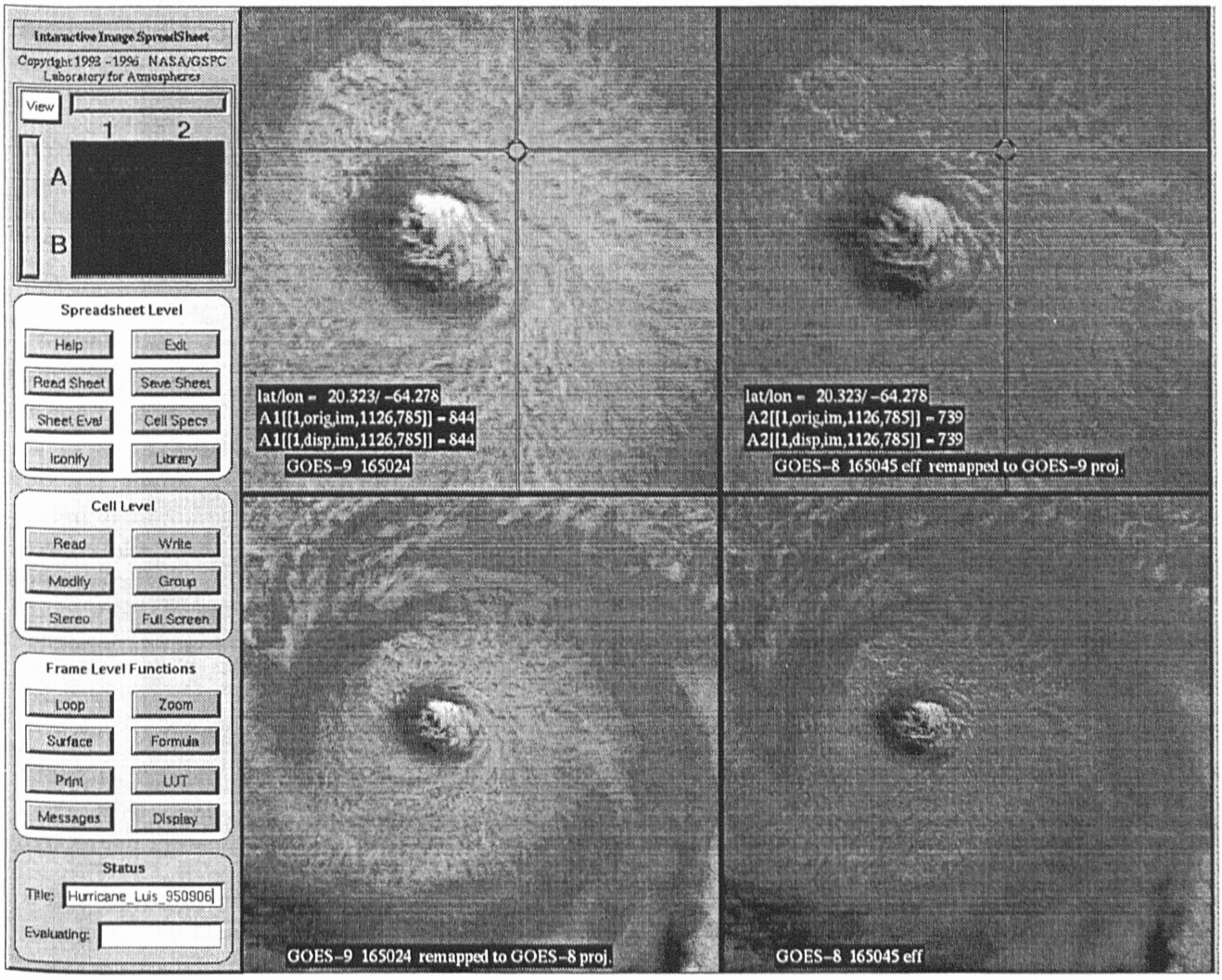

Figure 1: The IISS being used to examine simultaneous views of a hurricane.

3. ANIMATION EXAMPLE

Figure 2 shows a close-up view of southern Florida during a day of 1-minute interval imagery over the southeastern United States during a GOES-9 performance test by NASA. The IISS was used to roam and zoom across a field of 3000x2000 pixels, finding many other storms of local interest. Such interactive power and flexibility is readily available with today's workstations.

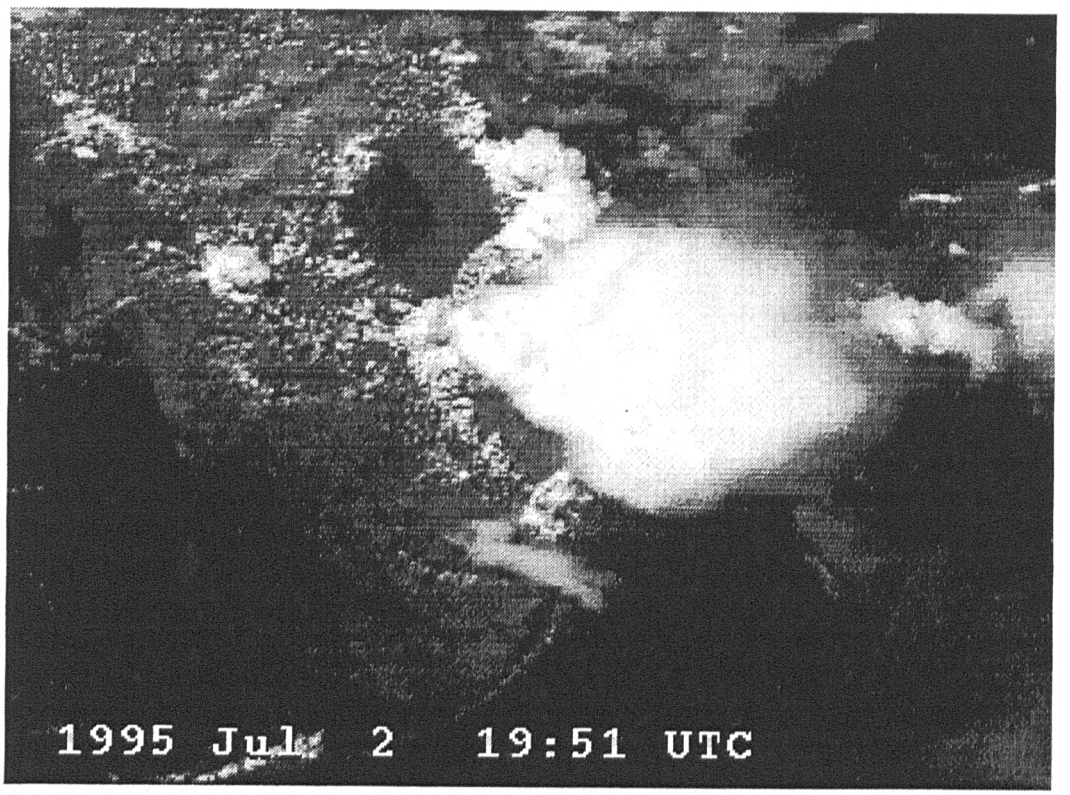

Figure 2: One frame from an animation of 1-minute interval GOES-9 scans over Florida.

In order to make these animations as smooth and pleasant as possible, bad scanlines were removed, and enhancements were applied that bring the dynamic range of the original GOES Imager data into the more limited human bandwidth[1] .

4. SUMMARY

High performance animation of large volumes of high precision GOES images is now relatively easy and affordable using modern hardware and software packages like the Interactive Imaging Spread Sheet (IISS). The IISS was useful in discovering and displaying the progress in GOES Image Navigation and Registration (INR) during the post-launch checkouts. During the very busy 1995 hurricane season, the IISS was used to animate each day's activity and pipe the animations directly to NASA Select TV, where they were occasionally picked up and used by the national TV broadcast networks.

NOAA's National Weather Service (NWS) field offices could be empowered with similar animation engines to combine imagery from two GOES satellites with digital radar and investigate it all interactively, as the weather develops.

5. ACKNOWLEDGMENTS

The IISS software was enhanced for GOES use by Mike Manyon. Hal Pierce was instrumental in processing the stereo images from GOES-8 and -9.

6. REFERENCES

1) http://rsd.gsfc.nasa.gov/912/trmm/spread.htm
2) http://climate.gsfc.nasa.gov/~chesters/goesproject.html
3) http://rsd.gsfc.nasa.gov/rsd/movies/preview.html
4) "GOES image enhancements and quality control", Jentoft-Nilsen, J., F. Hasler, D. Chesters, K. Palaniappan, SPIE Conf. *GOES-8 and Beyond*, Denver, CO, 1996.

IMPACT OF THE NEW GENERATION GOES ON THE DETERMINATION OF SEA SURFACE TEMPERATURE

Xiangqian Wu, W. Paul Menzel, and William L. Smith

Cooperative Institute for Meteorological Satellite Studies
University of Wisconsin, Madison, Wisconsin 53706

Abstract

The new generation GOES, with significantly higher spatial resolution and signal to noise ratio than its predecessors for the split window channel, makes it feasible for the first time to derive SST from a geostationary platform. The GOES data are well calibrated and navigated. The temporal information from GOES can be used to identify residual cloud contamination and detect diurnal variation of SST. All these features are valuable asset for monitoring the earth environment from space.

Key words: Sea surface temperature; GOES; Cloud identification

1. INTRODUCTION

The new generation Geostationary Operational Environmental Satellite (GOES) represents major improvements in our capability of monitoring the earth's environment. This paper examines the impact of sampling characteristics of new generation GOES imager on the determination of sea surface temperature (SST), in comparison with the SST derived from the Advanced Very High Resolution Radiometer (AVHRR) onboard the National Oceanic and Atmospheric Administration's (NOAA) Polar Orbiting Environmental Satellite (POES).

With few exceptions, most of the satellite data used in this paper are collected by GOES-9 Imager over the area of (0-20°N, 170-180°W), from 19 March to 15 April 1996. The SST retrieval scheme is based on the "split window" principle (McMillin 1975):

$$SST = T_b(4) + a + b[T_b(4)-T_b(5)] \qquad (1)$$

The coefficient, a = -1.7011 and b = 2.5860, are based on the regression of the surface temperatures from a selection of profiles against the computed GOES-9 radiance using those profiles. All the 110 profiles selected for regression have surface temperature above 290°K and $1°K<T_b(4)-T_b(5)<5°K$; the satellite view angle is set to 45° in computing GOES-9 radiance. In other words, the regression was specially tailored for GOES-9 viewing the area at the time. Though not constructed for general applications, Eq. (1) is representative of the operational AVHRR SST algorithm and suffices in our study of the sampling characteristics and its effect on the SST retrieval.

2. ADVANTAGES OF GOES SST

As far as the SST retrieval is concerned, the most important improvement of GOES-8/9, in comparison with previous GOES, is the much enhanced (about 28 times) signal to noise ratio (S/N) for the split window channel (12 micron). Its horizontal resolution has been reduced from 14 km to 4 km, yet the S/N is reduced from 0.7°K to 0.3°K. This is significant not only because one can determine SST more precise with higher spatial resolution, one also has a better chance of finding cloud free pixels. SST retrieval with infrared radiometry is to a large extent at the mercy of cloud. With a field of view (FOV) of 14 km, SST retrieval is only possible when and where cloud free region of 14 km or larger exists, which can be a serious restriction in many parts of the world. The new generation GOES relaxes this restriction such that it is now comparable to the AVHRR at the Global Area Coverage (GAC) resolution. In this regard, SST retrieval from GOES is practically feasible only with the advent of new generation GOES.

The GOES Imager is well calibrated and navigated, as has been documented elsewhere. Figure 1 is an example of GOES calibration accuracy. During

0-8194-2200-2/96/$6.00

Fig. 1

Comparison of Colocated Averaged HIS and GOES-8 Brightness Temperatures for Imager Channel 4. Jan. 16 HIS Flight.

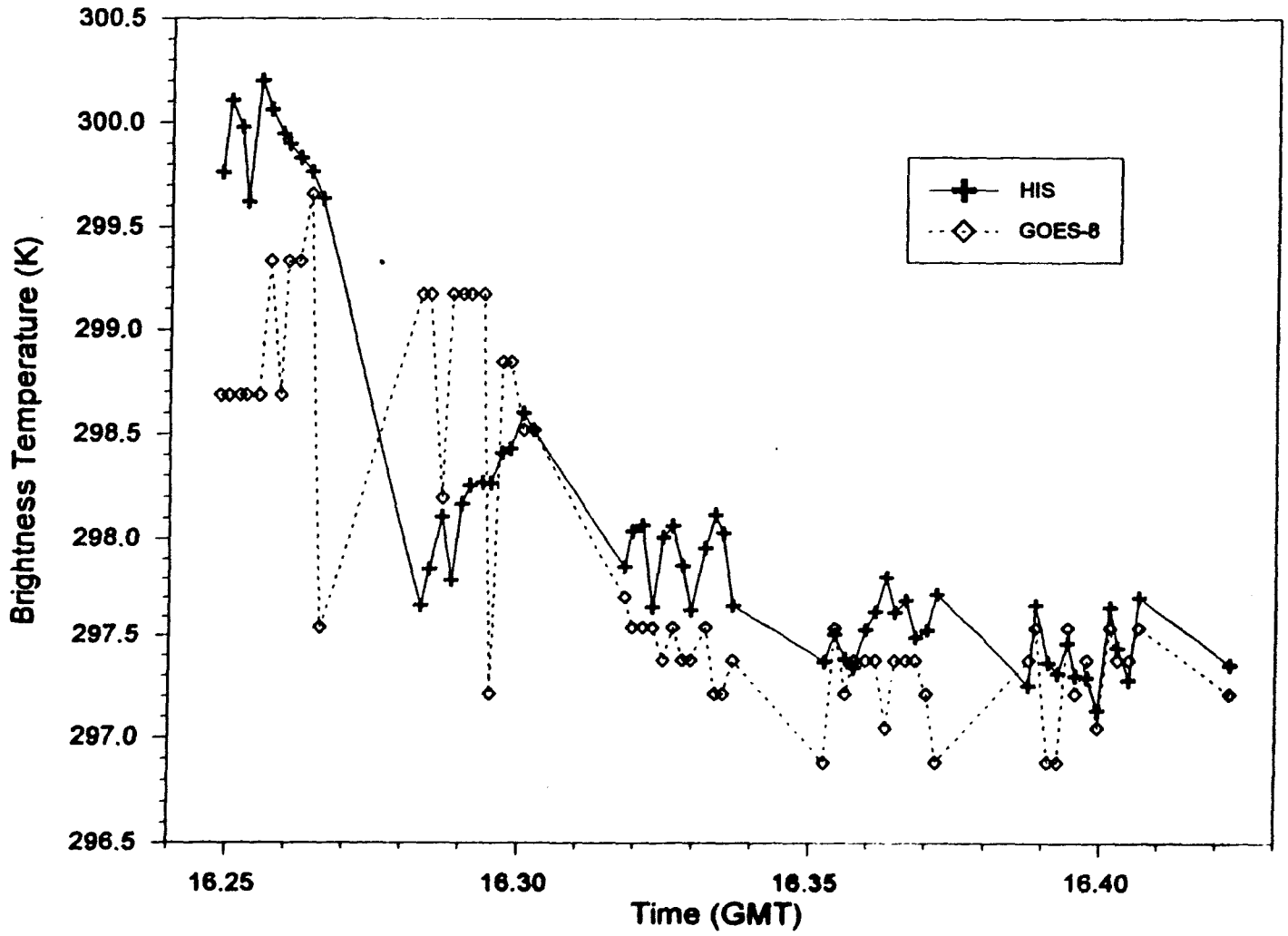

a calibration exercise on January 16, 1996, a High-resolution Interferometer Sounder (HIS) flew on a research aircraft at the altitude of 20 km over the Gulf of Mexico, under the surveillance of GOES-8. The high spectral resolution HIS data, which is calibrated to within 0.1°K, is convoluted to GOES brightness temperatures. Figure 1 shows a comparison of the colocated HIS and GOES brightness temperatures for GOES Imager Channel 4. The early part of the flight was over an area of varying SST with gradient as large as 2°K/km. Because of difference in FOV, the colocation between the two instruments is not exact, which caused large difference during the early part of the flight. In the later part of the flight (16:30 UTC and thereafter), the SST was much more homogeneous and the colocation error should be of secondary importance. Figure 1 shows that during this period of time the difference between HIS and GOES was less than 0.5°K in general.

As the *quality* of the GOES Imager data for SST retrieval is approaching to the standard of AVHRR SST, their *quantity* remains an order of magnitude more than POES can offer, albeit only for limited spatial coverage. As to be detailed later in this paper, this provides new opportunities to enhance satellite monitoring of SST. An obvious advantage of GOES SST is its ability to monitor the diurnal variation of SST. Our knowledge in this field is very limited at the present time; new information should be highly valuable. Another opportunity to improve SST retrieval with GOES measurements comes from the better handling of cloud by GOES, which is realized in two ways. Firstly, the temporal information available from GOES helps to identify pixels with residual cloud contamination that can be difficult for AVHRR to detect. Secondly, because of the complete temporal coverage by GOES, an area is more likely to be observed as cloud moves away, thus provide a more complete monitoring of SST.

3. COREGISTRATION ERROR

Figure 2 shows a 2-dimensional histograms composited from 24 hourly GOES-9 images on 29 April 1996 in western tropical Pacific (0-20°N, 100-110°W). The abscissa is 11 μm brightness temperature difference between the pixel and its neighboring pixels [$\nabla T_b(4)$]; the eight panels represent the eight directions. The coordinate is 11 μm and 12 μm brightness temperature difference [$T_b(4)$-$T_b(5)$] for a pixel. Shading represents, in logarithmic scale, number of pixels for a category of temperature differences in space and in spectrum: the outer-most shading represents 1-10 pixels, the next 11-100 pixels, ..., and the center-most shading represents more than 100,000 pixels. Thus, for example, the dark shading corresponding to (30,-4) in the upper central panel indicates that there are between one to ten pixels, out of the 24 images (about 4 million pixels), for which $T_b(4)$-$T_b(5)$ = -4°K and the $T_b(4)$ of the pixel to its north is 30°K cooler (e.g., cloud to the north).

For the majority of the pixels (the light spot in the center that represents about 90% of all pixels), spatial temperature gradient $\nabla T_b(4)$ is small (near zero) and spectral temperature gradient $T_b(4)$-$T_b(5)$ is in the range of 1 to 5°K. This is expected, considering the abundance of water vapor in the region and its differential absorption for the two channels. The interesting part is the *orientation* of the "ellipsoids" of relatively rare occurrence, which suggests certain dependence of the spectral brightness temperature gradient, $T_b(4)$-$T_b(5)$, on the spatial brightness temperature gradient in the north-south direction. One observes that $T_b(4)$-$T_b(5)$ for a pixel can be very negative if the pixel to its north is much cooler; $T_b(4)$-$T_b(5)$ for a pixel is *always* positive if the pixel to its north is sufficiently warmer.

This dependence of $T_b(4)$-$T_b(5)$ on $\nabla T_b(4)$ is common for GOES-9. Examination of all the GOES-9 data outlined in Section I shows that patterns similar to those in Fig. 2 persists in every day. On the other hand, GOES-8 data do not display such behavior. Figure 3 is the equivalent to Fig. 2 but with GOES-8 data. Patterns in Fig. 3 are quite different from those in Figure 2. In the east-west direction (middle panels of Figs. 2 & 3), the sampled temperature gradient $\nabla T_b(4)$ is notably smaller; the dependence of $T_b(4)$-$T_b(5)$ on temperature gradient is very weak (slightly stronger in some other days). These may be due to the oversampling in the east-west direction.

It is hypothesized that the dependence of $T_b(4)$-$T_b(5)$ on $\nabla T_b(4)$ stems from the coregistration error of GOES Imager, which is exaggerated in Fig. 4. This error is less than 1 km (Menzel and Purdom 1994), or a quarter of a pixel, however it may produce $T_b(4)$-$T_b(5)$ of 1°K or larger where $\nabla T_b(4)$ is 4°K/pixel or larger. Although $\nabla T_b(4)$ of such magnitude is infrequent (on the order of 1% in the example shown), its effect must be properly accounted for.

Details of the nature, cause, and effects of spatial gradients of GOES-8/9 brightness temperatures on their spectral gradient is a subject of further studies,

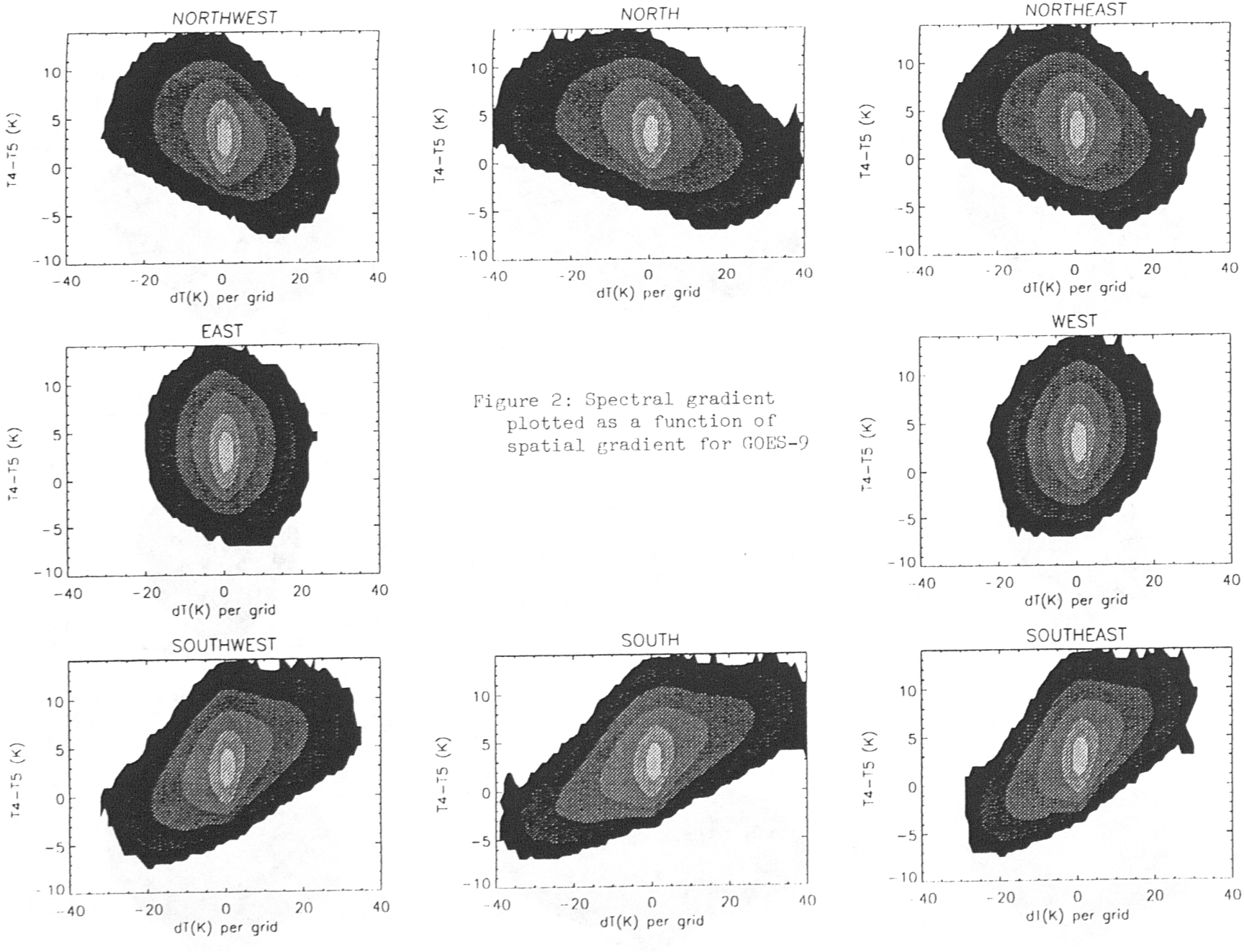

Figure 2: Spectral gradient plotted as a function of spatial gradient for GOES-9

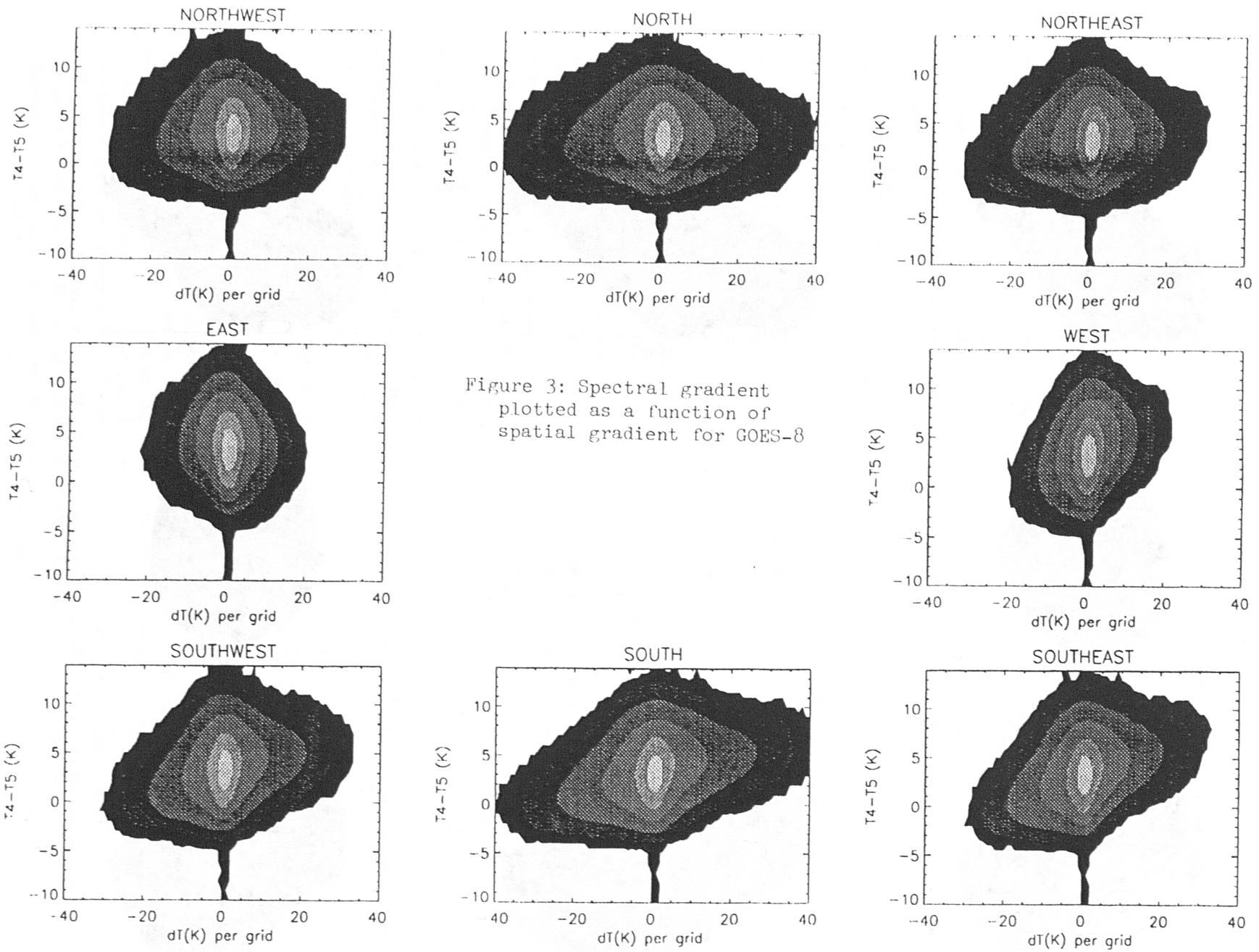

Figure 3: Spectral gradient plotted as a function of spatial gradient for GOES-8

particularly in collaboration with the study of $T_b(4)<T_b(5)$ that is possibly caused by convection dynamics and cloud microphysics (Moeller et al 1996). Our preliminary conclusion is that the coregistration error of GOES-9 Imager Channel 4 and 5 may result in systematic difference of the brightness temperatures measured by these two channels. As a precaution, data were discarded in this study where $\nabla T_b(4)$ is large.

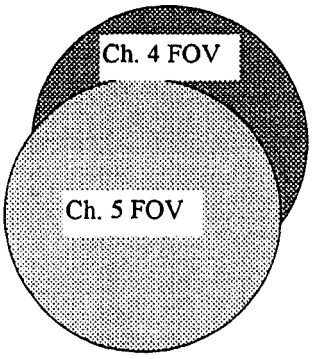

Figure 4: Illustration of coregistration error between channels

4. CLOUD CLEARING

Cloud clearing is a procedure by which potentially cloud contaminated pixels are identified and prevented from entering the data stream that generates the final SST product. This is done after the is quality control procedure, in which pixels with:

- $T_b(4) > 310°K$,
- $T_b(4)-T_b(5) < 0°K$,
- $T_b(4)-T_b(5) > 6°K$, and
- $\nabla T_b(4) > 6°K$/pixel

are eliminated. The first three criteria are based on observational and theoretical evidences; the last one is based on the observations presented in the previous section. Some of these criteria may be more stringent than necessary, but one can afford that with the abundance of GOES data. Collectively, they count for about 1% of total data.

The ensuing procedure of cloud clearing is based on the premises that: (1) Sea surface freezes at certain temperature; (2) Sea surface is warmer than cloud top. Consequently, a pixel is deemed cloud contaminated, and removed from further processing, if it possesses one of the following properties:

1) $T_b(4) < 270°K$
2) $T_b(4)$ is cooler ($<0.3°K$) than any one of its neighbors (3-by-3 pixels)
3) SST is cooler ($<1°K$) than any one of its neighbors in space (3-by-3 pixels) and in time (±1 hour)
4) SST is cooler ($<5°K$) than the past (5 days) maximum

Test 1 is based on the fact that sea water freezes at 270.5°K; it eliminated ~40% of pixels. Test 2 makes sure that no neighbors is 3σ warmer, noting that S/N for $T_b(4)$ is 0.1°K. It is desirable in theory to enlarge the searching area, but in practice the 3-by-3 searching area performs satisfactorily and using a larger searching area slows down the processing significantly. Test 2 detects another 45% pixels that are possibly contaminated by cloud. Note that this is different from the test of "looking for hot spot", which admits only pixels warmer than its neighbors. That test tends to exclude truly cloud free pixels in a large homogeneous region and retains only pixels near cloud edge.

The first two tests can be applied to "snap-shot" data like those from AVHRR. The next two tests are applicable only to data with temporal information, such as those from GOES. They are designed to deal with the problem where all pixels in an area are partially contaminated by cloud (or by clouds of sub-FOV scale), but the pixel in consideration happens to be less contaminated and thus passes the first two tests. Test 3 assures that the pixel in consideration is not cold not only in space but also in time. Pixels with partial cloud contamination will be caught by this test as long as the partial contamination is not overly persistent. Because temperature comparison is made in time as well, water vapor variation may cause variation in $T_b(4)$, therefore the comparison is made of the retrieved SST that should be independent of water vapor variation. However, since both $T_b(4)$ and $T_b(5)$ are used to produce SST and the S/N for $T_b(5)$ is 0.3°K, the precision of SST is about $\sqrt{(0.1^2+0.3^2)}$, assuming independence between $T_b(4)$ and $T_b(5)$ errors. This leads to $3\sigma \cong 1°K$, as used in Test 3. The time window of ±1 hour is again a compromise between effectiveness and efficiency. This test filters out another 10% of pixels.

Among the remaining 6% pixels there are unfortunately still a few pixels (~0.2%) that are possibly contaminated by cloud. As a final resource, Test 4 requires that all SST at a position is no more

Figure 5: IMPACT OF CLOUD CLEARING ON DERIVED SST

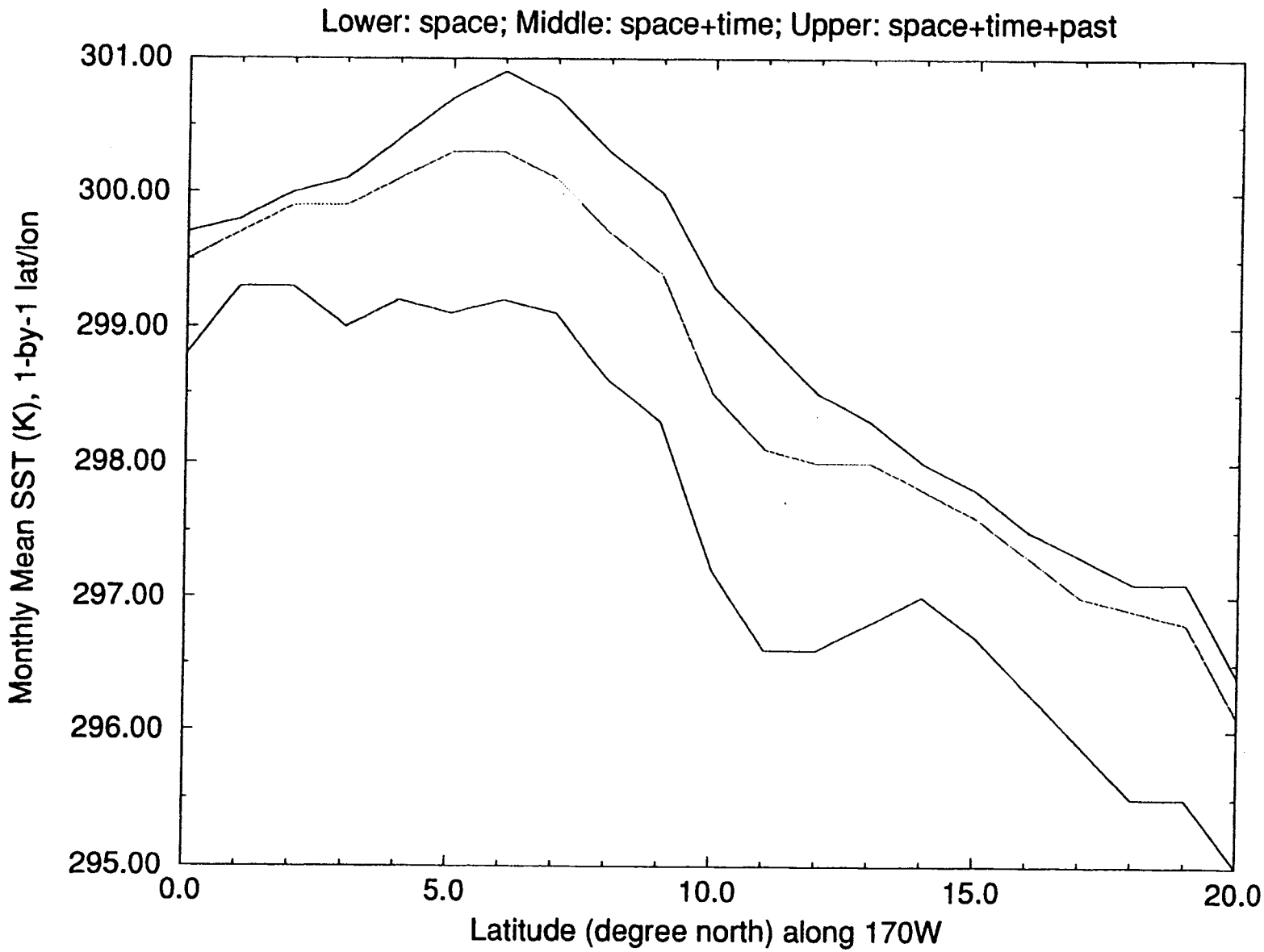

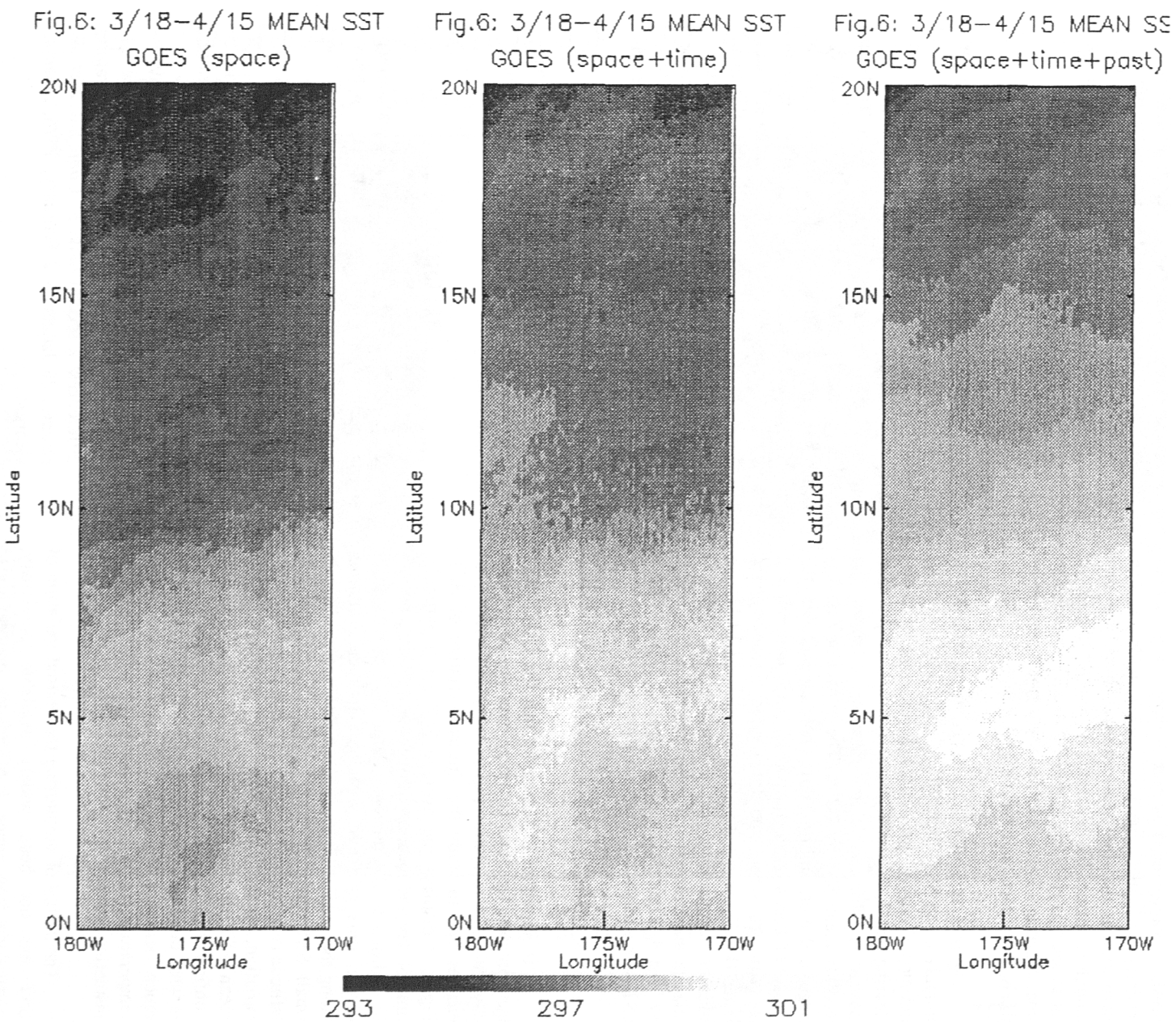
Fig.6: 3/18-4/15 MEAN SST
GOES (space)
Fig.6: 3/18-4/15 MEAN SST
GOES (space+time)
Fig.6: 3/18-4/15 MEAN SS
GOES (space+time+past)
20N
15N
10N
5N
0N
Latitude
180W
175W
170W
Longitude
293
297
301

than 5°K cooler than its past 5-day maximum. To prevent an erroneous maximum from rejecting all good SSTs, the 5-day maximum for a pixel is actually the average of its neighboring 3-by-3 pixels. The threshold values of 5°K and 5 days are somehow arbitrary and are subject to further revision. The motivation is that the time criterion should be long enough to ensure the existence of a valid maximum but as short as could be to avoid true SST variation in time. Although Test 4 affects only a small number of pixels, its impact can be significant.

Figure 5 is a plot, as a function of latitude, of monthly mean SST along 170°W. The lower, middle, and upper curves are results at the end of cloud clearing test 2, 3, and 4, respectively. It can be seen that more stringent cloud clearing increases the monthly mean SST by 1-2°K. The impact of Test 3 is larger and more uniform throughout all latitudes; the impact of Test 4 is generally small but is noticeable in the latitudes where the InterTropical Convergence Zone (ITCZ) was active at the time (5-13°N). In addition, results at the end of Test 2 & 3 both show a relative minimum at 11-12°N, which was eliminated by Test 4. Figure 6 shows the spatial distribution of SST with various cloud clearing methods.

5. DIURNAL VARIATION OF SST

It is important to remember that the GOES SST has complete temporal coverage over the course of a day with high resolution (up to every half hour). This enables one to study the diurnal variation of SST. Figure 7 displays the average SST for a particular time of day and location throughout a 28-days period. In addition to the relatively large SST variation for certain time of the day along a latitude (variation along the vertical direction), one also notes relatively small SST variation with time of the day at any latitude (variation along the horizontal direction). This variation, on the order of 0.5°K, is the signature of mean SST diurnal variation. Ship data (Figure 8) confirms that the sea surface skin temperature, which is what most infrared radiometers measures, responds much stronger than the subsurface sea water temperature to surface processes such as solar insulation, surface wind, and precipitation.

The ability of monitoring the diurnal variation of SST has not been widely available previously, particularly from space. It affords the opportunity to diagnose possible bias in the AVHRR SST due to its limitation in sampling. For the most part in the past two decades, the 5-channel AVHRR instrument that was used for SST derivation was placed on the afternoon POES only, whose orbits (and thus the local overpass times) drifted significantly over the years. For areas where SST experiences consistent and considerable diurnal variations, this orbit drift may induce artificial trend, which may be detected by GOES SST. Diurnal variation of SST also has important applications in, for instance, studies of coastal processes.

6. CONCLUSION

The new generation GOES makes it feasible for the first time to derive SST from a geostationary platform. The GOES data are well calibrated and navigated. The spatial resolution and signal to noise ratio of GOES Imager is comparable to AVHRR at GAC resolution. The abundance of GOES data affords better handling of cloud: on one hand it helps to identify the presence of cloud in a pixel, thus to improve the quality of SST; on the other hand it can "wait" for cloud to move away to observe the area. The GOES SST also has complete temporal coverage with high resolution, with which it is possible for one to monitor the diurnal variation of SST. All these features are valuable asset for monitoring the earth environment from space.

Acknowledgment: We thank Dr. Robert O. Knuteson of CIMSS for providing Fig. 8. This research was supported by the GOES I-M Product Assurance Activity.

7. REFERENCES

McMillin, L. M., 1975: Estimation of sea surface temperatures from two infrared window measurements with different absorption. *J. Geophys. Res.*, **80**, 5113-5117.

Menzel, W. P., and J. F. W. Purdom, 1994: Introducing GOES-I: The first of a new generation of geostationary operational environmental satellites. *Bull. Amer. Meteor. Soc.*, **75**, 757-781.

Moeller, C. C., S. A. Ackerman, K. I. Strabala, W. P. Menzel, and W. L. Smith, 1996: Negative 11 micron minus 12 micron brightness temperature differences: a second look. *8th Conf. Sat. Met. & Ocean.*, 28 January - 2 February, 1996, Atlanta, Georgia.

FIG.7: DIURNAL VARIATION OF SST AS OBSERVED BY GOES-9
(3/18-4/15 average for every half-hour along 170W)

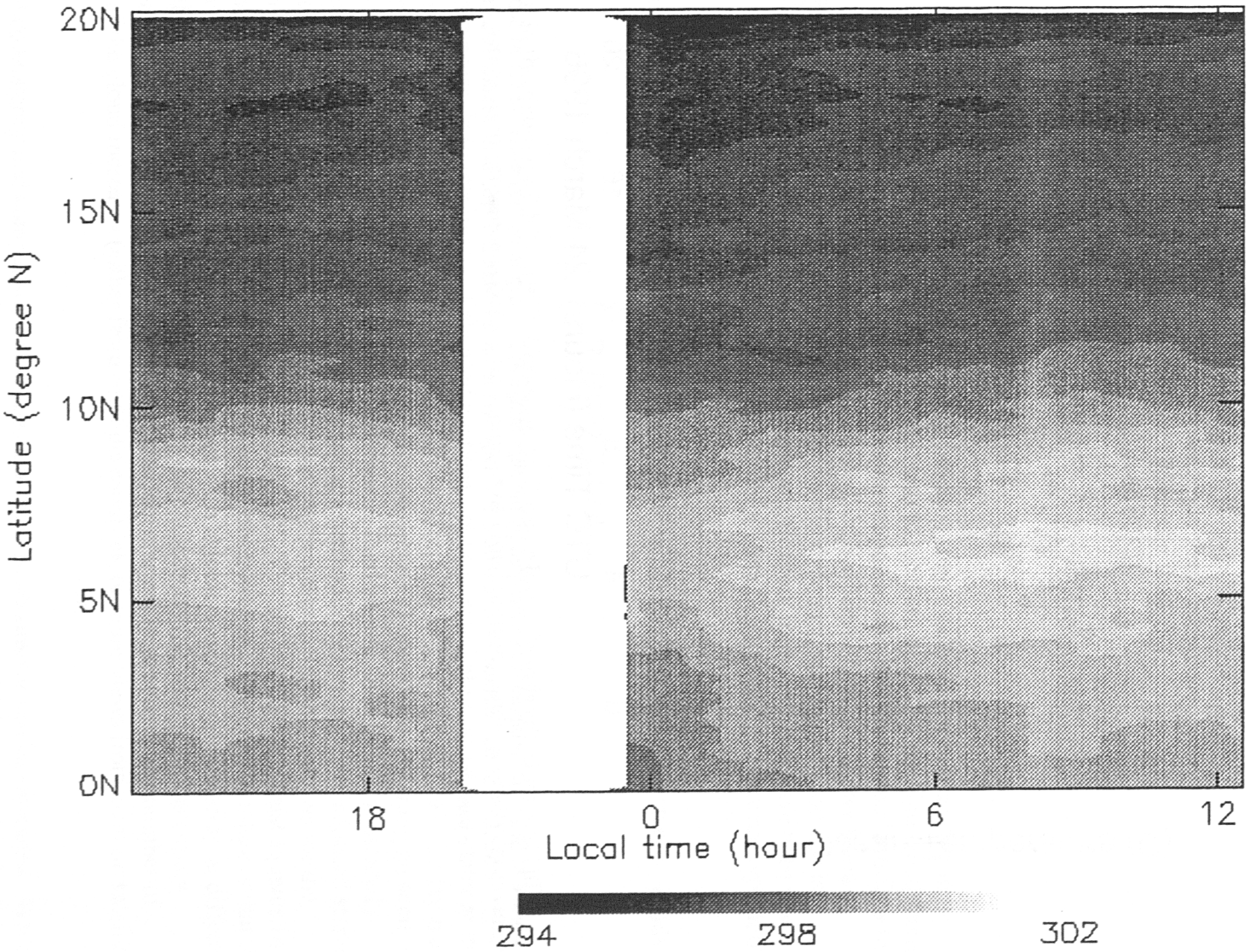

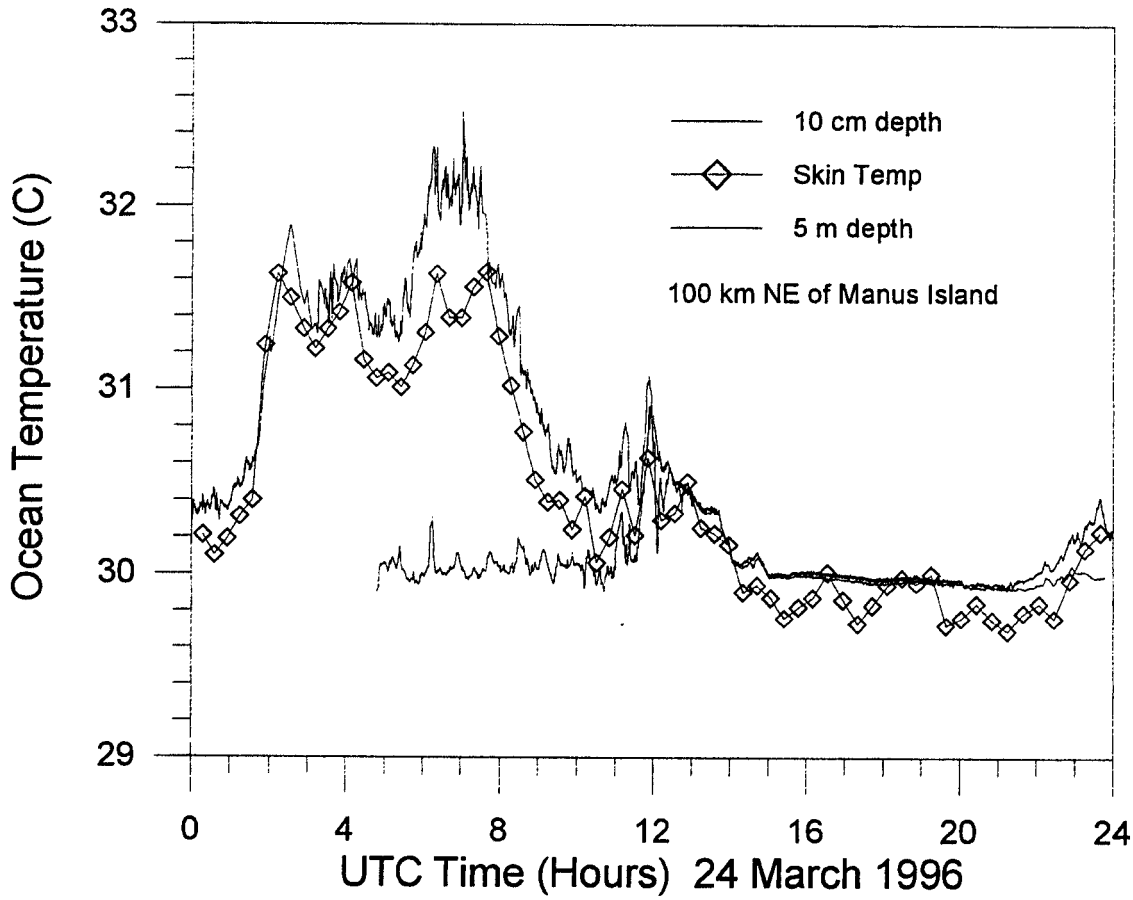

Figure 8: Sea water temperatures measured by the ship intake at 5 m depth, by "skimmer" at 0.1 m depth, and by MAERI at the surface skin, onboard RV Discoverer on 24 March 1996, near Manus Island, Tropical Western Pacific.

Asynchronous Stereo Height and Motion Estimation from Multiple Satellite Images

G. Garrett Campbell [2], James F.W. Purdom [1,2] and Carol E. Vaughn [2]

[1]Regional and Mesoscale Meteorology Branch NOAA/NESDIS
[2]Cooperative Institute for Research in the Atmosphere
Colorado State University
Fort Collins, Colorado 80523

USA

ABSTRACT

A method has been developed to derive both height and motion from satellite images using a purely geometrical technique. This is a combination of using stereo to measure height by viewing cloud from two view point and using several images in time to measure motion of clouds. The method requires that the cloud be viewed from two or more different perspectives with at least two of the views being at different times. With the new method time coincidence is a disadvantage, and higher accuracy is obtained when all views are at different times. For height verification, improvements have been made in the cloud height by shadow method. Accuracies of better than 1 km height and 0.5 m/sec are typical of the results.

Keywords: satellite winds, stereo heights, cloud heights, cloud winds, geosynchronous satellite, winds.

1. INTRODUCTION

As pointed out in the February 20-21, 1992 Workshop on Cloud Motion Winds (Purdom and Dill, 1993), the need exists to improve the accuracy and number of cloud motion winds, globally in coverage and eventually mesoscale in resolution. This need continued to be stressed almost two years later at the Second International Wind Workshop that was held in Tokyo from 13-15 December, 1993. Today many of the major problems remain at operational wind production centers. Foremost is assigning an accurate height for the tracer in question. At the last winds conference, Purdom and Dills (1993) presented a framework for deriving highly accurate cloud heights using a method they termed "time adjusted stereo." Since that initial work, research at CIRA has developed an improved method which allows for the determination of both cloud height and velocity simultaneously. The new method is a least squares fit for the position of the cloud as a function of time from many observations. The method requires that the cloud be viewed from two or more different perspectives with at least two of the views being at different times. With the new method time coincidence proves to be a disadvantage, with higher accuracy obtained when all views are at different times. In addition, accuracy is improved as the number of observations of the cloud increases (either from multiple satellites, or more views from a single satellite at other times).

Using internal consistency and comparison between nearby clouds, accuracies can be estimated. With 1 km resolution visible imagery, cloud motions remain very accurate (to within 0.5 m/s) while cloud

0-8194-2200-2/96/$6.00

height accuracies of better than 1 km are being realized. For height verification, improvements have been made in the cloud height by shadow method to give an independent verification method.

This paper addresses improvements in cloud motion accuracy, both velocity and height which have been major culprits inhibiting progress in wind improvement. After the methodology is presented, the accuracy factors will be discussed and results will be shown.

2.0. REVIEW OF PAST CLOUD HEIGHT ASSIGNMENT

2.1 Infrared based techniques

From satellites, both high resolution visible and infrared imagery are used for the tracking of clouds, while infrared imagery is used for cloud height assignment. Two major problems encountered when using infrared imagery for cloud height assignment are: 1) cloud emissivity; and, 2) knowledge of the lapse rate to which the cloud's temperature will be matched. A technique known as CO_2 slicing that uses multi-spectral aspects of GOES-VAS was developed to aid in cloud height assignment. That technique eliminates some of the uncertainties due to cirrus emissivity, however, the problem of a representative lapse rate in the vicinity of the cloud remains. In addition, CO_2 slicing is not be possible with the new GOES series of spacecraft since one of the needed channels is not included on those spacecraft's imagers. Instead, a technique that is not as accurate as CO_2 slicing will be employed: water vapor slicing.

2.2 Geometric techniques

Since geometry does not rely on cloud properties, that methodology may be preferable for use in deriving cloud heights. Recognizing the problem encountered using infrared imagery for cloud height assignment stereographic techniques were developed to very accurately determine cloud heights using imagery from two geostationary satellites. Early stereo techniques provided accurate cloud height assignment, however, there was a requirement for the satellites to observe the cloud at the same time or height errors would be introduced due to the cloud's motion. For instance for a 10 m/sec speed, the cloud will move one GOES pixel in one minute leading to height errors of similar size. The requirement for time synchronous viewing was eliminated with "time adjusted stereo," however, that technique required the cloud velocity be very well known. In addition, time adjusted stereo was a two step process, and (as with normal stereo) accuracy was not improved with multiple observations.

A geometrically based technique that overcomes the requirement for two satellites the calculation of cloud height using shadows (Purdom and Dills,1993). That technique is limited to daytime and performs best early or late in the day when the satellite , cloud shadow perspective is optimized (long shadows).

2.3 Stereo errors from different platforms.

A initial study of the accuracy of stereo height estimation from different view points was prepared. This considered different satellite view points and resolutions. Figure 1 shows the height errors from observation from the current GOES 8 and 9 satellite view points (75 ° West and 135° West). These were

estimated by adding random errors to the a set of reference view angles. Then the root mean square deviation of the resulting height

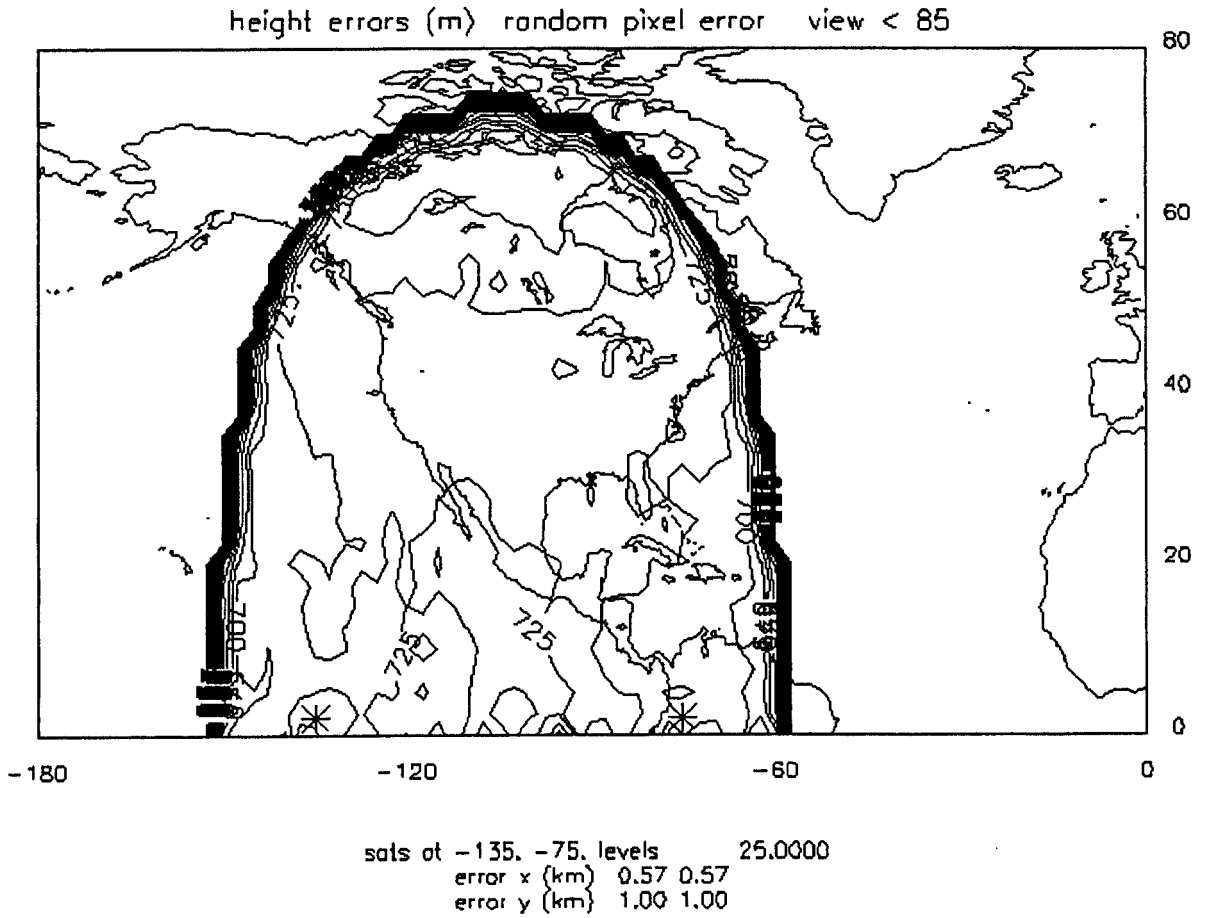

Figure 1 Pure stereo errors from GOES at 75° West and 135° West. The geometric height errors are very uniform across the area seen by both satellites.

analysis relative to the reference heights represents the uncertainty of the heights. Errors were added with Gausian random noise with variance of 1 pixel (± .57 km East West or 1 km North South for GOES).

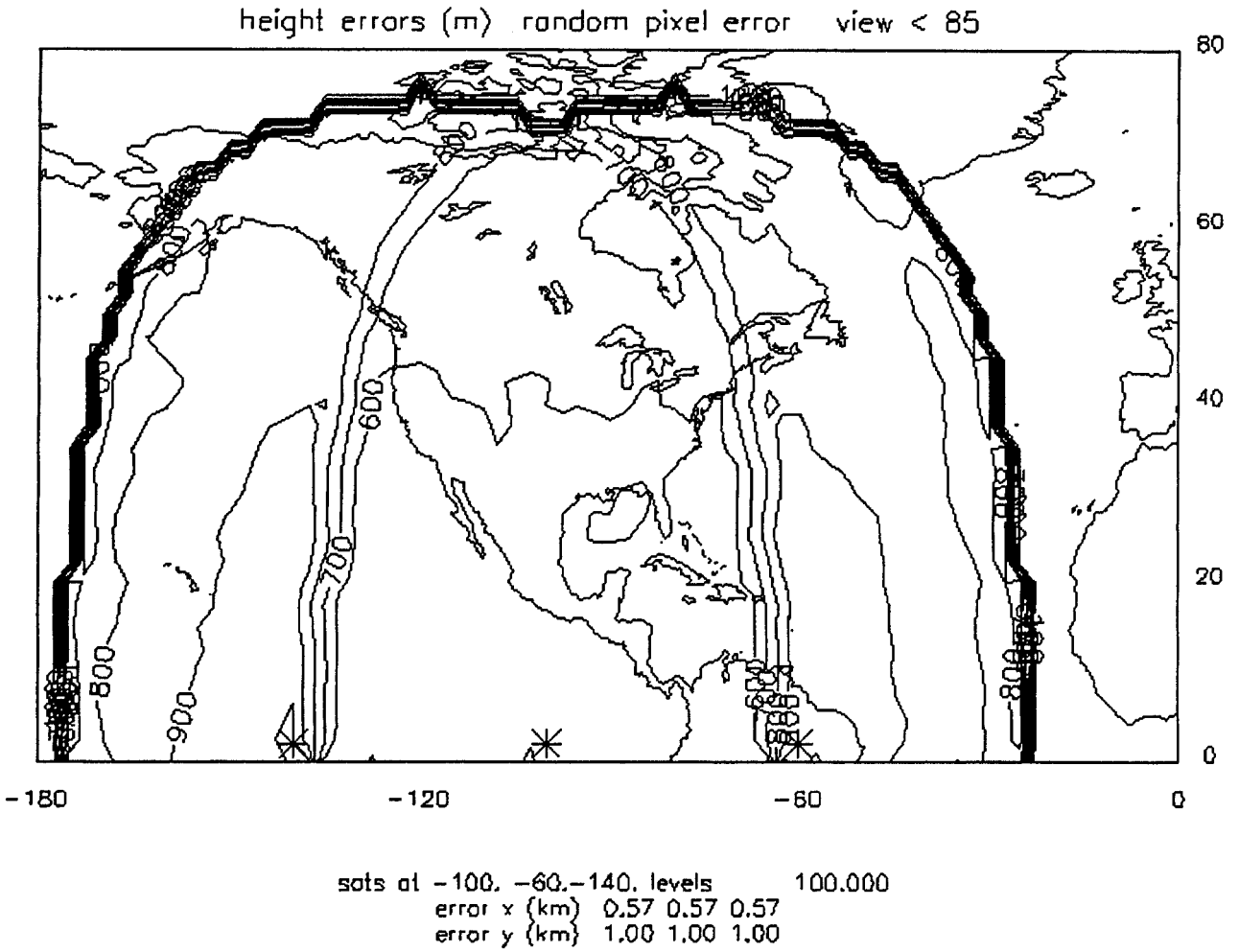

Figure 2. Pure stereo errors from GOES at 60° West and 140° West and 100° West. In the central region, errors are reduced because the redundant observations average out some of the noise. To the west and east, useful results are still obtained with just two measurements. This situation is proposed when the U.S. has 3 GOES operational

Figures 2 and 3 show that improvements occur with the introduction of a third satellite. Good results can be obtained with the mixture of Polar and Geosynchronous satellites. This last idea has been very difficult to implement until now because simpler algorithms require simultaneity. Finally some useful results can be obtained by mixing GOES and METEOSAT with its lower spatial resolution (figure 4). Small errors like these are possible with the mixed height/wind estimation discussed below.

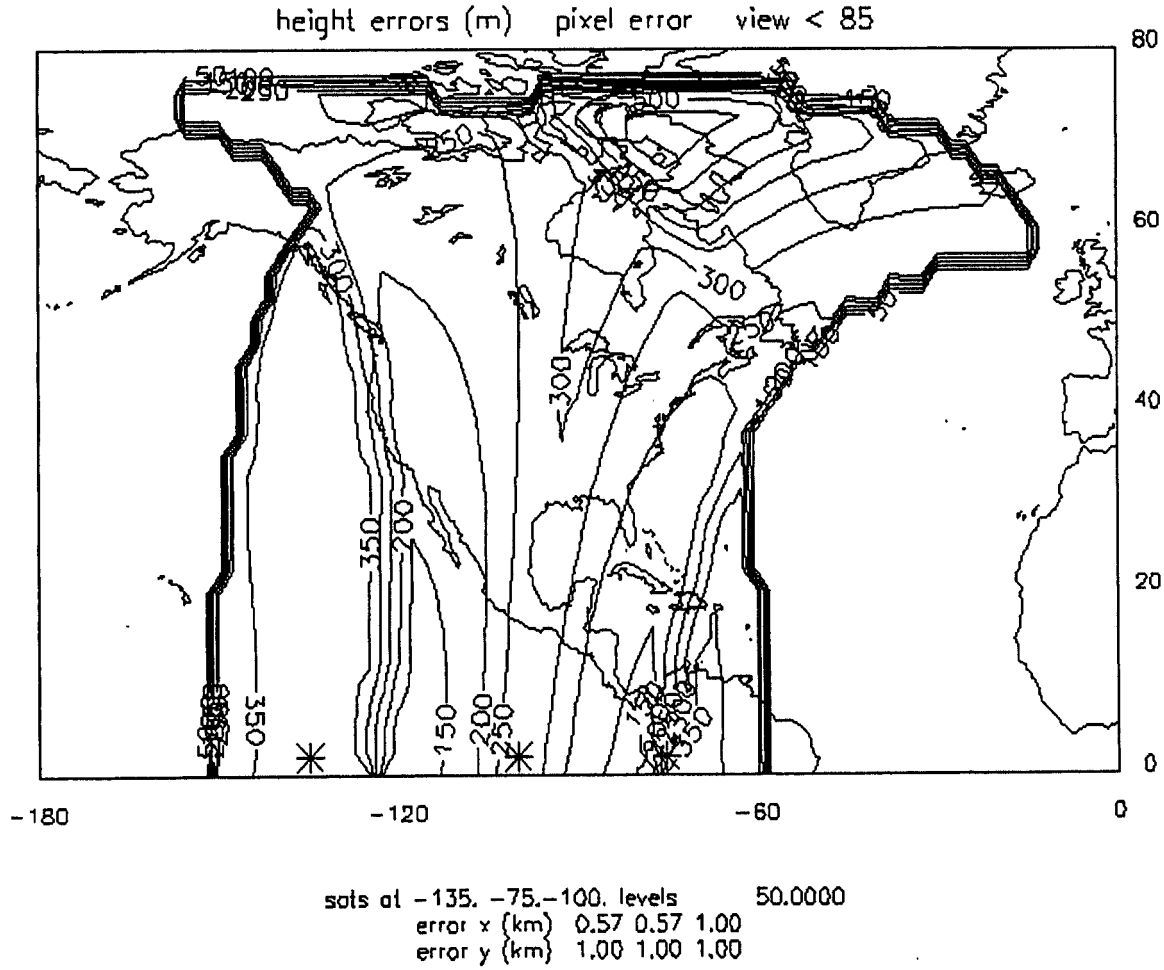

Figure 3 Pure stereo errors from GOES at 75° West and 135° West with one AVHRR 1 km resolution data (one orbit). The errors are reduced by the inclusion of more observations with three satellites in comparison to figure 1.

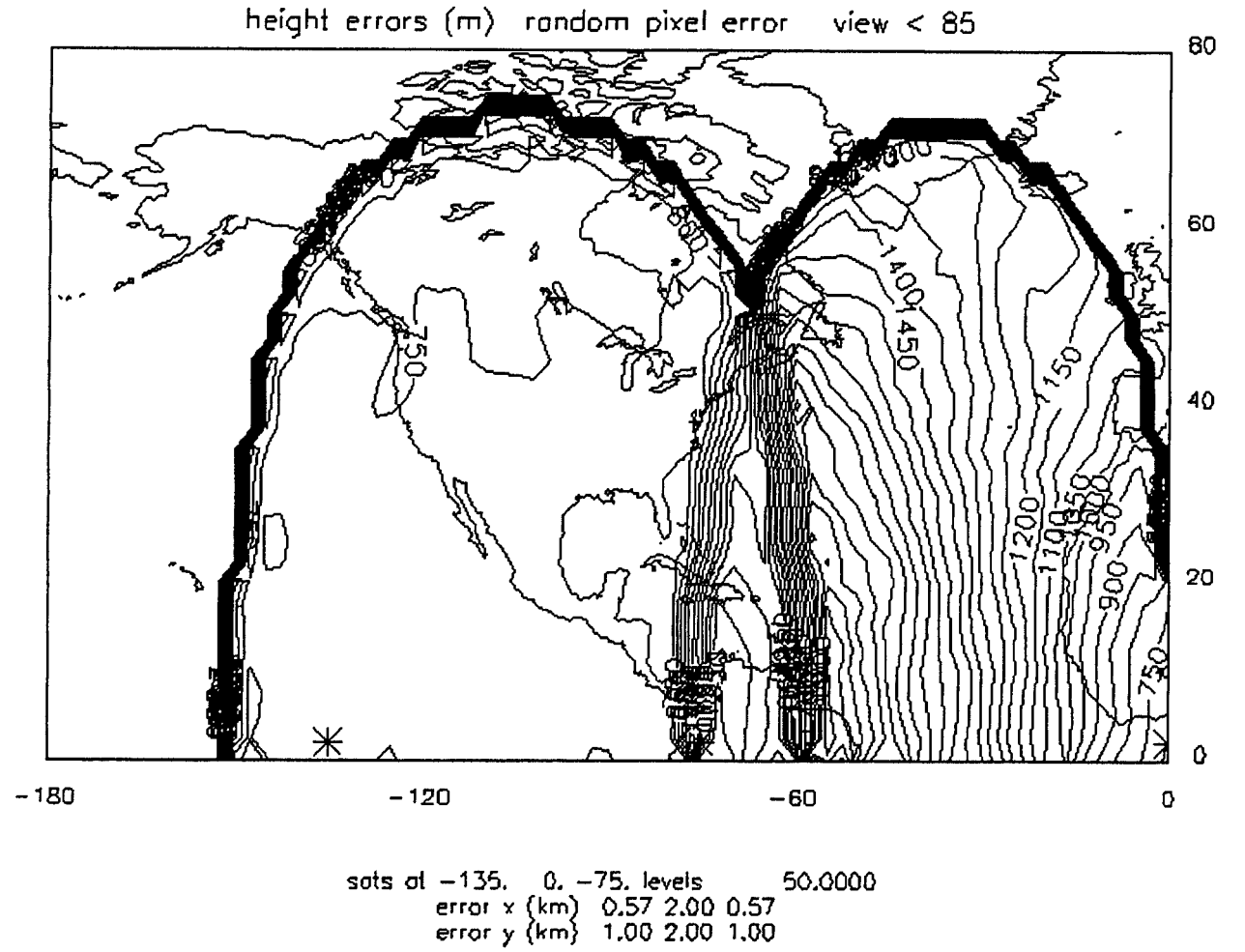

Figure 4 Mixture of GOES and METEOSAT whose resolution is 2 km at best. The use of 2 km resolution data does provide useful results across the Atlantic.

3.0 ASYNCHRONOUS STEREO HEIGHT AND MOTION ESTIMATION

The essence of the method is a least squares fit to all observations minimizing the difference between the apparent position from the observing satellites and an ideal vector which moves in time. By assuming constant velocity many measurements over time can be combined to decrease random noise due to quantized pixel locations.

Let **R**(t) represent the vector position of the cloud in time, t, then equation 1 represents the cloud position with a starting point **R**(0), a velocity **V**(0) and a acceleration, **S**:

1. $$\mathbf{R}(t) = \mathbf{R}(0) + \mathbf{V}(0)\, t + 1/2\, \mathbf{S}\, t^2$$

At first we considered the solution for constant velocity, but then we realized that a cloud would rise significantly over one hour for high winds (100 km/hour > .7 km rise/hour). The acceleration term was

added to tip the wind into approximately horizontal motion. S is approximated by centripetal acceleration (V^2/Rearth) pointing toward the center of the earth. This still allows the potential to measure vertical motion.

For the angles of observation from a satellite, **Rs**, the apparent location, **P**(t), of the cloud is derived for a point on the Earth's geoid from standard navigation software. The true location is located on the line of sight between the satellite and the apparent location, equation 2.

2. $$\mathbf{R}(t) - \mathbf{Rs} = f(\mathbf{P}(t) - \mathbf{Rs})$$

The factor f is unknown and is different for every observation event. Rearranging this and recognizing that no measurement is perfect, eq. 3 represents the error vector between the ideal and the real measurement:

3. $$\mathbf{E}(t) = \mathbf{R}(t) - \mathbf{Rs} - f(\mathbf{P}(t) - \mathbf{Rs}_i)$$

By summing over many observations, a minimum of the Σ ($\mathbf{E}(t) \cdot \mathbf{E}(t)$) provides an estimate of the initial position and initial velocity. The subscript has been added to the satellite view point because more than one viewpoint is needed to solve the equations. The smallest number of observations is two times from one view point and one observation from a different view point. As long as a single cloud facet can be identified, it is best not to have time coincidence between the two view points. This formalism is general enough to accommodate mixtures of Geosynchronous and Polar orbiter observations.

3.1 Implementation

Practically this has been implemented in the MCIDAS system using the operator to manually select a target cloud. Then a small region around the target is correlated to later images in a time loop to derive the sequence of **P**(t) observations relative to view point $\mathbf{Rs}_1$. The operator also selects a point near the cloud later in the time loop as a first guess for the cloud motion. The other geosynchronous image is remapped to the projection of the first and the target patch is correlated to it to find the best match cloud for the other satellite view. A small region around this matched location is correlated in a second time loop from the other satellite providing more **P**(t) observations relative to the second satellite $\mathbf{Rs}_2$. The manual operations might be eliminated in the future but it has been much more practical to deal with selected targets for algorithm development and testing.

3.3 Example 1: Cloud off Baja California

For example we will discuss the detailed analysis procedure for a case from March 3, 1996 between 17 and 18 Z with GOES 8 at 75° West and GOES 9 at 135° West. There was cirrus moving rapidly over the Baja California peninsula. Figures 5 a, b and c show the view of these clouds from GOES 8.

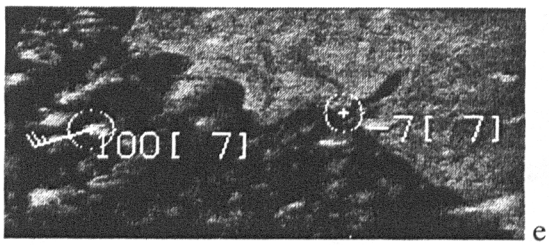

a

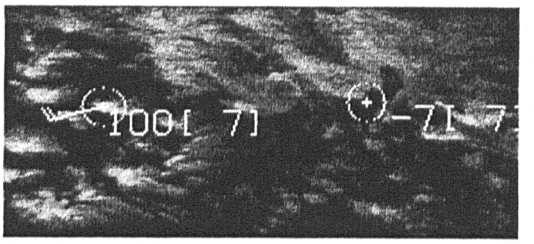

e

GOES 8 17:20 at the cloud

GOES 9 17:19 at the cloud

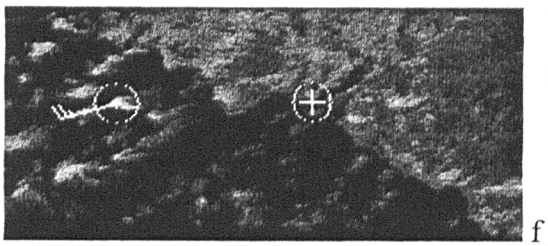

b

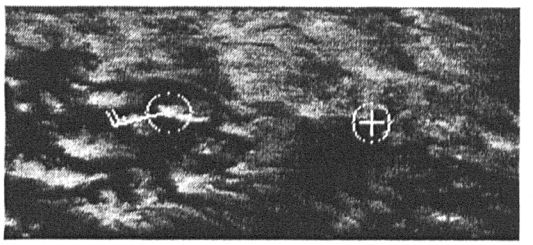

f

GOES 8 17:34 at the cloud

GOES 9 17:35 at the cloud

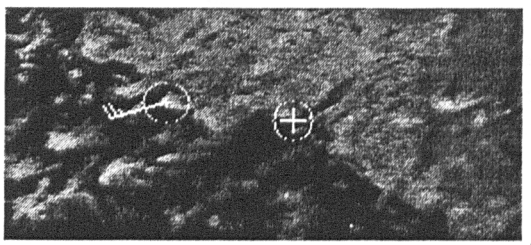

c

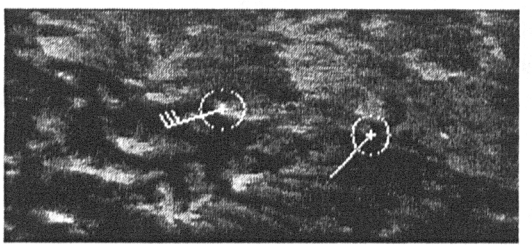

g

GOES 8 17:52 at the cloud

GOES 9 17:49 at the cloud

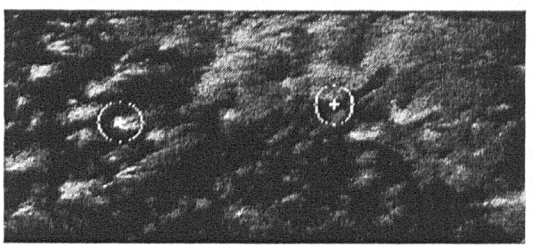

d

Remapped GOES 9 image into GOES 8 projection.

Figure 5: March 3, 1996 clouds near Baja California, Mexico. a,b,c,d from GOES 8 view point and e,f and g from GOES 8 view point.

The operator selected the cloud (or surface point) in the first image in the sequence from the GOES 8 view point (figure 5 a). Then a guess end point location was selected in last image in the loop (figure 5 c). Correlations were performed for times b and c to improved the cloud location matches. Next the program searched the remapped image to find a match to the patch from the first time. This is the

essence of any stereo method, find the object from the two view points. Finally the object is tracked in the second time loop (figure e,f, and g). The + sign indicates the correlation center, the circles show the correlation region, the wind barb shows the estimated wind and the height is displayed in hectometers (100 meters). The number in brackets shows the error estimate obtained by random perturbations added to the pixel locations. Notice that the observation times at the clouds can be different by several minutes because of the different operational scan modes used with GOES (Menzel and Purdom, 1994).

There are two wind and height estimates displayed, one for a cloud and the other for a surface point which should not move and should have 0.0 height (sea level):

Cloud: u	23.9	±0.57 m/s	Surface	u	.38	±0.56 m/s
v	11.1	±0.61 m/s		v	.08	±0.61 m/s
h	9986.	±696. m		h	-711.	±702. m

To give a larger view of this example, Figure 6 shows many cloud height and winds estimated for a 500 km region.

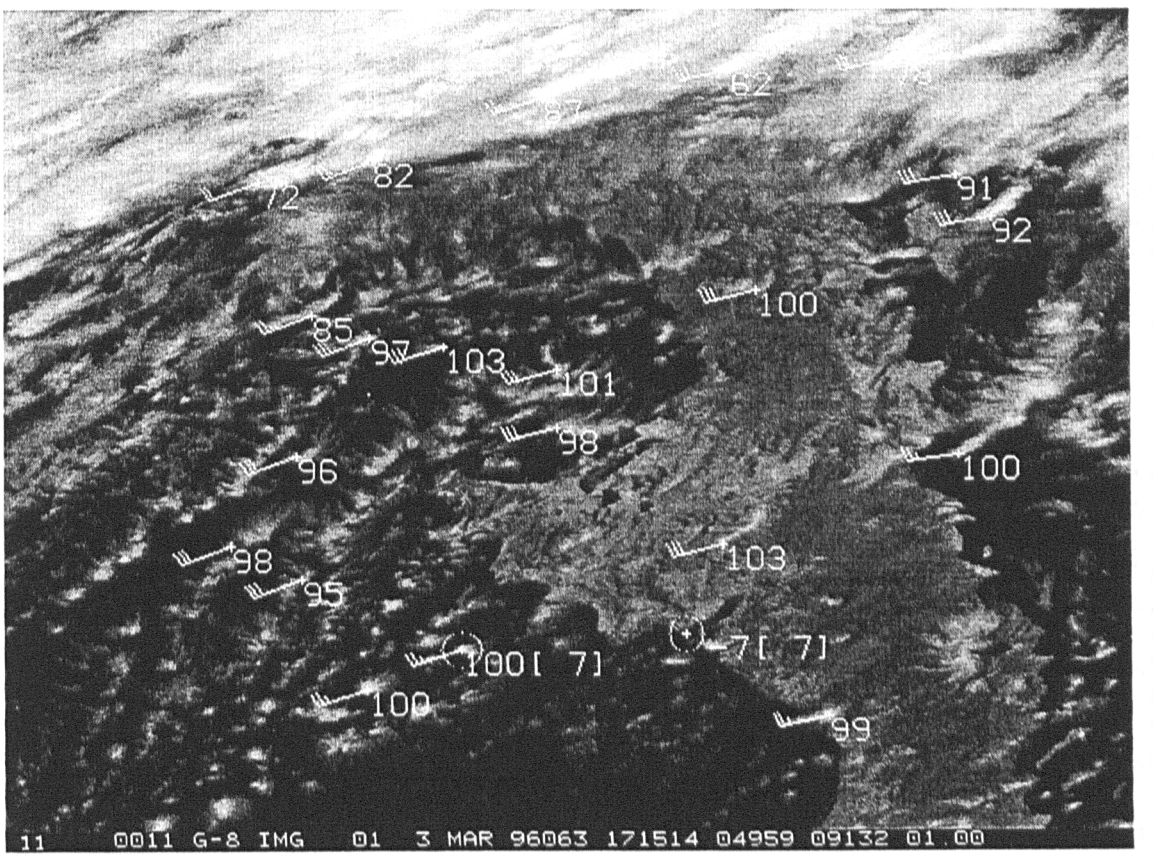

Figure 6, March 3, 1996 analysis, heights shown in hectometers.

3.4 Example 2: Clouds over Texas with 1 minute sampling.

As a second example, one minute interval data was collected over Texas on May 23, 1996 from GOES 8. The GOES 9 data transmitted data at a 7.5 minute interval. Figure 7 shows one image from that sequence with clouds at different heights. The numbers up and the right of the + are the cloud heights based upon the cloud's shadow. The lower numbers come from the composite analysis from 20 to 20:45 Z with the asynchronous stereo height and motion analysis. The two height analyses generally agree on the cloud heights to .5 km accuracy. The shadow height estimate is less accurate because it involves the analysis on only one image and typically the edges of shadows are not distinct.

In more detail, table 1 shows a list of the measurements which went into the asynchronous analysis. One can get an estimate of the cloud motion from each pair of images analyzed. The asynchronous analysis uses the times and apparent locations from all the times.

GOES 8 observations, apparent locations and image to image winds.

200458 *	31.245	98.077	0.	0.
200602	31.257	98.067	15.71	19.54
200706	31.268	98.056	15.72	19.55
200810	31.279	98.046	15.72	19.55
200913	31.290	98.035	15.96	19.86
201017	31.302	98.032	5.23	20.00
201121	31.313	98.028	5.23	20.00
201225	31.325	98.025	5.23	20.01
201909	31.369	97.968	13.27	12.26
202558	31.426	97.915	12.28	15.33
203236 *	31.471	97.866	11.77	12.54
203558	31.493	97.838	13.25	12.29
203701	31.504	97.827	15.93	19.93
203805	31.516	97.816	15.68	19.63
203909	31.527	97.813	5.22	20.07
204013	31.527	97.806	10.45	-.44
204117	31.527	97.799	10.45	-.44
204220	31.538	97.795	5.30	20.40
204324	31.549	97.785	15.67	19.64
205036 *	31.606	97.718	14.70	14.42
GOES 9 observations				
200421 *	31.242	97.893	0.	0.
201219	31.304	97.841	10.24	14.33
201948 *	31.366	97.772	14.71	15.52
202439	31.391	97.740	10.27	9.66
203419	31.466	97.663	12.57	14.37
204218 *	31.517	97.609	10.77	11.66
204947	31.567	97.545	13.43	12.57
hr/min/sec	latitude	- longitude	u (m/sec)	v (m/sec)

Final analysis

u 12.3 $\pm$ 0.2 m/sec

v 13.7 $\pm$ 0.3 m/sec

h 9838. $\pm$ 491. m

9.3 km shadow height estimate for the 200458 image.

Conventional wind estimate (first to last GOES 8 image)

13. to 15. m/sec

14. to 16. m/sec

Table 1: Detailed data on one particular cloud.

There is considerable fluctuation in the image to image wind estimate. These use the conventional method of estimating the motion: just difference the apparent position and divide by the time interval. The fluctuations occur because the time interval is very short and the cloud does not move very far. For a 5 m/sec motions, the cloud will only move 300 meters in one minute or less than one GOES pixel. In the current version of the program, clouds centers are located at pixel centers. This introduces some round off error which might be reduced by an analysis of the shape of the correlation function used to measure the movement of the cloud. We are studying this problem now, especially in view of the applications with lower resolution data (IR).

The conventional motion method can also be applied to the beginning and ending cloud giving a variety of results depending upon which facet of the cloud is tracked. In fact this particular cloud under goes some change in shape so there is some ambiguity in cloud motion or development.

To look at the impact of numerous observations, just a few selected observations were extracted for the sequence of observations above. For just the 6 observations with a * in the table, the analysis gives:

u 12.4 $\pm$ 0.4 m/sec
v 14.4 $\pm$ 0.5 m/sec
h 10473. $\pm$ 664. m

The biggest impact of the extra observations is to reduce the uncertainty of the result. The analysis with just 6 observations is useful.

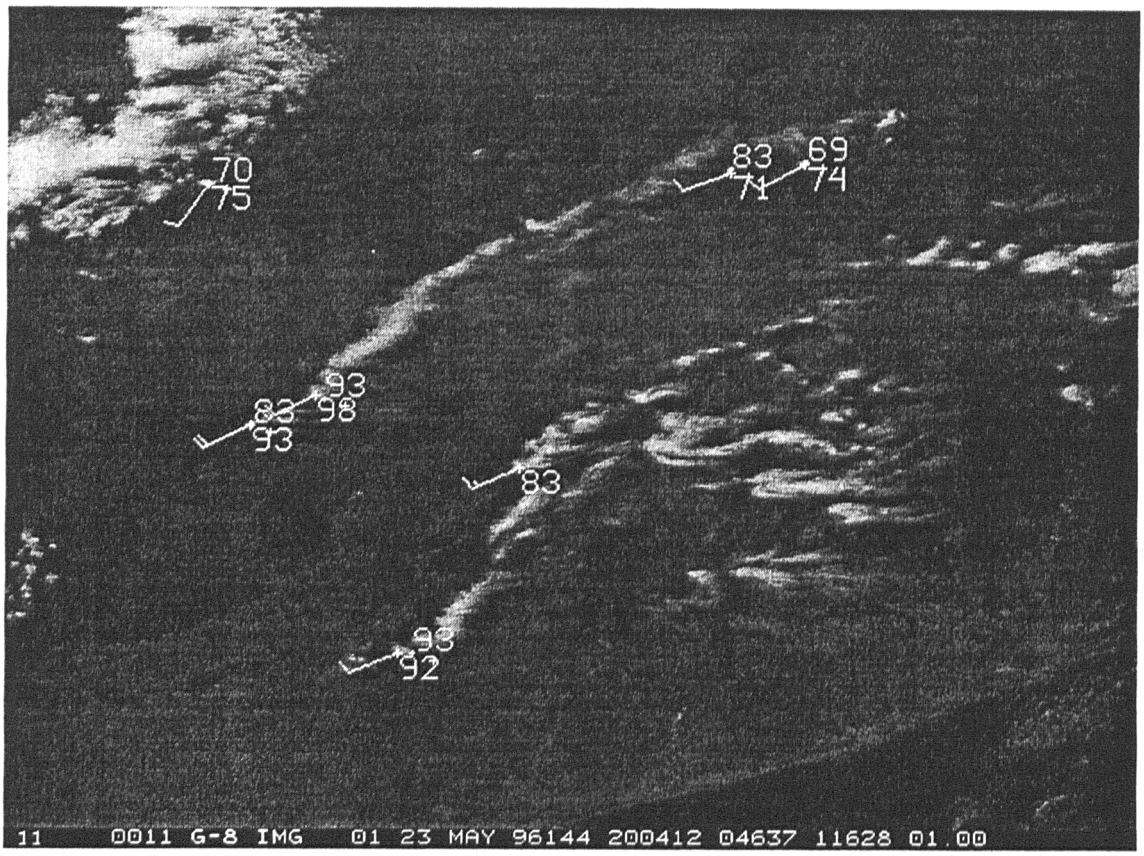

Figure 7: May 23, 1996 GOES 8 image with cloud height estimated by shadow (upper right) and asynchronous stereo (lower right). Heights in hectometers (100m).

Example 3, Multiple cloud levels and motions

This example shows a much more complex case with clouds which often did not last for 30 minutes. The shadow method lists the height of the cloud above the ground which is generally less that the cloud heights. But the height of the mountains are higher than the real mountains. Similarly the height of the fog is higher that the plains of Colorado by about 1 km. This is evidence that either GOES 8 or GOES 9 had some navigation error. We plan to modify the analysis program to incorporate a ground reference point to remove this bias. The 4.2 km cloud height was assigned incorrectly because the cloud was not matched between the two view points.

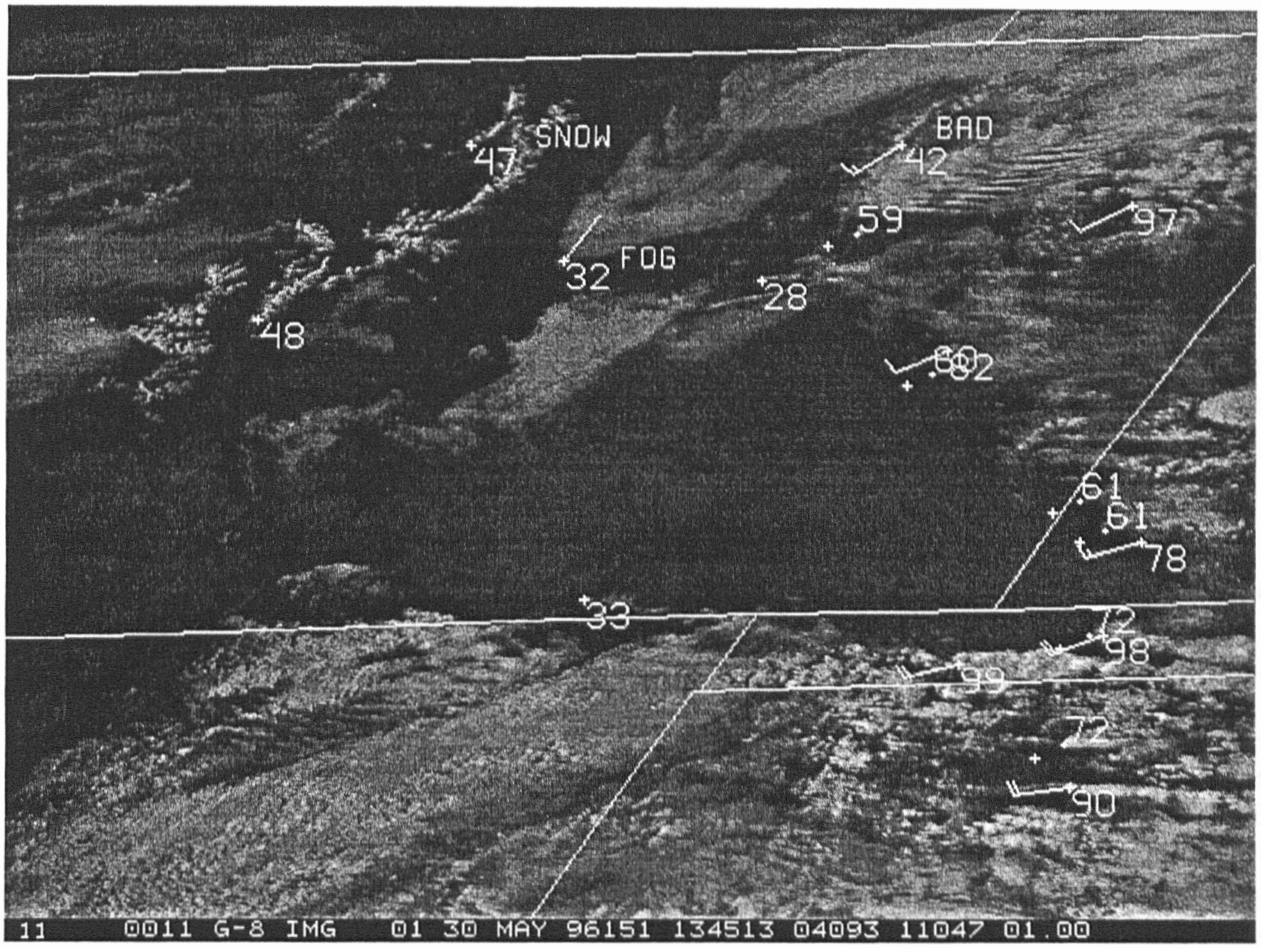

Figure 8, Complex case for example 3. Heights in 100 of meters.

4. VERIFICATION

4.1 Internal or regional consistency

Looking back at figure 6, one sees two types of clouds and two groups of cloud heights: around 10 km and around 8 km. These are not grouped randomly, but are associated with the particular cloud type. Trying to derive cloud height for the cirrus cloud in the southern part of this image from IR data would be difficult because none of these clouds would completely file the 4 km IR field of view and also the emissivity of the clouds would be less than 1.0. Finally he fact that the land height was near zero height verifies the analysis.

4.2 Shadow heights

Dills and Purdom (1993) discussed a shadow height estimation method at the last winds conference. This method has been improved by selecting the shadow and allowing the computer to search for the cloud. Since the cloud edge is more distinct than the shadow, it is easier to find. This provides an independent geometrical cloud height to be used to verify the results shown above. Distinct shadows are

more difficult to find than clouds so the multi-satellite cloud height methods is more widely applicable. Also the shadow method is less accurate at certain times of the day (near local noon). Still as shown in example 2 above shadows provide some useful results.

4.3 Ground Truth

A final opinion on the accuracy of our technique must await a comparison between a cloud and some ground based height measurement. There will be a special experiment over Oklahoma in June 1996, Cloud Layer Experiment (CLEX) sponsored by the Center for Geosciences at CSU. This will provide detailed cloud observations by airplanes and ground based measurements. The asynchronous stereo analysis will be carried out for comparison to these "ground truth" observations

5.0 FACTORS AFFECTING ACCURACY

The asynchronous algorithm now calculates height and motion together so improvements in one component generate improvements in the other component.

5.1 Remapping and Registration

Among the factors which affect the cloud height accuracy is precise remapping and registration between images. With the GOES 8 and 9 this is a smaller problem than older satellites, but can still be a significant. For special observation series like 5 minute or 1 minute sequences where clouds do not move very far between sequential images, and for slow moving clouds in 15 and 30 minute interval sequences, registration accuracy becomes more important. For special studies, adjustment of the navigation is fairly easy in the MCIDAS environment. For automated unsupervised estimates, poor navigation will cause larger problems.

For cloud motion measurements, the cloud can be identified by hand or by a correlation technique. Similarly for the height estimate to work correctly, some method is needed to match a cloud feature between the different view points. Our current algorithm does this by remapping an image from one view point into the other and then correlating the selected cloud feature. Then the cloud feature is tracked automatically in the image sequences from both satellites (one or more times). This transfer is critical and systematic navigation errors will amplify the errors.

Notice that the correlation between satellites is identical to the time coincident stereo method. But the information about the times of the two images is now included in the analysis. Inherent in all cloud tracking is the assumption that the cloud does not change it shape over the time interval of correlation. For clouds which change shape more rapidly than the observation interval, neither velocity or height would be accurate. This fact shows the advantage of rapid sequences of observations.

There is a related problem, cloud motion and height can not be determined for horizontally homogeneous clouds like some cirrus or stratocumulus clouds. Ultimately geometry methods can only analyze cloud edges in contrast to the temperature lapse rate technique which assumes horizontal homogeneity and fails when there are many cloud edges.

5.2 Number of observations

Improvements in cloud velocity and height accuracy occur with the new method with the inclusion of more observations of the same cloud facet. We have tested several cases with as many as 20 observations (within a one hour period) to derive an initial height and velocity. Cloud continuity in time can be improved by frequent viewing. If a cloud is changing shape rapidly in time, it can still be tracked by successive pair correlations. Suppose one has a sequence of 4 images 5 minutes apart. the simplest correlation method compares 1 to 2, 1 to 3 1 to 4. but a better method would be to correlate 1 to 2. Then compare the best match location in 2 to 3 and similarly the best location in 3 to 4. This shows the advantage of frequent viewing, 1 or 5 minute observations allow many more targets to be tracked than 15 minute or 30 minute interval observations. This will happen either because the target cloud changes shape or gets lost in a field of many similar clouds.

By providing many measurements in time, it is easier to maintain cloud continuity in situations with many similar small clouds. Yeisley (1996) discussed this for several case studies which showed the advantage of 5 minute interval observations for tracking low level scattered cumulus. He also pointed out that cloud lifetimes limit the number of cloud candidates for observation frequencies longer than 15 minutes.

5.3 Is cloud motion wind?

The motion of the correlation center may or may not represent the wind, but it can still be used to measure height. For instance wave cloud height can be measured even though the cloud motion does not represent the wind. The problem of connecting cloud motion to wind has been discussed extensively at this workshop by others, and is beyond the scope of this study.

5.4 Resolution

Estimation of the height of clouds and their motions depends fundamentally on how well a cloud patch can be aligned with one later in time (or from the other view point). This is limited to zero order by the pixel resolution of the images. By matching extended patches it may be possible to estimate subpixel scale latitude longitude differences in the position of the patches by careful examination of the shape of the correlation function in space. This would especially be needed for the analysis of IR data which at best has resolution of 4 km from current geosynchronous platforms. Mixing different resolutions appears possible and the simulation study results shown in figure 4 show promise that 2 and 1 km resolution data can be used together.

6.0 GOES OPERATIONAL ISSUES.

Many new opportunities exist with the GOES 8 and 9 satellites because of the diverse observation schedule. Generally the western continental U.S. is sampled every 15 minutes from both view points. Thus given a typical 30 minute cloud life time, 6 or more observations can be incorporated into one height wind analysis. For servere weather events, observations from 1 to 5 minute interval is routinely available. Precise navigation is a continuing problem, but is being improved by NESDIS. The possibility of a third GOES satellite next year makes the opportunities for short interval multiple

measurements even more wide spread. Routine observations from 3 geosynchronous satellites will improve the precision of the winds and heights.

7.0 CONCLUSIONS

Asynchronous stereo and motion analysis uses stereographic techniques, but does not require time synchronization between the different satellite images. Also the inclusion of many measurements improves the accuracy of the height and the motion. It is hoped that asynchronous stereo and motion analysis will replace temperature dependent methods with geometric calculations where the opportunity exists, and help refine temperature dependent methods in other situations. Cloud optical properties like emissivity could also be derived from the temperature lapse rate analysis given the geometric height of the cloud.

8.0 ACKNOWLEDGMENTS:

Portions of this research were supported by NOAA grant number NA37RJ0202-10. The Center for Geosciences at Colorado State University also provided support. A substantial portion of this research has also been reported at the Third International Wind Workshop sponsored by the World Meteorological Organization (Campbell et al. 1996).

9.0 REFERENCES

Campbell, G. Garrett, James F.W. Purdom and Carol E. Vaughn, 1996; Update on Accurate CloudMotion and Heights Using Time Adjusted Stereo; Third International Wind Workshop.

Menzel, W.P. and J.F.W. Purdom, 1994: Introducing GOES-I: The first of a new generation of geostationary operational environmental satellites. *Bull. Amer. Meteor.* Soc., **75**, 757-781.

Purdom, J.F.W., and P.N. Dills, 1993: Cloud motion and height measurements from multiple satellites including cloud heights and motions in polar regions. Second International Wind Workshop, Tokyo, EUMETSAT, Darmstadt-Eberstadt, Germany, 245-248, ISSN 1023-0416.

Yeisley, M. O., 1996, Low Level Mesoscale Wind Field Generation from Cloud-Track Winds Using GOES-8 Imagery. M.S. Thesis, Dept of Atmospheric Science, Colorado State Univ.

Meteorological features from principal component image transformation of GOES imagery

Donald W. Hillger

NOAA / NESDIS / ORA / RAMM
CIRA - Colorado State University
Fort Collins CO 80523-1375

ABSTRACT

A major problem with multi-spectral satellite imagery is that images in many of the spectral channels (or bands) contain redundant information about the atmosphere. By using Principal Component (PC) analysis to transform multi-channel satellite images, this information redundancy can be reduced. PC Image (PCI) analysis finds the information that is common among the various channel images and puts that information into the PCIs in descending order of significance. The first PCI contains common information, leaving other (channel-difference) information for higher-ordered PCIs. A second PCI is then formed which contains information common to the channel images other than that explained by the first PCI. The process continues until the number of PCIs is equal to the number of channel images being transformed. If none of the original channel images contains redundant information, then a PCI transformation is not needed. However, this is not the case with most satellite images. Because of channel image redundancy, the number of useful PCIs is often less than the number of channel images being transformed. The highest-order PCIs may contain only noise or slight differences among some of the channel images, however, these differences are of importance, especially for less obvious meteorological features in the atmosphere.

Many interesting examples of PCIs created from GOES-8/9 Imager and Sounder data are possible. For the 5-channel GOES Imager, the interpretation of the PCIs is fairly predictable when they are created on a large spatial scale. The main difference in interpretation occurs between day and night when the presence or lack of visible radiation is an important factor.

For the GOES Sounder, the interpretation of the PCIs is more complex, considering that input can consist of up to 19 channel images (1 visible channel and 18 IR channels). Different subsets of the Sounder channel images result in different products. With proper selection of channel images, emphasis can be placed upon either temperature or water vapor features in the atmosphere, or on features of the ground surface or clouds.

Keywords: GOES, Imager, Sounder, satellite, imagery, principal component analysis, meteorology

1. INTRODUCTION TO PCI TRANSFORMATION

Principal Components (PCs) have many uses, among them is the ability to compress the information content (or signal) and simplify multivariate data by reducing the dimensionality of the data set[1]. Certain features that are hidden in the data are also brought out by PC analysis[2]. PC theory dictates that the information content of the PCs is compressed into the PCs in descending order of significance, with the lower-order PCs containing the primary information content, and the higher-order PCs containing other information and noise. Both Morrison[3] and Preisendorfer[4] give good graphical representations of the PC transformation process. The process can be summarized as a translation and rotation of the original coordinate system into a new coordinate system that better reflects the principal modes of variability in the data set being analyzed.

2. APPLICATION TO GOES IMAGER AND SOUNDER

In the case of multi-spectral satellite imagery, there is usually a high redundancy in the multitude of channel images. By using PCI analysis, this image redundancy can be eliminated, parsing the channel images into basic image components[5,6]. This allows the user to concentrate on the similarity in the channel images, as well as on the differences among the channel images. Satellite images are also inherently noisy. PCI analysis can help suppress noise too. Since noise is random, it is a higher-ordered component in images compared to other signal information in the satellite images. Noise is typically relegated to the higher-order image components, components which contain little, if any, other information. Often these higher-ordered image components can be ignored.

The process of transforming satellite imagery into PCIs is based on statistics generated from the satellite images. A vector of satellite imagery consists of one measurement from each channel image over a given location. The number of elements in the vector

is equal to the number of channel images that are transformed. Satellite images may be manifest in several different measurement units. In the case of GOES imagery, the basic units supplied to data users are 10-bit GVAR (GOES Variable) counts (0-1023), a non-dimensional scaled unit which has a fixed and linear scaling to radiance units measured directly by satellite instruments. Other possible measurement units include radiances, radiance temperatures/albedos, and 8-bit display counts. Radiances are linear with 10-bit GVAR counts, but due to variations in the magnitudes of radiances for the channel images, there is a difference in the resulting PCIs when using radiance units as input. Likewise, since the transformation of radiances into radiance temperatures uses the inverse of the non-linear Plank function, the resulting PCIs are different from those created from satellite imagery either input as 10-bit GVAR counts or input as radiances. PCIs created from 10-bit GVAR counts and those created from IR temperatures (or albedos for the visible channel) are not significantly different, as shown in later examples. Finally, the transformation into 8-bit display counts is another non-linear process from IR radiance temperatures (a two-part linear process with an inflection point, which will not be explained here) or from visible albedos (a square root function). This form of satellite imagery is common because image display systems are almost universally 8-bits deep. Display counts, being 8-bits deep as opposed to 10-bits deep, lack the precision of the original 10-bit GVAR counts. The resulting PCIs generated from 8-bit display counts are again different from PCIs generated from other input measurement units. Examples of PCIs generated from either radiances or from 8-bit display counts are not shown in this writeup.

Regardless of the input measurement units, the transformation of each channel image vector, designated by CH for channel images, into a principal component image vector, designated by PCI for principal component images, takes on the form

$$PCI = E\ CH$$

where E is the eigenvector matrix, which is obtained from the covariance matrix of the satellite channel images through the use of standard mathematical packages for eigenvector transformation. This covariance matrix is easily generated from the satellite imagery (or just a sample of the satellite imagery) being analyzed. The covariance matrix explains the relationships among the channel images, allowing the eigenvector transform to parse that information into the component images. This parsing separates common and difference information from the multi-spectral imagery. The result of the eigenvector transformation is a concentration of the satellite information into as many image components as the number of available channel images. The first image component looks similar to the image from the channel (or channels) with the maximum signal, and higher-order image components contain primarily image-difference information and noise.

In the simplest 2-dimensional case, two channel images, ch1 and ch2, are transformed into two PCIs (pci1 and pci2) using

$$pci1 = e1 * ch1 + e2 * ch2$$

and

$$pci2 = f1 * ch1 + f2 * ch2$$

where e and f are linear transformation vectors (eigenvectors, or columns in the eigenvector matrix). The same e's and f's are used to transform each pixel (or picture element) in the original channel images. In this case, the pci1 will contain the information that is common to ch1 and ch2 images, and pci2 will contain the information that is different between ch1 and ch2 images.

3. EXAMPLES OF GOES AND PC-TRANSFORMED IMAGES

PCIs are created by the PC transformation of channel images from both the GOES Imager and Sounder instruments. The number of possible PCIs is equal to the number of satellite channel images being transformed. The significance of the PCIs is quantified by the eigenvalues, which are the variances explained by each eigenvector (or the PCIs resulting from each eigenvector). The eigenvalues contain information on the transformation process from channel images to PCIs. The first eigenvector gives the transformation for the first PCI, the second eigenvector gives the transformation for the second PCI, etc. In the case of GOES Imager, the first three PCIs typically contain more than 98% of the information content in all the channel images, while the higher-ordered PCIs contain information of much lesser magnitude, as well as noise. Hillger[5] gives an example using polar-orbiting satellite sounding imagery of the distribution of information (or signal) in satellite channel images. Also shown in that reference are the explained variances of the resulting PCIs generated from those sounding channels. The result of the PCI transform is the concentration of the signal into the first few PCIs, while higher-ordered PCIs contain little or no significant information.

In Figure 1 (a thru d) are a set of images from the GOES Imager for 31 January 1995 at 1645 UTC. Only four of the five GOES Imager channels are shown. Figure 1a is the visible channel image at 0.7 μm. The bright area over most of the northern half

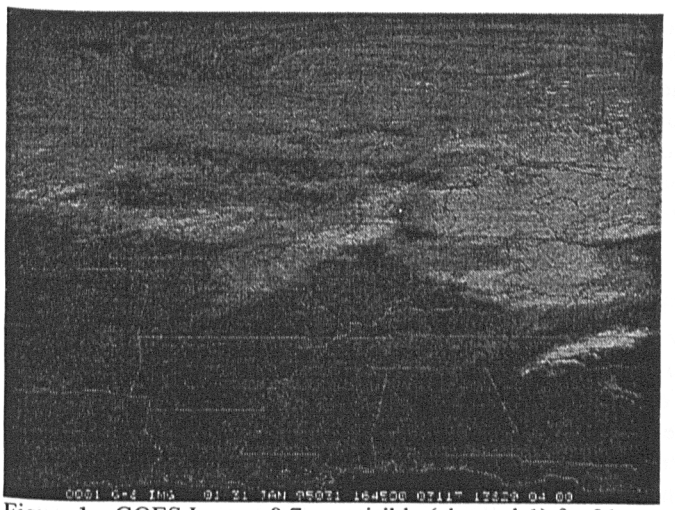

Figure 1a. GOES Imager 0.7 μm visible (channel-1) for 31 January 1995 (year/day 95031) at 1645 UTC.

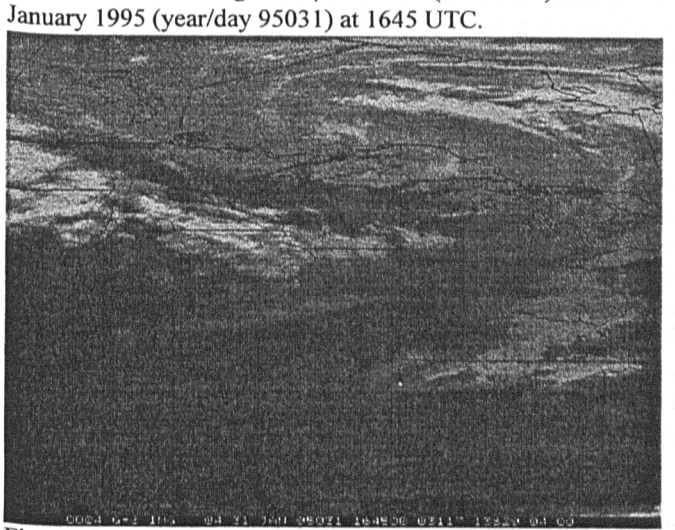

Figure 1b. Same as Figure 1a, but for 10.7 μm IR (channel-4).

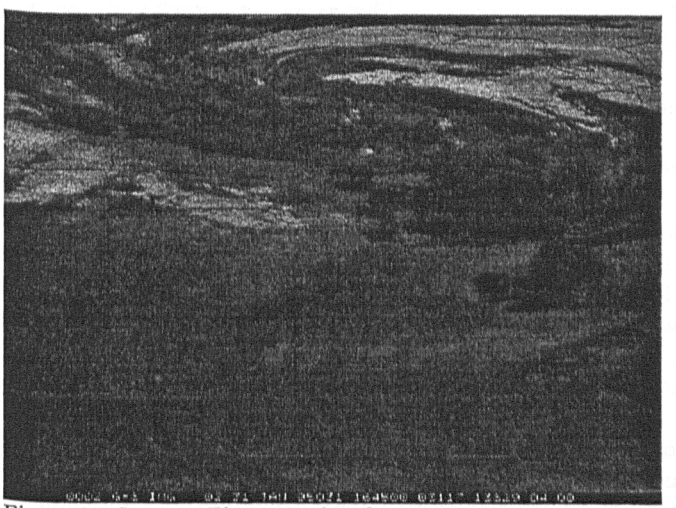

Figure 1c. Same as Figure 1a, but for 3.9 μm IR (channel-2).

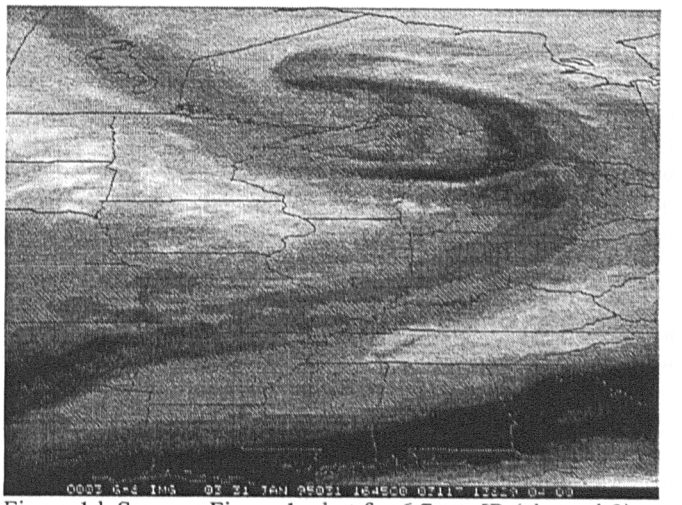

Figure 1d. Same as Figure 1a, but for 6.7 μm IR (channel-3).

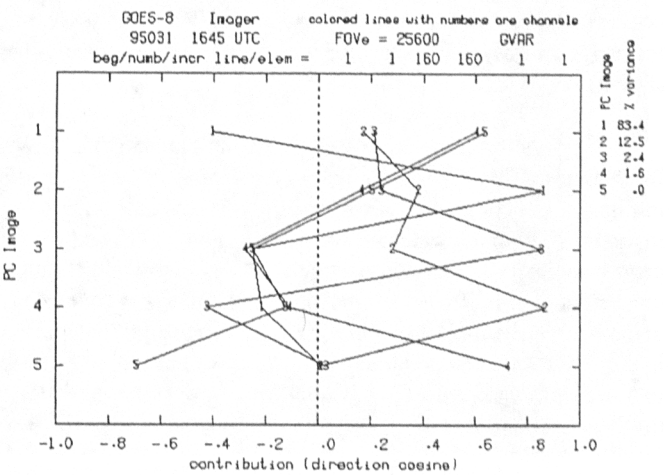

Figure 2a. PCI transformation vectors for all 5 GOES Imager channels for the case shown in Figure 1.

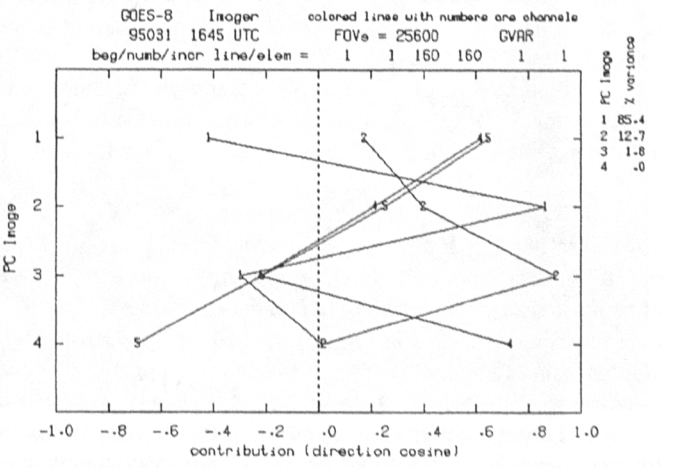

Figure 2b. Same as Figure 2a, but for 4 of the 5 GOES Imager channels (without channel-3).

of the image is due to reflected radiation from clouds and snow cover on the ground. Figure 1b is the same area as seen in channel-4 at 10.7 μm, which is an emitted thermal IR channel. The grey shades in IR channels are normally inverted so that IR images look similar to visible images. Emphasis in this thermal IR channel is on the highest clouds, since they are the coldest and have the lowest radiances. Figure 1c is similar to Figure 1b, but channel-2 at 3.9 μm has a reflected radiation component in addition to emitted radiation. Emphasis in this spectral channel is again on the highest (coldest) clouds, but important differences exist for lower clouds which may have both reflected and emitted radiation components. Finally, Figure 1d is the water vapor channel image at 6.7 μm. In this channel, the upper-level water vapor field associated with upper-air currents is most easily distinguished. Channel-5 at 12 μm is very similar to channel-4 at 10.7 μm and is not shown.

The PCI transform vectors for the channel images shown in Figure 1 are given in Figure 2. Figure 2a gives the PCI number along the vertical axis. The GOES spectral channels are designated by the numbered lines in the figure. On the horizontal axis is the weight given to each of the spectral channels in the transformation into each of the PCIs. The units of the horizontal axis are direction cosines (-1.0 to 1.0). The square of this number gives the weight for each channel image. Anything above a direction cosine of 0.7 (or below -0.7) has a weight of more than 50%. From this figure, the channels contributing significant information to each PCI are easily determined. As an example, PCI-1 is composed of positive contributions from IR channels 4 and 5 and a negative contribution from visible channel-1. Channel 2 and channel 3 have only a minor contribution to PCI-1. One way to think of this channel combination is the emitted IR radiation among the various channel images is being added and will become dominant, while reflected visible radiation is being subtracted from this image. The resulting image is similar to a pure IR channel image. This channel image combination can be confirmed by looking at PCI-1 in Figure 3a. Emphasis in PCI-1 is on the highest clouds, and on the other end of the range of grey shades are the warmest ground surfaces. This is similarly true for channel-4 in Figure 1b and for channel-5 (not shown).

Back to Figure 2a, PCI-2 (shown in Figure 3b) is composed primarily of visible channel-1 with lesser contributions from the IR channels. This figure is similar to the visible channel shown in Figure 1a, but with the highest clouds de-emphasized. Next, PCI-3 in Figure 2a is composed primarily of water vapor channel-3 and lesser contributions from the other Imager channels. Compare PCI-3 in Figure 3c with the water vapor channel shown in Figure 1d. Next, PCI-4 in Figure 2a is composed primarily of channel-2 and lesser contributions from the other channels. PCI-4 (shown in figure 3d) should be compared to channel 2 (shown in Figures 1c). What is most evident in PCI-4 is the emphasis upon the snow-covered areas. The snow-covered area is best seen in the original GOES images in the visible channel shown in Figure 1a. The emphasis upon snow cover is a result of the particular combination of channel images in this PCI. Reflected visible radiation in channel-2 is emphasized and emitted IR radiation is de-emphasized. The particular channel image combination in PCI-4 is good for snow cover detection with less possibility of confusion with low clouds as is the case with the visible channel alone.

Finally, PCI-4 (shown in Figure 3e) is constructed as a channel-4 minus channel-5 difference. Usually the only difference between channel 4 and channel 5 is the amount of atmospheric absorption due to water vapor. This channel difference normally shows low-level water vapor information, but due to the winter season, little water vapor is present. What appears are small variations in surface emittance between these two channels. A summer season image would give a better water vapor signal with which to work.

It appears that most of the GOES Imager channels are fairly independent. Several of the PCIs are composed of one primary GOES channel. However, even minor contributions from channels other than the primary channel may make a significant difference in the detection of certain meteorological or surface features. The snow cover detection in PCI-4 is one of the best examples.

Next, we'll see what happens if one of the GOES channels is deleted from the PCI transformation. This is shown in Figure 2b, where the PCI transform vectors are given for four of the five GOES channels. GOES Imager channel-3 is not used in this transformation. The resulting PCI transform vectors are similar to the PCI transform vectors shown in Figure 2a with the elimination of PCI-3 and a re-numbering of the higher-ordered PCIs. Thus the new PCI-3 is similar to the old PCI-4, and the new PCI-4 is similar to the old PCI-5. PCI-3 in Figure 4, showing snow-covered ground, is almost identical to PCI-4 in Figure 3d. This means it is the combination of channels which is important for feature detection, and not the PCI number.

To get a better understanding of the PCI transformation process, Figure 5 shows scatter diagrams of some pairs of GOES Imager channels. Correlations between the measurements in each scatter diagram are given in the upper right-hand corner of each figure. The axes on each graph are labeled according to radiance temperature even though 10-bit GVAR counts are the measurement unit used for the PCI transform. Figure 5a is a scatter diagram of channel-2 vs. channel-4 for the case shown in Figure 1. This figure shows a strong correlation (0.71) between these spectral channels. Differences between these channels are due to the fact that channel-

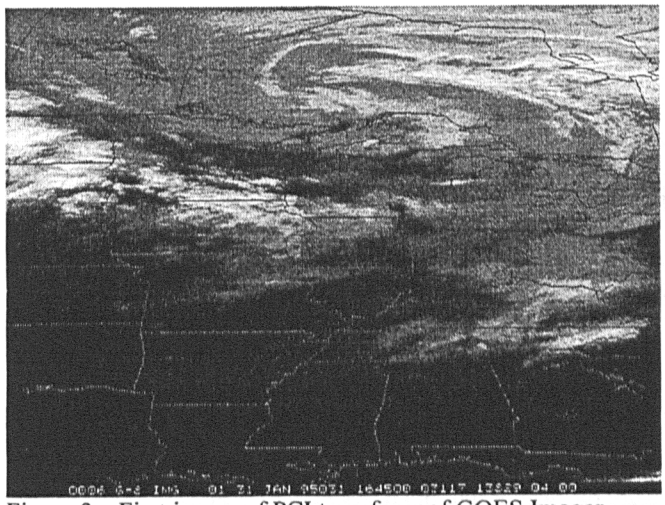

Figure 3a. First image of PCI transform of GOES Imager channels for the case shown in Figure 1.

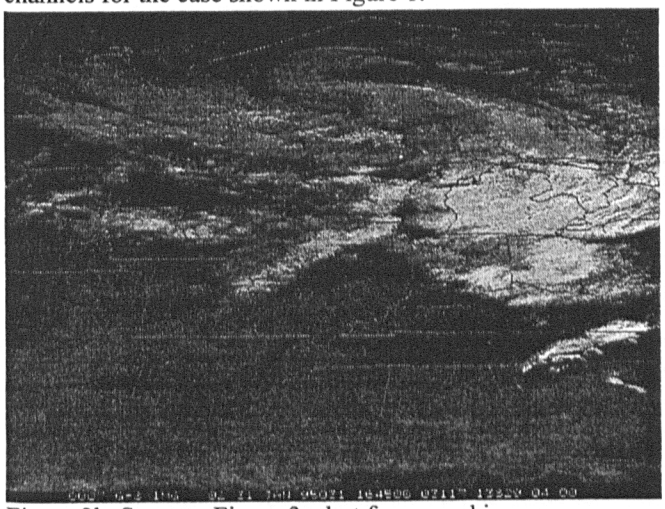

Figure 3b. Same as Figure 3a, but for second image.

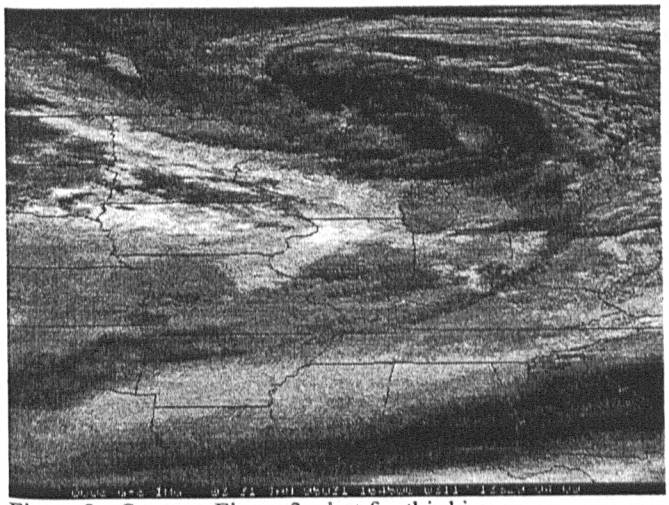

Figure 3c. Same as Figure 3a, but for third image.

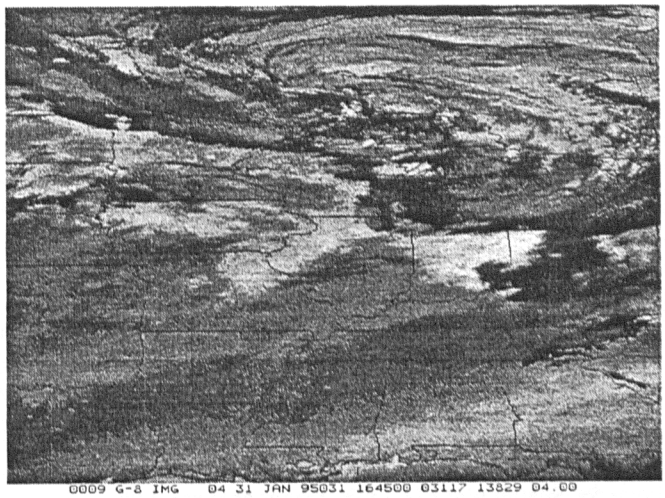

Figure 3d. Same as Figure 3a, but for fourth image.

Figure 3e. Same as Figure 3a, but for fifth image.

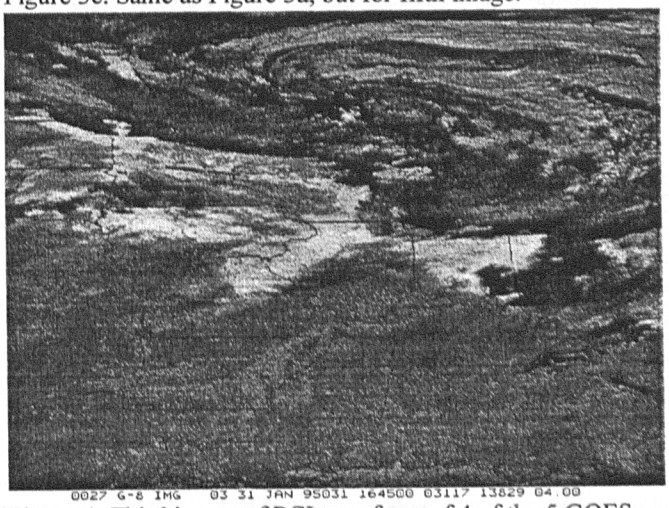

Figure 4. Third image of PCI transform of 4 of the 5 GOES Imager channels (without channel-3) for the case shown in Figure 1. Compare to Figure 3d.

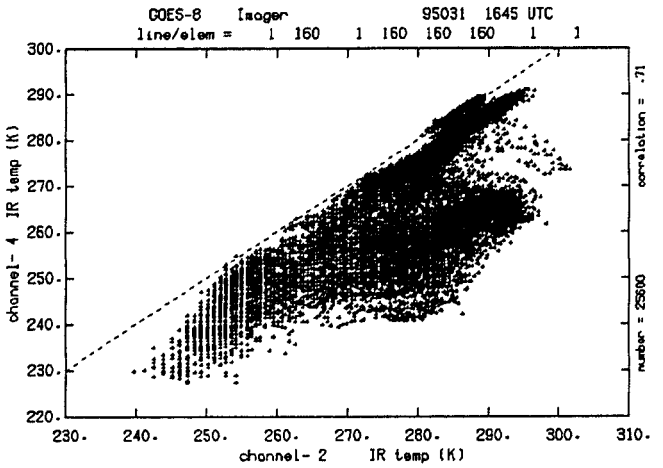

Figure 5a. Scatter plot of GOES Imager channel-2 vs. channel-4 IR temperatures for the case shown in Figure 1.

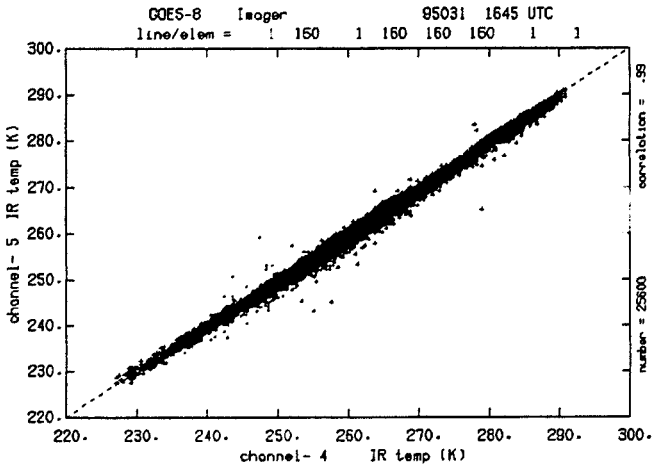

Figure 5b. Same as Figure 5a, but for GOES Imager channel-4 vs. channel-5.

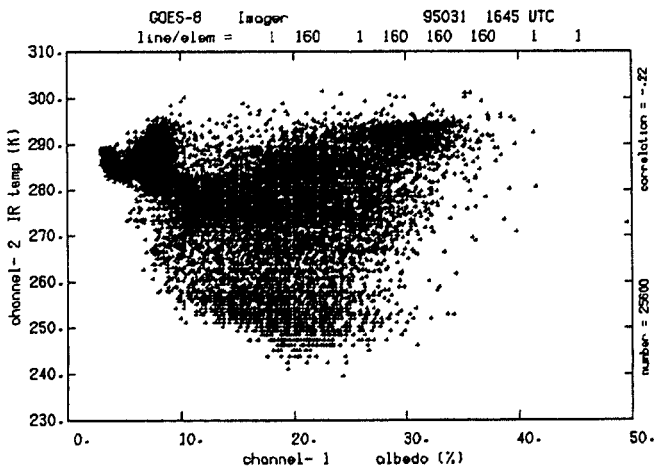

Figure 5c. Same as Figure 5a, but for GOES Imager channel-1 visible albedos vs. channel-2 IR temperatures.

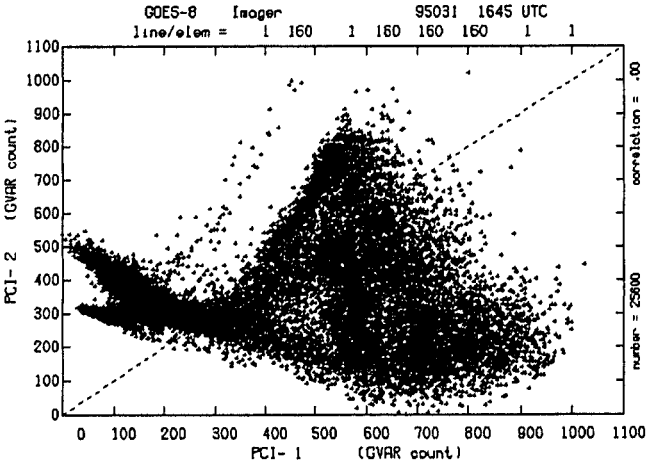

Figure 6a. Scatter plot of GOES PCI-1 vs. PCI-2.

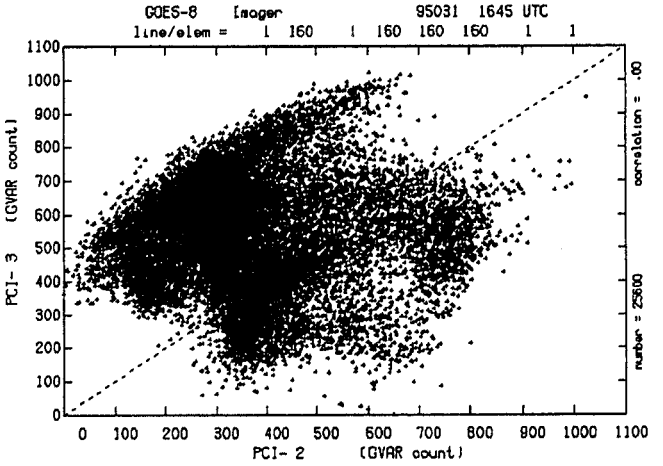

Figure 6b. Same as Figure 6a, but for PCI-2 vs. PCI-3.

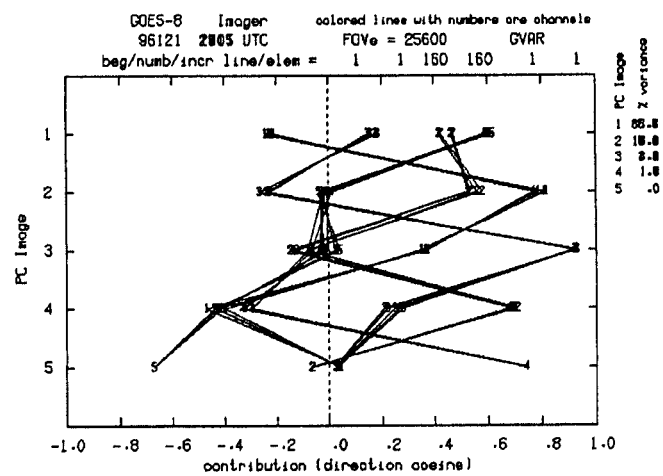

Figure 7. PCI transformation vectors for all 5 GOES Imager channels for 5 different times at 1-hourly intervals.

2 at 3.9 μm has a reflected radiation component in addition to an emitted radiation alone in channel-4. Figure 5b shows the very strong correlation (0.99) between channel 4 and channel 5. Next, Figure 5c shows a weak correlation (-0.22) between the visible channel and IR channel 2. The slight correlation between these channels is due to a reflected radiation component in channel-2.

Similar scatter diagrams of the resulting PCIs are shown in Figure 6. Because the PCI axes are a new coordinate system in which the axes are independent, there is no correlation among the components. This is seen as a zero correlation in Figure 6a showing PCI-1 vs. PCI-2, and as a zero correlation in Figure 6b showing PCI-2 vs. PCI-3.

The next question may be about the temporal stability of the PCI products. Figure 7 shows the PCI transform vectors generated independently at five times separated by one hour each. This is for a case on 30 April 1996 for which the channel images are not shown in this writeup. The PCI transform vectors (or eigenvectors) are very stable over time. The channels contributing significant information, those with direction cosines greater than 0.7 (or less than -0.7), are the same channels as those for the first case shown in Figure 2a. It should be mentioned however, that a big difference in PCI transform vectors occurs between day, when there is visible channel information, and night, when there is no visible channel information. Slight seasonal variations in PCIs are also expected, but in general the PCIs are a stable product when created from GOES Imager channels.

4. THE CHOICE OF INPUT MEASUREMENT UNITS FOR PC IMAGES

As mentioned above, the PCIs can be created from the GOES channels with a choice of measurement units for the channel images. The resulting PCIs may differ as a result of the magnitude of the measurement units alone, especially among various spectral channels, or the PCIs may differ due to nonlinear transformations between measurement units. One case with two different input measurement units will be shown.

Figure 8 shows GOES Imager channels for 31 March 1995 at 1615 UTC. The same combination of channels 1, 4, 2, and 3 are displayed as in the previous case. The PCI transformation vectors are shown in Figure 9a, which is similar to Figure 2a for the previous case with the following exceptions. The first exception is a reversal in the signs of the channels contributing to PCI-1. This sign reversal is merely the result of the software package being used, and the effect can be reversed by inverting the grey shades on PCI-1. This means that PCI-1 for this case (shown in Figure 10a) has the same interpretation as PCI-1 for the previous case (shown in Figure 3a). Another exception is that both channel 1 and channel 2 are major contributors to PCI-2, unlike primarily channel-1 alone in the previous case. The remaining exception is a reversed order of the channel information that goes into PCI-3 and PCI-4. PCI-4 in this case gets its primary contribution from channel 2 and best shows the snow cover as seen in Figure 10c. The snow cover is in the mountains of Colorado and New Mexico as well as in some of the other mountain ranges in the west.

PCI transform vectors generated for the same case but with the channel images input as IR temperatures (or albedos for the visible channel) are shown in Figure 9b. Here again, there is a reversal in the sign of the major contributing channels to PCI-1 from those shown in Figure 9a, making the signs of the channels contributing to this PCI the same as those for PCI-1 shown in Figure 2a. But again this reversal in sign is immaterial and can be corrected by inverting the grey shades used to display the image. The remaining difference is a reversal in sign of the channel images contributing to PCI-3. Some of the lower-order components are different, but PCI-3 (with image displayed in Figure 11) shows an almost identical analysis of snow cover compared to PCI-3 generated from 10-bit GVAR counts (shown in Figure 10c). Again, it is the combination of channels which is important, not the sign of the resulting PCI.

5. WEIGHTING FUNCTIONS HELP EXPLAIN SOUNDER PC IMAGES

For the GOES Sounder, there are up to 19 spectral channels (1 visible and 18 IR channels) which can be input into a PCI transform. Because of the high redundancy among many of these channels, Sounder information is a good candidate for PCI analysis. Weighting functions, which show the vertical distribution of information in each channel image, can help interpret the PCIs created from the original GOES channels.

Only one Sounder case will be presented in this article. Figure 12 shows three of the GOES Sounder water vapor channels for 1 May 1996 at 1746 UTC. This case presents a strong jet stream over the eastern U.S. The three Sounder water vapor channels are channels 10, 11, and 12 at 7.4 μm, 7.0 μm, and 6.5 μm, respectively. These three water vapor channels have weighting functions which peak at approximately 700, 500, and 300 hPa, respectively. The weighting functions are displayed graphically on top of the images for each channel. Each successive channel measures water vapor at higher levels in the atmosphere. The weighting functions are broad, indicating that these channels receive information from a large depth of the atmosphere. Information in these channels is

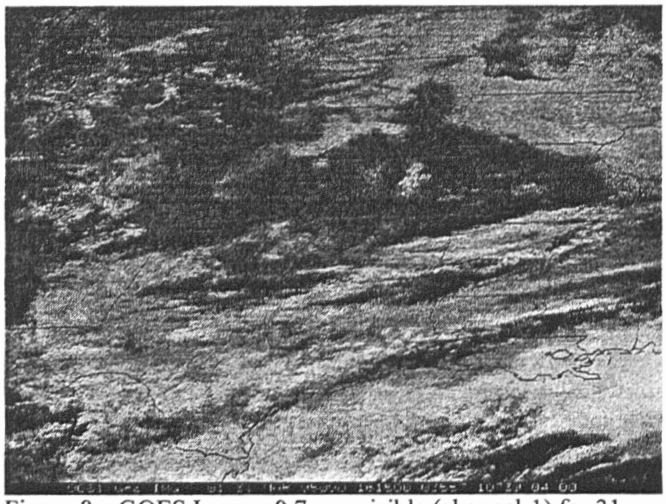

Figure 8a. GOES Imager 0.7 μm visible (channel-1) for 31 March 1995 (year/day 95090) at 1615 UTC.

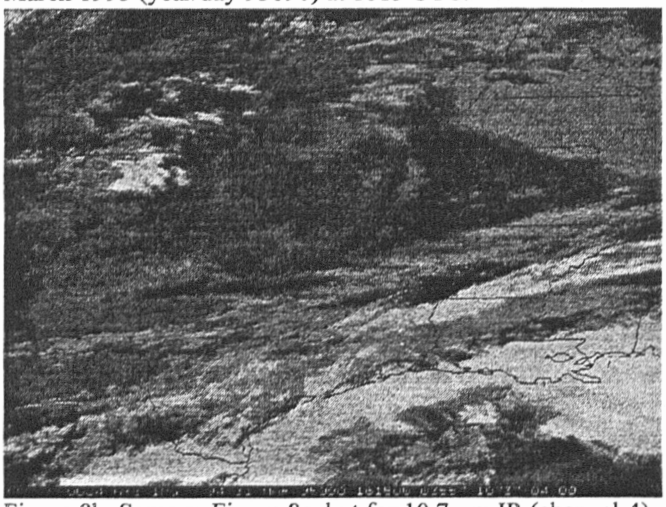

Figure 8b. Same as Figure 8a, but for 10.7 μm IR (channel-4).

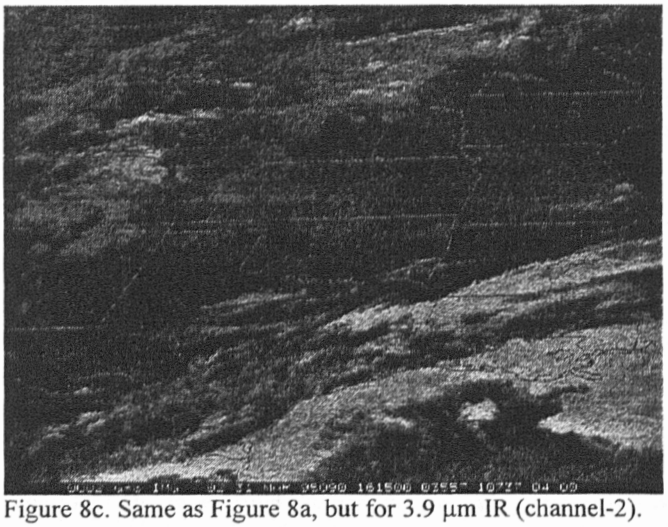

Figure 8c. Same as Figure 8a, but for 3.9 μm IR (channel-2).

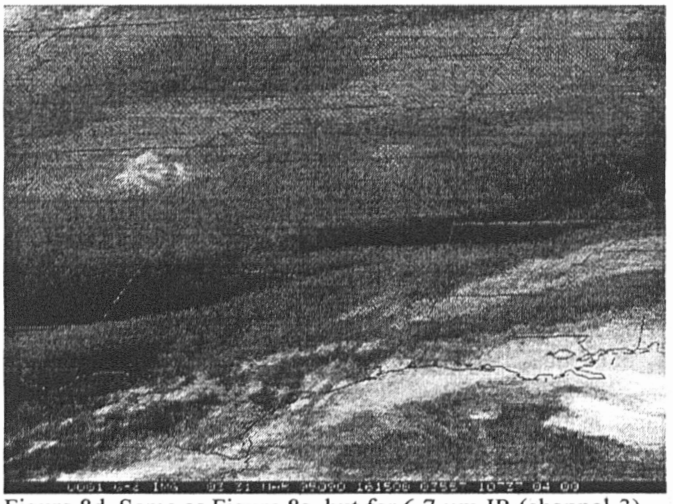

Figure 8d. Same as Figure 8a, but for 6.7 μm IR (channel-3).

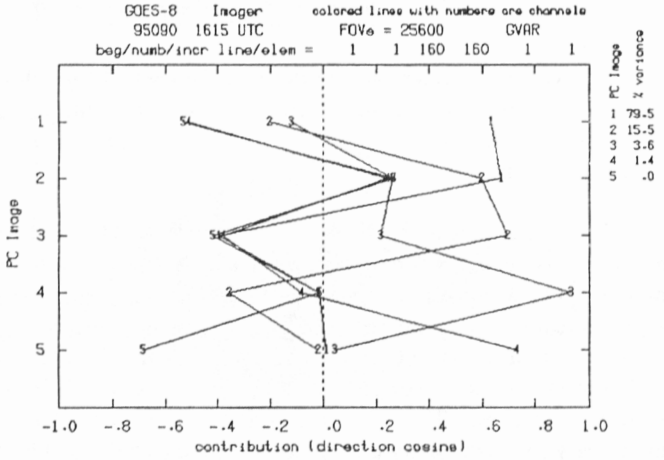

Figure 9a. PCI transformation vectors for all 5 GOES Imager channels for the case in Figure 8 input as 10-bit GVAR counts.

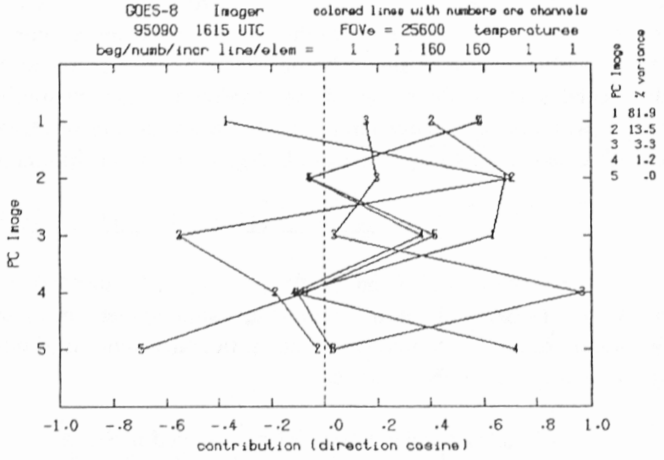

Figure 9b. Same as Figure 9a, but for GOES Imager channels input as IR temperatures (or visible albedos).

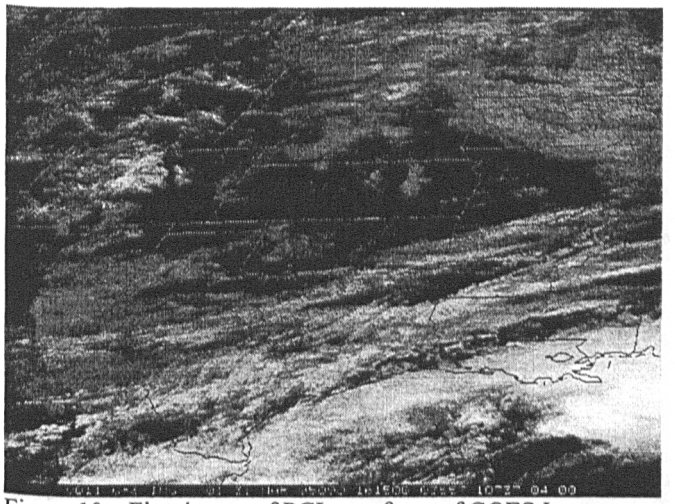

Figure 10a. First image of PCI transform of GOES Imager channels for the case shown in Figure 8. Input units are 10-bit GVAR counts.

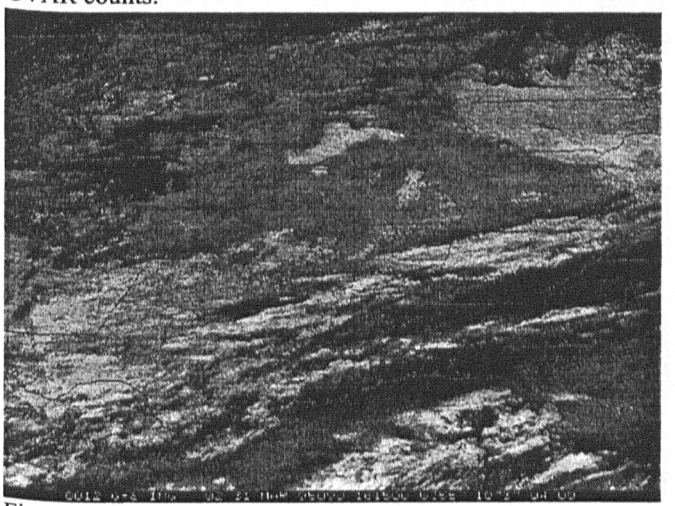

Figure 10b. Same as Figure 10a, but for second image.

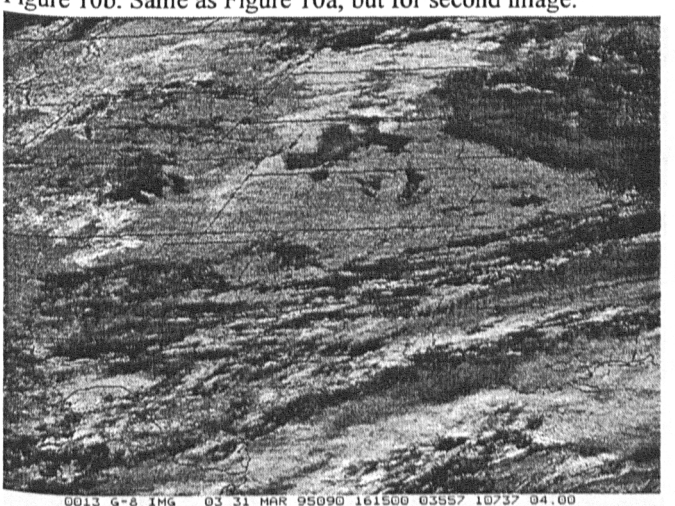

Figure 10c. Same as Figure 10a, but for third image.

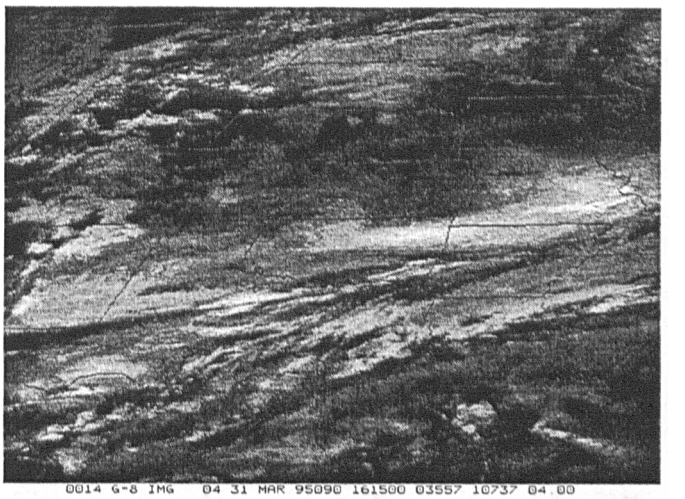

Figure 10d. Same as Figure 10a, but for fourth image.

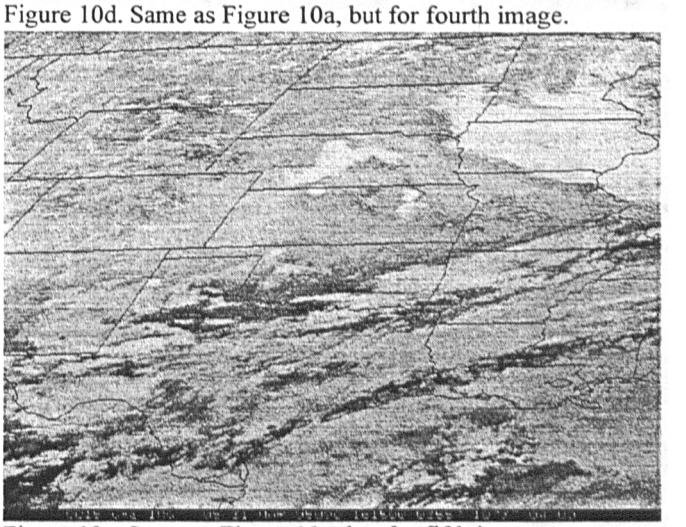

Figure 10e. Same as Figure 10a, but for fifth image.

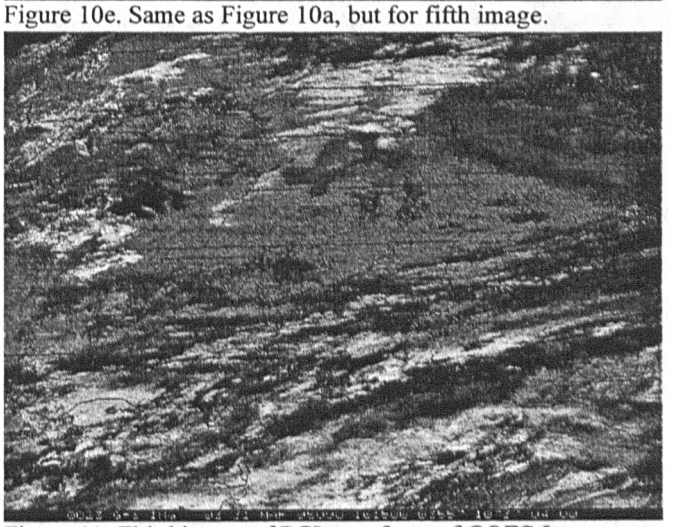

Figure 11. Third image of PCI transform of GOES Imager channels for the case shown in Figure 8. Input units are IR temperatures/visible albedos. Compare to Figure 10c.

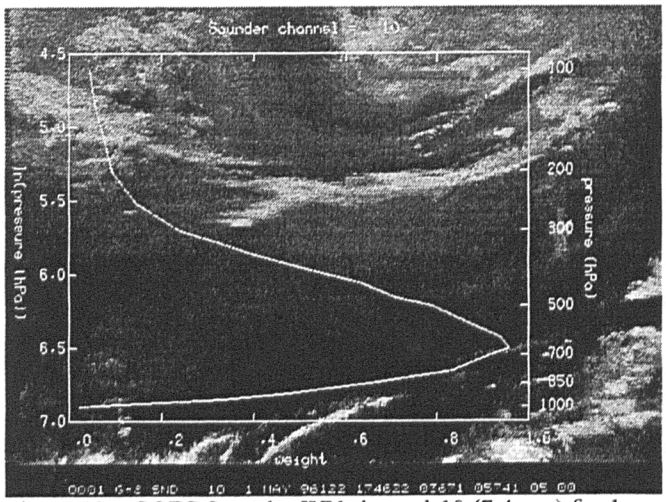

Figure 12a. GOES Sounder WV channel-10 (7.4 μm) for 1 May 1996 (year/day 96122) at 1746 UTC.

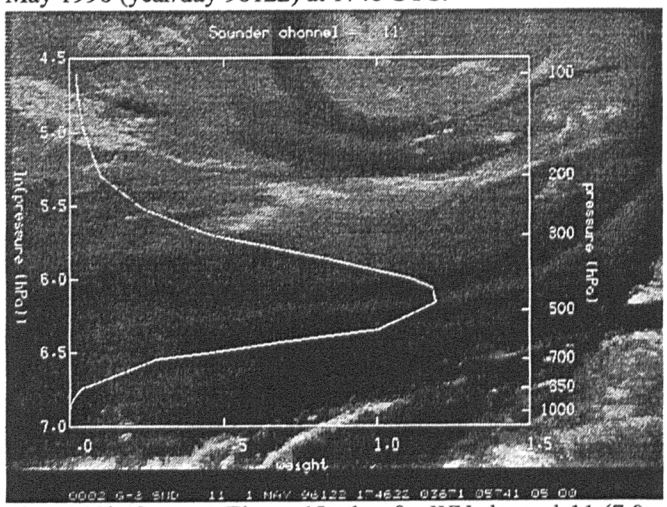

Figure 12b. Same as Figure 12a, but for WV channel-11 (7.0 μm).

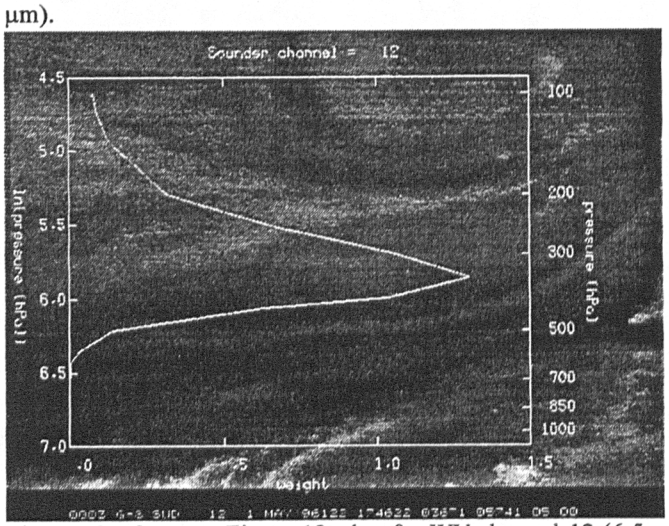

Figure 12c. Same as Figure 12a, but for WV channel-12 (6.5 μm).

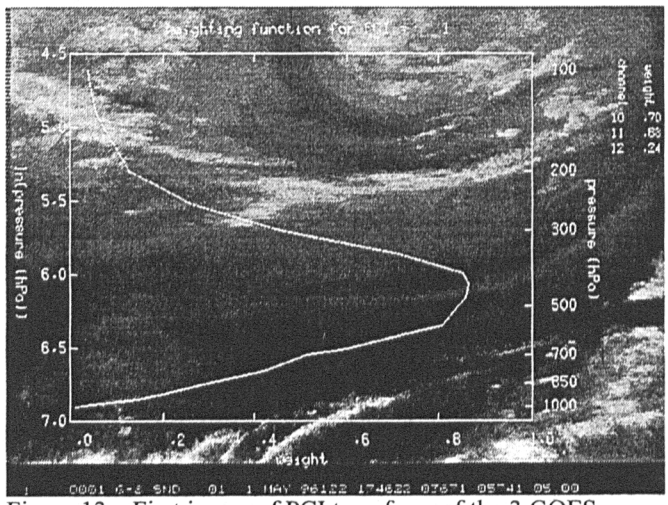

Figure 13a. First image of PCI transform of the 3 GOES Sounder WV channels for the case shown in Figure 12.

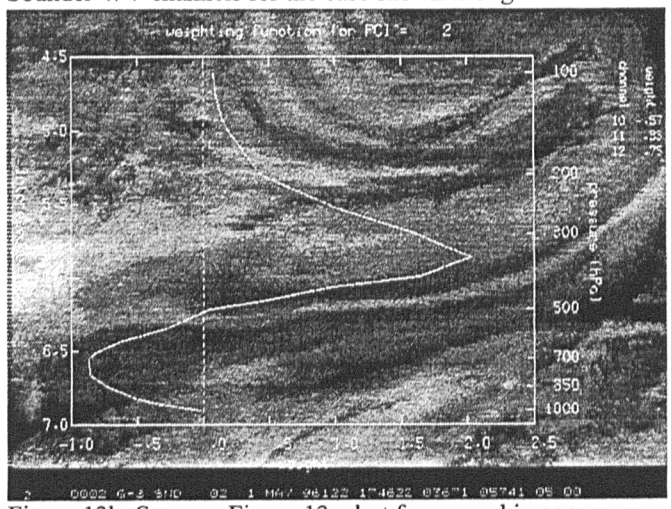

Figure 13b. Same as Figure 13a, but for second image.

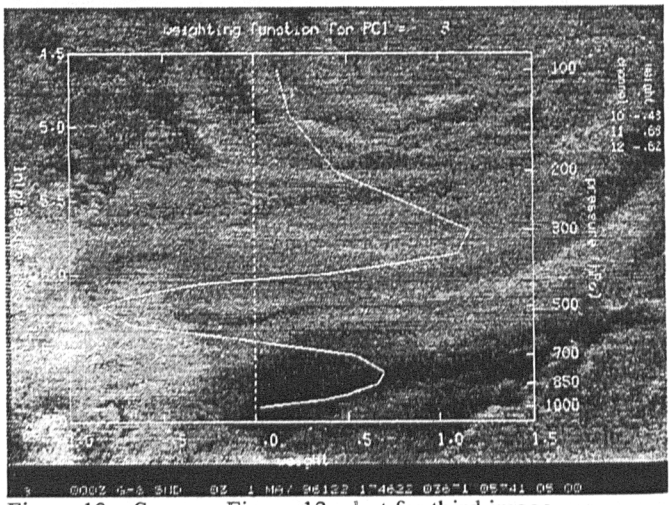

Figure 13c. Same as Figure 13a, but for third image.

also somewhat redundant due to the overlap in the weighting functions. This results in a certain similarity in the channel images shown in Figures 12a, b, and c, but there are also differences among those three images. However the differences are subtle and are best seen in the PCIs created from the water vapor channels.

In Figure 13 are three PCIs resulting from a transform of the three channels shown in Figure 12. Instead of showing the PCI transform vectors, only the resulting PCIs are shown. The weighting functions for each PCI are again displayed graphically over the component images. The combination of channels in each PCI is indicated by small numbers in the upper right corner of each figure. PCI-1 in Figure 13a captures the broad vertical features present in all three water vapor channels. Weights for the input channels are all positive. The weighting function for PCI-1 is even broader than any of the individual channel weighting functions. Next, PCI-2 in Figure 13b displays the second vertical mode of variation among these three water vapor channels. In this case, the lowest water vapor channel, channel-10, is subtracted from the other two water vapor channels. This combination of channels is indicated as well in the weighting function generated for this PCI. Emphasis in PCI-2 is upon differences in the vertical distribution of water vapor across the image. Finally, for PCI-3 in Figure 13c channels 10 and 12 are subtracted from channel 11. The weighting function for PCI-3 reflects the third mode of vertical variability in water vapor across the image. In this case the middle levels are de-emphasized compared to the upper and lower levels. The exact interpretation of the water vapor features in these PCIs is still uncertain, but the PCIs indicate that differences in the vertical distribution of water vapor exist. Those differences are important in the meteorological analysis of the water vapor channels on the GOES Sounder.

6. IMAGES RE-CREATED FROM THE PC IMAGES

The inverse transform

$$CH = E\ PCI$$

can be used to re-construct the original channel images, or CHs, from the component images, or PCIs. If all of the eigenvectors are used in the re-transform, then the process is completely reversible, and nothing is lost (or gained). However, images can be re-created from fewer than the maximum number of PCIs. A series of such images re-constructed from varying numbers of PCIs can show the effect of eliminating noise in GOES images. However, no examples of this image reconstruction are shown in this article. Typically, by not using the highest-ordered eigenvectors, the re-constructed image quality is improved as a result of eliminating noise from the other signal information. These highest-ordered image components are simply eliminated by zeroing a column of the eigenvector matrix E. The user, however, must be careful to not eliminate higher-ordered eigenvectors which still may contain subtle meteorological information other than noise.

7. CONCLUSIONS

Images created from the PCI transformation of GOES channel images can be instructive in learning about meteorological information in un-transformed GOES imagery. The user has to understand what is being presented, but with that knowledge, the PCIs can help interpret the meteorological information in redundant Imager and especially in highly-redundant Sounder channels.

8. ACKNOWLEDGMENTS

This research was sponsored by NOAA Grant NA37RJ0202.

9. REFERENCES

1. Gauch, H. G. Jr., "Prediction, parsimony, and noise," *American Scientist,* 81(5), 468-478, 1993.
2. Loughlin, W. P., "Principal component analysis for alteration mapping," *Photogrammetric Engineering and Remote Sensing*, 57(9), 1163-1169, 1991.
3. Morrison, D. F., *Multivariate statistical analysis*, McGraw-Hill, New York, 415 p., 1976.
4. Preisendorfer, R. W., *Principal component analysis in meteorology and oceanography*, Elsevier, New York, 425 p., 1988.
5. Hillger, D. W., "Image and graphical analysis of principal components of satellite sounding channels." *Sixth Conf. on Satellite Meteorology and Oceanography,* AMS, 5-10 January, Atlanta GA, 28-31, 1992.
6. Hillger, D. W., "Use of truncated principal component analysis to improve images from satellite sounding channels," *Seventh Conf. on Satellite Meteorology and Oceanography,* AMS, 6-10 June, Monterey CA, 540-541, 1994.

Automated cloud-drift winds from GOES images

Chandra Kambhamettu, K. Palaniappan and Frederick A. Hasler
Mesoscale Dynamics and Precipitation Branch
NASA Goddard Space Flight Center, Code 912
Greenbelt, MD 20771
chandra/palani/hasler@gloria.gsfc.nasa.gov, Tel: 301-286-5786, Fax: 301-286-1762

ABSTRACT

Estimation of the atmospheric wind field based on cloud tracking using a time sequence of satellite imagery is an extremely challenging problem due to the complex dynamics of the imaging instruments and the underlying non-linear phenomena of cloud formation and weather. Cloud motion may involve both partial fluid motion and partial solid motion, which we model as semi-fluid motion. Motion algorithm with subpixel accuracy using differential geometry invariants of surfaces was developed to track clouds. The motion model is general enough to include both physical and geometrical constraints. Typically, a polynomial displacement function is used to model the local deformation behavior of a surface patch undergoing semi-fluid motion. The cloud tracking algorithm recovers local cloud surface deformations using a sequence of dense depth maps and corresponding intensity imagery, that captures the time evolution of cloud-top heights. Either intensity or depth information can be used by the semi-fluid motion analysis algorithm. A dense disparity or depth map that can be related to cloud-top heights is provided by the Goddard Automatic Stereo Analysis (ASA) module for input to the motion analysis module. The results of the automatic cloud tracking algorithm are extremely promising with errors comparable to manually tracked winds. Experiments were performed on GOES images of Hurricanes Frederic, Gilbert and Luis, and a temporally dense 1.5 minute time interval thunderstorm sequence covering Florida region. Future work involves using multispectral information, incorporating robustness, cloud motion segmentation and adaptive searching for improving operational cloud-tracking performance.

1 Introduction

The estimation of cloud-top structure and motion using multiple satellite views is an extremely challenging problem due to the complex dynamics of the imaging instruments and the underlying non-linear phenomena of cloud formation and weather. Accurate cloud heights and winds are important for a number of meteorological and climate applications [3, 10, 11, 1] such as cloud model verification, physically-based numerical weather prediction and data assimilation, and radiation balance estimation for Mission to Planet Earth type climate baseline studies. Stereoscopic multispectral measurement of cloud heights and time sequential estimation of cloud winds using geostationary and polar orbiting satellite-based instruments are essential because they provide information which is independent of other meteorological measurements.

The computational approach to cloud structure and motion estimation involves two primary modules [14]. The first module estimates stereo-based cloud structure using a hierarchical, multi-resolution coarse-to-fine search strategy with image warping at each level [15] and has been parallelized for the Maspar parallel machine having 16,384 processors. The second module estimates motion using a sequence of dense depth maps and corresponding intensity imagery, in order to capture the time evolution of cloud heights and has also been parallelized on Maspar parallel machine [12]. The IISS is a visualization tool that was developed for rapidly analyzing gigabyte-sized geophysical datasets [4], and was enhanced to visualize the results of the stereo analysis and semi-fluid motion estimation algorithms. This paper addresses motion

0-8194-2200-2/96/$6.00

analysis part of our earlier work, which appeared in the *International Conference on Computer Vision '95* [14]. A brief overview of motion analysis for cloud tracking is presented next, followed by a description of the algorithms.

1.1 Motion Analysis

There can be two types of motions in general: *rigid* and *non-rigid* [8]. Cloud motion is a special case of non-rigid motion, where there is both partial fluid and partial solid motion, that we describe as being *semi-fluid motion*. The motion of objects exhibit a wide variation in behavior ranging from the simplest ideal frictionless rigid motion to the most complex turbulent fluid motion. Elastic motion deals with shape changes of continuous surfaces, and fluid motion deals with particle motion in which there is usually no continuity constraint among neighboring particles that are free to move according to the underlying dynamics. Although there has been an increasing amount of research in the individual categories of motion behavior, there have not been many attempts to combine different classes of motion models. In the fluid motion case when the local continuity of a surface is partially preserved, it should be advantageous to use both the characteristics of local continuity required for estimating surface properties, along with the flexibility of larger localized particle motion that would otherwise violate most local continuity assumptions. An ideal example of this category of motion, which we call *semi-fluid motion* is the non-rigid motion of clouds. Other examples may be found in the atmospheric sciences, as well as in hydrospheric modeling of ocean eddies and currents that mix and split thus maintaining some larger scale features identifiable in multi-spectral imagery, or biological cells that undergo fission or fusion processes. Time varying properties of clouds represent a prototypical example of semi-fluid motion behavior and offers a new experimental area for further investigation of non-rigid motion models.

We now present definitions of each motion type based on differential geometric variations during the motion [8]. Corresponding error measures are also presented, which can be used to estimate motion parameters and point correspondences for each nonrigid motion model. Error measure is represented by ε_R, which is expressed in terms of differential geometric parameters such as Gaussian curvature (K), mean curvature (H), Unit-normal (n), coefficients of first fundamental form (E, F, G) and Discriminant (D). Note that the parameters corresponding to the deformed surface are represented by primes such as K' for Gaussian curvature, n' for unit-normal etc. Each model is based on geometry only, and new motion models can be added to the list by forming more generic relationships. The reader is suggested to refer to [2] or any other related text for a detailed description of differential geometry.

Rigid motion preserves the 3-D distances between any two points in an object. The object does not stretch or bend; hence both mean curvature and Gaussian curvature on the surface of the object remains invariant.

$$\varepsilon_R = (K' - K)^2 + (H' - H)^2$$

Isometric motion is nonrigid motion which preserves lengths along the surface as well as angles between curves on the surface.

$$\varepsilon_R = (K' - K)^2$$

From the Figure 1.1, we can deduce that AB=A'B', AC=A'C' and $\theta = \theta'$ in this type of motion.

Homothetic motion is a uniform expansion or contraction of a surface, where stretching (t) is constant throughout the surface.

$$\varepsilon_R = (K't^2 - K)^2$$

Figure 1: Changes in Lengths and Angles Between Curves for Characterization of Nonrigid Motion Types

From the Figure 1.1, we have the ratio between the curves as constant, i.e, (AB/A'B' = AC/A'C' = constant), and also $\theta = \theta'$.

Conformal motion is nonrigid motion which preserves angles between curves on the surface during motion, but not lengths. Stretching (t) is different at different points of the surface, however is same in different directions of any given point.

$$\varepsilon_R = (E' - t^2E)^2 + (F' - t^2F)^2 + (G' - t^2G)^2$$

From the Figure 1.1, we can deduce that $\theta = \theta'$ in this type of motion.

Elastic motion is a nonrigid motion whose only constraint is some degree of continuity or smoothness. Motion at each point can be described by any polynomial function s. This kind of solid object motion is the most difficult to analyze. Following relations represent elastic motion when sufficiently small.

$$\varepsilon_R = (n' - n \times \mathbf{rot}s)^2 \;\; \& \;\; \varepsilon_R = (D' - D\mathbf{div}s)$$

rot$s$ can be defined as follows:

$$rot\ \mathbf{s} = \frac{1}{E}\mathbf{r}_1 \times \mathbf{s}_1 + \frac{1}{G}\mathbf{r}_2 \times \mathbf{s}_2.$$

where, r is the position vector of a point, represented by $(u, v, z(u, v))$ and E, G are the first fundamental coefficients. Note that the subscripts $1, 2$ indicate differentiation w.r.t to u, v respectively.

Semi-fluid motion is a combination of elastic and fluid motion. This motion type will be elaborated more in coming sections.

Fluid motion is general nonrigid motion that need not be continuous. It may involve topological variations and turbulent deformations.

Each motion model presented above is a subset of the one at a higher level. Thus, the motion parameter becomes more generic as the complexity of the motion model used is increased. Input to these models can be a pair of range, intensity, or both types of images. In order to estimate point correspondence, error measure (ε_R) is applied to each correspondence hypothesis over a template map. Each hypothesis

correspondence will then have a corresponding error measure, the minimum of which represents a good estimate for the correspondence. More than one correspondence can also be estimated with confidence measures for each hypothesis. ε_R represents confidence measure when the underlying motion assumption is followed.

2 Automatic Motion Analysis

In this paper, we present a novel approach to estimate the point correspondences and motion parameters of a cloud element undergoing deformation. A unified algorithm having two approaches of motion analysis has been developed on the Maspar parallel machine. First approach utilizes a *continuous motion model*, where individual cloud elements under deformation are assumed to be continuous. Second approach assumes a *semi-fluid motion model*, where local continuity constraints are violated during deformation. Detailed description of the mathematical formulation used in these approaches is given below.

A local small deformation assumption can be used to derive relationships between unit-normals of a point on the surface before and after motion, and also between the curvatures at the point during deformation. We build on these derivations [16, 7] for automatic motion analysis of clouds. Consider a point defined parametrically as, $z(x, y)$, on a surface that undergoes small deformation changes and is transformed to the point $z'(x', y')$. The following relationship holds between the corresponding unit-normals [16, 7]:

$$\mathbf{n}' = \mathbf{n} - \mathbf{n} \times rot\ \mathbf{s} \tag{1}$$

where $\mathbf{n}$ corresponds to the unit-normal of a point before motion, and $\mathbf{n}'$ is the unit-normal of the same point after motion. The displacement function, $\mathbf{s}$ models the non-rigid motion of the local neighborhood or small patch around the point of interest and can be expressed in the imaging instrument coordinate system at the initial time step as,

$$\mathbf{s} = (x' - x, y' - y, z'(x', y') - z(x, y)). \tag{2}$$

The rotation or *curl* of the displacement function denoted as, *rot* $\mathbf{s}$, is given by,

$$rot\ \mathbf{s} = \frac{1}{E}\mathbf{z}_1 \times \mathbf{s}_1 + \frac{1}{G}\mathbf{z}_2 \times \mathbf{s}_2. \tag{3}$$

The subscripts 1 and 2 indicate differentiation with respect to the parameters x and y respectively and the denominators, $E\ (= z_1 \cdot z_1)$ and $G\ (= z_2 \cdot z_2)$, are coefficients of the first fundamental form [16]. Polynomial functions are the simplest models for the local displacement function of a small patch undergoing small deformation. In our cloud-motion experiments, and in order to derive simple analytical relationships for differential geometry parameters, a small patch is assumed to undergo a local affine transformation defined as,

$$\mathbf{s}(x, y) = (a_i x + b_i y + c_i, a_j x + b_j y + c_j, a_k x + b_k y + c_k). \tag{4}$$

Let the unit-normal of a point before motion be defined as, $\mathbf{n} = (n_i, n_j, n_k)$ and the unit-normal of the same point after motion as, $\mathbf{n}' = (n_i', n_j', n_k')$. Surface normals and other intrinsic surface properties are estimated by using locally fitted quadratic surfaces for each small patch though the relationship between the normals (1) holds for all surface models. From (1), (2), (3) and (4), the following linearly independent equations can be derived [7, 9]:

$$\left[\frac{-n_k z_1}{E}a_i + \left(\frac{n_i - n_k z_2 - n_j}{G}\right)b_i + \left(\frac{n_j - n_k z_1 - n_i}{E}\right)a_j - \frac{n_k z_2}{G}b_j + \frac{n_k}{E}a_k + \frac{n_k}{G}b_k - n_i + n_i' - n_j + n_j'\right] = 0, \tag{5}$$

$$\left[\frac{n_i z_1}{E}a_i + \frac{n_i z_2}{G}b_i + \frac{n_j z_1}{E}a_j + \frac{n_j z_2}{G}b_j - \frac{n_i}{E}a_k - \frac{n_j}{G}b_k - n_k + n'_k\right] = 0. \quad (6)$$

The components of the displacement function, $\mathbf{s}(\cdot)$, are the unknowns in the above equations. Although the displacement function has nine unknowns, Eq. (2) can be used to solve for the constant terms. Using (5) and (6) provides two independent constraints for each point correspondence, so three point correspondences are needed to solve for the six unknowns in the affine displacement model (4). Using just three point correspondences is not as reliable as the least squares minimization approach described next.

Since each small patch is assumed to experience small continuous deformations locally, the continuity constraint can be used to hypothesize a set of point correspondences or equivalently a template mapping η_R, between corresponding patches. The hypothesis point set or search area is defined as L_R with the subscript R used to indicate that the hypothesis testing is done using range or disparity data. The best match is the hypothesis which minimizes the total sum of the squared errors, given by (5) and (6) defined as $\varepsilon_{R_1}(x, y)$ and $\varepsilon_{R_2}(x, y)$ respectively,

$$\varepsilon_R(x, y) = \sum_{i \in \eta_R} (\varepsilon_{R_1}(x, y))_i^2 + (\varepsilon_{R_2}(x, y))_i^2. \quad (7)$$

The error function (7) can be minimized w.r.t each of the six unknowns, (a_i, b_i, a_j, b_j, a_k, b_k), in the affine displacement function, resulting in six equations that can be solved using the hypothesized patch correspondence(s). Once c_i, c_j, c_k are calculated using Eq. (2), the displacement function (4) for a local patch is completely specified. Using the estimated displacement function associated with each hypothesis the errors $\varepsilon_R(x, y)$ can be ranked. The matching hypothesis associated with the smallest error is assumed to represent the deformable motion.

The minimization procedure is suitable for locally continuous surfaces that have small deformations. However, it needs to be modified to include semi-fluid motion where the continuity constraint is relaxed locally. Intensity-based information is used to complement the matching process discussed above which relies primarily on local surface shape characteristics and depth analysis. The algorithm for semi-fluid motion analysis has three steps. The first step deals with determining a set of possible semi-fluid template mappings using intensity information for each local patch. The second step evaluates the error for each hypothesized correspondence provided by the template mapping and selects the most reliable semi-fluid mapping. The third step is to refine the motion parameters of the semi-fluid mapping to sub-pixel accuracy.

The neighborhood template mapping for η_R can be continuous as shown in Fig. 2(a), or quite discontinuous under semi-fluid motion as shown in Fig. 2(b). Evaluating all possible semi-fluid template mappings between corresponding neighborhoods is combinatorially explosive. Determining the most plausible semi-fluid template mapping is made more tractable by using intensity information and tracking intensity features. For the cloud motion experiments, the discriminant was used as an intensity-based differential geometry parameter [9, 16]. The intensity-based algorithm allows small local regions within the template to undergo discontinuous semi-fluid motion. Other techniques such as optic flow-based segmentation that can be adapted to robustly estimate the local semi-fluid template mapping for motion tracking are also being investigated [5]. In order to determine the best semi-fluid mapping, Eq. (7) that measures the error in the surface or range normal constraint, is evaluated for each correspondence hypothesis using the semi-fluid template maps generated in the previous step. The error $\varepsilon_R(x, y)$ is computed within a small patch neighborhood for the pixel of interest and overlapping windows are used in computing the errors (5) and (6). The reliability in selecting the appropriate template mapping is improved by evaluating the error function over the entire neighborhood of points (η_R), rather than at a single feature or individual pixel. The template mapping correspondence hypothesis with the minimum error is assumed to represent the best estimate of the local semi-fluid motion behavior. The total error $\varepsilon_R(x, y)$ can be used as a confidence

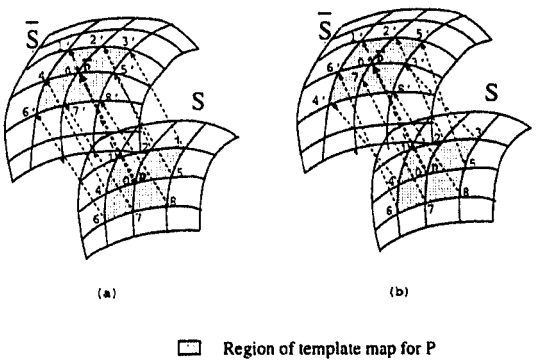

Figure 2: Local non-rigid deformation can be continuous as shown in the template mapping (a), or discontinuous under semi-fluid motion as shown in (b).

measure when the underlying motion assumption is valid. In our implementation, one can choose continuous, or semi-fluid motion model for cloud motion analysis. Figure 3 describes the processing steps of our algorithm as a flow chart. Semi-fluid motion tracking to sub-pixel accuracy is obtained by minimizing an energy function involving Gaussian curvature variations within the pixel. For a small patch defined by the vector function, $\mathbf{r}(x, y, z)$, that undergoes small deformation, the Gaussian curvatures before and after motion, K and K' respectively are related as [9],

$$K' = \frac{-1}{2D(1+\theta)}\left[\left(\frac{G + 2r_2 \cdot s_{21}}{D(1+\theta)}\right)_1 + \left(\frac{E + 2r_1 \cdot s_{12}}{D(1+\theta)}\right)_2\right]$$
$$= \frac{1}{(1+\theta)^2}K + f(x, y) \tag{8}$$

The discriminant (or infinitesimal area) at the point of interest is D $(= EG)$, and θ is the divergence or dilation at the same point. Dilation can be defined as the unit expansion/contraction of the feature during deformation and is expressed as,

$$\theta = div\ \mathbf{s} = \frac{1}{E}\mathbf{r}_1 \cdot \mathbf{s}_1 + \frac{1}{G}\mathbf{r}_2 \cdot \mathbf{s}_2\ . \tag{9}$$

3 Experiments

Motion analysis experiments are performed on GOES images of Hurricanes Frederic, Gilbert and Luis, and a temporally dense 1.5 minute time interval thunderstorm sequence covering Florida region. In this section, we present the analysis of hurricanes Frederic and Luis, and Florida thunderstorm. The output of motion analysis algorithm (implemented on the Maspar) is a dense estimate of tracked fields on the cloud images. Thresholding based on local intensity variations is performed to filter out point tracks in non-cloudy regions. A local quadratic surface is fitted to estimate the various differential geometric measures that were used in the algorithm.

Figure 4 shows the thresholded particles that were tracked through the four frames of hurricane Frederic having a time interval of 7.5 minutes between each successive frame. Stereo of all the four frames are available from GOES-E and GOES-W satellites which subtend an angle of about 135° with respect to the center of the Earth providing a very large baseline for stereo analysis. Automatic stereo analysis was first performed on the stereo pairs to estimate the disparity. The estimated depth map time sequence

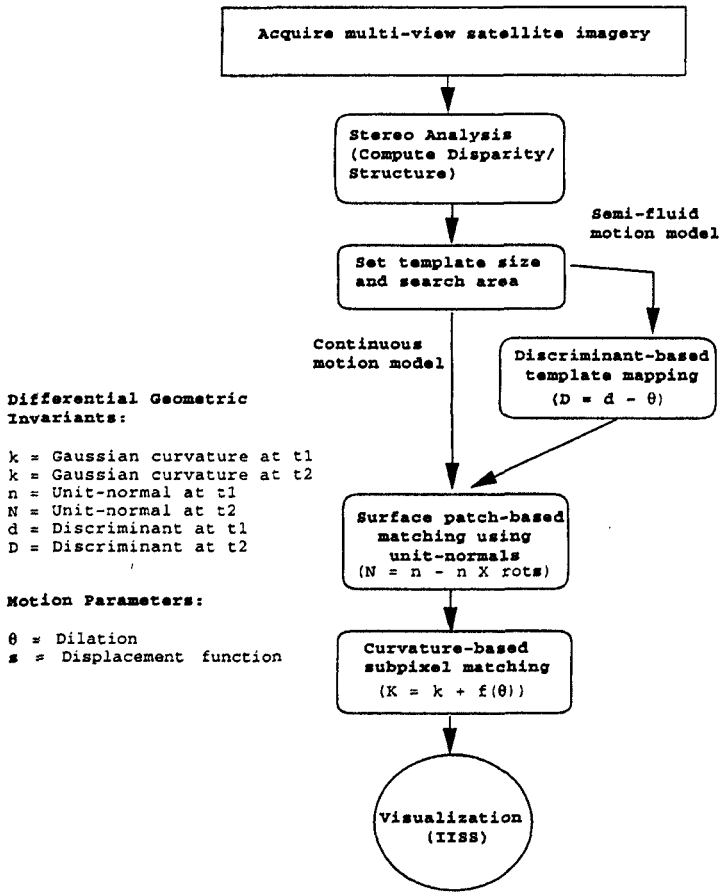

Figure 3: Automatic Motion Analysis

along with corresponding intensity images from the eastern satellite were used to perform semi-fluid motion analysis. Since the time interval between frames is comparatively high, we perform semi-fluid motion analysis with larger template and search areas than those used for other data sets below (template=121X121, search=13X13).

Figure 5 shows the thresholded particles that were tracked in a Florida thunderstorm sequence. There are 49 image sequences of this data with a 1.5 minute time interval (stereo is not available). Top row represents the tracked results of a continuous motion model (template=11X11, search=9X9) applied to this data set, and the bottom row represents results generated by a semi-fluid motion model (template=11X11, search=9X9). Typically, it has been observed that continuous motion model estimates better tracks than semi-fluid model when the time interval is small; continuity constraints are preserved in short intervals.

Finally, motion analysis was performed on 490 frames of one-minute hurricane Luis data (10:23 UTC to 22:26 UTC, 06 Sep. 1995). Figure 6 depicts the thresholded particles that were tracked. Top row indicates the tracked particles at a given instant (1128 UTC), and the bottom row indicates tracked particles for the successive frame (1129 UTC). Continuous motion model (template=11X11, search=9X9) is used for the analysis, as the time interval is short enough so as to maintain continuity constraints of the cloud elements. Visualization of color-coded velocity tracks has also been generated for a qualitative assessment

Figure 4: Semi-fluid motion analysis of Hurricane Frederic

Figure 5: Motion analysis of Florida Thunderstorm

Figure 6: Continuous motion analysis of Hurricane Luis

of the cloud-drift wind estimation. Please contact one of the authors to request for a corresponding video.

Validation of the cloud motion analysis is underway. So far, evaluation of the algorithm is performed by comparing the automatic tracking results with manual tracking analysis. An integrated system has been developed wherein the user can track a cloud element in a time sequence and immediately initiate the automatic tracking system. Cloud-drift winds can be generated from both the manual and automatic methods for validation. A complete statistical analysis of the tracked cloud-drift wind velocities can be obtained using the above mentioned system. Results thus far have been very promising, with RMS error as low as 5 mt/sec when well-defined cloud structures are being tracked. The algorithm fails when the cloud elements being tracked do not have structural variations or if there are multiple motions of clouds. We concentrate on this problem in our future direction, where cloud motion classification is performed before applying the motion model. A comprehensive error analysis of the algorithm in tracking different types of clouds is currently being performed.

4 Conclusions

We present a parallel algorithm for motion analysis that can produce dense motion fields (at every pixel) for a time-varying sequence. This algorithm has been implemented on the massively parallel Maspar computer. The algorithm can be applied to a pair of time-varying intensity data, surface or range data, or both intensity and surface data. A number of experiments using real satellite GOES imagery were performed. The algorithm produces favorable results compared to manually tracked cloud winds. However, additional validations are necessary for an operational performance of the algorithm in cloud-drift wind estimation.

Further research is needed to develop automatic parameter tuning methods for selecting optimum window sizes and various thresholds for different scenes using possibly machine learning methods. In addition to affine, higher-order polynomial and non-linear displacement functions guided by experiment can be used. Future work involves using adaptive hierarchical non-square template and search windows, using multispectral information, coupling stereo and motion estimation [6], improving the accuracy of the estimated motion field by using robust estimation [13], relaxation labeling or regularization, and post processing the motion field by using cloud classification.

5 Acknowledgements

Research funding was provided by the Applied Information Systems Research Program (NASA NRA-93-OSSA-09) managed by Glenn Mucklow, in the Office of Space Science at NASA HQ. GOES-9 data sets were acquired with the help of Marit Jentoft-Nilsen using the real time ingest system set up by Dr. Dennis Chesters, the GOES project scientist at NASA/GSFC. Acknowledgements are due to Dr. Peter Black of NOAA/Hurricane Research Division and Harold Pierce of Mesoscale Atmospheric Processes Branch at NASA/GSFC for manual tracking of clouds.

References

[1] G. G. Campbell, J. W. F. Purdom, and C. Vaughn. Cloud height and motion from multiple satellite observations. *SPIE*, August 1996.

[2] W. C. Graustein. *Differential Geometry.* Macmillan, New York, 1935.

[3] A. F. Hasler. Stereoscopic measurements. In P. K. Rao, S. J. Holms, R. K. Anderson, J. Winston, and P. Lehr, editors, *Weather Satellites: Systems, Data and Environmental Applications, Section VII-3*, pages 231–239. Amer. Meteor. Soc., Boston, MA, 1990.

[4] A. F. Hasler, K. Palaniappan, M. Manyin, and J. Dodge. A high performance interactive image spreadsheet (IISS). *Computers in Physics*, 8(3):325–342, 1994.

[5] Yan Huang, K. Palaniappan, Xinhua Zhuang, and Joe Cavanaugh. Optic flow field segmentation and motion estimation using a robust genetic partitioning algorithm. *IEEE Trans. Pattern Analysis and Machine Intelligence*, To be published.

[6] C. Kambhamettu, K. Palaniappan, and A. F. Hasler. Coupled, multi-resolution stereo and motion analysis. *IEEE International Symposium on Computer Vision*, pages 43–48, November 1995.

[7] Chandra Kambhamettu, Dmitry B. Goldgof, and Matthew He. Determination of motion parameters and estimation of point correspondences in small nonrigid deformations. *Proc. IEEE Conf. Computer Vision and Pattern Recognition*, pages 943–946, June 1994.

[8] Chandra Kambhamettu, Dmitry B. Goldgof, Demetri Terzopoulos, and Thomas S. Huang. Nonrigid motion analysis. In Tzay Young, editor, *Handbook of PRIP: Computer vision*, volume II, pages 405–430. Academic Press, San Diego, California, 1994.

[9] ChandraSekhar Kambhamettu. *Nonrigid Motion Analysis Under Small Deformations*. PhD thesis, University of South Florida, December 1994. Department of Computer Science and Engineering.

[10] Robert T. Merrill, W. Paul Menzel, Wayman Baker, James Lynch, and Eugene Legg. A report on the recent demonstration of NOAA's upgraded capability to derive cloud motion satellite winds. *Bull. American Meteorological Society*, 72(3):373–376, March 1991.

[11] S. J. Nieman. Goes-8/9 cloud drift winds. *SPIE*, August 1996.

[12] K. Palaniappan, M. Faisal, C. Kambhamettu, and A. F. Hasler. Implementation of an automatic semi-fluid motion analysis algorithm on a massively parallel computer. *IEEE International Parallel Processing Symposium*, pages 864–872, 1996.

[13] K. Palaniappan, Y. Huang, X. Zhuang, and A. F. Hasler. Robust stereo analysis. *IEEE International Symposium on Computer Vision*, pages 175–181, November 1995.

[14] K. Palaniappan, Chandra Kambhamettu, A. Frederick Hasler, and Dmitry B. Goldgof. Structure and semi-fluid motion analysis of stereoscopic satellite images for cloud tracking. *Proceedings of the International Conference on Computer Vision*, pages 659–665, 1995.

[15] H. K. Ramapriyan, J. P. Strong, Y. Hung, and C. W. Murray, Jr. Automated matching of pairs of SIR-B images for elevation mapping. *IEEE Trans. Geosciences and Remote Sensing*, 24(4):462–472, 1986.

[16] C. E. Weatherburn. *Differential Geometry in Three Dimensions*, volume II. Cambridge University Press, Cambridge, 1930.

Enhancement and quality control of GOES images

Marit Jentoft-Nilsen[†], K. Palaniappan[†], A. Frederick Hasler, Dennis Chesters

[†]Science Systems Applications Inc.
Laboratory for Atmospheres
NASA Goddard Space Flight Center, Greenbelt, MD 20771
Email: marit@camille.gsfc.nasa.gov, palani@camille, hasler@agnes, chesters@climate

ABSTRACT

The new generation of Geostationary Operational Environmental Satellites (GOES) have an Imager instrument with five multispectral bands of high spatial resolution, and very high dynamic range radiance measurements with 10-bit precision. A wide variety of environmental processes can be observed at unprecedented time scales using the new Imager instrument. Quality assurance and feedback to the GOES Project Office is performed using rapid animation at high magnification, examining differences between successive frames, and applying radiometric and geometric correction algorithms. Missing or corrupted scanline data occur unpredictably due to noise in the ground based receiving system. Smooth high resolution noise-free animations can be recovered using automatic techniques even from scanline *scratches* affecting more than 25% of the dataset. Radiometric correction using the local solar zenith angle was applied to the visible channel to compensate for time-of-day illumination variations to produce gain-compensated movies that appear well-lit from dawn to dusk and extend the interval of useful image observations by more than two hours. A timeseries of brightness histograms displays some subtle quality control problems in the GOES channels related to rebinning of the radiance measurements. The human visual system is sensitive to only about half of the measured 10-bit dynamic range in intensity variations, at a given point in a monochrome image. In order to effectively use the additional bits of precision and handle the high data rates new enhancement techniques and visualization tools were developed. We have implemented interactive image enhancement techniques to selectively emphasize different subranges of the 10-bits of intensity levels. Improving navigational accuracy using registration techniques and geometric correction of scanline interleaving errors is a more difficult problem that is currently being investigated.

Keywords: radiometric correction, histogram arrays, geometric registration, geostationary, GOES, satellite imaging

1. INTRODUCTION

A wide variety of atmospheric, land and ocean processes can be observed at unprecedented temporal and spatial resolution using the GOES Imager instrument. Examples of environmental and anthropogenic processes that we have observed over the past two years include rapid thunderstorm and front development, convective outbreaks along outflow boundaries, multilayer wind shear, evolution of hurricane cloud-top structure, microphysical properties of clouds, atmospheric gravity waves, Kelvin-Helmholtz and solitary waves in hurricane cloud structures, fog dissipation, plumes from shuttle launches, contrails from jet aircraft, snow deposition and evaporation, sun glint from clouds and water, urban heat islands, moon's shadow during solar eclipses, African and Amazonian dust storms, ash and heat from volcanic eruptions, smoke from forest fires and biomass burning, deforestation in Amazonia, atmospheric disturbances due to ship tracks, diurnal heating of land and water, river flooding and gyres in ocean currents[1].

The new generation of GOES have separate imaging and sounding instruments, additional spectral channels, improved spatial resolution, better spectral sensitivity, expanded number of quantization levels, a more accurate and stable sensor calibration, more precise pointing, navigation and registration accuracy, and adjustable scanning field of view[2]. The new GOES are also three axes stabilized providing nearly continuous temporal coverage of the hemisphere. Some characteristics of the five channels of the GOES Imager instrument are shown in Table 1. The GOES Imager senses radiant (emitted) and solar-reflected energy in five channels from sampled areas of the Earth that provide spatial coverage from full-earth disk images to rapid scan continental USA (CONUS) and super-rapid scan sectors. Each sample (pixel) from the Imager is quantized to 10-bit accuracy linearly (versus 6-bits for GOES-7). A complete full earth image scan requires about 26.5 minutes and occurs every 3 hours and a sector scan covering 3000km × 3000km takes about 3 minutes to complete.

0-8194-2200-2/96/$6.00

Channel No. (Wavelength)	Wavelength (μm)	Resolution (μrad)	IGFOV at Nadir (km) E/W x N/S	SSR (km) E/W x N/S
1 (visible, 0.65μm)	0.52 to 0.72	28	1.0 x 1.0	0.57 x 1.0
2 (shortwave IR, 3.9μm)	3.78 to 4.03	112	4.0 x 4.0	2.29 x 4.0
3 (water vapor, 6.7μm)	6.47 to 7.02	224	8.0 x 8.0	2.29 x 4.0
4 (longwave IR, 10.7μm)	10.20 to 11.20	112	4.0 x 4.0	2.29 x 4.0
5 (IR, 12.0μm)	11.50 to 12.50	112	4.0 x 4.0	2.29 x 4.0

Table 1 GOES Imager characteristics including instantaneous geometric field of view (IGFOV), sampled subpoint resolution (SSR) which accounts for scanline oversampling by 1.75 for visible, 1.75 for IR window and 3.75 for H_2O band. The Imager data rate is about 2.6 Mb/s (1.2 GB/hour).

We have three main objectives in processing and enhancing GOES images. First, we want to identify and characterize problems with the images for quality assurance to provide feedback to the GOES Project Office at NASA Goddard Space Flight Center (GSFC), as this relates to satellite stability, instrument and ground sensor processing performance. Quality assurance consists of checking for and quantifying problems such as impulse or *salt and pepper* noise, scanline noise or *scratches*, line dropouts, scanline misregistration, detector striping, detector drift, stray light affecting detectors, radiometric bias, geometric distortion due to optics or spacecraft motion, all of which are readily apparent in multispectral images of single scenes. More subtle problems such as image jitter, small image misregistration and navigation errors can be found using timeseries animations of images. Second, we want to produce high quality science data of severe storms and mesoscale phenomena using automatic satellite data product generation such as stereo cloud heights[3] and multispectral winds[4] for numerical weather modeling. Third, we want to use timeseries animations and color enhancements of GOES data to qualitatively study weather patterns and provide World Wide Web Internet access to realtime full resolution datasets for public interest and education.

Many similar processing steps are used to meet these three objectives in processing a sequence of images. It requires that radiometric and geometric flaws be fixed so that the eye is not distracted from seeing more subtle details. Radiometric errors due to noise, light leakage, or detector scanning and performance have been well characterized for the new GOES Imager and automatic algorithms for correcting for most of these errors have been developed a few of which will be described in Section 2. Maintaining good cloud top detail from dawn to dusk for the visible channel is necessary for tracking a cloud's details during all stages of its formation and dissipation and extends the period over which visible data can be analyzed. Section 3 describes an automatic gain adjustment that compensates for the solar zenith angle and normalizes the albedo variation due to changes in illumination angle over the course of the day. For GOES Imager data it is also necessary to reduce the 10-bits of grayscale levels in the data to match the smaller range that can be more readily perceived by the human eye. Reducing the range of graylevel quantization within a GOES image usually destroys some of the perceivable fine scale structure, so techniques for enhancing the images before or during the grayscale requantization step is described in Section 4. Geometric errors caused by image jitter due to abrupt fixes in the GOES Image Navigation and Registration (INR) system or due to uncorrected spacecraft attitude changes can usually be corrected by applying advanced image registration techniques. However, as described in Section 5, local geometric distortion due to scanline shear from east-west or north-south interleaving errors is more difficult to correct.

GOES-8 and GOES-9 each generate over 13 GB of data per day. It would be time consuming and inefficient to manually examine every Imager frame in detail, and the computing resources necessary to correct and archive all of the original as well as the corrected data generated by the quantitative quality control algorithms is prodigiously expensive. Furthermore, most of the quantitative algorithms that need to be applied, currently cannot keep up with the real-time data rate even when running on a fast supercomputer graphics workstation like the Silicon Graphics Inc. (SGI) Onyx with two R8000 (90 MHz) CPUs with a peak performance of 720 MFlops. Manually reviewing the output of these algorithms if they were run on every image is impractical without substantial resources. We use the following strategy to accomplish the three objectives described above in a cost effective manner. The Interactive Image SpreadSheet (IISS) developed in our laboratory is a powerful and versatile visualization software with a spreadsheet paradigm for handling large data volumes with high dynamic range measurements[5]. The IISS running on fast SGI workstations with large amounts of memory is used to view from several large to dozens or hundreds of smaller unenhanced GOES sectors from the realtime *ftp* server[1] singly or in animation. This allows us to find the most obvious quality control (QC) problems and observe the development of interesting weather situations. Then

semiautomatic processing software developed in our laboratory is run on the most interesting sector(s) of the day. The software fixes and enhances the images in the sector to produce an image animation suitable for further QC work or output to a NASA-TV video clip[6]. In the future, the GSFC GOES Web server is planned to have interactive sectorization and enhancement capabilities to provide data on demand from the rotating archive.

2. REPAIRING SCANLINE *SCRATCH* ERRORS IN GOES IMAGER DATA

Many of the missing and noisy GOES Imager scanlines are the result of bad reception at our antenna. Since the scanline scratches do not occur regularly within an image they cannot be readily identified and removed using Fourier transform methods. Figure 1a shows a GOES-9 visible scene from a series of 1-minute interval images with the noisy lines typical of bad reception at the NASA GSFC antenna. The scanline errors appear as horizontal *scratches* in the image and pose a challenge for creating smooth animations. Near the top of the image, there is also a line dropout (solid black line) of unknown origin. The noisy lines we see almost always occur singly, while the line dropouts often occur as gaps many lines wide. Software routines were written in the Interactive Data Language (IDL)[7] to automatically recognize and replace these two types of bad lines.

Repairing bad lines in a GOES visible image

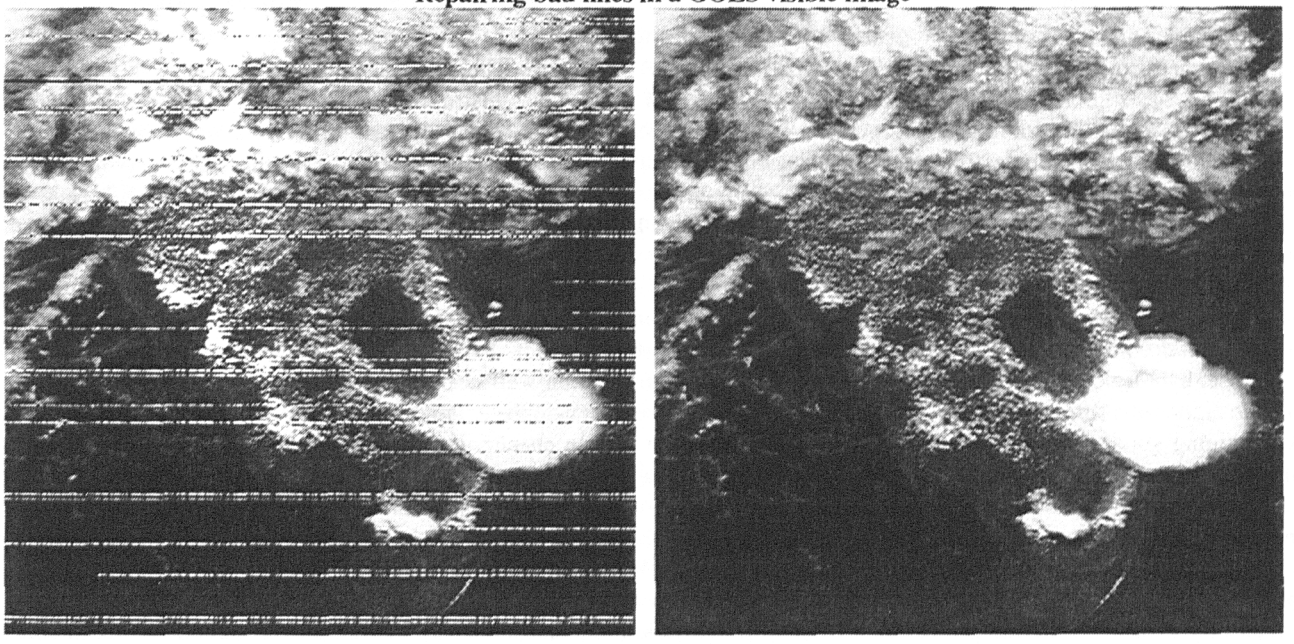

a. original image with bad lines

b. image with lines repaired by interpolation

Figure 1 (a) Original GOES-9 Imager picture (visible channel) of Florida from July 2, 1995 at 1844 UTC showing full and partial scanline scratches and dropouts. (b) The same image after application of automatic scanline repairing techniques.

Automatic average scanline radiance and correlation-based algorithms were developed to detect bad scanlines that extend most of the way across an image and interpolate across the noisy radiance measurements using spatially and temporally adjacent valid data. The line average,

$$\ell_{ave}(y) = \frac{1}{N_x}\sum_{x=0}^{N_x-1} I(x,y) \begin{cases} \geq T_\ell \text{ , normal scanline} \\ < T_\ell \text{, corrupt scanline} \end{cases} \tag{2.1}$$

is thresholded to identify and flag bad lines; T_ℓ is a user-defined value, typically a fraction (*e.g.* 0.25) of the spacelook value in each channel. The scanline autocorrelation (each line's correlation to a copy of itself that has been shifted horizontally by one or more pixels) is computed for each scanline,

$$r(x,y) = \frac{1}{N_x}\sum_{m=0}^{N_x-1} I(m,y)I(x+m,y) \begin{cases} \geq T_a \text{ , normal scanline} \\ < T_a \text{, corrupt scanline} \end{cases} \tag{2.2}$$

Scratchy scanlines are noisy and have low autocorrelation values, so scanline autocorrelations of lag one $r(1,y)$ that are less than the cutoff are used to detect corrupt scanlines. Both tests are needed since scanline dropouts which are nearly constant in value will have high autocorrelation values. The two tests can identify most of the bad lines, however, the two user-specified thresholds must be set differently depending on which of the five Imager channels is being processed. This technique does not work as well on visible Imager data near the terminator, because nighttime visible data, which is basically noise, is very uncorrelated.

Once a list of bad lines is generated, they are grouped into sets or gaps of adjacent bad lines and fixed in their entirety. For scanline gaps of one to three lines, the corrupt lines are replaced by interpolating between the previous and following good lines. Longer contiguous scanline gaps are replaced with data from a time-adjacent image. The data replacement is usually much less obvious in animation than when viewing a single image. When large gaps were repaired by interpolating between the previous and following time-adjacent images, the result was much more obvious and distracting in animations.

Figure 1a also shows several partially noisy lines that are only bad for a small fraction of the line. In order to minimize the amount of data replacement, a slightly different method is used to identify and replace partially scratchy scanlines. The absolute value of the difference between a line and its shifted copy is calculated and the differences are tested for segments with anomalous difference values to find sharp transitions.

$$\ell_{diff}(x,y) = |I(x,y) - I(x+1,y)| \begin{cases} \geq T_d \text{ , partially corrupt scanline} \\ < T_d \text{ , normal scanline} \end{cases} \tag{2.3}$$

Segments of the line with bad values are marked in a mask for the whole image. After all the bad segments are found, each column is checked for bad pixels which are replaced with values interpolated between the preceding and following good pixels. The whole series of 1-minute GOES-9 images from which Figure 1a was taken had many noisy scanlines; in some scenes up to 25% of the image was corrupted. Repairing the images produced a satisfactory high-resolution animation and that could be used for testing automatic cloud tracking algorithms.[8]

3. SOLAR ILLUMINATION ANGLE CORRECTION

The GOES Imager visible channel measures reflected solar radiation. Figure 2 shows a histogram array for a day long GOES-9 series with each image of size 2444 x1380 pixels, full resolution, and centered at (lat, lon) = (19.4°, -63.9°). The left histogram array, which is shaded to show highly populated bins in black and zero populated bins in white, shows the change in overall scene brightness as a function of time of day for raw images. When the scene is not illuminated (near 0900 UTC and 2330 UTC) the histogram distributions are centered on the spacelook count value with a very small spread. As the scene begins to be illuminated, the distributions begin to spread out and shift up in count space. At midday the process reverses and the range of counts diminishes until sunset. The two maxima in the histogram distributions, seen as dark regimes, are the maxima for land or water (low counts) and clouds (high counts).The two vertical stripes at 1545 UTC and 2030 UTC are due to very noisy data for these images.

The solar illumination angle correction assumes a Lambertian (diffuse) reflection model for the clouds being viewed and ignores any atmospheric effects between the clouds and the top of the atmosphere. In this simplified case, the reflected radiance from a scene, R, is the product of the scene albedo, ρ, the incident solar radiation, E, falling on the scene, and the cosine of the solar zenith angle,

$$R = \rho E \cos(z) \tag{3.1}$$

The equation converting GOES Imager counts X to radiance at the sensor is,

$$R = m(X - spacelook) \tag{3.2}$$

where m is a NOAA supplied calibration coefficient. This means that in count space, the sun illumination angle correction that converts measured counts to counts normalized to a sun zenith angle of zero is,

$$X' = \frac{(X - spacelook)}{\cos(z)} + spacelook \tag{3.3}$$

For display purposes, we enforce the constraint that the cosine term in (3.3) needs to be greater than or equal to 0.1 in order to make the transition over the terminator smooth and to avoid dividing by zero in unilluminated parts of a scene.

The two solid black lines plotted on the left histogram array of Figure 2 are theoretical count values for $\rho = 0$ and $\rho = 1$ for the pixel in the scene with the maximum solar illumination. The lines were calculated using Equation 3.3 and the relationship, $\rho = cR$, where c is a NOAA supplied radiance to albedo conversion coefficient for converting mW/(m^2 ster cm^{-1}) to albedo. The line for $\rho = 0$ is a flat line at the spacelook count value. The line for $\rho = 1$ is a curve that nearly coincides with the envelope of the histogram array. It is interesting to note, that there are a fair number of populated bins above the theoretical maximum count, especially at sunrise and sunset.

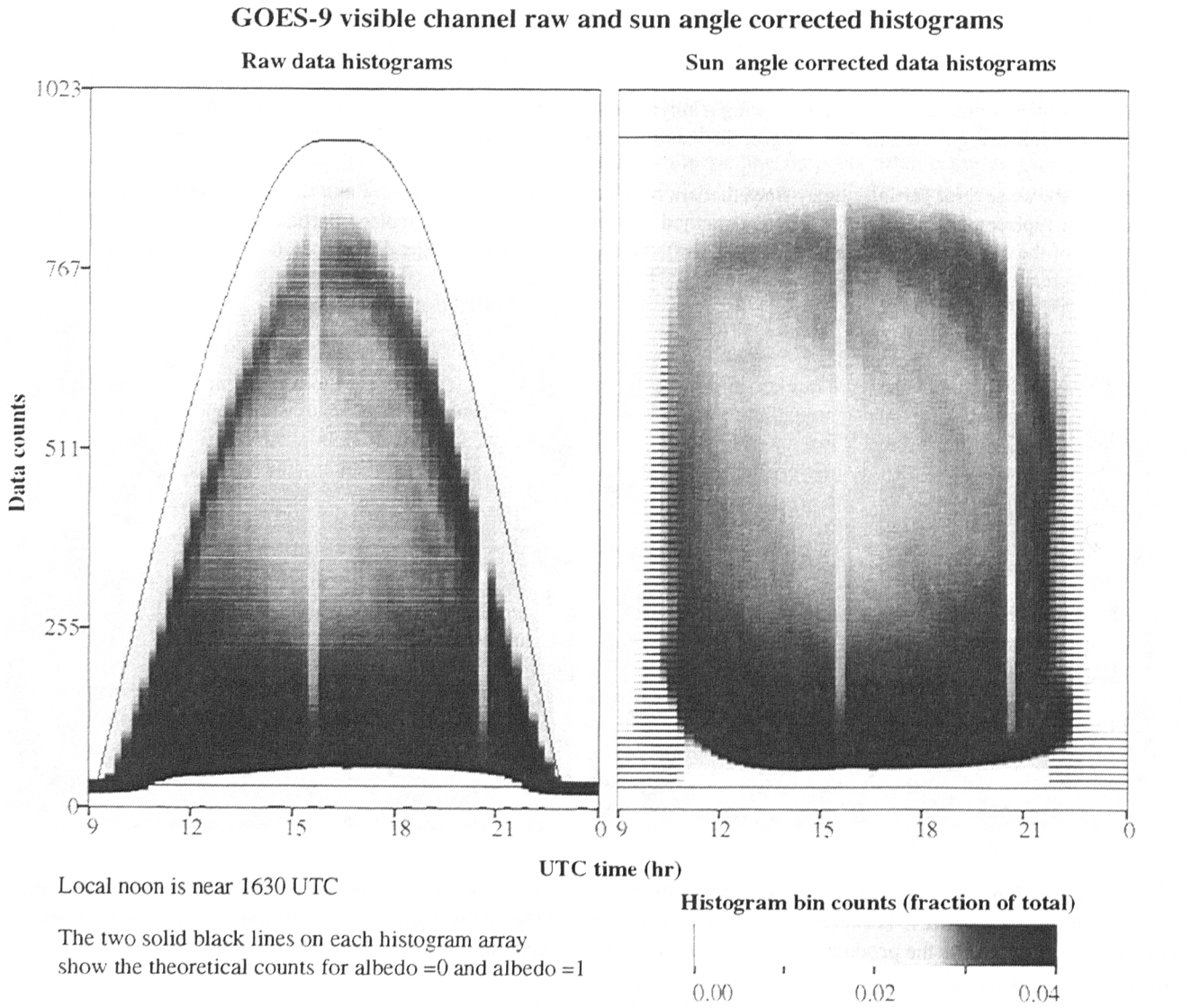

Figure 2 The left histogram array shows histograms for a day long series of GOES-9 Imager visible channel frames for scenes centered at (latitude, longitude) = (19.4°, -63.9°). The two solid black lines on each array show the theoretical count value for $\rho = 0$ and $\rho = 1$. The right histogram array is the result of applying the solar zenith angle correction.

The histograms of the same images after the solar zenith angle correction has been applied are on the right half of Figure 2. As expected, the gray levels of the images are much more level over the course of a day after the correction, and the theoretical $\rho = 1$ line becomes a straight line because all the histograms have been normalized to the same amount of incident radiation. The clouds with apparent albedo greater than one are much more obvious in the corrected histogram array, and it is more evident that they occur most frequently for larger solar zenith angles. Some possible reasons why these clouds appear so bright are: they have higher altitudes and are illuminated longer than lower clouds or land, the lambertian reflection model is a

poor assumption for the clouds, that near sunrise and sunset the path in the atmosphere between the cloud top and top of atmosphere is longer so the amount of path scattered radiation is larger. The NOAA supplied radiance to albedo conversion factor is only an approximate conversion since the true albedo of any particular target would depend on all these factors listed.

The automatic processing software uses the `xephem` program[9] to calculate the subsolar point at the frame start time and then uses the solar zenith angle of the pixel closest to the subsolar point for the whole image. This is computationally much faster than calculating the zenith angle for every pixel in an image. For the images used to produce the histograms in Figure 2, calculating and applying the true correction for each pixel took 20 times longer (in IDL) than calculating the correction for one pixel and applying it to the whole image. The global approximation works well for scenes smaller than about 20 degrees of longitude. Figure 3 shows several raw and solar illumination angle corrected GOES-9 images of hurricane Luis.

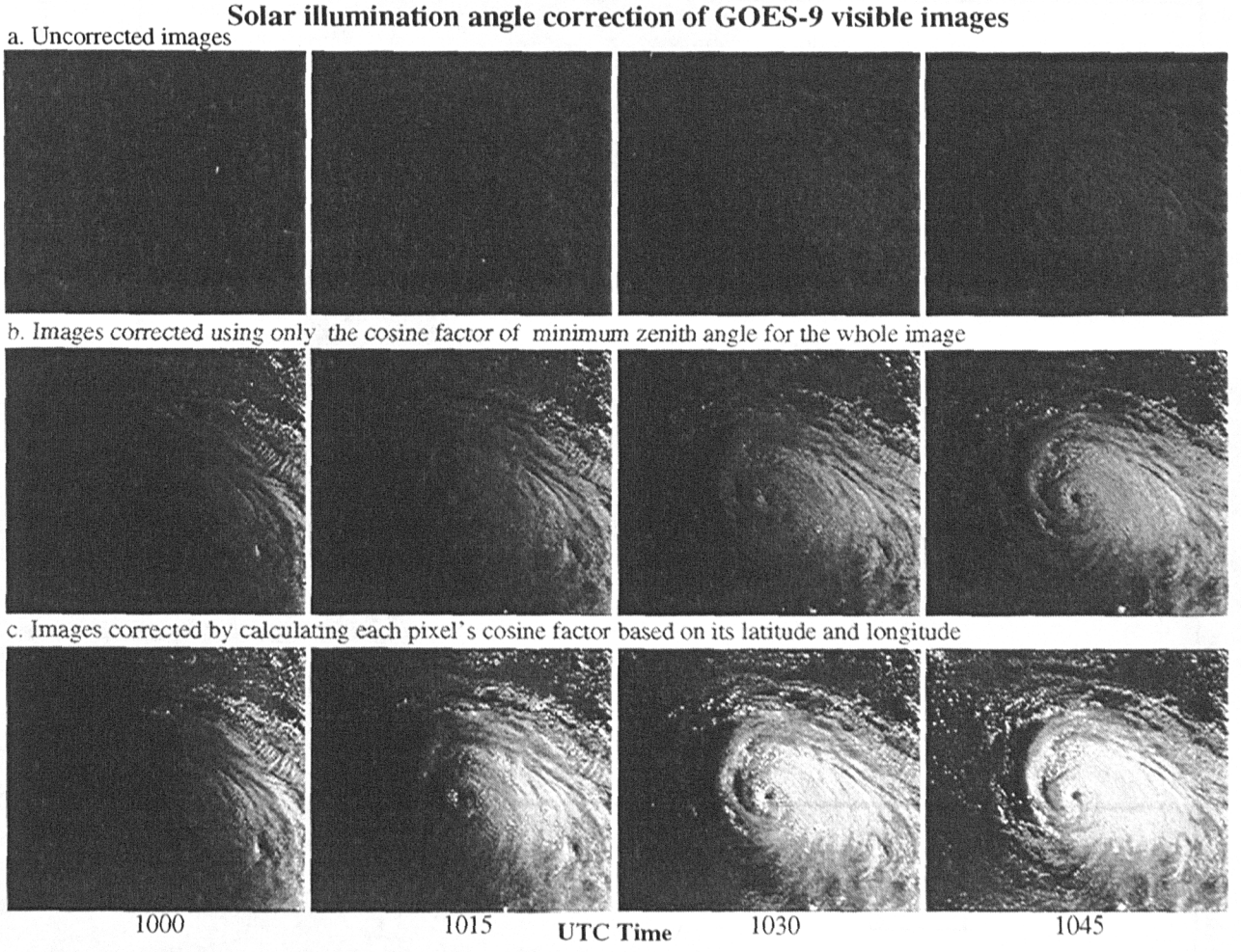

Figure 3 Results from two different techniques of solar illumination angle correction of GOES images from 6 Sep 95.

4. GRAY LEVEL QUANTIZATION AND IMAGE SHARPENING

The range of GOES multispectral Imager data is 10-bits or 1024 levels, which is wider than the limits of human perception for discriminating grayscale quantization levels. Figure 4 shows histogram arrays for a typical scene over a period of about 60 hours for each of the five GOES Imager channels from GOES-8. The visible channel has the largest range of gray levels, the 12μm and 11μm have slightly smaller min-max ranges, and the 3.9 μm and 6.7 μm channels have the smallest range.

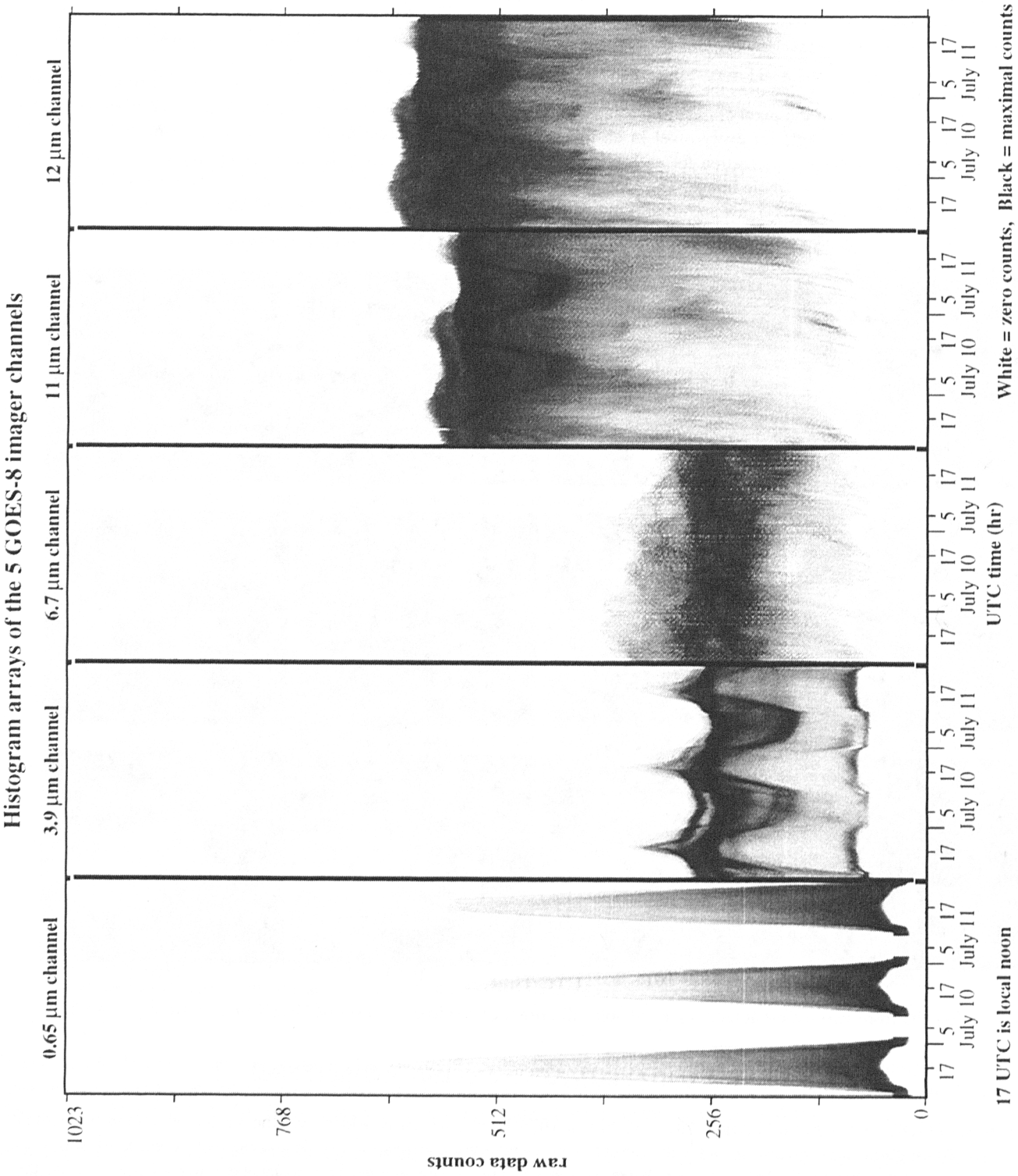

Figure 4 Histogram arrays for five channels of the GOES Imager collected over a 60 hour period at approximately 15 minute intervals.

Note that the histogram arrays are composed of a sequence of histograms with each individual scene histogram shown as a column of intensities in Figure 4. The effects of the daily solar illumination cycle can be seen not only in the visible channel (the gaps are during nighttime periods which would be seen as a black line), but also 3.9 μm, 11μm and 12 μm channels. The 3.9 μm channel saturates at the cold end during the nighttime; the detector clipping can be inferred from the sharp horizontal boundaries in the 3.9 μm histogram array. The 6.7 μm and 11μm channels have distinct rebinning effects, which appear as holes in the respective histogram arrays, from processing done at NOAA before the data is rebroadcast in *gvar* format. All these features need to be considered when compressing the gray level counts to an appropriate range for human perception.

The human visual system is sensitive to only about 5-bits (32 levels) at a given point in a monochrome image which is half the 10-bit dynamic range in the Imager data. Additionally, most computer display monitors such as cathode ray tube (CRT) screens, liquid-crystal displays (LCD), plasma panels, or electroluminescent displays, as well as printed paper are capable of presenting even a smaller range of intensity levels (4 to 5-bits). We have tried several methods to enhance detail in GOES visible and IR images. The techniques we have used include contrast stretching, sharpening, unsharp masking, local and general histogram. Each of these methods has trade-offs in terms of computational speed, preservation of radiance information, stability over a timeseries of images, ability to enhance detail at all gray levels and amount of image dependent fine tuning of filtering parameters. In general it is not too hard to enhance a single GOES Imager channel using any of the techniques listed above to get informative and nice looking results. It is a little more difficult to enhance a timeseries of images for animation without introducing artifacts that cause distractions during the animation. Figure 5 shows a GOES-8 image of Hurricane Bertha showing subregions that were enhanced using different enhancement techniques. Corresponding animations will be available at http://climate.gsfc.nasa.gov/~chesters/goesproject.html and http://rsd.gsfc.nasa.gov/rsd/movies/movies.html.

Several enhancement techniques applied to a GOES8 visible image

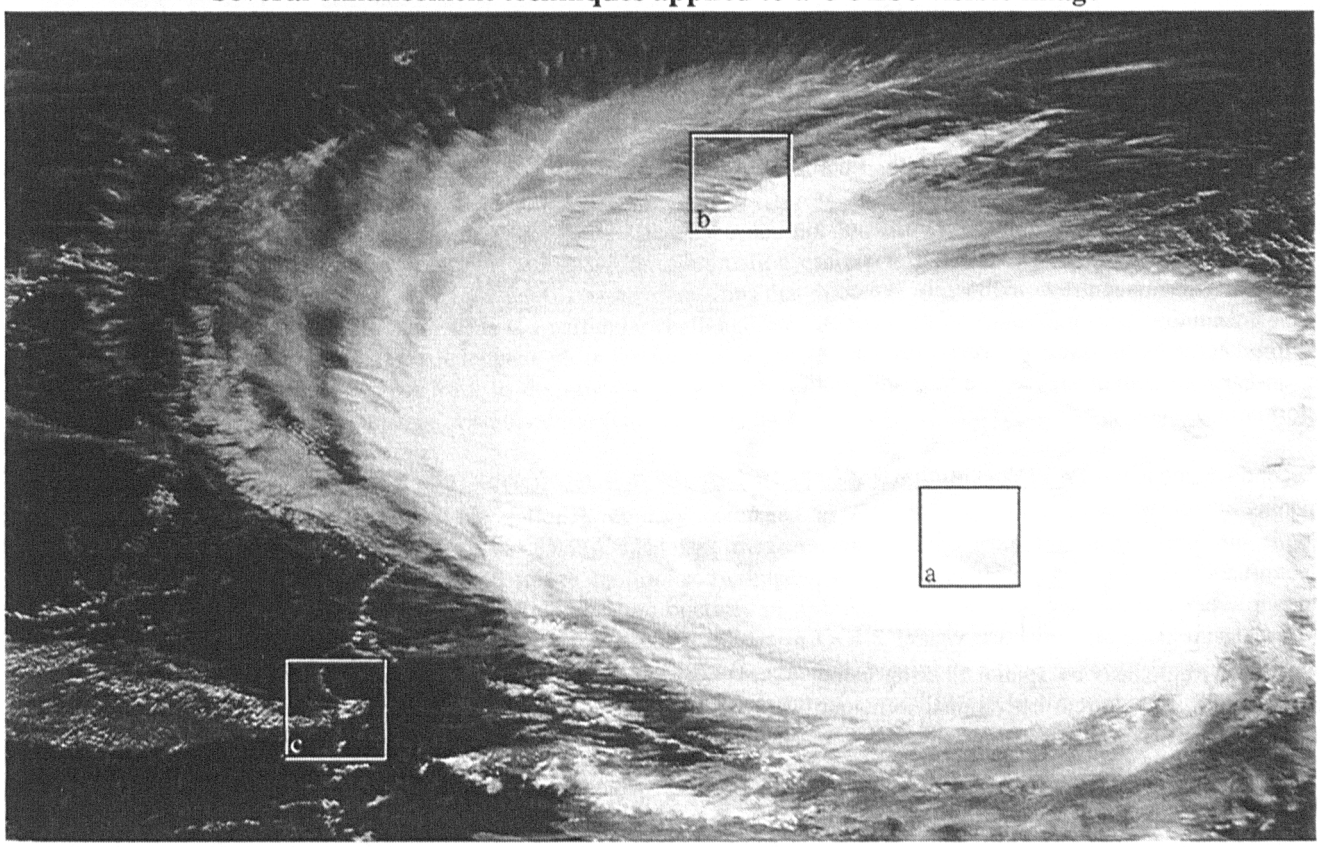

Regions a,b and c are shown enhanced with several techniques in the second part of this figure

Figure 5a Visible GOES-8 image at 1 km resolution from 9 July 1996 showing three regions selected for enhancement.

The simplest and fastest method of improving image contrast is to apply a lookup table that maps input data counts to the desired range of gray levels. If the mapping colormap lookup table mapping is monotonic, it is possible to calculate an approximate radiance for each rescaled gray level. Applying (colormap) lookup table transformations is stable for a timeseries of images and does not require any fine tuning to the particular image being enhanced. The main drawback with the lookup table approach is that it is not very good at compressing the number of gray levels in an image when there are details that need to be preserved throughout the quantization range. For GOES visible Imager data, it is possible to either enhance the cloud tops or to enhance the land and oceans. However, it is not possible to enhance both with a monotonic grayscale lookup table. Non-monotonic lookup tables can be used, but these lead to perceptual artifacts by adding structure to an image where the grayscale transformation mapping changes direction or has a discontinuity. The images available on the GOES public file server at GSFC-NASA[1] were all enhanced using lookup tables because it is fast and those downloading the images would then be able to calculate radiance from the gray levels. Figure 5a shows a GOES-8 visible image of Hurricane Bertha with three regions selected for enhancement. Figure 5b is divided into six rows, each showing the result of a different enhancement scheme. Row one in Fig. 5b shows the original image regions linearly stretched between minimum and maximum data counts, while Row 2 shows the same regions with a non-linear monotonic lookup table (i.e. square root transformation).

The second technique we use is convolution with a sharpening kernel such as

$$\begin{bmatrix} -1 & -1 & -1 \\ -1 & A & -1 \\ -1 & -1 & -1 \end{bmatrix} \qquad (4.1)$$

High frequency emphasis by spatial filtering using small kernels is our current operational technique for the sector of the day because it is fast and it sharpens images without changing their low frequency characteristics. Figure 5b Row 3 shows an image that has been enhanced using the kernel in (4.1) with $A = 12$. Outlier pixels such as salt and pepper noise only effect their immediate neighborhood, so they do not produce large scale flickering in a timeseries of images. Radiance

Several enhancement techniques applied to a GOES8 visible image

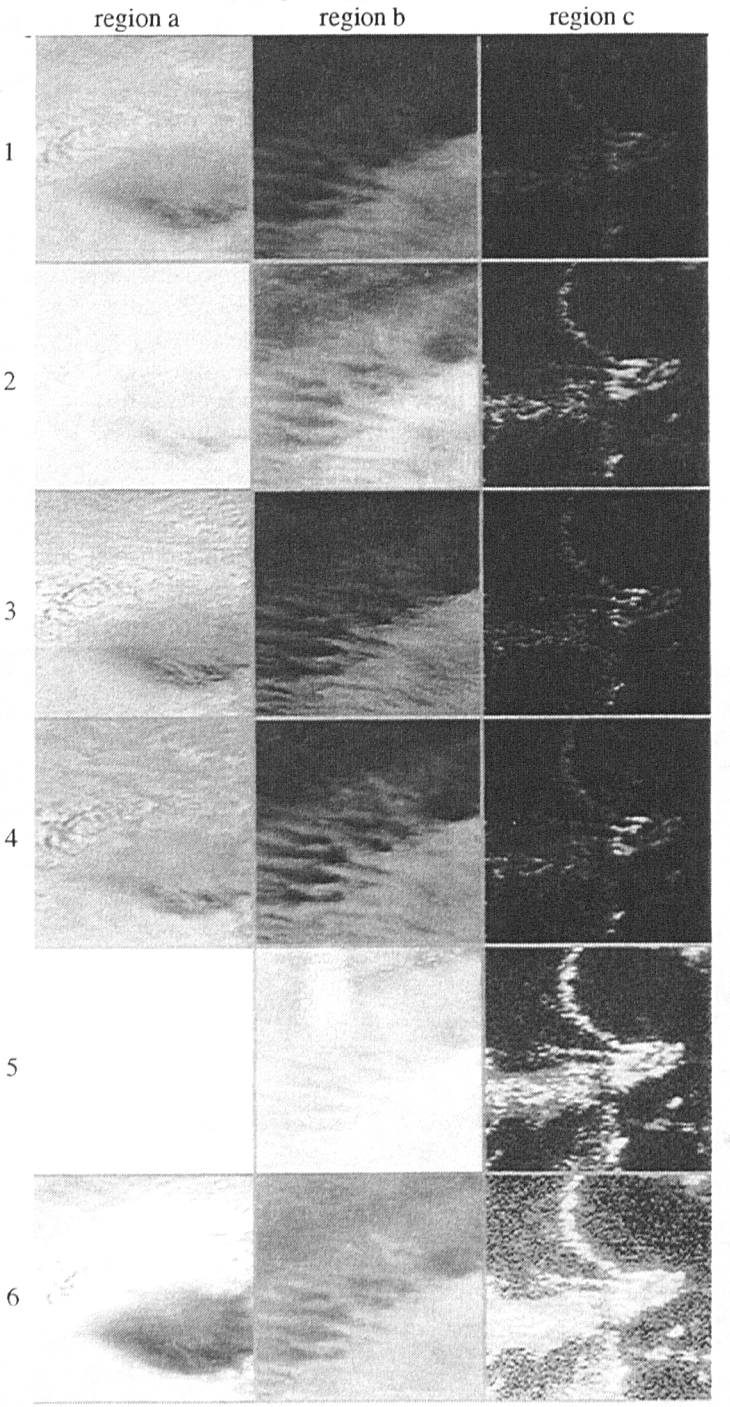

1 - original image 2 - nonlinear lookup table
3 - convolution with sharpening kernel 4 - unsharp mask
5 - histogram equalization 6 - local histogram equalization

Figure 5b Images enhanced by applying six different graylevel enhancement techniques to the 3 regions shown in Fig. 5a to bring out cloud-top structure. Each technique incorporates graylevel quantization reduction to 8-bits.

values cannot be reliably retrieved from images processed with type of convolution.

Unsharp masking or high-boost filtering can also be implemented using a kernel similar to (4.1) but is usually done in two steps instead of one. The idea is to subtract a smoothed version of an image from itself. This is similar to applying a band stop filter to an image, where the stopped frequency corresponds to the size of the box used to create the smoothed version of the image. Correct radiance values cannot be retrieved from the data values in images enhanced this way. Unsharp masking is a moderately fast technique, but since the amount of enhancement depends on the input scene, it is sensitive to outlier pixels, noise or even general changes in image brightness. This is most evident in timeseries when using a medium-large box size for the smoothing step. For example, the appearance of a bright cloud can brighten nearby areas in the smoothed image whose brightness may not have changed in the original image. This will make the sharpened image darker in those areas. For a single image, this is not a problem, but it can cause flicker in a timeseries. The same effect causes 'ringing' around the edges in the sharpened image. One big advantage of unsharp masking as we use it (as a band stop to stop low frequencies) is that it enhances detail at all gray levels. The disadvantages are its moderate speed, the flicker mentioned about and the fact that is can need some tuning to the input data. Figure 5b Row 4 shows an image to which unsharp masking has been applied.

We have also tried various types of local and general histogram modification. General histogram equalization is the process of calculating and applying a lookup table to an image to make it have a flat (or any other shape) histogram. Histogram equalization is fast and preserves radiance values, but does have some problems when used to compress gray levels. One difficulty that arises for GOES Imager data is that the cloud top data counts are often in the tail at either end of the original histogram distribution. During the process of equalization, the original distribution tails are often mapped into a very small number of values in the output image, with the result that the cloud tops end up saturated. Figure 5b Row 5 shows an image that has been histogram equalized.

Local histogram modification is the same as general histogram equalization, except a histogram is calculated for a local area around each pixel in the input image and each pixel's value is adjusted according to it's own histogram. This method enhances local detail better than the general histogram algorithm, but is much more computationally expensive. Also, depending on the size of the local area that is used to calculate the histograms, gray level shifts can occur in various parts of the output images making them unsuitable for animation. Figure 5b Row 6 shows an image that has been local histogram equalized.

Image enhancement for series of images involves some difficulties that are not present when processing a single image. For example, overall gray level changes from image to image in an animation can create a distracting flicker or strobing effect. When we enhance a series of images, we either have to avoid algorithms that effect the overall gray level or fine tune them to effect it consistently from image to image. This is a particular challenge for weather satellite images, since the scenes we are interested in can start out with large gray level changes in the form of clouds forming, dissipating and moving in and out of the scene. The changes in average gray level in the raw images are generally not distracting because they are caused by a bright object appearing against a constant or smoothly varying background.

5. GEOMETRIC DISTORTION DUE TO SCANLINE INTERLEAVING ERRORS

The new GOES satellite has improved navigational accuracy compared to GOES-7 including more precise pointing, navigation and registration accuracy using star sensing, landmark measurements, range from signal transmission time, compensation for orbit and attitude contributed image motion and compensation for scanning mirror or other instrument motion. The Image Navigation and Registration (INR) system operates in near real-time and was designed to meet stringent geographical location accuracy requirements.[2] However, adjacent scanlines in GOES Imager data are sometimes misplaced in either the north-south or east-west direction. Figure 6a shows east-west scanline shearing in a time series of several GOES-8 10.7 μm images. The shearing in this example shows up as two lines shifted several pixels to the east, as marked by the arrows. Figure 6b shows a similar situation with GOES-9 visible channel in a small island off the coast of the Dominican Republic. In this case, groups of 8 lines are shifted, causing the shape of the island and the coastline to the northeast to vary from image to image. Animating a time series of images at high magnification makes such shearing errors very obvious. We are currently investigating advanced registration techniques that may be useful for correcting such local geometric errors. Highly accurate navigation is needed for registering and matching images both in a time series for cloud tracking and in a stereo sequence from the two GOES satellites for stereo cloud heights[4].

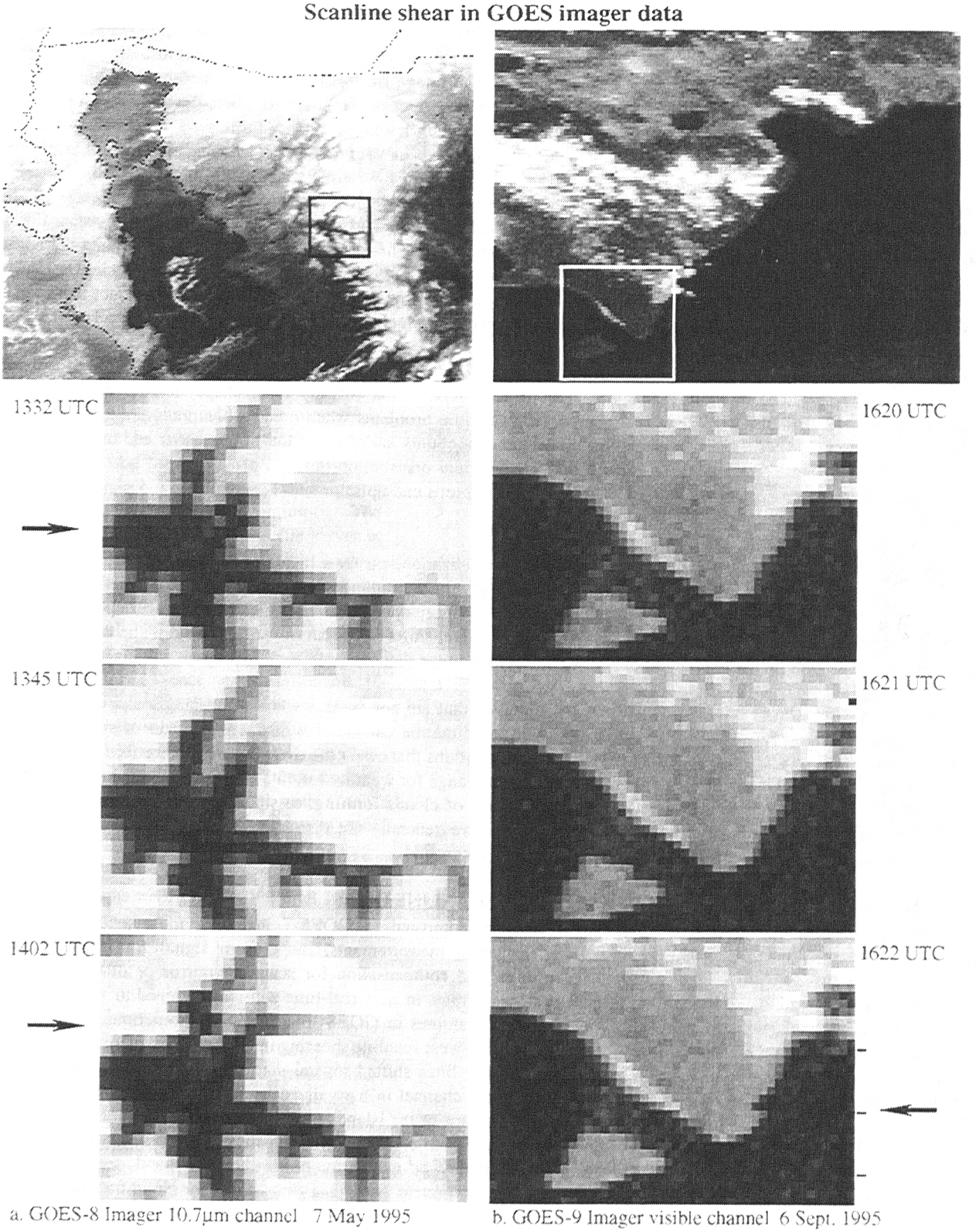

Figure 6 East-west scanline shear is evident in high contrast regions as shown in these (a) GOES-8 Imager scenes of the Sierra Madre mountains and (b) GOES-9 Imager scenes of Isla Beata off the coast of Dominican Republic.

6. CONCLUSIONS

A wide variety of atmospheric, land and ocean processes can be observed at unprecedented temporal and spatial resolution using the GOES Imager instrument. Smooth high resolution noise-free animations can be recovered using automatic techniques even from scanline *scratches* affecting more than 25% of the dataset. Radiometric correction using the local solar zenith angle was applied to the visible channel to compensate for time-of-day illumination variations to produce gain-compensated movies that appear well-lit from dawn to dusk and extend the interval of useful image observations by more than two hours. Image enhancement techniques and quantization methods for effectively using the full 10-bits of precision from the GOES Imager were developed.

7. ACKNOWLEDGMENT

This research was partially supported by the NASA RTOP 578-12-06-20, NASA AISRP program NRA-93-OSSA-09, NASA NRA-94-MTPE-02, NASA CAN-OA-94-01 and the NASA GSFC GOES Project Office.

8. REFERENCES

1. D. Chesters, O. Sharma, T. Nielsen, and A. F. Hasler, "GOES data ingest and public file service at NASA GSFC", *GOES-8 and Beyond*, SPIE Vol. 2812, Aug. 7-9, 1996 and http://climate.gsfc.nasa.gov/~chesters/goesproject.html.

2. W. P. Menzel and J. F. W. Purdom, "Introducing GOES-I: The first of a new generation of geostationary operational environmental satellites", *Bulletin of the American Meteorological Society*, Vol. 75, No. 5, pp. 757-781, May 1994.

3. K. Palaniappan, Y. Huang, X. Zhuang, and A. F. Hasler, "Robust stereo analysis", *IEEE Int. Symp. Comp. Vision*, IEEE Computer Society, Coral Gables, FL, pp. 175-181, Nov. 21-23, 1995.

4. K. Palaniappan, C. Kambhamettu, A. F. Hasler, and D. B. Goldgof, "Structure and semi-fluid motion analysis of stereoscopic satellite images for cloud tracking", *Int. Conf. Computer Vision*, IEEE Computer Society, Cambridge, MA. pp. 659-665, June 20-23,1995.

5. A. F. Hasler, K. Palaniappan, M. Manyin, and J. Dodge, "A high performance Interactive Image SpreadSheet (IISS)", *Computers in Physics*, Vol. 8, No. 4, pp. 325-342, May/June 1994.

6. Peter Jennings, World News Tonight, ABC-TV Network, Hurricane Luis 1-minute GOES-9 animation sequence, Aired Sept. 6, 1995, 6:30 to 7:00pm.

7. Research Systems Inc., Interactive Data Language, Version 4.0.1, Boulder, CO.

8. K. Palaniappan, M. Faisal, C. Kambhamettu, A. F. Hasler, "Implementation of an automatic semi-fluid motion analysis algorithm on a massively parallel computer", *10th Int. Parallel Processing Symp.*, IEEE Computer Society. Honolulu, HI, pp. 864-872, April 15-19, 1996.

9. E. C. Downey, xephem program, C code available from http://iraf.noao.edu/~ecdowney/xephem.html, 1996.

GOES-8/9 data ingest and public file service at NASA-GSFC

Dennis Chesters, Om Sharma, Fritz Hasler

NASA, Goddard Space Flight Center, Greenbelt, MD 20771

Torben Nielsen

Information and Computer Sciences Dept., University of Hawaii, Honolulu, HI 96822

ABSTRACT

Desktop computers have evolved to the point where they can process GOES variable-length (GVAR) data blocks at 1 Gbyte/hour, despite the complexity of the data stream and the varied demands of realtime users. Because of the lack of off-the-shelf GVAR processing packages before the launch of GOES-I in 1994, we assembled a custom Open System at NASA-GSFC to automatically ingest, process and disseminate full-resolution GOES-8 and GOES-9 imagery 24 hours per day. This data service is now widely used by the Internet community. The hardware-software package described here can be copied freely. Similar systems are now available from commercial vendors.

Keywords: goes, gvar, ingest

1. DATA FLOW - OVERVIEW

Figure 1 sketches the GOES data ingest and distribution architecture at NASA-GSFC. The GOES-8 and GOES-9 "data product" broadcasts are captured by two antennas at NASA-GSFC, and converted to GVAR data blocks (bit-packed scanlines) using custom cards in a SUN workstation. After a GOES Imager scan ends, the GVAR blocks are converted using a home-grown software package to parse the complicated GVAR format into full-resolution images and sounding files in standard formats. Calibrated and navigated GOES images for the last 24 hours are offered to the public in TIFF format, accessible to everyone with World Wide Web (WWW) browsers[1] or anonymous FTP[2]. An archive of historically interesting images and technical notes is also maintained by the GOES Project Scientist[3], providing an attractive and informative[4] public interface.

For the scientific analysis of large GOES datasets, the Interactive Image Spread Sheet (IISS)[5] is used on well-equipped workstations from Silicon Graphics Inc. (SGI) at the Goddard Laboratory for Atmospheres (GLA)[6]. For automated analysis of large amounts of data, custom IDL scripts are employed[7]. For smaller analyses and custom visualization in the GOES Project scrapbooks[8] and in the Remote Sensing Datasets (RSD) program[9], Macintosh personal computers are employed. Digital image animations are piped to a rack of television video equipment. High-quality dye sublimation printers are used for hardcopy. The ensemble of computers and visualization equipment scattered throughout the earth sciences building at NASA-GSFC is facilitated with FDDI and ethernet LANs that have very good connectivity to the Internet "cloud" of casual browsers and scientific users.

0-8194-2200-2/96/$6.00

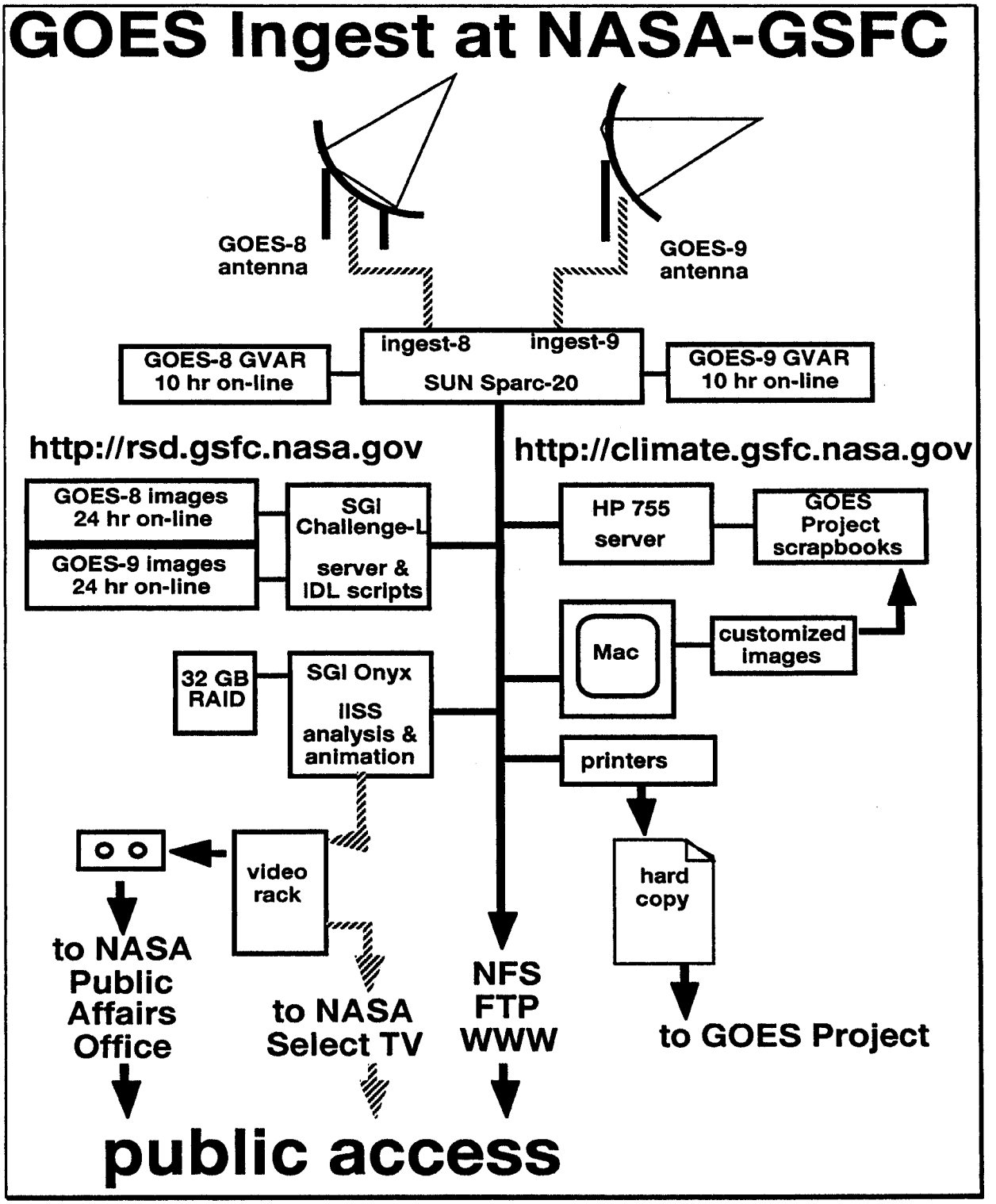

Figure 1: Hardware used to ingest GOES-8/9 data at NASA-GSFC for the GOES Project and for public service for schools, broadcast TV, and the Internet.

2. S-BAND FRONT END

The radio frequency (RF) front end for GOES GVAR reception begins with two 16-foot parabolic antennas with F/D ratios 3.5. One antenna is an old solid dish on a manually operated altitude-azimuth mount, normally fixed on GOES-EAST at 75W. The other dish is lightweight mesh on a motorized polar mount, purchased from Antenna Technology Communications, Inc. (ACTI). The newer antenna has a remote control for slewing to GOES-9 check-out station at 90W, and for fine-pointing in any weather at the operational station at 135W, low on the western horizon. Both dishes are mounted on top of the main earth sciences building at NASA Goddard Space Flight Center (GSFC) in Greenbelt, MD. The 5-story building is located on a hill near the watershed between the Patuxent and Potomac River basins, with a wide horizon in all directions, as shown in Figure 2.

Figure 2: GOES steerable 5-meter S-band antenna on rooftop at NASA-GSFC.

The wide horizon is a source of potential interference from the many government and military communications facilities in the Washington-Baltimore-Annapolis region. Consequently, we use 5 meter dishes, where 3- to 4-meter dishes are normally sufficient collecting area for the GVAR broadcasts. The large dishes have about the central 70% of their areas illuminated with feeds that have a F/D ratio of 3.9, instead of a dish-filling 3.5, with the aim of using the edge of the dishes as a "dark band" to minimize potential interference.

Nevertheless, bursts of interference occur occasionally, especially near dawn in mid-winter, presumably when the leafless trees allow greater visibility to the military radars on the horizon. The episodes of interference are visible as bursts of narrow-band spikes, observed with a power spectrum analyzer tuned within ±20 MHz of the GVAR downlink frequency at 1685.7 MHz.

The vulnerability to interference is exacerbated by the front end design, which amplifies and conducts the entire S-band down a 150-foot coaxial cable to the RF receiver, instead of down-converting the S-band inside the feed to a standard low frequency carrier such as 70 MHz. The long coaxial cable can be an

antenna for high frequency interference. Considerable time and effort has gone into shortening the run and optimizing the cable. Ideally, this design should be limited to less than 50 foot runs and be used in radio-quiet suburban areas, as it is at Colorado State University[10] using the front end supplied to them and to us by Western Engineering and Satellite Technology (WEST) of Melno Park, CA.

3. GVAR INGEST

Each antenna feeds a RF demodulator and bit-synch receiver also supplied by WEST. The output from each receiver is a clock-and-data bit stream that feeds a corresponding bit-handling S-bus card installed in one SUN SPARC-20 workstation. The cards are semi-generic bit-correlation engines supplied by Apogee Solutions (associated with the University of Hawaii). Apogee supplies proprietary C language software in the SUN workstation to locate the bit-synch pattern at the start of each GOES data block (scanline) using only a few percent of the SUN's CPU cycles. Apogee's ingestors are very efficient, each using about 5% of the CPU on the SPARC-20. Similar ingestors are also used at NASA Ames Research Center (ARC) in Palo Alto, CA, to ingest GOES-8/-9 images for the popular and completely automated "Explorer"[11] anonymous FTP site there. At NASA-ARC, these software-driven S-bus ingestors operate completely autonomously on two separate SPARC-5 stations. At NASA-GSFC, both S-bus cards run simultaneously inside one SPARC-20 station. The ingest is autonomous, automatically restarting each time the computer is rebooted by power outages.

There is an advantage to controlling the ingest process in high level software instead of PROM hardware. We have modified software several times to correct errors and to optimize throughput, and also to correct for problems in the SUN operating system (Solaris), which changes with each version. For example, the character-string version of the Solaris clock, which should be accurate to a millisecond, is only updated once every 4 minutes in Solaris 2.3 and 2.4. Because we use the date-time stamp from Solaris to label our raw GVAR datasets each time an image begins, we could not capture 1-minute interval images from GOES without a software work-around in the naming convention.

On the SUN, the GVAR data blocks are written into a UNIX disk file, named with a date-time-satellite stamp corresponding to the beginning of each new Imager frame. For example, the raw GVAR file named "9607041745G8w" was captured on the 4th of July 1996 at 1745 UTC by GOES-8. In this case, the suffix "w" is an character drawn sequentially from the alphabet, to ensure that rapid multiple image-starts will all have different names.

This ingest scheme generates several GVAR files per hour for processing and/or archiving to tape. Operational files are typically a few 100 MBytes each. We maintain a pool of raw GVAR data 10 hours deep for each GOES satellite, each on a 8-Gbyte disk pack. We have a UNIX script automatically delete the oldest files on each pack to maintain at least 500 MBytes of free space for the incoming GVAR data. The deep pool of recent GVAR data allows us to reprocess interesting events and to re-extract special features at full resolution and precision. The SUN disk packs are NFS-mounted to the workstations at NASA-GSFC, with as many as 6 stations drawing simultaneously on the raw GVAR data pool to create special-purpose imagery. The SUN has both FDDI and 10BaseT connections to facilitate GVAR data transfer at rates greater than the realtime flow (2.1 Mbits/sec from each satellite).

4. GVAR PARSING

NOAA's GVAR data format packs the GOES scanlines into long, variable-length blocks described in two thick books about the software in the GOES Operational Ground Equipment (OGE)[12]. There are copies of these OGE books on-line in several word-processing formats[13]. The demonically complex

GVAR blocking and packing requires well-structured code to deal with the many variations of Imager and Sounder blocks.

```
Usage:gvar [OPTIONS] <RawGvarDataFile> [MoreRawGvarDataFiles]
VERBOSE      -h more verbose description of the following options
INSTRUMENT   -i <instrument>              default: none
                 [none imager sounder iIcse
                  sIcse iSpacelookStats iNav sNav]
 FILETYPE    -f <file>                    default: none
                 [none bin jpeg tiff tifftile tiffstrip ncdf]
 TIMESTAMP   -T <stamp>                   default: fromFilename
                 [fromFilename framestart]
 START       -s <VISpixel,VISline>        default: from gvar
 END         -e <VISpixel,VISline>        default: from gvar
 AREA        -A <[+/-] Mbytes>            default: inactive
 LINKNAME    -l toggle link to latest     default: none
 CHANNEL     -c <channel>                 default: all
                 [all 1 2 .. ]
  WORDTYPE   -w <wordtype>                default: none
                 [none char uchar short ushort int uint float double]
  UNITS      -u <units>                   default: counts
                 [counts radiance
                  tstar tscene modeA      (for IR )
                  albedo albedo2]         (for VIS)
  GAIN       -g <gain> {y=((x-b)/g)^G}    default: 1.0
  BIAS       -b <bias>                    default: 0.0
  GAMMA      -G <gamma>                   default: 1.0
  XSCALE     -x <pixels>                  default: 1.0
  YSCALE     -y <lines>                   default: 1.0
  DIRECTORY  -p <output_path>             default: ./
  HOURS      -H <start,end>               default: 0,23
                 GMT hours
  MAP        -M <map>                     default: none
                    [none grid1 grid2 grid12 ]
  MAPVALUE   -m <counts>                  default: 1023
  COMPRESS   -C <scheme|QUALITY>          default: none|75
                 for tiff:
                 [cittrle ccittfax3 ccittrlew lzw
                  next packbits thunderscan pixarfilm]
                 for jpeg: QUALITY [0 - 100]
SNOOZE       -S <directory>               default: off
DEBUG        -D <mode>                    default: none
                [none header lineDoc block0time SAD CRC]
COUNTER      -K toggle counter off        default: on
CMDFILE      -F <fileName>                default: none
XECUTE       -X <scriptName>              default: none
 Version @ Tue Sep 26 12:26:11 EDT 1995
```

Figure 3: The command-line options for the "gvar" parsing freeware application that converts NOAA's raw, packed GVAR scanline format into images in common scientific formats.

The GVAR parser used at NASA-GSFC was written in C++. It is portable software, having been compiled and tested on the SGI, HP, SUN and GNU's C++ compilers in mid-1995. The source code and make files are freeware. They can be downloaded from the public domain[14]. The "gvar" software offers

a large number of command-line options when you type the command "gvar", listed in Figure 3. Each option is explained in greater length by invoking the verbose form "gvar -h".

The "gvar" options listed in Figure 3 offer choice of instrument (Imager or Sounder), choice of output file type (binary, JPEG, TIFF, tiled TIFF, etc.), choice of the time and place ranges of observation (in instrument scan coordinates), and choice of channel selections. Channel output options include the computer word type (short or long, integer or floating point), physical units (radiance, brightness temperature, or albedo), intensity rescaling options for the output in the form `y=((x-b)/g)^G` to reset gains and offsets, and horizontal and vertical rescaling. Either or both of NOAA's dot-maps containing geopolitical boundaries can be embossed in the images with a user-specified numerical value for the dots to make them stand out in the image. The "gvar" code offers several programmer conveniences, such as output path names, debug modes, running counts of blocks processed, and a link to other command files to be run after each raw GVAR block is process (such as the removal of old files or the creation of multi-spectral combinations of new images).

The "gvar" channel selection block can be repeated as many as 36 times within a single invocation of the application, each with its own output path. This means that it can create as many as 36 different sectors, each with it own image characteristics, while reading the raw GVAR data stream just once. The "gvar" parser can operate on one or more named raw GVAR files. It can also just "snooze" along, waiting for a new raw GVAR file to appear in the input directory path, allowing continuous automated processing.

The "gvar" parsing code does most of its work very efficiently using pointers and lookup tables. On modest RISC workstations (100 to 200 MHz CPUs), the "gvar" code processes local raw GVAR at rates limited by the SCSI disk bus -- about 10 times faster than the raw data comes from the satellite. Over a NFS-mounted FDDI network, a remotely running "gvar" parser can still process raw GVAR 4 times faster than the satellite downlink (2.1 Mbits/sec) while creating 36 sectors of calibrated, full resolution imagery in all channels of the GOES-8 Imager and Sounder.

5. DATA DISTRIBUTION

As each GOES Imager scan is completed, the "gvar" software immediately parses the stream of raw data, converting a large-area Imager scan into dozens of smaller megapixel sectors. Consequently, we maintain a realtime data pool of images that are no more than 30 minutes old.

These realtime images are written to a workstation dedicated to public file service of Remote Sensing Data (RSD) in the Mesoscale Processes[15] branch at NASA-GSFC-GLA (**http://rsd.gsfc.nasa.gov**). GOES images are written in TIFF format to preserve radiometric accuracy. The images remain on-line for 24 hours. The images are organized into 36 directories, one for each sector. Each realtime Imager sector contains a 1200x1000 pixel visible image and four corresponding 300x250 pixel infrared images, each in its own directory: vis, ir2, ir3, ir4, ir5.. Most sectors are supplied at full resolution (over-sampled by the satellite by a factor of 7/4ths in the east-west direction, making the earth appear oblate). The larger area sectors, such as full earth, Conterminous US (CONUS), Brazil, etc., are subsampled to round-earth infrared resolution.

In addition to realtime digital file service, the data stream can be run through a video rack to produce live video for NASA Select TV and broadcast quality BETA videotapes for immediate use by local broadcast meteorologists[16], some of whom routinely enhance the full-resolution images for broadcast and provide them, in turn, as "value added" to the Web[17]. More than once during the active 1995 hurricane season, we

would go home from an interesting day at the workstation terminals at NASA-GSFC to see our products on local or national broadcasts.

Sometimes the GOES ingestor at NASA-GSFC get personally involved in the weather it captures. For example, the GOES-8 ingest at NASA-GSFC captured the clouds containing the tornado in Fairfax VA on 24 June 1996 (Figure 4)[18] within a minute or two of the touchdown time officially estimated by the National Weather Service[19]. Shortly after taking this picture, the GOES ingestor at NASA-GSFC was knocked out by the enormous surges in the local power grid due to storm damage.

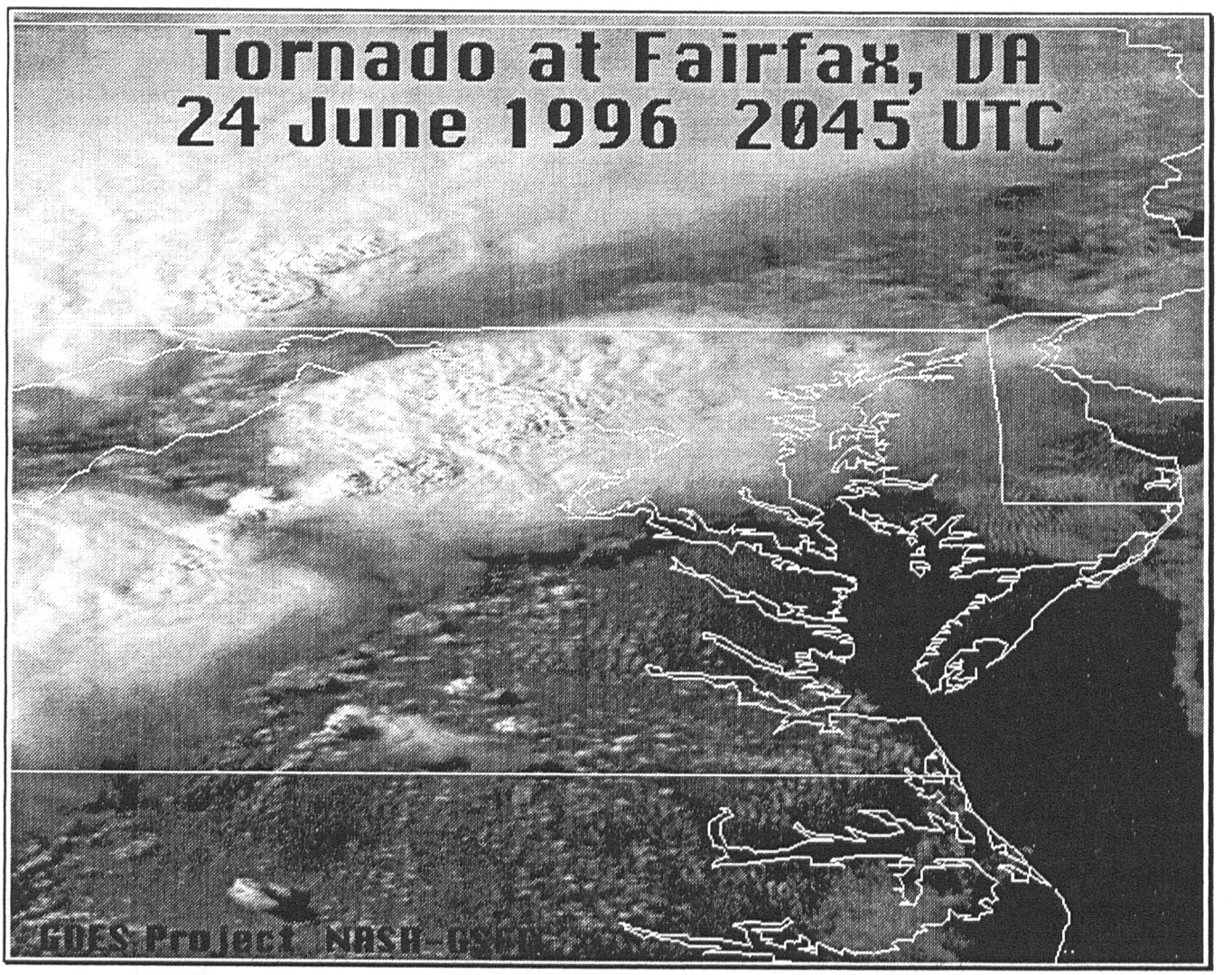

Figure 4: Enhanced GOES-8 image of Fairfax VA tornado, taken as the tornado was occurring, and just before the storm knocked out the GOES ingestor at NASA-GSFC in Greenbelt, MD.

To assist image navigation, each directory has an image file named "MAP.TIFF" containing geopolitical outlines for the area. This map can be overlaid on the GOES images to provide subjective location of weather events. This map is based on the navigated locations of every pixel, derived from NOAA navigation software, which is available on-line[20]. The latitude-longitude locations of each pixel are also listed to the nearest 1/100th of a degree in a corresponding file named "goes.nav", and is described by the file named "readme.nav".

In addition to the realtime images, the GOES Project Scientist in the Climate and Radiation[21] branch at NASA-GSFC-GLA maintains a lively 2-year deep on-line scrapbooks of GOES-8[22] and GOES-9[23] images and other GOES technical information (**http://climate.gsfc.nasa.gov**). Internet users currently fetch about 500 MBytes/week of archived images from the project scrapbooks. The most popular items are a "hot stuff"[24] list containing the most recently enhanced GOES images, and two repositories of dramatically enhanced multi-spectral images[25] and movies[26].

For high-end analysis of technical quality and scientific content of the GOES-8 and GOES-9 datasets, we employ the Interactive Image Spread Sheet (IISS), developed at NASA-GSFC.. At GLA, the IISS resides on a SGI Onyx with 512 MBytes of RAM and 32 Gbytes of dual-striped RAID disk packs capable of full screen color animation at 30 frames per second, with output to broadcast video. This high-performance system allows us to roam and zoom through day-long animations of CONUS visible imagery at full resolution, to probe for small differences among the GOES Imager channels, and to navigate images from different aspects and sources into a common coordinate system.

For example, Figure 5 shows a coordinated IISS probe among enhanced copies of the GOES-8 Imager channels examining the cloudtop temperatures to within a fraction of a degree over Hurricane Luis, with cell B2 equal to the difference in brightness temperatures between the 6.7 micron water vapor channel and the 11 micron window channel (cells A2 and B1, respectively). In this case, we were looking for signs of water vapor being injected into the stratosphere above the outflowing cirrus in the vigorously convective region that normally occurs northwest of the eye of a hurricane -- we did not find any.

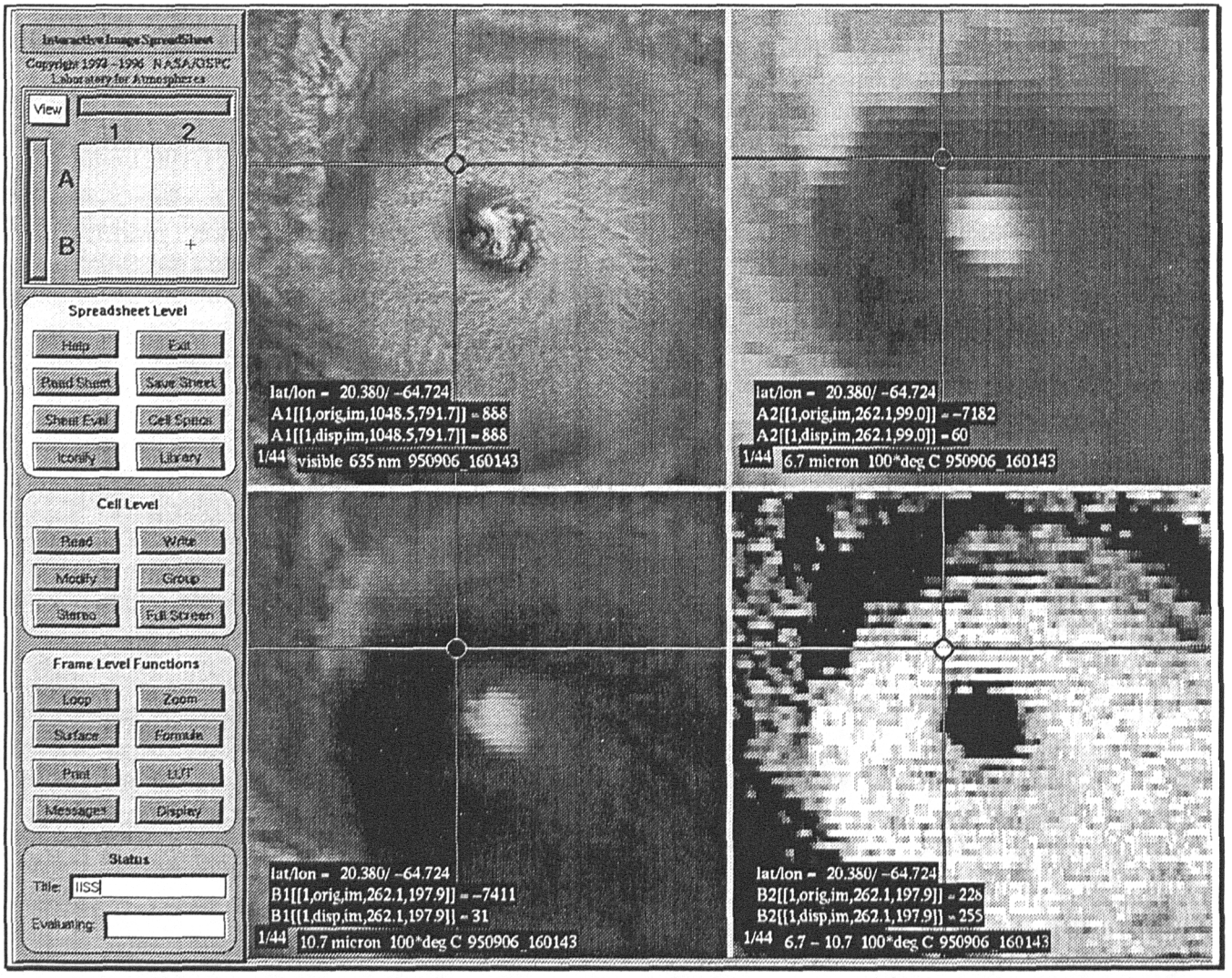

Figure 5: The IISS being used on Hurricane Luis to make a coordinated probe of cloudtop temperatures observed by the GOES-8 Imager channels.

Figure 6 presents another example of IISS analysis. In this case, GOES-8 and GOES-9 had simultaneously observed the eye of Hurricane Luis, and the two images are being navigated to a common latitude-longitude grid where the discrepancies in the apparent positions of cloudtops are being translated into stereoscopic height estimates. In this case, the unusual clouds within the eye are a secondary storm, a meso-vortex that occurs in the northwest quadrant of the eye, releasing energy and causing it to tilt. The animated version of Figure 6 is used to estimate wind speeds in the eye[27] for comparison to aircraft radar data that was taken by the National Hurricane Center (NHC) from a plane flying inside the eye of Hurricane Luis at the same time.

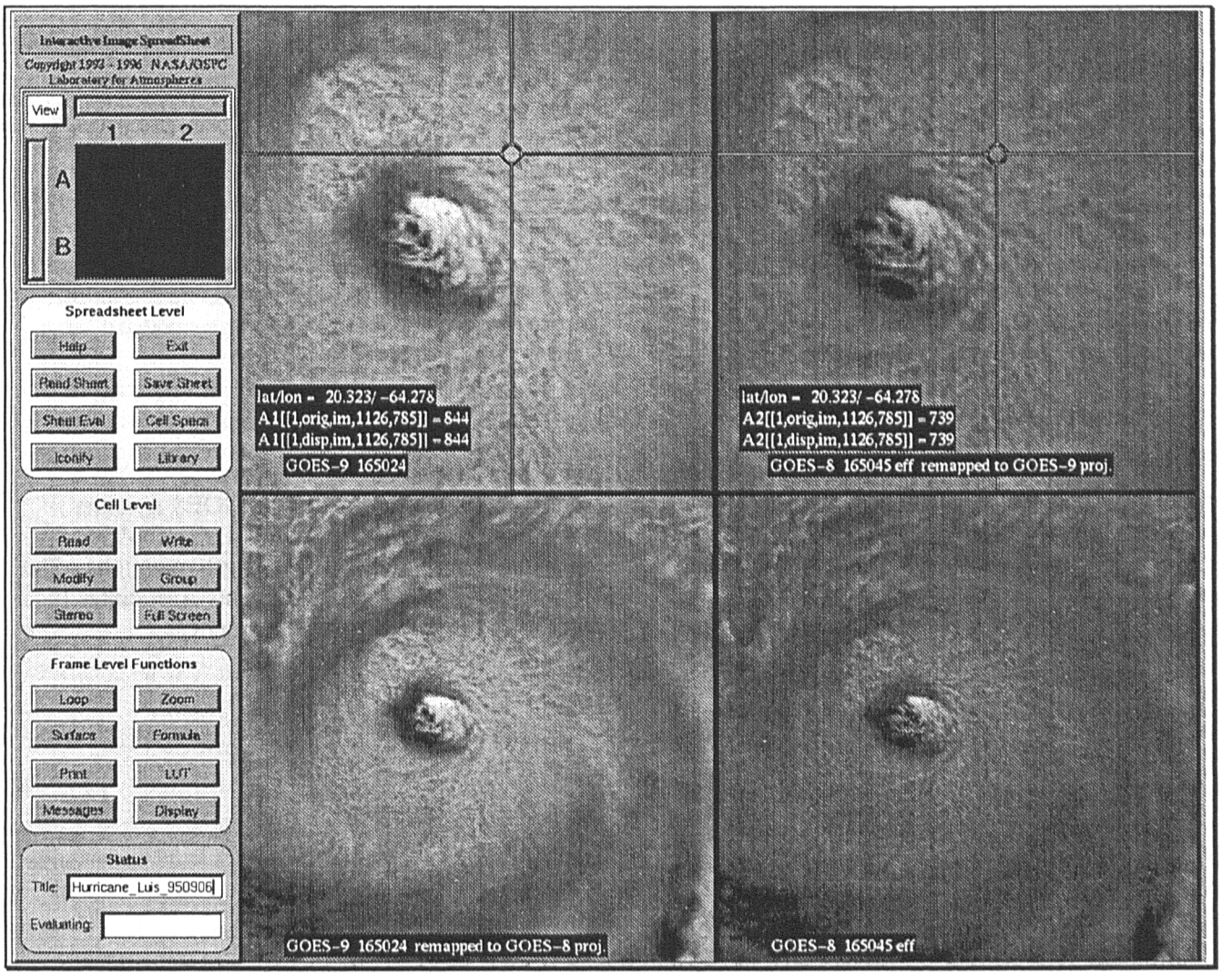

Figure 6: The IISS is used to map coordinated views of Hurricane Luis observed from GOES-8 and GOES-9 into the same coordinate system, to determine stereo cloud height and wind speed.

Finally, for NASA-funded science projects, we set up special GOES science data capture operations during field experiments. For example, we have provided GOES imagery over the internet to the 1995 stratospheric lightning chase[28] in Peru, enabling them to fly to the midnight locations of the most intense thunderstorms in the Amazon basin. On a more massive scale, we helped the Smoke/Sulfate Clouds and Radiation (SCAR)[29] experiment archive all the GOES-8 imagery of the Amazon basin during the summer of 1995, using FTP to move 20 Gbytes per day over FDDI into mass storage at NASA-GSFC. At the moment, we are providing daily images of Brazil to the Tropical Rainfall Measuring Mission (TRMM)[30] ground truth experiment, to help them calibrate their cloudtop/rainfall algorithm in preparation for the TRMM satellite launch in 1998. Finally, we are now routinely processing GOES Imagery in the California and Peru eastern Pacific Ocean basins to develop a reliable climatology of multi-layer, sub-resolution Marine Stratocumulus Clouds (MSC)[31].

6. SUMMARY

This GOES ingest system at NASA-GSFC automatically processes a significant flow of digital data with minimum customization with maximum openness and user software flexibility, assembled from "off the shelf" hardware components augmented by software. Multiple "gvar" processes can drink realtime data from the raw GVAR data pool using NFS over FDDI. The "gvar" image processing C++ software is efficient, self-explanatory, portable, and in the public domain. The Internet community gets free Web access to realtime images from GOES-8 and GOES-9, and to a rich scrapbook of interesting weather events ever since the launch of GOES-I in mid-1994. The science community gets free and easy access to full resolution, navigated and calibrated GOES data 24 hours per day, with special assistance from during NASA-supported field experiments. Similar systems are now available from commercial vendors[32] at modest cost, and other public servers have sprung up[33].

7. ACKNOWLEGEMENTS

The GOES Project provided the funds for the purchase of the hardware and development of the "gvar" software. Steve Eigsti of WEST was very helpful in suggesting causes and cures for GOES antenna reception and interference problems. Mort Friedman of the Search and Rescue (SAR) Lab at NASA-GSFC was generous with his time and equipment in debugging cables and signal strength questions. Shu Yang of Research and Data Systems (RDS) and Marit Jentoft-Nilsen of Science Systems Associates Inc. (SSAI) provided valuable assistance in maintaining antenna operations and data flow quality.

8. HYPER-REFERENCES

[1] http://rsd.gsfc.nasa.gov/
[2] ftp://rsd.gsfc.nasa.gov/
[3] http://climate.gsfc.nasa.gov/~chesters/chesters.html
[4] http://climate.gsfc.nasa.gov/~chesters/text/goestechnotes.html
[5] http://rsd.gsfc.nasa.gov/912/trmm/spread.htm
[6] http://dao.gsfc.nasa.gov/lab/lab_brochure.html
[7] "GOES image enhancements and quality control", Jentoft-Nilsen, J., F. Hasler, D. Chesters, K. Palaniappan, SPIE Conf. *GOES-8 and Beyond*, Denver, CO, 1996.
[8] http://climate.gsfc.nasa.gov/~chesters/goesproject.html
[9] http://rsd.gsfc.nasa.gov/rsd/
[10] http://www.cira.colostate.edu/earthsta/overview.htm
[11] ftp://explorer.arc.nasa.gov/
[12] *GOES IJK/LM Operations Ground Equipment (OGE) Interface Specification*, Revison D -- Parts 1 and 2, DRL 504-02-1 and 504-02-2, Space Systems/Loral, under NASA Contract NAS5-29500, June 1995.
[13] ftp://climate.gsfc.nasa.gov/pub/chesters/OGE_D/
[14] ftp://goes.gsfc.nasa.gov/pub/sharma/gvar
[15] http://rsd.gsfc.nasa.gov/912/
[16] http://wxnet4.nbc4.com/
[17] http://wxnet4.nbc4.com/satelliteimages.html
[18] http://climate.gsfc.nasa.gov/~chesters/text/goes8results.html#960624.fairfax.gif
[19] http://wxnet4.nbc4.com/jun24tornado.html
[20] ftp://climate.gsfc.nasa.gov/pub/chesters/navigation.FORTRAN/
[21] http://climate.gsfc.nasa.gov/

[22] http://climate.gsfc.nasa.gov/~chesters/text/goes8results.html
[23] http://climate.gsfc.nasa.gov/~chesters/text/goes9results.html
[24] http://climate.gsfc.nasa.gov/~chesters/text/hot.stuff.html
[25] http://rsd.gsfc.nasa.gov/rsd/images/
[26] http://rsd.gsfc.nasa.gov/rsd/movies/preview.html
[27] "High performance animation of GOES weather images", Hasler, F., D. Chesters, M. Jentoft-Nilsen, K. Palaniappan, SPIE Conf. *GOES-8 and Beyond*, Denver, CO, 1996.
[28] http://elf.gi.alaska.edu/
[29] http://climate.gsfc.nasa.gov/Projects.html#SCAR
[30] http://trmm.gsfc.nasa.gov/
[31] Molnar, G.I. and D. Chesters, "Variability of marine stratocumulus clouds derived from GOES-8 imagery", SPIE Conf. *GOES-8 and Beyond*, Denver, CO, 1996.
[32] http://climate.gsfc.nasa.gov/~chesters/text/goesvendors.html
[33] http://climate.gsfc.nasa.gov/~chesters/text/goesds.html

Blank page retained for pagination

SESSION 3

Imager and Sounder

The GOES Imager: overview and evolutionary development

Kathleen A. Hursen and Robert W. Ross

McDonnell Douglas Aerospace,
7404 Executive Place, Seabrook, Maryland 20706-0001

Goddard Space Flight Center
Greenbelt, Maryland 20771

ABSTRACT

This paper addresses imager evolution from the early geostationary imagers to the present and includes changes in requirements which drove instrument development and design. The GOES missions are compared with emphasis on development, performance differences, and design challenges.

The Imager overview section focuses on the current system design and contains a system description, instrument characteristics, operational performance, a summary of the test program, and the launch schedule. The key instrument design areas discussed are the optical design, scan control and operation, thermal control design, in-flight calibration, and operational data distribution. Technical advancements and differences between the current GOES Imager and its immediate predecessors are addressed. Plans for follow-on GOES missions beyond the GOES I-M series, in the context of the evolution of GOES Imager instruments, provide a view into technological developments in the near-future.

Keywords: GOES, Imager, predecessor, weather forecasting, radiometer, evolutionary, meteorological, satellite

1.0 HISTORY OF GEOSTATIONARY ORBITAL IMAGING INSTRUMENTS

The success of today's geostationary imaging (and sounding) missions can be attributed to the development of the first geosynchronous orbiting satellite in the early 1960's -- SYNCOM-3 in 1964. A geostationary satellite situated approximately 36000 kilometers (km) above the Earth's equator offers a wider viewing angle and more frequent monitoring of global atmospheric weather patterns then provided by low-altitude, sun-synchronous satellites.

1.1 Evolution of the geostationary imager

Technological advancements in meteorological instruments are summarized[1] in Table 1.1-1. The first imaging instrument on a geosynchronous satellite, Applications Technology Satellite-1 (ATS-1) was launched in 1966, only two years after spin-stabilized geostationary orbiting capabilities were proven. The National Aeronautics and Space Administration's (NASA) ATS program contained demonstration flights for a variety of satellite and instrument technologies. The ATS spin-scan cloud camera (SSCC) was the first imaging instrument to be operated in geostationary orbit.

The SSCC used spin stabilization to generate visible images of the Earth disk from 50 degrees South to 50 degrees North latitude. During the 360 degree rotation, 20 degrees was dedicated to Earth viewing. Small scale weather systems were studied over the 7-year operational life of the SSCC. The sensor capabilities were modified for the ATS-3 to provide a three-color (green, red, blue) visible imaging channel (multi-color SSCC-MSSCC) for better contrast of high to low clouds and clearer distinction between land and clouds. Full Earth coverage was achieved with an increase in the elevation angle range of the camera relative to the satellite's spin axis[2].

The ATS-6 Geosynchronous Very High Resolution Radiometer (GVHRR) had revolutionary advances in both the satellite and instrument. The satellite was 3-axis stabilized offering a much greater Earth viewing time versus that achieved by spin-stabilized satellites.[3] ATS-6 was primarily a communications satellite stationed over India, so it was not a major contributor to improved weather forecasting. The GVHRR did incorporate significant technology advancements. Unfortunately, the chopper motor, which operated as an effective "pass through" for visible radiant energy and as a reflector for the infrared (IR) band, failed after only 2.5 months. As a result, not all of the capabilities had an opportunity to be tested on-orbit, although several hundred images were generated.[4]

The most significant features of the GVHRR included dual channel visible and IR capability providing day and night imaging, 20 x 20 degree full frame and sector scans, improved resolution for study of severe local storms, and improvement in surface temperature estimations. Wind velocity predictions from cloud movement improved the existing weather analysis tools of the time.

0-8194-2200-2/96/$6.00

Instrument / Satellite (Stabilization)	Customer / Launch (Operational)	Technology Advancement	Evolved From
SSCC	NASA/GSFC	• First visible imagery from geostationary orbit • Visible imagery generated during satellite rotation data period • First weather monitoring and studies of small-scale weather systems from geosynchronous orbit	First technology demonstration
ATS-1[1] (Spin)	1966 (7yrs)		
MSSCC	NASA/GSFC	• Improved sensor capabilities (multi-color visible imaging, improved off-axis imagery) • First full disk Earth coverage • Ground processing overlay (green, red, and blue data for integrated color images)	ATS-1 SSCC
ATS-3[2] (Spin)	1967 (6.5 yrs)	• Longer wavelength channel reduced scatter and haze • Improved computer models for mid-latitude weather	
GVHRR	NASA/GSFC	• First radiometer to provide near continuous Earth viewing • Dual channel visible and IR capability provided day and night imaging • First use of Cassegrainian telescope provided higher spatial frequency resolution	ATS-3 MSSCC
ATS-6 (3-axis)	1974 (2.5 mos.)	• 20 x 20 degree full frame and sector-scans • First 2-axis gimballed scan mirror • Proved feasibility of wind velocity estimations from cloud movement	
VISSR[3]	NASA/NOAA	• First satellite dedicated to the instrument • Improved discrimination of altitude differences • Programmable N/S scan frame capability • Improved visible resolution to 0.5 nmi	ATS-6 GVHRR
SMS-1,2 GOES-1[4] GOES-2,3 (Spin)	1974-1978 (avg 2-4 yrs)	• High reflectance coating on scan mirror and telescope reduced stray light/thermal affects • Satellite data retransmission to/from the ground • First IR channel redundancy design • First in-flight IR radiometric calibration	
VAS	NOAA	• Proved feasibility of the first geostationary sounding experiment • Multi-purpose application with multi-spectral imaging and dwell sounding modes • On-board microprocessor controlled scan mirror N-S movement for extended dwell sounding or multispectral imaging. • Automated scan control processing of spin budget for dwell sounding	SMS-1, 2, GOES-1, 2, 3 VISSR
GOES-4, 5, and 7[5] (Spin)	1980-1987 (avg 2 yrs, GOES-7: 9 yrs)	• Improved SNR from dwell sounding • Investigated hourly temporal variations in atmospheric temperature/moisture profiles • First ground data retrieval system developed to process data -- McIDAS • Provided mesoscale measurements not previously available for severe weather forecasting	
VISSR	ESA	• First visible imaging with solid state detectors • First water vapor image from geostationary orbit • On–board duty cycle stretching	GOES-1, 2, 3 VISSR
Meteosat (Spin)	1977-1993 (2-4 yrs)		
VHRR	ISRO	• Dichroic mirror improved reliability in separation of visible and IR radiation and reduced time sharing of a mechanical chopper • Bearing lubrication changed for longer scanner assembly life • Space clamp circuit for dc restoration provided IR amplifier stability	ATS-6 GVHRR TIROS-N AVHRR
INSAT-1B[6] (3-axis)	1983 (7 yrs)	• HgCdTe detectors reduced susceptibility to noise pickup and stray capacity effect • Servo control via Inductosyn® instead of position reference analog encoder	

Table 1.1-1 Chronology of Imaging Development Leading to GOES I-M

[1]ATS-2 did not achieve stable orbit.
[2]ATS-4 did not achieve stable orbit; ATS-5 did not achieve orbit (went into a flat spin when apogee boost motor failed to re-ignite).
[3]Japan's GMS has the VISSR design on-board and was first launched in 1977.
[4]SMS-C became operational as GOES-1
[5]GOES-G did not achieve orbit, so GOES-H became GOES-7 on-orbit.
[6]INSAT-1A satellite failed after 5 months and the INSAT-1C satellite operated for 1 year and 4 months.

The GVHRR was physically similar to the current GOES I-M Imager with a large passive radiative cooler, telescope/scan mirror configuration, and separate electronics/power modules.

The Synchronous Meteorological Satellite (SMS) Program significantly improved visible resolution from two nautical miles (nmi) to 0.5 nmi. SMS-1 was launched the same year (1974) as the ATS-6 in support of improved weather forecasting. SMS-1 and -2, funded by NASA, were designed for operational use. The GOES-1 (SMS-3) cost was shared between NASA and NOAA. All subsequent flights have been NOAA-funded.

SMS-1 was the first satellite dedicated to the on-board instrument. This instrument, Visible Infrared Spin-Scan Radiometer (VISSR), used spin stabilization for image generation since 3-axis stabilized satellites were more expensive and was not an adequately proven technology at the time. The positive experience from other spinner programs influenced the decision to continue using the spin-stabilized satellite design. The VISSR had eight visible channels with photomultiplier tubes (PMTs) and one IR channel which allowed measurement of cloud temperatures to improve detection of altitude differences[5]. Also the study of mesoscale weather features was made possible with N-S motion of the scanner. Programmable capability to scan a section of the Earth on command allowed for tracking the formation of storms. Of equal importance was the VISSR data interface to the ground system. The analog video signal was digitized on the satellite. Wideband image data was transmitted to the ground station and then stretched for improved decoding at a data rate that could be handled by the user's receiving ground equipment. The data was then relayed during the satellite back-spin for retransmission to ground stations for wider data distribution. The VISSR flew aboard five geosynchronous satellites prior to the VISSR Atmospheric Sounder (VAS).

The VAS flew on GOES-4, -5, and -7 and validated the feasibility of dwell sounding. The most significant technology advancement was the addition of a filter wheel for sounding thereby providing two additional operational modes: multi-spectral imaging and dwell sounding[6]. The multi-spectral imaging mode provided normal cloud mapping. The dwell sounding mode, a selected spectral band for a specified number of satellite rotations on one scan line, provided the first sounding data for vertical temperature and moisture profiles. The programmable N-S scan frame and automated scan control processing allowed for dwelling, which improved the signal-to-noise ratio (SNR) and provided mesoscale weather data not previously available[7]. The first ground sounding retrieval system (Man-Computer Interactive Data Access System - MCIDAS) developed for processing and analyzing VAS sounding data is still in use today as a comprehensive data analysis system.

The spin stabilized Meteosat-1 VISSR[8], built for the European Space Agency (ESA), had two technology improvements over the GOES VISSR -- first use of solid state detectors for visible imagery and duty cycle stretching processed on-board. The second generation Meteosat instrument is of VISSR heritage and design.

The lineage of the ATS, SMS, and GOES series was used in part to develop the INSAT Very High Resolution Radiometer (VHRR) for the Indian Space Research Organization (ISRO). The VHRR had many design enhancements: a dichroic mirror for visible and IR energy direction to detectors instead of a mechanical chopper; a space clamp circuit for direct current (dc) restoration instead of a reference look-up table to improve IR amplifier stability; an Inductosyn® instead of an optical encoder to provide finer servo control in position reference control; and a change in the type of bearing lubrication to extend the life of the scanner assembly. The VHRR design was the immediate precursor to the GOES I-M series of meteorological satellites.

1.2 Summary performance and features of previous imaging instruments

Table 1.2-1 compares geostationary orbital imaging capabilities from the SSCC to the GOES I-M Imager. Initially only the visible spectrum was available for measurement. Multi-color visible channels led to development of thermal channels. Visible channels operated with separate PMTs until visible silicon diode detectors provided consistency in responses from detector to detector and reduced image stripping affects. IR channels, first tested on the GVHRR, complemented the visible channel and provided vital knowledge of global weather patterns improving computer modeling from local areas to mesoscale. IR channels provided critical data at night maintaining near continuous tracking of weather patterns and major storms. The IR channel became so critical that it has been redundant on every operational satellite since its initial demonstration.

The Instantaneous Field of View (IFOV) for PMTs ranged from approximately 110 μrad square to 21 x 25 μradians (μrad) trending towards smaller IFOVs. Silicon detectors shifted the IFOV size to 60 μrads for Meteosat and 76.8 μrads for the INSAT instrument. Visible channel spatial resolution improved to 1 km after the initial ATS satellite series and has effectively remained unchanged except for the European and Indian instruments. IR detector technology has improved resulting in successively smaller IFOVs (except for the VHRR which was based upon the GVHRR). Resolution generally remained in the 11 km range. Spatial resolution from instrument to instrument was dependent upon program constraints.

Instrument	Nadir Spatial Resolution (km)	Number of Channels		Spectral Band (μm)		IFOV (μrad)	S/N@ 100% Albedo (on-orbit)	NEΔT (on-orbit)	Total Weight (lbs)	Earth Viewing Efficiency (Full Disk)
		Visible	Infrared	Visible	Infrared					
SSCC	VIS 3.6 (~ 2nmi)	1	–	.47-.60	–	VIS 100	~ 155	–	20	5
MSSCC	VIS 3.6	3	–	.38-.48 .48-.58 .55-.63	–	VIS 100	~ 155 ~ 236 ~ 136	–	23	5
GVHRR	VIS 5.5 IR 11	1	1	.55-.75	10.5 - 12.5	VIS 150 IR 300	300	.50@ 300K	90	80
VISSR	VIS 0.9 IR 6.9	8	1†	.55-.72	10.5 - 12.6	VIS 25 IR 250	225	0.4@ 300K	132	5
VAS	VIS 0.9 IR 13.8 IR 13.8 IR 6.9 IR 13.8	8	6	.55-.72	3.8 - 4.0 6.4 - 7.0 10.2 - 12.0 12.5 - 12.8	VIS 21X25 IR 384 IR 384 IR 192 IR 384	225	.25@ 300K 1.0@ 230K .15@ 300K .40@ 300K	173	5*
Meteosat VISSR	VIS 2.5 IR 5	8	2†	.40-1.1	5.7- 7.1 10.5-12.5	VIS 60 IR 125	225	.40@ 230K .20@ 300K	132	5
VHRR	VIS 2.75 IR 11	1	1†	.55-.75	10.5-12.5	VIS 76.8 IR 307	250	.11@ 300K	88	82
GOES-9 Imager	VIS 1 IR 4 IR 8 IR 4 IR 4	1	4†	.55-.75	3.8 - 4.0 6.5 - 7.0 10.20 - 11.20 11.50 - 12.50	VIS 28 IR 112 IR 224 IR 112 IR 112	250	.12@ 300K .11@ 230K .09@ 300K .19@ 300K	260	82

*The Sounder portion of the VAS dwell sounding mode used 1/3 of the 5-percent total instrument viewing time available.

†Redundant

Table 1.2-1 Comparison of Geostationary Orbital Imaging Capabilities

The SSCC and MSSCC cameras used a "pin-hole" opening to the PMTs. The GVHRR changed to a 2-axis gimballed scan mirror with an 20 cm diameter aperture. The VHRR's unique requirements led to a smaller telescope and aperture diameter. The larger VISSR and VAS had a 40 cm diameter aperture thus an overall increase in weight. The SMS/GOES optical design determined the aperture size because of a large central obscuration from the telescope design. The GOES I-M Imager provides similar or better performance as the VAS with a 30 cm aperture.

The GVHRR digital resolution was 9 bits. While the VISSR and VAS quantized the visible to 6 bits and IR to 8 bits. The VHRR had similar quantization requirements as the VAS. The GOES I-M improved Imager quantization to 10 bits and Sounder to 13 bits. The scan time for a full-disk image generally remains at approximately 30 minutes. The GOES-8 and -9 scan time is 26 minutes. The percentage of Earth viewing time is approximately 5% for spin stabilized satellites and 82% for 3-axis stabilized satellites in full disk imaging.

The VISSR/VAS had an open-loop servo system for mirror control. An optical encoder (an incandescent lamp and a mask for fine or coarse traces) determined the position of the gimbal shaft. This approach began with the VISSR and continued through the GOES instruments. Reliability was poor since the lamps often burned out after a short period ultimately causing a shorter instrument life. The GOES-7 employed LEDs instead of lamps, resolving the lamp failure issue, and became the longest lived geostationary Imager of any in the series. The VHRR employed a closed-loop servo which provided active control of scan mirror position. The analog encoder, an Inductosyn®, provided positional control as well as position location. The GOES I-M Imager uses an improved Inductosyn® design. The VHRR bearing lubrication was also changed to extend instrument life by reducing a lube hill affect on the scan mirror bearings[9].

Visible channel in-flight calibration was first performed on the VISSR with a small collecting aperture and used the sun as a source to simulate an effective albedo level[5]. Following on-orbit experience, the visible calibration was changed to normalize outputs on the ground and incorporate ground truth measurement corrections. Each subsequent instrument calibrated the visible channel in the same manner. IR channel in-flight radiometric calibration was first performed using a shutter which reflected blackbody energy into the focal plane during non-Earth views. However, this on-orbit thermal calibration did not measure total instrument response and was not adequate when compared to ground truth measurements. The effects of the foreoptics, scan mirror, and structure had to be added to the calibration data correction algorithm in ground data processing. The Imager provides a complete end-to-end full aperture IR calibration with a blackbody.

2.0 GOES I-M IMAGER OVERVIEW

The GOES I-M series is funded and managed by the National Oceanic and Atmospheric Administration (NOAA) and operated by NOAA's National Environmental Satellite Data and Information Service (NESDIS). The design, development, test, launch, and postlaunch test of each satellite is managed by the NASA's Goddard Space Flight Center (GSFC). The National Weather Service (NWS) will be "modernized" through major technological advancements in the next generation of Earth observing meteorological satellites[10]. The GOES Imager of today

embodies a combination of advancements and upgrades from GOES predecessor missions. Specifically a 3-axis body stabilization satellite (provides a stable Earth pointing platform to more fully use the meteorological instruments on-board with independent imaging and sounding increasing the frequency of data collected and the opportunity for sounding); greater scan flexibility; one minute rapid scan imaging (provides severe storm forecasting); two additional IR channels; data resolution improvements; radiometric improvements (e.g., spectral resolution, SNR, smaller FOV, etc.); image navigation and registration (INR) (provides improved earth-referenced location determination and measurement accuracy); active in-flight full system IR calibration; and calibrated data (i.e., GVAR) in a simplified format to end users are included in today's imager missions. Each have provided significant steps in furthering the mission of the NWS over previous imagers. The GOES I-M Imager is part of the full instrument system presented below.

2.1 System description

The GOES I-M system consists of a space and ground segment. The space segment contains three instruments providing environmental remote sensing, a data collection system, and data broadcast system. The ground segment receives and processes raw data and retransmits it to the satellite for relay to the end users.

2.1.1 GOES instrument system

The GOES instruments are the Imager, Sounder, and Space Environment Monitor (SEM). The Imager and Sounder are radiometers that scan the Earth to monitor and measure dynamic weather patterns and events and operate independently -- a first. The Imager has one visible and four IR channels, provides cloud and water vapor measurements, and generates both visual and infrared images. The Sounder has one visible and 18 IR channels, provides vertical temperature and moisture profiles, layer mean temperature and moisture, total precipitable water, and a stability index. The SEM is a combination of five sensors that survey the sun and measure its effect on the near-Earth solar-terrestrial electromagnetic environment[11]. The SEM sensors include the X-Ray Sensor (XRS), Energetic Particles Sensor (EPS), High Energy Proton and Alpha Particle Detector (HEPAD), and magnetometers. The SEM's Solar X-Ray Imager (SXI) is planned for the GOES-M mission.

The data collection system receives and distributes meteorological data from ground-based Data Collection Platforms (DCP) to end users. The data broadcast system consists of a dedicated communications link for the search and rescue (SAR) transponder for detection and relay of distress signals from aircraft and ships to emergency on-call ground services. The continuous relay of Weather Facsimile (WEFAX) and processed weather data is also provided[11].

2.1.2 Imager system block diagram

The Imager has three separate modules (Figure 2.1.2-1): power supply, electronics, and sensor. The power supply module contains three power converters, fuses, and a relay control. The electronics module contains all the command, control, and signal processing elements and the scan control electronics for the instrument. The sensor module[12] (Figure 2.1.2-2) is approximately 115 x 80 x 75 centimeters (cm) and contains the optical subsystem and servo scan control and drive subsystem.

The Imager sensor module is mounted on the northwest corner of the Earth facing side of the spacecraft with the optical port pointing to the Earth. The power supply and electronics modules are also mounted on the north panel within the spacecraft. Primary spacecraft to instrument interfaces include command and telemetry, primary bus voltage input, and attitude and orbit control electronics (AOCE) input. The INR function is an integral part of the AOCE and provides imagery and sounding data on fixed Earth coordinates that define latitude and longitude for each picture element (pixel) within an image and between images. Imager command control is provided via the spacecraft command unit interface to the electronics module's proportional command subsystem.

The power supply module is 29 x 20 x 16 cm and provides an average of 134 watts distributed within the instrument. Within the power supply, the spacecraft primary bus voltage is converted to required voltages. Telemetry and electronics converter voltages are input to the electronics module for internal distribution and secondary regulation. Scanner power is input to the electronics module as a regulated input. The power supply's heater power bus is input to the sensor module's heater relays for distribution.

The electronics module is 67 x 43 x 19 cm and contains interface electronics, servo scan control drive subsystem, video processing subsystem, heater control circuit, and the data processing subsystem. The video and bi-level wideband telemetry data are integrated and the analog narrowband telemetry (e.g., temperature, voltage, current, servo error, etc.) are processed for downlink. Redundant circuitry is provided for the primary subsystem components (e.g., visible and IR processors, N-S and E-W address system, etc.).

The sensor module's optical subsystem contains the scan mirror, telescope, and optical train/detectors. The associated optical electronics and servo scan control subsystem are distributed between the electronics and sensor modules.

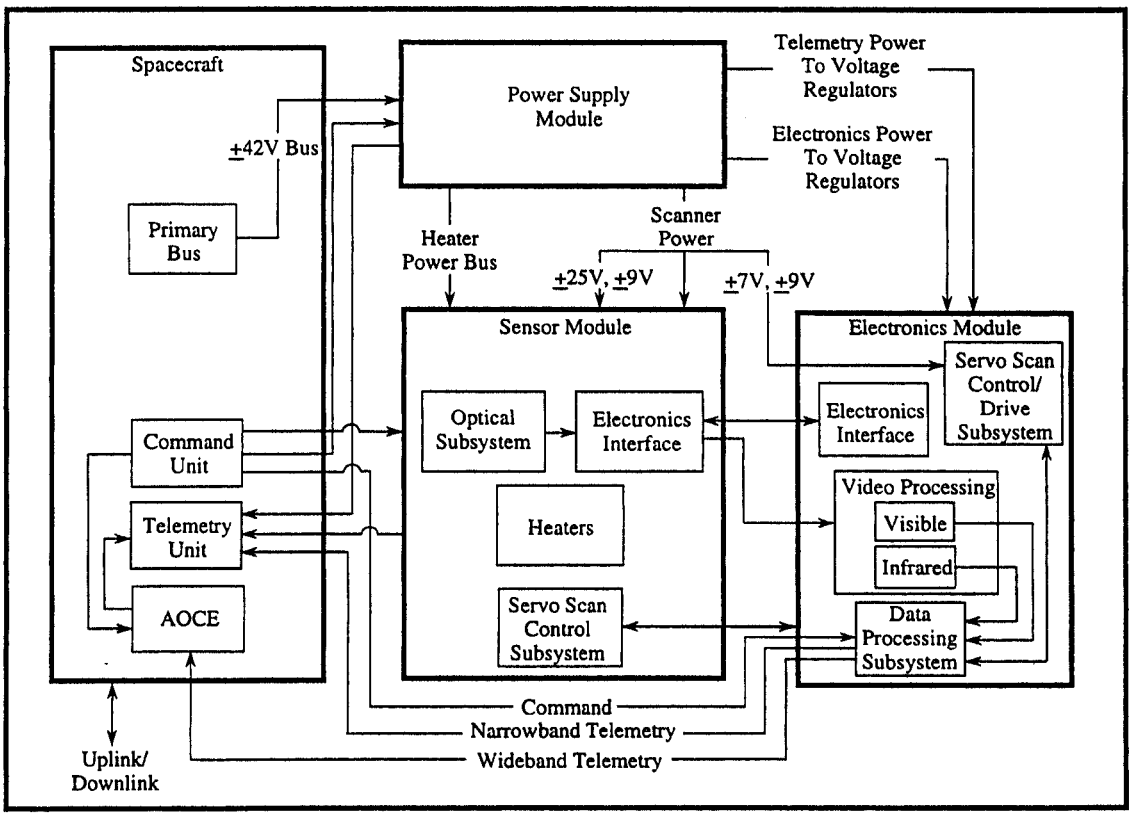

Figure 2.1.2-1 Imager Functional Block Diagram

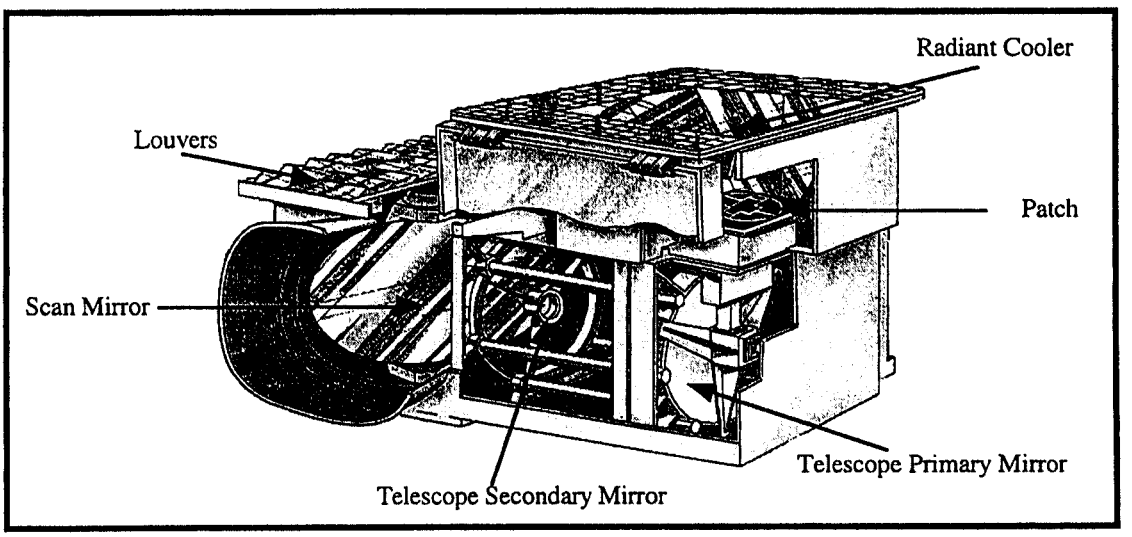

Figure 2.1.2-2 Imager Sensor Module
(Electronics and Power Supply not shown)

Heaters are strategically placed to thermostatically control the baseplate, patch, radiant cooler, and cooler outgas and anti-ice functions to commandable set points. The sensor module's scanner assembly includes the servo motors, Inductosyns®/preamplifiers, gimbals, rotating shaft, CEI/AEI circuitry, direct drive torque motors, and servo amplifiers.

2.2 Instrument characteristics and operational performance

The basic characteristics of the GOES I-M Imager are summarized[11] in Table 2.2-1. Each channel is described and the improved operational performance from previous Imagers is addressed.

Channel	Detector Type	Wavelength Range (μm)	Range of Measurement	IGFOV at Nadir (km)	Meteorological Objective
1-Visible	Si	0.55 to 0.75	1.6 to 100% albedo	1	Cloud cover
2-Shortwave	InSb	3.80 to 4.00	4 to 320 K	4	Nighttime clouds
3-Moisture	HgCdTe	6.50 to 7.00	4 to 320 K	8	Water vapor
4-Longwave	HgCdTe	10.20 to 11.20	4 to 320 K	4	Surface temperature
5-Longwave	HgCdTe	11.50 to 12.50	4 to 320 K	4	Sea-Surface temperature/ water vapor

Table 2.2-1. Imager Characteristics

2.2.1 Optical design

The portions of the sensor and electronics modules that contain the optical subsystem and provide video data processing[13] are shown in Figure 2.2.1-1. The Imager scans the Earth through the motion of an elliptical plane mirror which directs reflected sunlight and IR thermal emissions into a Cassegrain telescope. The scan mirror is a triangular-cell honeycomb structure of beryllium with a polished nickel plating and aluminum reflective surface. Mirror deformations are minimized by tailoring the plating thickness on the front and back surfaces of the mirror. The telescope is composed of a 31 cm primary mirror and a 5.3 cm secondary mirror, both of front-surface aluminized ULE glass. The focused visible and IR emissions are divided into five wavelength bands by dichroic beamsplitters, first separating the visible from the IR and further dividing the IR into four spectral bands, or channels. These four channels are centered at 3.9 μm, 6.75 μm, 10.7 μm and 12 μm. The visible signal focuses onto a silicon detector and the IR signals are directed to the cooled detectors through wavelength defining bandpass filters. Figure 2.2.1-2 conceptually illustrates the instrument optics[11].

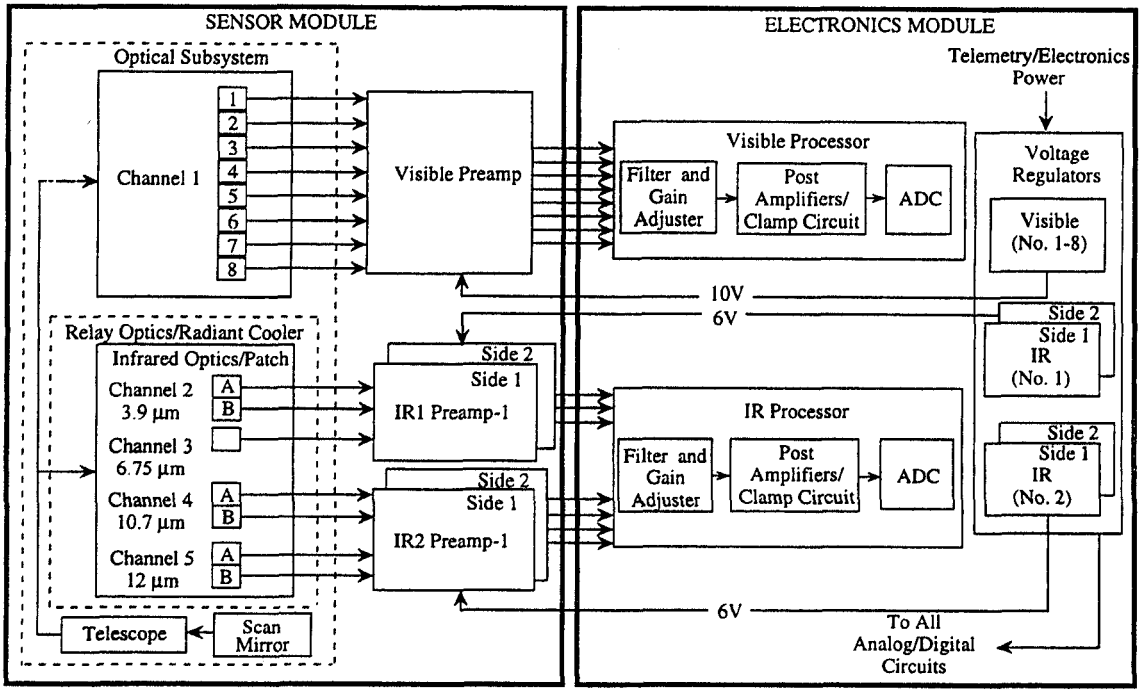

Figure 2.2.1-1. Optical Subsystem and Video Data Processing

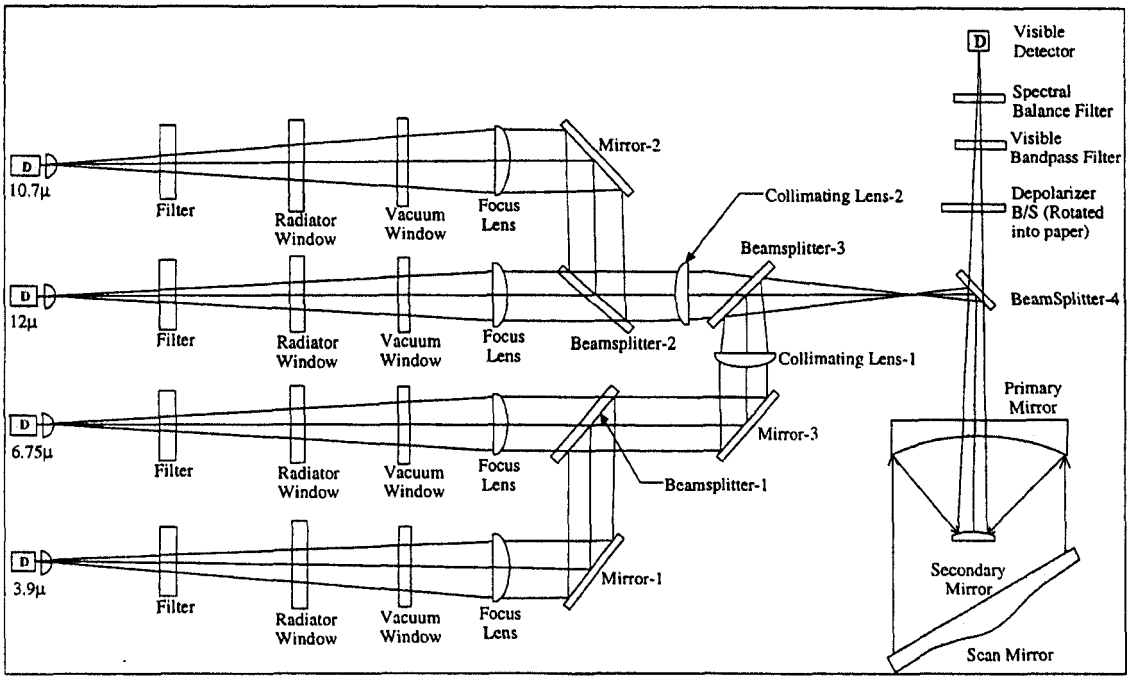

Figure 2.2.1-2 Representative Optical Design

The visible portion of the incident energy (550 nm to 750 nm) is directed to a linear array of eight 12.5 μm square silicon detectors which provide a nominal Instantaneous Geometric Field of View (IGFOV) of 28 μrad. This corresponds to a one kilometer square on the Earth. The detectors for the shortest wavelength energy of the four IR channels, 3.9 μm, is a cooled four-element indium antinomide (InSb) detector array used pairwise, to provide two adjacent 112 μrad (4 km) scan lines across the scene. A second pair in the array provide redundancy. The longer wave band emissions at 10.7 μm and 12.0 μm are detected by photoconductive (PC) mercury cadmium telluride (HgCdTe) detectors, packaged as four element linear arrays of 50 μm by 50 μm, which are scanned pairwise and the nominal IGFOV is 112 μrad (4 km). The single 6.75 μm detector is a two element PC HgCdTe nominal 100 μm square, with an associated IGFOV of 224 μrad (8 km). The separate paths in the instrument optics serve to separate the five wavelength channels. Required coregistration accuracy from any channel to any other is 28 μrad or less.

2.2.2 Scan control and operation

The portions at the sensor and electronics modules that contain the servo scan control and drive subsystem[13] are shown in Figure 2.2.2-1. The scan control forms images by actively controlling movement of the scan mirror in a raster-scan pattern across the Earth. The mirror is mounted on a two-axis gimbal system, allowing controlled scan motion in the east-west axis as well as north-south deflections. Each axis is driven by a direct drive motor and the gimbal position is sensed by an Inductosyn® position sensor. The scan control logic applies the desired mirror scan position value to each Inductosyn®. An error signal (difference between the target and the current mirror position) is fed to the torque motor which drives the mirror mount until null is achieved. Corrections to servo pointing errors (nonorthogonality and fixed-pattern errors) are determined during testing and compensating values are stored in the PROM. The E-W servo loop has a coherent error integrator (CEI) that automatically corrects for changes in bearing drag, cable torque or other systematic disturbances. The servo system achieves position errors of only a few microradians.

In addition to the instrument error corrections, the spacecraft supplies an Image Motion Compensation (IMC) signal which compensates for various deterministic spacecraft motions, such as thermal distortion, orbital deviations, and spacecraft attitude disturbances. The image remains fixed with respect to the Earth. In a typical scan operation, the start and end locations of the desired image frame are loaded by input command. The mirror is moved in eight microradian steps at 10 degrees/second. At the scan line end location, the mirror is decelerated and moved 224 μrad to the south. The mirror is then accelerated in the west-to-east direction and the next scan line begins. This process continues to the southern limit of the commanded frame.

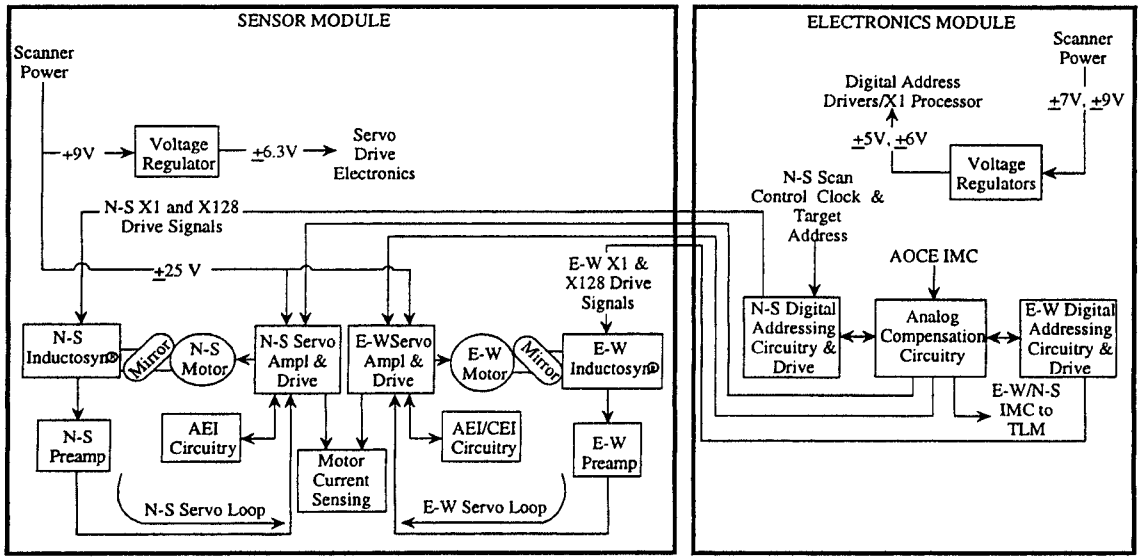

Figure 2.2.2-1 Servo Scan Control and Drive Subsystem

2.2.3 Thermal control design

The IR detectors are cooled to cryogenic temperatures using a passive, three-stage, radiative cooler. The first and warmest stage of the cooler is the vacuum housing which is thermally decoupled from the sensor module, conductively through a high resistance mounting structure and radiatively by using low emittance, gold-plated facing surfaces. It is cooled by radiation to space using optical solar reflector (OSR) surfaces which minimize heat gains when sunlit. The second stage of the cooler, called the radiator, is conductively and radiatively decoupled from the vacuum housing and is cooled by radiation to space from a black-painted surface. The sunshield prevents solar illumination of this surface. The final and coldest stage, the patch, can attain temperatures below 90 degrees Kelvin (K) under low sun angle conditions. The patch temperature is maintained at one of three commandable setpoints with a proportionally-controlled heater.

The thermal control of the sensor module is very challenging due to the large scan aperture, which allows large energy gain during part of the diurnal cycle when direct sun illuminates the aperture and large energy loss to space during the cold portion of the diurnal cycle. Solar energy into the scan cavity is reduced by a shield surrounding the aperture. Heat is dissipated from the sensor module with a radiator and louver system. A fixed sunshade prevents direct sunlight from reaching the louver assembly. Low temperature extremes are decreased by the use of thermal control heaters on the sensor baseplate. Since the instrument baseplate serves as an optical bench for the telescope, redundant sets of six individual proportionally controlled heaters are arranged to minimize gradients which would distort the telescope. Conductively and radiatively isolated sun shields are placed over the E-W motor and Inductosyn® housing and secondary mirror assembly and support. The back surface of the scan mirror is painted white which couples it to the warm scan assembly when viewing the Earth and reduces energy gain while the back is facing the sun when viewing the internal calibration target.

2.2.4 In-flight calibration

The in-flight calibration system calibrates the complete optical train from scan mirror to detectors. Effects of diurnal variations on the instrument's radiometric data quality are reduced on board. The combination of on-board calibration references and ground processing algorithms produce the radiometric image quality expected by users. The IR channels employ "spacelook" and a full-aperture blackbody to provide full-field calibration.

The IR Blackbody calibration consists of a sequence of spacelook, electronic calibration, and blackbody calibration every 10 minutes after completion of a frame without interruption of a scan[12]. Spacelook occurs automatically every 9.2 or 36.6 seconds. The detector electronics calibration (ECAL) signal ensures that the electronic gains are functioning properly. Update of the clamp circuitry occurs every 2.2 seconds for the visible and IR signal levels. Both thermal and electrical stability of the instrument are important to calibration. An absolute accuracy of 1.0 degree K results from the calibration process. On the ground, visible data is normalized and IR data is calibrated using look-up tables. The ground calibration system extracts the radiometric reference signal, compares it with the calibrated reference, and derives the differences to determine the correction factor to be applied to the Imager down-linked data.

2.2.5 Operational data distribution

The on-orbit instrument data processing subsystem[13] shown in figure 2.2.5-1 shows that portion of the electronics module that is associated with data processing and its interfaces. Energy from an Earth scene is input as analog signals to the sensor module's preamplifiers. The electronics module processes and converts the analog signals to digital signals which are formatted into 10 bit words. This improves image quality, star sensing capability, and radiometric measurements over previous instruments. These instrument raw data (wideband) are input to the satellite's sensor data (SD) transmitter for downlink to the ground. Wideband data includes all instrument outputs (e.g., video, servo, telemetry, etc.) used to generate weather products, monitor instrument status, and analyze on-orbit instrument anomalies. The sensors' analog and bi-level telemetry (narrowband) are input directly to the satellite's Telemetry and Command Subsystem's (TCS) telemetry unit for transmission to the ground via the Command and Data Acquisition (CDA) telemetry transmitter. Narrowband data are individual hardwired data outputs which are used to monitor the health and safety of the instrument and are an additional source for monitoring instrument status in the event the electronics data processing subsystem or its interfaces malfunction. The Multi-purpose Data Link (MDL) data (i.e., mirror slew events, N-S and E-W servo error), a diagnostics tool, is input to the satellite's attitude data multiplexer (ADM) via the AOCE and output to the MDL transmitter for downlink.

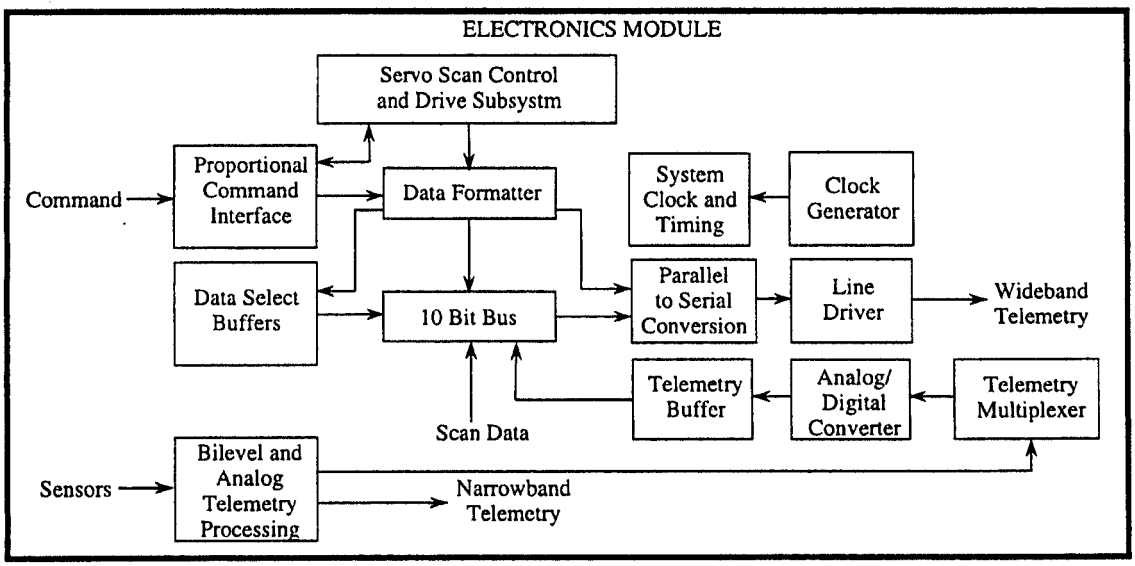

Figure 2.2.5-1. On-Orbit Instrument Data Processing Subsystem

The GOES data links and product distribution network are shown in figure 2.2.5-2. Satellite telemetry, raw instrument data, GOES Variable (GVAR) data, Data Collection System (DCS), SAR, and WEFAX are the data links between the GOES-8 and -9 satellites and the ground. The satellite is operated from the CDA Station in Wallops, Virginia and the SOCC in Suitland, Maryland. The CDA receives Imager raw data at 2.6 Mbps and Sounder data at 40 kbps which are processed into GVAR data (calibrated, normalized, gridded, Earth located), and retransmitted to the satellite for distribution to the users. The CDA also receives the DCS Platform data for transmission to DCS users and receives WEFAX data which are transmitted to the satellite for wide distribution to users.

The NESDIS Satellite Operations Control Center (SOCC) receives the retransmitted GVAR data, MDL diagnostic data, and WEFAX data from the satellite and generates command schedules which are transmitted to the satellite via the CDA. The Central Environmental Satellite Computer System (CESCS) receives both polar data and geostationary GVAR data for analysis and distribution. For wide distribution of data products, the SOCC and CESCS send the data via microwave to the Central Data Distribution Facility in the World Weather Building. The GVAR data are used to derive weather data products (e.g., realtime remapped images, global winds, moisture analysis, etc.) which are distributed to National Centers for severe weather forecasting and analysis. Regional field data facilities receive GVAR data and distribute products (e.g., imaging, rainfall estimates, mercator maps, etc.) to regionally located weather forecast offices across the country. A telephone service (GOES Tap) is also available to users (e.g., television, radio, airports, etc.) for easy access to various derived products.

The NOAA Environmental Research Laboratories (ERL) receive GVAR data from the satellite and extract and format the SEM data for users. The DCPs receive downlinked DCP Interrogation (DCPI) data and uplink the DCP Report (DCPR) for relay to the CDA and real-time users. The Emergency Locator Transmitter (ELT)/ Emergency Position

Indicating Radio Beacon (EPIRB) Search And Rescue (SAR) uplink to the satellite are relayed to the SAR ground station for emergency rescue services.

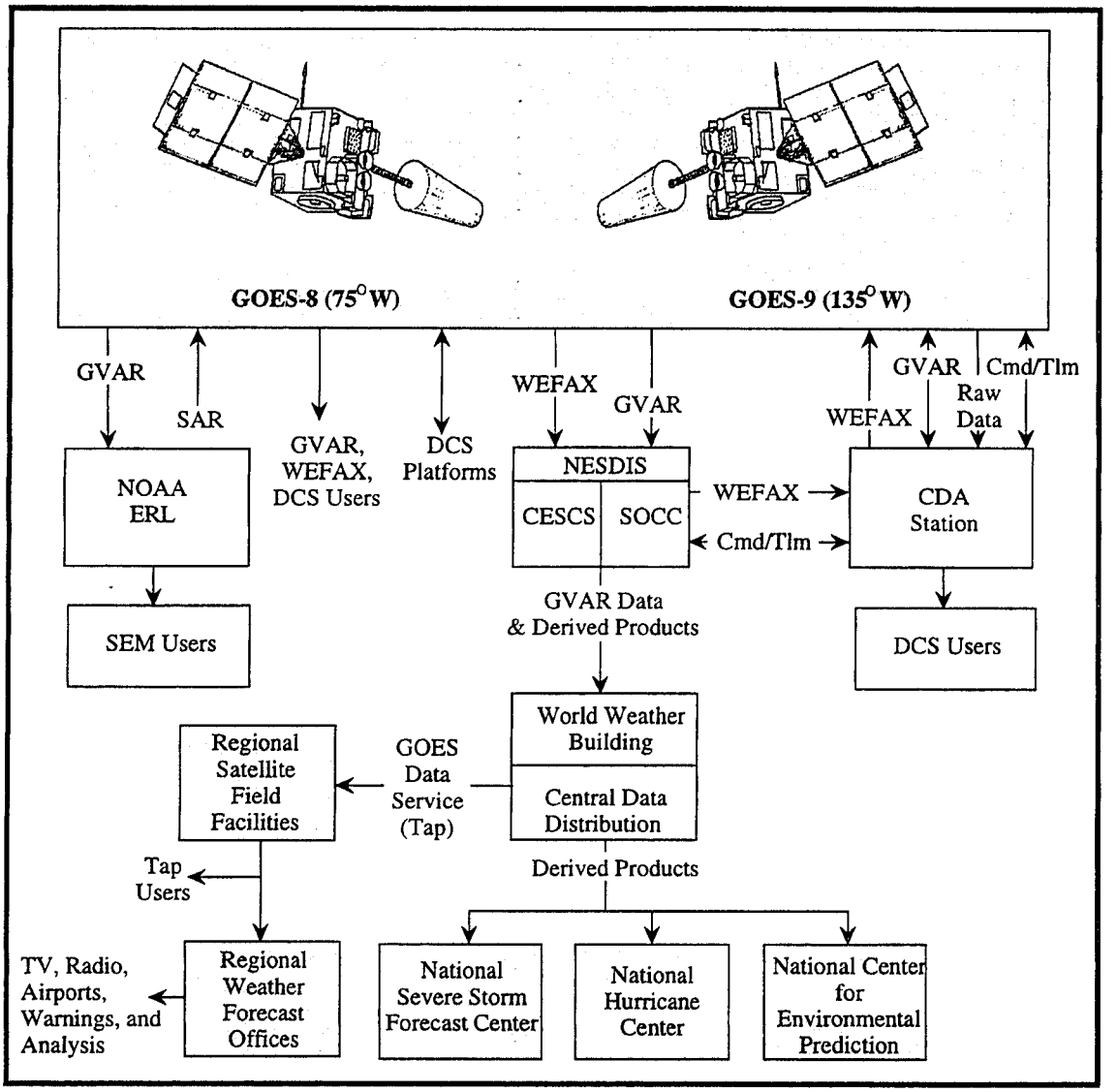

Figure 2.2.5-2 GOES System Produces Data for Regional and National Forecasting

2.3 Test program

Technology advancements made since the GOES-7 launch (1987) necessitated a comprehensive qualification test program for GOES-8 and GOES-9, as will the remaining instruments in the GOES series (GOES-K, L, M) to ensure successful operation on-orbit. This test program contains three levels of test that culminate in launch readiness: pre-integration, instrument system, and spacecraft. The test results are used to accurately characterize the instrument, verify system performance, and prepare the instrument for launch and on-orbit conditions.

Pre-integration testing includes life, component, subassembly ("box" level), and module testing. Life tests are conducted on new designs that have not been operated or reliably test flown on-orbit and component level and box level tests provide the qualification of critical flight components prior to use in the instrument. Module level testing is conducted on the three separate units (sensor, electronics, power supply) prior to integration as an instrument. The power supply and electronics are bench tested for functionality at ambient and mass properties measurements are performed. The power supply as a unit undergoes environmental testing for qualification. During the build-up of the sensor module, optical alignments are performed and again immediately prior to system integration. Visible and IR

optical subsystem tests (e.g., MTF, IFOV, coregistration, throughput measurements, etc.) are taken and validated against the specification. A few sensor module components are not tested directly; however their expected performance is verified by analysis. System integration follows with assembly and interconnect of the three instrument modules, the first power-on functional tests, and initial tailoring of electronic gains.

Instrument system level acceptance testing is comprised of five major phases: preliminary bench, preliminary thermal vacuum, EMI/EMC, vibration, and final thermal vacuum (t/v)[14]. Throughout the system acceptance testing, particular functional and performance tests are repeated to ensure that performance will not degrade over time or under environmental stress, that inherent design issues affecting performance are resolved, and overall performance confirmed. These "standard" tests include electrical performance, critical alignments, visible and IR calibration and star sense tests, coregistration, system MTF, scan accuracy validation, electro-optical tests, and contamination control inspections/optics cleaning. Power configurations for both side 1 and side 2 are tested.

Preliminary instrument level bench testing characterizes system performance and baselines are set so that instrument performance can be referenced throughout the complete test program. The bench tests include electrical performance that measures command, telemetry, and servo performance, optical train characterization, wideband telemetry verification, and the standard tests described above. In preliminary thermal vacuum, the IR gains are set, instrument performance over mission operating temperatures is measured, and the IR channels are calibrated. The standard functional, cooler performance, and baseplate heater tests and a 24-hour continuous operational scenario are run with the sensor module in the t/v chamber and the electronics and power supply modules at ambient to more easily adjust IR gains and troubleshoot any electrical or power module anomalies. Expected on-orbit performance is determined by comparing the t/v test results to thermal model predictions.

Electromagnetic compatibility is validated by performing electromagnetic interference testing with the results compared to the baseline electrical performance data to ensure that the instrument will operate nominally during RF exposure. Vibration testing follows with instrument random, sine, and shock specification levels applied to the sensor and electronics units. Post-vibration tests (i.e., standard functional, dynamic interaction, cooler cover pyro deployment, and external cube alignment) determine the effects on instrument alignment, image quality, and scan performance and are compared to a pre-vibration baseline previously established to build confidence in the flight instrument's proper operation under predicted launch loads. A final thermal vacuum test (i.e., standard functionals, alignment measurements, cold start, and three-day continuous operational scenario) with all three instrument modules under thermal vacuum is conducted to ensure the instrument is ready to be integrated and tested at the spacecraft level.

Spacecraft level testing, complete with the instruments integrated, includes reference comprehensive performance, RF link, acoustics, thermal vacuum, magnetic field, final alignment, end-to-end, and final comprehensive performance tests. Launch preparations are conducted at the launch site as part of the integrated spacecraft test activities. Following successful completion of the instrument tests (i.e., alignments, visible and star channel aliveness, scan operations, limited IMC electrical, electronic calibration, command functional, power consumption, cooler door deployment, torque margin measurement, and optics/cooler inspection and cleaning) the GOES instruments are ready for launch.

2.4 Launch schedule

The GOES I-M on-orbit operational system includes the GOES-8 positioned at 75 degrees West and the GOES-9 at 135 degrees West both at a geostationary altitude of 35790 km providing comprehensive coverage for the Western hemisphere. GOES-I was launched on April 13, 1994 and was renamed GOES-8 upon reaching synchronous orbit. GOES-J was launched on May 23, 1995 and renamed GOES-9 upon reaching synchronous orbit. After successful post launch testing and initiation of on-orbit operation of both GOES-8 and -9, GOES-7, originally launched in 1987 and operational for 9 years, was placed in a stable orbit and partially deactivated. It will be available for emergency back-up to the GOES operational system. The remaining satellites in the GOES I-M series (GOES-K, GOES-L, and GOES-M) are scheduled for launch in 1997, 2001, and 1999 respectively. GOES-M will be launched out of sequence due to the planned availability of the SXI instrument.

3.0 POSSIBLE TECHNOLOGY ADVANCEMENTS FOR FOLLOW-ON IMAGERS

The evolutionary growth from the GOES I-M will be in the GOES-NO/PQ series and GOES-R. The NWS preliminary plan is to implement "clone-like" requirements on GOES-NO/PQ and then possibly significant block changes on GOES-R. GOES-R will develop significant advancements in capabilities and is to be launched in 15 to 20 years. The NWS is formalizing goals and the desired capabilities are summarized[15] in Table 3-1. Though the NWS and NOAA have defined preliminary plans and would like to continue to implement these goals and desires, the real world of budget constraints, technology availability, and the desire to more fully use existing technology will determine the future capabilities of the GOES. As a result, NWS and NOAA are undergoing a major reassessment of GOES program goals . The intention is to begin an assessment of the current application of the GOES I-M and define possible subsequent changes in design requirements. A range of outcomes are possible from more fully utilizing current products, downgrading the existing design requirements for GOES NO/PQ to meet reassessed requirements, or upgrade

to operate in the state-of-the-art technology. Ultimately time will tell where we proceed from the current instrument technology operating on-orbit to the next generation of instruments.

The GSFC GOES Program is following the NWS near-term requirements on GOES-N, O for instrument design changes intended to provide primarily a reliability upgrade via modification of existing designs for engineering improvements (e.g., vacuum housing seals, heaters, etc.) and to eliminate design problem areas (i.e., solar intrusion) inherent in the GOES I-M series. The NOAA has also defined requirements for a Double Rate Imager (DRI) currently in the definition phase planned for completion in early 1997. The plan is to use existing GOES I-M Imager technology with the addition of reasonable upgrades in performance. The earliest the DRI may be considered for launch is in the GOES-P, Q timeframe. The DRI design intends to provide double the scene coverage rate, three additional IR 4 km IFOV channels with goals for improved Noise Equivalent Temperature Difference (NEΔT), eight additional visible 1 km IFOV detectors, channel 3 will have two 4 km IFOV detectors instead of one 8 km IFOV detector, electronics redundancy with dual visible and IR processor architecture design, and accommodation for the raw and GVAR data rate increase[16]. However, upon completion of the definition phase there may be a reduction in requirements based upon predicted design and operational costs.

Goals	Desired Capabilities
• Improve observational capabilities • Support increased demand for products • Improve data distribution • Improve regional forecasting displays • Develop new types of observations • Develop more sophisticated models • Support more sophisticated use of combined satellite/observational platforms	• Simultaneous local severe storm scanning with full Earth disk scans • Add two IR bands (mid-tropospheric winds/clouds) • Add one near-IR band (distinction between clouds/snow) • Updated full disk image every 15 minutes • Updated image data every 5 minutes over 3000x3000 km and visible data (rapid scan) over 1000x1000 km • Each IR band coregistered to the center of each corresponding field of view by +/-25% of the IR spatial resolution • On-board visible channel absolute and in-flight IR calibration within 0.2 degrees K relative accuracy and 1 degree K absolute accuracy • Continuous imaging and sounding through midnight • 24-hour operations during eclipse period • Visible resolution to 0.5 km and IR to 2 km • Lightning mapper • Measurements to benefit oceanography, climate, and hydrology monitoring and research • Microwave Imaging • Larger focal plane arrays with improved cooler technology • Improved data handling • Miniaturized technologies
• Satellite navigation accuracy of 1.25 km • Improvement in pixel-to-pixel registration within a frame • Visible image-to-image registration of 0.5 km or less over consecutive images during a 60-minute period • Data to users in real-time and from all bands simultaneously for a specific area within five seconds • One hour recovery time or less from a routine maneuver • Minimize performance degradation around local midnight	

Table 3-1. NWS & NOAA GOES Long-Term Goals and Desires

The working relationship developed between GSFC and NOAA throughout the history of the GOES Program can continue to be used to further the advancement of state-of-the-art instrument technology and environmental monitoring goals. GSFC's plan to focus potential technology development applications in instrument, spacecraft and ground systems and potential technology transfer from other NASA programs for future missions is proposed in the GSFC Technology Infusion Plan[17]. An example would be the New Millennium Program (NMP) that may provide possible advances in sensor technology, new approaches to low cost programs, and micro-miniaturization for incorporation into the future GOES Program.

With the NWS/NOAA reassessment of the GOES Program requirements and longterm goals, it is unclear how consistent future results will be with published plans. However, with the continued cooperation between NWS and NOAA defining observational requirements and GSFC's system development capabilities, the future GOES program can continually provide the critical component of the NWS's global weather forecasting system and satisfy the users needs with continuing performance and product development improvements.

4.0 SUMMARY

The GOES satellite system is an integral part of the NWS global weather data network and provides a critical resource for tracking severe weather activity that saves lives and property. In addition, daily local television forecasts using the GOES satellite data have significantly contributed to a better understanding of the complexity of weather and its

forecasting and ensuring that the American citizen has accurate and current information. This has been the result of major technological advances in the geostationary imager and data distribution since the first on-orbit geostationary demonstration in 1966 and the first operational instrument in 1974. GOES-8 and GOES-9 are the result of imaging and sounding instrument evolution in detector technology, cooler performance, independent imaging and sounding operations, navigation and registration, scanning modes (in particular one minute rapid scan imaging for severe storm forecasting), and radiometrics (e.g., SNR, NEΔT, resolution, etc.). The heritage of the current operational satellites is to keep pace with the needs of the users within the technology capabilities available.

The next series of GOES to follow GOES I-M will most likely contain performance improvements determined by a combination of budget constraints, user requirements, and existing technology capabilities available from the 1990's. Gradual design changes should be anticipated through the year 2003 and forthcoming revolutionary state-of-the-art technology should be available on-orbit in the next 20 years providing proposed long-term performance requirements and new technology from other programs can be applied to the GOES program. To ensure that the envelope of technology advancements continues to be pushed to the limits of practicality, decisions need to be made now to lay the foundation for satisfying the increasing performance and data needs of the user as understanding of meteorological events and global and mesoscale weather patterns expands and computer forecasting models evolve. An evolutionary approach to introduce new technologies into the operational GOES satellites will need to be implemented for NOAA and NASA to provide the NWS users continual growth over the next 20 years.

5.0 ACKNOWLEDGEMENTS

The authors thank Dr. W. P. Menzel/NOAA for reviewing and critiquing the accuracy of key tables included in this paper. Also thanks to many people from NASA and NOAA, and SS/L, ITT, and other government contractors who provided key background, technical, and programmatic inputs during the research phase. Special thanks to Lisa Smith of MDA for her commitment in preparation of a high quality product through many revisions and being accountable for excellence in the final version of this manuscript.

6.0 REFERENCES

1. NASA, Advanced Scanners and Imaging Systems For Earth Observations, SP-335, 1972.
2. Verner E. Suomi and Robert J. Krauss, University of Wisconsin, "The Spin Scan Camera System: Geostationary Meteorological Satellite Workhorse for a Decade," *Optical Engineering*, Vol. 17, No. 1, 1978.
3. W. E. Shenk, C.C. Stephanides, G.E. Sonnek, L.D. Howell, "ATS-6 The Geosynchronous Very High Resolution Radiometer," *IEEE Transactions on Aerospace and Electronic Systems*, Vol. AES-11, No. 6, 1975.
4. NASA, ATS-6 Final Engineering Performance Report, Volume 1 Program and System Summaries, Volume VI Scientific Experiments, Reference Publication 1080, 1981.
5. Santa Barbara Research Center (SBRC), Final Report-VISSR for a SMS, 1974.
6. SBRC, System Description VISSR Atmospheric Sounder, Revision A, 1976.
7. NASA, VAS Demonstration: Description and Final Report, Reference Publication 1151, 1985.
8. Eumetsat, The European Organization for Meteorological Satellites, 1981.
9. ITT Aerospace/Optical Division, Short Form Technical Description of a VHRR for the INSAT Spacecraft, BID 17604, 1977.
10. W. J. Hussey/NOAA/NESDIS, "Preparing for NOAA's Geostationary Operations of the 1990's," *GOES I-M Operational Satellite Post-Conference Summary Report*, page 19, 1989.
11. Space Systems/Loral (SS/L), "GOES I-M DataBook," DRL 101-08, 1994
12. ITT Aerospace/Communications Division, Imager Operational Reference Manual, 6281320-1D, 1993.
13. SS/L, GOES I-M Program Spacecraft Operations Handbook: Spacecraft Description, DRL 503-02, Volume III, 1994
14. ITT Aerospace/Communications Division, Test Procedure System Integration/Acceptance Test For Imager SN05, 8165957, 1994.
15. NOAA, National Weather Service Observational Requirements for the Evolution of Future NOAA Operational Geostationary Satellites, NWS Draft, 1995.
16. ITT Aerospace/Communications Division, Draft Instrument Level Performance Specification for the GOES-N/Q Double Rate Imager (DRI) and Interferometer Sounder (GHIS) Instruments, S 415-xx, 1996
17. GSFC, Technology Infusion Plan for the Mission to Planet Earth Program, 170-03-06, 1996.

GOES Sounder overview

Jeanine E. Murphy and Sanford W. Hinkal

NASA, Goddard Space Flight Center
Greenbelt, Maryland 20771

ABSTRACT

The GOES Sounder is similar in appearance, size, and design to the GOES Imager. It provides independent radiometric sounding of the atmosphere from GOES-East and GOES-West (GOES 8 and 9), which was accomplished on previous GOES by a single instrument with responsibility split between the functions of imaging and sounding. With 19 channels ranging from 0.70 μm to 14.71 μm, the Sounder probes the atmosphere to measure radiance at different depths (altitudes) while also monitoring surface and atmospheric temperatures, ozone, water vapor content, and cloud cover by means of the calibration of radiance data at selected wavelengths.

Like the Imager, the Sounder scans the full earth, and can be commanded to scan local regions of interest. The scan mirror steps across the disk of the earth in synchronization with a dead zone on a filter wheel. The filters define 18 of the channels as they rotate on the wheel in the path of light split into three beams traveling to detectors divided into longwave, midwave, and shortwave arrays. For visible (0.70 μm) sounding of cloud cover, energy is split off ahead of the filter wheel and passed to the 19th channel and also to star sensing detectors used for instrument navigation.

Keywords: GOES, sounder, weather, satellite

2. INTRODUCTION

The GOES Sounder is one of the two primary instruments on the Geostationary Operational Environmental Satellites (GOES). This instrument is a radiometer similar to the GOES Imager but with 19 distinct bandwidths or channels and with 13 bit resolution. Eighteen of these channels are selected by a rotating filter wheel ahead of three arrays of detectors which select the seven longwave (LW) (12.0 to 14.7 μm), five midwave (MW) (6.5 to 11.0 μm), and six shortwave (SW) bands (3.7 to 4.6 μm). One visible band (0.7 μm) is split off ahead of the filter wheel. These channels are chosen for the functional relationships between the energy radiated in each band and the atmospheric temperatures and moisture content at different altitudes, surface and cloud temperatures, and ozone distribution.

This paper presents an overview of the instrument from an instrument manager's perspective. The optical design of the instrument is described with an overview of the mechanical and electronic layout. Data products are described, with a discussion of some of the uses of the data. Calibration methods are summarized. The instrument has undergone continuous improvement and the effect of this is briefly discussed in terms of the data products of GOES Sounders now on orbit, presently undergoing assembly, and planned for the future.

3. DESIGN

The Sounder instrument consists of the sensor module (Fig. 1), which occupies a 1.2 X 0.8 X 0.7 meter volume within the 6.4 meter cube envelope of the spacecraft body, the electronics box, and the power supply. This hardware contributes 129 kg of the total spacecraft mass of 977 kg excluding fuel and pressurizing gas. The sensor module is mounted on the north end of the spacecraft surface which faces Earth, with the radiant cooler pointed north and the Sounder optical port facing the earth. The electronics box and the power supply are mounted within the spacecraft (Fig. 2) on the north panel.

Light enters the Sounder optical port (see Fig. 3) and falls on the lightweighted elliptical (0.51 m x 0.32 m) beryllium scan mirror, directing radiation into a 0.31 m aperture Cassegrain telescope which focuses it on the optical

0-8194-2200-2/96/$6.00

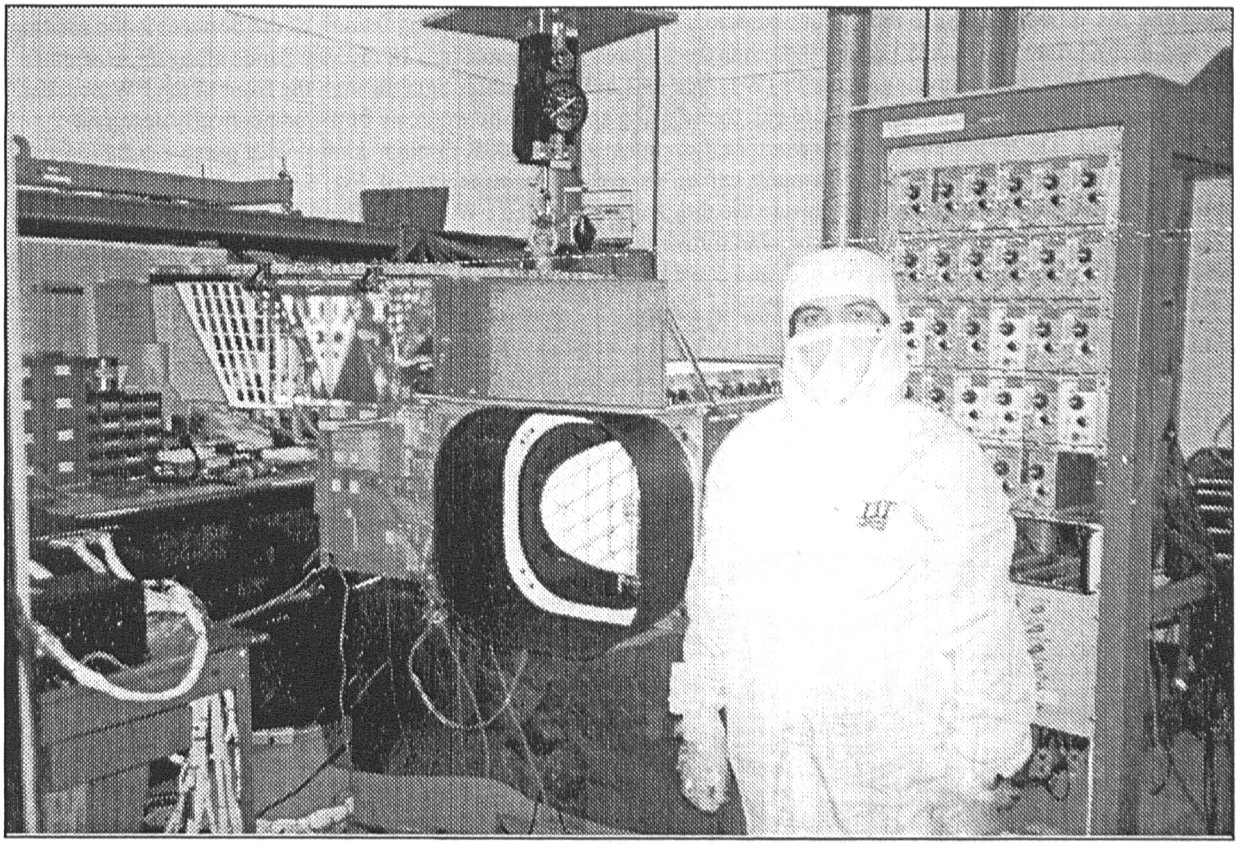

Fig. 1. The SN06 Sounder and J.E. Murphy in the ITT-Fort Wayne vibration test facility (April, 1996). This Sounder is slated for launch on GOES-M in August, 1999.

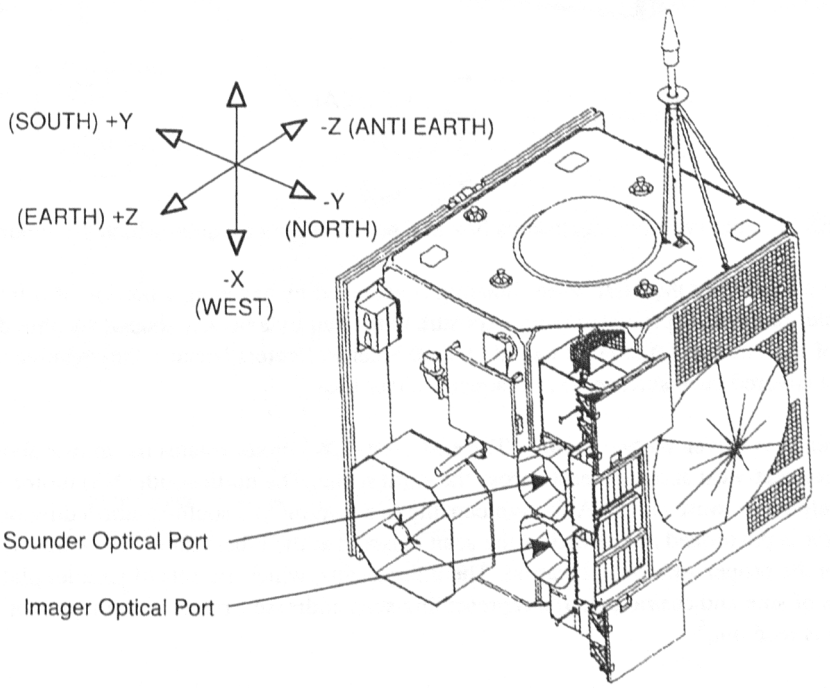

Fig. 2. GOES I-M Spacecraft

train and five different paths to the various detectors (Fig. 4). The distinguishing feature of the Sounder is the rotating cooled (235K) filter wheel (FW) which separates the infrared (IR) signals into 18 discrete bands along three of those paths. Three FW vacuum housing windows (W1, W2, W3 in Fig. 4) admit light through the front of the FW housing. Three identical windows allow the light to exit the housing and enter the windows of the adiabatically designed detector cooler. The temperature of the detectors is maintained near 100K through control with passive radiation and heaters. The selection of the bands or channels can be understood by inspection of Fig. 5. A synchronous hysteresis motor spins the filter wheel at 600 rpm inside the thermally-controlled FW housing. Notice that 25% of the filter wheel has no filters. Stepped motion of the scan mirror is synchronized with this "dead zone" so that its motion is stopped during data sampling. Figures 3, 4, and 5 are from the GOES I-M DataBook[2], published before the launch of GOES-I.

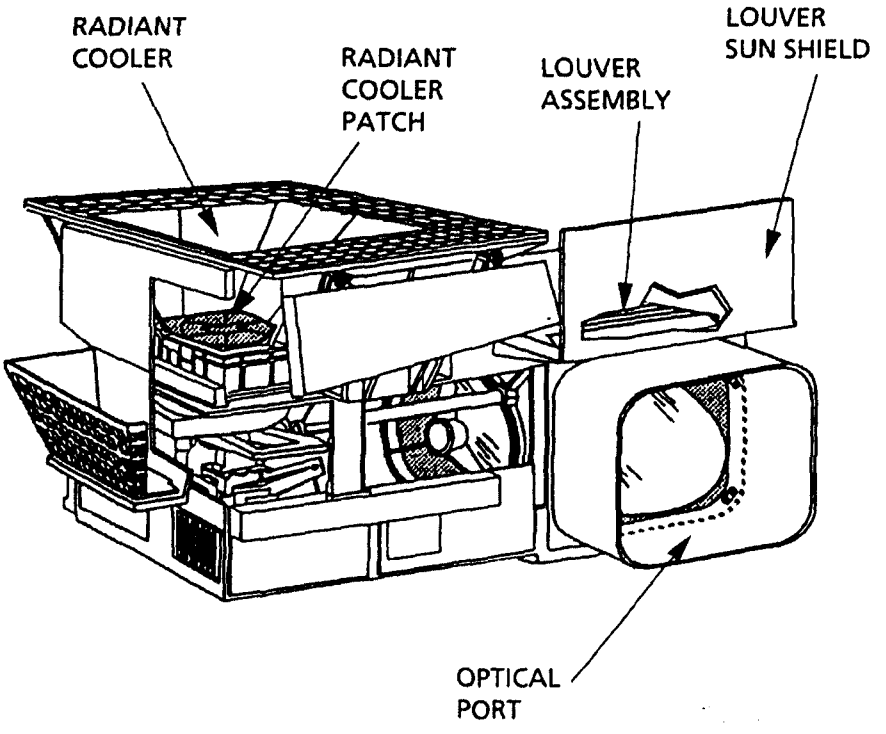

Fig. 3 The GOES Sounder (without electronics box and power supply module, which are mounted separately)

The radiative cooling of the filter wheel housing is achieved by exposing a portion of it into space, where it, like the detector cooler radiator, is protected from exposure to the sun by a bucket-shaped sunshield. The inner sides and the outer sides of the sunshield (the latter called Optical Solar Reflectors because they receive solar radiation directly) are made of silvered back surface 25 mm square mirror tiles.

The scan mirror is driven by two motors. The east-west (EW) motor rotates the mirror about its shorter axis for stepping the mirror east-west and west-east across the earth scene. The north-south (NS) motor steps the mirror from north to south after east-west scans. (Although capable of scanning in a south-to-north direction, this is never done.) The EW motor is positioned at one end of the scan axis and at the other end is the inductosyn which is used to position the mirror at the proper addressed location. The inductosyns, which are sets of parallel plates encoded with unique combinations of sine and cosine patterns representing scan addresses, rotate with the mirror axis until the commanded address is read out.[3]

Scan coordinates are apportioned into EW and NS cycles and each cycle is divided further into 2805 increments. The X1 inductosyn positions the mirror at the proper EW cycle. The scan coordinates divide the range of

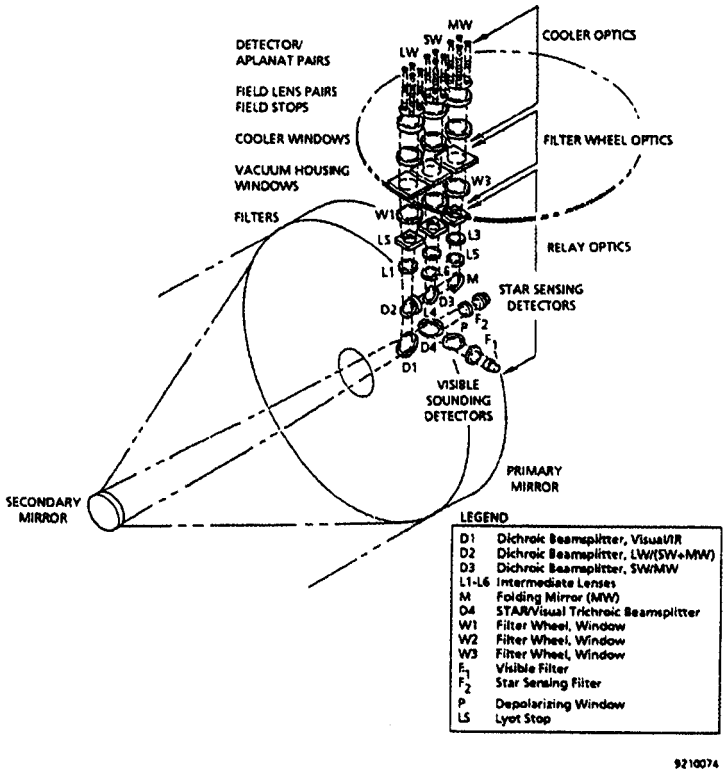

Fig. 4. Sounder optical elements.

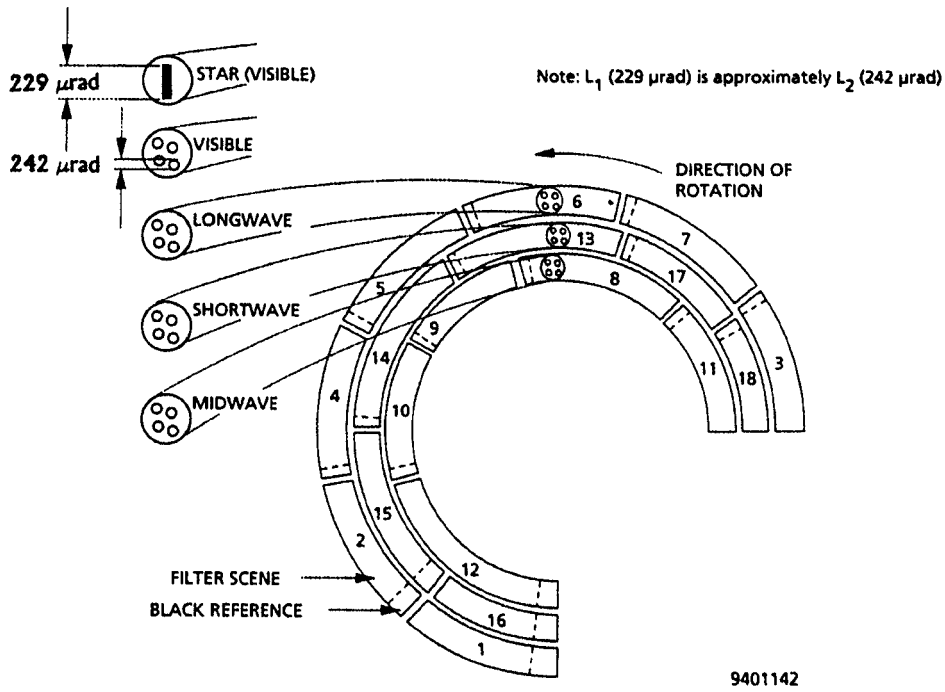

Fig. 5. Filter wheel and channel separation.

possible scan addresses into cycles and then further into increments. The X128 inductosyn positions the mirror at the proper increment. The same is true for the NS motor except that the motor and inductosyn are collocated. The mirror is stepped 280 microradians in 0.028 second in the EW direction while the dead zone in the filter wheel passes in front of the detectors. Each sounding requires 0.1 second to complete one step and one rotation of the filter wheel. The timing of the servo system is synchronized with timing signals from the wheel electronics. Fig. 6 represents the scan pattern produced by one scan across an area (whole Earth or smaller). The left side of the figure shows the relative spacing of a set four IR detectors in the focal plane. The circles represent any set of four LW, MW, SW, or visible detectors as shown in Fig. 5. These four detector sets are coregistered N-S and E-W in order to view the same areas simultaneously. Fig. 6 illustrates how the detectors are stepped through a line in 280 μm E-W or W-E increments to produce the pattern shown. Each detector is 242 μm in diameter and placed 280 μm center-to-center from the detector above it, where 280 μm at the detector corresponds to 10 km on the ground. At the end of each scan, the scan mirror is stepped four scan lines south, then it is stepped back across the area in the opposite direction from the previous scan.

In order to coregister the separate IR and visible bands so that each covers the same column of atmosphere with each scan mirror step, several of the optical components are designed to be adjustable during instrument assembly to achieve coregistration. The final coregistration is determined by summing the optical coregistration with the "step and settle" error introduced when positioning the scan mirror. The scan mirror does not fully "settle" before the end of the filter wheel dead zone as the mirror steps from one EW location to another.

Two additional inputs into scan mirror control are the Mirror Motion Compensation (MMC) and the Image Motion Compensation (IMC). The three-axis stabilized design of GOES I-M renders the system pointing accuracy more susceptible to spacecraft disturbances than the previous GOES spacecraft, which were spin-stabilized. One of the largest of these disturbances is the rotation of the Imager and Sounder scan mirrors to and from the black body source reference position during the calibration process. An MMC signal is sent to the servo loop to change the scan mirror position to compensate for this disturbance to the spacecraft attitude. The IMC is a signal supplied from the spacecraft Attitude Orbital Control System to compensate instrument pointing for spacecraft drift.

Thermal noise is minimized by placing the detectors on a "patch" which is exposed to space. A lower patch temperature allows the detectors, especially the longwave, to provide better IR sensitivity. The patch is the third stage of a three-stage cooler. The first stage is a vacuum housing which allows the cooler to be evacuated for ground testing purposes. The second stage is a radiator which is thermally isolated from the rest of the instrument. Finally, the patch is the space-exposed surface upon which the IR detectors are located inside their position-adjustable housings. A highly reflective vacuum-deposited aluminum surface shades the exposed patch from the sun and reflects away energy from the spacecraft solar sail. The patch temperature is controlled with heaters to provide three separate, commandable temperatures which is necessary due to seasonal variations in spacecraft attitude relative to the sun. The low patch temperature for all Sounders has ranged from 94K for GOES-8 to 89K for GOES-M. The mid-temperature point is at 101K for GOES-8 and 9 and 100K for GOES-K and L. "Patch high" is a backup temperature set point at

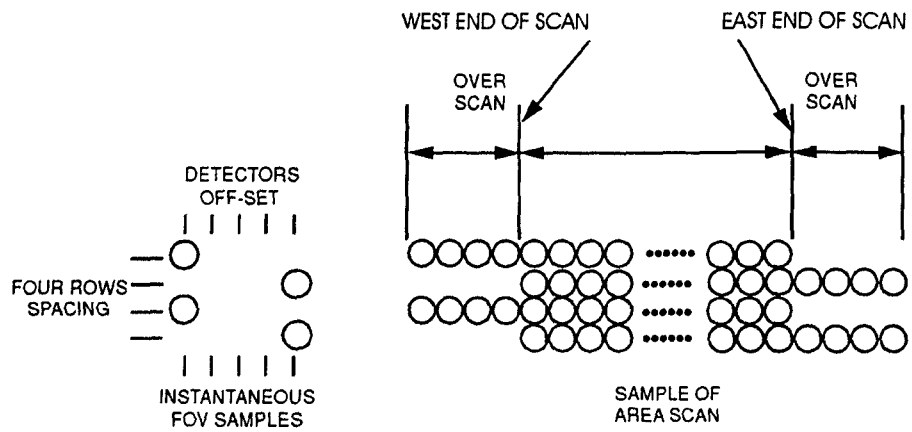

Fig. 6 Scan pattern

104K in case cooler performance degrades substantially at end of life. The patch low set point has been successively lowered as thermal margins have been verified on orbit and as design changes are made to the cooler.

A deployable cover is fitted over the radiant cooler to protect the patch and shroud surfaces from contaminates before and during launch, to regulate cooling during the cold transfer orbit after launch, and to maximize the temperature of the cooler for outgassing prior to deploying the door to its open position. The cooler door was enlarged for the GOES-K and later Sounders so that it would extend over the enlarged filter wheel cooler sunshade for contamination control purposes prior to deployment.

The instrument is powered by a 42V bus from the spacecraft. The bus voltage enters a set of four power convertors and to relays in the instrument power supply. The four different power convertors feed the proper voltages to the scan motors, filter wheel, signal processing and command electronics, detectors, and other circuits. Baseplate and outgas heaters are fed directly from the power relays. A fuse assembly and EMI filters are also contained in the power supply. The GOES-M Sounder power consumption is about 125 watts while scanning, including black body calibrations. To minimize power loading during routine scanning, power is shared between the scan motors and the six baseplate heaters. The baseplate is the instrument structure which supports the telescope. When the scan motors draw peak current, the baseplate heaters are briefly turned off.

When the instrument is in standby mode, as it is during launch and for all eclipses of the sun by the earth, power is supplied to the telemetry convertor to provide temperature status, to the filter wheel heater, the baseplate heaters, the patch temperature control, and to the filter wheel motor, drawing a total of 20 watts. During outgassing in standby mode, power is also supplied to outgas heaters on the cooler and filter wheel.

4. DATA PRODUCTS

The wavelengths of the 19 channels are distributed as listed in Table 1. Table 1 gives the central wavelength, noise specification (the NEΔN, *or noise equivalent delta radiance*, is a specification for maximum noise permissible in each channel), and application of each channel.[4]

Channel	Central Wavelength μm	Specified NEΔN mW/(m^{2}sr·cm^{-1})	Meteorological Parameter Determined
1	14.71	0.66	Stratosphere temperature
2	14.37	0.58	Tropopause temperature
3	14.06	0.54	Upper-level temperature
4	13.64	0.45	Mid-level temperature
5	13.37	0.44	Low-level temperature
6	12.66	0.25	Total precipitable water
7	12.02	0.16	Surface temp, moisture
8	11.03	0.16	Surface temperature
9	9.709	0.33	Total ozone
10	7.435	0.16	Low-level moisture
11	7.018	0.12	Mid-level moisture
12	6.515	0.15	Upper-level moisture
13	4.570	0.013	Low-level temperature
14	4.525	0.013	Mid-level temperature
15	4.454	0.013	Upper-level temperature
16	4.132	0.008	Boundary layer temperature
17	3.979	0.0082	Surface temperature
18	3.744	0.0036	Surface temperature, moisture
19	0.696	0.0010A	Cloud cover

TABLE 1 GOES I-M Sounder Spectral Bands
(A = Albedo. 0.0010A Signal/Noise is quoted for the Visible band.)

Vertical temperature and moisture profiles are obtained from Sounder radiance measurements and derived data products from the Sounder include thermal gradient winds, land-sea temperature, lifted index, total precipitable water vapor, and cloud product[5]. Lifted index is an estimate of atmospheric stability, and can indicate potential for severe storms. Cloud product is a term applied to information on clouds which are above 12,000 feet and is provided hourly to support forecast and aviation activities. Use of temperature and moisture profiles from the GOES Sounder in forecast models will assist plans for improved weather forecasting, especially over ocean areas which otherwise have very little data available.

The Sounder also has a star sensing capability to support instrument pointing requirements. For star sensing, the scan mirror slews to a star address and the star drifts across the field of view of the star array. Star sense detection is performed by a vertical array of eight detectors with IFOVs (Instantaneous Field of View) of 28 microradians. The Sounder does not provide landmark information as does the Imager due to the relatively large field of view (nominally 210 microradians) of the Sounder IR and visible detectors.

5. CALIBRATION

Calibration of the Sounder during ground testing is done by scanning an external calibration target set at seven different temperatures in evenly-spaced radiances between 200K and 320K. The slope is calculated and a non-linear (quadratic) fit is determined. Only the relative difference between the hot and cold targets is needed to determine a slope. Calibration at the seven different target temperatures is completed at hot and cold instrument temperatures and at patch low and patch mid temperatures to determine the nonlinear calibration coefficients for these conditions.

While ground calibrations are done at stable temperature conditions, the on-orbit temperature conditions, and therefore the energy coming into the detector, are constantly changing. This makes it mandatory that only the difference between the hot black body and cold space are used to determine the calibration.

On-orbit calibration is accomplished by scanning space, then scanning an internal black body target. A two-point slope is then determined by ground processing software. The nonlinear term is also added at this time. This is the nonlinear coefficient determined during thermal vacuum testing on the ground. The signal counts generated by each detector are inserted into this quadratic equation and radiances are calculated and sent to the data users. The calibration routine is executed every twenty minutes, interrupting the sounding in progress, and applied to the next 20 minutes of sounding data. Sounding resumes at the location it was interrupted. Between these twenty-minute calibrations, a space look is performed every two minutes for reference.

Calibration of the visible channel is performed on the ground by scanning a calibrated integrating sphere at ten different albedo levels between 0 and 100%. The integrating sphere is also used to check the star sense signal-to-noise ratio.

6. IMPROVEMENTS AND FUTURE PLANS

The GOES Sounders on the new GOES-East and GOES-West spacecraft are a splendid success, giving data users continual operational access to data that had to be acquired on a shared basis from GOES spacecraft before GOES-8, which switched between imaging and sounding functions within the same instrument. We who manage the design and build of the instruments hear from the users that they are continuing to learn how to use the wealth of new data being provided. Despite the success and quality of the data, improving significantly on what was available previous to the new GOES series, reviews of performance and requirements have resulted in decisions to make small design upgrades to enhance instrument performance, reliability, or testability. These are the major enhancements over the series: a more powerful NS scan motor, a lower-temperature filter wheel cooler for improved radiometric noise performance, a redesigned radiator cooler for lower detector temperature (hence lower noise) and for contamination control improvement, and a more thermally stable scan mirror for improved MTF. With these and other enhancements, the Sounder longwave IR sensitivity has improved about threefold over the first flight model.

The next proposed generation of GOES Sounder, called the GOES High resolution Interferometer Sounder (GHIS), will replace the filter wheel with a Michelson interferometer to achieve higher spectral resolution, which will enhance vertical (altitude within the atmosphere) resolution of temperature and moisture.

7. ACKNOWLEDGMENTS

Technical data was provided by ITT Aerospace/Communications Division in Fort Wayne, Indiana, which builds the Sounder under the direction of Space Systems/Loral, which is the prime contractor to NASA-Goddard Space Flight Center to build GOES I-M.

Further information can be found on the Internet. Start with the home page of the GOES Project Scientist, Dr. Dennis Chesters, **http://climate.gsfc.nasa.gov/~chesters/goesproject.html**
and information from the University of Wisconsin at **http://oldthunder.ssec.wisc.edu/goes/goes.html**.

8. REFERENCES

1. Geostationary Operational Environmental Satellite GOES I-M System Description, Space Systems/Loral, December 1992.

2. GOES I-M DataBook, DRL 101-08, Space Systems/Loral .

3. Sounder Operational Reference Manual, Document 6281320-2C, ITT Aerospace/Communications Division, October 1993.

4. Sounding Subsystem Performance Specification, Rev E, Space Systems/Loral, SS/L Doc No 565054, September 19, 1994.

5. Menzel, W. Paul and James F.W. Purdom, Introducing GOES-I: The First of a New Generation of Geostationary Operational Environmental Satellites, Bulletin of the American Meteorological Society, Vol. 75, No. 5, May 1994.

Polarization contributions from optical components on infrared sounding instruments

James B. Heaney and Kenneth P. Stewart

Goddard Space Flight Center
Greenbelt, MD 20771

Scott E. Bradley

Orbital Sciences Corporation
7500 Greenway Center Drive, Suite 700
Greenbelt, MD 20770

Phillip W. Alley

Physics Department, The State University of New York
Geneseo, NY 14454

ABSTRACT

Measured infrared reflectance and transmittance data, as a function of wavelength and incidence angle, are presented for polarization inducing components on a typical Geostationary Operational Environmental Satellite (GOES) atmospheric sounding instrument. The data are then used to construct Mueller matrices from which instrument polarization is computed. The computed results identify those components that are the source of a sounder's polarization sensitivity, not only to incoming radiance from an observed scene, but also to the instrument's own radiant signature. A comparison is made between the polarizing characteristics of a typical filter-type infrared sounding radiometer and a proposed Michelson-type Fourier transform alternative.

Key Words: Polarization, beamsplitters, Mueller matrices, reflectance, transmittance, emittance.

2. INTRODUCTION

A thorough compendium of polarization definitions and terminology, the origins of polarization in the natural environment and in optical components, and the effects of polarization sensitivity on remote sensing radiometer performance can be found in a methodical series of SPIE publications.[1-7]

In general, if an optical instrument is not designed with the specific intent of extracting information from the polarization state of incident scene radiance, then it should be designed with minimal polarization sensitivity. This is a prudent measure taken to reduce the likelihood of unpredictable radiometric errors caused by intrinsic instrument polarization sensitivity. Although the GOES atmospheric sounding instruments are not designed to extract information from the polarization content of an observed scene, the accuracy with which they can measure radiant intensity can be corrupted by intrinsic instrument

0-8194-2200-2/96/$6.00

sensitivity to the polarization state of incident scene radiance. The Sounder's polarization sensitivity originates primarily in mirrors and beamsplitters that encounter incident electromagnetic radiation at angles other than normal incidence. Figure 1 presents an optical layout for the GOES Sounder instrument that identifies schematically the relative position and orientation of key polarizing components with respect to an incident beam. Note that the scan mirror is not shown in the layout. It is the first optical element to encounter incident radiation and the rays incident on the telescope primary arrive from the scan mirror. Ideally, instrumental polarization sensitivity should remain constant as a function of time. However, the polarization sensitivity of a scanning mirror positioned directly in front of the instrument's telescope can be a complicated function of variable incidence angle and changing temperature. In principle, the scanning mirror polarization characteristics can be calibrated prior to launch, or even after launch from observations taken of a known target. However, this is made difficult by the fact that the instrument's responsivity to incoming scene radiance varies with incidence angle and by the change in instrument radiant signature with changing scan mirror temperature. Calibration would have to be performed by exposing a complete instrument to linearly polarized radiation that was incident over a wide range of angles, wavelengths, and component temperatures. Since the scan mirror is the only component whose contribution to instrument polarization sensitivity is likely to vary with temperature, as well as incident angle, it may be sufficient to construct a single polarization matrix for all the other instrument optical components that can then be convolved with each of a series of matrices representing various operating modes of the scan mirror.

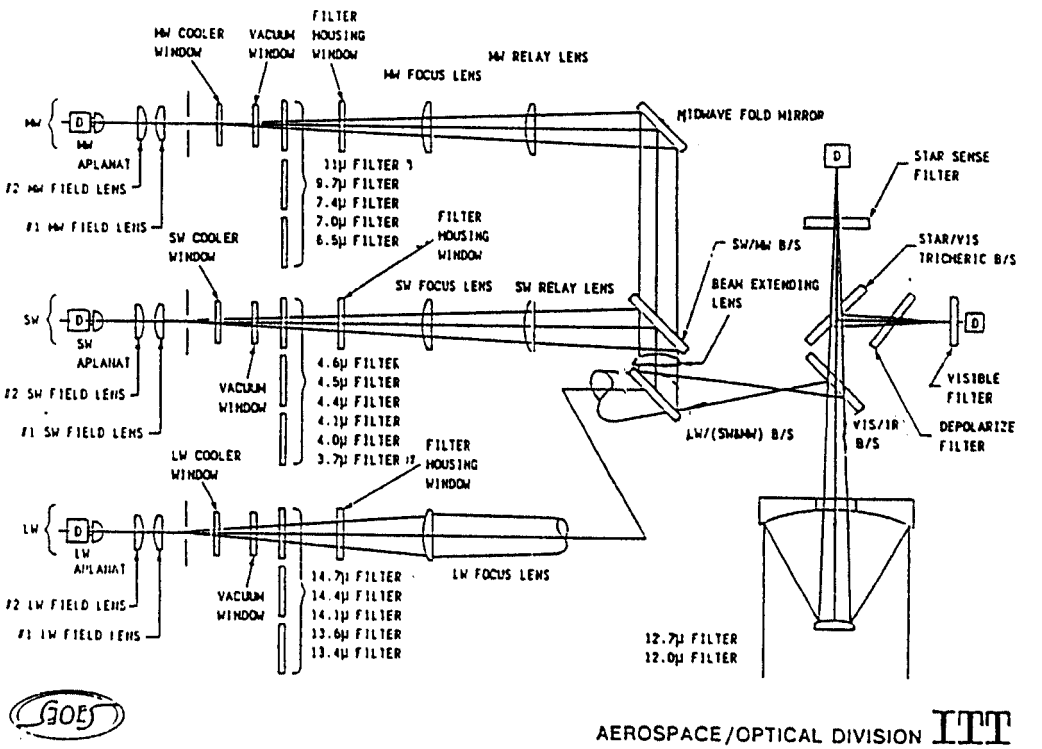

Figure 1: An optical layout sketch of the GOES Sounder instrument.

For the sake of brevity and ease of measurement, we will assume that radiation is incident on the scan mirror at an incidence angle of 45°, although in practice a wider range of angles is encountered. The degree of induced polarization is generally not significant for incident angles less than about 20°. On-axis telescope mirrors, lenses, windows, and filters that are used at near-normal incidence introduce little or no polarization into an infrared optical instrument. Also, uncoated metal surfaces do not significantly alter the polarization state of incident radiation until much higher angles are reached, especially at infrared wavelengths. However, thin film coatings applied to metal mirror surfaces in order to increase handling and cleaning durability and for slight reflectance enhancement can significantly alter a mirror's polarization sensitive reflectance.[8] As a consequence, mirror emittance is also rendered polarization sensitive. This latter point is relevant to the scan mirror.

Efforts to control and characterize instrument polarization sensitivity should concentrate on the polarization characteristics of dielectric substrate materials and mirror coatings for those components that are used at off-normal incidence angles. The degree of polarization sensitivity of dielectric materials is wavelength dependent and not constant over the entire operating bandwidth of a typical remote sensing instrument. This paper will present reflectance and transmittance data for selected optical components, such as the scan mirror, beam turning flat mirrors, and some beamsplitting elements used on the GOES Sounder instruments. The manner in which the polarization sensitivity of these components influences instrument measurement accuracy will also be demonstrated.

The current series of GOES atmospheric sounding instruments uses a series of wheel-mounted infrared bandpass filters to provide spectral selectivity. The filters are positioned at normal incidence with respect to the incoming beam and do not alter its state of polarization. However, a proposed Michelson-type Fourier transform spectrometer, used in a straightforward substitution for the filter wheel, will alter the polarization state of incident radiance and thereby change the instrument's polarization sensitivity. This change is due to the introduction of a coated dielectric beamsplitter in the Michelson interferometer that is used at an off-normal angle, as well as the presence of some beam turning flat mirrors.

3. REFLECTANCE AND TRANSMITTANCE MEASUREMENTS

A Nicolet 8000HV Fourier transform infrared spectrometer (FTIR) was used to perform reflectance and transmittance measuremnents over the 2μm to 20μm wavelength range applicable to the GOES Sounder instruments. The FTIR was equipped with a standard globar radiation source and a liquid nitrogen cooled HgCdTe detector. A grid-type linear polarizer on a KRS-5 substrate was placed directly in the infrared beam that was incident on the sample, usually at an angle of 45°. The principal transmittances, T_1 and T_2, of this polarizer are presented in Figure 2. (The principal reflectances shown in the figure are not relevant to this work.) Reflectance was measured relative to freshly evaporated Al or Au reference mirrors, whose reflectances were well characterized.

The measured reflectances and transmittances of the GOES Sounder's polarizing optical elements are presented in the following series of figures in the order in which they are encountered by incident radiance, beginning with the scan mirror, as sketched in the optical layout diagram of Figure 1. Data for both s- and p- polarization states are presented in the figures.

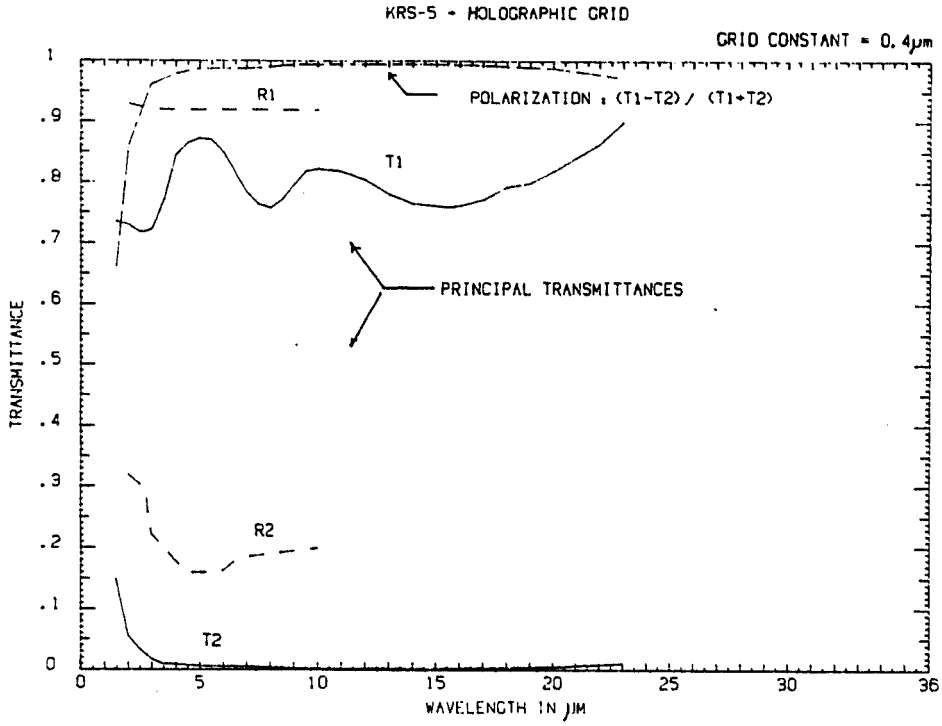

Figure 2: **The principal transmittances of the KRS-5 grid-type linear polarizer used for reflectance and transmittance measurements at off-normal incidence angles.**

Figure 3 - reflectance of the scan mirror;
Figure 4 - reflectance of the beamsplitter that transmits into the Sounder's visible and star sensing channels, and reflects into the infrared sounding portion of the instrument (3μm - 15μm);
Figure 5 - reflectance of the LW/(SW + MW) beamsplitter that reflects into the Sounder's shortwave and midwave channels (3μm - 11.5μm);
Figure 6 - transmittance of the LW/(SW + MW) beamsplitter that transmits into the Sounder's longwave channels (13μm - 15μm);
Figure 7 - reflectance of the SW/MW beamsplitter that reflects into the Sounder's shortwave channels (3μm - 5μm);
Figure 8 - transmittance of the SW/MW beamsplitter that transmits into the Sounder's midwave channels (6μm - 11.5μm).
Figure 9 - reflectance of the MW fold mirror used as a turning flat in the Sounder's midwave channel (6μm - 11.5μm).

4. MUELLER MATRICES FOR SOUNDER POLARIZING COMPONENTS

The R_s,R_p,T_s, and T_p measured data of figures 3 - 9 are sufficient to provide a Mueller matrix description for each of the Sounder's key polarizing elements. A straightforward multiplication of the individual matrices for a given path through the instrument will yield a final polarization matrix for that path. A general description of this process can be found in a number of references[7,9] and only a cursory description is provided here.

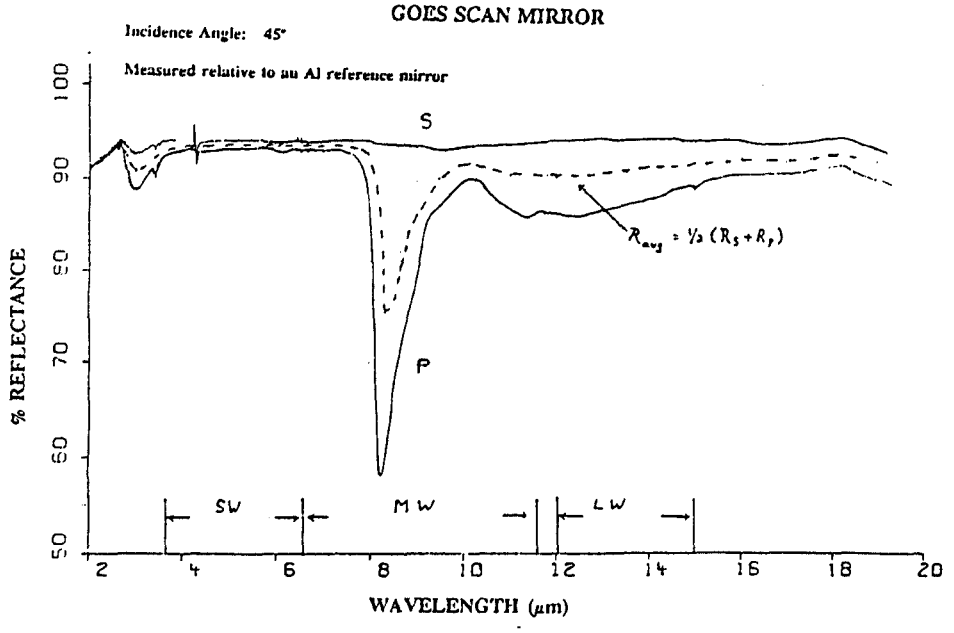

Figure 3: The reflectance of a GOES Sounder scan mirror witness sample measured relative to an evaporated Al reference mirror, at an incidence angle of 45°, over the 2μm to 20μm wavelength region.

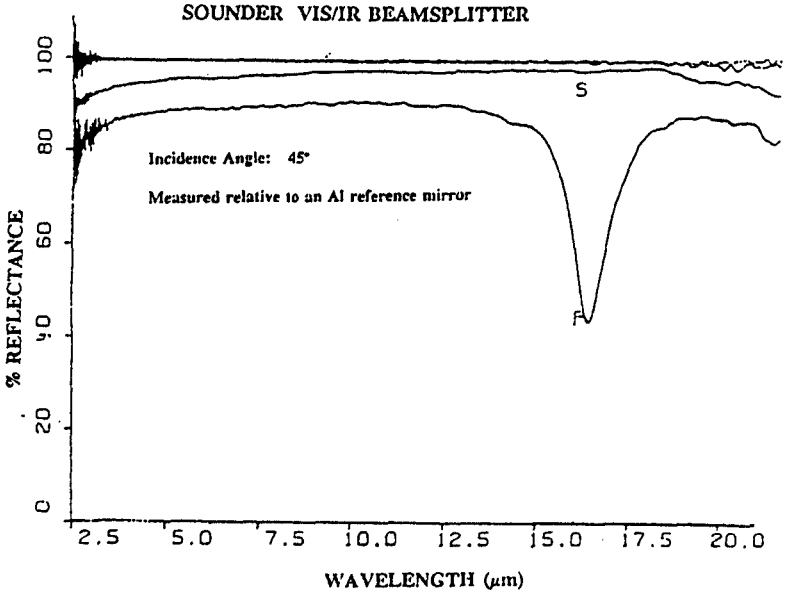

Figure 4: The reflectance of the Sounder VIS/IR beamsplitter, that transmits into the instrument's visible and star sense channels and reflects into the infrared sounding portion of the instrument, measured relative to an evaporated Al reference mirror, at an incidence angle of 45°, over the 2.5μm to 20μm wavelength region.

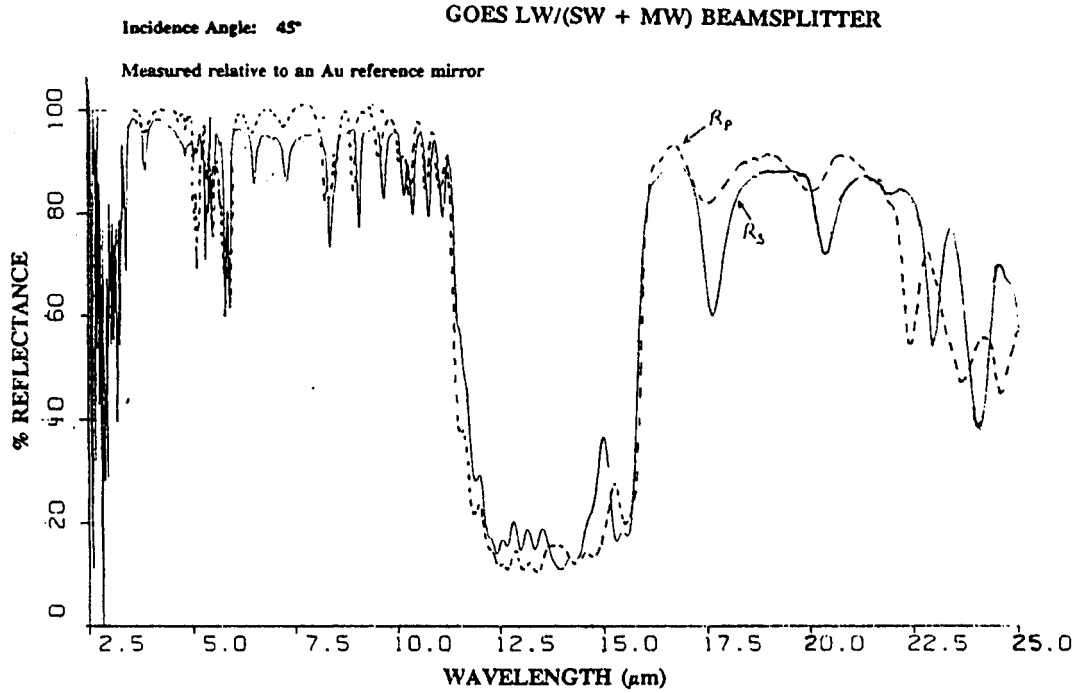

Figure 5: The reflectance of the GOES Sounder LW/(SW + MW) beamsplitter that reflects into the instrument's shortwave and midwave bands and transmits into the longwave band, measured relative to an evaporated Au reference mirror, at an incidence angle of 45°, over the 2.5mm to 25μm wavelength band.

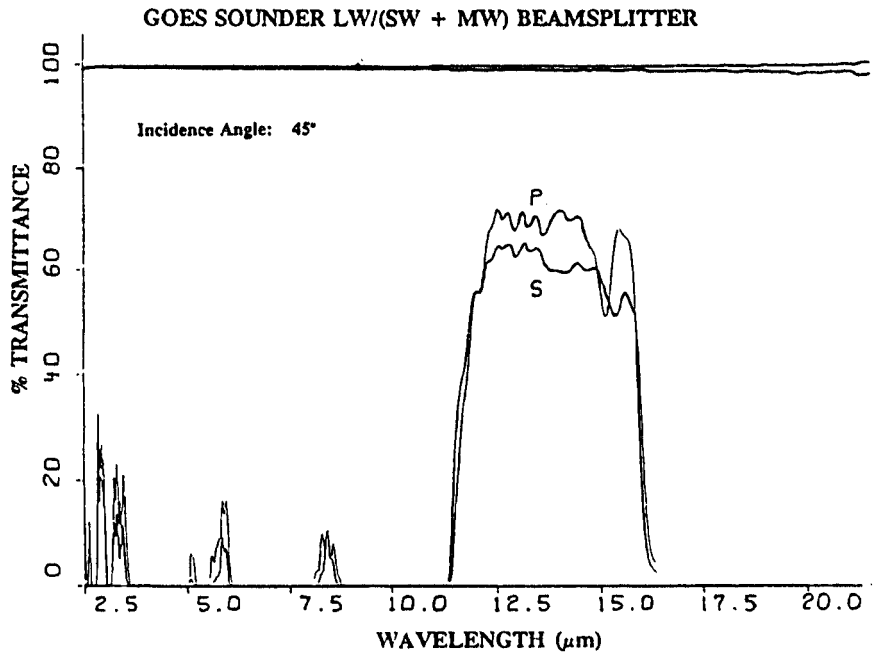

Figure 6: The transmittance of the GOES Sounder LW/(SW + MW) beamsplitter that transmits into the instrument's longwave channels, measured at an incidence angle of 45°, over the 2.5μm to 25μm wavelength region.

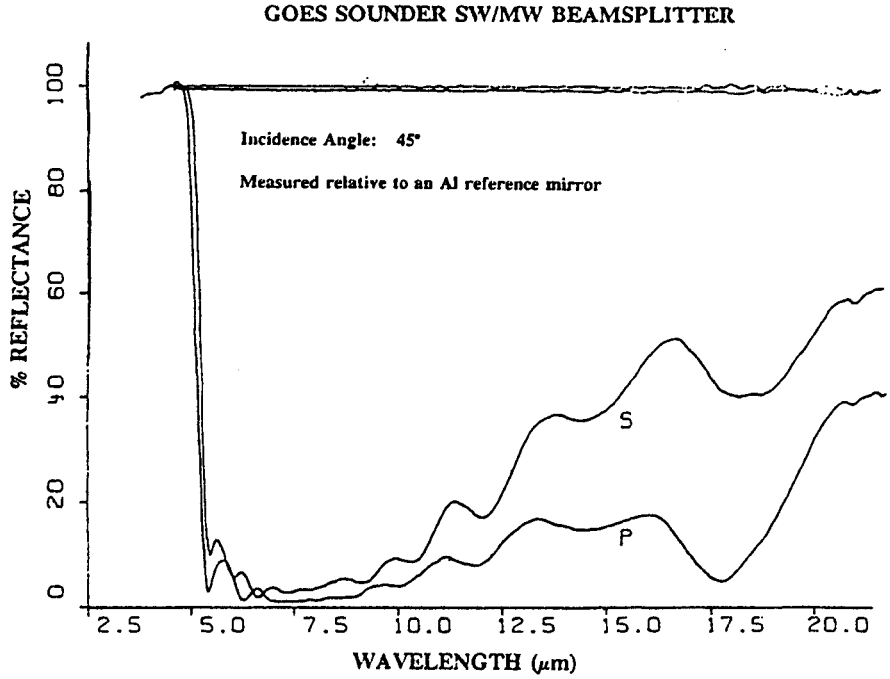

Figure 7: The reflectance of the GOES Sounder SW/MW beamsplitter that reflects into the instrument's shortwave channels, measured relative to an evaporated Al reference mirror, at an incidence angle of 45°, over the 2.5μm to 20μm wavelength region.

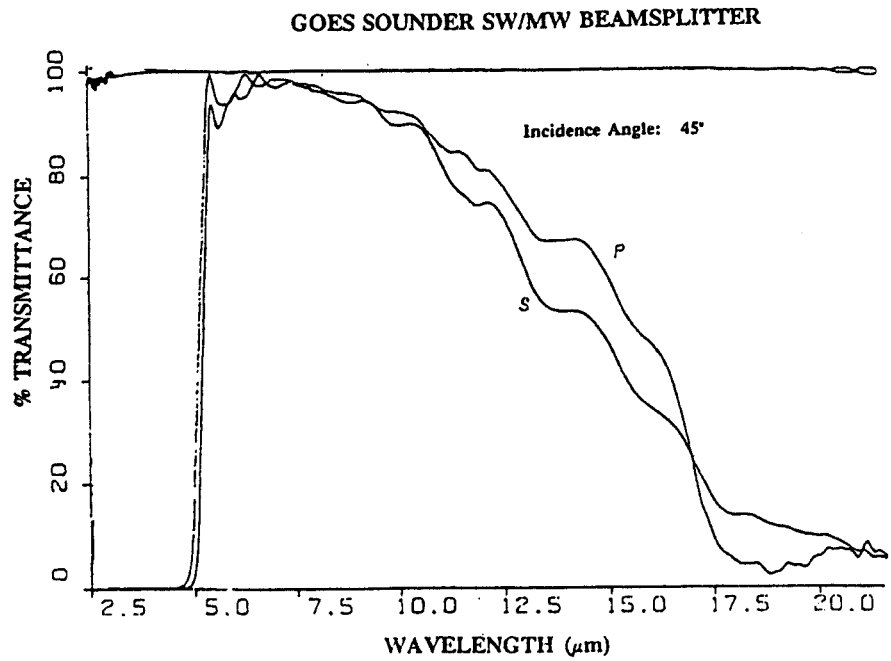

Figure 8: The transmittance of the GOES Sounder SW/MW beamsplitter that transmits into the instrument's midwave channels, measured at an incidence angle of 45°, over the 2.5μm to 20μm wavelength region.

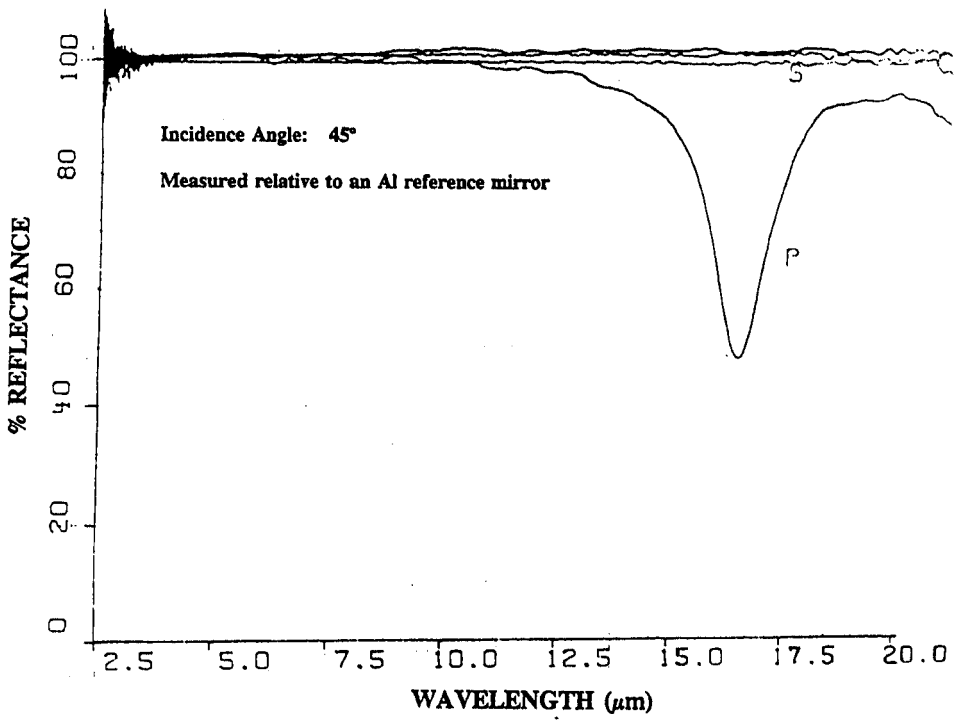

Figure 9: **The reflectance of the GOES Sounder MW fold mirror that reflects into the instrument's midwave channels, measured relative to an evaporated Al reference mirror, at an incidence angle of 45°, over the 2.5μm - 20μm wavelength region.**

The polarization state of scene radiance incident on the scan mirror can be described by the four element Stokes vector:

	Unpolarized incident beam
I - Intensity	1
M* - Preference for horizontal polarization	0
C - Preference for +45° polarization	0
S - Preference for right circular polarization	0

* - (+) is horizontal; (-) is vertical.

A Mueller matrix for a typical component would look as follows:

$$\begin{bmatrix} (X_s+X_p)/2 & (X_s-X_p)/2 & 0 & 0 \\ (X_s-X_p)/2 & (X_s+X_p)/2 & 0 & 0 \\ 0 & 0 & (X_s*X_p)^{1/2}\cos\phi & -(X_s*X_p)^{1/2}\sin\phi \\ 0 & 0 & (X_s*X_p)^{1/2}\sin\phi & (X_s*X_p)^{1/2}\cos\phi \end{bmatrix}$$

where X represents R or T. Reflectance and transmittance are wavelength dependent. Therefore, a separate Mueller matrix must be formulated for each wavelength in a polarization sensitivity computation.

Table 1 presents a summary of the method used to construct Mueller matrices for each of eight optical elements in the Sounder's shortwave beampath, stopping just prior to the filter housing window (see Fig. 1). The chosen wavelength was 4.1μm. Only those optical elements for which X_s and X_p differ contribute to an ultimate polarization sensitivity. The telescope primary and secondary mirrors, as well as the relay and focus lenses, do not alter the polarization state of an incident beam, but they do reduce its intensity, the first term in the Stokes vector that describes an incident ray.

Table 1: Mueller matrix construction for the GOES Sounder's shortwave beampath.

Matrix	Element	Values for short-wavelength path (SW 4.1 μm)	
M1	Scan mirror	Rs - 0.92	Rp - 0.91
M2	Telescope Primary mirror	Rs - 0.98	Rp - 0.98
M3	Telescope Secondary mirror	Rs - 0.98	Rp - 0.98
M4	VIS/IR beamsplitter	Rs - 0.92	Rp - 0.84
M5	LW/(SW+MW) beamsplitter	Rs - 0.97	Rp - 0.95
M6	SW/MW beamsplitter	Rs - 0.97	Rp - 0.92
M7	SW relay lens	Ts - 0.90	Tp - 0.90
M8	SW focus lens	Ts - 0.90	Tp - 0.90

$(\mathbf{I}_{in})$ **Input beam is assumed unpolarized.**

$$(\mathbf{M}_{final}) = (M8)(M7)...(M2)(M1)$$

$$(\mathbf{M}_{final})(\mathbf{I}_{in}) = (\mathbf{I}_{out})$$

Stokes Vectors

$(\mathbf{M}_{final})$ (4.1 μm)

$$\begin{bmatrix} 0.575 & 0.051 & 0.000 & 0.000 \\ 0.051 & 0.575 & 0.000 & 0.000 \\ 0.000 & 0.000 & 0.573 & 0.000 \\ 0.000 & 0.000 & 0.000 & 0.573 \end{bmatrix}$$

$(\mathbf{I}_{in})$

$$\begin{bmatrix} 1 \\ 0 \\ 0 \\ 0 \end{bmatrix}$$

$(\mathbf{I}_{out})$ (4.1 μm)

$$\begin{bmatrix} 0.575 \\ 0.051 \\ 0.000 \\ 0.000 \end{bmatrix}$$

An unpolarized input beam is assumed. The ordering of matrix elements in the computation leading to a final, or output, matrix is significant, because matrix multiplication is non-commutative. The computed output Stokes vector, compared to the input vector, indicates a 57.5% resultant intensity, with a 5.1% preference for horizontal over vertical polarization.

Similar Mueller matrix computations were carried out for four additional wavelengths - 6.8μm, 8.4μm, 11.5μm, and 13.4μm - representing selected bands in the Sounder's midwave and longwave paths. The values of R_s, R_p, T_s, and T_p that were used to construct the Mueller matrix for each component are listed in Table 2, together with the computed final path matrix and the resultant output Stokes vector for each wavelength. One wavelength - 8.4μm - was chosen because it represents a case of extreme polarization sensitivity driven by the resonant infrared absorption characteristics of the scan mirror's thin film dielectric overcoat. See Figure 3. It should be noted that the Sounder is not designed to sense scene radiance in this band and there is no consequent impact on radiometric accuracy. However, the mirror's lower reflectance due to this thin film polarization phenomenon raises its emittance and contributes a larger background signal into the instrument than would be received from either a bare metal mirror surface, or from a dielectric thin film with a much weaker resonant absorption. This point will be discussed further below.

Table 2: Computed final matrices and output Stokes vectors for the 6.8μm, 8.4μm, 11.5μm, and 13.4μm wavelength regions.

Listing of Elements Most Effecting Polarization			Matrices and Stokes Vectors MW & LW Wavelengths	
Matrix	Element	Values for MW & LW paths	(M_{final})	Stokes Vector (I_{out})
M1	Scan mirror	(6.8 μm) Rs - 0.91 Rp - 0.90 (8.4 μm) Rs - 0.91 Rp - 0.57 (11.5 μm) Rs - 0.92 Rp - 0.84 (13.4 μm) Rs - 0.92 Rp - 0.85	(6.8 μm) $\begin{bmatrix} 0.511 & 0.012 & 0.000 & 0.000 \\ 0.012 & 0.511 & 0.000 & 0.000 \\ 0.000 & 0.000 & 0.511 & 0.000 \\ 0.000 & 0.000 & 0.000 & 0.511 \end{bmatrix}$	(6.8 μm) $\begin{bmatrix} 0.511 \\ 0.012 \\ 0.000 \\ 0.000 \end{bmatrix}$
M4	VIS/IR beamsplitter	(6.8 μm) Rs - 0.93 Rp - 0.85 (8.4 μm) Rs - 0.94 Rp - 0.86 (11.5 μm) Rs - 0.94 Rp - 0.86 (13.4 μm) Rs - 0.96 Rp - 0.86	(8.4 μm) $\begin{bmatrix} 0.419 & 0.095 & 0.000 & 0.000 \\ 0.095 & 0.419 & 0.000 & 0.000 \\ 0.000 & 0.000 & 0.408 & 0.000 \\ 0.000 & 0.000 & 0.000 & 0.408 \end{bmatrix}$	(8.4 μm) $\begin{bmatrix} 0.419 \\ 0.095 \\ 0.000 \\ 0.000 \end{bmatrix}$
M5	LW/(SW+MW) beamsplitter	(6.8 μm) Rs - 0.92 Rp - 0.95 (8.4 μm) Rs - 0.87 Rp - 0.93 (11.5 μm) Rs - 0.87 Rp - 0.88 (13.4 μm) Ts - 0.64 Tp - 0.70	(11.5 μm) $\begin{bmatrix} 0.435 & 0.018 & 0.000 & 0.000 \\ 0.018 & 0.435 & 0.000 & 0.000 \\ 0.000 & 0.000 & 0.435 & 0.000 \\ 0.000 & 0.000 & 0.000 & 0.435 \end{bmatrix}$	(11.5 μm) $\begin{bmatrix} 0.435 \\ 0.018 \\ 0.000 \\ 0.000 \end{bmatrix}$
M6	SW/MW beamsplitter	(6.8 μm) Ts - 0.88 Tp - 0.91 (8.4 μm) Ts - 0.91 Tp - 0.94 (11.5 μm) Ts - 0.80 Tp - 0.88		
M9	MW fold mirror (45°)	(6.8 μm) Rs - 0.97 Rp - 0.96 (8.4 μm) Rs - 0.97 Rp - 0.96 (11.5 μm) Rs - 0.96 Rp - 0.94	(13.4 μm) $\begin{bmatrix} 0.470 & 0.023 & 0.000 & 0.000 \\ 0.023 & 0.470 & 0.000 & 0.000 \\ 0.000 & 0.000 & 0.469 & 0.000 \\ 0.000 & 0.000 & 0.000 & 0.469 \end{bmatrix}$	(13.4 μm) $\begin{bmatrix} 0.470 \\ 0.023 \\ 0.000 \\ 0.000 \end{bmatrix}$

Table 2 exhibits the computed intensity reduction and polarization sensitivity for the four selected wavelengths corresponding to the Sounder midwave and longwave beam paths. Note the extreme polarization sensitivity (9.5%) of the 8.4μm wavelength case.

5. SCAN MIRROR EMITTANCE

As the scanning mirror moves, it projects a varying angle to the Sounder's telescope optics. Let's assume that this angle is, on average, 45°. Although the scan mirror reflectance data of Figure 3 are for one incidence angle only, i.e. 45°, it can be readily demonstrated by measurements at other incidence angles that $R_s \neq R_p$ for angles other than 0° or 90°. This polarization effect carries over into mirror emittance, e, since e = 1 - R. Consequently, e is a function of wavelength and viewing angle. The radiant power emitted into the instrument by the scan mirror is given by $\Phi = e\sigma T^4$, where T is the mirror's temperature. The power radiated by the scan mirror into any instrument path will be a complicated function of viewing angle, wavelength band, and mirror temperature.

Figure 10 contains the results of radiant power calculations for three types of radiating surfaces. The top curve is for a blackbody (e = 1) at a temperature of 300K and is presented for reference purposes only. The bottom curve is the calculated spectral radiant power expected from a mirror, also at 300K, whose surface emittance = 0.03 and is approximately invariant with wavelength, as is the case for the current Sounder scan mirror at near normal incidence angles. The middle curve represents the spectral radiant power from the current scan mirror, at a temperature of 300K, viewed at an average angle of 45°.

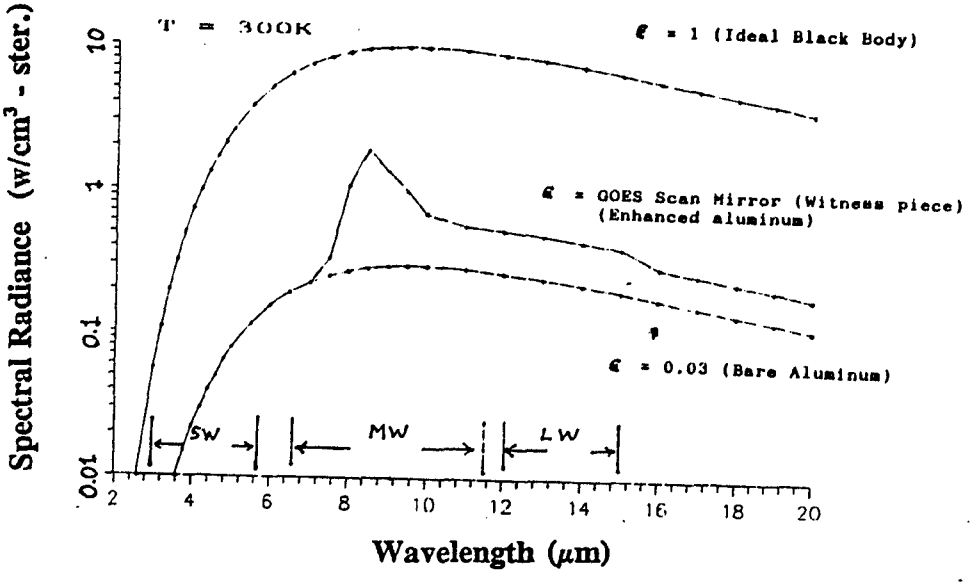

Figure 10: **The computed effect of the GOES scan mirror reflectance, at a 45° incidence angle, on mirror radiance for a mirror temperature of 300K.**

The scan mirror's total emittance, e(T) for a mirror at temperature T is given by:

$$e(T) = \int (1-R_\lambda)E_\lambda(T)\, d\lambda \,/\, \int E_\lambda(T)\, d\lambda$$ where $E_\lambda(T)$ is the Planckian spectral

radiance function for a surface at temperature T. As scan mirror temperature varies from 300K, the Planckian weighting function in the above integral will modify the mirror's emittance and e(T) will also vary. this would not happen if R were constant over the weighted wavelength band (essentially from 2μm to 50μm for temperatures in the vicinity of 300K).

This complicated dependence of scan mirror radiant background signal is a direct consequence of the mirror's polarization sensitivity that arises in its dielectric film overcoat.

6. COMPARISON OF THE POLARIZATION SIGNATURES OF A SOUNDER-TYPE FILTER RADIOMETER AND A MICHELSON-TYPE FOURIER TRANSFORM SPECTROMETER ALTERNATIVE

If the current Sounder's filter radiometer were to be replaced with a Michelson-type Fourier transform spectrometer, the instrument's polarization sensitivity would also change. The predominant cause of this change would be the dielectric beamsplitter of the Michelson interferometer that would be deployed at some angle other than normal to the incident beam. Any additional mirrors used at off-normal angles would also contribute to an altered polarization sensitivity.

This point can be demonstrated by considering one example of a Michelson-type interferometer/ spectrometer that has been proposed as a substitute for the Sounder's wheel mounted filters, that is the GOES High-Resolution Interferometer Sounder (GHIS). Figure 11 is a preliminary optical layout sketch of one proposed concept. Proceeding in the same manner as outlined above, a series of Mueller matrices were computed for the GHIS case. Matrix elements M1 through M4 are the same as above, since the optical components are common to both instruments. The values of R_s, R_p, T_s, and T_p for each optical element used to formulate the matrices are listed in Table 3a for the same five selected wavelengths. Table 3b contains the final matrix computed separately for rays following predominantly 'reflected' and 'transmitted' paths through the interferometer's beamsplitter. The resultant Stokes vectors for each case are then summed to yield the resultant vector that describes the output beam, up to the same instrument location as was calculated above for the filter case, i.e., just prior to the filter housing window. Detailed computations are shown for only one wavelength - 4.1μm - in Table 3b. However, computations were carried out for all five wavelengths.

The results are expressed in Figure 12 in terms of the 'Fraction of Polarization' (M*/I), a ratio of the first two terms of the output Stokes vector that expresses the degree of polarization of the beam transmitted into the detector end of the Sounder instrument. The figure contains a comparison of the filter wheel Sounder with the proposed GHIS interferometer/spectrometer in terms of M*/I. The wavelength dependence of the degree of polarization sensitivity for both designs is evident in Figure 12. The difference between the two instrumental approaches is most pronounced in the longwave channels.

Table 3a: R_s, R_p, T_s, and T_p used to formulate the Mueller matrices for the GHIS interferometer/ spectrometer at wavelengths 4.1μm, 6.8μm, 8.4μm, 11.5μm, and 13.4μm.

GHIS/ INTERFEROMETER INSTRUMENT

Matrix	Element	Values for all wavelengths - path (SW 4.1 μm)
Elements M1 thru M4 are the same as the SOUNDER.		
M5	GHIS turning flat	(4.1 μm) Rs - 0.99 Rp - 0.98 (6.8 μm) Rs - 0.99 Rp - 0.99 (8.4 μm) Rs - 0.98 Rp - 0.98 (11.5 μm) Rs - 0.97 Rp - 0.97 (13.4 μm) Rs - 0.99 Rp - 0.98
M6	GHIS collimator	(4.1 μm) Rs - 0.98 Rp - 0.98 (6.8 μm) Rs - 0.98 Rp - 0.98 (8.4 μm) Rs - 0.98 Rp - 0.98 (11.5 μm) Rs - 0.98 Rp - 0.98 (13.4 μm) Rs - 0.98 Rp - 0.98
M7	GHIS second turning flat	(4.1 μm) Rs - 0.99 Rp - 0.98 (6.8 μm) Rs - 0.99 Rp - 0.99 (8.4 μm) Rs - 0.98 Rp - 0.98 (11.5 μm) Rs - 0.98 Rp - 0.98 (13.4 μm) Rs - 0.99 Rp - 0.98
M8	GHIS I/F beamsplitter	(4.1 μm) Rs - 0.49 Rp - 0.23 (6.8 μm) Rs - 0.63 Rp - 0.38 (8.4 μm) Rs - 0.59 Rp - 0.32 (11.5 μm) Rs - 0.49 Rp - 0.23 (13.4 μm) Rs - 0.46 Rp - 0.22
M9	GHIS I/F beamsplitter	(4.1 μm) Ts - 0.49 Tp - 0.77 (6.8 μm) Ts - 0.35 Tp - 0.62 (8.4 μm) Ts - 0.40 Tp - 0.68 (11.5 μm) Ts - 0.47 Tp - 0.74 (13.4 μm) Ts - 0.46 Tp - 0.73
M10	GHIS I/F compensator	(4.1 μm) Ts - 0.95 Tp - 0.95 (6.8 μm) Ts - 0.95 Tp - 0.95 (8.4 μm) Ts - 0.95 Tp - 0.95 (11.5 μm) Ts - 0.96 Tp - 0.96 (13.4 μm) Ts - 0.96 Tp - 0.96
M11	GHIS I/F fixed mirror	(4.1 μm) Rs - 0.98 Rp - 0.98 (6.8 μm) Rs - 0.98 Rp - 0.98 (8.4 μm) Rs - 0.98 Rp - 0.98 (11.5 μm) Rs - 0.98 Rp - 0.98 (13.4 μm) Rs - 0.98 Rp - 0.98
M12	GHIS I/F moving mirror	(4.1 μm) Rs - 0.98 Rp - 0.98 (6.8 μm) Rs - 0.98 Rp - 0.98 (8.4 μm) Rs - 0.98 Rp - 0.98 (11.5 μm) Rs - 0.98 Rp - 0.98 (13.4 μm) Rs - 0.98 Rp - 0.98
Three mirror focus group. M13, 14, & 15	GHIS focus group	(4.1 μm) Rs - 0.98 Rp - 0.98 (6.8 μm) Rs - 0.98 Rp - 0.98 (8.4 μm) Rs - 0.98 Rp - 0.98 (11.5 μm) Rs - 0.98 Rp - 0.98 (13.4 μm) Rs - 0.98 Rp - 0.98
M16	GHIS LW/(SW+MW) beamsplitter (reflectance mode) same as M5 of SOUNDER.	
M17	GHIS SW/MW beamsplitter (reflectance mode) same as M6 of SOUNDER.	
M18	GHIS SW turning flat	(4.1 μm) Rs - 0.98 Rp - 0.98
M19	GHIS SW field lens	same as M8 of SOUNDER

Table 3b: Final computed matrices for beams following predominantly reflected and transmitted paths through the GHIS interferometer/spectrometer and the Stokes vector for the emergent ray.

(I_{in}) Input beam is assumed unpolarized,

Beam from telescope is reflected at I/F beamsplitter.

$$(M_{reflect}) = (M10)(M9)(M11)(M8)...(M1)$$

$(I_{reflect})$ is Stokes vector leaving interferometer.

$$(M_{reflect})(I_{in}) = (I_{reflect})$$

Stokes Vectors

$(M_{reflect})$ (4.1 μm) (I_{in}) $(I_{reflect})$ (4.1 μm)

$$\begin{bmatrix} 0.152 & 0.023 & 0.000 & 0.000 \\ 0.023 & 0.152 & 0.000 & 0.000 \\ 0.000 & 0.000 & 0.150 & 0.000 \\ 0.000 & 0.000 & 0.000 & 0.150 \end{bmatrix} \quad \begin{bmatrix} 1 \\ 0 \\ 0 \\ 0 \end{bmatrix} \quad \begin{bmatrix} 0.152 \\ 0.023 \\ 0.000 \\ 0.000 \end{bmatrix}$$

Beam from telescope is transmitted through the I/F beamsplitter.

$$(M_{trans}) = (M10)(M8)(M10)(M12)(M10)(M9)...(M1)$$

(I_{trans}) is Stokes vector leaving interferometer.

$$(M_{trans})(I_{in}) = (I_{trans})$$

Stokes Vectors

(M_{trans}) (4.1 μm) (I_{in}) (I_{trans}) (4.1 μm)

$$\begin{bmatrix} 0.131 & 0.028 & 0.000 & 0.000 \\ 0.028 & 0.131 & 0.000 & 0.000 \\ 0.000 & 0.000 & 0.128 & 0.000 \\ 0.000 & 0.000 & 0.000 & 0.128 \end{bmatrix} \quad \begin{bmatrix} 1 \\ 0 \\ 0 \\ 0 \end{bmatrix} \quad \begin{bmatrix} 0.131 \\ 0.028 \\ 0.000 \\ 0.000 \end{bmatrix}$$

$(I_{I/F\ out})$ is beam leaving interferometer.

$$(I_{reflect}) + (I_{trans}) = (I_{I/F\ out})$$

$$(I_{reflect}) \begin{bmatrix} 0.152 \\ 0.023 \\ 0.000 \\ 0.000 \end{bmatrix} + (I_{trans}) \begin{bmatrix} 0.131 \\ 0.028 \\ 0.000 \\ 0.000 \end{bmatrix} = (I_{I/F\ out}) \begin{bmatrix} 0.283 \\ 0.051 \\ 0.000 \\ 0.000 \end{bmatrix}$$

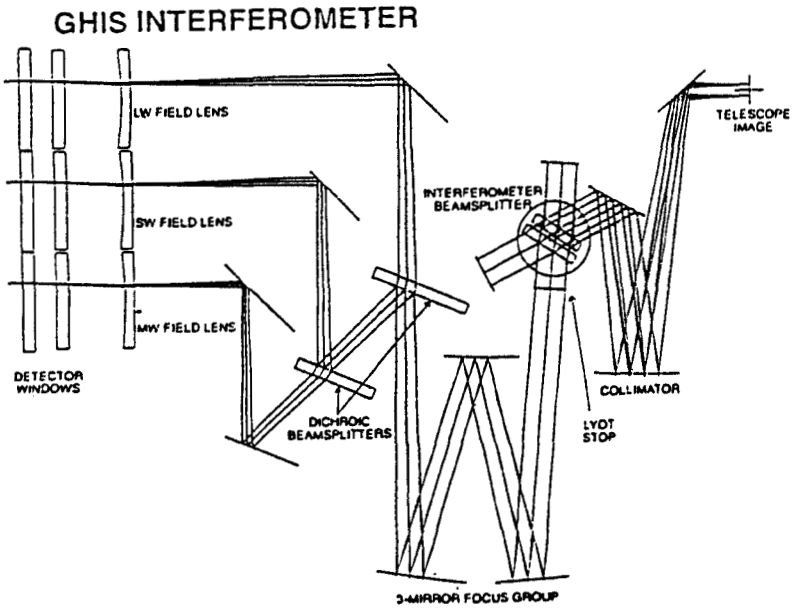

Figure 11: Optical layout sketch of a proposed Sounder Michelson-type interferometer/spectrometer (GHIS).

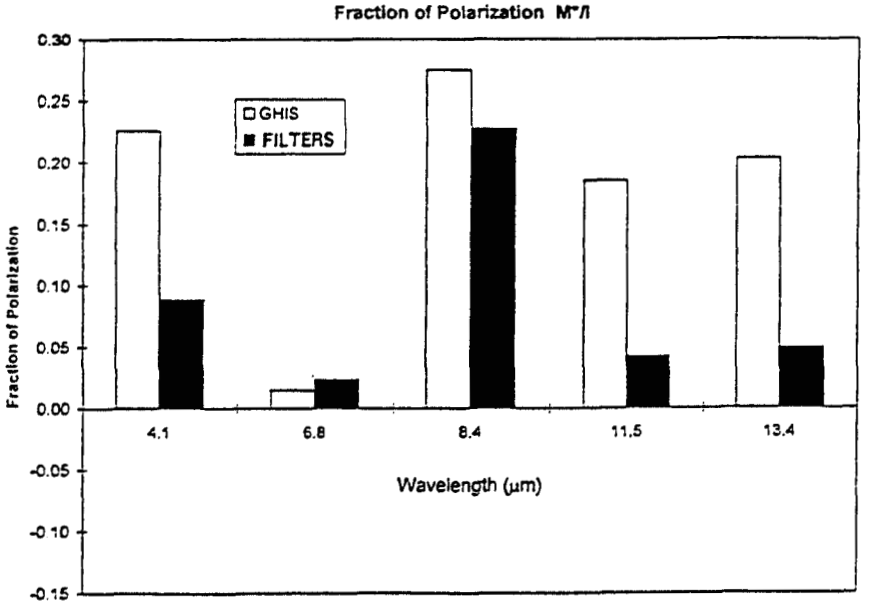

Figure 12: A comparison of the fractional polarizations of the emergent beams from a filter-type and a Michelson-type interferometer/spectrometer (GHIS).

7. Conclusions

Although the GOES Sounder filter wheel infrared radiometer is not designed to extract polarization information from incident scene radiance, it contains components that alter the polarization state of incident radiance. If incident radiance is polarized in a constant and random way, then the Sounder's radiometric accuracy is not affected by its polarization sensitivity. However, variations in the polarization state of incident scene radiance will produce instrument throughput variations that will influence radiomatric accuracy if not corrected by some independent calibration.

The principal contributor to instrument polarization sensitivity is the dielectric protective coating deposited over the scan mirror's reflective metal layer. The average reflectance of this mirror can vary from near 98% at normal incidence to below 75% for angles of 45° or higher. The emittance varies inversely with reflectance and the polarization related properties of the mirror's coating will cause the power radiated by the scan mirror into the instrument to vary with temperature and viewing angle.

Finally, a replacement of the Sounder's filter wheel with a Michelson-type Fourier transform spectrometer will produce a polarization sensitivity that is a function of wavelength and is most pronounced in the longwave channel. Changes in the Stokes vector that describe the radiant beam incident on the detector optics will require a modified instrument calibration procedure to insure continued radiometric accuracy.

8. REFERENCES

1. *Polarization Considerations for Optical Systems,* SPIE Vol. 891, Russell A. Chipman, ed., Los Angeles, CA, 1988.

2. *Polarization Considerations for Optical Systems II,* SPIE Vol. 1166, Russell A. Chipman, ed., San Diego, CA, 1989.

3. *Polarization Analysis and Measurement,* SPIE Vol. 1746, Dennis H. Goldstein and Russell A. Chipman, eds., San Diego, CA, 1992.

4. *Selected Papers on Polarization,* SPIE Milestone Series Vol. MS 23, Bruce H. Billings, ed., Bellingham, WA, 1990.

5. *Selected Papers on Applications of Polarized Light,* SPIE Milestone Series Vol. MS 57, Bruce H. Billings, ed., Bellingham, WA, 1992.

6. R. E. Fuller, R. A. Chipman, J. P. McGuire,Jr., "Bibliography of optical polarization papers", SPIE Vol. 1166, *Polarization Considerations for Optical Systems II,* Russell A. Chipman, ed., San Diego, CA 1989, p. 420-431.

7. P. W. Maymon and R. A. Chipman, "Linear polarization sensitivity specifications for space-borne instruments", SPIE Vol. 1746, *Polarization Analysis and Measurement,* Dennis H. Goldstein and Russell A. Chipman, eds., San Diego, CA, 1992, p. 148-156.

8. G. Hass, J. B. Heaney, and W. R. Hunter, "Front Surface Mirrors from the UV to the IR", in *Physics of Thin Films, Vol. 12,* G. Hass, M. H. Francombe, and J. L. Vossen, eds., Academic Press, New york, 1982, p. 29ff.

9. W. A. Shurcliff, Polarized Light, Harvard University Press, Cambridge, MA, 1962.

10. W. L. Smith, et al., "GHIS - The GOES High-Resolution Interferometer Sounder", *Jour. of Applied Meteorology, Vol. 29, No. 12,* pp. 1189-1203, Dec. 1990.

Improved pointing accuracy using high precision theodolite measurements

Ramuhalli Krishna

ITT Defense & Electronics, Aerospace Communications Division
P.O. Box 3700, Fort Wayne, In 46801

ABSTRACT

Geostationary earth observation satellite applications almost always require high pointing accuracy. The ability to meet very high pointing accuracy , at or below microradian levels, is limited by our ability to measure and correct pointing errors in the laboratory environment. Certain types of pointing errors are invariant over time and appear as fixed pattern over the field of view. These errors may not even be sensed by the servo. Such errors can be measured by other means and corrected through the servo in an open loop manner. This paper describes the method developed to measure the Fixed Pattern Errors (FPE) associated with a servo controlled, two degrees of freedom mirror arrangement by autocollimation of a theodolite. This system has been developed for GOES-8 and above S/C instruments. Several interesting optical phenomena were observed during measurement of the FPE. Mathematical models have been developed to help understand and explain these phenomena. The paper also describes how several numerical techniques were used to simplify the laborious testing by minimizing the number of measurements without compromising pointing accuracy. Fourier Analysis of the test data show that the FPE's are reduced to within +/- 4.5 microradians. The measurement accuracy obtained in these tests are believed to be at least two times better than the measurement accuracy reported so far using theodolites or other similar instruments.

1. INTRODUCTION

1.1 Background

The GOES-8 and above series of spacecraft are three axis stabilized geo-synchronous platforms for Imager and Sounder radiometric instruments devoted for round the clock weather observation. Both Imager and Sounder instruments have identical scan mechanisms with identical servo designs for scan mirror pointing control. However, there are some differences in the operation of the two instruments. The Imager scans the field of View (FOV) at 20 deg/sec in the EW direction and, at the end of the scan line, steps 224 microradians in the north or south direction . The Sounder steps in the EW direction 280 microradians every 0.1 seconds and, at the end of the scan line, steps 1120 microradians in the north or south direction. The Sounder collects radiometric data for 0.075 seconds after a delay of 0.025 seconds following each step. The FOV of the instruments is 23 deg EW and 21 deg NS. The Imager is capable of scanning the full earth disk in about 25 minutes and provides imagery with 16 microradian x 28 microradian pixel size. The Sounder requires about 3 hours to scan the earth full disk and provides images with 280 microradian x 280 microradian pixel size.

1.2 Scanner Mechanism

Fig. 1 shows the scanner part of the instrument (Imager/Sounder) which is set up on the optical bench along with a theodolite to measure scanner pointing accuracy. The scan system consists of a scan mirror attached to a yoke through a shaft and ball bearings at both ends of the shaft(Fig. 1). One end of the yoke carries a DC motor for servo control and the other end carries an Inductosyn for measuring the shaft angle (or the pointing direction of the mirror) which is the EW rotation of the mirror (rotation about 'Y' axis). The yoke with the mirror assembly is rigidly fixed to another shaft (NS shaft) which enables the mirror rotation in the NS direction (rotation about 'X' axis) orthogonal to EW rotation. The NS housing assembly supports NS shaft, NS motor and the NS inductosyn. The yoke is attached to the NS shaft at a 45 deg angle so that the rays of light from the scene will be reflected by the mirror into the telescope and converges on the detectors through an assembly of lenses and mirrors. It should be noted that a rotation of the mirror about the axis causes the scene at the detector to move by twice the rotation of the mirror in the EW direction whereas the rotation about the NS axis generates the same rotation along the NS axis. Thus in

0-8194-2200-2/96/$6.00

order to scan 23 deg (FOV) in the EW direction, the EW shaft moves through only +/-5.75 deg from nadir location. The NS motion is restricted to about -13 deg to +180 deg from nadir.

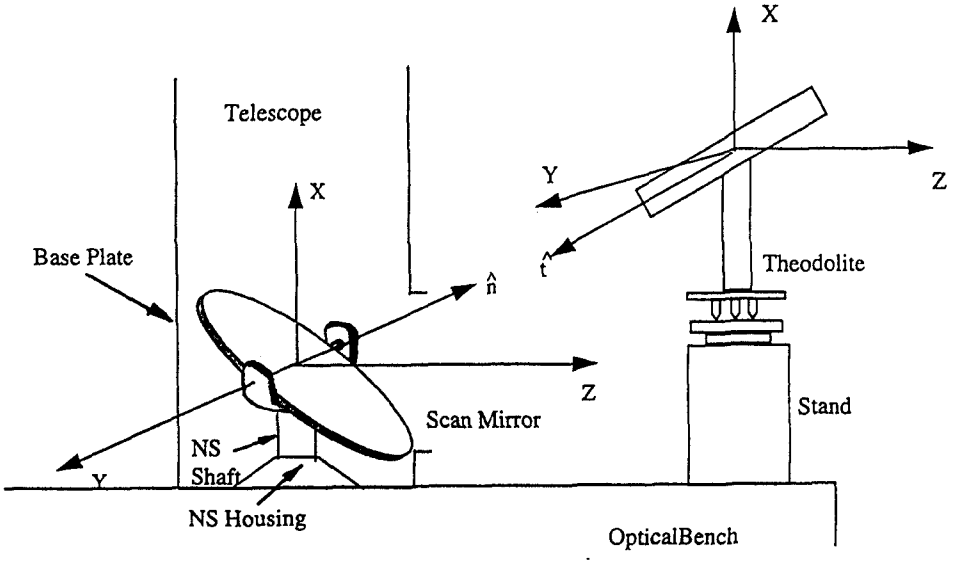

Fig. 1. Imager/Sounder test set up to measure pointing Errors.

The Inductosyn is an analog position encoder manufactured by Farrand Industries. The Inductosyn is graduated into 128 parts over 360 deg of shaft rotation. Thus, each part or a cycle represents 2.8125 deg. Each cycle is further divided into 6136 increments (8 microradians/increment) in the Imager and 2805 increments (17.5 microradians/increment in the Sounder). Approximately half a cycle past the FOV in the EW direction , there are two mechanical stops (one at each side of the FOV) restricting the mirror motion. There is also a mechanical stop half a cycle past the north edge of the FOV of Imager (for the Sounder this is the south edge) and another mechanical stop, approximately 175 deg, past the other edge of the FOV.

1.3 Servo System

NS and EW servo system design are almost identical. A functional block diagram of the servo system is shown in Fig. 2. The scan mirror position as a function of time is computed by scan control from the commanded start/stop addresses. These addresses are updated by a comparator to account for corrections due to four different types of error sources, namely, Image Motion Compensation (IMC), Mirror Motion Compensation (MMC), Orthogonality errors, and Fixed Pattern errors. The IMC/MMC signal is generated by the S/C to correct for orbit drift, effect of mirror motion of one instrument on the other, and instrument thermal deformation. The orthogonality errors result from the non-orthogonality between the NS and EW axes of the scanner. The instrument has an orthogonality correction CCA that provides a signal to correct EW position of the mirror as a function of NS position. The FPE correction CCA (Circuit Card Assembly) contains PROMs with FPE values (Obtained by the test) which are functions of NS and EW addresses and do not change over time.

The fixed pattern errors originate mainly from the Inductosyn. Inductosyns have several mechanical and electrical error sources that are characteristics of each Inductosyn. These errors generally appear as fundamental, in phase and out of phase second harmonics, and fourth harmonics of the 2.8125 deg cycles. These errors do not change over the useful life time of the instrument after the Inductosyns are fixed on the shaft and the Inductosyn drive circuits are tailored. The magnitude of these errors are in the range of 40 microradians mechanical angle, peak to peak. A typical pattern is shown in Fig. 3. Since these errors are not seen by the servo, the FPE correction CCA is designed to correct for the FPE based on measurements made on ground in an openloop manner. The servo system has a bandwidth of approximately 35 Hz. The objective of the servo system is to meet a pointing accuracy of 21 microradians 3 sigma from all error sources (not discussed in this paper). The objective of this paper is to discuss how effectively the FPE and the orthogonality errors can be measured and corrected.

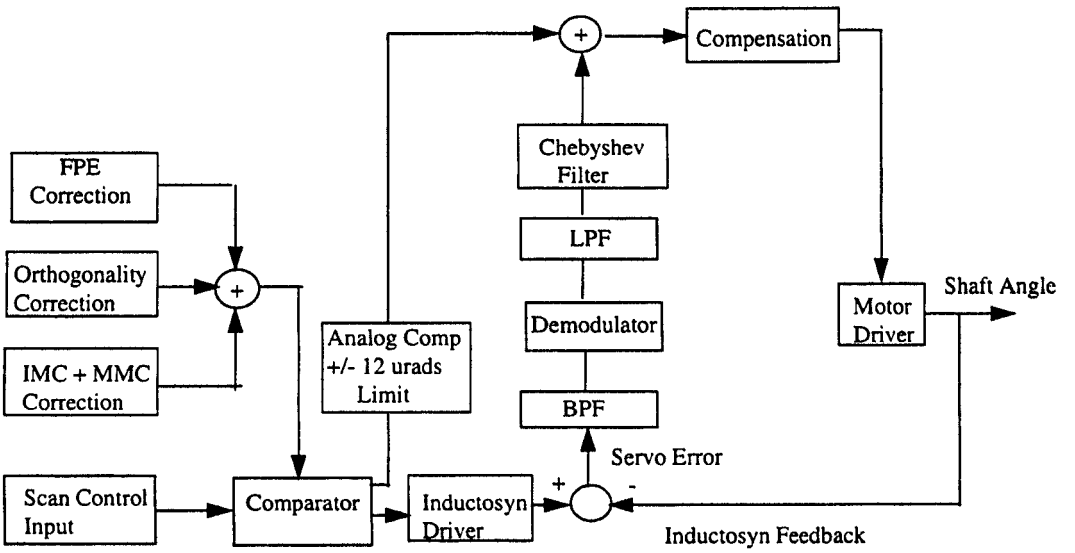

Fig. 2. Functional Block Diagram of the Servo System.

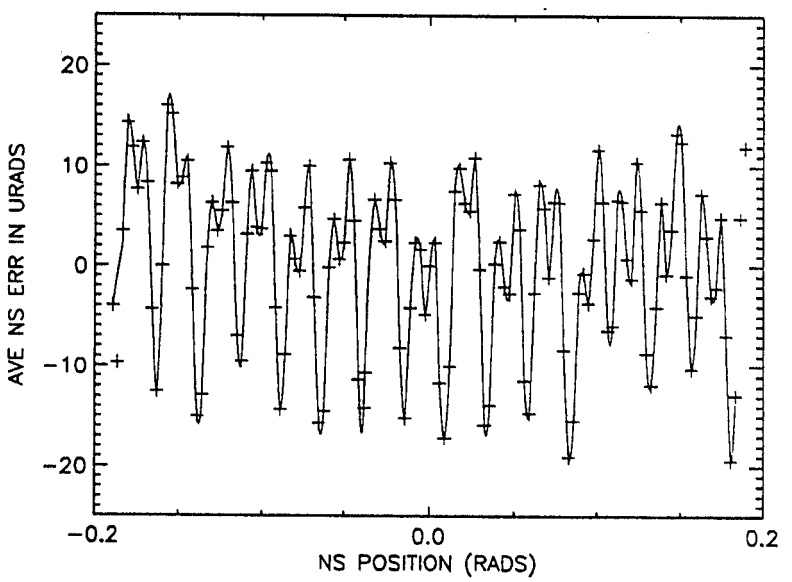

Fig. 3. A Typical Pattern for the NS/EW FPE.

2. DESCRIPTION OF TEST

2.1 Test Method

The test set up (Fig. 1) is used to measure the orthogonality angle between the NS and EW axes of the scanner, the FPE, and to verify pointing errors of the mirror over the full FOV of the instrument. The orthogonality error is measured by aligning the theodolite to the EW axis of the scanner and then measuring the EW errors while traversing in the NS direction. A resistor in the orthogonality compensation CCA is directly tailored to reduce the non-orthogonality angle to within +/- 3 microradians.

The FPE correction CCA consists of approximately 750 addresses for each PROM (NS/EW) . Corresponding to these addresses an equal number of FPE correction values can be blown into the PROMs. Since these measurements are very laborious, it is important to minimize the number of measurements. There are approximately 3.5 cycles in the EW direction and the FPE has the highest frequency at the fourth harmonic of the Inductosyn cycle. Therefore there are about 14 fourth harmonic cycles in the EW direction. By selecting about 10 points per cycle, equally spaced, about 140 measurements need to be taken to measure the FPE accurately. Using these 140 values a smooth fixed pattern error function can be obtained by interpolation (Lagrange's interpolation formula is being used with excellent results[1]). Using this FPE function, the FPE correction values are computed for each location. The FPE compensation method is to first measure FPEs , for both NS and EW axes separately, with PROMs having zero correction values. The interpolated values are then blown into the PROMs . The test is then repeated for about half of the locations in order to minimize the test time. This repeat test verifies that the FPE is properly corrected. The objective is to correct the FPE 's to within +/-4.5 microradians. In order to reduce measurement errors, the measurements are made three times along each axis and an average is taken.

2.2 Theodolite T3000

The instrument used to measure angular positions of the mirror is Leica Heerbrugg T3000 theodolite. This is a high precision theodolite capable of measuring angular positions to an accuracy of +/- 3 microradians. The theodolite consists of a telescope which can rotate about a horizontal axis (to measure elevation angle) and also about a vertical axis (to measure azimuth angle). The elevation angle and the azimuth angle are measured by two separate encoders. The telescope has a built in autocollimation eyepiece with a cross hair. The measurements are taken by manually centering the cross hair on the return image . The encoder readings may be directly read by a computer through the theodolite RS232 port. Each autocollimation takes about 30 seconds on the average for an experienced operator. The theodolite has three foot screws for leveling . These screws are also used for alignment of the theodolite axes to the instrument axes. The theodolite has several built in error compensation very similar to the GOES Imager/Sounder servos. The theodolite has an orthogonality compensation to make the theodolite horizontal and vertical axes orthogonal to each other that may change during shipping and handling. The theodolite also compensates for any errors due to misalignment from the local vertical and any fixed pattern errors due to mechanical inaccuracy during manufacturing. Since it is very difficult to align both instrument and the theodolite to local vertical at the same time , it was decided to turn off the compensation due to nonalignment to local vertical. This also turned off the theodolite fixed pattern errors. However, it was found later that these errors in the selected theodolites were small enough to be ignored. It should be noted that the theodolite measures the angular motion of the shaft/mirror (mechanical angle) and not the optical angle of the mirror. The optical angle for the EW direction is obtained by multiplying the mechanical angle by a factor of 2.

2.3 Test Procedure

The tests are done in a temperature controlled laboratory (23 +/- 5 deg F). Prior to starting the test , the theodolite is calibrated by a procedure recommended by the theodolite manufacturer to minimize the non-orthogonality of the theodolite. The theodolite is then fixed to an optical bench facing the instrument and about a foot away from the scan mirror. The RS232 port is connected to a computer so that the computer reads and stores both elevation and azimuth angles upon a trigger issued by the operator. The scan mirror is positioned at its nadir location and at approximately +/-10 deg (NS) from nadir location successively and at each location the elevation errors are minimized by adjusting the theodolite feet. This aligns the theodolite vertical axis to the instrument vertical axis. Next, the orthogonality correction test is performed. The FPE test is then performed with a zero correction FPE PROM.

The first attempt to measure FPE resulted in a pattern similar to shown in Fig. 3, but with a slope of almost 30 microradians peak to peak. The repeat test with the measured and interpolated values in the PROMS showed that the FPE's were reduced to within +/-5 microradians, but also showed a slope different from the previous test. Several repetitions of the test showed that the slope was probably due to alignment. The alignment process did not make the vertical axis of the theodolite parallel to the vertical axis of the scanner. Also, several small but different patterns were noticed that could not be visualized or explained. Hence, a mathematical model has been developed to understand the optical phenomena.

3. MATHEMATICAL MODEL

3.1 Mathematical Model Development

Fig . 4 shows the body fixed coordinate system (x_m, y_m, z_m) for the scan mirror along with the inertial coordinate system X,Y,Z. ' $\hat{n}$ ' is a unit vector normal to the plane of the mirror. Another unit vector, $\hat{t}$, is defined along the line of sight (LOS) of the theodolite. The rotation of the mirror in the inertial co-ordinate system may be represented by the following transformation. Rotate the inertial axes X, Y, Z through an angle, ϕ , to get X, Y', Z' axes. Rotate the X, Y', Z' axes about Y' axis through an angle, θ, to get X'', Y', z_m axes. Finally rotate X'', Y', z_m axes about z_m axis through an angle, ψ, to get the mirror fixed coordinate system x_m, , y_m , z_m .

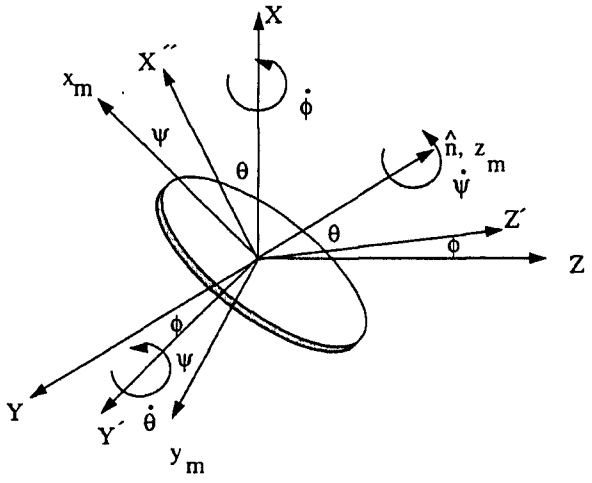

Fig. 4. Euler angle transformation between the mirror fixed coordinates and the inertial Reference System . [2]

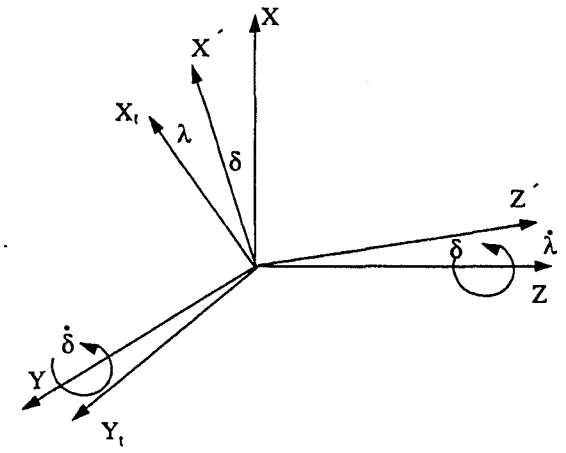

Fig. 5. Misalignment between the theodolite fixed coordinates and the inertial reference system.

These transformations may be represented by,[2]

$$\begin{bmatrix} X \\ Y \\ Z \end{bmatrix} = \begin{bmatrix} 1 & 0 & 0 \\ 0 & C_\phi & -S_\phi \\ 0 & S_\phi & C_\phi \end{bmatrix} \cdot \begin{bmatrix} C_\theta & 0 & S_\theta \\ 0 & 1 & 0 \\ -S_\theta & 0 & C_\theta \end{bmatrix} \begin{bmatrix} C_\psi & -S_\psi & 0 \\ S_\psi & C_\psi & 0 \\ 0 & 0 & 1 \end{bmatrix} \begin{bmatrix} x_m \\ y_m \\ z_m \end{bmatrix}$$

where, the notation $S_\theta = \sin\theta$, $C_\theta = \cos\theta$, etc. has been used. Matrix multiplication gives:

$$\begin{bmatrix} X \\ Y \\ Z \end{bmatrix} = \begin{bmatrix} C_\theta C_\psi & -C_\theta S_\psi & S_\theta \\ S_\theta S_\phi C_\psi + C_\phi S_\psi & -S_\theta S_\phi S_\psi + C_\phi C_\psi & -S_\phi C_\theta \\ -S_\theta C_\phi C_\psi + S_\phi S_\psi & S_\theta C_\phi S_\psi + S_\phi C_\psi & C_\theta C_\phi \end{bmatrix} \begin{bmatrix} x_m \\ y_m \\ z_m \end{bmatrix}$$

Representing the above transformation by matrix A, the equation can be rewritten as:

$$\begin{bmatrix} X \\ Y \\ Z \end{bmatrix} = [A] \begin{bmatrix} x \\ y \\ z \end{bmatrix} \tag{1}$$

In the test set up , 'θ' corresponds to EW motion and 'ϕ' corresponds to NS motion of the mirror. Let us assume that the misalignment angle between the inertial reference system X, Y, Z and the theodolite fixed co-ordinate system x_t, y_t, z_t be represented by δ and λ as shown in the Fig. 5 . 'δ' represents the elevation angle and 'λ' represents the azimuth angle misalignments. The inertial co-ordinate system may be related to the theodolite coordinate system by the following .

$$\begin{bmatrix} X \\ Y \\ Z \end{bmatrix} = \begin{bmatrix} C_\delta & 0 & S_\delta \\ 0 & 1 & 0 \\ -S_\delta & 0 & C_\delta \end{bmatrix} \begin{bmatrix} C_\lambda & -S_\lambda & 0 \\ S_\lambda & C_\lambda & 0 \\ 0 & 0 & 1 \end{bmatrix} \begin{bmatrix} x_t \\ y_t \\ z_t \end{bmatrix}$$

The relation between the inertial and the misaligned theodolite coordinate system may now be related as,

$$\begin{bmatrix} X \\ Y \\ Z \end{bmatrix} = [B] \begin{bmatrix} x_t \\ y_t \\ z_t \end{bmatrix} \tag{2}$$

where

$$[B] = \begin{bmatrix} C_\delta C_\lambda & -C_\delta S_\lambda & S_\delta \\ S_\lambda & C_\lambda & 0 \\ -S_\delta C_\lambda & S_\delta S_\lambda & C_\delta \end{bmatrix}$$

The theodolite reference system x_t, y_t, z_t may also be related to the theodolite fixed system by the same order of rotation used in deriving equation (1) above. Specifically, rotating axes x_t, y_t, z_t about x_t through an angle α, rotating the resultant coordinate system about the new y_t axis through an angle β, and finally rotating the coordinate system about z_t through an angle γ to get the theodolite fixed coordinate system x_t, y_t, z_t.

$$\begin{bmatrix} X_t \\ Y_t \\ Z_t \end{bmatrix} = [C] \begin{bmatrix} x_t \\ y_t \\ z_t \end{bmatrix} \tag{3}$$

where [C] is obtained by replacing the angles θ, ϕ, ψ in [A] by α, β, and γ respectively. The relationship between the theodolite fixed coordinate system and the inertial reference system is expressed as,

$$\begin{bmatrix} X \\ Y \\ Z \end{bmatrix} = [B][C] \begin{bmatrix} x_t \\ y_t \\ z_t \end{bmatrix} \tag{4}$$

Multiplication of [B][C] gives:

$$[B]\,[C] = \begin{bmatrix} C_\delta C_\lambda C_\beta C_\gamma - C_\delta S_\gamma (S_\alpha S_\beta C_\gamma + C_\alpha S_\gamma) & -C_\delta C_\lambda C_\beta S_\gamma - C_\delta S_\gamma (C_\alpha C_\gamma - S_\alpha S_\beta S_\gamma) & C_\delta (C_\lambda S_\beta + S_\lambda S_\alpha C_\beta) + S_\delta C_\beta C_\alpha \\ + S_\delta (S_\alpha S_\gamma - C_\alpha S_\beta C_\gamma) & + S_\delta (C_\alpha S_\beta S_\gamma + S_\alpha C_\gamma) & \\ S_\lambda C_\beta C_\gamma + C_\lambda (S_\alpha S_\beta C_\gamma + C_\alpha S_\gamma) & -S_\lambda C_\beta S_\gamma + C_\lambda (C_\alpha C_\gamma - S_\alpha S_\beta S_\gamma) & S_\lambda S_\beta - C_\lambda S_\alpha C_\beta \\ -S_\delta C_\lambda C_\beta C_\gamma + S_\delta S_\lambda (S_\alpha S_\beta C_\gamma + C_\alpha S_\gamma) & S_\delta C_\lambda C_\beta S_\gamma + S_\delta S_\lambda (C_\alpha C_\gamma - S_\alpha S_\beta S_\gamma) & C_\delta C_\alpha C_\beta - S_\delta C_\lambda S_\beta - S_\delta S_\lambda S_\alpha C_\beta \\ + C_\delta (S_\alpha S_\gamma - C_\alpha S_\beta C_\gamma) & + C_\delta (C_\alpha S_\beta S_\gamma + S_\alpha C_\gamma) & -S_\delta (C_\lambda S_\beta + S_\lambda S_\alpha C_\beta) + C_\delta \end{bmatrix}$$

Since the theodolite is autocollimated at all positions of the mirror, the line of sight vector , $\hat{n}$, of the theodolite is always along the unit vector, $\hat{n}$ normal to the plane of the mirror and opposite in direction. The unit vectors , $\hat{n}$ and $\hat{t}$ are represented in the respective body fixed coordinate systems as

$$\hat{n} = [0 \quad 0 \quad 1]^T \quad \text{and} \quad \hat{t} = [0 \quad 0 \quad -1]^T$$

With this selection of unit vectors $\alpha = \phi + \pi$. Using these vectors in Eqs. (1) and (4) and equating the resulting matrices we get,

$$\begin{aligned} S_\theta &= -(C_\delta C_\lambda S_\beta + C_\delta S_\lambda S_\alpha C_\beta + S_\delta C_\beta C_\alpha) \\ S_\phi C_\theta &= S_\lambda S_\beta - C_\lambda S_\alpha C_\beta \\ C_\theta C_\phi &= -(C_\phi C_\delta C_\alpha C_\beta - S_\delta C_\lambda S_\beta - S_\delta S_\lambda S_\alpha C_\beta) \end{aligned} \tag{5}$$

'δ' and 'λ' are the misalignment angles between the theodolite vertical axis and the instrument vertical axis. By commanding the mirror to extreme NS locations and minimizing the EW error by adjusting the theodolite feet it is possible to reduce 'λ' to within +/- 3 microradians. Angle 'δ' can not be minimized by this method. Thus , if the alignment is made carefully, 'λ' may be assumed to be zero. The set of equations (5) may then be written as,

$$S_\theta = -C_\delta S_\beta - S_\delta C_\alpha C_\beta \tag{6}$$

$$S_\phi C_\theta = -S_\alpha C_\beta \tag{7}$$

$$C_\theta C_\phi = S_\delta S_\beta - C_\delta C_\alpha C_\beta \tag{8}$$

From Equations (6) and (8) we get,

$$S_\beta = S_\delta C_\theta C_\phi - C_\delta S_\theta \tag{9}$$

When the mirror is at its nominal reference position, $\phi = 0$.

$$\therefore \ \beta = \delta - \theta$$

This shows that β has the opposite sign of θ and differs by δ which is consistent with the geometry of the test set up.

Eliminating β from Eqs. (6) and (8) and using Eq. (7) we get the expression for α in terms of ϕ and θ.

$$\text{Tan}\,\alpha = \frac{S_\phi C_\theta}{(S_\delta S_\theta + C_\delta C_\theta C_\phi)} \qquad (10)$$

Eqs. (9) and (10) give solutions for α and β. In order to find errors associated with the misalignment angle δ, the measurement errors are defined as,

NS error = $(\alpha - \phi) - (\alpha - \phi)_{ref}$ and EW error = $(\beta - \theta) - (\beta - \theta)_{ref}$

The reference locations for theodolite measurements are taken when the mirror is in the nadir position. At nadir position $\phi = 0$ and $\theta = 45$ degrees.

From Eq. (10) $\alpha = 0$ when $\phi = 0$. Therefore, NS error = $\alpha - \phi$.

Substituting $\beta = \delta - \theta$ for $(\beta - \theta)_{ref}$, EW error = $(\beta + \theta - \delta)$

3.2 Analysis:

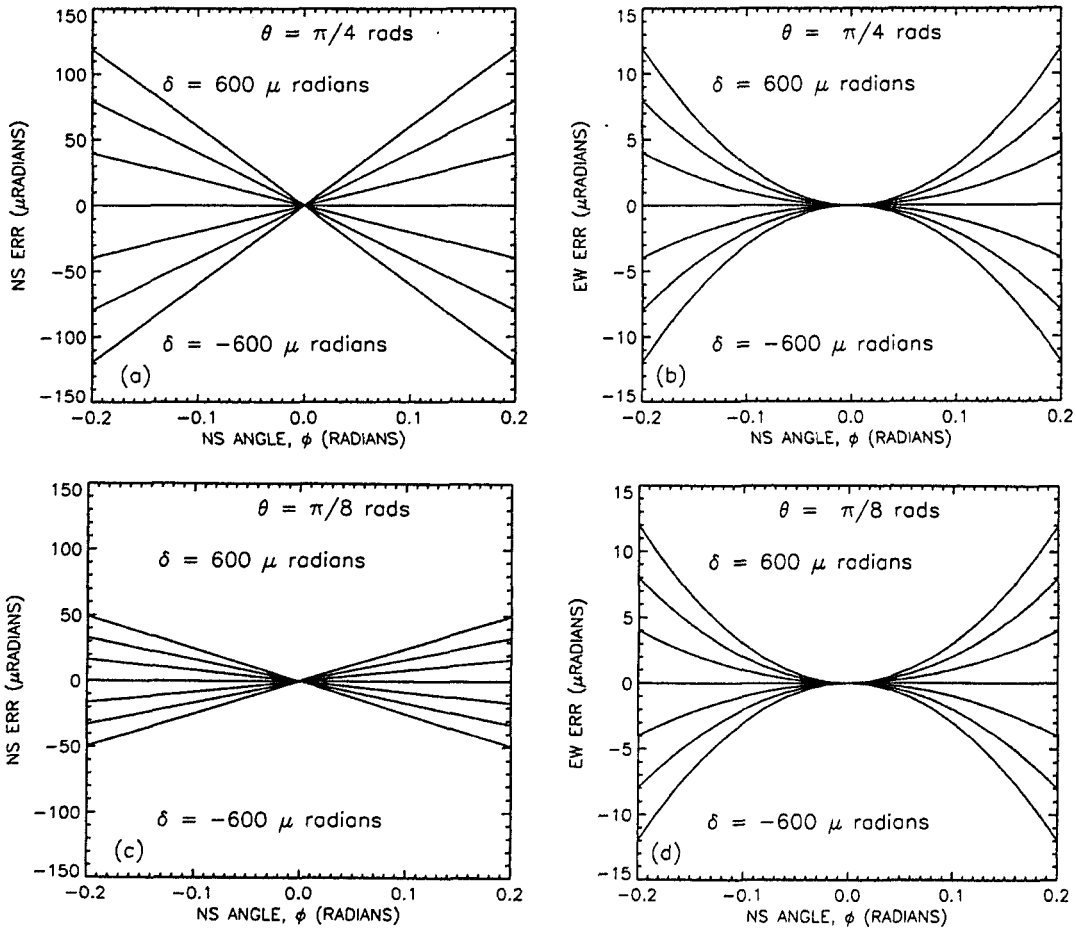

Fig. 6. NS and EW measurement errors as a function of NS position..

Figs. 6(a) and 6(b) show NS and EW errors as a function of NS angle, respectively, at the EW nominal angle of 45 degrees as δ is changed from -600 microradians to + 600 microradians in steps of 200 microradians. It is clear that there is a systematic NS

error, linearly proportional to the misalignment angle δ. This error is as much as 40 microradians at $\phi = 0.2$ rads, for $\delta = 200$ microradians. This misalignment also causes a non-linear error in the EW positions as a function of NS angle(Fig. 6b). Figs. 6(c) and 6(d) show corresponding results for $\theta = 22.5$ degrees. The NS error has reduced to 50 microradians from 120 microradians for the case of $\delta = 600$ microradains. Thus, the NS error as a function of NS angle is also a function of θ, but is nonlinear. The EW error as a function of EW angle (Fig. 6b) is independent of θ. Figs. 7(a) and 7(b) are obtained for the case of $\theta = (\pi/4) - 0.1$ rad corresponding to an extreme EW location. It may be noted that NS error as a function of NS position or the EW error as a function of EW position denote the FPE . The EW error as a function of NS position or NS error as a function of EW position may be referred to as orthogonality error due to misalignment.

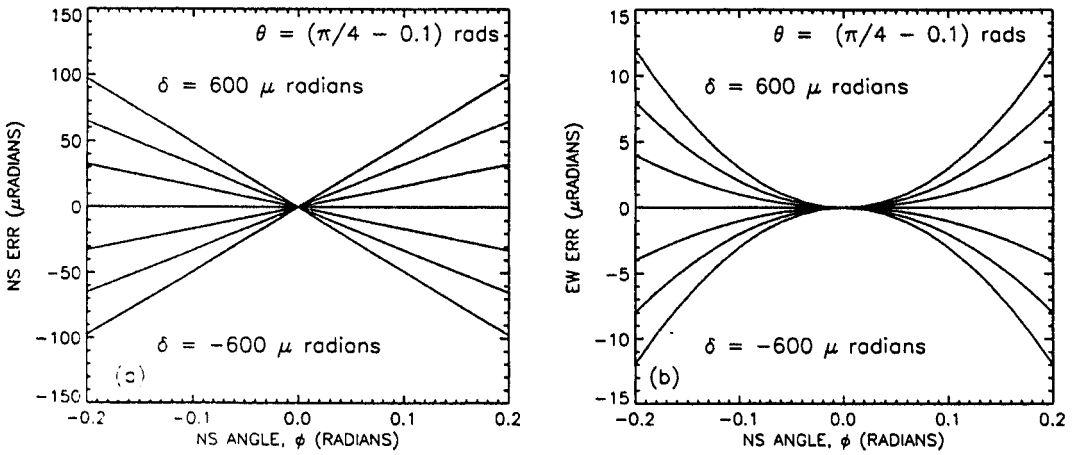

Fig. 7. NS and EW measurement errors as a function of NS position for $\theta = (\pi/4 - 0.1)$ rads.

Figs. 8a and 8b show NS and EW errors as a function of EW position for the extreme NS position $\phi = 0.2$ rads. Fig. 8b shows the effect of δ on EW FPE. Fig. 8a shows another interesting phenomena. The NS error changes at a given NS position , if the EW position changes. This is also due to the effect of δ and not the orthogonality between the NS and EW axes.

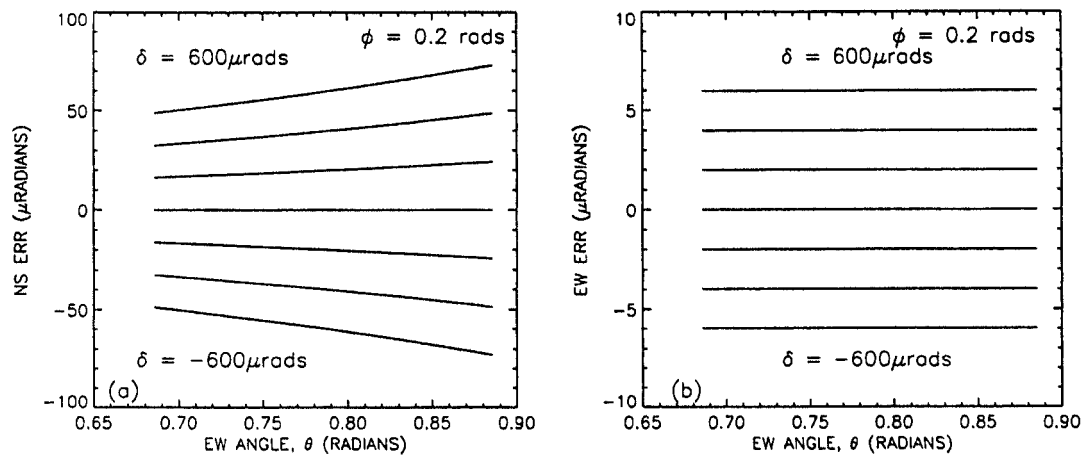

Fig. 8. NS and EW measurement errors as a function of EW position.

The mathematical analysis thus establishes that the measurement errors could be tens of microradians due to the misalignment angle, δ. This analysis has been very helpful in explaining test data (Section 4).

4. TEST RESULTS

Fig. 9(a) shows the first attempt to correct for FPE in the NS direction. The slope in the residual errors is clearly due to the misalignment , δ. This was confirmed by moving the theodolite elevation angle approximately equal to 180 microradians (refer to Fig. 7(a) for explanation) after NS alignment and repeating the test. The test data (Fig. 9b) showed no slope. There was no appreciable change in EW FPE before or after correcting for the misalignment . Also, the EW FPE has not shown any slope in any of the test data. A procedure has been developed to minimize δ in a similar way as part of the initial test set up for the theodolite. With this modified test set up, the following results were obtained.

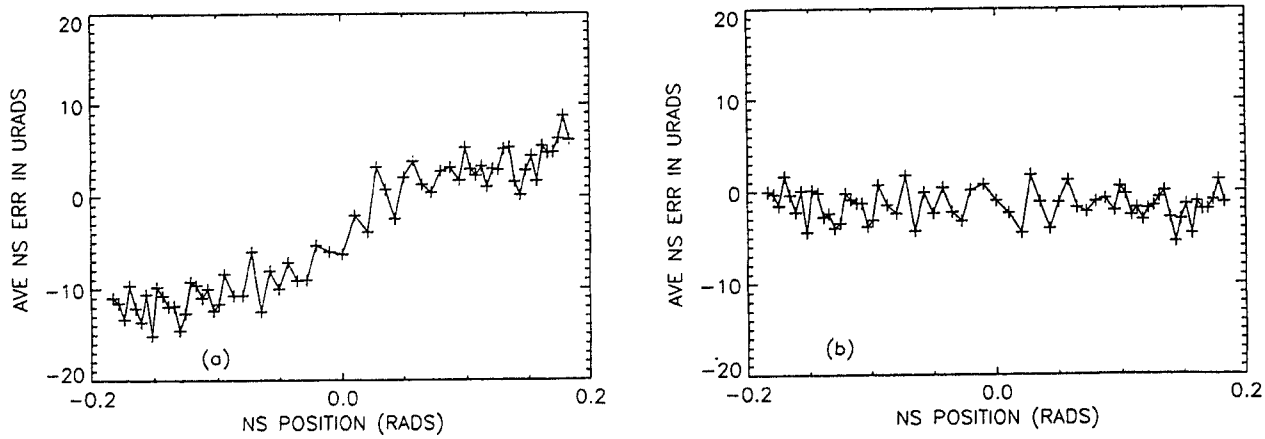

Fig. 9. NS Fixed pattern errors.

Another phenomena that has been understood recently, after the model was well developed, is shown Fig. 10(a) and 10(b). The data is collected over 20 locations which are off NS and EW axes. Originally it was thought the spike seen at the extreme left and right were due to residual non-orthogonality effect. If we look at the plot carefully, we can see a slope of about -12 microradians in the NS plot. This is because the δ minimization process was not carefully done for this test. The total shift may also be a combined effect of misalignment and the non-orthogonality. This is yet to be verified.

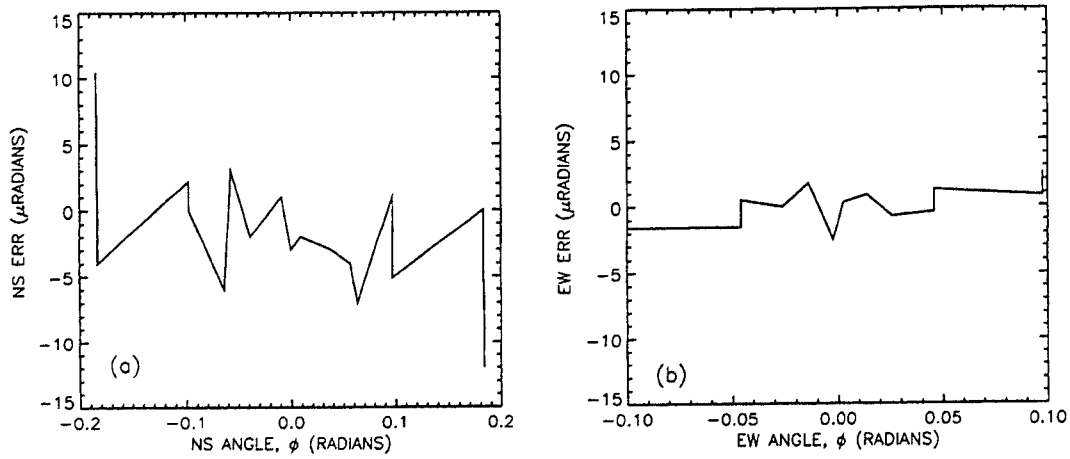

Fig. 10. Measurement errors over selected points over the full FOV.

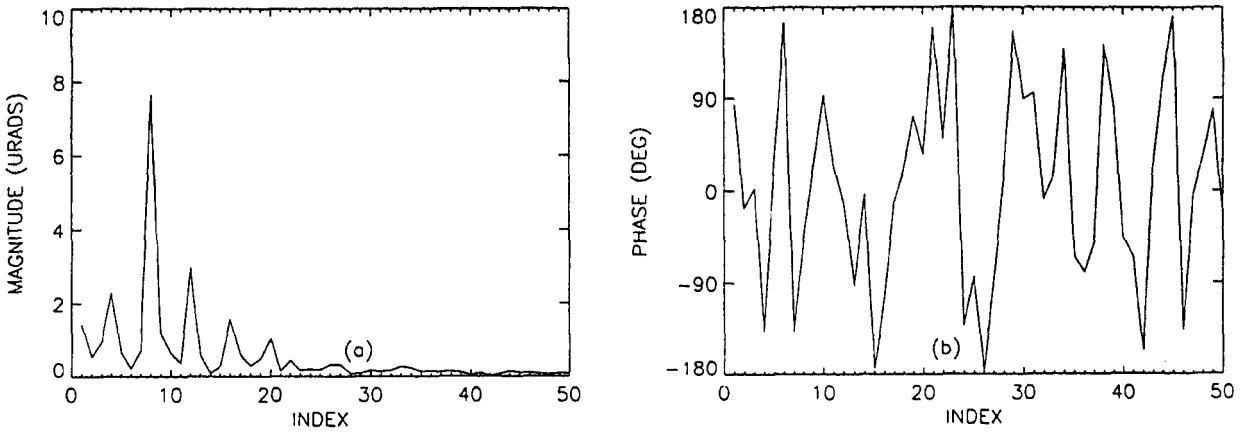

Fig. 11. FFT of a residual FPE for a special case.

Interesting results are found from the test even after having run this test a number of times. In one such case , the residual FPE's was obtained to be within +/- 4.5 microradians. The test was repeated after the instrument went through a vibration test. The residual FPE's were found to be about 25 microradians. An FFT was run on this data and the FFT was plotted (Fig. 11a, the FPE function contained data over 4 inductosyn cycles). The magnitude plots show that the errors were mainly of the second harmonic of the Inductosyn. A corresponding phase plot (Fig. 11b) showed that the phase at this frequency was -90 deg. This pointed towards a component change in the Sin/Cos drive of the Inductosyn. It was later found that a component had been replaced in the Sin/Cos drive CCA with a component of a slightly different value.

5.0 CONCLUSIONS

The mathematical analysis appears to explain all the phenomena associated with the test data. It has been shown analytically that the misalignment angle, δ , is the primary cause of most of the optical phenomena in the test data. The misalignment is caused by the fact that the scan mirror has a 45 deg tilt with respect to NS axis of rotation. The test results show that the static measurement accuracy that can be achieved is better than 4.5 microradians mechanical angle. This is 2 to 4 times better than reported previously[3]. Use of interpolation technique has made this possible. Use of a wide field collimator along with a well defined target has been proposed to measure the pointing accuracy even better (3 to 4 microradians optical angle) in a dynamic mode with less cost and time.

6. ACKNOWLEDGMENTS

The work reported here has been done under the GOES Project (NOAA/NASA Contract to ITT). I extend my appreciation to every member of GOES test team for their patience in doing these tests and to Systems Engineering , especially to Richard Hertel for encouraging me to write this paper.

7. REFERENCES

1. C.R. Wylie, *Advanced Engineering Mathematics*, McGraw Hill, New York,1982.
2. H. Goldstein, *Classical Mechanics*, Addison Wesley, Reading, Ma,1980.
3. W.L. Eichhorn, "Optical alignment measurements at Goddard Space Flight Center," Applied Optics, Vol. 21, No. 21, pp 3891-3895, Nov. 1982.

On-orbit determination of focal plane detector positions

James J. Shea

Swales & Associates, Inc.
5050 Powder Mill Road, Beltsville, MD 20705

1. ABSTRACT

Post Launch Tests on the GOES satellite cameras called for determination of the positions of various imaging detectors. The GOES spacecraft's two cameras, the imager and sounder, are both scanners that use focal plane arrays. The below method determines their detectors' relative positions by recording detector outputs as the edge of the moon drifts past their instantaneous fields of view (IFOVs). While this method works well with simulated data, it is still experimental and is still being tested with flight data.

Keywords: coregistration, colocation, focal plane arrays (FPA), positioning, image registration

2. OBJECTIVE

For the GOES 8 check-out, this test was used to locate the position of each of the imager's side one infrared channel detectors with respect to the center of the visible array. The approach is to stare at the moon, allow the moon's edge to drift past the positions of the detectors' IFOVs, and use the different edge transitions to determine the detectors' positions[1].

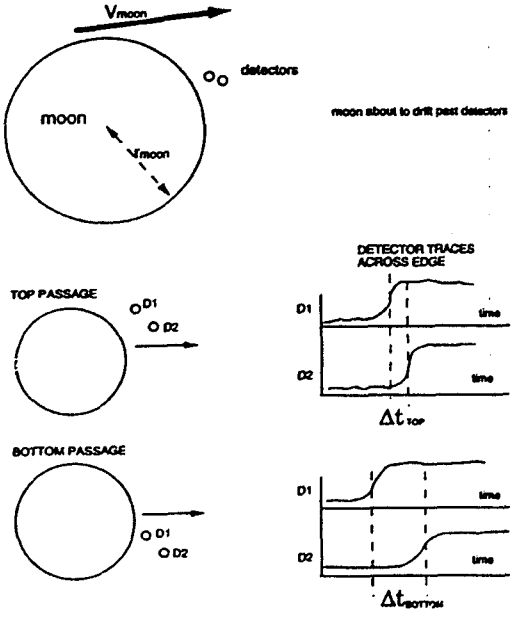

Figure 1. General approach to detector coregistration

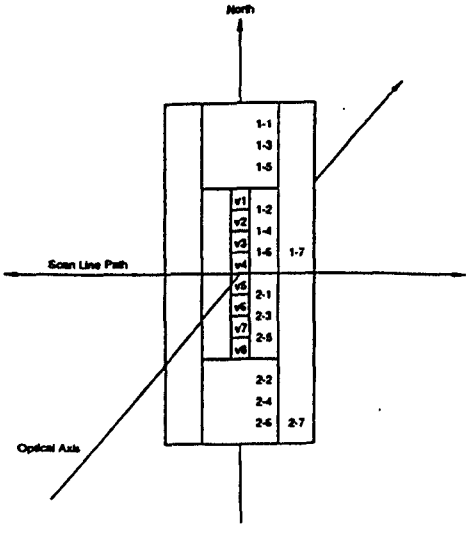

Figure 2. Imager focal plane

0-8194-2200-2/96/$6.00

To determine a detector's position, one passage across an edge is not sufficient. To uniquely colocate a pair of detectors, two independent passes must be made. The general approach is pictorially described in Figure 1.

3. BACKGROUND

The eighth Geostationary Operational Environmental Satellite (GOES) was launched in April, 1994. It has two imaging cameras, an imager (four infrared and one visible channel) and a sounder (eighteen IR and one visible channel). They both use a scan mirror that sweeps vertically (north/south) and horizontally (east/west). They both have focal plane arrays, with anywhere from one to eight detectors per channel. See Figure 2 for the imager's focal plane array.

4. TEST PROCEDURE

Moon sightings must be planned when the moon enters the instrument's field of view. The moon must offer a sharp, lit edge, so phases such as the new moon are not useful. Further, the test operator must see to it that the phase is such that the moon's drift brings the detectors from space onto the edge. If the other side of the moon is the lit edge, the detectors should stare onto the moon first and look for the edge as it trails off. Since the moon travels west to east in the instrument's field of view, this means that if the east side is lit, then a stare in front of the moon will allow the detectors to see space then a sharp transition to the lit edge. If however, the moon is lit on the west side, the detectors will see a sharp transition only from staring at the moon itself and waiting for the limb/space edge to drift into view.

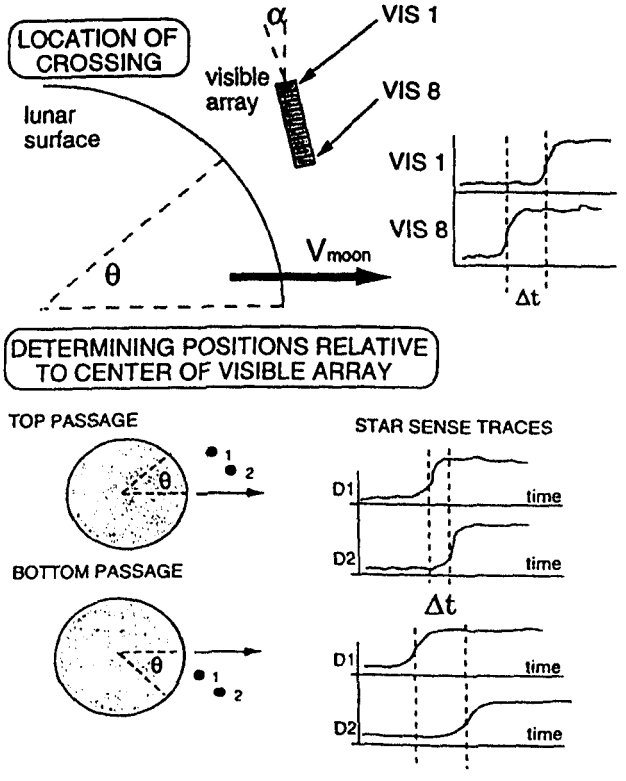

Figure 3. Data collection to determine limb crossing location and detector positions

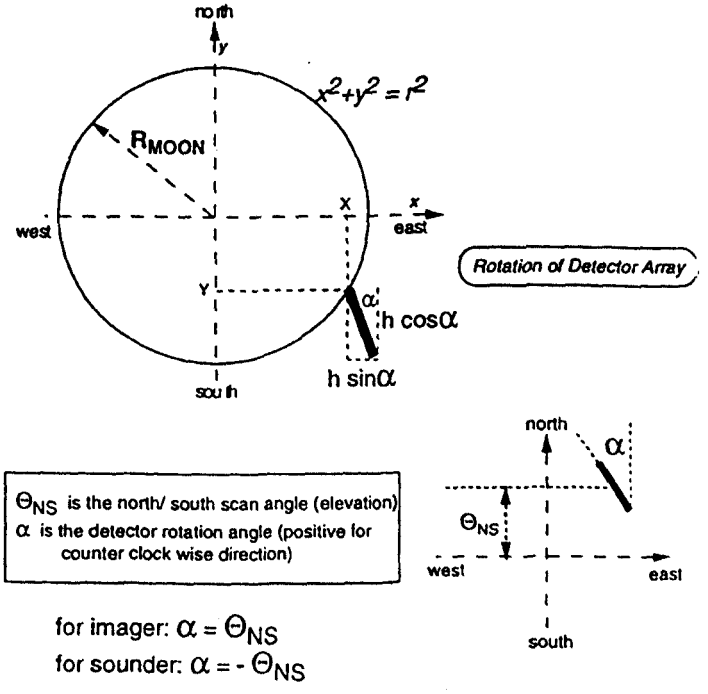

Figure 4. Origin moon circle and detector rotation

After an appropriate moon sighting has been chosen, the operator must decide at which point on the moon's limb he wishes to observe. It is best to look for crossings above and below the lunar equator. In this way, the delta times are as different as possible and allow for better accuracy. It is best to avoid both the equator (since the surface is too flat) and the poles (which produce great time differences and risk having a detector miss the limb entirely - a scenario that has occurred). The scanning coordinates and the limb crossing position can be scheduled by an OATS calibration routine. The accuracy with which the limb position can be placed is sufficient for this data collection procedure, but a more accurate determination of the limb crossing position must be made analytically once the data are available.

Finally, the analyst must have:

- the satellite/moon distance (which varies by as much as ten percent over two weeks' time),
- the relative velocity of the moon with respect to the geostationary satellite,
- some nominal information regarding the reference detector - for the GOES application, the reference detector was the center of the visible array, thus certain parameters of the array (dimensions and orientation) have to be assumed, and
- the position of the moon in the instrument's field of view.

5. TECHNIQUE FOR DETERMINING THE DETECTOR POSITION

The actual determination of the detector position occurs in two steps. The first step determines where on the moon's limb the center of the visible array the crossing occurred. The second step is to use the knowledge of the crossing position and the above parameters to solve for the detector position with respect to the center of the visible detector array.

5.1 Limb crossing position

The first step, determining the position on the moon's limb where the visible array actually crossed, can be performed by looking at the time difference between edge crossings for the top detector of the visible array (vis #1) and the bottom detector (vis #8). See Figure 3. Given traces from visible detector one and detector eight, an appropriate edge crossing is determined for each, and the time difference between them, Δt, is determined by subtraction. This piece of information, together with the parameters listed above, is sufficient to fix where on the moon the center of the visible array crossed.

a) let the time that the reference detector crosses the origin be $t_0 = 0$. Consider a circle representing the moon at $t_0 = 0$. The equation of this circle is $x^2 + y^2 = r^2$, where r is the radius of the moon in angular coordinates, x and y being respectively east/west and north/south positions, all in microradians with respect to the spacecraft. See Figure 4.

b) it follows that the reference detector is somewhere on this circle. If the particular stare is a "top passage" (*i.e.* in the northern hemisphere of the moon), then the reference detector can be said to be on the semicircle $y = \sqrt{r^2 - x^2}$ for $x > 0$. For a bottom passage (southern hemisphere), the reference detector is situated on the semicircle $y = -\sqrt{r^2 - x^2}$ where $x > 0$. The middle diagram of Figure 3 shows an array making a bottom passage.

c) it also follows that for every possible point (x_1, y_1) which may be the location of the top detector (visible detector #1), there is another point (x_8, y_8) which is the position of the bottom detector (visible detector #8). The distance between the detectors is h, where h is the height of the detector array. However, their IFOVs are not necessarily separated in the north/south direction by a distance h. This is because the projection of the focal plane array into space is rotated by an amount that depends on the north/south scan angle. See the bottom of Figure 4.
For the imager, a detector array that is looking at a point having a vertical angle Θ_{NS} is rotated counterclockwise by an angle equal to this north/south scan angle $\alpha = \Theta_{NS}$. (The sounder rotates

in the opposite sense.) Thus the bottom detector is $h \sin\alpha$ to the east, $h \cos\alpha$ to the south of the top detector. If the position of the top detector is somewhere on the origin-centered "moon circle" of part (b), the bottom detector is somewhere on the circle shifted by $(h \sin\alpha, -h \cos\alpha)$, or along the top circle in Figure 5:

$$(x - h\sin\alpha)^2 + (y + h\sin\alpha)^2 = r^2. \tag{1}$$

d) after time Δt, the bottom detector is, by definition, somewhere on the moon's edge. Also, the moon circle has moved a distance $v_x\Delta t$ in the east/west direction, $v_y\Delta t$ in the north/south direction. The equation of this displaced circle containing the bottom detector is that of a circle of radius r shifted by $(v_x\Delta t, v_y\Delta t)$:

$$(x - v_x\Delta t)^2 + (y - v_y\Delta t)^2 = r^2. \tag{2}$$

See the bottom of Figure 5. For a top moon passage, the positive semicircle for $x > 0$ describes the solution set for the bottom detector's crossing, for the bottom passage, the negative semicircle is taken.

e) the bottom detector's position at $t = \Delta t$ is somewhere on both the semicircle from Eq. (1) and the $t=0$ semicircle from Eq. (2). Since they both describe the same position in the same reference frame, their solution yields the unique coordinate position: See the bottom of Figure 5. Solving simultaneously:

$$\text{from (1): } y = -\sqrt{r^2 - (x - h\sin\alpha)^2} - h\cos\alpha \tag{3}$$

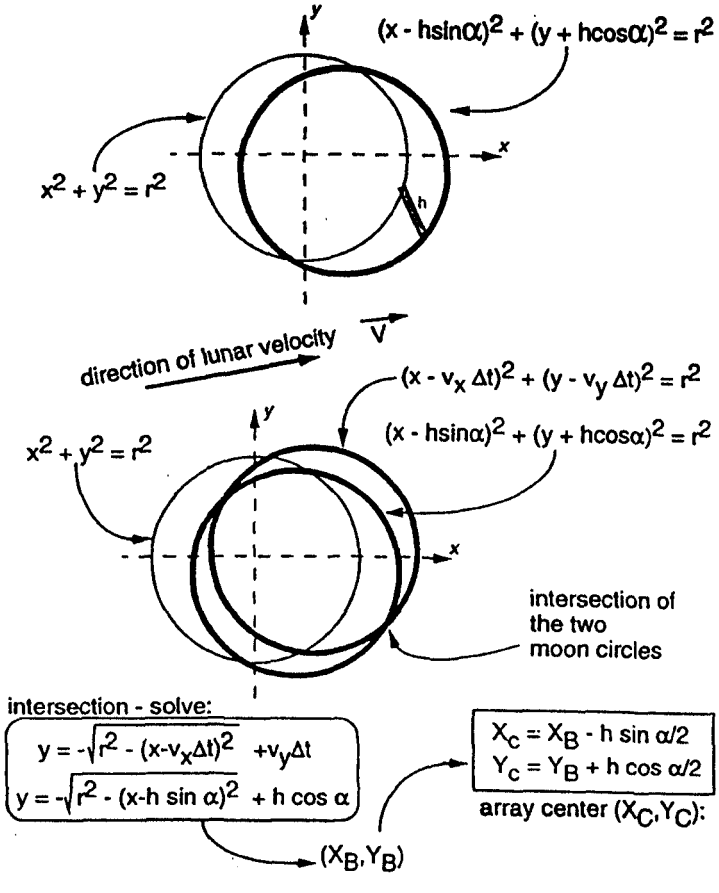

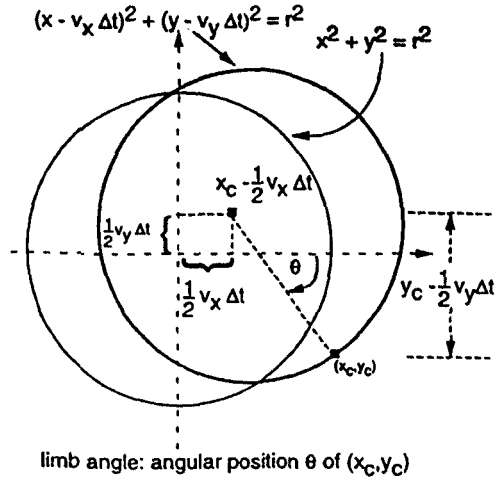

Figure 5. (left) Solving "moon circles" for visible array crossing point.

Figure 6. (above) Solving for the limb angle

$$\text{from (2): } y = -\sqrt{r^2 - (x - v_x\Delta t)^2} + v_y\Delta t \qquad (4)$$

yields x_g, and knowing x_g, one finds y_g. This is the intersection of the solid circles in Figure 5.

f) it remains to find the position of the center of the array, (x_c,y_c), (the eventual reference point for the channel detectors) through simple geometry:

$$x_c = x_g - \tfrac{1}{2} h \sin\alpha \qquad (5)$$

$$y_c = y_g + \tfrac{1}{2} h \sin\alpha \qquad (6)$$

g) the final step is to use (x_c,y_c) to find the limb angle, θ, the "lunar latitude" angle describing where the center of the visible array crosses. One can not simply say $\tan\theta = y_c / x_c$ because these values are referenced to the *t=0* origin but are not on the *t=0* moon circle. See Figure 6. (Another way of looking at it is that $x_c^2 + y_c^2 \neq r^2$ so they can not be used directly to find the lunar angle.) Assume that the time from the top detector crossing to the center of the array crossing is one half of Δt. The moon has then moved a distance $\tfrac{1}{2}v_x\Delta t$ to the east, $\tfrac{1}{2}v_y\Delta t$ to the north. Subtracting these distances from (x_c,y_c) allows us to determine the limb angle:

$$\tan\theta = \frac{y_c - \frac{1}{2}v_y\Delta t}{x_c - \frac{1}{2}v_x\Delta t} \qquad (7)$$

5.2 Position of the channel detector

The above steps for determining the angle at which the center of the visible array crosses the lunar limb have to be implemented for each edge crossing. Despite the fact that the OATS operator (person responsible for orbit and attitude tracking) may schedule a passage at, for instance, -25° (*i.e.* 25° latitude in the moon's southern hemisphere), the actual angle at which the array crosses may be quite different.

With the position of the array at the crossing known, one may now look at the traces from the channel detectors. To colocate a given detector, one considers two passages, a top and a bottom, the limb angle for each, and the trace for the particular detector from each passage. The steps to implement the procedure are as follows:

a) calculate the Δt values. This time, the Δt for a particular detector for a particular passage is the time difference between the crossing of the center visible array and the crossing of the IR detector. See Figure 7. Let Δt be positive if the detector crosses after the visible array; thus a Δt of, for instance, -0.8 seconds means that the IR channel detector crossed 0.8 seconds before the visible array. There will be a Δt_T for the top passage and a Δt_B for the bottom passage.

b) for the top passage, imagine another "moon circle", $x^2 + y^2 = r^2$, representing the position of the moon when the center of the visible array crosses. In effect, this establishes a coordinate system which will be used to write and then solve the algebraic expressions necessary to fix uniquely the channel detector's position. The center of the visible detector array is on the semicircle:

$$y = \sqrt{r^2 - x^2} \qquad (8)$$

(for a top passage), its specific position being at limb angle θ, *i.e.* at

$$X_{CT} = r\cos\theta \ , Y_{CT} = r\sin\theta \ . \qquad (9)$$

c) after time Δt, the channel detector is on the moon circle. Also, the moon circle has moved a distance $v_x\Delta t$ in the east/west direction, $v_y\Delta t$ in the north/south direction. See Figure 8. The equation of

this displaced circle containing the channel detector is that of the above moon circle shifted by $(v_x\Delta t_T, v_y\Delta t_T)$:

$$(x - v_x\Delta t_T)^2 + (y - v_y\Delta t_T)^2 = r^2. \quad (10)$$

The channel detector is somewhere on the positive semicircle of this equation.

d) the same procedure is used to place the moon circles generated by the bottom passage. The only complication here is that the moon circles from the bottom passage have to be algebraically expressed in the same reference frame as the top passage. (Otherwise there would be no way to solve simultaneously. Note that Figure 8 expresses the passages' equations in different reference frames.) The way to relate the top passage moon circles to the bottom passage moon circles is to "overlap" the circles such that the position of the center of the visible array in the top passage (X_{CT}, Y_{CT}) is the same as that of the bottom passage (X_{CB}, Y_{CB}). Thus, the above steps are repeated and the final equations shifted by X_{CT}-X_{CB} in the east/west direction, Y_{CT}-Y_{CB} in the north/south direction. (Remember that Y_{CT} and Y_{CB} will have opposite signs since Y_{CB} is negative, so the magnitudes will add.) See Figure 9. Thus the moon circle equations become:

i) top passage at visible array crossing: $x^2 + y^2 = r^2$ (9)

ii) top passage at channel detector crossing: $(x - v_x\Delta t_T)^2 + (y - v_y\Delta t_T)^2 = r^2$ (10)

iii) bottom passage at visible array crossing:

$$[x - (X_{CT} - X_{CB})]^2 + [y - (Y_{CT} - Y_{CB})]^2 = r^2 \quad (11)$$

iv) bottom passage at channel crossing:

$$[x - (X_{CT} - X_{CB}) - v_x\Delta t_B]^2 + [y - (Y_{CT} - Y_{CB}) - v_y\Delta t_B]^2 = r^2 \quad (12)$$

Solving Eqs. (10) and (12) simultaneously would yield the detector position.

e) the correction factor to this approach concerns the rotation of the focal plane. The routine determining the limb angle took into account the rotation, whereas the correction has not yet been applied here. In effect, one assumes above that the four moon circles can be laid over each other by

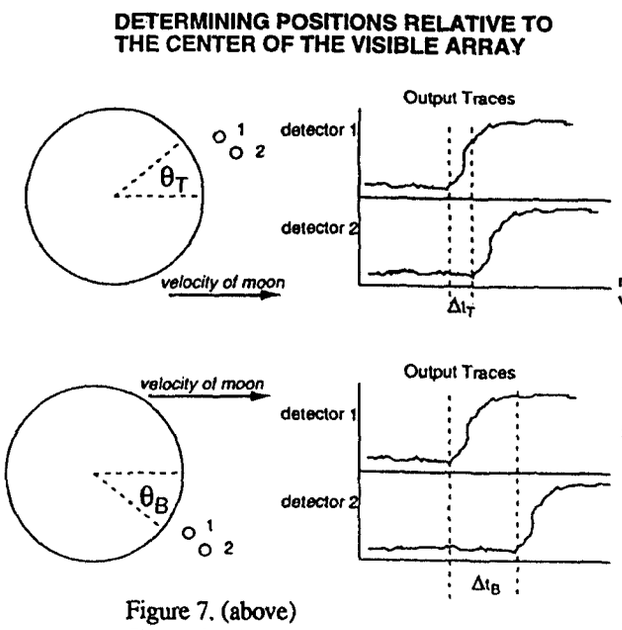

Figure 7. (above)

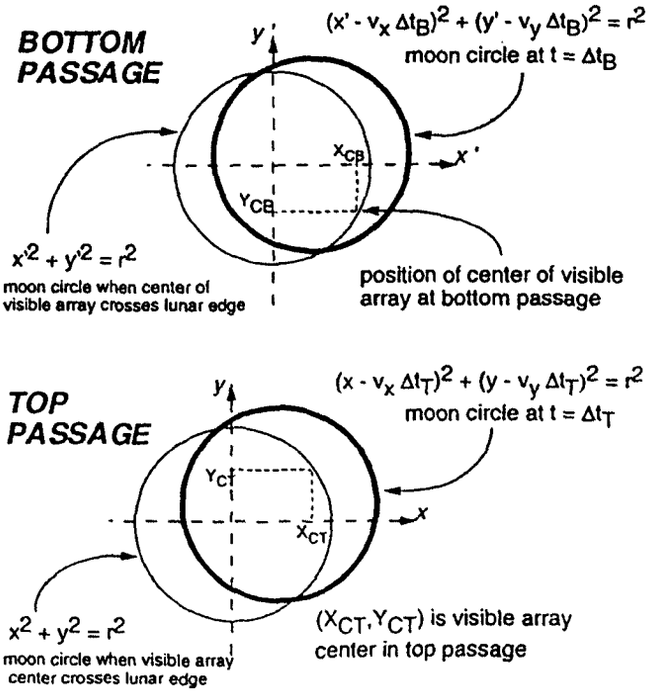

Figure 8. (right)

aligning the (X_{CT}, Y_{CT}) and (X_{CB}, Y_{CB}) positions. This is not true - the circles have to be "derotated" back to the reference plane of the spacecraft.
The rotation is effectively corrected for the algebraic solution described above if the (X_{CT}, Y_{CT}) and (X_{CB}, Y_{CB}) positions and the direction of the lunar velocity are modified. Before using Eq. (9) to determine the visible detector positions, subtract the rotation angle, α, from the limb angle θ. Then shift the direction of the moon's motion back to the spacecraft frame by subtracting the rotation angle. See Figure 10. Thus:

- $\theta' = \theta - \alpha \Rightarrow X_{CT} = r\cos\theta', Y_{CT} = r\sin\theta'$
- $v_x = v\cos(\gamma - \alpha)$ (13)
- $v_y = v\sin(\gamma - \alpha)$, where (14)

  v is the magnitude of the moon's velocity with respect to the spacecraft
  γ is the direction of the moon's velocity with respect to the spacecraft

One recalls that each of these quantities is different from top passage to bottom passage, with the exception of the moon's velocity which can be assumed constant over the course of the data collection, which is roughly 5 - 10 seconds for each trial for the imager and up to 40 - 50 seconds for the sounder.

Using these corrected values, then, one may calculate the requisite parameters and solve Eqs. (10) and (12) to get the channel detector's position with respect to the reference position, the center of the visible array. The entire set of calculations must be repeated for each detector.

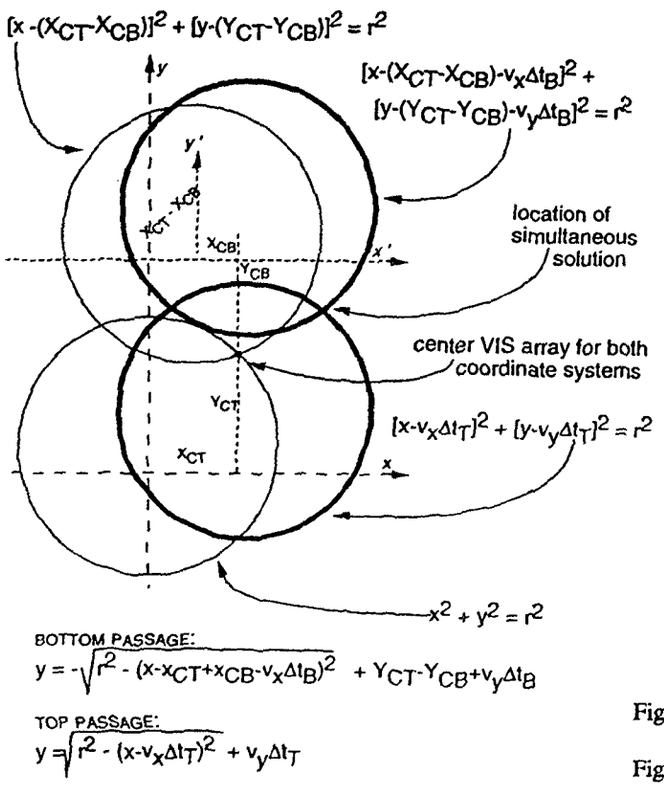

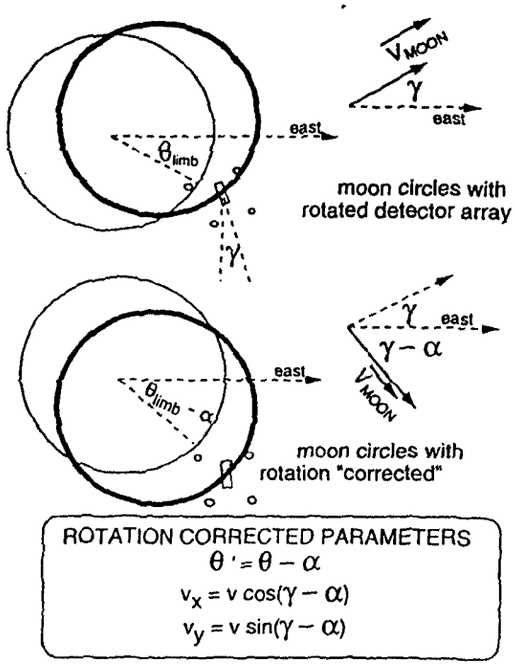

Figure 9. (left) Solving top and bottom channel crossings
Figure 10. (above) Correction detector rotation

6. PRACTICAL CONSIDERATIONS

The principle mechanism in implementing the above approaches is to solve equations simultaneously. The solutions were obtained through iteration. Such an approach lacks efficiency and requires an appropriate expression to determine the starting point of the iteration. The accuracy of the solution depends upon the interval by which the variable x is incremented. However, the lack of efficiency in this respect is not a problem and an expression for a starting value is not difficult, although care must be taken since the equations are quadratic and only one of the two roots is physically meaningful. The errors due to this iteration are actually rather minor as a part of the entire process.

7. VALIDATION

While this method depends solely on manipulating plane geometry, there are many details to consider and several signs and reference planes that need to be strictly correct. To test these routines before implementation, a simulator was independently developed. This separate software routine was written to do the opposite of the colocation routine, that is, to start with a focal plane (shapes, dimensions and positions), a simulated circle representing the moon, lunar velocities, observations times, rotation angles, and lunar subtense and then to produce traces of what the detectors "see" as they cross from space to the moon. To avoid repeating any conceptual errors, the author of the detector determination method had no hand in the development of the simulator.

With these simulated traces, top and bottom passages were performed and Δt values were measured and applied to the colocation routine. The results were then compared to the original focal plane. The errors for a simulated imager focal plane array were on the order of 5 μrad in each direction.

8. TRAILS WITH REAL DATA

The actual data collection was performed for the imager on August 12, 1994. Three trials were performed with the intention of averaging the results. (In reality, four trials were performed but, since the moon was very low in the field of view - around -10.4° - the bottom passage of the fourth trial missed the limb.)

The locations on the moon that were commanded were 20° latitude and -20° latitude. The actual measured surface moon crossings diverged from these values by as much as 20 degrees lunar latitude. Such discrepancies are not surprising. The precision with which OATS can target the moon is rather limited. (The subtended moon diameter is less that one half of a degree.) Also, there was an OATS failure the day before this test, affecting the image navigation and registration (INR) system.

Three complete trials were processed to produce three sets of detector positions. THey were then averaged. The results indicated a shift northward for all the detectors of roughly 20 - 30 μrad and a shift of roughly 8 μrad to the west. (The trial was performed at conditions approximating mission high.)

9. ERROR MARGIN

The sources of error in this trial include:

- numerical imprecision in the routines
- errors in assuming that the visible array is perfectly straight in the north/south direction
- imprecision in picking out transition points off of the traces
- irregularity of the moon

9.1 Numerical errors from the routines

The errors in the numerical manipulations of the routines are rather slight. The limb angle may be off by as much as two degrees although it is usually off by roughly one degree for "reasonable" limb angles (between 10 and 50 degrees). There seems to be more error in determining the top passage angles then the bottom ones for reasons that are unclear.

Even with one degree errors in limb angle, the channel detector routine determined the detector placement usually to within a 3 - 4 μrad, often less, with the simulated data.

9.2 Errors in assuming a perfectly straight visible array in north/south direction

This method only locates the IR channel detectors with respect to the center of the visible array. To do so, it assumes that the visible array is to specifications. While this is not quite true, the total north/south misalignment in the SN03 imager was reported to be roughly 6 - 8 μrad. (This figure varies with mission conditions.) Taking as much as 10 μ rad of misalignment, the resulting error in detector position is within a few microradians.

9.3 Imprecision in picking out transition points

A major error contributor is the imprecision with which one is forced to read the traces. The traces from the visible detectors are fairly clear in that they locate the starting point and ending point of the space/moon transition to within a few samples. There is a much more gradual transition, however, for the IR detectors (at least for the imager, the only instrument for which the method was performed thus far).

To estimate how much error may be involved, a spread of values of transition points was used to get a spread of Δt values. These spreads were then used as input to the simulator and the differences in resulting positions compared. This measure is at least partly subjective since different analysts may declare starting and ending points (or space and surface points) differently. Some sample traces are included as Figures 11 (visible detector) and 12 (IR channel two detector). The analyst who produced the above results (and who actually wrote the routines) found an error of about 5 samples taken at 54.6 Hz, or 0.09 seconds, conservatively yielding position errors of 15 - 20 μrad.

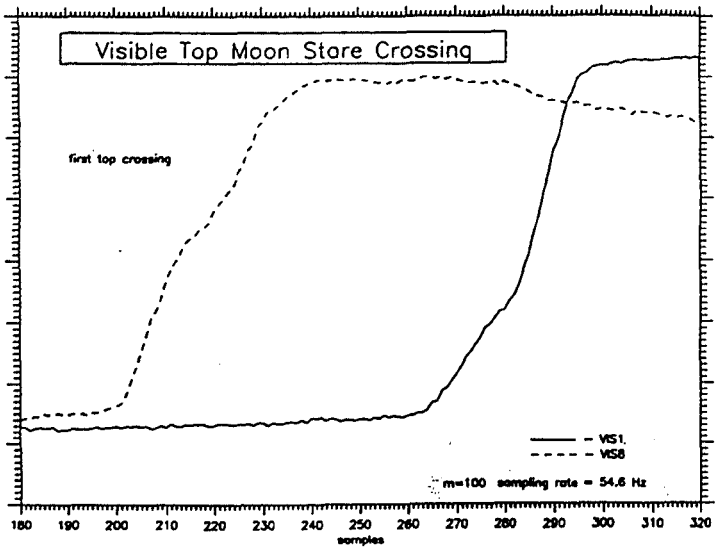

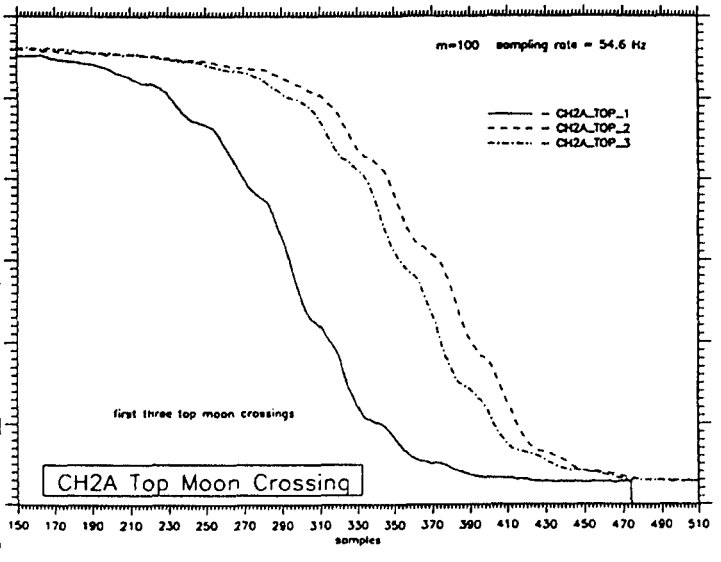

Figure 11. (top) Plot of visible detectors #1 and #8
Figure 12. (bottom) Plot of IR detector CH2A

Both the analysis and the simulator assume that the moon is a perfect circle with a smooth surface. Clearly, it is not a perfect sphere and irregular surface topology lends itself to details on the traces which will not be repeatable. These surface details in turn may produce ambiguities in determining the transition points needed for calculating the delta time values. Since the traces are somewhat irregular, it is not possible to automate the delta calculation process (such automation was performed with the simulated data). Still, given the distance involved, the footprint of the IR IFOVs on the moon is on the order of 112 μrad • 400,000 km ≈ 45 km, possibly enough to average out many of the effects of mountains, shadows, etc.

9.4 Method results

The test results indicate that at the time of the observation, under the given conditions, the IR detectors appeared to be shifted to the north of their nominal position by roughly one visible pixel. No conclusion can be made about the east/west shift since the average shift detected (~ 8 μrad) is much less than the margin for error of this test.

10. UNRESOLVED PROBLEMS

These results were compared to on-orbit images used to determine the visible/IR offset. Users compared visible images to those from channel four. The offset was determined by shifting one image to overlap the other and counting the pixel displacement needed to align landmarks. The offset was determined to be between one and two visible pixels south - the opposite direction of the results as determined by the moon edge test. These images were taken in the scanning mode, or dynamic mode, whereas the moon test was performed in the staring or static mode. However, there should not be a great deal of difference between these two parameters, especially in the north/south direction.

Further, the imager's manufacturer, ITT, projected the offset, based on ground testing performed pre-launch, to be south also.

The reasons for this discrepancy are unclear. The simulator results validate the general approach as well as the implementation of the code. Other possibilities include a mix-up in detector data, inaccuracies in assuming that the moon is circular, and irregularities in the moon's topology.

[There is also the theoretical possibility that the visible/IR offset changed between the time that the moon edge test was run and the time that the image shift determination was performed. It is unlikely however, that this passage of time - roughly a year - would account for such a change.]

The possibility that the detector traces were confused and/or mislabeled is unlikely. The traces are qualitatively consistent with their trials. In general, any such mix-up would produce large errors, yielding values that are unreasonable. While the visible/IR offset results may be off compared to the pre-launch test and the image shift test, they are within the range of values for this parameter.

The major difference between the simulator and the real on-orbit test is the assumption that moon's profile is perfectly circular. In reality, it is not far from being a good sphere. According to a report studying altimetry data from the recent Clementine lunar probe[2], the difference between the polar diameter and the equatorial diameter is roughly two km, compared to a mean diameter of 1,736 km. Altering the code to use an eclipse with these axes produces marginal differences in the detector positions.

Finally, the topology of the moon introduces a random irregularity to this test that may account for discrepancies. The stares were roughly in the same general areas of the moon and it is therefore at least possible that any large deviation in any of these areas such as a mountain or valley could have corrupted the results. The above report studied the surface variation and found that the standard deviation in lunar radius on the near side is about 1.4 km. Thus the moon has remarkably little ellipticity at the

equator. The effect of particular artifacts at the exact location of the limb crossing however are difficult to estimate.

11. RECOMMENDATIONS

Random effects are reduced when many trials are averaged. As of this writing, this test has been performed only on these three trials and only for the imager. As noted, the observation was performed while the moon was at the limit of the imager's field of regard - actually crossing the edge of the FOR. It would thus be interesting to see test results where the moon is well within the instrument's window.

It would be helpful to repeat the test or to perform more trials on successive instruments. This would also allow operators to gauge the test's repeatability. Only then will test operators be able to assess thoroughly the method's viability.

12. SUMMARY & CONCLUSIONS

Using geometry and parametric equations, it is theoretically possible to determine the relative positions of two detectors by comparing the traces they make as the moon's edge drifts past their field of view. A solution that works well with simulated data is presented here. This solution depends upon having two observations of the moon's edge, one in each hemisphere, by the detector pair. Further trials are necessary to validate this procedure for field testing.

13. ACKNOWLEDGMENTS

This work was performed at Swales & Associates, Inc. as part of the GOES project. Swales & Associates contracts through the Goddard Space Flight Center in Greenbelt, Maryland. The author expresses his appreciation to Swales for their support of this effort.

A special note of acknowledgment is reserved for Smiley Hsu, formerly of Swales. Although the author developed this approach and implementation, it was Mr. Hsu that came up with the notion of using the moon's edge to colocate detectors, recognizing that two independent crossings would be required to solve the problem uniquely. Mr. Hsu also developed the simulator to test this routine, which proved invaluable in validating the code.

14. REFERENCES

1. Initial suggestion from Smiley Hsu, formerly of Swales & Associates, Inc.

2. M. T. Zuber, D. E. Smith, G. A. Neumann, & F. G. Lemoine, "What factors control the long wavelength shape of the moon," Lunar & Planetary Institute Proceedings, page 1511 - 1512, February, 1996

On-orbit MTF measurements

James J. Shea

Swales & Associates, Inc.
5050 Powder Mill Road, Beltsville, MD 20705

ABSTRACT

The GOES program seeks a reliable method to measure the imager's modulation transfer function (MTF) once the instrument is in orbit. This has proven difficult since there is no convenient target. It has been proposed to use the edge of the moon as a high contrast target, offering the possibility of performing a "knife-edge" MTF test. The following treatment produces a visible, east-west edge spread function (ESF) from imager scans over the lunar limb. The ESF is used both to produce a visible knife-edge MTF estimate as well as to produce, through differentiation, a visible line spread function (LSF), which also is used to produce an MTF. While the results do not rigorously conform to ground tests, they track low and medium spatial frequency test values reasonably well and offer a means to test the instrument's imaging fidelity on-orbit.

Keywords: MTF, knife-edge, line spread function, post launch test (PLT)

2. BACKGROUND

The GOES program conducts a check-out phase to evaluate the instruments' radiometric and optical operations immediately after proper orbit is attained. For most parameters, it is possible to compare pre-launch and on-orbit performances at corresponding environmental conditions. Evaluating the imager's imaging fidelity, however, requires an appropriate target. While it would theoretically be possible to measure an MTF from a point source, such as a star, there is no star that is bright enough to produce a usable point spread function in the imager's scanning (imaging) mode. Stars are routinely detected for navigation purposes, but such detection occurs in a special mode, where the detectors "stare" into space and the gain is increased. The effective signal to noise ratio is thereby increased, but this approach is not possible in the scanning mode.

It has been informally proposed[1] to measure the MTF by using the edge of the moon as a high contrast target. With the appropriate viewing angle, this would allow a sharp edge to be seen by the imager. The exact profile will be different for the visible and infrared channels. In the visible wavelengths, the moon is essentially reflective, and since the lunar surface is, to first order, a lambertian scatterer, a full moon would appear roughly uniform. (The topology will obviously be irregular, but a uniform surface would produce a uniform irradiance profile. Since it is only the dark to bright transition that is of interest, large scale irregularities can be avoided.) In the infrared, however, the moon is essentially radiative, that is, is detectable from the radiation that it emits due to its temperature and emissivity. Thus, the lunar profile will depend upon the thermal profile. Since the edge of a full moon as seen by the imager will normally be the coolest portion of the lit moon, the edge would generally not offer a high IR contrast. (The bright edge of a crescent moon would offer a high IR contrast.) The present treatment will concentrate on the visible MTF taken from a full moon seen by the visible channel.

3. DATA ACQUISITION

The SN04 imager, housed on the GOES-9 satellite, took a scan of the moon on November 11, 1995, at approximately 17:00 GMT, viewing a roughly full moon. The image is reproduced here as Figure 1; the oval shape is due to east-west overscanning. The small sector scan was 160 scan lines, each line taking 460 data blocks, thereby producing a visible channel image of 1840 columns by 1280 rows. A line profile,

roughly through the equator, is given as Figure 2. The imager was in 36.6 second scan mode, which means that it performs a space clamp every 36.6 seconds. The moon was at an eight degree elevation in the imager's field of regard.

[The imager corrects for image rotation by adjusting the timing of the samples from the detectors. This does not correct for the orientation of the individual detectors, thus the effect of the rotation of the IFOV's projection into space is not corrected, only the rotation of the detector array. Since the traces are individually selected and combined to produce the most sequentially consistent edge - see below - the image rotation correction has no impact here. The rotation itself, however, is a factor in choosing which trace to use. See section 4.1.]

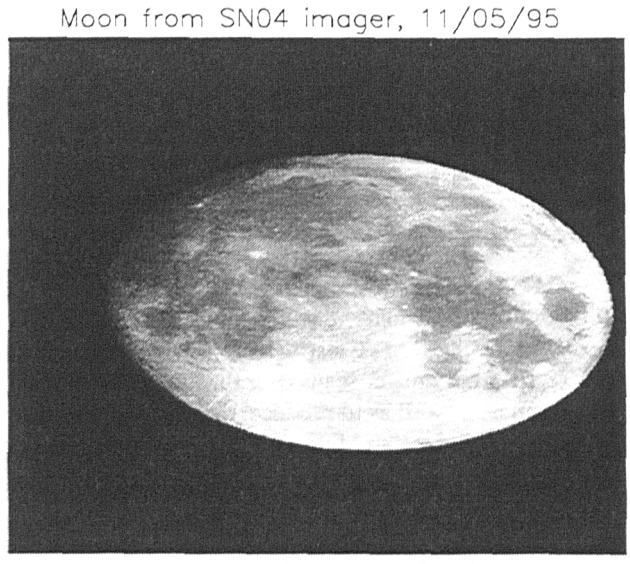

Figure 1. Image of moon from GOES-9 imager. Oval shape due to 1.75:1 instrument overscan.

One immediate consideration is any blurring of the image due to motion of the moon. One notices the staircase effect on the edge of the moon in Figure 1 due to the lunar drift. The image took 51 seconds to scan. During the scan, the moon was moving in the east/west direction at about 61 μradians/second. Thus the moon moved at total of 3,100 μradians, the equivalent of 110 IFOVs (instantaneous fields of view of a visible detector). However, this figure is not relevant to determining any blurring in an individual scan line. Blurring on the scan line would be due to significant lunar movement as the detector IFOV scans across the lunar edge. The detector samples at a rate of 21,840 samples/second, overscanning such that the samples are separated by a nominal center-to-center distance of 16 μradians. At this rate, it takes 80.1 μsec to completely cross an edge. During this time, the lunar edge moves about 0.005 μradians, or about 1.7×10^{-4} visible pixels. Thus the effect of the lunar drift rate on an edge transition profile is negligible.

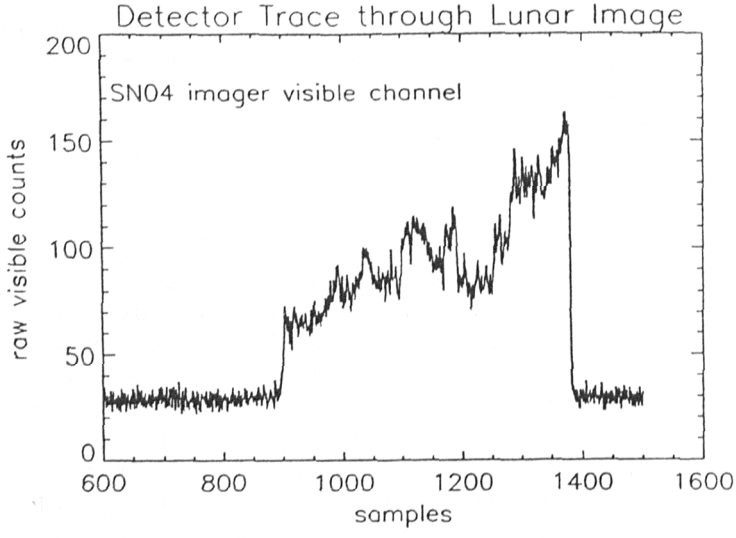

Figure 2. East-west detector trace through the moon image (shown above in Figure 1.).

4. PRODUCING THE EDGE SPREAD FUNCTION

From the array of samples comprising the visible image of the moon, an edge spread function, the system's image of a sharp contrast along a straight line (e.g. a step function), must be extracted. There are two separate concerns that will direct this effort. First, the particular east-west traces from the image were chosen. Second, traces are combined in the proper manner to generate a curve with sufficiently low noise levels.

4.1. Choosing east-west traces for edge spread function

In making this estimate of the east-west MTF, one needs to consider not only east-west pixel profiles but also the orientation of the detectors. The imager is a serial scanner and thus the scan mirror travels both east-west and north-south, progressing line by line. In doing so, a rotation of the IFOV is created, *i.e.* the detectors' projection into space rotates as a function of elevation. (There is no rotation induced as a function of east-west position.) This rotation is equal to the north-south elevation, and is in the counterclockwise direction (looking out to space in the instrument's reference frame) in the north, clockwise in the south.

Given that the moon was at eight degrees, each individual detector was rotated eight degrees counterclockwise as it crossed the lunar limb. Thus, the most parallel trace to the detector is the one that is at eight degrees north lunar latitude. See Figure 3.

4.2. Combining traces to produce optimum edge spread function

In an analog system, it would theoretically possible to use the single trace taken above for an east-west MTF estimate. However, in practical, electronic sampling systems, such an approach has two serious drawbacks. First, it would be too noisy. Noise corrupts the scans. Differentiation of the noisy scans to estimate the LSF amplifies the high frequency components of the scans, where the signal to noise ration is the lowest.

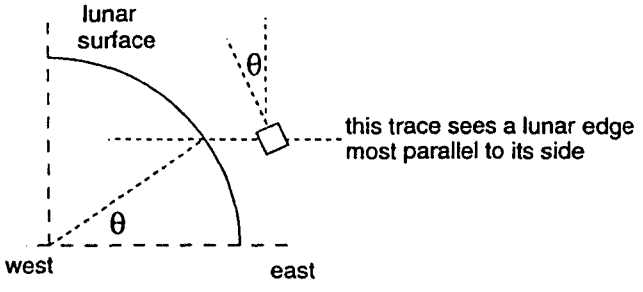

Figure 3. (above) Geometry of moon with detector rotation. Detector rotation is proportional to north-south scan elevation, counterclockwise in north as shown.

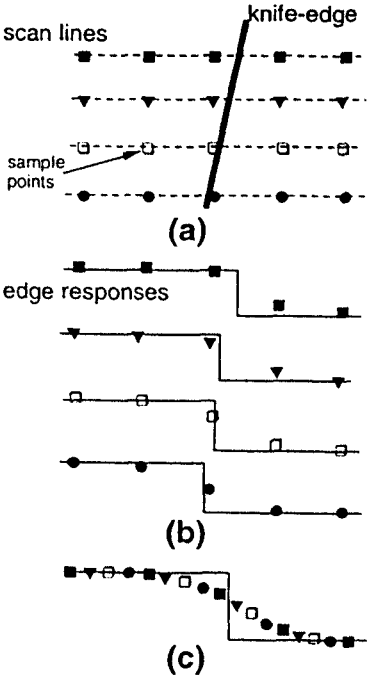

Figure 4. (right) Combining traces to produce the edge spread function. (a) knife-edge along sampling grid, (b) knife-edge traces, (c) combined scan for ESF[2]

Second, digital imaging systems typically undersample, causing aliasing of frequencies into the region below the Nyquist rate. While the GOES imagers employ 1.75:1 oversampling, this oversampling can be improved in a simulated trace to reduce aliasing further and increase the accuracy of the MTF estimate.

To produce an ESF having low noise and low aliasing potential, a simple technique of scan line averaging is used. This technique[2,3] has been used to improve the reliability of knife-edge MTF measures and LSF estimates for digital imaging systems, especially remote sensing systems for which edge contrasts are often the only available performance targets. Scan line averaging is implemented by collecting many scans across an edge. Then these scans are combined sequentially using estimates of the edge location, so that they corresponding samples from each scan follow each other. That is, the scans are shifted so that the edge points of all the scans are aligned. Figure 4 depicts a scan combination in this manner.

The noise in the combined scans can then be suppressed by smoothing and resampling, thereby sacrificing some spatial resolution in order to reduce noise. The resampling resolution should be at least as great as the MTF cutoff, and the smoothing filter should be matched to the resampling resolution. For typical digital image acquisition devices, twofold (or slightly higher) superresolution is usually sufficient.[2]

Once an acceptable visible east-west ESF has been created, it is compared to an ideal step function for a direct visible, east-west MTF calculation. It is also differentiated to produce an E/W LSF, whose Fourier transform is a one-dimensional MTF.

The limitation here is that the moon's edge is circular, not straight. While it may be approximated as a straightedge near the equator, there is only a limited number of scan lines that can be selected for combination as described in the above scheme. Thus one is limited in the degree to which the noise suppression technique can be achieved.

Given the increasing curvature of the lunar limb and the increase in incident angle, scans were taken roughly ten degrees above and below the matching angle of eight degrees, *i.e.* from the equator to roughly twenty degrees north. This produced twenty-four traces. The traces were truncated to twenty one samples, an example of which is Figure 5. (The transition, read from west to east, is actually from the lunar surface off to space.) They were then combined in a sequence that produced the smoothest overall transition, following the example described in Figure 4 but keeping in mind that the real traces were much more irregular. The finished, twenty-four trace combined edge is shown in Figure 6. The west side of the combined trace,

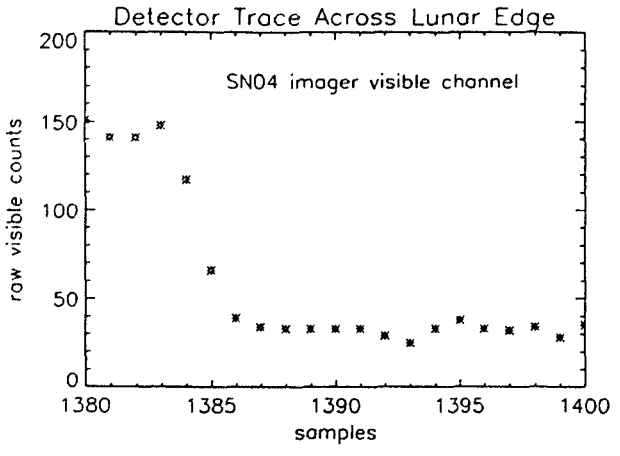

Figure 5. Samples across limb from a single trace

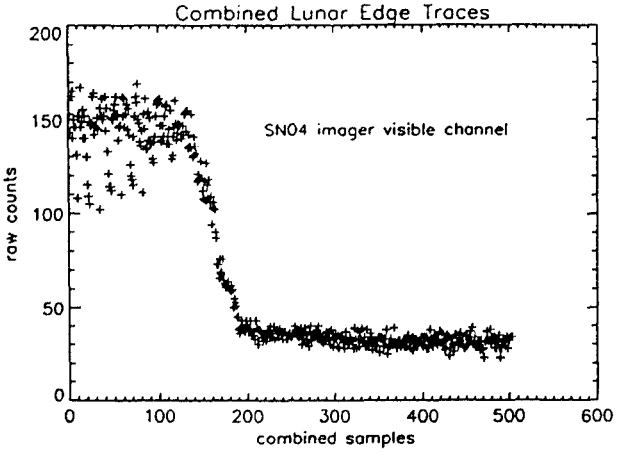

Figure 6. Combined scan, using 24 traces

representing the lunar surface, appears here as a random spread of samples. This is due to the irregularity of the surface; scans *n*, *n+5*, and *n+10*, for instance, will view different areas of the moon, perhaps covering craters, mountains, and shadows, thus there is no reason to expect them to have similar profiles. This is of little concern since it is the edge itself that is of primary interest.

Next, the trace was resampled, or "smoothed," by an averaging window. The intention was to have roughly twice as many samples as the original traces. Since the original trace had 21 samples, a averaging window of 11 was chosen. Thus, the combined trace, having 21 x 24 = 504 samples was resampled such that each 11 samples were averaged to produce a single sample, yielding a new trace of 45 samples. This new trace not only has reduced noise, it also places more samples across the edge, increasing the effective sampling rate. For the finished edge spread function, the DC bias was removed (so that the space edge would have a zero average value), the leading edge was truncated to eliminate the spread samples resulting from the surface topology; and the plot was "padded" with zeros such that the edge was the center of a 1024 sample scan. (1024 was chosen to make the later FFT more efficient.) The edge transition of the ESF is given as Figure 7. Since the resampled scan had 45 samples, the oversampling ratio for this resampled curve is 45/21 = 2.14. Note that this is the ratio from the resampled trace to the original trace and does not include the 1.75 overscan of the instrument itself. The 1.75 overscan is effectively accounted for in the later spatial frequency scaling by assigning a sampling rate of 16 μrad/sample.

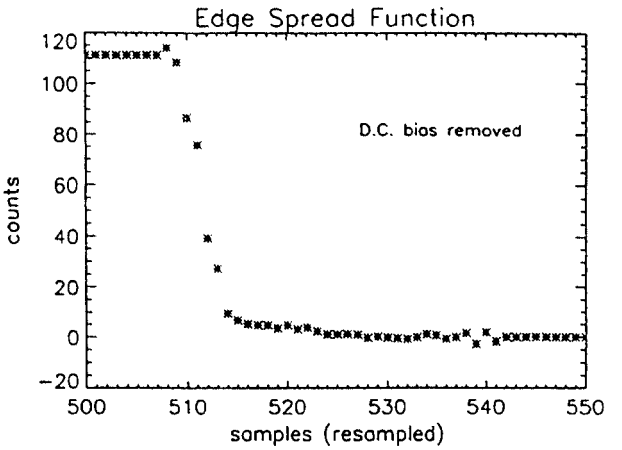

Figure 7. Edge spread function, resulting from resampling the combined traces with an 11-sample averaging window

This new trace constitutes the east-west visible edge spread function, which will be used to estimate the visible MTF in two different manners.

5.0 KNIFE-EDGE MTF

5.1. Generalities

The "knife-edge" MTF is calculated by taking the ratio of the Fourier Transform of the ESF and that of an ideal step function. One recalls that, for a linear shift invariant system, the input, output, and system response are related by the convolution:

$$r(x,y)*h(x,y) = s(x,y) \qquad (1)$$

where r(x,y) = input function
h(x,y) = system function (*i.e.* impulse response)
s(x,y) = output function

And the relation between the corresponding frequency terms by the product:

$$R(f_x f_y)\, H(f_x f_y) = S(f_x f_y) \qquad (2)$$

where f_x, f_y = horizontal, vertical spatial frequency
$R(f_x, f_y)$ = input spectrum (Fourier transform of

where the Fourier transform is defined as:

$$R(f_x, f_y) = \iint_{\infty} r(x,y) e^{-j2\pi(f_x x + f_y y)} dx\, dy \tag{3}$$

The spectrum of the system function $H(f_x,f_y)$ would in this case be the optical transfer function (OTF). The OTF can be expressed in magnitude and phase terms as:

$$OTF(f_x, f_y) = \left|OTF(f_x, f_y)\right| e^{-j\theta(f_x, f_y)} \quad \text{where} \tag{4}$$

$$\left|OTF(f_x, f_y)\right| \equiv MTF(f_x, f_y) \tag{5}$$

The system in question is the GOES imager. This analysis is restricted to the x-axis, that is, the east-west direction, along the direction of the scanning motion. The edge spread function represents the output function. The input function is assumed to be an ideal, one dimensional step function, often symbolized as *u(t)* or the Heavyside operator. Thus:

$$STEP(f_x)\, OTF(f_x) = ESF(f_x) \quad \text{or} \tag{6}$$

$$OTF(f_x) = \frac{ESF(f_x)}{STEP(f_x)} \quad \text{and}$$

$$\text{MTF}(f_x) = \left|\frac{ESF(f_x)}{STEP(f_x)}\right| \tag{7}$$

Adapting this expression for the sampled data, one accounts for the pixelization and the overscanning:

$$STEP(u)OTF(u)Sinc\left(\frac{u}{\alpha}\right) = ESF(u) \tag{8}$$

where u represents normalized spatial frequency (*i.e.* $u = 1.0$ corresponds to the imager's nominal sampling rate), and α is the overscan ratio (the ratio of samples before and after the resampling). The sinc is the spatial frequency representation of a unit pulse.

5.2 Application

Since the data are digitized, a discrete Fourier transform (DFT) is used. In practice, the "fast Fourier transform" was implemented to calculate the DFT. The DFT of the ESF is given as Figure 8. STEP(u) here is the spectrum of an ideal step function, given as:

$$\text{STEP}(u) = \begin{cases} \frac{1}{2}, & \text{for } u = 0 \\ -j/2\pi u & \text{otherwise} \end{cases} \tag{9}$$

The *sinc(u)* is takes its standard definition, increasing its size in the spatial frequency domain by α since it is reduced in size in the spatial domain by that amount:

$$Sinc(u) = \begin{cases} 1, & \text{for } u = 0 \\ \sin(\pi u)/\pi u & \text{otherwise} \end{cases} \tag{10}$$

Using an oversampling ratio of $\alpha = 2.14$ and a nominal sampling rate of $f_s = 1/16$ μrad = 62,500 cycles/radian (*i.e.* $u = 1.0$ corresponds to $f_x = 62{,}500$ cycles/radian), the absolute value of the OTF from Eq. (8) is shown in Figure 9.

The curve is plotted with the pre-launch test values (or specification values), which are at 4490, 9000, 13500, and 18000 cycles/radian. (These values correspond to $u = 0.07$, 0.14, 0.21, and 0.29 respectively.) The MTF estimate tracks the ground values to within about five percent for the low and mid spatial frequencies, starting to diverge dramatically approaching 0.25 (about 16,000 cycles/radian).

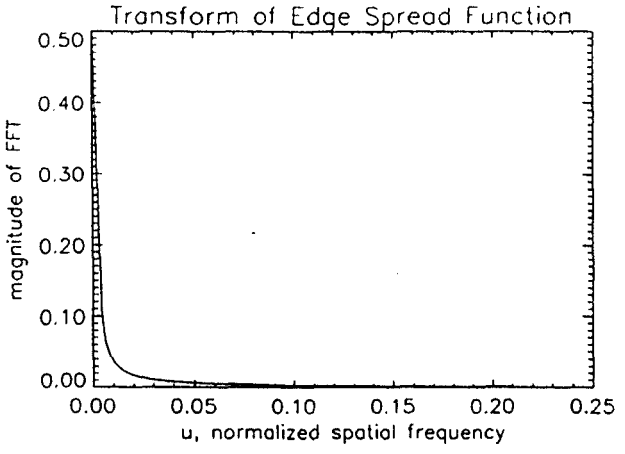

Figure 8. Fourier transform of the ESF

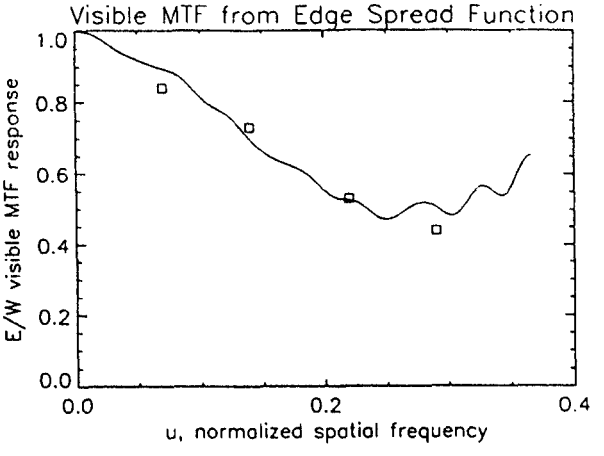

Figure 9. Visible east-west MTF from ESF

These two transforms are normalized from the nominal sampling rate of 1/16 μrad = 62,500 cycles/radian.

6. MTF FROM LINE SPREAD FUNCTION

Rather than ratio the ESF to an ideal step function, the ESF can be used to derive a line spread function. The Fourier transform of the LSF provides a one-dimensional MTF estimate. This has the advantage of ease of calculation, yet could potentially introduce high frequency noise, since the LSF is produced by differentiating the ESF, thus amplifying any noise.

The ESF was differentiated, yielding a line spread function given in Figure 10. Note that it goes negative then returns to zero, reflecting the fact that the edge transition is from high to low.

Taking the Fourier transform of the LSF produces another MTF estimate, given here as Figure 11. Like the MTF derived directly from the ESF, it is within about five percent of the first three test frequencies, and diverges significantly around the high frequency test value (18,000 cycles/radian).

7. DISCUSSION OF RESULTS

Both methods produce MTF estimates that are reasonably close for the first three spatial frequencies and yet have enough error at the fourth to be essentially unusable beyond 16,000 cycles/radian. Curiously, the

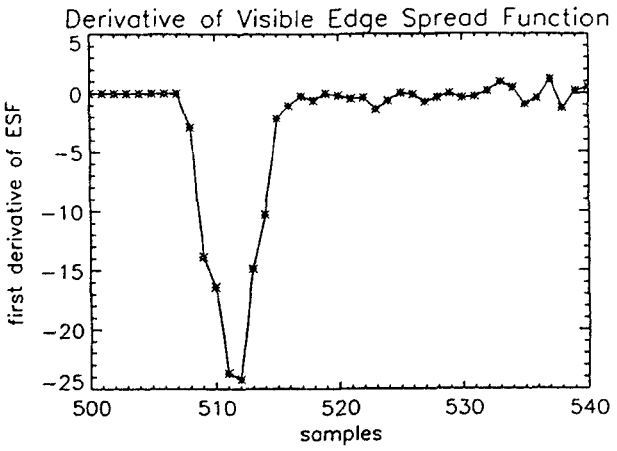

Figure 10. First derivative of ESF; effective line spread function (LSF) for imager

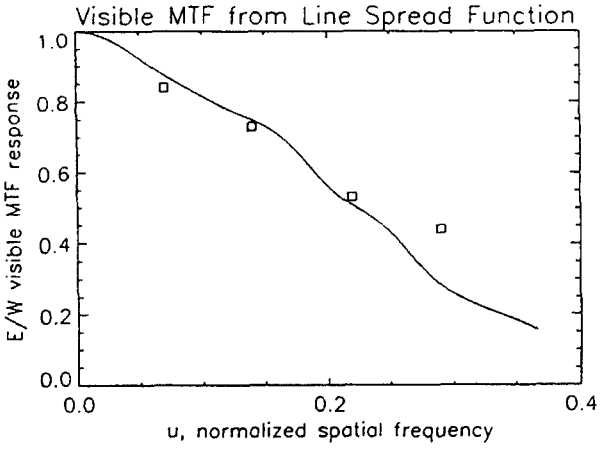

Figure 11. Visible E/W MTF from derived LSF

ESF MTF diverges from the ground values, and in fact, never drops off as would be expected but fluctuates between 0.6 and 1.0. In contrast, the LSF-derived MTF drops too quickly from the expected response.

The fact that the LSF-MTF drops too quickly suggests that the noise has been sufficiently reduced, although this is difficult to prove without more trials with this method. It is not immediately clear why the ESF-MTF blows up at higher frequencies, especially since both methods use the same edge trace.

As mentioned earlier, the major limitation in this method is the number of lines that can be combined for the edge spread function. Reinenbach[2] *et al* used 64 scans in a test case example, whereas it was only possible to use a third that number for this treatment, due to the dimensions of the moon with respect to the detector lines. One recalls that combining and resampling the traces not only reduces the noise but also extends the fidelity of the MTF curve in spatial frequency; the effective Nyquist rate, for instance, is not half the nominal sampling frequency, $f_S/2$ (62,500/2 cycles/radian), but rather is $\alpha\, f_S/2$ (2.14•62,500/2 cycles/radian). One could then speculate as to whether increasing the number of combined scans would improve the high frequency response. The question is somewhat moot however, since the existing dimensions fix the approach to more or less the parameters used here.

Another factor limiting the accuracy of this method is need to pad the response on the lunar surface. Since the scans cover different areas on the moon having differing topolgies, the combined scan produces a random scatter of samples on the moon side of the trace. See the beginning of the trace in Figure 6. This is obviously unusable and needs to be eliminated when constructing the ESF. Thus, this portion of the ESF is effectively lost, introducing a certain degree of error and possible accounting for the failed high frequency response. Further, there is a degree of subjectivity in choosing the exact sample at which to start the trace, leading to a small variation in ESF estimates.

Finally, this approach ignores the fact that the visible channel is made up of eight distinct detectors, each of which has a measured MTF response. This treatment combines them together, producing a composite MTF. Given the limited number of scans that are available when using the moon's edge, it is not possible to combine any useful number of scans for separate MTF measures. In any case, the pre-launch measurements vary little from detector to detector. One drawback in this respect is that if there is a single detector that

suffers an MTF degradation, such performance loss would translate into a less appreciable drop in the composite MTF as calculated here, possibly going unnoticed.

As it stands, this method offers post launch test engineers a means to measure the on-orbit MTF low and mid response to within roughly five percent.

8. FUTURE WORK

Two objectives immediately suggest themselves for follow-up work in this area.

One is to perform the same analysis using infrared data. It is not possible to use this same image to produce an IR MTF with the same fidelity as this visible example here, since the IR profile of a full moon is more of a curved slope rather than a sharp edge. Also, since a full moon would saturate most of the IR channels, a profile of a crescent moon would be needed. (See section 2.0.)

A second application is to estimate the MTF with staring data, as opposed to the scanning data used here. The imager's detectors can stare at a fixed point in space and allow the moon's edge to drift by. This operation collects data at a much higher spatial sampling rate. There would be only one data trace, but given the high sampling rate, it could still be resampled to reduce noise. This would produce a "staring MTF," a measure of the fidelity of the system that would be apart from the imaging mode.

Beyond these two tasks, this method can also be used trend the MTF performance as a function of mission level parameters, particularly as a function of scan mirror temperature. The difficulty in this respect is the availability of the lunar target. The moon is only visible to the GOES spacecraft once or twice a month. There is no guarantee that the profile will be usable each time, although most moon phases will offer sufficient contrast at the brighter limb for the visible channel. Still, the image used here was taken during the post launch check-out phase, using a small frame which is not part of the normal operations schedule. Therefore, it is not certain that analysts would have the flexibility to request such frames once spacecraft operations have been handed over to NOAA.

Finally, any MTF measure could be used as a starting point for image enhancement. Knowing the manner in which an imaging system attenuates its images allows users to compensate for the loss in spatial frequency, thereby "recovering" some of the image. Several digital image processing algorithms designed to remove the effects of an image acquisition device exist, such as the inverse filter, the Wiener filter, and the constrained-least-squares filter. All these approaches, however, are only as good as the knowledge of the imaging system fidelity. (Algorithms such as these often require phase information; estimating the phase transfer function was not addressed here, but the PTF can theoretically be extracted through similar means.)

9. SUMMARY & CONCLUSIONS

An image of the moon has been used to produce two visible, east-west MTF estimates. Twenty-one visible scan lines taken from the northern lunar hemisphere were sequentially combined and resampled to produce a visible east-west edge spread function having a higher effective sampling rate and reduced noise than the original traces. This ESF was used to produce a visible knife-edge MTF estimate. The same ESF was then differentiated to produce a visible line spread function, from which a second MTF was estimated. Both MTF estimates were within five percent of corresponding ground test values for three of four test and/or specification spatial frequencies. Both diverged significantly - and in opposite senses - at the highest test frequency. This method offers post launch test engineers a fairly practical means of estimating the on-orbit visible east-west MTF up to roughly 16,000 cycles/radian.

10. ACKNOWLEDGMENTS

The author is currently on the GOES contract through the Goddard Space Flight Center in Greenbelt, Maryland, as an employee of Swales & Associates, Inc. This work was performed at the NASA Resident Office, Space Systems Loral, in Palo Alto, California. The author wishes to thank Marvin Maxwell of Swales for helpful background discussion in the early stages of this project.

7. REFERENCES

1. From Marvin Maxwell, senior engineering consultant, Swales & Associates, Inc., October, 1993

2. S. E. Reichenbach, S. K. Park, & R. Narayanswamy, "Characterizing Digital Image Acquisition Devices," Optical Engineering, February, 1991, volume 30, number 2, pages 170 - 177

A background source for image processing techniques:

Kenneth R. Castle, *Digital Image Processing*, chapter 12, Prentice-Hall, Inc., Englewood Cliffs, New Jersey, 1979

GOES-8 Imager and Sounder Radiometric Performance Models: Methodology and Application

Peter McDonald

Lockheed Martin IR Imaging Systems
2 Forbes Road, M/S 345, Lexington, MA 02173

ABSTRACT

The GOES-8 Imager and Sounder Radiometric Performance Models are flexible tools intended to provide a intuitive user interface to instrument sensitivity analysis. The models were developed at Lockheed Martin IR Imaging Systems and transferred to the GOES modeling community as the standard for projecting the instruments' IR sensitivity in units of Noise-Equivalent Delta Radiance (NEDN), under arbitrary user-imposed conditions. In addition, the models provide an efficient means for selecting flight IR detectors with the highest possible instrument performance. The Radiometric Models have shown the way to several instrument-level performance improvements, and have also been a valuable tool in troubleshooting anomalous measurements at various stages of the GOES instrument build. The operation of the GOES-8 Sounder Radiometric Performance Model is described herein in terms of input parameters, calculational flow, and output results.

Keywords: GOES, model, radiometric, infrared, sensitivity, NEDN.

1. GOES RADIOMETRIC MODEL BACKGROUND

This text is intended to accompany the Lockheed Martin Radiometric Performance Model for the long-and-midwave infrared channels of the GOES-8 Sounder to provide documentation, and assist new model users in data entry. Although the GOES-8 Imager Model is not addressed directly in this document, the calculational methods and flow of the models are intended to be similar so that much of the system analysis is applicable to both models. In addition to explaining the operation of the Sounder model, the following text describes the theory, assumptions, and methodology behind the mathematics, and the database upon which they operate. It is therefore intended that the Lockheed Martin model is open and freely documented so that modifications and updates may be easily addressed. The revision number for the GOES radiometric model described herein is 4.1.

Since its inception in 1990, the Lockheed Martin model has evolved and its prediction accuracy has increased as GOES instrument and detector parameters became more clearly defined. For example, simplified 4-pole electrical filter approximations were updated in Rev. 3.01 to reflect more accurate knowledge of the instrument frequency response. The same is true of Rev. 4.1, in which the modified clamp circuit has been incorporated to accurately model the instrument's improved sensitivity. The Lockheed Martin GOES Radiometric Model is in a mature state, and has evolved into the standardized system model and NEDN predictor for the GOES instruments. The official model software repository is the ITT SDRL 27K document.

0-8194-2200-2/96/$6.00

The NEDN model is intended to be a flexible tool, not only for predicting system performance, but for troubleshooting instrument-level issues. Depending on the user's intent, any and all input values of the database may be overridden if more recent or accurate measurements are available, or a particular input is suspected to be affecting the NEDN measurement. The model is a convenient tool for quickly assessing the impact of any number of instrument parameters on the overall performance.

In projecting performance of future instruments, a nominal, or current instrument, database must be used. However, (as an example), to project performance of the instrument currently being built, the user might enter the bench-measured IGFOV values as they become available to override the ray-traced nominal values. Obviously, the intent of the model is to produce the most accurate prediction of system performance given the available data. This allows the model the flexibility to calculate "what-if" cases, as any parameters can be varied to determine the impact on final performance, whether hypothetical or real.

2. MODEL MECHANICS

The Lockheed Martin NEDN model may be run on any Macintosh or IBM personal computer with Mathcad 3.1 or higher. The paradigm for NEDN model 4.1 has changed from Excel to Mathcad for several reasons:

1. More powerful calculations: Noise bandwidth calculations performed rigorously.
2. Transparency of algorithms: No "hidden-in-cell" spreadsheet format. Hard copy is self-documenting.
3. Graphics capability: In-line plots of spectral NEDN, frequency response and clamp timeline provide visual verification of input/output.

Version 4.1 of the Lockheed Martin NEDN model is contained within 9 vertical pages of a Mathcad document. It was intended that this vertical flow illustrate a logical sequence of NEDN modeling and calculations. The following description is similarly written by page number sequence.

3. DESCRIPTION BY PAGE NUMBER

3.1. Overview

Pages 1 and 2 contain the substantial inputs to the model for the photoconductive Sounder detector channels (LW 1-7 or MW 8-12). This portion is intended to provide convenient front-end interfacing with the model for users who are interested in varying detector and instrument parameters to determine the impact on NEDN system performance. Such inputs as detector size, spectral responsivity, Simulator performance, and noise characteristics are entered here in the appropriate input "cell". These inputs are operated on by the calculations of the intervening Model Pages (3-6). The end result system NEDN performance is calculated on Model Page 7, and graphical analysis of frequency response is provided on Model Pages 8 and 9.

The following page-by-page breakdown examines each of these inputs and outputs in detail, providing units where appropriate in brackets [units] and comments in parentheses. Note that many inputs and calculations in the model are at least partially documented by text comments and prompts

alongside the "cell". This overview is intended to provide more complete documentation of the model calculations and guide new users through the inputs and calculations.

3.2. Model Page 1

3.2.1. Detector/Aplanat Parameters

L_d: Detector Length [mil] (current flow direction)

W_d: Detector Width [mil] (perpendicular to current flow)

These two inputs must be consistent with the detector dimensions which were used in the determination of detector responsivity.

R_λ: Detector Peak Responsivity [V/W]

The data as it appears on the vendor detector data sheet. Note that it is measured pre-aplanat (bare detector) in BB flood illumination. The detector bias and temperature (usually 102K), must be consistent with the noise parameters. System-type illumination correction is provided by the measured simulator factor. Operating patch temperature interpolation is provided by the tables on Page 2.

r_λ: Relative detector spectral responsivity [unitless] as it appears on the vendor detector data sheet. Defined as the ratio of detector responsivity at each GOES Sounder channel wavelength to the peak responsivity at the detector spectral peak wavelength.

N_w: Detector white noise spectral density [nV/rtHz]

f_k: Detector knee frequency [Hz]

β: Detector 1/f noise region power slope (nominal=1)

The accepted convention concerning the preceding three noise parameters is as follows: The three parameters are determined from an unweighted nonlinear least-squares curve fit to the measured vendor postaplanat spectral noise data. The discrete noise data frequencies used in the curve fit are a minimum of (10, 20, 40, 100, 250, 500, 4000) [Hz]. A curve fit to these frequencies is empirically known to provide a good representation of detector noise characteristics. Note that this curve fit to the measured noise data points is assumed to have been completed "off-line", so that the resulting three parameters become the model input.

$\tau_{aplanat}$: In-band aplanat transmission

Used only for Simulator factor prediction if measured Simulator data is not yet available.

$\tau_{simulator_factor}$: Simulator "throughput" factor

The LW and MW Sounder Simulators were designed and built at Lockheed Martin and maintained there from 1990 to early 1994. In mid-1994 the Simulators were transferred to ITT A/CD in Fort Wayne, Indiana. The Simulators provide (among other useful data) the effective system performance factor linking the vendor-measured flood responsivity (entered above) and detector performance to be expected under system illumination conditions. The Sounder Simulators contain all instrument optics except the telescope, with the goal that the flight optics, instrument temperatures, and surrounding baffles be entirely reproduced from the Lyot stop to the detector. The detector/aplanat unit is tested under the same conditions (e.g., F number, image size, focal plane temperature) that are present on the instrument. Thus Simulator testing is the highest-level subsystem measurement performed on a particular detector/aplanat unit. The Simulator factor (so-called "throughput") is defined as the ratio of the measured Simulator signal to the predicted ideal Simulator signal. The predicted ideal signal is calculated using standard radiometric equations to determine IR power incident on the detector under system conditions, which is multiplied by the vendor reported pre-aplanat responsivity. A Simulator throughput calculation is provided as an example in Appendix I.

Thus defined, the Simulator throughput contains all possible losses that the detector/aplanat will experience on the instrument (diffraction, collection efficiency, aplanat transmission and gain). Thus it can be thought of as the effective multiplier that bridges the gap between the flooded, pre-aplanat vendor performance and the expected performance in the Sounder instrument. Measured Simulator throughputs are documented and available for all detectors available for instrument selection at the time of the Simulator transfer.

Note that if the Simulator input is left zero, a "projected" Simulator throughput is calculated on Page 3 of the model, based on the existing database of measured throughputs correlated with detector area and aplanat gain. This feature was implemented in response to a customer request to provide a uniform rule in projecting and ranking detector performance at various stages of the detector/aplanat unit build.

3.2.2 Instrument Parameters

efl: effective focal length of Sounder optics [in]

Field_Stop_ Diameter: units of [in]

Primary Area$_{obsc}$: Area of primary mirror minus area of obscurations from struts and secondary mirror [cm^2]

The preceding three parameters are nominal values for the calculation of the "optical invariant" AΩ, known from raytracing of the Sounder optics.

$ifov_{meas}$: Instrument-measured instantaneous field of view for a particular detector (overrides nominal raytrace value) [μrad]

Ω: ifov converted to solid angle [sr]

τ_{optics}: Optical transmission by channel [unitless]

Product of all optical piece parts between the detector and the incoming radiation. By convention, the ITT "analytic gen" (AG) database is the accepted input for a given instrument. This AG data consists of peak in-band transmittance and spectral bandwidth for each channel.

$\tau_{polarization}$: Optical transmission including polarization losses.

Based upon experience with previous filter radiometers, the GOES modeling team has agreed upon a constant 5% polarization loss assumed for all GOES Sounder Channels.

$N_{instrument}$: Instrument noise [nV/rtHz]

This noise includes all instrument noise contributors: preamp, pickup, and any others. 4 nV/rtHz has been used as a typical representation for S/N03 and S/N04 instruments. It is important that the LW and MW detectors are biased at a current high enough such that their noise dominates the instrument noise (detector-noise-limited performance).

ν: Spec center wave number by channel [cm^{-1}]

λ_{av}: Band average wavelength [μm]

The preceding two cells are used only in the calculation of background radiation contributions from the filter wheel assembly.

Δν: Spectral bandwidth of each channel [cm^{-1}]

By convention, the source of this input is the ITT analytic gen transmission database.

T_{filter}: Temperature of filter wheel assembly [K]

T_{det}: Operating temperature of detector [K]

The next three input sections (scene, auto-zero, and channel clamp parameters) define the operation of the GOES clamp circuit. For further information, refer to the 1993 MIT/LL white paper on the subject[1]. The model contains nominal values for the existing S/N03 or S/N04 clamp parameters, but these may be overridden for "what-if" optimization. By convention, capital letters (T) refer to the duration of an event, while lower-case letters refer to the starting time of an event (e.g., t=0 msec corresponds to the start of a filter wheel revolution with period T=100 msec).

3.2.3. Scene Parameters

T_{sc}: Scene look duration [msec]

t_{sc}: starting time of each channel scene look [msec]

3.3. Model Page 2

3.3.1. Auto-Zero Clamp Parameters

T_z: Auto-zero clamp duration [msec]

t_z: starting time of auto-zero clamping [msec]

g_z: closed-loop gain of auto-zero circuit

RC_z: Time constant of auto-zero circuit [sec]

3.3.2.Channel Clamp Parameters

T_z: Channel clamp duration [msec]

t_z: starting time of channel clamp (by channel) [msec]

g_z: closed-loop gain of channel clamp circuit [sec]

3.3.3. Detector Temperature Scaling

r_T: Matrix of detector responsivity by channel relative to T_{det}

r_{Nw}: Matrix of detector white noise by channel relative to T_{det}

If projected performance is required for patch temperatures other than the detector input data temperature T_{det}, scaling factors are required for the signal and noise at the temperatures of interest. ITT has created a database for these relative signal and noise matrices for each detector in their inventory at various temperatures (usually 94, 101. 102, and 104K). Cubic spline interpolation is applied to predict performance at in-between temperatures. Note that if

temperature projection is not required, values of unity should be in the column representing the temperature of interest.

At this point, all substantial input parameters to the model have been completed. The remaining pages of the model (3-9) comprise the calculational operations performed on the preceding input database.

3.4. Model Page 3

3.4.1. Throughput Projection

This section (only applied if "0" is entered for $t_{simulator_factor}$ on page 1) is used to project an "expected" simulator throughput factor for detectors that have not yet undergone Simulator testing, such as detectors at the preaplanat build stage. The projection is comprised of two multiplicative factors: geometric collection efficiency (η) and effective aplanat gain. The collection efficiency is a function of the detector's dimensions and assumed image diameter (from optical raytracing). It is calculated as the ratio of the area of the intersection of the image circle and the detector rectangle to the area of the image circle. The effective aplanat gain is a constant multiplier (63%) of the "raytrace" gain (6.33) that was empirically observed to provide a good prediction of postaplanat simulator performance, based on the existing detector/aplanat database. Again, the intent of this portion is to provide a uniform rule for projecting Simulator performance based on what is known about the particular detector early in its build, and what has been measured for previous detectors. Obviously, if the detector/aplanat unit is available to the Simulator, the factor should be measured and this data should be input on Page 1.

3.4.2. Instrument Throughput

This section, included at the request of ITT test engineers, calculates a quantity that is proportional to ideal detector signal on the instrument. It is not used for any further calculation.

The calculations in the following three sections are derived from linear systems analysis of the reference and signal timing clamp circuit. Further detail on the derivation of these equations can be obtained in the aforementioned MIT/LL white paper reference.

3.4.3. White Noise Bandwidth

The channel clamp RC constant chosen for the S/N04 instrument was 1.55 sec for all four LW detectors. However, the optimum RC for a particular detector may be higher or lower depending on the 1/f characteristics of the noise. If the RC input on page 2 is set to 0, a "rough optimum" RC will be chosen based on a curve fit to the MIT/LL optimization data. White noise bandwidth of the instrument is determined (via Parseval's Theorem) by the RC, T_{sc}, and a small auto-zero contribution.

3.5. Model Page 4

3.5.1. Noise Bandwidth Calculations

The noise modeling of NEDN Model Rev. 3.01, and subsequently Rev. 4.1, grew out of signal processing analysis performed at Lockheed Martin that avoided the simplified modeling of the circuitry as a high-pass RC filter in favor of an exact frequency response determination. This electrical analysis was independently corroborated by the GOES detector evaluation team. After defining the parameters of the sampling algorithm f(t) of the sounder clamping circuitry, the exact bandwidth B (by definition) can be calculated using Fourier transform techniques:

$$F(\omega) \equiv \int_{-\infty}^{\infty} f(t) \cdot e^{i\omega t} \cdot dt \tag{1}$$

$$B = \int_{0}^{\infty} F^{*}(\omega) \cdot F(\omega) \cdot d\omega \tag{2}$$

Note that f(t) is a different function for S/N03 and the modified S/N04+ clamp circuit. In effect, the channel capacitors are tied together for the S/N04+ clamp to give a common reference, taken seven times per filter wheel revolution (LW), or five times (MW). In comparison to the once-per-revolution S/N03 clamp reference, the effects of 1/f noise drift are mitigated. Separate model documents have been compiled for the different clamp circuitry.

The total detector noise can then be calculated as a sum of the white noise and the 1/f contribution over the bandwidth:

$$\text{Noise Power} = N_w^2 \left[B_{wh} + B_{1/f} \right] \tag{3}$$

$$\text{Noise Power} = N_w^2 \left[\int_{-\infty}^{\infty} F^{*}(\omega) \cdot F(\omega) \cdot d\omega + \int_{-\infty}^{\infty} F^{*}(\omega) \cdot F(\omega) \cdot \left(\frac{\omega_{knee}}{\omega} \right)^{\beta} \cdot d\omega \right] \tag{4}$$

where the detector noise characteristics are defined as:

N_w^2 = high frequency white noise power [V^2/Hz)
ω_{knee} = knee frequency (defined as frequency where noise power = 2* N_w^2)
β = noise power slope in detector's 1/f region

Once the functional form of the Fourier Transform pair f (t) <=> F (ω) was determined, the two integrals in the brackets above could be performed. These functional forms are given by the equations in the "System Transfer Functions" subsection of Page 4. The first integral determines the white noise bandwidth and may be solved in closed form by Parseval's Theorem as mentioned above. The second integral however, represents the 1/f noise contribution and must be calculated numerically to give a quantitative result.

3.6. Model Page 5

3.6.1. 1/f Noise Bandwidth Integrations

The integrations are broken down and calculated by frequency decade. The results may be interpreted as an effective 1/f noise bandwidth that must be added to the real instrument white noise

bandwidth to determine the total electrical bandwidth. Alternatively, the result can be thought of as an effective (higher) white detector noise over the instrument white noise bandwidth (with no 1/f contribution). Both interpretations are calculated by channel on Page 5.

3.7. Model Page 6

3.7.1. Background Noise Calculations

This section calculates the filter wheel assembly contribution to background photon flux at the detector. It should be noted that previous revisions of the model (e.g. Rev. 3.01) calculated background flux from every element in the optical train of the Sounder, in every channel. These equations were calculationally intensive and comprised the bulk of the running time of the previous model. The results of these calculations showed that under standard conditions, the filter wheel assembly was by far the dominant contributor to background. This result was carried over to Rev. 4.1, in which only the filter wheel contribution to background is calculated as an excellent approximation to the rigorous result. This approximation is validated by measured results on the GOES instruments, where measured bench vs. thermal vac noise agrees with modeled improvement when the filter wheel is cooled to operating temperature.

The filter wheel flux contribution is compared with the flux present during the vendor detector testing. Any excess photon flux is converted to an rss-additive noise due to excess instrument background. Instrument noise is also rss'ed to give a total rms noise voltage used in the NEDN calculations on the following page.

3.8. Model Page 7

3.8.1. NEDN Calculation

At this point, all the pieces of the NEDN equation have been calculated for each Sounder channel. NEDN is calculated by channel using the fundamental IR sensitivity equation:

$$NEDN_{\lambda} = \frac{V_{rms}}{R_{\lambda} \cdot A_{o} \cdot \Omega \cdot \tau_{total} \cdot \Delta\upsilon} \tag{5}$$

The NEDN result is then compared to the system-level NEDN spec by ratio in each channel, and also by the weighted average of the ratio to spec that has come to be known as the Menzel Figure of Merit (FOM). Although this single number obscures much information specific to the individual detector, it has become a popular go/no-go criterion for detector selection. Since the LW detector with the least sensitivity on the S/N03 instrument achieved a 0.33 Menzel FOM, this level of performance has become an unofficial, but defacto, requirement for detector selection on future instruments.

3.9. Model Page 8

3.9.1. Transfer Function Plots

This section provides a visual illustration of the instrument frequency response. Both the white noise and the 1/f noise transfer functions are displayed as a function of frequency.

3.10. Model Page 9

3.10.1 Fourier Transform Of Transfer Function

The instrument frequency response is Fourier-transformed to give a visual illustration of the clamp circuit timeline. This section is particularly useful in displaying the scene vs. reference portions of the measurement. The significant differences between the S/N03 clamp (1 reference per revolution) and S/N04 clamp (7 references per revolution) can be easily visualized.

4. CONCLUSION

This text documents the Lockheed Martin GOES-8 Sounder Radiometric Model. The purpose of the model is to provide an intuitive user interface to GOES-8 instrument IR sensitivity analysis. The model software is freely available for distribution to interested parties by contacting the author.

5. ACKNOWLEDGEMENTS

These models were developed at Lockheed Martin (while known as Loral Infrared and Imaging Systems, LIRIS). The work was performed under LIRIS subcontract SS-274281-E with Space Systems Loral, for the GOES Program effort (US Govt Prime Contract NAS5-29500). The author would like to acknowledge the contributions of Lockheed Martin system engineers Chris Miller, Rich Hassler, Curtis Vock, and Neal Butler in the development of useful algorithms for the models. Additionally the author thanks the LIRIS GOES team, under the guidance of Pat Buckley, Fernando Faria, and Bruce Reynolds, for direction and support during a period of many challenges successfully met.

6. REFERENCES

1. L. Candell and D. Mooney, "Analysis of the GOES Sounder Clamp Circuit", MIT/LL Internal White Paper, 3/15/92.

APPENDIX I: LW Sounder Simulator Throughput calculation example:
LW-L020 (Large Area detector - 3.27 x 3.37 mil)

$$\text{Throughput (\%)} = \frac{\text{Signal}_{\text{measured}}}{\text{Signal}_{\text{ideal}}}$$

$$\text{Throughput (\%)} = \frac{V_{\text{signal}}}{(R)(F)(G)\left[\int L_\lambda R_\lambda \tau_\lambda d\lambda\right](A\Omega)}$$

where:

V_{signal}= measured LW-L020 detector signal in Sounder Simulator at 101 K, 3.5 mA bias=9.89 mV

R = Preaplanat peak responsivity measured on Lockheed Martin ADTS station = 14,317 V/W

F = rms chopper factor = 0.45

G = Sounder Simulator preamplifier measured gain = 994

$L_\lambda(T)$ = Signal spectral radiance, calculated from the blackbody function:

$$L_\lambda(T) = \frac{1.19\times10^4}{\lambda^5\left(e^{14388/\lambda T}-1\right)}\left(\frac{W}{cm^2\cdot sr\cdot\mu m}\right)$$

$L_\lambda(T)$ = L_λ(BB Temp) - L_λ(Room Temp) = L_λ(352 K) - L_λ(296 K)

R_λ = Relative spectral responsivity of detector/aplanat for Sounder Channel 5 = 91%

τ_λ = τ_λ(Dewar window)·τ_λ(Ch. 5 filter)·τ_λ(Radiator window)
·τ_λ(Field Lens 1)·τ_λ(Field Lens 2)·τ_λ(Aplanat)

τ(Ch. 5) = (0.73)(0.78)(0.88)(0.96)(0.96)(0.96)(0.96) = 44.1%

$$\int_{11.6}^{12.5} L_\lambda R_\lambda \tau_\lambda = (0.91)(0.441)\int_{13.33}^{13.59} L_\lambda d\lambda = 6.345\times10^{-5}\left(\frac{W}{cm^2\cdot sr}\right)$$

A_s = Source Area = Lyot Stop Area = $\pi(0.1465\text{ cm})^2 = 0.0674\text{ cm}^2$

Ω = Solid angle of field stop subtended at Lyot stop

Ω = $\text{Area}_{fs}/(\text{distance})^2 = \pi(0.124"/2)/(4.65")^2 = 5.596\times10^{-4}$ sr

$$\text{Throughput (\%)} = \frac{9.89\text{ mV}}{\left[14317\ \frac{V}{W}\right](0.45)(994)\left[(6.345\times10^{-5}\ \frac{W}{cm^2 sr}\right](0.0674\text{ cm}^2)(5.59\times10^{-4}\text{ sr})}$$

Throughput (%) = 64.6 %

GOES LW SOUNDER NEΔN MODEL

INPUT SECTION: Input system parameters below to predict NEΔN performance. DATE: 08/06/96

Detector S/N: **L017, S/N04 Longwave detector 1, 1.0 mA, 101K operation**

Comments: S/N 04 Clamp Circuit: RC=1.55, 0.7 msec channel clamp (tied), 16 msec autozero clamp.
S/N 04 Analytic Gen. transmissions, Δν; S/N 04 measured ifov.
Noise curve fit to LIRIS ADTS post burn-in repeatability data at 102 K.
Temperature spectral responsivity scaling from ITT measurements.

DETECTOR/APLANAT PARAMETERS: Det_SN := .017

$L_d := 2.33$ [mil] $W_d := 2.07$ [mil] $A_d := L_d \cdot W_d \cdot \left(\frac{2.54}{1000}\right)^2$

$R_{peak} := 31200$ [V/W at 102 K] $A_d = 3.112 \cdot 10^{-5}$ [cm²]

$r_\lambda := (.64 \ .77 \ .85 \ .94 \ .84 \ .90 \ .88)^T$ (Fraction of peak R in Channels 1...7 at 102 K)

$N_{wh} := 6.99$ [nV/rtHz] $f_k := 20$ [Hz] $\beta_{det} := 0.98$

$\tau_{aplanat} := 0.96$ $\tau_{simulator_factor} := 0.529$ (Leave zero if simulator measurement not available)

INSTRUMENT PARAMETERS:

Nominal Raytrace Values:

efl := 522.0648 [in] Field_Stop_Diam := 0.124 [in] $Primary_Area_{obsc} := 718.0$ [cm²]

$ifov_{meas} := 225.0$ [μr] (override value, leave zero for nominal AΩ)

$ifov := if\left(ifov_{meas} \neq 0, ifov_{meas} \cdot 10^{-6}, \frac{Field_Stop_Diam}{efl}\right)$ $ifov = 2.2500 \cdot 10^{-4}$ [radians]

(Selects nominal ifov unless override (measured) value has been entered)

$\Omega := \frac{\pi}{4} \cdot ifov^2$ $\Omega = 3.9761 \cdot 10^{-8}$ [sr] Instrument solid angle

$A_o := Primary_Area_{obsc} \cdot 10^{-4}$ $A_o = 7.180 \cdot 10^{-2}$ [m²] optical receiving area

$\tau_{optics} := (.269 \ .281 \ .372 \ .374 \ .408 \ .423 \ .390)^T$ (product of pieceparts, Channels 1...7)

$\tau_{polarization} := .95$ $N_{instrument} := 4.0$ [nV/rtHz]

$\nu := (680 \ 696 \ 711 \ 733 \ 748 \ 790 \ 832)^T$ [cm⁻¹] Spec Center Wavenumber

$\lambda_{av} := \frac{7 \cdot 10^{-2}}{\sum \nu}$ [m] $\lambda_{av} \cdot 10^6 = 13.49$ [Microns] Band Average Wavelength

$\Delta\nu := (11.62 \ 12.97 \ 13.18 \ 13.24 \ 14.30 \ 28.98 \ 49.91)^T$ [cm⁻¹] Analytic Spectral Response FWHM

$T_{filter} := 238$ [K] Filter Wheel Temperature $T_{det} := 101$ [K] Patch Temperature

SCENE PARAMETERS:

$T_{sc} := 7.575 \cdot 10^{-3}$ $t_{sc} := \left[(2.493 \ 13.270 \ 24.048 \ 34.826 \ 45.604 \ 56.381 \ 67.159) \cdot 10^{-3}\right]^T$

AUTO ZERO CLAMP PARAMETERS: Det_SN = 0.017

$T_z := 16 \cdot 10^{-3}$ [Sec] $t_z := 76.8 \cdot 10^{-3}$ [Sec] $g_z := 212.67$ [Gain] $RC_z := 7$

CHANNEL CLAMP PARAMETERS:

$T_{cl} := .7 \cdot 10^{-3}$ [sec] $t_{cl} := \left[(1.093 \quad 11.870 \quad 22.648 \quad 33.426 \quad 44.204 \quad 54.981 \quad 65.759) \cdot 10^{-3} \right]^T$

$g := 252.5$ [gain] $RC := 1.55$ (input RC=0 for selection of rough optimum channel clamp time constant)

DETECTOR TEMPERATURE SCALING

Responsivity Scaling

Required input: r_T= matrix of responsivity factors relative to 102 K for each spectral channel

Patch Temp: 94 101 102 104

$$r_T := \begin{bmatrix} 2.001 & 1.122 & 1.0 & 0.775 \\ 1.793 & 1.102 & 1.0 & 0.808 \\ 1.693 & 1.091 & 1.0 & 0.830 \\ 1.624 & 1.082 & 1.0 & 0.846 \\ 1.609 & 1.080 & 1.0 & 0.849 \\ 1.573 & 1.076 & 1.0 & 0.857 \\ 1.550 & 1.073 & 1.0 & 0.863 \end{bmatrix}^T$$

Ch 1 (14.7 μm)
Ch 2 (14.4 μm)
Ch 3 (14.1 μm)
Ch 4 (13.6 μm)
Ch 5 (13.4 μm)
Ch 6 (12.7 μm)
Ch 7 (12.0 μm)

$T_{patch} := (94 \quad 101 \quad 102 \quad 104)^T$ $m := 1 .. 7$

$r^{<m>} := \text{cspline}\left(T_{patch}, r_T^{<m>}\right)$ Cubic spline fit for each Channel

$r\left(T_{det}\right) := \text{interp}\left(r^{<m>}, T_{patch}, r_T^{<m>}, T_{det}\right)$ Cubic spline interpolation for any patch temperature

$R_{\lambda_m} := \left[R_{peak} \cdot r_{\lambda_m} \cdot r\left(T_{det}\right) \cdot (10)^{-3} \right]$ [V/mW]

White Noise Scaling (1/f parameters assumed invariant with temperature)

Required input: r_{Nw}= matrix of white noise factors relative to 102 K

Patch Temp: 94 101 102 104

$r_{Nw} := (1.0 \quad 1.0 \quad 1.0 \quad 1.0)^T$ White noise factor relative to 102 K

$vs := \text{cspline}\left(T_{patch}, r_{Nw}\right)$ Cubic spline fit for white noise vs temp.

$r_N\left(T_{det}\right) := \text{interp}\left(vs, T_{patch}, r_{Nw}, T_{det}\right)$ Cubic spline interpolation for any temp.

$N_w\left(T_{det}\right) := N_{wh} \cdot r_N\left(T_{det}\right)$

$N_w\left(T_{det}\right) = 6.99$ [nV/rtHz] Detector white noise scaled to operating temperature

------**END OF INPUT SECTION: CALCULATION SECTION BEGINS**------

THROUGHPUT PROJECTION: utilizes detector collection efficiency and aplanat gain. Det_SN = 0.017
Applied only if simulator measurements are unavailable.

$r_i := 1.4$ (mils, nominal image radius) $W_{d0} := W_d$

$W_d := if(W_{d0} < L_d, W_{d0}, L_d)$ $L_d := if(W_{d0} < L_d, L_d, W_{d0})$ (Forces Ld>Wd below)

$$P := r_i^2 \cdot acos\left(\frac{W_d}{2 \cdot r_i}\right) - \frac{W_d}{2} \cdot \sqrt{2 \cdot r_i \cdot \left(r_i - \frac{W_d}{2}\right) - \left(r_i - \frac{W_d}{2}\right)^2}$$

$$Q := if\left[\left(\frac{L_d}{2} \geq r_i\right), 0, r_i^2 \cdot acos\left(\frac{L_d}{2 \cdot r_i}\right) - \frac{L_d}{2} \cdot \sqrt{2 \cdot r_i \cdot \left(r_i - \frac{L_d}{2}\right) - \left(r_i - \frac{L_d}{2}\right)^2}\right]$$

$$\eta := if\left[\frac{W_d}{2} \geq r_i, 1, if\left[r_i < \left[\left(\frac{L_d}{2}\right)^2 + \left(\frac{W_d}{2}\right)^2\right], if\left(\frac{W_d}{2} < r_i, 1 - \frac{2 \cdot P + 2 \cdot Q}{\pi \cdot r_i^2}, \frac{L_d \cdot W_d}{\pi \cdot r_i^2}\right), \frac{L_d \cdot W_d}{\pi \cdot r_i^2}\right]\right]$$

$\eta = 0.77$ Geometric Collection Efficiency

$$Nominal_Gain := \left[\frac{\sin\left(1.385 \cdot \frac{\pi}{180}\right)}{\sin\left(.5395 \cdot \frac{\pi}{180}\right)}\right]^2 \cdot \tau_{aplanat}$$ Nominal_Gain = 6.33 Measured_Gain := 4

$$Post_ap_performance := \frac{Measured_Gain}{Nominal_Gain}$$ Post_ap_performance = 0.63

$Proj_Throughput := \eta \cdot Post_ap_performance$ Proj_Throughput = 0.484

$Throughput := if(\tau_{simulator_factor} = 0, Proj_Throughput, \tau_{simulator_factor})$ Throughput = 0.53

INSTRUMENT THROUGHPUT

$\tau_{total} := \tau_{optics} \cdot \tau_{polarization} \cdot Throughput$

$\tau_{total}^T = (\ 0.14 \quad 0.14 \quad 0.19 \quad 0.19 \quad 0.21 \quad 0.21 \quad 0.20\ )$

$System := \overrightarrow{\left(A_o \cdot \Omega \cdot \tau_{total} \cdot \Delta\nu \cdot R_\lambda\right)}$ [m^2*Sr*PerCm*V/mW] (Represents Signal)

$System^T = (\ 1 \cdot 10^{-7} \quad 1.38 \cdot 10^{-7} \quad 2.04 \cdot 10^{-7} \quad 2.25 \cdot 10^{-7} \quad 2.37 \cdot 10^{-7} \quad 5.31 \cdot 10^{-7} \quad 8.23 \cdot 10^{-7}\ )$

WHITE NOISE BANDWIDTH:

$d := 84.777 - 68.333 \cdot \beta_{det} + 70.671 \cdot \beta_{det}^2$ }
$q := 1.10275 + 1.4964 \cdot \beta_{det}$ } Curve Fit to MIT/LL optimum RC data. (AZ negligible).

$B_{wh} := if\left[RC \neq 0, \frac{1}{2 \cdot T_{sc}} + \frac{1+g}{4 \cdot RC}, \left(d + q \cdot f_k\right)\right]$ White noise BW calculated by Parseval's theorem.
If RC entered as zero, choose optimum RC.

$$\tau_{cl} := \frac{1}{4 \cdot \left(B_{wh} - \frac{1}{2 \cdot T_{sc}}\right)} \qquad RC := if\left[RC \neq 0, RC, \tau_{cl} \cdot (1+g)\right]$$

$$B_{wh} := B_{wh} + \frac{1+g_z}{4 \cdot RC_z}$$ (Add Auto-Zero BW contribution)

NOISE BANDWIDTH CALCULATIONS: Det_SN = 0.017

Transfer Function Parameters:

$\tau_{cl} := \frac{RC}{(1+g)}$ $T := .1$ $\tau_z := \frac{RC_z}{(1+g_z)}$ $\zeta := e^{\frac{-T_z}{\tau_z}}$ $\gamma_z := \frac{g_z}{1+g_z}$

$\gamma := \frac{g}{1+g}$ $m := 1..7$ $k := 1..7$ $\beta_{cl} := e^{-\frac{T_{cl}}{\tau_{cl}}}$ $\beta := \beta_{cl}^{7}$

System Transfer Functions:

$$H_{sc}(f) := \frac{1 - e^{-i \cdot 2\cdot\pi\cdot f T_{sc}}}{i \cdot 2\cdot\pi\cdot f\cdot T_{sc}} \qquad H_{cl}(f) := \frac{1 - \beta_{cl}\cdot e^{-i \cdot 2\cdot\pi\cdot f\cdot T_{cl}}}{1 + i \cdot 2\cdot\pi\cdot f\cdot\tau_{cl}}$$

$$H_{az}(f) := \frac{1 - \zeta\cdot e^{-i \cdot 2\cdot\pi\cdot f T_z}}{\left(1 + i \cdot 2\cdot\pi\cdot f\,\tau_z\right)} \qquad Z(f) := \frac{\gamma_z\cdot e^{\left[i \cdot 2\cdot\pi\cdot f\cdot\left(T_z + t_z\right)\right]}}{\left[1 - \zeta\cdot e^{(-i \cdot 2\cdot\pi\cdot f\cdot T)}\right]}\cdot H_{az}(f)$$

$$H_{clamp}(f) := \left[\begin{array}{l} \gamma\cdot\left[\sum_m\left[(m\le k)\cdot\left(\beta_{cl}^{\,k-m}\right)\cdot\left[e^{\left[i \cdot 2\cdot\pi\cdot f\cdot\left(t_{cl_m} + T_{cl}\right)\right]}\cdot H_{cl}(f) - \left(1-\beta_{cl}\right)\cdot Z(f)\right]\right]\right] \ldots \\ + \frac{\gamma\beta\cdot e^{-i \cdot 2\cdot\pi\cdot f\cdot T}}{1 - \beta\cdot e^{-i \cdot 2\cdot\pi\cdot f T}}\cdot\left[\sum_m\left[\beta_{cl}^{\,k-m}\cdot\left[e^{\left[i \cdot 2\cdot\pi\cdot f\cdot\left(t_{cl_m} + T_{cl}\right)\right]}\cdot H_{cl}(f) - \left(1-\beta_{cl}\right)\cdot Z(f)\right]\right]\right] \end{array}\right]$$

$$H_k(f) := \left[e^{i \cdot 2\cdot\pi\cdot f\left(T_{sc} + t_{sc_k}\right)}\cdot H_{sc}(f) - H_{clamp}(f) - Z(f)\right]$$ (Impulse response of entire measurement)

$U(f) := \left(\left|H_k(f)\right|\right)^2$ (white noise transfer function)

$V(f) := \left[\left(\left|H_k(f)\right|\right)^2\cdot\left(\frac{f_k}{f}\right)^{\beta_{det}}\right]$ (1/f noise transfer function)

1/f NOISE BANDWIDTH INTEGRATIONS: Det_SN = 0.017

$$I_{1_k} := \int_{.001}^{.1} V(f)\,df \qquad I_{1_4} = 0.00 \quad [Hz]$$

$$I_{2_k} := \int_{.1}^{1} V(f)\,df \qquad I_{2_4} = 0.65 \quad [Hz]$$

$$I_{3_k} := \int_{1}^{10} V(f)\,df \qquad I_{3_4} = 24.64 \quad [Hz]$$

$$I_{4_k} := \int_{10}^{100} V(f)\,df \qquad I_{4_4} = 35.01 \quad [Hz]$$

$$I_{5_k} := \int_{100}^{1000} V(f)\,df \qquad I_{5_4} = 3.15 \quad [Hz]$$

$$I_{6_k} := \int_{1000}^{10000} V(f)\,df \qquad I_{6_4} = 0.09 \quad [Hz]$$

$$B_{1overf} := \overrightarrow{(I_1 + I_2 + I_3 + I_4 + I_5 + I_6)}$$

$B_{1overf}^{T} = (\ 75.76 \quad 71.54 \quad 67.17 \quad 63.54 \quad 64.64 \quad 62.81 \quad 59.19\ )$ [Hz]

$B_{wh} = 114.52$ [Hz]

$B_{total} := B_{wh} + B_{1overf}$

$B_{total}^{T} = (\ 190.29 \quad 186.07 \quad 181.69 \quad 178.06 \quad 179.17 \quad 177.33 \quad 173.71\ )$ [Hz]

$$N_{det} := \overrightarrow{\left(N_w(T_{det}) \cdot \sqrt{\frac{B_{total}}{B_{wh}}}\right)}$$

$N_{det}^{T} = (\ 9.01 \quad 8.91 \quad 8.80 \quad 8.72 \quad 8.74 \quad 8.70 \quad 8.61\ )$ Equivalent white detector noise density [nV/rtHz]

$\left(\overrightarrow{\left(N_{det} \cdot \sqrt{B_{wh}}\right)}\right)^{T} = (\ 96.4 \quad 95.3 \quad 94.2 \quad 93.3 \quad 93.6 \quad 93.1 \quad 92.1\ )$ Equivalent white detector noise [nVolts rms]

Reorder results into spectral channels 1..7: (Time Order 1,2,4,5,6,7,3) (Chan Order 1,2,3,4,5,6,7)

reorder := B_{1overf} $B_{1overf} := (reorder_1 \ reorder_2 \ reorder_7 \ reorder_3 \ reorder_4 \ reorder_5 \ reorder_6)^{T}$

reorder := B_{total} $B_{total} := (reorder_1 \ reorder_2 \ reorder_7 \ reorder_3 \ reorder_4 \ reorder_5 \ reorder_6)^{T}$

BACKGROUND NOISE CALCULATIONS: Det_SN = 0.017

$K_b := 14387.9$ $h := 6.626 \cdot 10^{-34}$ $c := 3 \cdot 10^{8}$ $\eta_q := 0.7$ $\kappa := 188.365 \cdot 10^{21}$

Instrument Background

$\Omega_b := 2 \cdot \pi \cdot \left(1 - \cos\left(\frac{40 \cdot \pi}{180}\right)\right)$ [sr] $Q_b := \left[\frac{\kappa}{\pi} \cdot \int_{11.3}^{15.0} \frac{1}{\lambda^4} \cdot \frac{1}{e^{\frac{K_b}{\lambda \cdot T_{filter}}} - 1} d\lambda\right] \cdot \Omega_b$ Instrument background photon flux

$Q_b = 1.09 \cdot 10^{17}$ photons/(sec*cm^2)

Detector Test Background

$T_b := 300$ [K] $\Omega_t := 2 \cdot \pi \cdot \left(1 - \cos\left(\frac{24.5 \cdot \pi}{180}\right)\right)$ [sr]

$Q_t := \left[\frac{\kappa}{\pi} \cdot \int_{11.3}^{15.0} \frac{1}{\lambda^4} \cdot \frac{1}{e^{\frac{K_b}{\lambda \cdot T_b}} - 1} d\lambda\right] \cdot \Omega_t$ Detector test station background photon flux

$Q_t = 1.11 \cdot 10^{17}$ photons/(sec*cm^2)

BACKGROUND NOISE

$R_{av} := \frac{\sum R_\lambda}{7} \cdot 10^3$ Average in-band responsivity $R_{av} = 28218$ [V/W]

$N_{bkg} := \text{if}\left(Q_b - Q_t > 0, \overrightarrow{\left[\frac{2 \cdot h \cdot c \cdot R_{av}}{\lambda_{av} \cdot \eta_q} \cdot \sqrt{(Q_b - Q_t) \cdot A_d \cdot 10^9}\right]}, 0\right)$ Noise due to excess instrument background

$N_{bkg} = 0.00$ [nV/rtHz]

$N_{rms} := \overrightarrow{\left(\sqrt{N_{det}^{\ 2} + N_{instrument}^{\ 2} + N_{bkg}^{\ 2}}\right)}$ (total rms noise voltage density) [nV/rtHz]

$V_{rms} := \left(\overrightarrow{\left(N_{rms} \cdot \sqrt{B_{wh}}\right)} \cdot 10^{-9}\right)$ (total rms noise voltage) [Volts rms]

Noise Voltages:

$\left(N_{bkg} \cdot \sqrt{B_{wh}}\right) = 0.00$ [nVolts rms]

$\overrightarrow{\left(N_{det} \cdot \sqrt{B_{wh}}\right)}^T = (\ 96.4 \quad 95.3 \quad 94.2 \quad 93.3 \quad 93.6 \quad 93.1 \quad 92.1\ )$ [nVolts rms]

$N_{instrument} \cdot \sqrt{B_{wh}} = 42.8$ [nVolts rms]

$V_{rms}^{\ T} \cdot 10^9 = (\ 105.5 \quad 104.5 \quad 103.5 \quad 102.6 \quad 102.9 \quad 102.5 \quad 101.6\ )$ [nVolts rms]

Noise Voltage Density:

$N_{bkg} = 0.00$ [nV/rtHz]

$N_{det}^{\ T} = (\ 9.01 \quad 8.91 \quad 8.80 \quad 8.72 \quad 8.74 \quad 8.70 \quad 8.61\ )$ [nV/rtHz]

$N_{instrument} = 4.00$ [nV/rtHz]

$N_{rms}^{\ T} = (\ 9.86 \quad 9.77 \quad 9.67 \quad 9.59 \quad 9.61 \quad 9.57 \quad 9.49\ )$ [nV/rtHz]

NEΔN CALCULATION:

Det_SN = 0.017

$$NE\Delta N_\lambda := \frac{\overrightarrow{V_{rms}}}{R_\lambda \cdot A_o \cdot \Omega \cdot \tau_{total} \cdot \Delta v}$$

$$NE\Delta N_\lambda = \begin{bmatrix} 1.05 \\ 0.76 \\ 0.51 \\ 0.46 \\ 0.43 \\ 0.19 \\ 0.12 \end{bmatrix} \begin{matrix} \text{Ch 1} \\ \text{Ch 2} \\ \text{Ch 3} \\ \text{Ch 4} \\ \text{Ch 5} \\ \text{Ch 6} \\ \text{Ch 7} \end{matrix} \quad [mW/(m^2*sr*cm^{-1})]$$

$$NE\Delta N_{spec} := \begin{bmatrix} 0.66 \\ 0.58 \\ 0.54 \\ 0.45 \\ 0.44 \\ 0.25 \\ 0.16 \end{bmatrix} \qquad \frac{\overrightarrow{NE\Delta N_\lambda}}{NE\Delta N_{spec}} = \begin{bmatrix} 1.59 \\ 1.30 \\ 0.94 \\ 1.01 \\ 0.99 \\ 0.77 \\ 0.77 \end{bmatrix}$$

$$NFOV := (25 \;\; 25 \;\; 9 \;\; 9 \;\; 9 \;\; 1 \;\; 1)^T$$

$$FOM_{Menzel} := \frac{\sqrt{\sum_m \left[\frac{NE\Delta N_{\lambda_m}}{NE\Delta N_{spec_m} \cdot \sqrt{NFOV_m}} \right]^2}}{\sqrt{\sum_m \left(\frac{1}{NE\Delta N_{spec_m} \cdot \sqrt{NFOV_m}} \right)^2}} \qquad FOM_{Menzel} = 0.17$$

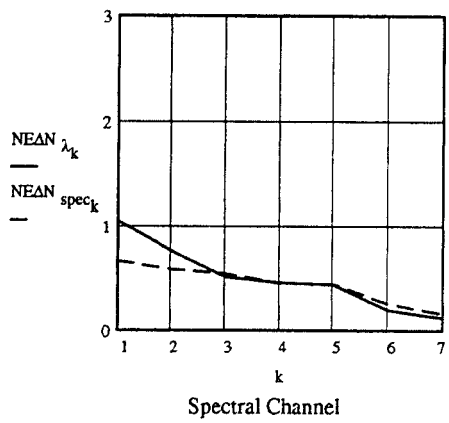

Spectral Channel

TRANSFER FUNCTION PLOTS: $W := 4$ Channel (time order) for plots Det_SN = 0.017

$$N(f) := \sqrt{1 + \left(\frac{f_k}{f}\right)^{\beta_{det}}}$$ Normalized noise voltage vs frequency

$$H_{clamp}(f) := \left[\gamma \cdot \left[\sum_m \left[(m \le W) \cdot \left(\beta_{cl}^{W-m}\right) \cdot \left[e^{\left[i \cdot 2 \cdot \pi \cdot f \cdot \left(t_{cl_m} + T_{cl} \right) \right]} \cdot H_{cl}(f) - \left(1 - \beta_{cl}\right) \cdot Z(f) \right] \right] \right] \ldots \right.$$
$$\left. + \frac{\gamma \cdot \beta \cdot e^{-i \cdot 2 \cdot \pi \cdot f \cdot T}}{1 - \beta \cdot e^{-i \cdot 2 \cdot \pi \cdot f \cdot T}} \cdot \left[\sum_m \left[\beta_{cl}^{W-m} \cdot \left[e^{\left[i \cdot 2 \cdot \pi \cdot f \cdot \left(t_{cl_m} + T_{cl} \right) \right]} \cdot H_{cl}(f) - \left(1 - \beta_{cl}\right) \cdot Z(f) \right] \right] \right] \right]$$

$$H_k(f) := \left[e^{i \cdot 2 \cdot \pi \cdot f \cdot \left(T_{sc} + t_{sc_W} \right)} \cdot H_{sc}(f) - H_{clamp}(f) - Z(f) \right]$$

points := 500 n := 1 .. points

$f_{min} := .01$ $f_{max} := 1000$ $r := \log\left(\frac{f_{max}}{f_{min}}\right)$ $freq_n := f_{min} \cdot 10^{\frac{r \cdot n}{points}}$ Plots equally spaced points on a frequency log axis

$U(f) := \left(\left| H_k(f) \right| \right)^2$ $V(f) := \left[\left(\left| H_k(f) \right| \right)^2 \cdot \left(\frac{f_k}{f}\right)^{\beta_{det}} \right]$

RC = 1.55 B_{wh} = 114.5

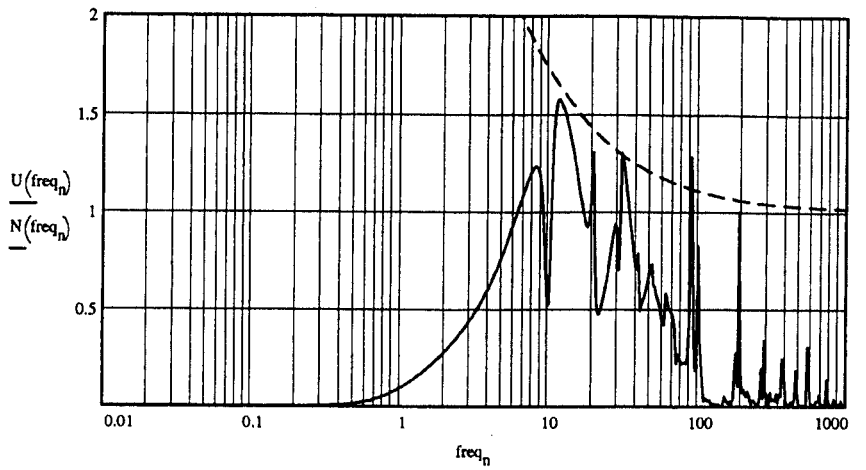

RC = 1.55 B_{1overf_4} = 67.17

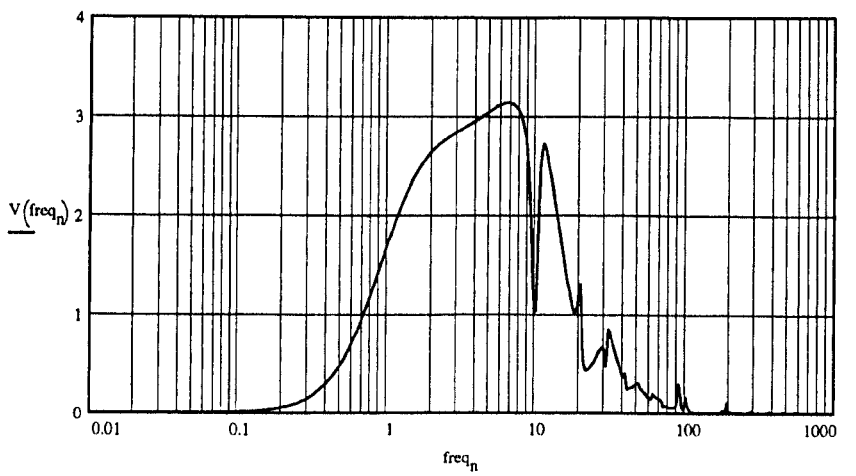

FOURIER TRANSFORM OF TRANSFER FUNCTION Det_SN = 0.017

$p := 12$ $points := 2^p$ $points = 4096$ $m := 1 .. points$ $f_H := 10000$ $f_L := .01$

$$freq2_m := \frac{(m-1)\cdot(f_H - f_L)}{points} + f_L \qquad H_{k2_m} := \left(H_k\left(freq2_m\right)\right)$$

$$H_{k3} := \overrightarrow{\left[H_{k2}\cdot e^{-i\cdot 2\cdot\pi\cdot freq2\cdot W\cdot\left(t_{cl_2} - t_{cl_1}\right)}\right]}$$

Phase delay sets start of scene at origin

$Timeline := icfft\left(\overrightarrow{H_{k3}}\right)$ inverse FFT of frequency response

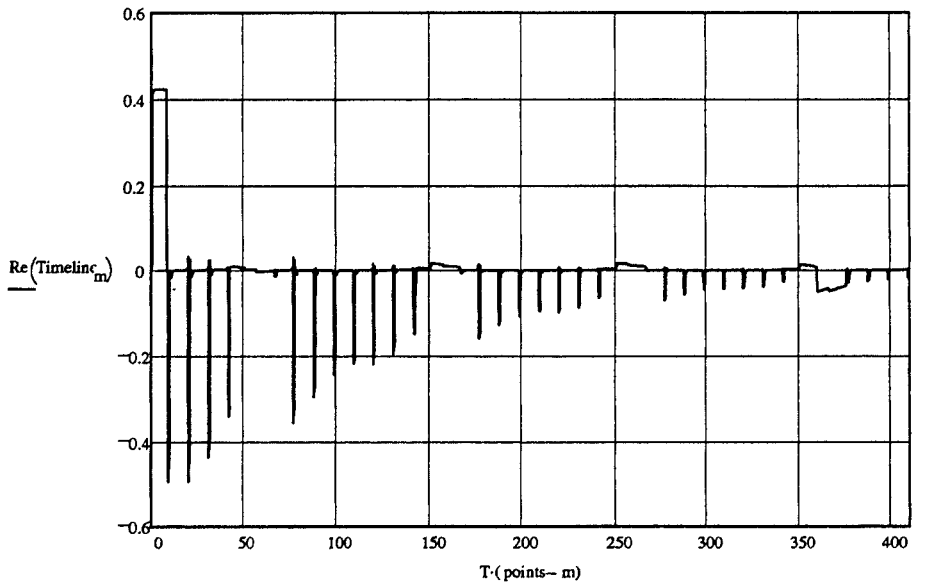

Time (msec)

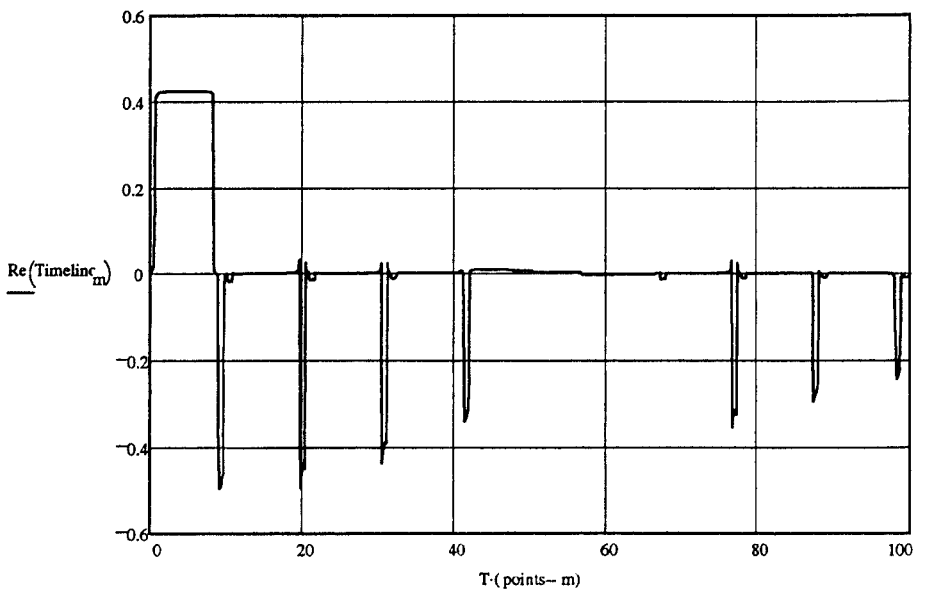

Time (msec)

Solar Intrusion Thermal Analysis

Benny Ghaffarian
ITT/ACD Technical Staff Engineer,
Fort Wayne, Indiana 46801
&
Kent Sprunger
ITT/ACD Senior Technical Staff Engineer,
Fort Wayne, Indiana 46801

ABSTRACT

During the Fall of 1994 eclipse season, GOES-8 Sounder telescope secondary mirror temperature exceeded qualification limits, while operating normally in the vicinity of the Sun. Based on a simple conservative thermal analysis, which was performed in January of 1995, it was determined that there was a health and safety issue with operating Imager or Sounder in the vicinity of the Sun. As a result, a set of operating constraints were levied on both instrument normal operations, limiting them from scanning in the vicinity of the Sun. Since the simple thermal analysis was believed to be conservative, ITT was tasked to develop a detailed model of the secondary assembly and to determine the effect of focused energy on the secondary assembly critical components. The detailed model of the secondary assembly was developed and several full disk frame cases were analyzed to determine if the keep out zone may be eliminated or reduced. In addition to the full disk frame cases several CEI initialization cases were also analyzed for the Imager post eclipse instrument turn on scenario. The results of the detailed analysis indicates that the simple thermal analysis done in January of 1995 was in fact not conservative. It was determined that the Imager secondary temperature will far exceed the mission allowable temperature of 47C (52C Instrument qualification temperature -5C), while performing full disk frames in the vicinity of the Sun. The Maximum inner baffle temperature was predicted to get as high as 130C for the worst full disk frame case analyzed. The Thermal modeling effort as well as the results of the analysis and recommendations for future instrument qualification test and design changes will be documented in this paper.

Keywords

Solar Intrusion, Focused Energy, Secondary Assembly Thermal Model, Keep-Out-Zone, Health and Safety

INTRODUCTION

During the first eclipse season after launch of the GOES-8 satellite (Fall of 1994), temperature telemetry for Sounder telescope secondary mirror exceeded the maximum mission allowable limit. This was observed during normal operations with the optical axis pointing in the vicinity of the sun. Optical ray trace analysis confirmed that impingement of solar energy, focused by the telescope primary mirror, onto components of the secondary mirror assembly caused the high temperature.

The mission allowable temperature limit is based on the temperature range over which the telescope components were tested during pre-launch qualification tests. Allowing the telescope to operate above the established maximum limit poses a health and safety concern for the instrument. The primary concern relates to risk of a permanent change in the position of the secondary mirror, thereby incurring degradation of visible MTF and/or star sense signal/noise. Small secondary mirror displacements, i.e. 0.0001 inch in axial position and 0.002 inches in radial position, can produce a measurable change in instrument performance.

Initially this concern was thought to apply only to the Sounder. The Sounder stepping mode allows impingement of focused solar energy onto the secondary mirror assembly for up to 87 seconds per east/west (E/W) scan line, whereas the Imager scanning mode limits the impingement to ≤ 0.45 seconds. Simple thermal analysis performed in January of 1995 confirmed the health and safety concern when operating the Sounder in the vicinity of the sun. However contrary to the initial reasoning, it also indicated that there is a health and safety concern when operating the Imager in the vicinity of the sun.

Under these conditions, it predicted very large temperature gradients within the secondary mirror assembly such that the locations of the two secondary mirror temperature sensors do not provide the necessary information for all potential health and safety concerns. Operational constraints, i.e. solar intrusion keep-out zones, to protect the health and safety of the instruments were levied on the operations of both instruments. The Imager is prohibited from scanning within 6.25° of the sun. The Sounder is prohibited from stepping within 8.25° of the sun. For days when the sun declination angle is +7.25° to -7.25°, the Imager scan motors are prohibited from being turned on within 1.25 hours of local satellite midnight to prevent the automatic E/W Coherent Error Integrator (CEI) initialization scans from overlapping the 6.25° keep-out zone. As a result, many of the frames normally scheduled from 1030 to 0130 local satellite time cannot be executed. The data from these deleted frames is lost.

Since these constraints have significant, adverse impacts on users and since the thermal analysis was believed to have been conservative and overstated the temperature rise, ITT was tasked to perform the required detailed thermal modeling/analysis to characterize and better understand instrument solar intrusion.

The objectives of the solar intrusion thermal analysis were:

1. Predict on-orbit telescope secondary temperatures for the Imager instrument when performing full disk frames and CEI initialization frames in the vicinity of the sun to determine if the "keep-out" zone for Imager full disk frames and/or the constraint for Imager turn-on after eclipse can be reduced or eliminated.

2. Determine if the present design of the telescope secondary can possibly be qualified to operate over increased temperature limits necessary to allow further reduction or elimination of the Imager full disk frame "keep-out" zone and/or the Imager turn-on after eclipse constraint.

THERMAL ANALYSIS

Solar intrusion thermal analysis of the secondary mirror assembly was a unique and very sensitive study. An enormous amount of solar energy can be focused on the secondary mirror assembly during the E/W scanning motion of the scan mirror, when the north/south (N/S) position of the Sun is within 6 degrees of the N/S scan mirror position. The magnitude of the focused solar energy on the secondary mirror assembly components is approximately equivalent to fifty times the collimated solar heat load. The secondary mirror housing and its inner baffle are made of Invar which has a low Coefficient of Thermal Expansion (CTE) to maximize the optical performance over the on-orbit temperature range. However Invar has also a relatively low thermal conductivity (0.34 W/in-C) and when exposed to such large, focused solar loads will have very large temperature gradients, i.e. large localized temperature extremes. The secondary mirror and its Invar housing assembly have a very small conduction path through flexures to the aluminum spider assembly. The combination of the above mentioned solar loads and design characteristics contribute to high rates of temperature change and localized high temperatures of the secondary mirror inner baffle and housing. To accurately predict the effects of focused energy on the secondary mirror assembly, a detailed thermal model of the secondary mirror was developed. Every critical aspect of the model was independently verified, and finally the predictions from this model were compared to orbital data for two different days during the eclipse seasons. This model was then utilized to predict the Imager secondary mirror temperatures for several full frame and CEI initialization cases. Results of this analysis were then used to determine if the GOES-8 keep out zone can be reduced. This model will also be utilized in future analysis to evaluate possible design changes.

Methodology

Imager and Sounder instruments typically perform different frames at prescribed times according to a user defined schedule. The solar heat load profile for the thermal analyses of each frame is unique and different from every other frame, based on the frame type, size and relative location of the sun with respect to earth. The goal was to set up the thermal analysis programs such that any given frame size and type, for any given sun relative location could be analyzed. Hence, detailed radiation and conduction thermal models of the GOES secondary mirror assembly were developed utilizing the I-DEAS/TMG program. The NEVADA program was utilized to predict the solar heat loads on the secondary mirror assembly for 213 different sun vectors. The 213 sun vectors were defined such that the solar image could be mapped on the secondary assembly from its east to west and north to south edges at one degree increments. A mapping program was then developed to map the appropriate solar heat load results of the NEVADA program onto the secondary mirror assembly for different

frames. This process enabled us to analyze many different types of frames both for the Imager and the Sounder instruments. The Imager full disk frame was picked as the first set of frames to be evaluated. During a full disk frame, the scan mirror rotates in the E/W direction between the Beginning and the End Of the scan Line (BOL/EOL) at a constant rate of 20 degrees per second. The scan mirror then slows down to a stop at the Turn Around (T/A) point at the end of each scan line and speeds back up to the constant scanning rate between the T/A point and the BOL. The slowing down, stopping and speeding back up to constant scan rate takes 0.2 second. The scan mirror steps south 224 μrad during the turn around sequence after each scan line. A typical Imager full frame takes 26 minutes to complete. The analysis process was set up such that the absorbed solar heat loads were mapped on the secondary mirror based on instantaneous scan mirror position and the Sun location. However, even with a large matrix of 213 solar loads, some approximation had to be made on the N/S position of scan mirror location/motion. Since the solar loads were calculated at one degree N/S increment, north to south stepwise motion in one degree increments was assumed for the transient runs. For example, during the time at which the relative angle between the scan mirror position and sun location was between 4.5 to 5.5 degrees, the E/W absorbed solar heat loads of cases associated with the 5.0 degree N/S relative angle were utilized in the transient analysis. Multiple transient runs were performed varying the N/S and E/W relative angle between scan mirror and the sun and interpolating between the corresponding E/W solar loads to simulate the scan mirror position and motion. The predicted temperature results at the end of each N/S position were used as the initial temperatures for the next N/S transient run until the solar image was moved off the secondary assembly. Results of the multiple runs were then concatenated into one file to produce temperature predictions for a full disk frame case.

Combined Radiation/Conduction Model

Detailed radiation and conduction thermal models of the secondary mirror assembly were developed using I-DEAS/TMG. The radiation model contained all the exterior surfaces of the secondary mirror assembly and the interior walls of the instrument scan cavity, scan mirror, primary mirror and limit frames. Figure 1 presents the geometric element layout of the radiation model. SS/L utilized the NEVADA program to generate the solar loads on the secondary mirror assembly for 213 different sun vectors. Table 1 presents the optical properties used in the NEVADA program.

	Emittance	Solar Absorptance
Black Paint	0.87	0.95
Scan Mirror	0.053	0.14
Primary Mirror	0.053	0.11
Secondary Mirror	0.053	0.11

Table 1: Optical Properties Used in the Radiation Model

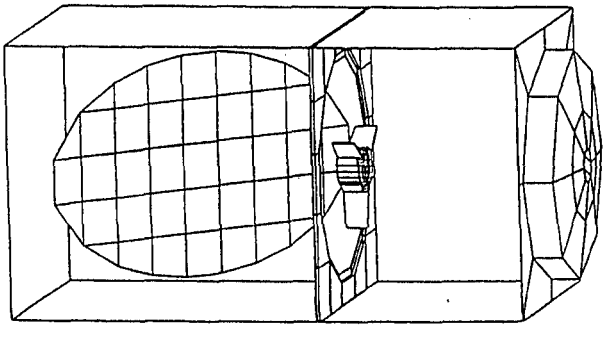

Figure 1: Geometric Nodal Layout of the Radiation Model.

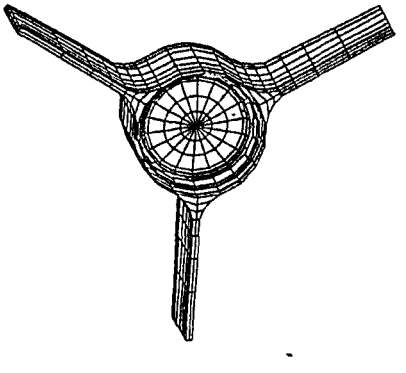

Figure 2: Geometric nodal layout of the secondary mirror assembly in the conduction model

The conduction model which contains 523 nodes includes all the secondary assembly components (the Invar inner baffle, secondary mirror housing, end plate, the ULE secondary mirror, the aluminum flexure, outer baffle and spider assembly). Figure 2 presents a plot of the secondary assembly. Table 2 presents the material properties used in the conduction analysis. The appropriate nodes of the conduction and radiation models were merged to generate a combined model. NEVADA solar loads were mapped on the secondary assembly for different full disk frame cases, and transient runs were performed at multiple N/S scan mirror positions (one degree increments) to complete a full disk frame case.

Material	ρ (lb/in^3)	C_p (W-hr/lb-C)	K. (W/in-C)	Comments
ULE	0.079	0.095	0.022	Secondary mirror.
Invar	0.29	0.065	0.34	Inner baffle, mirror housing, end plate
Al (6061)	0.098	0.10	4.35	Spider, Flexure
Mylar	0.047	0.2374	0.00404	Spacer (between secondary mirror & housing)
RTV 566	0.054	0.169	0.0082	Between mirror & housing, on Thermistor
Epoxy, Structural 3M-2216	0.048	unknown	0.005	Mechanical joints
Epoxy Epon	0.044	0.2321	0.0055	Between Flexure & Spider
Eccobond	0.083	0.121	0.038	On thermistor
Alumina 96%	0.144	0.131	0.628	Thermistor chip

Table 2: Material Thermal Properties Used in the Conduction Model.

Model Verification

The I-DEAS/TMG program was utilized to develop the model geometry. The geometric tolerances were picked such that the resulting calculated mass of each component was either equal to or slightly less than its actual measured weight. The material list was made available to Swales and GSFC Engineers for their recommendation of the material properties to be used. Table 2 represents the material properties used in the model.

The geometric tolerances were picked such that the resulting element thicknesses were smallest, hence the calculated conduction values were conservatively low. In addition all critical conduction values calculated by TMG program were verified against two sets of independent values hand calculated by ITT and Swales engineers.

Prior to performing 213 NEVADA solar runs, an extensive effort was put forward by the SS/L, ITT, Swales and GSFC engineers to verify the proper definition of the Scan mirror, Primary mirror, and Secondary mirror geometries, locations, and focusing. A boresight case verification analysis was conducted with the Sun at the optical axis. The scan mirror and primary mirror absorptance values were set to 0.01 and the secondary mirror absorptance was set to 1.0. The resulting total absorbed solar load compared closely with hand calculated values. Other geometry verification cases conducted included replacing the secondary mirror with a small surface at the primary mirror focal point and verifying that all of the solar energy is being focused properly on this surface. A small surface was also placed behind the primary mirror at the secondary mirror focal point to verify the geometric location and shape of the secondary mirror. For each of these cases, the verifications were made by ray tracing plots, and by comparing the total absorbed solar heat load with hand calculated values.

Once the radiation model was verified geometrically, the actual optical surface properties, of Table 1, were inputted in the model and the 213 sun vector NEVADA runs were initiated. GSFC in parallel, conducted similar analyses for several sun vectors using a different analyzer , Thermal Synthesizer System (TSS) , to verify the absorbed solar heat load values on the secondary assembly.

TEMPERATURE SENSITIVITY ANALYSIS

The thermal model was built to be conservative. The geometric tolerances were picked such that the resulting thermal masses and thermal conductor values were lowest. The boundary temperatures surrounding the secondary assembly were obtained from the system level model for the end of life (EOL) conditions. The EOL secondary mirror assembly initial temperature from the system level model is 30C, which is 10C higher than beginning of life (BOL) on-orbit temperatures. The solar heat loads were calculated with scan mirror and primary mirror BOL absorptance values. As a result, the secondary assembly calculated absorbed heat loads were 5% higher than corresponding EOL higher absorptance values.

The only remaining uncertainty was the material properties used in the model. The only significant discrepancy was the published values for Invar thermal conductivity. The variation found in the published values were from -20% to +5% of the value used in the model. As a result, parametric analyses were performed on two full disk frame cases, for which, the thermal conductivity and thermal capacitance of Invar were reduced by as much as 30% and 10% respectively. Table 3 shows the predicted maximum secondary temperature for each case. As shown in this table, the variation in predicted maximum temperature for the higher heat load level case (case 8) was 9.7C, and for the lower heat load level case (case 12) the variation was 6.2C. The two cases which were picked for sensitivity analysis were case 8 (see table 4) which predicted the highest inner baffle temperature of 130.7C, and case 12 (see table 4) which predicted a maximum inner baffle temperature of 72.3C.

Hence based on the results of this sensitivity study, the recommended level of uncertainty was set at +10 and -0C on predicted temperatures above 70C, and +5 and -0C on predicted temperatures of 70C or below.

		Case 8		Case 12	
Cp_Invar	K_Invar	Tmax	Delta	Tmax	Delta
100%	100%	130.7	-	72.3	-
90%	90%	134.3	3.6	74.6	2.3
90%	70%	140.4	9.7	78.5	6.2

Table 3: Inner Baffle Predicted Maximum Temperatures

ON-ORBIT THERMISTOR COMPARISON

To verify the solar mapping procedure, predicted thermistor temperatures were compared with two different GOES-8 on-orbit secondary mirror thermistor temperature profiles. The first comparison case picked was GOES-8 Imager data from a full disk frame performed on day 290 of 1994. For this case the sun declination was -9.18 and the E/W starting sun location was -0.31 degrees. Figure 3 shows the frame size and the relative position and size of the sun. Figure 4 shows the relative size of the solar image on the secondary mirror assembly. This figure also depicts a box which represents the path of the center of the sun on the secondary during the full disk frame imaging. As shown in this figure, the solar image passes directly over portions of the secondary mirror assembly including the thermistor number 2 location.

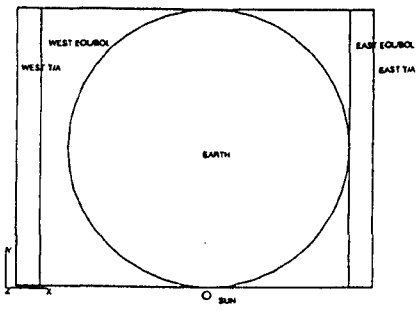

Figure 3: GOES-8 Imager full disk frame description for day 290, 1994

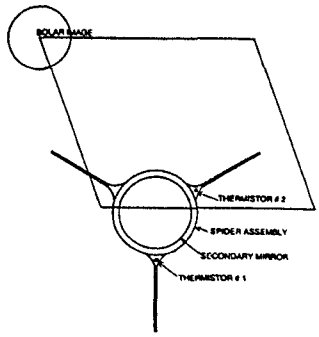

Figure 4: Solar image path on secondary mirror assembly viewed from primary mirror, Day 290, 1994

Figure 5 presents the actual relative N/S angle of the sun and the corresponding relative N/S and E/W position of the sun used in the model. Figure 6 shows the comparison of the predicted thermistor number 2 temperature with on-orbit data. As shown in this figure, the predicted time and the slope for the temperature rise compares very well with the data. The predicted slope of the thermistor temperature rise changes several times. This is due to the one degree incremental stepping of the scan mirror during the analysis. The secondary mirror assembly and a primary mirror baffle create a shadowed spot in the center of the solar image. One noticeable difference between the predicted and on-orbit temperature is during the time when the shadowed spot on the center of the solar image is traveling over the thermistor. Figure 7 shows the mapped solar load profiles on the thermistor for two scan lines for -3 degree south sun position. As shown in this figure the solar load during the scan line does go to zero, representing the shadowed spot on the thermistor. However with the discrete number of solar loads available, the continuous change of the magnitude of the solar energy on the thermistor could not be captured. Over all, the comparison for this case was considered to be very good, because the predicted time for temperature rise and initial slope matched well. The thermistor maximum temperature and the time of occurrence for the maximum temperature were predicted accurately (45.2C predicted maximum temperature compared to on-orbit peak temperature of 44.5C). The predicted slope of the cool down also compared well with flight data. This comparison verified the solar heat load mapping scheme. Figure 8 shows the predicted maximum temperature profile of the secondary assembly (Inner Baffle), secondary mirror housing and the thermistor during this frame. As shown in this figure the maximum predicted temperature of the secondary assembly was 87C while the maximum predicted temperature of the thermistor is only 45C.

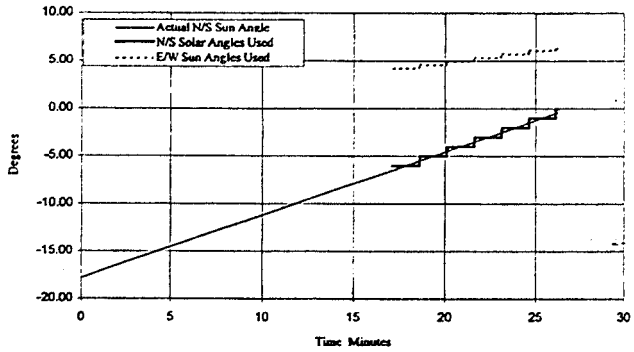

Figure 5: Relative sun angles utilized in analysis of case 1.

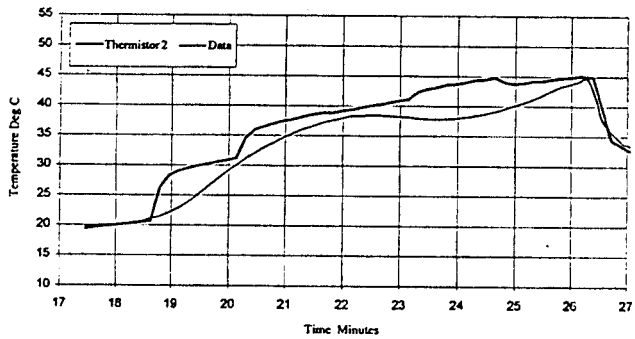

Figure 6: GOES-8 thermistor 2 comparison for day 290, 1994

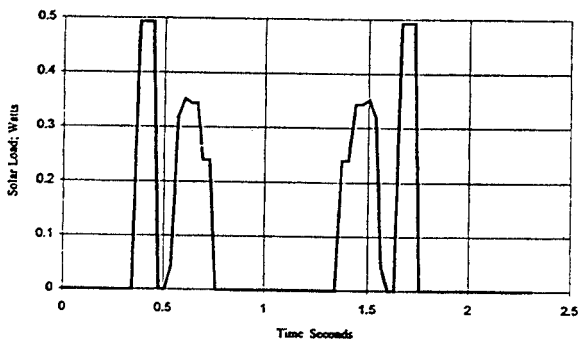

Figure 7: Absorbed Solar Load Profile on Thermistor 2
N/S Relative Sun Angle to Scan Mirror = -3°

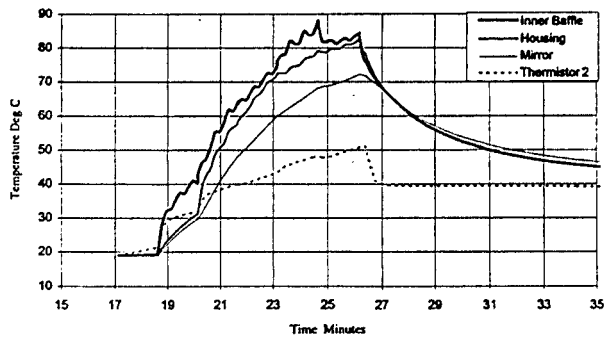

Figure 8: Predicted Secondary Assembly Maximum Temperatures, GOES-8, Day 290, 1994

The next case used for comparison with on-orbit data was GOES-8 Imager data from a full disk frame performed on day 237 of 1994. For this case the sun declination was 10.83 and the E/W starting location was -0.49 degrees. Figure 9 shows the frame size and the relative position and size of the sun. Figure 10 shows the relative size of the solar image on the secondary mirror assembly. This figure also depicts a box representing the path of the center of the sun on the secondary during the full disk frame imaging. As shown in this figure the edge of the sun illuminates the thermistor number 2 for a short time. Thermistor number one, however, is exposed to the sun for much longer duration. Thermistor number one is known not to be reliable therefore it was not used for comparison purposes. Comparison with the data for thermistor 2 on this day was considered to verify the conduction paths within the spider assembly. Figure 12 compares the predicted temperature profile of thermistor 2 with on-orbit data. While during the first 0.23 minutes, the actual N/S position of the sun varies from 0.34 to 0.5 degree, the mapping program used the higher solar heat load values associated to 0 degree N/S position. This resulted a higher slope for initial predicted temperature rise compared to the flight data. After 0.23 minutes, when the solar image has moved off the thermistor 2, the remaining temperature rise is strictly due to the conduction through the secondary spider assembly. As shown in Figure 12, the remaining temperature rise slope and the predicted peak temperature matches the on-orbit data well. The predicted maximum thermistor temperature was 31.7, compared to the maximum on orbit thermistor temperature of 30.5C.

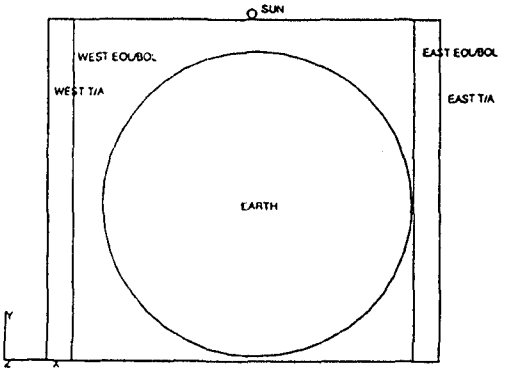

Figure 9: GOES-8 Imager full disk frame description day 237, 1994

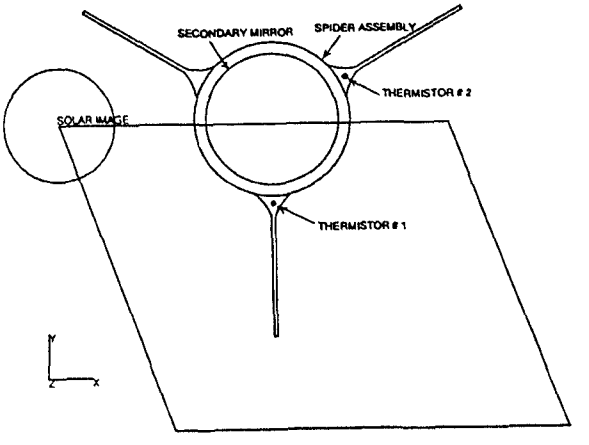

Figure 10: Solar image path on secondary mirror assembly viewed from primary mirror ,Day 237, 1994

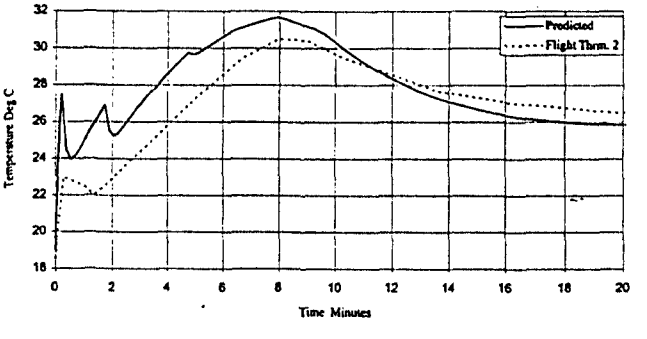

Figure 11: GOES-8 Imager Thermistor 2 Comparison for Day 237, 1994

ON ORBIT PREDICTION CASES

Transient analyses were performed for nineteen full disk frame cases and twenty two CEI initialization cases. The sun declination and E/W position of sun were the variable elements for each case. The combination of the results from these analyses were used to determine by how much the Imager operational constraints may be reduced. Table 4 lists the details of the frame boundaries and the sun initial position for each case. Also included in this table are the maximum predicted temperature for any component on the secondary (titled as Tmax All), as well as the maximum predicted temperature for secondary mirror housing (titled as Tmax Housing). The Tmax All most often reflects the inner baffle temperature. Since the inner baffle does not have any structural importance, this temperature was used to identify concerns for outgassing of materials only. The predicted housing temperature was used to identify structural and optical performance concerns for the secondary mirror assembly. The maximum predicted inner baffle and mirror housing temperatures were 130.7C and 118.4C for cases 8 and 17, respectively. Similar information for the twenty two CEI initialization cases are tabulated in Table 5. The maximum predicted inner baffle and housing temperatures for the CEI initialization cases were 82C and 56.6C for case numbers 103 and 105, respectively. Detailed temperature plots for all the analyzed cases are documented in reference 1.

CONCLUSION

An extensive effort was put forth by ITT, SS/L, Swales and GSFC engineers to develop a detailed thermal model of the secondary mirror assembly. This model has been thoroughly verified by the involved engineers of these organizations. The temperatures predicted by this model are conservative, and as reliable as analytically achievable. Analyses were performed for nineteen Imager full disk frames as well as twenty-two CEI initialization frames.

The results indicate that the simple thermal analysis done in January of 1995 was in fact not conservative. The Imager secondary mirror assembly temperature will far exceed the mission allowable temperature (MAT) when performing worst case full disk frames and CEI initialization frames in the vicinity of the sun. A MAT of 47°C has been established for the GOES-8 and GOES-9 secondary mirror assemblies. It is based on the fact that they were temperature cycled up to 52°C during instrument qualification testing. Detailed evaluation of the present design has revealed that the GOES-8 and GOES-9 secondary mirror assemblies may not be qualified by similarity to operate over increased temperature limits. Therefore, on-orbit temperatures, including 5° analysis uncertainty, must be limited to the MAT to avoid incurring a high risk of permanent degradation in visible MTF and/or star sense signal/noise.

Operational constraints, i.e. solar intrusion keep-out zones, must be maintained to protect the health and safety of the GOES-8 and GOES-9 Imager and Sounder instruments. A systems engineering evaluation of the temperature predictions revealed that to maintain the GOES-8 and GOES-9 Imager secondary mirror temperatures below the MAT, the keep-out zone can only be marginally reduced by 0.25 degree. A 0.25 degree reduction in the keep-out zone only eliminates ≈3 days/year when frames intrude into the keep-out zone.

The temperature predictions also confirm that present locations of the two secondary mirror temperature sensors do not provide the necessary information for health and safety monitoring. Moving the sensors to different locations could only verify, not reduce, keep-out zones.

The solar intrusion phenomena is now well understood and it's effects can be analytically predicted. This thermal model will be used to evaluate all future potential design changes which could reduce the secondary mirror assembly peak temperatures. With a reduction of secondary mirror assembly peak temperatures and pre-launch qualification testing at increased temperatures , the keep-out zones for future satellites can be greatly reduced.

ACKNOWLEDGMENTS

The authors wish to acknowledge the efforts of team members at ITT, Space Systems/Loral, GSFC and Swales Associates. Their work was performed under a contract from NASA on the GOES project, contract number SC92800-AZ.

REFERENCES

1) ITT Final Report: Solar Intrusion Analysis, Phase A, Dated January 29, 1996.

Case	Tmax		Sun Decl.	Start Sun	Stop Sun	West	West	East	East	Frame Start	Frame	Solar Exposure
No.	All	Housing	Deg	Angle E/W	Angle	EOL/SOL	T/A	EOL/SOL	T/A	N/S Position	Duration (min)	time (min)
Case 1	-	-	-9.18	-0.31	6.23	-10.4	-11.88	8.7	10.17	8.68	26.15	9.13
Case 2	127.7(-0+10C)	108.8(-0+10C)	10.83	-0.49	6.87	-10.4	-11.88	8.8	10.28	10.49	29.42	9.276
Case 3	92.2(-0+10C)	87.6(-0+10C)	-1.35	-15.53	-9.03	-8.69	-10.17	10.4	11.88	8.6	25.97	19.58
Case 4	117.5(-0+10C)	97.4(-0+10C)	-8.7	-11.85	-5.35	-8.69	-10.17	10.4	11.88	8.6	25.97	9.6
Case 5	114.4(-0+10C)	99.1(-0+10C)	-8.7	-10.72	-4.23	-8.69	-10.17	10.4	11.88	8.6	25.97	9.69
Case 6	124.9(-0+10C)	109.1(-0+10C)	8.7	3.9	10.39	-10.4	-11.88	8.7	10.18	8.6	25.97	9.62
Case 7	101.5(-0+10C)	97.4(-0+10C)	2.11	8.51	15	-10.4	-11.88	8.7	10.18	8.6	25.97	19.55
Case 8	130.7(-0+10C)	116.3(-0+10C)	7.425	4.99	11.49	-10.4	-11.88	8.7	10.18	8.6	25.97	11.54
Case 9	31.3(-0+5C)	31.3(-0+5C)	-1.35	-19.9	-13.41	-8.69	-10.17	10.4	11.88	8.6	25.97	19.58
Case 10	36.6(-0+5C)	34.6(-0+5C)	-1.35	-18.9	-12.41	-8.69	-10.17	10.4	11.88	8.6	25.97	19.58
Case 11	56.5(-0+5C)	53.7(-0+5C)	-1.35	-17.9	-11.41	-8.69	-10.17	10.4	11.88	8.6	25.97	19.58
Case 12	72.3(-0+10C)	69.4(-0+5C)	-1.35	-16.9	-10.41	-8.69	-10.17	10.4	11.88	8.6	25.97	19.58
Case 13	119.8(-0+10C)	99.6(-0+10C)	-8.95	-4.56	1.93	-8.69	-10.17	10.4	11.88	8.6	25.97	9.34
Case 14	32.5(-0+5C)	32.5(-0+5C)	14.6	-1.93	4.56	-10.4	-11.88	8.7	10.18	8.6	25.97	0.753
Case 15	69.3(-0+5C)	41.9(-0+5C)	13.6	-1.93	4.56	-10.4	-11.88	8.7	10.18	8.6	25.97	2.259
Case 16	81.8(-0+10C)	58(-0+5C)	12.6	-1.93	4.56	-10.4	-11.88	8.7	10.18	8.6	25.97	3.765
Case 17	128.3(-0+10C)	118.4(-0+10C)	-4.63	-14.88	-8.39	-8.69	-10.17	10.4	11.88	8.6	25.97	15.833
Case 18	100.7(-0+10C)	97.2(-0+10C)	5.32	9.2	15.69	-10.4	-11.88	8.7	10.18	8.6	25.97	14.73
Case 19	42.1(-0+5C)	32.9(-0+5C)	2.6	14.67	21.16	-10.4	-11.88	8.7	10.18	8.6	25.97	12.8
Case 20	47.5(-0+5C)	35.6(-0+5C)	2.6	13.67	20.16	-10.4	-11.88	8.7	10.18	8.6	25.97	15.814

Table 4: Maximum Predicted Temperatures and the Frame Details for Imager Full Disk Frame Cases

Case	Tmax		Sun Decl.	Start Sun	Stop Sun	West	West	East	East	Frame Start	Frame
No.	All	Housing	Deg	Angle E/W	Angle	EOL/SOL	T/A	EOL/SOL	T/A	N/S Position	Duration (min)
Case 101	59.6(-0+5C)	50.9(-0+5C)	0	8.95	9.12	-10.4	-11.88	10.4	11.88	0	0.7
Case 102	68.6(-0+5C)	49.9(-0+5C)	1	8.89	9.06	-10.4	-11.88	10.4	11.88	0	0.7
Case 103	82(-0+10C)	54.7(-0+5C)	2	8.72	8.89	-10.4	-11.88	10.4	11.88	0	0.7
Case 104	78.6(-0+10C)	54.6(-0+5C)	3	8.43	8.6	-10.4	-11.88	10.4	11.88	0	0.7
Case 105	74.5(-0+10C)	56.6(-0+5C)	4	8.01	8.17	-10.4	-11.88	10.4	11.88	0	0.7
Case 106	78.4(-0+10C)	54.1(-0+5C)	2	10.79	10.96	-10.4	-11.88	10.4	11.88	0	0.7
Case 107	61.3(-0+5C)	49.9(-0+5C)	2	12.79	12.96	-10.4	-11.88	10.4	11.88	0	0.7
Case 108	48.4(-0+5C)	46.1(-0+5C)	2	14.79	14.96	-10.4	-11.88	10.4	11.88	0	0.7
Case 109	59.5(-0+5C)	50.2(-0+5C)	0	11.79	11.96	-10.4	-11.88	10.4	11.88	0	0.7
Case 110	60.3(-0+5C)	51.2(-0+5C)	0	11.54	11.71	-10.4	-11.88	10.4	11.88	0	0.7
Case 111	58.7(-0+5C)	49.8(-0+5C)	0	11.29	11.46	-10.4	-11.88	10.4	11.88	0	0.7
Case 112	61.4(-0+5C)	51.8(-0+5C)	0	11.04	11.21	-10.4	-11.88	10.4	11.88	0	0.7
Case 113	62.7(-0+5C)	53.4(-0+5C)	0	12.04	12.21	-10.4	-11.88	10.4	11.88	0	0.7
Case 114	60.4(-0+5C)	51.4(-0+5C)	0	12.29	12.46	-10.4	-11.88	10.4	11.88	0	0.7
Case 115	62.4(-0+5C)	52.6(-0+5C)	0	12.54	12.71	-10.4	-11.88	10.4	11.88	0	0.7
Case 116	36(-0+5C)	36(-0+5C)	-6	6.64	6.81	-10.4	-11.88	10.4	11.88	0	0.7
Case 117	47.9(-0+5C)	42.4(-0+5C)	-5	7.42	7.59	-10.4	-11.88	10.4	11.88	0	0.7
Case 118	67.9(-0+5C)	42.6(-0+5C)	5	7.42	7.59	-10.4	-11.88	10.4	11.88	0	0.7
Case 119	34.7(-0+5C)	34.7(-0+5C)	6	6.64	6.81	-10.4	-11.88	10.4	11.88	0	0.7
Case 120	35.3(-0+5C)	35.3(-0+5C)	3	16.4	16.57	-10.4	-11.88	10.4	11.88	0	0.7
Case 121	41.7(-0+5C)	35.8(-0+5C)	0	17.29	17.46	-10.4	-11.88	10.4	11.88	0	0.7
Case 122	43.9(-0+5C)	35.2(-0+5C)	-3	16.4	16.57	-10.4	-11.88	10.4	11.88	0	0.7

Table 5: Maximum Predicted Temperatures and the Frame Details for Imager CEI Initialization Cases

Comparison between subsystem and system optical MTF for GOES Imager

Frederick L. Williams, John C Ehlert, David R. Wickholm

ITT Aerospace Communications Division
For Wayne, Indiana

ABSTRACT

Starting with SN05 Imager the optical MTF of the visible optics assembly has been measured at subsystem and at system level testing. For the visible detector MTF at 18,000 cycles/radian relative differences of 16 percent have been observed between system and subsystem data. The test setups are quite different, however, the MTF values should be dominated by the detector's field of view MTF and thus the differences should be small. Descriptions of the two configurations are given along wiht a discussion of some of the important differences.

The investigation into the differences led to the testing of the Imager and test collimator with a parabolic mirror as collimator and an MTF analyzer. The MTF values using the parabola with the instrument were about 12 percent better than with the test collimator. Observations of the image of a pinhole at the Cassegrain focus led to the analysis of spider vane diffraction which accounts for 2.7 percent MTF reduction. In addition analysis has also been performed on the collimator interferogram that indicates a reduction in MTF due to a number of steep zones within the collimator wavefront. The analysis predicts a 9.7 percent reduction in MTF at 18,000 cycles/radian due to the test collimator of which 1.4 percent is a result of the collimator secondary spider vanes. The verification of the analysis awaits a new collimator with slope errors reduced to less than 0.12 waves/inch.

KEYWORDS: GOES, IMAGER, MTF, OPTICAL MTF, SLOPE ERRORS

1. INTRODUCTION

The visible channel modulation transfer function (MTF) is a key performance requirement for the GOES Imager. The GOES 8 and 9 Imager MTF performance of the visible channel appears very good based upon the images that they are producing. However, during instrument performance testing on the ground, the system and optical MTF for the visible channel measure below expectations. This is true for the four specified spatial frequencies on each Imager tested to date. The MTF for a diffraction limited f/12.25 system, the Imager, the cutoff frequency equals approximately 125.59 cycles/mm for a 0.65 μm wavelength. (The visible channel spectral bandpass is 0.55 +- 0.025 μm to 0.75 +- 0.025 μm) For the Imager the 18,000 cycles/radian spatial frequency corresponds to 4.72 cycles/mm or only 3.75percent of cutoff. This frequency is far enough from the cutoff frequency that small shifts in focus and small changes in aberrations should not dramatically reduce the MTF. For the 18,000 cycle/radian frequency the Imager visible channel MTF should be driven primarily by the field of view (FOV) of the detector which is required to be within 25.2 to 28.0 microradians with a nominal of 26.67 microradians.

As a result of the lower than expected MTF performance, starting with SN05 Imager, a measurement of the visible optics assembly MTF occurs during subsystem testing. This measurement includes the visible detector and other components within the visible optics assembly. The results of the 18,000 cycle/radian subsystem optical MTF measurements (EW), ~0.63, are very close to the expected values for MTF compared to the system optical MTF value for 18,000 cycles per radian of 0.53 (EW). The difference between the subsystem and system optical MTF measurements is approximately 16 percent. The differences between subsystem and system optical MTF measurements is the subject for discussion in this paper.

2.0 BACKGROUND

The Imager visible optical system consists of the scan mirror, telescope primary and secondary mirrors, the visible-infrared beamsplitter, depolarizer, spectral balance filter, spectral bandpass filter, detector window and detector. Figure 1 shows an optical layout of the Imager visible optics. The telescope[1,2] is a Cassegrain design with a 30.5 cm diameter primary mirror and a 3.8 cm diameter secondary mirror. The telescope has an effective focal length of 150 inches and a 2 milliradian total field of view. The secondary mirror has 3 spider vanes equally spaced at 120 degrees apart supporting it. The scan mirror is a nickel plated beryllium mirror with an aluminum coating on top of the nickel. The visible-infrared beamsplitter and depolarizer are each tilted at 45 degrees relative to the optical axis and tilted about axes orthogonal to each other to correct for polarization

0-8194-2200-2/96/$6.00

effects and to balance astigmatism. The spectral filters limit the wavelengths of light reaching the detector to 0.55 +/- 0.025 μm to 0.75 +/- 0.025 μm. The two filters are both normal to the optical axis as are the detector window and detector.

FIGURE 1
GOES IMAGER VISIBLE OPTICAL SYSTEM

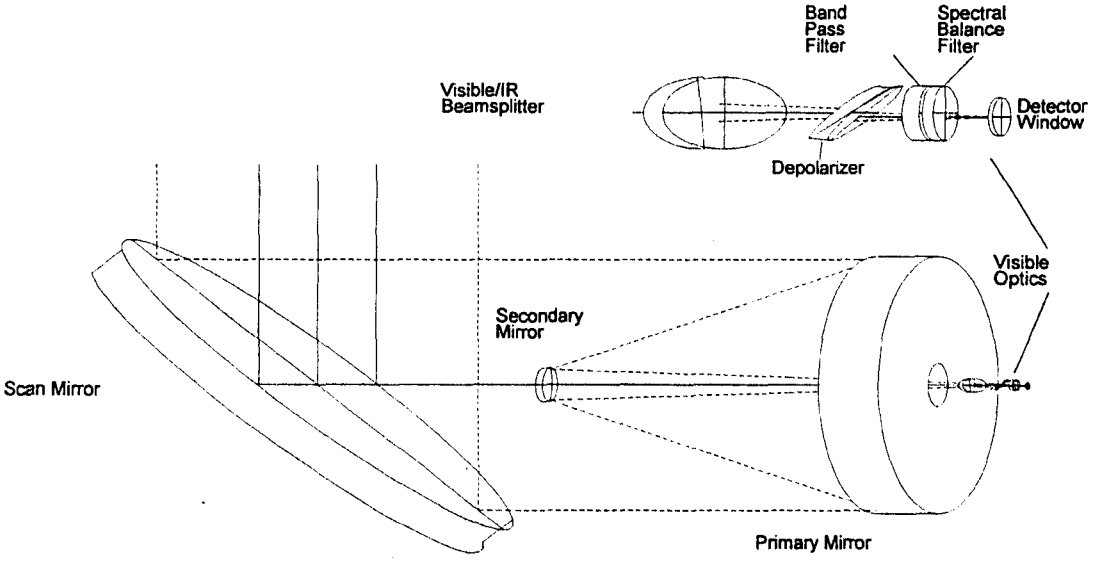

The MTF of the GOES Imager visible optical system is the product of the individual components MTF. Except for the telescope all of the components in the visible optics are flat and should have minimal impact on MTF. The most significant component affecting MTF is the detector field of view. The equation below gives the detector MTF at a spatial frequency ν for a field of view θ.

$$MTF = \frac{\sin(\pi\nu\theta)}{\pi\nu\theta} \tag{1}$$

For a nominal size detector of 26.67 microradian FOV the MTF at 18,000 cycles/radian equals 0.662. Table I shows the detector FOV MTF for the other frequencies of interest. The MTF of the telescope is a more complex calculation due to the secondary obscuration. The equation for a diffraction limited system with a central obscuration[3] is:

$$OMTF = \frac{2}{\pi} * \left(\frac{D_o^2}{D_o^2 - D_i^2}\right) * \left(\phi_o - \sin\phi_o * \cos\phi_o\right) - 2 * \left(\frac{D_i^2}{D_o^2 - D_i^2}\right) + \left(\frac{2}{\pi}\right) * \left(\frac{D_i^2}{D_o^2 - D_i^2}\right) * \left(\phi_i - \sin\phi_i * \cos\phi_i\right) \tag{2}$$

where D_o = telescope diameter, D_i = secondary obscuration diameter, $\cos\phi_o = \lambda\nu/D_o$, $\cos\phi_i = \lambda\nu/D_i$, λ is the wavelength of light and ν is the spatial frequency. For D_o = 305 mm, D_i = 61 mm, λ = 0.65 μm, and ν = 18,000 cycles/radian, Table I shows the resultant MTF = 0.939. As this value shows the visible channel optical MTF at 18,000 cycles/radian depends primarily on the detector width, because the detector is the field stop in the case of the Imager. Table I shows the ideal visible optical MTF of an ideal Imager optical system at the specified frequencies.

TABLE I
IDEAL IMAGER OPTICAL MTF VALUES

FREQUENCY (cycles/radian)	TELESCOPE MTF diffraction limited	DETECTOR FOV MTF 26.67 microradians	VISIBLE OPTICAL MTF ideal
18000	0.939	0.662	0.622
13500	0.954	0.800	0.763
9000	0.969	0.908	0.88

4490	0.985	0.977	0.962

In practice no system performs at the ideal level. The scan mirror has some small imperfections, the telescope has aberrations, and the visible optics have aberrations also. The expectations for visible MTF need to have a more realistic estimate. The current method for estimating the visible MTF is to use measurements, such as wavefront error and FOV, to help predict the eventual MTF. The scan mirror and telescope wavefront error measurement computes the Zernike coefficients that CODE V can use to predict the MTF of a system having those measured aberrations. Likewise the FOV measurement of the visible detectors produces detector size data that the computer model uses to predict the detector MTF. Using the measurements of the SN05 and SN06 Imager Table II shows the expected visible optical MTF values, not including the effects of stray light, for a nominal 26.67 microradian detector FOV. These are the values to compare with the subsystem and system level MTF measurements for SN05 and SN06.

TABLE II
OPTICAL MTF PREDICTIONS FOR SN05 AND SN06
IMAGER VISIBLE CHANNEL

FREQUENCY	OPTICS		DETECTOR	EXPECTED OPTICAL MTF	
cycles/radian	SN06	SN05	26.67 microradian	SN06	SN05
18000	0.935	0.932	0.662	0.619	0.617
13500	0.953	0.951	0.800	0.762	0.761
9000	0.969	0.968	0.908	0.88	0.879
4490	0.985	0.985	0.977	0.962	0.962

Table III and Table IV show the results for the visible optical MTF measurements at subsystem and system level testing. Both SN05 and SN06 MTF results indicate a significant difference in performance ~16 percent at 18,000 cycles/radian. At the other spatial frequencies the difference between subsystem and system MTF values show a maximum of only 8 percent. Something appears to be reducing the MTF at system compared to subsystem with the largest difference occurring at 18,000 cycles/radian. This then is the frequency that we will address to begin understanding the influences that the instrument or test conditions have on the MTF measurements.

TABLE III
SUBSYSTEM OPTICAL MTF MEASUREMENTS
IMAGER VISIBLE CHANNEL

cycles/radian	18000		13500		9000		4500	
	SN06	SN05	SN06	SN05	SN06	SN05	SN06	SN05
east west	0.63	0.634			0.815	0.829	0.918	0.906
north/south	0.616	0.626			0.81	0.817	0.914	0.911

TABLE IV
SYSTEM OPTICAL MTF MEASUREMENTS
IMAGER VISIBLE CHANNEL

cycles/radian	18000		13500		9000		4490	
	SN06	SN05	SN06	SN05	SN06	SN05	SN06	SN05
east west	0.535	0.525	0.669	0.651	0.809	0.772	0.886	0.851
north/south	0.53	0.494	0.663	0.615	0.787	0.742	0.875	0.849

3.0 SUBSYSTEM OPTICAL MTF MEASUREMENTS

Subsystem level MTF measurements utilize a telescope simulator (TESI), a one-to one conjugate Offner relay, to simulate the f/12.25 beam incident on the visible optics assembly. The TESI image plane location occurs at the same nominal position as the telescope focal plane relative to the three mounting pads on the back of the primary cell. This assures that the position of the visible optics assembly with respect to the optical axis on the TESI is identical to the position of the visible optics assembly in the instrument relative to the telescope optical axis. TESI is a well-corrected symmetric optical imaging system due to the fact that the center of curvature of the two spherical mirrors is the same. The imaging performance of the telescope simulator is very nearly diffraction limited and unlike the flight telescope TESI has no obscuration.

Figure 2 is a diagram of the TESI optical configuration. At the source end the target and fiber optic light source mount on a set of translation stages that move the target during the subsystem scans. A fold flat in the input arm to the spherical primary of TESI allows for the physical separation of the object and image planes. The visible optics assembly mounts to the TESI cell plate that simulates the telescope primary cell reference datum. At the primary mirror of TESI there is a mask that defines the entrance pupil and exit pupil of the TESI.

The MTF measurements at subsystem use several discrete bar targets with different spatial frequencies as the periodic objects to image. The bar targets set in a holder that has been positioned at the input focus of the TESI and a fiber optic light source illuminates the bar target. (The subsystem bar targets are physically the same bar targets as the ones used at system level tests. However, because the collimator to instrument focal length ratio is 2 to 1, the bar targets at subsystem represent half the spatial frequency that they do at system.). The target and light source assembly mounts to a set of 0.1 micrometer resolution, computer-controlled translation stages.

FIGURE 2
TELESCOPE SIMULATOR OPTICAL CONFIGURATION

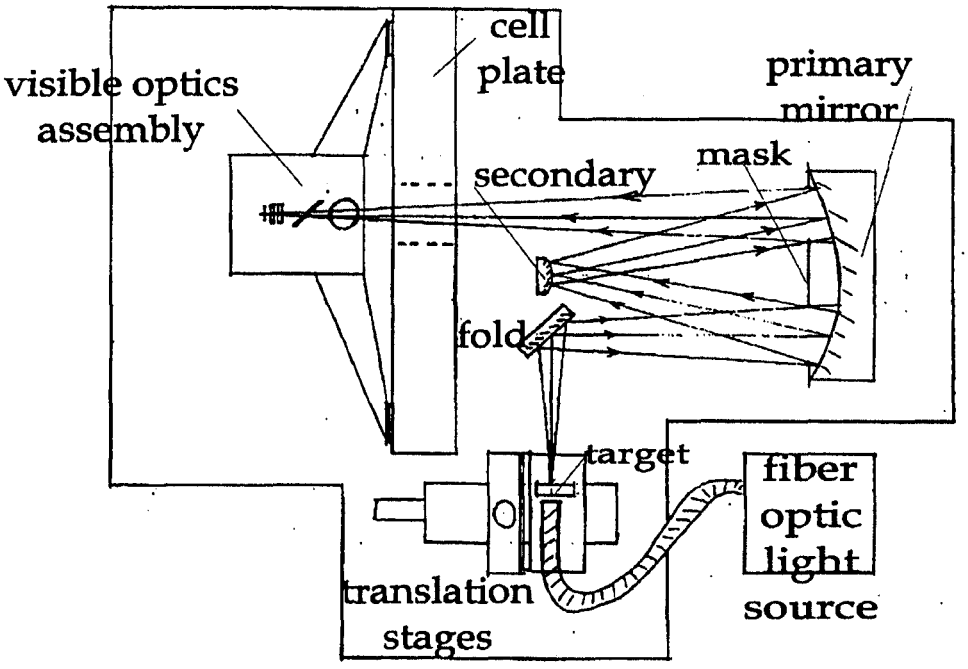

The MTF data collection process at subsystem uses a step-collect-average-store sequence. The computer commands the target's translation stage to step in uniform increments. At each step of the target, the computer averages N samples of each visible detector and stores the result to a file. This process continues until the entire bar target scans across the detectors FOV. The scan for the orthogonal axis proceeds similarly with the bar target rotated 90 degrees in the holder.

Following the acquisition of data comes the processing of the data to calculate the MTF. The subsystem MTF calculations use the same algorithm as system level to perform a least squared error fitting of the measured data to the calculated data to determine the coefficients in the Fourier series. Using the coefficients, the algorithm computes the amplitude of the fundamental frequency or sinusoidal MTF. Table III shows the results of the subsystem measurements of optical MTF for SN05 and SN06 Imager. As stated previously, the measured optical MTF values at subsystem are very close to expected optical MTF values, assuming a nominal visible detector size.

4.0 SYSTEM OPTICAL MTF MEASUREMENTS

Figure 3 shows the optical configuration for the system level MTF measurements. The system level tests use the system test collimator and its light source assembly to illuminate the Imager. The test collimator is a Cassegrain telescope with an effective focal length of 300 inches and a clear aperture of 14 inches. The collimator secondary mirror diameter is approximately 2 inches which matches the instrument secondary obscuration size very closely. The collimator secondary has four support vanes positioned at 45 degrees with respect to the vertical and horizontal axes. There is a fold mirror that inserts from the primary mirror end to reflect the collimator's optical axis to the side of the collimator housing where the target focal plane resides. The collimator light source assembly contains both a visible and infrared source. The visible source is a helical tungsten wire filament source operating at 150 watts. A zinc selenide beamsplitter combines the visible beam with the infrared beam by reflecting the visible and transmitting the infrared radiance. In the visible source optical path is a condenser lens that images the filament about 3 inches behind the secondary mirror and provides reasonably uniform light to the target. The condenser lens and secondary mirror together image the filament onto the primary mirror of the collimator. Typically the collimator to Imager separation is approximately three feet.

FIGURE 3
SYSTEM TEST OPTICAL CONFIGURATION

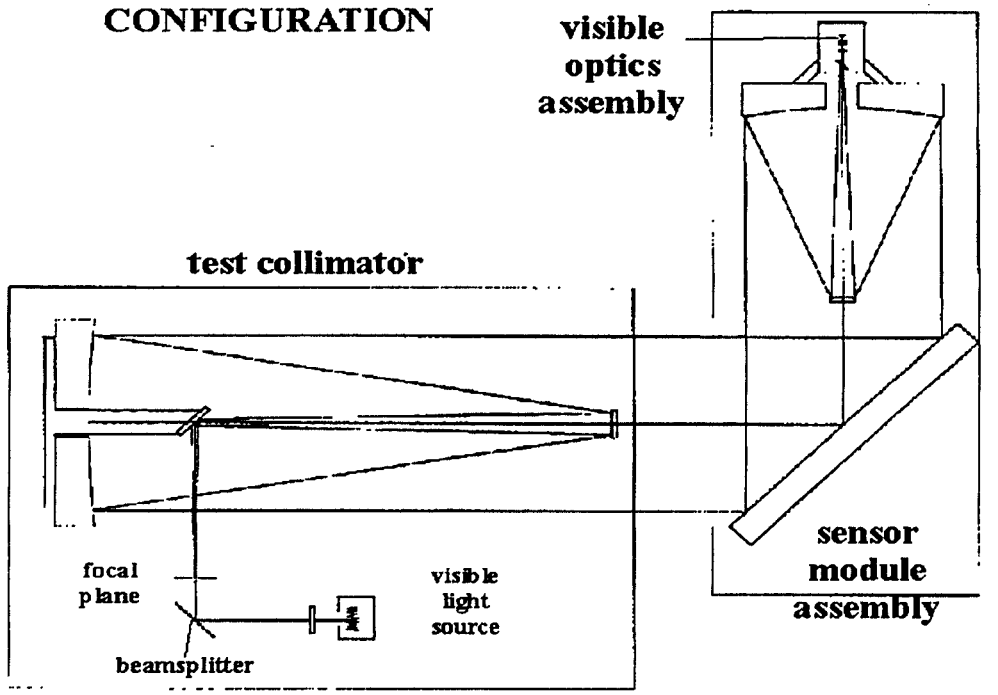

The discrete bar targets that are used at subsystem as periodic objects are also used during system optical MTF measurements. The target holder locates the target at the focal plane of the collimator. The pair of computer-controlled linear translation stages also with 0.1 μm resolution supports the target assembly and locates the target on the optical axis of the collimator.

The alignment of the collimator to instrument uses the telescope's back of secondary reference mirror to achieve an angular alignment with the telescope. The translational alignment puts the collimator and instrument secondary obscurations overlapping within 1/4 to 1/2 inch.

The optical MTF measurement at system test collects wideband data during a sweep of the scan mirror. The motion of the scan mirror serves to sweep the bar target image coming from the collimator across each detector's field of view. The data collection begins following an image motion compensation (IMC) command to the scan mirror to move approximately 2 milliradians. An externally generated square wave whose frequency is 1 kHz controls the speed of the scan mirror motion.

This reduces the speed of the scan mirror so that it moves much slower than the standard 20 degrees per second. The software stores the wideband data to a file for subsequent processing.

The data processing follows the data collection. The same algorithm that calculates the subsystem MTF calculates the system optical MTF. The MTF calculation uses a single scan line of data and not an average of numerous scans of the bar target. Table IV shows the results of the system optical MTF measurements.

In addition to the system optical MTF measurements there are sensor module MTF measurements that use the subsystem data collection methodology. This test verifies that no stress or force is acting on the telescope as the sensor module assembly progresses. The sensor module MTF measurement is a very good bridge between the subsystem and system MTF measurements. The test configuration is the same as system test, i.e., test collimator and Imager, and the data collection and data processing are the same as subsystem, following the step-collect-average-store sequence.

Table V shows the MTF values from the sensor module integration MTF measurement. As Table V indicates the sensor integration MTF measurements use only the 18,000 and 4490 cycle per radian targets to perform the health check. The MTF values agree very well with the system optical MTF values. This indicates that the data collection and processing that are different between the system and subsystem tests do not produce significant differences in the determination of MTF values.

TABLE V
SENSOR INTEGRATION MTF MEASUREMENTS
IMAGER VISIBLE CHANNEL

cycles/radian	18000		13500		9000		4490	
	SN06	SN05	SN06	SN05	SN06	SN05	SN06	SN05
east west	0.539	0.507					0.87	0.852
north/south	0.531	0.484					0.871	0.84

5.0 DIFFERENCES BETWEEN SYSTEM AND SUBSYSTEM TESTS AND MEASUREMENTS.

From the descriptions above there are significant differences between the system and subsystem MTF measurement situations. The most noticeable differences are the following:

1. On axis configuration vs. off axis configuration
   1A. central obscuration vs. no obscuration
2. Light sources
3. wavefront errors
4. Focus

Other differences that are not as obvious are the following:

5. vibrations
6. air turbulence
7. Light scattering
8. Bar targets

5.1 On-axis vs. off-axis

The difference between an on-axis and off-axis system has two aspects: obscurations and multiple reflections. The off-axis TESI obviously does not have an obscuration and may therefore have a higher MTF at 18,000 cycles/radian. The optical modeling of the Imager visible optics includes the effect of the secondary obscuration and the reduction in MTF is small approximately 1.2 percent when comparing to an unobscured f/12.25 system at 18,000 cycles/radian. The test collimator also has a secondary obscuration approximately the same size as the telescope obscuration. If the alignment of collimator to instrument places the two secondary obscurations overlapping each other there is no effect on MTF of the additional obscuration. However, the possibility exists for a degradation in MTF if the alignment is incorrect. The reduction in MTF expected should only be ~1 percent. In addition to the central obscurations the Imager and test collimator have spider vanes supporting each secondary mirror. The area of the vanes is small and so the effect of scattering and diffraction should also be small. The effect of central obscurations on MTF is then expected to be about 1 percent to 1.5 percent.

The TESI also minimizes any chance for multiple reflections within the test setup with its off-axis configuration. The only multiple reflections other than within the visible optics have to return to the target and back to the detector. Since that side of the targets is black, it is unlikely to create any measurable reflectance at the detector. At system test it is possible for a portion of the light reflected from the telescope's back of secondary mirror to reach the detector of the instrument. This effect is again a small effect but may be as much as one percent depending upon how well the secondary of the collimator overlaps the instrument secondary. Another concern is the light from the target that bypasses the secondary of the collimator and enters the instrument. This light originates from outside the field of view of the instrument and should not reach the detector. Measurements show that blocking the light that bypasses the collimator secondary does not affect the measured MTF values. The conclusion is that the on-axis configuration may bring a slight degradation in MTF but the expectations are that this level is about 2 percent worst case.

5.2 Light sources

The light source of the test collimator images the filament at the primary mirror of the collimator. The alignment of the mirror behind the source fills the gaps between the filament coils to make the image of the filament more uniform. The magnification of this image is such that only about two cycles of the filament actually fit inside the diameter of the primary mirror. This pupil illumination pattern is not uniform having dips in the intensity across the pupil of approximately 20 percent. If the pupil is not uniform it is possible to reduce the MTF of the system much like an obscuration does. However as stated earlier the frequency range over which the instrument operates is small compared to cutoff and these large slow varying pupil intensity functions do not significantly affect the MTF at 18,000 cycles/radian and lower. The TESI fiber optic light source does not appear to image the filament within the TESI optical path and therefore has a nearly uniform intensity distribution across the target and pupil planes. The only noticeable effect of the TESI light source is that for the larger targets at the lower spatial frequencies the intensity begins to fall off at the edge of the target.

5.3 Wavefront errors

At system level tests a wavefront error measurement of the telescope and scan mirror mounted on the baseplate verifies that the scan mirror and telescope do not have excessive aberrations. The wavefront error for SN05 Imager shows 0.832 waves peak to valley and 0.129 waves rms. The wavefront error measurement for SN06 Imager shows 0.679 waves peak to valley and 0.099 rms. This much distortion in the wavefront has a slight impact on MTF at 18,000 cycles/radian. Using the Zernike coefficients from the wavefront measurement CODE V optical analysis software predicts the MTF of a system with those errors. The results show less than a 1 percent reduction in the MTF at 18,000 cycles/radian as Table II indicates. The test collimator also has its wavefront measured periodically. The resultant peak to valley wavefront error is approximately 0.5 waves and could cause some degradation in MTF. The wavefront errors are smaller than that of the instrument and are not additive to the instrument wavefront errors. Thus the impact of the collimator and instrument wavefront errors is expected to be small, less than one percent.

5.4 Focus errors

Being two different optical systems it is possible to have a focus difference between them. For this reason and because the telescope has a +/- 0.050 inch tolerance on its back focal distance, each test determines a best focus position. To find best focus requires the determination of the modulation for the 18,000 cycle/radian bar target as a function of axial position. At subsystem the modulation is monitored on a storage oscilloscope while moving the bar target image across the detector field of view. At system level test the optical MTF both EW and NS is measured as a function of axial position to determine the best focus. The measurements show that the MTF does not change appreciably over a 0.010 inch axial position change. This corresponds well with the quarter wave criterion which in this case is 0.007 inch. To have a 15 percent reduction in MTF due to defocus requires more than a full wave of focus error or more than 0.030 inch. Using the 0.010 inch range or +/- 0.005 inch and assuming the MTF is linear with focus, which it is not, the worst case reduction in MTF due to focus error would be ~2.5 percent. However, this could result in the system level situation being better than the TESI situation or visa versa.

5.5 Vibrations

The conditions in the two rooms used for these tests are quite different. The system test room has a slab of concrete sunk to a depth of three feet with a gap between it and the concrete basement floor which in theory should decouple the slab from the building vibrations. In practice it is difficult to isolate a small section of a building from vibrations that occur within and

outside the building. To reduce the vibrations the instrument sits on an eighteen inch thick honeycomb optical bench with pneumatic isolation legs. The weight of the table, the instrument and its holding fixture and the collimator requires six legs operating at about 100 psi to support the optical table. The sources of vibrations are two large vacuum chambers operating within 50 feet of the slab room for system test. When either chamber is operating, the vibrations increase the noise in the visible detector signal output if the optical table is not isolated. Therefore the requirement for MTF measurements is that the optical table be floating or isolated from floor vibrations. This minimizes the vibrations but may not completely eliminate the effect of vibrations. As for vibrations at TESI, the measurements with the TESI do not appear to require pneumatic isolation of the optical table even though it is available. The vibration level is certainly less as the room is over 100 feet from the chambers mentioned above. The TESI measurements may not be as sensitive to vibrations due to the averaging that the subsystem data collection does. In the tests at system level the effect of floor vibrations reduces the MTF at 18,000 cycles/radian by several percent. However the test requires that the table be floating or pneumatically isolated which reduces the effect on MTF to within the repeatability or less than 2 percent.

5.6 Air turbulence

To keep the instrument in clean air a laminar flow air duct positioned directly above the instrument directs clean air downward all around the instrument. This necessitates that the laminar flow units be off or that a tent encloses the instrument and collimator during MTF measurements. At the TESI location the air ducts are not laminar flow units and are not directly above the test setup. The path length of exposed air for the TESI is about five feet within a five or six square feet whereas the system air path is about 14 feet but only about three feet are in open air which covers only slightly more square feet. The other factor is that TESI uses a 2 inch diameter beam and the system level test uses the 12 inch diameter beam. For the larger diameter beam the air turbulence can become a significant factor if no provision is made to control the air. Tenting or covering the instrument and or turning the laminar flow units off does reduce the variations in the measurements of MTF. The room air flow may also have a small effect but measurements are again within the repeatability of 2 percent.

5.7 Light scattering

The light scattering within either the TESI or the collimator and instrument can reduce the MTF by creating a higher than expected minimum signal. Although frequency dependent, the light scattering at the lower spatial frequency is usually a good indicator of the presence of scattered light. From Tables III and IV the 4490 cycles/radian MTF values show approximately 6 percent to 7 percent difference This indicates that at least at 4490 cycles/radian the light scatter in the collimator and instrument is for the worst case about three percent more than in TESI.

5.8 Bar targets

The bar targets are actually thin metal disks that have etched bar patterns in them. The metal disks are glued to a holder that has a rectangular hole over which the bar pattern sits. There are multiple targets for each frequency. This opens the possibility for a different target to be used during different tests. Some of the targets have accidentally been touched and have minor imperfections, such as one bar pushed slightly inward. The effect of the imperfections is that the frequency of the bar pattern is not the same across the target. This will obviously reduce the amplitude of the fundamental frequency since the algorithm assumes a fixed frequency for the entire target when fitting the measured data to the calculated data. The reduction in MTF due to a slightly altered target could be as much as 5 percent. However, with careful examination of the targets prior to use the effect of the target non-uniformity is approximately 2 percent to 3 percent.

5.9 Interim summary

Although it appears as though the MTF reduction may be a result of many minor influences, the repeatability of the difference between subsystem and system test for SN05 and SN06 Imager indicates that these minor concerns are under control. There must be another factor that is the major contributor to the reduced MTF at system test. The desired test to perform is a test using an optical system similar to TESI, i.e., an unobscured system, to illuminate the instrument. This test would at least show whether the deficiencies exist in the instrument or in the collimator.

Modifying the existing test collimator is undesirable due to its need for testing other instruments. Not having another suitable collimator in house, ITT requested the use of a parabolic collimator 16 inches in diameter from OCA of Garden Grove, California. The goal of the tests with a different collimator is to identify whether the degradation in MTF at 18,000

cycles/radian belongs with the collimator or the instrument. In addition to the parabola the use of a commercial MTF analyzer as an independent measurement of MTF should help remove any uncertainties in the bar target and data processing.

6.0 INDEPENDENT COLLIMATOR TESTING

The parabola is a 120 inch focal length 16 inch diameter parabola of good quality. The wavefront error of the parabola measures 0.188 waves peak to valley. The MTF analyzer is the Eros 2000 made by Ealing Corp. The plan is to make independent MTF measurements of the instrument and the test collimator, the instrument and the parabola as collimator, and the test collimator and parabola.

The first measurements with the MTF analyzer are with the standard system test configuration - test collimator + SN05 Imager. The MTF analyzer replaces the visible detector in the instrument. A 10 μm slit replaces the target at the collimator focal plane. The visible optics assembly with its components is still present in the instrument. Table VI shows the results of the MTF analyzer testing for a 5 line pair per mm spatial frequency and for both 5x and 10x microscope objectives. The change in magnification changes the area of the image used for determining MTF. As the Table shows, the MTF results for the 10x and the 5x magnifications are close in most measurements. However, since the scans for collecting MTF data cover a broad extent at the focal plane, the 5x magnification is probably the one to compare to the bar target MTF data. The MTF analyzer results for the SN05 Imager and test collimator agree closely with measured MTF values for the system optical MTF without a detector. Multiplying the nominal detector (width of 26.67 microradians) MTF of 0.662 by the MTF analyzer values yields MTF values of 0.497 and 0.510, ns and ew respectively. Compare these values to the measured system optical MTF values 0.49 and 0.52 for SN05 Imager.

FIGURE 4
OPTICAL CONFIGURATION FOR IMAGER AND PARABOLA

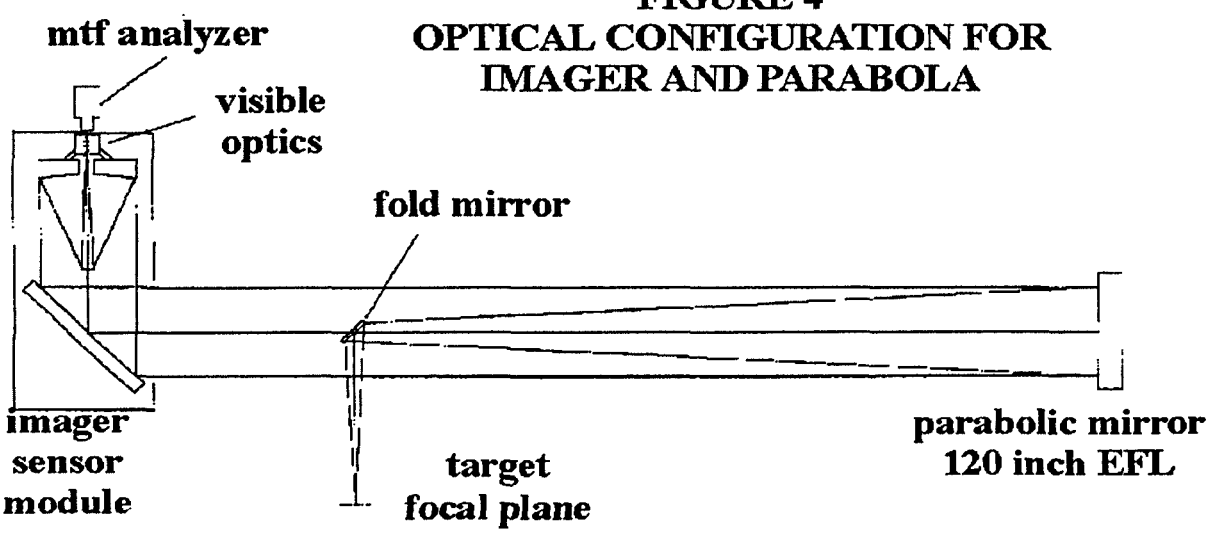

Next the analyzer measures the MTF of the TESI with no visible optics assembly present. The MTF results are very nearly diffraction limited at 0.9 and 0.93. (The MTF analyzer results are repeatable within 2 percent under these test conditions.) The parabola as collimator then replaces the test collimator and is aligned to the instrument. Figure 4 shows an optical layout of the test configuration. The parabola is centered on the optical axis of the Imager telescope. A fold mirror placed in the obscuration of the secondary mirror reflects the axis of the system to the side where the target focal plane and light source assembly are located. The MTF analyzer results are about the same 0.78 as with the test collimator and instrument in one axis but better in the other axis 0.87 using a fiber optic light source. If the light source is the test collimator source, the MTF values from the analyzer drop slightly but within the repeatability error (+/- 2 percent). The fact that one axis shows improvement of approximately 12 percent with the parabola indicates that improvement is possible and thus something with the test collimator is degrading the MTF performance.

The last test involving the parabola is with the test collimator facing the parabola. Ideally the results should look like the TESI results. The results show 0.88 and 0.84 for the two axes. While one axis is very close the other is still 9 percent less than TESI. Even allowing for the measurement uncertainty it appears that the collimator is not diffraction limited.

TABLE VI
MTF Analyzer Results

	5X Microscope Objective		10X Microscope Objective	
	Radial (NS)	Tangential (EW)	Radial (NS)	Tangential (EW)
ITT Collimator + SN05 Imager	0.75	0.77	0.80	0.79
Reduced Height of Slit				0.83
Telescope Simulator (TESI)	0.90	0.93	0.94	0.93
Parabolic Collimator + SN05 Imager				
Fiber Source	0.78	0.87	0.80	0.85
ITT Source	0.77	0.84	0.76	0.83
ITT Collimator + Parabolic Collimator	0.88	0.84	0.90	0.87
Reduced Height of Slit	0.90	0.88	0.91	0.89

During the course of making measurements with the MTF analyzer the image of a pinhole was observed at the instrument focal plane with a HeNe laser as the source. The airy pattern was present as expected but in addition there was a significant amount of diffracted light from the spider support vanes for the secondary mirror. When viewing this pattern with the parabola collimator and SN05 Imager, the diffracted pattern looked similar to the sketch in figure 5. Considering the angular extent of the diffraction from the spider vanes it seemed that the MTF should vary as a function of angle within the focal plane. To verify this the MTF analyzer was rotated to various angles and the MTF measured. The result shows a variation in MTF with angle where the maximum MTF occurs where the diffraction is a minimum and the lowest MTF occurs at the angle where there is the most diffracted light as figure 5 indicates. Figure 6 shows the pupil configuration when viewing the pinhole image.

FIGURE 5
PINHOLE IMAGE OBSERVATIONS

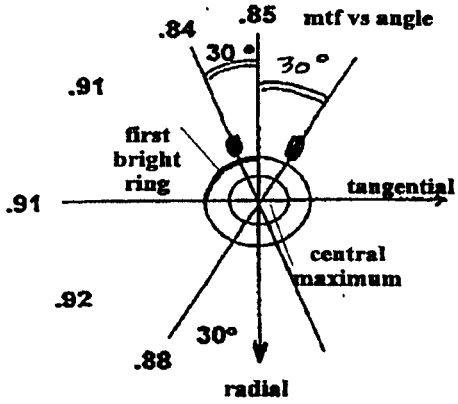

FIGURE 6
ENTRANCE PUPIL CONFIGURATION

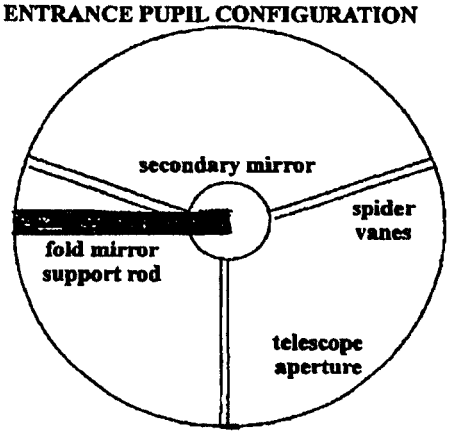

Having observed the diffraction from the spider vanes, the question arose as to whether this diffraction was included in the optical model for the instrument. The answer is no it has not been included up to this point in time. The next step was to use CODE V to model the diffraction from the spider vanes. The spider vanes are 0.200 inch thick by 5.025 inches long and there are three vanes in the aperture as figure 6 shows. CODE V estimates that the diffracted light will reduce the MTF at 18,000 cycles/radian by 0.027 or 2.7 percent in the EW axis and 0.017 or 1.7 percent in the NS axis. The effect is less at the lower spatial frequencies. Although not as much of an effect as expected, it reduces the difference between subsystem and system level MTF.

The results from the MTF analyzer and parabola as collimator are not as definitive as desired. The telescope simulator measures near diffraction limited as expected. The test collimator with the parabolic collimator measures somewhat below diffraction limited which suggests that the collimators are not as good as expected. The fact that the reduced height slit improves the MTF slightly suggests that the test collimator's MTF performance could be better. The measurements using the parabola with the SN05 Imager are inconclusive because one axis differs from the other. The fact that one axis is better by ~12 percent using the parabola rather than the test collimator indicates that the test collimator is degrading MTF performance.

The results of the testing prompted a more detailed look at the test collimator starting with the wavefront error of the test collimator.

7.0 ANALYSIS OF COLLIMATOR WAVEFRONT

The test collimator is periodically refocused as a part of its calibration cycle. During calibration, a wavefront measurement is made using a Zygo mark 4 interferometer. The test collimator interferogram, shown in figure 7, was obtained by taking the raw phase data from the Zygo and converting it into a format that could be analyzed using the CODEV optical design and analysis software package. The interferogram reveals a number of prominent zones (as well as a chip adjacent to the central hole in the primary mirror). The local surface slope error of the steepest zone is approximately 1 wave/inch. According to CODEV the MTF of a collimator with this wavefront error is 0.852 at 18,000 cycles/radian. That is a 9.7 percent reduction in MTF relative to the diffraction limited MTF value of 0.944 at the same frequency for an unobscured system. A small portion of the reduction at 18,000 cycles/radian, 0.014 or 1.4 percent, is caused by the four spider vanes of the test collimator. The zonal figure slope errors are responsible for the rest of the MTF reduction.

CODEV was also used to determine what an acceptable level of zonal figure error might be if a new collimator was to be procured. Analysis showed that the MTF losses could be kept below 1 percent at 18,000 cycles/radian if the maximum surface slope errors were less than 0.12 waves/inch. An intuitive feel for the impact of slope errors can be obtained by recognizing that local errors in the mirror's surface figure reflect energy away from the Airy pattern. A local surface slope error of 3 microradians (0.12 wave/inch = 3 urad) deviates a ray 6 urad. With a 300 inch focal length collimator the ray is displaced 0.0018 inch at the focal plane. For comparison, the diameter of the Airy disk is 0.0015 inch at 0.65 microns with the collimator stopped down to the 12.25 inch aperture of the Imager and the width of a single bar in the 18,000 cycle/radian target pattern is 0.0083 inch. The CODEV results are consistent with a requirement that all rays deviated by local slope errors fall within the second bright ring of the Airy pattern. If this condition is satisfied, the optical system should not degrade the MTF at 18,000 cycles/radian. The effect of slope errors on MTF is highly dependent on the spatial frequency of interest and a more stringent requirement is needed if the MTF at higher frequencies is to be measured. This should be kept in mind when designing a test collimator because "one size" definitely will not fit all applications.

FIGURE 7
TEST COLLIMATOR INTERFEROGRAM

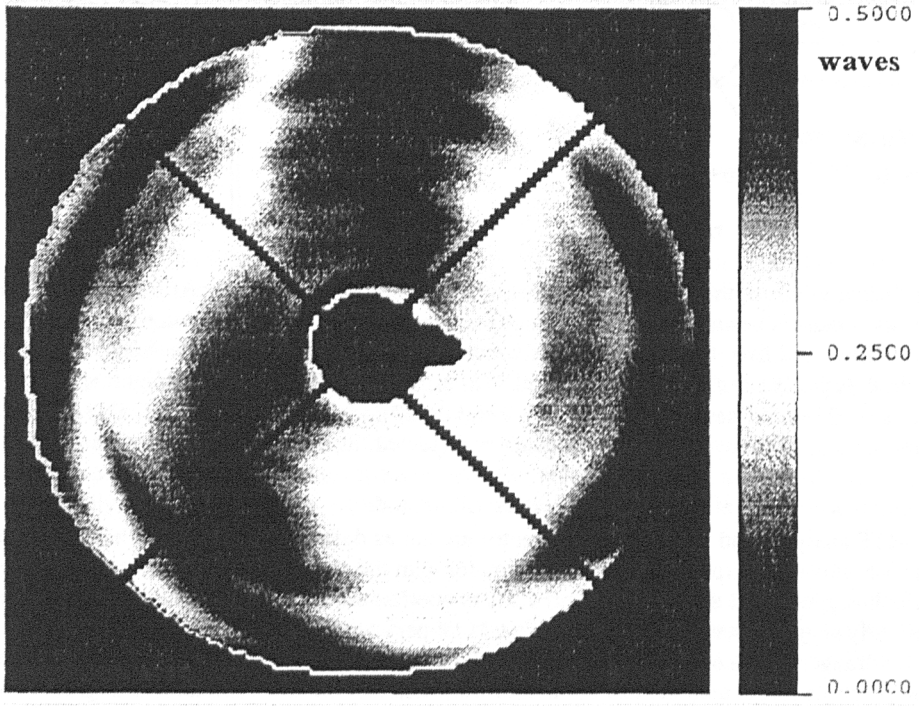

8.0 CONCLUSIONS

The comparison between the subsystem and system level MTF performance has led to a better understanding of the Imager instrument MTF performance and the limitations of the test equipment. The computer model used to calculate Imager MTF performance now includes the effect of spider diffraction. Procedural steps have been added to ensure that all the minor concerns relative to MTF performance, such as vibrations, air flow and bar targets are under control. In addition there is strong evidence from the analysis that the zones in the collimator wavefront having slopes of ~1 wave/inch are degrading the measurement of the Imager optical MTF. If indeed the analysis is correct, the Imager optical and system MTF performance is better than the measured values by 9 percent to 10 percent at 18,000 cycles/radian. The proof of the analysis will have to wait until a new collimator with reduced slope errors is available for test.

9.0 ACKNOWLEDGMENTS

The authors would like to thank the many persons at ITT Aerospace/Communications Division in Fort Wayne, Indiana who helped during this investigation. Thanks also to Roger Johnston and Richard Rhay of OCA for their assistance in making measurements and assessing performance. The GOES program funded this work through Space Systems Loral, Palo Alto, California. ITT is a subcontractor to SSL providing instruments for the GOES spacecraft.

10. REFERENCES

1. G. E. Zurmehly and R. A. Hookman,"Thermal.Optical Test Setup for the Geostationary Operational Environmental Satellite Telescope," *Precision Engineering and Optomechanics*, D. Vukobratovich, editor, Proc. SPIE vol. 1167, pp. 360-367, 1989.
2. R. A. Hookman, "Design of the GOES Telescope Secondary Mirror Mounting," *Precision Engineering and Optomechanics*, D. Vukobratovich, editor, Proc. SPIE vol. 1167, pp. 368-374, 1989.
3. R. Shannon and James C. Wyant, *Applied Optics and Optical Engineering*, Chapter 6, William B. Wetherell, editor, Academic Press, 1980.

Blank page retained for pagination

SESSION 4

Space Environment Monitoring

The NOAA Space Environment Center mission and the GOES space environment monitoring subsystem

G. Heckman, D. Speich,, J. W. Hirman, and T. DeFoor

NOAA R/E/SE
325 Broadway
Boulder, Colorado 80303

ABSTRACT

The mission of the NOAA Space Environment Center (SEC) is to serve the nation's need to reduce adverse effects of solar-terrestrial disturbances on humankind's activities. To meet this need, SEC

- acquires, interprets, and disseminates space weather information
- prepares and disseminates forecasts and alerts of conditions of the space environment
- conducts research and development in solar-terrestrial physics and in techniques to improve monitoring and forecasting
- prepares high quality data for national archives
- uses its expertise to advise and educate those affected by variations in the space environment.

Users are provided information in the form of forecasts, nowcasts, data, advice, support, expertise, and publications about conditions in the solar-terrestrial environment. The Space Environment Monitors on GOES spacecraft provide space weather observations from the Sun to Earth and form the basis of the SEC real-time operation. The X-ray Sensor (XRS) monitors solar flare activity and serves as the international standard for rating the intensity of flares. Flares are observed and classified according to the intensity of their emission on the XRS sensor. Forecasts of the occurrence of solar flares are expressed in terms of the measurements from the XRS. SEC also issues a daily index of the background solar radiation based on the XRS measurements. Solar particle events (SPE) and energetic electron events (increases in the charged particle radiation environment near Earth) are detected using the Energetic Particle Sensors (EPS) on GOES. Alerts and forecasts of the occurrence of SPE are made in terms of the fluxes of charged ions—mostly protons—measured by the EPS. Alerts are issued for energetic electron events based on the EPS measurements.

Keywords: Space Environment, Space Weather Services, GOES Space Environment Monitor

2. INTRODUCTION

The Space Environment Monitors (SEM) on the GOES spacecraft are vital to the U.S. space weather program. The observations from the GOES instruments are critical to the operation of the Space Environment Center and its operational arm, Space Weather Operations (SWO). SWO is a joint NOAA and USAF real-time space weather center located in Boulder, Colorado. The SWO collects observations in real time from NOAA and cooperating federal agencies including the DOD, NASA, the Department of Interior, the Department of Energy, and many foreign countries. These data are collected in the SWO by the Space Weather Data System. The Space Weather Data System provides on-line data storage, helps in the detection of events and disturbances in the solar-terrestrial environment, provides displays for analysis and forecasting at the SWO, and assists in providing alerts, watches, warnings, forecasts, summaries, and then distributes the products to users through a variety of distribution systems. The products of the SWO are available on the Internet and are also distributed by military data networks, over World Meteorological Organization circuits, by direct satellite broadcast, through WWV short-wave radio time service and by telephone recording.

0-8194-2200-2/96/$6.00

3. EFFECTS OF SOLAR-TERRESTRIAL VARIATIONS ON TERRESTRIAL SYSTEMS

Variations in the solar-terrestrial environment cover time scales from minutes to years. Bursts of X-rays, energetic charged particles, and radio emissions occur in minutes and hours. Solar EUV radiation, important in heating the Earth's upper atmosphere (including both the ionosphere and the upper neutral atmosphere at the height of satellite orbits) varies on time scales of days and months. The Sun also produces variations in plasma emission, including ejections of its own mass in a phenomena called a Coronal Mass Ejection (CME) and increased continuous emission of plasma in localized areas called Coronal Holes. Coronal holes and CMEs are the source of the disturbances in the solar wind—the ever-blowing transport of plasma from the sun to the distant reaches of the solar system. The plasma ejections are the source of the disturbances in the magnetic field of Earth called Geomagnetic Storms. The effect is to disturb the Earth's magnetic field, triggering the acceleration of charged particles and the flow of electric currents. These magnetospheric currents cause problems when they induce secondary currents in power systems, pipelines, and other long-distance conducting systems. Electric currents heat the neutral atmosphere, causing it to expand and change the drag force on low-orbiting satellites. The variations that are produced in Earth's magnetic field are a problem for terrestrial systems that use the magnetic field as a reference. Aeromagnetic surveying, some navigation systems, and very sensitive electronic manufacturing systems are sensitive to these rapid variations.. The plasmas that are formed or convected by the magnetospheric activity are themselves a potential source of surfacing charging problems for satellites in orbit. Energetic charged particles are a hazard for crews in space and for satellite hardware including command and control electronics, solar power cells, and star sensors. The current Space Environment Monitors (SEM) on GOES provide direct measures of the solar X-ray emission, solar energetic particles, and the in-situ magnetic field at the GOES orbit [1,2,4,5,6,7]. The GOES X-ray and energetic particle data are the primary source of these measurements in SWO operations. The magnetic field variations are used with magnetic field measurements from the surface of the Earth (data collected in large part by the GOES Data Collection Platforms (DCS)) to form a more complete picture of Earth's magnetic field environment. Table 1 summarizes space environment variations and their impact on terrestrial systems. GOES observations are the sole source of measurements in Columns B and C; provide the standard data for alerts and forecasts in Columns A, C, and G; and are basic to detection and forecasting of effects listed in Columns A through F. An EUV detector providing the measurements for Column G is desirable in the future. A detector for lower energy particles provides the data described in Column E. The Solar X-ray Imager being built for GOES-M and follow-on missions will provide the basic observing and forecasting information for the mass ejections and coronal holes that are the source of the variations listed in Columns C through F.

Table 1. Space weather variations and their effect on terrestrial systems

Terrestrial Systems Impacts	Sources							
	A	B	C	D	E	F	G	H
	Energetic particle emission from the Sun	Solar X-ray Bursts	Variation in geomagnetic field	Effects of electric currents in heating ionosphere and neutral atmosphere	Plasma variations in Earth's magnetosphere (low-energy particles)	Energetic particles accelerated in Earth's magnetic field	Solar EUV variation	Solar radio emission
Radiation hazard to crews in space and on high-flying aircraft	•							
Interference with satellite star sensor systems	•							
Lack of complete knowledge of background conditions during environmental experiments (e.g. ozone depletion due to solar events)	•			•				
Degradation of satellite surfaces including solar cells	•					•		
Satellite electronics upsets due to single charge ionization effects	•							
Errors in lab experiments due to changes in background radiation environment at Earth's surface	•							
Signal fade and phase change on satellite up- and down-links		•		•				
Location errors and reception problems using GPS navigation system		•		•				
Location errors in remote sensing of satellites when signal propagates through the ionosphere		•		•				
Location errors in using over-the-horizon radar systems		•		•				•

Terrestrial Systems Impacts	Sources							
	A	B	C	D	E	F	G	H
Location errors in using VLF navigation systems (Loran and Omega)		•		•				
Location errors in remote sensing of HF radio signals		•		•				•
Errors in remote detection of satellites		•						•
Errors in satellite magnetic torque systems when the local field is toot disturbed to provide a reference			•					
Errors in control of high-sensitivity manufacturing operations due to variations in Earth's magnetic field			•					
Errors in high-precision magnetic based navigation systems			•					
Experiments in animal navigation during geomagnetic storms			•					
Increased atmospheric drag leading to orbit changes				•				
Lost space debris that poses a danger to satellites and space missions				•				
Induced currents in long-distance power systems and pipelines				•				
Errors in surveying Earth's crust using magnetic field sensing systems				•				
Satellite electronics upsets due to surface charging					•			
Satellite electronics due to internal depth charging						•		
Radio noise interference with ground reception of satellite signals								•
Radio noise interference with air-to-ground communications								•

4. CUSTOMERS FOR SPACE ENVIRONMENT SERVICES

The national real time space weather services are provided by two operating centers. The SWO at Boulder provides services to all users except the DOD. DOD users are serviced by the 50th Weather Squadron stationed at the Space Command of Falcon Air Force Base, Colorado. Figure 1 shows the distribution of users by application for the SWO operation in Boulder[3]. The percentages shown are from an in-depth survey in 1991. The numbers do not reflect any numerical value assigned to individual users, so one short-wave radio user is counted the same as one electric power utility. The table does not show the numbers of secondary users who receive services indirectly from the SWO. For example, one power company redistributes alerts of geomagnetic storms to several additional users. One alert distributed through the Federal Aviation Administration or its contractors can reach many users through the network of FAA information services and flight service stations.

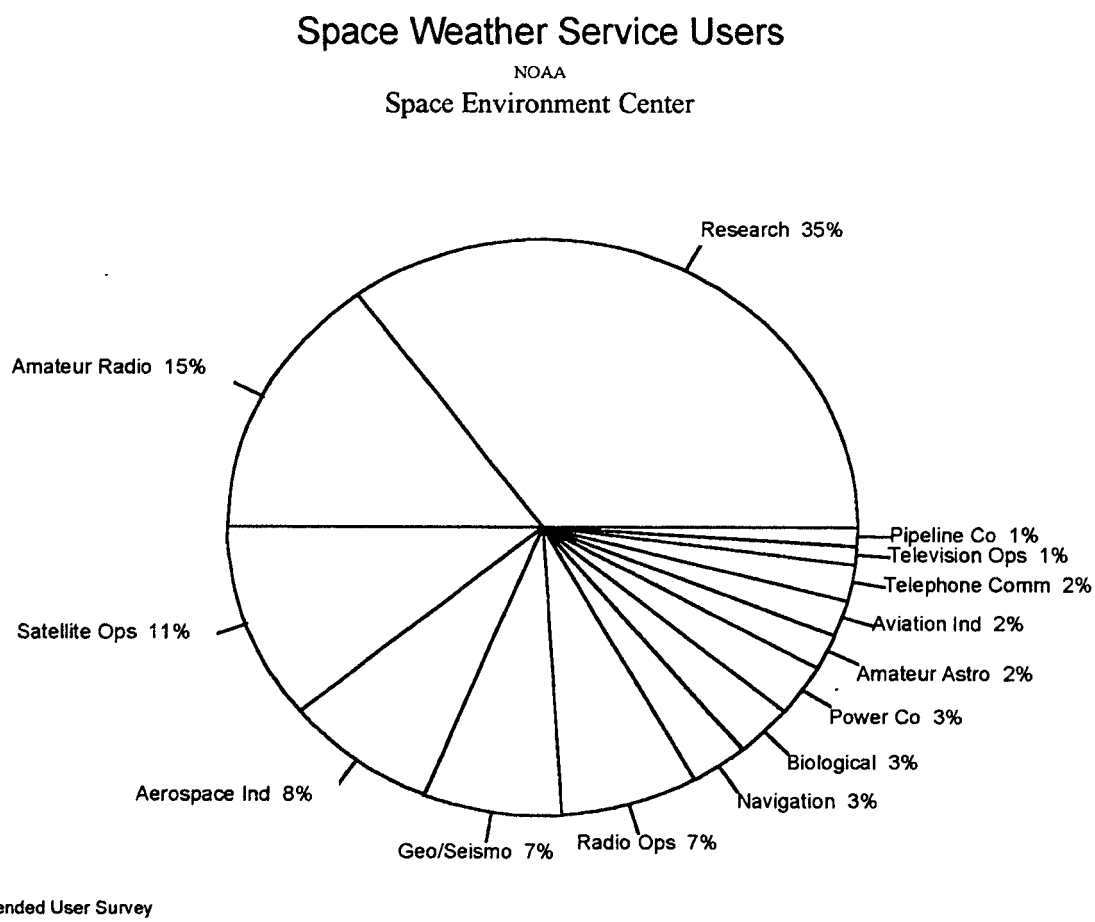

Figure 1. Distribution of customers for space environment (space weather) services from the Space Environment Center (SEC) Space Weather Operations (SWO) center. The percentages shown are the percentages of the approximately 500 users who voluntarily responded to a survey of Space Weather Operations users in 1991.

5. SPECIFIC APPLICATIONS OF GOES SEM DATA IN SPACE WEATHER OPERATIONS

GOES SEM data form an integral part of SWO operations. The individual SEM instruments are described in more detail in the companion paper. The data from the X-ray Sensor (XRS) are used to classify the intensity of solar flares according to their peak intensity in the 0.1-0.8 nm detector. The classification system, now accepted as the

international standard for research and operations, was developed by the SWO using sensors that flew as research predecessors to the GOES operational spacecraft. The classification system was developed to reflect effects on the ionosphere such that a moderate class flares (Class M) would be sufficiently large to induce short-wave effects on high frequency signals propagating through, or being reflected by, the ionosphere. To be classified as a M-flare, the peak 0.1-0.8 nm flux must equal or exceed 10^{-5} W m^{-2}. A flare equaling or exceeding 10^{-4} W m^{-2} is classified as Class X. In a Class-X flare, high frequency radio propagation on the day-lit side of the Earth is virtually non-existent. The flare classification system based on GOES replaced an older classification system based on the optical size and brightness of a flare as observed through ground-based telescopes. Forecasts of solar flares are issued by the SWO in terms of their X-ray emission using the GOES XRS. Forecasts, stated as the probability of occurrence in a 24-hour period, are made for one, two, and three days into the future. Alerts of flares in progress are issued by SWO for Class X flares and for flares exceeding 5 x 10^{-5} W m^{-2} (termed a Class M5, taking the mantissa as the second term of the classification).

Increased fluxes of energetic protons from the Sun arriving in the vicinity of Earth are classified according to their flux as measured by the GOES Energetic Particle Sensors (EPS). After averaging over one minute intervals, an integral particle spectrum is fit to the data. A Solar Proton Event is declared when the flux at energies greater than 10 MeV exceeds 10 particles cm^{-2} s^{-1} sr^{-1}. Alerts are issued for other levels of integral flux greater than 10 MeV and greater than 100 MeV. Alerts for Energetic Electron Events are issued when the integrated electron flux exceeds 10^3 cm^{-2} s^{-1} sr^{-1}.

Future uses of GOES data in space weather operations include expanded utilization of current data and the use of data from new sensors. The Solar X-ray Imager will provide unique real-time data for observing and forecasting solar activity. Major analysis and development efforts will go into developing this capability. Future alerts using the magnetometer data from GOES will provide notice of the compression of Earth's magnetosphere to the point where geosynchronous satellites are in the magnetosheath. Future improvements to fill gaps in the measurements [5] in Table 1 include better monitoring of the spatial distribution (Column F) and lower energies fluxes (Column E) of energetic particles and the addition of EUV (Column G) and hard X-ray sensors (Columns A and B).

6. SUMMARY

The Space Environment Monitors on GOES form an integral and essential basis of the Space Weather Operations in the NOAA Space Environment Center. The observations from GOES are used for detection of events in the solar-terrestrial environment, issuing of alerts to users, and making forecasts for future conditions. An essential aspect of this process is the use of the GOES data to define events according to standards developed specifically for GOES and which are now accepted as national and international definitions of these events.

7. BIBLIOGRAPHY

Space Environment Services Center Products and Services Users Guide, Space Environment Laboratory, U.S. Department of Commerce, Boulder, Colorado, January, 1993.

Glossary of Solar-Terrestrial Terms, Space Environment Laboratory, U.S. Department of Commerce, Boulder, Colorado.

8. REFERENCES

1. P.L., Bornmann, D. Speich,, J. Hirman, V. Pizzo, R.N., Grubb, C. Balch, and G. Heckman, in these Proceedings, "The GOES Solar X-ray Imager: Overview and Operational Goals."

2. P. L. Bornmann, D. Speich, J. Hirman, L. Matheson, R. N. Grubb, R. Viereck, and H. Garcia, in these Proceedings, "The GOES X-Ray Sensor and its Use in Predicting Solar-Terrestrial Disturbances."

3. L.E. Combs, T. A. Nichol, and N. L. Cohen, Survey of the Space Environment Services Center Users and Services, in *Solar-Terrestrial Predictions - IV, Proceedings of a Workshop at Ottawa, Canada, May 18-22, 1992*, J. Hruska, M. A. Shea, D. F. Smart, and G. Heckman, ed., NOAA, Boulder, Colorado, 1993.

4. R.N. Grubb, "The SMS/GOES space environment monitor subsystems," *NOAA Tech. Memo. ERL SEL-42*, NOAA, Boulder, CO, 1975.

5. R.N. Grubb, P.L. Bornmann, G. Heckman, T.G Onsager, H.J. Singer, R. Viereck, in these Proceedings, "The space environment monitoring mission beyond GOES M."

6. T.G. Onsager, R. Grubb, J. Kunches, L. Matheson, D. Speich, R. Zwickl, and H. Sauer, in these Proceedings, Operational uses of the GOES energetic particle sensors

7. H.J. Singer, L. Matheson, R. Grubb, A. Newman, and S.D. Bouwer, in these Proceedings, Monitoring space weather with the GOES magnetometers

Operational uses of the GOES energetic particle detectors

T. G. Onsager, R. Grubb, J. Kunches, L. Matheson, D. Speich, R. Zwickl, and H. Sauer†

NOAA Space Environment Center
325 Broadway
Boulder, CO 80303

†also at: CIRES, University of Colorado
Boulder, CO 80303

ABSTRACT

A central mission of the GOES Space Environment Monitor program is to provide continuous, real–time monitoring of the near–Earth space environment. The GOES Energetic Particle Sensor (EPS) and High Energy Proton and Alpha Detector (HEPAD) obtain measurements of the energetic electron, proton, and alpha particle fluxes at geosynchronous orbit. These measurements serve as the basis for a variety of services that are provided to numerous government and private organizations, including the forecasting of adverse conditions, providing a characterization of the current conditions in the Earth's environment, and providing the necessary measurements to allow comprehensive post–event analyses. Numerous products are derived from the GOES EPS measurements and made available to industry, government agencies, and research institutions throughout the world. The particle fluxes in the Earth's environment are comprised of three main components: (1) particles trapped within the geomagnetic field, (2) particles of a more direct solar origin, and (3) a cosmic ray background. These particle fluxes are quite dynamic, varying on times–scales ranging from seconds to decades. In this paper, we describe the GOES–8 and GOES–9 EPS and HEPAD instruments and the operational uses of the energetic particle measurements made at geosynchronous orbit.

Keywords: GOES, energetic particles, radiation, geosynchronous, solar, magnetosphere, cosmic ray, space environment

1. INSTRUMENT DESCRIPTION

The energetic particle environment at geostationary orbit is measured on the GOES spacecraft using two independent instruments: the Energetic Particle Sensor (EPS), with telescope and dome detectors, and the High Energy Proton and Alpha Detector (HEPAD). These detectors are illustrated in Figures 1–3. The EPS detectors and the HEPAD are often referred to collectively as the Energetic Particle Sensors on the GOES Space Environment Monitor package. The detector channel energies and geometric factors are given in Table 1. The EPS measures protons at energies between 0.7 MeV and approximately 900 MeV, alpha particles at energies between 4 MeV and 500 MeV, and electrons greater than 0.6 MeV. The EPS uses two different detector designs to measure the particles over these energy ranges. A telescope detector (Figure 1) is used to measure the lower energy protons (0.7 to 15 MeV) in three differential channels and lower energy alpha particles (4 to 61 MeV) in three differential channels (Table 1). The telescope consists of two silicon surface barrier detectors with thicknesses of 50 μm and 500 μm, and it has a field of view of approximately 35 degrees half–angle. Sweeping magnets are used to exclude electrons below about 100 keV, and light shielding is provided with an aluminum foil. The telescope is passively shielded with no active anti–coincidence.

Three wide–aperture dome detector assemblies (Figure 2) are used to measure medium–energy protons (15–900 MeV) in four differential channels and alpha particles (60–500 MeV) in three differential channels (Table 1). The dome detectors also measure electron fluxes in three integral channels (greater than 0.6, greater than 2, and greater than 4 MeV). The dome detector consists of three sets of two solid state silicon surface barrier detectors (both with 1500 μm thickness) with independent fields of view. Moderators of different thicknesses cover each of the three detector sets to provide the different energy thresholds, as shown in Figure 2. The fields of view of the dome detectors are about 30 degrees half–angle in the equatorial plane and about 60 degrees half–angle in elevation.

The high–energy portion of the proton and the alpha particle spectra is measured with the HEPAD. This detector is illustrated in Figure 3. Protons are measured with energies from 330 MeV to greater than 700 MeV and alpha particles at energies from 2560 to greater than 3400 MeV. The HEPAD uses a telescope geometry with two silicon surface barrier detectors and a Cerenkov radiation photomultiplier tube detector. The instrument field of view is approximately 34 degrees half–angle.

The particle and energy discrimination for the EPS telescope and dome and the HEPAD are accomplished with coincidence/anticoincidence logic on the pulses produced by the two detectors in each subassembly. Because the detectors are

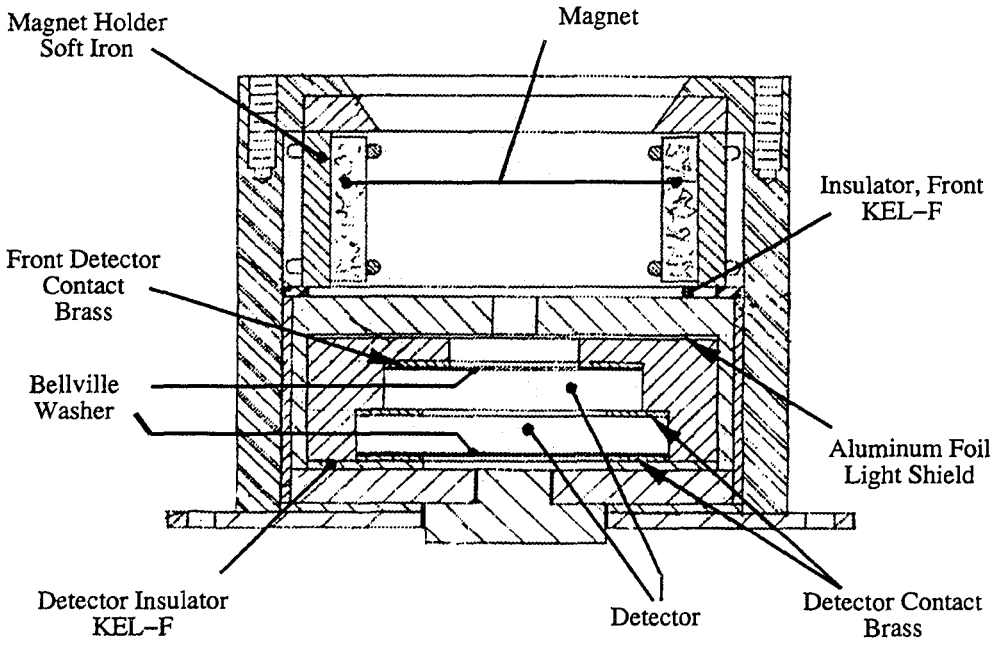

Figure 1: Cross–sectional diagram of the GOES EPS Telescope Detector.

only passively shielded, some high–energy particles and out–of–aperture particles will be able to penetrate the shielding and contribute a secondary component to the measured counts (see Table 1 for a list of allowable energies). As described below, a procedure is used to correct for these secondary counts in the EPS telescope and dome detectors.

Beginning with GOES–8, the GOES–series spacecraft are no longer spinning. The EPS telescope and dome detectors are mounted on the spacecraft with their fields of view directed westward. The HEPAD is mounted with its field of view directed away from the Earth.

2. DATA PROCESSING

The data are obtained in real time at the NOAA Space Environment Center in Boulder, CO with temporal resolution of roughly 20 sec. The data are processed and archived as raw telemetry and as five–minute averages. The data processing consists of the basic conversion from count rates to particle flux units as well as the application of correction algorithms.

The electron detectors have a wide energy passband, and therefore the energy–dependent response of the detectors has been taken into account by estimating an effective geometric factor that depends on the inferred spectral shape of the electron distributions. The electron data processing involves estimating the spectral slope from neighboring pairs of the three electron channels and then using this spectral slope to compute the effective geometric factor based on the laboratory calibration. The response of the dome detectors to greater than 2 MeV electrons (E2) was found to be nearly independent of energy, and therefore a fixed geometric factor of 0.05 (cm^2 sr) is used. The geometric factor used for E1 is typically 0.075 ± 0.025 (cm^2 sr) and for E3 typically 0.017 ± 0.006 (cm^2 sr). A correction algorithm is also applied to the electron fluxes to remove contamination from energetic protons. This correction depends linearly on the proton flux levels and is based on laboratory calibration data and the measured proton fluxes in the 8.7–200 MeV range.

The proton fluxes measured by the EPS telescope and dome are corrected for both the cosmic ray background and for the response from particles either out of the primary energy range or out of the design acceptance aperture (see Table 1). This

Table 1: GOES–8 and GOES–9 Energetic Particle Channels

		Primary Detector Response		Secondary Detector Response	
Proton Channels	Detector Type	Energy Range (MeV)	Channel Response Factor† (cm^2 sr MeV)	Energy Range (MeV)	Geometric Factor (cm^2 sr)
P1	Telescope	0.7–4.2	0.194	50–200	0.02
P2	Telescope	4.2–8.7	0.252	50–125	0.04
				125–200	0.007
P3	Telescope	8.7–14.5	0.325	60–125	0.07
				125–200	0.014
P4	Dome 3	15–40	5.21	80–115	0.038
				115–150	0.25
P5	Dome 4	38–82	14.5	80–110	0.091
				110–150	0.57
				150–190	0.21
P6	Dome 5	84–200	129.	80–110	0.15
				110–130	0.84
				130–200	0.80
				200–300	0.26
P7	Dome 5	110–900	839.	80–110	0.03
				110–170	0.15
				170–250	1.5
				250–500	1.9
				500–900	0.56
P8	HEPAD	330–420	65.7		
P9	HEPAD	420–510	65.7		
P10	HEPAD	510–700	139.		
P11	HEPAD	> 700	G = 0.73 cm^2 sr		
Electron Channels					
E1	Dome 3	> 0.6	Spectrum Dependent (see text)		
E2	Dome 3	> 2	0.05		
E2	Dome 4	> 4	Spectrum Dependent (see text)		
Alpha Channels					
A1	Telescope	4–10	0.342		
A2	Telescope	10–21	0.638		
A3	Telescope	21–61	2.22		
A4	Dome 3	60–160	21.		
A5	Dome 4	160–260	36.		
A6	Dome 5	330–500	176.		
A7	HEPAD	2560–3400	613.		
A8	HEPAD	> 3400	G = 0.73 cm^2 sr		
Derived Proton Integral Flux Values					
		> 1			
		> 5			
		> 10			
		> 30			
		> 50			
		> 60			
		> 100			

†Flat–spectrum detector response determined over the specified primary energy range (Panametrics Document FH–CAL–0053195).

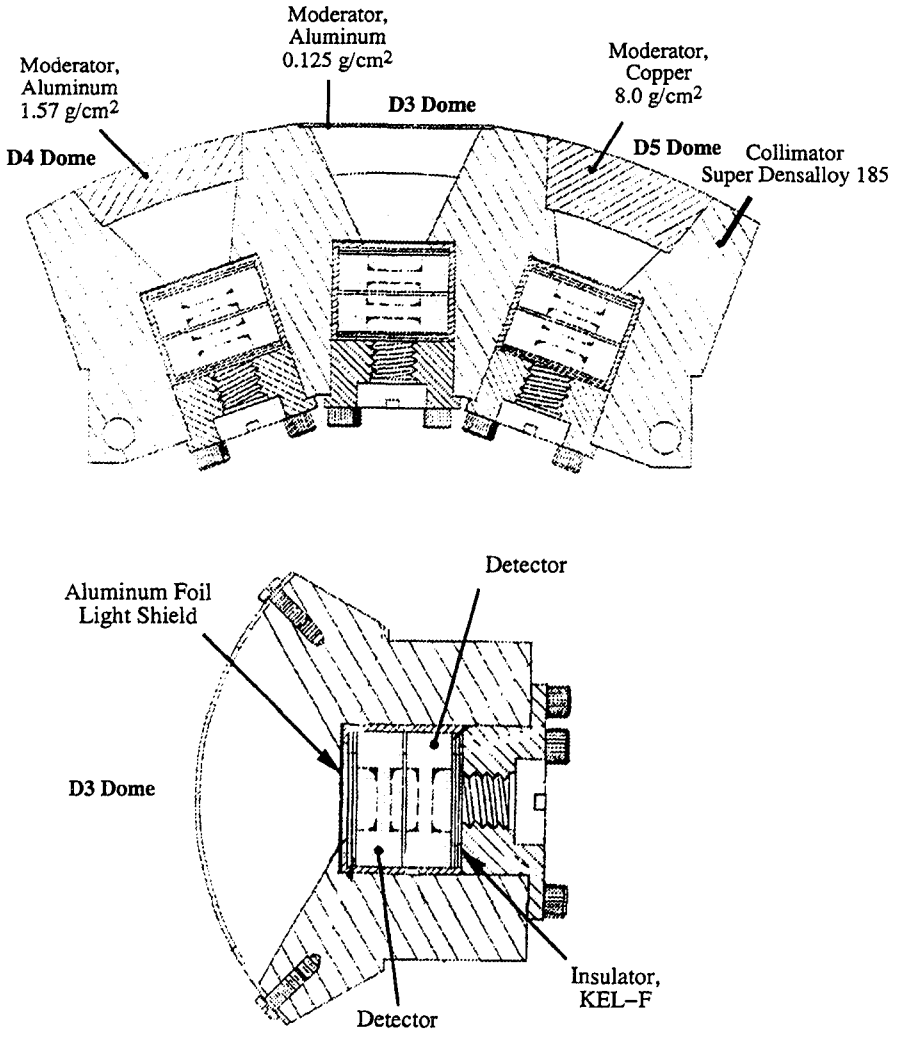

Figure 2: (Above) cross-sectional diagram of the EPS Dome detector illustrating the three separate modules, and (below) cross-sectional diagram of the D3 Dome module, showing the detector assembly details.

correction algorithm uses a ten-day, low-pass filter to determine the minimum count level over the previous ten-day period that is subtracted from the measured count rate. In order to avoid using an artificially high minimum count level, such as may occur during a prolonged period of elevated fluxes from a solar source, the new ten-day minimum flux level must be within a specified range of the previous ten-day level before the new level will be applied. If the new minimum level is outside this range, the background level from the previous ten-day period is used.

The second correction involves subtracting the counts due to the secondary detector response. The energy ranges of this secondary response and the geometric factors determined from laboratory calibration are listed in Table 1. In practice, the correction algorithm begins at the highest energies (P7), and by assuming a power-law spectrum between adjacent channels estimates the contribution to the count rate from the secondary energy passbands. This secondary response is subtracted from the total to create the corrected fluxes. The secondary response of the lower-energy channels is then estimated using the corrected count rates from the higher-energy channels. The correction algorithm was designed to work on each five-minute averaged data sample, independent of the previous or following five-minute data.

After the initial processing, the data are available in real time to the NOAA Space Weather Operations Group, to the US Air

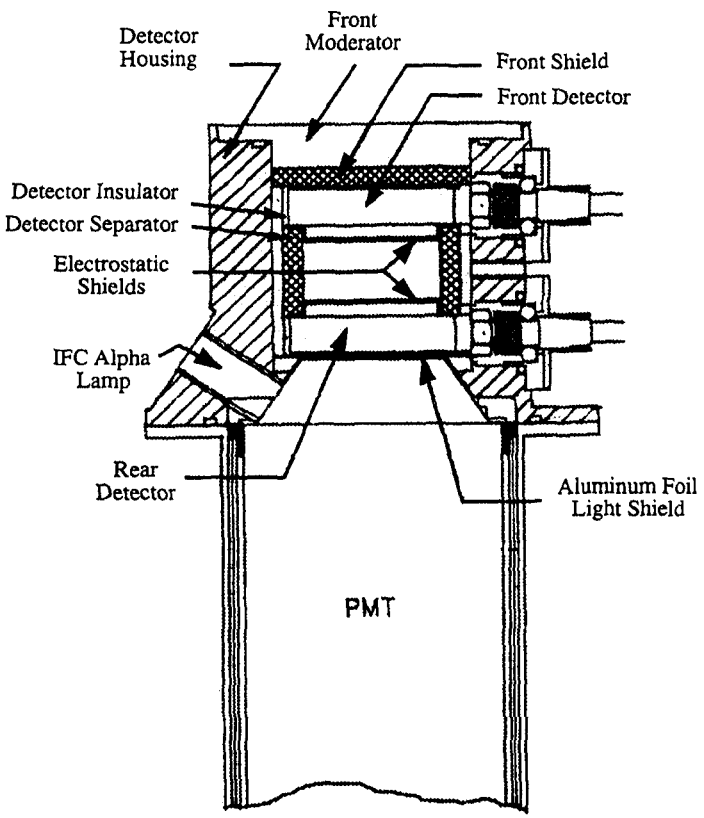

Figure 3: Cross–sectional diagram of the High Energy Proton and Alpha Detector (HEPAD).

Force 50th Weather Squadron located in Colorado Springs, and a subset of the data are made available over the World Wide Web. The data are also archived at the NOAA Space Environment Center and at the NOAA National Geophysical Data Center. Here the data are made available for a broad spectrum of applications, including satellite design and anomaly assessment and both applied and basic research.

3. THE PARTICLE ENVIRONMENT AT GEOSYNCHRONOUS ORBIT

The GOES EPS and HEPAD are designed to provide continuous monitoring of the Earth's energetic particle environment. The Earth's particle environment can be broadly classed into three categories, each with important effects on spacecraft systems, humans, and on other regions of the environment such as the ionosphere and the atmosphere. These three catagories are: (1) geomagnetically trapped particles, (2) particles of direct solar origin, and (3) cosmic rays. The dynamics of the Sun, the heliosphere, and the Earth's magnetosphere/ionosphere system all contribute to the variability in the energetic particle fluxes at geostationary orbit. Consequently, these energetic particle populations are observed to vary over a wide range of time scales, from minutes to decades, and it is only through long–term monitoring that we are able to characterize, and in some cases to predict, the particle flux levels and their effects.

Typical measurements from the GOES EPS telescope and dome detectors are illustrated in Figure 4. These measurements include one month of five–minute averaged data and show some of the commonly measured features at geosynchronous orbit. The upper three panels contain integral electron flux from channels E1–E3, and the lower four panels contain differential proton flux in channels P1–P4 covering the energies shown in Table 1. The higher energy proton fluxes are not shown due to their low levels at this time.

A strong daily variation can be seen in the geomagnetically trapped particle fluxes (all electron channels and the lowest energy proton channel) that occurs as the GOES satellite travels from local noon (high fluxes) to local midnight (low fluxes). This variation is due to the motion of the energetic particles in the Earth's asymmetric magnetic field. Geomagnetic activity in response to energy input from the solar wind creates additional distortions in the Earth's magnetic field that result in further variability in the measured particle fluxes.

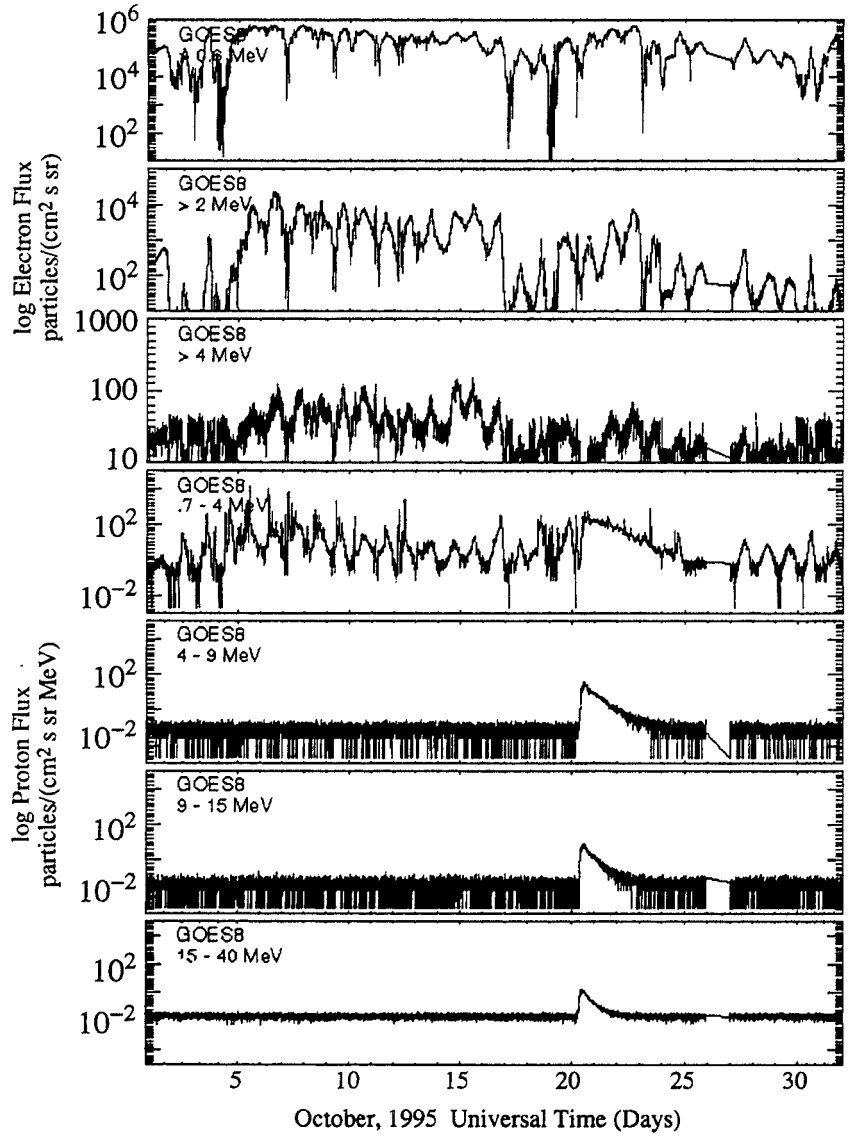

Figure 4: (Upper three panels) Electron flux at energies greater than 0.6 MeV, greater than 2 MeV, and greater than 4 MeV, and (lower panels) proton flux at energies from 0.7–4 MeV, 4–9 MeV, 9–15 MeV, and 15–40 MeV obtained with the GOES–8 EPS telescope and dome detectors during October, 1995. Note the strong daily variation due to the orbit of the satellite in the Earth's asymmetric magnetic field and also the small energetic proton event that began on October 20.

Typically, the higher energy proton channels are only above background levels during energetic solar proton events. An example of a small proton event can be seen beginning on October 20 and lasting for a few days. As discussed below, these proton fluxes originate from active regions on the Sun and often indicate that disturbed geomagnetic conditions may occur within one to two days.

3.1 Geomagnetically trapped particles

The trapped magnetospheric particles in the outer radiation belts are those that are confined by the Earth's magnetic field and remain within the magnetosphere for time periods ranging from many hours up to many days. These particles move in response to the magnetospheric electric and magnetic fields. They are injected into the near–Earth region primarily through processes occurring in the ionosphere and in the magnetotail, and they are lost through precipitation into the upper atmosphere, charge

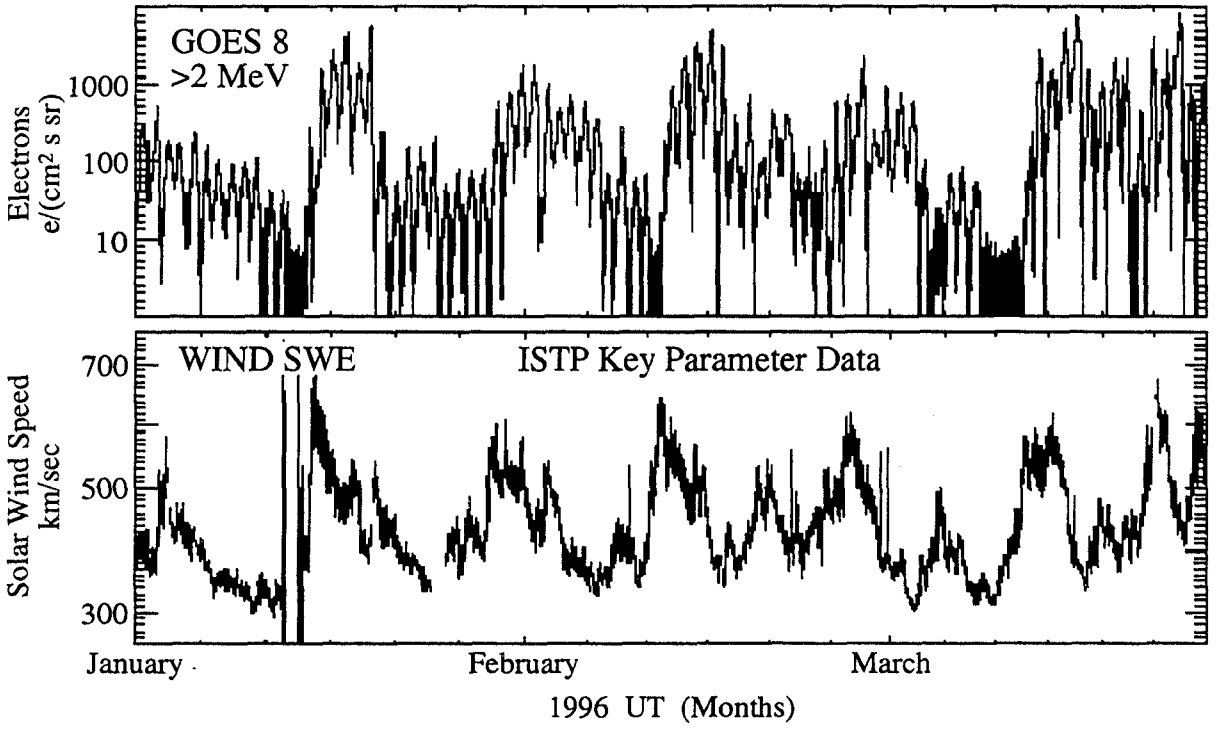

Figure 5: (Upper panel) electron flux at energies greater than 2 MeV and (lower panel) the solar wind speed obtained from the WIND SWE instrument (courtesy of A. Lazarus and J. Steinberg of MIT and K. Ogilvie of Goddard Space Flight Center). It can be seen that the energetic electron flux at geostationary orbit is highly correlated with the speed of the solar wind.

exchange with neutral particles, or by convection out through the magnetopause (the outer boundary of the magnetosphere). The primary operational concern regarding the trapped particles is from the energetic electrons. At the lower energies (greater than 10 keV), the trapped electrons contribute to spacecraft surface charging[1], while the higher energy electrons (greater than 1 MeV) are known to cause deep dielectric charging that can result in electrostatic discharge[2]. In addition, the electrons with energies above a few hundred keV are thought to have an effect on atmospheric chemistry[3].

An important aspect of the trapped energetic electrons is the fact that their flux levels appear to be strongly governed by the speed of the solar wind, with the flux levels greatly enhanced during periods of high solar wind speed[4]. Because of this dependence on solar wind speed, the electron flux levels are highest during the minimum of the solar cycle when high-speed streams emanating from large coronal holes are frequently encountered at the Earth. This effect can be seen in Figure 5 where the electron flux levels at energies greater than 2 MeV (as measured by the GOES-8 spacecraft) and the solar wind speed are shown. The solar wind measurements were obtained from the WIND spacecraft which is located upstream from the Earth in the solar wind[5]. It is important from an operational perspective to note that the prolonged levels of intense electron fluxes during late March, 1996 coincided with numerous reported spacecraft anomalies[6]. Although not well understood, the energization of these electrons within the magnetosphere appears to require prolonged time periods of high-speed solar wind, with the peak electron flux at geosynchronous orbit usually reached within about two days following the onset of the high-speed stream[7].

3.2 Solar energetic protons

Protons that are accelerated near the Sun and propagate through interplanetary space to the Earth form an important and potentially harmful component of the space environment. The occurrence of energetic proton events depends on the solar cycle, with highest likelihood around the years of solar maximum. Energetic proton events can, however, occur at any time within the solar cycle[8]. The proton energization has been shown to involve some combination of acceleration near the origin of a coronal mass ejection or flare, often with subsequent acceleration by a travelling interplanetary shock[9].

Table 2: Operational Uses of the GOES EPS and HEPAD Data

Alerts: Observed Conditions	Proton Events: > 10 pfu[1] at > 10 MeV > 1 pfu at > 100 MeV Electron Events: > 10^3 pfu at > 2 MeV
Warnings: Imminent Condition With a High Probability of Occurrence	Proton Events: > 10 pfu at > 10 MeV > 1 pfu at > 100 MeV
Real–time Data Availability Over the Internet	Integral Proton Fluxes at Energies: > 1 MeV > 5 MeV > 10 MeV > 30 MeV > 50 MeV > 60 MeV > 100 MeV Integral Electron Fluxes at Energies: > 0.6 MeV > 2 MeV > 4 MeV
Real–time Data Distribution to US Air Force Services Center	All derived quantities (Table 1) are made available.
Data Archival for Post–Event Analysis and Long–Term Studies	All derived quantities (Table 1) are archived and available from the NOAA National Geophysical Data Center, Boulder, CO.

[1]A Particle Flux Unit (pfu) is defined as 1 particle/(cm^2 s sr)

The energetic particles accelerated near the Sun propagate into space, primarily following the interplanetary magnetic field direction, but also convecting perpendicular to the magnetic field at the ExB drift speed[10]. Because of the typical spiral nature of the interplanetary magnetic field, there is a good correlation between the location of the active region on the Sun and the temporal flux profile arriving at the Earth[11]. The particle fluxes arrive most promptly when the observation point is magnetically connected to the source region; the location of an interplanetary shock relative to the connecting magnetic field affects the arriving particle flux. From the estimated location of the acceleration region, for example from X–ray measurements, and from the initial characteristics of the energetic proton flux, some prediction may be possible for the subsequent time evolution of the particle fluxes.

The energetic particles that propagate along the magnetic field can reach the Earth in tens of minutes. Because the particles with high speeds parallel to the magnetic field will be the ones that reach the Earth first, the initial particle fluxes will have a highly anisotropic, field–aligned distribution. The particle fluxes gradually become more isotropic due to scattering in the interplanetary medium well beyond the Earth.

The particle anisotropies present an operational concern during the initial detection of these events by the GOES spacecraft, since as mentioned above, beginning with GOES–8 the spacecraft are no longer spinning. With the previously spinning spacecraft, the initial onset time and the omnidirectional flux could be determined at any location in the spacecraft orbit with a time resolution of a few minutes. Currently, the initial onset of an event may be missed if the detectors are sampling away from the direction of the highly collimated particle fluxes. If the detectors sample outside the direction of the collimated flux, the omnidirectional flux will be underestimated, and if the detectors directly sample the collimated fluxes, the omnidirectional flux will be overestimated.

The prompt detection of energetic proton events and the accurate characterization of the particle fluxes are important operational concerns, due to the effects of these high fluxes on humans in space and on spacecraft systems. The large solar proton events represent a significant hazard to astronauts performing extra-vehicular activities, particularly at the high-inclination orbit envisioned for the International Space Station. These proton fluxes have also been shown to cause Single Event Upsets in spacecraft electronics, and have resulted in substantial degradation in the power generating capabilities of solar panels[2].

4. NOAA SPACE ENVIRONMENT CENTER OPERATIONS

At the NOAA Space Environment Center (SEC), the GOES energetic particle measurements are made available to a broad range of civilian and military users, fulfilling both commercial, military, and scientific needs. Current operational uses of these data are summarized in Table 2. As the data are received and processed in real time, they form the basis for the official government civilian alerts of currently existing flux levels and warnings that high flux levels are likely to occur.

The SEC alert and warning thresholds indicated in Table 2 have been established based on a combination of current customer needs, long-term studies of the environment and its effects on spacecraft systems and humans, and to some extent on historical practices. For example, the proton alert/warning threshold of 10 particles/(cm^2 s sr) at energies greater than 10 MeV corresponds to a flux level at which users consider the resulting Polar Cap Absorption to be of significant interest. More recently, the SEC began issuing alerts for energetic electron flux levels that relate to deep dielectric charging on geosynchronous spacecraft, as discussed above. The satellite user community was polled to solicit their input as to where the threshold should be set to best serve their needs. Since deep dielectric or bulk charging varies with different spacecraft shielding and with different electronic devices, many different levels were suggested. A moderately low level was chosen for the energetic electron alert (see Table 2) in order to accommodate the majority of the customer needs.

The measurement of energetic proton flux is used operationally as advance warning of enhanced geomagnetic activity that may occur within about two days following the onset of the solar protons. The measured particles, together with model calculations based on the locations of active regions on the Sun, are used to make these predictions. These real-time data are also used to support the Johnson Space Flight Center during missions of the Space Shuttle. Similar support is anticipated for the International Space Station.

The data obtained from the GOES instruments are also made available to the general public over the Internet. Plots covering the current day and the previous two days of the electron fluxes at greater than 0.6 MeV and greater than 2 MeV are available at the SEC WEB site (http://www.sec.noaa.gov) and are updated in real time. The proton and electron integral flux levels in the energy ranges given in Table 2 are also available in tabular form and can be downloaded from the SEC computers.

An important function of the GOES EPS and HEPAD measurements, in addition to the real-time operations, is to provide an extensive database for use in post-event analyses and long-term studies. When orbiting spacecraft experience anomalous behavior, the initial concern is often to determine if the anomaly resulted from conditions in the natural environment. The NOAA Space Environment Center and the USAF Services Center are frequently contacted in these situations, and then work to assess the possible role of the environment in the abnormal spacecraft behavior.

The GOES energetic particle measurements have also served as the basis for studies of various natural phenomena, including galactic cosmic rays, the Sun, the heliosphere, and the near-Earth space environment. The effects of the energetic particle populations on spaceborne systems, on other regions of the environment, and on humans are also investigated with these data. For example, cosmic radiation (greater than 200 MeV) is thought to have potential long-term human exposure risks. These very energetic particle fluxes are monitored continuously by the HEPAD. Long-term trends have been investigated using data from the GOES-6 spacecraft, and it has been demonstrated that a strong correlation exists between the HEPAD flux levels and the count rates measured by ground neutron monitors[12]. Studies of the cosmic ray modulation over solar cycles have led to the concept of an effective heliospheric potential that allows one to estimate the long-term cosmic ray dose that may be experienced over time by, for example, airline crews[13] or astronauts.

5. SUMMARY

The energetic particle instruments on the GOES spacecraft are providing a critical monitor of the environment at geostationary orbit. These instruments cover a broad energy range that is sensitive to processes occurring near-Earth, at the Sun, and throughout the heliosphere. The conditions of the geosynchronous energetic particle environment are not only important to the owners and the operators of the numerous satellites in geosynchronous orbit, but also provide key information on the conditions

at other locations in space where manned and unmanned spacecraft may be located. In addition, these data provide information on the particle fluxes that also affect the ionosphere and the upper atmosphere.

The GOES energetic particle measurements provide an important component of the civilian and the military real–time alerts and warnings of potentially hazardous conditions in the space environment. Relativistic electron fluxes, which are known to cause electrostatic discharge in spacecraft instrumentation, are continuously monitored, and alerts are issued by the NOAA Space Environment Center when potentially hazardous levels are reached. Research on the long–term trends of these energetic particles has, to some extent, enhanced our ability to predict these flux levels. The energetic proton fluxes that are monitored by the GOES spacecraft provide information for real–time alerts of potentially hazardous flux levels and also allow some predictability of future geomagnetic activity. Finally, the extensive database that has been established by GOES monitoring allows comprehensive analyses to be performed which will continue to lead to a better understanding of our space environment and its effects on human activities and other natural systems.

6. ACKNOWLEDGMENTS

The authors would like to thank A. J. Lazarus and J. T. Steinberg of the Massachusetts Institute of Technology and K. Ogilvie of Goddard Space Flight Center for providing solar wind data from their instrument on board the WIND spacecraft. We also thank H. J. Singer and L. Puga for their careful evaluation of this manuscript.

7. REFERENCES

1. N. J. Stevens, M. E. Kirkpatrick, R. C. Chaky, J. E. Howard, G. T. Inouye, and E. W. Beran, "Environmental interactions technology status," *Air Force Geophysics Laboratory Scientific Report No. 1*, AFGL–TR–85–0043, October, 1986.

2. E. G. Stassinopoulous and G. J. Brucker, "Radiation induced anomalies in satellites," *American Institute of Aeronautics and Astronautics 34th Aerospace Sciences Meeting*, 96–0739, January, 1996.

3. L. B. Callis, D. N. Baker, J. D. Lambeth, R. E. Boughner, M. Natarajan, R. W. Klebesadel, and D. J. Gorney, "Precipitating relativistic electrons: Their long–term effect on stratospheric odd nitrogen levels," *J. Geophys. Res., 96*, 2939, 1991.

4. G. A. Paulikas and J. B. Blake, "Effects of the solar wind on magnetospheric dynamics: Energetic electrons at the synchronous orbit," *Quantitative Modeling of Magnetospheric Processes, 21*, 180, Geophys. Monograph Series, 1979.

5. K. W. Ogilvie, D. J. Chornay, R. J. Fitzenreiter, F. Hunsaker, J. Keller, J. Lobell, G. Miller, J. D. Scudder, E. C. Sittler, Jr., R. B. Torbert, D. Bodet, G. Needell, A. J. Lazarue, J. T. Steinberg, J. H. Tappan, A. Mavretic, and E. Gergin, "SWE, A comprehensive plasma instrument for the WIND spacecraft," *Space Science Reviews, 71*: 55–77, 1995.

6. D. N. Baker, J. H. Allen, R. D. Bellian, J. B. Blake, S. G. Kanekal, B. Klecker, R. P. Lepping, X. Li, R. A. Mewaldt, K. Ogilvie, T. Onsager, G. D. Reeves, G. Rostoker, R. B. Sheldon, H. J. Singer, H. E. Spence, N. Turner, "An assessment of space environmental conditions during the recent Anik E1 spacecraft operational failure," *NASA ISTP Newsletter, Vol 6*, June, 1996.

7. Baker, D. N., R. L. McPherron, T. E. Cayton, and R. W. Klebesadel, "Linear Prediction Filter Analysis of Relativistic Electron Properties at 6.6 R_E," *J. Geophys. Res., 95*, 15,133, 1990.

8. M. A. Shea, "Intensity/time profiles of solar particle events at one astronomical unit," Interplanetary Particle Environment, *Proceedings of a Conference, JPL Publication 88–28*, 75, April, 1988.

9. S. W. Kahler, "Coronal mass ejections and long rise time of solar energetic particle events," *J. Geophys. Res., 98*, 5607, 1993.

10. E. C. Roelof, "Solar energetic particles: From the corona to the magnetotail," *Quantitative Modeling of Magnetospheric Processes, 21*, 220, Geophys. Monograph Series, 1979.

11. H. V. Cane, D. V. Reames, and T. T. von Rosenvinge, "The role of interplanetary shocks in the longitude distribution of solar energetic particles," *J. Geophys. Res., 93*, 9555, 1988.

12. H. H. Sauer, "GOES observations of energetic protons to E>685 MeV: Description and Data Comparison, *23rd Int. Cosmic Ray Conf., Vol. 3*, pp 250–253, 1993.

13. K. O'Brien, W. Friedberg, F. E. Duke, L. Snyder, E. B. Darden Jr., and H. H. Sauer, "The exposure of aircraft crews to radiations of extraterrestrial origin," *Radiation Protection Dosimetry, Vol. 45*, 145, Nuclear Technology Publishing, 1992.

The GOES X-Ray Sensor and its Use in Predicting Solar-Terrestrial Disturbances

P. L. Bornmann, D. Speich, J. Hirman, L. Matheson,
R. N. Grubb, H. A. Garcia, and R. Viereck
NOAA/Space Environment Center
325 Broadway, Boulder, CO 80303

ABSTRACT

The X-Ray Sensor (XRS) on the Geostationary Orbiting Environmental Satellite (GOES) provides a standard reference for essentially continuous monitoring solar activity and characterizing solar flares. Disk-integrated x-ray fluxes observed by XRS are used by forecasters and researchers around the world as a measure of the strength and duration of solar flares. The peak 0.1-0.8 nm x-ray flux during flares is used to distinguish between C, M, and X flares, flares that differ by an order of magnitude in the peak flux. Forecasters use this peak flux to predict the magnitude of proton events, and the x-ray duration is used to estimate whether coronal mass ejection may have occurred that could cause a geomagnetic disturbance if it hits the Earth. Recipients of the data use the peak flux and the duration of the flare to estimate the disturbances expected on radio communication systems. The magnitudes of XRS-observed flares are also used to determine when to issue alerts of changed ionospheric conditions that can disrupt communications and GPS signals. XRS fluxes are also used to augment solar radio observations to alert users of radio frequencies of times when the solar signal may interfere with their operations. The non-flaring x-ray flux, otherwise known as the x-ray background flux, is used as a proxy for the solar EUV emissions that are used to predict the atmospheric density as satellite orbits; variations in the daily averaged solar x-ray flux are used to estimate changes in the atmospheric drag on spacecraft orbits.

Keywords: GOES, x-rays, solar physics, x-ray instruments, space weather, solar-terrestrial disturbances, flares

1. INTRODUCTION

The X-Ray Sensor (XRS) on the Geostationary Orbiting Environmental Satellite (GOES) provides real-time monitoring for solar x-ray flares. Two ion chambers measure the electrons produced by incident solar x-rays in the 0.05 to 0.4 and 0.1 to 0.4 nm ranges. These bandpasses, shown in Figure 1, show a dramatic change of signal during solar flares[1]. To first order, the non-flaring solar spectrum[2] can be thought of as a step function, with a nearly flat spectrum for x-rays for wavelengths greater than about 0.1 nm, as shown in Figure 2. During solar flares, the x-ray emitting plasma temperature can rise to 20 x 10^6 K or more causing the step function to move to shorter wavelengths. As a result, the Sun starts emitting strongly in the XRS bandpass causing a strong increase in the XRS signal.

Disk-integrating x-ray sensors have been measuring solar fluxes in the 0.05 to 0.4 and 0.1 to 0.8 nm ranges since the early 1960s[4]. The early x-ray fluxes were measured by instruments flown by the Naval Research Laboratory (NRL) on the Solar Radiation (SOLRAD) program[3], the Orbiting Solar Observatory (OSO), and the Orbiting Geophysical Observatory (OGO) satellites[4]. The first XRS instruments were flown on the National Aeronautics and Space Administration's (NASA) Synchronous Meteorological Satellites (SMS) starting in 1974[5]. Two years later, in 1976, XRS were included on the first GOES spacecraft flown by the National Oceanic and Atmospheric Administration (NOAA)[6,7].

Because GOES is in a geosynchronous orbit, XRS provides nearly continuous monitoring for solar flares. The only loss of coverage for each XRS occurs during weekly electronics calibration (of about 10 minutes each), during spacecraft orbit adjustments (usually lasting 2-4 hours roughly every 45 days), and during the spring and fall eclipse seasons (up to 75 minutes per day for a total of about 90 days per year). Total coverage is maintained by operating two XRS instruments on two GOES spacecraft separated by roughly 60° in longitude. This can be compared with the 79% optical coverage provided by the U. S. Air Force's (USAF) ground-based Solar Observing Optical Network (SOON). Thus XRS provides the only instrument for continuous, real-time monitoring for solar flares.

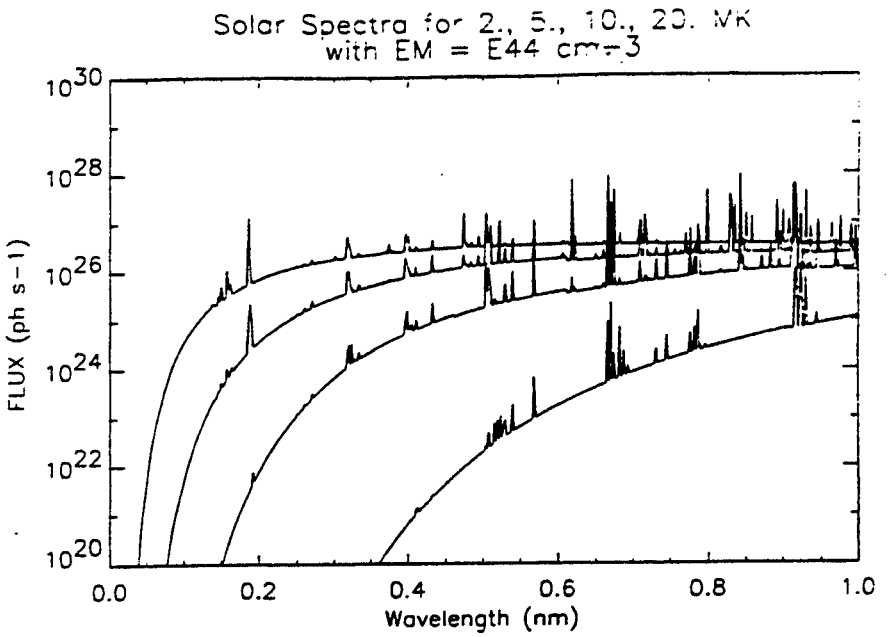

Figure 1. The solar spectrum for the XRS wavelength range for temperatures typcial of active regions to flares. Hotter spectra have larger fluxes at shorter wavelengths.

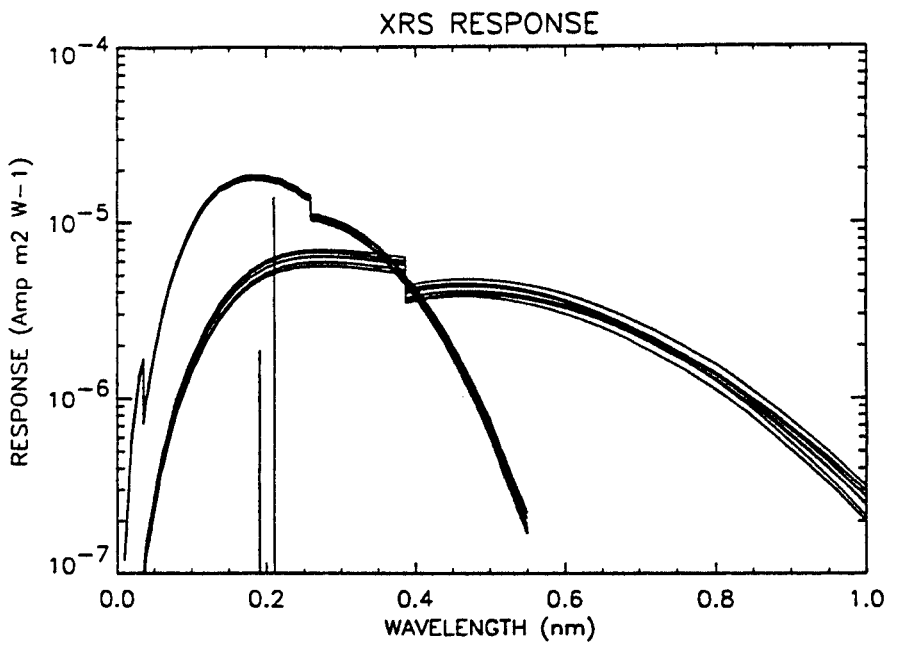

Figure 2. Wavelength dependence of XRS for GOES-4 through GOES-M. Vertical lines represent the relative intensities of the ^{55}Fe x-ray source used to calibrate the XRS.

XRS observes emissions originating from the solar corona high above the photosphere and chromosphere. Unlike most ground-based optical observations, which observe photospheric and chromospheric emissions, x-ray emission can be seen from regions beyond the solar limb. When no optical flare location is reported, forecasters must determine if the flare ocurred from a region beyond the solar limb. If it came from a strong flare that has recently rotated beyond the west limb, it could produce high energy particles. If the flare came from a region beyond the east limb, this region would be expected to produce additional flares as it rotates onto the front side of the Sun.

XRS data provide a long-term database of x-ray flare fluxes that provides a standard reference of comparing solar flares. The x-ray flare classification is based on the peak flux from the entire Sun as observed in the 0.1 to 0.8 nm XRS channels. This classification is reported as a leter and a multiplier. The letter represents factors of ten increase in flux, starting at 10^{-6} W m^{-2} for C flares. The letters can be thought of as representing C for Common flares, M for medium flares, and X or X-tra large flares. (The letter sequence has been extended to lower fluxes, giving a full sequence of A, B, C, M, and X.) The other standard flare classification, based on ground-based optical images, is more subjective. This optical classification is based on the spatial extent of the Hα flare reported as a numerical value (0-4) and letter indicating the flare brightness above a background that is manually adjusted to eliminate flare reports from small-scale fluctuations in the active region intensity. This optical classification uses the letters F for Faint, N for Normal, and B for Brilliant flares.

2. SOLAR X-RAY FLUX VARIATIONS

Disk-integrated solar x-ray fluxes vary on several timescales and are indications of changes in different solar features. Very long-term variations in the x-ray flux, on the order of years, are associated with the solar cycle. The number of active regions on the solar disk each day rises from zero at solar minimum to over thirty during solar maximum over the solar cycle of roughly 11 years. This causes the non-flaring solar x-ray flux (the "background flux") to vary over the solar cycle by nearly two orders of magnitude[8], from 8×10^{-8} to 1×10^{-6} W m^{-2}. And because flares come primarily from solar active regions, the number of flares also varies with the solar cycle.

Slowly evolving changes on the order of days are the result of solar active regions. These regions can last for days to weeks and will contribute to the XRS signal during the two week interval when the 27-day solar rotation brings them to the front side of the Sun. The contribution from individual active regions can be seen near solar minimum when only one strong active region is present; near solar maximum the overlapping signals from multiple active regions cause source confusion in this disk-integrated data and the contributions from individual regions cannot be extracted.

Short-term variations on the order of minutes to hours are caused by flares. The x-ray flux increases significantly during flares, with peak flare fluxes rising to three or more orders of magnitude above non-flaring levels. The slowly evolving flares are known as Long Duration Events (LDEs).

3. OPERATIONAL VALUE

X-ray fluxes are used to forecast the geomagnetic storms, ionospheric disturbances, and energetic particle events. The manifestation of a solar flare in the terrestrial environment and the effect of that manifestation are described in the following sections.

3.1. Radio Communications

Radio communications were the first systems known to be disturbed by solar activity. In the early 1940s engineers realized that radio communication difficulties occurred when the Sun was in the antenna's beam pattern. Even today radio communication along the line of sight to the Sun can be corrupted during solar flares. Radio fluxes from 245 MHz to 15.4 GHz are monitored in real time by the USAF's Radio Solar Telescope Network (RSTN), and XRS fluxes are used as verification that a solar flare has occurred.

Solar x-ray, EUV, and UV fluxes incident on the Earth's atmosphere affect the level of ionization within the ionosphere. This, in turn, affects radio communication passing through the ionosphere (e.g. ground-to-satellite communication) or

reflecting off the ionosphere (e.g. long-distance ground-to-ground communication). X-rays are absorbed in the D region of the Earth's ionosphere. This increases the local ionization and causes increased absorption of high frequency (HF) radio waves and shortwave fadeouts (SWF). In addition, the reflection height of very low frequencies (VLF) moves to lower heights during solar flares, causing sudden phase anomalies (SPA). The XRS fluxes are used as a proxy for radio disturbances, and alerts are issued when the x-ray flux exceeds the M5 and X1 (5×10^{-5} and 10^{-4} W m^{-2}) flux levels.

Increases in the EUV and UV fluxes can also increase the ionization of the ionosphere's E and F layers, which in turn affects radio waves entering these layers. This can corrupt LORAN navigation systems, shortwave radio broadcasts, spacecraft-to-ground and airplane communications, and also cause erroneous readings from the Global Positioning System (GPS). Solar EUV and UV fluxes are not monitored directly, but since solar fluxes increase in nearly all wavelengths during solar flares, x-ray and radio fluxes can be used as proxies. XRS fluxes are therefore used to estimate the severity and duration of disturbances to radio and other affected systems.

3.2. Satellite Drag

X-ray and EUV fluxes also affect the density of the Earth's upper atmosphere by heating the atmosphere and causing it to expand and rise. The net result is that at a given altitude, the density of the atmosphere will change. These density changes affect the drag experienced by satellites in low Earth orbit (LEO). Because EUV fluxes are not measured directly, the 10.7 cm solar radio fluxes are used as a proxy for solar EUV fluxes. The F10.7 flux is recorded three times a day, but can be interrupted by severe terrestrial weather conditions. Even though attempts are made to record these fluxes during non-flaring periods, flare contamination occasionally occurs. Furthermore, there is not always good correlation between the F10.7 flux that is observed and the EUV flux that affects the upper atmosphere.

For atmospheric density calculations, a direct measurement of the EUV fluxes would be a much better input because the EUV fluxes are affecting the atmospheric responses directly. Although these models are designed to use EUV spectra scaled by the 10.7 cm radio flux, we will not be able to advance our understanding of these physical processes without measuring the fluxes directly. Because of this, NOAA/SEC has been exploring cost-effective methods to include solar EUV monitoring on the GOES satellites[9].

Short-term predictions of the F10.7 cm flux are used to estimate orbit changes required to track thousands of satellites. Long-term predictions are used to estimate atmospheric density and orbit drag changes that will affect the orbital lifetime of future satellites.

3.3. Atmospheric Models

Solar EUV radiation not only heats the upper atmosphere, but also influences the chemical reactions. For example, the production of nitric oxide (NO) in the lower thermosphere is directly related to the action of both EUV and soft X-ray radiation on the neutral atmosphere. Because the EUV fluxes are not routinely measured, models of atmospheric chemistry scale several solar EUV reference spectra[10,11] based on the 10.7 cm solar radio flux. One of the primary energy inputs to these models is therefore based on spectra observed in the late 1970's. Model calculations of the amount of atmospheric nitric oxide do not agree with reported x-ray fluxes, but could be explained if the incident solar x-ray flux was a factor of 2-3 larger[12,13,14], particularly near solar maximum, for wavelengths longward of XRS (*i.e.* in the 0.8 to 14.0 nm range) that are not directly measured. One attempt to study this discrepancy is re-examining the assummed solar temperatures used to derive the 4.4-6.0 nm fluxes reported from SOLRAD[15].

3.4. Particle Events

The x-ray flare flux is used to empirically estimate the anticipated peak particle flux based on historical data[16, 17]. The peak particle flux scales as the 4/3 power of the time-integrated x-ray flux[18], with a correlation coefficient[19] of 0.7. Because the particles with the highest energies can reach the Earth within about twenty minutes, the forecasters make an estimate of the anticipated peak XRS flux shortly before the flare reaches its x-ray peak in order to estimate the anticipated total x-ray flare flux. The total flux is used with the solar flare location and the solar wind velocity to predict the peak particle flux[18,19]. Flare

locations are usually available from ground-based optical observatories, and SXI[20] will monitor flares without interruptions from terrestrial weather. The solar wind velocities are currently available in real time for about two hours each day from the WIND spacecraft; a real-time solar wind monitor at the L_1 Lagrange point would be a much better solution.

Recent research[21] suggests the occurrence of a particle event may be related to changes in the hard x-ray spectra[22] and the solar plasma temperature derived from the XRS fluxes[23]. NOAA/SEC is pursuing opertunities to fly a Hard X-ray Spectrometer (XRS) for future testing of this technique.

3.5. Geomagnetic Disturbances

Long Duration x-ray flare Events, known as LDEs, are associated with Coronal Mass Ejections (CMEs) and filament disappearances, both of which are associated with geomagnetic disturbances. The XRS measures x-ray fluxes over a dynamic range of at least five orders of magnitude with a flux resolution of at least 2-3%. Therefore, XRS cannot observe small changes in flux that are less than 1% of the total solar flux. This makes it difficult to observe faint LDEs, particularly near solar maximum when the non-flaring x-ray flux can be three to four orders of magnitude greater than at solar minimum. Some faint LDEs may be observable when the background fluxes are low, but would not be observable when the background fluxes are higher. In fact, increases in x-ray flux observed by the Solar X-ray Telescope (SXT) on Yohkoh that were associated with CMEs are much less than the total x-ray flux observed across the solar disk[24]; these events could not be detected with the 1% flux resolution of XRS. For these weak events, spatially resolved x-ray images from the future GOES Solar X-ray Imager (SXI) will be used.

3.6. Research

The ratio of the fluxes in the two XRS wavelength bands can be used to derive an average flare temperature. Because the solar spectrum changes with the temperature of the emitting plasma, the response in each XRS waveband will change by a different amount, with the 0.05-0.4 nm channel increasing by larger factors than the 0.1-0.8 nm channels as the flare temperature increases. A simple, analytic formula is available for determining the flare temperature from the observed flux ratio[25]. More recent calculations[26]. with updated atomic physics calculations confirm this formula for temperatures above 3×10^6 K. Alternatively, tables of the ratio of the electrical current generated in the two XRS chambers can be used to derive the average solar plasma temperature[27]. These temperatures have been used with temperatures derived from other instruments to study flare properties[28,29].

Because XRS is a disk-integrating instrument, the derived temperature will be an average over all of the x-ray emitting structures of the sun, which has been illustrated in the analysis of XRS data during a lunar eclipse[30]. Thus proper subtraction of the pre-flare flux is required when deriving a temperature for the weaker flares[31].

4. FLUX CALIBRATION

The calibration of the XRS fluxes is of interest to groups using the reported fluxes in models of the chemical reactions in the Earth's atmosphere. It is also an issue of current investigation because the fluxes reported by XRS instruments on the three-axis spin-stabilized GOES-8 and GOES-9 are larger than reported by the spinning GOES-5 and GOES-7.

Whenever a new XRS is launched, its fluxes are compared with those of previously launched instruments. In most cases the fluxes agree to within the calibration uncertainty. XRS instruments are calibrated before launch with a reference ^{55}Fe x-ray source emitting at 0.18 nm (see Figure 2). These calibrations are accurate to at least 3σ = +/- 11%[32]. Occasionally the fluxes differ by more than the stated level of calibration uncertainty and a scaling factor is introduced in the ground processing of the XRS data. This was done for GOES-6, -8, and -9 to force the reported fluxes to agree with measurements from the previous satellites in the series. In these cases the XRS fluxes have been scaled to match the fluxes from all previous instruments; the scaling factors applied during SEC ground processing are summarized in Table 1. The physical explanation for these discrepancies is a subject of current investigation at SEC.

It should be noted that XRS fluxes were systematically 1.5 to 2 times greater than SOLRAD-reported fluxes in the 0.05-0.4 nm band and 2-4 times lower in the 0.1-0.8 nm band[4]. The bandpasses of the two instruments are similar, although the XRS instruments have greater response at the longer wavelengths in each band.

Table 1. XRS Scaling Factors (applied during ground processing

	0.5-4 A	1-8 A
GOES 5	1.000	1.000
GOES 6	1.000	0.833
GOES 7	1.000	1.000
GOES 8	0.920	0.790
GOES 9	0.920	0.790

5. CONCLUSIONS

Two XRS operating on GOES provide the only source of continuous flare patrol, which is critical for monitoring the Sun for sources of solar-terrestrial disturbances. XRS has a long history of providing reliable data, that together with its predecessors form a continuous data series covering over three decades. These data are now using the data as a measure of the total solar x-ray flux incident on the Earth. This raises questions that have not yet been fully resolved regarding the absolute flux calibration between XRS instruments on the spinning and non-spinning GOES and between the GOES XRS and the x-ray monitors flown on SOLRAD.

The XRS fluxes are used in numerous ways to assist in forecasting and monitoring solar disturbances. It is the only source of data that provides a continuous flare monitor. Data from other instruments are used to support the XRS observations. It should be noted that direct EUV monitoring system or better physical understanding of the relationship between the solar production of X-ray and EUV flux is required for models tracking the effects of the EUV fluxes; atmospheric density esimates will continue to have large uncertainties if these advances are not made.

6. REFERENCES

1. R. W. Kreplin, K. P. Dere, D. M. Horan, and J. F. Meekins, "The Solar Spectrum Below 10 Å," in *The Solar Output and Its Variation,* O. R. White (ed.), Colorado Univ. Press, 1977.

2. R. Mewe and E. H. B. M Gronenschild, "Calculated X-radiation for Optically Thin Plasmas IV. Atomic Data and Rate Coefficients for Spectra in the Range 1-270 Å," *Astron. Astrophys. Suppl. Ser.,* **45** 11-52, 1981.

3. D. M. Horan, R. W. Kreplin, and K. P. Dere, "The NRL SOLRAD 11 Satellites (1976-023C, 1976-023D) Description of Experiments," NRL Memorandum Report 4959, 1982

4. S. W. Kahler and R. W. Kreplin, "The NRL SOLRAD X-Ray Detectors: A Summary of the Observations and a Comparison with the SMS/GOES Detectors," *Solar Physics*, **133**, 371-384, 1991.

5. R. F. Donnelly, "SMS-GOES Solar Soft X-ray Measurements Part I. SMS-1, SMS-2, and GOES-1 Measurements from July 1, 1974, through December 31, 1976," NOAA Tech. Mem. ERL SEL-56, 1981.

6. S. D. Bouwer, R. F. Donnelly, J. Falcon, A. Quitana, and G. Caldwell, "A Summary of Solar 1-8 Å Measurements from the SMS and GOES Satellites," NOAA Tech. Mem. ERL SEL-62, 1982.

7. R. F. Donnelly, R. N. Grubb, and F. C. Cowley, "Solar X-ray Measurements for SMS-1, SMS-2, and GOES-1: Information for Users," NOAA Tech. Memo. ERL SEL-48, 1977.

8. W. J. Wagner, "Observations of the 1-8 Å Solar X-ray Variability During Solar Cycle 21," *Adv. Space Res.*, **8**, No. 7, 67-76, 1988.

9. R. N. Grubb, P. L. Bornmann, G. Heckman, T. G. Onsager, H. J. Singer, and R. Viereck, "The Space Environment Monitoring Mission Beyond GOES M," paper 2812-30 in these proceedings, 1996.

10. H. Hinteregger, K. Fukui, and B. R. Gilson, "Observational, Reference and Model Data on Solar EUV, From Measurements on AE-E," *Geophys. Res. Letters*, **8**, 1147-1150, 1981.

11. W. K. Tobiska and C. A. Barth, "A Solar EUV Flux Model," *J. Geophys. Res.*, **95**, No. A6, 8243-8251, 1990.

12. J. D. Winningham, D. T. Decker, J. U Kozyra, J. R. Jasperse, and A. F. Nagy, "Energetic (> 60 eV) Atmospheric Photoelectrons," *J. Geophys. Res.*, **94**, 15335-15348, 1989.

13. R. G. Roble, "Solar EUV Flux Variations During a Solar Cycle as Derived from Ionospheric Modeling Considerations," *J. Geophys. Res.*, **81**, 265-268, 1976.

14. D. E. Siskind, C. A. Barth, and D. D. Cleary, "The Possible Effect of Solar Soft X-rays on the Thermospheric Nitric Oxide," *J. Geophys. Res.*, **956**, 4311-4317, 1990.

15. F. G. Eparvier and P. L. Bornmann, "Solar Soft X-rays (1-60 Å): A Re-Analysis of the SOLRAD-11 Observations," 1996 in prep.

16. G. A. Kuck, R. R Davis, and G. J. Krause, "Prediction of Polar Cap Absorption Events," Air Force Weapons Lab. Tech. Report AFWL-TR-71-1, 1971.

17. C. Balch and J. Kunches, "SESC Methods for Proton Event Forecasts," in *Solar Terrestrial Predictions Workshop in Meudon France Jun 18-22, 1984*, P. A. Simon, G. Heckman, and M. A. Shea (eds.), 353-356, 1984.

18. G. R. Heckman, J. M. Kunches, and J. H. Allen, "Prediction and Evaluation of Solar Particle Events Based on Precursor Information," *Adv. Space Res.*, **12**, No. 2,. 313-320, 1992.

19. G. A. Kuck and S. L. Huston, "Prediction of Solar Proton Fluxes from X-ray Signatures," in *Solar-Terrestrial Predictions: Proceedings of a Workshop at Luera, Australia, October 16-20, 1989*, R. J. Thompson, D. G. Cole, P. J. Wilkinson, M. A. Shea, D. Smart, and G. Heckman (eds.), Vol. 1, 422-429, 1990.

20. P. Bornmann, D. Speich, Joseph Hirman, V. Pizzo, R. Grubb, C. Balch, and G. Heckman, "The GOES Solar X-ray Imager: Overview and Operational Goals," in these proceedings.

21. H. A. Garcia and A. L. Kiplinger, "Low-Temperatature X-ray Flares, Spectrally Hardening Hard X-ray Flares, and Energetic Interplanetary Protons," in *Solar Drivers of Interplanetary and Terrestrial Distrubances"*, K. S. Balasubramaniam, S. L. Keil, and R. N. Smartt (eds.), ASP Conf. Series, **95**, 91-99, 1996.

22. A. L. Kiplinger, "Comparative Studies of Hard X-ray Spectral Evolution in Solar Flares with High-Energy Proton Events Observed at Earth," *Astrophys. J.*, **453**, 973-786, 1995

23. H. A. Garcia, "Temperature and Hard X-ray Signatures for Energetic Proton Events," *Astrophys. J.*, **420**, 522-532.

24. A. H. McAllister, M. Dryer, P. McIntosh, H. Singer, and L. Weiss, "A Large Polar Crown CME and a Severe Geomagnetic Storm: April 14-17, 1994," in *Proc. Thrid SOHO Workshop - Solar Dynamic Penomena and Solar Wind Consequences*, p. 315-318, 1994.

25. R. J. Thomas, R. Starr, and C. J. Crannell, "Expressions to Determine Temperatures and Emission Measures for Solar X-ray Events from GOES Measurements," *Solar Phys.*, **95**, 323-329, 1985.

26. J. Sylwester, H. A. Garcia, and B. Sylwester, "Quantitative Interpretation of GOES Soft X-ray Measurements I. The isothermal Approximation: Application of Various Atomic Data," *Astron. Astrophys.*, **293**, 577-585, 1995.

27. H. A. Garcia, "Temperature and Emission Measure from GOES Soft X-ray Measurements," *Solar Phys.*, **154**, 275-308, 1994.

28. H. A. Garcia and F. Fárník, "Flare Plasma Diagnostics Based on the Soft X-ray Photometric Data from GOES and Prognoz," *Solar Phys.*, **141**, 127-146, 1992.

29. F. Fárník and H. A. Garcia, "Phobos-GOES Soft X-Ray Observations of the Sun," *Astrophys. J.*, **444**, 929, 1995.

30. P. L. Bornmann and L. D. Matheson, "Solar Flare Plasma Properties Derived from the Disk-Integrating GOES X-ray Sensors During an Eclipse," *Astron. Astrophys.*, **231**, 525-535, 1990.

31. P. L. Bornmann, "Limits to Derived Flare Properties using Estimates for the Background Fluxes: Examples from GOES," *Astrophys. J.*, **356**, 733-742.

32. Panametrics, Inc. "Summary Report #1 Status Review of X-Ray Sensor Subsystem GOES D, E, F" (see also more recent calibration reports for GOES I-M), PANA GOESX-SR-1, 1978.

J. F. Meekins, A. E. Unzicker, K. P. Dere, and R. W. Kreplin, "Absolute Calibration of X-ray Ionization Chambers," NRL Report 7698, 1971.

Monitoring space weather with the GOES magnetometers

H.J. Singer, L. Matheson, R. Grubb, A. Newman, and S.D. Bouwer[†]

NOAA Space Environment Center
NOAA R/E/SE, 325 Broadway, Boulder, CO 80303

[†]also at: CIRES, University of Colorado,
Campus Box 216, Boulder, CO 80309

ABSTRACT

Magnetic field measurements have been made from geosynchronous orbit for more than 20 years. These measurements are important for monitoring "space weather" and for providing a unique data base that can be used for improving our knowledge of the Earth's magnetosphere and solar-terrestrial interactions. This paper will focus on the variety of products and services provided by these measurements - those currently available, and those under consideration for the future. The magnetic field measured at the GOES is presently used to detect synchronous orbit magnetopause crossings and shocks in the solar wind, to assist forecasters in qualitatively assessing the level of geomagnetic disturbance, to interpret changes in energetic particle measurements, to provide data to the National Geophysical Data Center, to support in real-time scientific activities such as rocket launches, and to conduct research for a better understanding of the space environment. One important use of magnetometer data in the Space Environment Center is to alert customers when shocks occur in the solar wind. These shocks have the potential for energizing particles to multi-MeV levels, causing Single Event Upsets (SEU's) in spacecraft electronics, and at lower energy ranges causing deep-dielectric charging that produces spacecraft anomalies. Data from the new GOES-8 and GOES-9 spacecraft will be discussed along with prospects for future products and services.

Keywords: magnetometer, geomagnetic field, geomagnetic storm, geomagnetic substorm, geosynchronous, GOES

1. INTRODUCTION

In 1945, in the British radio journal *Wireless World*, Arthur C. Clarke was the first to propose the use of three satellites, located 22,300 miles above the equator, to provide global TV coverage. As he wrote about this proposal in the early 1960's in the book Profiles of the Future, he noted that preparations were underway by the Hughes Aircraft Company and the United States Army to launch communications satellites into this 24 hour orbit[1]. On July 26, 1963, Syncom 2 was launched, becoming the first communications satellite in geosynchronous orbit. It was only a few years later, in 1966, that the first magnetic field measurements were made in geosynchronous orbit by the ATS-1 (Application Technology Satellite), and operational measurements began with the SMS (Synchronous Meteorological Satellite) in May 1974[2].

Since those early days of the space age, hundreds of satellites valued at billions of dollars have been placed in geosynchronous orbit to provide a multitude of services like improved global communications and weather monitoring. These resources, satellites in other orbits, and many ground-based technological systems are vulnerable to "space weather" effects like those caused by damaging energetic particles and severe geomagnetic disturbances. Consequently there is a need for monitoring, specifying, and predicting conditions in the near-Earth space environment where these systems operate. The Geostationary Operational Environmental Satellite (GOES) magnetometer is one of the instruments that provides these functions, and it is included in the NOAA Space Environment Center Space Environment Monitor (SEM) package that is operational on each GOES. The other instruments in the SEM package, an Energetic Particle Sensor (EPS) and a solar X-ray Sensor (XRS) are described elsewhere. In addition, a new operational instrument to provide Solar X-ray Images (SXI) will be flown on GOES around the year 2000. As described below, the geosynchronous environment is not only an important location for monitoring space weather, but it is also a unique location for providing data that can be used for improving our knowledge of the Earth's magnetosphere and solar-terrestrial interactions.

Following two SMS satellites, the first GOES was launched in October 1975, and they have continued to this day with the currently operational GOES-8 and GOES-9 spacecraft[3]. The magnetic field data, beginning with SMS-1, are used for space

weather operations, and are collected and processed by the NOAA Space Environment Center to be archived and distributed through the NOAA National Geophysical Data Center. The continuous record spanning several decades is one of the values of these measurements over measurements made in other orbits over more limited time spans. This paper will describe the magnetometer instrument, the geosynchronous space environment, and operational and scientific uses of the GOES magnetometer data.

2. MAGNETOMETER INSTRUMENT: DESCRIPTION, TESTING, AND OPERATION

The magnetometers on the three-axis stabilized GOES I-M (called GOES 8-12 after launch) series of satellites are three-axis fluxgate magnetometers manufactured by the Schonstedt Instrument Company and integrated on the spacecraft by Space Systems/LORAL. The magnetometer electronics are inside the spacecraft, and the sensors are mounted on a three-meter boom attached at the north west corner of the anti-Earth panel, with the primary sensor at the end of the boom and a second redundant sensor located 0.3 meters inboard of the first. Only one magnetometer may be operated at a time. Each magnetometer axis is measured once a telemetry frame (0.512 seconds), with a 42 millisecond delay between sampling successive axes. To reduce aliasing, each of the three-axis magnetometer outputs is filtered through a five-pole 0.5 Hz Butterworth low-pass filter.

The magnetometer range is ± 1000 nanoTesla (nT), and is measured by a 16 bit analog-to-digital converter providing 0.03 nT sensitivity. With temperature compensation of the sensors and electronics, the accuracy of the instrument is 1 nT. The instruments are monitored for proper operation by adding a series of small fixed currents to a set of auxiliary windings during weekly calibrations and checking for proper magnetometer gains and transient responses.

To insure accurate measurements, the GOES magnetometers are thoroughly tested and calibrated. Prior to launch, the instruments are temperature calibrated, and sensor gains and offsets are determined. Because stray fields, generated by the spacecraft, can severely contaminate the measurement, a stray-fields test program identifies whether or not various spacecraft systems produce magnetic signatures that are likely to be detected in orbit. If there is a detectable signature, it is either reduced to an allowable limit through hardware modifications, or a correction scheme is instituted in the ground-based data processing. Efforts are also made to minimize and control magnetic materials on the spacecraft and boom. An initial calibration of the spacecraft torquer coils is also made prior to launch.

Absolute magnetic field measurements require accurate knowledge of magnetometer offsets that result from the spacecraft and the sensor electronics. A spinning spacecraft continuously provides the opportunity to measure these values for the spin plane sensors; however, on the three-axis stabilized GOES-8 and GOES-9, we must rely on a one time satellite maneuver. In orbit, just after the magnetometer boom deployment, the spacecraft is rotated about 3 axes to determine magnetic offsets that result from a combination of the spacecraft field and the magnetometer sensors. This maneuver cannot be performed again after all spacecraft appendages are deployed and the spacecraft becomes operational. Following the initial offset determination, data comparisons with magnetic field models are used to monitor for any major changes in these offsets.

On GOES-8 and GOES-9, the spacecraft torquer coils are the major system contributing offset fields to the measurements that must be corrected during data processing. The magnetic torquers, along with two momentum wheels, a reaction wheel, the solar panel trim tab and 22 thrusters, maintain the proper attitude of the spacecraft. They are controlled by an attitude and orbit control subsystem. At the launch of GOES-8, the torquers could change current at a 20 minute interval. The currents could change from full scale of one polarity to full scale of the other polarity at one of these steps, could make a small step, or the current might not change at all at one of the possible current change times. A maximum size step can produce as much as a 400 nT magnetic signature at the magnetometer sensors. The control of the torquers has evolved into a small fixed size step in the torquer current at a much faster rate. The current operation of the torquers sets the current change at a level that causes a 1.5 nT magnetometer step at a minimum change interval of 2.56 seconds. In actual operation not every possible change interval has a torquer current change. GOES-8 torquer currents change from 600 to 800 times a day.

A calibration between torquer currents and magnetic field signatures was made both on the ground and in space for correcting the magnetic field measurement; however, on GOES-8, noise in the torquer current telemetry introduced artificial noise in the "corrected" magnetic field at the few nanoTesla level. A correction has been instituted on GOES-8, and will be included on following spacecraft, to allow use of torquer command data for torquer current correction. The problem has been further dealt with on GOES-9, and future spacecraft, by filtering the torquer current telemetry before it is transmitted.

3. THE GEOSYNCHRONOUS MAGNETIC ENVIRONMENT

Geosynchronous magnetic field measurements have proven useful for both operational and scientific purposes, in part because the orbit is in a strategic location for monitoring the effects of the major magnetospheric current systems. Much can be learned about solar-terrestrial interactions from analysis of these data. These currents described below[4], are superimposed on the Earth's internal dipole-like field that has a value of about 110 nT at geosynchronous orbit located at 6.6 Earth radii from the center of the Earth. The Earth's internal magnetic field is modified at this location by perturbations that range from fractions of a nanoTesla to sometimes more than 100 nT, but are more typically on the order of 40 or 50 nT. The variations of concern occur on a wide range of time scales: seconds for solar wind shocks and magnetic pulsations, minutes and hours for substorms, a day for local time variations in magnetospheric structure, days for magnetic storms, and months and years for solar cycle effects.

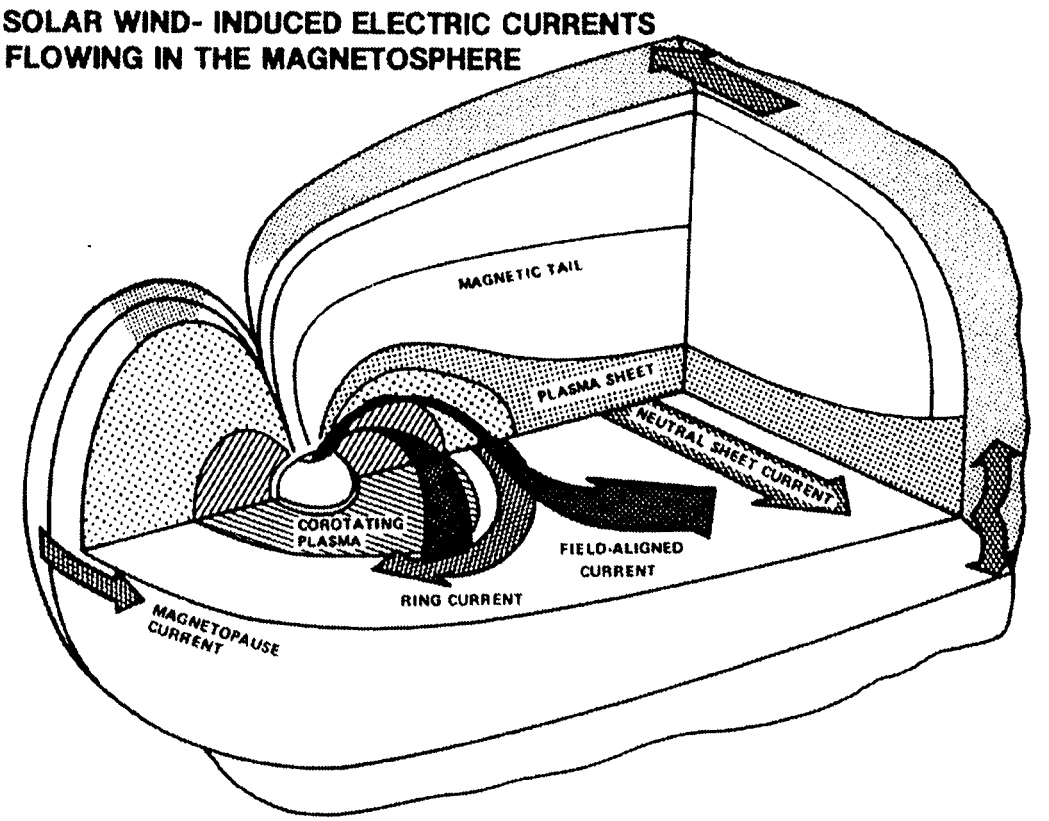

Figure 1: Solar-wind induced electric currents flowing in the magnetosphere. G K Parks, PHYSICS OF SPACE PLASMAS: AN INTRODUCTION, (portion of figure 7.1 from page 224), © 1991 Addison-Wesley Publishing Company Inc. Reprinted by permission of Addison-Wesley Longman Publishing Company, Inc.

As the solar wind streams past the Earth it distorts the Earth's dipole-like magnetic field into a shape that is compressed on the dayside, and drawn out into a geomagnetic tail hundreds of Earth radii long on the nightside (Figure 1). The velocity and density of the solar wind plasma, and the strength and direction of its imbedded magnetic field, influence not only the structure of the magnetic field surrounding the Earth, but also control the processes by which mass, momentum, and energy are transferred from the solar wind to the Earth's magnetosphere-ionosphere system. This interaction between the solar wind and the Earth's magnetic field creates the complex and dynamic magnetosphere which can be monitored by the GOES field and particle instruments.

The perturbations in the Earth's dipole field are caused by current systems external to the Earth that result from the coupling between the time varying solar wind and its interaction with the Earth's magnetic field. The primary current systems affecting geosynchronous observations are the magnetopause current, the ring current, magnetic field-aligned currents, and the neutral sheet or cross-tail current. Figure 1 shows the Earth's magnetosphere and the location of the major current systems in relation to magnetospheric regions and boundaries. Although the boundaries are dynamic, geosynchronous orbit is located in the equatorial region, typically between the plasma sheet and corotating plasma regions.

The magnetopause current system is at the magnetopause boundary that separates the region of space dominated by the Earth's field from the region dominated by the solar wind and its imbedded Interplanetary Magnetic Field (IMF). This interface is typically at about 10 Earth radii upstream of the Earth, between the Earth and Sun, but extends in a long downstream wake that is on the order of 100 Earth radii or more. The magnetopause current on the dayside enhances the field at geosynchronous orbit. The magnetopause boundary is dynamic, and when it is pushed in past the geosynchronous orbit location, satellites operations at that location can be affected.

The ring current is caused by radial gradients in the density and temperature of typically 1 to 200 keV ions that surround the Earth. This current typically maximizes at about 3 to 4 Earth radii, its strength can be asymmetric around the Earth, and its radial location can extend over a distance of several Earth radii. The ring current is a westward current that produces a strong depression in the field in the inner magnetosphere and at the surface of the Earth during geomagnetic storms.

Magnetic field-aligned currents that communicate information and electrically couple the ionosphere and the magnetosphere are quite complicated as a function of latitude, local time, and solar wind conditions. One of the most significant field-aligned currents that is detected at geosynchronous orbit is the current system associated with substorm expansion onsets in the midnight sector. Substorms typically occur every few hours, although their frequency and intensity are quite variable and dependent on solar wind conditions. The perturbations caused by the substorm related field-aligned currents are most notable in the east-west deflections of the geosynchronous magnetic field.

The last current system described, the neutral sheet current, is located in the center of the plasma sheet region and supports the oppositely directed magnetic fields in the tail lobes. Field lines threading the plasma sheet are closed, with one foot in each ionosphere. The foot points form an oval shaped region surrounding the polar cap where the most intense auroral activity occurs in the high latitude ionosphere. When the tail currents are strong the magnetic field at GOES in the midnight region departs from its dipole-like shape and becomes very stretched. When substorm expansions occur, in addition to the field-aligned currents mentioned previously, there is a reduction of the neutral sheet or cross-tail current that causes the field geometry to revert to a more dipole-like shape.

4. USES OF THE GOES MAGNETOMETER DATA

There are a variety of uses of the GOES magnetometer data for both operational and scientific needs. These are outlined in Table 1 and a few examples are discussed in greater detail below.

4.1. Assessing the level of geomagnetic disturbances

The geosynchronous magnetic field data can be used to assist forecasters in qualitatively assessing the level of geomagnetic disturbances. Figure 2 illustrates some of the information that can be learned from the examination of a simple time series of the data; it shows one-minute averages of three components of the magnetic field and the total field measured by GOES-9 for the entire month of January 1996. The three components are: Hp, perpendicular to the satellite orbital plane or parallel to the Earth's spin axis in the case of a zero degree inclination orbit; He, perpendicular to Hp and directed earthwards; and Hn, perpendicular to both Hp and He and directed eastwards. (This is the same coordinate system used for all the GOES magnetic field measurements since GOES-5; prior to GOES-5, Hn was directed westwards.)

4.1.1 Diurnal variations

An obvious feature in the data is the diurnal variation observed in all components and the total field. The diurnal variation is caused by the asymmetry in the Earth's field with respect to the solar direction. Hp (the parallel component) and Ht (the total

OPERATIONAL AND SCIENTIFIC USES OF THE GOES MAGNETOMETER
• Detecting magnetopause crossings
• Alerting customers to solar wind shocks or sudden impulses
• Assessing the level of geomagnetic activity
• Distinguishing among different sources of energetic particle events
• Developing techniques for new operational applications
• Providing data to NGDC for archives and the scientific community
• Real-time data to the US Air Force 50th Weather Squadron
• Supporting rocket launch decisions and other real-time activities
• Conducting research for understanding the space environment

Table 1: Operational and scientific uses of the GOES magnetometer data.

field strength) typically maximize on the dayside near local noon, where the field is compressed by the solar wind pressure. Hp and Ht are reduced near local midnight where the Earth's field is stretched out into a long geomagnetic tail, so the Hp or Ht diurnal variation can be used to quickly assess the local time of the GOES satellite at a particular UT. In this case, during the month of January, GOES-9 was being moved from 115.8 degrees west geographic longitude to its more permanent position at 134.7 degrees. (Typically one GOES satellite is at 75 degrees west geographic longitude and one is at 135 degrees.) At the end of the month the total field (Ht) maximized near 21 UT when the satellite was near local noon and Ht minimized near 09 UT when the satellite was near local midnight.

4.1.2 Solar wind dynamic pressure

Another feature seen in the data, the magnitude of the field strength (Ht) maximum, can be used to infer the solar wind dynamic pressure, since this pressure is one of the factors controlling the compression of the Earth's magnetic field and therefore the strength of the dayside field. During January 1996 the maximum varied by about 35 nT, and during the 4 to 6 hours-per-day when the satellite is within 2 or 3 hours of local noon, these data can be used to monitor the solar wind influence on the magnetosphere. With two satellites separated by about 4 hours local time, as is typical for the GOES satellites, we could have an indicator of solar wind dynamic pressure during about 10 hours each day. These increases in solar wind dynamic pressure can at times be so large as to move the magnetopause inside geosynchronous orbit, causing major changes in the particle and field environment at this location.

4.1.3 Substorms, field-aligned currents and magnetic field reconfigurations

Substorms include brilliant activation of the aurora, the development of new and enhanced current systems in the ionosphere and magnetosphere, the reconfiguration of the magnetic field geometry in the magnetotail and geosynchronous regions, the injection and energization of particles into geosynchronous altitudes, and the formation of plasmoids that are ejected down the magnetotail. Substorms can be detected in both Hp and Ht and are most noticeable in Figure 2 where magnetic fluctuations

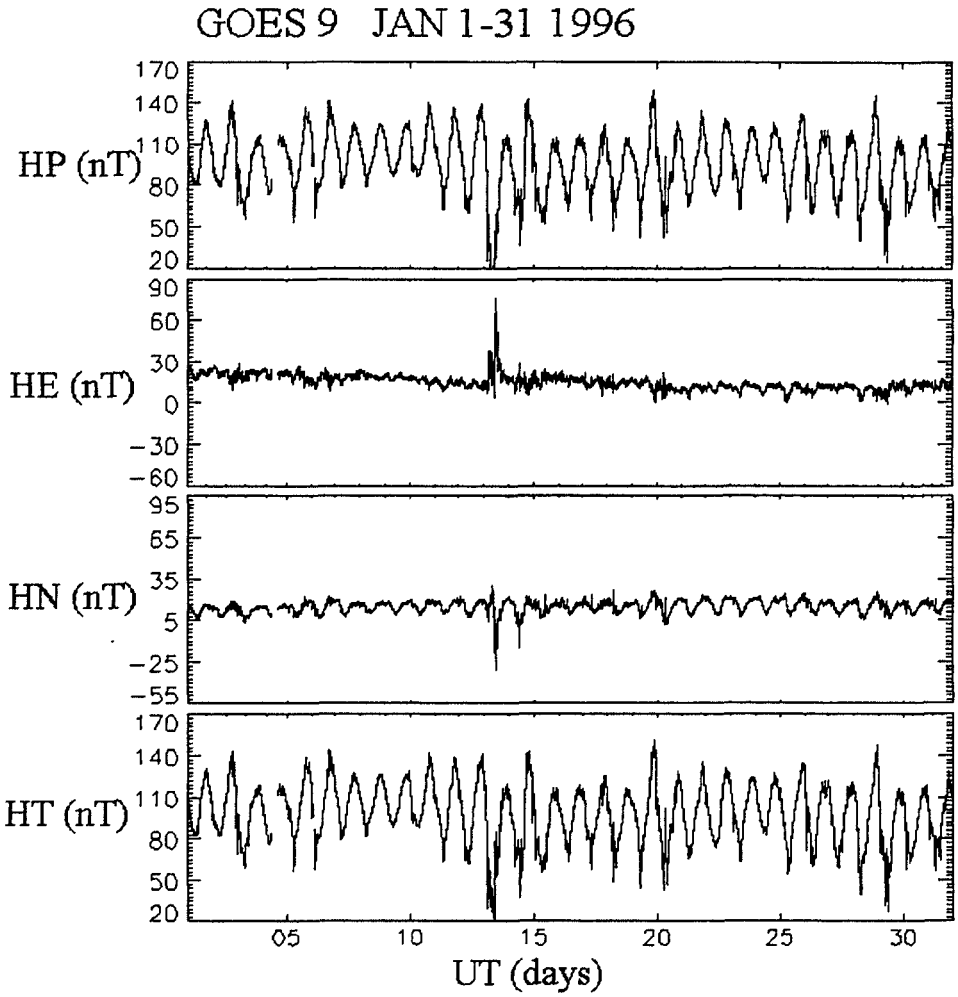

Figure 2: GOES 9 magnetic field data for January 1996.

cause a "hashy" appearance in the display around local midnight; good examples of this are seen on Jan 13, 14, and 15 and again around January 29. The geomagnetic activity index, Kp, indicates that these were the most disturbed days of January 1996.

Just as the Hp component at local noon can be useful for determining how compressed the magnetic field is on the dayside, the Hp component near local midnight can be used to indicate how stretched the field is on the nightside. The more stretched the field the weaker the Hp component near midnight, and as can be seen in the top panel of Figure 2, this component can vary substantially from day to day. Magnetic field stretching in the magnetotail is the result of a complex process that begins with the transfer of energy from the solar wind to the magnetosphere (where energy is stored in the form of increased magnetic flux in the tail lobes of the magnetosphere) enhancing the cross-tail current sheet and causing field-line stretching near geosynchronous orbit. Eventually this energy is released in the substorm process, causing the sudden relaxation, or dipolarization, of the stretched field. The sudden relaxation can be observed as an abrupt increase of the Hp component of the field, as seen on January 20 in Figure 2.

Substorm activity and other processes related to energy coupling between the solar wind and the magnetosphere often result in increased field-aligned currents. These currents can cause variations in the east-west (Hn) component of the magnetic field at

geosynchronous altitude. A major increase in these currents is seen on January 13 in association with tail stretching and substorm activity. Although these dynamic phenomena have been studied for many years and are among the most fundamental processes in space plasma physics, they are far from understood. They are known, however, to be related to the space weather effects such as spacecraft charging that can affect satellite operations, and ionospheric currents and heating that can effect communication systems that depend on ionospheric properties. In the future, the GOES magnetometer data could be used to develop new substorm indices based on magnetic field stretching, dipolarizations, and the disturbances described above.

4.1.3.1 Magnetic field observations and auroral substorm images

The magnetic field variations observed by GOES magnetometer during substorm expansion onsets, such as tail stretching and dipolarization, are related to a variety of global scale magnetospheric features. Observations from the recently launched NASA Polar satellite provide a new opportunity to explore further the relationship between GOES substorm observations and simultaneous auroral features monitored by imaging the Earth's polar regions in the visible, ultraviolet, and x-ray wavelengths. These comparisons may lead to a better understanding of substorms and to improvements in forecasting and monitoring their effects on ground and space-based systems.

The top portion of Figure 3 shows a gray scale version of an image made by the Polar satellite on May 15, 1996[5]. The entire auroral oval can be seen in this picture, along with a brightening of the aurora on the nightside. This figure, along with many others, are available at the World Wide Web (WWW) site http://www-pi.physics.uiowa.edu/www/vis/. The top portion of Figure 3 is described at this site as, "A sudden, intense bulge in the auroral oval signals the start of an auroral substorm over North America. The bulge can be seen easily over northern United States and southern Canada. A map of the coastal outlines has been superposed on the image. This image has been acquired by the Earth Camera that is one of the three cameras in the Visible Imaging System (VIS) on board the Polar spacecraft. In this mode, an image of Earth can be acquired every 53 seconds with the VIS Earth Camera. This image was taken at 07:13 UT on May 15, 1996. At the time of this image, the Polar spacecraft is located at 82.1° latitude, 74.2° longitude, and is at an altitude of 41,900 km as it approaches apogee. The filter for this image passes ultraviolet emissions that are not directly visible to the human eye. The intensities of this light from atomic oxygen in Earth's atmosphere at altitudes in the range of about 100 to 500 km are color-coded in the image with dark red as lowest intensities and whitish yellow as the brightest intensities."

The bottom portion of Figure 3 shows one-minute averages of the GOES-8 and GOES-9 magnetometer Hp component from 0600 to 0800 UT. While GOES-8 shows little activity, there are two dipolarizations at GOES-9, and the larger second dipolarization at about 0713 UT coincides with the auroral brightening in the Polar image data. On May 15, 1996 GOES-8 was located at 75 degrees west geographic longitude, and GOES-9 was located at 135 degrees west geographic longitude. The foot of the magnetic field line through GOES-9 intercepts the Earth approximately in western Canada just north of the bright aurora, while the GOES-8 field line intercepts the Earth in eastern Canada, far to the east of the bright aurora. These results illustrate how the GOES satellites can be used as a diagnostic of magnetospheric substorms — the two satellites provide information about the substorm expansion onset time and on the strength and spatial extent of the current systems. The high time and spatial resolution Polar images will provide a new opportunity to examine this relationship between the geosynchronous and ionospheric manifestations of the substorm processes.

4.1.4 Magnetopause crossings and shocks

An important operational use of the GOES magnetometer data is related to the need to monitor magnetopause crossings and interplanetary shocks. As described earlier, magnetopause crossings at geosynchronous orbit are caused by increases in solar wind dynamic pressure. The largest increases are often, but not always, associated with shocks in the interplanetary medium and geomagnetic storms. Magnetopause crossings at geosynchronous orbit can have serious effects on those satellites that depend on magnetic torquer coils to adjust for satellite momentum changes caused by solar radiation pressure. Some satellite operators have indicated that they would turn off torquers during these intervals rather than torque against a magnetic field that differs substantially from what is expected[6]. The largest geomagnetic storms often begin with the arrival of a shock in the solar wind[7] and these shocks can cause transient geomagnetic disturbances that affect ground-based electric power systems. In addition, large shocks, such as one on March 24, 1991, can produce new radiation belts of MeV electrons and protons in a matter of seconds[8]. These radiation belts can be long lasting and can damage, destroy, or limit the lifetime of satellite electronics.

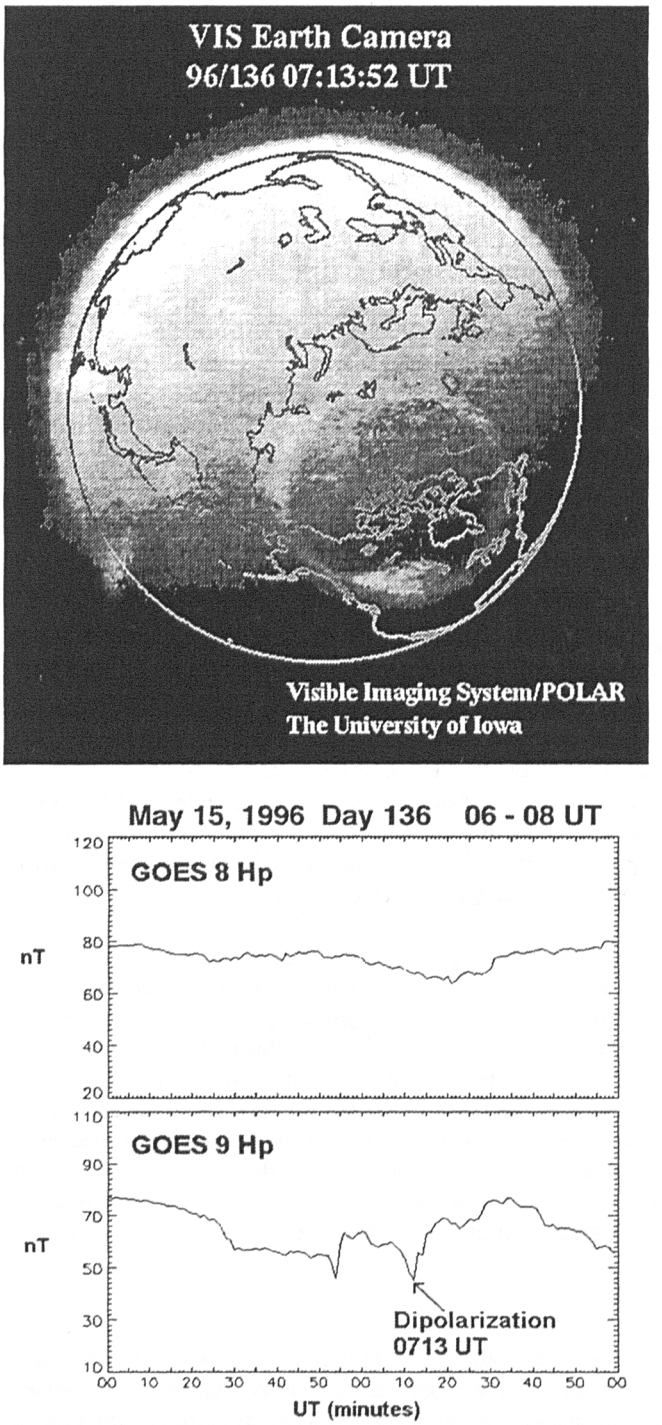

Figure 3: (Top) This image was acquired with the Earth Camera that is one of three cameras in the Visible Imaging System (VIS) which was designed and constructed at The University of Iowa. The VIS is one of twelve instruments on the Polar satellite of the NASA Goddard Space Flight Center. The Principal Investigator is Dr. L. A. Frank and the Instrument Scientist and Manager is Dr. John. B. Sigwarth. (Courtesy L. Frank) (Bottom) GOES-8 and GOES-9 magnetometer Hp component from 6-8 UT on May 15, 1996.

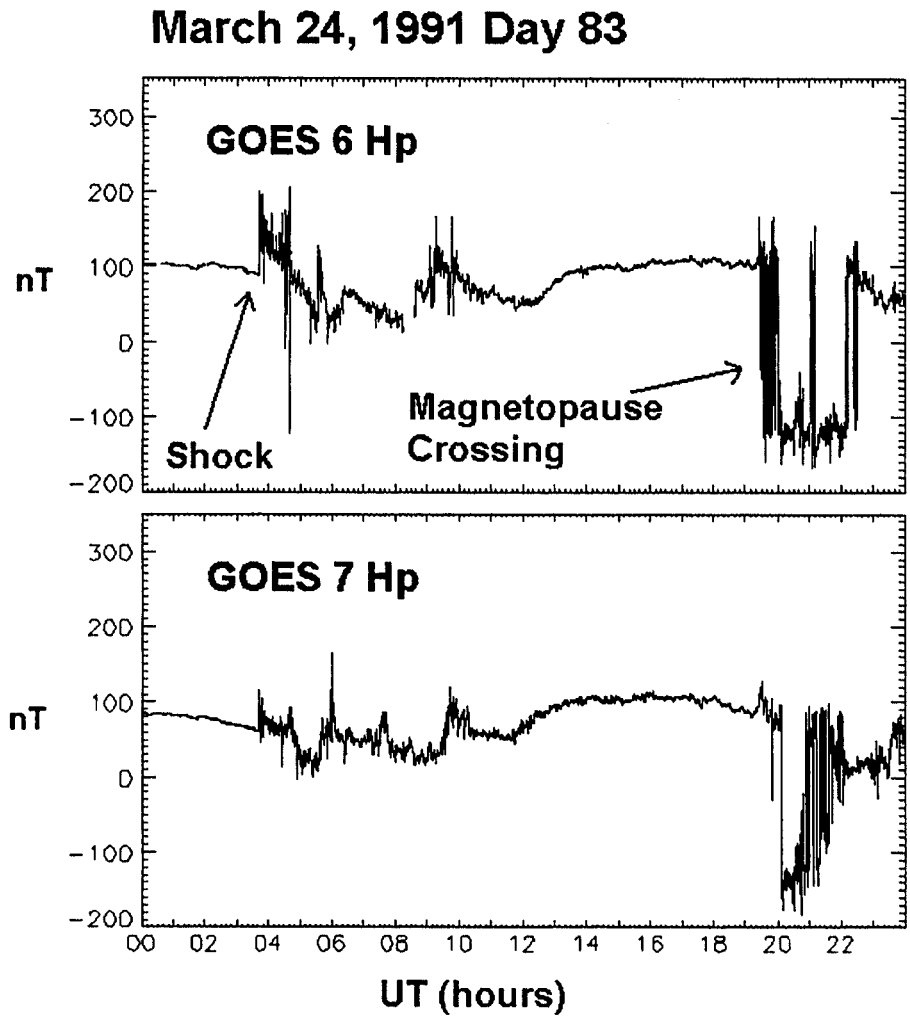

Figure 4: GOES 6 and 7 magnetic field Hp component at the onset of the March 24, 1991 magnetic storm.

The March 24, 1991 geomagnetic storm is one example in the GOES data base that illustrates magnetic field effects during a large storm. These data, from GOES-5 and GOES-6, are shown in Figure 4 as 3.06 second data from the parallel (Hp) component for the entire day. At 3:41 UT a shock in the solar wind encountered the Earth's magnetosphere, compressing the magnetic field to nearly twice its normal value at GOES-6 and slightly less at GOES-7. Later in the day, as indicated in Figure 4, the field normally positive and on the order of 100 nT, reversed sign to a large negative value, indicating a magnetopause crossing. An accurate magnetopause model and solar wind measurements from an upstream monitor, such as the currently operating NASA WIND spacecraft or the future NASA ACE spacecraft, could provide a 30-60 minute forecast of these conditions; current model results, however, are least valid during extreme solar wind conditions, when they are most needed. Therefore, there is a need for improved magnetopause models, the testing of these models under extreme conditions, and monitoring what actually occurs at the geosynchronous location at GOES.

In the Space Weather Operations office at NOAA SEC, an automated computer procedure monitors the GOES spacecraft and the Boulder ground magnetometer for rapid changes in the geomagnetic field. When two out of three of the sensors indicate a rapid change, an alarm is sounded to alert forecasters to a possible sudden impulse or shock, and they can give increased attention to the data, and if necessary, send out an alert to customers.

5. SUMMARY

The GOES magnetometer measurements provide crucial information about the geospace environment that is used to protect military and civilian ground and space-based assets that are vulnerable to space weather effects. In this paper we have briefly described the magnetometer instrument, the environment the instruments monitor, how to interpret the data, and how the data are used to support real-time operations at the NOAA Space Weather Operations and the US Air Force 50th Weather Squadron. The data are archived at the NOAA National Geophysical Data Center. The data are also made available to real-time users through a variety of delivery systems, including the World Wide Web (http://www.sec.noaa.gov), and are archived and used at SEC for anomaly assessments, developing new techniques for operational applications, and for conducting research to better understand the space environment.

6. ACKNOWLEDGMENTS

The authors thank a large number of NOAA, NASA/Goddard Space Flight Center, and Space Systems Loral personnel who have contributed to the success of the GOES magnetometer measurements. In particular, we are grateful to Ed Bielecki, Sandra Cauffman, Eric Chipman, Warren Dunham, Harry Farthing, Ron Hooker, Herb Sauer, Charlie Upton, and Frank Zimmermann. We also appreciate the NOAA SEC operations personnel who utilize these data and contribute to real-time data display and distribution. Thanks to Chris Balch, Tad Sargent, and Dave Speich who provided helpful information about GOES operational use and to Terrance Onsager and Larry Puga for providing helpful criticism of this manuscript. Special thanks to Dr. Louis A. Frank, The University of Iowa, and NASA for generously contributing the Polar spacecraft VIS data. Finally, H.J.S. thanks all my predecessors who have made the GOES magnetometer data set a long-term and valuable resource.

7. REFERENCES

1. Clarke, A. C., *Profiles of the Future*, Bantam Books, Inc., New York, pp. 186-196, 1972.
2. McPherron, R.L., "The synchronous orbit magnetic field data set," *Quantitative Modeling of Magnetospheric Processes*, ed. by W. P. Olson, American Geophysical Union, Washington, D.C., pp. 35-47, 1979.
3. P.K. Rao, S.J. Holmes, R.K. Anderson, J.S. Winston, and P. E. Lehr, editors, *Weather Satellites: Systems, Data, and Environmental Applications*, American Meteorological Society, Boston, pp. 14-16, 1990.
4. Parks, G.K., *Physics of Space Plasmas An Introduction*, Chapter 7, Addison-Wesley Publishing Company, Redwood, City, CA, 1991.
5. Frank, L.A., J.B. Sigwarth, J.D. Craven, J.P. Cravens, J.S. Dolan, M.R. Dvorsky, P.K. Hardebeck, J.D. Harvey, and D.W. Muller, "The visible imaging system (VIS) for the Polar spacecraft," *Space Science Reviews*, vol 71, pp. 297-328, 1995.
6. Singer, H.J., T.R. Detman, G. Burkhart, H. Sauer, and D. Sibeck, "Magnetopause location and geosynchronous spacecraft operations," *EOS (Trans. Am. Geophys U.)*, vol 75, No. 16, p. 318, 1994.
7. Gonzalez, W.D., J.A. Joselyn, Y. Kamide, H.W. Kroehl, G. Rostoker, B.T. Tsurutani, and V.M. Vasyliunas, "What is a geomagnetic storm," *J. Geophys. Res.*, vol. 99, pp. 5771-5792, 1994.
8. Li, X., I. Roth, M. Temerin, J.R. Wygant, M.K..Hudson, and J.B. Blake, "Simulation of the prompt energization and transport of radiation belt particles during the March 24, 1991 SSC," *J. Geophys. Res.*, vol. 20, pp. 2423-2426, 1993.

The GOES Solar X-ray Imager: Overview and Operational Goals

P. L. Bornmann, D. Speich, J. Hirman,
V. Pizzo, R. N. Grubb, C. Balch, and G. Heckman,
NOAA/Space Environment Center
325 Broadway, Boulder, CO 80303

ABSTRACT

The first Solar X-ray Imager (SXI) will provide a major advance in real-time, continuous monitoring of solar-terrestrial conditions. This instrument, which will fly on a Geostationary Operational Environmental Satellite (GOES), will provide full-disk images of the Sun once a minute in the 0.6-6 nm range with 5 arcsec pixels. SXI's images will complement x-ray fluxes from the disk-integrating GOES X-Ray Sensor (XRS) and optical images from ground-based observatories. The automated sequence of SXI images will make it easy for forecasters, researchers, and image processing algorithms to interpret the images.

SXI is being built to meet five operational goals for real-time prediction of solar-terrestrial disturbances: (1) SXI will provide clear evidence of x-ray coronal holes that are associated with recurrent geomagnetic storms. (2) SXI will provide flare locations that are used to estimate the magnitude and timing of energetic particle events, including flares from regions behind the solar limb that are not visible at other wavelengths. (3) SXI could provide a significant improvement in forecasting geomagnetic disturbances if CME-associated brightenings can be readily observed. (4) SXI will provide advance warning of solar active regions that will be rotating onto the solar disk. (5) SXI images will show the complexity of the active regions, which will be used to estimate each region's flare potential.

Keywords: GOES, x-rays, solar physics, instruments, space weather, solar-terrestrial disturbances, flares, coronal holes, active regions

1. INTRODUCTION

The Solar X-ray Imager (SXI) will provide full-disk x-ray images of the Sun in several wavelength bands from 0.6 to 6 nm. The 42 arcmin field of view will extend beyond the solar limb to observe features rotating onto and off the 32-arcmin diameter solar disk. A regular sequence of exposures at one-minute intervals will be used to cover the full dynamic range required to monitor solar activity.

SXI is a cooperative effort among the National Oceanic and Atmospheric Administration (NOAA), the National Aeronautics and Space Administration (NASA), and the United States Air Force (USAF). Initial funding was provided by the USAF, and the instrument is being built by NASA's Marshall Space Flight Center (MSFC) through a contract with the NASA Goddard Space Flight Center (GSFC). The instrument will be operated after launch from NOAA's Spacecraft Operations Control Center (SOCC), and the data will be analyzed at NOAA's Space Environment Center (SEC) and shared with the USAF's 50th Weather Squadron (formerly the Space Forecasting Center).

The first SXI will fly on GOES-M as part of the spacecraft's Space Environment Monitor (SEM). GOES-M is currently scheduled to launch in December 1999, prior to the launch of GOES-L in December of 2003. Subsequent SXIs will be included on future GOES spacecraft to provide the continuous series of SXI's required for real-time forecasting and monitoring of solar-terrestrial disturbances.

In rough order of importance, the following operational goals for SXI are summarized here:

(1) SXI will provide clear images of coronal hole boundaries, which appear in x-rays as regions of low emission and are sources of high-speed solar wind streams associated with recurrent geomagnetic disturbances.

(2) SXI will continuously monitor the Sun to determine flare locations, including flares from regions beyond the east and west limb; flare locations are used to predict the magnitude, arrival time, and spectrum of energetic particle events.

(3) SXI may improve the forecasting of geomagnetic disturbances if the post-ejection signatures of Earthward directed Coronal Mass Ejections (CMEs) are observable as bright arcades of x-ray loops or transient darkenings.

(4) SXI will be used to observe emission from active regions rotating over the east limb onto the visible solar disk, providing advance notification of the appearance of flare-producing region.

(5) SXI will observe the intensity and morphology of coronal magnetic structures above solar active regions, which are used qualitatively to estimate each region's flare potential.

2. SXI'S HERITAGE

SXI builds on a long heritage of solar x-ray instruments that were first developed for research. The first solar x-ray instruments had limited spatial resolution and integrated the solar flux over large fields of view. These instruments matured and NOAA has been including one in the GOES SEM package for many years as the GOES X-Ray Sensor (XRS). The XRS has been the backbone of solar-terrestrial observations for many years[1] and will continue to provide a very unique and useful data set for characterizing the magnitude and temporal evolution of solar flares.

The second generation of solar x-ray instruments used grazing-incidence mirrors to image the Sun. The first long-term series of images from these instruments was made by American Science and Engineering's (AS&E) x-ray telescope S-054 on Skylab launched in 1974[2,3]. These Skylab images clearly showed the utility of full-disk solar images for studies of coronal holes and solar flares. Further research instruments continued with the raster-scanning X-Ray Polychromator[4] on the Solar Maximum Mission (SMM) in the 1980's and the images from the Solar X-ray Telescope[5] (SXT) on Yohkoh in operation since 1991.

SXI is based on technology developed for the Skylab and Yohkoh instruments. For example, SXI improves upon the film detection of Skylab by using digital detection. SXI's mirror uses the same technology used by SXT to create a dual-surface, single-unit mirror, which simplifies alignment and reduces weight. And ground analysis of SXI images will likely use software developed for SMM and extended for SXT.

Research and instrumentation continue to advance, with the third generation of EUV instruments having normal-incidence mirrors with multi-layer coatings to give narrow EUV bandpasses. This work started with rocket observations made by several groups[6,7,8] and continues with satelliate observations. The Observatory (SOHO)[9] launched in December of 1995, uses this technology for its Extreme-ultraviolet Imaging Telescope (EIT)[10]. Images from EIT clearly show coronal holes at a time in the solar cycle when active-region emission is weak and coronal holes are near the sensitivity limit of the Yohkoh/SXT. The wavelength range of SXI is between that of SXT and EIT, leading us to believe that SXI's response to coronal holes will be better that SXT's.

3. SPACECRAFT CONSIDERATIONS

The geosynchronous orbit of the GOES spacecraft provides nearly continuous viewing of the Sun, and two SXI in operation would give complete solar coverage. SXI observations will be interrupted for less than 10 minutes each week for calibration. Additional interruptions of usually 2-4 hours occur roughly every 45 days for station-keeping maneuvers when SXI and the XRS are stowed to protect them from thruster gases. Regular outages will also occur during the fall and summer

Table 1. Comparison of Solar X-ray Instruments

	Skylab AS&E	SMM/FCS	Yohkoh/SXT	SOHO/EIT	GOES/SXI
Launch Date	1973 May 14	1980 Feb 14	1991 Aug 30	1995 Dec 2	1999 Dec 15 scheduled
End of Operation	1974 Feb 8	1989 November	still operating July 1996	still operating July 1996	3 yr mission life
Orbit	LEO	LEO	LEO	L_1	Geosynch.
Power			7-12 W + heaters		57 W
Mass		~ 115 kg	14.7 kg telescope + 9.0 kg electronics		14.76 kg telescope + 7.9 kg electronics
Length		1.5 m	1.7 m		0.76m
Width	0.23 m (mirror)	0.65 m	0.30 m		~ 0.20 m (0.16 m mirror)
Optics	nested pair of Wolter I paraboloid hyperboloids	Collimator	Nariai double hyperboloid	Normal incidence, Multilayer, Ritchey-Cretien	Wolter I paraboloid hyperbaloid
Focal Length	2.13 m	1 m collimator	1.54 m	1.65 m	0.657 m
Peak Effective Area			78 mm^2		~50 mm^2
Detector	film	gas proportional counter	X-ray CCD	back-illuminated CCD	MCP, phosphor, and optical CCD
Wavelength Coverage	0.2-6.0 nm	x-ray lines from 0.18 - 2.0 nm	0.6-1.2 nm	EUV Lines	0.6-6.0 nm
Wavelength Choices	6 filters	7 x-ray lines	5 filters	17.1, 19.5, 28.4, and 30.4 nm	6 filters
FOV	48 arcmin	7 x 7 arcmin	42 x 42 arcmin	45 x 45 arcmin	42 x 42 arcmin
Pixel Size	1 arcsec grains	14x14 arcsec	2.5 arcsec (5 arcsec for most full disk images)	2.6 arcsec	5 arcsec
Exposure Times	1/64 to 265 s		0.077 ms to 242 s		1 ms to 3 s (6 s occasionally)
Temporal Resolution	greater than 2.5 s	4.5 min for 7 x 7 arcmin raster		greater than 2 min	1 minute (35 s max)
Full-Disk Image Cadence	30-300 images per day	not done	about 5 per day	3 per day at each wavelength (up to 1 image per 24 min)	1 per minute (up to 1 image per 35 s)
Duty Cycle	~ 22% ??	~65%	~67%		~98%
Data Delay	months	hours	hours		minute

eclipse seasons when the Earth blocks the spacecraft's view of the Sun and therefore limits the power generated by the solar arrays.

GOES eclipses occur daily during each 45-day eclipse season, with each eclipse growing progressively longer and then shorter with a maximum duration of about 72 minutes. The SXI will be placed in its survival mode during these eclipses, and routine image patrol will not restart until SXI has returned to operating temperatures and the detector voltages have been brought back to operating values, which can take up to 45 minutes after power is returned to the SXI. Another eclipse complication is insufficient power to maintain the optimized observing tables stored in the random access memory (RAM). After eclipses SXI will operate from tables that were loaded into the read-only memory (ROM) during instrument assembly. SOCC should be able to upload enough commands within a few hours after each eclipse to return the SXI to its optimized observing sequences that may differ from the ROM tables.

Because the first SXI was funded well into this block of spacecraft, the solar pointing capabilities were based on the less stringent requirements for the XRS. The north/south pointing is maintained by the X-Ray Positioner (XRP) to which both the XRS and SXI are mounted. The XRP's closed-loop control maintains the north/south pointing within 0.005° (18 arcsec) of Sun center. A bias current has been added to the XRP on GOES-M to allow the solar image to drift through the allowable range, rather than keeping it at the limit of acceptable pointing.

The east/west pointing is determined by the solar array yoke. The actual pointing is a function of the spacecraft orbit and the stepping of the Solar Array Drive Assembly (SADA). The spacecraft is being modified to accept discrete SADA-step commands, and SOCC has agreed to command the spacecraft to add or delete SADA steps at least four times per day to maintain east/west pointing to within the desired ±0.005° east/west pointing accuracy.

Each step of the SADA introduces oscillations (sometimes called jitter) into the solar array[11,12,13], which affect the pointing stability of the XRP. For GOES-M the SADA will be operated in the double-step mode. This increases the time between steps, thereby allowing longer SXI exposure times of up to 3.36 s. It also improves the pointing stability because the second step is timed to minimize oscillations at the natural frequency of the solar array. Because the optimum delay time between double steps cannot be adequately determined prior to launch, it will be adjusted during post-launch testing to minimize the spacecraft-induced smear. Models of the spacecraft oscillations indicate that after optimization 80% of the energy of a point source should fall within a single 5-arcsec SXI pixel and 98% should fall within two pixels. In addition, SXI can time each image to finish just before each SADA double step so that exposures are taken when the oscillation amplitudes have had time to damp down.

4. TELESCOPE HIGHLIGHTS

SXI's design incorporates requirements for operational solar monitoring from the three-axis spin-stabilized GOES spacecraft. Design considerations include limited exposure times caused by the repointing rate of the solar array and limited space on the spacecraft's solar array yoke. SXI consists of an x-ray telescope, a high accuracy Sun sensor (HASS), and three electronics boxes. These components were required to fit within the limited space between the structural elements of the yoke. In addition, SXI must fit within a cutout in the spacecraft body during launch when the solar array is folded against the body of the spacecraft.

SXI's capabilities differ somewhat from that of its predecessors, as summarized in Table 1. SXI was designed to observe the development of solar activity and therefore was designed to maintain a continuous cadence of full-disk images, rather than focus on small, flaring regions. SXI was also designed to maximize the wavelength response at the longer wavelengths where cool coronal features, such as coronal holes, are most prominent.

SXI focuses solar x-rays with a Wolter Type 1, grazing-incidence mirror. Both the parabolic and hyperbolic surfaces were ground from a single piece of Zerodur glass. The mirror's nickel coating was chosen to maximize the response to long wavelength photons, particularly in the 2-6 nm range.

The focused x-rays are detected by an intensified CCD detector stack consisting of a microchannel plate (MCP), a phosphor-coated fiber optic taper (FOT), and an optical charge coupled device (CCD). The MCP converts the x-rays into a cascade of electrons, which cause the phosphor to emit optical photons. These optical photons travel through the FOT and are recorded at the CCD. A 1:1.2 taper was chosen to match the 19 micron CCD pixel size with the desired 5 arcsec field of view for each pixel. The photon-counting ability of this detector (as opposed to energy-detecting sensors) further improves the instrument response at the longer wavelengths.

Images will be taken using polyimide and Beryllium filters to adjust the wavelength response within the system's 0.6-6 nm (0.2-2 keV) passband, as shown in Figure 1. (For comparison, the wavelength response of the Yohkoh/SXT is shown in Figure 2). The 12-position filter wheel includes redundant x-ray filters, a solid radiation shield, and a UV disperser to be used with the internal UV lamp for aliveness testing and limited in-flight calibration. The full wavelength response will be comparable to Skylab's, and SXI's narrower bandpasses will be comparable to SXT's widest bandpasses.

The Sun will drift in front of the SXI between SADA steps at the rate of 15 arcsec per second. This image drift will be removed by stepping the charges within the CCD at the same rate. Pointing knowledge will be available from two sensors: the SXI's High Accuracy Sun Sensor (HASS) will provide pointing knowledge to 5 arcsec, and the spacecraft's Sun Analog Sensor (SAS) on the XRP will provide coarser pointing knowledge to at least ±1 arcmin. If the solar pointing is adjusted during an exposure by either the SADA or the XRP, SXI can be set to automatically retake the image. If pointing is affected by other sources, such as other equipment on the spacecraft[14] SXI images may be affected.

The resolution of the images will be somewhat less than the 5 arcsec pixels, due to limitations of the mirror, the detector stack, and the spacecraft stability. Estimates from early mirror metrology suggest that the mirror resolution will be about 4.4 arcsec, and resolution tests have given detector resolutions of 7.5 arcsec. The oscillations from the spacecraft are expected to contribute 2.0 arcsec to the reduced system resolution. Taken together, these three sources indicate that the resolution of the SXI images will be between 9 arcsec and 14 arcsec, depending on whether these effects add in quadrature or linearly.

Exposure times can be chosen in 1 ms increments from 1 ms to 65 s, although the actual exposure time will be slightly longer because the circuitry adds 0.5 ms to each exposure. In practice the longest exposures will be much shorter than what is allowable by the software. SADA double steps occur every 3.36 s, which places a practical limit on the exposure times during routine operations. We will, however, acquire longer exposures at least four times per day when SOCC commands the spacecraft to drop a SADA double step and take a longer exposure.

5. SOLAR FEATURES

There are four basic features that SXI was designed to observe: coronal holes, solar active regions, flare locations, and signatures of coronal mass ejections. Each of these solar features is used for monitoring and forecasting solar-terrestrial disturbances.

5.1. Coronal Holes

X-ray images from Skylab showed clear evidence of x-ray coronal holes. These regions of extremely low x-ray emission can persist for months, appearing for approximately two weeks during each solar rotation. Coronal holes, particularly during solar activity minimum, are associated with high-speed solar wind streams and recurring geomagnetic disturbances, making them extremely useful for predicting recurrent geomagnetic disturbances.

For many years, solar forecasters have relied on images taken in the infrared He 1083 nm line observed at the National Solar Observatory's Kitt Peak Observatory. Coronal holes are not as striking in these images, and a coronal hole expert determines the location of the holes and sends this information to forecasters in Boulder. Since 1991, NOAA/SEC has been using x-ray images from the Yohkoh/SXT to locate x-ray coronal holes. These images have provided very clear indications of coronal hole locations for much of the solar cycle, but are a bit difficult to use during the current solar minimum when overall solar fluxes are low.

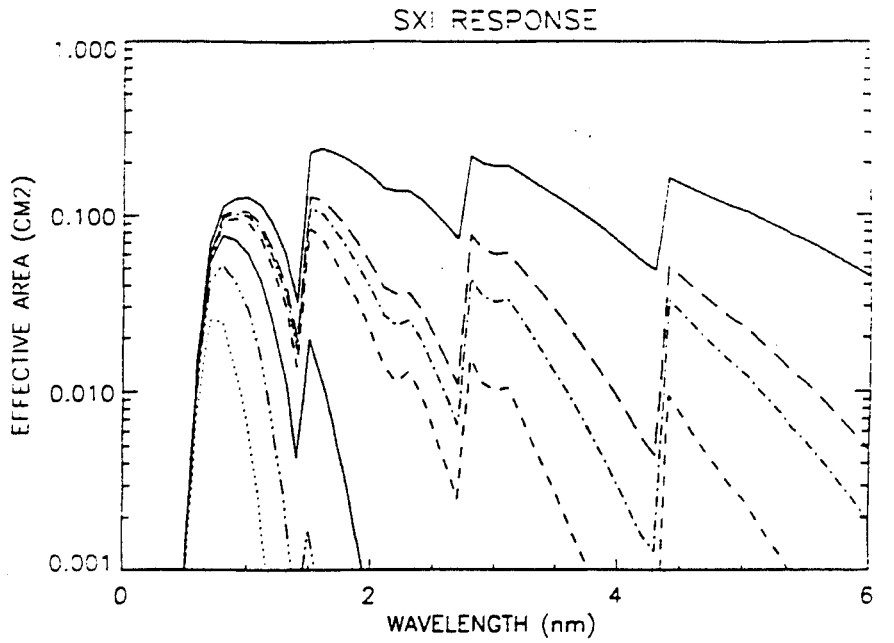

Figure 1. Wavelength dependence of entire SXI system (prefilter, mirror, filter, and detector). From top to bottom curves represent different filters: solid line is no filter, longdashed is thin polyimide, dash-dot is medium polyimide, short-dashed is thick polyimide, solid dashed is thin beryllium, dash-triple-dot is medium beryllium, and dotted is thick beryllium.

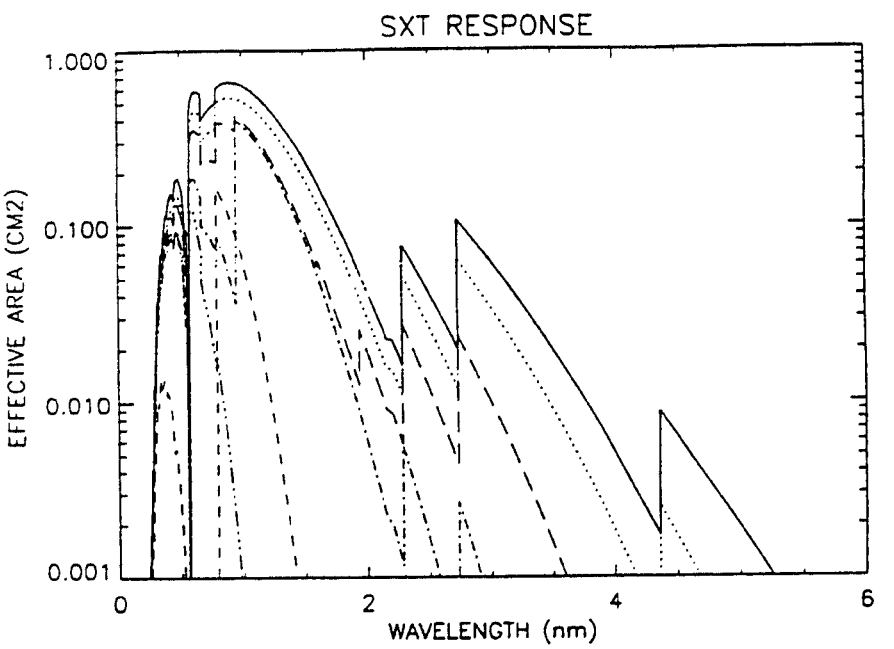

Figure 2. Wavelength dependence of Yohkoh's SXT through the different filters in the entire sytem. Solid is with no filter, dotted 1265 Å Al, long-dashed is Al/Mg/Mn/C filter combination, dash-dot is 2.52 μm Mg, short dashed is 11.7 μm Al, dash-triple-dot is 119 μm Be.

Since early 1996, SEC has also been using coronal hole locations observed in EUV images from SOHO's EIT. These images clearly show coronal holes during the current solar minimum, as did Skylab. SXI's wavelength response falls between that of SXT and EIT. The SXI's wavelength range extends to longer wavelength ranges than SXT and is comparable to Skylab's. Therefore we expect SXI's images to do well in detecting coronal holes, although SXI's exposure times will be limited. To counteract this, images will be added during ground processing to increase the signal to noise of these faint features. In addition, SXI's point response will be better than Skylab's, although not quite as good as SXT's. Thus the apparent haze in Skylab images caused by scattered light should not be an issue for SXI.

5.2. Active Regions

Optical emission from active regions originates close to the surface of the solar disk, while the x-ray emission extends into the corona above the solar disk. As a result, x-ray emission provides an indication of active regions that will be rotating onto the solar disk in the next day or two. This gives forecasters advance warning that a new or returning active region will be rotating into a position to affect the 10.7 cm radio flux and cause solar-terrestrial disturbances.

The complexity of active regions is used to estimate the degree of development and rate of growth of solar active regions; these factors are used to predict the region's flare probability. Hα images, which forecasters have relied on for many years, and x-ray images give very different, but complementary views of active regions. The Hα emission comes from the chromosphere close to the solar surface, and active regions are seen as a complex structure of dark fibrils that trace the low-level magnetic field. In the x-rays the active regions appear as loops of material suspended along magnetic field lines extending far above the chromosphere. Theory suggests that the coronal structure will provide information about the magnetic field structure that cannot be determined from Hα images alone. Thus, both types of images will be used to estimate each active region's flare potential.

5.3. Flares

Forecasters use data from the XRS to alert them that a flare has occurred, and they use reports from the USAF's Solar Observing Optical Network (SOON) to provide flare locations. Flare locations are used to adjust the predicted magnitude and temporal evolution of energetic particle events[15,16,17], which depends on whether the flare occurs at a location that is magnetically well connected to the Earth.

On average, the five SOON observatories provide 86% coverage of the Sun, with outages primarily due to terrestrial weather. If the USAF proceeds with plans to consolidate its operations into fewer observatories, this optical coverage is expected to drop to 79%. During times without optical coverage, forecasters will know if a flare has occurred but have no direct information about the flare's location.

SXI will provide nearly continuous coverage for flare locations, as will the Solar Radio Burst Locator (SRBL) currently being tested by the USAF. SRBL monitors the 2-18 GHz microwave emissions from the Sun and uses frequency-agile interferometry to derive the locations of strong radio bursts. (The antenna beam pattern depends on the observing frequency, so flare location can be derived from the amplitude observed at the different frequencies.) SRBL should give flare locations to within 2 arcmin for all bursts greater than 500 sfu. The peak fluxes for solar radios bursts at these frequencies range from 1 to 10^5 sfu, so SRBL should work well for all large flares, but may not have sufficient signal to derive locations for the weaker flares, including the long-duration events.

SXI will provide flare locations to within 10's of arcsec for all flares, without restriction on the flare area or intensity. Observing sequences will provide images every 1-3 minutes that can be used to derive these flare positions. Although SXI will saturate for many of the stronger flares, these images will clearly indicate the location of the flare because non-flaring regions will not be saturated. Moreover, images taken during the rise or decay of the flare should not be saturated, and therefore can easily be used to locate solar flares.

5.4. *Coronal Mass Ejections*

Coronal Mass Ejections (CMEs) are associated with geomagnetic disturbances. CMEs are generally believed to cause these disturbances if they hit the Earth with a magnetic field oriented opposite to that of the Earth's magnetosphere. CMEs are best observed in white light scattered by electrons high in the corona, which can only be observed when the bright solar disk is occulted in a coronagraph. Unfortunately, coronagraph observations rarely observe CMEs that are directed toward Earth.

CMEs have been associated with the disappearance of solar filaments observed in Hα and Long Duration x-ray Events (LDE) observed by XRS. Hα images are used to determine if a filament has disappeared based on visual interpretation of these images. NOAA forecasters suspect that many of these filament disturbances are not reported.

Early observations from Skylab[18] gave intriguing indications that x-ray images provide evidence of solar mass ejections, and recent work with Yohkoh/SXT images[19] show an arcade of bright loops that form along the filament channel near the time of CME onset. The emission from these CME-associated arcades is typically much less than the total emission from all other x-ray sources on the solar disk. As a result, the increase in brightening is often too faint to be recorded by XRS as an LDE. SXI's observing sequences are being designed to observe at cadences that will provide properly exposed images to monitor for these CME indicators. Thus we hope that SXI will provide a useful monitor for CME occurrences.

6. OBSERVING PLANS

SXI is controlled by pre-loaded and editable tables that specify the exposure sequences and observing parameters such as exposure time and MCP voltage. These tables are currently being developed to meet SEC's goals for observing evolving solar features, summarized in Table 2, that are associated with solar-terrestrial disturbances.

Standardized images will be taken at regular intervals so that forecasters can immediately interpret the images and the rate of development of the various solar features. The actual observing sequences cover the full dynamic range of the solar features by taking images with different exposure times. (SXI's detector is digitized to 10 bits *i.e.* 1024 counts, although the true dynamic range is expected to be about 300.) During routine patrol the longest useful exposure time is limited by the SADA stepping, which occurs every 3.36 s. Current plans are to cycle through exposures of 1, 50, and 3000 ms to cover the full dynamic range of the solar features of interest. Longer exposures of 6 s will be taken at least four times per day, when the solar array is halted briefly via ground command from SOCC.

Image sequences are being created that use the filter wheel to varying degrees; sequences that make minimal use of the filter wheel are included as a contingency, in case the filter-wheel motor shows signs of reaching the end of its operational lifetime. Some of these sequences will use a single filter and others will use all filters. In this way, we expect to have an adequate ROM table for all on-orbit conditions. Images taken through different filters will be used to derive temperatures and emission measures of solar features. The different filters will also be used to optimize images for different solar features, with thin filters used to observe weak features and thick filters for bright flares.

7. IMAGE ANALYSIS

The SXI data is transmitted from the spacecraft at 100 Kbps and will be received directly at SEC's GOES Ground Station with 6.2 m dishes installed for this purpose. After ingest of the raw telemetry stream, the various types of packet data will be separated into image files and housekeeping data files. These files will be made available for real-time access by image processing computers and forecaster workstations.

Image processing will be used to enhance SXI images. Images will be deconvolved with the point response function to improve the spatial resolution. Additional image corrections will be made to correct for instrument degradation; a running total of the total charge extracted from the MCP will be kept for each pixel and used to estimate the detector stack's degradation at individual pixels.

Table 2. Desired Cadences to Observe Solar Features

Solar Feature	Property	Required Cadence	Goal
Flares	location	2 min	1 min
"	statistics *	as possible	as possible
Active Regions	images	10 min	10 min
"	statistics *	1 hour	10 min
CMEs	filament arcade images	10 min	5 min
Coronal Holes	images (incl. transient holes)	30 min	10 min
	deep exposures	6 hour	1 hour

* statistics include temperature and emission measure, which require images using different filter combinations

SXI images will be arriving at a higher data rate than any other data source used by the NOAA/SEC. Unlike research instruments where data can be analyzed for many months, operational data must be ready for interpretation within minutes. For this reason SEC has been working on computer-automated feature recognition[20,21,22]. These computer algorithms are currently being developed to recognize solar features such as filaments observed in Hα, sunspots observed in white light, and large-scale magnetic field patterns observed in line-of-sight magnetograms. After the features have been recognized, their properties (e.g. width, length, location, intensity, proper motion, and lifetime) can be calculated and used for further analysis. By the time SXI is operating on-orbit, we should be able to display the outlines and derived properties of these solar features on the SXI images in near real time.

In the near future, feature-recognition algorithms will also be developed to identify x-ray coronal holes and flares observed in Yohkoh/SXT images. After SXI's launch these algorithms will be adjusted to recognize the same features in SXI images. Our goal is to continuously process images in the background, interpret the image, and alert the forecaster whenever a significant change has occurred.

Composite images will be created from images using three or more different exposure durations. These composite images will show the full dynamic range of solar features in a single image and will incorporate multiple long exposures to enhance the signal from faint solar features.

We will also be able to display movie sequences of images, including solar images that have been converted into rectangular latitude-longitude coordinates. These rectangular displays make it easy to study the evolution of solar features because solar rotation has been removed.

8. CONCLUSIONS

Additional information about SXI has been published in two earlier papers[23,24], and in several SXI documents. The instrument operation is described in the Telemetry and Control Document[25], and the predicted performance is described in the Sensitivity document[26] and in the Optical Performance document[27]. Details about the observing plans are being documented in the Concept of Operations and Observing Sequences document[28], and two additional presentations at this conference[29,30] will discuss the SXI instrument.

Data will be made available to forecasters and researchers around the world, and we encourage studies that lead to improvements in predicting and interpreting solar changes that affect the solar-terrestrial environment.

9. ACKNOWLEDGEMENTS

This project would not be possible without the contributions of many individuals. We would like to recognize the contributions of Tom Shaner, Sherry Buschmann, Shawn Wallace, Kevin Russell, John Davis, Deborah Bagdigian, Tim Page (all from NASA/MSFC), Sandra Cauffman (NASA/GSFC), Ron Hooker (NOAA/GSFC), Greg Berthiaume (MIT/LL), Jon Chappell (SAO), and the many other contributors to this instrument who are too numerous to mention but not too numerous to appreciate.

10. REFERENCES

1 P. L. Bornmann, D. Speich, J. Hirman, L. Matheson, R. N. Grubb H. Garcia, and R. Viereck, 'The GOES X-Ray Sensor and its Use in Predicting Solar-Terrestrial Disturbances," in these Proceedings, 1996.

2. R. Tousey, "Apollo Telescope Mount of Skylab: an Overview," *Applied Optics*, **16**, 825-836, 1977.

3. G. S. Vaiana, L. Van Speybroeck, M. V. Zombeck, A. S.Krieger, J. K. Silk, and A. Timothy, "The S-054 X-ray Telescope Experiment on Skylab," *Space Sci. Inst.*, **3**, 19-76, 1977.

4. L. W. Acton, J. L. Culhane, A. H. Gabriel, R. D. Bentley, J. A. Bowles, J. G. Firth, M L. Finch, C. W. Gilbreth, P. Guttridge, R. W. Hayes, E. G. Joki, B. B. Jones, B. H. Kent, J. W. Leibacher, R. A. Nobles, T. J. Patrick, K . J. H. Phillips, C. G. Rapley, P. H. Sheather, J. C. Sherman, J. P. Stark, L. A. Springer, R. F. Turner, and C. J. Wolfson, "The Soft X-ray Polychromator for the Solar Maximum Mission," *Solar Physics*, **65**, 53-71, 1980.

5. S. Tsuneta, L. Acton, M. Bruner, J. Lemen, W. Brown, R. Caravalho, R. Catura, S. Freeland, B. Jurcevich, M, Morrison, Y, Ogawara, T. Hirayama, and J. Owens, "The Soft X-ray Telescope for the Solar-A Mission," *Solar Physics*, **136**, 37-67, 1991.

6. A. B. C. Walker, Jr., T. W. Barbee, Jr., R. B. Hoover, and J. F. Lindblom, "Soft X-ray Images of the Solar Coroina with a Normal-Incidence Cassegrain Multilayer Telescope," *Science*, **241**, 1781-1787, 1988.

7. L. Golub, M. Herant, K. Kalata, I. Lovas, G. Nystrom, F. Pardo, E. Spiller, J. Wilczynsi, "Subarcsecond Observations of the Solar X-ray Corona"

8. J. H. Underwood, M. E. Bruner, B. M. Haisch, W. A. Brown, and L. W. Acton, "X-ray Photographs of a Solar Activbe Region with a Multilayer Telescope at Normal Incidence,", *Sciencd*, **238**, 61-64, 1987.

9. V. Domingo, and A. I. Poland, "SOHO - An Observatory to Study the Solar Interior and the Solar Atmospehre," in *The SOHO Mision - Scientif and Technical Aspects of the Instruments,"* ESA SP-1104, 1989.

10. J. -P. Delaboudiniere, G. E. Artzner, J. Brunaud, A. H. Gabriel, J. F. Hockedez, F. Miller, X. Y. Song, B. Au, K. P. Dere, R. A. Howard, R. Kreplin, D. J. Michels, J. D. Moses, J. M. Defise, C. Jamar, P. Rochus, J. P. Chauvineau, J. P. Marioge, R. C. Catura, J. R. Lemen, L. Shing, R. A. Stern, J. B. Gurman, W. M. Neupert, A. Maucherat, F. Clette, P. Cugnon, and E. L. Van Dessel, "EIT - Extreme-Ultraviolet Imaging Telescope for the SOHO Mission, " *Solar Phys.* **162**, p. 291, 1995

11. S. Tadikonda, "Understanding GOES-8 Dynamics" 1996, paper 2812-64 in these proceedings, 1996.

12. J. Sudey, Jr., W. Dellinger, and M. Hagopian, "On-orbit Jitter Performance of the GOES Spacecraft and Instruments" paper 2812-61 in these proceedings, 1996.

13. J. Knack, and M. Phenneger, "Using the Sun Analog Sensor Data to Investigate Solar Array Yoke Motion on the GOES-8 and -9 spacecraft," paper 1812-69 in these proceedings, 1996.

14. W. C. Bryan, "GOES on-orbit INR system performance," paper 2812-83 in these proceedings, 1996.

15. E. Barouch, M. Gros, P. Masse, "The Solar Longitude Dependence of Proton Event Delay Time," *Solar Phys.*, **19**, 483, 1971.

16. M. A. I. Van Hollebecke, L. S. Ma Sung, E. B. McDonald, "The Variation of Solar Proton Energy Spectra and Size Distribution wiuth Heliolongitude," *Solar Phys.*, **41**, 189, 1975.

17. H. V. Cane, D. V. Reames, an dT. T. von Ronsenvinge, "The Role of Interplanetary Shocks in the Longitude Distribution of Solar Energetic Particles," *J. Geophys. Res.*, **93**, No. A9, 9555-9567, 1988.

18. Rust, D. M. and Hildner, E. H. "Expansion of an X-ray Coronal Arch into the Outer Corona," *Solar Phys.*, **48**, 381-387, 1976.

19. A. H. McAllister, M. Dryer, P. McIntosh, H. Singer, and L. Weiss, "A Large Polar Crown CME and a Severe Geomagnetic Storm: April 14-17, 1994," in *Proc. Thrid SOHO Workshop - Solar Dynamic Penomena and Solar Wind Consequences*, p. 315-318, 1994.

20. P. L. Bornmann, "Automatic Recognition of Solar Features," in *Proc. First SOHO Workshop*, ESA SP-348, 1991.

21. P. L. Bornmann, C. Kohl, T. Kohl, and F. Glazer, "Solar Image Processing and Feature Recognition," in *X-ray Solar Physics from Yohkoh*, Y. Uchida, T. Watanabe, K. Shibata, and H. Hudson (eds.), 329-332, 1995.

22. P. L. Bornmann, J. R. Winkelman, D. Cook, D. Speich, and T. Kohl, "Automated Solar Image Processing for Flare Forecasting," to appear in *Solar Terrestrial Predictions Workshop*, 1996.

23. P. L. Bornmann, R. Grubb, D. Speich, E. Hildner, and V. Pizzo, T. Shaner, S. Buschmann, K. Russell, S. Wallace, J. Davis, S. Cauffman, Hooker, R., "A New Solar Monitor for Solar Forecasters: the GOES Solar X-ray Imager," to appear in the *Solar-Terrestrial Predictions Workshop*, 1996.

24. J. M. Davis, D. Bagdigian, S. Buschmann, K. Russell, and K. Wallace, The Solar X-Ray Imager for the Geostationary Operational Environmental Satellite (GOES), *AIAA Space Programs and Technologies Conference*, 94-4645, 12 pgs., 1994.

25. K. Freestone, and S. Wallace, "Telemetry and Control for the Solar X-ray Imager (SXI)," MSFC Document SXI-013, 1996.

26. J. M. Davis, 1995, MSF Document SXI-029, "Solar X-ray Imager Sensitivity Analysis", 1995.

27. D. E. Zissa, and M. E. Smithers, "Solar X-ray Imager (SXI) Optical System Performacne Analysis," MSFC Document SXI-022, 1994.

28. P. L. Bornmann, D. Speich, V. Pizzo, S. Wallace, J. Davis, K. Russell, J. Hirman, "SXI Concept of Operations and Observing Sequences," SEC document, 1996.

29. K. Russell, E. L. Corder, J. Briscoe, S. Wallace, and J. H. Chappell, "Solar X-ray Imager (SXI) Detector Calibration and Characterization," paper 2812-59 in this proceedings, 1996.

30. M. E. Smithers, and D. E. Zissa, "Solar X-ray Imager (SXI) Optical Performance Analysis," paper 2805-14 in these proceedings, 1996.

The space environment monitoring mission beyond GOES M

R. N. Grubb, P. L. Bornmann, G. Heckman,
T. G. Onsager, H. J. Singer, R.Viereck

NOAA Space Environment Center, R/E/SE, 325 Broadway, Boulder, CO, 80303

ABSTRACT

Conditions in the near-Earth space environment are of ever increasing importance to our human activities on Earth and in space. The provision of the space environment services required in future depends on improving our understanding of solar activity and the coupling of this activity to our local region of space, as well as improving our remote sensing and in-situ monitoring of conditions and events in the solar system. Our present service is largely analogous to the state of terrestrial weather forecasting from a local weather office before the advent of numerical modeling and remote atmospheric sensing technology. Numerical models of the local space environment and of interplanetary space are being developed. However, these models are limited in performance by our understanding of the underlying physical processes, and their practical application is restricted by the paucity of observational data.

Instruments on the Geostationary Orbiting Environmental Satellite (GOES) provide a critical resource to NOAA's space environment services. GOES is our most effective operational platform for real-time remote sensing of the Sun, the near-Earth environment, and processes in interplanetary space. It also makes important in-situ measurements in a critical region of space that is now of huge commercial importance. This paper will discuss the planned and potential extensions of the GOES Space Environment Monitor (SEM) in the overall context of the data required to meet the future needs for space environment services.

Keywords: Future, GOES, space, solar, services

1. BACKGROUND

The importance of understanding and treating "Space Weather" on a par with terrestrial weather is now widely appreciated. Our nation's reliance on technological systems that are sensitive to space weather is increasing at an exponential rate. Under the guidance of the Federal Coordinator for Meteorological Services and Supporting Research, the Committee for Space Environment Forecasting has formulated the National Space Weather Program Strategic Plan, which sets out the needs for improvement and the steps which must be taken over the next ten years to provide the needed timely, accurate and reliable space environment observations, specifications and forecasts[1]. To quote from the introduction to the plan :

" "Space Weather" refers to conditions on the sun and in the solar wind, magnetosphere, ionosphere and thermosphere that can influence the performance and reliability of space-borne and ground-based technological systems and can endanger human life or health. Adverse conditions in the space environment can cause disruption of satellite operations, communications, navigation, and electric power distribution grids, leading to a variety of socioeconomic losses."

Many of the present systems affected by space weather have been discussed in the companion papers. As these systems are further developed and deployed they may become more sensitive to the effects of space weather. For instance, the nations' power grids are becoming more interconnected and less autonomous and therefore more sensitive to induced currents from geomagnetic storms. National strategy now places emphasis on rapid deployment and flexibility in the use of military forces. Reliability of the nations' satellite communications infrastructure becomes critical under this approach, and space weather services are vital to this reliability.

New systems, either under implementation, or active planning, will require more, not less, understanding of the space environment and support from space environment services. Long-term habitation in the International Space Station and the large amount of space-suited construction activity, although shielded by Earth's magnetic field, will require support for planning and conducting operations at the Station to minimize astronaut radiation exposure. New communication services

 0-8194-2200-2/96/$6.00

using constellations of spacecraft in low and medium Earth orbit are planned to use lower UHF and even VHF frequencies which are readily disrupted by ionospheric scintillation during disturbed conditions. More widespread and critical civilian uses of the Global Positioning Satellite navigation system can be similarly disturbed. The planned return of humans to the moon and projected manned missions to Mars can only be conducted responsibly with a thorough understanding of the radiation risks to the astronauts and the systems that will be required to mitigate those risks.

The applications of the data required to provide a full 'Space Weather' service fall into four categories, each of which is used to determine if an event is likely to occur and affect a given system;

a) Monitoring or 'Nowcasting', i.e., measuring the conditions in the space environment at this moment with limited extrapolation, and providing data to system operators that enables them to assess the effect on their system operation.

b) Warnings are issued when conditions indicate that a disturbance may occur, e.g., complex solar active regions are present that are expected to produce a flare.

c) Alerts are issued when a condition has occurred that frequently leads to a disturbance, e.g., a large flare has been observed and therefore a solar proton event is possible.

d) Forecasts provide longer term predictions of conditions based on the currently observed conditions on the Sun and in interplanetary space, e.g. a previously observed coronal hole will rotate into a position likely to result in a geomagnetic disturbance.

In many cases 'modeling' can be used to aid the extrapolation over space or time. Models can fall into two categories or combinations thereof. They can be based on an understanding of the physical processes or on empirical relationships based on historical data. A good example of the newer generation of physically based models is the Magnetospheric Specification and Forecast Model (MSFM)[2] developed at Rice University with USAF support. This model computes the fluxes of energetic charged particles that contribute to spacecraft charging in the inner and middle magnetosphere using magnetic indices and data from interplanetary, geostationary and polar spacecraft.

The current state of the art in providing space weather services is limited by two factors:

a) Inadequate understanding of the physical processes underlying solar activity, the propagation of the resultant disturbances outward into interplanetary space, and their interaction with our local space environment.

b) The difficulty and resulting expense of obtaining the data that would be necessary to provide a high quality reliable service, e.g., observation of the solar hemisphere invisible from Earth and adequate sampling of the conditions in interplanetary space and Earth's magnetosphere.

The situation is similar to the state of terrestrial weather services 50 years ago, particularly by analogy with the limitations of a single 'weather station', i.e., the Earth, at one point in space. The first factor, inadequate physical understanding, is being attacked by the research community, and considerable advances in understanding should result from the current and future scientific spacecraft deployed by the international community, e.g., the Yohkoh, SOHO, WIND, Polar, and ACE missions etc. The second factor, the limitations of present and currently planned data collection systems, will improve as society deploys new systems to provide benefits that can justify the cost of the required new space environment services and data collection systems. Better modeling will in general follow the advance of physical understanding. The development of the present models is being supported actively by the National Science Foundation, NASA and the USAF in part as a component of the National Space Weather Program. Models require evaluation of their practical value to space environment services using operationally available data before they can be adopted.

The U.S. Department of Commerce has had the mission to provide space environment services almost from the very first realization that solar activity could adversely affect radio communication systems critical to national commerce and defense. It was therefore quite natural that, from their inception, the geostationary (GOES) and polar (POES) operational

meteorological satellite systems were put to dual use to monitor the space environment in addition to providing meteorological data. However, the ultimate goal of a fully reliable and comprehensive space weather service will probably require additional spacecraft in other orbits to provide better remote sensing of the Earths' space environment, direct monitoring of conditions in interplanetary space remote from Earth and continuous observation of much more of the sun's surface than is visible from Earth. The remainder of this paper will describe how the GOES SEM is expected to evolve and its place in the total 'space weather' monitoring system that we anticipate will be required to support our expanding technological infrastructure in the 21st century.

2. RESEARCH DIRECTIONS

The NOAA Space Environment Center (SEC) is continually monitoring advances in research and technology that could improve our space environment services. In some cases we have concluded that the research is not ready to justify setting requirements for additional real-time monitoring instruments, as is the case for solar vector magnetographs. This was a research topic that many felt had great promise for improving flare forecasts. At this point, research has not shown that vector magnetograph data will produce a significant improvement in forecasts[3,4]. In other cases, where a research topic looks promising, it is tested in parallel to current operations. For example, NOAA/SEC is currently testing the Sheeley/Wang technique[5] for predicting solar wind speed from solar line-of-sight magnetic field measurements. The current analysis is showing that predictions of geomagnetic activity from this technique are comparable in accuracy to those of human forecasters; this technique will be considered further if it can be fully automated and thereby free the forecasters for their many other responsibilities. Another example of a tested research idea was the use of Interplanetary Scintillation. Two years of data were examined in real time to determine if they could be used to track solar disturbances as they traverse the interplanetary medium and cause scintillation of distant radio sources. In this case the technique looked promising, but data interpretation was too ambiguous from a single observing site to justify adopting this technique for real-time monitoring and forecasting operations[6].

As always, as some techniques are completing their evaluation periods, new advances are becoming available and are ready for implementation. One such advance, discussed in more detail in the next section, is the use of solid state detectors to measure solar EUV fluxes. This new technology much reduces the mass and power required by earlier solar-disk-integrating EUV instruments. Recent results from instruments using this technology in space on the Solar and Heliospheric Observatory (SOHO) look promising, leading us to believe that this could be applied immediately in the next generation of GOES instruments to directly measure the EUV fluxes of interest, rather than relying on 10.7 cm radio fluxes as proxy. If implemented, users of the proxy10.7 cm fluxes would have to transition because their models are based on this proxy and may have built in corrections for cases when the radio fluxes deviate from the EUV fluxes that are causing the changes in Earth's upper atmosphere. But the only way to improve our understanding of these physical processes is to have a large data set that can be used to develop better models and understanding.

Another example of new technology being considered is the normal-incidence EUV imaging telescopes, such as the Extreme-ultraviolet Imaging Telescope (EIT)[7] on SOHO. EIT images have shown clear evidence of coronal holes even when the x-ray images from the Solar X-ray Telescope (SXT) on Yohkoh have had difficulty in times of low solar activity. The wavelength response of the new GOES Solar X-ray Imager (SXI) is between that of EIT and SXT, and therefore, we anticipate that the SXI images will be sufficient to locate the coronal holes, which are the sources of recurrent high-speed solar wind streams and geomagnetic disturbances.

A third example is recent work that indicates an improvement in predicting the occurrence of proton events from the behavior of hard X-ray spectra during solar flares[8]. This new technique requires additional testing before it is ready for real-time operations. Therefore NOAA/SEC is pursuing opportunities to include a Hard X-ray Spectrometer on a research mission.

3. THE FUTURE GOES SEM

The GOES SEM system is critically important to the present space environment services and will play an increasing role in the future for a number of reasons:

a) The simplicity and efficiency of real-time control and data acquisition from a geostationary platform.

b) The position of the geostationary orbit close to the boundary with interplanetary space and open to the measurement of energetic solar particle events.

c) The importance of measurements of the local geostationary orbit environment to the enormous investment in other geostationary spacecraft.

d) The successful adaptation of the GOES three-axis-stabilized spacecraft design to almost continuous solar observation in wavelengths inaccessible to ground-based observatories.

3.1. Solar Observation

The current systems for measuring the total solar X-ray flux with the X-Ray Sensor (XRS) and the new Solar X-ray Imager (SXI) have been described in companion papers. We expect to augment both these types of measurements by extending their wavelength ranges.

3.1.1. Measurement of whole Sun EUV flux

The solar EUV flux is a critically important input to both empirical and physically based models of the density of the neutral and ionized atmosphere. At these wavelengths the radiation is absorbed primarily in Earth's upper atmosphere at altitudes greater than 100 km. Currently, models of Earth's upper atmosphere rely on 10.7 cm solar radio flux as a proxy for EUV radiation. This radio flux is an acceptable proxy for long-term average EUV fluxes over time scales of months and years. But on shorter time scales, on the order of days, the 10.7 cm flux is of less value; the correlation between 10.7 cm radio and EUV fluxes on the time scale of a solar rotation is only 50%[9]. These measurements and models can be used to calculate parameters that affect satellite drag and radio communications. At a recent scientific meeting (CEDAR, Boulder, June 1996) many of the upper atmospheric researchers agreed that uncertainties in the solar EUV flux introduce some of the largest errors into their models.

3.1.1.1. Proposed EUV instrument parameters

Consideration of the EUV solar spectrum, the cost, and the instrument complexity suggest that five spectral channels could provide a vast improvement in our knowledge of the solar EUV flux. The five channels are chosen to be centered at or near the brightest emission features and to cover as much of the solar spectrum as possible. The table below shows the required sensitivity and dynamic range required for the channels based on our present knowledge of the solar flux and spectrum.

Channel	Wavelength range (nm)	Threshold Flux (W/m^2)	Min. Dynamic range
EUV-A	5 - 25	$1x10^{-4}$	10^3
EUV-B	25 - 40	$5x10^{-4}$	10^2
EUV-C	40 - 65	$1x10^{-4}$	10^2
EUV-D	65 - 103	$3x10^{-4}$	10^2
EUV-E	5 - 103	$1x10^{-3}$	10^2

Until recently, an instrument to make these measurements would have been both a major addition to the SEM system in terms of volume and weight, as well as being of highly questionable calibration stability. However, new developments in silicon detectors and transmission grating technology, partially funded by NOAA under an SBIR contract,[10] have made it practical to realize the required measurements with a simple lightweight and stable instrument that could probably include the functions of the present XRS by integrating the two shorter wavelength X-ray channels into the same instrument using the same new technology.

The new silicon diode detectors have 100% quantum efficiency at these wavelengths and are quite stable over time. In fact, these devices are now used as secondary standards by the National Institute of Standards and Technology (NIST). The technology is well established and has been flown on both the space shuttle and on research satellites such as SOHO[11] (now

observing the sun from the L_1 point). The necessary wavelength selectivity can be provided by a combination of thin metallic filters, some of which can be deposited on the surface of the detectors, and the use of transmission gratings. These gratings, constructed by the technology of the integrated circuit industry, consist of parallel wires of only 200 nm or more separation. As no reflection is required to produce the desired diffraction pattern, the gratings are immune to the contamination effects common to conventional ruled gratings used at these wavelengths. Diffraction orders cannot be selectively enhanced by blazing and overlapping orders of diffraction must be carefully considered in design.

A possible design for a slitless spectrometer to provide the desired channels is shown in Figure 1. A combination of filtering alone in the zero order response and filtering plus dispersion by the grating is used to obtain the desired channels. The angles and coatings of each of the detectors are listed, and the drawing shows the relative detector positions. It should be noted that the entire package is only 10 x 12 x 1.5 cm, and there are no moving parts. The plot in Figure 2 shows the grating characteristics for the first, second, and third orders and the sensitivity of the detector and filter combinations. Extensive passive, and perhaps active, radiation screening would be required to reduce contamination of the measurements by charged particles reaching the detectors. Additional detectors to monitor and provide correction for such effects may also be required.

3.1.2. Observing and forecasting solar activity

Just as in terrestrial weather forecasting, advances in the forecasting of solar activity must rest on better quantitative observation and understanding of the physics of what we call solar activity. Sunspot activity has been observed from the ground for centuries, and solar active regions have been observed in more detail using optical narrow-band imaging for more than 60 years. More recently optical techniques have made it possible to measure both the magnetic fields that control active-region structure and the bulk line-of-sight velocities using Doppler shifts. However, the range of temperatures occurring in the solar atmosphere is greater than 1000 to 1, ranging from a few thousand degrees Kelvin at the photosphere to millions of degrees in the solar corona and in the core heated regions of solar flares. Thus the emissions available to observe activity ranges from near IR for the base of the photosphere, through the X-ray spectrum and beyond for flares and the top of the corona. The SXI, imaging with soft X-rays, is primarily designed for two purposes. Firstly to image the corona and the important structure in that region which channels the outflow of the solar wind streams responsible for the recurrent geomagnetic storms at Earth. Secondly to provide a more reliable monitor of flare position than the ground-based observatories, and also a view of the upper structure of active regions well before they rotate onto the optically visible disk.

For the first time, the SOHO EIT instrument is providing us with research quality solar images in the EUV part of the solar spectrum that enable us to observe structure in the important transition region below the corona. In many cases this proves to be an invaluable supplement to the Yohkoh soft X-ray images in understanding the coronal hole structure and the connections to the underlying regions. Future GOES Solar Imagers need to extend their wavelength coverage into the EUV region to exploit this capability.

3.2. In-Situ measurements

3.2.1. Charged particles

The companion papers have described the present GOES measurement of energetic solar particles and the local trapped medium-energy protons and electrons. Historically, the GOES measurements of charged particles were primarily directed at monitoring the radiation hazards to astronauts, and passengers and crew of high flying aircraft. Currently, there are three main areas of the charged particle environment that represent our primary operational concerns. These areas are: (1) the energetic ions (>10 MeV) that contribute to, for example, single event upsets, solar panel degradation, and present a hazard to humans in space; (2) energetic electrons (> 1 MeV) that contribute to deep dielectric charging of electronic components; and (3) medium-energy electrons that are responsible for spacecraft surface charging. As our use of and reliance on space continues to increase, our ability to accurately monitor these important characteristics of the environment becomes increasingly more critical.

Our energetic particle monitoring capabilities need to be enhanced in two areas: (1) the directional coverage and (2) the energy coverage of the measured fluxes. The additional directional resolution is needed for the accurate characterization of the onset time and total fluence of solar proton events. During the early stages of particle events the particle fluxes can be highly anisotropic. On the earlier GOES the spacecraft spin was used to average the particle fluxes within the spin plane, but

this capability has been lost on the new three-axis-stabilized spacecraft. There is now a danger that the early stages of a solar particle event might be underreported by the present sensors if the majority of the flux is outside the detector's field of view. At the energies currently measured by the EPS it is difficult to construct particle sensors with a much larger field of view without degrading the energy resolution. However duplicate sensors, with different look directions can be added to provide greater coverage.

While the current GOES instrumentation is providing measurements of electrons of energies that contribute to deep dielectric charging (>1 MeV), the lower energy portion of the electron spectrum that is responsible for spacecraft surface charging (30 keV-600 keV) is not being measured. This additional portion of the electron distribution could be measured with conventional solid state detectors similar to those used for the higher energies. The enhanced coverage of the particle energy and directional spectra would allow the GOES spacecraft to provide a more comprehensive characterization of the properties of the space environment that are known to have a variety of effects on spacecraft.

3.2.2. Magnetic fields

The ambient magnetic field measurements on GOES will continue to meet the requirements as we currently envisage them. The measurements are important for monitoring magnetopause crossings at geosynchronous orbit and assessing the level of geomagnetic activity as well as a number of uses described in the companion paper. Because of the use of magnetic torquing and the comparatively short sensor boom, the magnetometer sensor and the spacecraft must be treated as a combined system in which the spacecraft must supply information needed to correct the sensor data during ground processing for the offsets introduced by the spacecraft system. Although the present system design is capable of working well, these are quite sensitive measurements. Therefore vigilance will be necessary as the spacecraft design is evolved or new designs are introduced to ensure that the magnetic field measurements are not compromised.

4. THE FUTURE SPACE ENVIRONMENT MONITORING SYSTEM

A future space environment monitoring and forecasting service is expected to include most or all of the following components, depending on the activities requiring the support of space environment services.

1. A continuing ground-based component for radio and optical observation of the Sun and ground-based magnetometer measurements to provide indices of ionospheric and magnetospheric currents.

2. The GOES SEM for energetic solar particle measurement at Earth, measurement of the geostationary orbit environment, and routine whole-sun flux and solar imaging in wavelengths inaccessible to ground-based observation because of atmospheric absorption.

3. The POES polar orbiting SEM to monitor the properties of Earth's polar regions which have direct magnetic field connection to interplanetary space and the auroral regions where substantial energy is deposited into Earth's upper atmosphere from the precipitation of magnetospherically trapped charged particles.

4. A spacecraft orbiting the L_1 Lagrange point between Earth and the Sun to monitor the solar wind and interplanetary magnetic field and provide advance warning of solar wind disturbances in the solar wind traveling towards Earth.

5. Two spacecraft in solar orbit matched to that of Earth so as to provide solar imaging from approximately east and west perpendicular positions to the Sun-Earth line. These will provide the necessary observation of the evolution and activity of solar active regions as they rotate behind the Sun from our normal viewpoint and before they reappear to our view as well as monitoring the activity of regions rotating off the visible disk but still capable of influencing our local space environment through the interplanetary field connections. Suitably spaced observations can also be used to develop 3D views of solar structures that may be invaluable for observing Coronal Mass Ejections (CME) directed at Earth.

6. A spacecraft in eccentric polar orbit equipped to image energy deposition in the upper atmosphere of the Earth using the UV and other radiation produced in the excited regions.

7. In the case of manned missions into interplanetary space, additional interplanetary monitoring spacecraft may be required that are positioned to provide advance warning of solar particle events for the astronauts.

The most vital core components will require dedicated long-term operational systems which are maintained, operated, and replenished as necessary to guarantee the reliability of the service. However some components may be appropriately deployed as necessary to meet specific mission needs, or may be provided as opportunities occur to make use of instruments intended primarily for research that can be arranged to provide operationally useful data. As our knowledge of the space environment and monitoring technology improve, this list of will be modified by adding new components and discarding those made redundant.

4.1. Example applications

Some of the most significant adverse effects on terrestrial systems caused by solar activity are those due to geomagnetic storms. These disturbances in the magnetic field of the Earth cause induced currents in long conductors, particularly those at higher latitudes. In interconnected power grids these currents can cause damage to transformers and affect protective control systems. If a highly reliable warning of a disturbance could be provided to power system operators, even with small lead times, it would be possible to reconfigure networks to reduce the possibility of the network becoming unstable and collapsing. Such a collapse, triggered by a solar disturbance, which happened in the north east US and Canada in 1989, cost power utility companies and consumers billions of dollars in lost revenue and disruption of work. Major geomagnetic disturbances are caused by the arrival at Earth of a shock wave in the solar wind which has the right interplanetary magnetic field configuration to couple effectively to Earth's field. Irrespective of the ability to observe and forecast the origin of the shock at the sun, it is possible to provide reliable warnings of their impending arrival by monitoring the solar wind at a 'weather' station between Earth and the Sun. It is practical to maintain a spacecraft to do this by placing it in orbit around the force balance between the Earth and the Sun at the Lagrange L_1 point about 1.6×10^6 km from Earth. For typical shock speeds this can give 20 minutes to one hour warning of a shock arrival and the information necessary to predict the effects. Data from L_1 have been available in the past from the research spacecraft ISEE 3 and is currently available in real time for a few hours a day from the NASA WIND spacecraft. Data will become available nearly continuously from the NASA ACE spacecraft to be launched in 1997. However, if the benefits are shown to justify the cost, a dedicated operational space environment monitoring spacecraft will be required at L_1, or, if the technology can be developed, at other intermediate distances between Earth and the Sun to provide greater lead time for warnings.

A challenging future task for the Space Environment Service will be if and when the manned exploration of space is resumed. A recent study[12] has explored the risks and risk management strategies for future manned missions to the Moon and to Mars. The challenge is to protect the astronauts from radiation exposure to the maximum practical extent. The radiation received is from two sources, the continuous Galactic Cosmic Ray background, and the infrequent, but much larger solar proton events. The magnitude of the problem posed by solar proton events is illustrated by the August 1972 event, which occurred between the Apollo 16 and 17 missions. When modeled for shielding typical of a space vehicle structure alone (2g cm^{-2}) this event would have resulted in an astronaut reaching the lifetime limit for exposure to the more sensitive body organs within 10 hours of the start of the event. In the absence of reliable forecasting of proton events, it will be necessary to base mission planning on the contingency of detecting the start of an event locally to the astronauts, and providing shelter which can always be reached within a few hours. It is now understood that the largest proton events are created by the shock waves accompanying coronal mass ejections rather than within solar flares, although a mass ejection may be accompanied by a flare or flares. The techniques for reliably observing mass ejection events are only now being developed. Ejections can be observed reliably when at the solar limb using optical coronagraphs but they are difficult to observe against the face of the sun except by the large scale reordering of the coronal structure that may be left. The coronal mass ejection itself, traveling in interplanetary space, may be detectable using a newly proposed more sensitive optical technique[13]. Reliable detection and forecasting of these solar events will undoubtedly require a combination of techniques deployed, both locally by the astronauts, and on multiple other spacecraft around the sun, including multispectral imaging (radio, optical, EUV, X-Ray) of the solar atmosphere and the early detection of solar proton events by spacecraft nearer to the sun than the astronauts.

5. CONCLUSION

An overview of this brevity can only indicate the general directions that may be taken in Space Environment Monitoring and the Space Environment Services of the future. New research results are continuously improving our

understanding of solar activity and our local space environment. New technological systems and endeavors will have new sensitivities to our space environment. The monitoring systems and space environment services must continue to evolve in response to these changes.

6. REFERENCES

1. "The National Space Weather Program. The Strategic Plan" Office of the Federal Coordinator for Meteorological Services and Supporting Research, FCM-P30-1995
2. B. Bales, J. Freeman, B. Hausman, R. Hilmer, R. Lambour, A. Nagai, R. Spiro, G. H. Voight, R. Wolf, W. F. Denig, D. Hardy, M. Heinemann, N. Maynard, F. Rich, R. D. Belian, and T. Cayton, "Status of the Development of the Magnetospheric Specification and Forecast Model." Terrestrial Predictions IV: Proceedings of a Workshop at Ottawa, Canada, May 18 -22, 1992, NOAA Environmental Research Laboratories, Boulder, pp.467-478.
3. D. M. Speich, and J. W. Hirman, 1996, "Operational Uses of Vector Magnetograph Data," in Proceedings of the Solar-Terrestrial Predictions Workshop, Hitachi, Japan, 23-27 January 1996, ed. K. Nozaki, (in press).
4. J. B. Smith Jr., D. F. Neidig, P. H. Wiborg, E. A. West, M. J. Hagyard, M. Adams, and P. H. Seagraves, "An Objective Test of Magnetic Shear as a Flare Predictor", Solar Drivers of Interplanetary and Terrestrial Disturbances, ASP Conference Series Vol 95, 1996, pp 55 - 65,
5. Y. M. Wang , N. R. Sheeley Jr, "Solar Wind Speed and Coronal Flux Tube Expansion", The Astrophysical Journal Vol 355, pp 726 - 732, 1990, June 1
6. H. Leinbach, and S. Ananthakrishnan, "IPS g-Maps: A Viable Forecasting Tool for Solar Wind Disturbances?", Solar-Terrestrial Predictions - IV, Proceedings of a Workshop at Ottawa, Canada, May18 -22, 1992, NOAA Environmental research laboratories, Boulder, pp.587 - 595.
7. J. P. Delaboudiniere, G. E. Artzner, J. Brunaud, A. H. Gabriel, J. F. Hockedez, F. Miller, X. Y. Song, B. Au, K. P. Dere, R. A. Howard, R. Kreplin, D. J. Michels, J. D. Moses, J. M. Defise, C. Jamar, P. Rochus, J. P. Chauvineau, J. P. Marioge, R. C. Catura, J. R. Lemen, L. Shing, R. A. Stern, J. B. Gurman, W. M. Neupert, A. Maucherat, F. Clette, P. Cugnon, and E. L. Van Dessel, "EIT - Extreme-Ultraviolet Imaging Telescope for the SOHO Mission," Solar Phys., Vol. 162, p. 291, 1995
8. A. L. Kiplinger, "Comparative Studies of Hard X-ray Spectral Evolution in Solar flares with High Energy Proton Events Observed at Earth." The Astrophysical Journal 453:973-986 1995 November 10
9. S. D. Bouwer, "A Suggested Proxy Index for Estimating Solar Lyman β" Proceedings of the Workshop on the Solar Electromagnetic Radiation Study for Solar Cycle 22, ed. R. F. Donnelly, NOAA ERL SEL, Boulder CO 80303, pp. 371 - 382, July, 1992
10. SBIR Contract NOAA 50-DKNA-2-00148 with International Radiation Detectors, R. Korde Principal Investigator.
11. H. S. Ogawa, D. R. McMillin, D. L. Judge, R. Korde, "Normal Incidence Spectrophotometer with High Density Transmission Grating Technology and High Efficiency Silicon Photo Diodes for Absolute Solar Extreme Ultra-Violet irradiance measurement." Optical Engineering, Vol 32 no 12, Dec 1993, pp 3121 - 3125.
12. R. Turner, Principal Investigator, "Risk Management Strategies during Solar Particle Events on a Human Mission to Mars or the Moon." ANSER Corporation Technical report under NASA Grant NAGW-4166
13. S. L. Keil, R. C. Altrock, S. W. Kahler, B. V. Jackson, A. Buffington, P. L.Hick, G. Simmett, C. Eyles, D. F. Webb, and P. Anderson, "The Solar Mass Ejection Imager (SMEI): Development and Use in Space Weather Forecasting", Solar Drivers of Interplanetary and Terrestrial Disturbances, ASP Conference Series Vol 95, 1996, pp 158- 165

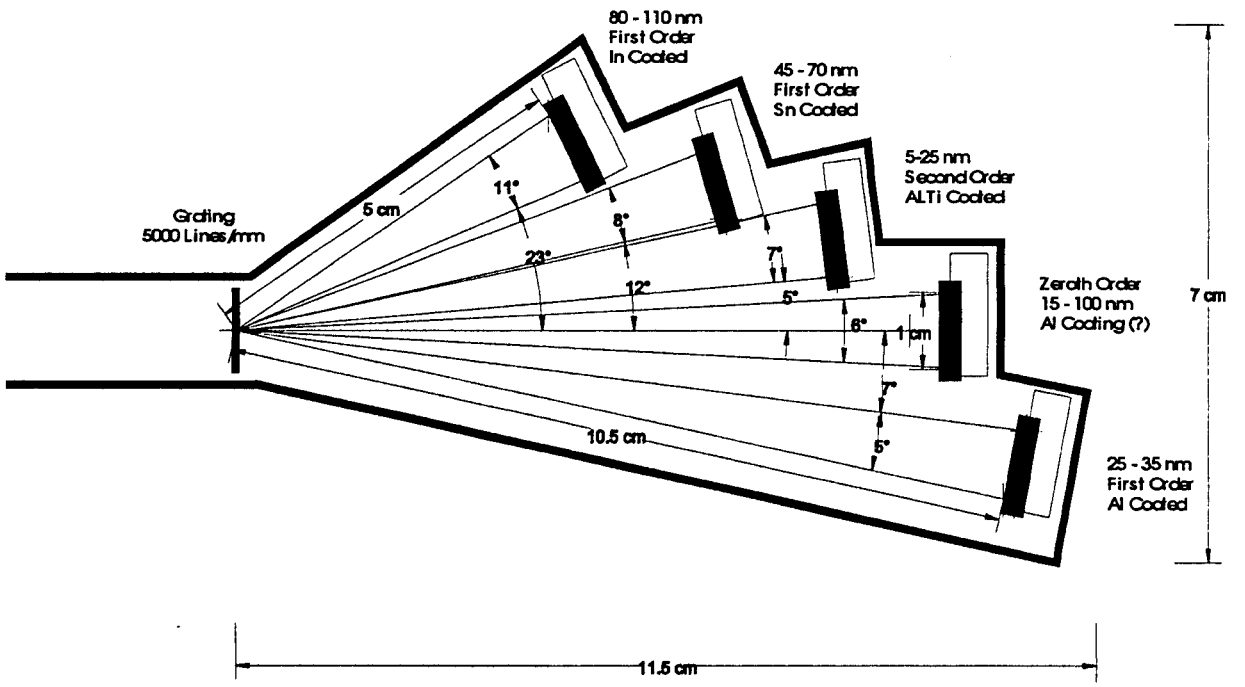

Figure 1. Possible design for a slitless spectrometer meeting the requirements for Solar EUV monitoring.

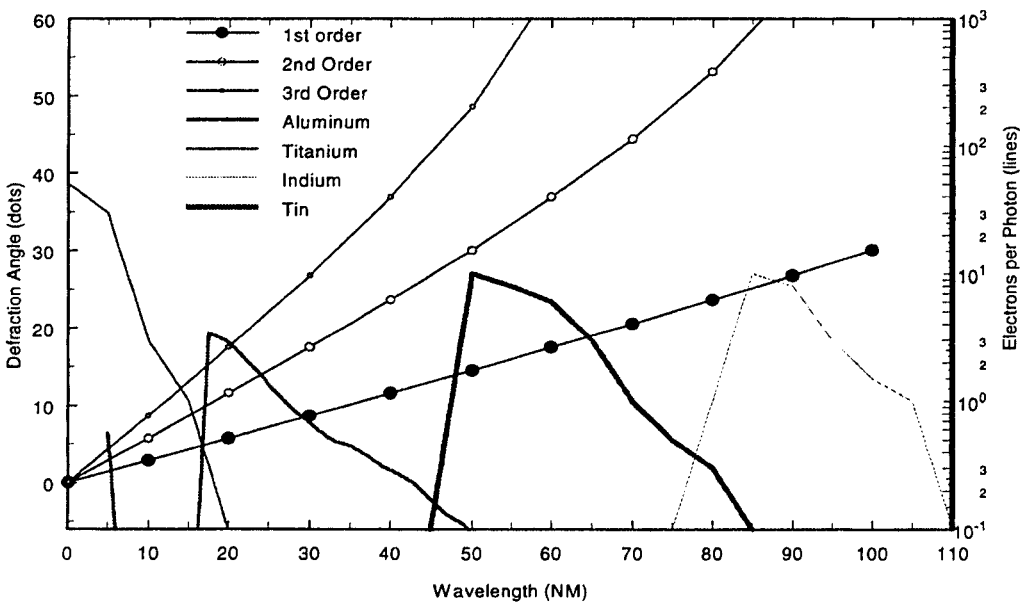

Figure 2. Plot of grating dispersion and detector sensitivity as functions of wavelength for the spectrometer of Figure 1. The dispersion angle for first, second, and third order diffraction from a 5000 lines/mm grating are shown with large medium and small dots respectively. The sensitivities of the diodes coated with different thin-film materials are plotted as various thicknesses of solid lines respectively.

Compensating GOES-8&9 magnetometer data for spacecraft induced errors

Frank Zimmermann

Space Systems /Loral
3825 Fabian Way, Palo Alto, CA 94303

Sandra Cauffman

NASA /GSFC
Code 415, Greenbelt MD 20771

Winfield Farthing

Swales and Associates
5050 Powder Mill Rd., Beltsville Rd. MD 20705

Ronald Hooker

NOAA
NASA /GSFC Code 415, Greenbelt MD 20771

1. ABSTRACT

This paper discusses the issues associated with correcting GOES spacecraft magnetometer data for the effects of the spacecraft platform. The effects discussed include: varying fields due to moving permanent magnets, stray spacecraft fields resulting from the flow of electric currents, the effects of spacecraft noise, and magnetometer shift due to temperature. Issues associated with the interpretation of on-orbit data are discussed, and approaches to overcoming these issues are offered. The use of ground processing to compensate for spacecraft magnetic effects is analyzed based on the results from on-orbit data and pre-launch test data. The results from analyzing GOES-8 and GOES-9 on-orbit data indicate that the combined effect of the errors associated with torquer current ambiguity, torquer corrections, other un-corrected stray fields, results in a root of the sum of the squares (RSS) error of 0.4 nT. The most significant concern in achieving high accuracy in magnetic measurements of the earth's magnetic field with these GOES Spacecraft was found to be the control of magnetic contamination on the magnetometer boom.

Keywords: magnetic fields, earth's fields, magnetometers

2. INTRODUCTION

The magnetic field measured by the magnetometers on board the GOES Spacecraft can be considered to be a combination of the following components:

1. The Earth's magnetic field.
2. Non-varying Fields due to permanently magnetized materials on-board the spacecraft.
3. Varying Fields due to moving permanently magnetized materials on-board the spacecraft.
4. Stray Spacecraft Fields resulting from the flow of Electric Currents.
5. Measurement Noise.
6. Steady State Sensor Error after Temperature Correction.

The Specification[1] for the GOES Spacecraft puts limits on errors due to:

1. Varying Fields due to Permanently Magnetized Materials.
2. Stray Fields from of Electric Currents.
3. Measurement Noise.
4. Temperature Corrected Sensor Error.

Steady state fields, due to permanently magnetized materials on-board the spacecraft, are compensated for based on the results of on-orbit measurements.

2.1 Varying fields due to moving permanent magnets

The primary items of concern are:

1. The permanent magnets in the X-Ray Sensor (XRS) which are rotated about two axes by the Solar Array Drive Assembly (SADA) and the X-Ray Positioner (XRP).
2. Movable magnetic materials which may reposition as the result of the firing of the spacecraft propulsion thrusters.

2.1.1 XRS permanent magnets

A model has been developed to provide the correction for the XRS magnets as a function of the pointing angle of the SADA and the XRP. The description of the model and tabular listing of the corrections are presented in Reference Two.

2.1.2 Movable magnetic materials

The movement of magnetic materials on the magnetometer boom is by far the most critical concern. The region closest to the sensors is the most important due to the inverse cube relationship of magnetic fields in the far field. The solution is to remove all magnetic material from the magnetometer boom except for the magnetometers.

2.2 Stray spacecraft fields

A Stray Magnetic Field is a "Magnetic Field resulting from the flow of current"[3] The stray magnetic field generated by the Spacecraft magnetic attitude control torquer is the primary stray field at issue. The torquer current telemetry for the GOES Spacecraft is limited to 9 significant bits. This results in a resolution of magnetic torquer current of .78 milli-Amps, which corresponds to an ambiguity of up to 0.5 nT at the magnetic sensors.

2.3 Measurement noise

This refers to relatively small errors not otherwise accountable or suitable for modeling. An example of noise encountered in the GOES Spacecraft is the error associated with the noise in the torquer current telemetry. The magnetometer readings are corrected for the magnetic torquer generated magnetic field by ground processing based on the magnetic torquer telemetry. Noise spikes due to anomalous torquer current telemetry can translate to magnetic field measurement ambiguities of up to 5 nT.

2.4 Sensor temperature corrected measurements

This error relates to the accuracy of the sensor after temperature compensation and is dependent on the sensing instrument.

The following table shows estimates of the above contributing effects, and the resultant Root of the Sum of the Squares of the Magnetic Field Measurement Accuracy for GOES-8&9:

Magnetic Field Measurement Accuracy per Axis

	Varying Permanent S/C Fields	Stray S/C Fields	Measurment Noise	Sensor T-Corrected	Root of Sum of Squares
Goal	+-0.5 nT	+-0.5 nT	+-0.3 nT	+-1.0 nT	+-1.3 nT
GOES-8 (Mag. #1)	+-2.0 nT	+-0.6 nT	+-1.1 nT	+-1.0 nT	+-2.6 nT
GOES-9	+-1.0 nT	+-0.6 nT	+-1.1 nT	+-1.0 nT	+-1.9 nT

3. MEASUREMENT ACCURACY

The relative significance of the components which contribute to the total error can be seen from this table. The larger errors dominate the overall performance indicated by the Root of the Sum of the Squares (RSS). The specific cause of the most significant errors are varying permanent fields.

3.1 Varying permanent fields

The largest source of error in measuring magnetic fields with the GOES-8 magnetometers is the varying magnetic field. This is caused by small pieces of magnetic hardware on the magnetometer boom in the proximity of the magnetic sensors which can move when thrusters are fired. The majority of these items were eliminated from the GOES-9 magnetometer boom and all have been removed from GOES-K. The effect of the magnets in the XRS, moving with the solar array and the XRS Positioner (XRP) is typically less than 0.2 nT, and can be compensated for[4,5].

3.1.1 Stray fields

The most significant stray fields, generated by a spacecraft electrical currents, are the magnetic fields generated by the magnetic torquers. Other sources, such as bus currents and heater currents have been controlled by limiting the cross-section of current loops. Particular attention was paid to the design of the solar panel, which is a movable magnetic field source. Excluding the magnetic torquer, there are no other current loops that effect the magnetometers by more than 0.2 nT[6].

3.1.2 Measurement noise

The largest part of the noise contribution is ambiguity errors due to imperfect correction of the magnetic torquer generated fields.

3.1.3 Sensor error

The resultant sensor error after temperature correction have been found to be +-0.5 nT[7].

4. MAGNETOMETER DATA CORRECTION ALGORITHM

The correction algorithm for the GOES magnetometer measurements is:

$$\mathbf{B}_{\text{ACTUAL i}} + \mathbf{B}_{\text{NOISE i}} = \mathbf{B}_{\text{MEASURED i}} - \mathbf{B}_{\text{S/C STEADY FIELDS i}} - \mathbf{B}_{\text{S/C VARYING FIELDS i}} \quad (1)$$

Where:

$\mathbf{B}_{\text{ACTUAL i}}$	=	Ambient field w/o S/C effects, ith axis
$\mathbf{B}_{\text{NOISE i}}$	=	Un-correctable measurement errors, ith axis
$\mathbf{B}_{\text{MEASURED i}}$	=	Temperature corrected measured field, ith axis
$\mathbf{B}_{\text{S/C STEADY FIELDS i}}$	=	Spacecraft induced steady fields, ith axis
$\mathbf{B}_{\text{S/C VARYING FIELDS i}}$	=	Spacecraft induced varying fields, ith axis

For: i = x, y, z axes

4.1 Ambient field w/o spacecraft effects

Magnetic field to be measured. The value the actual magnetic field cannot be separated from the un-correctable measurement errors.

4.2 Un-correctable measurement errors

Effects which are not correctable and the error associated with corrections.

4.3 Temperature corrected measured field

Magnetic field measurements corrected for the effects of temperature on the sensor and the electronics box.

4.4 Spacecraft induced steady fields

The measurement of spacecraft induced steady magnetic fields is accomplished as part of the on-orbit Post Launch Test procedure, EF 0403, Satellite Intrinsic Magnetic Field/Sensor Axis Orientation[8,9]. This data is gathered during on-orbit testing in which the spacecraft is rotated about its principal axes to allow for measurement of the magnetometer zero off-sets. This test can only be performed prior to the deployment of the solar sail. The results of these tests are summarized in the following tables.

GOES 8 Spacecraft Induced Steady Fields, $\mathbf{B}_{\text{S/C STEADY FIELDS i}}$ (nT)

	Magnetometer 1			Magnetometer 2		
{PRIVATE }	x-axis	y-axis	z-axis	x-axis	y-axis	z-axis
$\mathbf{B}_{\text{S/C STEADY FIELDS i}}$	+ 21.00	+ 2.47	+ 1.77	+ 9.00	+ 9.58	+ 1.04
Std. Dev.	0.14	0.57	0.01	0.03	2.47	0.11

GOES 9 Spacecraft Induced Steady Fields, $\mathbf{B}_{\text{S/C STEADY FIELDS i}}$ (nT)

	Magnetometer 1			Magnetometer 2		
{PRIVATE }	x-axis	y-axis	z-axis	x-axis	y-axis	z-axis
$\mathbf{B}_{\text{S/C STEADY FIELDS i}}$	+6.65	-7.93	+3.30	+10.25	-12.70	-7.30
Std. Dev.	0.13	0.68	0.28	1.06	3.10	0.28

4.5 Spacecraft induced varying fields

The discussion of this category is divided into two topics: the effect of the magnetic torquers, and the effect of all other stray fields. The latter is the category of least concern.

4.5.1 Other than torquer stray fields

The review of magnetometer data during solar eclipses, when electric loads are abruptly changed, reveal that the measurement error due to stray magnetic Fields, other than the magnetic torquers, is on the order of +-0.2 nT. These findings correlate with the results of the ground based stray magnetics testing[10]. Because of the low level of these fields and the difficulty of tracing the origin of fields associated with thermostatically controlled heaters, it is not feasible to correct for these fields. This means that the effects of these currents are part of the un-correctable measurement errors

4.5.2 Magnetic torquer fields

The measurement of the effect of magnetic torquer induced magnetic fields is performed as part of the on-orbit test procedures. Torquer currents were individually manipulated to facilitate data collection[8,11]. The results of these tests, for GOES-8&9 are summarized in the following tables:

GOES-8 SPACECRAFT INDUCED VARYING FIELD CORRECTIONS

Magnetic Axis	Off-set	Torquer #1	Torquer #2
$\mathbf{B}_{\text{S/C VARYING FIELDS x}}$ (nT) =	+ 0.1000	+ 0.4092 I_1 (mA)	- 0.0769 I_2 (mA)
$\mathbf{B}_{\text{S/C VARYING FIELDS y}}$ (nT) =	+ 0.3200	+ 0.3390 I_1 (mA)	- 0.1208 I_2 (mA)
$\mathbf{B}_{\text{S/C VARYING FIELDS z}}$ (nT) =	- 0.0360	+ 0.0062 I_1 (mA)	- 0.1831 I_2 (mA)

GOES-9 SPACECRAFT INDUCED VARYING FIELD CORRECTIONS

Magnetic Axis	Off-set	Torquer #1	Torquer #2
$\mathbf{B}_{\text{S/C VARYING FIELDS x}}$ (nT) =	+0.0595	+ 0.4121 I_1 (mA)	- 0.0784 I_2 (mA)
$\mathbf{B}_{\text{S/C VARYING FIELDS y}}$ (nT) =	-0.1020	+ 0.3351 I_1 (mA)	- 0.1227 I_2 (mA)
$\mathbf{B}_{\text{S/C VARYING FIELDS z}}$ (nT) =	-0.3248	+ 0.0052 I_1 (mA)	- 0.1867 I_2 (mA)

The magnetic field coefficients associated with the torquer currents for GOES-8&9 are virtually identical. The differences in the off-sets are 0.5 to 2.0 mA for the x and y-axis and 2 to 4 mA for the z-axis. The effect of the differences in these off-sets is less than one nanoTesla. The magnetic torquer currents have almost identical effects on the magnetometers for GOES-8 and GOES-9.

4.5.3 Effect of XRS magnets

Compensation for the effect of the varying field caused by the movement of the XRS magnets can be added to the above $\mathbf{B}_{\text{S/C VARYING FIELDS i}}$, to increase accuracy of the correction. For convenience this correction, which is dependent on the time of day and the time of year, may be ignored. The magnitude of this effect is typically less than 0.2 nT, and is independent of the other error mechanisms. The impact on the total error, i.e. the root of the sum of the square of the errors, is almost negligible.

5. Algorithm validation, using on-orbit data

Validation of the magnetometer data correction algorithm was performed for both GOES-8 and GOES-9 data. The validation of the algorithm for GOES-8 was complicated by the existence of random noise and "beat frequency" noise on the magnetic torquer current telemetry[12]. These noise effects were removed from GOES-9 by installing low pass filters on the torquer current signal inputs to the telemetry units.

5.1 Goes-8 magnetometer data correction algorithm validation

Validation of the magnetometer data correction algorithm for GOES-8 was done for data collected during a time period when the current for the magnetic torquers was updated every twenty minutes. Results for filtering with 21 point averages, which cause a five second delay, showed good results. Even better results are obtained by averaging over a greater number of data points. Transitions in torquer current, and segments of torquer current data with "beat frequency" noise can be automatically detected using a 21 point moving variance[12].

5.1.1 Data sample used for algorithm testing

Figure 1 shows a plot of the data used for this validation. This data provides a good sample of GOES-8 data due to the diversity in the data. It includes torquer current with and without the "beat frequency" noise. It contains a torquer current transition in the midst of the "beat frequency" noise; torquer current transitions of the same magnitude as the noise; and a transition which is an order of magnitude greater than the noise.

5.1.2 21-point moving variance threshold

Figure 2 shows a comparison of the 21-point variance with filtered and un-filtered torquer current. The variance clearly indicates the step change in the torquer current.. The 21-point moving variance is a good indicator for determining when the 21-point moving average filter is creating unwanted artifacts.

5.1.3 21-point moving average filter performance

Figure 3 shows the results of filtering the magnetic torquer current telemetry data using a 21-point moving average filter. The scale for the filtered data has been changed to avoid overlap in the plots. The 21-point averaging filter provides good filtering of the spiky noise and a good filtering of the "beat frequency" noise with a delay of 5 seconds plus processing time. Figure 4 shows a portion of the data in figure 3 which is centered around the torquer change in current. There is a period of about 11 seconds for which the moving average filter yields a bad result.

5.1.4 Component of data with eight minute period

The "beat frequency" noise has two principle components. The first of these components has a time period of about 1.5 seconds. This component is adequately removed by the 21-point moving average as shown for torquer current #1 in figure 4. The second component has a time period of about 8 minutes. This component can be seen as the envelope of the "beat frequency" noise on the torquer #1 current as shown in figure 3, and in figure 5 which is scaled for better visibility of this component. From figure 5 it can be seen that the zero to peak magnitude of this component is about 1.8 mA. In order to remove this component, a filter with a span larger than the 8 minutes period is required.

5.2 GOES-8 magnetometer data correction validation results

Figure 6 shows the un-corrected x-axis magnetometer flux data and the unprocessed magnetic torquer data for both torquers. After the torquer current data was filtered with a 21-point moving average filter, the magnetometer data was corrected for the magnetic torquer current generated fields per the magnetometer data correction algorithm. A threshold for the 21-point moving variance was used to identify ranges of data that are not appropriate for correction with the averaged torquer data. A threshold variance of 0.0001 was effective in identifying data that was unsuitable for correction; yet yielded a relatively small amount of discarded data. Figures 7 shows the before and after results of this correction process. Reference ten contains further details of this validation and additional examples of results. The scheme of filtering the torquer current data with a 21-point moving average and correcting the magnetometer data for torquer current with a moving variance under 0.0001 provided excellent results for the data sample used.

5.3 GOES-9 magnetometer data correction algorithm validation

Due to the fact that the random noise and the "beat frequency" noise found on the GOES-8 magnetic torquer current telemetry data is not found on the GOES-9 data, the validation of the magnetometer data correction algorithm for GOES-9 was considerably more straight forward. Figure 9 shows a plot of the torquer currents and the un-corrected magnetometer data. Figure 10 shows a plot of the results of the magnetometer data correction for the effect of the magnetic torquer generated magnetic fields. A constant 1.8 milli-second delay of the magnetic torquer current telemetry was used to compensate for temporal misalignment of the magnetometer and magnetic torquer current telemetry, including the effects of the magnetometer anti-aliasing filter in the magnetometer electronics box.

5.3.1 GOES-9 magnetometer data correction validation results

Figures 11, 12, 13 and 14 show a comparison of an x-axis magnetometer signal before and after filtering. The torquer currents are also shown in order to highlight the effect of the correction on the magnetometer signal. Within the time period plotted in these figures there is a region around the epoch 53:46 where the ambiguity in the torquer current is apparent. Figure 11 shows that the correction process introduces artifacts related to the torquer current ambiguity.

5.3.2 Lessening the appearance of torquer current ambiguity

Two possible approaches to lessening these artifacts were explored. The first was to apply recursive filtering to the torquer current signal before it was used to correct the magnetometer data. Figure 12 shows the before and after results of applying that technique. As can be seen from Figure 12, the effect of the torquer current ambiguity is greatly lessened. The second technique to reduce the effect of the torquer current ambiguity on the corrected magnetometer data was to perform a 5 second average on the magnetometer data subsequent to the correction process. The results of this approach are shown in figure 13. Again there is a significant reduction in the appearance of the torquer current ambiguity in the corrected magnetometer data. Figure 14 shows the results applying both of these techniques. As can be seen from this figure, the effect of using both of these techniques almost eliminates the appearance of the torquer current ambiguity artifacts.

6. SUMMARY OF RESULTS

6.1.1 Magnetic material effects

The most significant error is that associated with the magnetic measurements on both GOES-8 and GOES-9 is the presence of magnetic material on the magnetometer boom which has the ability to move in relation to the magnetometer sensors.

6.1.2 Telemetry accuracy effects

The effective nine bit accuracy of torquer current telemetry results in an ambiguity of +- 0.4 mA which can effect the magnetometer correction by +- 0.2 nT. This ambiguity can be seen in the torquer current telemetry signal in both figures 9 and 10 on the torquer 1 signal centered around the 54:00 epoch. The effect of this ambiguity on the corrected x-axis and y-axis magnetometer data can be seen in figure 10. The effect of the magnetic torquer current ambiguity is of the same order of magnitude as the glitches resulting from the correction for torquer currents.

6.1.3 Telemetry noise effects

The torquer current averaging is not required for GOES-9 (and subsequent spacecraft) to overcome the torquer current noise found on the magnetic torquer current telemetry on GOES-8. This is a result of the anti-aliasing filter that was added to the torquer current signal on board the GOES-9 spacecraft. Some averaging or filtering may be desirable to lessen the appearance of the torquer current ambiguity related artifacts on the corrected magnetometer data. This doesn't necessarily improve the accuracy of the data but may eliminate the misinterpretation of these artifacts.

6.1.4 Combined effects

The combined effect of the errors associated with torquer current ambiguity, torquer corrections, other uncorrected stray fields, and ignoring the XRS changing field; each of which has an impact on the order of 0.2 nT, results in a root of the sum of the square of these values of 0.4 nT.

7. REFERENCES

1. Performance Specification For Geostationary Operational Environmental Satellite System (GOES-IJK/LM), S-480-19B, Paragraph 3.5.1, "Magnetic Field Sensor".
2. Macintyre Electronic Design Associates Inc. Report "GOES X-Ray Sensor (XRS) Stray Magnetic Fields - Analytical Model for S/N 002" dated April 18,1994
3. NASA Space Vehicle Design Criteria, NASA SP-8037, " Assessment and Control of Spacecraft Magnetic Fields", September 1970.
4. MEDA Report, Dated: April 18,1994, Subject: GOES X-Ray Sensor Stray Magnetic Fields, Analytical Model for GOES-J XRS S/N 002 (On GOES-8).
5. MEDA Report 000104, Dated: July 2,1995, Subject: GOES X-Ray Sensor Stray Magnetic Fields, Analytical Model for XRS S/N 001 (On GOES-9).
6. GOES-9 Post Launch Test Report EF0404, "Magnetic Interference" (Draft), October 1995.
7. MEDA Report EAD-94-376-FZ, Dated August 31,1995, Subject: GOES Magnetometer Error Analysis.
8. NASA GOES-8 Post Launch Test Report, Volume IV - Thermal, SEM, Imager, Rev. 1; Dated: January 16, 1995.
9. GOES-9 Mission Performance Report, DRL 503-03, Dated: 23 August 1995; Chapter 11, Space Environment Monitoring.
10. Technical Memorandum GOES-PCC-TM-6291, Dated: March 30, 1994, Subject: Stray Magnetic Analysis Results for Thermostatic/ Proportional Heaters.
11. Swales letter; Dated June 29, 1995, Subject: GOES-9 Preliminary Test Report. EF0404, Magnetic interference.
12. Technical Memorandum GOES-PCC-TM-6441, Dated July 25, 1994, Subject: GOES-8 Magnetometer Calibration for Magnetic Torquer Generated Fields with Torquer Current Telemetry Noise as described in GOES-8 TIR-97 and TIR-151.

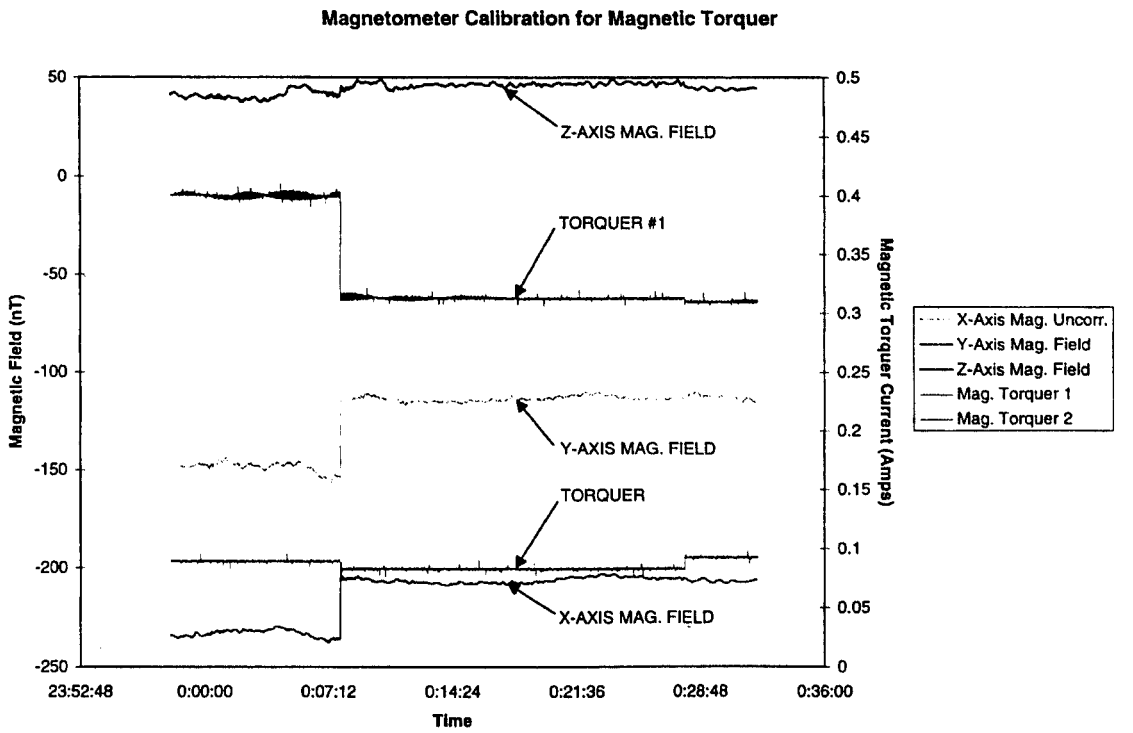

Figure 1

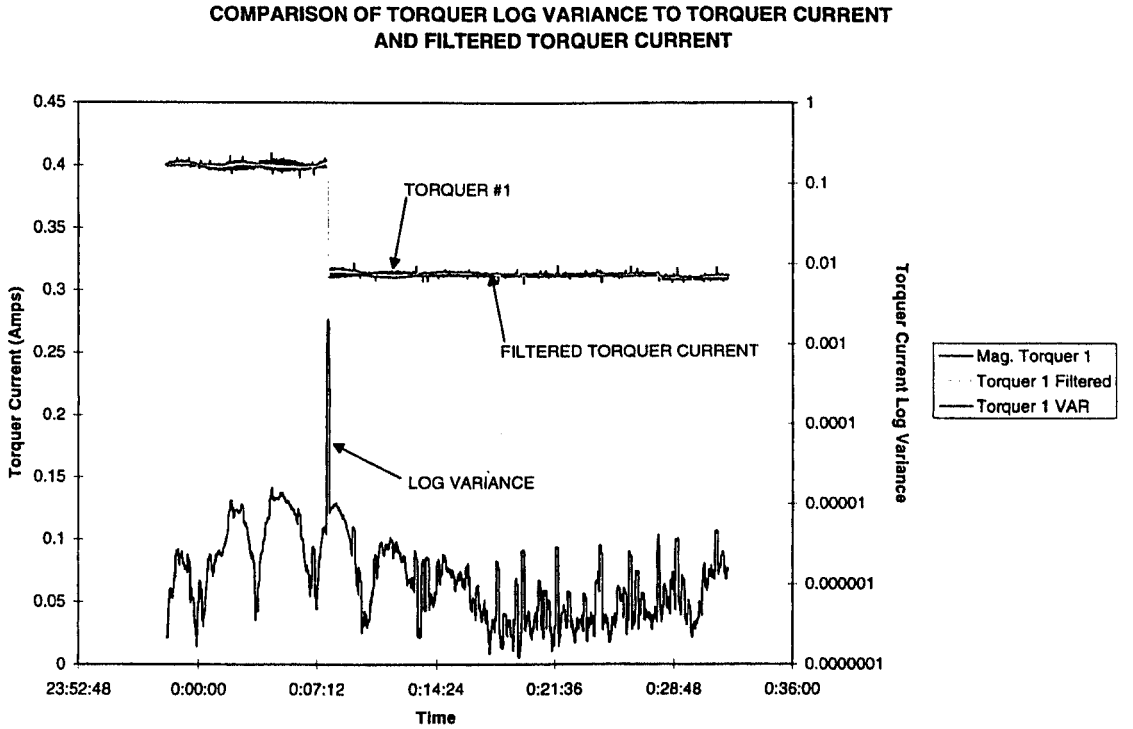

Figure 2

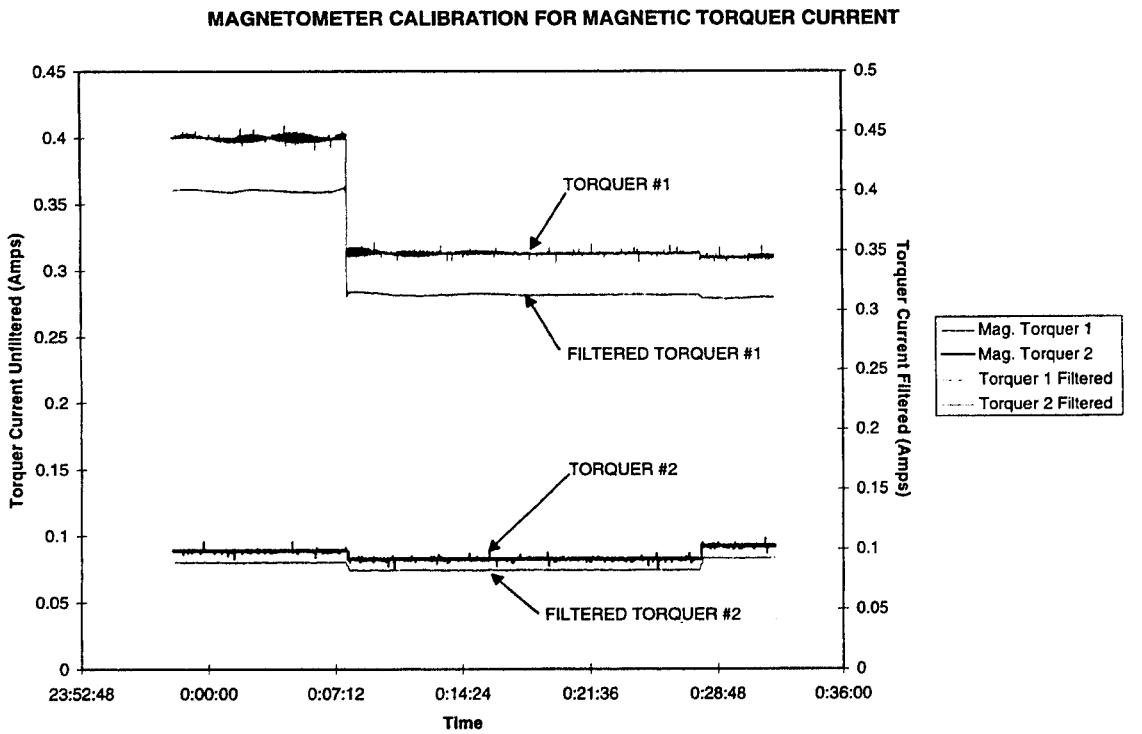

Figure 3

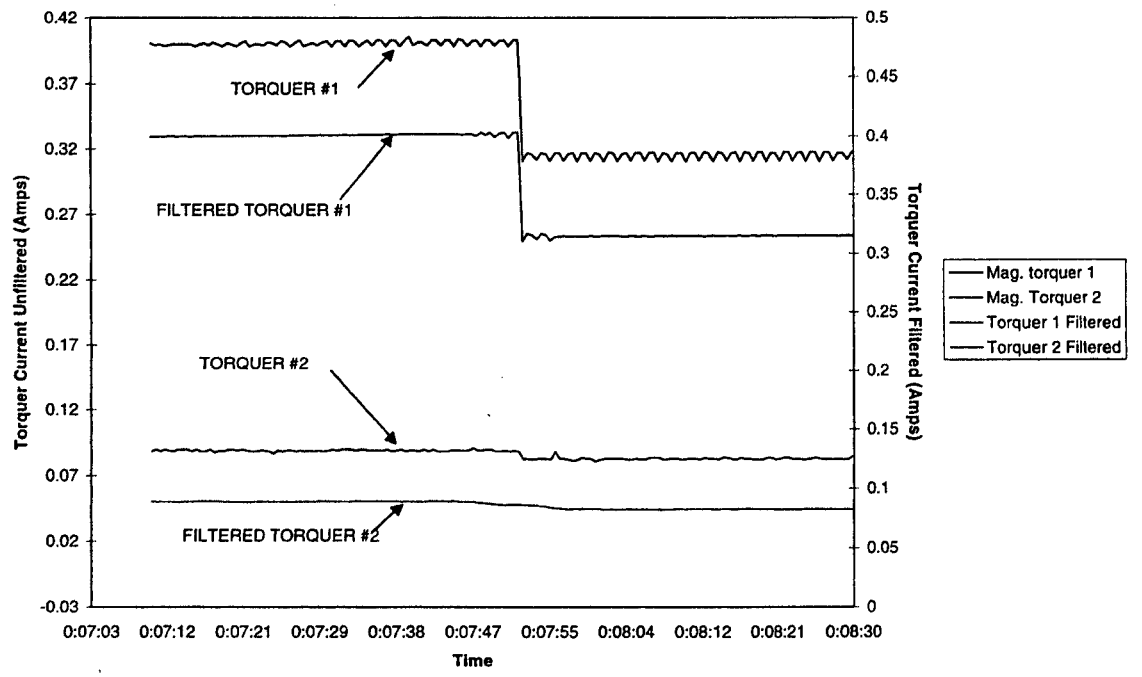

Figure 4

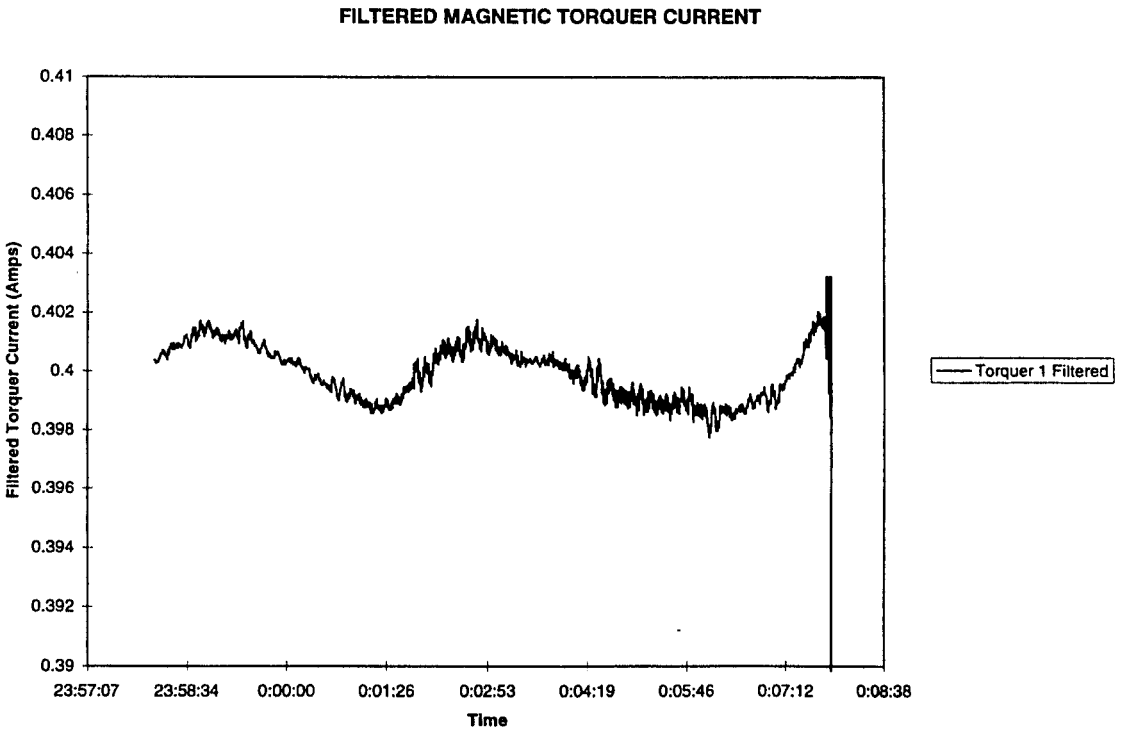

Figure 5

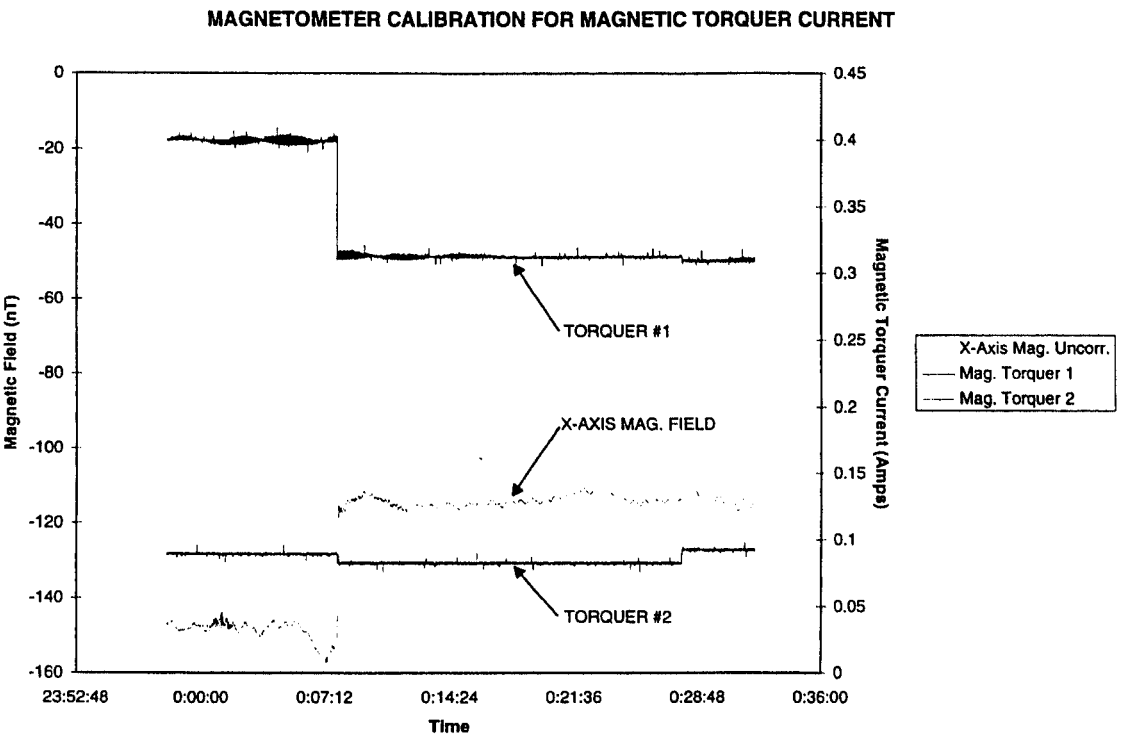

Figure 6

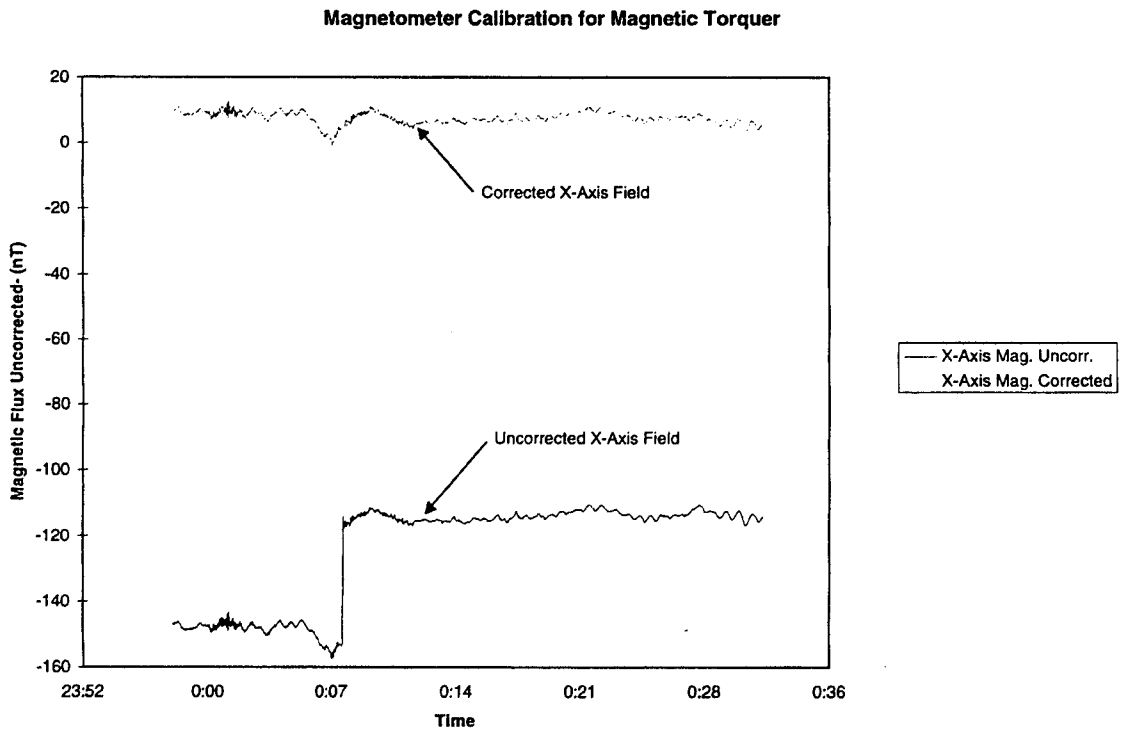

Figure 7

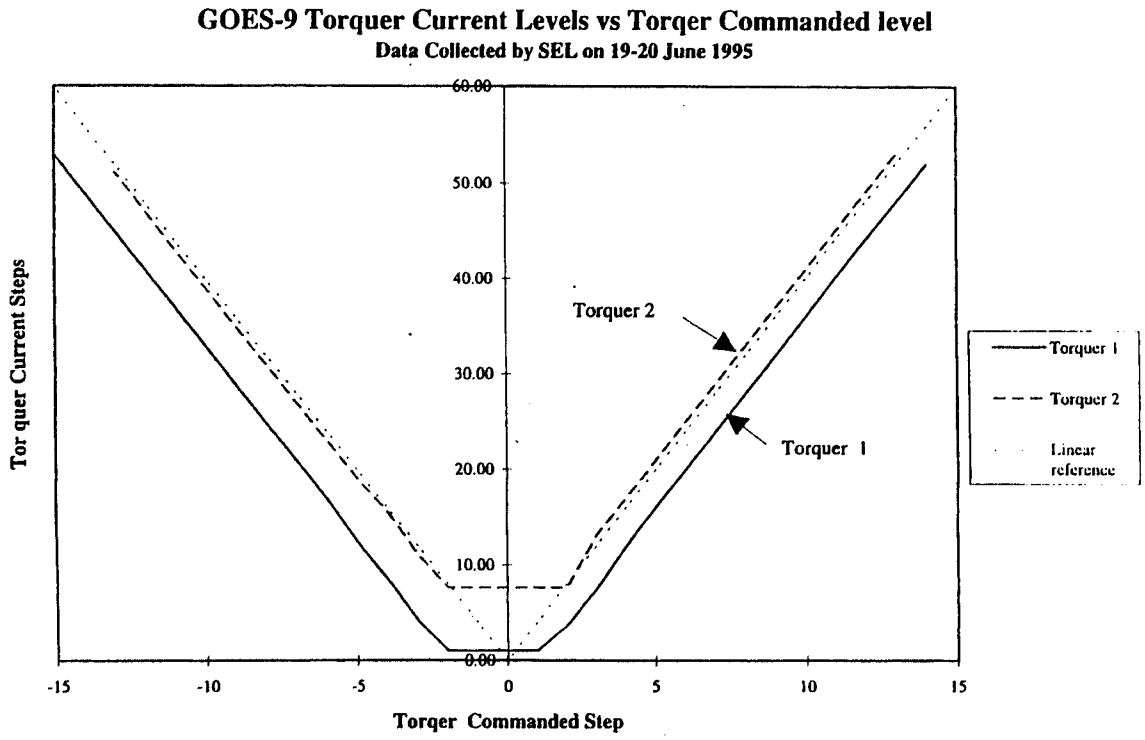

Figure 8

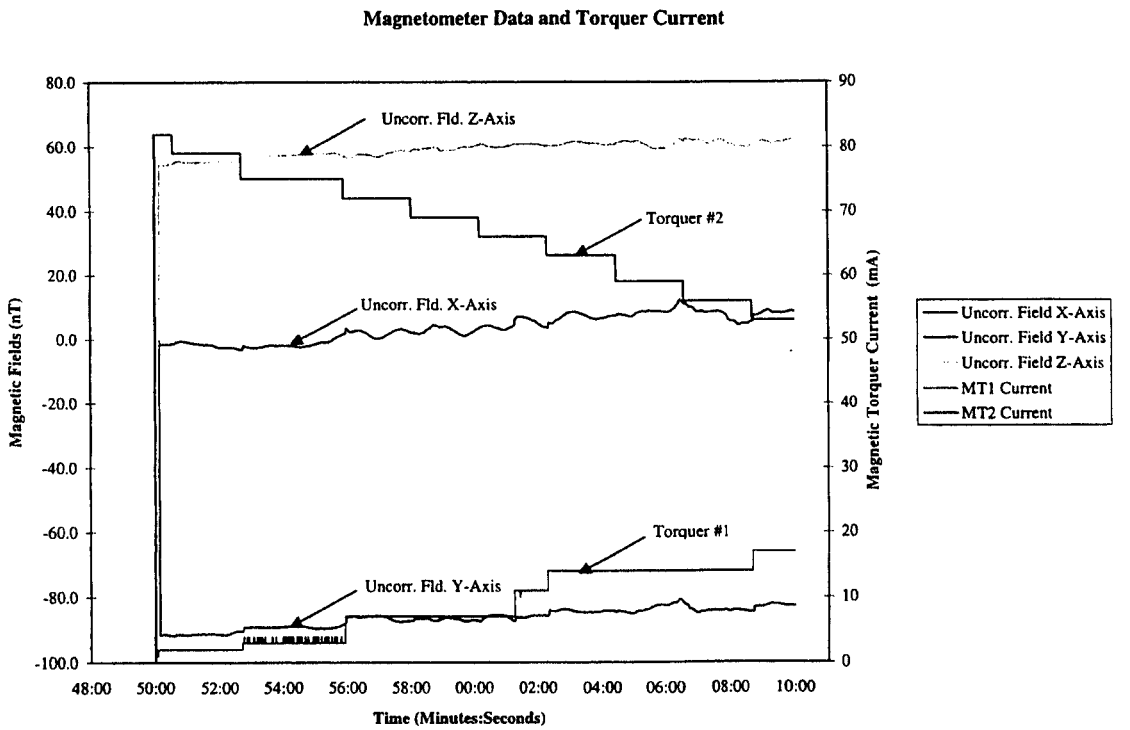

Figure 9

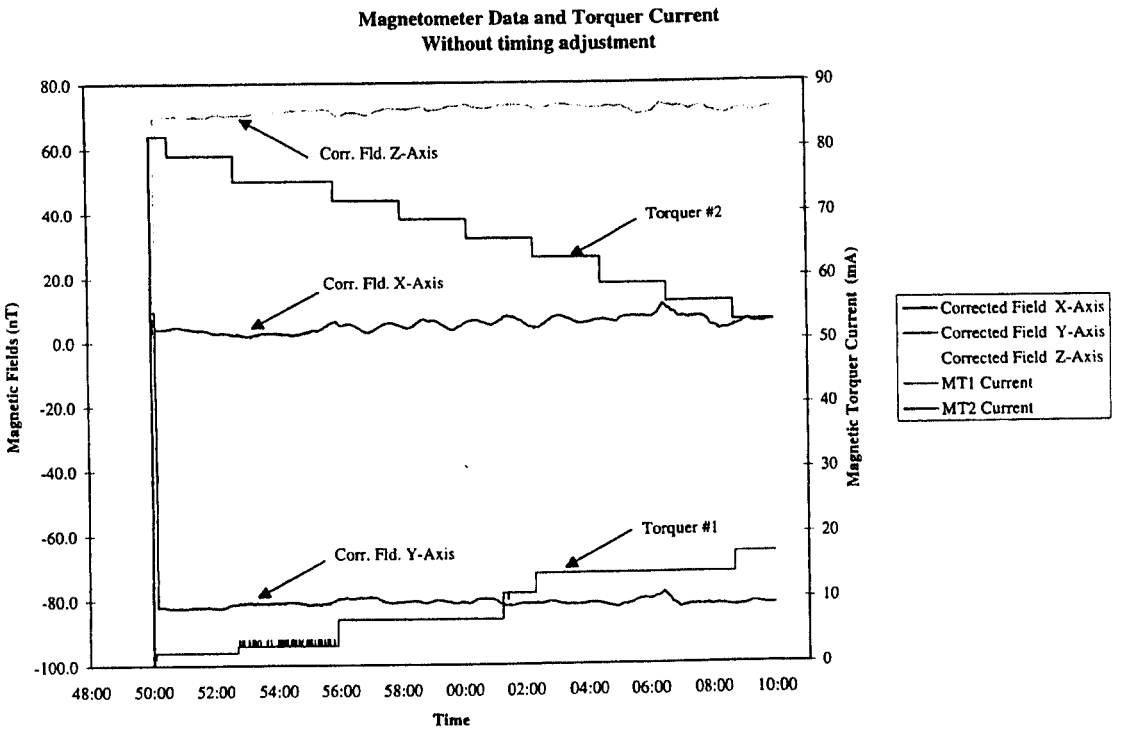

Figure 10

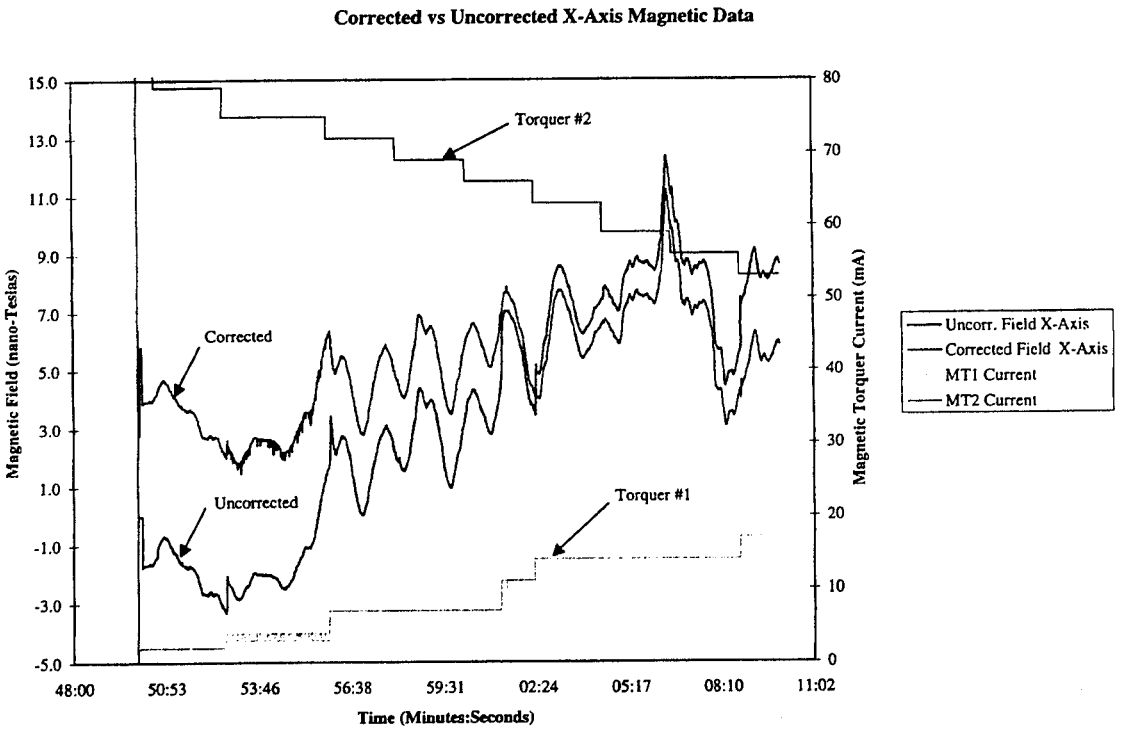

Figure 11

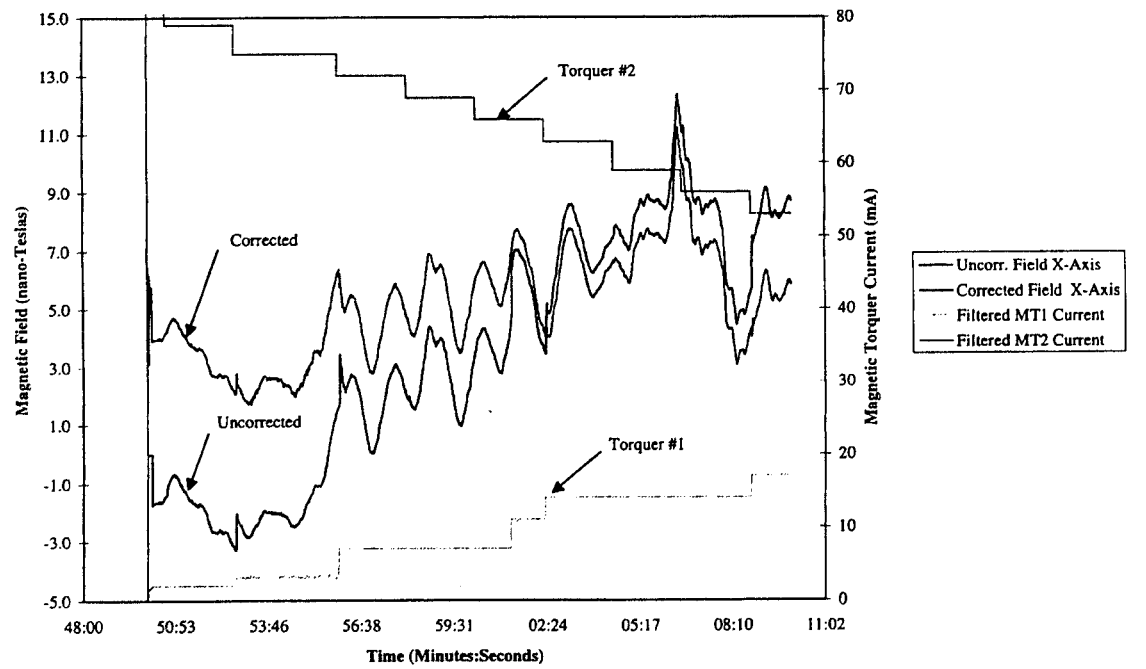

Figure 12

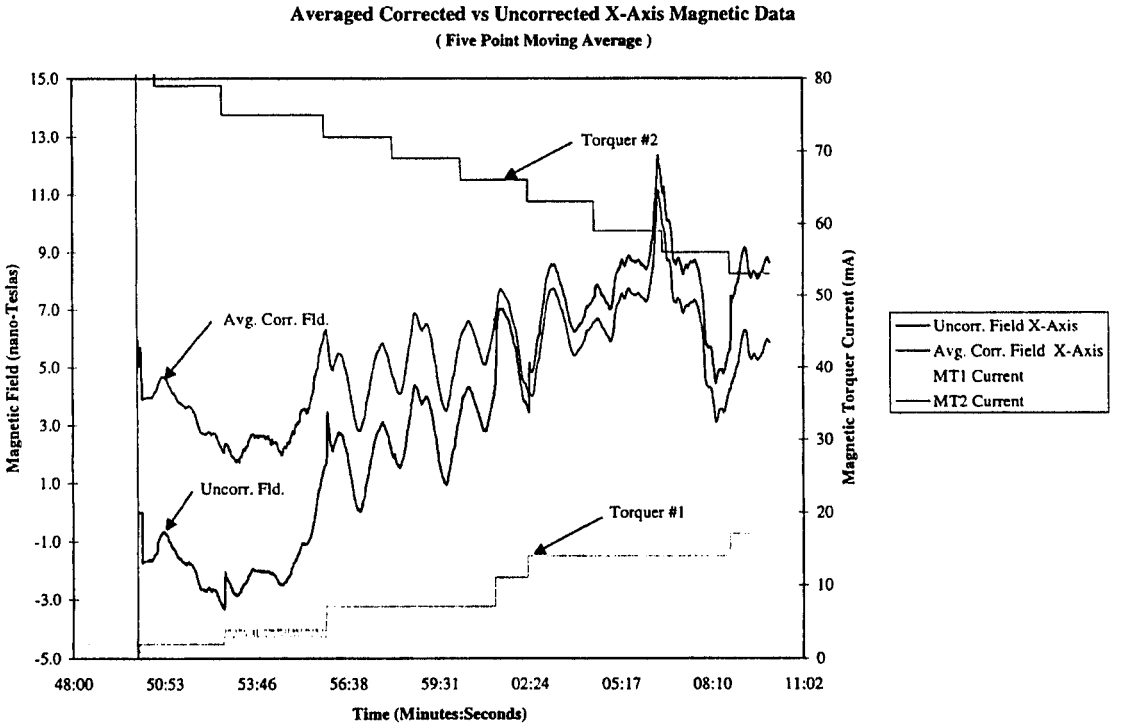

Figure 13

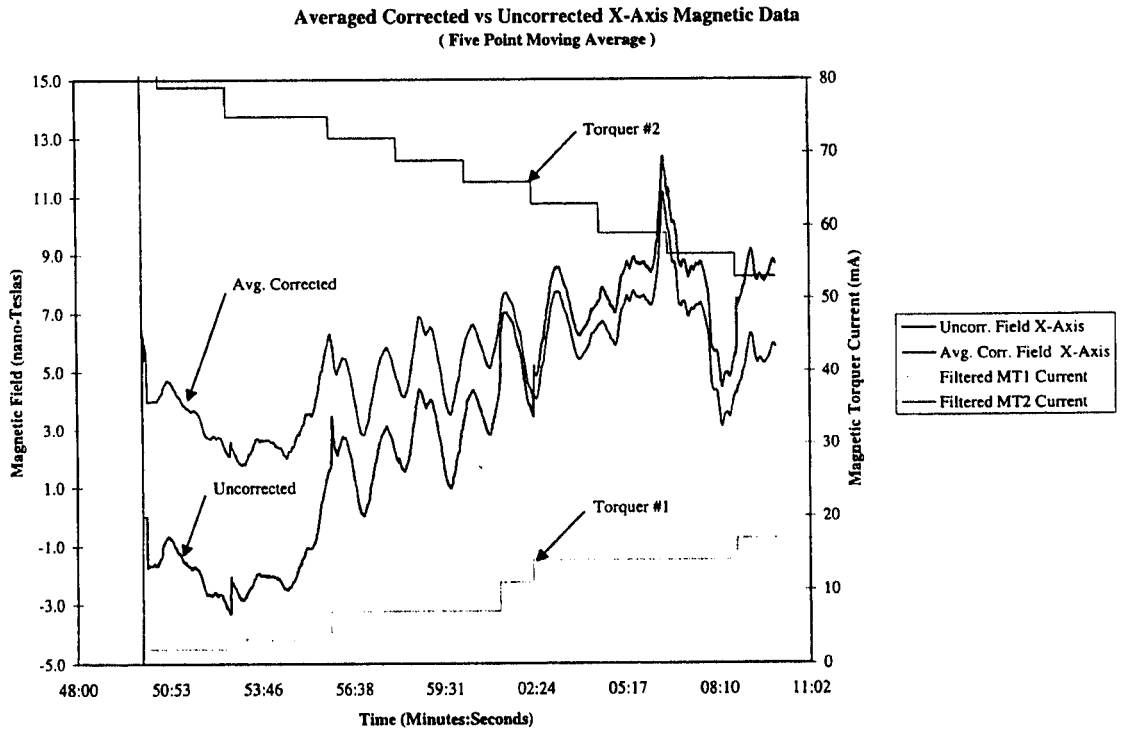

Figure 14

Design and calibration of the GOES-8 solar x-ray sensor: the XRS

Frederick A. Hanser and Francis B. Sellers

Panametrics, Inc.
221 Crescent St., Waltham, Massachusetts 02154

ABSTRACT

The GOES-8 Solar X-Ray Sensor (XRS) detects solar x-rays in two (2) wavelength bands of approximately 0.5 to 3 Å and 1 to 8 Å. The XRS uses a dual ion chamber design with beryllium windows and Xenon or Argon gas fills to provide the x-ray detection, and which determine the wavelength response functions. GOES (and SMS) spacecraft before GOES-8 were spinning, and the previous XRS design used this property to measure the solar x-rays as a "pulse" above the ambient particle background during the time when the XRS FOV scanned across the sun. GOES-8 and later spacecraft are three-axis stabilized, and the XRS now views the sun constantly from a mount on the solar panel yoke. This puts a severe requirement on the XRS for shielding of the ion chamber, since the background current from ambient particles must be well below the current from the design threshold x-ray fluxes. The design and calibration of the XRS is described, as are results from electron irradiation which were used to verify the immunity to ambient particle fluxes.

Keywords: x-rays, solar x-rays, x-ray detectors, spacecraft x-ray sensors

1. INTRODUCTION

The GOES spacecraft have monitored the solar x-ray emission since the launch of the SMS-1 spacecraft in May 1974.[1-4] The ion chamber detector design has not changed since the first units, so the basic wavelength response has been constant for the entire SMS/GOES archive of solar x-ray flux. Up to GOES-7 all of the XRS units were designed for use on a spinning spacecraft, and this was used to aid in eliminating the background from ambient particles, mostly electrons and their associated bremsstrahlung, by measuring the solar x-ray "pulse" as the XRS field-of view (FOV) scanned across the sun. For the 3-axis stabilized GOES-8 and later spacecraft this is not possible, since the XRS is now located on the solar panel yoke on the south side of the spacecraft. This provides the XRS with a constant view of the sun, but it also results in the spacecraft providing minimal particle shielding for the XRS. Thus the XRS must use tighter FOV collimation and improved shielding to reduce the ambient particle background to well below the desired x-ray threshold response. The XRS electronics processing of the ion chamber currents is also different for the units on GOES-8 and on, since the response is now a DC current rather than the solar x-ray pulse of the previous units. The following sections contain descriptions of the GOES-8 XRS design, with special attention to the ion chamber shielding and the x-ray calibration.

2. DESIGN AND RESPONSE OF THE XRS

The external appearance of the XRS is shown in Fig. 1, while details of the x-ray collimation and ion chamber shielding are shown in Fig. 2. Since electrons in the MeV energy range can penetrate the ion chamber window and produce ionization in the fill gas, a strong permanent magnet and baffles are used in the telescope collimator to prevent electrons below several MeV from being able to reach the ion chamber directly. Since electrons scatter very strongly, and produce a significant bremsstrahlung (x-ray) flux, the collimator design is extremely important. The collimators closest to the ion chamber are of a layer design, using aluminum in front to reduce the bremsstrahlung production, and copper or lead in the rear to provide better particle and x-ray shielding. The front collimator is made of copper which provides better particle and x-ray absorption than aluminum, and is far enough from the ion chamber so that the electron bremsstrahlung are still well absorbed. The entire ion chamber is well shielded by lead in all directions except the FOV, so response to bremsstrahlung generated in the outer XRS housing is strongly reduced, particularly since the outermost layer is beryllium. This is important since the XRS location on the GOES-8 solar panel yoke means that the spacecraft provides minimal particle shielding for the XRS, less than 2π sr, so the XRS housing is exposed directly to most of the ambient particle fluxes at geosynchronous orbit. A more detailed discussion of the ion chamber shielding is given in Section 4. The bucking magnet is not essential for the XRS operation, but is added to provide cancellation of the remnant

 0-8194-2200-2/96/$6.00

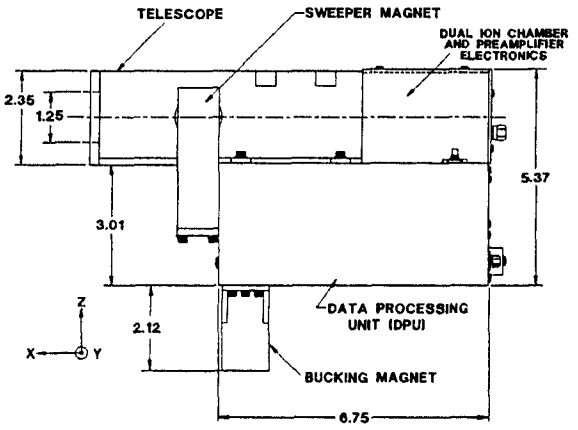

Figure 1. External view of the GOES-8 XRS. Dimensions listed are in inches.

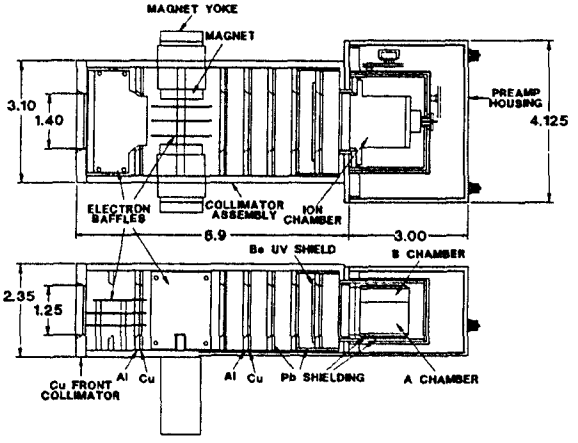

Figure 2. Detailed view of the XRS x-ray collimation and ion chamber shielding. Dimensions listed are in inches.

dipole field from the sweeping magnet, reducing the effect of the XRS on the GOES magnetometer.

The x-rays are detected by a dual ion chamber, with the characteristics given in Table 1. The wavelength dependent response of the ion chambers to x-rays is given by[5]

$$G(\lambda) = (q_e A/W)e^{-\mu Be(\lambda)\ tBe}(1 - e^{-\mu g(\lambda)\ tg})C_F(\lambda), \quad (1)$$

where q_e is the electron charge, A is the ion chamber window area, W is the energy/ion pair for the ion chamber gas , $\mu Be(\lambda)$ is the absorption coefficient of Be for x-rays of wavelength λ , tBe is the Be window thickness, $\mu g(\lambda)$ is the absorption coefficient of the gas fill for x-rays of wavelength λ, tg is the ion chamber gas thickness along the FOV direction, and $C_F(\lambda)$ is a correction for fluorescent radiation escape.[5] For long wavelengths $C_F(\lambda) = 1$, while for wavelengths shorter than the gas fill K or L absorption edge

$$\begin{aligned} C_F(\lambda) &= 1 - 0.032\lambda,\ 0.358\ \text{Å} < \lambda < 2.59\ \text{Å} \\ &= 1 - 1.6\lambda,\ \lambda < 0.358\ \text{Å}, \end{aligned} \quad (2)$$

for the Xenon-filled A chamber and

$$C_F(\lambda) = 1 - 0.015\lambda,\ \lambda < 3.87\ \text{Å} \quad (3)$$

for the Argon-filled B chamber. The nominal values of the various constants are given in Table 1 for the 0.5 to 3 Å A chamber and for the 1 to 8 Å B chamber. Using the x-ray absorption coefficients for Be,[6] Ar[6] and Xe[7,8] the nominal ion chamber response functions are plotted in Fig. 3. The actual calibrated XRS A and B chamber response functions are modified slightly from the nominal values, as described in Section 5. The response constants for the ion chambers are calculated for a flat (in wavelength) x-ray spectrum, using

$$\bar{G}(\Delta\lambda) = \int_0^\infty G(\lambda)\, d\lambda/\Delta\lambda \quad (4)$$

where $\Delta\lambda = 3 - 0.5 = 2.5$ Å for the A chamber and $\Delta\lambda = 8 - 1 = 7$ Å for the B chamber. For the nominal responses shown in Fig. 3 the results are

$$\bar{G}(A) = 1.8\times10^{-5}\ A\text{-}m^2/W$$
$$\bar{G}(B) = 4.6\times10^{-6}\ A\text{-}m^2/W. \quad (5)$$

The XRS FOVs are designed to be as narrow as possible to minimize the background from particles entering the telescope opening. The two sets of electron baffles help reduce the electron background, which is usually the dominant particle flux at geosynchronous orbit. The low energy x-ray FOV is calculated from the shielding of the ion chamber windows by the baffles and the front collimator edges. For the Y direction (see Fig. 1 for coordinate orientation) the A and B chambers have the same symmetrical FOV plotted in Fig. 4. The FOVs in the Z direction are different for the A and B chambers, and are plotted in Figs. 5 and 6. Positive angles denote an x-ray source displaced in the positive Y or Z direction from the XRS FOV axis. The FOV responses are within 97.5% of the peak for a width of 0.74° in the Y direction, and for a width of 0.68° (A chamber) and 1.06° (B chamber) in the Z direction, which allows coverage of the full solar disk of 0.5° diameter. These results are similar to the Z FOVs of the previous spinner XRS design, where the calculated values agreed reasonably well with in-orbit measurements. [4]

Table 1. Dual ion chamber properties

Item	A Chamber	B Chamber
Nominal x-ray detection range	0.5 to 3 Å	1 to 8 Å
Beryllium window thickness, tBe	20 mils	2 mils
Fill gas and pressure	Xenon/180 mm Hg	Argon/800 mm Hg
Window area, A	5.80 cm^2	1.90 cm^2
FOV direction gas thickness, tg	5.051 mg/cm^2	6.831 mg/cm^2
Energy to produce an electron-ion pair, W	22.0 eV	26.2 eV

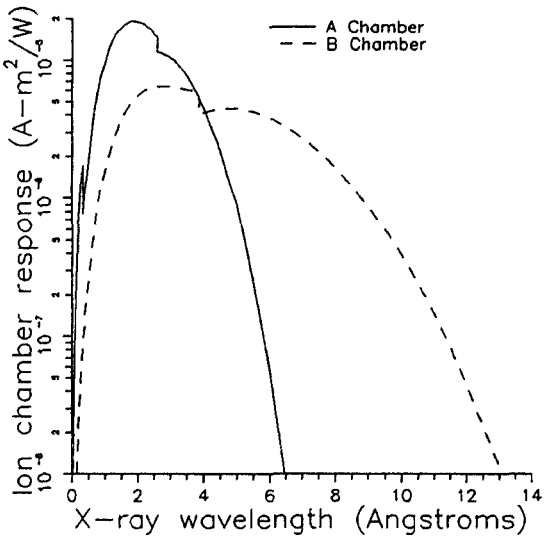

Figure 3. Nominal response function G(λ) for the XRS.

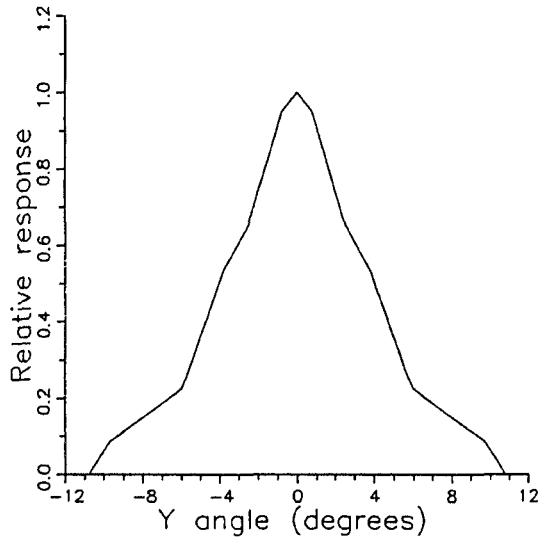

Figure 4. XRS FOV response in the Y direction.

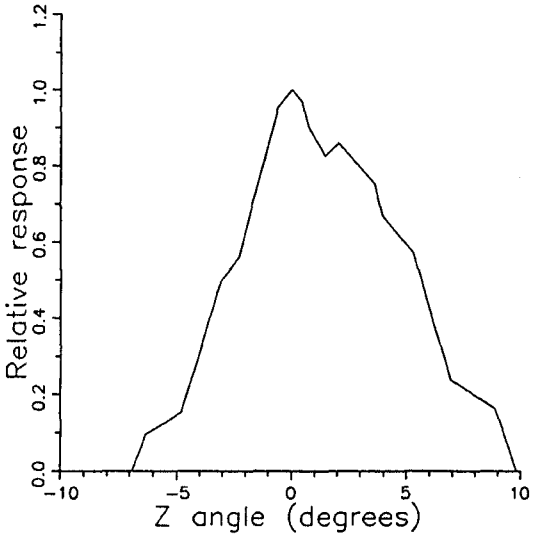

Figure 5. XRS A chamber FOV response in the Z direction.

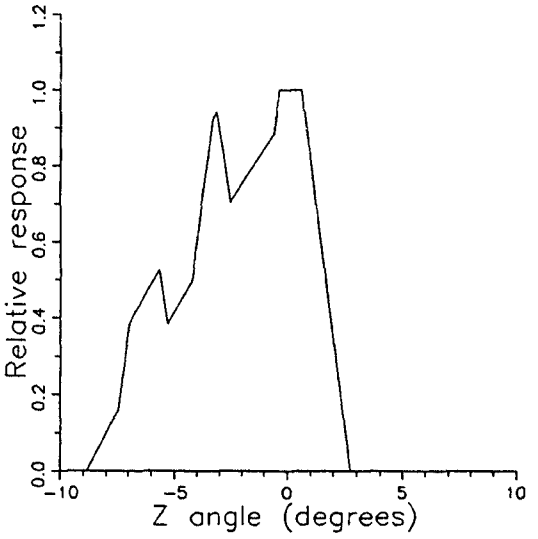

Figure 6. XRS B chamber FOV response in the Z direction.

3. DESIGN OF THE XRS ELECTRONICS

A block diagram of the XRS electronics design is shown in Fig. 7. The GOES-8 XRS covers an x-ray flux range of 5×10^{-9} to 5×10^{-4} W/m^2 for the A chamber and 2×10^{-8} to 2×10^{-3} W/m^2 for the B chamber. The XRS units up to GOES-7 covered 10^{-9} to 10^{-4} W/m^2 and 10^{-8} to 10^{-3} W/m^2 for the A and B chambers, but this resulted in saturation at some of the largest solar x-ray flares.[1,2] Since large x-ray flares have the most effect on the earth's ionosphere, it is important to avoid saturation at the high flux end, and the XRS range was shifted upward starting with GOES-8. The nominal response constants from Eq. 5 give ion chamber currents of about 9.0×10^{-14} to 9.0×10^{-9} A for the A chamber and 9.2×10^{-14} to 9.2×10^{-9} A for the B chamber. The low threshold x-ray flux currents of $<10^{-13}$ A put stringent requirements on the XRS preamplifier electronics and on the ambient particle shielding for the ion chamber.

The x-ray flux ranges of five decades are covered by four linear ranges of the output analog signal, accomplished by changing the preamplifier gain by a factor of 100 and by attenuating the output signal by a factor of 10. The four possible combinations of preamplifier gain and signal attenuation provide the four analog ranges for each chamber, with adjacent ranges differing by about a factor of 10 in gain. The spacecraft telemetry system digitizes the x-ray analog output signal (range 0 to 5 V) to an 8-bit word, so in order to reduce the effects of digitization resolution, the analog signal has an added 0.5 V offset. The range switching takes place when an increasing x-ray signal reaches 95% of full scale (4.8 V output of a 5 V maximum; with the 0.5 V offset this is a net x-ray signal of 4.3 V), or when a decreasing signal reaches about 8% of full scale (0.9 V output; with the 0.5 V offset this is a net x-ray signal of 0.4 V). The range switch points are adjusted to allow about 25% hysteresis so that frequent range switching ("hunting") at the range boundaries is minimized. Since the XRS output signal has a 1 second time constant, the XRS output is set to mid-range (2.5 V) after a range switch to minimize the time to approach the new output voltage value.

The electronic gains for all four ranges are monitored in-orbit by an In-Flight-Calibration (IFC) cycle, which measures the zero level and 60% of full scale for each range. Since the ion chambers are not disconnected from the preamplifier input during the IFC, any solar x-ray fluxes present will be added to the IFC signals. Normally the IFC will be valid for the two or three highest ranges, with only the lowest having a significant probability of solar x-ray flux interference. If desired, the XRS can be pointed off-sun to eliminate the x-ray flux interference with the IFC, but this is not usually necessary. Stable IFC data for the higher ranges indicates proper operation of the XRS electronics, and with high probability also verifies the lowest range when x-ray fluxes are present. The lower range IFC data can be corrected for the presence of solar x-ray signals by subtracting the pre- and post-IFC solar x-ray signals, although this leads to

greater signal uncertainties. If the solar x-ray signal is not in the lowest range, then the lowest range IFC signals will be saturated and of no use. Normal in-orbit operation performs an IFC measurement once per week, and this is sufficient to verify proper XRS operation over long time periods.

The GOES environment has high radiation levels, with expected maximum radiation doses for the five year lifetime being 10^5 rad(Si) for a spherical shielding thickness of about 1 g/cm^2 Al.[9] The electronics are designed for radiation hardness by use of radiation-hard devices or by shielding individual packages when necessary.

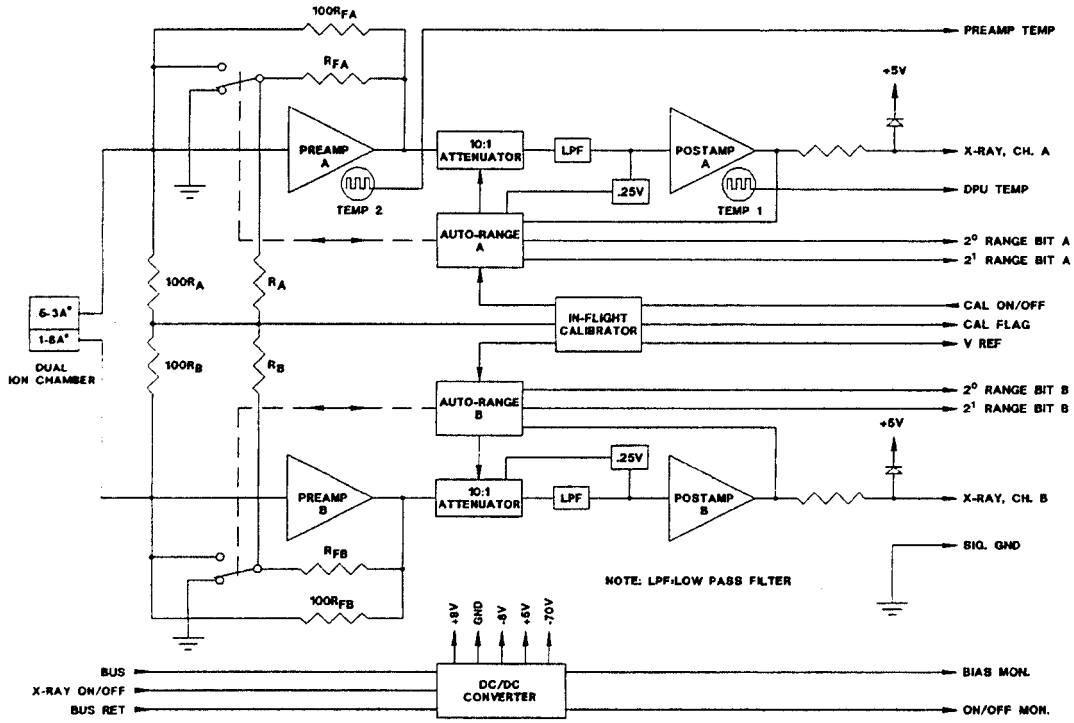

Figure 7. Block diagram of the XRS electronics.

4. DESIGN OF THE ION CHAMBER SHIELDING

The ion chamber response functions in Fig. 3 show that both chambers have some response to high energy x-rays with $\lambda < 1$ Å ($E_x > 12.4$ keV), particularly the A chamber. The worst case >2 MeV omnidirectional electron flux at geosynchronous orbit (160° W) is about 3.4×10^4 e/(cm^2-s),[9] while the XRS design specifications for GOES are that the XRS operate without interference from >1.9 MeV electron fluxes of 1.5×10^5 e/(cm^2-s). This requires considerable care in the design of the ion chamber shielding to minimize the effects of direct electron irradiation and of electron bremsstrahlung.

The basic ion chamber shielding configuration is shown in Fig. 2. Direct electron irradiation is minimized by the sweeper magnet, the electron baffles, and the various collimator assemblies. The sweeper magnet consists of sets of rare-earth-cobalt magnets with a soft iron return yoke. The field at the gap center is >1.3 kG and rises to >4 kG at the pole faces, which are 1 inch in diameter and separated by 1.5 inches. The magnetic field direction is such that electrons are bent up toward the B chamber, since this is a more effective shield for the larger window area A chamber. The integrated field strength along the FOV axis is >4.5 kG-cm, which is sufficient to shield both ion chamber windows from electrons below about 4 MeV on the worst-case trajectory. The baffles serve to collimate the incoming electrons parallel to the telescope FOV, and thus make the electron shielding by the magnet more effective. The ion chambers are shielded from electrons up to several MeV for most of the possible entering directions of the telescope aperture. The various collimators help shield the ion chambers from scattered electrons and from the electron bremsstrahlung.

An important part of the ion chamber shielding is from the electron bremsstrahlung produced in the outer walls of the XRS housing, especially the part surrounding the ion chamber. Since bremsstrahlung production is proportional to the square of the atomic number (Z) of the target material, while the x-ray absorption cross sections are larger for high Z materials, the best shielding design is to use a low Z material on the outside to reduce bremsstrahlung production and a high Z material inside to absorb the bremsstrahlung more effectively. In the XRS the ion chamber has walls of a minimum of 0.060 inch stainless steel (about 1.2 g/cm^2 Fe equivalent, Z = 26) and has 0.062 inch thick Pb (Z = 82) shields attached directly to the sides, top and bottom. A 0.062 inch thick enclosure of Al (Z = 13) with a 0.062 inch thick Pb shield attached encloses the entire ion chamber except for the FOV aperture. The outer housing for the ion chamber section is 0.100 inch thick Al with a final outer later of 0.062 inch thick Be (Z = 4). In this manner the outermost layers which stop the electrons are of low Z material (Be and Al), while the inner x-ray shielding is mostly by high Z material (Pb). Note that the collimators in the telescope assembly are also constructed in this low-Z/high-Z pairing.

An approximate upper limit response of the ion chambers to the electron bremsstrahlung was calculated using approximate functions for the electron stopping power, and bremsstrahlung yields for Be, Al, Fe and Pb of Berger and Seltzer.[10] The bremsstrahlung spectrum was approximated by a flat (in energy) spectrum[11], which is most accurate at low energies, but should still be a reasonable approximation up to a few MeV. Since electrons scatter significantly while stopping in matter, the bremsstrahlung generated were taken to be isotropic. A numerical integration was then used to approximate the ion chamber current generated by the worst case electron spectrum. This calculation took account of the fact that electrons generated in the ion chamber gases generally have a range longer than the chamber dimensions, and so only a part of the electron energy is absorbed by the gas.[12] A similar calculation was made for the current generated by direct electron irradiation through the shielding magnet, and gave results that were about 8% (A chamber) and 23% (B chamber) of the bremsstrahlung generated currents.[12] The calculated results are given in Table 2, along with the threshold x-ray flux currents and some beta source measurements.

The ion chamber responses to a 100 mCi Sr-Y-90 beta source (2.5 MeV end point energy) were measured with an Engineering Model (EM) XRS. The measurement is difficult, especially for the direct electron response which is easily contaminated by the bremsstrahlung produced in the beta source itself. The procedure and corrections have been described in detail, and the results compared with the threshold x-ray currents.[12] The results are listed in Table 2, along with the above discussed calculations. The agreement between the measurements and the calculations is reasonable, and both the calculations and the data show that in-orbit electron fluxes should not compromise the solar x-ray measurements. Note that the calculations and measurements take no account of the shielding by the XRS DPU or the spacecraft, so the results are upper limit, worst case responses, and in-orbit responses should be lower. This has been verified by in-orbit operations of the GOES-8 and GOES-9 XRS units, which have shown no noticeable effects from the ambient electron fluxes.

The XRS ion chambers may show some background current generation from high energy protons in solar particle events. Since we are currently near the minimum of the solar sunspot cycle there have been no significant solar proton events since the GOES-8 launch in April 1994. A large, high energy proton event will produce some background ion chamber currents, since it is impossible to shield the ion chambers from protons above a few tens of MeV, and the shielding magnet is not effective for protons in the MeV range. For such conditions the XRS will have to be pointed off-sun several times during the solar proton event to measure the proton-induced background current for subtraction from the on-sun current to provide the net x-ray flux current. The GOES EPS and HEPAD data[13] should be able to allow calculation of the XRS proton-induced background by interpolation between XRS off-sun measurements.

Table 2. Calculated and measured ion chamber electron responses		
Item	A Chamber	B Chamber
Nominal response threshold x-ray flux current	9.0×10^{-14} A	9.2×10^{-14} A
Calculated maximum electron flux bremsstrahlung response	2.5×10^{-14} A	1.0×10^{-14} A
Calculated maximum electron flux direct response	2.1×10^{-15} A	2.3×10^{-15} A
Corrected measured beta source bremsstrahlung response	3.9×10^{-14} A	1.1×10^{-14} A
Corrected measured beta source direct response	$<2.4\times10^{-14}$ A	$<2.7\times10^{-14}$ A

5. CALIBRATION OF THE XRS

The actual XRS ion chamber responses differ from the nominal responses of Eq. (5) because of slight variations in the Be window thicknesses, slight differences in fill gas pressure, and variations in the shielding of the charge collection anodes (which is actually neglected in the Eq. (5) responses). The ion chamber Be window thicknesses are obtained by measuring the area and mass before the windows are epoxied onto the ion chamber body. The gas fill pressures are nominally for 25°C, but the filling is usually done in a vacuum chamber at elevated temperature with the actual pressure at fill time being adjusted for the measured ion chamber temperature. The response of the completed ion chamber is checked with radioactive sources at several points on the window areas to verify window uniformity and the absence of epoxy wiped onto the sensitive area. The fill gases contain 0.4% He which is used to check the finished chamber for leaks, and the gas densities in Table 1 take this factor into account.

The first five XRS ion chambers for SMS and GOES were calibrated at a number of x-ray wavelengths by Unzicker and Donnelly[5], but for later ion chambers the calibration has been limited to use of one wavelength from calibrated radioactive sources. Since the detailed calibrations showed good agreement with the theoretical form of Eq. (1), the time and expense of doing a multiple wavelength calibration for later ion chambers has been replaced by calibration at one wavelength. The later ion chambers are calibrated by measurement of the ion chamber responses to a strong ^{55}Fe x-ray source, which has been calibrated against a standard ^{55}Fe source purchased from NIST (formerly the NBS). The absolute ion chamber response at the 5.9 keV (2.2 Å) x-ray line is used with the calibrated response of the XRS electrometer to produce the overall ratio of XRS signal current to input ion chamber x-ray flux.

Strong ^{55}Fe sources (sources are in the tens of mCi range) are calibrated against a NIST ^{55}Fe Standard Reference Material, which has a calibrated forward emission in K x-rays/(s-sr). Note that ^{55}Fe sources emit predominantly two Mn x-ray wavelengths: the $K_{\alpha1,2}$ x-rays at 5.895 keV (2.103 Å) with an intensity of 0.2268; and the $K_{\beta1,3}$ x-rays at 6.490 keV (1.910 Å) with an intensity of 0.0303. The different intensities and absorptions of these x-rays must be taken into account to produce accurate source and ion chamber calibrations. The source cross-calibrations are performed using a proportional counter and polyethylene attenuators. Since attenuations in excess of a factor of 10 are used, all attenuation data must account for the presence of the two different x-ray energies with different attenuation coefficients. The ^{55}Fe half life of 1009 days must also be taken into account to correct all measurements for source decay. The ion chambers are calibrated in vacuum using a fixture which holds a number of the calibrated strong ^{55}Fe sources at a fixed distance from the ion chamber. The ion chamber currents are then measured and used with the fixture geometry (there are correction factors for source parallax, and for x-ray intensity variation over the depth of the ion chamber because of $1/r^2$ variation with distance from the source), the absolute source intensities, and the response of Eq. (1) for the ^{55}Fe x-rays using the true window thicknesses, to derive a calibration constant for the chamber response. The result is a pair of calibration constants for the A and B chambers, given by

$$B_m = G_m(^{55}\mathrm{Fe})/\bar{G}_c(^{55}\mathrm{Fe}). \tag{6}$$

In Eq. (6)

$$G_m(^{55}Fe) = I_m(^{55}Fe)/J_x \quad (7)$$

where $I_m(^{55}Fe)$ is the measured ion chamber current and J_x is the corrected effective x-ray flux intensity at the ion chamber, and

$$\bar{G}_c(^{55}Fe) = (0.2268\ G_c(2.103\ \text{Å}) + 0.0303\ G_c(1.910\ \text{Å}))/0.2571 \quad (8)$$

where $G_c(\lambda)$ is the calculated response of Eq. (1) using the actual ion chamber Be window thickness. J_x must be calculated in A-m^2/W to match the units of Eq. (1). The calibration constants obtained from Eq. (6) are generally found to be close to 1.0, with the average for several chambers being within 5% of 1.0, and almost no ion chambers deviating from 1.0 by more than 10%. The estimated absolute accuracies of the calibration constants B_m are ±10% for the A chamber and ±15% for the B chamber, on a three standard deviation basis.

The response of the ion chamber in the XRS has two additional factors which must be included along with the absolute calibration constant of the bare chamber obtained from Eq. (6). First, the effect of the Be UV shield (0.3 to 0.5 mil thick) must be included in the calibrated response function, $G_{cal}(\lambda)$, and second the shielding effects of the electron baffles must be included. The Be UV shield was essential for the spinner XRS design, since the induced photoelectron current pulse on the ion chamber window when the FOV scans across the sun produces a small feedthrough into the ion chamber x-ray produced currents, and this would interfere with low level x-ray flux measurements[1]. The Be UV shield is not essential for the GOES-8 XRS design, but was retained to avoid possible problems from the photoelectron current and to provide some protection to the ion chamber from solar heating and long term UV irradiation. The Be UV shield also ensures that the XRS response curves, especially that for the B chamber, are nearly identical to the previous XRS units. The shielding effects of the electron baffles is purely geometric from the 0.015 inch thick stainless steel baffles, and are given by $F_{elbf} = 0.924$ for the A chamber and $F_{elbf} = 0.963$ for the B chamber.

The calibrated response functions are calculated from

$$G_{cal}(\lambda) = G_c(\lambda)\ T_{BeUV}(\lambda)\ B_m\ F_{elbf} \quad (9)$$

where $G_c(\lambda)$ is the response function of Eq. (1) calculated with the actual ion chamber Be window thickness and the Be UV shield transmission is given by

$$T_{BeUV}(\lambda) = e^{-\mu Be(\lambda)\ tBeUV} \quad (10)$$

where tBeUV is the measured thickness of the Be UV shield. The calibrated response constant for a flat (in wavelength) spectrum is calculated from

$$\bar{G}_{cal}(\Delta\lambda) = \int_0^\infty G_{cal}(\lambda)\ d\lambda/\Delta\lambda \quad (11)$$

which is identical to Eq. (4) except for the use of the calibrated response $G_{cal}(\lambda)$. Solar flare x-ray spectra are generally not flat in wavelength. For more accurate x-ray flux values the actual response functions $G_{cal}(\lambda)$ can be used to provide better estimates of the actual solar x-ray spectrum.[4] Thus use of the GOES XRS A and B chamber data can provide both a solar x-ray flux intensity and effective temperature.

The remaining part of the XRS calibration is the electronic gain for each chamber in each of the four output ranges. The calibration is made with a calibrated picoampere source during thermal vacuum testing of each XRS. These calibrations must be made in hard vacuum, since moisture in the air can affect the preamplifier feedback resistance in the highest gain range. The electronic calibrations are made at temperatures of -20°C and +25°C to allow for temperature correction of the in-orbit data. The calibrations provide both the offset voltage C_x (V) and the range gain S_x (A/V). The measured x-ray telemetry signal V_x (V) then gives the measured solar x-ray flux from

$$J_x(\Delta\lambda) = (V_x - C_x)/(S_x\ \bar{G}_{cal}(\Delta\lambda)). \quad (12)$$

Each GOES XRS unit is provided with a Calibration Report, which contains tabular listings of the $G_{cal}(\lambda)$ from Eq. (9) and the $\bar{G}_{cal}(\Delta\lambda)$ from Eq. (10) for the A and B chambers. The Calibration Report also provides the calibrated values of C_x and S_x for each of the four ranges, and the IFC output values for each of the four ranges, all at two temperatures (generally -20°C and +25°C) for both the A and B chambers. The Calibration Reports are designated by the XRS Serial Number (SN), with the 3-axis stabilized XRS designs starting at SN/001; GOES-8 has XRS SN/002,[14] while GOES-9 has XRS SN/001.[15]

6. ACKNOWLEDGMENTS

The GOES-8 version of the XRS was developed by the Space Instrumentation Division (SID) of Panametrics, Inc. under the sponsorship of the NOAA. The electronics design was done under the supervision of Jean L. Hunerwadel, who has since retired from the SID. Much of the work was contracted through Space Systems/Loral. We would also like to acknowledge the technical support of Richard N. Grubb of the NOAA Space Environment Center in Boulder, CO.

7. REFERENCES

1. R. F. Donnelly, "SMS-GOES solar soft x-ray measurements, Part I. SMS-1, SMS-2, and GOES-1 measurements from July 1, 1974, through December 31, 1976," *NOAA Tech. Memo. ERL SEL-56*, Space Environ. Center, Boulder, CO, 1981.

2. R. F. Donnelly, "SMS-GOES solar soft x-ray measurements, Part II. SMS-2, GOES-1, GOES-2 and GOES-3 measurements from January 1, 1977, through December 31, 1980," *NOAA Tech. Memo. ERL SEL-57*, Space Environ. Center, Boulder, CO, 1981.

3. S. D. Bouwer, R. F. Donnelly, J. Falcon, A. Quintana and G. Caldwell, "A summary of solar 1-8Å measurements from the SMS and GOES satellites, 1977-1981," *NOAA Tech. Memo. ERL SEL-62*, Space Environ. Center, Boulder, CO, 1982.

4. R. F. Donnelly, R. N. Grubb and F. C. Cowley, "Solar x-ray measurements from SMS-1, SMS-2, and GOES-1, information for data users," *NOAA Tech. Memo. ERL SEL-48*, Space Environ. Center, Boulder, CO, 1977.

5. A. Unzicker and R. F. Donnelly, "Calibration of x-ray ion chambers for the space environment monitoring system," *NOAA Tech. Report ERL 310-SEL 31*, Space Environ. Center, Boulder, CO, 1974.

6. B. L. Henke and R. L. Elgin, "X-ray absorption tables for the 2-to-200Å region", in *X-Ray Analysis, Vol 13*, B. L. Henke, J. B. Newkirk and G. R. Mallett, editors, 639-665, Plenum Press, NY, 1970.

7. F. Wuilleumier, "Determination of mass-attenuation coefficients in Krypton and Argon by continuous analysis between 8 and 0.8 keV," *Phys. Rev. A6*, 2067-2077, 1972.

8. E. F. Plechatz and J. R. Terrall, "Photon cross sections 1 keV to 100 MeV," *UCRL-50400, Vol. VI; TID-4500, UC-34*, LRL Univ. of CA, Livermore, CA, 1968.

9. E. G. Stassinopoulos and J. M. Barth, "The space radiation environment for GOES missions," *NASA Report X-601-84-2*, Goddard Space Flight Center, Greenbelt, MD, 1984.

10. M. J. Berger and S. M. Seltzer, "Tables of energy losses and ranges of electrons and positrons," *Report NASA SP-3012*, NASA, Washington, DC, 1964.

11. R. D. Evans, *The Atomic Nucleus*, McGraw-Hill, NY, 1955.

12. "Test report on telescope effectiveness of shielding," *NXT-ENG-103*, report submitted to Ford Aerospace and Communications Corp., Panametrics, Inc., Waltham, MA, 1987.

13. F. B. Sellers and F. A. Hanser, "Design and calibration of the GOES-8 particle sensors: the EPS and HEPAD," *SPIE Proceedings 2812*, this volume, 1996.

14. "Calibration report for x-ray sensor (XRS) SN/002," *NXT-CAL-115, Rev. A*, report submitted to Space Systems/Loral, Inc., Panametrics, Inc., Waltham, MA, 1995.

15. "Calibration report for x-ray sensor (XRS) SN/001," *NXT-CAL-114, Rev. A*, report submitted to Space Systems/Loral, Inc., Panametrics, Inc., Waltham, MA, 1995.

Design and calibration of the GOES-8 particle sensors: the EPS and HEPAD

Francis B. Sellers and Frederick A. Hanser

Panametrics, Inc.
221 Crescent St., Waltham, Massachusetts 02154

ABSTRACT

The Energetic Particle Sensor (EPS) and the High Energy Proton and Alpha Detector (HEPAD) measure protons, alpha particles and electrons in several energy ranges. The latest version of the EPS for GOES-8 and succeeding GOES spacecraft detects protons in 7 energy ranges from 0.8 to 500 MeV, alpha particles in 6 energy ranges from 4 to 500 MeV, and electrons in 3 integral channels of 0.6, 2 and 4 MeV. The HEPAD measures protons in four energy ranges from 350 to greater than 700 MeV, and alpha particles in 2 energy ranges from 2560 to greater than 3400 MeV. Most of the particle channel responses of the EPS and HEPAD have been calibrated directly at available accelerators. The GOES particle data are used to monitor the ambient, trapped, particle radiation, which is predominantly MeV electrons, and the proton and alpha particle fluxes from solar particle events. The data are used for various types of warnings and are archived by the NOAA Space Environment Center.

Keywords: Solar particle detection, particle detectors, spacecraft instruments, proton sensors, electron sensors

1. INTRODUCTION

The GOES spacecraft have had ambient particle monitors since the initial SMS spacecraft in the 1960s. The initial spacecraft had only an EPS which measured protons, alpha particles and electrons. The HEPAD was added later to provide early warning of very high energy solar proton fluxes which could be a hazard to high altitude aircraft flying over the earth's polar cap regions and to manned spaceflight missions.

The EPS consists of two separate units, the Dome and the Telescope, with the Dome covering the upper end of the ~1 to 500 MeV energy range measured by the EPS. Actually, the GOES particle sensors operate as a single sensor system, as shown in the block diagram in Fig. 1. The Signal Analyzer Unit/Data Processing Unit (SAU/DPU) provides all interfaces with the spacecraft, and it controls and receives data from the three sensor assemblies.

The EPS is located in the main body of the spacecraft, with the Dome and Telescope view directions in the West, i.e., detected particles travel East at the GOES location. The HEPAD is located next to the EPS and views in the anti-Earth direction. On the spinning GOES-7 and earlier spacecraft the EPS and HEPAD viewed in the spacecraft equatorial plane, which allowed viewing of a large range of particle arrival directions and a measurement closer to the local isotropic particle flux. For the 3-axis stabilized GOES-8, the location near the outer boundary of the earth's magnetosphere provides some scattering of solar particles, so the measurements are not expected to differ significantly from those of the earlier, spinning GOES.

The following sections contain descriptions of the GOES-8 particle sensor designs and operation, with special attention to the calibration data.

2. DESIGN AND OPERATION OF THE EPS

The present EPS uses two detector sets, the Telescope and the Dome, which detect and sort the particles by suitable energy deposition measurements. The EPS Telescope consists of two silicon surface barrier solid state detectors (SSDs) operated in a coincidence/anti-coincidence mode for particle selection in a series of energy bins, while the Dome utilizes three independent SSD sets in highly-shielded configurations, to measure particles above several integral energy thresholds. The Telescope detects protons (0.8 - 15 MeV) in three energy bins, and also alpha particles (4-60 MeV) in three energy bins. The Dome detects electrons (>0.6 to > 4.0 MeV) above three integral energy thresholds, protons (15-500 MeV) above four such energy thresholds, and alpha particles (60-500 MeV) above three such energy thresholds. These two units, the Telescope and the Dome, are described in detail below.

2.1 Telescope

The block diagram of the Telescope in Fig. 2 shows the interfaces to the SAU/DPU (Fig. 1). The detailed design of the Telescope, provided in Fig. 3, shows how the two SSDs are mounted to form the aperture's Field-of-View (FOV), with a 50-micron thick, 100 mm^2 front detector, and a 500-micron thick, 200 mm^2 rear detector (detectors D1 and D2). Tungsten is used for the collimators, and as shielding for out-of-aperture particles. Magnets shield the detectors from direct irradiation by electrons of less than about 100 keV.

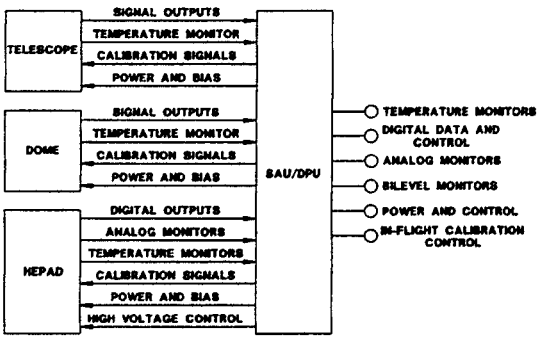

Figure 1. Particle sensor - system block diagram.

Fig. 4 shows the calculated energy losses in both the front and rear detectors, for normally-incident protons and alpha particles. The parametric values along each curve are the energies of the incident particles that produce the energy losses at those particular points on the curves. The maximum half-angle of incidence allowed by the collimation is 35°, and that is taken into account in defining the average energy widths of the bins, determined by the energy deposition threshold levels (numbered 1-5) in the figure. Table 1 shows the actual values of these energy loss threshold levels, the coincidence/anti-coincidence logic associated with each of the energy bins, and the channel designations, as shown in Fig. 4.

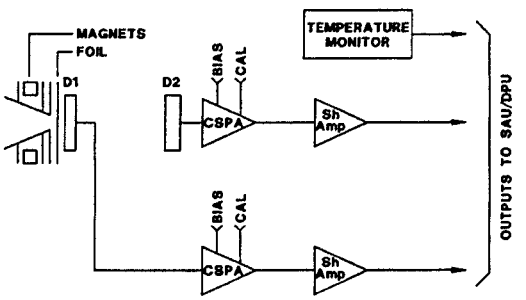

Figure 2. EPS Telescope block diagram.

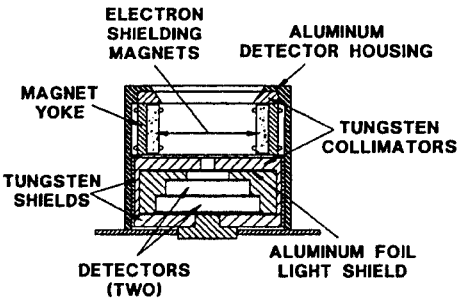

Figure 3. EPS Telescope detector cross section.

2.2 Dome

The block diagram of the Dome in Fig. 5 shows the interfaces to the SAU/DPU (Fig. 1). The detailed design of the Dome, provided in Fig. 6, shows how a set of two 1500-micron thick, 25 mm^2 silicon surface barrier detectors is mounted in each of the Dome assemblies (detectors D3-D5). The two output pulses are summed, to produce the energy deposition signal analyzed by the threshold circuitry. Tungsten shielding of > 20 g/cm^2 is used for collimation and for out-of-aperture shielding. This shields completely for protons below about 120 MeV. Hence, it is very effective for the two lowest energy Domes (D3 and D4), but the response becomes significantly omnidirectional for the highest energy particles detected by D5. These effects were measured during the calibrations reported in Section 4.2.

Energy deposition calculations were carried out for all three Domes shown in Fig. 6,[1,2] in order to define the threshold levels required to define the energy bins of interest. A typical set of calculations is shown in Fig. 7, for the D4 Dome. The maximum half-angle of incidence is 60°, at which angle the particles miss the second detector, and the pathlength is the same as for a normal incidence particle penetrating both detectors. These angles produce the minimum pathlength. The maximum pathlength occurs for a 45° half-angle particle, which just penetrates both detectors. For electrons, the energy deposition is severely affected by scattering. Shown in Fig. 7 are the two limits: the lower two curves are based simply on stopping power calculations[2], while

Table 1. EPS Telescope thresholds and energy bin logic			
Detector	Threshold	Energy Loss (MeV)	
Front/D1	1	0.325	
Front/D1	2	0.49	
Front/D1	3	2.92	
Rear/D2	4	3.20	
Rear/D2	5	14.2	
Energy bin logic requirements			
Channel	Particle		Logic
	Type	Energy (MeV)	
P1	Proton	0.8-4.2	$1\cdot2\cdot\bar{3}\cdot\bar{4}$
P2	Proton	4.2-8.7	$1\cdot2\cdot\bar{3}\cdot4\cdot\bar{5}$
P3	Proton	8.7-14.5	$1\cdot\bar{2}\cdot4\cdot\bar{5}$
A1	Alpha	3.8-9.9	$1\cdot3\cdot\bar{4}$
A2	Alpha	9.9-21.3	1·3·4
A3	Alpha	21.3-61.0	$1\cdot2\cdot\bar{3}\cdot5$

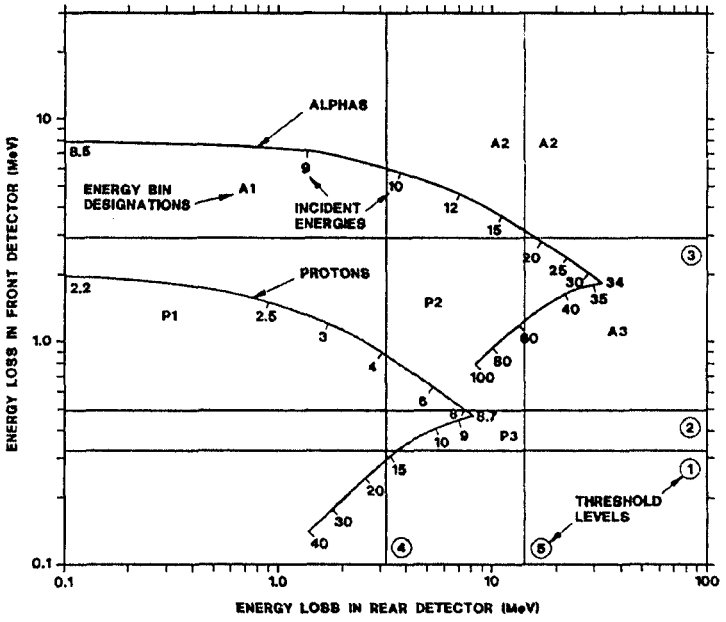

Figure 4. EPS Telescope energy loss and threshold levels diagram.

the upper curve assumes that the entire energy remaining, after passing through the moderator, is deposited in the detector--due to multiple scattering effects. Thus, for example, threshold 10 is used with the D4 Dome to define the 4 MeV integral-type energy bin for electrons.

Table 2 shows, for all three Domes, the actual values of the energy loss thresholds, the coincidence/anti-coincidence logic associated with each of the energy bins, and the channel designations (with E3, P5, and A5 being shown in Fig. 7). Note that the EPS units on GOES-7 and earlier only had one electron channel, equal to the E2 channel of the GOES-8 design.

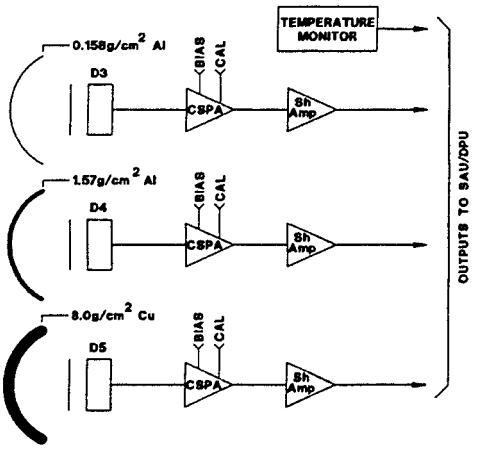

Figure 5. EPS Dome block diagram.

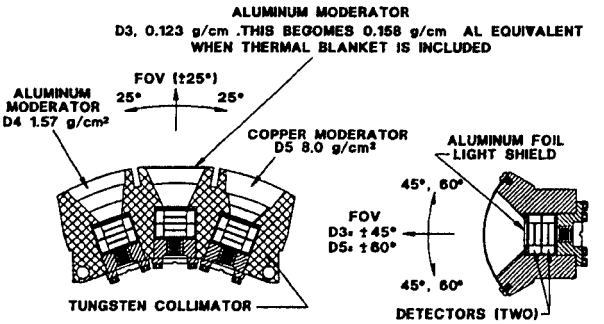

Figure 6. EPS Dome detector cross section.

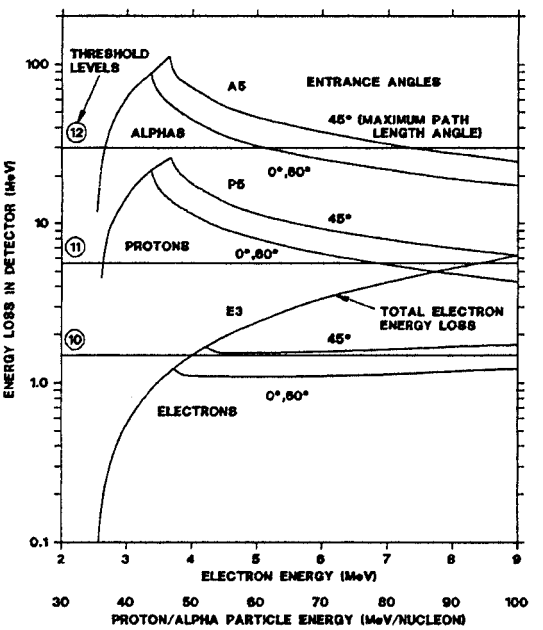

Figure 7. EPS Dome D4 energy loss and threshold levels diagram.

3. DESIGN AND OPERATION OF THE HEPAD

The HEPAD is designed to measure high energy (relativistic) protons and alpha particles in the presence of intense fluxes of lower energy particles. The basic design is a solid state detector (SSD) telescope with a quartz Cerenkov radiator/PMT for detection of the relativistic particles.

The block diagram of the HEPAD in Fig. 8 shows the interface to the SAU/DPU (Fig. 1). In contrast to the Telescope and Dome, the HEPAD contains the necessary logic circuitry to define the digital outputs, for the channel designations shown. These channels are discussed below.

Table 2. EPS Dome thresholds and energy bin logic		
Detector	Threshold	Energy Loss (MeV)
D3	6	0.25
D3	7	1.77
D3	8	10.5
D3	9	40.0
D4	10	1.53
D4	11	5.6
D4	12	30.0
D5	13	1.6
D5	14	3.5
D5	15	28.0

Energy bin logic requirements			
Channel	Particle		Logic
	Type	Energy (MeV)	
P4	Proton	15-40	$6 \cdot 8 \cdot \overline{9}$
P5	Proton	36-80	$10 \cdot 11 \cdot \overline{12}$
P6	Proton	80-180	$13 \cdot 14 \cdot \overline{15}$
P7	Proton	165-500	$13 \cdot \overline{14}$
A4	Alpha	60-180	9
A5	Alpha	145-250	12
A6	Alpha	320-500	15
E1	Electron	≥ 0.55	$6 \cdot \overline{7}$
E2	Electron	≥ 2	$6 \cdot 7 \cdot \overline{8}$
E3	Electron	≥ 4	$10 \cdot \overline{11}$

The detailed design of the HEPAD detector assembly is provided in Fig. 9. The principal energy-determining sensor is the Cerenkov radiator, which is inherently discriminatory against low energy particles (≤ 350 MeV for protons, ≤ 640 MeV/nucleon for alpha particles). The front surface of the Cerenkov radiator is painted black to reduce response from rear entry particles. In order to define the approximately 0.9 cm^2-sr geometric factor, the radiator output is placed in coincidence with the two 500-micron thick silicon, 3 cm^2 (SSD) surface barrier detectors. The outer aluminum housing and shield stop most electrons and reduce bremsstrahlung production. The tungsten inner shield stops lower energy protons and shields the SSDs from bremsstrahlung. In flight calibration is provided by light pulses from the "alpha lamp," a combination of a low-intensity ^{241}Am alpha-emitting radioactive source with a plastic scintillator.

Energy deposition calculations for the SSDs[1] were combined with the theoretical Cerenkov radiator response[3] to define the SSD energy loss and PMT photoelectron thresholds required to establish the desired energy bins. The results are provided in Fig. 10.

The HEPAD SSD energy losses show almost no variation for protons > 350 MeV, so the proton energy separation is only through the Cerenkov light variation. The latter saturates above 1000 MeV, so in practice it becomes difficult to separate proton energies above about 700-800 MeV. Alpha particles are separated from protons by the SSD energy losses, as well as the Cerenkov light pulse amplitude. The general features of the theoretical calculations shown in Fig. 10 are, in fact, valid, but the actual proton energies are somewhat different, based on the calibration data (Section 5). Table 3 shows the actual values of the energy loss and photoelectron thresholds, the coincidence/anti-coincidence logic associated with each of the energy bins, and the channel designations. In addition to these channels, diagnostic measurements are also made of four singles and one fast coincidence channel, designated S1-S5 in Fig. 8.

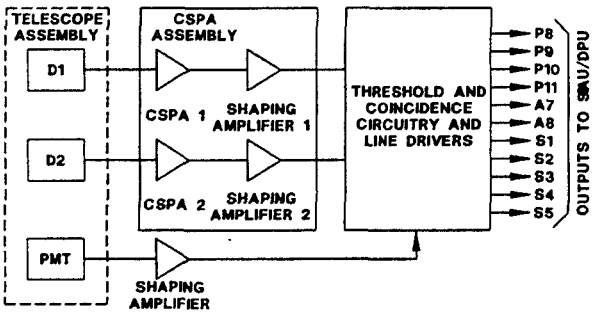

Figure 8. HEPAD block diagram.

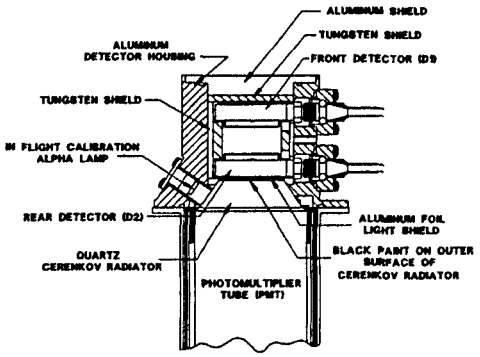

Figure 9. HEPAD detector cross section.

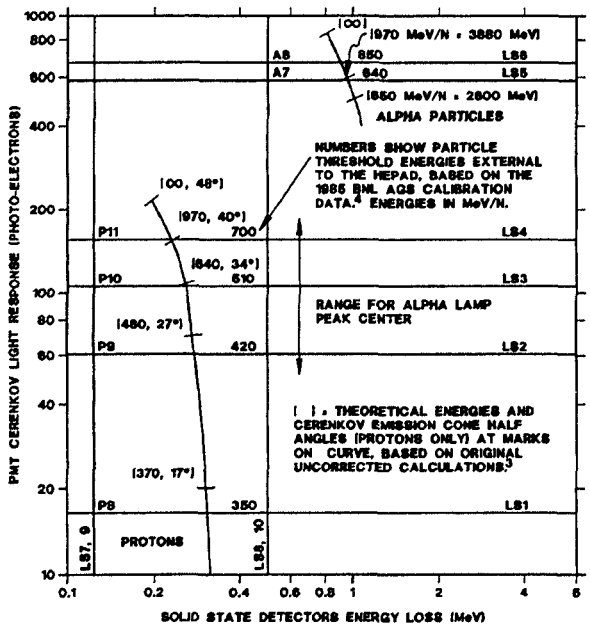

Figure 10. HEPAD energy loss and threshold levels diagram.

The particle energies required to exceed any particular HEPAD pe threshold (Table 3) depend on the PMT gain, which is adjustable by changing the HV setting through ground command. The gain is monitored by measuring the count rates of the two

lowest thresholds, LS1 and LS2 (= S3 and S4 counts), for the alpha lamp light pulses. One HV step changes the PMT gain for the thresholds by about 5%, and, in general, changes the S4/S3 count rate ratio by about 0.1 (at S4/S3 = 0.5). The actual detected particle energies may thus vary with time if the PMT gain changes and is not adjusted by the necessary HV step changes.

4. CALIBRATION OF THE EPS

The EPS was calibrated with protons and alpha particles up to about 40 MeV at a tandem Van de Graaff accelerator at Brookhaven National Laboratory (BNL), and with protons up to about 150 MeV at the Harvard University Cyclotron. Additionally, the Dome electron channels were calibrated at the Rome Air Development Center (RADC) electron linear accelerator, at Hanscom AFB, MA. In all instances, we were able to rotate the sensor assemblies in such a way as to determine the angular response for at least one energy--usually more than one. The purpose of the cyclotron measurements for the Telescope was to determine the spurious response to such out-of-aperture high energy protons, over entrance angles up to 180° from the entrance direction.

Table 3. HEPAD Thresholds and energy bin logic

Detector	Threshold	Energy loss (MeV) or photoelectrons (pe) emitted
PMT	LS1	13.5 pe
PMT	LS2	69 pe
PMT	LS3	114 pe
PMT	LS4	164 pe
PMT	LS5	608 pe
PMT	LS6	729 pe
Rear SSD	LS7	0.125 MeV
Rear SSD	LS8	0.500 MeV
Front SSD	LS9	0.125 MeV
Front SSD	LS10	0.500 MeV

Energy bin logic requirements

Channel	Particle		Logic
	Type	Energy (MeV/nucleon)	
P8	Proton	350-420	P·$\overline{LS2}$
P9	Proton	420-510	P·LS2·$\overline{LS3}$
P10	Proton	510-700	P·LS3·$\overline{LS4}$
P11	Proton	> 700	P·LS4·$\overline{LS5}$
A7	Alpha	640-850	A·LS5·$\overline{LS6}$
A8	Alpha	> 850	A·LS6

C = Fast Coincidence of PMT (LS1), D1 (LS9) and D2 (LS7)
P = Slow Coincidence of $\overline{LS8}$, $\overline{LS10}$, and C
A = Slow Coincidence of LS8, LS10, and C

If it is assumed that the incident particle spectrum j(E) $(cm^2\text{-sr-s-MeV})^{-1}$ is isotropic within the aperture of the sensor, then the detector count rate c (cps) can be written

$$c = \int_0^\infty j(E)\, G(E)\, dE \tag{1}$$

where G(E) (cm^2-sr) is the geometric factor for energy E (MeV), and is obtained from the calibration data. The measured in-orbit count rates c are converted to a first-order spectrum point by assuming that j(E) is independent of energy. Under this assumption the integral in (1) can be evaluated and the particle flux obtained from the measured count rate c_m as

$$j(E_0) = c_m/G_E \tag{2}$$

where E_0 (MeV) is the average energy of the detected particles and G_E (cm^2-sr-MeV) is the energy-geometric factor. The values of E_0 and G_E are calculated using the calibrated values of G(E) from

$$G_E = \int_0^\infty G(E)\, dE \tag{3}$$

$$E_0 = \left(\int_0^\infty E\, G(E)\, dE\right)/G_E \tag{4}$$

The calibration values of G(E) are calculated from detection areas measured at several angles in the FOV and integrating over solid angle. The detection areas are obtained by comparing the measured channel count rate against that of a pair of calibrated monitor detectors, in a monoenergetic particle beam.[5,7]

4.1 Telescope

The EPS telescope was calibrated at the BNL tandem Van de Graaff accelerator[5] for protons up to 25 MeV and for alpha particles up to 40 MeV. Extensive angular response measurements were made up to a 40° entrance angle at 5° intervals. At the Harvard Cyclotron[5], proton measurements were made at energies between about 33 and 144 MeV at 0° entrance angle, and at several energies between 60 and 90 MeV for angles up to 180°--mainly to determine the spurious response.

At BNL the accelerator-produced proton beam impinged upon a scattering foil, and the Telescope, and a scattered-beam intensity monitor detector, were set up at angles β to the beam direction, on opposite sides of the beam. The BNL experimental angular response data obtained were integrated over entrance angle, including the effect of solid angle variation with entrance angle, to provide the results given in Figs. 11 and 12.

Two factors require explanation in the proton data shown in Fig. 11. At high energies (channel P3), some particles are not counted due to their loss below threshold level 1 (Fig. 4) as a result, principally, of energy loss straggling in the front detector. Thus, the P3 decrease at high energies is not sharp. In fact, the maximum value of G(E) near 12 MeV does not quite reach the theoretical maximum of about 0.056 cm^2-sr because of this effect.

In the low energy proton bin, P1, the geometric factor exceeds that expected (the alpha particle low energy geometric factor, Fig. 12, is generally as expected). The scattering cross section from the foil is proportional to the factor $\sin^{-4}(\beta/2)$, which varies strongly with scattering angle β. A 20% variation in scattered intensity is caused by about 1° variation in β. Such a variation could easily be caused by the earth's field (for 1-5 MeV protons) following the last focusing magnets in the beam line. The effect would be much less for alphas due to their greater mass. A similar effect was also seen in the GOES B and C instruments[6]. We believe the P1 channel low energy proton data should be normalized downward somewhat, in such a way that the peak of G(E) is located as expected, while the variation of G(E) with E is retained.

With the exception of channel P1, all of the measured results are within ± 8% of an analytically determined[5] maximum G(E) value of 0.0557 cm^2-sr. We cannot, however, state with certainty that any particular experimental problem caused this effect. Nevertheless, we know no reason that it should be higher than the analytical maximum. Our best judgment is that the correct value is nearer 0.056 cm^2-sr, within the experimental uncertainties.

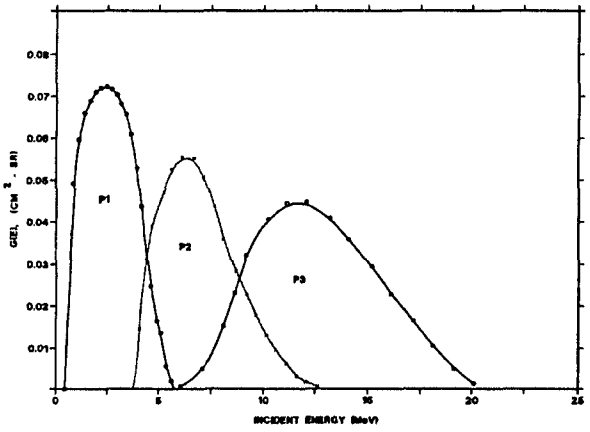

Figure 11. Telescope proton energy dependent geometric factors.

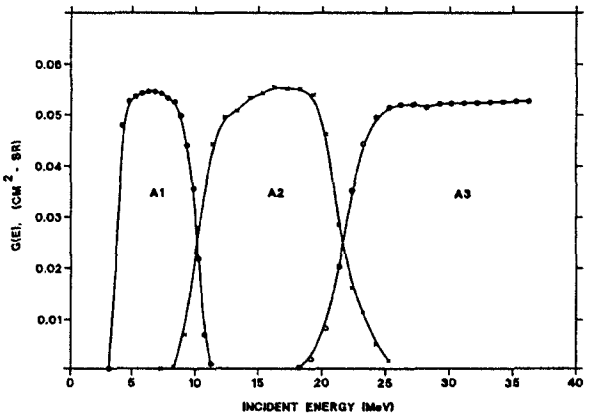

Figure 12. Telescope alpha particle energy dependent geometric factors.

The only significant spurious effects expected are due to very energetic protons that can penetrate the out-of-aperture shielding of the Telescope. Although all alpha channels are affected to a small degree by > 100 MeV protons, none are affected significantly by lower energies, except for a very narrow region near 90 MeV that affects A2. The method of approach was to determine the results expected analytically, correlate these with experimental data, and combine the two approaches to obtain the best estimate of the spurious geometric factors. Because the problem is one of, essentially, finding the background effects in the primary channels, the variation of the spurious G(E)s with E was not measured in the same detail as it was for the in-aperture particles. Since both the out-of-aperture solid angle, and the sensitive energy range (10 to 100 MeV) are large, the resulting spurious counts would be significant for essentially flat energy spectra. Nevertheless, for the Telescope these spurious counts will usually be only a small correction to the primary count, because the shape of solar particle spectra are such that the flux normally decreases rapidly with energy. A condition in which this is not true, however, can occur in the first few hours of a solar particle event, when only the most energetic particles have had time to arrive. In that instance, the Dome data should be used to calculate the corrections, and these should only be applied when they represent small corrections to the observed Telescope count rates.

A summary of the above calculations has been provided in a detailed report (Ref. 7, Table 3.15), with the results being reproduced in Section 6 below.

4.2 Dome

The EPS Dome was calibrated with protons at the Harvard Cyclotron[7] up to about 144 MeV. Because of the wide angular response of the three Domes (Fig. 6), it was necessary to make measurements over the entire angular response range for each dome, usually in 10° or 15° intervals. Results for the P5 and E3 channel in the D4 Dome (Fig. 7) are shown in Fig. 13, where the proper solid angle values have been used to obtain the angle-integrated geometric factors. As can be seen from the energy loss curves in Fig. 7, sufficiently energetic protons can lose small enough amounts of energy in these detectors to be counted in the E3 channel (i.e., below threshold 11)--hence the form of proton response shown in Fig. 13 for E3.

The spurious, out-of-aperture, energy-dependent geometric factors were calculated for all three Domes[7]. The results show that it is necessary only to include the in-aperture G(E) data for Domes D4 and D5, because most solar proton event spectra decrease rapidly with E. For Dome D6, however, it is necessary to include both the spurious and in-aperture G(E) data. A summary of these calculations has been provided in a detailed report (Ref. 7, Table 3.15), with the results being reproduced in Section 6 below.

The electron response of the Dome electron channels E1, E2, and E3 (Table 2) was measured at the RADC electron linear accelerator[8]. The facility can provide analyzed beams in the range 5-15 MeV. The 5 MeV beam was degraded by use of aluminum absorbers to obtain three lower energies, down to about 1 MeV. We also supplemented these measurements for the D3 Dome E1 and E2 electron channels with Sr-Y-90 and Ru-Rh-106 beta sources. The total air path to the Dome detector was

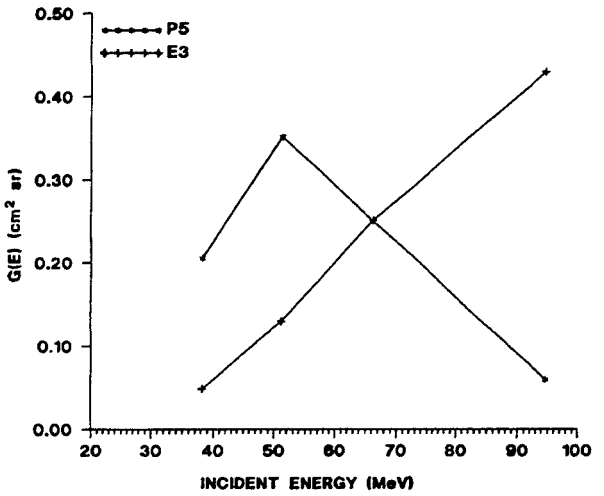

Figure 13. D4 Dome proton energy dependent geometric factors.

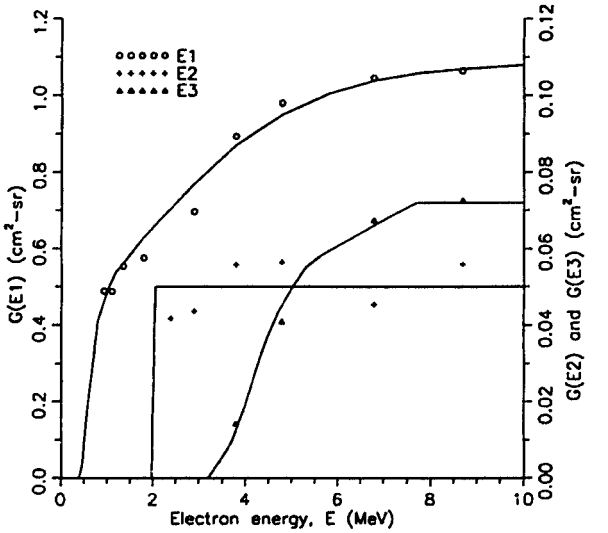

Figure 14. Dome electron channels energy dependent geometric factors.

about 0.15 g/cm^2, and this was used to correct the beta spectra in the data analysis. The Sr-Y-90 beta source has 546 keV (maximum) electrons from Sr-90 and 2.27 MeV (maximum) electrons from Y-90, so the source can be considered as emitting only a Y-90 spectrum. For the Ru-Rh-106 beta source, the Ru-106 has a 39-keV endpoint and Rh-106 a 3.54-MeV endpoint, so the source is effectively only Rh-106 for calibration purposes.

Angular response measurements were made up to entrance angles of about 60°, and those were used, along with the angular-dependent solid angle factors, to calculate the energy-dependent geometric factors in Fig. 14. These response curves demonstrate clearly the integral character of these particular channels. Hence, it is not possible to obtain meaningful values of G_E and E_0 by use of Eqs. (2), (3), and (4), as it is for the proton responses. Accordingly, in order to determine an on-orbit electron spectrum by use of the three E1, E2, and E3 counts, it would be necessary to utilize the energy dependencies shown in Fig. 14, and determine the assumed electron spectrum parameters by fitting the count data.

5. CALIBRATION OF THE HEPAD

The HEPAD has been calibrated extensively with high energy protons at the BNL Alternating Gradient Synchrotron (AGS), using a secondary beam, magnets for coarse energy selection, and a time-of-flight (TOF) system for fine energy selection[9]. We verified earlier angular response[4] measurements which showed that the response at a 12° entrance angle was the same as that averaged over the entrance aperture, including the solid angle variation. The relative response for the P8-P11 channels (Table 3) is shown in Fig. 15. We were able to normalize the curves to obtain the actual geometric factors by use of the absolute count rate of the front SSD, the PMT, and the known areas. We also measured the response to rear entry protons, where we found that the P10 and P11 channel responses can be neglected for essentially all energies. There are small correction factors for the P8 and P9 channels' response to very relativistic particles.

The cross-over points between the energy bins shown in Fig. 10 are marked in Fig. 15. The initial Cerenkov emission calculations[3] neglect the effects of collection efficiency variation in the Cerenkov radiator PMT due to emission cone half angle variation with energy. These are largely responsible[4] for the differences between the measured bin cross-over energies and those calculated earlier.[3]

6. SUMMARY OF GEOMETRIC FACTOR RESULTS

The 1995 Calibration Report[7] on the EPS Dome proton response was used to summarize all of the earlier geometric factor results described above, as given in Table 4. Note, in particular, that these electron channel responses are for protons (Section 4.2); their response to electrons is provided in Fig. 14.

Table 4. Summary of EPS/HEPAD channel response factors

Channel (Sensor*)	Average Particle Energy E_0 (MeV)	G_{E0} (cm^2-sr-MeV)	Particle Energy Range (MeV)
P1 (T)	2.5	0.194	0.74 - 4.2
P2 (T)	6.5	0.252	4.2 - 8.7
P3 (T)	11.6	0.325	8.7 - 14.5
P4 (D)	30.6	5.21	15 - 40
P5 (D)	63.1	14.5	38 - 82
P6 (D)	165.	129.	84 - 200
P7 (D)	433.	839.	110 - 900
P8 (H)	375.	65.7	330 - 420
P9 (H)	465.	65.7	420 - 510
P10 (H)	605.	139.	510 - 700
P11 (H)	(> 700.)	(G = 0.73 cm^2-sr)**	> 700
A1 (T)	6.9	0.342	3.8 - 9.9
A2 (T)	16.1	0.638	9.9 - 21.3
A3 (T)	41.2	2.22	21.3 - 61.
A4 (D)	120.	21.	60 - 160
A5 (D)	210.	36.	160 - 260
A6 (D)	435.	176.	330 - (500)
A7 (H)	2980.	613.	2560 - 3400
A8 (H)	(> 3400.)	(G = 0.73 cm^2-sr)**	> 3400
E1 (D)	638.	686.	15 - 1000
E2 (D)	348.	536.	15 - 800
E3 (D)	360.	480.	38 - 800

*T: EPS Telescope; D: EPS Dome; H: HEPAD.
**G is the geometric factor for an integral flux $(cm^2\text{-sr-s})^{-1}$, above the energies shown.

NOTES: Pi channel responses are for protons; Ai channel responses are for alpha particles. Ei channel responses are for protons. The HEPAD channel responses are for the PMT gain set to the correct value.

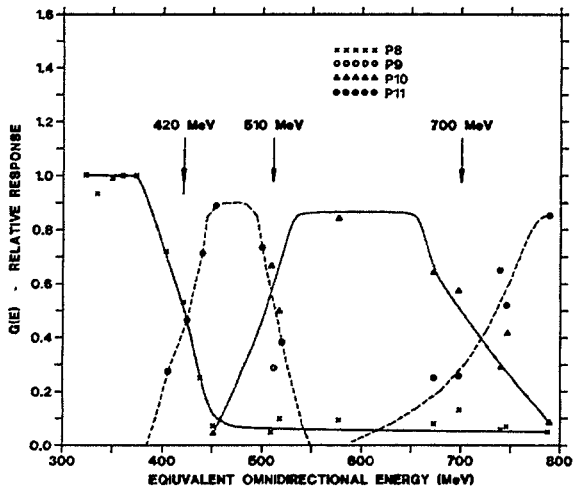

Figure 15. HEPAD proton channel energy dependent geometric factors, relative responses.

7. ACKNOWLEDGMENTS

This instrumentation was developed by the Space Instrumentation Division (SID) of Panametrics, Inc. under the sponsorship of the NOAA. The electronics design was done under the supervision of Paul R. Morel, who manages the Systems Department of the SID. Much of the work was contracted through Hughes Aircraft Company's Space and Communications Group, and through Space Systems/Loral. Some of the calibration work was supported directly by NOAA, with calibration facility support by Brookhaven National Laboratories and by the Rome Air Development Center facility at Hanscom, AFB.

We are pleased to acknowledge the continuing technical support of Mr. Richard N. Grubb and Mr. Herbert H. Sauer of NOAA's Space Environment Center in Boulder, CO.

8. REFERENCES

1. J.F. Hanni, "Calculations of energy loss, range, pathlength, straggling, multiple scattering, and the probability of inelastic nuclear collisions for 0.1 to 1000-MeV protons," *Technical Report No. AFWL-TR-65-150, AFWL/AFSC*, Kirtland AFB, NM, 1966.

2. M.J. Berger and S.M. Seltzer, "Tables of energy losses and ranges of electrons and positrons," *Report NASA SP-3012*, NASA, Washington, DC, 1964.

3. M.C. Rinehart, "Cerenkov counter for spacecraft application," *Nucl. Inst. and Meth.* 154, 303-316, 1978.

4. "Report on the Proton Calibration of HEPADs SN6 and SN9 at the Alternating Gradient Synchrotron of Brookhaven National Laboratory," *PANA-NOAA-CAL1*, submitted to NOAA/ERL/SEL, Panametrics, Inc., Waltham, MA, 1986.

5. "GOES D, E, F progress report, energetic particle sensor telescope calibration work, analysis report," *PANA-GOESP-CR2*, submitted to Hughes Aircraft Company, Panametrics, Inc., Waltham, MA, 1979.

6. M.C. Rinehart, "SMS - A, B, C EPS Calibration," *3G4600-74-079, Rev. A, SMS-PCC-6252*, Philco-Ford Corporation, 1974.

7. "Calibration report for the EPS Dome sensor response to protons," *NXT-CAL-102*, submitted to Space Systems/Loral Inc., Panametrics, Inc., Waltham, MA, 1995.

8. "GOES I, J, K, L & M EPS Dome electron channel calibration report," *NXT-CAL-101*, submitted to Ford Aerospace Corporation., Panametrics, Inc., Waltham, MA, 1988.

9. "Report on the proton calibration of HEPAD SN 002 consisting of HEPAD: FAC PN 571774-01, Serial No. 002 at the Alternating Gradient Synchrotron of Brookhaven National Laboratory," *NXT-CAL-107*, submitted to Ford Aerospace Corporation., Panametrics, Inc., Waltham, MA, 1990.

Design and performance of the GOES-8 high resolution magnetometer

Warren D. Dunham, Steven A. Macintyre and Charles R. Upton

Macintyre Electronic Design Associates (MEDA), Inc.

ABSTRACT

The GOES-8 Magnetometer is one of the most sophisticated and highest performance fluxgate magnetometers to be flown in space. Its 16-bit Analog-to-Digital converter (ADC) can resolve magnetic field strengths as low as 0.03 nT. It can measure fields to an accuracy of 1 nT over a temperature range of -80°C to 72°C. This paper describes the GOES-8 Magnetometer design and performance. The magnetometer consists of a very low noise three-axis analog magnetometer, a high resolution dual slope integrating ADC, and a redundant digital serial spacecraft interface. Another feature of the magnetometer is its ability to generate a calibration sequence upon command. The 16-bit ADC design was the most challenging. There were no 16-bit Grade 1 ADCs on the market at the time (1986), so it was necessary to design the ADC using the limited number of Grade 1 parts that were available.

Keywords: GOES-8, fluxgate, magnetometer, analog-to-digital converter, ADC, instrument, sensor

1. INTRODUCTION

The fluxgate magnetometer has been the primary instrument used to map the magnetic field of space since the space age began. Fluxgate magnetometers are rugged, reliable, small, and require very little power to operate. The first instruments were relatively crude by today's standards. The typical accuracy of the early fluxgate magnetometer was on the order of 5% and its resolution was in the nanotesla (nT) range. Since these early days, there have been steady improvements in the quality of the magnetic cores and materials used to construct fluxgate sensors and in the topology of the electronic circuits which excite the sensor core and convert the sensor signal into a dc voltage. These improvements have resulted in analog magnetometers that have high accuracy, wide dynamic range and very low noise. An analog fluxgate magnetometer can now be produced with an initial accuracy of 0.01% and a dynamic range greater than 85 dB. Unfortunately, space qualified analog-to-digital converters (ADC) that have the dynamic range to exploit these improvements have been slower in development.

The fluxgate magnetometer used on the MAGSAT satellite[1] (launched in Oct. 1979) was the earliest high resolution magnetometer to be used in space. It made precise measurements of the geomagnetic field vector in support of the work being performed by the international science community to improve the geomagnetic field model. The MAGSAT magnetometer used an analog magnetometer with a fixed ±2000 nT field range followed by a 12-bit ADC to achieve a resolution of 0.5 nT. Field offsets in increments of 1000 nT were applied to the sensors to keep the magnetometer output on scale. This technique gave the MAGSAT magnetometer an effective operating range of ±64,000 nT.

There were two high resolution fluxgate magnetometers on the Galileo satellite[2] launched ten years later (Oct. 1987). These magnetometers were used to investigate the structure and dynamic variations of Jupiter's magnetosphere. Each magnetometer had two analog ranges (outer: ±32 and ±512 nT; inner: ±512 and ±16,384 nT). These signals were digitized using a 12-bit ADC with 15 bit accuracy. The digital data were averaged to achieve a resolution equivalent to a 16-bit ADC. The resolution of the magnetometers, which was limited by their noise level, was about 0.1 nT.

The Ulysses satellite[3] launched in Oct. 1990 carried a fluxgate magnetometer that was quite similar to the Galileo satellite magnetometers. It had four analog magnetometer ranges (±8, ±64, ±2,048 and ±44,000 nT) and used a 12-bit ADC to convert the analog signals. Resolution was 0.0039 nT on the ±8 nT range. There was no noise performance data provided in the cited publication.

The Mars Observer satellite[4] carried two fluxgate magnetometers. Both magnetometers were mounted on a boom outside the spacecraft. The outer unit was at the end of the boom, and the inner one was 2/3 of the distance between the outer unit

and the spacecraft body. This arrangement allowed for the first order correction of the spacecraft generated magnetic field. The magnetometer design was similar to the Galileo and the Ulysses magnetometers. The only real difference was the number of analog magnetometer ranges. The Mars Observer magnetometer had eight ranges. The resolution on the most sensitive range (±4.0 nT) was 0.002 nT. The magnetometer noise level was reported to be 0.006 nT rms over a 10-Hz bandwidth.

These magnetometers had to resort to analog magnetometer range changing or the application of magnetic field offsets to achieve a wide dynamic range because space qualified ADCs with spans greater than 12 bits (72 dB) were not available. Changing ranges or applying magnetic field offsets requires complex hardware arrangements and controlling software. Whenever the magnetometer changes ranges or a magnetic field offset is applied, some time must be allocated to allow transients in the system to die. Since the basic dynamic range of the analog magnetometer section is better than 85 dB, being able to use a 16-bit ADC (96 dB dynamic range) would have significantly reduced or eliminated the number of analog ranges or offset fields required to cover the desired field range.

The GOES magnetometer design took advantage of the basic dynamic range of the analog magnetometer by custom designing a 16-bit ADC using available (in 1986) space grade electronic parts. The GOES magnetometer had to meet the highest level of reliability so only Grade 1 (S level) parts could be used. The resulting magnetometer has a resolution of 0.03 nT over a field range of ±1000 nT and requires no range changing or magnetic field offsets. It has an absolute accuracy of 1 nT over the sensor temperature range of -80°C to +72°C.

2.DESIGN OVERVIEW

Table 1 lists the overall magnetometer performance requirements.

Table 1. GOES Magnetometer performance requirements

PERFORMANCE	
Range:	±1000 nT
Sensitivity:	10 mV/nT
Non-linearity:	≤ 0.02 % of full scale
Noise:	≤ 0.1 nT rms
Bandwidth:	dc to 0.5 Hz
Initial accuracy:	1 nT (over temperature)
Resolution:	0.03 nT
Sensor alignment error:	≤ 0.25°
ENVIRONMENT	
Sensor Temperature Range:	-80°C to 72°C
Electronics Temperature Range:	-40°C to 72°C
OUTPUT DATA	
ADC Span:	16-bits no missing codes
Format:	48-bit serial stream representing the X, Y, Z magnetic field values
Sample rate:	2 samples/second
RELIABILITY	
Mission Life:	7 years
MTBF:	232 years

Figure 1 is a block diagram of the GOES magnetometer. The magnetometer consisted of a sensor unit (SU) and an electronics unit (EU). The EU mounts inside the spacecraft main body. The SU mounts on a boom outside the main body of the spacecraft and is subjected to a much wider operating temperature range than is the EU (see Table 1).

The EU is divided into five separate modules: the analog signal processor module, the anti-alias filter module, the ADC module, the spacecraft interface module and a dc-dc converter module. Each of these modules was built and tested separately and then integrated into the final EU. Error budgets were assigned to each module so that the only adjustments required after final assembly were the scale factors and zero offsets of the analog signal processor.

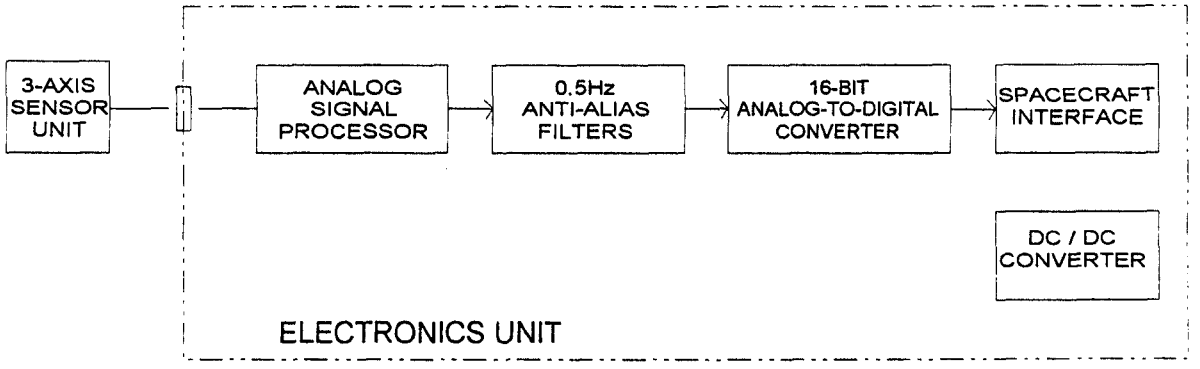

Fig. 1 Block diagram of the GOES Magnetometer

The SU along with the analog signal processor module constitute the analog magnetometer portion of the instrument. The SU consists of three Schonstedt type fluxgate sensors mounted at right angles to one another and aligned to the base plate surface and one of its edges. The EU analog signal processor provides sensor excitation and sensor signal processing.

The outputs of the analog signal processor module are filtered by a five-pole Butterworth low pass filter to prevent aliasing of the signal by the ADC process. This provided about 30 dB of attenuation at the Nyquist frequency (1 Hz).

The three filtered analog signals are applied to the input of the ADC which sequentially converts each signal into a sixteen bit digital representation. A dual slope integration technique is used to perform the conversion. The output of the ADC is serially transmitted to the spacecraft interface module which stores the data until it is interrogated by the spacecraft data acquisition system.

The spacecraft interface module processes timing and control signals received from the spacecraft data acquisition system. These signals control the start of data sampling and conversion and the transfer of data from the magnetometer to the spacecraft data acquisition system. A magnetometer calibration circuit is included in this module. When commanded by the spacecraft, it generates a sequence of known magnetic field steps that are superimposed on the ambient field being measured by the SU. A digital output signal indicates the state of the calibration circuit.

The dc-dc converter converts the 28 volt nominal input power into the ±14 volts and 5 volts that are used to power the other EU modules. A digital input signal from the spacecraft controls the on/off state of the dc-dc converter. A digital output signal indicates the state of the converter.

Figure 2 shows the EU mechanical assembly with the cover removed. Each module is encapsulated as a separate unit. The modules are then stacked one on top of the other with a grounded aluminum shield sandwiched between each layer to minimize electromagnetic interference between the modules. The cover and modules are secured by four long screws which pass through the top of the cover, through collinear mounting holes in the modules and then into tapped standoffs in the analog signal processor module.

Internal electrical connectors were not permitted because of their poor reliability, therefore all wires between modules were terminated in a solder joint. Each wire passes through a strain relief hole before being terminated. All five modules can be separated while remaining electrically connected when performing final adjustments.

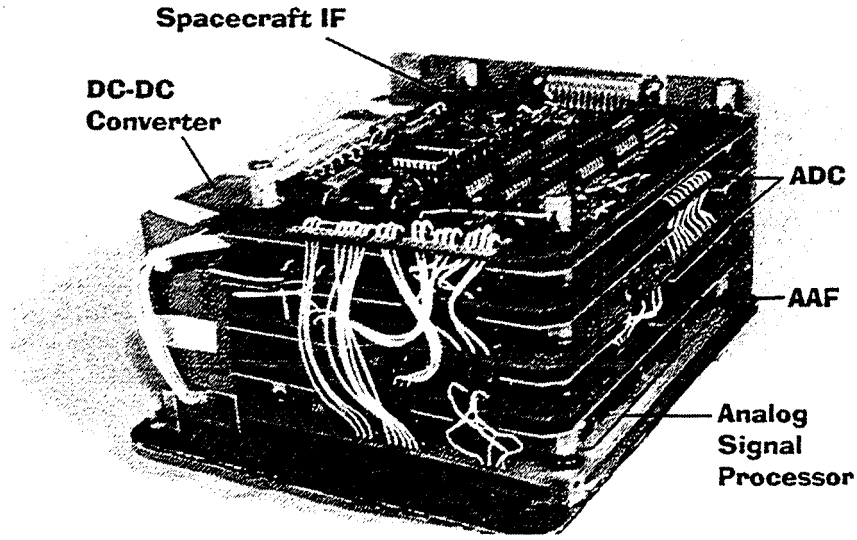

Fig2. Magnetometer EU mechanical assembly

3. ANALOG MAGNETOMETER

The block diagram given in figure 3 of the analog magnetometer portion of the instrument is typical of a second harmonic field feedback magnetometer. A brief description of its operating principle follows. Refer to Primdahl[5] for a comprehensive description of fluxgate magnetometer theory.

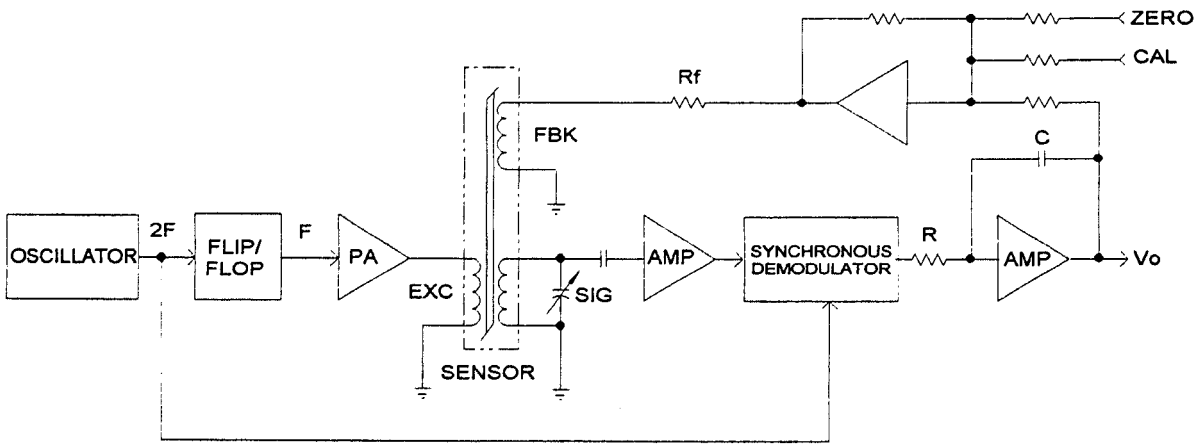

Fig. 3 Block diagram of the analog portion of the magnetometer

The sensor is driven into saturation twice each excitation cycle (F). This produces a signal in the sensor signal winding that is at twice the excitation frequency (2F) and has an amplitude that is proportional to the magnetic field vector component along the sensitive axis of the sensor. The sensor signal is tuned, amplified and then synchronously demodulated to produce a dc voltage with a magnitude proportional to the magnitude of the field and a polarity that corresponds to the direction of the field vector.

The demodulated signal is integrated (low pass filtered), and the output voltage of the integrator is fed back through a resistor to a second (feedback) winding wrapped around the sensor. The current passing through the feedback winding

produces a magnetic field that opposes the ambient field along the sensor's sensitive axis thus forming a negative feedback loop. This circuit topology produces a very linear and stable magnetometer with controllable performance characteristics.

The feedback loop includes a summing amplifier that is used to sum the signals from the integrator output with a zero offset adjustment signal and the calibration signal.

4. ANTI-ALIAS FILTER

The block diagram of the antialias filter is show in figure 4. A front end differential amplifier provides ground isolation between the analog magnetometer and the filter. Since the value of the least significant bit of the ADC is 153 μVolts, it was important that every precaution be taken to minimize potential error sources. The overall filter transfer function was realized by cascading a passive single pole low pass filter with two active two pole low pass filters.

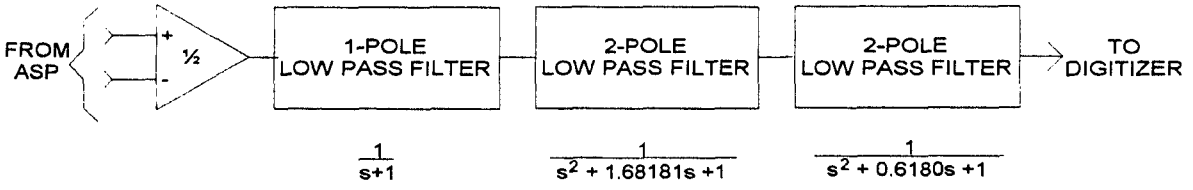

Fig. 4 Block diagram of the anti-alias filter

Stable 1% Polycarbonate capacitors and 0.1 % wirewound resistors were used to provide the necessary transfer function stability over the operating temperature range and the lifetime of the satellite. Precision wirewound resistors were selected instead of the more common fixed film resistors since their aging factor is significantly lower. When operated at less than 10% of its power rating, a wirewound resistor has an aging factor of 0.03% over seven years whereas a fixed film resistor has an aging factor of 1% over the same period.

5. ANALOG-TO-DIGITAL CONVERTER

The most challenging part of the GOES magnetometer design was the ADC. There were no commercially available Grade 1 (S level reliability) 16-bit ADCs in 1986. The ADC was designed using CD4000 series CMOS logic circuits and the limited selection of analog ICs that could be procured to the S level reliability requirement.

At first a successive approximation technique was investigated using two 12-bit digital-to-analog converters (DAC). Unfortunately the linearity of the 12-bit DACs was inadequate. The GOES ADC had to have monotonic linearity (i.e., no missing codes) over the complete 16-bit dynamic range. A range change technique was not satisfactory because it did not maintain the specified resolution. The field offset technique could provide adequate resolution, but it introduced transients when the offset fields were applied, and the offset field generator had to be monotonic and have 16-bit accuracy and stability. It was decided that the dual-slope ADC technique (which is inherently monotonic) would provide the required accuracy and stability at the lowest level of circuit complexity. The reduced circuit complexity also improved reliability. A simplified schematic of the GOES ADC is given in figure 5.

The input stage of the ADC consists of a four channel multiplexer that is used to select the axis to digitize followed by a summing and inverting amplifier that conditions the bipolar ($-V_{ref}$ to $+V_{ref}$) analog magnetometer output voltage so that the integrator input voltage ranges from 0 to $-V_{ref}$. Semiconductor switches on the input of the integrator are used to select one of the following signals for integration : the output of the conditioning amplifier, the reference voltage or zero volts.

The integrator is an operational amplifier with a very stable capacitor (C) connected from the amplifier's output to its negative input and a resistor (R) connected from the amplifier's negative input to the signal to be integrated. The integrator output is amplified and applied to the input of a comparator. The comparator output controls the gating of clock pulses to a 16-bit counter.

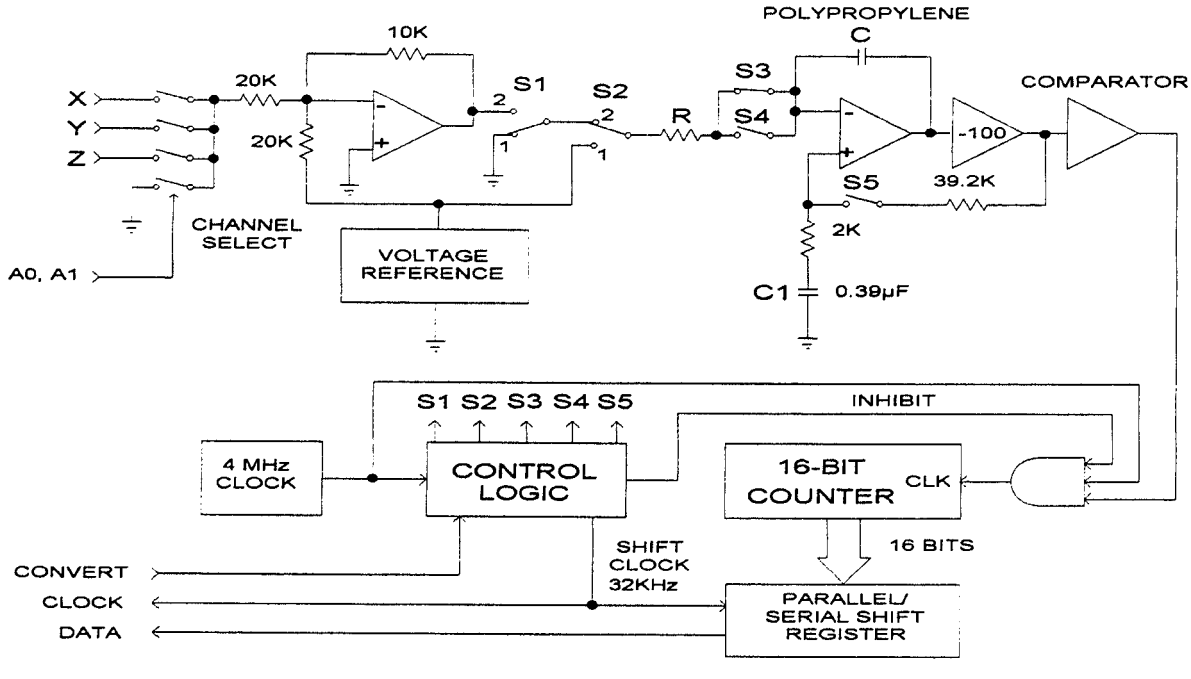

Fig. 5 Simplified schematic of the ADC

A 4 MHz clock controls the ADC timing and provides the clock pulses to the counter. Signals from the spacecraft interface module select the channel to be digitized and initiate the conversion process. The timing diagram for a single conversion is given in figure 6.

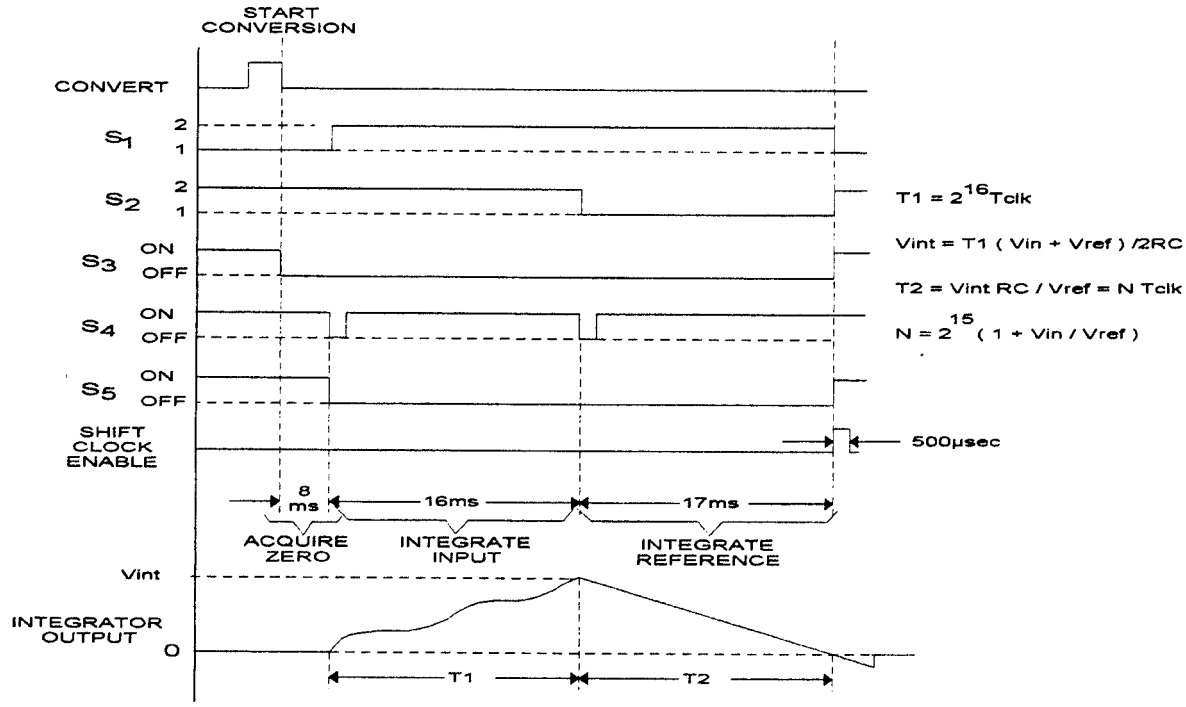

Fig. 6 ADC timing diagram

The analog-to-digital conversion process begins on the falling edge of the Convert pulse. The integrator input is set to zero volts for the first 8 milliseconds (ms) of the conversion cycle, with the integrator circuit configured as a voltage follower (S_5 closed). This causes C1 to charge to the input zero offset of the integrator. Upon completion of the zero offset acquisition, the integrator circuit is configured for integration by opening S_5. At the same time, the integrator input is switched to the input signal (S_1 in position 2) and integrated for 2^{16} clock cycles (approximately 16 ms). During this period the counter is inhibited from counting.

Once the input signal integration period is completed, the integrator input is switched to the reference voltage (S_2 in position 1), and the counter is enabled for counting clock cycles. The integrator output voltage declines at a constant rate and the counter accumulates clock cycles. When the integrator output voltage crosses zero, the comparator switches states, thereby disabling the clock input to the counter. This completes the conversion process. The counter output is then transferred to a parallel/serial shift register and serially shifted out to a 64-bit storage register on the spacecraft interface module.

Between conversions the integrator input resistor is shorted (S_3 closed), and the integrator input is connected to zero volts (S_1 in position 1) to discharge the integrator capacitor and prepare it for the next conversion process. Also note that the integrator input is opened briefly (S_4 open) during switching operations to minimize switching transient errors.

The integrator capacitor determines the overall linearity of the ADC. A Polypropylene capacitor was selected for this function. A Polystyrene capacitor would have been the best choice since it has the lowest dissipation factor and dielectric absorption, but it was not approved for S level space applications. The ADC is not sensitive to changes in R, C or clock frequency since these items drop out of the scale factor and zero offset equations.

The stability of the voltage reference and the resistors in the first stage determines the overall accuracy and stability of the ADC. The sensitivity of the scale factor is 1 for changes in the reference voltage. The zero offset sensitivity is 0.5 for voltage reference changes. The sensitivity of the scale factor is also 1 for changes in the ratio of the feedback resistor to the input resistor. Neglecting aging effects, the worst case scale factor stability for the ADC is 486 parts-per-million (ppm) (0.5 nT full scale), and zero offset stability is 35 counts (1 nT). If aging over the seven year lifetime of the satellite is taken into account, the scale factor could change as much as 2,322 ppm (2.3 nT full scale), and the zero offset could change by 162 counts (5 nT). The reference voltage aging accounts for 90% of these changes.

6. SPACECRAFT INTERFACE

The Spacecraft Interface module transforms the spacecraft data bus control signals into the signals that execute the required magnetometer functions. These functions include analog-to-digital conversion, data transfer, starting/stopping a calibration sequence and turning power on or off.

6.1 ADC controller

Figure 7 is a block diagram of the ADC controller portion of the Spacecraft Interface.

A frame sync pulse from the spacecraft arrives at the magnetometer every 512 ms and initiates the analog-to-digital conversion function. The ADC controller then sequentially selects the magnetometer axis to be converted and sends a convert signal to the ADC. After each conversion the 16-bit digital data from the ADC is serially clocked from the ADC into a 64-bit storage register. When all three magnetometer channels plus the ADC zero input have been digitized, the ADC resets and waits for the next frame sync pulse.

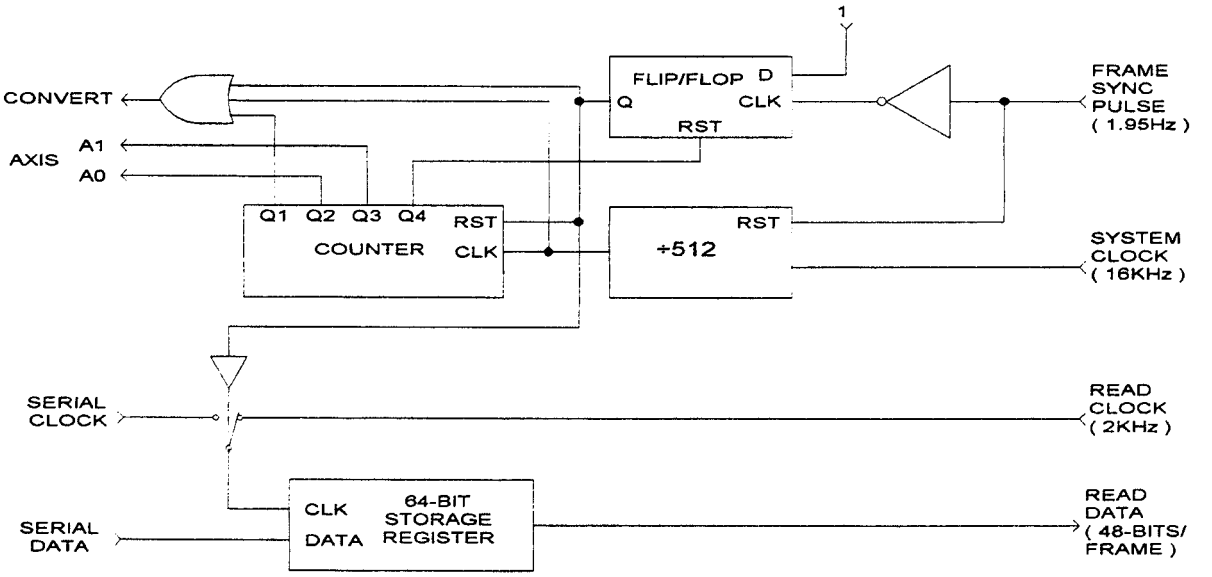

Fig. 7 Block diagram of the ADC controller

During conversion the clock input to the 64-bit storage register is connected to the ADC serial clock output. This input is switched to the Read Clock signal from the spacecraft after the conversion function is complete to allow the spacecraft to serially transfer the data to the spacecraft data bus. A timing diagram for the ADC controller is shown in figure 8.

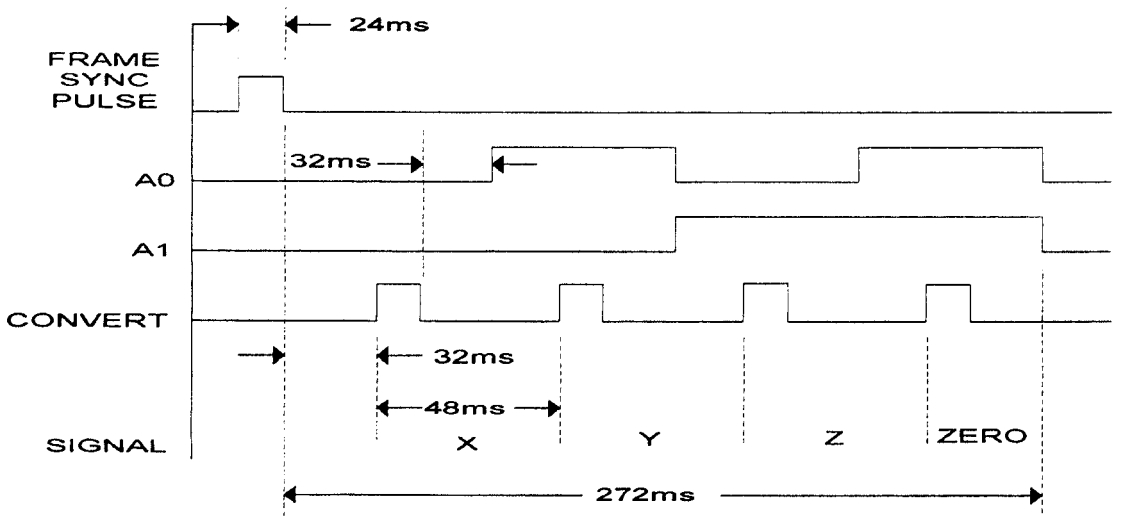

Fig. 8 ADC timing diagram

6.2 Calibration circuit

A block diagram of the calibration circuit is shown in figure 9. The spacecraft can initiate or terminate a calibration sequence. When a calibration (CAL) command is received, it causes a flip flop to change states. If a calibration sequence is in progress, it is immediately terminated otherwise a new calibration sequence is initiated. The calibration function sequentially superimposes five different field levels on the ambient field being measured by the magnetometer. Each field level has a fixed duration of 32 Frame Sync pulse periods (16.38 seconds). After the fifth step the circuit resets and waits until a new CAL command is sent.

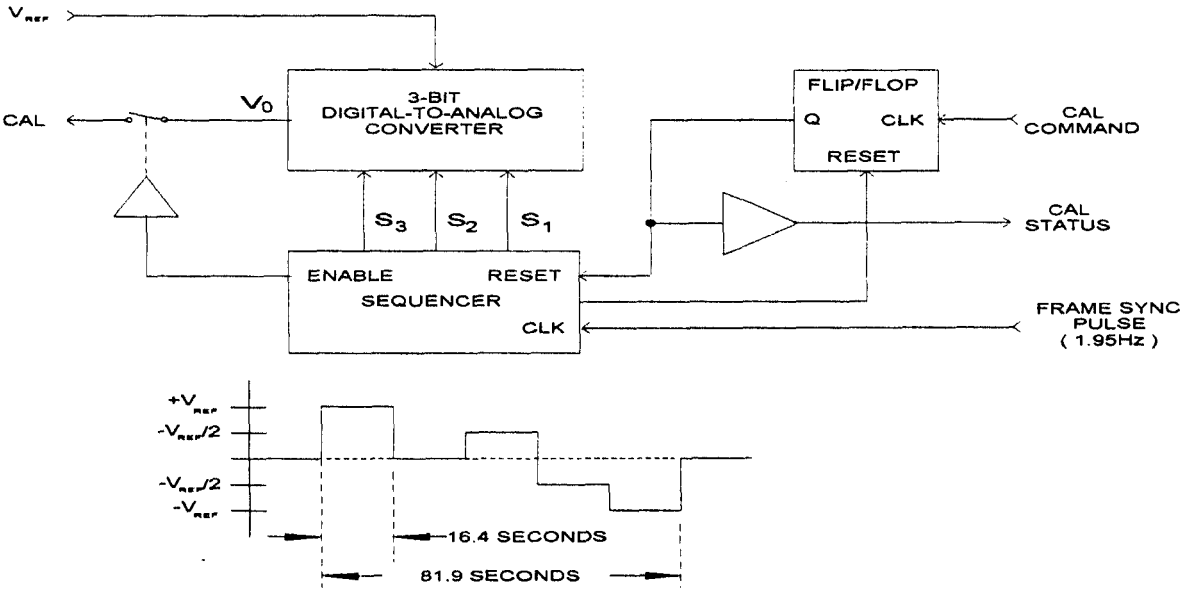

Fig. 9 Block diagram of CAL circuit

The field levels are generated by applying the digital outputs from a sequencer to the inputs of a 3-bit digital-to-analog converter (DAC).. Figure 10 is a simplified schematic of the DAC.

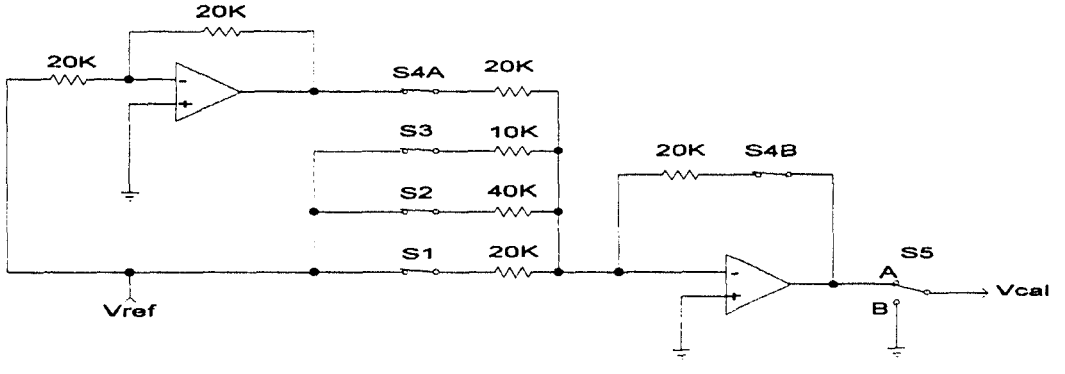

Vcal = Vref (1 - S1 - S2/2 - 2*S3)

S1	0	1	0	1	0
S2	0	0	1	1	0
S3	0	0	0	0	1
Vcal / Vref	1	0	½	-½	-1

* S4 = 1

* S5 IS IN 'A' POSITION DURING CAL AND IN 'B' POSITION OTHERWISE.

Fig 10. Calibration circuit 3-bit ADC

The ADC voltage reference is also used by the DAC. The semiconductor switch in series with the feedback resistor of the summing amplifier partially compensates for the on resistance of the semiconductor switches S1,S2, S3 and S4A.

7. CONCLUSIONS

Table 2 lists the measured performance of the GOES-8 magnetometer over its operating temperature range.

Table 2 GOES-8 Magnetometer Performance

PARAMETER	VALUE
Scale Factor Stability	0.30 nT
Zero Stability	0.68 nT
Non-linearity	0.2 nT
Noise	0.1 nT pk-pk
Alignment Error	0.11 degrees

The overall magnetometer linearity and noise performance were determined strictly by the analog magnetometer section. The ADC linearity, resolution and noise were under 1 least significant digit (0.03 nT), thus the objective of using a 16-bit ADC was met: the GOES magnetometer performance was limited only by the analog magnetometer's characteristics and not by the limitations of the analog-to-digital conversion process. Using a wide dynamic range, ADC eliminated the need for range changing or the application of field offsets to achieve the needed magnetic field measurement range and resolution.

9. REFERENCES

1. M. H. Acuna, C. S. Scearce, J. B Seek and J. Schelfile, "The MAGSAT vector magnetometer-a precision fluxgate magnetometer for the measurement of the geomagnetic field," *NASA Tech. Memo. 79656,* Oct. 1978.

2. M. G. Kivelson, K. K. Khurana, J. D. Means, C. T. Russell and R. C. Snare, "The Galileo magnetic field investigation," *Space Science Review,* Vol. 60, pp. 357-383, 1992.

3. A. Balogh, T. J. Beek, R. J. Forsyth, P. C. Hedgecock, R. J. Marquedant, E. J. Smith, D. J. Southwood and B. T. Tsurutani., "The magnetic field investigation on Ulysses mission: instrumentation and preliminary scientific results," *Astron. Astrophys. Suppl. Ser,.* Vol. 93, pp. 221-236, 1992.

4. M. H. Acuna, J. E. P. Connerney, P. Wasilewski, R. P. Lin, K. A. Anderson, C. W. Carlson, J. McFadden, D. W. Curtis, H. Reme, A. Cros, J. L. Medale, J. A. Sauvaud, C, d'Uston, S. J. Bauer, P. Cloutier, Michael Mayhew and N. F. Ness , "Mars Observer magnetic fields investigation," *Journal of Geophysical Research,* Vol. 97, E5, pp. 7799-7814, May 1992.

5. F. Primdahl, "The fluxgate magnetometer," *J. Phys. Sci. Instrum.,* Vol. 12, 1979.

SESSION 5

Advanced Technologies and Instruments

GOES imager upgrade design for minimum system impact

D. Cousins, M.S. Cafferty and L.M. Candell

MIT Lincoln Laboratory
244 Wood Street, Lexington, Massachusetts 02173

J. Kimchi

EG&G Judson Inc.
221 Commerce Drive, Montgomeryville, Pennsylvania 18936

ABSTRACT

An engineering design of an Imager upgrade is under consideration for the GOES-N/Q series. The upgrade consists of adding up to three new IR channels at 4 km resolution and doubling the earth coverage rate. The design approach introduces advanced technology as needed to minimize impacts to the sensor optical and mechanical configuration, electronics box layout, data communication links and ground systems. By operating presently redundant portions of detector arrays and developing double rate signal processors, the scanning servo system and electronics modules are largely retained. Bicolor detectors and optical coatings are used to add channels while retaining the present relay optics and radiant cooler layouts. Lossy data compression of visible imagery and lossless data compression of IR imagery are used to preserve the sensor data and processed data relay communications links. System NEDT and SNR performance and implementation issues for new technologies are addressed.

Keywords: GOES, infrared design, bicolor detectors, data compression

1. INTRODUCTION

Based on the success of GOES-8 and -9, NOAA is planning on the continued use of the present design through the GOES-Q launch in roughly 2008. Improvements to GOES sensors in this timeframe will be modifications of the present designs[1] rather than completely new designs. A modification to the GOES I/M Imager is being considered that would add up to 3 IR bands at 4 km resolution and double the earth coverage rate. The engineering philosophy for the design is to meet requirements with minimum impact to the entire GOES system. It is assumed that all present users should have access to expanded double rate data. Table 1 lists the basic requirements for the Imager upgrade. Minimum impact is interpreted as:

avoid significant changes to the optical and mechanical configuration of the Imager;

continued use of the present detector materials;

continued use of the present frequency allocation and modulation for data transmission.

avoid significant hardware changes at CDA/SOCC and at direct readout sites

This work was sponsored by the National Oceanic and Atmospheric Administration under Air Force Contract No. F19628-95-C-0002.

0-8194-2200-2/96/$6.00

Table 1. Imager Upgrade Basic Requirements

Channel No.	Bandpass (μm)	Resolution (μrad)	NEDT (K) or SNR
1	0.52 - 0.72	28	200 at 100% albedo
2	3.73 - 4.07	112	0.20 K at 300 K
3	13.0 - 13.7	112	0.70 K at 300 K
4	10.2 - 11.2	112	0.20 K at 300 K
5	5.8 - 7.3	112	0.30 K at 230 K
6	11.5 - 12.7	112	0.25 K at 300 K
7	5.2 - 5.5	112	0.30 K at 250 K
8	1.5 - 1.7	112	250 at 100% albedo

2. IMAGER UPGRADE SYSTEM DESIGN

The system schematic for the Imager upgrade is shown in Figure 1.

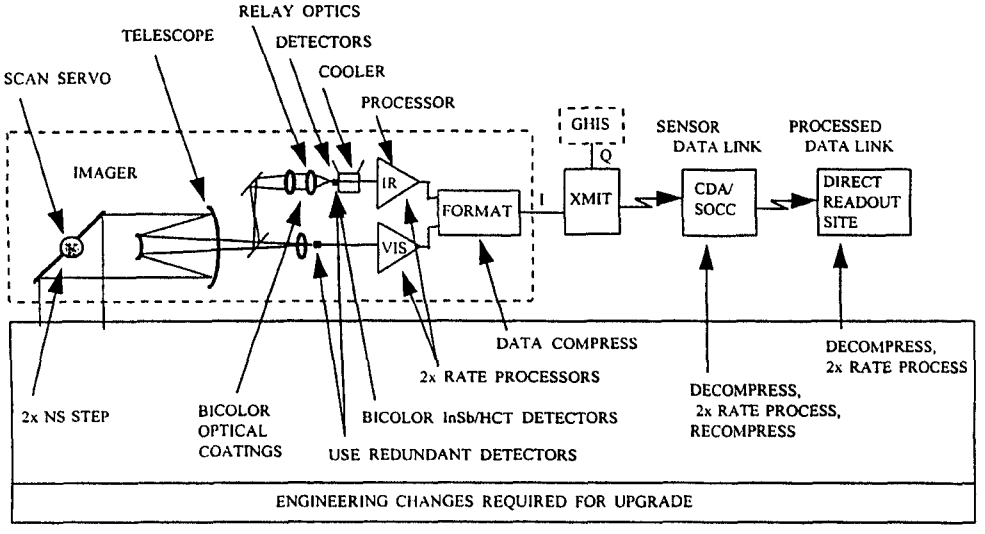

Figure 1. Engineering approach to imager upgrade design.

The approach to doubling the coverage rate is to activate the presently redundant set of IR detectors and use them to form a wider scan line. An extended 1x16 array of Si detectors is used for the VIS channel. Only very minor servo system modifications are needed; the east-west scan rate is unchanged while the north-south step size is doubled. In order that the power and volume used for signal processing electronics not significantly increase, double rate signal processing circuits are used.

The approach to adding channels to the optical system is based on the observation that a single path in present relay optics will focus a range of wavelengths at slightly different focal positions. Therefore, if suitable optical coatings can be developed to direct two bandpasses along a single relay optics path and a detector developed that independently senses both bandpasses, then channels can be added without changing the relay optics configuration. These modifications are referred to as bicolor optics and detectors. The signal processing required for the bicolor channels are additional double rate circuits in spare slots in the present electronics box.

The approach to data handling system modifications is based on making suitable alterations of the sensor data to preserve the present communications links. Since the unmodified raw data rate from the Imager upgrade would exceed the present link capacity, data compression is used. Artifacts of compression are made insignificant and the final decompressed images meet all requirements.

For conciseness, only the bicolor optics and detector for the channel 2/4 combination are described in detail here. Extension of the bicolor design approach to the channel 7/6 combination is straightforward. Furthermore, the addition of channel 8 at 1.6μm is not described in detail here. It is assumed that channel 8 can be added by a straightforward extension of the visible relay optics using an uncooled InGaAs detector.

3. BICOLOR OPTICAL COATINGS

Bicolor optical coatings are used to separate, transmit and filter the required spectral bandpasses through the IR relay optics. A total of 17 specific coatings[2] are used in this approach, as listed in Table 2. Figure 2 shows where each coating is used in the relay optics and which channels are directed in each path.

Table 2. Bicolor Optical Coatings

Coating Properties	Substrate	No. of Layers
Filter 1: Dual Bandpass 3.7-4.0 μm, 10.2-11.2 μm	Ge @ 0 deg	136
Filter 2: Dual Bandpass 5.2-5.5 μm, 11.5-12.7 μm	Ge @ 0 deg	TBD
Beamsplitter 1: Transmit 5.2-5.2, 11.5-12.7 μm; Reflect 3.7-4.0, 10.2-11.2 μm	ZnSe @ 45 deg	61
Beamsplitter 2: Transmit 5.8-7.1 μm Reflect 13.0-13.7 μm	ZnSe @ 45 deg	20
Beamsplitter 3: Transmit 5.8-7.1, 13.0-13.7 μm; Reflect all other bands	ZnSe @ 45 deg	92
AR1: Antireflect 5.8-7.1, 13.0-13.7 μm	ZnSe @ 45 deg	6
AR2: Antireflect 5.8-7.1 μm	ZnSe @ 45 deg	4
AR3: Antireflect 5.8-7.1 μm	ZnSe @ 0 deg	4
AR4: Antireflect 13.0-13.7 μm	ZnSe @ 0 deg	4
AR5: Antireflect 5.8-7.1 μm	Ge @ 0 deg	5
AR6: Antireflect 13.0-13.7 μm	Ge @ 0 deg	3
AR7: Antireflect 5.2-5.5, 5.8-7.1, 10.2-11.2, 11.5-12.7 μm	ZnSe @ 0 deg	10
AR8: Antireflect 5.2-5.5, 11.5-12.7 μm	ZnSe @ 45 deg	6
AR9: Antireflect 5.2-5.5, 11.5-12.7 μm	ZnSe @ 0 deg	6
AR10: Antireflect 3.7-4.0, 10.2-11.2 μm	ZnSe @ 0 deg	6
AR11: Antireflect 5.2-5.5, 11.5-12.7 μm	Ge @ 0 deg	7
AR12: Antireflect 3.7-4.0, 10.2-11.2 μm	Ge @ 0 deg	5

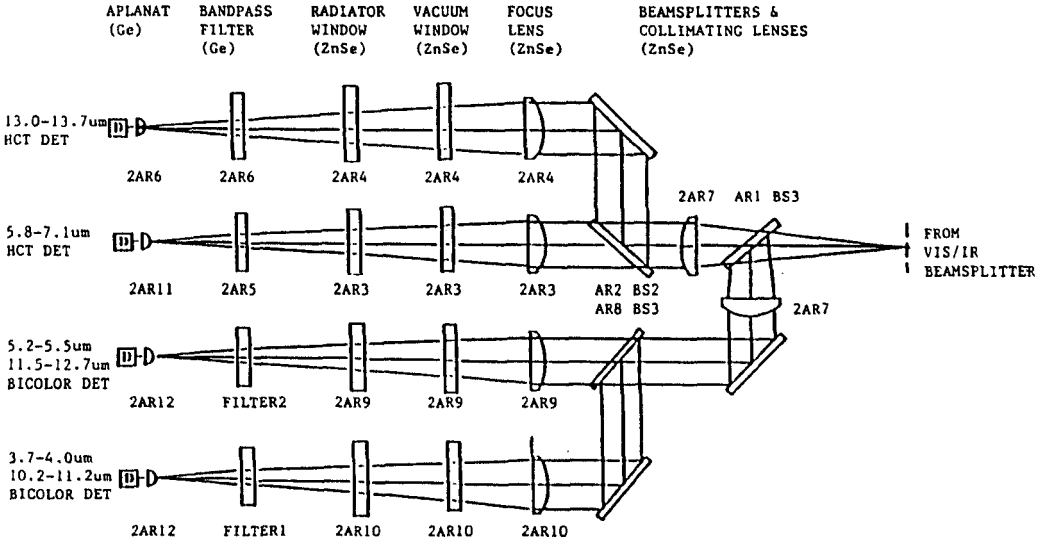

Figure 2. Bicolor IR relay optics.

As an example, Figure 3 shows the thin film design and predicted transmission spectrum of beamsplitter 3. Figures 4 and 5 show the combined spectral transmission for the complete bicolor relay optics for the channel 2/4 path. In these figures, the bandpass filter transmission is taken from measurements of an actual prototype filter. Note that the transmission of the combined coatings prior to the bandpass filter is narrowband, therefore minimizing the optical heat load into the radiant cooler.

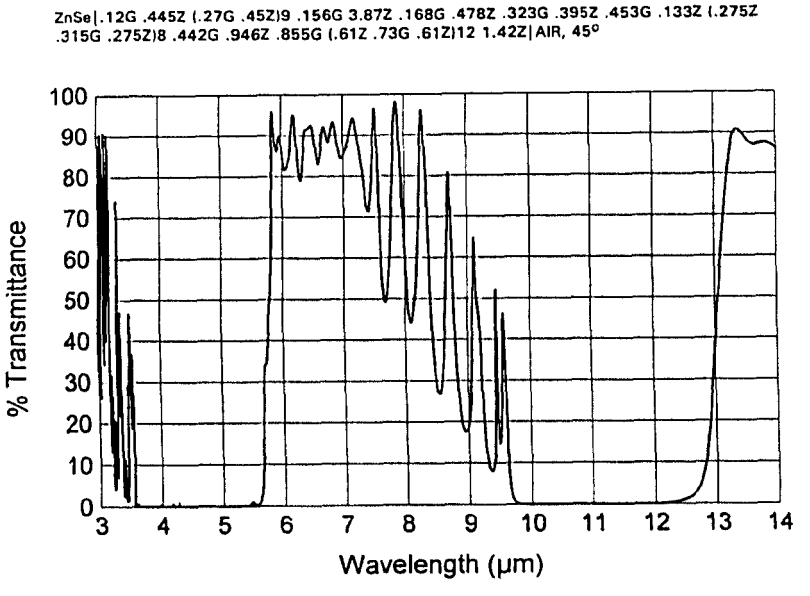

Figure 3. Bicolor optics beamsplitter 3.

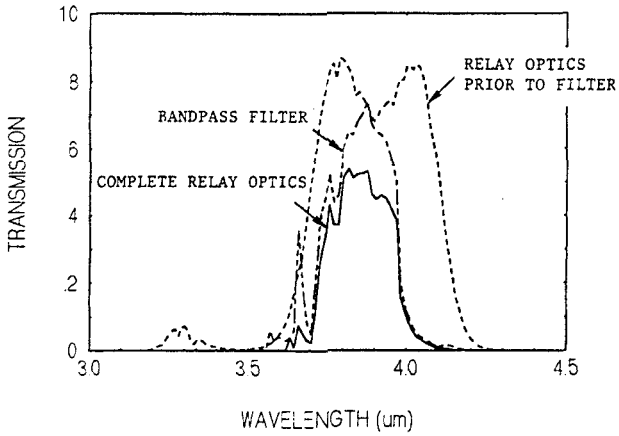

Figure 4. Spectral bandpass for channel 2.

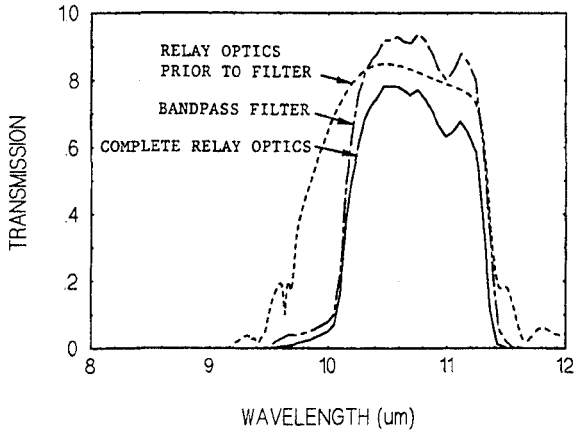

Figure 5. Spectral bandpass for channel 4.

Table 3 lists the average inband transmission for each bicolor coated component and the complete path transmission for all channels. Small amounts of substrate absorption are included as appropriate for channels greater than 10μm. The complete path transmissions are used to estimate NEDT performance.

Table 3. Average In-Band Transmission for Bicolor Optics

	3.7-4.0 μm	5.2-5.5 μm	5.8-7.1 μm	10.2-11.2 μm	11.5-12.7 μm	13.0-13.7 μm
Beamsplitter 3	0.99	0.99	0.83	0.99	0.99	0.75
Collimating Lens	0.92	0.90	0.92	0.92	0.92	0.87
Fold Mirror	0.98	0.98	-	0.98	0.98	-
Beamsplitter 2	-	-	0.90	-	-	0.99
Beamsplitter 1	0.99	0.91	-	0.99	0.90	-
Fold Mirror	0.98	0.98	0.98	0.98	0.98	0.98
Focus Lens	0.96	0.96	0.94	0.98	0.96	0.95
Vacuum Window	0.96	0.96	0.94	0.98	0.96	0.95
Radiator Window	0.96	0.96	0.94	0.98	0.96	0.95
Bandpass Filter	0.75	0.75	0.82	0.75	0.75	0.82
Aplanat	0.96	0.96	0.94	0.91	0.90	0.86
Complete Relay Optics	0.55	0.50	0.43	0.56	0.47	0.38
Mirrors and VIS/IR BS	0.83	0.86	0.86	0.82	0.82	0.82
Complete Optics	0.46	0.43	0.37	0.46	0.39	0.31

Only ZnSe and Ge layers are used in the thin film design of each bicolor coating. The bicolor coatings, particularly the beamsplitter and bandpass coatings, require more layers than the coatings they are replacing in the present design. In order to assess manufacturability of the coatings, transmissions were calculated assuming small random layer thickness variations. The results indicate that bicolor coatings have no greater sensitivity to layer thickness variations than conventional coatings. Probably the most challenging aspect of bicolor coating manufacturability is achieving extremely accurate placement of both cut-on and cut-off wavelengths for the dual bandpass filters.

4. BICOLOR FOCUSING OPTICS

A ray trace of the present 10.7 μm relay optics path (neglecting coatings) shows that a 3.9 μm focus is produced on the optical axis at a position about 160 μm closer to the aplanat than the 10.7 μm focus. Figure 6 shows the position of the 10.7 μm focus after refraction by a 270 μm thickness of 100K InSb placed at the 3.9 μm focus. The 10.7 μm focus position is about 90 μm from the back surface of the InSb. Note the nominal size of the detector. At the respective 3.9 μm and 10.7 μm focal positions, the geometric focus size is insignificant compared to the detector size and diffraction effects. For either wavelength, the relay optics contribution to overall system MTF is small.

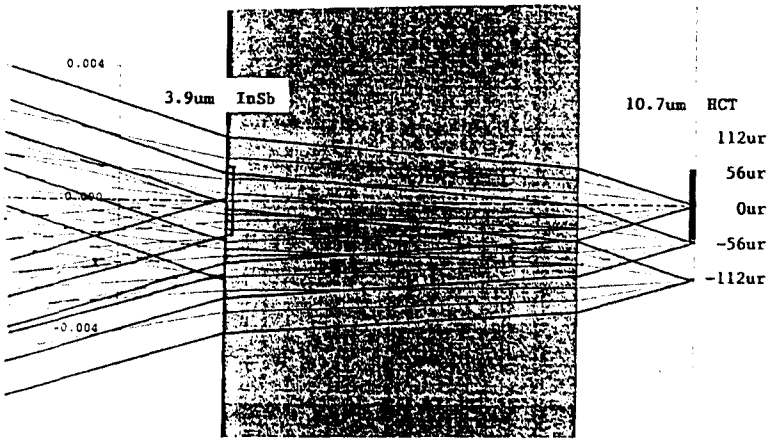

Figure 6. Channel 2/4 bicolor optics geometric focus.

The 270 μm InSb thickness and 90 μm gap form a basis for the design of an InSb/HCT bicolor detector. Other combinations of InSb thickness and gap could be used. Since the relay optics do not allow separate adjustment of the 3.9 μm and 10.7 μm focal positions, it is important that the InSb thickness is carefully controlled. The effects of relay optics focal length variations, tilts and decentrations are similar for both 3.9 μm and 10.7 focuses.

Due to the optical properties of InSb[3], radiation less than about 5.5 μm is absorbed very near the InSb front surface. The transmission of 10.7 μm radiation through the InSb layer is determined by a small amount of absorption within the InSb and reflections at the front and back surfaces. With perfect antireflection coatings applied to both surfaces, the transmission through the layer would be about 0.93. Realistic performance of actual high quality coatings will likely produce a transmission of 0.80.

5. BICOLOR InSb/HCT DETECTOR

An InSb/HCT bicolor detector assembly consisting of an InSb detector 270 μm thick positioned 90μm above an HCT detector allows the present 10.7 μm relay optics (with suitable bicolor coatings) to be used as the channel 2/4 bicolor

relay optics path. The bicolor detector consists of coaligned InSb and HCT 1x4 detector arrays with 0.002" nominal square elements. Based on review of actual detector manufacturing processes at EG&G Judson Inc., the InSb thickness, InSb-HCT gap and coalignment tolerances can be maintained to less than 5 μm. The bicolor detector is housed together with a bandpass filter and aplanat and has the same mounting footprint as the present HCT detector, although with more electrical leads. A structural analysis of the detector assembly indicates that natural resonant frequency is sufficient high (500 kHz) to insure compatibility with the required launch mechanical environment. Figure 7 shows a cross section of the bicolor detector assembly.

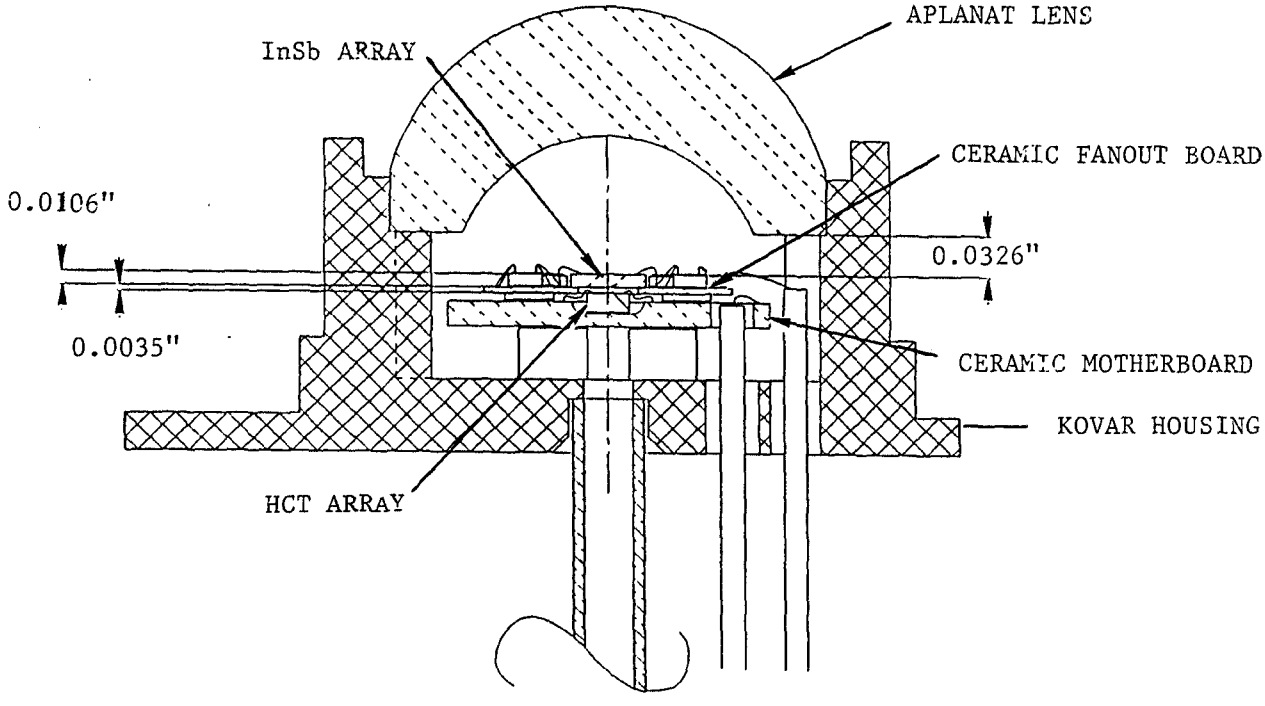

Figure 7. Channel 2/4 bicolor InSb/HCT detector, cross section.

Since the detector types used in the bicolor assembly are used in the present Imager, it is reasonable to assume that D* and responsivity will be identical to the present values, except for losses through the InSb layer.

As shown in Figure 8, the InSb element active area uses a grounded p-type guard ring to control potential out-of-area response surrounding the active p-n junction. The InSb element metal contacts slightly obscure longwave radiation passing to the underlying HCT elements. Based on the ratio of area obscured, it is estimated that this metal contact causes about a 3% longwave transmission loss. An oversized opaque metal mask placed on the front InSb surface reduces the potential for internal reflections of longwave radiation leading to out-of-area response of the HCT elements.

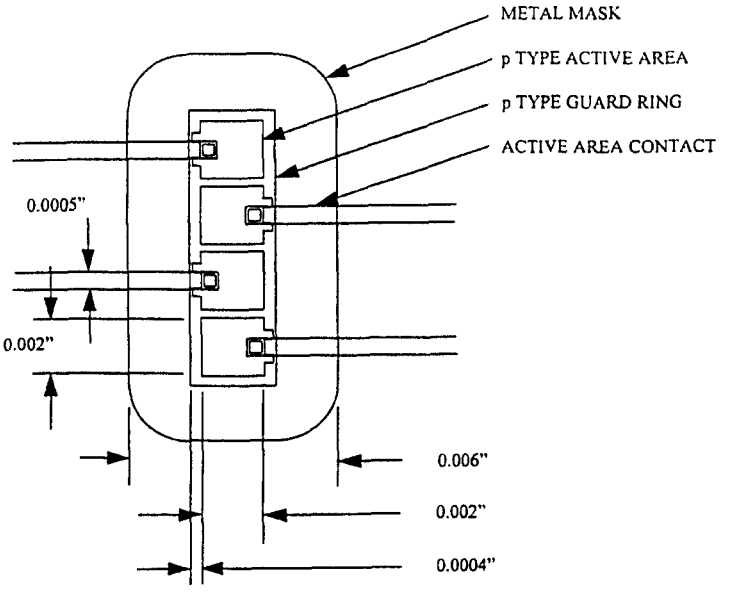

Figure. 8. Channel 2/4 bicolor InSb/HCT detector, InSb array.

EG&G Judson Inc. has identified a processing sequence for manufacturing bicolor detectors that minimizes handling risks and maximizes yield of high quality assemblies. Both HCT and InSb detectors can be separately tested as modules and screened prior to assembly. The InSb module can be replaced after assembly if needed. No significant optical or electrical crosstalk is anticipated between HCT and InSb elements.

The addition of detectors to the focal plane and the operation of presently redundant detectors lead to increased heat load to the radiant cooler. It is estimated that the heat load increases about 40mW compared to the present heat load of 101mW (equinox) and 158 mW (summer). The bicolor detector approach does not increase heat load more than simply adding the corresponding number of discrete detectors. Without changing the cooler design, the added heat load would lead to a 6K increase in detector operating temperature. There are several cooler modifications that can be used to offset the added heat load and maintain the present operating temperature including electropolishing to reduce cooler interstage radiative coupling and the use of a spectrally selective patch coating to reject astromast heatload. It is assumed the cooler is suitably modified and that the new detector configuration with bicolor detectors operates near the present 100K.

Table 4 lists NEDT estimates based on

$$NEDT = \frac{\alpha f^2 \sqrt{\Delta f}}{\sqrt{Ad}\, A_o\, \tau\, D^*\, \Delta\nu \left| \frac{dN}{dT} \right|_{Tspec}}$$

Table 4. NEDT Estimates

Channel Number	2	5	4	6	7	3
α	1.1	1.3	1.3	1.3	1.1	1.3
λ (μm)	3.9	6.5	10.7	12.0	5.3	13.3
$\Delta\nu$ (cm^{-1})	223	315	88	85	105	40
Tspec (K)	300	230	300	300	250	300
$\frac{dN}{dT}\Big\vert_{Tspec}$ $(\frac{mW}{m^2 srcm^{-1}K})$	0.038	0.15	1.6	1.7	0.071	1.7
D^* (100K) (cm $\sqrt{Hz}$/W)	1.0E12	1.4E11	7.7E10	4.4E10	1.0E12	4.0E10
τ optics	0.46	0.37	0.46	0.39	0.43	0.31
τ detector	1.0	1.0	0.8	0.8	1.0	1.0
NEDT (K)	0.09	0.15	0.09	0.18	0.11	0.42

$$f = 52cm;\ \Delta f = 1650\ Hz;\ \sqrt{Ad} = 58\ \mu m;\ A_o = 720cm^2$$

where:
- α = detector excess low frequency noise factor
- f = optics focal length
- Δf = electrical white noise bandwidth
- Ad = detector active area
- A_o = optics collecting area
- τ = transmission
- D* = detector detectivity at operating temperature
- $\Delta\nu$ = optical bandwidth
- dN/dT = thermal derivative of source at specified temperature

6. DOUBLE RATE SIGNAL PROCESSOR

Modification to the present signal processing circuit allows two independent signals to be processed by a single circuit thereby preserving the electronics box layout. Figure 9 shows a schematic of the double rate signal processor. In this circuit the clamp, sample/hold and digital conversion functions are shared between two separate inputs. The circuit preserves the low noise and independent gain selection of the separate inputs. More complex timing functions are required and the two resulting samples are offset in time by one half of the sampling period. Other circuits based on further downstream placement of the mux function can be considered to allow nearly simultaneous dual channel sampling but with fewer shared components.

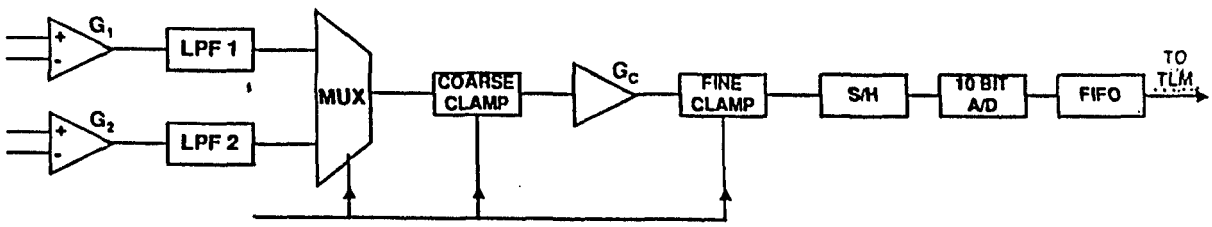

Figure 9. Double rate signal processor schematic.

A prototype of the double rate IR signal processor was manufactured and tested. The circuit preserved circuit card area, power consumption and number of components. Table 5 lists the results of the circuit tests.

Table 5. Double Rate Signal Processor Prototype Test Results

worst case clamp offset	+/- 2.5 volt
noise level	0.0286 volt
dual channel isolation	< 0.3 %
number of op amps	13
sampling period	90 μsec
power consumption	1.2 W

7. DATA HANDLING

The Imager upgrade results in more than twice the sampling rate of the present Imager. Sensor data rate, R, can be calculated by

$$R = \sum_i \frac{\Delta\theta}{\Delta t} \frac{1}{IFOV} n_s\, n_b\, CR\, n_i + OVERHEAD$$

where

$\Delta\theta/\Delta t$	=	east west scan rate
IFOV	=	instantaneous field-of-view
n_s	=	number of east west samples per IFOV
n_b	=	number of bits per sample
CR	=	compression ratio
n_i	=	number of north south samples per channel i

The present Imager generates about 2.6Mbps. Without data compression, the Imager upgrade would generate about 5.5Mbps. Assuming that 10 bit data and the present 7:4 east-west oversampling are maintained, data compression

with an average ratio of about 2.1:1 must be used to maintain the sensor data rate and preserve the present communication links.

Data compression is lossless if the original data stream can be exactly reproduced. Lossless compression can be based on the process of taking differences between successive samples in a data stream and encoding frequently occurring differences with fewer bits than infrequently occurring differences. The degree of lossless compression achieved varies depending on the scene entropy. Computer simulations of lossless compression show that GOES IR images can be compressed with a compression ratio (CR) of about 1.7:1.

Data compression with CR of more than about 1.7:1 will necessarily result in some degradation (or noise added) to the data. Since the visible data is used primarily for visual interpretation rather than quantitative derived products, it is more suitable for lossy compression than the IR data. The most widely used version of lossy compression for image data is based on the direct cosine transformation (DCT) and sometimes referred to as JPEG compression. It operates on blocks of 8x8 pixels based on a quantization table derived from a standard image and a desired CR. Lossy compression can be performed at arbitrary CR resulting in various amounts of compression noise. The root mean squared (rms) difference between pixels of the original and decompressed images is a measure of the compression noise. A conservative estimate of the total noise after decompression is the root sum square of the electronic and compression noise.

Assuming that lossless compression is used on the IR data, lossy compression at 3:1 CR is needed for the visible data to maintain the present Imager data rate at all times. If scan data is transmitted during scan turnaround periods, then the required CR is less than 3:1 depending on the image size. Figure 10 shows the compression noise for various degrees of lossy compression on visible data compared to the visible channel electronic noise. Note that at 3:1 CR, the rss noise is 10% higher than the electronic noise only. The resulting visible SNR is about 220. No 8x8 blocking artifacts can be observed in decompressed images at 3:1 CR.

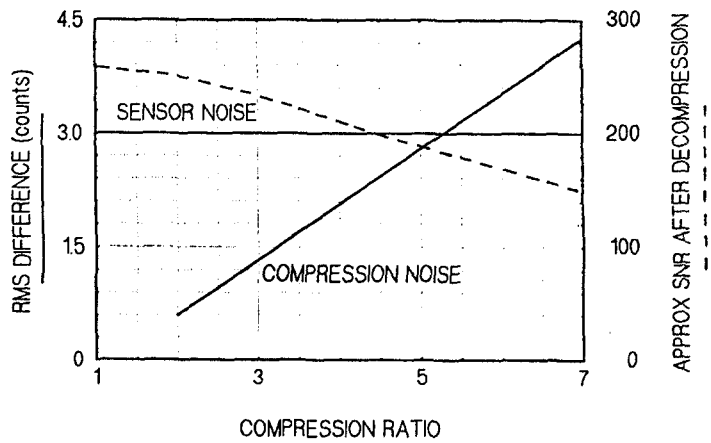

Figure 10. Compression noise for GOES visible images.

The sensor implementation of data compression is shown in Figure 11 and is based on the USES chip, a space qualified component developed by NASA/GSFC. A space qualified component for the DCT function must be developed. Since the output data rate following compression is variable, packetization and buffering of the data are required. Several quantization tables representing less than 3:1 CR can be made available for the lossy compression and selected depending on the occupied size of the buffer. The packet header indicates the quantization table being used at all times.

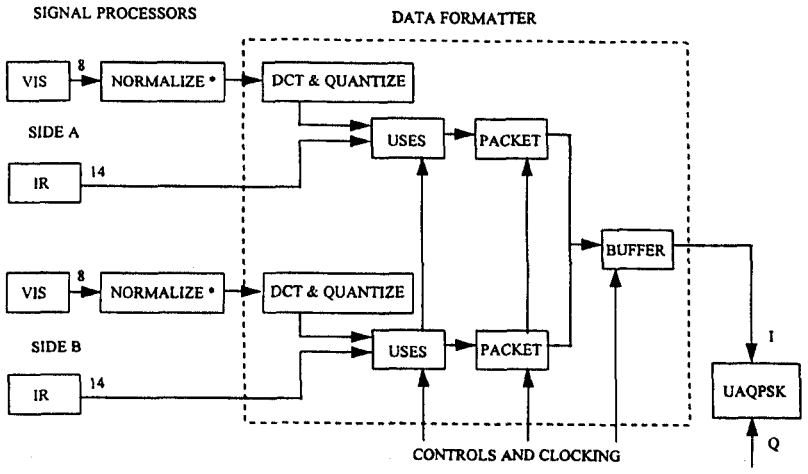

Figure 11. Data compression sensor implementation.

The impact to ground systems is shown in Figure 12. Decompression is accomplished in special hardware at CDA/SOCC followed by double rate image processing in software. Recompression of the data is used on the processed data link. No additional degradation of the visible data will occur if the same algorithm is used on the same pixel boundaries. Decompression is accomplished in hardware at the direct readout sites.

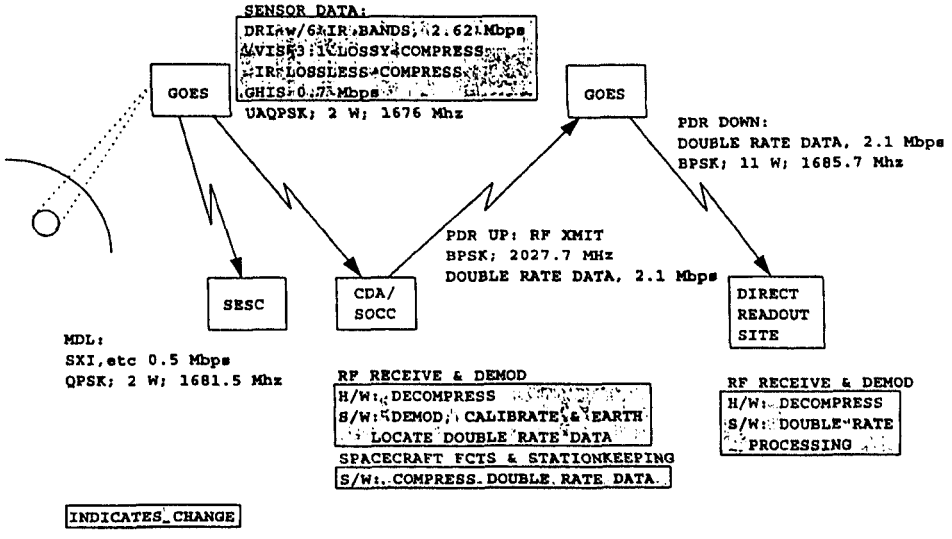

Figure 12. Imager upgrade ground systems impacts.

8. CONCLUSIONS

The Imager upgrade design uses bicolor optics and detectors to preserve the optical and mechanical radiant cooler configuration of the sensor. Data compression is used to preserve both sensor data and processed data communications links, while the image data meets all SNR and NEDT requirements. Modest changes are required at CDA/SOCC and direct readout sites.

Efforts are underway to resolve the following issues:

Bicolor optical coatings need to be flight qualified, with special attention given to achieving the required spectral definition in the bandpass filters and high transmission in all components.

Bicolor InSb/HCT detector need to be flight qualified, with special attention given to achieving accurate IFOV, low out-of-area response and low crosstalk among InSb elements.

A double-blind test with users is being conducted to insure that a slight decrease in SNR compared to the present Imager does not affect the utility of visible data.

A space qualified implementation of lossy compression electronics and resulting Imager output data format need to be developed.

The required hardware to decompress data at ground stations needs to be demonstrated.

9. ACKNOWLEDGMENTS

The authors wish to thank Bill Brown for his insightful guidance of this project and Karen Hovsepian for helping prepare the report for publication. This work was sponsored by the National Oceanic and Atmospheric Administration under US Air Force contract No. F19628-95-C-0002.

10. REFERENCES

1. J. Savides, "Geostationary Operational Satellite GOES I-M," Space Systems/Loral, Dec.1992.

2. D. Cousins and M. Cafferty, "The use of Bicolor Coatings, Optics and InSb/HCT Sandwich Detectors for Adding Bands to the GOES Imager," MIT Lincoln Laboratory, PM No. 96PM-GOES-0009, 30 Mar. 1996.

3. S.W. Kurnick and J.M. Powell, "Optical Absorption in Pure Single Crystal InSb at 298K and 77K," Physical Review Vol. 116, No. 3, 1 Nov 1959, pp.597-604.

Overview of GOES high-resolution interferometer sounder (GHIS) brassboard development and test program

W. E. Bicknell

MIT Lincoln Laboratory
244 Wood Street, Lexington, Massachusetts 02173

ABSTRACT

Replacement of the sounder filter wheel in one of the clones of the GOES I-M satellite series with a Fourier Transform Infrared (FTIR) interferometer would improve retrieval performance and could be a pathfinder for technology employed in the next generation Geostationary Operational Environmental Satellite (GOES) series. Based on examination of an earlier proposal, NOAA decided to pursue the feasibility of a such a FTIR replacement.

The FTIR interferometer is to be as nearly a "plug-in" replacement for the sounder filter wheel as possible. This imposes some interesting and challenging optical, mechanical, and electronic constraints on the design and fabrication of the interferometer.

This overview describes a brassboard design for a replacement FTIR interferometer and provides the background and the status of GHIS brassboard work-in-progress at MIT Lincoln Laboratory.

1. BACKGROUND OF GHIS BRASSBOARD EFFORT

Based on research that demonstrated improved sounding retrieval accuracy can be achieved by use of more and higher-resolution infrared channels, a team headed by the NOAA Cooperative Institute for Meteorological Satellite Studies (CIMSS) at the University of Wisconsin prepared a proposal in 1988 for the development of a FTIR interferometer sounder for the GOES.[1,2] Action on the proposal was postponed at that time until completion and launch of the then ongoing development of the GOES I-M 18-channel filter wheel sounder.[3]

As the first GOES I-M series satellite launch of April 1994 approached, NOAA turned attention to future sounding requirements. Motivated partly by the possibility of sounding improvements foreseen from use of more and higher-resolution channels, NOAA stated requirements for future sounders that were a significant improvement over those achievable with the 18-channel filter wheel.[4] The observational accuracy requirements are given in Table 1.

Table 1. Observational Accuracy Requirements (RMS Error)

Altitude Range	Temperature	Humidity	Vertical Resolution
Sfc-300 mb	1K	10%	1-2 km layers
300-100 mb	1K	20%	2-3 km layers
Above 100 mb	1K	-	3-6 km layers

In addition, NOAA set a requirement to achieve, within 1 hour, a sounding of a synoptic 3000 km x 3000 km area as well as, when needed, a mesoscale 1000 km x 1000 km area.

Since a new design and replacement of the GOES I-M satellites is not foreseen until the 2005 time period, an interest developed in the possibility of modifying one or more of the later GOES I-M satellite sounders so that the desired improvement in observational accuracy and sounding time could be achieved, or nearly achieved, before then.

This work was sponsored by the National Oceanic and Atmospheric Administration under Air Force Contract No. F19628-95-C-0002.

MIT Lincoln Laboratory was asked by NOAA to review the 1988 CIMSS proposal for a FTIR interferometer sounder to determine if such an instrument could be used as a replacement for the filter wheel. The concept is illustrated in Figure 1. There, the filter wheel is shown in the GOES I-M sounder located between a beam-splitting and wavefront-dividing relay optics assembly and the Northeast panel, behind which are cooled detectors and associated optics. The filter wheel itself is cooled to approximately 220K by a dedicated thermal radiator. The idea was to determine if an FTIR interferometer with its optics, metrology reference and zero phase difference (ZPD) sources, moving mirror, and support structure could be built and installed in place of the filter wheel and cooled to 220K. The telescope and the cooled detectors were to remain unchanged. And the relay optics assembly housing was to remain in place.

The MIT Lincoln Laboratory review study proceeded in two phases: In the first phase the feasibility of an FTIR interferometer replacement was examined from a conceptual viewpoint. Upon finding no insurmountable issues, the second phase examined a point design that was developed for a replacement interferometer.

The major conclusion of the review was that a replacement appeared feasible.[5] It was also concluded that the FTIR interferometer would significantly improve sounding performance, although would not fully meet the NOAA requirements cited in Table 1. This is illustrated in Figure 2 which shows the results of simulated temperature retrieval for 2 km layers using a 0.4 sec scan time mode of the FTIR interferometer and using the 0.1 sec duty cycle, 18 channel filter wheel.[6] To put the comparison on equal footing, it was assumed that 4 samples were averaged by the filter wheel for each interferometer scan. It is seen that in the altitude range of about 900 to 100 mb (1 hPa $\approx$ 1 mb) that a 1K RMS error can be achieved by the interferometer. At other altitudes the error is greater than 1K RMS, but is generally smaller than the filter wheel result.

The review did reveal some concerns: The required compactness of the interferometer would make it a challenge to fabricate and assemble. Its placement between two optical systems that are not rigidly registered to an optical bench introduces issues with regard to both initial alignment as well as maintaining alignment upon cooling to 220K.

The review concluded with three recommendations: The first was that a brassboard of a flight-sized FTIR interferometer by built and tested. The second was that a science team be formed to quantify the merits of sounding improvement predicted for the FTIR instrument. Finally, it was recommended that an effort be initiated to develop a plan and schedule for the filter wheel replacement and to evaluate its effect on the ongoing GOES I-M program.

2. GHIS BRASSBOARD OBJECTIVE AND PLAN

NOAA decided to pursue the possibility of an FTIR interferometer replacement with a plan of making a decision on whether to proceed or not at the end of the second quarter of FY 1997. MIT Lincoln Laboratory was asked to build and test a brassboard. NOAA also formed a science team and asked NASA Goddard Space Flight Center (GSFC) to formulate a plan for fabricating a flight FTIR interferometer replacement with Space Systems Loral, Palo Alto, CA, and ITT, Fort Wayne, IN, the manufacturers of the GOES I-M satellite and the filter wheel sounder.[7]

The brassboard is being built and tested both at ambient and at 220K at MIT Lincoln Laboratory. It is currently planned that the brassboard will be installed, aligned, and tested in an early development model (SN02) of the GOES I-M sounder at ITT in Fort Wayne. The objective is to accomplish this in time to provide NOAA with information from the tests in support of the decision on whether or not to proceed.

NASA GSFC is significantly contributing to several areas of the brassboard effort. Contributions include optical diffraction and scattering analysis, procurement and testing of beamsplitters, development of a space-qualified metrology reference source, and examination of magnetic bearing moving mirror designs.

3. BRASSBOARD DESIGN

The wavelength coverage and the operating modes of the brassboard are shown in Table 2.

Table 2. Summary of Wavebands and Operating Modes

Band		Longwave	Midwave	Shortwave
Wavenumber Range (cm^{-1})		620-1150	1210-1740	2150-2721
Operating Modes				
Mode	Dwell (Sec)	Resolution (cm^{-1})		
Full Res	0.4	0.63	1.25	2.5
Fast Scan	0.125	0.68	5.0	5.0
Low Res	0.10	3.85	5.0	5.0

The moving mirror stroke length is set by the highest required resolution. Both the Medium and Low operating modes employ double-sided strokes. The Fast Scan mode is a single-sided stroke that rapidly moves through (without collecting data) the mid optical phase difference (OPD) range. The Fast Scan mode provides nearly the same resolution as the Full Resolution in the Longwave band, but requires a significantly shorter Dwell time. Reduced resolution in the Midwave and Shortwave bands for the modes results from recording data for less than a full stroke extent for those bands.

The estimated RMS noise-equivalent difference temperature (NEDT) for these modes is plotted in Figure 3.

3.1 Optics

Figure 4 shows the optical ray-trace and layout of the FTIR interferometer sounder.[8] There are three subsystems: the GOES I-M sounder telescope, the interferometer, and the existing GOES I-M sounder detectors.

The f/11.9 telescope brings an earth image to focus at the exit of the GOES relay optics housing. A field stop aperture is placed at the telescope image to define four, 244 micro-radian instantaneous field of views (IFOVs), each providing an ≈ 9 km instantaneous ground field of view (IGFOV). The interferometer subsystem, placed in the filter wheel volume, collimates the bundle of four beams and passes the bundles through a FTIR interferometer. After passing through a Lyot stop, the bundles are focused to an f/42 cone and divided into three wavebands. The field stop is re-imaged at the location of a cold glare stop in front of each of the three waveband detector optics. The glare stop is a 20% oversized aperture for each IFOV. The detector optics form an image of the Lyot stop at the detectors. For simplicity, the ray trace for only one IFOV bundle is shown.

The location of the field stop at the telescope image insures that all three wavebands have overlapping IFOVs. However, special thermal and mechanical design is required to maintain alignment with the visible sounder IFOV upon cooling the interferometer to 220K.

A de-centration budget of 0.002 inch and an angular alignment budget of 0.02 degrees is required for the positioning all but the active interferometer components. Diffraction analyses and scattering analyses have been undertaken.[9] Scattering analysis to date has led to a proposed baffling system that isolates the components on either side of the Lyot Stop.

The mirrors are aluminum and have diamond turned surfaces with vacuum- deposited gold coatings. Both a ZnSe and a KBr design will be compared in the brassboard testing.[10]

3.2 Mechanical

The mechanical design of the GHIS brassboard uses an aluminum bench to support the planar optical design.[11] Figure 5 shows a top view of the brassboard mounted on a surrogate filter wheel K-bracket support. The unit is quite compact owing to space constraints. The telescope image plane occurs at the field stop cap in the lower right hand corner of Figure 5. The three separate waveband bundles pass out of the housing through a field lens bracket shown in the upper right. The moving mirror is a leaf-spring porch swing that is suspended below the housing and is not shown.[12]

The bench is held with titanium thermal insulation posts that are located and sized to cause a 220K cooldown zero-shrink point to lie along the centerline of the input telescope image plane and the Longwave band output bundle. This provides design control of cooldown de-centration of the Midwave and Shortwave optical output bundles.

Because of the constrained space, very few of the aluminum component mounts are identical. Figure 6 shows the design of mirror 3 that represents the general approach. As indicated in Figure 4 this mirror is a turning flat just on the telescope side of the interferometer components. It services a metrology reference beam on top and the infrared beam on the bottom. It employs a cantilevered support that provides good thermal conduction from the reference bench while also imparting low stress to the mirror.

The baseline brassboard design does not include a dynamic alignment system for the porch swing moving mirror. It does, however, employ a commandable mirror for the non-moving arm of the interferometer, which is labeled number 4 on Figure 4. The commandable mirror is illustrated in Figure 7. It employs two piezoelectric PZT stacks to control the mirror tilt. The PZT stacks have a nearly zero coefficient of thermal expansion over ambient to 220K and are held by a an invar support bracket that minimizes mirror tilt shift upon cooldown. Strain gauges mounted to the actuator are used to sense and control its length. The mirror tilt has about a 350 microradian dynamic range and can be set to a precision of about 1 microradian.

Vibration testing of the brassboard is not scheduled for the current phase of work. However, the mounts and components have been designed to withstand and maintain alignment under vibration and acceleration loads of an Atlas class rocket launch.

3.3 Electronics

The electronics for the brassboard is being developed for laboratory testing and is not aimed at flight packaging.[13] Figure 8 shows the overall electronics architecture. Experiment control and data storage will use PC based software. Data processing, display, and archiving will done at an accompanying workstation.

Data processing will emulate a technique that could be employed in flight hardware: Interferogram data from each waveband is sampled at a rate to satisfy the Nyquist criterion with margin. The sampled data will be decimated prior to transmission from the satellite to earth The data rate resulting from this process is about 360 kBits/Sec and can be accommodated by changes in the GOES telemetry transmitter power rationing between the sounder, imager, other instrumentation, and housekeeping.

Operation of the brassboard and data collection will utilize a 16 bit A/D converter and a digital signal processing board. Analog electronic bandpass filters having a flat phase delay characteristic will be fabricated for handling up to four detectors at a time. This will be sufficient to simultaneously measure either 1 detector in each of the three wavebands or all four detector channels in any one waveband.

Real time control of the brassboard employs a metrology reference beam fringe counter. This counter utilizes quadrature zero crossing signals derived from a stable reference source that operates in parallel with the infrared beam in the interferometer.[14] As illustrated in Figure 9, by use of an eighth-wave plate retarder in the fixed arm of the interferometer for the metrology beam path, two interferograms having orthogonal linear polarization are derived. The two interferograms are electrically 90 degrees out phase when intensity detected.

Two orthogonal reference signals implement sensing the direction of moving mirror motion. Zero crossing counts from the two signals can be maintained through moving mirror turn-around. This facilitates keeping track of the absolute position of the moving mirror and eliminates the need for a separate zero phase difference (ZPD) source and detector. The zero crossings are used to derive sample triggers for the A/D converter and to control the speed of the moving mirror.

The metrology reference beam is introduced into the interferometer through an optical elevator that is held on a loft shelf situated just below the top plate of the interferometer housing. Mounting chucks for the fiber optic cables that receive and transmit the reference beam, along with the optical elevator are shown in Figure 10.

4. BRASSBOARD ASSEMBLY AND TESTING

The objective of the brassboard assembly and testing is to assess the feasibility of using the GHIS interferometer as a low-risk substitute for the existing GOES sounder.[15]

Assembly and testing of the brassboard has involved four steps: First, testing mirrors and mounts upon procurement and fabrication for initial performance and testing for changes in alignment and wavefront error upon cooldown to 220K. Second, assembly and testing of the components and mounts at ambient temperature. Third, examining alignment changes in the assembled GHIS brassboard for changes in ensquared energy and co-registration upon cooldown. Finally, assembling the GHIS brassboard with infrared components and testing its performance at ambient and at 220K.

4.1 Component testing

Mirrors and mounts were tested using a small dewar and a Zygo interferometer. Changes upon cooldown in mirror wavefront error indicated that for this application diamond turned, vacuum-deposited gold coated aluminum mirrors are superior to polished aluminum mirrors that require a nickel overcoat to achieve final surface finish polish. The latter were found to exhibit wavefront error distortion upon cooldown due to differences in coefficients of thermal expansion of the bi-metallic nickel coating and the aluminum substrate. Diamond turned mirrors were determined to have about 10-50 nanometer RMS surface roughness. The impact of the surface roughness at infrared wavelengths on instrument background scatter signature was judged less than that of wavefront error distortion, but is still to be assessed.

4.2 Assembly and testing at ambient temperature

Assembly and positioning of the brassboard components and mounts on the optical bench was facilitated by use of a Cordax measurement table used in the MIT Lincoln Laboratory mechanical inspection shop. The table provided measurement of position over the bench to an approximate ± 0.0001 inch accuracy. Components were mounted to within ±0.001 inch uncertainty in accordance with the optical prescription. By pre-setting the elevation angle of each optical component to be orthogonal to its mount base, final alignment required adjustments in azimuth. These adjustments were accomplished by use of a Zygo alignment interferometer operating at 0.6328 microns.

Ensquared energy and co-registration for the three wavebands were examined at ambient temperature for the assembled GHIS brassboard Tests were undertaken at 0.6328 microns to characterize the overall, front-to-back wavefront error, magnification, and alignment. Results indicated that ambient assembly wavefront error, magnification, and alignment achievable will meet GOES co-registration and ensquared energy requirements.

4.3 Cooldown testing

Figure 11 is a picture of the laboratory used for both ambient and cooldown tests. Cooldown tests are conducted by placing the interferometer in a vacuum chamber with optical input and output ports. In the chamber the interferometer is cooled to 220K by coupling it via braided copper straps to a liquid nitrogen cold plate. Steady-state temperature is controlled to within ±1K.

Figure 12 illustrates a nominal chamber test setup. The Zygo interferometer emits a collimated 0.6328 μm beam that is focused by an input lens and transmitted through a window into the vacuum chamber and into the interferometer. Referring to Figure 4, it may be noted that an f/11.9 beam that emulates the telescope cone and passes into the interferometer through the field stop at the telescope image will be reflected back out of the interferometer by both mirror #4 and mirror #6. For front-end testing, this is exactly what the input lens shown in Figure 12 accomplishes. A beam blocker can be placed at or near the Lyot Stop to prevent spurious reflections from components #7 through #18.

By blocking either mirror #4 or #6 a single return beam is obtained. The reflected beam is collimated by the focusing lens shown in Figure 12 and returns to the Zygo interferometer. The Zygo compares the wavefront of the collimated, emitted beam to that of the returned beam. The Zygo instrument both displays the resulting interference pattern as well as can be commanded to compute a variety of statistics on the interferogram, including the RMS wavefront error. The wavefront error measured is for a double pass through the components in the optical path and for single reflection off

of either mirror #4 or #6. Use of mirror #6 allows testing the beamsplitter assembly, component #5, in reflection while use of mirror #6 assesses that component in transmission.

Referring again to Figure 4, it may be noted that the re-imaging mirror set #7,#8, and #9 turn the collimated working beam that passes through the Lyot Stop into a cone that forms a re-image of the input field stop outside the rear exit of the interferometer housing. The re-imaging mirror set forms an f/33 cone and the field lenses #16, #17, and #18 convert this into the required f/42 cone. During tests the field lenses were not in service.

Continuing to refer to Figure 4, it can be seen that if the interferometer housing were reversed, so that the interferometer exit ports faced the Zygo in Figure 12, a situation analogous to the front-end tests described would exist: An f/33 beam emulating the exit beam cone that is focused at the field stop image plane and transmitted into the interferometer will be reflected by both mirror #4 and #6. In this case a beam blocker can be placed in the interferometer to prevent spurious reflections from mirrors #1, #2, and #3. This set-up is referred to a back-end test.

The front-end and back-end wavefront errors may be analytically combined to provide a measurement of the overall front-to-back wavefront error of the GHIS brassboard.

Figure 12 also shows some reference flat mirrors employed in the chamber. These mirrors are placed in the collimated beam emitted by the Zygo. The measured tilt of the return wave monitors GHIS table, test bracket, and box motion. The Zygo information is used to assess the changes in alignment of these structures upon cooldown.

Figure 13 shows also a typical interferometer pattern shown on the Zygo display There are several interference patterns displayed each serving a purpose just described.

Dial gauges have also been employed to measure GHIS housing and surrogate K-bracket support de-centration upon cooldown and warm-up to a resolution of 0.0002 inches.

It has been found that changes in the housing support, housing orientation, and internal front-end optics of the GHIS brassboard retain alignment upon cooldown to satisfy GOES co-registration and ensquared energy requirements. To date, tests on the back-end optics indicate that the Longwave band optics also satisfy these requirements. Midwave and Shortwave band alignment exhibits some alignment change on cooldown that is thought attributable to tilt of the dichroics, #10 and #11. Data has been taken, but has not yet analyzed to ascertain if the observed change is within specification.

4.4 Infrared testing

Installation of infrared components into the brassboard is being undertaken at the time of the preparation of this manuscript. It is planned that testing will include a repeat of cooldown alignment and performance evaluation in the test chamber. It is also currently planned that the brassboard will be evaluated by a test installation into the ITT prototype model SN02 for determination of suitability for substitution into the GOES production filter wheel sounders.

5. SUMMARY

The current GOES sounder is providing data to the National Weather Service that will improve weather products. However, higher spectral resolution instrumentation is recommended by the meteorological community to further improve weather prediction. Within the context of the GOES sounder production now in progress, an FTIR filter wheel substitute instrument is proposed as method of providing improved weather prediction obtainable from such a higher spectral resolution instrument with a minimum current sounder modification.

A brassboard of an FTIR interferometer brassboard suitable for filter wheel substitution has been developed and is under test. The major subject investigated to date is maintaining alignment upon cooldown to 220K. To date, brassboard testing has revealed no impediment to utilization of such an instrument.

6. ACKNOWLEDGEMENTS

The author would like to acknowlege the contributions of W. M. Brown.

7. REFERENCES

1. University of Wisconsin-Madison Cooperative Institute for Meteorological Satellite Studies, Santa Barbara Research Center, and ITT Aerospace/Optical Division, "High-Resolution Interferometer Modification of the GOES L/M Sounder: Feasibility Study," September 1988.

2. W. L. Smith, et al, "GHIS-The GOES High-Resolution Interferometer Sounder," Journal of Applied Meteorology, vol 29, No. 12, pp. 1189-1204, December 1990.

3. H. Savides, "Geostationary Operational Environmental Satellite GOES I-M System Description," Space Systems/Loral, GOES Program Office, 3825 Fabian Way, Palo Alto, CA, 94303, December 1992.

4. National Oceanic and Atmospheric Administration, "National Weather Service Observational Requirements for the Evolution of Future NOAA Operational Geostationary Satellites," Review Copy, 7 September 1994.

5. W. E. Bicknell, et al, "GOES High-Resolution Interferometer Study," MIT Lincoln Laboratory Project Report NOAA-12, 5 June 1995.

6. J. P . Kerekes and H. R. Finkle, "GOES high-resolution interferometer sounder retrieval performance simulations," to be published in this SPIE proceedings.

7. GHIS Science Team is led by P. Menzel of CIMSS, University of Wisconsin-Madison.

8. D. P. Ryan-Howard, "GHIS optical design," to be published in this SPIE proceedings.

9. Analyses were performed by Lambda Research Corporation, Acton, MA and by a team led by Eric Young, GSFC.

10. Beamsplitters for the brassboard were procured and tested by Jim Heaney, GSFC.

11. D. E. Weidler, "Mechanical Design of GHIS Brassboard," to be published in this SPIE proceedings.

12. A magnetic suspension drive porch swing for GHIS is being developed by Willie Blanco, GSFC and is planned for testing in the brassboard in FY 97.

13. L. M. Candell, D. M. Weitz, "Electronics considerations for a geostationary interferometer sounder," to be published in this SPIE proceedings.

14. The 1.55 micron stabilized diode laser reference source is being developed provided by Anthony Martino, GSFC. The long and short wavelength stability of this source is to be 10 ppm.

15. A. B. Plaut, A. C. Parker, D. Weitz, "Assembly, alignment, and testing of a GHIS brassboard instrument," to be published in this SPIE proceedings.

SOUNDER

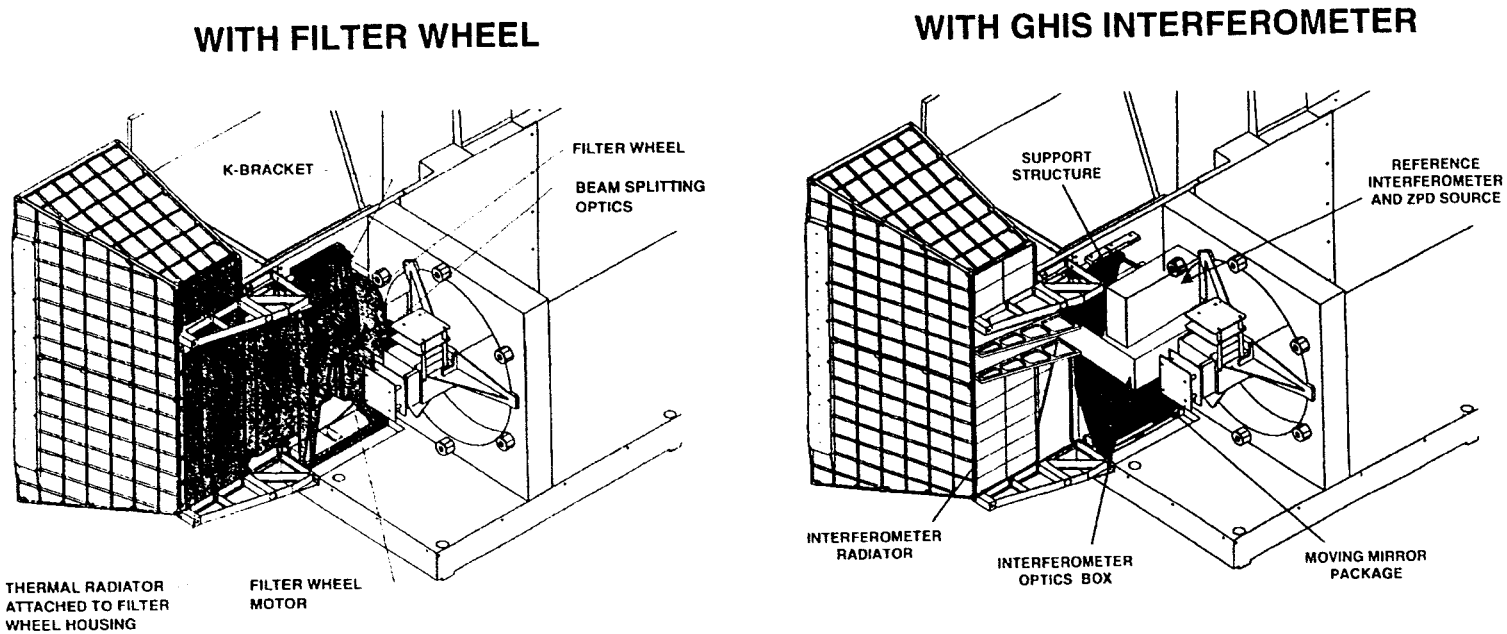

Figure 1. Concept of FTIR interferometer replacement of GOES I-M sounder filter wheel.

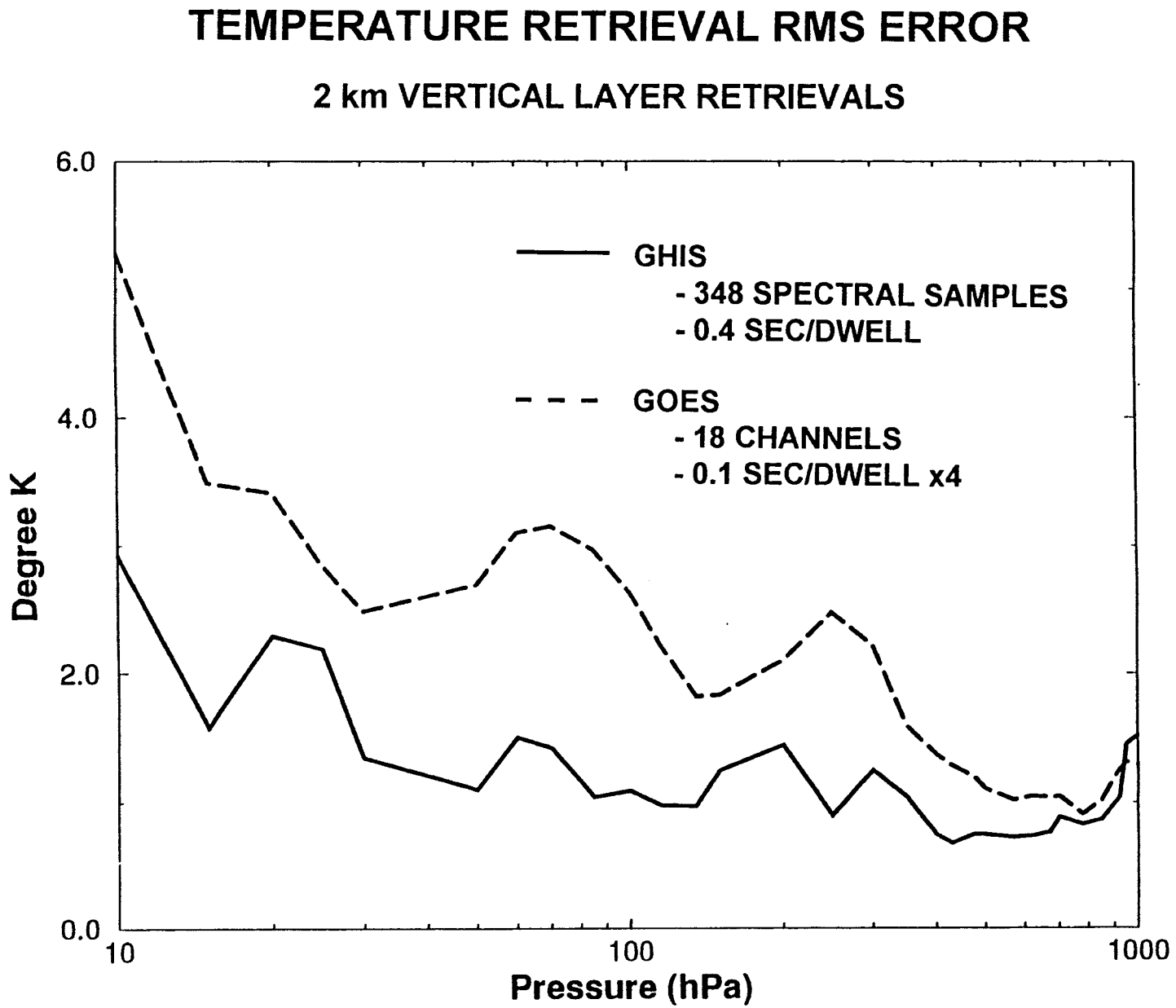

Figure 2. Simulated temperature retrieval error.

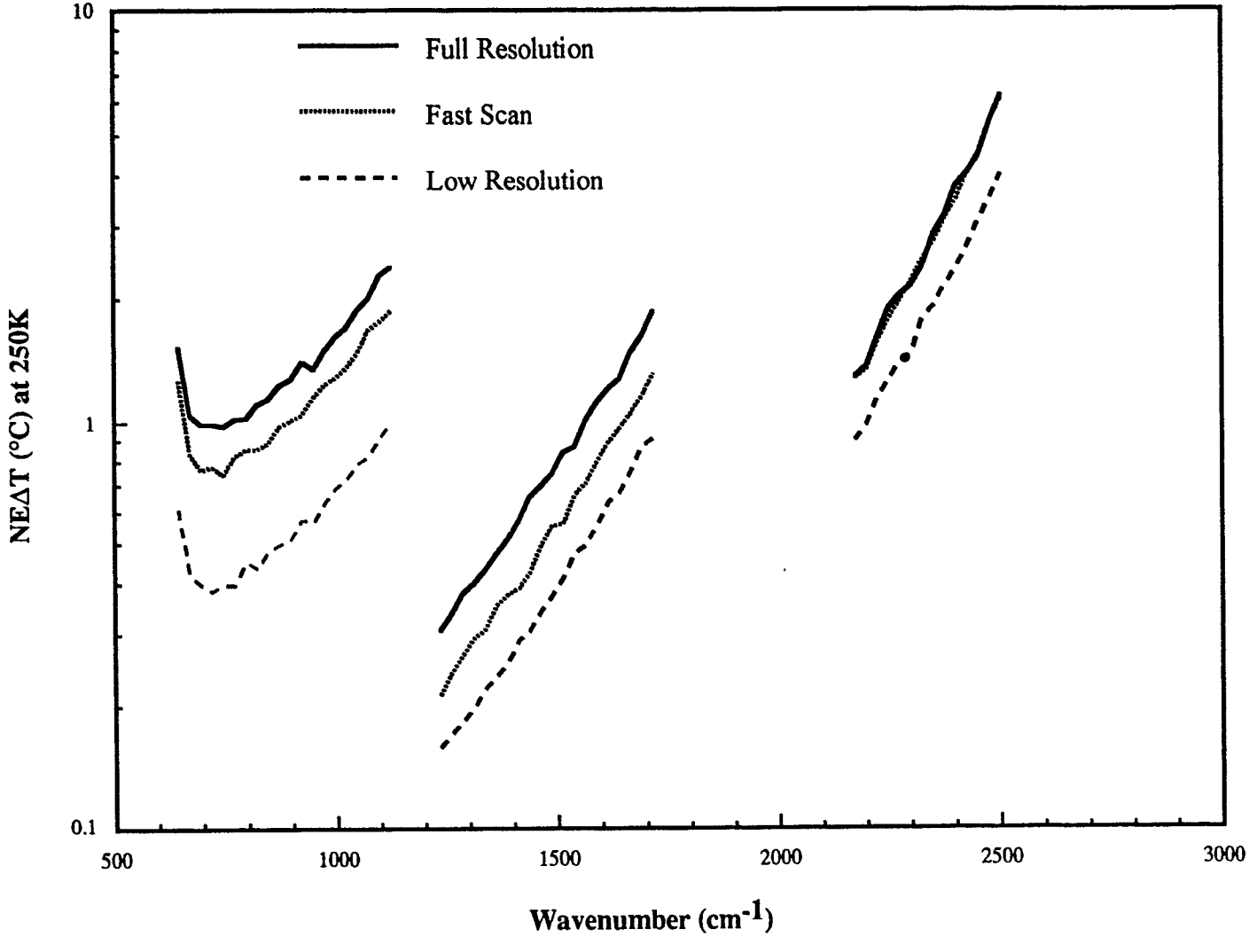

Figure 3. Estimated NEDT.

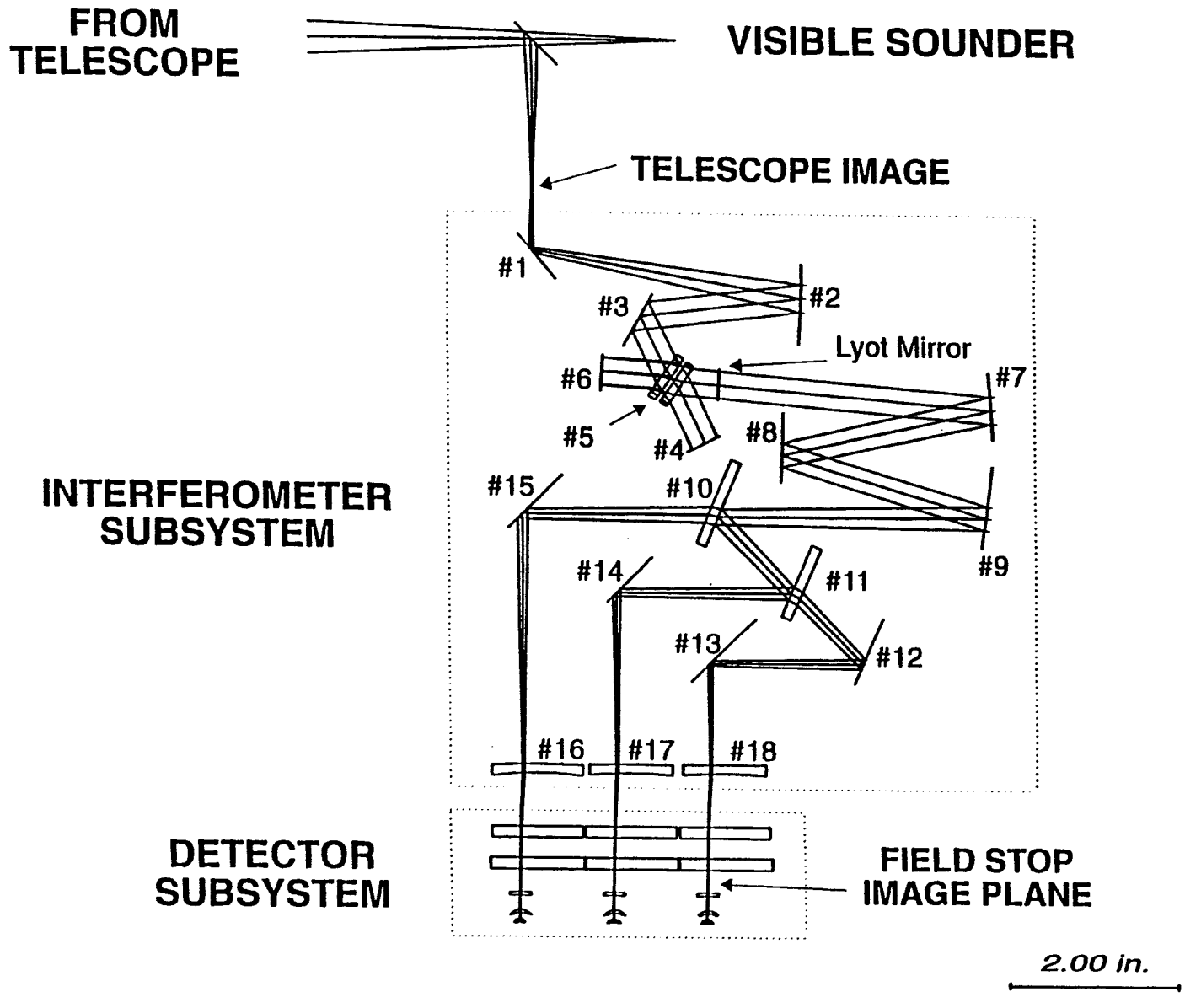

Figure 4. FTIR Interferometer optical layout.

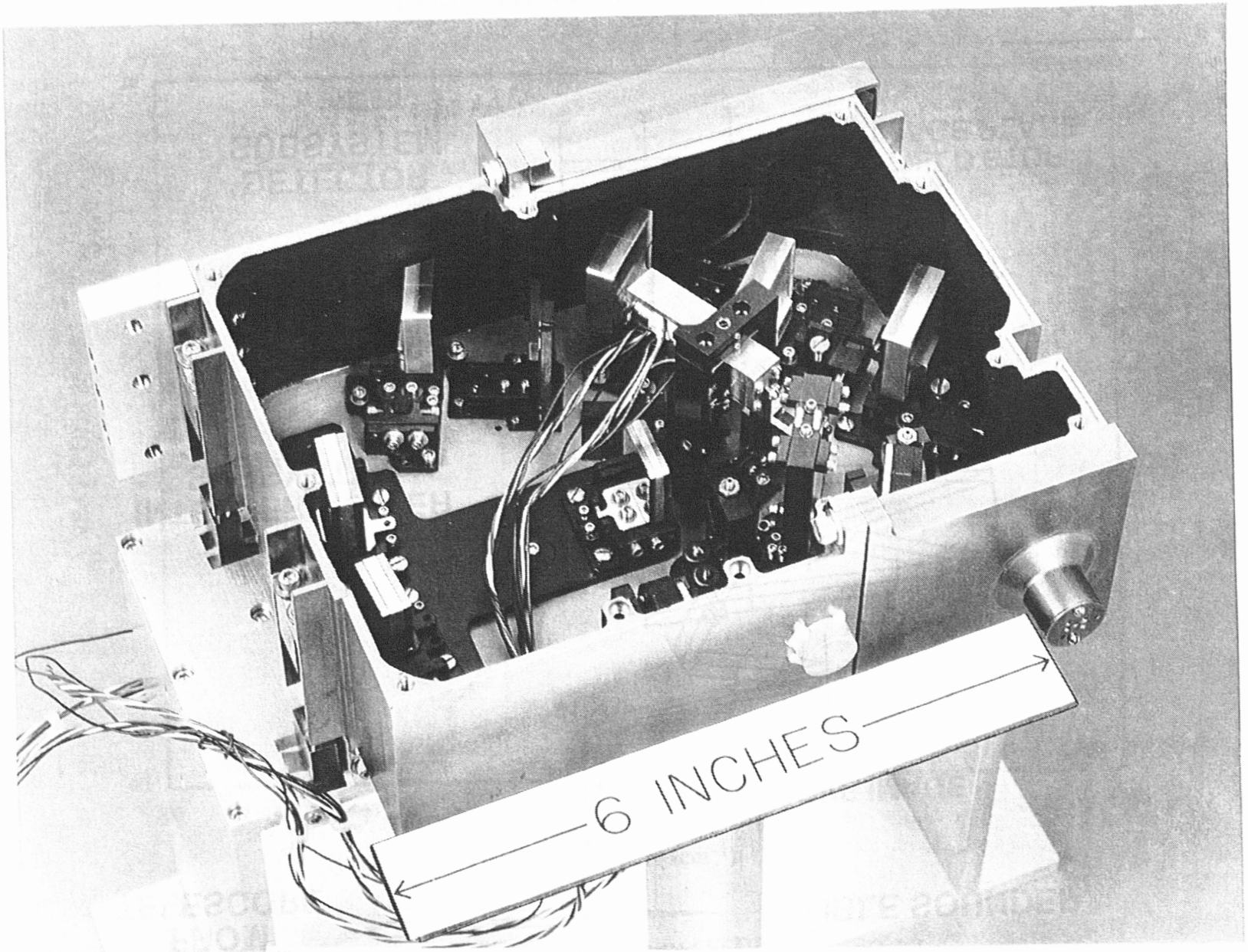

Figure 5. Brassboard mounted on surrogate K-bracket support.

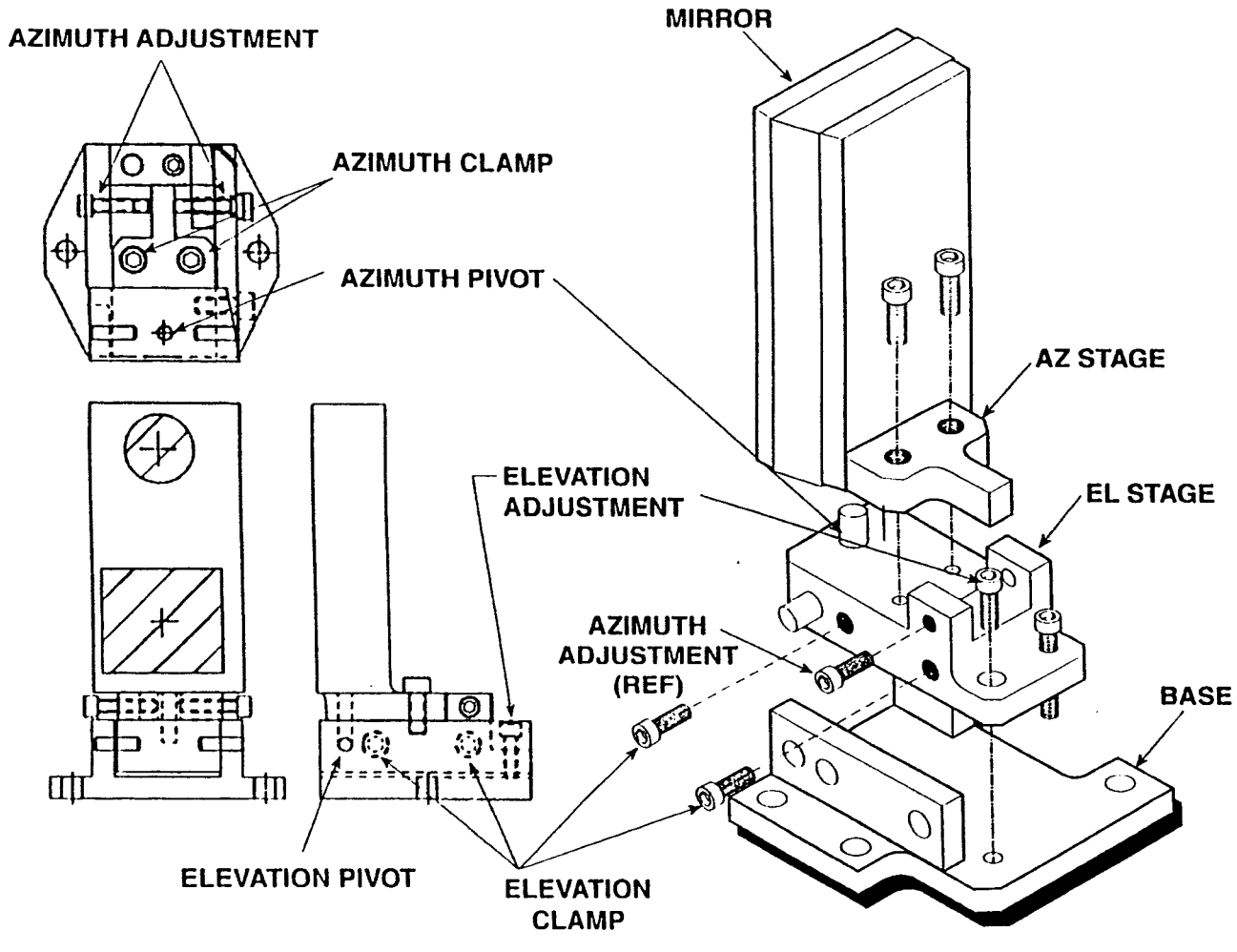

Figure 6. Representative mirror mount design.

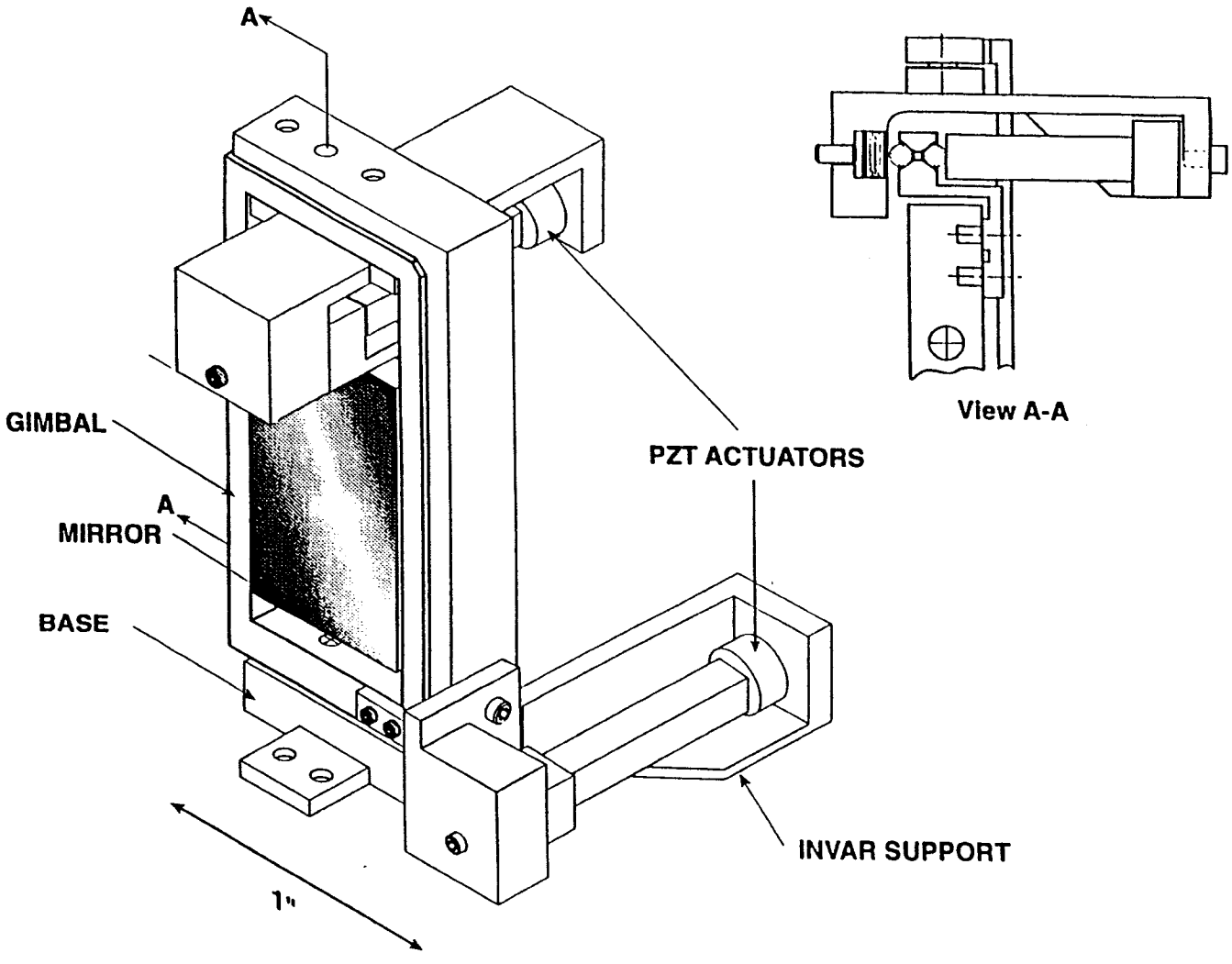

Figure 7. Commandable mirror.

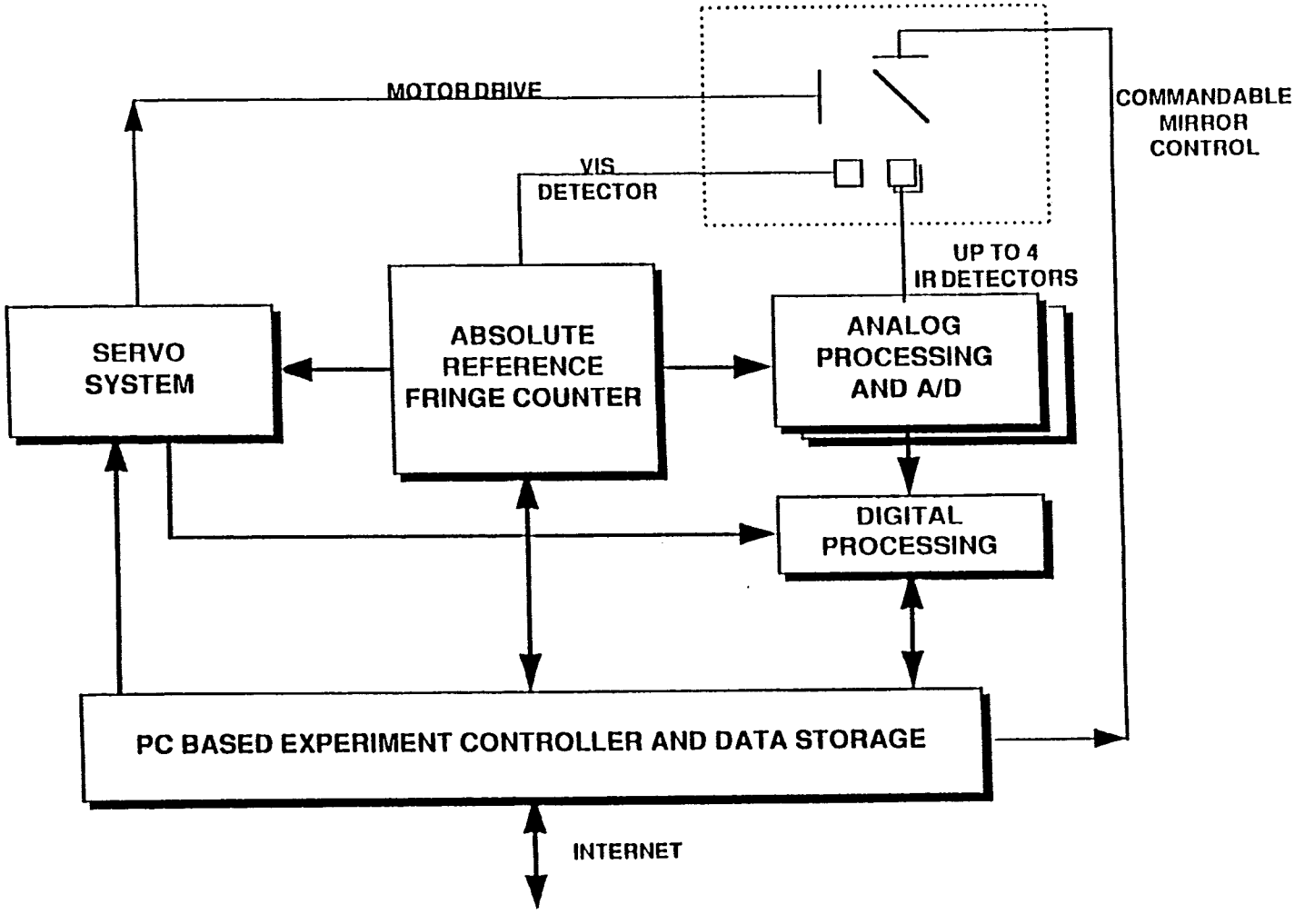

Figure 8. Brassboard electronics architecture.

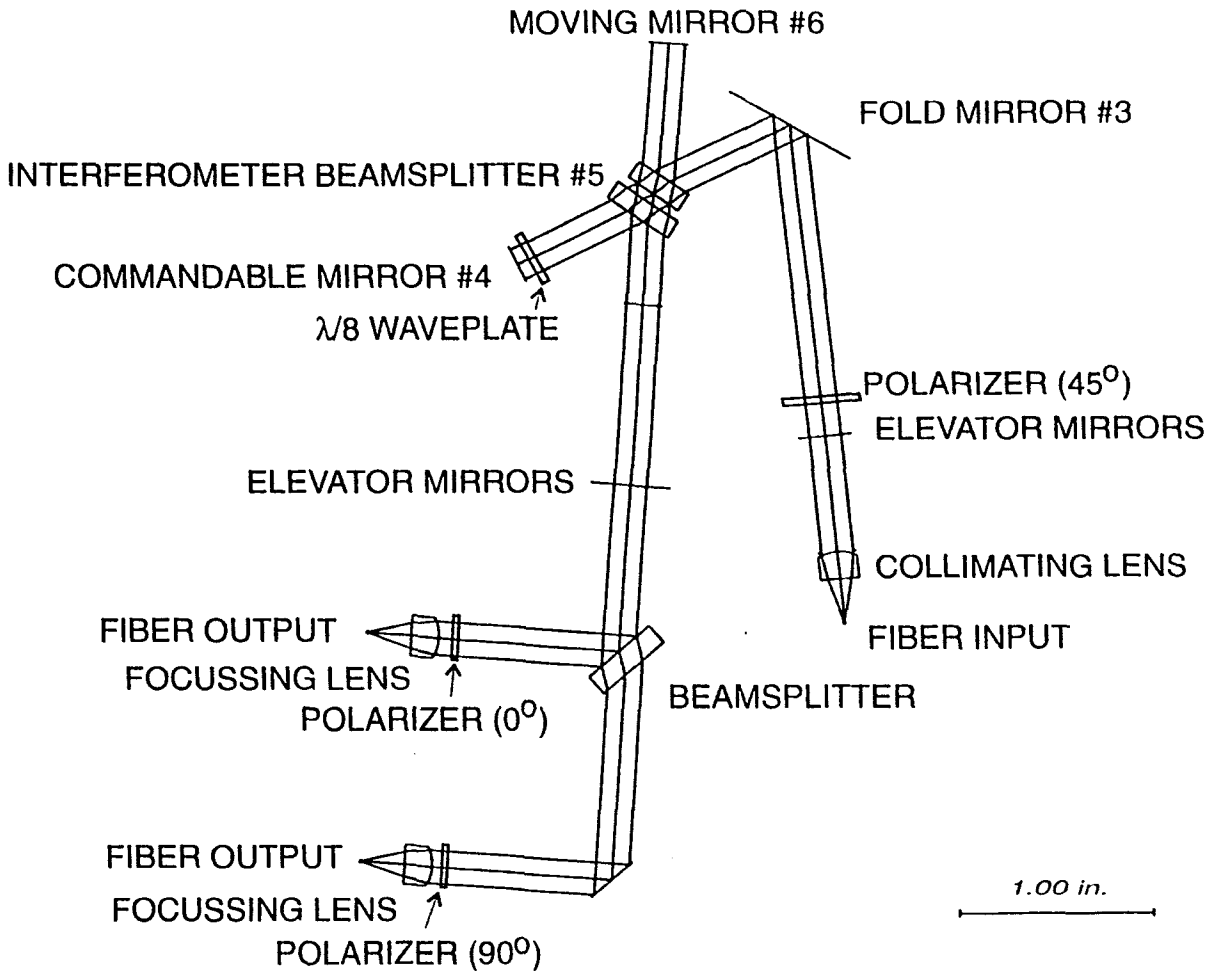

Figure 9. Optical set-up of metrology reference beam fringe counter.

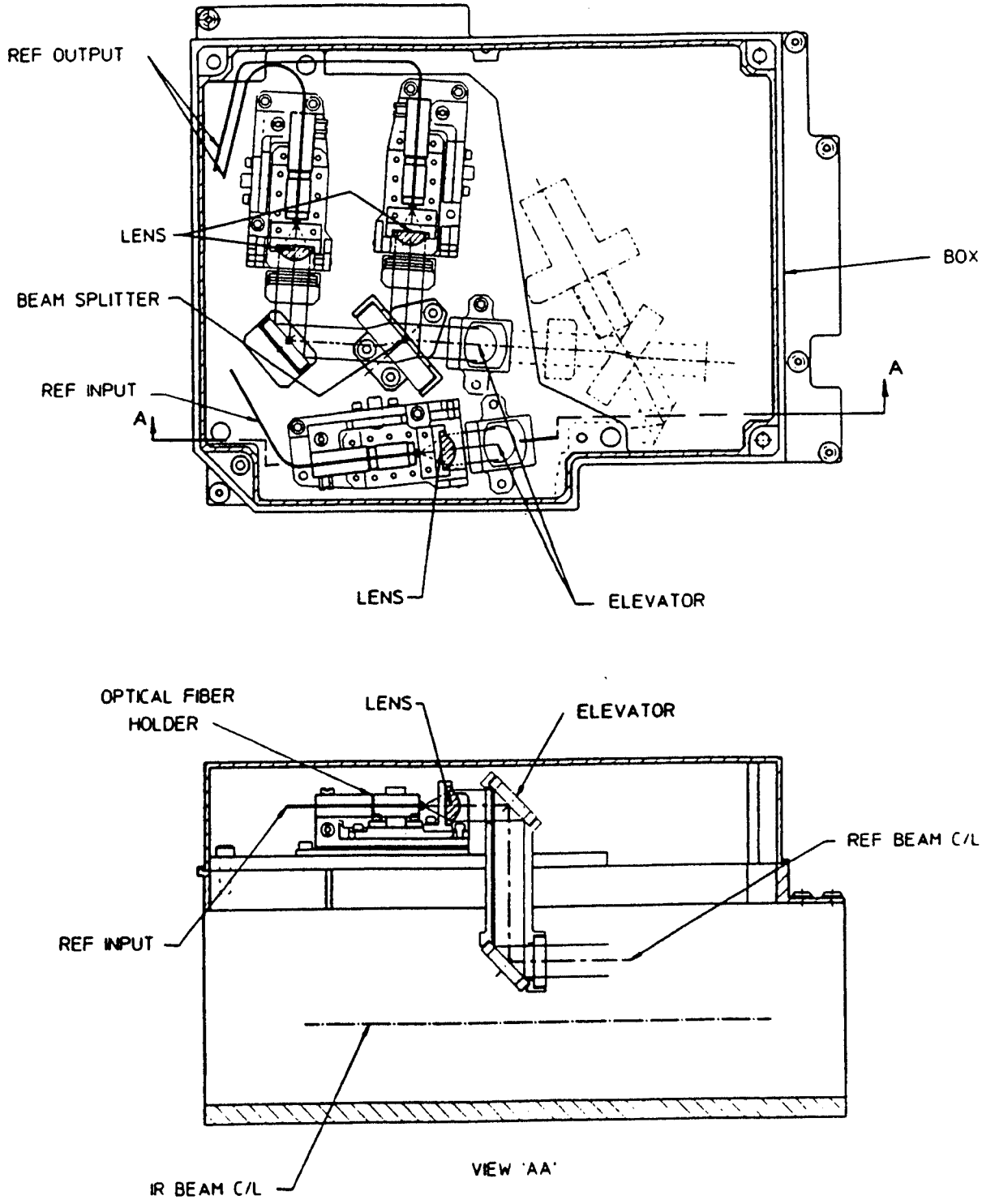

Figure 10. Meteorology reference beam interferometer loft.

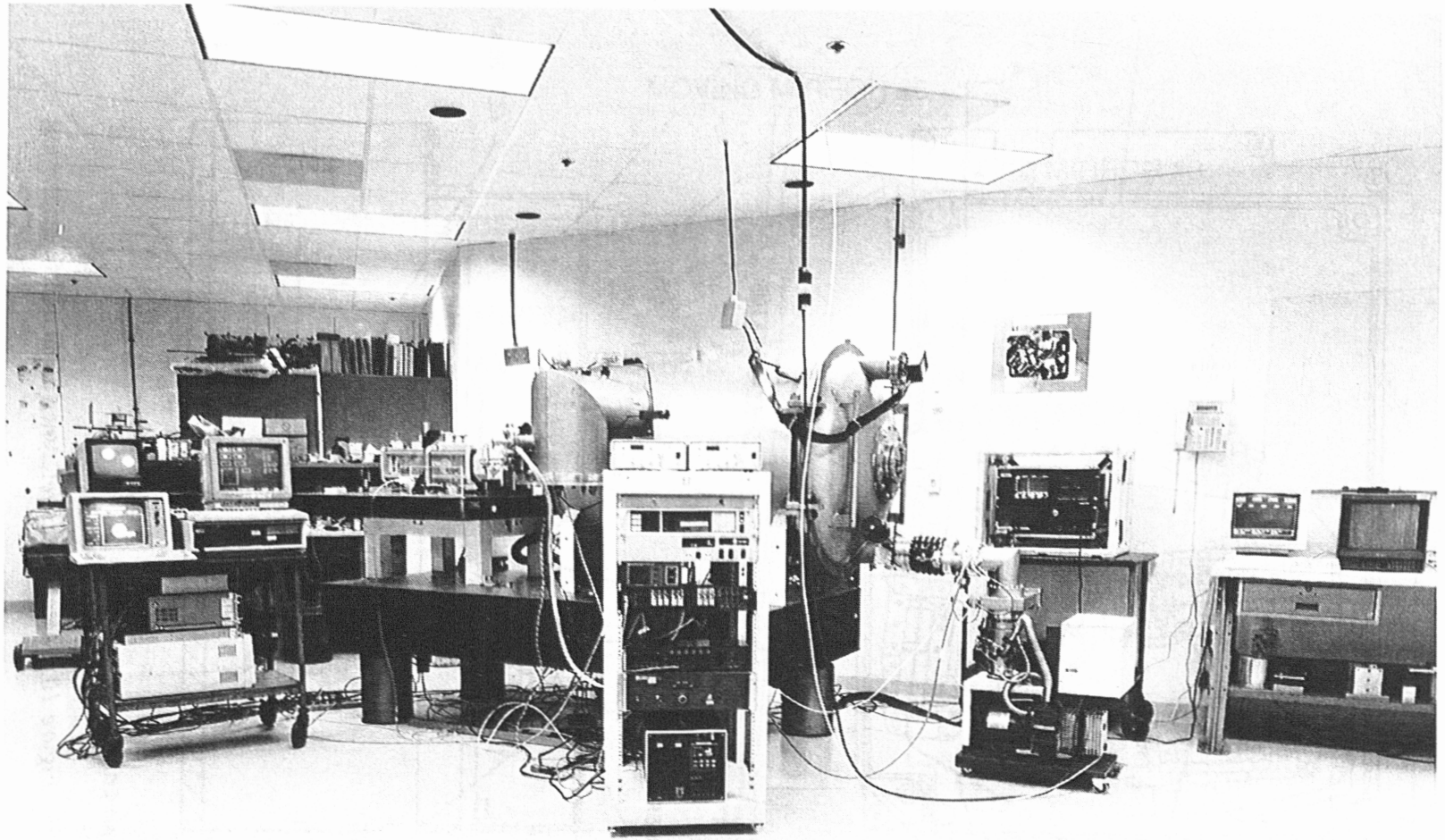

Figure 11. GHIS brassboard test laboratory.

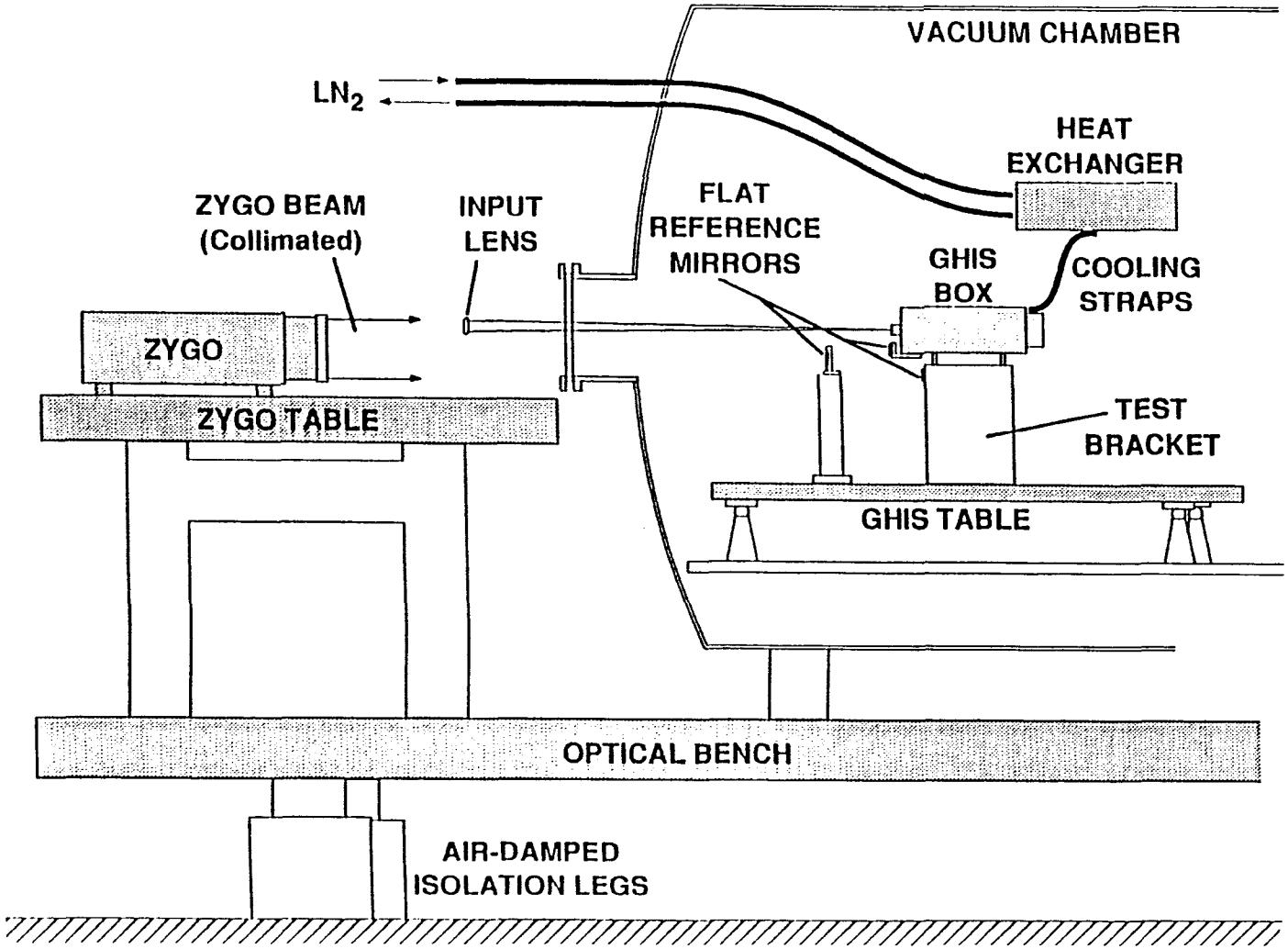

Figure 12. GHIS test set-up.

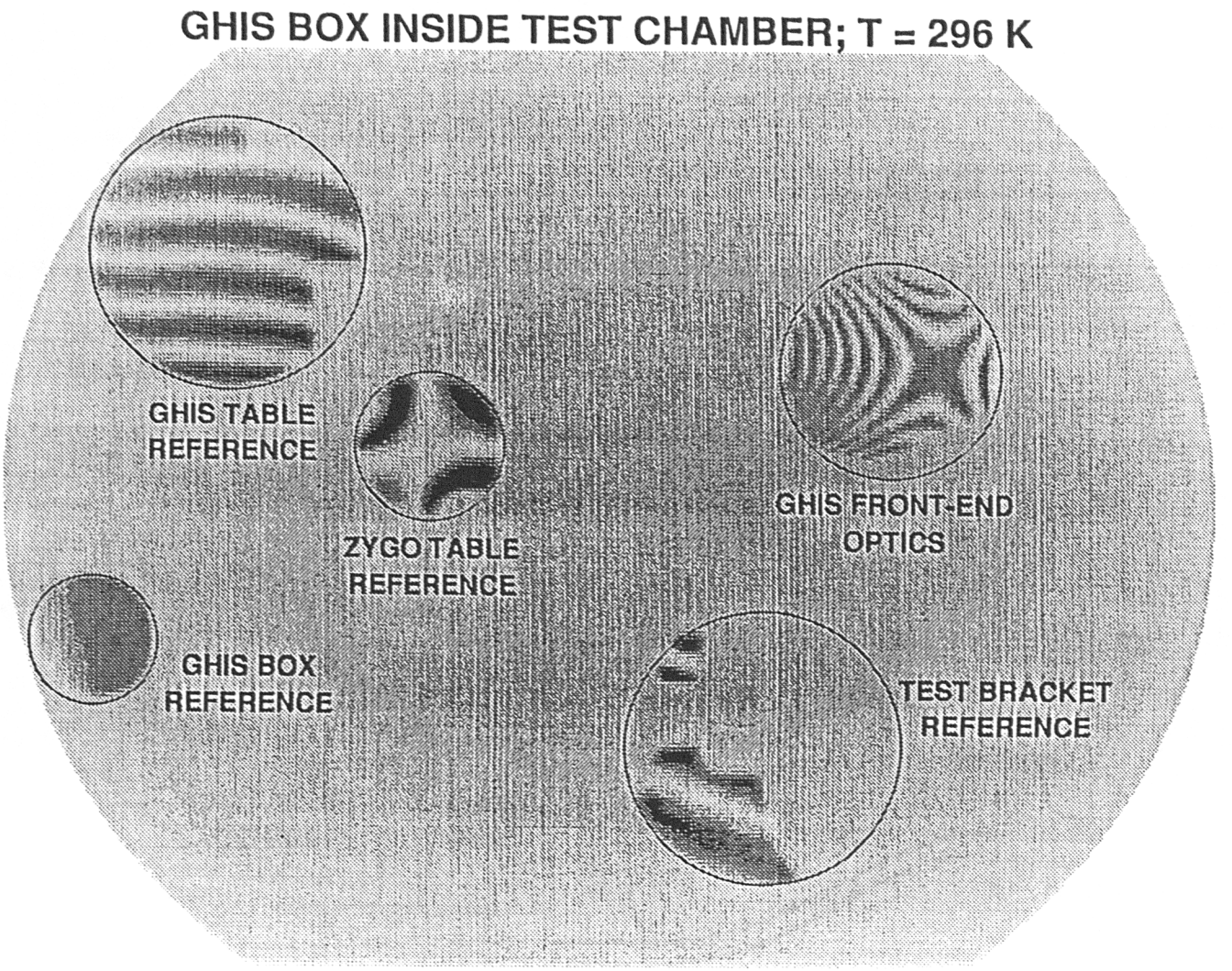

Figure 13. Zygo fringe monitor display.

GOES advanced sounder design study

W. E. Bicknell, J.P. Kerekes, and D. P. Ryan-Howard

Lincoln Laboratory, Massachusetts Institute of Technology
244 Wood Street
Lexington, MA 02173

ABSTRACT

Interim results of a current study on upgrading the geosynchronous operational environmental satellite (GOES) infrared (IR) sounder are presented. Considered are a 15 cm diameter telescope to reduce instrument size and weight, use of a Fourier Transform Infrared (FTIR) interferometer for high spectral wavelength resolution, a small detector focal plane array (FPA) operating at 65K, and combining the instrument with a microwave sounder. Retrieval performance improvement from the FTIR sounder is estimated.

1. INTRODUCTION

This is a report of some interim results from an on-going study being conducted at MIT Lincoln Laboratory. The study is examining IR sounding instruments to be employed on geosynchronous weather satellites in the early 2000 time period. The aim of the study is to determine sounder instrument designs and configurations that could improve performance and reduce cost. The purpose of this report is to describe a point design that illustrates some of the technical issues being considered.

Performance improvement could result from using a small, cooled FPA. The FPA would increase radiometric sensitivity as well as reduce time required for sounding a given geographical area. Combining the IR sounder with a microwave sounder would improve overall retrieval performance, particularly from cloud covered areas.

Cost could be reduced by utilizing smaller, less expensive boosters for launching satellite payloads into geosynchronous orbit. To accomplish this the current GOES payload consisting of an IR sounder, imager, and several other instruments might be separated into two packages. Figure 1 illustrates this concept where a microwave and IR sounder are on a separate satellite that is operated in close orbital proximity to a satellite for the imager and associated instruments. The idea is that of replacing a few large satellites with a constellation of smaller ones. This would lower individual launch costs and would also allow upgrading satellites with improved instrumentation on a less expensive and more timely basis.

Spacecraft weight savings may be achieved by using lightweight alloy structures, lithium batteries, and plasma thrusters. Weight savings could be achieved for an imager and an IR sounder by using lightweight optics and high density electronics packaging. Further weight reduction of an IR sounder might be achieved by utilizing a smaller telescope aperture than currently used.

Table 1 illustrates a weight budget for projected combined IR and microwave sounder.

Table 1. Projected Weight (lbs) of GOES Instruments

Instrument	Current	Advanced
IR Sounder	290	130
Microwave Sounder	-	220
Imager	270	-
Total Weight	560	350

This work was sponsored by the National Oceanic and Atmospheric Administration under Air Force Contract F19628-95-C-0002.

It is seen from Table 1 that a total weight reduction of about 200 lbs is sought. Combined with a possible, 150 lb weight reduction in the spacecraft, the total dry weight of an IR/microwave sounder could then be brought into the Delta 2 and Ariane 4 geosynchronous payload launch capability.

An estimate of the radiometric and retrieval performance that might be achieved with a geosynchronous IR sounder that is mated to a microwave sounder has been developed. The IR sounder point design employs a cryogenically cooled FPA and a 15 cm, rather than the current GOES 31 cm, telescope aperture diameter.

2. IR SOUNDING REQUIREMENTS

Next generation GOES sounding instrumentation should satisfy geosynchronous sounding requirements of the National Weather Service (NWS). Table 2 shows a summary of the required temperature and moisture sounding accuracy.[1] In addition to Table 1, requirements include the capability of sounding both a 3000 x 3000 km^2 synoptic scale area and a 1000 x 1000 km^2 mesoscale area in 60 minutes.

Table 2. Observational Accuracy Requirements (RMS Error)

Altitude Range	Temperature	Humidity	Vertical Resolution
Sfc-300 mb	1K	10%	1-2 km layers
300-100 mb	1K	20%	2-3 km layers
Above 100 mb	1K	-	3-6 km layers

The NWS will require high IR spectral resolution soundings with a resolution on the order of that achievable with FTIR, grating, etalon, or other relatively high-resolution interferometers.[2] Other high-resolution instruments will be examined before completion of the study. However, this report considers a point design for a compact FTIR interferometer of the type being developed for the GOES High-Resolution Interferometer Sounder (GHIS) brassboard.[3,4]

3. MICROWAVE SOUNDER

There is a benefit from simultaneously combining geosynchronous IR sounding with microwave sounding.[5] A microwave sounder has the capability to provide temperature and humidity profiles in the presence of clouds. Although not a major subject of this study, several aspects of a microwave design will be described to illustrate mating a microwave and IR sounder.

If a microwave sounder and IR sounder operate together, both will need to meet the NWS coverage rate requirements. This requirement is assumed to necessitate an hourly 45 minute synoptic scale coverage, a 5 minute mesoscale coverage, and an allowance of 10 minutes for IR calibration and satellite positioning.

A 2 meter antenna microwave sounder strawman design being considered by a geosynchronous microwave sounder working group study has been adapted to the NWS coverage and rate requirement.[6] The operating frequencies are at 118 and 400 GHz for temperature sounding in oxygen bands and at 183 GHz for water vapor sounding. The 400 GHz frequency was chosen to provide high resolution with a 2m antenna with the knowledge that water vapor continuum absorption may prevent sounding below a few km altitude in the tropical latitudes. Table 3 shows a summary of the microwave sounder parameters.

Table 3. Microwave Sounder Parameters

Nominal Frequency (GHz)	118	183	400
Wavelength, λ, (mm)	2.54	1.64	0.75
IGFOV (Diam.) at 36,000 km (km)	60	38	18
IGFOVs in 3000^2 km^2	2600	6200	28000
IGFOV Integration Time, T_i (Sec)	1.1	0.43	0.10
Noise Temperature, T_N (K)	1000	1000	2000
DT_{rms}(K) BW: 100 - 400 MHZ	0.1 - 0.05	0.15 - 0.08	0.64 - 0.32
Azimuth Scan Rate (Degrees/Sec)	0.09		

The instantaneous ground field of view (IGFOV) is evaluated over a 3000 km x 3000 km plane normal to the equatorial satellite projection axis as indicated in Figure 1. The plane subtends a 4.8 degree x 4.8 degree solid angle at the satellite. No spherical geometric projection factors have been used.

The 50% beam response IGFOV shown in Table 3 is given by

$$IGFOV = \frac{1.3\lambda}{D} \times 36000 \text{ km} \quad (1)$$

where D is the antenna diameter. The IGFOV integration time is then 45 minutes (2700 Sec) divided by the number of IGFOVs in 3000^2 km^2.

The receiver sensitivity, ΔT_{rms}, is given by

$$\Delta T_{rms} = \frac{T_N}{\sqrt{BW \times T}} . \quad (2)$$

The front end mixer noise temperatures in Table 3 are projected values assuming about a factor of two reduction from those that are currently available. With this assumption, which is not considered unreasonably optimistic, a receiver sensitivity less than 1K would be achieved at all frequencies.

Since the IGFOVs of the three frequencies are different, it is assumed that the 183 GHz and 400 GHz IGFOVs are raster scanned over the larger, 60 km, 118 GHz IGFOV while all three are being scanned in azimuth. The raster scan might be achieved by scanning the antenna feeds. The overall azimuth scan rate is then given by the requirement of 50 (3000 km/60 km) azimuth scans over a 4.8 degree swath in 2700 seconds. The scan pattern is illustrated in Figure 2. One method for scanning the microwave antenna and IR sounder might be to scan the entire satellite using incremental braking and acceleration of sets of otherwise balanced momentum wheels.

4. INFRARED SOUNDER

A point design IR sounder is assumed to employ a small, 6 x 6 or 8 x 8, array of cooled HgCdTe photovoltaic detectors. Each detector will view an approximately 9 km diameter patch with a 10 km patch spacing. A scan pattern for obtaining a simultaneous microwave and IR sounding then becomes an issue.

4.1 Scan pattern

Figure 2 shows the IGFOV footprint of the 6 x 6 array co-aligned with the 118 GHz microwave sounder footprint. Figure 2 illustrates one mode of simultaneous operation of the two instruments. A turning flat in the IR sounder optical train will be used to counter-scan against the microwave azimuth scan, thereby holding the IR field of view (FOV) steady during an integration period. The counter-scan mirror will periodically be reset in step with the motion of the 118 GHz azimuth scan and the raster scan of the 183 GHz and 400 GHz receivers. For integration time estimates to be described, a 25 mSec counter-scan mirror reset time is assumed

4.2 Optics

The IR sounder optical train is assumed to be a re-imaging design similar to the current GOES, three-waveband sounder except that it, like GHIS, employs an FTIR interferometer rather than a filter wheel. The design is illustrated in Figure 3 for one waveband. A field stop at the telescope focus defines the overall field of view (FOV). A collimating mirror with its focus at the telescope focus collimates the incoming radiation and directs it into an FTIR interferometer. The collimating mirror images the entrance pupil at the Lyot stop that lies at the end of the FTIR interferometer working distance. A re-imaging mirror images the front field stop onto a set of microlenses. The diameter of the microlens defines the instantaneous field of view (IFOV) which, in turn, determines the IGFOV. Finally, the microlenses in combination with the re-imaging mirror image the Lyot stop onto each detector of the 65K FPA.

Figure 3 does not show two dichroic filters after the Lyot Stop that are used to separate the sounder into three waveband channels. And, although a detector bandpass filter and the microlens array should be cold, the cryogenic configuration is illustrative only. Figure 3 does contain notation for optical parameters for a point design described in Table 4.

Table 4. Point IR Sounder Optical Design Parameters

Design Parameters		Dependent Parameters	
IFOV (μrad)	244	Collimator to Lyot Stop (cm), Sw	11
Diag. FOV (mrad), 6x6 Array	2.36	Lyot Stop Diameter (cm), D_{ls}	1.25
Entrance Pupil Diameter, (cm) D_{ep}	15	IFOV Micro-Field Lens Diameter (mm)	1
Primary Mirror Focal Length (cm) f_p	120	FOV Micro-Field Lens Diameter (mm)	10
Collim. Mirror Focal Length (cm) f_c	10	Interferometer IFOV Angle (mrad)	3
Re-Image Mirror Focal Length (cm) f_r	35	Interferometer Diag. FOV Angle (mrad)	28.3
Micro-field Lens Focal Length (cm) f_m	0.14	Detector Focus Distance (mm), f_d	1
Primary to Entrance Pupil (cm) S_p	5	Detector Size (mm), Ddet	0.05

Table 4 describes a point optical design based on simple paraxial ray formulae. The design parameters in the left column determine the dependent parameters shown in the right column. The IFOV is the same as the current GOES filter wheel sounder. The 15 cm entrance pupil, is just less than one-half the current GOES sounder. An f/8 telescope with a 120 cm effective focal length, f_p, is indicated. This can be compared to the approximately 370 cm effective focal length of the GOES f/11.9 telescope.

A 10 cm focal length collimating mirror is indicated. This gives a 11 cm interferometer working distance, Sw, which is tight, but is similar to the compact GHIS brassboard design. The ratio of the telescope and the collimating focal lengths, fp/fc, gives a x12 magnification of the FOV angle for the FTIR interferometer working angle. This may be compared to a x36 magnification for the proposed GHIS system. This smaller magnification helps reduce self-apodization effects in the FTIR interferometer.

The microlens array employs 1mm individual lenses operating at f/1.4. A detector size of 50 μm is nominally matched to HgCdTe IR photovoltaic FPA sizes.[7] The detector FPA and the microlens array are items that are not currently available. However, they are developable and within the range of current technology.[8]

The use of detector readout integrated circuits (ROICs) pose a challenge to timing requirements needed for accurate sampling of an interferogram.[9] It is likely that a 6 x 6 HgCdTe photovoltaic array can be implemented with direct leads which will circumvent this issue. However, employment of an 8 x 8 or larger array may require ROIC development.[8]

Figure 4 shows a ray trace of an optical system based on the parameters of Table 4. The figure shows a two-element unobscured telescope. It also shows the use of a visible/IR beamsplitter to provide a visible image of the sounding that is used in retrieval. Figure 4 shows use of dichroics to divide the radiation into three wavebands.

It has been estimated that approximately 200 mW of cooling would be sufficient to obtain 65K operation of a thermally insulated bandpass filter, microlens, and 6 x 6 FPA. Required refrigeration for three wavebands might then be achieved with Stirling-cycle or pulse-tube cryocoolers that could maintain a 65K cold tip while providing a total of 600 mW of cooling. One refrigeration configuration that might achieve this is the employment of three miniature 250 mW, 65K cold tip pulse-tube cryocoolers.[10] This refrigeration package would weigh about 20 lbs and require about 50 watts of electrical power. Isolation of the FTIR porch swing from the small, but finite, cryocooler vibration is an important consideration that remains to be investigated.

Detailed layout of the instrument depends on the supporting spacecraft design. However, Figure 5 is an artist's illustration of an instrument package. The illustration indicates use of a scanning mirror similar to the current GOES instrument. Also shown are two North-facing radiation coolers. One radiation cooler is used to maintain the optics interferometer at 220K, while the other radiates heat from the cryocooler refrigerator.

4.3 Radiometric performance

Detector sensitivity is a major issue, particularly for the longwave (LW) band. For a photovoltaic detector, the peak D* is given by

$$D^*_{pk} = \frac{\frac{q\eta}{hc}\lambda_{pk}}{\sqrt{\frac{2kT}{R_o A_d}\left(\exp\left(\frac{qV}{kT}\right)+1\right) + 2\eta q^2 Q + \frac{\left[V_{na}^2\right]\exp\left(\frac{2qV}{kT}\right)}{(R_o)^2 A_d}}} \qquad (3)$$

where

q	=	charge of an electron
k	=	Boltzman's constant
h	=	Planck's constant
c	=	velocity of light
h	=	quantum efficiency
Q	=	detector photon flux
T	=	detector temperature
V_{na}	=	preamp noise voltage/√Hz
A_d	=	detector area
R_o	=	detector zero-bias resistance
V	=	detector bias (< 0)

Figure 6 shows a plot of Eq.(3) for a peak D* at 650 cm^{-1} using ambitious, but achievable, detector parameter values.[8] The background flux, Q, assumed was based on calculations of 220K GHIS FTIR instrument NEΔN.[11] The plot indicates that with modest bias at 65K, a peak D* of 1.2×10^{12} can be obtained. This is within about 80% of BLIP. Also shown is a nominal photoconductive

HgCdTe peak D*. The use of the biased, 65K photovoltaic detector provides a gain of about x4 in sensitivity. This and other parameters assumed for the IR sounder are given in Table 5.

Table 5. Geosynchronous IR Sounder Performance Parameters (15 cm Aperture)

Band	Longwave		Midwave		Shortwave	
Wavelength (cm^{-1})	650 - 1150		1210 - 1740		2150 - 2721	
Spectral Resolution (cm^{-1}), $\Delta\nu$	0.625		1.25		2.50	
Scene Flux (Ph/cm^2-Sec)	1×10^{16}		1×10^{15}		0.4×10^{14}	
220K Instrument Flux (Ph/cm^2-Sec)	8×10^{16}		6×10^{15}		1×10^{14}	
Total Detector Flux (Ph/cm^2-Sec), Q	9×10^{16}		7×10^{15}		1.4×10^{14}	
65 K PV HgCdTe R_oA_d (Ohm-cm)	1.2		1000		10000	
Preamp Noise (Volt/√Hz), V_{na}	4					
Quantum Efficiency, η	0.7					
PV D_{pk}*(cm√Hz/Watt)	1.2×10^{11}		2.90×10^{11}		1.12×10^{12}	
GHIS D_{pk}*(cm√Hz/Watt)	3.0×10^{10}		1.37×10^{11}		1.07×10^{12}	
<Diff Loss>/<GHIS Diff Loss>	0.93		0.96		0.98	
Detector Size (cm^2)	$2.5\ 10^{-5}$					
GHIS Detector Size (cm^2)	3×10^{-5}		6×10^{-5}		7×10^{-5}	
Focal Plane Array Size	6 x 6	8 x 8	6 x 6	8 x 8	6 x 6	8 x 8
Max. Self-Apodization Factor	0.993	0.987	0.996	0.993	0.997	0.996
Integration Time, T_i(Sec),	1.06	1.90	1.06	1.90	1.06	1.90
<NEDN> (mw/M^2-cm^{-1}-Sr)	0.80	0.60	0.16	0.12	0.05	0.03
GHIS Integration Time, T_{io}(Sec)	0.10					
GHIS <NEDN> (mw/M^2-cm^{-1}-Sr)	2.5		0.36		0.06	
Noise Factor	0.091	0.070				
GHIS Noise Factor	0.283					

Table 5 cites the wavebands and resolutions that are being used for the GHIS brassboard system. The Table indicates that the background flux on the detector is dominated by instrument radiation in the Longwave and Midwave bands. Decrease of the instrument temperature to below 220K is an option that might be considered. It would improve achievable sensitivity in all wavebands.

Diffraction loss contribution to an instrument transmission, τ, has been estimated. At 650 cm^{-1} the geometric IFOV stop diameter lies just outside the second dark ring of the Airy function at the focus of the 31 cm GHIS system, giving a diffraction transmission loss factor of 91%.[12] For the 15 cm aperture system the geometric IFOV stop diameter (image of microlens diameter) lies

just at the first dark ring, giving a loss factor of 82%. The ratio of the loss factors of the 15 cm aperture to the 31 cm aperture is 0.9 at 650 cm^{-1}. Table 5 shows the ratio:

$$\frac{\tau_{diff}}{\tau_o} = \frac{<Diff\ Loss>}{<GHIS\ Diff\ Loss>}$$

where <Diff Loss> is an average over the waveband. The effect of diffraction on allowable IGFOV cross-talk is a subject to be further explored.

Interferometer self apodization has been considered.[13, 14] The estimate uses an unpublished analysis of self-apodization developed at MIT/LL that employs Lommel functions.[11] The effects are small and are smaller in the Shortwave band than in the Longwave because of the decreased optical phase difference (OPD) used to achieve the required resolution.

For an FTIR interferometer system the noise equivalent differential radiance, NEΔN, is given by

$$NE\Delta N = \frac{1}{A\Omega\tau\Delta\nu D^*}\sqrt{\frac{A_d}{T_i}} \qquad (4)$$

where

A	=	Entrance pupil aperture area
Ω	=	IFOV solid angle
τ	=	Optical transmission
Δν	=	Wavenumber resolution
D*	=	Detector specific detectivity
A_d	=	Detector area
T_i	=	Integration time.

Equation (4) shows that reduction in entrance pupil aperture diameter increases the NEΔN by the square of the reduction factor. The equation also shows that changes in optical transmission, τ, and in D* scale the NEΔN by the ratio of the change, while increases in the integration time or decreases in the detector area decrease the NEΔN by the square root of the ratio of the change.

Results summarized in Table 5 indicate that the combination of improvement in peak D*, increased integration time, and slightly smaller detector size is adequate to offset the approximately x4 increase in NEΔN due to reduction in entrance pupil area and the effects of diffraction loss and self apodization. Further, the improvements appear sufficient to reduce the NEΔN in each waveband to a value less than that for the 31 cm aperture GHIS system. For the LW band the improvement is most significant and critically depends on an improvement in the peak D*.

Results in Table 5 include a noise factor for the LW band which can be used to estimate the effects of improved NEΔN on temperature retrieval error.

5. ESTIMATED TEMPERATURE RETRIEVAL ERROR

During the course of the GHIS effort, retrieval analysis simulations have been undertaken to estimate the performance improvement over the current GOES filter wheel sounder. The current simulations use a subset of TOVS Initial Guess Retrieval (TIGR) atmospheric profiles for training and a second, independent, TIGR set for statistically evaluating retrieval performance for a given set of GHIS waveband NEΔNs.[15]

Analyses have shown that the temperature retrieval is most sensitive to the LW band NEΔN. Providing NEΔNs of the Midwave and Shortwave bands are not significantly different, changes in temperature retrieval error have been found to almost singularly depend on the LW <NEΔN>. This has led to the development of a simple scaling factor applied to the LW band <NEΔN>, called the noise factor, that can be used in predicting and describing results.[16] A set of noise factor scaling results from recent retrieval

simulations has been made available and are used to estimate the improvement in temperature retrieval due to the projected improvement in <NEΔN> suggested in Table 5. The results used are for a 1 km vertical resolution layer.

The noise factor, nf, is a scaling factor used for the effect of the LW band NEΔN. It is given by

$$nf = \frac{<NE\Delta N>}{<NE\Delta N_o>} \sqrt{\frac{1}{NS}} \propto \frac{A_o \Omega_o \tau_o \Delta \nu_o D^*_o}{A \Omega \tau \Delta \nu D^*} \sqrt{\frac{1}{NS} \frac{A_d}{A_{do}} \frac{T_i}{T_{io}}} \tag{6}$$

where the notation has been previously described and the subscript "o" refers to a reference <NEΔN> value used to compare one retrieval simulation to another. The factor NS is the number of number IGFOV sounding samples averaged. For a given ground cell size being evaluated by sounding, it is given by

$$NS = (1 - \text{Percent Cloud Cover}) \left(\frac{\text{Averaged Cell Size}}{\text{IGFOV Spacing}} \right)^2 \tag{7}$$

Typically, a 50% cloud cover is assumed for a 50 km cell size with a 10 km IGFOV spacing, giving NS = 12.5. For the IR sounder being considered compared to GHIS

$$\Omega_o = \Omega, \Delta \nu_o = \Delta \nu$$

and

$$nf \propto \frac{A_o \tau_o D^*_o}{A \tau D^*} \sqrt{\frac{A_d}{A_{do}}} \sqrt{\frac{1}{NS} \frac{T_i}{T_{io}}} \equiv \epsilon_f \sqrt{\frac{1}{NS} \frac{T_i}{T_{io}}} . \tag{8}$$

The parameter ϵ_f reflects noise factor scaling due to fixed design parameters.

Figure 7 shows an estimate of the improvement in average RMS temperature error sounding provided by the 15 cm aperture, cooled photovoltaic FPA sounder. The temperature error is an average from 1000 to 300 mb. The GHIS temperature errors are from a study which predicted errors using an average over the TIGR data sets.[16] The advanced sounder RMS sounder errors in Figure 7 were obtained by scaling the GHIS results using the improved noise factors shown in Table 5 that result from the lower LW <NEDN>.

It is seen from Figure 7 that the projected performance is an improvement over the GHIS design, as expected. The temperature retrieval error also falls within the NWS requirement boundary. That the estimated error only "clips" or somewhat marginally falls within the boundary is not unexpected: It has been found in simulations that reduction in LW <NEΔN> by a factor of 2 reduces the retrieved temperature error by approximately 20%. Also, it should be considered that the estimate here does not include improvement that will be derived from incorporating microwave sounding with the IR retrieval. In addition to a providing larger sounding measurement data base, the microwave sounder will greatly diminish the effect of cloud cover.

6. SUMMARY

This report describes interim results of an MIT/LL study on development of an advanced GOES IR sounder. The study is to explore possibilities for reducing cost and improving performance. A point design example has been given of a potentially smaller, compact IR sounder based on GHIS technology, lightweight, smaller aperture optics, and a 65K 6 x 6 or 8 x 8 photovoltaic HgCdTe FPA. The IR sounder operates with a microwave sounder housed in the same satellite. The example illustrates some of the issues encountered in providing an advanced geosynchronous sounder instrumentation system.

Results suggest that the retrieval performance from such a sounder system will be improved over the current GHIS design, will meet NWS requirements, and will provide soundings much less susceptible to cloud cover conditions.

Possible further improvement in IR performance might be achieved by operating the FTIR interferometer at a temperature lower than 220K. Operating the FPA at slightly higher than 65K temperature might be traded against a slightly larger aperture to arrive at an overall minimized weight.

It has been projected that the payload weight of such a combined microwave and IR sounder could be less than the current GOES series combined sounder and imager instruments. This invokes separation of the current imager and other instruments into a separate companion satellite. Interim results of ongoing studies of advanced IR and microwave geosynchronous sounders have been described. Final results on the merit and feasibility of a combined IR and microwave sounder instrumention awaits the completion of both studies.

Technology that might be further pursued in preparation for development of an IR instrument includes LW photovoltaic HgCdTe FPAs, ROICs, microlens systems matched to such FPAs, and continued development of space-qualified cryocoolers.

7. ACKNOWLEDGEMENTS

In addition to those cited, the authors would like to acknowledge the contributions of W. M. Brown to the advanced sounder concept, D. L. Mooney for helpful technical discussions and critique, and D.E. Weidler for consultation on mechanical and thermal issues.

8. REFERENCES

1. National Oceanic and Atmospheric Administration, "National Weather Service observational requirements for the evolution of future NOAA operational geostationary satellites," Review Copy, 28 November 1995.

2. ibid.

3. W. L. Smith, et al, "GHIS-The GOES High-Resolution Interferometer Sounder," Journal of Applied Meteorology, 29, No 12, pp. 1189-1204, December 1990

4. Also see "Advanced Technologies and Instruments" in this Proceedings

5. D.H. Staelin and J.P. Kerekes,"Combined Microwave and Optical Atmospheric Remote Sensing Techniques: A Review," Proc. of 2nd Topical Symposium on Combined Optical-Microwave Earth and Atmosphere Sensing (CO-MEAS), April 3-6, 1995, pp. 3-6.

6. D. H. Staelin, Private Communication

7. E. E. Krueger, et al, " Extending HgCdTe Photovoltaic Detector Technology to Cutoff Wavelengths of 17 μm," 1993 Spring Meeting of the Materials Research Society, San Francisco, CA, April 1993

8. M. Reine, Private Communication

9. L.M. Candell and D. M. Weitz, , "Electronics Considerations for a Geostationary Interferometer Sounder," to be published in this SPIE Proceedings

10. E. Tward, *et al.*, "Miniature Long-Life Space-Qualified Pulse-Tube and Stirling Cryocoolers," pp. 329-336, *Cryocoolers 8*, R.G. Ross, Jr., Editor, Proceedings of the 8th International Cryocooler Conference, Vail, Colorado, June 1994, Plenum Press, NY

11. D. R. Hearn, Private Communication

12. M. Born and E. Wolf, Principles of Optics, MacMillan, New York, 1964

13. R. J. Huppi, R.B.Shipley, and E. R. Huppi, "Balloon-borne Fourier spectrometer using a focal plane detector array," Proc. Soc. Photo-Opt. Instrum. Eng. 191, pp. 26-32, 1979

14. B.K. Yap, W. A. M. Blumberg and R. E. Murphy, , "Off-axis effects in a mosaic Michelson interferometer," Applied Optics, 21, pp. 4176-4128, November 1982

15. Allen Huang, Private Communication

16. W. L. Smith, Private Communication

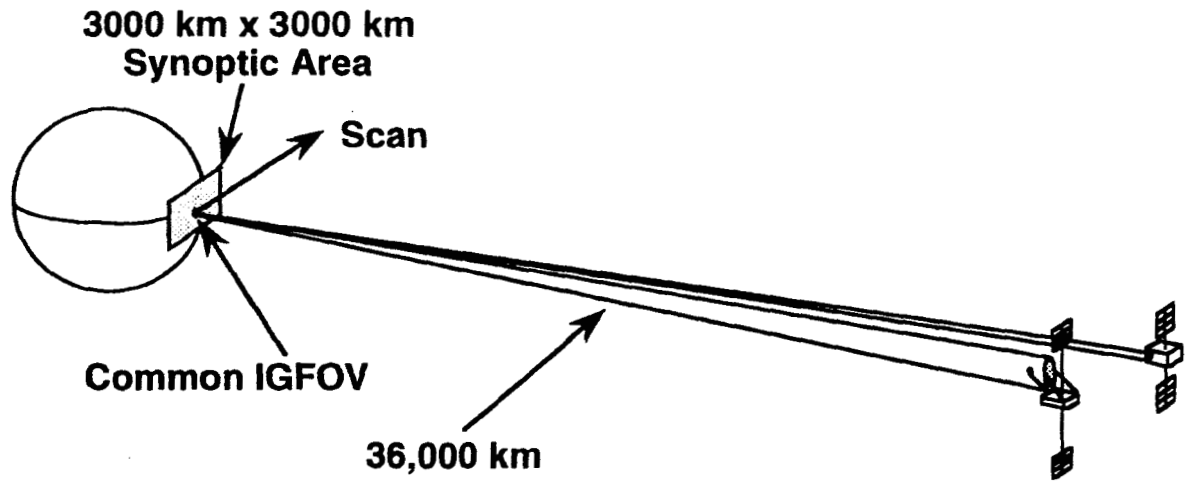

Figure 1. Advanced sounder concept.

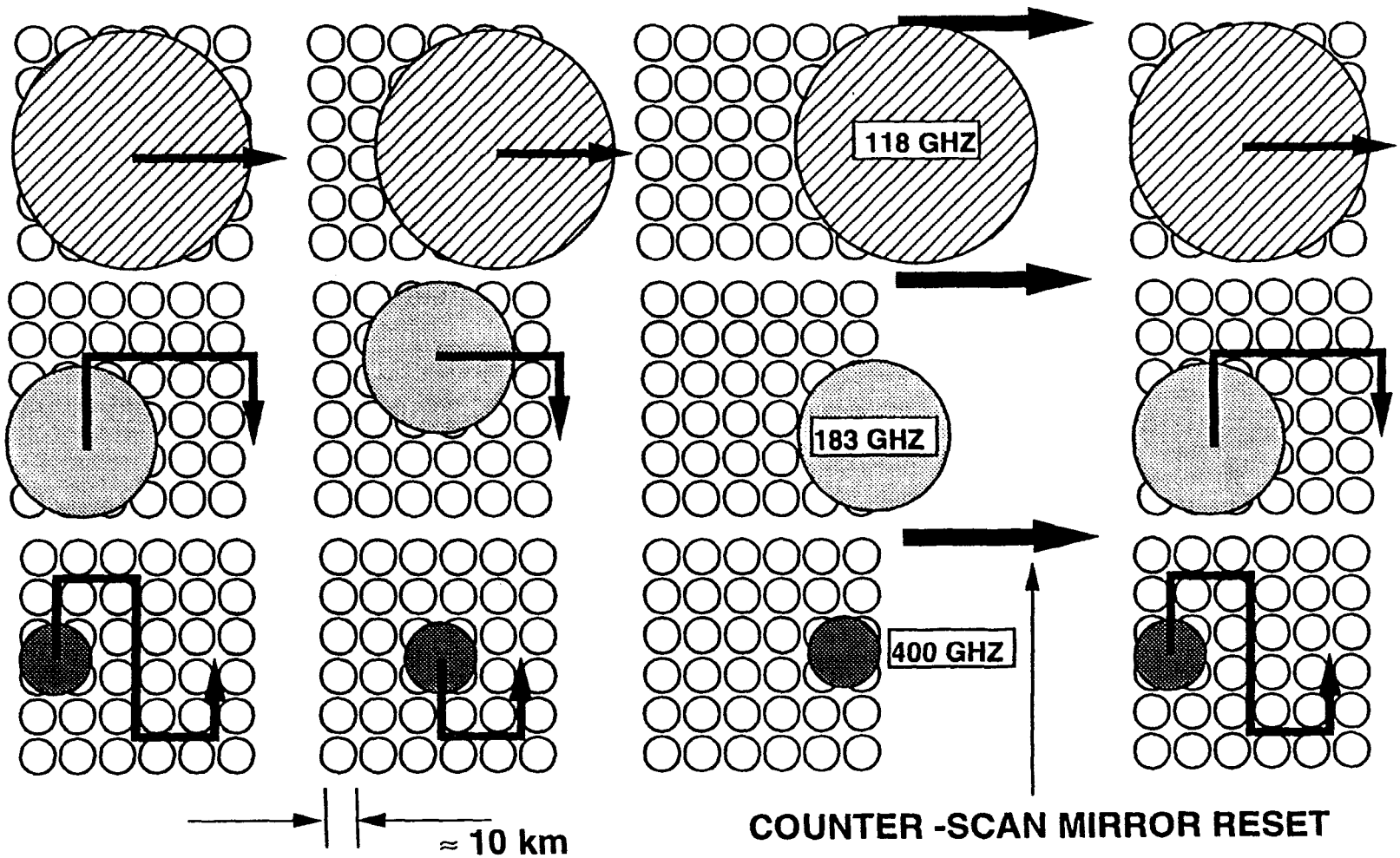

Figure 2. Microwave and IR scan pattern.

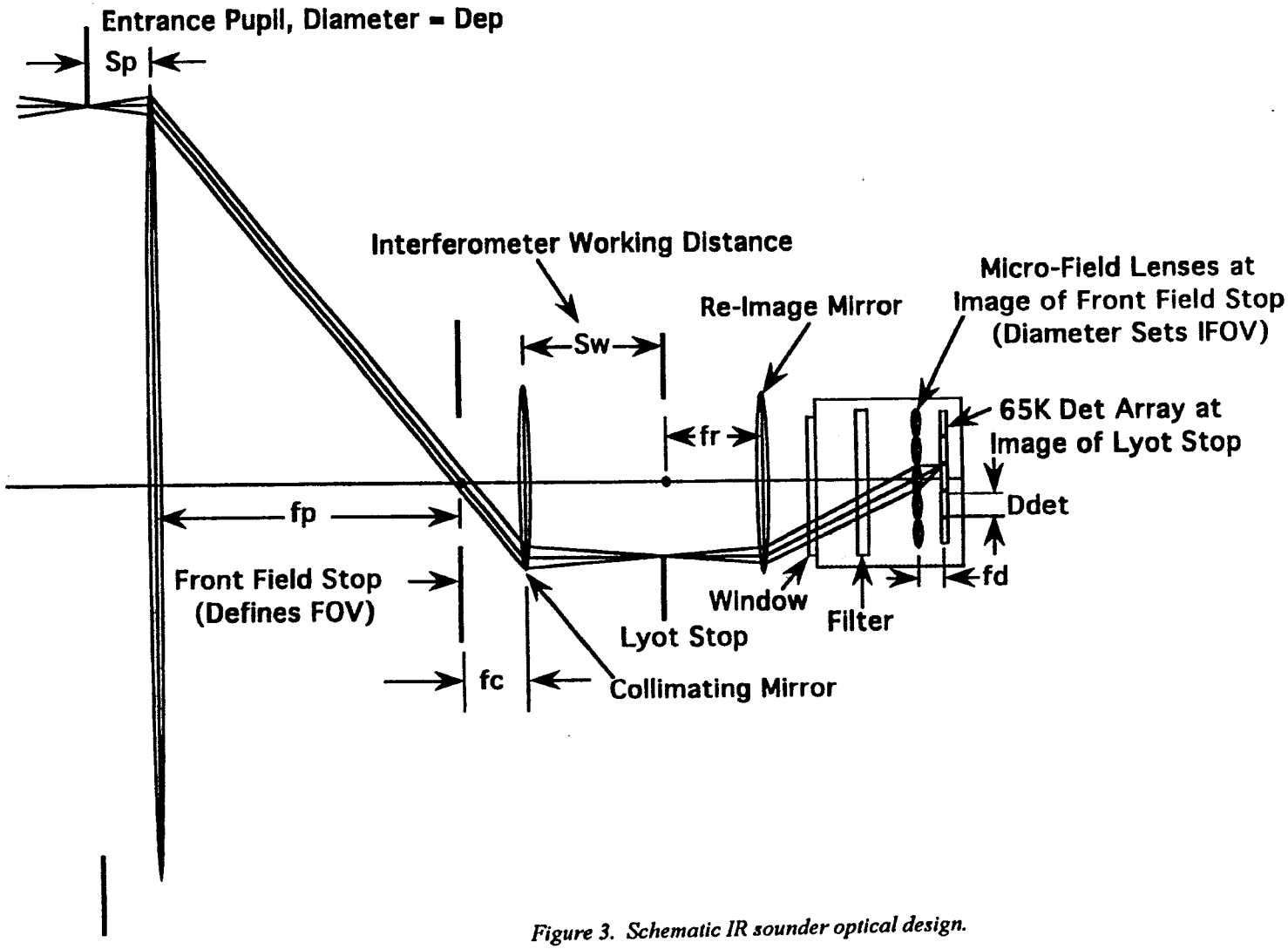

Figure 3. Schematic IR sounder optical design.

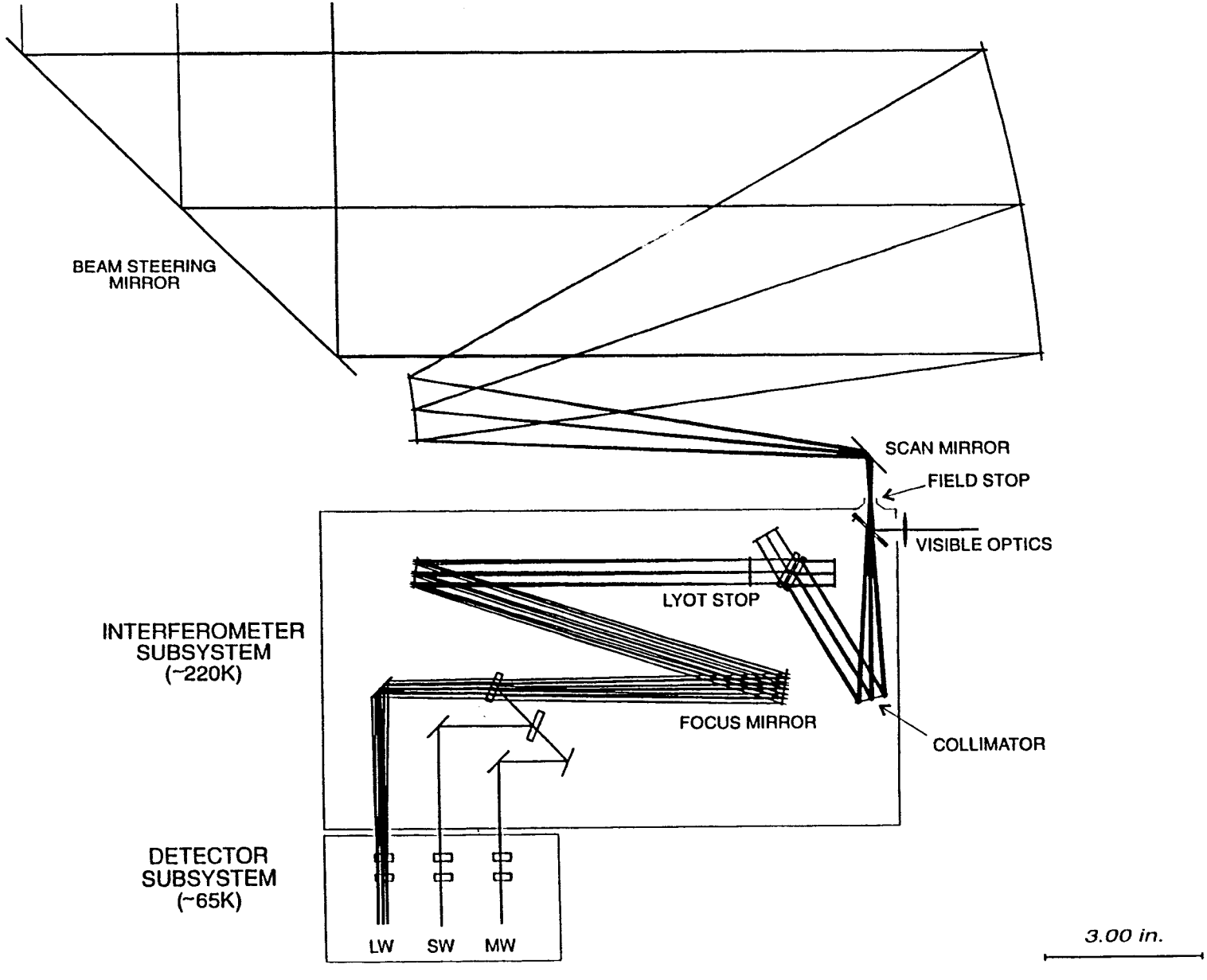

Figure 4. Ray trace and layout of IR sounder optics.

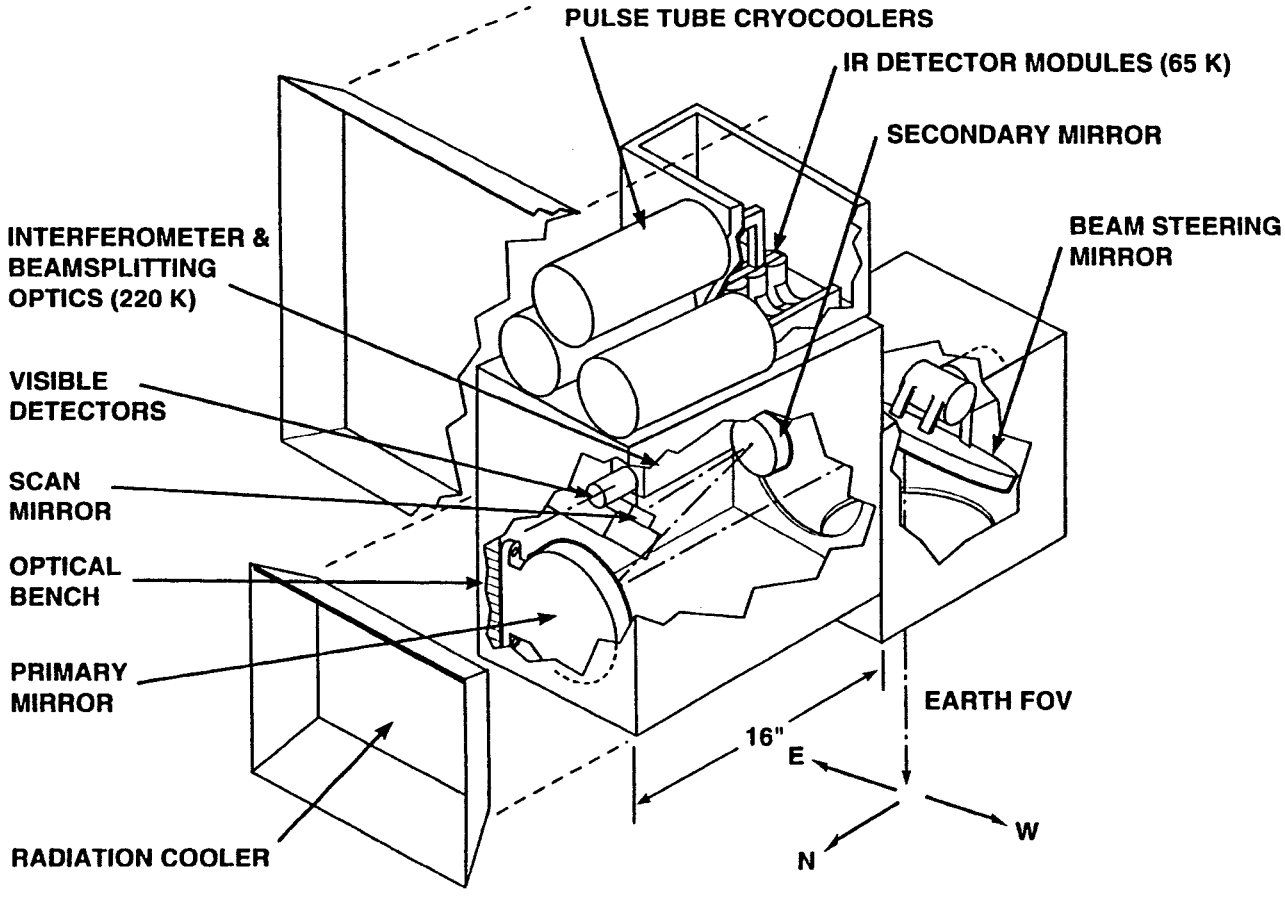

Figure 5. IR sounder instrument package.

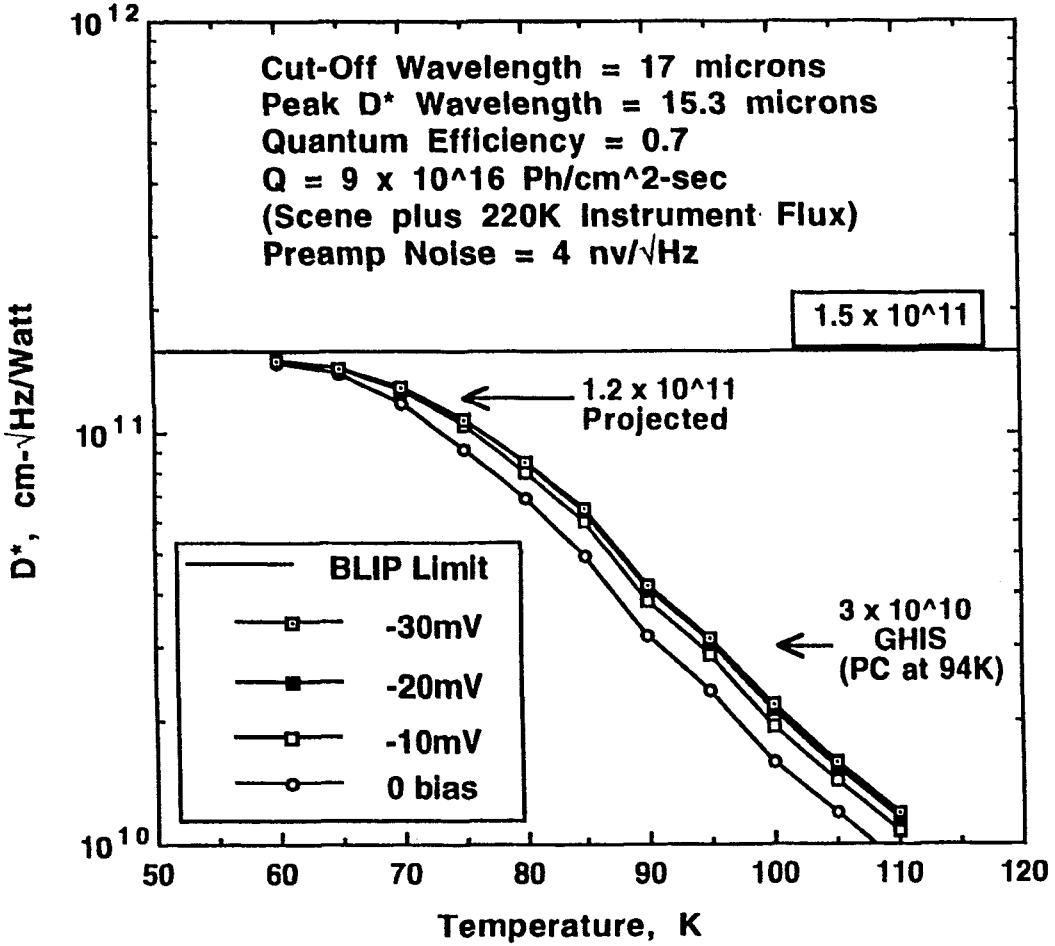

Figure 6. LW PV D^*_{pk} vs. temperature and bias.

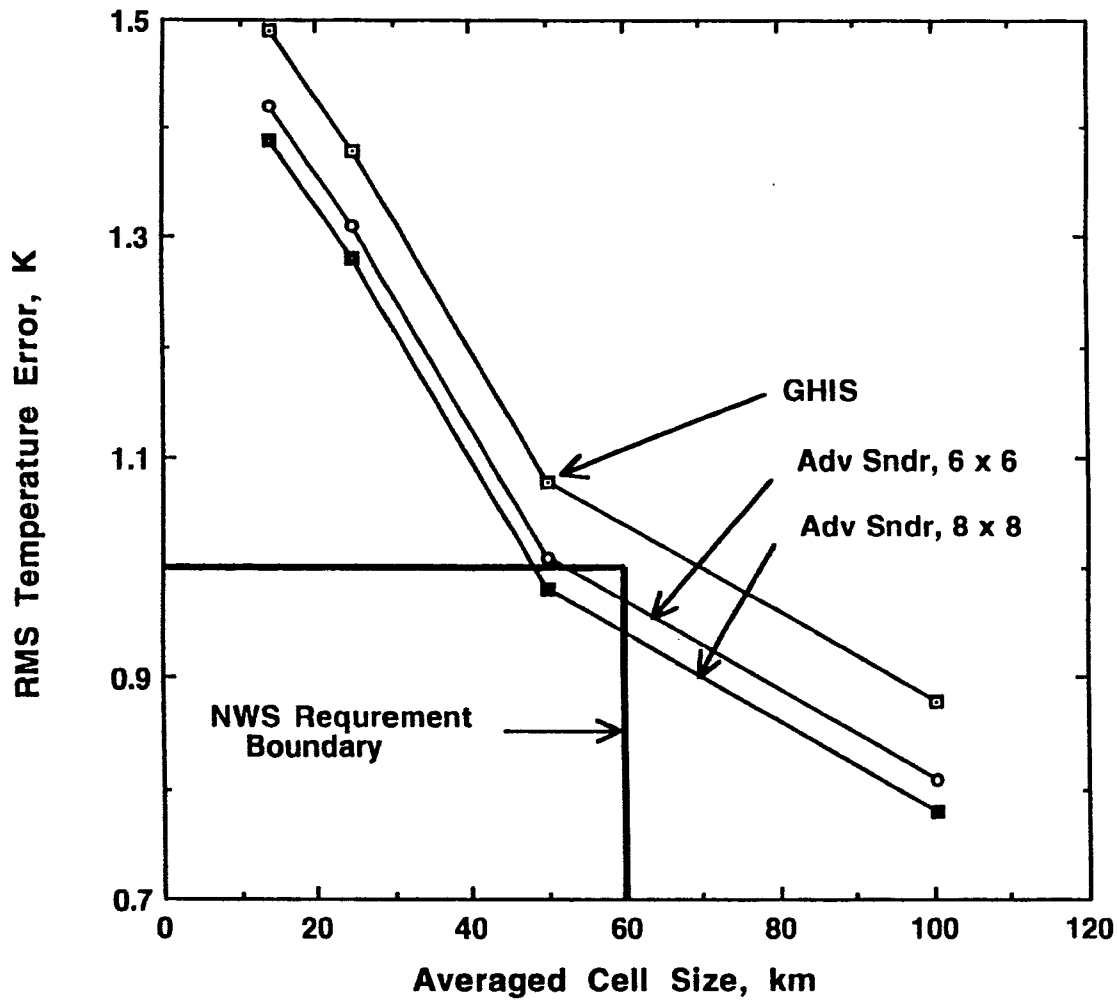

Figure 7. Estimated temperature retrieval performance (15 cm aperture, 65K FPA).

An advanced imager concept for GOES-R

D.E. Lencioni and D.R. Hearn

Lincoln Laboratory, Massachusetts Institute of Technology
244 Wood Street
Lexington, MA 02173

ABSTRACT

The results of a conceptual design study of an advanced Imager for GOES-R is presented. Tentative performance requirements are established from NOAA operational and science communities. A performance scaling law is developed which provides a quantitative measure of sensor capability and insight into the key design parameter tradeoffs. The basic design concept is described and estimates for sensitivity and resolution are given.

1. INTRODUCTION

The spacecraft and Imager and Sounder instruments in the current geostationary operational environmental satellite series (GOES I-M) provide a significant improvement in measurement capability over the previous GOES series. The Imager and Sounder instruments are developed by the Aerospace/Communications Division of ITT Corporation under subcontract to Space Systems/Loral (SS/L). The program which began in October 1985 had a successful launch of GOES-I in April 1994.

The National Oceanic and Atmospheric Administration (NOAA) GOES Program is considering additional instruments beyond the current series which provide enhanced capability at minimum risk by making evolutionary upgrades to the GOES I-M series. Potential Imager upgrades include the addition of three new IR bands improving the resolution of the 6.5 μm band to 4 km, and doubling coverage (reduced frame time) by adding eight new visible band detectors, using the redundant sets of IR detectors and using data compression. At this time there is no official decision on implementation.

NOAA has also initiated a process to define the next generation (GOES-R) system. MIT/Lincoln Laboratory is providing early support to NOAA for this effort. The initial operational and science requirements[1,2] which have emerged from this process indicate the need for a significant improvement in the capability of the Imager. This is driven by requirements for improved resolution, increased signal-to-noise ratio, increase in number of spectral bands and more rapid imaging rates. The technology strategies required to meet this performance and a design concept for an advanced Imager for GOES-R are discussed below.

2. REQUIREMENTS

At this time there is no official comprehensive set of NOAA requirements for the GOES-R system which can be used for the designs of the spacecraft, instruments and ground segment. There has been, however, considerable progress in defining measurement requirements and goals for the various NOAA offices. In particular the National Weather Service (NWS) has defined[1] hydrometeorological observational data requirements for the GOES-R Imager. These have been incorporated into a tentative set of requirements used as the focus of the advanced Imager design concept described in this paper.

The requirements for other elements of the NOAA GOES Program are also being developed.[2] For example, the NESDIS ocean research community has expressed a strong interest in geostationary ocean color observing capability. The requirements for this capability have also been incorporated into the tentative requirements for future programmatic review. These specifications are summarized in Tables 2-1 and 2-2.

This work was initiated by the National Oceanic and Atmospheric Administration under Air Force contract no. F19628-95-C-0002.

 0-8194-2200-2/96/$6.00

Table 2-1. Advanced Geostationary Imager Tentative Requirements

Band	Wavelengths (μm)	SNR or NEΔT
Visible (or PAN) Band: 0.5 km IGFOV		
1	0.55 - 0.75	600:1
Ocean Color Bands: 1.0 km IGFOV		
2	0.402 - 0.422	300:1
3	0.433 - 0.453	300:1
4	0.480 - 0.500	300:1
5	0.500 - 0.520	300:1
6	0.545 - 0.565	300:1
7	0.660 - 0.680	300:1
8	0.745 - 0.785	300:1
9	0.845 - 0.885	300:1
Infrared Bands: 2.0 km IGFOV		
10	1.3 - 1.9	300:1
11	3.8 - 4.2	0.1 K @ 270 K
12	6.5 - 7.0	0.3 K @ 240 K
13	7.0 - 7.5	0.3 K @ 240 K
14	10.2 - 11.2	0.1 K @ 300 K
15	11.5 - 12.5	0.1 K @ 300 K
16	13.2 - 13.8	0.4 K @ 270 K

Table 2-2. Imaging Time Tentative Requirements

	Full Earth	3000 x 1000 km	1000 x 1000 km
NWS Bands (1, 10 - 16)	15 min.	5 min.	1 min. (Simultaneous and independent)
Ocean Color Bands (2 - 9)	60 min.	60 min.	60 min.

This report does not address the requirements for improved calibration or improved image navigation and registration.

3. DESIGN APPROACH

The Advanced Imager requirements contained in the previous section represent a revolutionary increase in capability compared to the current GOES Imager. This is driven by a factor of two improvement in instantaneous geometric field-of-view (IGFOV) in all bands down to 2 km at 14 μm wavelength; a factor of two improvement in signal-to-noise ratio (SNR); and an increase in the number of spectral bands from the current five to sixteen with the inclusion of the eight ocean color bands; a reduction in the imaging or frame time with the ability to simultaneously and independently do one minute imaging of mesoscale and local storms and do 15 minute full disk imaging.

A quantitative measure of the improved capability and insight into the key tradeoffs can be obtained from the performance scaling law derived here. Figure 1 illustrates a linear array of N detectors, each subtending a square IGFOV, which scans a field-of-view (FOV) in some total frame time (T_F). The dwell time (τ_D) per ground sample distance (GSD) is given by

$$\tau_D \propto T_F \, N \, \frac{IGFOV^2}{FOV^2} \tag{1}$$

This represents the amount of time a detector can collect photons from one GSD. If the sensor is scene photon noise limited then the signal to noise ratio (SNR) is given by

$$SNR \propto [\Phi \times D^2 \times IGFOV^2 \times \tau_D]^{1/2} \tag{2}$$

where Φ is the scene photon radiance in the spectral band and D is the effective aperture diameter of the optical system of the Imager. This expression can be rewritten as

$$\frac{SNR^2 \times FOV^2}{\Phi \times T_F \times IGFOV^4} \propto D^2 \times N \tag{3}$$

This performance scaling law contains the critical system requirements on the left as a "figure of merit" for the system capability. The right hand side contains the two key design parameters and represents a measure of the technical complexity (cost) of the sensor.

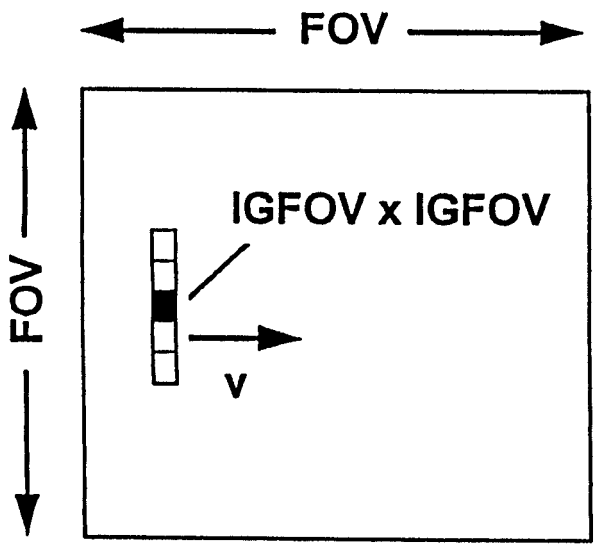

Figure 1. Linear array of N detectors which scans a scene FOV x FOV in size at scan rate V.

As can be seen a given level of system capability can be achieved by trading aperture area and number of detectors. Both parameters can be varied within restricted regions of parameter space. Increasing the diameter, for example, rapidly increases the weight of the optical system (approximately as $D^{2.5}$) which of course can have major impact on the total system. At the other extreme the diameter can be reduced until diffraction effects limit the Imager resolution. In the case of the number of detectors the maximum limit may be determined by the availability of appropriate large count focal plane arrays or by the fact that a large number of detectors occupies a large optical field-of-view with adequate image quality to support the resolution requirements. This in turn drives the optical design complexity.

The advanced Imager requirements contained in Tables 2-1 and 2-2 represent a factor of 640 increase over GOES I-M in the figure of merit for the system capability as expressed in Eq. (3). The Imager design concept described in this report achieves this by exploiting the advances in detector array technology that have occurred in the past two decades. As an example in the GOES I-M Imagers there are eight visible band detectors in a linear array, two detectors each in the 3.9 μm, 10.7 μm and 12.0 μm bands and only one detector in the 6.75 μm band.

One of the most challenging requirements of the advanced Imager is the ability to simultaneously and independently image the global/synoptic scales and the mesoscale. This can be accomplished in a single instrument if the full earth imaging time is sufficiently short so as to satisfy the requirement on each frame, i.e., one minute full earth imaging time or if a duplex mode can be used to interleave full earth scans and mesoscale scans. The full earth frame time for an advanced Imager is shown in Figure 2 as a function of the number of visible band detectors and required optical field-of-view (FOV). The scan rate required to achieve the SNR is 0.63° per second which is a factor 32 lower than the GOES I-M 20° per second rate. The IGFOV = 0.5 km represents an angular extent of 14 μrad. For large fields-of-view the optical image quality required to support this IGFOV becomes difficult. At a 2° FOV the total number of visible detectors in a linear array is 2500 and the full earth frame time is 5 minutes. The detector count for the ocean color bands is 1250 per band and for the IR bands 625 per band. These array sizes are well within current technology capabilities. Optical systems which support a 2° FOV with a 14 μrad resolution are practical.[3]

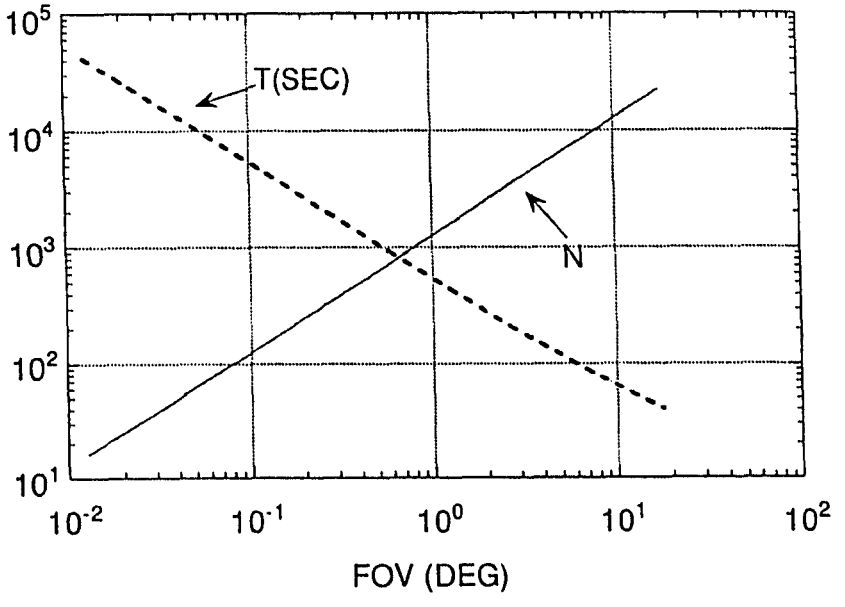

Figure 2. Full earth imaging time (T) as a function of number of detectors (N) and optical field-of-view (FOV). Each visible band detector subtends a square IGFOV of 0.5 km.

4. DESIGN CONCEPT

4.1 Focal Plane Configuration

The basic sensor concept consists of an all reflective, 35 cm aperture diameter, f/4 optical system, with a 1° x 2° field-of-view, similar to published designs[4]. As illustrated in Figure 3 a dichroic beamsplitter is used to split the image onto two sets of detector arrays.

One contains the MWIR and LWIR bands and is cooled with a Sterling cycle or pulse-tube cryocooler[5] to a temperature ~80K. The other set of detector arrays contains the visible, near infrared and short wave infrared (SWIR) bands and is assumed to operate at moderate temperatures (T > 220K) with no active cooling. Discrete spectral band filters are located at the focal plane to simplify the spectral separation. The ocean color bands can be obtained using either eight discrete filters or by using a Wedge Imaging Spectrometer[6] (WIS) technique to obtain continuous hyperspectral coverage over the range 0.4 μm to 0.9 μm. This approach is illustrated in Figure 3. A silicon photovoltaic detector array with approximately 200 detectors in the wavelength dimension could provide spectral resolution $\Delta\lambda/\lambda \sim 1\%$. The WIS approach provides flexibility in spectral band selection, e.g., Sea WIFS or MODIS, provides atmospheric attenuation information and is a rich data source for new earth science opportunities.

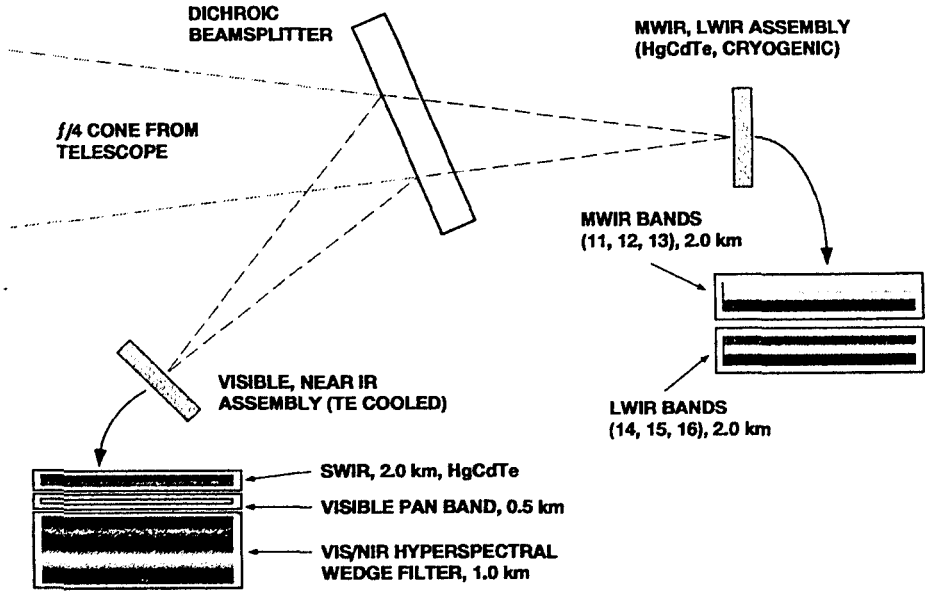

Figure 3. GOES-R Imager focal plane concept.

As the earth's image is scanned across the arrays the detectors for a given waveband are sampled at a rate such that the detectors in different spectral bands sequentially sample the same spot on the earth.

4.2 Operating Modes

Three basic scan modes are illustrated in Figure 4. The first shows a full earth frame covering 17.4° x 17.4°. The 2° dimension of the focal plane is in the north/south direction and the scene is scanned east/west. The 2° corresponds to a swath width of 1250 km at the earth's equator. At the scan rate of 0.6° per second the full earth can be covered in 5 minutes. Each of the nine scans requires approximately 30 sec with another 30 sec for retrace time.

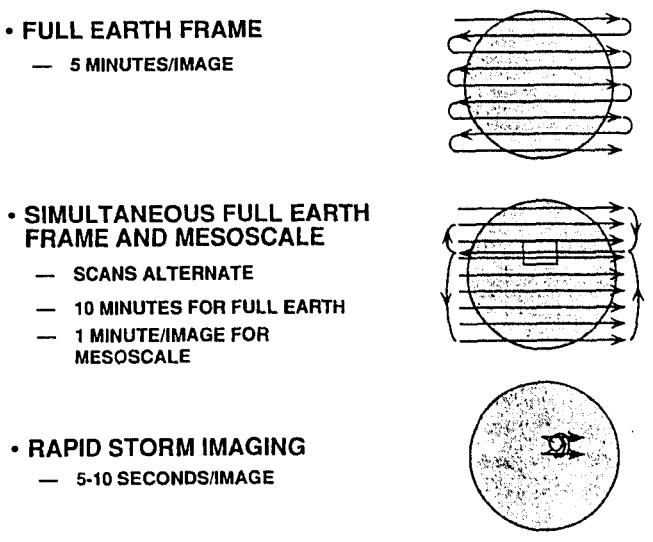

Figure 4. Imager scan mode options.

The second mode shown in Figure 4 illustrates a way to achieve simultaneous full earth and mesoscale coverage. Here, after each west to east scan of the full earth frame, the sensor scans east to west at the latitude of interest. Thus that region is revisited every 60 seconds and the full earth frame requires 10 minutes.

The third mode illustrates rapid storm imaging where, for example, a 1250 km x 1250 km region can be imaged as often as every 10 seconds.

4.3 Data Rates

The data rates, assuming approximately one sample per IGFOV and 12 bit digitization, are: 20 Mbps for the visible pan band, 5 Mbps each for the ocean color bands and 1.25 Mbps each for the IR bands. The total rate for all 16 bands is approximately 68.75 Mbps. This is roughly a factor of 25 larger than the current GOES I-M Imager.

Some form of onboard data processing and data compression may be required to manage the down link rates. The ocean color bands are required only over a small fraction of an earth scene. Moreover, twelve 5 minute frames can be averaged and still satisfy the 60 minute frame rate requirement of Table 2-2. This also will increase the effective SNR for these images by a factor of about three and as will be seen in the following section this brings all the SNRs above the required values of Table 2-1. For the visible pan band frame to frame subtraction can be used to report only image changes. Data compression may also be desirable for data rate management.

If a WIS approach is used for the ocean color bands the maximum data rate can be as high as 1 Gbps. Clearly onboard spectral band synthesis and processing is indicated. Moreover the full hyperspectral capability can be restricted to small regions of interest and with lower frame rates. Data would then be stored onboard and down linked at a lower more manageable rate.

In any case maximum utilization of the advanced imager capabilities will require advances in onboard processing, data storage, the communication link and ground segment capability.

5. PERFORMANCE ESTIMATES

5.1 Spatial Resolution

The spatial resolution of an imaging instrument is best described by its modulation transfer function (MTF). The MTF is defined for each coordinate direction (in-scan and cross-scan), and it is generally a function of position in the field-of-view. It is also a function of the wavelength band. We have chosen a few representative wavelengths for the purpose of estimating MTF's.

Factors which contribute to the system MTF include optical diffraction, optical aberrations, detector size, and scan motion during pixel integrations. Optical aberrations can be subdivided into design residuals, component figure errors, and alignment errors. We base the estimate of fabrication and alignment errors on the measured performance of systems which have been built in the past.

Diffraction fundamentally limits the resolution, based on the wavelength, λ, and the aperture diameter, D. No angular frequencies above D/λ, the "optical cutoff frequency," are passed by the optical system. For our initial diffraction MTF estimates, we have used the expression for an unobscured circular aperture, with $D = 350$ mm.

The size of each detecting element also contributes to the system MTF. We assume that the detector pixels have a sharp-edged response distribution, with a filling factor of 90% in the cross-scan direction. The "pixel MTF" is thus a simple sinc function. Initially at least, we assume that each detector area is square. For this system, the pixel sampling frequency (in the cross-scan direction) is less than the optical cutoff frequency for all wavelength bands. The resolution is thus detector-limited.

Scan motion during the integration time for each pixel contributes to the system MTF in the scan direction. The "motion MTF" is also a simple sinc function, exactly analogous to the pixel MTF. In this case however, the integration time can be shortened to limit the blur, as long as signal-to-noise performance does not suffer unduly. The in-scan extent of the detectors can also be reduced, to compensate for the motion MTF.

The modulation transfer functions are shown for two different wavelength bands in Figures 5 to 8. In each case, both the system MTF and the major component MTF's are shown. The system MTF is the product of the component MTF's. In Figures 5 and 6, the cross-scan and in-scan MTF's of the PAN band (0.65 μm) are plotted. Figures 7 and 8 show the corresponding MTF's for band 15 (12 μm).

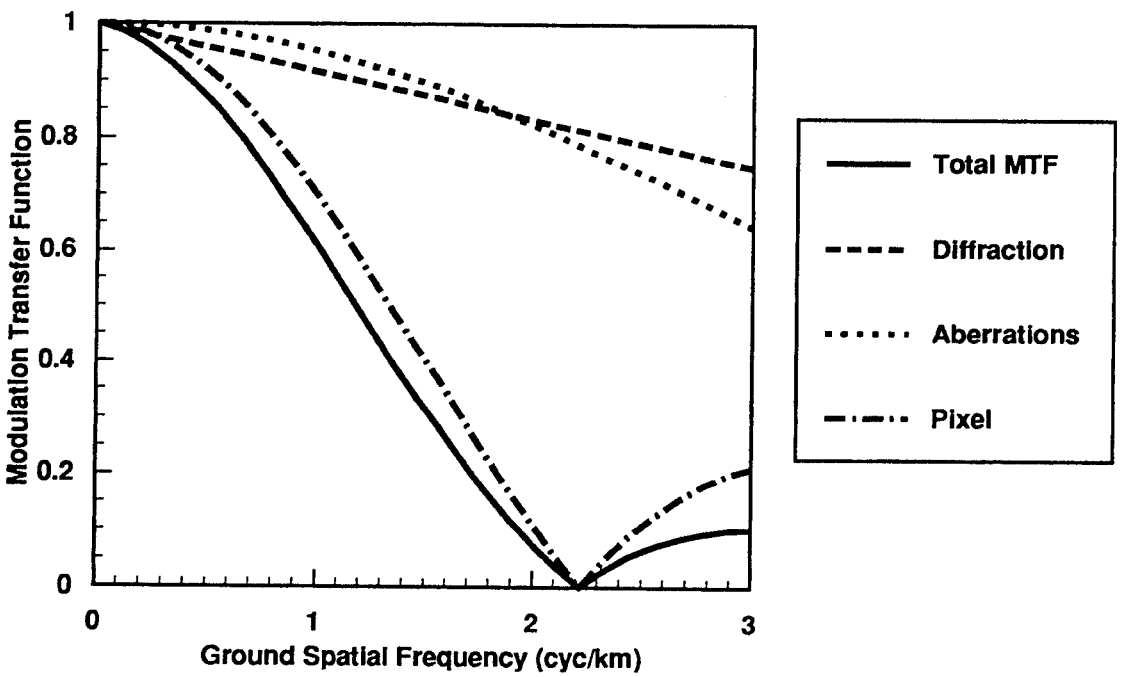

Figure 5. Modulation transfer function for the PAN band, across the scan direction. The median wavelength is 0.65 μm.

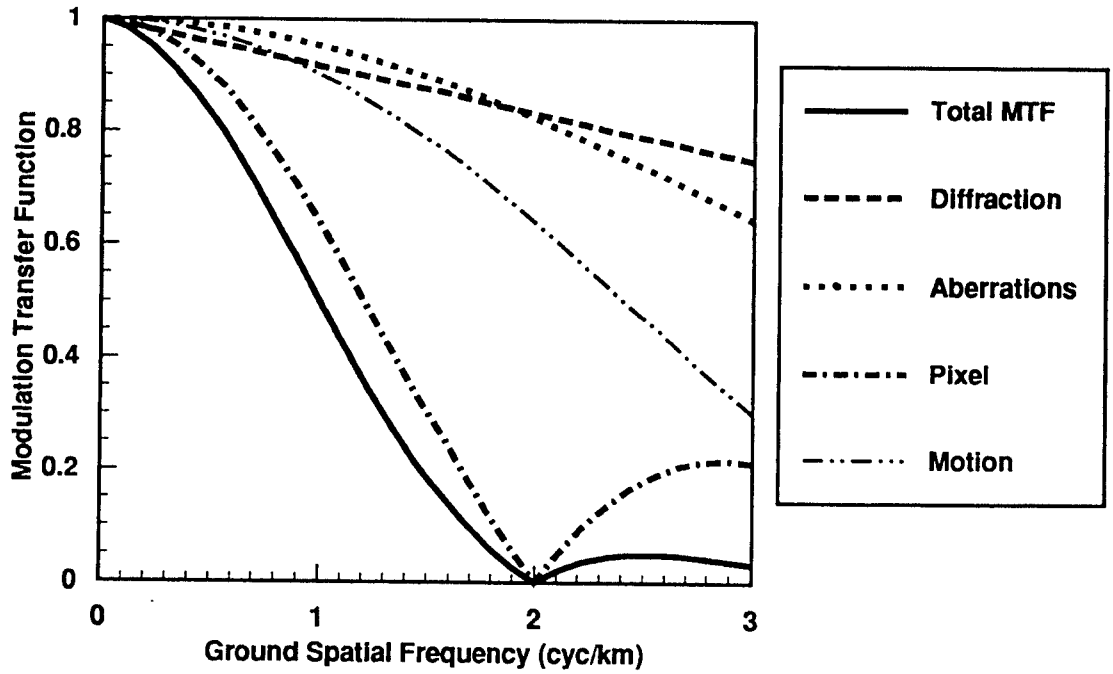

Figure 6. Modulation transfer function for the PAN band, in the scan direction. An exposure duty cycle of 50% is assumed.

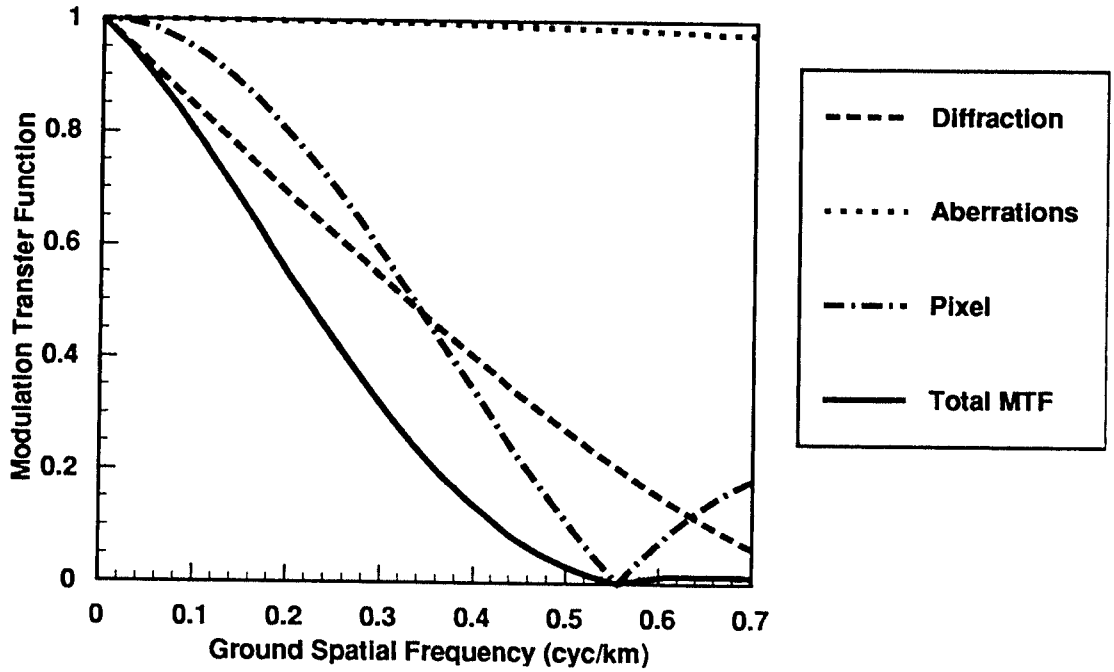

Figure 7. Modulation transfer function for band 15, across the scan direction. The median wavelength is 12 μm.

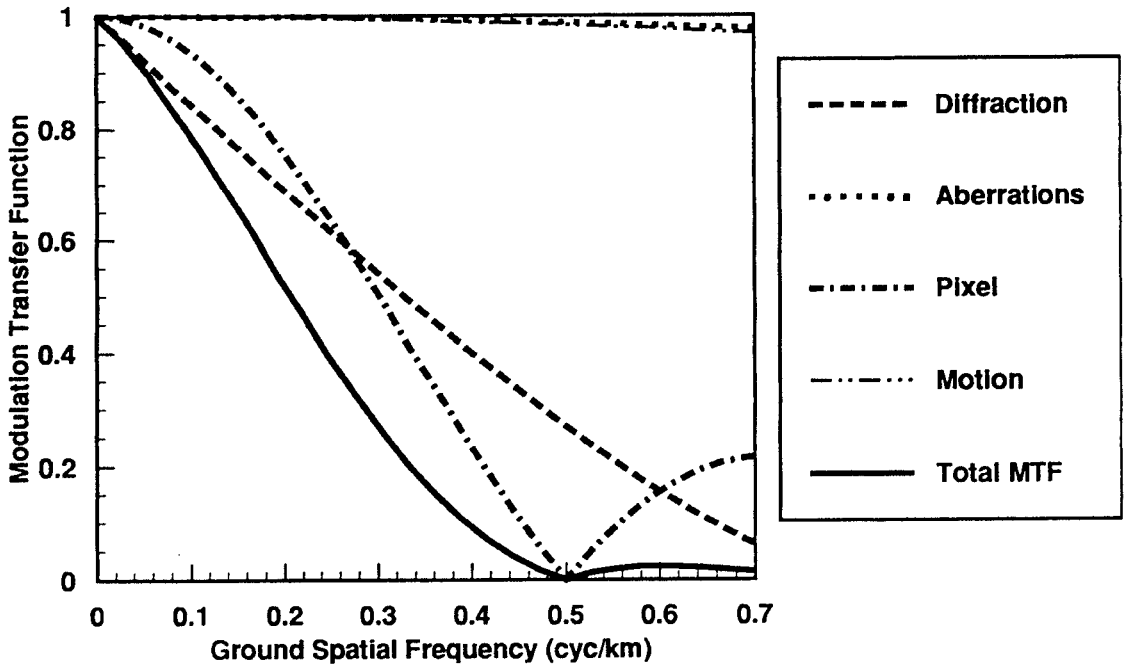

Figure 8. Modulation transfer function for band 15, in the scan direction. An exposure duty cycle of 10% is assumed.

The separate "diffraction" and "aberration" MTF's deserve some explanation. In principle, there is an optical transfer function which incorporates both diffraction and aberration effects. For these initial performance estimates, we have used a separate gaussian factor to represent all optical aberrations, including design residuals, figure errors, and alignment uncertainties. It can be thought of as a ratio of the true optical MTF to a diffraction-only optical MTF.

A comparison of the PAN band and band 15 MTF components shows the greater relative importance of diffraction in the 12 μm band. The PAN band is detector-dominated. The in-scan plots for the two bands show the effects of different duty cycles on the motion MTF components. For the PAN band, a 50% duty cycle was assumed, while for band 15, where the photon signal is very large, a 10% duty cycle was used. Aberrations are significant for the PAN, but negligible in the LWIR band.

5.2 Radiometric Performance

Signals and noise from the detecting arrays have been estimated, based on typical properties of the types of detectors to be employed. Silicon photovoltaic detectors are assumed for the visible and near infrared (VNIR) bands, i.e., the panchromatic and ocean color bands. The rest of the detectors would be HgCdTe (MCT), tailored to several different cutoff wavelengths. Band 10 can use photovoltaic MCT detectors at a moderate temperature[7] (~ 220 K), with a cutoff around 2.4 μm. Bands 11, 12 and 13 use a cutoff of 8 μm, at ~ 80 K or less. Bands 14, 15 and 16 should have a 14 μm cutoff, and also operate at 80 K. All of the MCT detector are assumed to be photovoltaic in operation.[8]

The sources of noise include photon statistical fluctuations (photon noise), spatial noise resulting from response non-uniformity (residuals, after correction), electronic noise, and quantization noise. Electronic noise was characterized as a "read noise" of so many electrons per pixel readout, depending on the type of detector. Residual non-uniformity was estimated to be 0.05% for silicon detectors,

and 0.1% for MCT detectors. All noise components were evaluated in terms of electrons per pixel sample, and then added in quadrature to find the total noise. One of the challenges of focal plane arrays is to get detector performance so that striping is not evident.

Signals were estimated from incident solar spectral irradiances and typical albedo values (ρ) for the visible and short-wave IR bands. Scene effective temperatures (as seen from space) were used to compute the mid- and long-wave IR signals. All signals were expressed as electrons per pixel sample, which, when divided by the total noise electrons, yields the signal-to-noise ratio (SNR). For the thermal infrared bands(MWIR and LWIR), the performance is expressed as a noise-equivalent difference in temperature, NEΔT.

Estimated values of the system radiometric sensitivity are presented in Table 5-1. The table also shows the wavelength range for each band.

Table 5-1. Advanced Geostationary Imager Performance Estimates

Band	Wavelengths (μm)	SNR or NEΔT
Visible (or PAN) Band: 0.5 km IGFOV		
1	0.55 - 0.75	800:1 @ ρ = 40%
Ocean Color Bands: 1.0 km IGFOV		
2	0.402 - 0.422	190:1 @ ρ = 4%
3	0.433 - 0.453	260:1 @ ρ = 4%
4	0.480 - 0.500	320:1 @ ρ = 4%
5	0.500 - 0.520	280:1 @ ρ = 3%
6	0.545 - 0.565	240:1 @ ρ = 2%
7	0.660 - 0.680	100:1 @ ρ = 0.5%
8	0.745 - 0.785	110:1 @ ρ = 0.5%
9	0.845 - 0.885	100:1 @ ρ = 0.5%
Infrared Bands: 2.0 km IGFOV		
10	1.3 - 1.9	300:1 @ ρ = 40%
11	3.8 - 4.2	0.1 K @ 270 K
12	6.5 - 7.0	0.3 K @ 240 K
13	7.0 - 7.5	0.3 K @ 240 K
14	10.2 - 11.2	0.1 K @ 300 K
15	11.5 - 12.5	0.1 K @ 300 K
16	13.2 - 13.8	0.4 K @ 270 K

6. SUMMARY

The results of a conceptual design study of an advanced Imager for GOES-R has been presented. A set of potential performance requirements for this instrument was generated from a combination of NWS future operational requirements[1] and ocean color observing capability desired by the NESDIS ocean research community.[2] This report described the basic design approach and illustrated the improvement in the performance "figure of merit" by exploiting advances in detector array technology.

The design concept represented a highly integrated sensor which satisfied both the NWS and NESDIS requirements and in particular was able to simultaneously and independently image the mesoscale and do full disk imaging. The resolution performance was estimated in terms of the MTF and the sensitivities were estimated in terms of the SNR or NEDT.

The results indicate the feasibility of achieving significant improvement in system capability by exploiting advanced technologies for focal plane arrays, cryocoolers, optical design and fabrication.

7. REFERENCES

1. National Oceanic and Atmospheric Administration, "National Weather Service Observational Requirements for the Evolution of Future NOAA Operational Geostationary Satellites," Review Copy, 28 November 1995.

2. P. Menzel, J. Purdom and R. Heymann, "Plans and Requirements for GOES-N," unpublished draft, January 1995.

3. D. Wang, SSG, Inc., private communication.

4. J. Robichaud, M. Anapol, L. Gardner, and P. Hadfield, "Ultralightweight Off-Axis Three Mirror Anastigmatic SiC Visible Telescope," SPIE vol. 2543, 8/95, p. 180.

5. E. Tward, et. al., "Miniature Long-Life Space-Qualified Pulse-Tube and Stirling Cryocoolers," pp. 329-336, Cryocoolers 8, R.G. Ross, Jr., Editor, Proceedings of the 8th International Cryocooler Conference, Vail, Colorado, June 1994, Plenum Press, NY

6. G.T. Elerding, J.G. Thunen, and L.M. Woody, "Wedge Imaging Spectrometer: Application to Drug and Pollution Law Enforcement," in Surveillance Technologies, Proc. SPIE, Vol. 1479, 1991.

7. E.A. Patten, et. al., "Room Temperature SWIR Double Layer PV HgCdTe Detector Arrays," IRIS Specialty Group on Infrared Detectors, Johns Hopkins University, Laurel, MD, August 1995.

8. E.E. Krueger, G.N. Pulz, K.R. Maschhoff, S.P. Tobin, P.W. Norton, J.H. Rutter, and M.D. Reine, "Extending HgCdTe Photovoltaic Detector Technology to Cutoff Wavelengths of 17 μm," Materials Research Society Symposium Proceedings 299, 85 (1994).

GOES High-Resolution Interferometer Sounder Retrieval Performance Simulations[1]

John P. Kerekes and Harry R. Finkle
Lincoln Laboratory, Massachusetts Institute of Technology
244 Wood St., Lexington, MA 02173-9185
kerekes@ll.mit.edu

ABSTRACT

An evolutionary improvement to the existing GOES I-M Sounder has been proposed as the GOES High-Resolution Interferometer Sounder (GHIS). This instrument will be based upon technology developed during successful demonstrations of an airborne Michelson interferometer instrument for the temperature and moisture sounding of the atmosphere from passive infrared measurements. The spectral resolution afforded by the interferometer technology will substantially improve retrieval accuracy and vertical resolution of the sounding information. Simulations of the spectral radiance measurements have been used to study the expected retrieval performance of the GHIS. A fast transmittance code has been used in the simulations and in the calculation of the retrieval operator in an iterative, non-linear physical retrieval scheme. The effects of instrument noise and spectral operating mode have been considered in the retrieval simulation. A measure of the vertical resolution of the retrieved profiles has been developed. This measure considers the correlation in the retrieval error between atmospheric levels of the retrieved parameters. The effects of both the instrument characteristics and those of the retrieval algorithm are thus considered in this measure. The results indicate that the GHIS is expected to provide temperature retrieval accuracy on the order of 1 °C throughout the troposphere which will be a significant improvement over the existing GOES-8 sounder. The vertical resolution simulations also show improvement over GOES-8 capabilities.

Keywords: GOES, Interferometer Sounder, Retrieval Simulation, Vertical Resolution

1. INTRODUCTION

With the advent of the first two flight spacecraft of the GOES-Next series, GOES-8 and -9, full time operational geostationary sounding has become a reality. The hourly satellite soundings retrieved from the data have proven to be useful aids in qualitative interpretation as well as quantitative inputs to numerical weather prediction models. These applications of sounder data represent a major step forward in the development of geostationary sounders begun with the VISSR Atmospheric Sounder first flown on GOES-4 in 1980.

While the ultimate utility of the GOES-Next Sounders is just being explored, planning and development work has been ongoing for the next generation of geostationary infrared sounders. In 1988, the University of Wisconsin, the Hughes Santa Barbara Research Center, and ITT Aerospace/Communications Division prepared a study of a concept for replacing the filter wheel in the GOES-Next Sounder with a Michelson interferometer as a potential upgrade[1,2]. This concept, named the GOES High-Resolution Interferometer Sounder (GHIS), offered an attractive way to implement a high-resolution sounder onboard the GOES platform without having to redesign the entire instrument.

Since 1993, MIT Lincoln Laboratory has been performing risk-reduction technology development on the GHIS concept. Lincoln is currently developing a hardware prototype of the GHIS which will be integrated into the GOES Sounder pathfinder instrument and undergo a variety of instrument-level testing to demonstrate fit and functionality. This demonstration will hopefully smooth the procurement of flight models.

In parallel with the hardware risk reduction activity, Lincoln has been exploring system performance trades through the use of radiometric performance models and retrieval simulations. Through detailed detector and system models we obtain estimates of the NEΔN which is then used in the retrieval simulation to explore the impact of noise and spectral resolution on atmospheric profile retrieval performance.

---

[1]This work was sponsored by the National Oceanic and Atmospheric Administration under Air Force Contract F19628-95-C-0002.

2. GHIS UPGRADE

This section briefly describes the origin of the GHIS concept, the risk-reduction effort at Lincoln Laboratory and covers the general instrument specifications as they were at the time of writing.

2.1 *GHIS Concept*

In the late 1980's it was recognized that advances in weather forecasting would drive requirements on satellite sounding accuracies higher than those developed for the GOES-Next Sounder. Higher vertical resolution and more accurate soundings would soon be necessary to support the next-generation numerical weather prediction models. Based on their experiences with the airborne High-resolution Interferometer Sounder (HIS)[3], University of Wisconsin (UW) scientists recognized that a Michelson interferometer with approximately 1 cm^{-1} spectral resolution could possibly meet those requirements.

Working together with engineers at Santa Barbara Research Center and ITT Aerospace/Optical Division, the UW scientists explored the feasibility of replacing the filter wheel section of the GOES-Next Sounder with a Michelson interferometer without a major redesign of the instruments optics, housing, detectors, and cooling assemblies. Their study produced a preliminary concept and recommended proceeding forward.

Unfortunately, about the same time this study was being released, the fabrication and test of the GOES-Next satellite instruments was running into several technological problems which were delaying development of the series. Being preoccupied with these problems, the proposal for the sounder upgrade languished on the shelves.

In 1993, with the GOES-Next program back on track, NOAA initiated a two phase review of the UW/SBRC/ITT GHIS proposal at MIT Lincoln Laboratory. In phase 1, Lincoln engineers reviewed the technology and risks associated with the GHIS concept. They concluded that the concept appeared feasible, but identified several risk areas. During phase 2, they developed a detailed point design that established the feasibility of the concept and recommended an approach to risk-reduction through a technology demonstration effort including a brassboard prototype.

2.2 MIT/LL Brassboard Development

Starting in mid-1995, Lincoln Laboratory begun development of a GHIS brassboard prototype to explore design issues and reduce risks associated with flight-model development by demonstrating a design, fabrication and test approach that will result in a GHIS module that will operate as specified in a modified GOES-Next sounder. This effort is well under way[4] and in 1997 will demonstrate through thermal vacuum testing the operation of GHIS integrated into an early engineering model of the Sounder. The experience and lessons learned through this activity will be shared with the instrument vendor for the flight model procurement. Together with an engineering study at ITT, this effort will provide input to NOAA for a decision on the upgrade by mid-1997. If approved for development, the GHIS module could be carried on GOES-N slated for launch in 2004.

2.3 GHIS Specifications and Radiometric Performance Predictions

In the time since the original GHIS feasibility study, the design specifications for GHIS have evolved through additional experience gained with the HIS instrument and through additional engineering design and trade studies. While the final instrument specifications have yet to be decided, the following describes the relevant instrument parameters as of this writing.

Since the GHIS concept replaces only the spectral selection subsystem of the GOES-Next Sounder, many of the characteristics will remain the same including the spatial resolution, scan strategies and calibration techniques. However, with the inclusion of the Michelson interferometer, many of the radiometric, calibration and registration requirements may have to be tightened to obtain the desired improvements in performance of the sounder.

Table 1 presents a summary of the GHIS specifications that relate to sounding performance as explored in this study. As mentioned above, these parameters are subject to change as the design and development process proceeds. Given a

nominal set of optical parameters, detector performance and instrument temperatures, the predicted radiometric accuracy in terms of noise-equivalent delta temperature (NEΔT) is shown in Figure 1.

Table 1. GHIS spectral specifications used in retrieval simulation study.

Parameter	Band 1	Band 2	Band 3
Spectral band range	620 - 1150 cm^{-1}	1210 - 1740 cm^{-1}	2150 - 2720 cm^{-1}
Interferometer scan pattern by spectral operating mode			
Full Resolution (double-sided)	-0.8 to 0.8 cm	-0.4 to 0.4 cm	-0.2 to 0.2 cm
Partial Scan (single-sided)	-0.05 to 0.10 cm 0.58 to 0.73 cm	-0.05 to 0.1 cm	-0.05 to 0.1 cm
Low Resolution (double-sided)	-0.13 to 0.13 cm	-0.1 to 0.1 cm	-0.1 to 0.1 cm
Spectral resolution* by spectral operating mode			
Full Resolution	0.76 cm^{-1}	1.5 cm^{-1}	3.0 cm^{-1}
Partial Scan	0.75 cm^{-1}	6.0 cm^{-1}	6.0 cm^{-1}
Low Resolution	4.64 cm^{-1}	6.0 cm^{-1}	6.0 cm^{-1}

*Defined as the FWHM of the main lobe of the unapodized spectral response function.

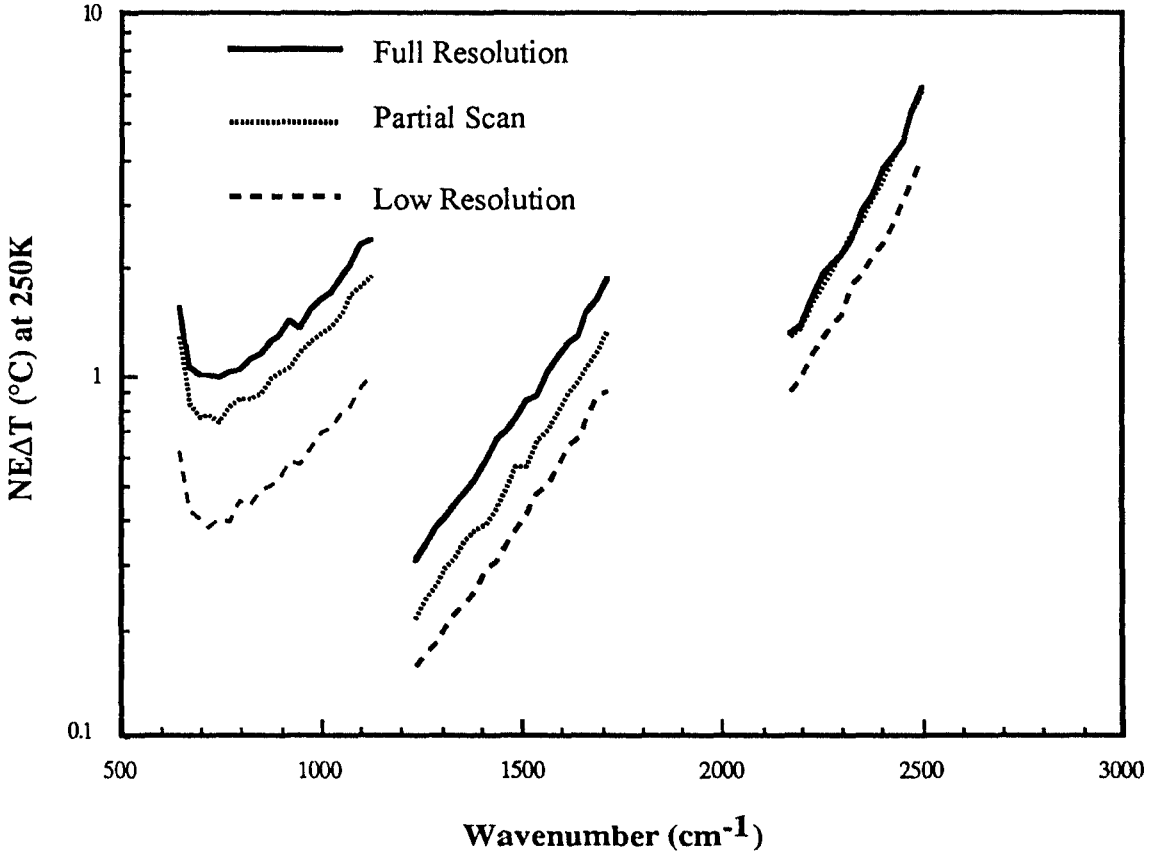

Figure 1. Nominal NEΔT prediction for GHIS given typical instrument parameters and specifications shown in Table 1.

The Partial Scan mode was added to the concept to allow high spectral resolution data to be collected at a rate required by the National Weather Service, but with lower noise. The NWS has specified a coverage rate of scanning a 3000 x 3000 km area within one hour. The Partial Scan mode works in Band 1 by scanning the interferometer mirror slowly through ZPD (Zero Path Difference), rapidly slewing to an OPD (Optical Path Difference) of 0.58 cm, and then taking data slowly out to 0.73 cm. Bands 2 and 3 are the same as in the Low Resolution mode except data is collected on only one side of the interferogram. This scan pattern was adopted from earlier work[5] and is matched to the resonance of the 15 μm CO_2 band which appears in the interferogram at ~0.65 cm OPD.

The Low Resolution mode is included to also meet the spatial coverage rate requirement as well as to provide a lower resolution double-sided interferogram which typically has fewer potential calibration problems than the single-sided Partial Scan interferogram.

3. RETRIEVAL SIMULATION METHODOLOGY

This section details the approach developed for exploring the retrieval performance of the GHIS concept.

3.1 Simulation Methodology

The basic approach is to simulate atmospheric radiances as will be measured by the instrument in space (including the effects of radiometric noise), perform retrievals, and then compute accuracies by comparing the retrieved profiles to the original ones used to generate the atmospheric radiance. Two sets of atmospheric profiles are used in the process; one for use in "training" and developing the background statistics and a first guess linear regression operator, and the second for use in "testing" by actually performing the retrievals and determining accuracy. This approach is shown in Figure 2.

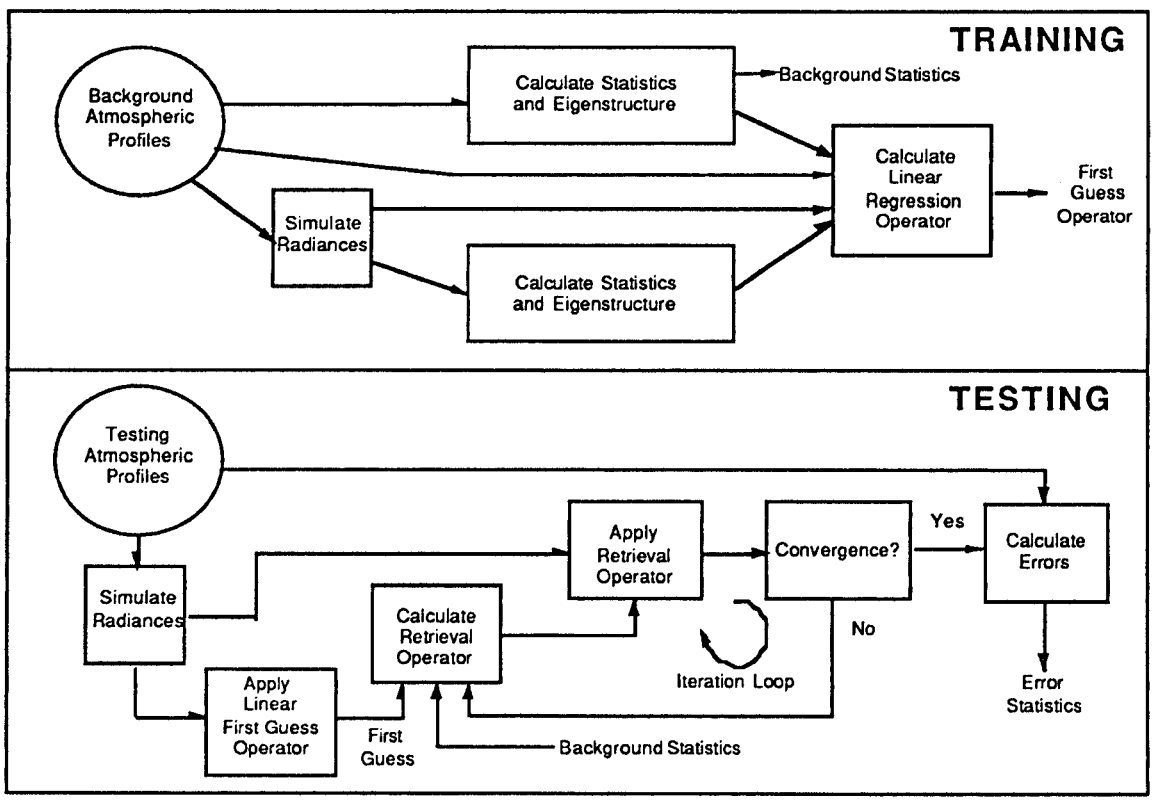

Figure 2. Block diagram of retrieval simulation approach.

The two key components of this simulation approach are the model used to simulate the atmospheric radiance and calculate the transmittance for use in the full retrieval operator, and the particular algorithm used in deriving the equations defining the operator. These two components are described in the following two sections.

3.2 Fast Transmittance Code

The fast transmittance code is used in two separate places in the retrieval simulation. It is used to generate the atmospheric radiance as seen by the satellite as well as to calculate level-to-space transmittances within the full retrieval operator. The simulation of atmospheric radiances need not be necessarily fast, but it is convenient to be consistent with the retrieval code. The retrieval operator transmittance calculations, however, need to be fast since they must be performed for slightly different conditions to calculate derivatives and they are recomputed for each iteration and for each profile in the retrieval simulation.

The fast transmittance code used in this study was developed by scientists at the University of Wisconsin under a subcontract. The code follows an approach developed by scientists at the European Center for Medium-Range Weather Forecasts[6] and uses a regression between atmospheric profiles and transmittances as calculated by the USAF line-by-line atmospheric code FASCD3P. The regression data base was interpolated to 0.1 cm^{-1} resolution to which the GHIS Full Resolution unapodized spectral response was then applied.

This code was used as provided for the Full Resolution mode, but required additional processing for use in the other two modes. For the Partial Scan and Low Resolution mode, the spectral transmittances were transformed to the interferogram domain through the use of an FFT algorithm, a mask applied to simulate the interferogram mirror scan pattern for the appropriate mode, and then transformed back to the spectral domain. This has the effect of applying the appropriate spectral response and works fine, although it is computationally burdensome. A much better approach would be to implement the fast code with the proper spectral response initially applied; however, while design studies are still under way it is nice to have the flexibility of trying arbitrary scan patterns.

This same fast transmittance code was also used to simulate the GOES-8 Sounder radiances and transmittances by applying the measured instrument spectral responses to the high-resolution output of the code. This was done to ensure consistency among the different comparisons.

3.3 Retrieval Algorithm

The retrieval algorithm is an adaptation of a published algorithm[7] designed for the TIROS Operational Vertical Sounder (TOVS) instrument suite on the NOAA polar orbiters. The algorithm is simultaneous in temperature and water vapor, uses a linear regression first guess based on eigenvectors, and iterates until convergence criteria are met.

3.4 Atmospheric Profiles

The training and testing profiles are extracted from a subset of the TOVS Initial Guess Retrieval (TIGR) profiles. A version of the TIGR dataset with 1761 profiles has been used by the NASA/EOS AIRS Science Team for algorithm development. Scientists at the University of Wisconsin[8] have ordered these profiles based on the residual error between the original profiles and ones reconstructed using a limited number of eigenvectors from the temperature covariance matrix. Profiles with sharp gradients and complicated vertical structure have a greater residual error We have used a set of 587 profiles from the middle of this ordering which implies they are of a "moderate" degree of retrieval difficulty (at least in temperature). Of these, 440 profiles were used to calculate the background statistics and the other 147 profiles were used to provide an independent set for retrieval performance prediction.

4. RETRIEVAL RESULTS

Retrieval simulations were performed for the three proposed GHIS operating modes along with GOES-8 characteristics to investigate their relative performance.

4.1 Review of Conditions

For these experiments we used a subset of the spectral channels available from the GHIS instrument. Table 2 shows the number of channels used for each operating mode. Also, the retrievals were done assuming the radiance measurements are the average of cloud-free samples within a 50 x 50 km grid (5 x 5 IFOV's) which was 50% cloudy. This results in lowering the noise shown in Figure 1 by the square root of the number of samples (we assume the measurements are independent samples of a homogenous area). The numbers here were derived assuming each mode was operated in such a way as to meet the NWS requirement of covering a 3000 x 3000 km area in under one hour.

Table 2. Number of spectral channels and noise factors assumed for retrieval simulation study.

GHIS Operating Mode	Number of Spectral Channels	Spatial/Temporal Noise Factor
Full Resolution	369	0.558
Partial Scan	333	0.288
Low Resolution	150	0.288
GOES-8	18	0.288

4.2 Results

The following tables show the 1 km layer averaged accuracies for the different modes and for different stages of the retrieval algorithm. The Linear First Guess result is that obtained using the linear regression operators derived from the background set of profiles. Temperature and water vapor are retrieved separately in this step using channels sensitive to each parameter. The Iteration Result is the final answer from our current algorithm which stops iterating when the forward brightness temperature calculation converges to a constant value.

Table 3. Tropospheric (1000-100 mbar) RMS temperature errors (°C) for 1 km layers.

GHIS Operating Mode	Linear First Guess	Iteration Result
Full Resolution	1.53	1.14
Partial Scan	1.42	1.16
Low Resolution	1.56	1.47
GOES-8	2.11	1.76

Table 4. Stratospheric (100-10 mbar) RMS temperature errors (°C) for 1 km layers.

GHIS Operating Mode	Linear First Guess	Iteration Result
Full Resolution	1.64	1.57
Partial Scan	1.60	1.55
Low Resolution	1.90	2.05
GOES-8	3.57	2.95

Table 5. Tropospheric (1000-300 mbar) RMS water vapor mixing ratio errors (g/kg) for 1 km layers.

GHIS Operating Mode	Linear First Guess	Iteration Result
Full Resolution	0.57	0.53
Partial Scan	0.68	0.63
Low Resolution	0.53	0.56
GOES-8	0.87	0.69

These results provide an example of the improvement in retrieval accuracy possible for the GHIS as compared to the current GOES-8 Sounder. In all cases an improvement is seen. The higher resolution modes improved tropospheric temperature accuracies by ~ 50% and stratospheric accuracies by nearly a factor of two. Even the Low Resolution mode (which offers slightly faster coverage rates and lower data rates) promises a significant improvement over GOES-8. The improvements are less dramatic in the water vapor, but the GHIS results are expected to improve with further algorithm development.

As a design issue, the Full Resolution and Partial Scan modes are seen to provide comparable performance, although the Partial Scan did do poorly on the water vapor in these experiments. This may be due to the lower resolution and fewer channels available in the water vapor band of the Partial Scan mode. However, since the Full Resolution mode in these experiments had higher noise corresponding to an equivalent spatial coverage rate of the Partial Scan, and it did as well (or better), it would seem preferable to the added design complexity required by the Partial Scan mode.

5. VERTICAL RESOLUTION

This section discusses the concept, algorithm, and results of calculations of the vertical resolution for the GHIS.

5.1 Vertical Resolution Algorithm

In the sounding retrieval community the term "vertical resolution" has been used to mean a variety of quantities. One definition has been the full-width half-maximum (FWHM) of the instrument's weighting function, $d\tau/d\ln p$. This quantity is a fair representation of the thickness of an atmospheric layer sensed by an individual channel, but ignores the added information present from other channels, or the retrieval algorithm. Another definition has been the thickness of the vertical layer over which points in the retrieved profile are averaged. This definition ignores the instrument characteristics and leads to an arbitrary number that does not fit with our intuitive understanding of resolution.

A more useful approach to the concept of vertical resolution is to consider an application of the retrieved profiles and define a measure that is significant in this application, as well as fits our intuitive model. A primary application of satellite soundings is their use in Numerical Weather Prediction (NWP) models. There, atmospheric layers are defined and the values of temperature and water vapor quantities are state variables in the model. One issue of importance in these models is the correlation in the values of the state variables between layers. An important feature of new data to be inserted in the model is the correlation of errors between layers. It is undesirable to adjust a model profile to a retrieved profile that has correlated errors over several layers.

Thus, a useful definition of vertical resolution is the distance, or correlation-length, between atmospheric levels over which the error in the retrievals are uncorrelated. Figure 4 shows the correlation functions of retrieval error at three different altitudes: 1 km, 10 km and 20 km. As one can see, the correlation functions approximate the shape of a sin (x)/x curve. Just as in considering the resolution of unapodized interferograms which typically have a sin(x)/x instrument line shape, a useful definition is the FWHM. Here, this definition is seen to result in resolutions of approximately 1 km in the lower troposphere, 2 km in the upper troposphere and 3 km in the stratosphere which fit well with intuition.

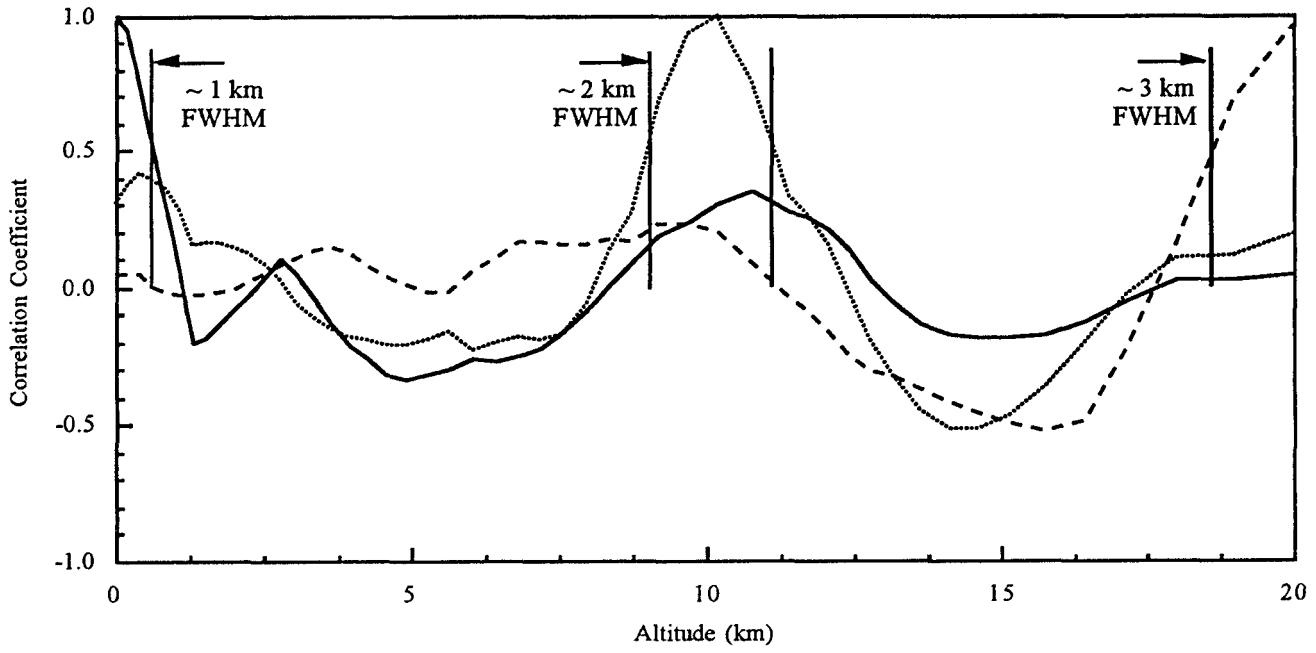

Figure 4. Typical retrieval error correlation coefficient functions for three difference altitudes.

5.2 GHIS Vertical Resolution Results

The following tables show the results of applying this vertical resolution algorithm to GHIS and GOES-8. They provide a glimpse at the expected improvement in going from the filter wheel to the interferometer. The improvement is pretty dramatic in the stratosphere, but not quite as significant as expected in the troposphere. This may be attributed more to the capabilities of the GOES-8 Sounder than the deficiencies of the GHIS.

The GHIS is shown to achieve vertical resolutions in the troposphere of just over 2 km, instead of the anticipated 1 km resolution. Further work will be done to fine tune the vertical resolution algorithm, but these results indicate that even with GHIS there may be significant correlations between errors over several kilometers in the retrieved profiles. Data assimilation methods have been developed for NWP models using current sounder data and these results suggest they will still be required in the future, although the correlations show promise of being reduced. Also, the resolution reported for the tropospheric region is an average from the surface to 100 mbar while the actual results show a profile with the resolution being 1 km near the surface and increasing to 3 km at 100 mbar.

Table 6. Tropospheric (1000-100 mbar) temperature vertical resolutions (km).

GHIS Operating Mode	Linear First Guess	Iteration Result
Full Resolution	2.6	2.4
Partial Scan	2.6	2.2
Low Resolution	2.6	2.4
GOES-8	3.2	2.7

Table 7. Stratospheric (100-10 mbar) temperature vertical resolutions (km).

GHIS Operating Mode	Linear First Guess	Iteration Result
Full Resolution	3.6	3.4
Partial Scan	3.5	3.3
Low Resolution	3.9	4.0
GOES-8	6.1	5.6

6. SUMMARY AND CONCLUSIONS

The retrieval performance of an upgrade for the GOES-Next Sounder has been studied through simulations. The GHIS design is seen to provide retrieval performance improvements relative to the GOES-Next Sounder by 50 to 100% in temperature retrieval accuracy. Water vapor improvements are less dramatic, but nonetheless significant. A measure of the vertical resolution achieved by these sounders based on the correlation of retrieval error has been developed and used to show the improvement possible from the GHIS upgrade. The retrieval performance shown for GHIS should be considered as a minimum and is expected to improve as the understanding and capability of performing retrievals with high resolution, high dimensional spectral data develops.

7. ACKNOWLEDGMENT

The authors would like to thank David Hearn of MIT/LL for performing the GHIS radiometric noise calculations.

8. REFERENCES

1. University of Wisconsin-Madison Cooperative Institute for Meteorological Satellite Studies, Santa Barbara Research Center, ITT Aerospace/Optical Division, "High-Resolution interferometer modification of the GOES L/M Sounder: Feasibility Study," September 1988.

2. W. L. Smith, et al, "GHIS-The GOES High-Resolution Interferometer Sounder," *Journal of Applied Meteorology*, Vol. 29, No. 12, pp. 1189-1204, December 1990.

3. H. E. Revercomb, et al, "Radiometric calibration of IR Fourier transform spectrometers: solution to a problem with the High-resolution Interferometer Sounder (HIS)," *Applied Optics*, vol. 27, pp. 3210-3218, 1988.

4. W. E. Bicknell, "Overview of GOES High-Resolution Interferometer Sounder (GHIS) brassboard development and test program," to be published in this proceedings.

5. T. G. Kyle, "Temperature soundings with partially scanned interferograms," *Applied Optics*, vol. 16, no. 2, pp. 326-333, February 1977.

6. J. R. Eyre, "A fast radiative transfer model for satellite sounding systems," Technical memorandum No. 176, European Centre for Medium-Range Weather Forecasts, March 1991.

7. J. R. Eyre, "Inversion of cloudy satellite sounding radiances by nonlinear optimal estimation. I: Theory and simulation for TOVS," *Royal Quarterly Journal of the Royal Meteorological Society*, vol. 115, no. 489, pp. 1001-1025, July 1989 Part B.

8. A. Huang and W. Smith, personal communication, May 1996.

Electronics Considerations for a Geostationary Interferometer Sounder[†]

Lawrence M. Candell and David M. Weitz

MIT Lincoln Laboratory
244 Wood St, Lexington, Massachusetts 02173

ABSTRACT

Future GOES sounders will likely require increased spectral resolution and number of channels in order to meet the sounding vertical resolution and accuracy specifications set forth by the science community. The Sensor Technology and Systems group at MIT Lincoln Laboratory has pursued the use of a high resolution interferometer (GHIS) in order to meet these spectral needs. This paper will focus on the electronics and signal processing necessary for achieving the noise fidelity, dynamic range and data rate constraints for the GHIS instrument. This will include the absolute fringe counting interferometer, analog filtering, A/D conversion, and digital processing. The paper will highlight techniques for reducing the interferometer dynamic range and data rate in order to simplify a GHIS flight design.

Keywords: GHIS, interferometer electronics

1. INTRODUCTION

The Sensor Technology and Systems Group at MIT Lincoln Laboratory has been designing and implementing a prototype interferometer for studying the possibility of replacing the filter wheel section of the present geostationary sounder (GOES Sounder) with an interferometer package (GHIS)[1,2]. This paper will discuss some of the electronics consideration that we have addressed in building this measuring device. First, a high level block diagram of the system is presented. In Section 3, we discuss sampling methods and issues than arise in an interferometer. In Section 4, the concept and utility of absolute fringe counting is established. Section 5 discusses methods of controlling the interferometer moving mirror. Section 6 explores the A/D quantization noise effects on spectral performance, and Section 7 explores the data rate and sampling rate reduction.

2. GHIS ELECTRONICS BLOCK DIAGRAM

The heart of an interferometer is a moving mirror mechanism. As it moves the optical path difference (OPD) in one arm of the interferometer changes–causing different optical frequencies to move in and out of constructive and destructive interference. The electronics system must measure and record the sum total of all of these interferences as a function of OPD as measured by a detector. This signal is called the interferogram. The analog processing and A/D block in the block diagram (Figure 1) acquire samples that are ideally uniformly spaced in OPD (Sections 3 and 6 discuss the sampling process).

It is the job of the absolute reference fringe counter to maintain a measure of the moving mirror position at any time. This measurement is useful for accurately positioning the mirror, for knowing when to take samples, and for enabling the alignment of multiple interferograms (as vectors) during downstream processing. Section 4 discusses considerations for absolute fringe counting.

[†] This work was sponsored by the National Oceanic and Atmospheric Administration under Air Force Contract F19628-95-C-0002.

 0-8194-2200-2/96/$6.00

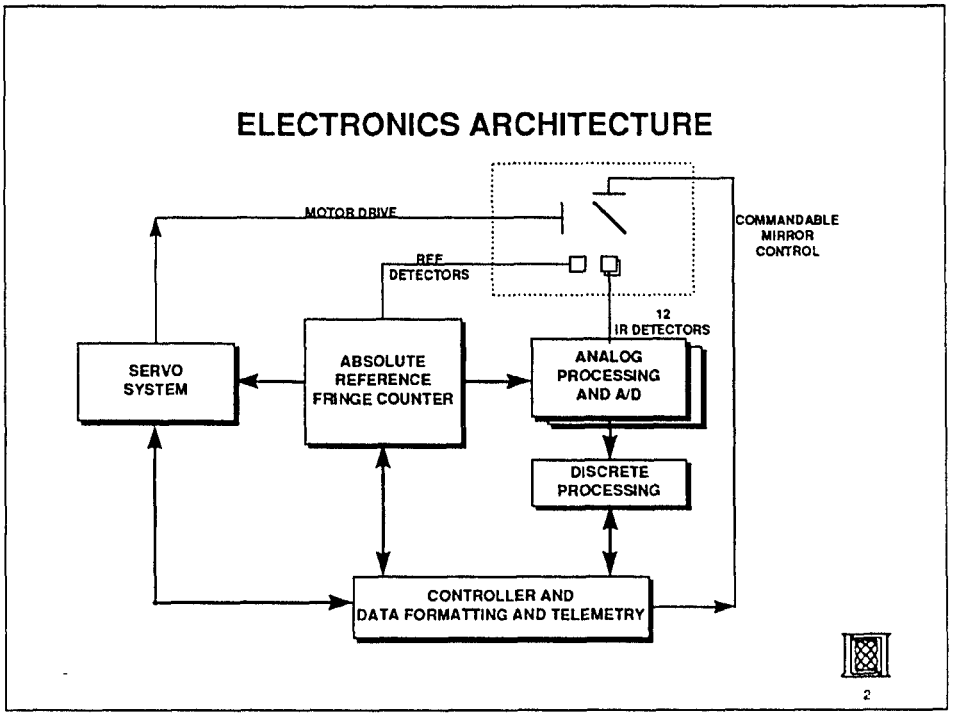

Figure 1

If the mirror were moving at a constant velocity, then the uniform spatial samples would correspond exactly to uniform temporal samples; hence, the temporal frequencies of the interference would be constant, making the frequency response variation of the system unimportant. This places tight demands on the servo system that velocity during the active portion of the data collection be nearly constant. Section 5 will discuss the servo system in more detail

There is also a block shown in Figure 1 for discrete processing. This processing takes place after the samples have been collected and as we will see in Section 7, the primary function of this block is for data reduction. Finally, there is a controller that coordinates the entire process.

3. SAMPLING OF INTERFEROGRAMS

3.1 Sampling in position

Although the interferometer produces a signal that is a function of time, the interferogram would ideally be known as a function of position. After all, we wish to find out how many cycles per centimeter are present in a given signal. The interferometer gives us a clever method of generating spatial samples— passing light of a known wavenumber (cycles/cm) through the moving mirror mechanism and using the resulting interference pattern (a sine wave) to determine sample positions. Figure 2 demonstrates a system where samples of the IR interferogram are taken on rising and falling zero crossings of the reference signal. Note that as the mirror changes velocity, the time axis for both the IR and reference change in tandem.

The frequency of this reference fringe clock must be high enough so that the Nyquist criteria can be satisfied with the derived sample positions. In practice, a highly oversampled system will yield better system performance by allowing simpler analog anti-aliasing filters as well more coarse quantization of the interferogram samples.

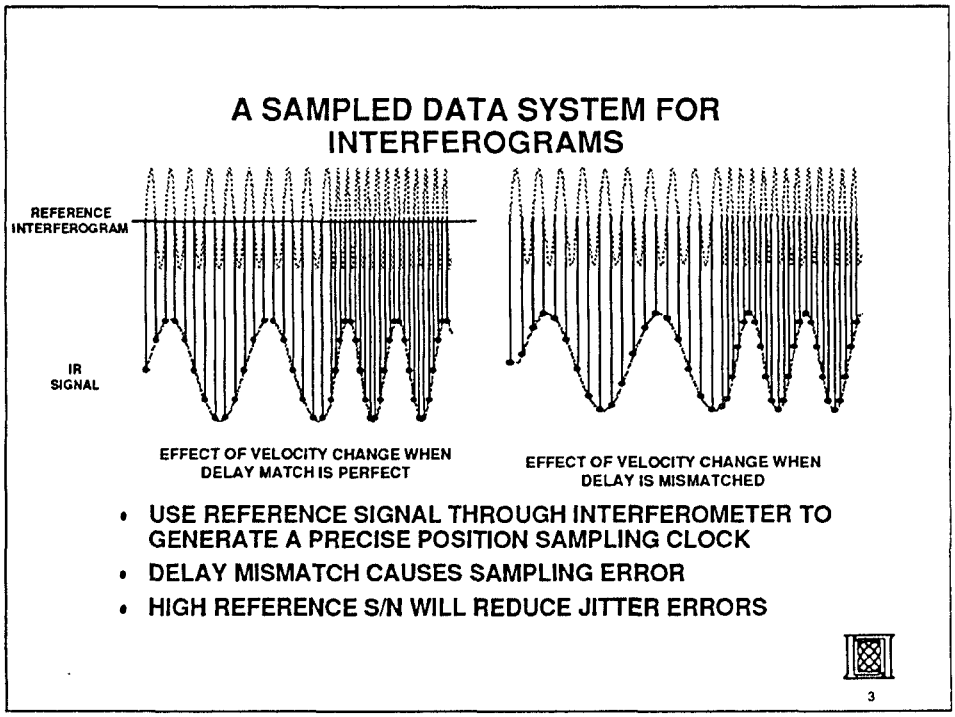

Figure 2

3.2 Delay matching

Figure 2 shows two sampling scenarios: one where the delay in both the IR and reference are equal, and one where there exists a mismatch in the delay of the two signals. A delay is caused by the fact that these signals will likely be passed through analog filters with different group delays. If the delay match is perfect, then any changes in mirror velocity will affect the IR and reference signal simultaneously; thus, the set of samples from this case is unaffected by the velocity change (note that the sample values are in identical positions before and after the velocity change. However, when the delays are not perfectly matched, we notice that extra samples are taken before the IR signal has changed to the higher temporal rate. Also the apparent phase of the samples changes as well.

3.3 Sampling jitter

Since the sample clock is derived from a signal that comes out of the interferometer, its signal to noise ratio becomes an important issue in being able to accurately place the reference zero crossings. This results in an apparent clock jitter that is random in nature. Sampling at incorrect times results in noisy samples where the level of noise is dependent on the rate of change of the IR signal as well as the S/N ratio of the reference signal.

4. ABSOLUTE FRINGE COUNTING

The sampling method described in Section 3 locally determines where samples are taken, but it is impossible to say where the mirror is in an absolute sense (a sine wave is inherently ambiguous to anything greater than one wave). By counting fringes, the ambiguity can be resolved to some degree; however, it is not possible to tell which direction the mirror is moving in when a zero crossing occurs. Many interferometers make use of a white light source (which has an unambiguous large spike at the zero path difference) to establish an absolute position.

4.1 Implementing absolute fringe counting with a quadrature reference

Another option is to add a quadrature signal which permits the determination of direction of travel. This quadrature signal can be generated optically by exploiting the passing a reference signal of both polarizations through the interferometer. Figure 3 illustrates the functionality of the quadrature signal. In the case where no quadrature signal is present, it is impossible to decide which direction the mirror is moving. When the quadrature is present, the sign of the quadrature signal helps to decode the mirror direction. If the quadrature signal is positive on a reference rising edge, then by convention the mirror is moving from left to right. If we move across the diagram from right to left, then rising edges of the reference coincide with places where the quadrature signal is negative. With quadrature signals, the direction can be determined even as the mirror turns around (velocity =0); therefore, whether to add or subtract from the count can be determined. Figure 3 shows the fringe counter output of the GHIS brassboard when the interferometer is in the low resolution mode and a HeNe reference laser (15823 cm^{-1}) is used. The maximum OPD in the low resolution mode is 0.16cm which is 2531 HeNe waves. The turn around section uses about 400 fringes where the velocity is not constant.

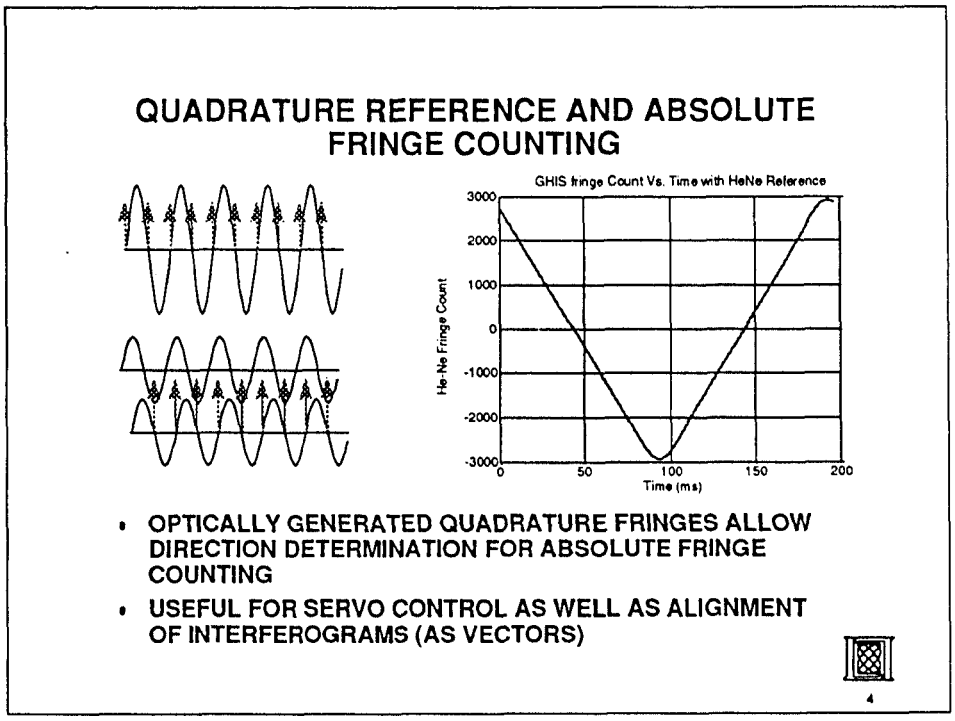

Figure 3

4.2 Utility of absolute fringe counting

Knowing the absolute position of the mirror to the nearest fringe has great benefits for a number of reasons. First, it lets the reference system be easily used as the position sensor for the servo system. Fringe counts can be sent to the servo and the noise will be set by the fringe quantization. For HeNe, this resolution is 632nm— difficult to achieve at a 5000 Hz bandwidth with other techniques.

Second, A/D samples can always be taken at the same fringe position. This greatly simplifies ground processing by allowing two interferograms to easily be subtracted (background subtraction, for instance). Without absolute fringe counting, a new phase correction would need to be computed for every interferogram collected, since the sample positions would vary.

5. MOVING MIRROR CONTROL

5.1 Desired velocity profile

Imagine that the IR signal consisted of a single sine wave. Looking at Figure 2, as the velocity varied, the samples would still be perfect so long as the delays are matched. On the other hand, the illustration assumes that the analog filters before the A/D have a constant flat response. Since the temporal frequency changes with velocity, the sine wave amplitude would vary to the degree that the frequency response changed. This sensitivity is dealt with in two ways: first, the pass band of the analog filter is designed to be as flat as possible and wider than the actual signal (making oversampling desirable). Second, one must maintain tight control of the mirror velocity variation. Except for the turnaround, the velocity is commanded to be constant.

5.2 Achieving small velocity variation

The constant velocity of the mirror is made difficult by a number of issues. Figure 4 shows the actual velocity profile of the GHIS brassboard. It is normalized so that 1 is the nominal velocity. The mirror must rapidly turn around at the end of a scan. This produces a step like input into the velocity portion of the control loop. Furthermore, phase margin is such that some ringing is inevitable.

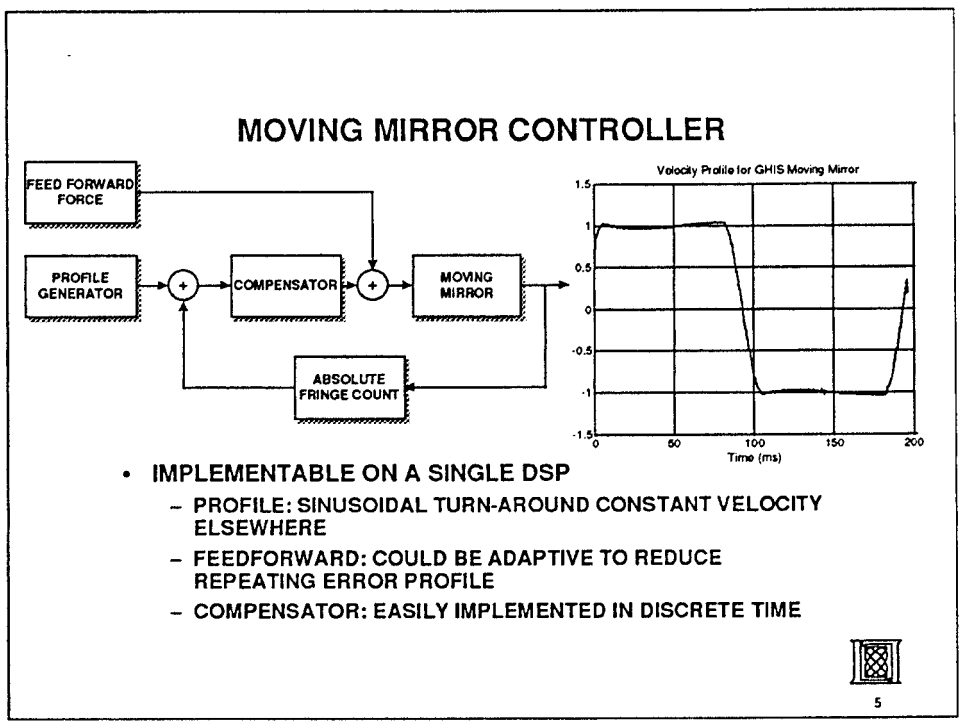

Figure 4

The effects are mitigated in a number of ways. First, the constant velocity regions of the velocity profile are connected by a cosine. This increases the peak actuator requirements, but smoothes out the command. Second, the servo systems makes use of a feed forward forcing term. This term is either derived beforehand or determined adaptively. It supplies the nominal forces needed to move the mirror through the desired profile, so that the control loop ideally would not see any errors except for disturbances.

6. SAMPLE QUANTIZATION

In a sampled data system, the question of the number of required quantization bits often arises. For an interferometer, this issue becomes more complicated because the dynamic range of the interferogram can be quite different from the spectral domain where noise is typically defined. A method must be developed to map dynamic range from one domain to the other. Figure 5 demonstrates how this can be accomplished.

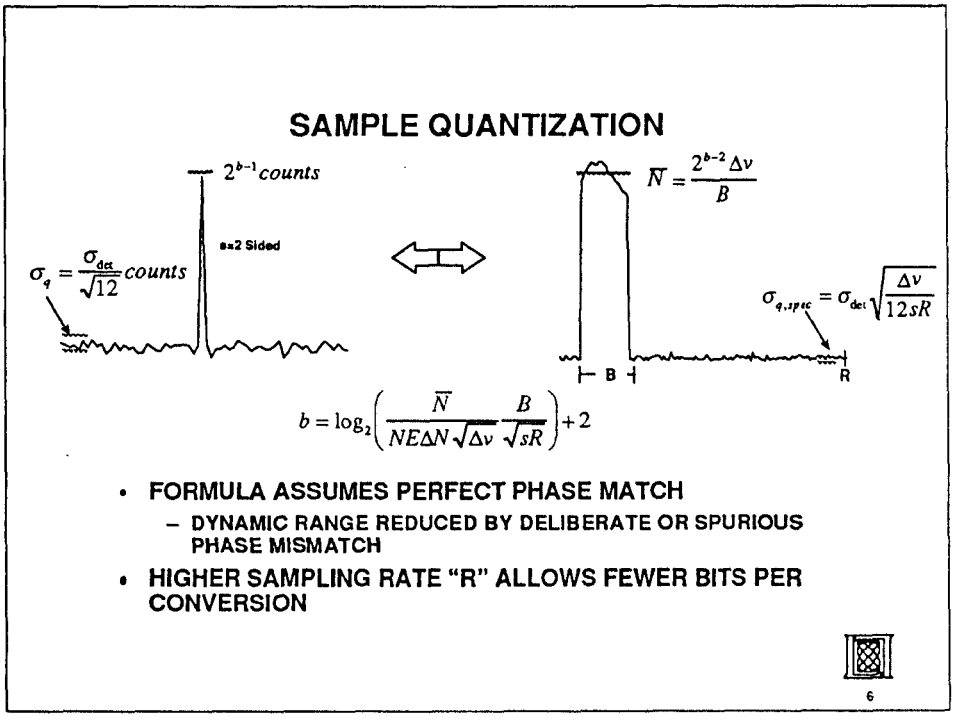

Figure 5

The high end of the interferogram dynamic range is set by the height of the Zero Path Difference (ZPD) peak, and the low end is determined by the rss of the many noise sources in the data samples. From Figure 5, we see that the quantization level is set so that its standard deviation is 1/sqrt(12) of the detector noise. This is equivalent to setting the size of the quantization cell equal to the standard deviation of the detector noise. With this setting, quantization noise will be 4% of the detector noise level and well uncorrelated with the signal of interest. Also the ZPD peak is set so that half of the full bipolar range is used to capture the peak.

The ZPD peak height can be shown to be governed by the mean level of the spectral response and the relationship is shown on the Figure 5. The quantity N is the average radiance reaching the detector weighted by the responsivity of the detector. The noise in the interferogram domain is assumed to be white; thus it maps with a scale constant into spectral domain. R is the sampling rate (cycles/cm), Δv is the spectral resolution of the channel (cycles/cm) and B is the channel bandwidth (cycles/cm). Notice that as the sampling rate is increased, the noise in the spectral domain due to quantization will decrease, suggesting a benefit of oversampling.

Taking the ratio of signal to noise in the spectral domain generates a formula for the number of bits needed in the A/D. This formula is given in Figure 5. Using typical values for the longwave band N=150 mW/m^2/sr/cm^{-1}, NEdN=1mW/m^2/sr/cm^{-1}, Δv=.625 cm^{-1}, B=530 cm^{-1}, and R=12900 cm^{-1}, yields a number of bits, b=11.3 bits for the converter. A twelve bit converter would therefore suffice (leaving some margin for A/D nonlinearities and headroom).

This formula is derived assuming that the interferogram is a linear phase sequence. This leads to a maximum peak at ZPD since all the cosines add in phase. Phase distortion actually decreases the dynamic range of the

interferogram. Phase distortion occurs inadvertently due to non linear phase analog filters and background levels. Also, it would be possible to add small phase distortion to reduce the dynamic range. With absolute fringe counting, the phase could be recovered and corrected.

7. DATA RATE REDUCTION

We have seen that the analog filtering requirements and the A/D quantization both benefit from a high A/D sampling rate. This does, however, lead to many more samples than are theoretically needed to express the interferogram. This, of course, implies that the downlink data rate must increase to accommodate the increased number of samples. The alternative is to perform processing on the data samples to enable a resampling at a slower rate.

This process is shown in Figure 6. The downsampling approach (decimation)[3] involves two steps. First, filter out unwanted portions of the spectrum, and second decrease the sampling rate. Even though aliasing will occur, the filtering has removed any spurious signals that might alias onto signal of interest.

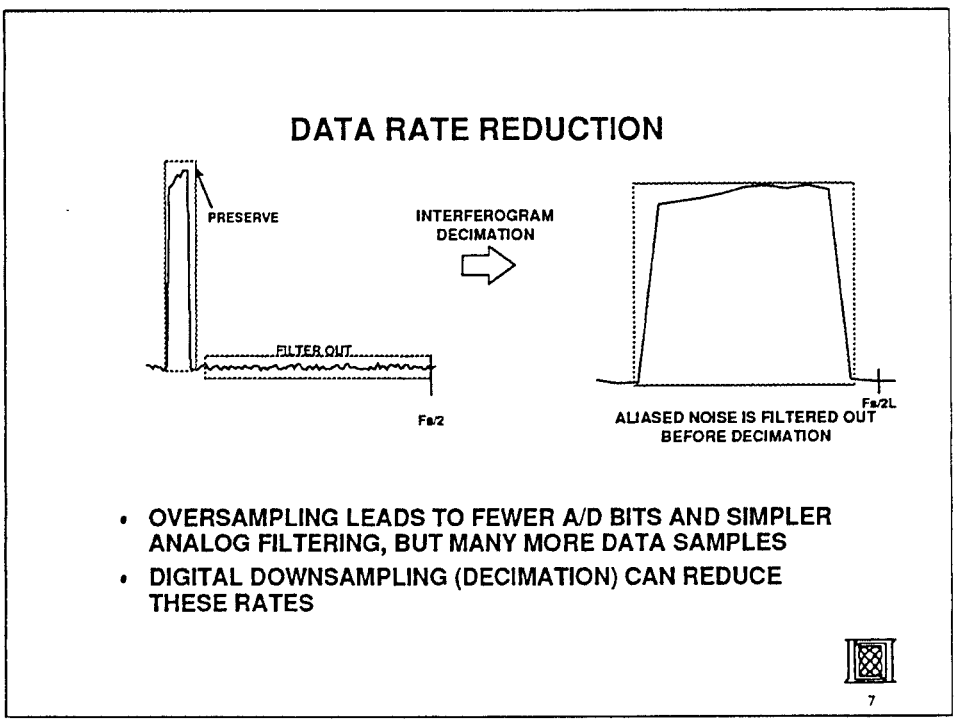

Figure 6

The processing demands for the filtering are quite modest, since the filter output need only be computed at sample outputs which will not be thrown away. A typical processor uses an FIR filter of length 200 and can reduce the unprocessed data rate by a factor of ten. This requires roughly one million multiplies and adds per second.

8. REFERENCES

1. W.E. Bicknell et al, *GOES High Resolution Interferometer Study,* MIT Lincoln Laboratory Project Report, NOAA-12, 5 June 1995.
2. W.E. Bicknell, "Overview of GOES high resolution infrared sounder (GHIS) brassboard development and test program", *1996 SPIE Proceedings, Session 2812-36* (to be published)
3. A.V Oppenheim and R.W. Schafer, *Discrete-Time Signal Processing*, Prentice Hall, Englewood Cliffs, NJ, 1989

GHIS optical design

Danette P. Ryan-Howard

MIT Lincoln Laboratory
244 Wood Street, Lexington, Massachusetts 02173

ABSTRACT

The GOES Sounder is a 19-channel discrete filter radiometer. Studies by the University of Wisconsin[1] and MIT Lincoln Laboratory indicate that retrieval performance could be improved by replacing the filter wheel with a Michelson interferometer. The interferometer system is to replace the relay optics and filter wheel and is required to use the existing GOES telescope and detector subsystems. Numerous configurations were considered in an effort to define a design which meets the optical specifications and fits within the limited available space with sufficient clearance around the optical components for the mechanical housings. The selected interferometer subsystem design fits within the available volume without rotation of the star sensor. Performance, diffraction and sensitivity analysis results are included.

Keywords: optical design, GOES, GHIS

1.0 INTRODUCTION

The GOES optical system comprises an f/11.9 telescope subsystem, relay optics for each of three infrared channels, a filter wheel assembly and a detector optics subsystem. A schematic of the GOES Sounder Optical System is shown in Figure 1. The visible channel is transmitted through the first dichroic beamsplitter and the three infrared channels are reflected. The infrared channels are separated using dichroic beamsplitters. There are independent refractive relay optics for each channel. The relay optics are followed by the sounder filter wheel and the detector optics.

The GOES Sounder is a 19-channel discrete filter radiometer. Studies by the University of Wisconsin[1] and MIT Lincoln Laboratory indicate that the sounder temperature resolution could be improved by replacing the filter wheel with a Michelson interferometer. The GOES High-Resolution Interferometer Sounder (GHIS) system is required to use the existing GOES telescope and detector subsystems. The relay optics and filter wheel assembly are to be replaced with an interferometer subsystem. The interferometer subsystem must therefore accept the f/11.9 beam at the GOES telescope image and produce an f/42 beam at the field stop aperture which is located within the detector subsystem. The telescope primary aperture must be imaged onto a Lyot stop and then reimaged onto the detector. The image at the field stop must be matched to that of the GOES system in both size and angle. The change is to be transparent to the telescope and detector subsystems.

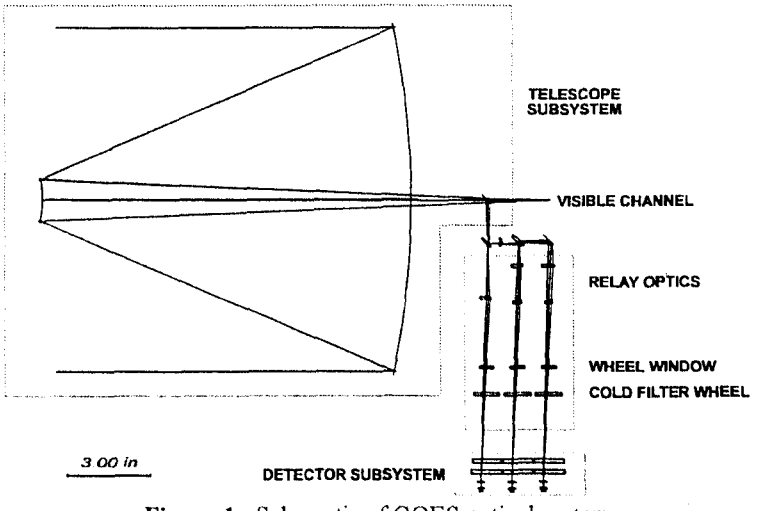

Figure 1: Schematic of GOES optical system

This paper describes the optical performance requirements, the optical system design and the effects of deviations from the design parameters on the system performance. An overview of the GHIS brassboard development and test program which employs the optical system described here is given in a paper by Bicknell[2].

2.0 GHIS OPTICAL REQUIREMENTS

For the change from the filter wheel sounder to an interferometer sounder to be transparent to the telescope and detector subsystems, the GHIS system must accept the f/11.9 beam at the GOES telescope image and produce an f/42 beam at the field

stop aperture which is located within the detector subsystem. The telescope primary aperture must be imaged onto a Lyot stop and then reimaged onto the detector. Because of the moving mirror in the interferometer, the Lyot stop must be located on the detector side of the interferometer and must be the limiting aperture for the system. The image at the field stop must be matched to that of the GOES system in both size and angle. The field stop parameters are shown in Figure 2[3]. The GHIS optical requirements are summarized in Table 1.

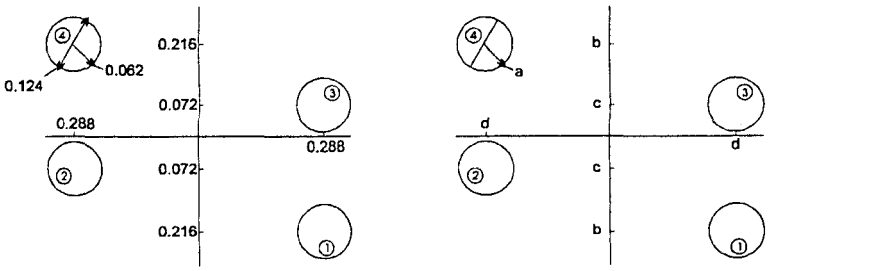

	a	b	c	d
Longwave	0.006985	0.024129	0.008043	0.032153
Shortwave	0.006963	0.024147	0.008049	0.032198
Midwave	0.006970	0.024147	0.008049	0.032206

Figure 2: GOES field stop parameters

Table 1: GHIS optical requirements

Wavebands	3.7 - 4.7 μm (shortwave) 5.8 - 8.3 μm (midwave) 8.7 - 16.1 μm (longwave)
GFOV	± 820 μrad (± 0.047°)
IGFOV	244 μrad (0.014°)
F/number at Telescope Image	f/11.9
F/number at Field Stop	f/42
Interferometer Aperture Diameter	0.33 in. (recommended by Wisconsin[1])

2.1 Pupil and field stop imaging

The GOES system is a pupil imaging system. With a pupil imaging system, information from any point in the field-of-view is uniformly distributed across both the pupil and the detector. Intensity fluctuations on the detector due to ground structure are therefore minimized. An image of the ground is formed at the field stop. The diameters of the four apertures shown in Figure 2 define the IGFOV of the system. The locations of the four apertures determine the location of the IGFOV within the GFOV.

2.2 Co-registration and percent energy

Table 2 summarizes the sounder performance requirements.

Table 2: Sounder performance requirements

Parameter	Value	Source[4]
Encircled Energy	70, 85, 90% (vis, sw) 65, 78, 84% (mw) 60, 73, 79% (lw) @ 1.0, 1.25, 1.5 IGFOV	SS/L Doc. 565054 Rev. E, p27
IGFOV Size	244 μrad diameter	NASA 3.12.8.1 FACC 3.2.4.1
Channel-to-Channel Registration	± 22 μrad IR (± 9%) ± 22 μrad vis[5]	NASA 3.12.8.4 FACC 3.2.5.1

The encircled energy requirement specifies that 70, 70, 65, 60% of the energy from a 244 μrad IGFOV must fall on the detector for the visible, shortwave, midwave and longwave channels respectively. The second and third number in the encircled energy value specification are for 1.25 and 1.5 IGFOV respectively. The encircled energy specification does not include component transmission losses. The channel-to-channel registration is required to be within ± 22 μrad. Specified as a fraction of the IGFOV, the co-registration requirement is ± 9%. The co-registration requirement assures that the detectors for the visible channel and the corresponding detectors for the three infrared channels are all receiving information from the same region on the ground.

3.0 OPTICAL SYSTEM

3.1 Optical design history

For compatibility with the GOES telescope and detector subsystems and proper operation of the interferometer, the following components are required: A collimator to form the input beam for the interferometer, a Lyot stop following the interferometer, a focussing lens to reimage the telescope image onto a field/glare stop, and a field lens which in combination with the other optical components forms an image of the Lyot stop on the detector.

Numerous configurations were considered in an effort to define a design which meets the optical specifications and fits within the available space with sufficient clearance around the optical components for the mechanical housings. Systems employing a beamsplitter in the interferometer which have a 30° angle-of-incidence were preferred to systems with a beamsplitter which have a 45° angle-of-incidence since the coating efficiency is slightly higher. An unobscured telescope, an off-axis parabola and a tilted spherical mirror were considered for the collimator. Both the unobscured telescope and the off-axis parabola fit within the available space, but yield a tilted pupil image at the Lyot stop. The tilted spherical mirror was preferred for a baseline design since the pupil image is perpendicular to the optical axis.

Designs which employed a refractive field lens near the telescope image had unacceptable amounts of chromatic aberration. To reduce the chromatic aberration, it was necessary to remove all refractive lenses from the region in which all three infrared channels are combined and place one field lens in each channel after the infrared channels are separated by the dichroic beamsplitters. A single reflecting component was initially used to form the f/42 focus at the field stop. The resulting system had excessive residual aberrations and it was necessary to use a three-mirror focussing group to improve the image quality.

3.2 Selected design

Figure 3 is a schematic of the GHIS optical system with the GOES telescope and detector subsystems. Figure 4 is an enlarged view of the interferometer subsystem. The interferometer subsystem comprises a tilted spherical mirror which serves as the collimator, an interferometer with the beamsplitter tilted at 30°, a three-mirror focussing group which forms the required f/42 beam, dichroic beamsplitters to separate the three infrared channels, and a refractive field lens for each channel which, in combination with the three-mirror system and the detector optics, forms an image of the Lyot stop on the detector element. A stop is located at the telescope image. As recommended in the Wisconsin proposal[1], the collimated beam diameter at the interferometer is 0.33 inches. The interferometer subsystem is designed for an operating temperature of 220 K. The interferometer subsystem is athermalized so that it can be aligned at room temperature and operated at 220 K. Figure 5 shows the detector subsystem and one of the four detectors of the longwave channel with its associated lenses. The location of the image plane at the field/glare stop position is shown. Approximate temperatures of the components within the subsystem are indicated on the figure. The GOES

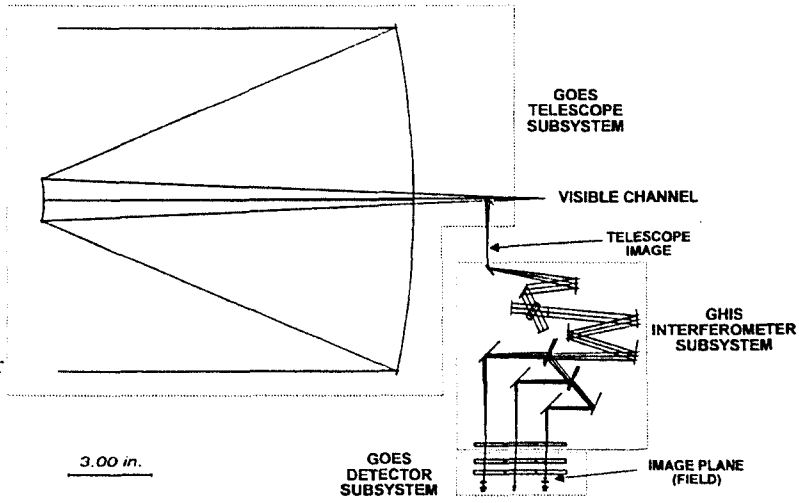

Figure 3: Schematic of GHIS optical system

system has wavelength filtering coatings on the detector window. Similar wavelength filters will be required for the GHIS system.

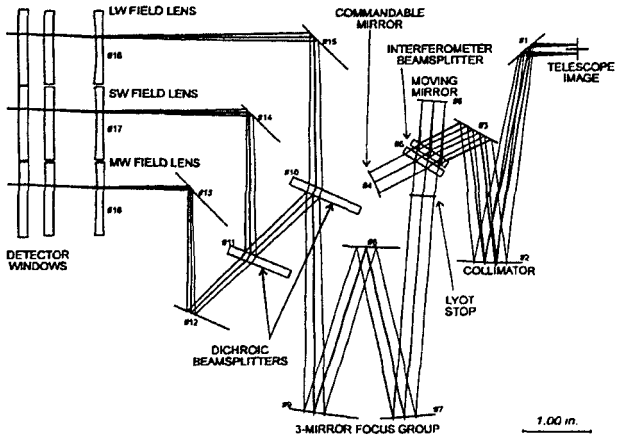

Figure 4: Englarged view of the GHIS interferometer subsystem

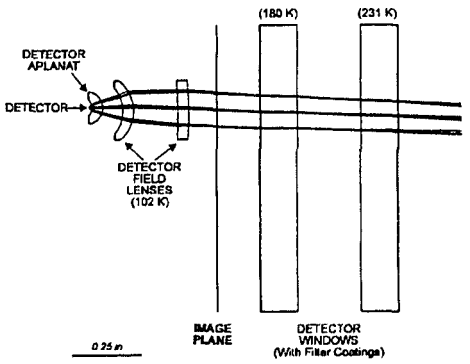

Figure 5: Detector subsystem - longwave channel

The preferred GHIS system fits within the available space and is an in-plane design which simplifies mounting and alignment. All optical surfaces within the interferometer subsystem are either spherical or planar and can be manufactured using conventional fabrication techniques. Table 3 lists the percent energy on the detector for the infrared channels. The similar percent energy numbers for the GHIS and GOES optical systems show that the optical parameters of the GHIS interferometer subsystem are appropriately matched to those of the GOES relay optics. The change from the relay optics and filter wheel to the interferometer subsystem is transparent to the telescope and detector subsystems.

Table 3: Percent energy on detector (nominal)

Channel	GHIS	GOES
Longwave	86 %	90 %
Midwave	92 %	94 %
Shortwave	90 %	92 %

3.3 Visible detector configuration

The GOES relay optics subsystem has an even number of reflections. (See Figure 1.) It should be noted that with one exception, all configurations considered for the GHIS system had an odd number of reflections within the interferometer subsystem. This difference in the number of reflections means that the image at the infrared field stops will be a mirror image of the image at the visible field stop. A modification to the infrared detector package would be difficult since each aperture in the field stop is followed by three lenses and a detector. There are, however, no individual optics for each of the four detectors in the visible sensor. A schematic of the visible optics channel is shown in Figure 6. A mask is used to define the visible detector configuration on the focal plane. Fabrication of a new mask for the visible detectors is a minimal modification to the existing system.

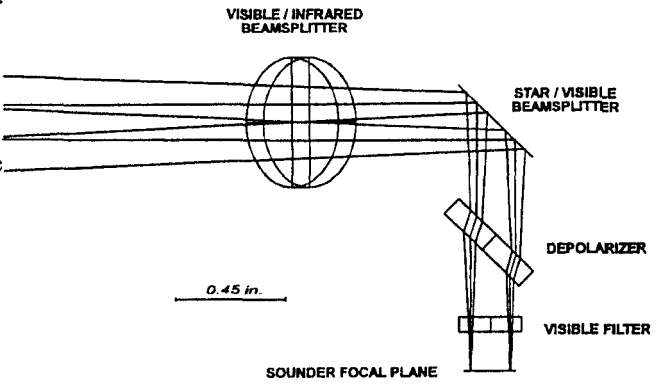

Figure 6: Sounder - visible channel

3.4 Field stop location

The GOES sounder has infrared field stops located within the detector subsystem. For the GHIS system, two options were considered: 1) use the field stops in the existing locations and 2) place a single field stop at the input to the GHIS subsystem and substitute glare stops for the field stops in the detector subsystem. The single field stop in the front has advantages. Since the field stop at the input defines the field-of-view for all three channels, co-registration among the infrared channels is assured. Since the co-registration with the visible channel is determined by the front field stop, the components within the interferometer subsystem and within the detector subsystem do not affect the co-registration.

Diffraction analyses for both options were run using GUERAP[6]. Results showed that there were no negative consequences of placing the single field stop at the input to the interferometer subsystem.

3.5 Co-registration sensitivities

To assure that the three infrared channels and the visible channel are receiving radiation from the same region on the ground, there is a maximum allowable co-registration error of 9% at the field stop. (See Section 2.2.) A co-registration error between the visible and the infrared channels can result from a placement error of the interferometer subsystem relative to the telescope subsystem. Because the field stop is located at the input to the interferometer subsystem and is common to all three infrared channels, co-registration errors among the infrared channels do not occur.

The interferometer subsystem must be aligned in both position and angle relative to the telescope subsystem. Each subsystem is subject to manufacturing and alignment tolerances In addition to the alignment variations, thermal variations during the mission can lead to decentrations of one subsystem relative to the other. Figure 7 shows the reference points about which the decentration and tilt sensitivities of the subsystems were calculated. The reference point selected for the interferometer subsystem is the point which is static when the subsystem is cooled from room temperature to its operating temperature of 220 K. The convention used for x, y, and z is based on an optical design convention. The x axis is perpendicular to the optical axis in and out of the plane of the paper. The y axis is perpendicular to the optical axis in the plane of the paper. The z axis is along the optical axis.

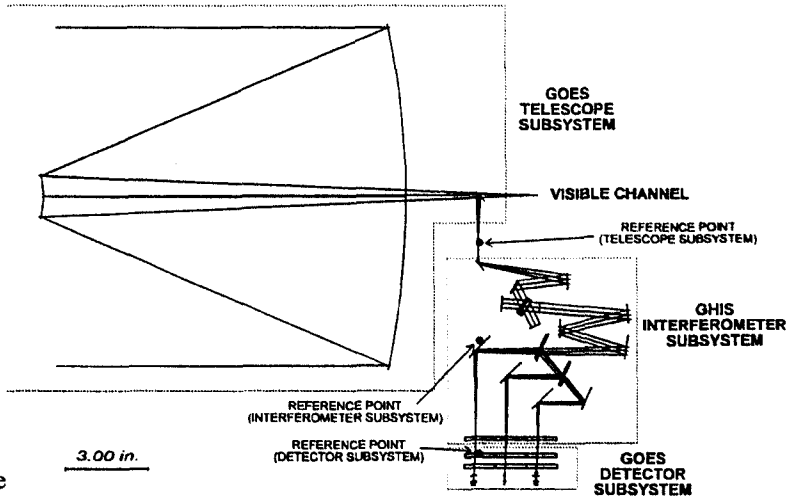

Figure 7: Reference points for sensitivity analyses

Figure 8 shows the image at the field stop for the nominal placement of the interferometer subsystem and an example of a 0.003" decentration of the interferometer subsystem relative to the telescope subsystem. For each field stop aperture shown, four field points at the maximum half-field angle specified for an individual aperture were selected as source points. Each source

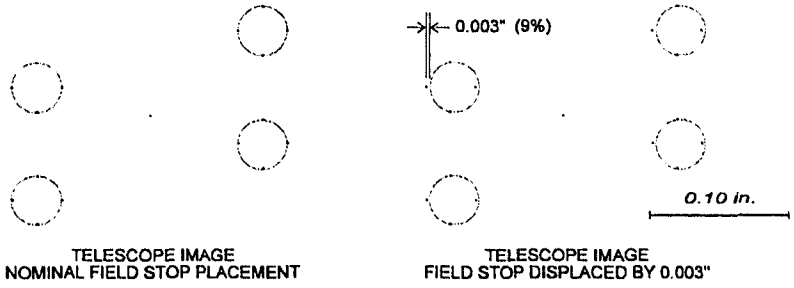

Figure 8: Telescope image on field stop aperture

point on the ground is imaged at the field stop. For the nominal placement of the interferometer subsystem, the field stop image is centered relative to each 0.035" diameter aperture and has information from each of the selected field points. As shown, the center of the field stop image is displaced by 9% when the interferometer subsystem is displaced by 0.003". Information which was on the one side of the field-of-view is clipped by the field stop and does not reach the detector. Information which was outside the original field-of-view can be transmitted through the aperture on the other side. Table 4 summarizes the co-registration errors due to subsystem placement errors using the centers of rotation shown in Figure 7. Percent errors listed are between an infrared channel and the visible channel.

Table 4: Co-registration sensitivity due to subsystem placement errors.

Placement Error	Percent Co-Registration Error		
	X	Y	Z
0.001" Decenter	2.85	2.85	0.01
0.02° Tilt about axis (telescope)	0.00	0.00	0.10
0.02° Tilt about axis (interferometer)	3.68	3.68	0.10

3.6 Percent energy sensitivities

Percent energy calculations have been made to determine the change in the percent energy on the detector with subsystem placement errors. The aplanat-detector unit in the GOES detector subsystem has translation adjustments which are used to maximize the percent energy on the detector in the current GOES system. The location of the aplanat-detector unit was optimized to maximize the nominal percent energy on the detector for the GHIS longwave channel optical design. The field stop was located at the input to the interferometer subsystem. A twenty percent oversized glare stop was located at the field stop plane in the detector subsystem. The optimized percent energy on the detector is 86%. Table 5 lists sample subsystem placement errors with the percent energy and change in percent energy from the nominal design. The aplanat-detector unit was not moved from the optimized nominal position. Subsystem tilts are about the reference points shown in Figure 7.

Table 5: Percent energy sensitivity to subsystem placement errors for the longwave channel (13.64 μm)

Subsystem	Subsystem Error	Percent Energy (change)		
		X	Y	Z
Telescope	0.001" Decenter	85 (-1)	84 (-2)	86 (0)
	0.02° Tilt about axis	85 (-1)	85 (-1)	86 (0)
Interferometer	0.001" Decenter	85 (-1)	85 (-1)	86 (0)
	0.02° Tilt about axis	85 (-1)	84 (-2)	86 (0)
Detector	0.001" Decenter	87 (+1)	85 (-1)	86 (0)
	0.02° Tilt about axis	85 (-1)	84 (-2)	86 (0)

The minimum allowable percent energy for the longwave channel is 60%, i.e., a change of 26%. An allowance of 15% has been made for diffraction losses. This leaves a maximum change of 11%. The RSS of the change in the percent energy due to the sample subsystem placement errors listed in Table 5 is 4.6%. Tilt of the interferometer subsystem about the z axis is expected to have a larger effect on the midwave channel since the output of the midwave channel is offset from the center of rotation. For the midwave channel, however, a tilt of 0.02° about the z-axis leads to a decrease from 92.18% to 91.98%, i.e. a change of only 0.2%.

The percent energy changes due to the interferometer components have been computed parametrically for each of the components in the longwave channel. These parametric curves can be used in conjuction with tilt or decentration estimates to assess the impact of motion during cooldown on the final system performance. The component reference numbers are shown on

Figure 4. The term box on the figure refers to the interferometer subsystem. Figure 9 shows the effect of an uncompensated component decentration on the geometrical percent energy. It shows that small decentration errors lead to a minimal drop in the percent energy. For example, for any individual component , a 0.001" decentration leads to a decrease of less than 1.5 percent. Figure 10 shows the effect of an uncompensated component tilt on the geometrical percent energy. For any individual component, the percent energy decrease is less than two percent for tilts of less than 0.01°.

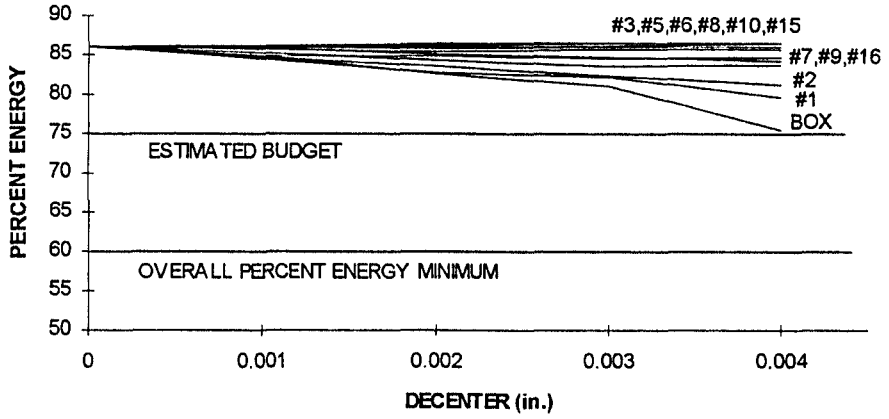

Figure 9: Geometrical percent energy vs uncompensated decenter (longwave)

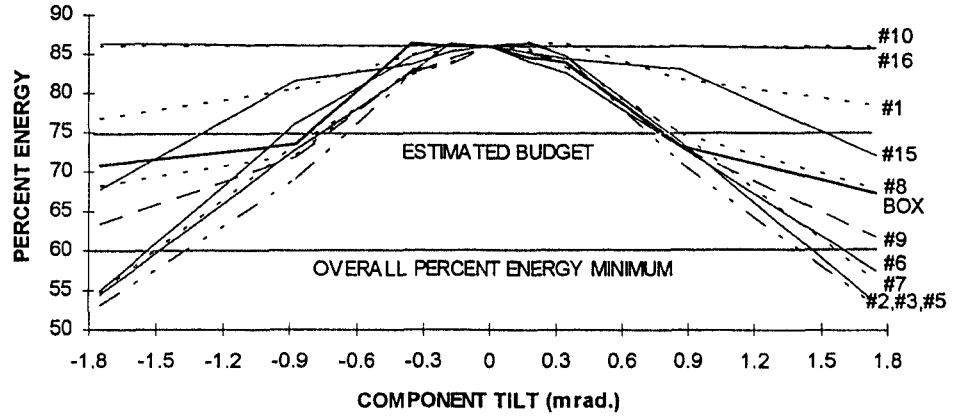

Figure 10: Geometrical percent energy vs uncompensated tilt (longwave)

3.7 Performance summary

To evaluate the system performance in the presence of subsystem placement errors, interferometer component placement errors and subsystem placement variation due to diurnal temperature variation or cooldown, estimates were used. Subsystem placement was assumed to be within 0.001" centration and less than 0.01° tilt (For the center of rotation shown in Figure 7). The expected co-registration error due to these subsystem placement errors is 4.8%. If the subsystem placement is relaxed to 0.002" centration and less than 0.01° tilt, the expected co-registration error due to these subsystem placement errors is 8.5%. Diurnal temperature variation data was obtained from ITT[7]. The range of co-registration errors due to diurnal temperature variation is from 1% to 3% depending upon the time of day. The worst case error of 3% is used here. Table 6 summarizes the estimated co-registration errors.

Table 6: Co-registration errors based on estimated subsystem errors

	Co-Registration Error 0.001" centration, 0.01° tilt	Co-Registration Error 0.002" centration, 0.01° tilt
Subsystem Placement Errors	4.8 %	8.5 %
Diurnal Temperature Variation	3.0 %	3.0 %
RSS	5.7 %	9.0 %

The total co-registration error allowance is 9%. The components within the interferometer and detector subsystems will not affect the co-registration since co-registration is measured at the field stop which is located at the input to the interferometer subsystem. If it is found that the diurnal temperature variation numbers are too pessimistic, it would be possible to relax the subsystem decentration tolerances.

The percent energy on the detector is affected by subsystem placement errors, diurnal temperature variation, component alignment errors (compensated during alignment) and component cooldown errors (uncompensated). A CodeV model of the GHIS longwave channel was used to compute the effect of tilts and decenters on the percent energy on the detector. Initial subsystem placement errors were assumed to be 0.001" and 0.01°. Diurnal temperature variation was assumed to give a maximum decentration of the telescope to the interferometer subsystem of 0.001". Standard component assembly tolerances were assumed (0.002" decenter, 0.002" airspace or thickness, 0.02° tilt or wedge, and 0.1% radius) for the interferometer subsystem components. These initial assembly errors can be compensated by adjusting the final fold flats in the interferometer subsystem. Although the GHIS interferometer subsystem is designed to be aligned warm and operated either warm or cold, small motions of either the GHIS box or an internal component may occur on cooldown. These are the uncompensated errors. Worst case errors of 0.001" and 0.01° were assumed. Although the GOES telescope and detector subsystem components will influence the percent energy change, they are not included in these estimates since the GOES detector and telescope optics were assumed to be completed subsystems that remain unchanged. Table 7 summarizes the changes in the percent energy for the longwave channel. The cooldown error includes tilt and decentration of the interferometer subsystem.

Table 7: Change in percent energy based on estimated errors (longwave channel)

Error Source	Estimated Error	Change in Percent Energy
Initial Subsystem Placement	0.001" decenter, 0.01° tilt	-3.9
Diurnal Temperature Variation	0.001" decenter	-1.2
Interferometer Assembly (compensated errors)	0.002" decenter or thickness 0.02° tilt or wedge	-1.1
Cooldown (uncompensated errors)	0.001" decenter, 0.01° tilt	-6.1
RSS		-7.4

The maximum allowable decrease in the percent energy for the longwave channel is 11%. The RSS of the change in the percent energy due to the errors listed in Table 7 is 7.4% which is within the 11% budget. The uncompensated errors assumed here are much larger than the expected errors. The actual errors will be determined using a thermal model and data generated during testing of the brassboard unit which is currently being fabricated.

4.0 SUMMARY

A GHIS interferometer subsystem can replace the GOES relay optics and filter wheel. The change from a filter wheel sounder to an interferometer sounder is transparent to the existing GOES telescope and detector subsystems. The system is designed to be aligned at room temperature and operated at 220 K. Analyses indicate that both co-registration and percent energy on the detector are within allowed bounds for nominal tolerances assigned or expected on cooldown.

5.0 ACKNOWLEDGEMENTS

This work was sponsored by the National Oceanic and Atmospheric Administration under Air Force Contract F19628-95-C-0002.

6.0 REFERENCES

1. High-Resolution Interferometer Modification of the GOES L/M Sounder: Feasibility Study, University of Wisconsin-Madison Cooperative Institute for Meteorological Satellite Studies (CIMSS), Santa Barbara Research Center (SBRC), and ITT Aerospace/Optical Division, September 1988.

2. W. E. Bicknell, "Overview of GOES High-Resolution Interferometer Sounder (GHIS) Brassboard Development and Test Program", this proceedings.

3. GOES Imager and Sounder Prescription Suites, Lockheed Missiles and Space Company, Inc., Sunnyvale, CA. 1990.

4. FACC numbers refer to SE-565056 spec. paragraph., NASA numbers refer to S-480-19A spec. paragraph.

5. Except for ±4 hrs around midnight.

6. This analysis was done under subcontract to Lambda Research Corporation using GUERAP 5 software.

7. Private Communication.

Assembly, alignment and testing of a GHIS brassboard instrument

A. B. Plaut, D. P. Ryan-Howard, A. C. Parker and D.M. Weitz

Lincoln Laboratory, Massachusetts Institute of Technology
244 Wood Street
Lexington, MA 02173

ABSTRACT

The GHIS (GOES High-Resolution Interferometer Sounder) FTIR spectrometer is designed to be a plug-in replacement for the low-resolution filter wheel spectrometer employed in current GOES sounders. State-of-the-art retrieval algorithms will be able to produce atmospheric temperature and humidity profiles with improved vertical resolution and smaller uncertainties as a result of the instrument's higher spectral resolution. MIT Lincoln Laboratory has designed, assembled, and performed visible-wavelength tests of a GHIS brassboard spectrometer. Details of the assembly procedure will be presented, showing how the optical components were individually tested, then pre-aligned and integrated into the instrument at room temperature for eventual operation at a nominal 220 K.

1. INTRODUCTION

The GHIS FTIR spectrometer is designed to be a plug-in replacement for the low-resolution filter wheel spectrometer employed in current GOES sounders. MIT Lincoln Laboratory has designed, assembled and performed visible-wavelength tests of a GHIS spectrometer. Figure 1 is a schematic of the GHIS optical system. The individual component numbers are noted. The assembly methodology for the GHIS instrument sought to prealign and integrate the interferometer components at room temperature before actual operation at nominally 220 K. The small form factor of the instrument necessitated several distinct alignment steps. Each stage in the assembly and alignment procedure addressed component positioning at a progressively finer measurement scale.

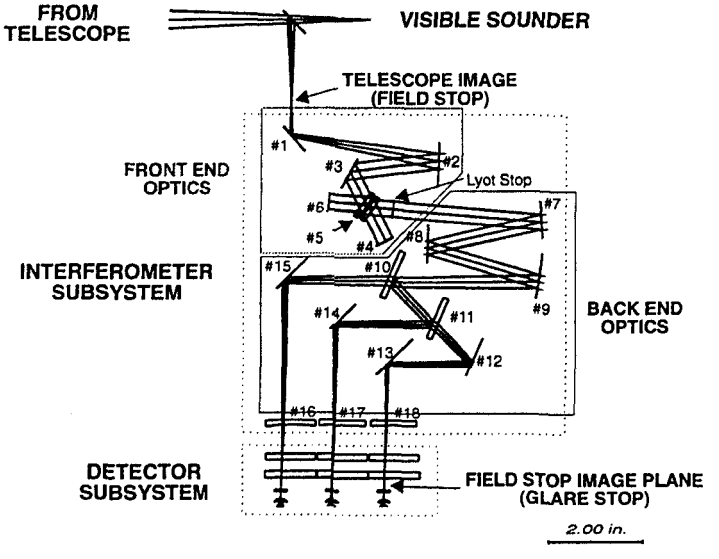

Figure 1. Schematic of the GHIS optical system.

This work was sponsored by the National Oceanic and Atmospheric Administration under Air Force Contract No. F19628-95-C-0002.

0-8194-2200-2/96/$6.00

2. INDIVIDUAL COMPONENT TESTING

The small vacuum chamber shown in Figures 2 and 3 was used to established wavefront characteristics of each individual component at both ambient temperature and at the operating temperature of 220 K. Figures 4a and 4b show the results of the tests on one of the powered mirrors in the focussing group. It shows that the component has a peak-to-valley (P-V) wavefront irregularity of 0.111 waves ($\lambda = 633$ nm) at room temperature and a P-V wavefront irregularity of 0.142 waves at 220 K. The specification called for a P-V wavefront error less than 0.25 waves. Other individual component tests yielded similar results.

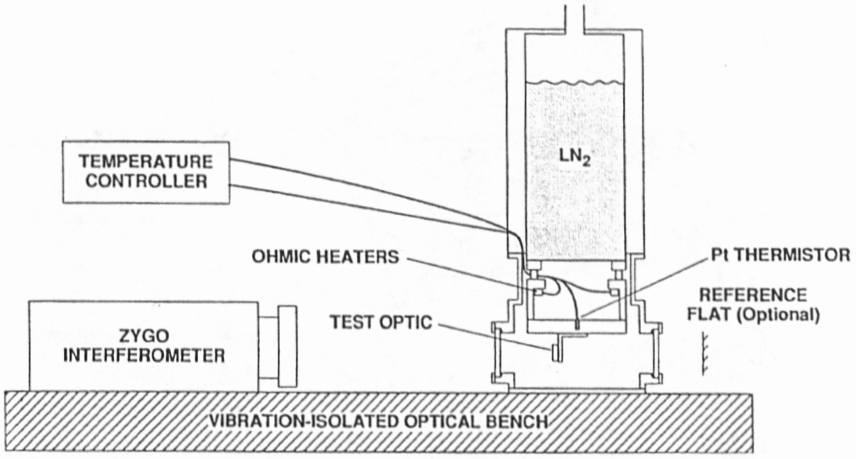

Figure 2. Schematic of the vacuum chamber used for component testing.

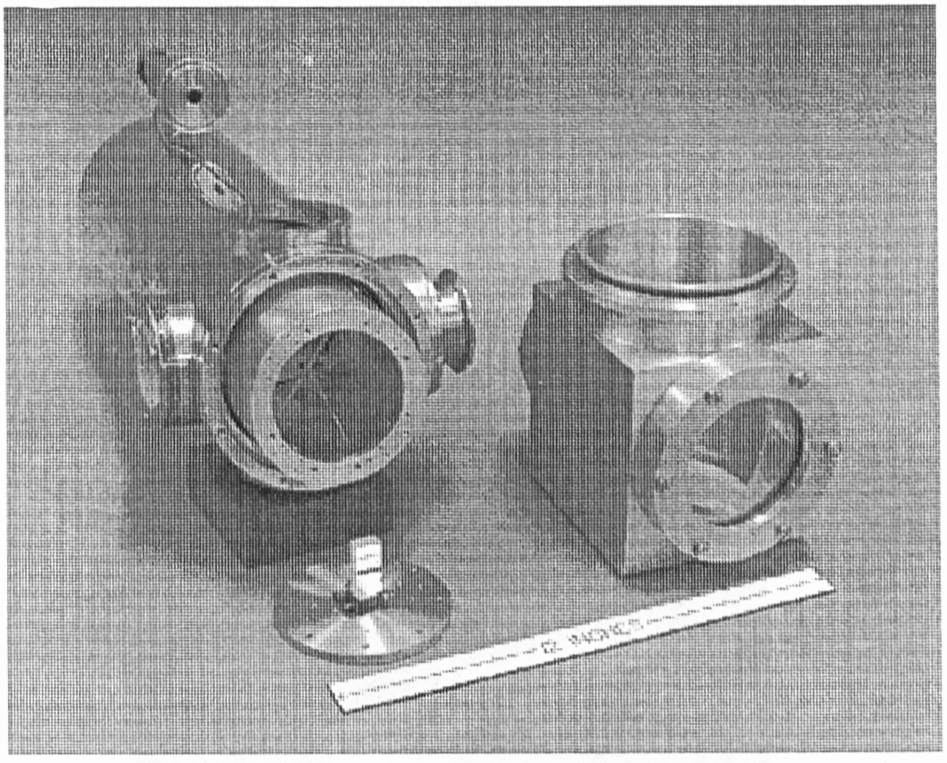

Figure 3. Photograph of the vacuum chamber showing a component under test.

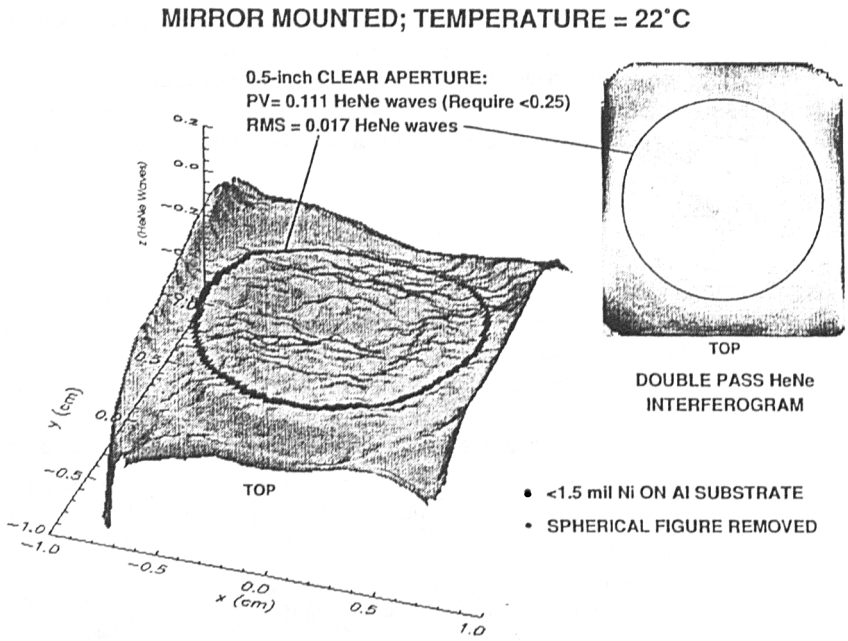

Figure 4a. Wavefront irregularity of mirror #7 at ambient temperature.

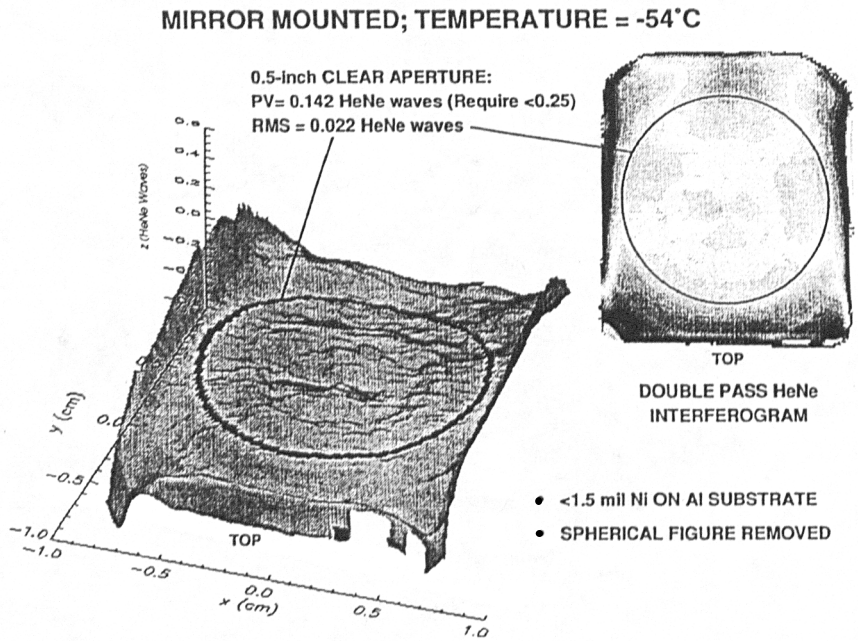

Figure 4b. Wavefront irregularity of mirror #7 at the operating temperature of 220 K.

3. ASSEMBLY AND AMBIENT TEMPERATURE TESTS

Following the individual component wavefront error tests, the component mounts were adjusted to yield orthogonal elevation angles between the optics and their respective mount bases. These adjustments were performed at room temperature using a Zygo interferometer operating at 632.8 nm. Measurement accuracy was approximately 10-20 microradians.

Component placement within the instrument, as dictated by the optical prescription, was next performed at room temperature using a CORDAX metrology system. The CORDAX consists of a video camera mounted to a computer-controlled xyz translation stage (See Figure 5). By establishing appropriate reference angles, and using miniature mechanical adjustment tools, the optical components were positioned to within 0.001 inches of their prescribed locations. Figure 6 shows the GHIS Brassboard with the mounted optical components.

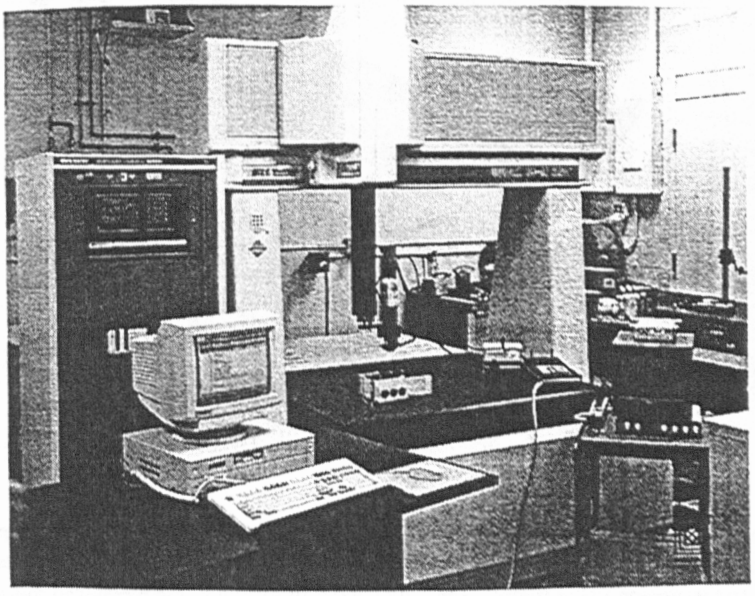

Figure 5. Photograph of the Cordax instrument with the GHIS brassboard.

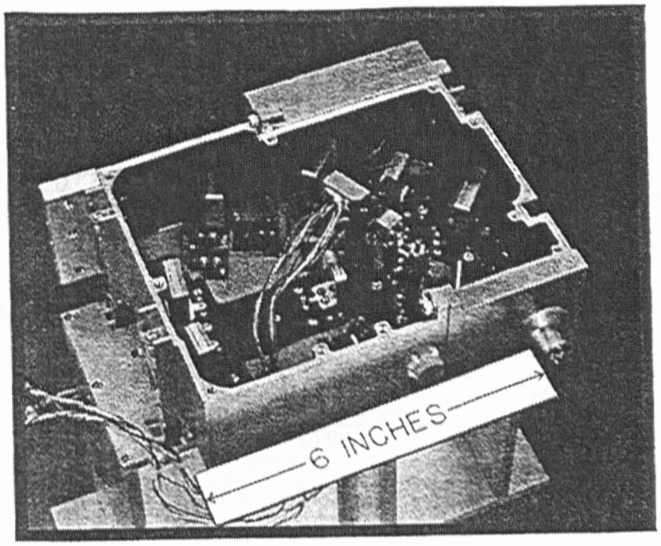

Figure 6. Photograph of the GHIS brassboard.

The Zygo visible interferometer facilitated final alignment of the GHIS instrument, especially the non-common path components. Performed at room temperature, these fine-scale adjustments assured optimal ambient alignment for optical testing at 632.8 nm. Figure 7 shows the measured wavefront error for the first four mirrors in the interferometer subsystem. The measured P-V wavefront error for those components was 2.9 waves at $\lambda = 633$ nm. The wavefront error predicted using the CodeV optical design package was 3.2 waves. The P-V wavefront error was also measured for the subsequent components in the system. The measured wavefront error for the longwave channel of 0.65 waves compare favorably with the 0.7 wave error predicted using CodeV. The overall measured P-V wavefront error of 2.3 waves agrees well with the overall predicted wavefront error of 2.4 waves.

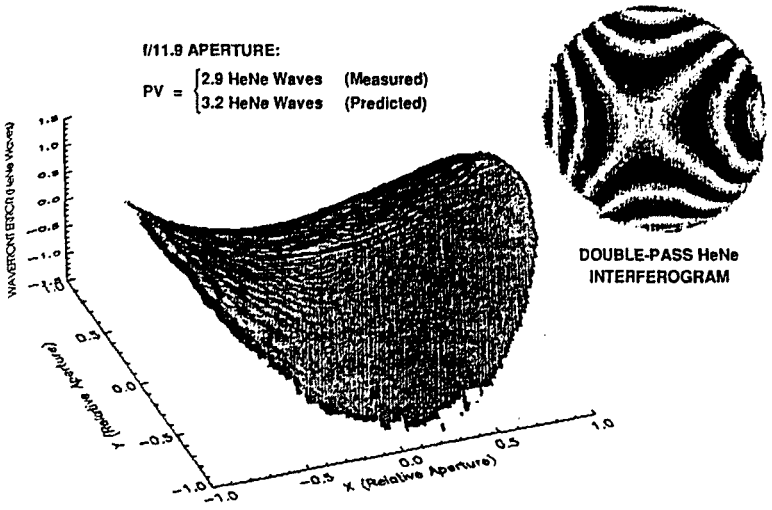

Figure 7. Wavefront error for the first four mirrors in the GHIS brassboard (ambient).

The magnification of the interferometer subsystem was also measured to verify system performance. The system was designed to have a magnification of 3.5. To assure compatibility with the GOES telescope and detector subsystems, the magnification must be matched to the design value within 10%. As shown in Figure 8, the measured magnification was 3.7 ± 0.1 and satisfies the requirement.

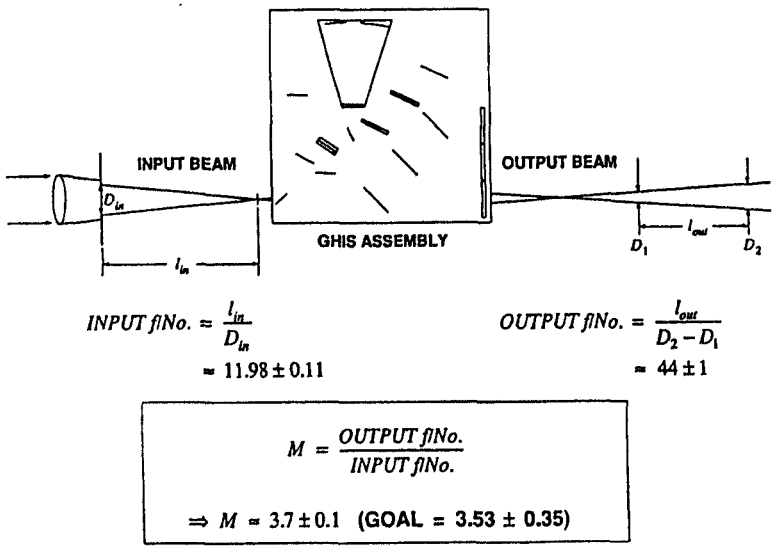

Figure 8. Measurement of the magnification of the GHIS brassboard.

4. AMBIENT AND OPERATING TEMPERATURE TESTS

Lincoln Laboratory has a dedicated vacuum facility for cooling the GHIS interferometer subsystem to 220 K. A photograph of the vacuum facility is shown in Figure 9. A schematic of the optical bench portion of the system is shown in Figure 10. The system is used to make measurements of wavefront error and instrument and component motion caused by cooldown from ambient temperature to 220 K. Figure 11 shows the GHIS interferometer subsystem in the vacuum chamber. The system is instrumented with dial gauges and thermocouples so the motions which occur as a consequence of cooldown can be tracked. Table 1 lists the results of the warm/cold tests of the first six elements in the optical system. As can be seen from the table, the wavefront error is the same at ambient and 220 K.

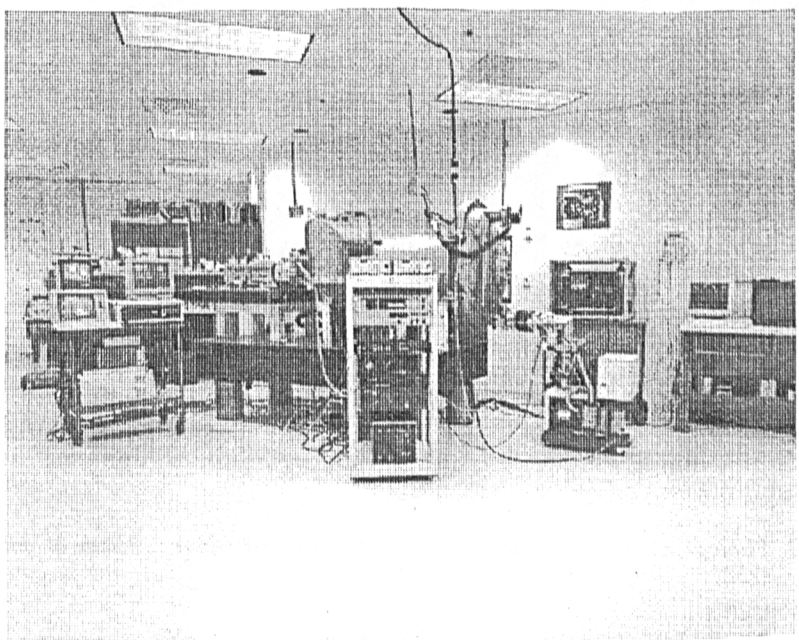

Figure 9. Photograph of the vacuum facility used for cooling the GHIS brassboard.

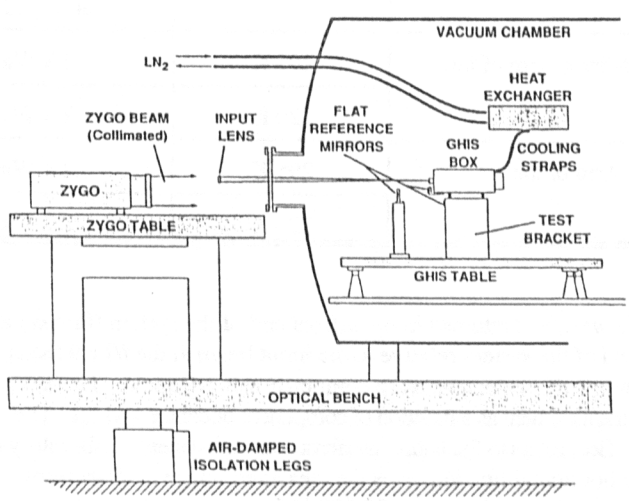

Figure 10. Schematic of the GHIS test setup.

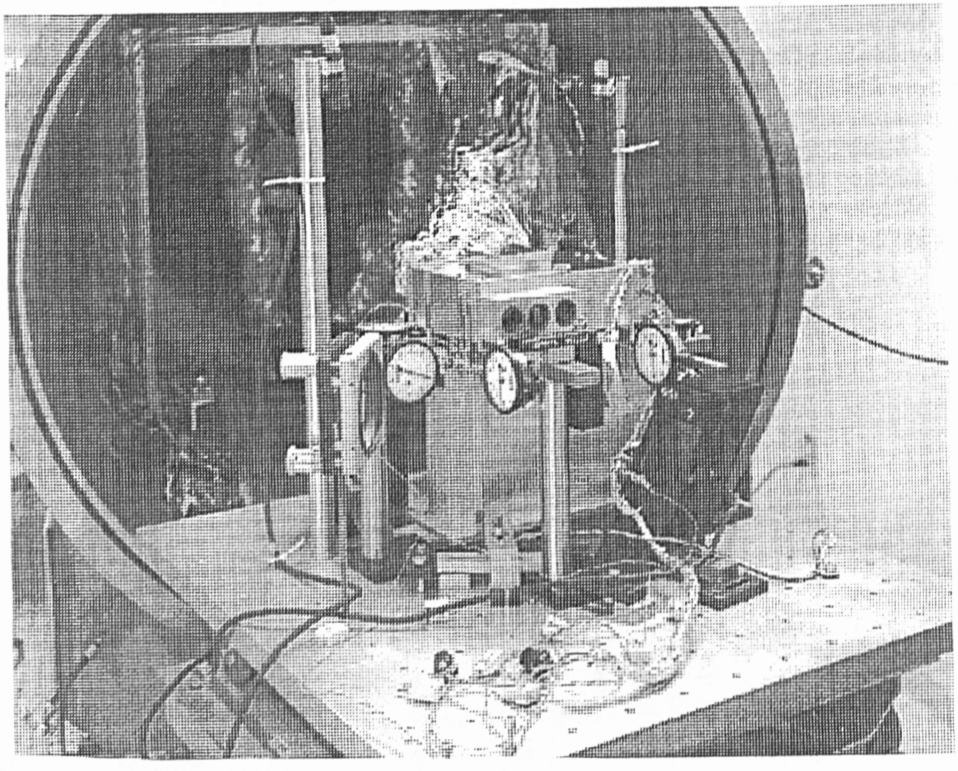

Figure 11. Photograph of the instrumented GHIS brassboard with the vacuum chamber.

Table 1: Results of Front-End WFE Measurements

Path	Temperature	Wavefront Error (at $\lambda = 633$ nm)
Commandable Mirror Arm of the Interferometer	295 K	2.3 Waves
	220 K	2.3 Waves
Moving Mirror Arm of the Interferometer	295 K	2.4 Waves
	220 K	2.3 Waves

Measurements of the tilt of a wavefront returned from the front end of the system (first six elements) yield the displacement of the beam returned from the front end of the system relative to the input beam at the f/11.9 focus. Individual component motions which would yield the measured image displacement were computed using CodeV. The top graphs in Figures 12 and 13 are parametric curves which give image displacement as a function of component decenter and tilt. The component numbers correspond to those shown in Figure 1. The term 'Box' refers to the entire interferometer subsystem. Laboratory measurements yielded an image displacement of 0.004 inches. The horizontal line indicates the measured image displacement. As can be seen from the graphs, that implies that there is a maximum component decenter of 0.002 inches or a maximum component tilt of 1.35 mrad. To assess the impact of the component decenter or tilt, it is necessary to relate it to the system performance parameters. The longwave channel performance is used here as a benchmark. The GHIS optical system is required to have 60% of the energy on the longwave detector.

It is estimated that 15% of the energy will be lost due to diffraction. It is therefore required that the percent energy not dip below 75% as a consequence of the individual component tilts or decenters. The nominal percent energy for the longwave is 86%. The lower plots of Figures 12 and 13 show the percent energy as a function of component decenter or tilt. The percent energy values were computed on CodeV. As can be seen in the figures, the predicted percent energy is above 75% for the component errors which would correspond to the measured image displacement of 0.004 inches.

The ensquared energy parametric study was also run for the back half of the system (components 4,5,6,7,8,9,10 and 15). For any tilt or decenter which resulted from the measured image displacement, there was a decrease in the percent energy of less than 3.5%, i.e. the percent energy is well within the acceptable limits.

5. SUMMARY

The GHIS brassboard has been assembled aligned. Tests indicate that the system can be aligned warm and operated cold. The ensquared energy parametric study indicates that component tilts and decenters which occur due to cooldown are within acceptable limits. The next phase of testing will examine alignment and interferometric performance in the infrared.

6. ACKNOWLEDGMENTS

The authors would like to acknowledge the contributions of E.J. Ringdahl to this effort.

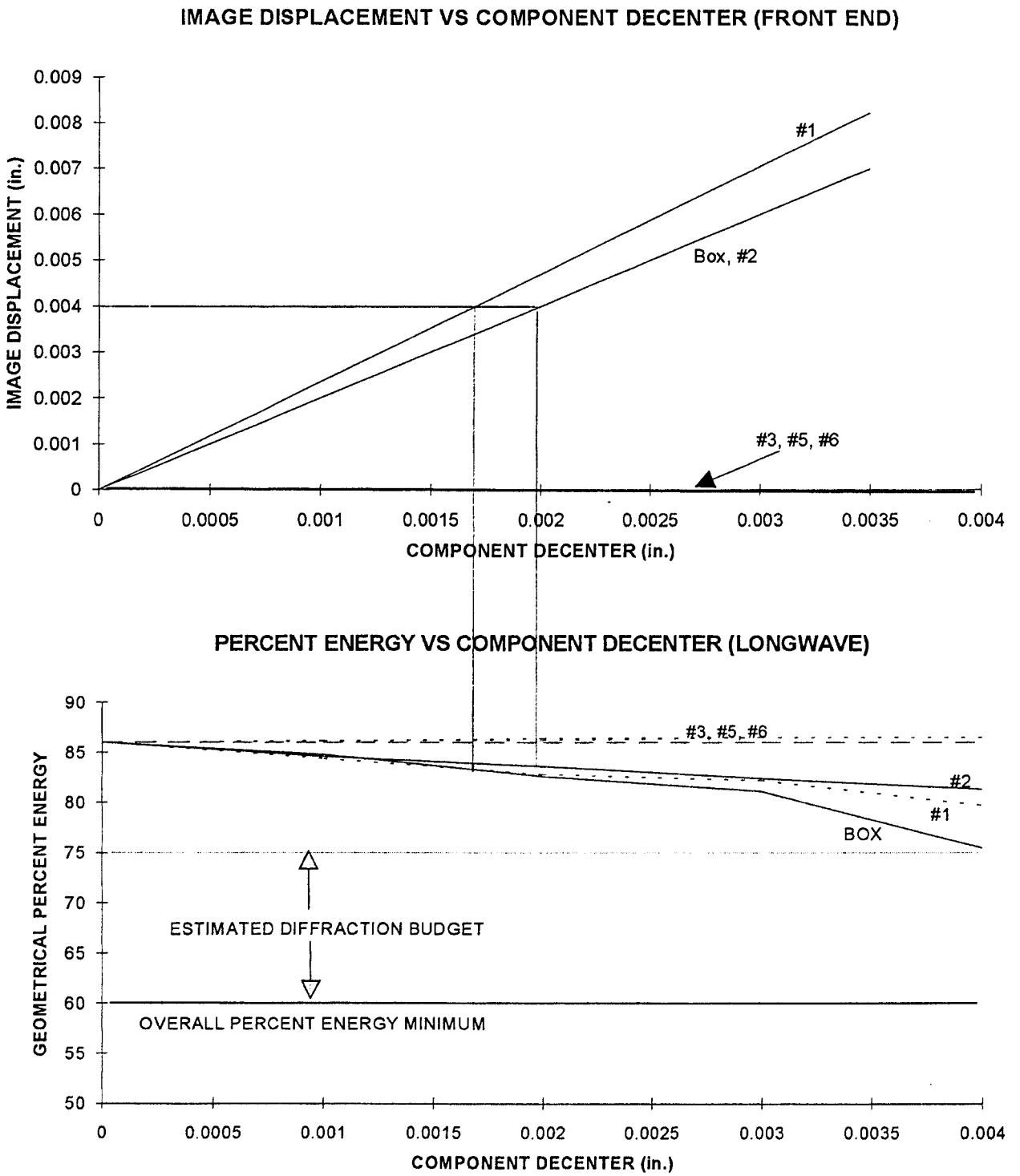

Figure 12. Parametric curves showing the measured image displacement and predicted percent energy on the detector as a function of component decenter.

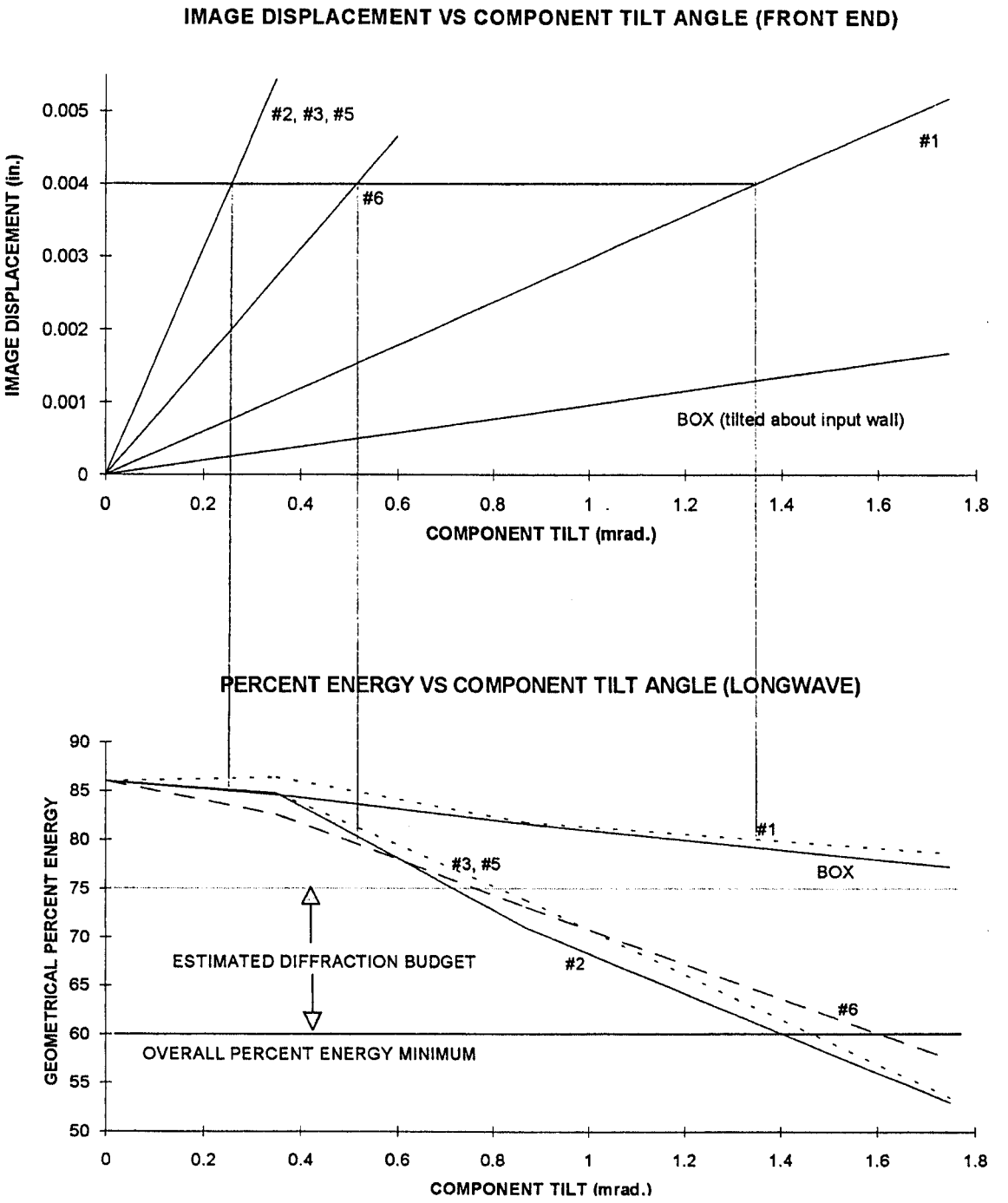

Figure 13. Parametric curves showing the measured image displacement and predicted percent energy on the detector as a function of component tilt.

Comparative performance analyses of passive microwave systems for tropospheric sounding of temperature and water vapor profiles

William J. Blackwell and David H. Staelin
Research Laboratory of Electronics, Room 26-341
Massachusetts Institute of Technology
Cambridge, Massachusetts 02139-3594

May 31, 1996

ABSTRACT

Advances in receiver technology permit the use of microwave spectrometers at 100-500 GHz in combination with economically affordable antennas on geostationary meteorological satellites. Microwave systems operating at 118 GHz, 183 GHz, 380 GHz, and 425 GHz have been compared. With an antenna of just over 2 meters in diameter, a system operating at 380 GHz and 425 GHz is capable of sounding temperature and water vapor profiles with 20-km horizontal resolution, and a system operating at 118 GHz and 183 GHz is capable of 70-km resolution. Analyses show that integration of such microwave spectrometers with a high performance infrared sounder would provide a nearly all-weather continuous-observation geostationary sounding system with accuracies approaching those of low-earth-orbit observatories.

Keywords: sounding, temperature, water vapor, microwave, geostationary

1 INTRODUCTION

Passive microwave soundings from geosynchronous orbit have received serious consideration only recently, principally because technology and economics previously had posed too great a problem. Advances in precision reflector antennas, low-noise receivers, and remote sensing technology in the 100-500 GHz region have been very important, as has the growing realization in the meteorological community of the importance of the cloud-penetration capabilities of passive microwave sensors in active meteorological zones.[1] In this paper we evaluate the performance of a simulated microwave system operating at frequencies from 118 GHz to 425 GHz for tropospheric (100 mb – 1000 mb) sounding of atmospheric temperature and water vapor (relative humidity) profiles in the presence of clouds. Finally, we examine the cloud-contaminated temperature profile retrieval accuracy when the microwave system is combined with a high performance infrared sounder, such as the Atmospheric Infrared Sounder (AIRS).[2]

2 MICROWAVE CONFIGURATION

Microwave frequencies between 10 GHz and 600 GHz are useful for passive remote sensing because of oxygen and water vapor absorption lines distributed throughout the band, as shown in Figure 1. Higher frequencies permit increased spatial resolution, but at the cost of noisier receivers and screening of the lower troposphere due to water vapor continuum absorption.

2.1 Microwave channel groups

Channel group A consists of seven temperature channels centered at the 118.75-GHz oxygen resonance and four water vapor channels centered at the 183.31-GHz water vapor resonance. The weighting functions for these channels are shown in Figure 2 and Figure 3.

0-8194-2200-2/96/$6.00

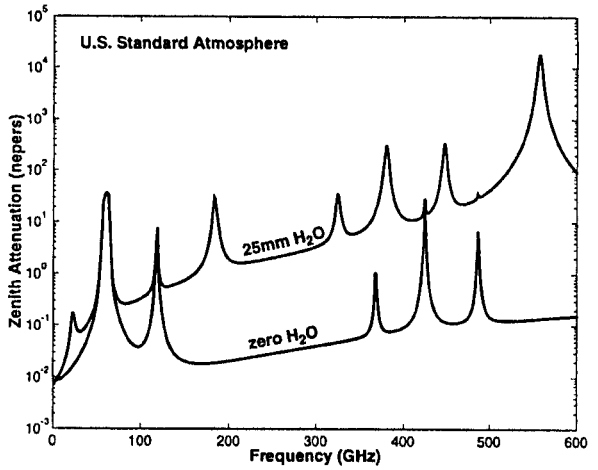

Figure 1: Zenith attenuation through the 1976 standard U.S. atmosphere.

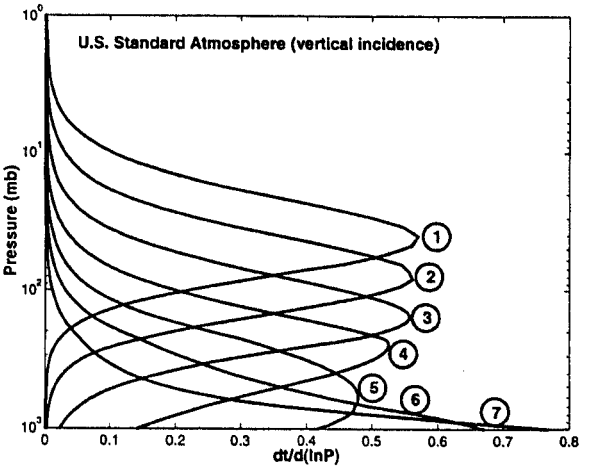

Figure 2: Weighting functions for channel group A temperature sounding channels.

Channel group B consists of seven temperature channels centered at the 424.76-GHz oxygen resonance, four water vapor channels centered at the 380.2-GHz water vapor resonance, and a window channel centered at 340 GHz. The weighting functions for these channels are shown in Figure 4 and Figure 5.

2.2 Horizontal resolution

For a two meter circular antenna, a half-power beamwidth of 0.75λ radians and a first side-lobe level of 31 dB can be achieved with nonuniform-amplitude illumination.[3] This translates into a 70-km horizontal resolution for channel group A (118/183 GHz) and a 20-km horizontal resolution for channel group B (340/380/425 GHz)[1].

2.3 Microwave system sensitivities

It is important in simulation studies to accurately represent instrument noise. For these simulations, a coverage of a 5000 km × 5000 km area in one hour is assumed. This requires an integration time of approximately 50 milliseconds for the 20-km resolution sys-

[1]The resolution of the high-frequencies channels is degraded to match the resolution of low-frequency channels for simplicity.

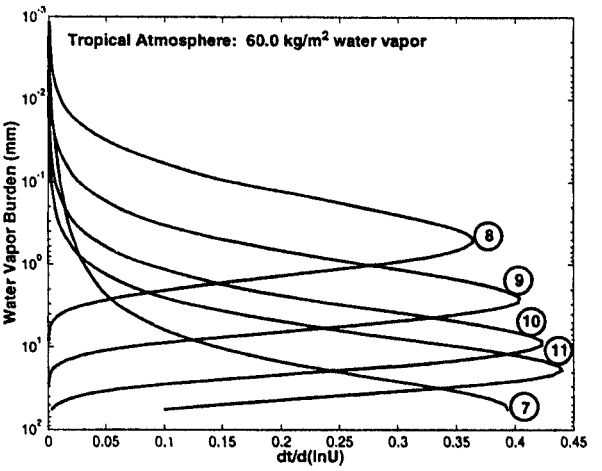

Figure 3: Weighting functions for channel group A water vapor sounding channels plotted against water vapor burden.

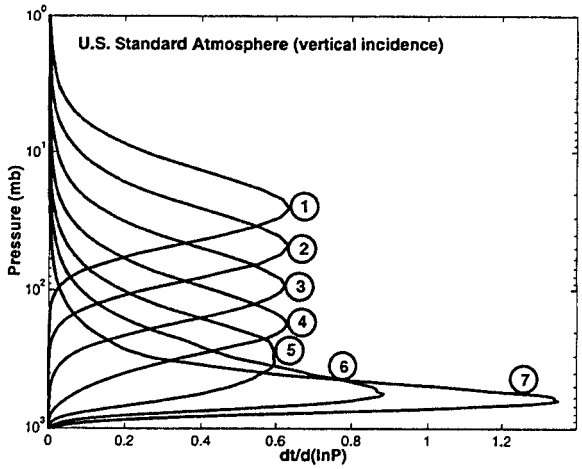

Figure 4: Weighting functions for channel group B temperature sounding channels.

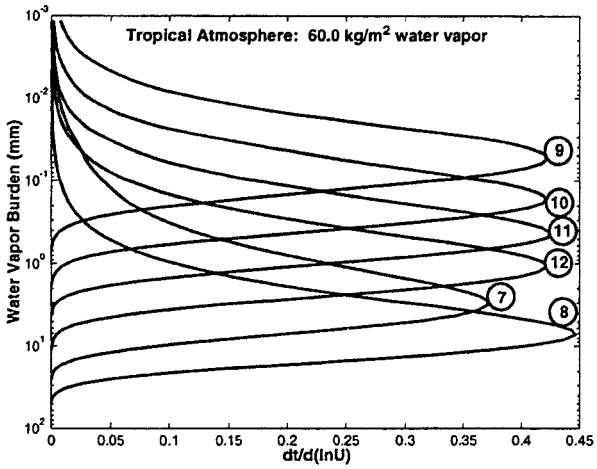

Figure 5: Weighting functions for channel group B water vapor sounding channels plotted against water vapor burden.

tem and approximately 700 milliseconds for the 70-km resolution system. For a double-sideband receiver, the system sensitivity for a particular channel is calculated using the following equation:

$$\Delta T_{RMS} = \frac{T_{sys}}{\sqrt{2B\tau}} \quad (1)$$

where T_{sys} is the system temperature, B is the bandwidth of a single sideband, and τ is the integration time. The following system temperatures were chosen for these simulations:

118 GHz	183 GHz	340-425 GHz
1500 K	2000 K	3000 K

The following tables summarize channel offsets, bandwidths, and RMS sensitivities.

No.	Frequency Offset (MHz)	Bandwidth (MHz)	Sensitivity (RMS K)
1	± 113	74	0.15
2	± 225	150	0.10
3	± 450	300	0.07
4	± 850	500	0.06
5	± 1450	700	0.05
6	± 2300	1000	0.04
7	± 4000	2000	0.03
8	± 1000	500	0.08
9	± 3000	1000	0.05
10	± 7000	2000	0.04
11	± 14000	4000	0.03

Table 1: Specifications for microwave sounding system A. The center frequency for the temperature channels (1-7) is 118.75 GHz and for the water vapor channels (8-11) is 183.31 GHz. The bandwidth given in the table is for a single sideband. A double-sideband receiver is assumed in the sensitivity calculation.

3 PROFILE DATA

For the simulation studies presented here, profile data created by the AIRS Science Team at NASA/JPL was used. The data can be described as follows. The

No.	Frequency Offset (MHz)	Bandwidth (MHz)	Sensitivity (RMS K)
1	± 113	74	1.10
2	± 225	150	0.77
3	± 450	300	0.55
4	± 850	500	0.42
5	± 1450	700	0.36
6	± 2300	1000	0.30
7	± 4000	2000	0.21
8	0	8000	0.15
9	± 850	700	0.36
10	± 1800	1200	0.27
11	± 3350	1900	0.22
12	± 6150	3700	0.16

Table 2: Specifications for microwave sounding system B. The center frequency for the temperature channels (1-7) is 424.76 GHz, for the window channel (8) is 340.0 GHz, and for the water vapor channels (9-12) is 380.2 GHz. The bandwidth given in the table is for a single sideband. A double-sideband receiver is assumed in the sensitivity calculation, with the exception of the 340-GHz channel.

profile data used for these simulations were created using a general circulation model. Every profile contained two cloud layers between 100 mb and 850 mb at least 200 mb apart. The cloud fractions of the two layers were adjusted nonlinearly to achieve an average cloud fraction of about 50% for the sum of the two layers. The positions of the cloud layers were determined from a regional eta model used by NOAA/NMC. The microwave surface emissivity was approximately uniformly distributed from 0.85 to 0.95. The infrared surface emissivity was distributed from 0.94 to 1. The emissivity of the cloud tops was 0.9, independent of frequency. The profiles were approximately uniformly distributed over latitude and longitude as well as seasonal period. Figure 6 shows a histogram of integrated water vapor for the profiles used in the simulation and it is observed that this set of profiles is very moist.

The band-averaged brightness temperatures were simulated using a discrete version of the radiative transfer equation for a 64-level atmosphere. Absorption due to oxygen, water vapor, and liquid water was taken into account; it was modelled after Rosenkranz.[4] No scattering was modelled. 5000 profiles were randomly chosen for the training set and a different set of 2500 profiles

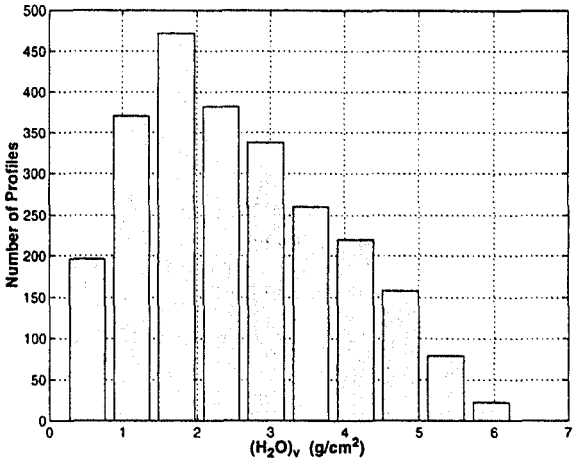

Figure 6: Histogram of integrated water vapor.

were randomly chosen for the validation set. Layer-averages of approximately 1-km thickness of the temperature profile from 100 mb to 1000 mb were retrieved. For the water vapor retrievals, relative humidity was retrieved for 22 points in the atmosphere between 100 mb and 1000 mb.

4 RETRIEVAL IMPLEMENTATION

4.1 Microwave only

Multilayer Feedforward Neural Networks (MFNN)[5] trained with backpropagation[6] have been shown to be effective for retrieving temperature[7] and water vapor[8] profiles from spectral radiance observations, and are used here.

4.1.1 Temperature retrievals

For the microwave-only temperature retrievals, neural networks with a single hidden layer employing sigmoidal activation functions were used with a linear output layer with 15 neurons. The physics of the inversion problem associated with channel group A are sufficiently linear that only 20 hidden neurons were needed to re-

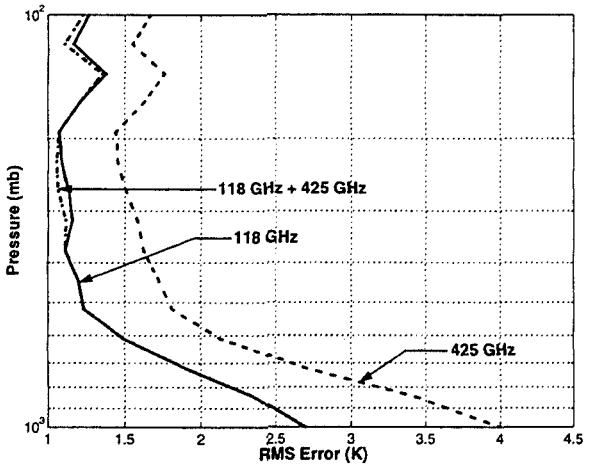

Figure 7: Microwave-only temperature retrieval.

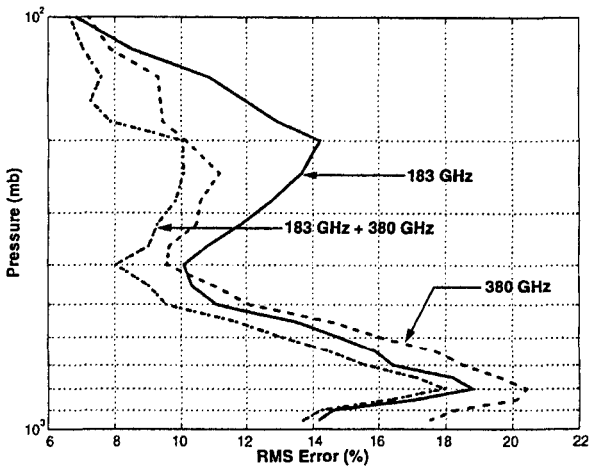

Figure 8: Microwave-only relative humidity retrieval.

trieve temperature. A larger network was needed for channel group B to correct for the water vapor screening effect, therefore 40 hidden neurons were used. For the combined retrieval, 50 hidden neurons were used. The results for the temperature retrievals with channel group A, channel group B, and groups A and B are shown in Figure 7.

4.1.2 Relative humidity retrievals

The microwave brightness temperatures depend nonlinearly on the water vapor profile of the atmosphere making relative humidity retrievals more difficult than temperature retrievals. We therefore use neural networks with two hidden layers to retrieve relative humidity. In all cases, 50 neurons were used in the first hidden layer, 30 neurons were used in the second hidden layer, and 22 neurons were used in the linear output layer. The results for the relative humidity retrievals with channel group A, channel group B, and groups A and B are shown in Figure 8.

4.2 Microwave with infrared

High spectral resolution infrared sounders offer superior performance to microwave sounders in clear-air, but are severely handicapped by clouds. By synergistically using infrared and microwave channels, retrieval accuracies can be greatly improved when clouds pervade the field of view.[9]

For the final simulation, we evaluate the temperature retrieval performance when all the microwave channels are combined with an AIRS-like instrument, referred to hereafter as GAIRS, or Geostationary AIRS. The spectral coverage and spectral resolution of GAIRS is assumed to be same as AIRS, namely 2371 channels distributed from 3.7 μm to 15.4 μm with a spectral resolution of $\nu/\Delta\nu \approx 1200$. The horizontal resolution of GAIRS is assumed to be 20 km in order to match the resolution of channel group B. The instrument noise (NEΔT) of current geostationary infrared sounders such as GOES-8 and GHIS is greater than that of AIRS by a factor of about five to ten.[10] Therefore, three different instrument noise vectors were used: GAIRS_{10} assumes instrument noise which is a factor of ten larger than AIRS, GAIRS_5 assumes instrument noise which is a factor of five larger than AIRS, and GAIRS assumes instrument noise identical to AIRS. Instrument noise can be reduced by active cooling of the receivers and longer dwell times, such that the noise specifications of AIRS can be approached.

For each retrieval, nine 20-km fields of view are formed, each with the same temperature and water vapor profile, but with different cloud amounts and surface properties. Nine 20-km resolution fields of view (channel group B and IR) are combined with one 70-km field of view (channel group A). This permits the use of the

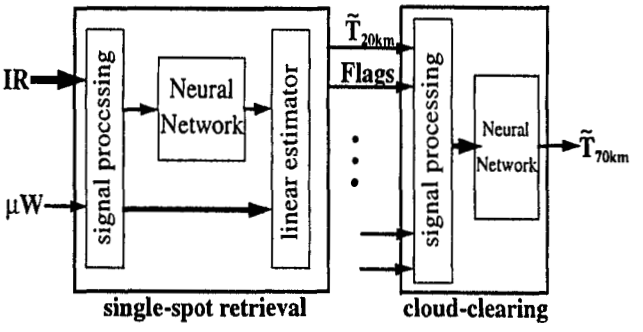

Figure 9: Microwave/Infrared temperature retrieval block diagram.

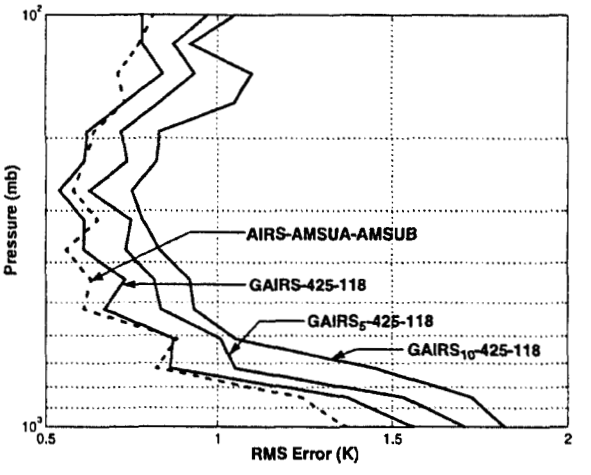

Figure 10: Microwave/Infrared temperature retrieval.

high resolution microwave channels for cloud-clearing.

The retrieval algorithm is shown in Figure 9. A retrieval is produced for each of the 20-km spots using all microwave and infrared channels as follows. The radiance data is first processed using a Noise-Adjusted Principal Components Transform.[11] The processed data is then passed to a neural network followed by a linear estimator. In addition to retrieving the temperature profile for each spot, a "cloud flag" profile is also produced, which estimates how the retrieval at each level is impacted by clouds. These 18 profiles (nine temperature and nine cloud flags) are then input to a neural network which estimates the final 70-km temperature profile. The results are shown in Figure 10. On the same graph, results for a 50-km retrieval using the same method with AIRS-AMSUA-AMSUB[12] are plotted.

5 RESULTS

As shown in Figure 7, the 118-GHz channels are clearly superior to the 425-GHz for sounding temperature. However, as will be seen later, the high resolution 425-GHz channels are useful for characterizing clouds when combined with an infrared sounder. A small improvement in performance results over the 118-GHz channels when all microwave channels are used. Figure 8 demonstrates that the 380-GHz channels offer little improvement to the 183-GHz channels for sounding water vapor in the lower atmosphere. This is due to the water vapor screening effect mentioned earlier. However, above 400 mb, the 380-GHz channels are superior to the 183-GHz channels. Again, this advantage can be used to detect and characterize clouds.

Perhaps the most compelling evidence of the utility of the high resolution microwave channels can be seen when microwave and infrared channels are used together to sound temperature. Here the microwave channels can identify and correct cloud contaminated fields of view. It is seen in Figure 10 that the geostationary instrument suite rivals the performance of the AIRS-AMSUA-AMSUB low-earth-orbit package.

6 CONCLUSIONS

Analyses show that the performance of a geostationary infrared/microwave sounder could approach that of low-earth-orbit instrument suites such as AIRS-AMSUA-AMSUB. In addition to improving cloudy soundings, high spatial resolution microwave temperature and water vapor channels could prove very useful. Recently, high resolution microwave imagery has been used for precipitation estimates[13] and hurricane warm core measurements.[14] Access to this information on a global scale could lead to improved shortrange forecasts, including those for severe weather, floods, and hurricane

tracks. Further work, however, is needed to characterize the degree to which microwave scattering due to both cloud liquid water and ice will affect sounding performance.

Acknowledgements. The authors wish to thank Dr. P. W. Rosenkranz for his assistance. This research was supported by a National Science Foundation Graduate Fellowship and National Aeronautics and Space Administration Grants NAG5-2545 and NAS5-31276.

7 REFERENCES

[1] D. H. Staelin. Passive microwave sensing of the atmosphere from space. *Microwave Radiomet. Remote Sens. Appl.*, pages 151–167, 1989.

[2] H. H. Aumann and R. J. Pagano. Atmospheric infrared sounder on the earth observing system. *Optical Engineering*, 33(3):776, March 1994.

[3] F. T. Ulaby, R. K. Moore, and A. K. Fung. *Microwave Remote Sensing – Active and Passive: Volume I.* Artech House, Norwood, Massachusetts, 1981.

[4] P. W. Rosenkranz. Absorption of microwaves by atmospheric gases. *Atmospheric Remote Sensing by Microwave Radiometry*, pages 37–82, 1993.

[5] K. M. Hornik, M. Stinchcombe, and H. White. Multilayer feedforward networks are universal approximators. *Neural Networks*, 4(5):359–366, 1989.

[6] D. E. Rumelhart, G. Hinton, and R. Williams. *Parallel Distributed Processing: Explorations in the Microstructure of Cognition. Vol. 1: Foundations.* D. E. Rumelhart and J. L. McClelland (Eds.). MIT Press, Cambridge, MA, 1986.

[7] H. E. Motteler, et al. Comparison of neural networks and regression-based methods for temperature retrievals. *Applied Optics*, 34(24):5390–5397, August 1995.

[8] C. R. Cabrera-Mercader and D. H. Staelin. Passive microwave relative humidity retrievals using feedforward neural networks. *IEEE Trans. Geosci. Remote Sens.*, 33(6):1324–1328, November 1995.

[9] W. J. Blackwell. Atmospheric temperature profile estimation from infrared and microwave spectral radiance observations using principal components analysis. Master's thesis, Massachusetts Institute of Technology, Department of Electrical Engineering and Computer Science, September 1995.

[10] J. P. Kerekes. Personal communication. 1996.

[11] J. B. Lee, A. S. Woodyatt, and M. Berman. Enhancement of high spectral resolution remote-sensing data by a noise-adjusted principal components transform. *IEEE Trans. Geosci. Remote Sens.*, 28:295–304, 1990.

[12] R. W. Saunders. Note on the advanced microwave sounding unit. *Bulletin of the American Meteorological Society*, 74(11):2211–2212, November 1993.

[13] P. Racette, et al. An airborne millimeter-wave imaging radiometer for cloud, precipitation, and atmospheric water vapor studies. *Journal of Atmospheric and Oceanic Technology*, 13(3):610, 1996.

[14] M. J. Schwartz, et al. Observations of thermal and precipitation structure in a tropical cyclone by means of passive microwave imagery near 118 GHz. *J. Appl. Meteor.*, 35(5):671–678, May 1996.

Mechanical design of GHIS brassboard*

Darryl Weidler

Lincoln Laboratory, Massachusetts Institute of Technology;
244 Wood Street; Lexington, Massachusetts 02173-9108

ABSTRACT

The GHIS optics assembly was designed as a replacement for the filter wheel assembly in an upgraded GOES Sounder Sensor for the year 2000+. An overview of the entire effort is presented elsewhere in these proceedings.[1] The assembly includes miniature optics consisting of a Michelson interferometer with compatible input and output optics. It is to be aligned at room temperature and operated at -55°C without realignment; therefore, an athermal design approach was chosen. Several aspects of the opto-mechanical design will be discussed herein, namely: the support, attachment, and adjustment of the miniature optics; investigation and fabrication of various types of aluminum mirrors; a remotely adjusted mirror for on-orbit alignment using PZT actuators; a moving-mirror supported on a leaf-spring, flexure mechanism moved by a voice-coil actuator; a laser, reference-beam, optical assembly, with fiber optic input and output, to control the velocity and position of the moving-mirror; the support structure; and the thermal control design.

KEYWORDS: GOES, GHIS, mechanical, design, mechanism, optical mount, thermal, structure

1.0 INTRODUCTION

The GHIS brassboard optics assembly was designed as a replacement for the filter wheel assembly and beam splitting optics in an upgraded GOES Sounder Sensor, see Figure 1. The GHIS enhancement will permit improved data collection which is expected to significantly improve atmospheric temperature measurements to permit more accurate weather predictions. It will collect interferometric data of the earth's radiance over a wavelength band from 3 to 16 microns. The Sounder upgrade will include an optics package, control electronics, a data processor, and new detectors. This paper will describe the mechanical design of the optics package with its supporting structure.

The GHIS optics package, see Figure 2, will fit between the existing Sounder telescope optics and the IR detector package to minimize the impact on the sensor and thus the cost of the upgrade. A single IR beam enters the GHIS package through the field stop from the Sounder telescope optics. After the beam is collimated to 0.33" diameter it passes through a Michelson interferometer and is split into three output beams, each with separate wave bands, to align with the existing detector's positions on the Sounder. On orbit alignment of the interferometer is accomplished with a PZT actuated commandable mirror. The variable-length optical leg of the interferometer is accomplished by a moving-mirror utilizing leaf-springs flexures and voice-coil actuator. The moving-mirror position and velocity are controlled by signals from a separate optical "Reference Beam" 0.23" in diameter.

The GHIS box is supported on titanium flexures which simultaneously provide structural support and thermal isolation. The flexures and their attachment points are designed to maintain minimum motion of the input and output beams when the box is cooled from room temperature to -55°C (its normal operating temperature). A support bracket is mounted to the detector mounting panel. The package is cooled to -55°C by a thermal radiator, radiating to cold space, the same size and position as is used for the filter wheel assembly.

2.0 IR OPTICS & BOX ENCLOSURE

To ease assembly and alignment it was decided, at the beginning of the design phase, to make a GHIS assembly which could be aligned at room temperature and operated at -55°C without requiring any alignment changes or offset adjustments to accommodate expected thermal motions. This type of design is referred to as an "athermal" design. As the temperatures change, the positional relationships and surface figures of the components remain aligned. To accomplish an athermal design all components are made of the same material. The material chosen, 6061-T6 aluminum, is commonly used for both structures and optical components, has a high thermal conductivity, is commonly available, and is easy to machine. In some cases 7075-T651 aluminum is used for the mirror material, because it has similar mechanical properties. The initial testing of the assembled unit at both warm and cold temperatures has shown that the design concept does indeed work as planned.

* This work was sponsored by the National Oceanographic and Atmospheric Administration.

0-8194-2200-2/96/$6.00

2.1 Box enclosure

The box enclosure, approximately 5" by 7" by 2.2", is machined from a solid block of aluminum, see Figure 3. It is designed with a 2" deep cavity and a 0.2" thick base which was machined flat and functions as an optical bench for mounting and alignment of all the internal components. Removable brackets are incorporated to support the input field-stop aperture and the 3 output lens. An aluminum frame is bolted to the top of the box, roughly the same shape as the box outline, to incorporate supports for the "reference beam" components and mounting plate (referred to as the "loft", Figure 13). The top cover of the box attaches the loft-frame to make a light-tight enclosure. Analyses and test results show that the optical bench (base of the box) performs as expected when cooled down to -55°C with thermal gradients of less than 2°C. All interior walls and the top are painted black to minimize optical reflections. The inside base surface is alodined aluminum. It is not painted because it formed the optical bench for the box. The external surfaces of the assembly were gold plated to minimize thermal radiation input.

2.2 IR Optical Components

The optical components in the box, see Figure 4, consist of one input field-stop aperture; twelve (12) aluminum reflective mirrors (eight flat and four with spherical surfaces); one potassium bromide beam splitter with its compensator plate for the interferometer; one Lyot-stop; two zinc selenide dichroics to separate the signal into the three output wave bands; and three zinc selenide output lenses.

The following paragraphs in this section discuss the types of aluminum mirrors evaluated, the different techniques used to support the components, and the azimuth and elevation adjustments built into the holders.

2.2.1 Aluminum mirrors evaluation

All mirrors are made of aluminum. Three different mirror types with two different fabrication techniques are used to evaluate the optical effects of each. Four mirrors are plated with 0.002" thick nickel to permit polishing to a low scatter surface, three mirrors are plated with only 0.001" thick nickel, and four mirrors are diamond turned with no nickel plating. All have a gold overcoat to improve reflectivity and/or protect the aluminum from corrosion. When each mirrors is received, its surface figure is evaluated both warm and cold using a Zygo interferometer.

The nickel plated mirrors are plated on both the front and the back surfaces to minimize the thermal distortions caused by the bimetallic bending when changing from room temperature to -55°C. NASTRAN finite element models of each are required to insure that the thermal distortions are within acceptable limits. The thinner platings cause less distortion than the thicker platings. Since the main IR beam and the "reference beam" are separate and parallel in the interferometer section, the mirrors are rectangular with their heights approximately twice their widths. Bimetallic distortions of these mirrors cause the beams to converge, rather than remain parallel, as the mirrors are cooled. The beam convergence, of the mirrors with the thicker nickel coating, consumes the entire alignment tolerance budgeted for these components in the interferometer section.

The unplated diamond turned mirrors do not distort when changing from room temperature to the cold operating environment. Also the scatter, due to the tool marks from the diamond turning, is barely detectable when observed in the visible wavebands. The scatter from the tool marks in the longer IR wavebands is expected to have a negligible affect on the final GHIS assembly. Therefore, the final versions of the mirrors used in the interferometer section are diamond turned with no nickel plating to eliminate the bimetallic distortions. BRDF measurements are being considered for quantifying scatter from the diamond turned mirrors when they are received.

2.2.2 Optic component attachments

There are four basic types of optic attachments used in the final GHIS design. One type is used for the non-moving aluminum mirrors, a second type is used for the moving-mirror, a third type is used for the elements transmitting the IR beam, and a fourth type is used for the beam splitter and compensator plate. The azimuth and elevation adjustments built into the mounts are similar for all designs except for the special case of the moving mirror.

Most of the aluminum mirrors are either machined with an azimuth adjusting base plate, see Figure 5, or attached to an azimuth adjusting base plate with two screws tapped into the bottom of the mirrors. The beam positions on the mirrors are designed to be far enough from the mounting surface to insure no beam distortions.

Each of the two zinc selenide dichroics is mounted in an aluminum bezel using steel sheet metal clips attached with screws threaded into the bezel, see Figure 6. The clips provide sufficient preload to keep the optic from moving when subjected to expected loads. An earlier design, which did not work properly, involved potting each dichroic into an aluminum bezel using a low-out-gassing, vacuum-compatible RTV. Using the known coefficients of thermal expansion of aluminum, zinc selenide, and the RTV; the width of the potted gap was designed and specified to produce an athermal design which would maintain the optical element stress-free as the temperature changed from ambient to the cold operating temperature. The design worked fine when the beam was transmitted through the dichroic. However, thermal vacuum tests of the system indicated that the reflected beam tilted through unacceptably large angles in azimuth and/or elevation when the dichroic and holders were cooled to operating temperature. It was found that some of the RTV leaked between the zinc selenide and the bezel locating pad, and that the RTV thicknesses could not be maintained uniform enough to be used in the reflection mode. Since both dichroics are used in the reflection mode, the designs were changed to use steel clips which provided positive mechanical location.

The beam splitter design is a special case, see Figure 7. The assembly is made of two potassium bromide optical elements; a beam splitter and separate compensator plate. Potassium bromide has a yield strength of less than 160 psi. The extremely low yield strength requires a method of holding that insures that the beam splitter and compensator plate are not overstressed. To accomplish that, small compression springs preload Teflon plungers against the potassium bromide components at each support point. The springs provide sufficient force to insure no movement under twice the expected loading (factor of safety of 2), even with adverse spring tolerances. This method is chosen to provide a positive location of the components, and a kinematic mount provides non-redundant and simple load paths. There are three preloaded points normal to the component face, two preload points in one lateral direction, and one preload point in the orthogonal direction. Opposite each spring loaded support point is a raised pad on the bezel to assure that the potassium bromide is in compression and not in bending. Thin sheets of mylar were used between the potassium bromide and the aluminum bezel to provide a compliant interface material and insure no point loadings.

2.2.3 Optical component adjustments

Each optical component mount design has built-in alignment capability for azimuth and elevation. A typical mount with adjustments is shown in Figure 5. The mirror mounted to an azimuth plate can be pivoted about a front pin or countersunk screw and secured with two tie-down screws once adjusted. The elevation plate is attached to a base plate clevis with two pins forming a horizontal pivot axis under the mirror. Once adjusted in elevation, it can be secured to the base plate with two screws into the edge of the elevation plate. When a mirror is adjusted in elevation, the mirror center line simultaneously translates as well as rotates because the pivot axis is below the mirror center line. To negate the translation effect, all components are preadjusted in elevation to make the mirror surface perpendicular to the base within approximately 50 microradians using a Zygo interferometer. Each component is placed in the GHIS box on the optical-bench-base at the appropriate position within ± .002" by using an overhead viewing system on a Cordax Inspection Station. Once all components are located in this manner, the box is taken to a Zygo interferometer test station where the mirrors are adjusted in azimuth by evaluating the wavefront errors. Since the mirror elevation angles are preadjusted, only azimuth adjustments are required in the box.

The mirror support and adjustment for the moving-mirror is a special case because it must fit through a hole in the base of the box. Figure 8 is a sketch of the mirror and mount. The mirror attaches to the mount at three points to assure no distortion to the mirror. The aluminum mount has two orthogonal flexures machined as part of the mount for azimuth and elevation adjustments. Aluminum adjustment screws are used to maintain alignment when the temperature changes.

3.0 MOVING-MIRROR

The moving-mirror assembly, see Figures 9 through 11, is used to produce the adjustable leg of the Michelson interferometer. It is mounted to the outside bottom of the base of the optics box. It is designed to the following requirements.

Stroke:	± 0.157" (± 4mm) maximum plus turn-around
Velocity:	0.84"/s (2.134 cm/s) within ± 10% during data collection
Turn-around time:	0.025 s
Design loads:	40 Gs each axis
Caging mechanism:	required to provide restraint for launch loads
Mirror alignment:	± 15 microradians

The mirror is cantilevered from the top of the moving mechanism and protrudes through a hole in the base of the box to intercept the IR and reference beams within the box. Three different interferometer operating modes are currently planned which require three different mirror stroke lengths. The moving-mirror is designed to permit a stroke of up to 0.2" to accommodate the maximum stroke plus a large turn-around margin.

The moving-mirror is attached to its mount by three screw threads tapped into the back of the mirror. See Figure 8.

The mechanism used to control the mirror motions is basically a four-bar linkage to maintain the moving-mirror parallel to itself at any position during the stroke, Figures 9, 10, and 11. The slight vertical motion of the mirror is acceptable because it has no curvature. In this design, the two upright bars of the four-bar linkage are beryllium copper leaf-spring flexures 1.5" wide by 1.5" high by 0.005" thick. The upright leaf springs are positioned parallel to each other and 3" apart by a fixed, aluminum base and a moving aluminum platform. The upright flexures are attached to the ends of the base and moving platform using aluminum, clamping bars and screws. The mirror component is attached to an adjustable bracket which mounts to the movable platform. The effects of dimensional or fabrication tolerances on the detail parts are adequately described in the literature.[2,3] The mechanism base is attached along its edges to brackets which mount at three points to the under side of the GHIS box.

A caging mechanism, Figure 10, is used to restrain and preload the moving platform to withstand launch loads. The preload is accomplished using a screw through the base plate which engages a cone on the base of the motor assembly attached to the moving platform. The preload screw is driven by an electric motor through a gear train. The screw mechanism applies a load which pre-tensions the leaf-spring flexures to a level of stress lower than encountered when on orbit but higher than will be encountered during launch so that the flexures do not buckle when loaded to launch loads. The flexure springs are made of beryllium copper. Assuming a requirement to operate for 5 years at 5 Hertz, the springs are sized for a minimum of $8x10^8$ repeated stress cycles. Fatigue life versus stress data are provided by the material manufacturer for various alloys of beryllium copper. The leaf-spring flexures are designed to one-half the allowable stress level (30,000psi) at $8x10^8$ cycles to provide a factor of safety of 2.

The motion of the mechanism is produced by an off-the-shelf voice coil motor. Most of the electrical power dissipated in the motor occurs in the voice coils. Therefore, the voice coil is mounted to the non-moving base of the mechanism. Thermal isolator supports minimize the heat conducted to the base. The heat is conducted through thermal straps to the side supporting brackets. The magnets and the metal magnetic flux return path are bolted to the moving platform. The power allocated in the thermal budget for this design is 0.5 watt. The start-up control of the platform motion is maintained by a signal from a LVDT (linear velocity displacement transducer). After motion is established and the reference beam is working properly, the LVDT is turned off and the position and velocity of the mirror are maintained by counting the fringes from the reference beam. The mechanism is enclosed by thermal covers to minimize thermal radiation to the unit.

4.0 COMMANDABLE MIRROR

The Commandable Mirror, see Figure 12, is designed to be remotely controlled to permit on-orbit alignment of the interferometer system. Both the IR and the reference beams reflect from the commandable mirror; therefore, both beams are adjusted simultaneously during the alignment process. The mirror is a solid, diamond-turned aluminum mirror with a gold overcoat, approximately 0.6" by 1.25" by 0.2" thick. It is supported in a classic, 2-axis, gimbal design with PZT piezoelectric position actuators. The PZT actuator is used because of its small size, its ability to operate from room temperature to below -55°C, and it requires less than ± 100 volts DC to operate. The same actuators are used in a JPL satellite experiment launched in June 1994. Each actuator is a ceramic stack 0.2" by 0.2" by 0.7" long with a 0.31" diameter by 0.2" thick disk of Invar bonded to one end. The end disk has a threaded hole for mounting the stack. There is an end plate of 0.02" thick stainless steel on the "pushing surface". The position is controlled by a strain gage mounted to the surface of the ceramic. The actuators are capable of moving the mirror ± 150 microradians about each axis to within a few microradians. When the temperature changes, the lengths change which results in a repositioning of the commandable-mirror if no compensation are made. The PZT actuators are attached to the mirror assembly through a combination of Invar and aluminum members so that the mirror will maintain alignment from ambient to -55°C. The assembled unit is aligned warm and the alignment is checked when cold. The design is made with lengths of aluminum and Invar which may be adjusted, by machining, to obtain the desired athermal design.

5.0 REFERENCE BEAM ASSEMBLY

In the current GHIS brassboard, the reference beam is generated by a helium-neon (HeNe) laser. NASA/GSFC is developing a 1.5 micron laser which will ultimately be used as the operational reference beam. The reference beam laser is housed in a rack mounted test configuration assembly. The signal is sent to the GHIS optics box through an optical fiber. Inside the GHIS optics box, see Figure 13, the input fiber is clamped in position and the beam is collimated with a lens. The beam then passes into a periscope on the upper level of the box, down, and out of the periscope 0.61" above the main IR beam. The reference beam passes through the interferometer parallel to and in the same direction as the main IR beam. It then enters another periscope where it is returned to the upper box level. The beam then passes through a beamsplitter. The two resulting output beams pass through filters and lenses which focus the beams onto the two output optical fibers. The two output fibers are routed out of the GHIS box and back to detector assemblies for counting the fringes and controlling the moving-mirror.

Each fiber optic with its collimating lens is assembled and pre-aligned as a unit. Within each unit, the fiber optic is secured by a commercial fiber optic chuck which is clamped to a vee block azimuth plate for focus adjustments. A collimating lens bracket is adjusted laterally and shimmed vertically to center the lens on the fiber optic beam. The fiber optic units also contain azimuth and elevation adjustments similar to those used with the other optics in the GHIS assembly. However, the input fiber optic unit requires much finer pointing adjustments; therefore, differential screws replace the conventional fine pitch screw used in the two output fiber optic units.

6.0 THERMAL CONTROL

The GHIS assembly operating temperature was chosen to be -55°C to limit the IR radiation from the GHIS transmissive components to the detectors. The final operating temperature of the GHIS package will be determined when the operating parameters of the final unit are measured. The only components that require cooling are the beam splitter assembly, the two dichroics, and the three output lenses. However, it is thought to be easier to cool the entire assembly than to cool and maintain alignment of only the few transmitting elements within the relatively small total assembly. The amount of heat that is be removed from the GHIS assembly is limited by the design of the existing Filter Wheel thermal radiator. The Filter Wheel radiator design can radiate from 3 watts at -73°C to 4.5 watts at -55°C. The operating temperature of the radiator is determined by the amount of power that is removed from the GHIS assembly. The issue is to limit the heat input to the GHIS box to insure adequate margin when operating the box at -55°C.

The overall thermal control concept shown in Figure 14 is:

(1) to minimize the thermal radiation input by using a low emissivity gold plating on the outside of the cold assembly and inside of a warm thermal shield,

(2) to minimize the thermal conduction input by supporting the box with titanium thermal isolators,

(3) to minimize the heat input through the cables by minimizing the wire's sizes and insulating the wires with either space blankets or a low emissivity enclosure, and

(4) to limit the amount of heat generation within the assembly.

A tentative overall thermal budget is shown below. The "box" in the thermal budget is meant to be the entire cooled assembly. It includes the optics box and its contents, the moving-mirror, the thermal radiator, and all cables. The warm thermal shields and support bracket are not included since they remain at the Sounder ambient temperature.

THERMAL CONTROL BUDGET

RADIATION INPUT TO THE BOX	1.3 W
CONDUCTION INPUT THRU ISOLATORS	1.3 W
CONDUCTION INPUT THRU CABLES	0.5 W
INTERNAL POWER GENERATION	0.6 W
TOTAL	3.7 W

Thermal vacuum test results indicate that the gold coating on the box is not adequate to limit the radiation input to the budgeted value. It has been decided to add low emissivity thermal shields around the assembly to reduce the thermal radiation input by 50% and remain within the thermal budget. The measured thermal conduction through the titanium isolators is slightly higher than expected due to additional radiation input from the cavity effect of the structure surrounding the isolators but remains within a slightly adjusted the thermal budget.

A thermal model was developed to estimate the performance of the GHIS assembly. The model included details of the optical housing, the thermal isolators, the support bracket, the thermal radiator, and the internal walls of the Sounder instrument. No details of the optical components within the box were included since they should reach equilibrium with the local box temperatures. Both conduction and radiation coupling between the GHIS components and the Sounder were included. The model was used to estimate box temperatures for both the thermal vacuum test conditions and on-orbit conditions. For the on-orbit conditions, the heat inputs to the GHIS assembly were from the Sounder housing. The diurnal temperature variations of the Sounder housing were obtained from ITT for the summer solstice, winter solstice, and equinox conditions. The estimated thermal gradients across the floor of the optical housing were estimated to be less than 2°C.

7.0 SUPPORT STRUCTURE

The support structure attaches to the Sounder and supports the box with the appropriate thermal isolation. The first support bracket design was based on the "replacement module" concept, see Figure 1. In that concept the Filter Wheel assembly was to be removed and, with some disassembly but no re-machining of parts, the GHIS was to be installed and aligned in its place. The removed Filter Wheel "K-bracket" attach points were to be used as the mounting points for the GHIS assembly. The support bracket was designed to maintain a natural frequency above 200 Hertz, to permit installation and alignment in a 1-G (one-gravity) environment without changing significantly when it reaches the zero gravity environment, but below 300 Hertz to minimize the input from the shock environment which increases with frequency. The bracket designed incorporated mounts for the optics box and the two smaller boxes which house the reference beam transmitter and the receiver/detector optics. The mounting concept was later modified as ITT began their preliminary design concepts.

The current concept is to support the GHIS box on a bracket which attaches to the same panel to which the detectors are mounted. The panel has natural frequencies below 100 Hertz. The challenge is to find attach points near the edges of the panel which are stiff enough to provide the necessary support to obtain the desired 200+ natural frequency for the GHIS support bracket with optics box. The design of this support bracket is not completed at this time.

However, the previously developed interface between the box and the support bracket will be maintained. The design uses titanium support flexures with a circular cross section like a column, see Figure 15. Titanium (6Al-4V) provides excellent strength and good stiffness while providing very low thermal conductivity for good thermal isolation. The flexures have large axial spring rate relative to their small lateral spring rate. They can maintain position firmly in one direction while being relatively free to move laterally in the other two directions. This technique is sometimes referred to as a kinematic support.

Kinematic support is accomplished in this design in the following way. Three flexures support the box in the vertical direction defining a horizontal plane and preventing rotation about the two horizontal axes. Two flexures support the box in one horizontal direction and prevent rotation about the vertical axis. One flexure supports the box in the orthogonal horizontal direction. These attachments between the box and the support bracket have four somewhat conflicting requirements. They are:

(1) to provide adequate structural support,
(2) to maintain the natural frequency between 200 and 300 Hertz,
(3) to maintain good thermal isolation, and
(4) to maintain the input optic axis at the same position (without moving) when cooled from room temperature to -55°C.

To obtain "adequate structural support", the attachments should be short to prevent buckling, and they should also have a large area to keep the stresses low. To maintain the natural frequency between 200 and 300 Hz, the spring rates must be kept within a small range. To maintain good thermal isolation the attachments should be kept long and the area should be kept small. To maintain the input optic axis at the same position warm or cold required a specific ratio between the titanium support length and the aluminum attach point relative to a "contraction point".

To accomplish the "zero motion" of the input optical axis when cooling from room temperature to -55°C, a special design technique was used. The point-that-is-not-supposed-to-move when the temperature changes is defined to be the "contraction-point". The attachment technique is such that (in the vertical direction) the "contraction-point" shrinks toward the box attachment point the same distance that the titanium support shrinks down toward the support bracket attach point. Therefore, the "contraction-point" does not move with a decrease in temperature. The above technique describes how one direction or plane can be kept from moving. The technique must be applied in three orthogonal planes to maintain a fixed point. Test results have shown that this technique has been quite effective.

The areas and lengths of the titanium support columns were adjusted to provide an appropriate balance between the conflicting requirements.

8.0 SUMMARY

A GHIS optics assembly is designed and fabricated as a replacement for the filter wheel assembly in an upgraded GOES Sounder Sensor. The initial version is tested at .6328 microns using an existing Zygo interferometer. The design includes the optical components, a box enclosure for the optics, a support structure, and the overall thermal control system which permits alignment at room temperature and operation at -55°C without realignment. Three types of aluminum mirrors are evaluated and discussed. Four different techniques for mounting optical components with adjustments for azimuth and elevation alignment are described. The mechanical design of a remotely controlled alignment mirror is presented. A continuously moving mirror design, for use in a Michelson interferometer, is discussed. The design of a reference beam assembly for controlling the moving mirror is presented. Some test results are also included. The results to date indicate the assembly is performing as designed.

9.0 ACKNOWLEDGEMENTS

I would like to acknowledge the assistance provided by several of my colleagues at Lincoln Laboratory. The designs of the optical components and supports were the responsibility of Herbert Feinstein with the assistance of Randolph DiSanto and Paul Tirone. Vincent Cerrati was responsible for the design of the Moving Mirror with the assistance of Daniel Stremeckus. Eui In Lee and Ronald Efromson provided the thermal modeling support while Keith Doyle and Anne Vogel accomplished most of the NASTRAN analyses.

10. REFERENCES

1. W. E. Bicknell; "Overview of GOES high-resolution infrared sounder (GHIS) brassboard development and test program"; International Symposium on Optical Science, Engineering, and Instrumentation (SPIE's Annual Meeting); 4-9 August 1996; Denver, Colorado; Conference 2812, "GOES-8 and Beyond", paper # 2812-36; to be published by SPIE.

2. R. V. Jones, "Parallel and rectilinear spring movements", Journal of Scientific Instruments, volume 28, pp. 38-41, February 1951.

3. R. V. Jones and I. R. Young, "Some parasitic deflexions in parallel spring movements", Journal of Scientific Instruments, volume 33, pp. 11-15, January 1956.

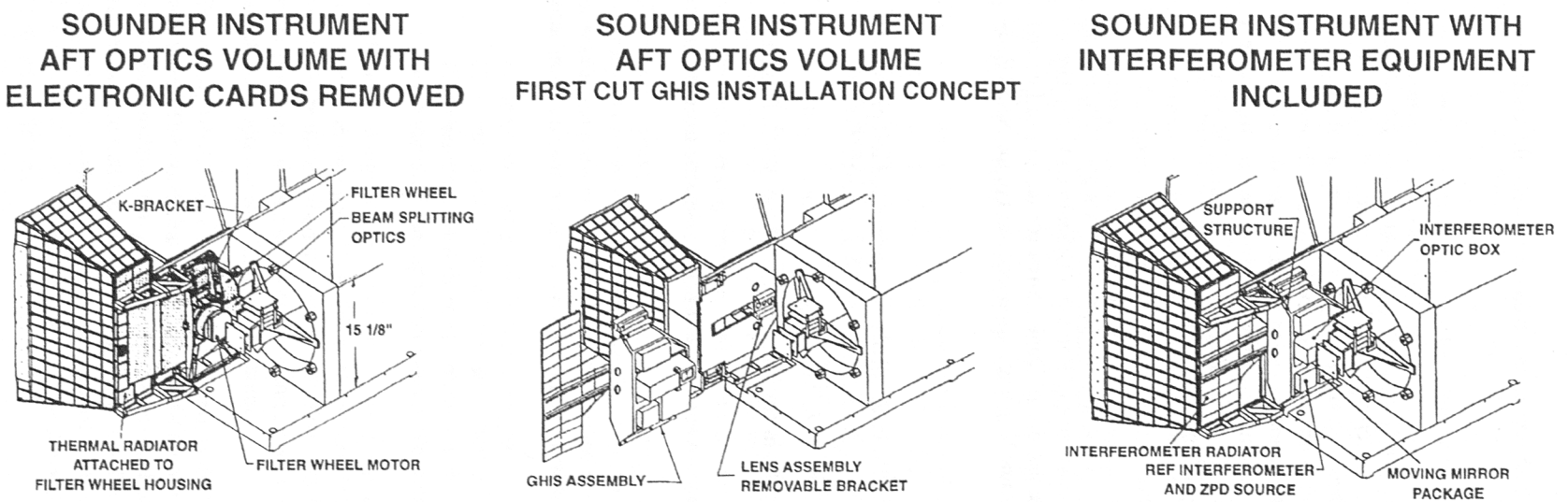

Figure 1. GHIS as a replacement for the filter wheel assembly.

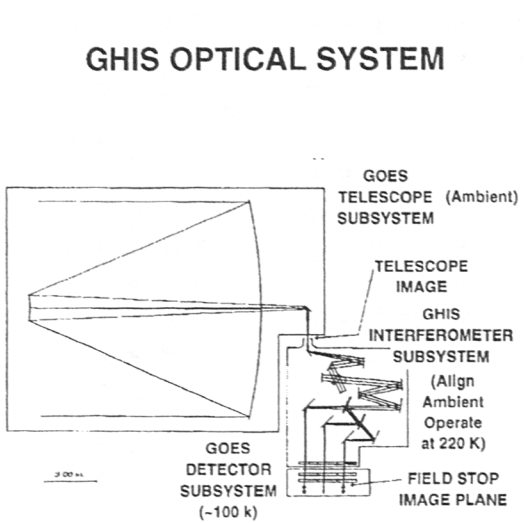

Figure 2. GHIS between existing telescope & detectors.

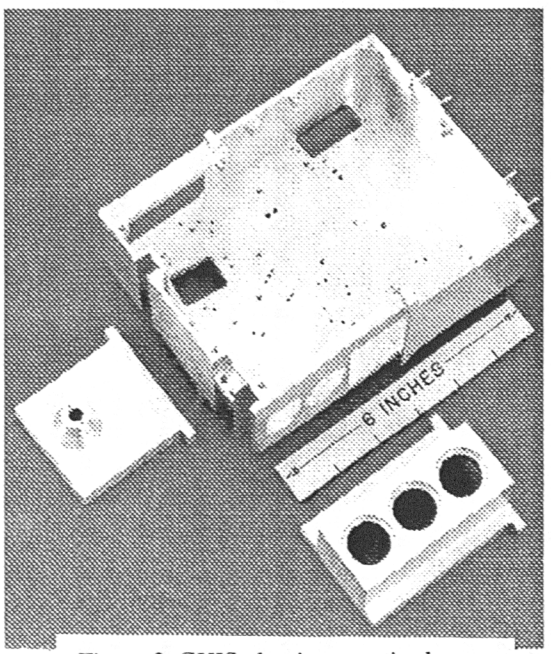

Figure 3. GHIS aluminum optics box.

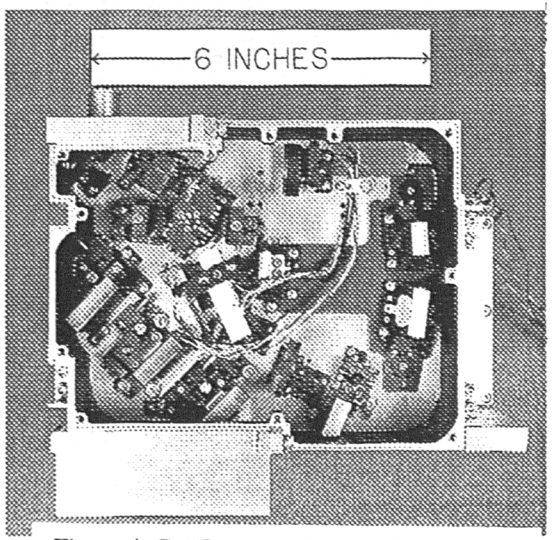

Figure 4. GHIS box with optical components.

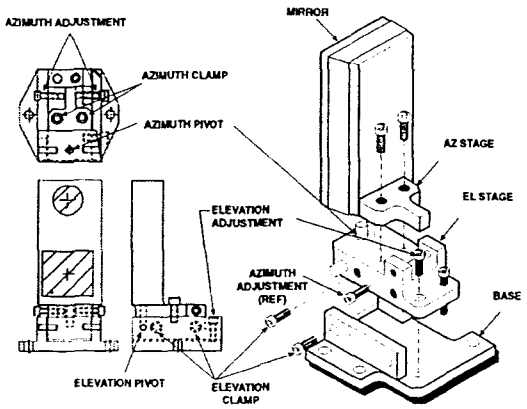

Figure 5. Mirror mount and adjustment mechanisms.

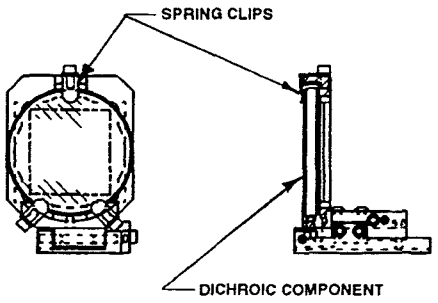

Figure 6. Dichroic mounting

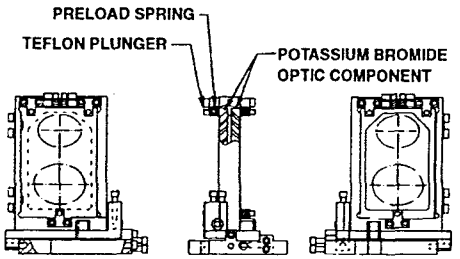

Figure 7. Beam splitter assembly mounting.

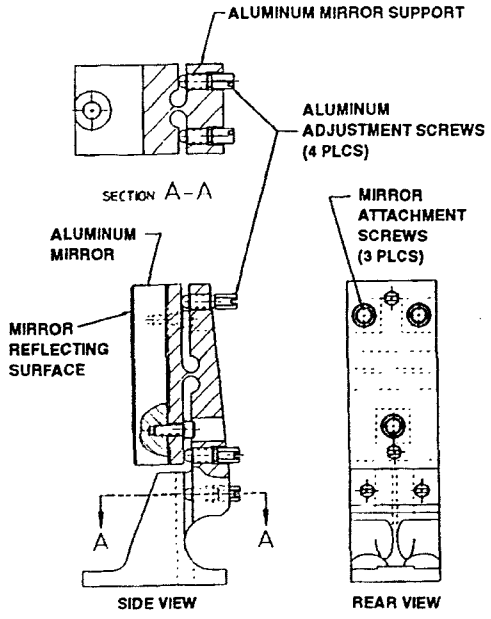

Figure 8. Moving mirror mount

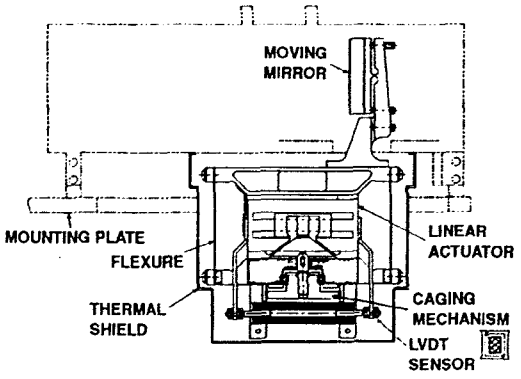

Figure 9. Moving mirror assembly side view.

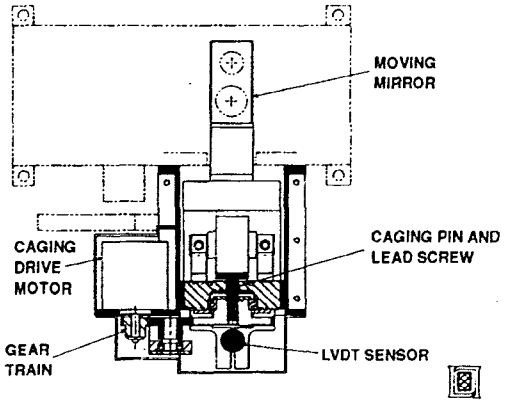

Figure 10. Moving mirror assembly end view

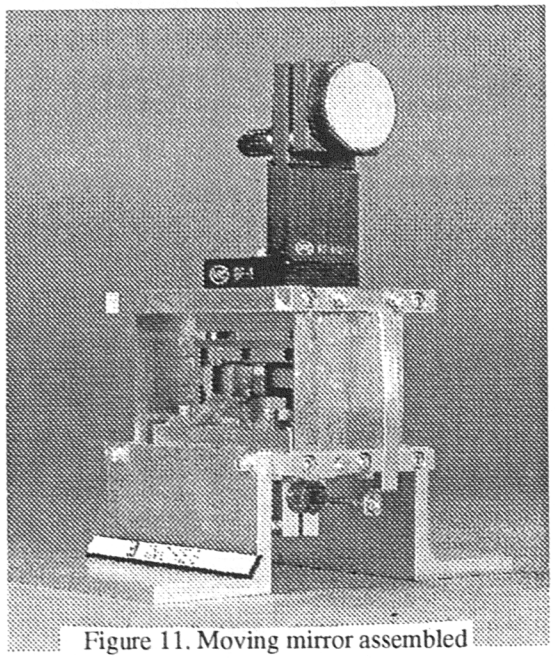

Figure 11. Moving mirror assembled

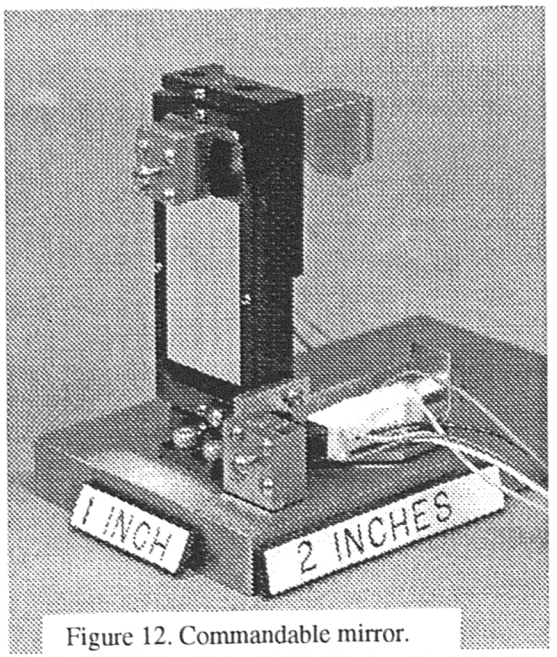

Figure 12. Commandable mirror.

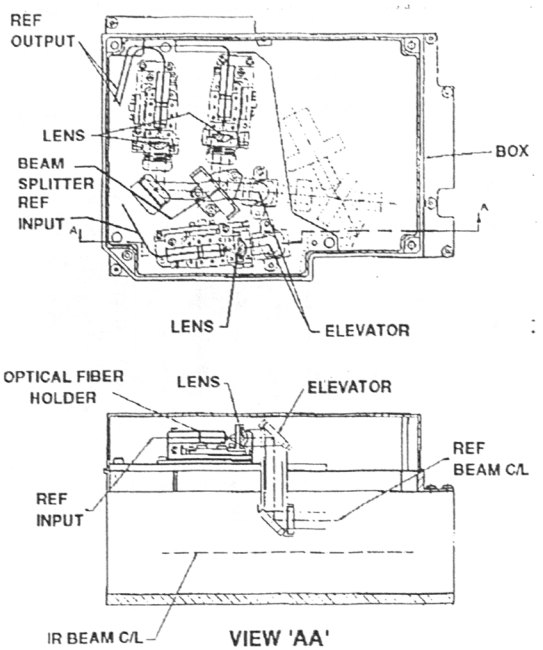

Figure 13. Reference beam assembly.

- USE FILTER-WHEEL RADIATOR TYPE DESIGN
- COOL INTERFEROMETER-OPTICS PACKAGE AT 220 K
- SURROUNDINGS AT ~290 K

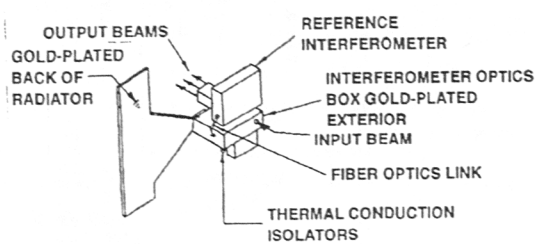

Figure 14. Thermal control concept.

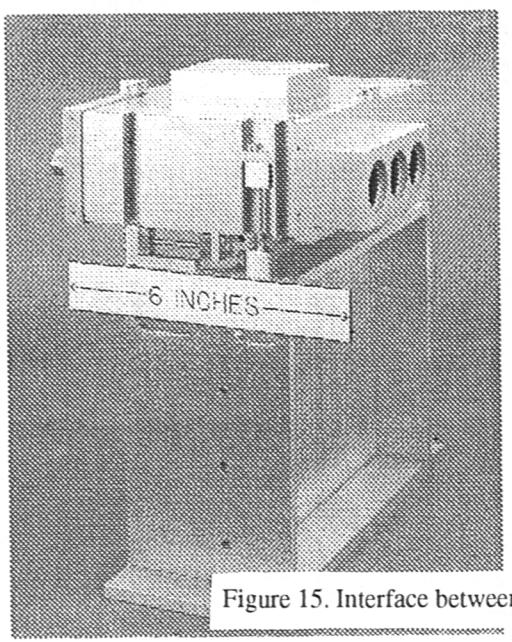

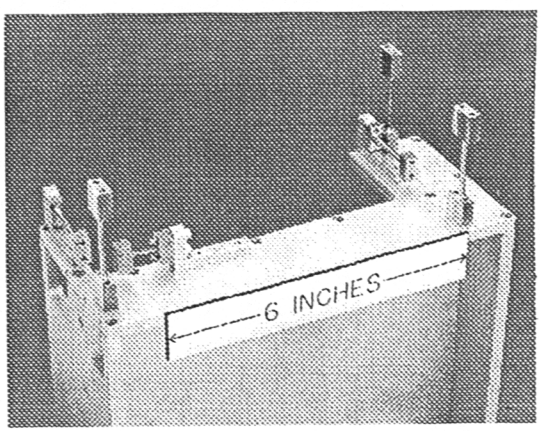

Figure 15. Interface between GHIS box and support structure.

SESSION 6

Detector Technologies and Modeling

High Performance HgCdTe Infrared Detectors for the GOES Long-Wave Sounder

R. J. Martineau, Kelley Hu*, S. Manthripragada, Jack Shi*, C. A. Kotecki, F. A. Peters, A. S. Burgess, D. J. Krebs, R. Johnson, D. B. Mott, P. K. Shu

NASA Goddard Space Flight Center, Greenbelt, MD 20771
*Hughes STX Corp., Lanham, MD 20706

ABSTRACT

GOES long wave sounder (LWS) detector requirements have always pushed the state-of-the-art for longwave detectors operating in the vicinity of 102 K. Performance and yield of acceptable detectors have always been problems and continue to be important issues affecting the performance of instruments of both present and future design. GSFC has been examining new device and operational concepts aimed at producing significant improvements in performance and yield. Our approach has been directed towards mitigating the deleterious effects of operating small geometry HgCdTe PC devices under heavy bias, that is, under minority carrier sweepout, as is typical in conventional LWS detector operation. Specifically, theory indicates that detectors of the new design operating under optimal bias conditions have significantly higher responsivity and D^*_λ's, lower power dissipation, and lower 1/f noise knees than conventional LWS detectors. In this paper we will describe the new LWS detectors fabricated at GSFC, present detector data, and review the theory of operation of these devices.

Keywords: HgCdTe, detector design, sweepout, performance enhancement.

1. INTRODUCTION

The Geostationary Operational Environmental Satellite (GOES) uses a variety of infrared sensors in its Imager and Sounder instruments to provide continuous weather monitoring. The crucial importance of timely and accurate data acquisition has placed increasing demands on the sensitivity of these detectors and the industry which supplies them. Operational requirements have not always been met as detectors of needed sensitivity have exceeded the state-of-the-art then available. This has been especially true for the more demanding Long Wave Sounder (LWS) detectors since they require high sensitivity at the longest wavelengths of interest.

Presently, LWS detectors are typically Photoconductive HgCdTe single element detectors of essentially square or slightly rectangular active area geometry having nominal active area of 50 μm x

0-8194-2200-2/96/$6.00

50 μm. They are usually biased at a reasonably high bias in an attempt to meet the responsivity requirement, but this enhances minority carrier sweepout, shortens the response profile, increases the 1/f noise knee, and makes the D^*_λ requirement difficult to meet. The difficulty is then of producing these small area devices meeting the active area size requirements as well as all performance requirements when these parameters have a significant dependence on the degree of sweepout. It is therefore no surprise that the yield of acceptable devices has been less than 1%.

To address these problems, Goddard Space Flight Center (GSFC) has recently examined the use of non-traditional split-geometry device structures to meet the peculiar LWS detector requirements. Split-geometry PC detectors are not new per se, but they are new to this application. In this paper we will show that these detectors are particularly well suited to operation under low bias powers, and to meeting LWS detector requirements.

2. DEVICE DESIGN

The LWS device design and construction is based on a ten-element split-geometry PC detector approach we used to produce arrays for the Composite Infrared Spectrometer (CIRS) instrument on the Cassini mission. The results of that program are described in an associated paper in this conference. There the active area was 200 μm on an edge and carrier sweepout was not an issue. A top view of a CIRS array is presented in Fig. 1. As can be seen in Fig. 1, each element is split down the center with a metal cap at the top for current return. The split-geometry design was used to increase detector resistance and responsivity, and to reduce power dissipation to meet the 0.5 mW/element requirement. The strategy worked quite well and allowed all performance requirements to be met. With the successful completion of the CIRS program, we then turned our attention to producing similar (although smaller) devices for GOES. We especially liked the approach for GOES because it was suited to low bias operation which would alleviate carrier sweepout effects.

Several split-geometry designs were examined. We fabricated some devices whose active areas were split down the middle with a metal cap like the CIRS detectors, and others whose active areas were split half way and had no caps. Fig. 2 shows a split-square detector of this type, and Fig. 3 shows a split-circle detector.

The split-geometry configuration is the most important design feature of these devices. Fabrication is standard and will not be described in detail. Wafers of low carrier concentration HgCdTe were purchased from LORAL. We found these wafers to be of excellent quality. The devices were delineated using bromine spray etching. They were anodized and AR coated with ZnS, then packaged for testing.

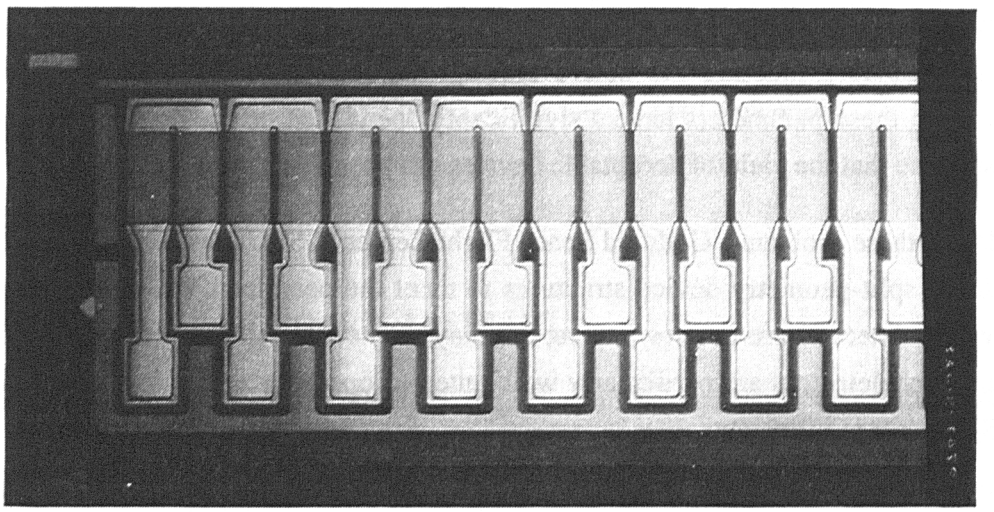

Fig. 1 Ten element split-geometry CIRS PC array.

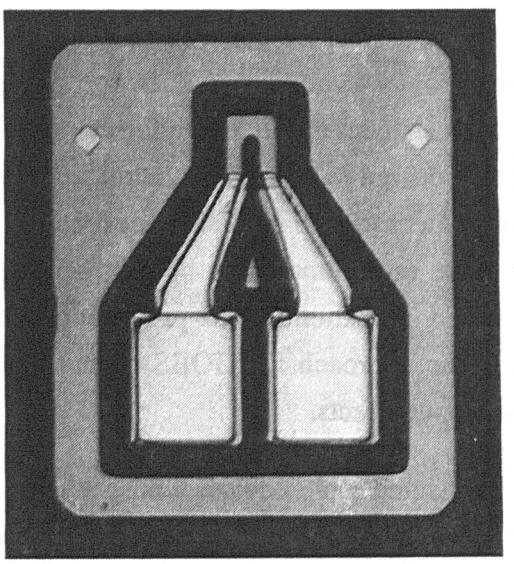

Fig. 2 A LWS detector of split-square design.

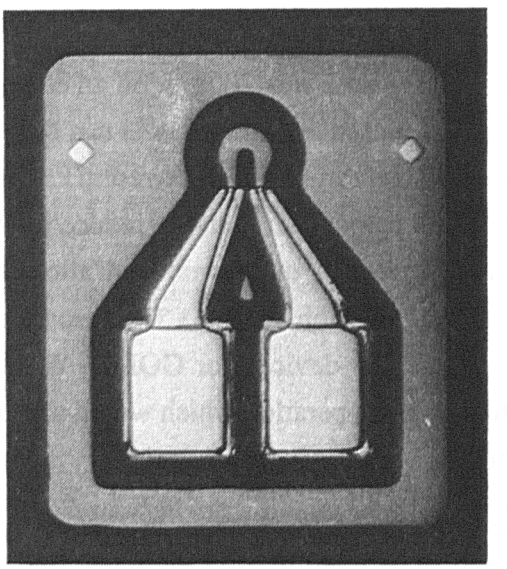

Fig. 3 A LWS detector of split-circle design.

3. DETECTOR DATA

The LWS detector performance specifications are set at 40 Hz and 100 Hz for 102 K operation, with vendor screening tests being performed mostly at 77 K. Most of our testing was done at 40 Hz to address the harder spec, and at 77 K for detector screening ease. For operation at 102 K, we usually see D_λ^*'s fall by about a factor of 2 to 3.

Detector responsivity was measured with a 500 K blackbody while under a background photon flux of $2.0 \times 10^{17}/cm^2$ sec. Noise was measured from 1 Hz to 100 Hz using an HP35661 spectrum analyzer. These measurements were usually made at a single bias for screening. The better devices were measured as a function of bias in order to determine parametric dependence on current, the optimum operating conditions for such detectors, and the level of performance achievable under optimum bias.

Table 1 shows the performance of a split-square LWS detector operated at biases ranging from 0.1 mA to 2.0 mA. Device resistance is 134 ohms, and cutoff wavelength is 17.2 μm. The noise frequency is 40 Hz. Notice that at the higher bias levels of 1.7 and 2.0 mA there is indication of Joule heating of the detectors as revealed by the shortening of the cutoff wavelength. Total noise measured at 0.1 mA is 2.7 $nV/\sqrt{Hz}$ which is encountering the preamp noise floor of 1.8 $nV/\sqrt{Hz}$.

Table 1 Performance of split-square LWS detector G2A-P12-B6 operated at different biases at 77 K.

λ_c (μm)	I_{bias} (mA)	Vnoise @ 40 Hz (V_{rms}/rtHz)	R_λ Peak (V/W)	D_λ^* Peak (cm rtHz/W)
17.2	0.10	2.66E-09	2.75E+04	5.15E+10
17.2	0.20	4.72E-09	5.52E+04	5.84E+10
17.2	0.30	6.92E-09	8.27E+04	5.98E+10
17.2	0.40	1.00E-08	1.10E+05	5.50E+10
17.2	0.50	1.22E-08	1.34E+05	5.48E+10
17.1	1.00	2.86E-08	2.40E+05	4.20E+10
17.1	1.27	3.96E-08	2.82E+05	3.57E+10
17.1	1.49	5.44E-08	3.11E+05	2.86E+10
16.4	1.71	6.45E-08	3.38E+05	2.62E+10
16.4	1.98	9.14E-08	3.52E+05	1.93E+10

To better illustrate the bias dependence of the data, we plotted D_λ^* and responsivity as a function of bias for this device as shown in Fig. 4.

The maximum D_λ^* observed for this device is $6.0 \times 10^{10}\ cm \cdot \sqrt{Hz}/Watt$. As seen in Table 1, it occurs at a bias of 0.3 mA. At higher biases, D_λ^* deteriorates because of increased sweepout and some Joule heating. At lower biases D_λ^* deteriorates as the detector noise approaches the preamp noise floor.

The responsivity is observed to increase with bias, but in sub-linear fashion due to saturation of responsivity caused by carrier sweep-out. This type of behavior is typical for LWS detectors of square or split-geometry design although the particular values of D^*_λ and responsivity differ. Typically, square LWS detectors have lower resistance and are operated at from 1 to 3 mA. This mode of operation induces significant sweep-out and because of signal saturation, makes it difficult to meet D^*_λ and responsivity requirements.

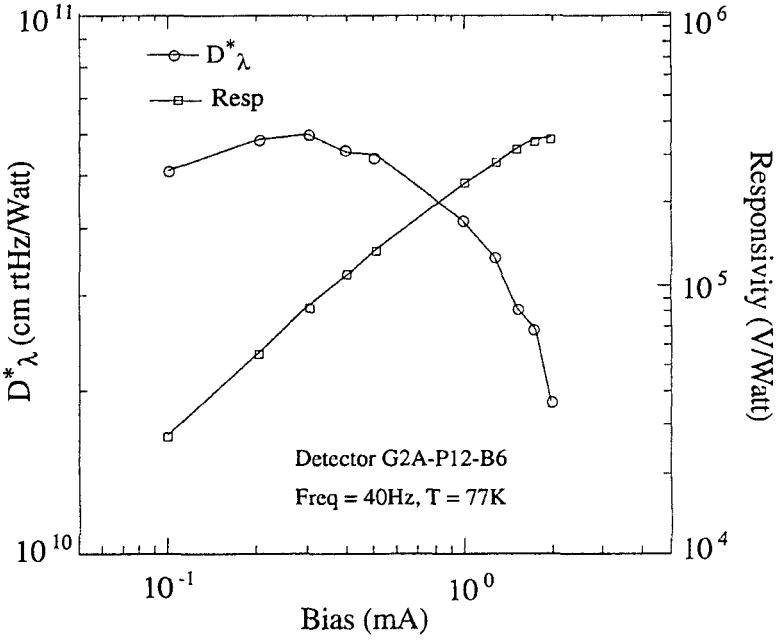

Fig. 4 Measured D^*_λ and Responsivity as a function of bias for a split-square detector .

Fig. 5 shows variable temperature D^*_λ data for a split-circle detector from LN2 to 105 K. The cutoff wavelength of this device is 16.7μm at 77K and the noise frequency is 40Hz. An exponential curve has been fitted to the data. At LN2, D^*_λ is about $6\text{x}10^{10}$ $cm \cdot \sqrt{Hz}/Watt$, and at 102 K it is slightly above $2\text{x}10^{10}$ $cm \cdot \sqrt{Hz}/Watt$.

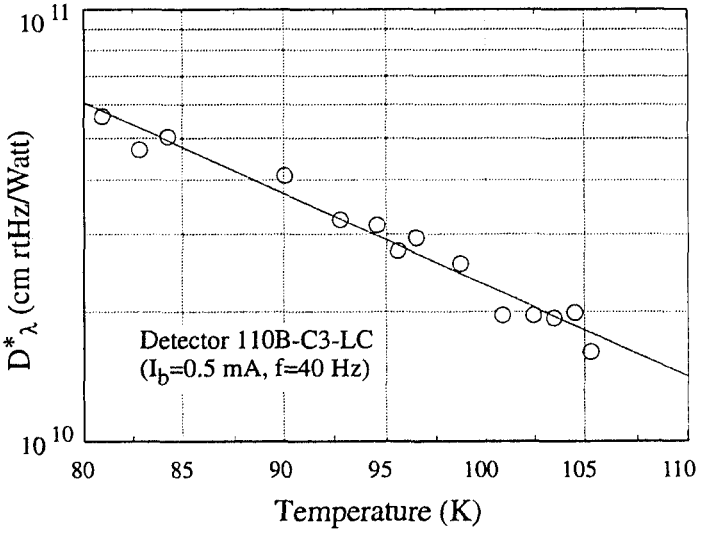

Fig. 5 D^*_λ vs. temperature for a split-circle detector.

Although this detector has not been anti-reflection (A/R) coated yet, it meets the 102 K D^*_λ specification of $2\text{x}10^{10}$ $cm \cdot \sqrt{Hz}/Watt$ at 40 Hz. We are performing annealing and other experiments to further increase D^*_λ. Even though this is a good LWS detector, we are losing lifetime, and estimate that there is still a factor of 1.5 to 2 to be gained with processing improvements for these devices.

4. DETECTOR MODELING

Split-circle and split-square detectors of the type described above are very difficult to model because of non-uniform fields and sweepout effects. In order to understand the general behavior of such detectors, some simplifying assumptions will be made. Instead of modeling a detector with a slit running halfway down the active area, we will model a detector with a slit extending the entire length to a metal shorting cap. This will produce more uniform field lines in the two halves of the detector. We also neglect carrier diffusion effects in comparison with carrier drift effects. This simplified model has the advantage of being able to be solved in closed form while still revealing the important mechanisms at work.

With these simplifications the detectivity of the device is given by the equation

$$D_\lambda^* = \frac{R_\lambda}{V_N} \cdot \sqrt{A} \ ,$$

where R_λ is the responsivity, V_N is the total noise per $\sqrt{Hz}$, and A is the active area. In turn, the responsivity and noise are given by the expressions

$$R_\lambda = \frac{\eta \cdot \lambda_c}{h \cdot c} \cdot \left(\frac{V_b \cdot \tau_e}{n \cdot l \cdot w \cdot t} \right) , \text{ and } V_N = \sqrt{V_{fn}^2 + V_{gr}^2 + V_a^2} \ ,$$

where the responsivity has the usual dependence on cutoff wavelength, λ_c, bias voltage, V_b, carrier concentration, n, and length, width, and thickness of the device, $l \cdot w \cdot t$. Because of sweepout, the lifetime dependence is on an effective lifetime, τ_e, given by the equation

$$\tau_e = \tau_b \left[1 + \frac{\tau_b}{\tau_d} \cdot \left(Exp\left(-\frac{\tau_d}{\tau_b} \right) - 1 \right) \right] ,$$

where τ_b is the bulk lifetime and τ_d is essentially the time it takes minority carriers to drift across the length of the device in the applied field. That is,

$$\tau_d = l^2 / (V_b \cdot \mu_a) \ ,$$

where μ_a is the ambipolar mobility, essentially the hole mobility in n-type material.

The total noise is the rms sum of the 1/f noise, V_{fn}, the gr-noise, V_{gr}, and the preamp noise, V_a. The 1/f noise is given by

$$V_{fn} = \beta \cdot \frac{V_b}{\sqrt{f}} ,$$

where f is the frequency, and β is a process dependent dimensionless constant. The gr-noise is given by the expression

$$V_{gr} = 2 \cdot \tau_e \cdot \left(\frac{V_b}{n \cdot t \cdot \sqrt{l \cdot w}} \right) \cdot \sqrt{\frac{n \cdot p}{n + p}} \cdot \sqrt{\frac{t}{\tau_e}} ,$$

where p is the hole carrier concentration.

There are general conclusions we can make just by examining the bias dependence of these equations. We first notice that the effective lifetime becomes the bulk lifetime for drift times significantly larger than the bulk lifetime, that is for long devices operated at low biases. When the drift time is much less than the bulk lifetime, that is, for heavy sweepout, then the effective lifetime tends to 1/2 the drift time, which decreases with increasing bias, i.e.,

$\tau_e \equiv \tau_d / 2$ (heavy sweepout).

Therefore, for heavy sweepout, the responsivity, being dependent on $V_b \cdot \tau_e$, no longer increases linearly with bias and ultimately saturates to a constant value. This of course makes it difficult to meet responsivity requirements by increasing bias on small devices.

If we now examine the gr-noise in the thermal limit, we notice a $\sqrt{\tau_e} \cdot V_b$ dependence, so the thermal gr-noise continues to increase with bias. For background limited operation V_{gr} has a $V_b \cdot \tau_e$ dependence because the excess holes have a τ_e dependence, so the background limited gr-noise also saturates. This means that a background limited detector will remain background limited but that a thermal limited detector will suffer D^*_λ degradation with increasing sweepout. Conversely, lowering the bias will reduce sweepout and improve D^*_λ until the total noise begins to be dominated by another noise source such as preamp noise, 1/f noise, or background photon noise.

The 1/f knee is defined as the frequency for which the 1/f noise equals the white noise. It is given by the expression

$$f_{knee} = \frac{(\beta \cdot V_b)^2}{V_{gr}^2 + V_a^2} .$$

When a thermal gr-limited device is operated in sweepout sufficiently above the preamp noise floor, the bias dependence of the 1/f knee becomes proportional to $\left(V_b/V_{gr}\right)^2$ or to $1/\tau_e$, and therefore to V_b. This means that the 1/f knee will decrease with decreasing bias, another reason, besides improved D^*_λ's, for avoiding sweepout as much as possible. If the device is driven out of sweepout and the gr-noise is still greater than the preamp noise, then the 1/f knee will not change with bias. Finally when the gr-noise approaches the preamp noise, the 1/f knee will again drop with bias.

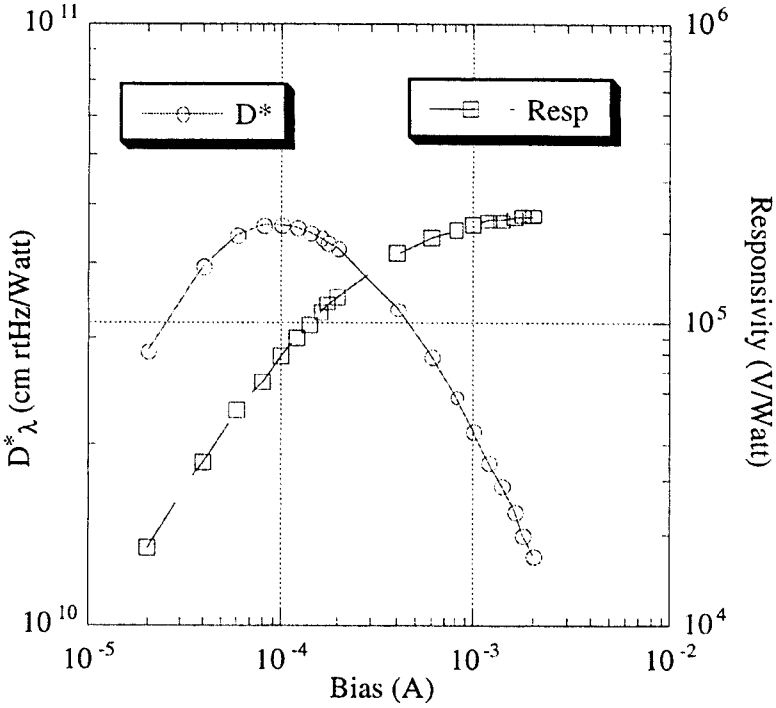

Fig. 6 D^*_λ and Responsivity vs. Bias

Graphical results of the modeling illustrating this general behavior for 102 K operation are shown in Figs. 6 through 10. In Fig. 6 we observe that the responsivity goes like V_b at low bias and begins to saturate at high bias when sweepout becomes appreciable. Because of this, the D^*_λ curve shows significant improvement when bias is reduced so as to take the device out of heavy sweepout, goes through a maximum value, and decreases when the total noise begins to be dominated by the preamp noise.

The bias dependence of the various noise terms is shown in Fig. 7. We notice that the 1/f noise goes like V_b, and the gr-noise goes like V_b at low bias and $\sqrt{V_b}$ at high bias. Figures (6) and (7) reveal that D^*_λ degrades at higher bias because the responsivity cannot keep up with the noise. At lower bias responsivity again tracks the gr-noise and 1/f noise, but not the preamp noise, which soon dominates, causing D^*_λ to drop. If it weren't for the preamp noise, at lower bias D^*_λ would saturate and become constant at a value determined by the gr-noise or 1/f noise, whichever dominates. We therefore conclude from figures (6) and (7) that D^*_λ can be further improved to its saturation value (either thermal gr, 1/f, or background limited) by reducing preamp noise. So the procedure to optimize D^*_λ is to design a device which reduces sweepout, to operate devices at the lowest possible biases whether

those devices are of optimum design or not in order to reduce sweepout, and to reduce the preamp noise floor when it is encountered. Then if 1/f noise dominates, one would reduce 1/f noise through better processing, generally of the contacts or passivation. Afterwards, what remains is the gr-noise limit which includes thermal gr-noise and background photon noise.

A comparison of D^*_λ for split and square detectors is shown as a function of bias in Fig. 8. Notice that the performance of both split and square detectors is improved as the detectors are driven out of sweepout, but that the split detector does better at low bias.

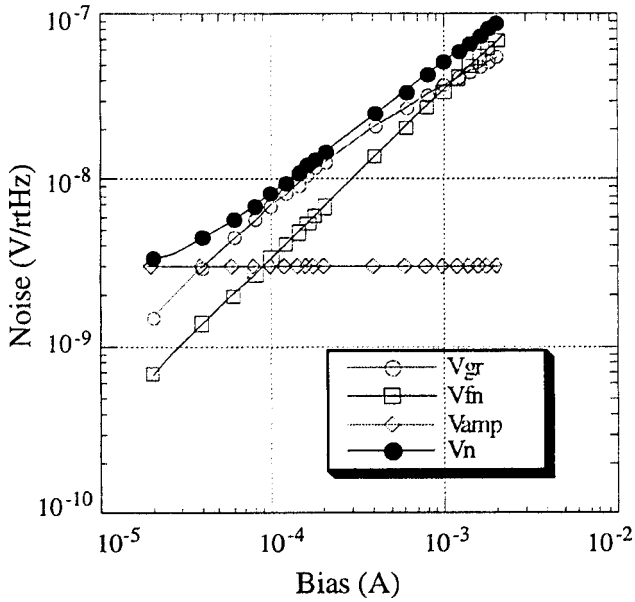

Fig. 7 Bias dependence of noise sources.

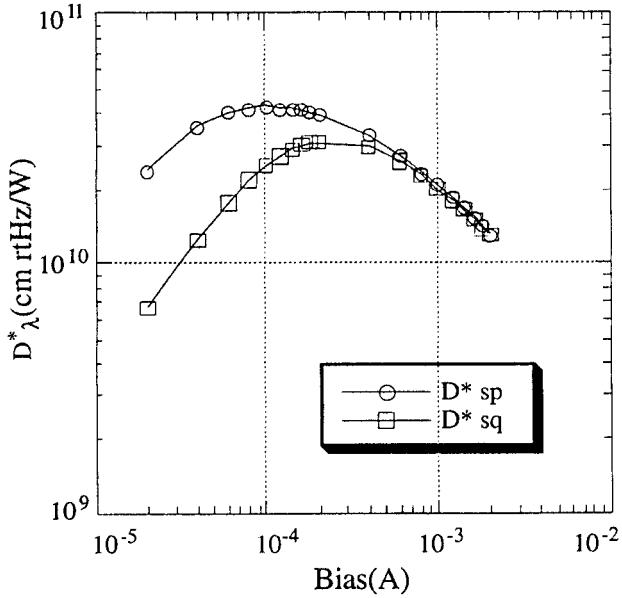

Fig. 8 D^*_λ comparison of split vs. square detectors.

Let us now examine the effects that improved processing and higher bulk lifetime will have on the performance of detectors in sweepout. We would normally expect that improved processing (better polishing, passivation, etc.) would produce longer lifetimes and together with higher bulk lifetimes would yield higher performance. In Fig. 9 we observe that if the device is operated in sweepout, higher lifetimes will have little effect on the level of performance achieved, but that the device will improve significantly when operated at low bias. There is little advantage to improving lifetime if the device is operated in heavy sweepout.

Before leaving this topic, let us examine the bias dependence of 1/f noise knees for thermal gr limited detectors. If we first take the preamp noise to be negligible in the f_{knee} expression, we see that the 1/f knee would fall like V_b as the device is driven out of sweepout, and would ultimately become constant when the device is no longer in sweepout. If V_a is not zero, we would encounter a region

where the 1/f knee would fall like V_b^2 when V_{gr} falls below V_a. This behavior is shown in Fig. 10. We conclude that avoiding sweepout for detectors not only improves D^*_λ, but also reduces 1/f noise knees.

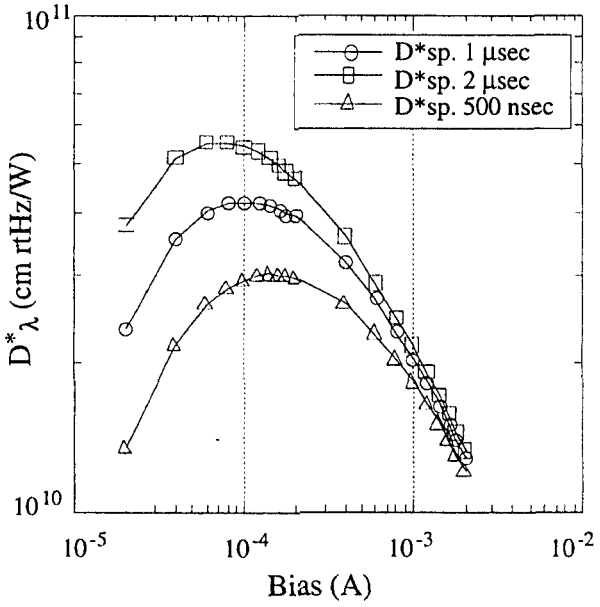

Fig. 9 Beneficial effects of high lifetimes are masked in heavy sweepout.

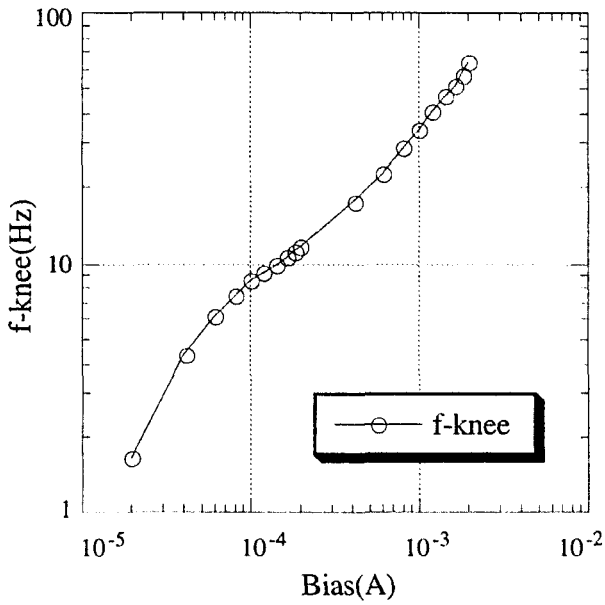

Fig. 10 The 1/f noise knee is reduced at lower biases.

5. CONCLUSIONS

Based on the devices we have built and tested, and on the theory of operation of such devices we can draw the following conclusions:

a) For GOES LWS type applications, one obtains higher D^*_λ's than normally achievable by using detectors of split-geometry and by operating the detectors at low bias.

b) Split-geometry detectors will provide higher resistance and responsivity than square detectors, yielding higher performance at lower bias.

c) Low bias operation will mitigate sweepout effects, allowing better processing and higher bulk lifetimes to have beneficial effects on performance. Conversely, strong sweepout masks the effects of high lifetime.

d) Power dissipation is significantly improved by operation at lower bias.

e) The 1/f noise knees are also reduced by operation at lower bias.

If vendors are being constrained to operate in sweepout in order to meet the responsivity requirement, it would be beneficial to relax the responsivity requirement and make up the signal shortfall with upstream electronic gain. This would allow detector operation at lower bias with all the attendant benefits listed above.

Acknowledgments

The authors gratefully acknowledge funding for this study provided by Marty Davis, GOES Project Manager, and express appreciation for his and NOAA's continued interest.

References:

1. R. J. Martineau, *et al.*, "HgCdTe Detector Technology and Performance for the Composite Infrared Spectrometer (CIRS)/Cassini Mission," to appear in Proceedings of SPIE'96 conference Cassini/Huygens, Denver, 1996.

Photovoltaic HgCdTe detectors for advanced GOES instruments

M. B. Reine, E. E. Krueger, P. O'Dette and C. L. Terzis

Lockheed Martin IR Imaging Systems
Lexington, Massachusetts 02173

ABSTRACT

There has been significant progress made during the past several years in PV HgCdTe technology for advanced long wavelength remote sensing applications. Useful cutoff wavelengths have been extended to beyond 17.0 μm. Junction quality has been improved to the point that $D^* > 3\times10^{11}$ cm-√Hz/W can be achieved at temperatures of 60-65 K. The Atmospheric Infrared Sounder (AIRS) instrument, scheduled for launch in the year 2000 as part of the NASA EOS Program, uses long linear multiplexed arrays of PV HgCdTe detectors with cutoff wavelengths extending as far as 15.0 μm at 60 K. PV HgCdTe offers many advantages over PC HgCdTe for advanced remote sensing instruments: negligible 1/f noise, much higher impedance so that cold preamps or multiplexers are possible, backside-illuminated two-dimensional arrays of closely spaced elements, 10X-100X better linearity, dc coupling for measuring the total incident photon flux, and a √2 higher BLIP D* limit. In this paper we compare the relative merits of PV and PC HgCdTe for advanced remote sensing instruments, we review recent data for linear arrays of PV HgCdTe with cutoff wavelengths as long as 17.5 μm at 70 K, and we project that PV HgCdTe should be able to meet or exceed the present demanding GOES LW Sounder D* requirements at T=100 K, with the additional benefits of negligible 1/f noise and better linearity.

Keywords: infrared detectors, HgCdTe, mercury cadmium telluride, GOES instrument, photoconductors, photodiodes, photovoltaic detectors, semiconductor devices

1.0 INTRODUCTION

Photoconductive (PC) HgCdTe infrared detectors[1-4] have been used by many NASA and DoD spaceborne remote sensing instruments over the past 25 years for highly sensitive detection of 8-20 μm radiation. These detectors have been single elements or small linear arrays having 2 to 8 elements, and were radiatively cooled to temperatures around 90-105 K, or mechanically cooled to temperatures near 77 K.

The HgCdTe PC detectors in the GOES (Geostationary Operational Environmental Satellite) Imager and Sounder instruments on the recently launched GOES-8 and GOES-9 satellites are excellent examples of HgCdTe PC technology for remote sensing applications.[5-8] Lockheed Martin IR Imaging Systems[5] built 7 of the 11 HgCdTe PC detector assemblies for the GOES-8 instruments and 9 of the 11 assemblies for the GOES-9 instruments. EG&G Judson Inc.[6] built the remainder of the GOES-8 and GOES-9 PC HgCdTe detector assemblies. These radiatively cooled PC HgCdTe detectors have cutoff wavelengths as long as 14.8 μm, operate at 90-105 K, and achieve D* that approach the theoretical D* limit set by thermal g-r noise in high quality n-type HgCdTe.

Advanced remote sensing instruments today are placing even greater demands on HgCdTe detector technology for the 8-20 μm spectral region. These increased demands are partly due to the lower temperatures now achievable with long-life advanced coolers, which are making possible detector operating temperatures of 60-65 K for long duration space missions. Advanced instruments want to realize fully the expected D* improvement in VLWIR HgCdTe detectors that results when the detector thermal noise is lowered (exponentially) by the lower operating temperature. Another reason for the increased demands is that advanced instruments are being designed for higher spatial and/or spectral resolution and require orders-of-magnitude more detector elements in the focal plane.

0-8194-2200-2/96/$6.00

Additionally, better linearity of the detector response at high photon fluxes is usually required, especially for interferometric sensors.

Photovoltaic (PV) HgCdTe detectors[2-4,9] offer many key system advantages over PC HgCdTe for 8-17 μm detection in advanced remote sensing instruments: negligible 1/f noise, much higher impedance so that cold preamps or multiplexers are possible, backside-illuminated two-dimensional arrays of closely spaced elements, 10X-100X better linearity, dc coupling for measuring the total incident photon flux, and a $\sqrt{2}$ higher BLIP D* limit. PV HgCdTe technology has advanced rapidly during the past 10 years as a result of massive investments by APRA, the DoD and industry for second generation hybrid Infrared Focal Plane Arrays (IRFPAs) for 8-10 μm detection. Interestingly, one of the first applications of PV HgCdTe for spaceborne remote sensing was a thermoelectrically-cooled single-element implanted n-on-p photodiode with a cutoff wavelength of 5.6 μm at T=185 K, designed and built by Lockheed Martin IR Imaging Systems for the Halogen Occultation Experiment (HALOE) remote sensor for the Upper Atmospheric Research Satellite (UARS).[10]

The Atmospheric Infrared Sounder[11-15] (AIRS) is an advanced remote sensing instrument that has pioneered the use of PV HgCdTe detectors to satisfy key system demands that are impossible to meet with PC HgCdTe. This high resolution, grating spectrometer, now being built by Lockheed Martin IR Imaging Systems, will utilize over 4000 PV HgCdTe detectors configured in 10 separate hybrid multiplexed arrays to cover the 3.7-13.8 μm spectral region, with the longest cutoff wavelength being 15.0 μm. Two linear arrays of PC HgCdTe detectors will cover the 13.7-15.4 μm band. All detectors will operate at a temperature of 60 K. The AIRS program has been responsible for extending the useful cutoff wavelength for PV HgCdTe from the 11-12 μm region out to beyond 17 μm, and for developing LPE film growth and array processing to the point that high quantum efficiencies (>70%) and D* values in the $3\text{-}5\times10^{11}$ cm-$\sqrt{\text{Hz}}$/W can be achieved at T=60 K.[16-19]

This progress has enabled PV HgCdTe to become a practical alternative to PC HgCdTe for 8-17 μm detection in advanced remote sensing applications. Still, PC HgCdTe will continue to be the better choice for certain instruments, such as those with relatively small numbers of detectors, with detection requirements out to extremely long wavelengths, or with very large detector optical areas. For example, the HIRDLS (High Resolution Dynamic Limb Sounder) is an instrument being built by Lockheed Martin which will use 21 individual PC HgCdTe detectors operating at 65 K, with the longest cutoff wavelength being 19.5 μm.

In Section 2 of this paper, we compare the relative merits of PC HgCdTe and PV HgCdTe for 8-17 μm detection in advanced remote sensing instruments. Section 3 summarizes recent data at T=60-70 K on high performance linear arrays of PV HgCdTe detectors with cutoff wavelengths out to 17.5 μm. In Section 4 we project that PV HgCdTe should be able to meet or exceed the present demanding GOES LW Sounder D* requirements at T=100 K, with the additional benefits of negligible 1/f noise and better linearity than PC HgCdTe.

2.0 COMPARISON OF PV AND PC HgCdTe FOR 15 μm REMOTE SENSING APPLICATIONS

Table 1 presents a comparison of the key features of PC and PV HgCdTe detectors. It is noteworthy that the most technologically significant and highest performance PC and PV HgCdTe detectors today both have a 10-15 μm thick n-type layer as the absorber layer in which photogeneration takes place. Photoconductors are processed from bulk-grown n-type HgCdTe wafers and are passivated with an n^+ surface accumulation layer. Many different photodiode architectures have been explored for HgCdTe over the years, but the one architecture that has emerged to have the broadest applicability, for cutoff wavelengths throughout the 2.5-17.5 μm, and to give the highest performance is the P-on-n structure. This structure is most commonly realized by a two-layer LPE growth process, although this same device architecture is being adopted for HgCdTe photodiodes being grown by MOCVD[20] and MBE.[21,22] Photoconductors usually require a relatively low donor concentration, on the order of $2\text{-}4\times10^{14}$ cm^{-3}, to make the resistance as high as possible and the power dissipation low. The preferred donor concentration for P-on-n

photodiodes is higher, in the $1\text{-}2\times10^{15}$ cm^{-3} range. Nevertheless, the fundamental operating temperature limits for both PV and PC are set by the Auger-1 recombination mechanism in the n-type absorber layer, and hence the operating temperatures for PC and PV needed to achieve a given thermally-limited D^*_λ are essentially the same.

The basic configuration for photoconductors is a single element or a linear array, with radiation incident on the frontside of the detector, i.e., the same side of the detector that has the contact metals. The basic configuration for photodiodes is the backside-illuminated two-dimensional array, illustrated in Figures 1 and 2, in which radiation is incident on an infrared-transparent wide-band-gap CdTe or CdZnTe substrate, with the two-layer P-on-n detector grown epitaxially on the opposite face. Bump interconnects affix this detector array to either a circuit board for fanout to nearby cold preamp stages, or, for the case illustrated in Figure 1, to a silicon CMOS ReadOut Integrated Circuit (ROIC) which constitutes a hybrid Infrared Focal Plane Array (IRFPA). Here the PV configuration is more flexible, allowing two dimensional arrays of closely spaced detectors instead of only a linear array. The entrance surface for the backside-illuminated photodiode array is planar, as contrasted to the PC case where there is considerable topology that can scatter radiation and lead to crosstalk. The planar surface can be coated with low-reflectivity (< 1%) multilayer antireflection layers to ensure that as much of the incident radiation as possible gets to the n-type absorber layer.

The process of photogeneration in the n-type absorber layers is the same for both photoconductors and photodiodes. However, the method whereby the two types of detector translate the photocarriers into external electrical signals is quite different. In the photoconductor, photogenerated carriers immediately cause a small but significant increase in the conductivity, and continue to do so until they recombine at a rate characterized by the excess carrier lifetime τ. Recombination can be dominated by bulk recombination via, e.g., the Auger-1 process, by surface recombination, or by contact recombination. In the photodiode, the photogenerated carrier pairs must first diffuse to the edge of the depletion region, where they are then separated and contribute to a photocurrent in the external circuit, or to a photovoltage in an open circuit arrangement. The quantum efficiencies of both photoconductors and photodiodes are essentially about the same, around 70-80%.

Resistances of photoconductors and photodiodes are vastly different. Typically, LWIR n-type HgCdTe photoconductors have resistances of 25-50 ohm per square, and there is negligible change in this resistance when low-level signal radiation is incident, typically less that one part in 10^5-10^6. Photodiode resistances usually decrease exponentially with increasing cutoff wavelength of the detector. They usually increase exponentially with decreasing operating temperature and with increasing reverse bias voltage. Typically, LWIR photodiode resistances range from as low as 1×10^4 ohm to 1×10^{10} ohm, depending on photodiode area, temperature, cutoff wavelength and bias voltage. Because of their low resistances, photoconductors do not match well to cold preamplifiers with tolerable amounts of power dissipation, and consequently there is no practical way to multiplex PC arrays containing large numbers of elements. Hence the number of photoconductors allowed in an array depends on how many leads can be handled and on how much bias power dissipation can be handled by the cooler. Moreover, the inability to have a cold preamp mounted next to the photoconductor element means that the noise level on the output leads is quite low, on the order of 10 $nV/\sqrt{Hz}$, and care needs to be taken to avoid pickup and ground loops. The much higher resistances of photodiodes allow them to couple well to a variety of CMOS or JFET cold preamp stages, and make it possible to multiplex large two-dimensional arrays in configurations as large as 128x128, 256x256 and 640x480.

Because the change in the photoconductor resistance is so small, only ac operation is possible, i.e., one detects only time-varying changes in the detector resistance, and it is not possible to determine the absolute value of the photon flux incident on the detector. An optical chopper is often used with PC HgCdTe to provide an ac input photon flux. Conversely, the photocurrent in a photodiode is proportional to the total photon flux incident, so one can determine the dc background photon flux as well as time-varying changes in photon flux.

Photoconductors require a dc bias voltage, usually 0.1-0.3 V, to convert the conductivity modulation into a signal voltage or current. Photodiodes are usually operated in a "short circuit" mode, with the preamp impedance much lower than that of the photodiode. It is usually desirable to operate the photodiode at a small reverse bias voltage of -15 to -30 mV for several reasons: realize a $\sqrt{2}$ decrease in the thermal noise current from the n-type absorber layer, to raise the junction resistance well above any series resistance that may be present in the photodiode itself or in the external circuit, and to suppress the preamp noise below the photodiode noise.

The upper frequency limits to the useful electrical bandwidth of LWIR HgCdTe photoconductors and photodiodes are about the same, on the order of 200 kHz to 2 MHz, and can be varied somewhat and optimized for certain applications by variations in device design and device operation. The useful bandwidth of the PV may also depend in some cases on the total capacitance in the junction and the external circuit.

Photodiodes have negligible power dissipation, whereas photoconductors have bias power dissipation typically on the order of 0.1-0.3 mW per element. However, the high impedance of PV devices renders them more susceptible to EMI, and consequently there is usually a need for a cold preamp stage proximate to the photodiode. For the hybrid multiplexed array configuration shown in Figure 1, each silicon CMOS preamp stage is directly beneath each photodiode. In non-multiplexed configurations, the preamp may be mounted on the cold fanout board adjacent to the photodiode, and the preamp may dissipate some amount of power itself, on the order of 1-3 mW.

There is a major difference in the 1/f noise characteristics of PC and PV HgCdTe detectors. The 1/f knee frequency for well made PC HgCdTe devices is in the range of 30-200 Hz, whereas the typical 1/f knee frequency for well-made PV HgCdTe devices is less than 0.3 Hz. This means that PV generally requires no optical chopper to raise the electrical frequency above the 1/f noise region.

Linearity of detector output signal at large signal photon flux levels is an important consideration for radiometric calibratability,[23-25] and is especially critical for detectors used at the output of interferometers.[26] Photoconductors should be biased in the constant voltage mode to achieve best linearity, rather than the constant current mode.[27] Another cause of nonlinearity, one that is more basic for both PC HgCdTe as well as PV HgCdTe, is the Auger-1 electron-electron recombination mechanism that, ideally, should dominate the excess carrier lifetime in the n-type absorber layer. If Δn is the photogenerated electron concentration in the n-type layer, and n_{DARK} is the steady-state electron concentration in the layer in the absence of photogeneration, then there are two limiting regimes:

linear region:	$\Delta n \propto Q$	for $\Delta n << n_{DARK}$
non-linear region:	$\Delta n \propto Q^{1/3}$	for $\Delta n >> n_{DARK}$

where the nonlinear (cube-root) dependence of Δn on photon flux Q at large values of Δn ($>> n_{DARK}$) is an inherent feature of the Auger-1 recombination mechanism. PV HgCdTe is less sensitive than PC HgCdTe to this characteristic Auger-1 nonlinearity for three reasons. First, the PC output signal is directly proportional to Δn, whereas the PV output signal is proportional to the rate of collection of photocarriers by the depletion region, which is much more weakly dependent on Δn. Second, PC devices are designed to make Δn as large as possible, whereas PV devices have Δn equal to zero at the edge of the depletion region. Third, n_{DARK} itself is much higher in PV ($1\text{-}2\times10^{15}$ cm^{-3}) than in PC ($2\text{-}4\times10^{14}$ cm^{-3}).

Surface passivation technology is well established for both PC and PV HgCdTe. PC devices are straightforwardly passivated with an n^+ surface accumulation layer, which has the disadvantage of inducing a shunt resistance that is comparable to the resistance of the n-type HgCdTe layer itself. The passivation of choice for PV HgCdTe has come to be an interdiffused layer of CdTe. Radiation hardness of both PC and PV is excellent for the

levels of total ionizing dose that spaceborne remote sensing instruments are likely to encounter. Both PC and PV HgCdTe are bake stable to temperatures of 95°-100° C.

In summary, we see that PV HgCdTe offers certain important over PC HgCdTe for advanced remote sensing instruments: negligible 1/f noise, much higher impedance so that cold preamps or multiplexers are possible, configurational versatility with backside-illuminated two-dimensional arrays of closely spaced elements, 10X-100X better linearity, dc coupling for measuring the total incident photon flux, and a $\sqrt{2}$ higher BLIP D* limit.

3.0 RECENT DATA FOR 15 μm PV HgCdTe ARRAYS AT T=40-100 K

In this section we review our recent data on VLWIR PV HgCdTe detector arrays. All photodiodes are in the backside-illuminated configuration shown in Figures 1 and 2. All photodiodes have the P-on-n heterojunction architecture shown in Figure 2. The two-layer HgCdTe films are grown at Lockheed Martin IR Imaging Systems by Liquid Phase Epitaxy (LPE), as described in References 16-18. The mesa photodiodes are formed by wet etching and are passivated with our interdiffused CdTe process. Most of the data presented in this section are for 20-100 element linear arrays consisting of two adjacent rows of 50x100 μm^2 elements, which is the AIRS array configuration. These arrays are bump mounted onto sapphire fanout boards, which are mounted into 121 pin grid array flatpacks for electrical, optical and radiometric characterization in variable temperature dewars over the 100-40 K temperature range.

The spectral response characteristics of these backside-illuminated VLWIR P-on-n LPE PV HgCdTe photodiodes are well behaved and are classical in shape, as illustrated by the data in Figures 3 and 4. Data for relative response per Watt (upper curve) and relative response per photon (lower curve) are shown in Figure 3 for a photodiode at T=60 K. The cutoff wavelength λ_{CO}, defined as the wavelength at the 50% point of the long wavelength fall-off of the relative response per Watt, is 15.4 μm at T=60 K. The peak wavelength in the relative response per Watt curve is at 14.0 μm, consistent with the empirical relationship for HgCdTe devices that the cutoff wavelength is about 10% longer than the peak wavelength. The fall-off of both curves is sharp, and the response (per photon) at wavelengths less than the peak wavelength is relatively independent of wavelength. The increase of the cutoff wavelength with decreasing temperature is well illustrated in the data in Figure 4 for a HgCdTe photodiode with a cutoff wavelength of 15.04 μm at T=60 K. These data were taken by K. Seaman at the Jet Propulsion Laboratory. Here the relative response per Watt curves show the expected increase in cutoff wavelength as temperature is lowered from 80 K to 40 K.

The most widely accepted figure of merit for quantitatively describing the quality of an infrared photodiode is the R_0A product, which is the product of the resistance R_0 at zero bias voltage and the photodiode area A. The upper limit to detectivity D* set by thermal noise in a photodiode operated at zero bias voltage is given by:

$$D^*_\lambda(V=0) = \frac{\lambda}{hc}\eta e\sqrt{\frac{R_0A}{4kT}} \tag{1}$$

where λ is the wavelength, h is Planck's constant, c is the speed of light, η is the quantum efficiency, k is Boltzmann's constant, and T is the photodiode temperature. The R_0A product is determined by those mechanisms that determine the junction current near zero bias voltage. The highest possible R_0A product is achieved when all defect-generated, tunneling and shunt leakage current mechanisms are suppressed through the use of the highest quality starting material and the use of well established device processing, and the only remaining current mechanism is diffusion current from an n-type absorber layer in which the lifetime is set by the Auger-1 electron-electron recombination mechanism. A useful estimate of the ultimate R_0A product achievable in the technologically perfect one-dimensional finite-base HgCdTe P-on-n photodiode is given by:

$$\frac{1}{R_0A} = \frac{e}{kT} j_{SAT} = \frac{e}{kT}(eg_{th}d) = \frac{e}{kT}\left(e\frac{n_i^2(x,T)}{N_D\tau_A}d\right) \quad (2)$$

where j_{SAT} in the saturation current density, g_{th} is the thermal generation rate per unit volume, $n_i(x,T)$ is the intrinsic carrier concentration for HgCdTe, d is the thickness of the absorber (or base) layer, τ_A is the Auger-1 lifetime, N_D is the donor concentration in the absorber layer, and e is the electron charge. Indeed, the goal of HgCdTe photodiode technology development has been, for a given combination of cutoff wavelength and operating temperature, to achieve a dependable capability for photodiodes that have their R_0A products as high as those given by this equation.

That this goal has been achieved in our best LPE P-on-n photodiode arrays is demonstrated by the R_0A data plotted in Figure 5 versus 1000/T for an element with a cutoff wavelength of 15.5 μm at T=60 K. The R_0A product increases exponentially with decreasing temperature. The data points agree well with the predictions for a photodiode limited only by Auger-1 n-side diffusion current down to temperatures below 60 K. The solid curve in Figure 5 is a plot of Equation 2 for d=20 μm and $N_D=1.0\times10^{15}$ cm^{-3}.

The I-V curves for this element, plotted in Figure 6 for temperatures of 40, 60, 70 and 100 K, illustrate that diffusion current limits the I-V curves over a considerably large region of reverse bias voltage, even down to temperatures as low as 60 K. VLWIR HgCdTe photodiodes are typically operated at reverse bias voltages in the -20 to -40 mV range. Note that at 100 K the current at reverse bias voltages out to -300 mV shows no sign of tunneling current. Some tunneling current can be seen as the temperature is lowered and as the thermal current mechanism decreases exponentially with decreasing temperature, until at 40 K tunneling current dominates the reverse bias I-V for voltages beyond -20 mV. At 60 K, the intended operating temperature for the AIRS IRFPA, tunneling current begins to dominate at -100 mV, well beyond the intended operating bias range of -20 to -40 mV.

The maturity of our VLWIR LPE P-on-n HgCdTe photodiode technology is demonstrated by the 60 K data for R_0A plotted versus the 60 K cutoff wavelength in Figure 7 for many AIRS-format linear arrays of 50x100 μm^2 elements. Each data point is the average R_0A of a linear array having from 20 to 100 elements. The average quantum efficiencies for these arrays at 60 K are in the 60%-80% range. The dashed curve is a plot of Equation 2, and the best data in this plot are at the limit set by Auger-1 n-side diffusion current. Also shown in Figure 7 are plots of Equation 1, showing the combinations of R_0A product and cutoff wavelength needed to achieve thermally-limited peak-wavelength D* values of 2×10^{11} and 1×10^{12} cm-$\sqrt{Hz}$/W at T=60 K. For these iso-D* curves we assumed that the peak wavelength λ_{PEAK} was equal to $0.9\times\lambda_{CO}$, and that the quantum efficiency was 70%, a value which is typical for the arrays represented in Figure 7.

Good uniformity of the R_0A product is illustrated in Figure 8 for a 20-element AIRS-format test array for temperatures of 100, 80, 70 and 60 K. The cutoff wavelength for this array at 60 K is 15.7 μm. Also plotted in this figure are the dynamic resistance-area products R_DA at reverse bias voltages of -20 mV and -40 mV. At the highest temperature of 100 K, thermal current dominates both the R_0A and the R_DA products, and the element-to-element profiles for all three are quite uniform, as expected for thermal current mechanisms. As temperature is reduced, there is exponentially less thermally generated current, and the reverse bias R_DA products become progressively less uniform, being influenced to a greater degree by non-thermal defect-related current mechanisms. The R_0A profile remains quite uniform, even down to 60 K. But the reverse bias R_DA products, especially at the larger reverse bias voltage of -40 mV, have much more variation from element to element. Nevertheless, this array is quite functional at 60 K when the reverse bias voltage is kept to -20 mV.

A summary plot of R_0A versus cutoff wavelength for T=70 K is shown in Figure 9. As in the analogous plot in Figure 7, the open data points are the average R_0A values at 70 K for AIRS-format linear arrays with 20 to 100

elements. The average quantum efficiencies for these arrays are in the 60%-80% range, just as for the data in Figure 9. Here we have added recent 70 K data for backside-illuminated circular mesa P-on-n LPE HgCdTe photodiodes. Each data point is the R_0A for the best of several 350 μm dia. mesa devices selected from a variable-area diagnostic array. The longest cutoff wavelengths at T=70 K are 17.4-17.5 μm. The quantum efficiencies for these circular mesa devices are in the 61-73% range.

4.0 PV HgCdTe SHOULD MEET OR EXCEED GOES LW SOUNDER DETECTOR REQUIREMENTS AT T=100 K

The Imager and Sounder instruments now successfully operating on the GOES-8 and GOES-9 satellites contain some of the most carefully designed and processed LWIR HgCdTe photoconductive detectors ever made.[5-8] These detectors, produced by Lockheed Martin IR Imaging Systems[5] and by EG&G Judson Inc.[6] are radiatively cooled and operate at temperatures between 90 K and 105 K. Of the five different types of detector in the Imager and Sounder instruments, the most demanding requirements were those for the LW detectors in the Sounder instrument, which had the longest cutoff wavelengths:

Active area:	50x50 μm²
Cutoff wavelength:	14.8 μm
Operating temperature:	100 K
Background photon flux:	1.2×10^{17} ph/cm²-sec
Detectivity:	2.7×10^{10} cm-√Hz/W at 100 Hz
	2.0×10^{10} cm-√Hz/W at 40 Hz
Bias power dissipation:	< 1.7 mW
Preamp & system noise:	4.0 nV/√Hz

These requirements are made difficult[7] because the required D* is just at the theoretical limit for n-type HgCdTe photoconductors for this combination of cutoff wavelength and temperature. Equally significant is the high preamp and system noise level of 4 nV/√Hz, which requires biasing the detector until the detector noise is well above this value, a challenging thing to do in view of the power dissipation limitations imposed by radiative cooling, and the decreasing Auger-1 lifetime in n-type HgCdTe at this temperature and cutoff wavelength.

Could PV HgCdTe meet these challenging requirements? It appears that it could. Recall from the previous section - Figure 6 in particular - that the behavior of VLWIR P-on-n HgCdTe photodiodes at higher temperatures becomes more and more dominated by the large amount of diffusion current thermally generated in the n-type absorber layer. Under these conditions the I-V curves follow the ideal Shockley relationship very well, and we can expect large increases in dynamic resistance at reverse bias voltage. This is illustrated well by the I-V curves in Figure 10 for a P-on-n photodiode at T=100 K with a cutoff wavelength of 13.4 μm at 100 K. Note that the reverse bias I-V curve shows hard saturation out to -300 mV, and that the dynamic resistance $R_D(V)$ increases by nearly two orders of magnitude from zero bias voltage to -50 mV. The dynamic resistance $R_D(V)$ follows very closely the exponential behavior, shown by the dashed line in Figure 6, that is expected for an ideal diode whose I-V curves are limited only by diffusion current.

The GOES LW Sounder PV HgCdTe detector would be operated at strong reverse bias (i.e., -eV/kT>>1) for several reasons. First, the thermal noise current is reduced by a factor of $1/\sqrt{2}$ from its value at zero bias voltage, so that the thermally-limited D* is $\sqrt{2}$ larger than that for zero bias voltage:

$$D^*_\lambda(-eV >> kT) = \frac{\lambda}{hc}\eta e\sqrt{\frac{R_0A}{2kT}} \qquad (3)$$

For T=100 K, kT=8.6 mV and a reverse bias voltage of -25 mV would be sufficient to reach the strong reverse bias regime. The second benefit of reverse bias is that the dynamic resistance is, for -eV=3×kT, about 20 times the zero bias resistance R_0, which would help raise the dynamic resistance well above any series resistance. The higher dynamic resistance would also help to suppress preamp noise below detector noise.

The various limits to D* are plotted versus R_0A product for the GOES LW Sounder detector conditions in Figure 11, for the case of a photodiode operated at T=100 K under strong reverse bias. We assumed a reasonable value for quantum efficiency of 70%, and a preamp noise voltage e_N of 4 nV/√Hz. We see that a D* value of 4.0×10^{10} cm-√Hz/W can be achieved for an R_0A product of 0.1 ohm-cm².

The required combination of R_0A product of 0.1 ohm-cm² and cutoff wavelength λ_{CO} of 14.8 μm at 100 K should be achievable in an LPE P-on-n HgCdTe photodiode, as shown by the plot of R_0A data for AIRS-format arrays at T=100 K versus cutoff wavelength in Figure 12. As in Figures 7 and 9, each data point is the average for an AIRS linear array with 20 to 100 elements. The data follow well the solid curve, which is the one dimensional R_0A expected for only diffusion current from an n-type absorber dominated by Auger-1 recombination (Equation 2). The longest cutoff wavelength at 100 K for which we have data thus far is 13.9 μm, but the trend of the data shows that an R_0A value of 0.1 ohm-cm² should be expected for a cutoff wavelength of 14.8 μm.

Hence the projected D* for an LPE P-on-n HgCdTe at T=100 K, operated at strong reverse bias, is at least 4.0×10^{10} cm-√Hz/W, which meets or exceeds the GOES LW Sounder requirement. An important advantage that PV enjoys for this application is the absence of 1/f noise; the 1/f knee frequency for PV HgCdTe would be less than 0.3 Hz, as compared to the knee frequencies of 50-200 Hz common for the GOES PC LW Sounder detectors. Another significant advantage is the one-to-two order of magnitude better linearity that PV HgCdTe enjoys over PC HgCdTe. The photodiode would be in the standard backside-illuminated configuration, with a planar CdTe entrance surface that has a low-reflectivity coating. The detector would be bump-mounted onto a sapphire fanout board, which would also hold a cold preamp and a temperature sensor.

5.0 CONCLUSIONS

There has been significant progress made during the past several years in PV HgCdTe for technology for advanced long wavelength remote sensing applications. Useful cutoff wavelengths have been extended to beyond 17.0 μm. Junction quality has been improved to the point that the R_0A products are limited by Auger-1 n-side diffusion current down to temperatures of 60 K for cutoff wavelengths as long as 15.5 μm, and D* > 3×10^{11} cm-√Hz/W can be achieved at temperatures of 60-65 K. The AIRS instrument, scheduled for launch in the year 2000 as part of the NASA EOS Program, uses 334-element bilinear multiplexed arrays of PV HgCdTe detectors with cutoff wavelengths extending as far as 15.0 μm at 60 K.

PV HgCdTe offers many advantages over PC HgCdTe for advanced remote sensing instruments: negligible 1/f noise, much higher impedance so that cold preamps or multiplexers are possible, configurational versatility with backside-illuminated two-dimensional arrays of closely spaced elements, 10X-100X better response linearity, dc coupling for measuring the total incident photon flux, and a √2 higher BLIP D* limit.

As an example of the applicability of VLWIR PV HgCdTe, we project that a PV HgCdTe should meet or exceed the demanding GOES LW Sounder D* requirements. A projected D* value of at least 4.0×10^{10} cm-√Hz/W should be achieved by an LPE P-on-n HgCdTe photodiode with a cutoff wavelength of 14.8 μm, operating at 100 K under strong reverse bias, with the additional advantages of negligible 1/f noise and one-to-two orders of magnitude better response linearity.

The advantages of PV HgCdTe will be more important for some remote sensing applications than for others, and the relative merits of PV versus PC for a given system will, as always, need to be considered in the context of overall system performance, cost, risk and schedule. PC HgCdTe is a more mature technology than PV HgCdTe, and PC HgCdTe is a more simple device. If PC HgCdTe can satisfy all the system technical performance requirements, then it would be the natural choice from the standpoint of cost, risk and schedule. However, PV HgCdTe now offers the system architect exciting new possibilities for advanced remote sensors that would not be achievable with PC HgCdTe. In the final analysis, the choice between PV and PC HgCdTe will depend on the precise details of the performance requirements, technological suitability, and programmatic constraints.

6.0 ACKNOWLEDGEMENTS

The VLWIR PV HgCdTe data reviewed in this paper originated mostly from the Atmospheric Infrared Sounder (AIRS) program at Lockheed Martin IR Imaging Systems, Contract 958606 from NASA Goddard Space Flight Center through the Jet Propulsion Laboratory (JPL). Mr. Fred O'Callagnhan of JPL is the AIRS Program Manager. Additional data were provided by the program "VLWIR PV HgCdTe Feasibility Study for the IMG-II" funded by the NEC Corporation, managed at Lockheed Martin IR Imaging Systems by Jan Williams. The P-on-n LPE films were grown for this program by Dr. Guy Plutz, Tim Robertson and Jim Hughes, and the variable-area VLWIR diagnostic arrays were processed by Dave McKee. The authors thank Mr. Kirk Seaman of JPL for providing spectral response data for one of our VLWIR HgCdTe photodiodes. We acknowledge several technical discussions on the applicability of PV HgCdTe to various advanced remote sensing instruments with Dr. Michael R. Gunson of JPL, with Dr. Daniel L. Mooney and Dr. W. Edward Bicknell of the MIT Lincoln Laboratory, and with our colleagues Chris Miller and Paul Morse at Lockheed Martin IR Imaging Systems. There have been many discussions about the GOES PC HgCdTe detector requirements with Dr. Ed Andrews and Jeff Derr of ITT Aerospace/Communications Division, Fort Wayne, Indiana.

7.0 REFERENCES

1. R. M. Broudy and V. J. Mazurczyk, "(HgCd)Te Photoconductors," Chapter 5 in Semiconductors and Semimetals, Vol. 18, edited by R. K. Willardson and A. C. Beer (Academic Press, New York, 1981).

2. M. B. Reine, K. R. Maschhoff, S. P. Tobin, P. W. Norton, J. A. Mroczkowski and E. E. Krueger, "The Impact of Characterization Techniques on HgCdTe Infrared Detector Technology," Semicond. Sci. Technol. 8, 788 (1993).

3. A. Rogalski, Infrared Photon Detectors (SPIE Press, 1995).

4. E. L. Dereniak and G. D. Boreman, Infrared Detectors and Systems (Wiley, New York, 1996).

5. J. Hartley, C. L. Terzis, M. B. Reine, R. Hassler and A. J. Verilli, "Photoconductive HgCdTe Detector Assemblies for the GOES Imager and Sounder Instruments," Proc. SPIE 2812 (1996).

6. J. Frederick, J. Kimchi and T. T. S. Wong, "High-Performance HgCdTe Photoconductive Detector Assemblies," Proc. SPIE 2812 (1996).

7. R. B. Schoolar, W. E. Bicknell and D. L. Spears, "HgCdTe LWIR Photoconductor Technology Review and Performance Projections for GOES Imager-4, Imager-5, and LW Sounder," Aerospace Corporation Report No. ATR-92(2826)-1, July, 1992.

8. D. G. Seiler, J. R. Lowney, W. R. Thurber, J. J. Kopanski and G. G. Harmon, "Improved Characterization and Evaluation Measurements for HgCdTe Detector Materials, Processes, and Devices Used on the GOES and TIROS Satellites," National Institute of Standards and Technology Special Publication 400-94, April 1994.

9. M. B. Reine, T. J. Tredwell and A. K. Sood, "Photovoltaic Infrared Detectors" in Semiconductors and Semimetals, Ed. by R. K. Willardson and A. C. Beer, Vol. 18 (Academic Press, New York, 1981).

10. P. W. Norton, P. H. Zimmermann, R. J. Briggs and N. M. Hartle, "Large Area Space Qualified Thermoelectrically (TE) Cooled HgCdTe MW Photovoltaic Detectors for the Halogen Occultation Experiment (HALOE)," Proc. SPIE 686, 138 (1986).

11. H. H. Aumann and R. J. Pagano, "Atmospheric Infrared Sounder on the Earth Observing System," Optical Engineering 33, 776 (1994).

12. P. Morse, C. Miller, M. Chahine, F. O'Callaghan, H. Aumann and A. Karnik, "Candidate Future Atmospheric Sounder for the Converged U. S. Meteorological System," Proc. SPIE 2553, 329 (1995).

13. H. Aumann and C. Miller, "Atmospheric Infrared Sounder (AIRS) on the Earth Observing System," Proc. SPIE 2583, 332 (1995).

14. J. Rutter, D. Jungkman, J. Stobie, E. Krueger, M. Krueger, J. Garnett, M. Reine, B. Denley, D. Kleinmann and M. Gurnee, "An Advanced PV/PC HgCdTe Hybrid IRFPA for Satellite Based High Resolution Multispectral Remote Sensing," Proc. SPIE 2553, 344 (1995).

15. J. H. Rutter, D. Jungkman, J. Stobie, E. E. Krueger, J. D. Garnett, M. B. Reine, B. Denley, M. Jasmin and A. Sofia, "Multispectral HYBRID HgCdTe/FPA Dewar Assembly for Remote Sensing in the Atmospheric Infrared Sounder (AIRS)," Proc. SPIE 2816 (1996).

16. E. E. Krueger, G. N. Pultz, P. W. Norton, J. A. Mroczkowski, M. H. Weiler and M. B. Reine, "Two-Layer LPE HgCdTe P-on-n 8-18 μm Photodiodes," Mat. Res. Soc. Symp. Proc. 216, 93 (1991).

17. G. N. Pultz, P. W. Norton, E. E. Krueger and M. B. Reine, "Growth and Characterization of P-on-n HgCdTe Liquid-Phase Epitaxy Heterojunction Material for 11-18 μm Applications," J. Vac. Sci. Technol. B9, 1724 (1991).

18. E. E. Krueger, G. N. Pultz, K. R. Maschhoff, S. P. Tobin, P. W. Norton, J. H. Rutter and M. B. Reine, "Extending HgCdTe Photovoltaic Detector Technology to Cutoff Wavelengths of 17 μm," Mat. Res. Soc. Symp. Proc. 299 (1993).

19. M. B. Reine, E. E. Krueger, C. L. Terzis, B. Denley, J. Hartley, J. Rutter and D. E. Kleinmann, "Advances in 15 μm HgCdTe Photovoltaic and Photoconductive Detector Technology for Remote Sensing," Proc. SPIE 2816 (1996).

20. P. Mitra, Y. L. Tyan, F. C. Case, R. Starr and M. B. Reine, "Improved Arsenic Doping in Metalorganic Chemical Vapor Deposition of HgCdTe and *in situ* Growth of High Performance Long Wavelength Infrared Photodiodes," 1995 U.S. Workshop on the Physics and Chemistry of Mercury Cadmium Telluride and Other IR Materials, Baltimore, Maryland, Oct. 10-12, 1995; to be published in Jour. of Electronic Materials (1996).

21. J. Bajaj, J. M. Arias, M. Zandian, J. G. Pasko, L. J. Kozlowski, R. E. De Wames and W. E. Tennant, "Molecular Beam Epitaxial HgCdTe Material Characteristics and Device Performance: Reproducibility Status," Jour. Electronic Materials 24, 1067 (1995).

22. O. K. Wu, D. M. Jamba, G. S. Kamath, G. R. Chapman, S. M. Johnson, J. M. Pearson, K. Kosai and C. A. Cockrum, "HgCdTe Molecular Beam Epitaxy Technology: A Focus on Material Properties," Jour. Electronic Materials 24, 423 (1995).

23. M. P. Weinreb, G. Hamilton and S. Brown, "Nonlinearity Corrections in Calibration of Advanced Very High Resolution Radiometer Infrared Channels," Jour. Geophysical Research 95, 7381 (1990).

24. I. L. Goldberg, "Two-Point Calibration of Non-Linear PC HgCdTe Channels," Infrared Physics 36, 785 (1995).

25. W. E. Bicknell, MIT Lincoln Laboratory, private communication on issues of HgCdTe detector nonlinearity and the GOES instrument calibration.

26. M. C. Abrams, G. C. Toon and R. A. Schindler, "Practical Example of the Correction of Fourier-Transform Spectra for Detector Nonlinearity," Applied Optics 33, 6307 (1994).

27. G. Eppeldauer and L. Novak, "Linear HgCdTe Radiometer," Proc. SPIE 1110, 267 (1989).

Table 1. Comparison of photoconductive (PC) and photovoltaic (PV) HgCdTe infrared detectors.

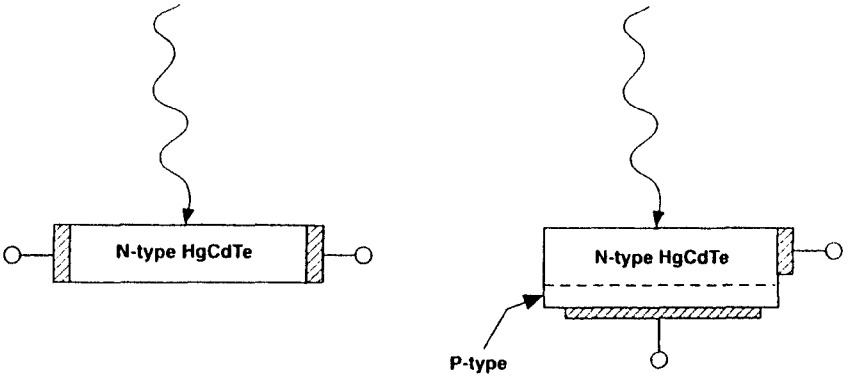

	PC	PV
Material	n-type bulk-grown	P-on-n two-layer LPE
Array configuration	60-180 element linear arrays	MxN mosaic arrays
Resistance	25-50 ohm per square	1×10^4 - 1×10^7 ohm
Gain	100-200	1
Quantum efficiency	70-80%	70-80%
Electrical coupling	ac only	ac and/or dc
Bias voltage	0.1-0.3 V required	15-30 mV reverse bias desirable
Power dissipation	0.1-0.5 mW per element	negligible
Electrical bandwidth	0.2-2 MHz	0.2-2 MHz
1/f noise knee frequency	30-200 Hz	< 0.3 Hz
Linearity	good	better than PC by 10X - 100X
Noise mechanisms	• thermal g-r noise • background g-r noise • 1/f noise	• shot noise on thermal current • shot noise on photocurrent
Surface passivation	n^+ accumulation layer	CdTe interdiffused layer
Radiation hardness	excellent	excellent
Thermal bake stability	95° C	100° C

- **Backside-illuminated NxN P-on-n HgCdTe detector array**
- **N = 64, 128, 128, 256, . . .**
- **Unit cell area: 40 x 40 μm^2 - 60 x 60 μm^2**
- **Indium bumps interconnect detector array to silicon CMOS multiplexer chip**

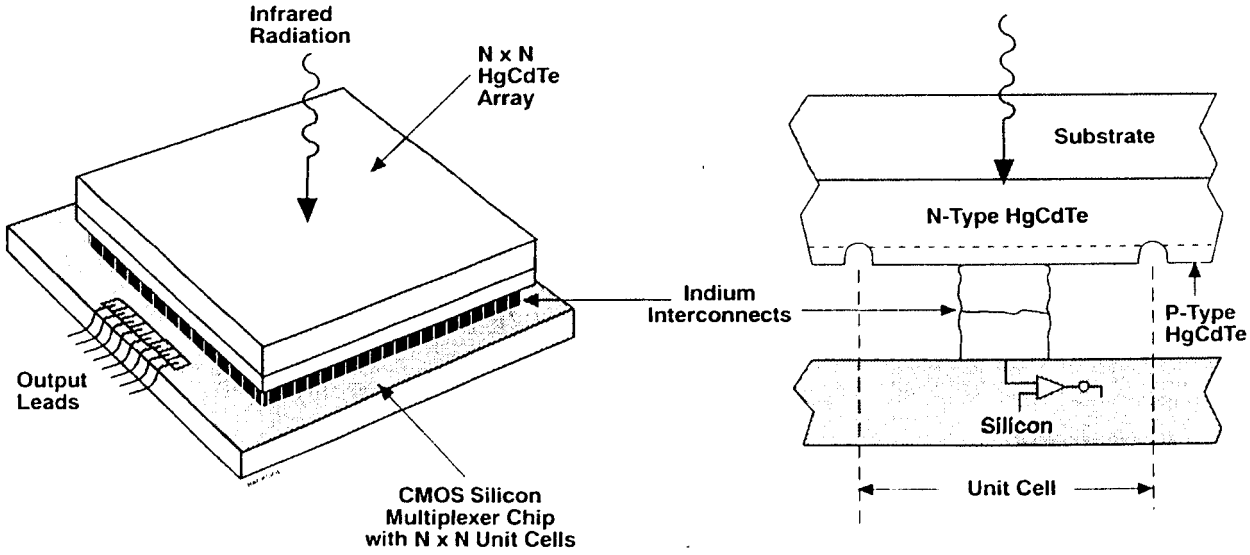

Figure 1. Two-dimensional arrays of backside-illuminated HgCdTe photovoltaic detectors are hybridized to silicon CMOS ROICs to form large Infrared Focal Plane Arrays (IRFPAs).

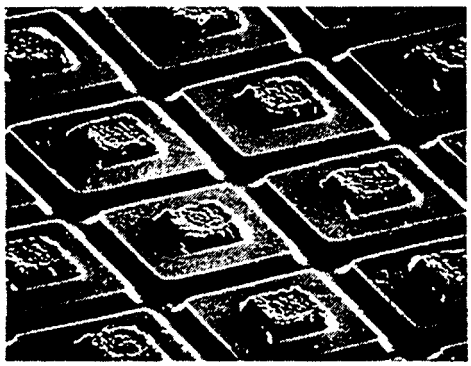

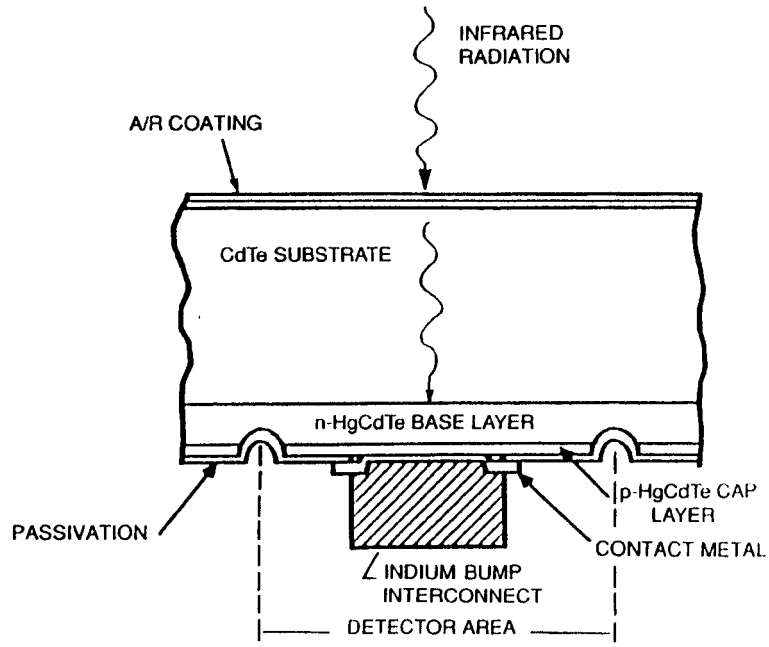

- **N-type base layer:**
  - **Tellurium-rich horizontal slider**
  - **Indium doping to 10^{15} cm^{-3}**
  - **15-20 μm thick**
- **P-type cap layer**
  - **Mercury-rich vertical slider**
  - **Arsenic doping to 10^{17} cm^{-3}**
  - **1 to 2 μm thick**

Figure 2. Cross section of a backside-illuminated LPE P-on-n HgCdTe photodiode. The SEM photo shown a two-dinemsional array of 50x50 μm^2 HgCdTe photodiodes prior to hybridization.

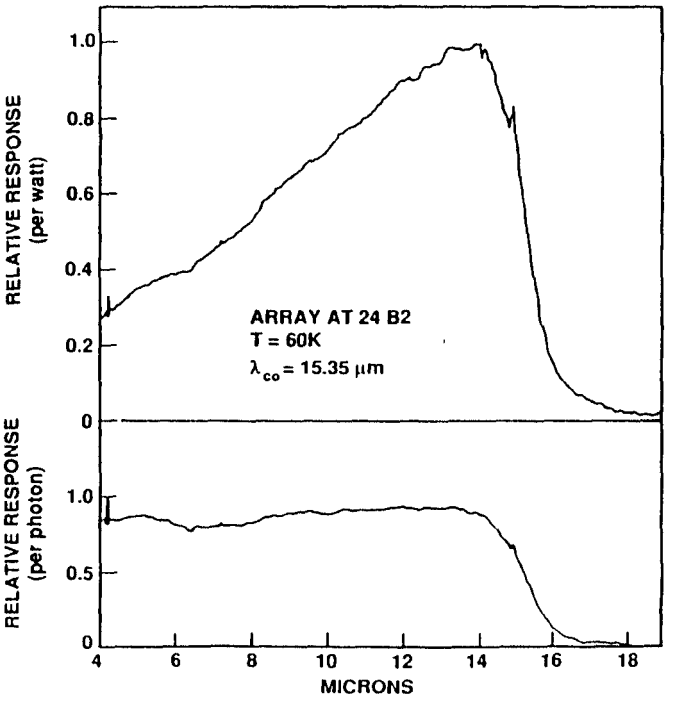

Figure 3. Relative spectral response per Watt (upper curve) and per photon (lower curve) for an LPE P-on-n HgCdTe photodiode at T=60 K with a cutoff wavelength of 15.4 μm.

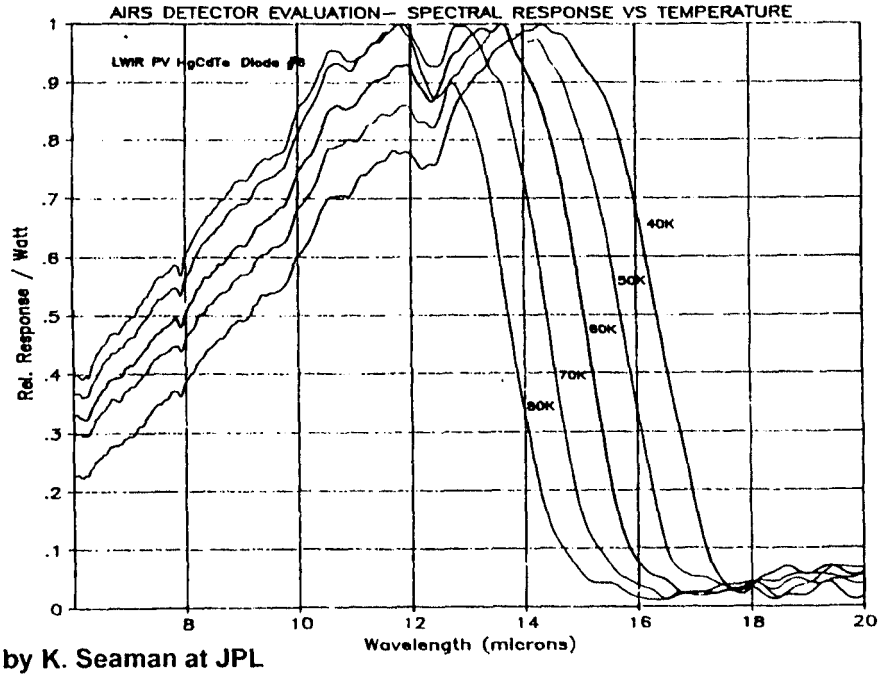

Data taken by K. Seaman at JPL
AIRS Array LD057FB
λ_{co}(60 K) = 15.04 μm

Figure 4. Relative spectral response (per Watt) for an LPE P-on-n HgCdTe photodiode for temperatures between 40 K and 80 K.

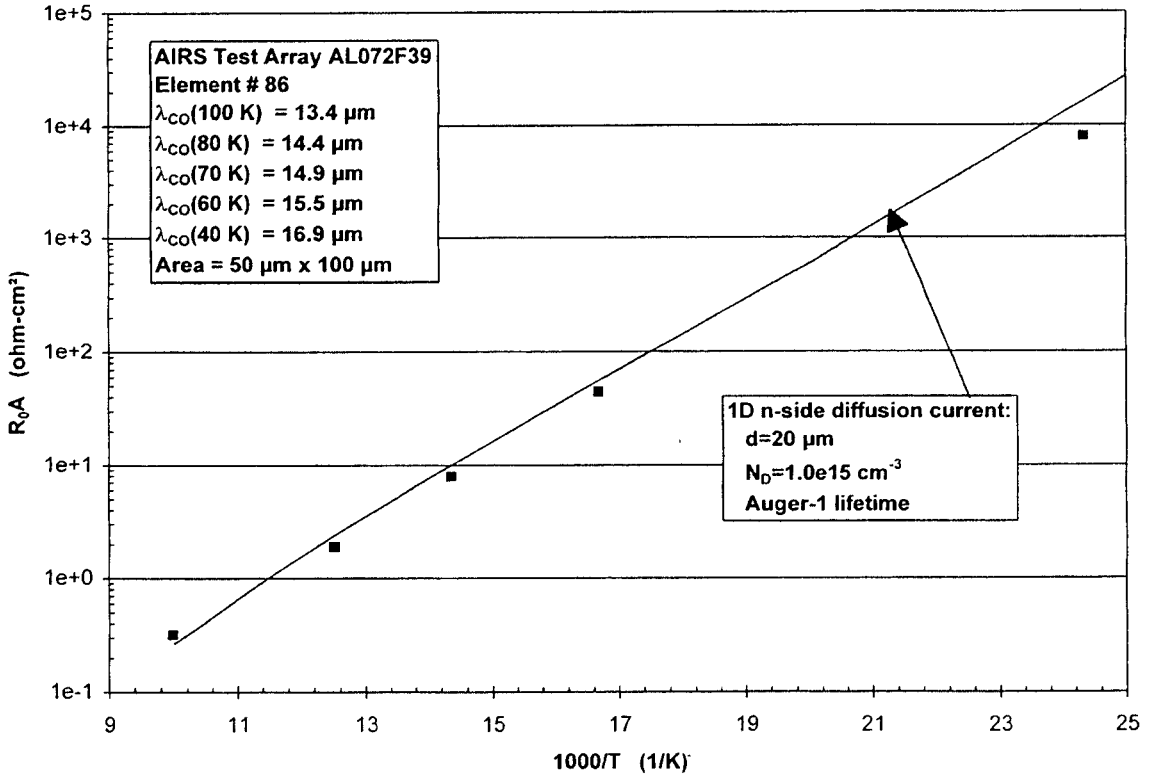

Figure 5. R_0A versus 1000/T for an LPE P-on-n HgCdTe photodiode over the 40-100 K temperature range.

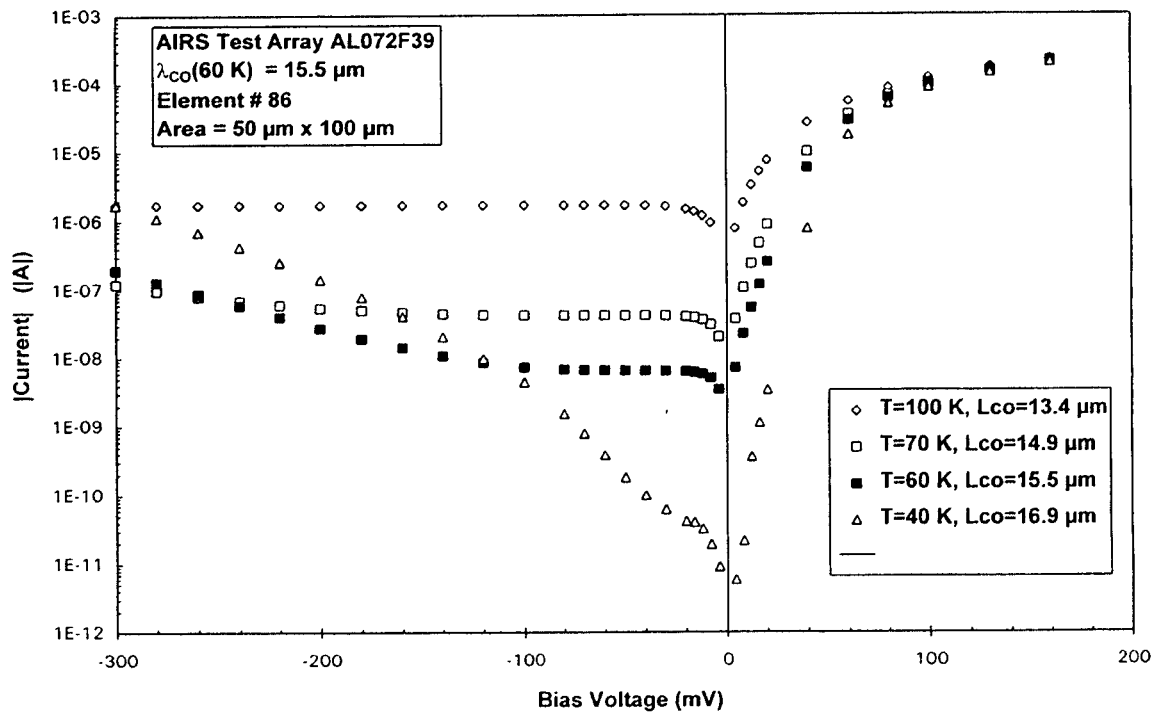

Figure 6. Current-voltage curves for the photodiode of Figure 5 over the 40-100 K temperature range.

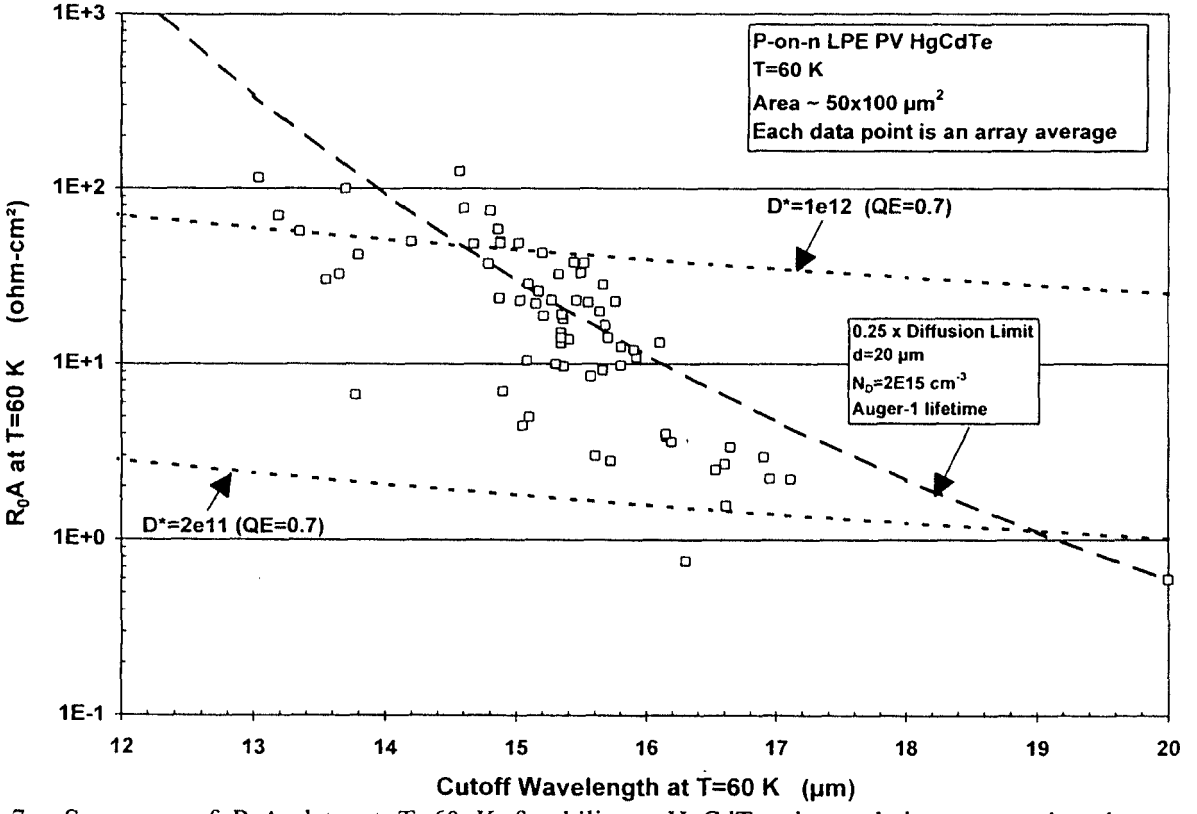

Figure 7. Summary of R_0A data at T=60 K for bilinear HgCdTe photovoltaic arrays, plotted versus cutoff wavelength. Each data point is the average R_0A for an array containing 20 to 100 elements.

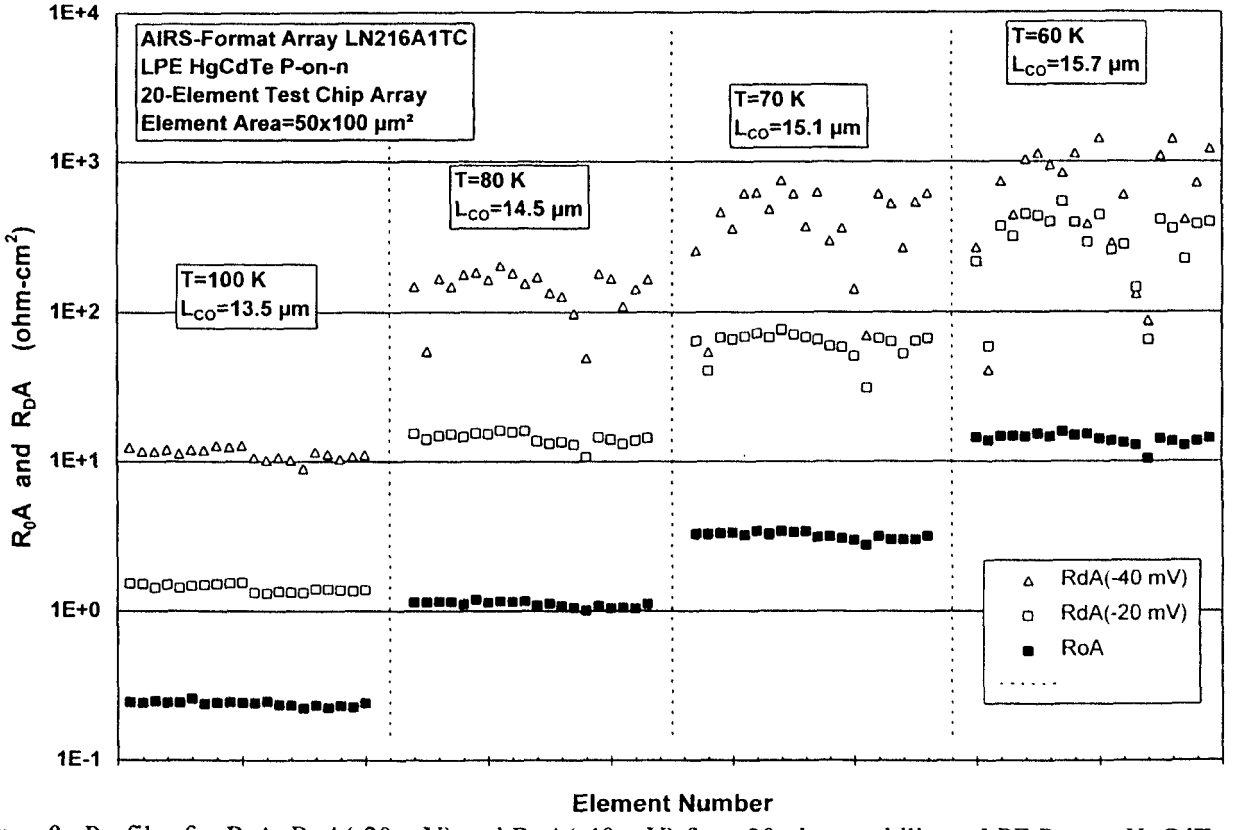

Figure 8. Profiles for R_0A, R_DA(-20 mV) and R_DA(-40 mV) for a 20-element bilinear LPE P-on-n HgCdTe array for four temperatures.

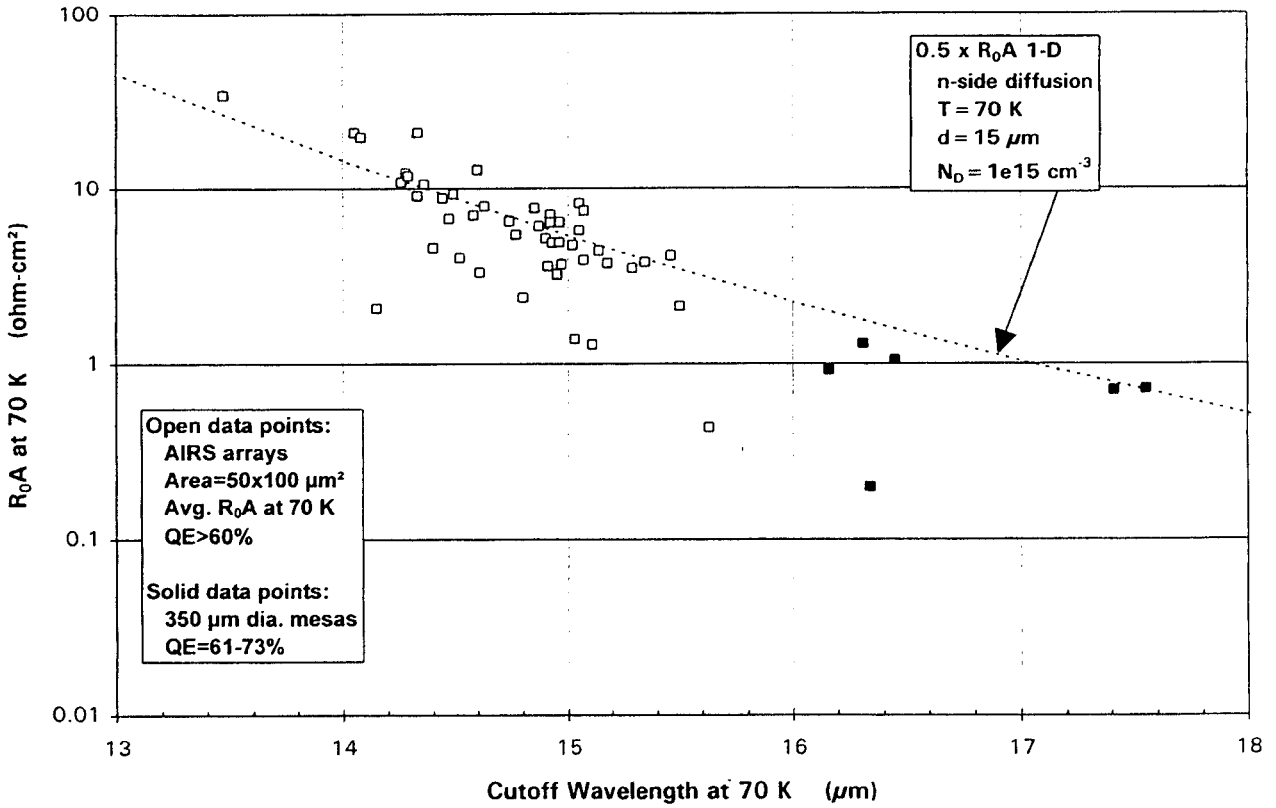

Figure 9. Summary of R_0A data at T=70 K for bilinear HgCdTe photovoltaic arrays, plotted versus cutoff wavelength. Each data point is the average R_0A for an array containing 20 to 100 elements.

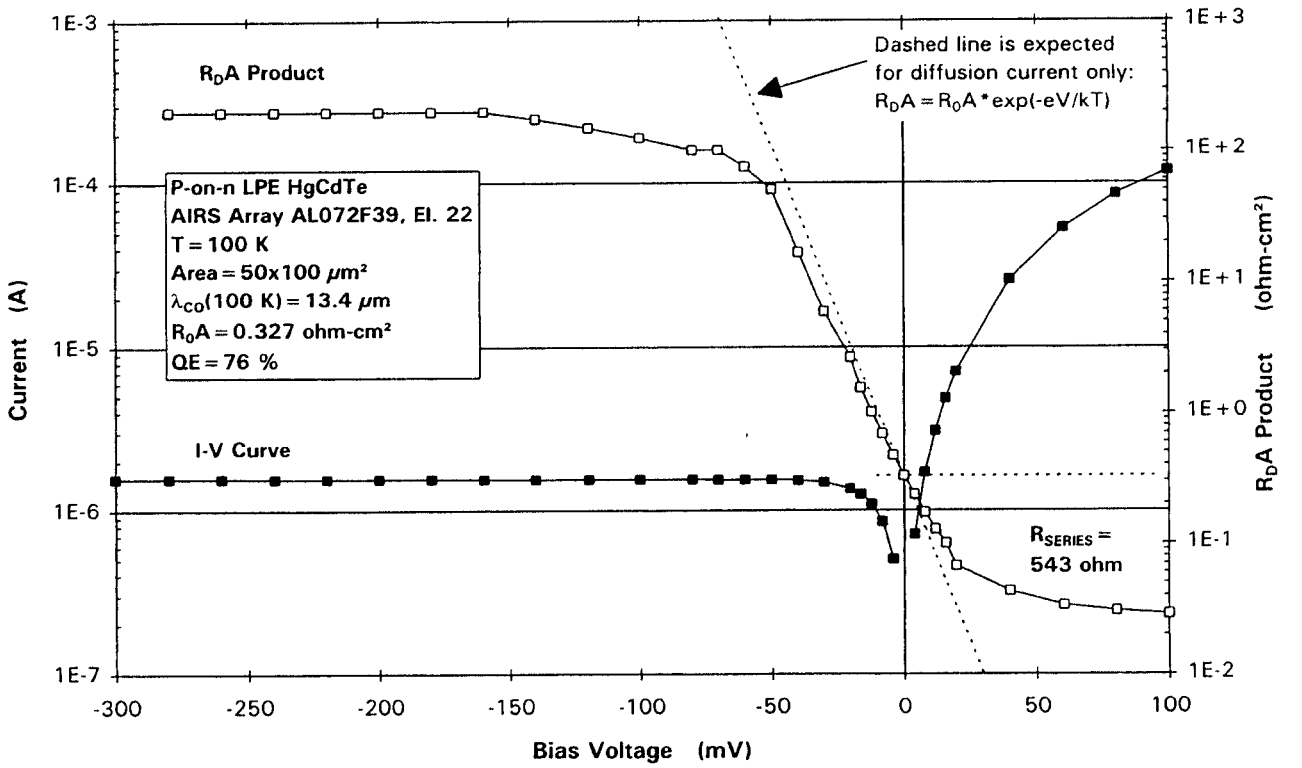

Figure 10. Current-voltage curves at T=100 K for an LPE P-on-n HgCdTe photodiode with a cutoff wavelength at 100 K of 13.4 μm.

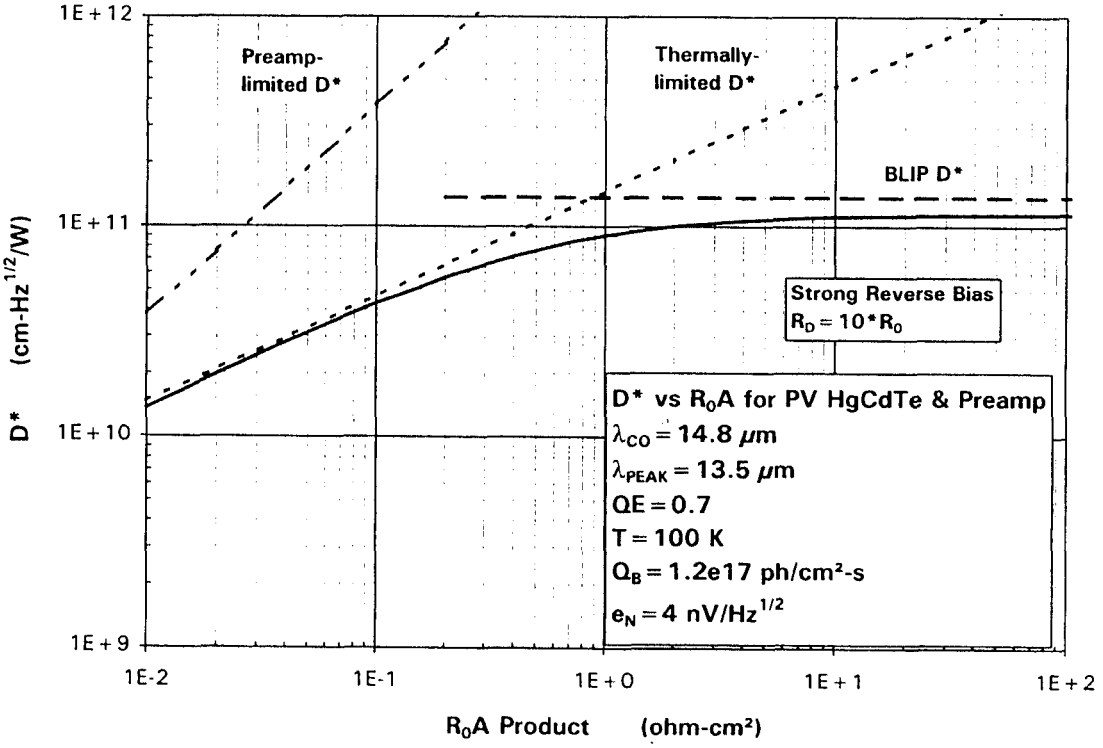

Figure 11. Calculated D* versus R0A product for a HgCdTe photodiode at T=100 K with a cutoff wavelength of 14.8 μm, for conditions representative of the GOES LW Sounder detector.

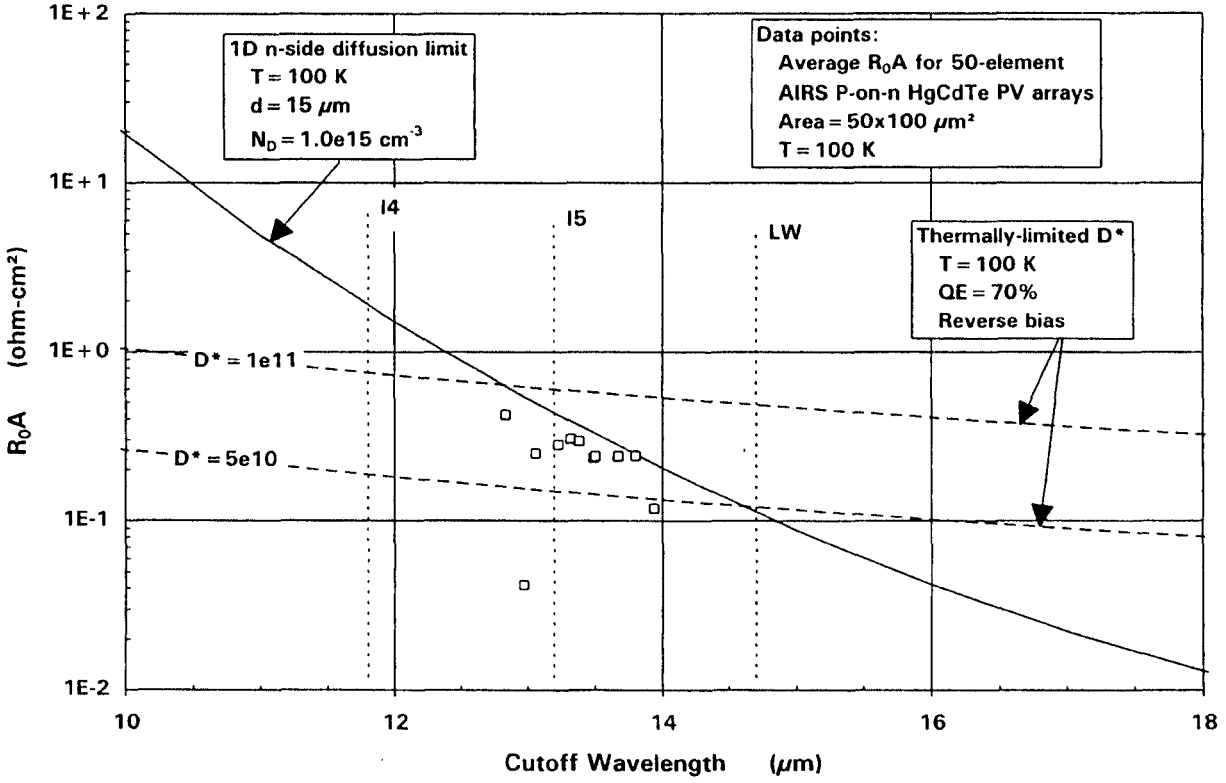

Figure 12. Summary of R_0A data at T=100 K for bilinear HgCdTe photovoltaic arrays, plotted versus 100 K cutoff wavelength. Each data point is the average R_0A for an array containing 20 to 100 elements.

Photoconductive HgCdTe Detector Assemblies for the GOES Imager and Sounder Instruments

J.M. Hartley, M.B. Reine, C.L. Terzis, A.J. Verrilli, R.T. Hassler, and E. Lesondak

Lockheed Martin IR Imaging Systems
2 Forbes Road
Lexington, Massachusetts 02173

ABSTRACT

The GOES Imager and Sounder Instruments each utilize several HgCdTe photoconductive (PC) detectors and detector arrays for detection over the to 6.5 to 14.7 μm region. These high performance detectors are integrated with germanium aplanat lenses and mounted in miniature hermetically sealed housings. There are demanding requirements on the radiometric performance of these detector assemblies. For LW Sounder detectors, the highest possible sensitivity achievable by a practical HgCdTe photoconductor at the operating temperatures of 100 to 105 K was required. Lockheed Martin designed, fabricated, tested, packaged, qualified, and delivered 7 of the 11 HgCdTe PC detector assemblies for GOES-8, and 9 of the 11 assemblies for GOES-9. All the n-type HgCdTe starting material was grown at Lockheed Martin.

This paper reviews the specification process, design, testing, packaging, and selection of the detector assemblies for the Lockheed Martin HgCdTe detector assemblies used in the GOES Imager and Sounder Instruments. We discuss the importance of the specification of HgCdTe detector assemblies to achieve the best match between the detector and sensor. The basic packaging considerations for ease of assembly, test, and instrument integration are also discussed. The levels of detector testing and the value these tests provide to the instrument integrator for diagnostic and long term science data are presented.

Keywords: Infrared detectors, mercury cadmium telluride, HgCdTe, GOES instrument, semiconductor devices, photoconductors

1. BACKGROUND

In February 1991, Lockheed Martin was contracted to build replacement HgCdTe photoconductive detectors for the GOES-I instrument with a six month delivery. The strategy Lockheed Martin pursued to fulfill this effort was to leverage our production experience and equipment from the Army Common Module program to change only what was necessary to meet the GOES objectives and minimize the risks of those changes. The approach was based on our ability to provide HgCdTe detectors with maximum uniformity, stability, and reliability in the minimum amount of time. Lockheed Martin used their own in-house design capabilities for photomasks and vacuum dewars to provide rapid turnaround of the hardware.

Existing test equipment was redesigned and modified for the five device types required. Because we grow our own HgCdTe material and maintain a large inventory of well characterized, high quality HgCdTe wafers covering a wide range of cut-off wavelengths, it was possible to design the detectors and start fabrication within two months of the contract award. Lockheed Martin also made use of its optical design and test capabilities to test the germanium aplanat lenses before mounting, and benefited from its experience in IR system modeling, and integration and test, to assist in selecting the best detectors for each instrument.

2. INTRODUCTION

The detector assemblies built for the GOES instruments fall into five categories. There are three devices for the Imager instrument and two for the Sounder instrument. Their device characteristics and the number of units required per instrument are described in Table 1. In total, 63 units of the five device types were delivered, including all of the Imager 3's and 4's, and the MW Sounders for all of the satellites. To perform quickly on such a diverse contract, it was necessary to approach the problem in a systematic way, starting with reviewing the specifications and using this information to design the detectors. A test approach to evaluate the devices must be chosen and the producibility of the packaging must be addressed to select the best detectors for timely delivery to the instruments.

0-8194-2200-2/96/$6.00

Table 1. Lockheed Martin IR Imaging Systems has made most of the HgCdTe Photoconductive Detectors for GOES-I and GOES-J Satellites

Band	Filter Wavelength Band (μm)	HgCdTe PC Detector Configuration	Element Area (μm^2)	Number of Units Required	GOES-I (GOES-8)	GOES-J (GOES-9)
Imager I3	6.5 - 7.0	2-element array	100 x 100	1	Lockheed Martin	Lockheed Martin
Imager I4	10.2 - 11.2	4-element linear array	50 x 50	1	Lockheed Martin	Lockheed Martin
Imager I5	11.5 - 12.5	4-element linear array	50 x 50	1	Judson	Lockheed Martin
Sounder, MW	6.2 - 11.8	single element	75 x 75	4	Lockheed Martin	Lockheed Martin
Sounder, LW	11.2 - 15.4	single element	50 x 50	4	Lockheed Martin: 1 Judson: 3	Lockheed Martin: 2 Judson: 2

2.1 Specification review

When designing a sensor, it is important to have a model to project the end system performance. The model utilizes the performance of the subcomponents under the operational conditions of the instrument. In a detector specification, the system designer must define operating temperature, background photon flux, detector size and configuration, maximum bias power dissipation allowable, and preamp noise voltage. The spectral bandpass to be covered and the number of detectors needed for coverage are also required. This information must be established prior to the design of the specific detector device.

For HgCdTe, the peak response of the detector performance is within 10 - 12% of the cutoff wavelength. After the system spectral filter is defined, the detector designer chooses the material cutoff wavelength to be 10 -12% longer than the system filter bandpass. This guarantees the filter cutoff is controlling the system response, not the detector cutoff. The bandpass for the long wave (LW) Sounder is defined to be 2.7 μm wide. Narrow spectral filters split the broader bandpass into seven individual channels. The LW Sounder's longest channel was specified at 14.7 μm. One of the difficulties encountered with the LW Sounder performance requirements was a combination of the long wavelength cutoff (16.17 μm), and the width of the bandpass to be covered.

Figure 1 shows the response curve of an HgCdTe detector. Note that the normalized response falls off at the shorter wavelengths and, over the 2.7 μm waveband of the LW Sounder, the response varies by up to 10%. Combining this response variation with the fact that the maximum attainable detectivity, D*, decreases with increasing cutoff wavelength, the amount of performance in channel 1 (the longest channel) vs. the performance in Channels 6 and 7 (near 12.5 μm) became a serious system level trade.

The performance in Channel 1 could be maximized only at a cost of reduced D* in Channels 6 and 7. It became an issue for the science team to select which area of the spectrum was of greater interest to the community. Because this decision was made after the detectors were fabricated, the opportunity to select material with a cutoff to optimize detector performance for Channels 6 and 7 never occurred. A potential solution to maximizing performance across the entire LW Sounder waveband would have been to split the bandpass over two separate detectors, each with a narrower bandpass. This was not viable for the detector retrofit portion of GOES NEXT, although these issues should be considered when designing additional instruments using long wavelength detectors.

Figure 1. Longwave HgCdTe Spectral Response from a Detector Fabricated at Lockheed Martin

2.2 Detector design

To design each GOES device, the Lockheed Martin photoconductive detector model was used. The sensor defined criteria, plus HgCdTe material characteristics and process-related parameters, are used to predict detector performance prior to fabrication and test. Detector design inputs to the performance model include the cutoff wavelength, the active area length and widths, contact extensions at both the positive and negative contacts, if required, and the antireflection (AR) coating thickness. Process-dependent parameters which effect detector performance, such as detector thickness, quantum efficiency at the peak response, surface recombination velocity, surface passivation conductance, and 1/f noise coefficient, are used in the model. These parameters are fed into the design of the different photomask layers and the choice of fabrication processes. The HgCdTe material characteristics used in the model are the measured FTIR cuton at 300 K, and the HgCdTe alloy composition, donor concentration and the electron mobility in the HgCdTe at 77 K. These material characteristics are used to choose the HgCdTe wafers to be processed from inventory. The model is used to predict detector performance. Some of the outputs include predictions of peak wavelength, detector resistance, bias power dissipation, detector response time, detectivity (without 1/f noise), and the voltage responsivity. Estimates of the noise characteristics such as the g-r noise voltage, Johnson noise voltage, 1/f noise voltage at 1 Hz, and the 1/f noise corner frequency are also generated by the model.

The information from the model is used for determining photomask layout and array processing steps, including the choice of passivation techniques utilized. As the GOES contract progressed, it became clear that detector arrays with higher performance levels than originally specified would be required to meet instrument performance. Using the detector model, and feeding back detector data from the early processing lots into the model, provided a method to initiate thoughtful changes to the detector designs to optimize performance, rather than a trial and error approach to better devices. Figure 2 shows how the detector performance changed to fit the changes in the LW Sounder specification. Lot 3 reflects the original specification. A change in the material selected and the extended contact mask increased the performance in Lot 6. Lot 9 data reflects a different passivation process from the earlier fabrication lots. Lots 13 and 15 contain devices where the active area was increased to increase the optical throughput of the system. Higher bias currents were required to reach performance levels equivalent to the smaller devices, due to the increased detector width. The performance of these devices became limited by the maximum power dissipation allowed. Detectors from Lots 6 and 9 are flying on GOES I and J.

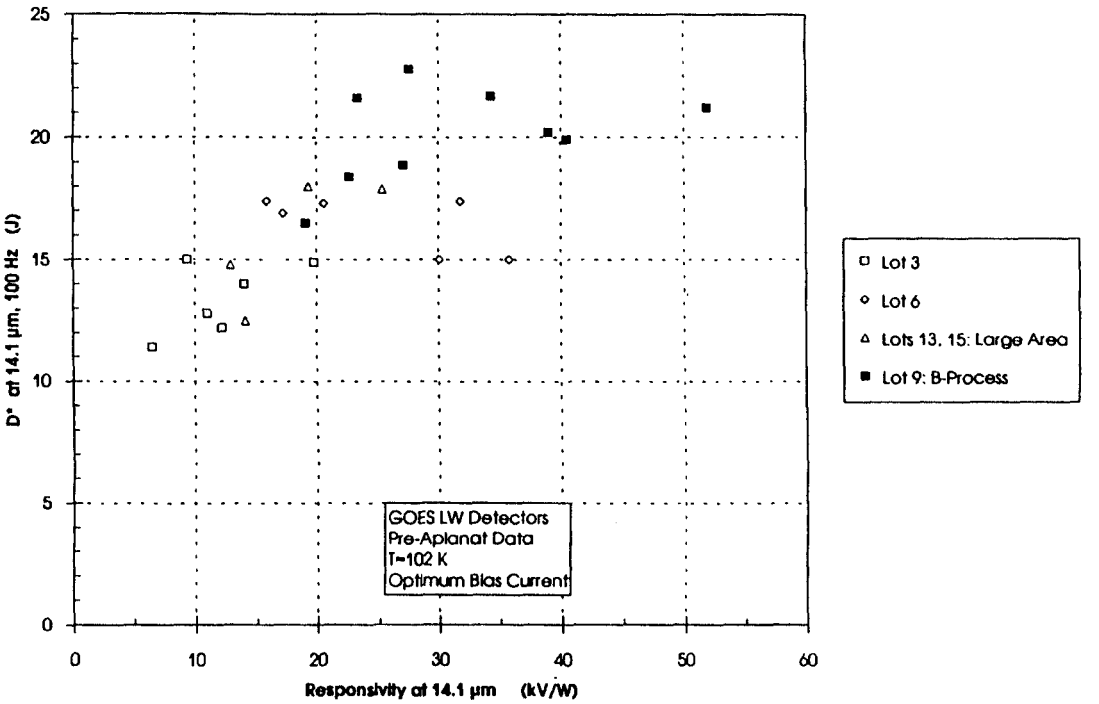

Figure 2. LW Sounder Performance Reflects Changes to the Specification

One portion of the detector design that does not come from the model is the physical dimensions of the die. The length of the die is determined by the distance required from the active area to the wire bonding pads. For single elements and very small arrays, the minimum width is determined by the smallest width that is mechanically stable; that is, the die must be wide enough to stand up on its own. Since the active area for the GOES detectors used only a fraction of the mechanically stable die, it was decided to use this dead space to replicate additional elements with different extended contact configurations. The minimum die size could support four elements. The Sounder devices each consist of a single element. Imager 3 is a two-element array, and the Imager 4 and 5 are four-element arrays of identical layout. Each of the final housing designs had sufficient space to allow for aligning any good detector, or array, on the die to the system interface. The Imager 4/5 housings could support a double die, one with two sets of four elements. This allowed every die to contain detector elements with at least two different extended contact configurations to help optimize detector performance (shown in Figure 3). Large quantities of data could be generated on each detector fabrication lot. This feature, combined with the ability to test at the wafer level, allowed the rapid learning curve needed for the original contract's short schedule and generated a large data base for optimizing performance.

2.3 Detector test and assembly

Because of the enormous amount of data required and the need for short turnaround time, Lockheed Martin treated the test planning structure as though it was a production program. A baseline was designed and modifications made for device-specific requirements. A common baseline for the software for all five devices reduced the cost of the software and the time required for bringing five sets of software online. All data sets contained information at both the Imager and Sounder test frequencies. Baseline software for the wafer cryoprobe equipment and one of Lockheed Martin's production test stations was written and debugged, prior to device specific modifications, such as active area size and appropriate constants being made. Data was taken automatically at multiple biases and frequencies. This data matrix was generated for rapid selection of optimum operating bias, provided a flexible diagnostic tool for detector processing and later, was used at an instrument level to choose detectors for optimum sensor performance. A standard reference detector was run each day to verify the test station's operation. The reproducibility of the data from the standard eliminates wasted time by separating detector test results from test station anomalies. A top-level flow chart for the Imager devices is shown in Figure 4.

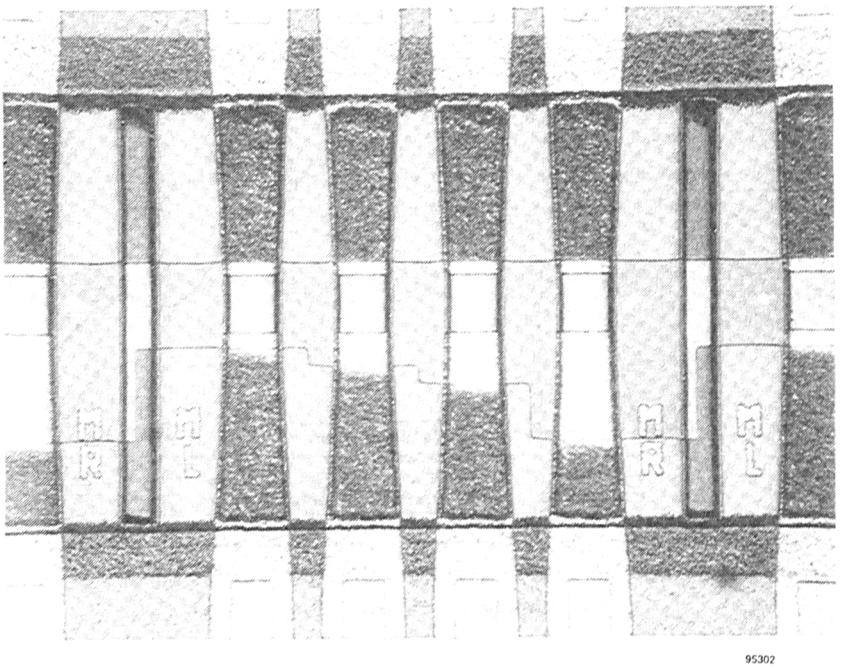

Figure 3. Detector Performance Optimized with Extended Contact Configurations

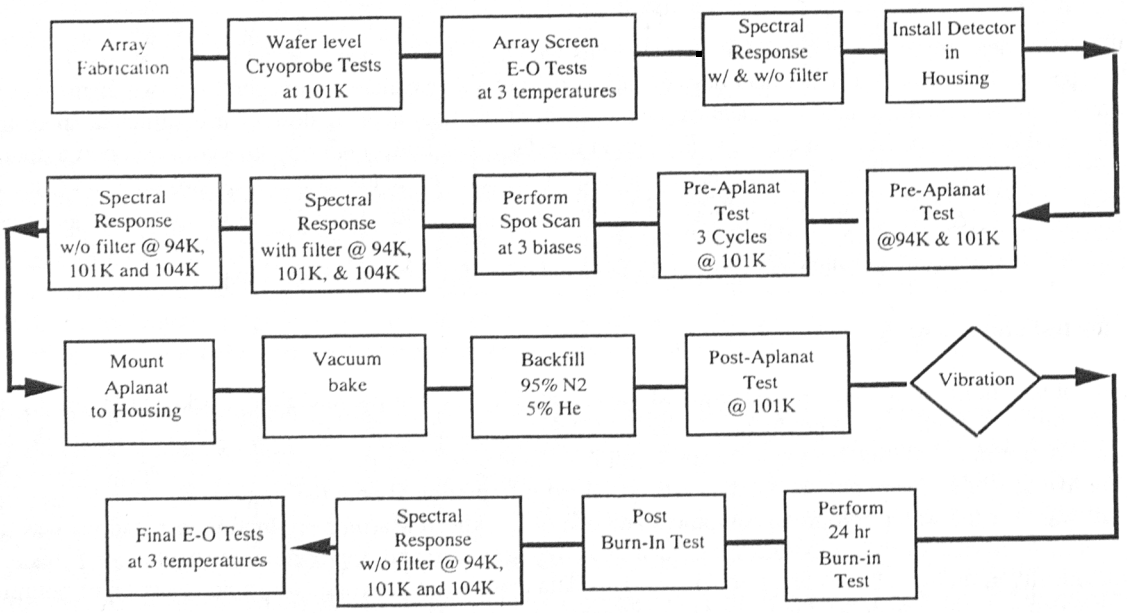

Figure 4. Top-Level Flow Shows Major Test and Assembly Points

The detectors were fabricated on the standard production line using customized processes when extra performance was required. The wafers were then moved into a wafer level screening, similar to the procedure for silicon processing, but performed at cryogenic temperatures. Then, the best die were diced from the wafers and mounted into pin grid arrays (PGAs) for further radiometric tests and spectral response testing. The selected detectors were mounted in the final housings and returned to test, prior to the mounting of the aplanat lens. Radiometric and spectral measurements at multiple temperatures were performed. For the Imagers, the radiometric testing was done three times at 101 K and once each at 94 K and 104 K. The spectrals were recorded with and without the filters at all three temperatures. Spot scans at multiple biases were used to determine the active area sizes for each element. After a source inspection, the aplanat was installed in the housing, and the unit was vacuum baked and backfilled with nitrogen and a helium tracer. The unit was then returned for radiometric tests at a single temperature only, sent for a vibration test to verify workmanship, and then a operating burn-in cycle at liquid nitrogen temperatures. The final series of tests repeated the radiometric measurements and the spectrals without filters.

One of the benefits brought from Lockheed Martin's production experience was using our cryoprobe test equipment, which allowed for a nondestructive, 100% screening, of the detectors at the wafer level. The existing equipment was modified to operate at operating temperatures for the Sounder or the Imagers. The cold shielding was modified for operating backgrounds between 3E15 -5E16 ph/cm/s. Software changes were made to increase the detector bias range and to allow for application of negative biases. This feature allowed for testing of different extended contacts lengths on the positive and negative sides of the device to establish the effectiveness of different contact extensions. The data output included responsivity and signal at 1 KHz, bias current, resistance, power dissipation, and 4 KHz noise. D* data was acquired at seven frequencies. These included 4 KHz, which is above any 1/f corner frequency; 500 Hz and 250 Hz, the test frequencies for the Imagers; and 100 Hz and 40 Hz, the test frequencies for the Sounders.

Other software features included the ability to easily change the detector area and background flux with each type of device tested, and the screening thresholds and defect codes installed for sorting out good die without reading each piece of data. If it were assumed an average wafer had 64 double die to be tested, with eight elements each, and that originally each element was tested at 8-bias currents, there were 28,672 pieces of data to be addressed for each cryoprobe test run. The defect codes allowed for rapid selection of the best devices, which were then diced out and sent for test dewar screening. The original defect codes identified pass/fail for D* at the two specified frequencies, power dissipation, and blackbody responsivity. As the detector requirements were changed and more was known about which information was useful for each individual detector type, the cryoprobe software was revamped to reduce the number of biases used and customized the choice of biases for the specific device type. The longest possible detector lifetimes were required in order to try to meet the newer specifications. A new figure of merit was added to the cryoprobe software (called $\eta\tau\zeta$ or zeta), which provided a measure of normalized detector lifetime. Zeta removed the bias current and the detector resistance from the detector lifetime calculation. The new defect codes for zeta increased the ability to identify die which would meet the newer specifications at wafer probe. This information was summarized into wafer tables and maps for array selection and further analysis. The selected die were then mounted into test dewars for radiometric and spectral testing with the channel-specific filters.

For array screening, the best die were mounted into PGAs for testing in liquid nitrogen dewars into which heaters and temperature sensors were installed. The purpose of this testing was to reproduce the final flux levels the devices will see as closely as possible before committing the die to the final housing. Up to 16 die could be tested in each PGA for screening of the single-die configuration devices, the Sounders and the Imager 3's. Eight each of the Imager 4 and 5 die could be tested. This maximized the number of detectors which could be tested on each cooldown cycle, thus increasing the throughput. After the first few screening cycles of each device type, the cryoprobe data were correlated to the dewar test data. Over time, it was shown that the best detectors could be found from the wafer level tests and that the array screen was needed only for differentiating the finer points between devices.

Standard formats on the detectors allowed for common test hardware and software. To facilitate the quantity of performance testing required, Lockheed Martin made use of its standard test dewar with wiring modified for GOES. With five physically similar, but spectrally different devices, careful attention was paid to correctly reproducing the flux levels for each device. The cold shielding for array screen and the pre-aplanat detector testing represented the flux levels seen in the sensor at the focal plane, whereas the flux levels at post-aplanat test reproduced the energy deposited on the outside of the aplanat lens in the instruments. Because the major mechanical aspects of the detector housings were common for the three Imagers and common between the two Sounders, the test fixturing for the Imager devices was common to all Imagers. The Sounder devices had fixtures common to the Sounder housings. The MW and LW Sounders had waveband-specific cold shields and apertures. The

bandpass filters, which were different for each channel, were mounted into fixtures specific to each device. Flight filters were used for the Imager channels and the larger radiator windows were used for Sounder testing. All test dewars were interchangeable between all devices, Imager or Sounder. This allowed for rapid turnaround of devices at radiometric test. After radiometric and spectral testing, the chosen die were mounted into their final housings.

At the beginning of the program, it was decided to standardize the housing designs. This reduced the complexity of building multiple device types simultaneously. The redesigned housings were common between the Imager 3, 4, and 5's and between the Sounders. As discussed above, standard housings allowed for common fixturing for performance testing and assembly. Standardization of the housing packages for all of the Imager and Sounder units led to faster turnaround of the housings for the short schedule. For the Sounder housings, only the height between the aplanat seat and the detector mounting surface was different. Differences on the Imager packages were limited to the number of pins (four on the Imager 3 vs. eight on the Imager 4 and 5 packages), and the position of the locating pin hole. The position of the evacuation tube was changed to increase the producibility of the design. Another change was the reduction in the pin circle for the Imager housings, to eliminate an interference between the holes for the pins and the aplanat mounting surface. All parts were completely interchangeable with previously existing devices. An example of the final Imager and Sounder devices are shown in Figure 5.

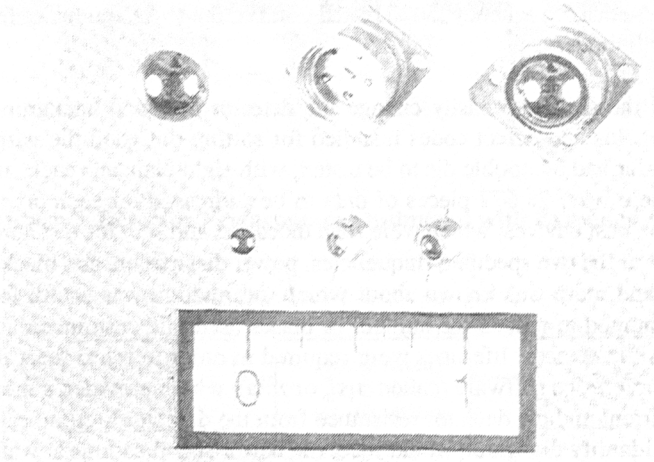

Figure 5. TOP: Imager Aplanat Lens, Detector Mounted in Housing and Final Imager Device BOTTOM: Sounder Aplanat Lens, Detector Mounted in Housing and Final Sounder Device

To provide reliable operation for up to ten years in space, Lockheed Martin treated the backfilled detector housing as though it were a vacuum housing. All seals are hermetic. Electrical feedthroughs are glass-to-metal sealed, similar to those used on the production programs. The housing is closed off with a copper evacuation tube, typical of all Lockheed Martin programs. The aplanat lens is sealed with an approved, low outgassing, epoxy. A desirable feature of all housings is the aplanat lenses self-jigging into their mounts, which makes for easy and accurate installation. There is only one position for each aplanat to sit into the housing, and the tolerances on the mounting diameter guaranteed the aplanat would be correctly centered over a properly aligned detector.

Housing standardization allowed for modular assembly tooling. A common carrier was used for alignment of the detector array into the housing, wire bonding, and aplanat installation. These carriers referenced the mounting surfaces of the housings to the alignment microscope and wire bonders. All assembly and inspection operations were carried out with the housings mounted in the carrier, and multiple units could be mounted in each carrier to increase throughput at each assembly step. The assembly and test tooling were designed with respect to the same mounting surfaces used by the instrument, assuring reproducibility of results between measurements made during the detector build and those required during instrument integration.

One aspect of the housing design which would have made both detector testing and instrument integration easier would have been the installation of temperature sensors inside each detector/aplanat/housing assembly. The original GOES design did not have extra pins to allow for them and, as these were direct replacements for the existing design, temperature sensors could not be added. The detectors are extremely sensitive to changes in temperature. Detector resistance, and therefore the voltage across the detector, changes with temperature. Accurate performance data are dependent on knowledge of the actual test temperature. A separate temperature sensor would allow knowledge of the temperature independent of using each detector's resistance.

2.4 Detector selection for system usage

When designing a sensor, it is important to have a model that uses the performance of the subcomponents, under the operational conditions of the instrument, to project the end system performance. Originally, this model is used to create the component and subsystem performance specifications. After the initial design phase, this model should be continually upgraded to reflect the actual measured performance of those subcomponents. One of the most significant aspects of the GOES detector contracts was the vast amounts of testing done on the detectors. These devices have had more test data taken on them than any other PC device ever built at Lockheed Martin IR Imaging Systems. The data were fed back into the various sensor models to improve the prediction of instrument performance.

When setting up the system model, thought needs to be given as to which figures of merit will be used to determine the "goodness" of each component. It is highly desirable that the data requirements passed down to the detector vendor, for example, include those parameters that can be fed back into the model for verification. Some of the models for the GOES instruments included the spectral response over the band of interest, active area size, the detector resistance and responsivity, and the area weighted measure of detector output signal. System designers often desire to see the detector data reported in a format familiar to them, that is, report the data in terms of NEDT. When system level parameters, like NEDT, are used to describe detector performance, potential for calculation errors is introduced which can create errors in the system performance prediction when the faulty data are used. It is important for the system designer to define the detector performance in terms of standard detector level test parameters. The detector data should be reported in terms as close to the actual measured signal and noise as is reasonable to reduce the chance of misinterpretation.

It would be desirable to test detectors, and report their performance, measured under a focused incoming beam which replicates the system optical path. In this situation, one has to choose different figures of merit to correctly use this information. All current detector performance figures of merit are defined to be under flood-illuminated conditions; therefore, the figures of merit, D* for example, become meaningless for a focused beam situation. Although creating figures of merit for the focused beam test configuration is under discussion in the industry, there is no current standard. The most accurate method for determining how a detector will behave under the focused beam case is to build a simulator which replicates the behavior of the actual optical system. To correctly predict the behavior of the devices for the GOES instrument, the program made use of Lockheed Martin's optical and mechanical departments to design and build simulators which replicated the two Sounders and the Imager 5 optical chains. The system engineers used the information from these simulators, in conjunction with the flood-illuminated detector data and the models, to choose the detectors that would operate best with the optical and electrical characteristics of the specific instrument.

The measurements made on each of the final GOES devices included D*, responsivity and noise at multiple frequencies, and spectral measurements, all at multiple temperatures. The temperatures represented the nominal operating temperature and the expected temperatures at beginning and end of instrument life. The spectral response of each element was recorded with and without the filters at all three temperatures. This data can be used to calibrate out the effects of radiation on the filters over the service life of the instruments. Spot scans were taken to determine the active area sizes for each element. All of this information was plugged into the system models and used to select the specific devices to be used on the GOES instruments.

The enormous quantity of testing on each device, partially described in Figure 4, was reformatted for use in selecting the best devices for each instrument. As part of the detector selection meetings, hundreds of graphs were created showing responsivity and low frequency noise vs. bias current, and the ratio of responsivity to the noise vs. bias current, for test data taken both before and after the mounting of the aplanat lenses. Because the GOES instruments, particularly the Sounder, operates at such low frequencies, the amount of low frequency noise and the location of the knee frequency was a critical parameter in predicting the instrument performance. Detector noise was measured at seven frequencies on all Lockheed Martin detectors

and all devices considered for flight use to identify the 1/f knee. The pre-aplanat noise at 10, 20, 40, 100, 250, and 500 Hz was plotted against bias current to choose the optimum bias for the detector as it will operate in conjunction with the system noise. The multiple bias and multiple noise frequency data allowed for the trade-off of signal-level with the signal-to-noise ratio. All of this data was plotted for every HgCdTe detector available for mounting into the Imager and Sounder instruments.

The value of having this data available for review to allow the system integrators to choose the detector with the most desirable characteristics is undeniable. The issue here is that very little of the data which was used at the time of detector selection was required to be taken or recorded. The actual specifications required data only at the optimum bias, as chosen by the detector vendor using his own test preamps. These preamps are often a factor of two or more better than the preamp noise in a real system with long cable runs, where additional noise can be picked up. The specification required data at only two noise frequencies; 40 and 100 Hz for the Sounders, and 250 and 500 Hz for the Imagers. It was only because Lockheed Martin chose to approach the contract as if it was a production order, use the single baseline for all five sets of software, and use programmable test equipment, that the multiple bias/multiple-frequency data was available for the detector selection meetings. The value of this type of data has made this the standard test approach for our remote sensing detector contracts.

3. CONCLUSIONS

We have reviewed how the correct specification of the detectors is a direct outgrowth of the system design and modeling efforts. It is recommended that the system model should utilize standard detector performance parameters to reduce the potential for calculation errors, which will create faulty system level performance predictions. The discussion of the detector design process shows how changes to the requirements after detector processing has started results in new fabrication runs, as the material selection and photomask design are critical to determining detector performance. The basic packaging considerations for easier assembly and test were discussed along with issues associated with instrument integration and test. It is shown how a solid test plan can maximize the amount of data taken in the fewest cooldown cycles, provide the data for in-process diagnostics to optimize detector performance and yield, and provide the information required to select the best device for the instrument. The value of correctly specifying all the detector test parameters to be reported can be seen in having the information available for selection of detectors, integration diagnostics, and assuring the long term science objectives are met.

4. ACKNOWLEDGMENTS

The authors acknowledge the efforts of the personnel at Lockheed Martin IR Imaging Systems including Dave Weir, Larry Gauthier, Karl Gustavsen and Tony Tocci, who assembled and tested the GOES devices; Mike Coole, Douglas Kleinmann, and Tony Carita, who managed the effort; Peter McDonald, Rich Hassler and Curtis Vock for their work on the Lockheed Martin Sounder and Imager system models and sharing it with us, and Ed Andrews at ITT A/CD in Ft. Wayne, IN, for his efforts on our behalf. Credit should also be given to the work done by Dr. Daniel L. Mooney of MIT/Lincoln Labs, Dr. David G. Seiler of National Institute of Standards and Technology, and all those who served on the Detector Evaluation Team. This work was funded by ITT A/CD in Ft. Wayne and Space Systems/Loral in Palo Alto, CA under NASA/Goddard contract NAS5-29500.

5. REFERENCES

1. W. M. Higgins, G. N. Pultz, R. G. Roy, R. A. Lancaster and J. L. Schmit, "Standard Relationships in the Properties of $Hg_{1-x}Cd_xTe$," J. Vac. Sci. Technol. A7, 271 (1989).

2. D. G. Seiler, J. R. Lowney, W. R. Thurber, J. J. Kopanski and G. G. Harmon, "Improved Characterization and Evaluation Measurements for HgCdTe Detector Materials, Processes, and Devices Used on the GOES and TIROS Satellites," National Institute of Standards and Technology Special Publication 400-94, April 1994.

3. J. R. Lowney, W. R. Thurber and D. G. Seiler, "Transverse Magnetoresistance: A Novel Two-Terminal Method for Measuring the Carrier Density and Mobility of a Semiconductor Layer," Appl. Phys. Lett. 64, (1994).

4. R. B. Schoolar, W. E. Bicknell and D. L. Spears, "HgCdTe LWIR Photoconductor Technology Review and Performance Projections for GOES Imager-4, Imager-5, and LW Sounder," Aerospace Corporation Report No. ATR-92(2826)-1, July, 1992.

5. R. M. Broudy and V. J. Mazurczyk, "(HgCd)Te Photoconductors," Chapter 5 in Semiconductors and Semimetals, Vol. 18, edited by R. K. Willardson and A. C. Beer (Academic Press, New York, 1981).

6. M. B. Reine, K. R. Maschhoff, S. P. Tobin, P. W. Norton, J. A. Mroczkowski and E. E. Krueger, "The Impact of Characterization Techniques on HgCdTe Infrared Detector Technology," Semicond. Sci. Technol. 8, 788 (1993).

7. A. Jozwikowska, K. Jozwikowski and A. Rogalski, "Performance of Mercury Cadmium Telluride Photoconductive Detectors," Infrared Physics 31, 543 (1991).

High Performance HgCdTe Photoconductive Detector Assemblies for Space Applications

J. Ray Frederick , Joseph Kimchi and Theodore T.S. Wong
EG&G Judson, Montgomeryville, PA 18936

ABSTRACT

Advanced detector fabrication technology and high reliability packaging processes have been developed for the manufacturing of high performance HgCdTe photoconductors. These infrared array assemblies for use in GOES and other weather satellites operate at radiative cooler temperatures ranging from 95 to 115K. A large quantity of flight detectors sensitive to spectral wavelengths ranging from 7 to 16μm have been fully characterized. Detector performance data as a function of bias, temperature, frequency and cutoff wavelength are presented. A computerized model has been developed and reasonable agreements between computer projections and measured performance are obtained. This model has been used successfully to identify an optimum set of materials and device parameters for a given set of system requirements. In addition, advanced assembly and packaging techniques have been developed to ensure tight alignment tolerances, long-life hermeticity, low-outgassing and low internal reflection. Detector array assemblies have been demonstrated to withstand extensive qualification and environmental tests and the results are summarized.

Keywords: GOES, TIROS, HgCdTe, Photoconductors, Infrared Detector, Remote Sensing

1. INTRODUCTION

Remote sensing of the earth from geostationary orbit in the infrared presents several challenges to the detector vendor. First, to be able to detect small variations in temperature or radiance requires detectors with high detectivity (D^*) and responsivity (R_λ). Second, to be able to maintain these qualities over the entire spacecraft lifetime requires high reliability detector and housing design and assembly processes. Since many of these application require operation at 100K temperatures as well as detection of wavelengths as long as 15 microns, photoconductive Mercury Cadmium Telluride (HgCdTe) is the detector of choice for these applications. EG&G Judson is one of the very few detector vendors in the world that is qualified to build these high-reliability HgCdTe photoconductors which perform at the theoretical upper limits, giving our customers the highest performance and most reliable systems possible. Along with HgCdTe, we have been producing Indium Antimonide (InSb), Indium Arsenide (InAs) and Indium Gallium Arsenide (InGaAs) detector assemblies for spaceborne applications for over 12 years. Highlights of these programs are summarized in Table 1. In the following sections, we will discuss detector electro-optical performance projections versus achievements, packaging and assembly technology, and reliability demonstration under various environmental conditions.

	HALOE	**DMSP**	**GOES**	**ADEOS-IMG**	**TIROS**	**MTSAT**	**SABER**	**INSAT**
Applications	Atmospheric Chemistry	Defense Weather Satellite	Civilian Weather Satellite	Greenhouse Gases Monitoring	Meteorological Data Base	Japanese Weather Satellite	Atmospheric Chemistry	Weather Data
Detector	InAs	HgCdTe	HgCdTe	HgCdTe/InSb	HgCdTe	HgCdTe	HgCdTe/InSb/ InGaAs	HgCdTe
Spectral	2.5 - 3.4	9-13	8-15	6-14/3-5	10-15	6-7, 10-13	1.3 - 16	6-7, 8-14
Operating Temp (K)	190-210	105-110	100-110	65-90	95-110	95-101	65-70	105-115
Detector Size (μm)	600	85 X 36	50-100	2000	170 - 2100	50	2000 X 140	33
Packaging	Hermetic Window	Hermetic Window	Aplanat Lens Seal	Hermetic Window	Aplanat Lens Seal	Aplanat Lens Seal	Window Seal	Aplanat Lens Seal

TABLE 1: SPACEFLIGHT DETECTOR PROGRAM SUMMARY

0-8194-2200-2/96/$6.00

2. ELECTRO-OPTICAL PERFORMANCE

The objectives of this section are two-fold. First, we will present a computerized model and show that the computed performance matches very well with the measured data. Secondly, we will present typical results obtained on recent space qualified HgCdTe flight detectors operating under low background conditions at low frequencies and radiatively cooled temperatures. EG&G Judson's success in producing high performance HgCdTe detectors with excellent stability is a direct result of the processing technology we have developed. This new process is based on a successful synthesis of a number of technological breakthroughs achieved at EG&G Judson including advanced surface passivation, stable and off-material contacts, ion beam delineation, and stoichiometric anneals.

EG&G Judson has developed a computer model for analyzing HgCdTe photoconductors. Figure 2.1 shows the basic algorithm in which feedback loops are utilized. First, input parameters such as carrier concentration, alloy composition, detector dimensions, and test conditions are fed into the computer. The computer model then calculates performance using equations either based on first principle or empirically derived, with a set of adjusting parameters such as surface state density and surface recombination velocity. The computed performance parameters include detectivity, responsivity, noise, resistance, and detector time constant. The next routines simultaneously match all these performance parameters to Judson's measured data over a wide range of alloy compositions, operating temperatures, background levels, detector dimensions, and bias currents. When the matching reaches an optimum point among all the performance parameters considered, the feedback loops stop and the computation is complete. Reasonable convergence between computed performance and measured data over a variety of test conditions have been obtained. In many situations, detector performance reaches the fundamental limits of photoconductors.

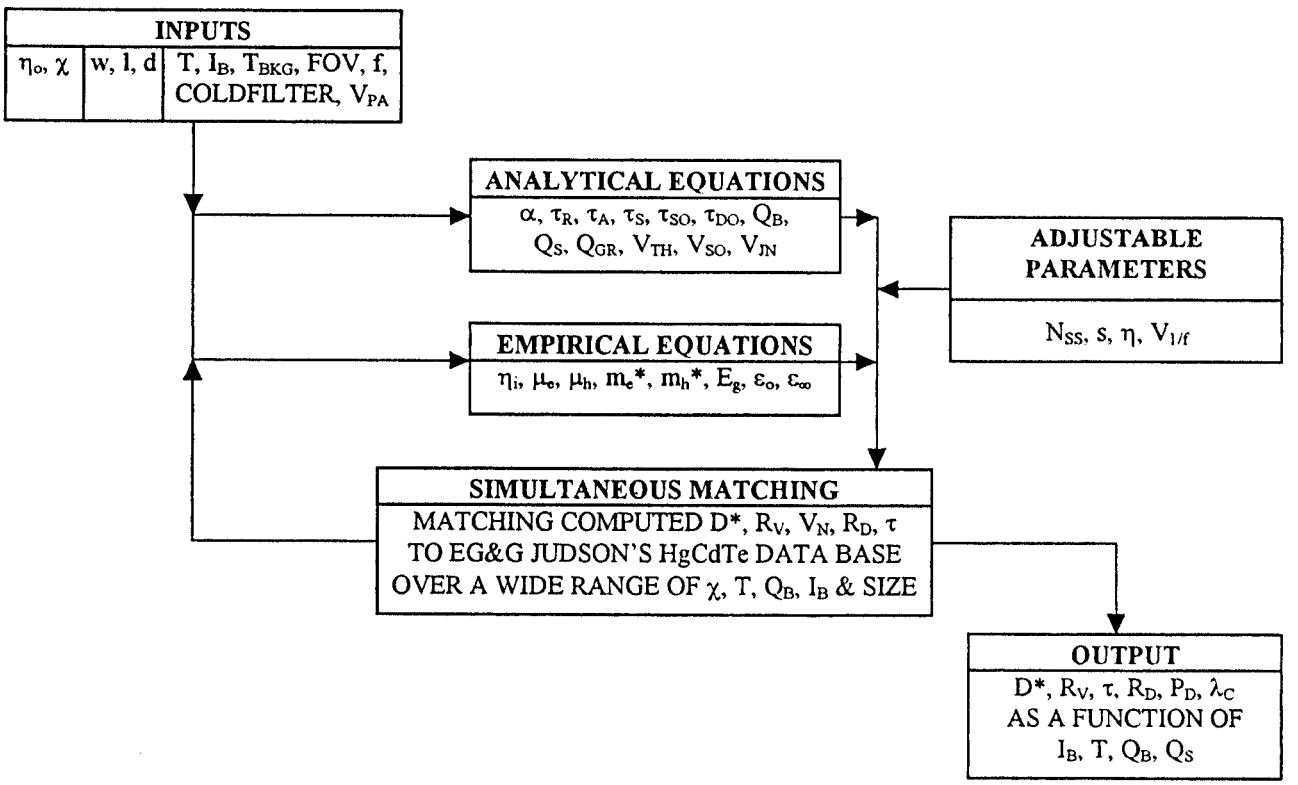

FIGURE 2.1 EG&G JUDSON'S HgCdTe PHOTOCONDUCTOR MODEL

Having briefly described Judson's computer model, we now focus on comparing calculations based on the model to long wavelength infrared (LWIR) HgCdTe data measured at temperatures from 77°K to 115°K. Figures 2.2 through 2.4 show detector performance versus temperature for 33 x 33 micron detectors with a cold field of view (FOV) of 71 degrees. Figure 2.2 compares calculated and measured detectivity at 500 Hz versus temperature from 77°K to 115°K. The solid squares are averages measured on 40 detectors and the triangles represent plus or minus one standard deviation. The dotted line represents calculated performance using a set of optimum parameters derived from the computer model. The agreement between data and computed performance is excellent. For a given alloy composition, the detector cutoff wavelength is an inverse function of temperature. Figure 2.3 shows both measured and calculated cutoff wavelength versus temperature. Again the agreement between calculations and measurements is exceptional. Figure 2.4 shows responsivity as a function of temperature. Not only that the agreement between data and theory is remarkable, the uniformity among the 40 detectors sampled, represented by the tight standard deviations, is strikingly good in view of the fact that no bias adjustment was made to match the signal response among the 40 detectors.

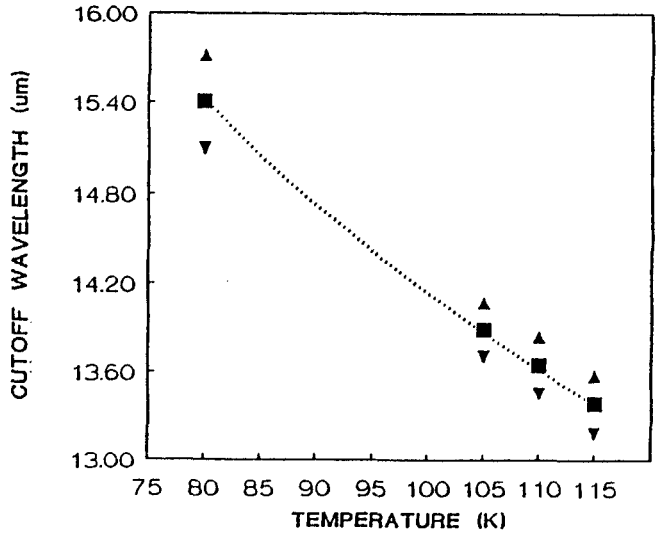

FIGURE 2.2. D* vs. TEMPERATURE

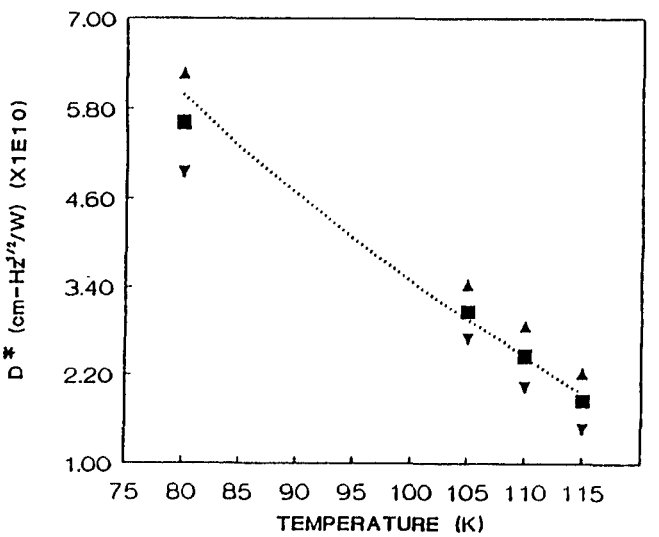

FIGURE 2.3. CUTOFF WAVELENGTH vs. TEMPERATURE

Figures 2.5 through 2.7 displays detector detectivity versus frequency for a series of different cutoff wavelength detectors that are 50 microns or less in size. Figure 2.5 shows the average detectivity for 14 detectors with a 9 micron cutoff at 105K with a 71 degree FOV. The various sources of detector noise are indicated in the legend. At high frequencies, D* is limited by the thermal g-r noise while at low frequencies, the D* is limited further by 1/f noise and the preamp used to measure signal and noise. Figure 2.6 shows the average D* for 38 detectors with a 13 micron cutoff under the same operating conditions as Figure 2.5. The 1/f knee, by definition, is the intersection of the g-r line and the 1/f line, and in this case is 150 Hz. Once again, the agreement between the model and data is very good. In Figure 2.7, the averaged D* for 30 detectors with a 15 micron cutoff at 102K with a 40 degree FOV is shown. These detectors have a 1/f knee below 60Hz, one of the lowest knee frequencies ever reported.

Figures 2.8 and 2.9 show D* as a function of bias power for 50 micron detectors. In Figure 2.8, average spectral D* at 250 Hz and 500 Hz for each detector is overlaid onto the model. In most cases, the spacing between the 250 Hz and 500 Hz data is no more than the spacing between the model lines, and the data distribution in this bias range follows the inverse relationship between bias and D* very nicely. Figure 2.9 shows the bias power dependency of the average spectral D* model at three frequencies with detector data points as indicated. Again, the data is grouped around the model with the frequency spacing agreement quite remarkable. Figure 2.10 presents D* versus wavelength data for 34 longwave GOES detectors with the projected spectral D* curves at 10Hz and 100Hz shown from 11 microns to 16 microns.

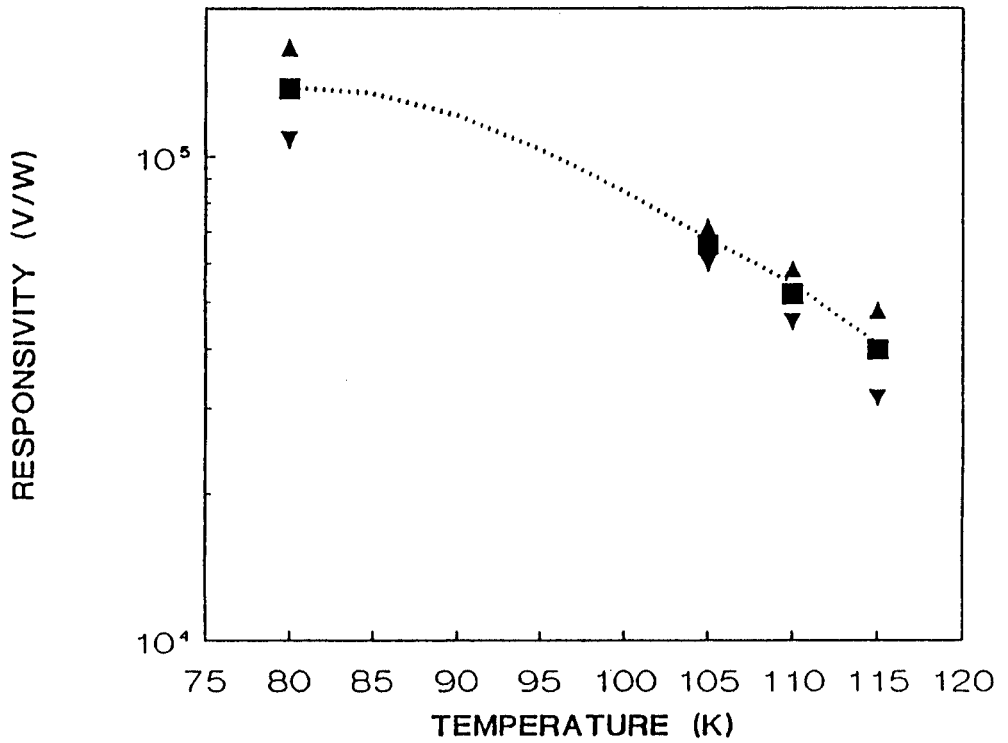

FIGURE 2.4. COMPUTED AND MEASURED RESPONSIVITY vs. TEMPERATURE

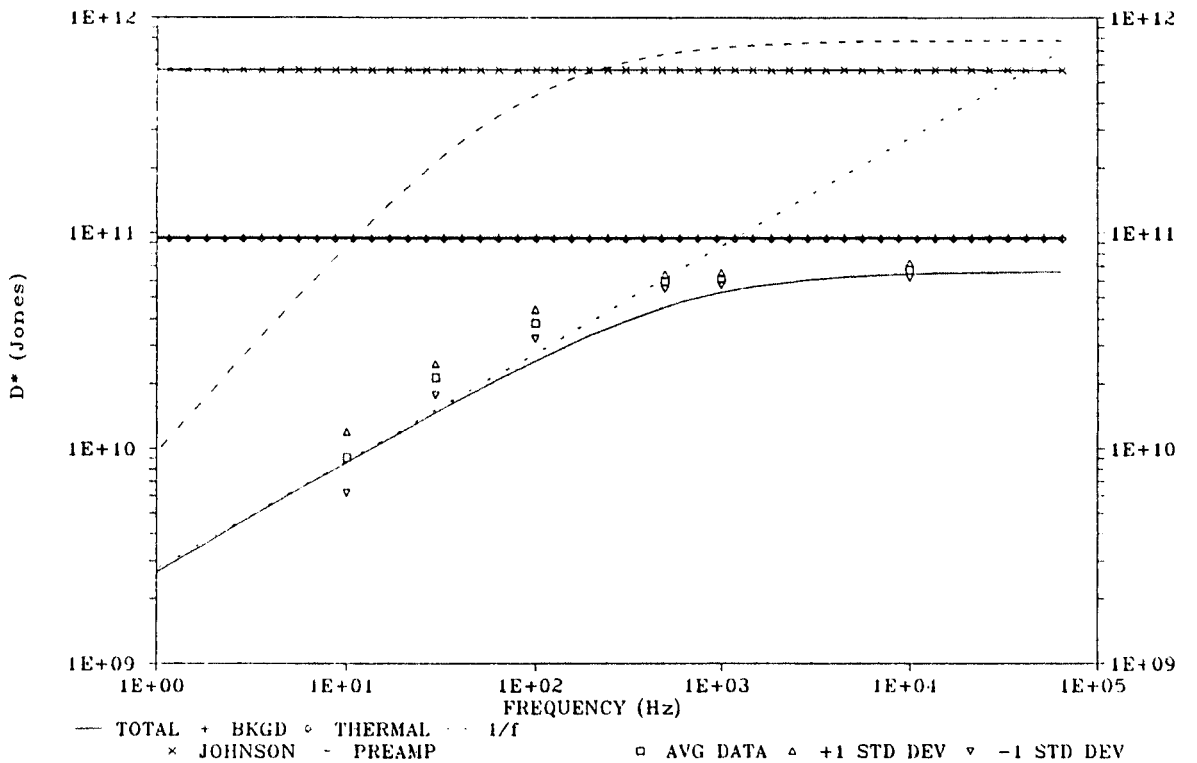

FIGURE 2.5. D* vs. FREQUENCY FOR 9 MICRON CUTOFF DETECTORS @ 0.5 mW BIAS POWER

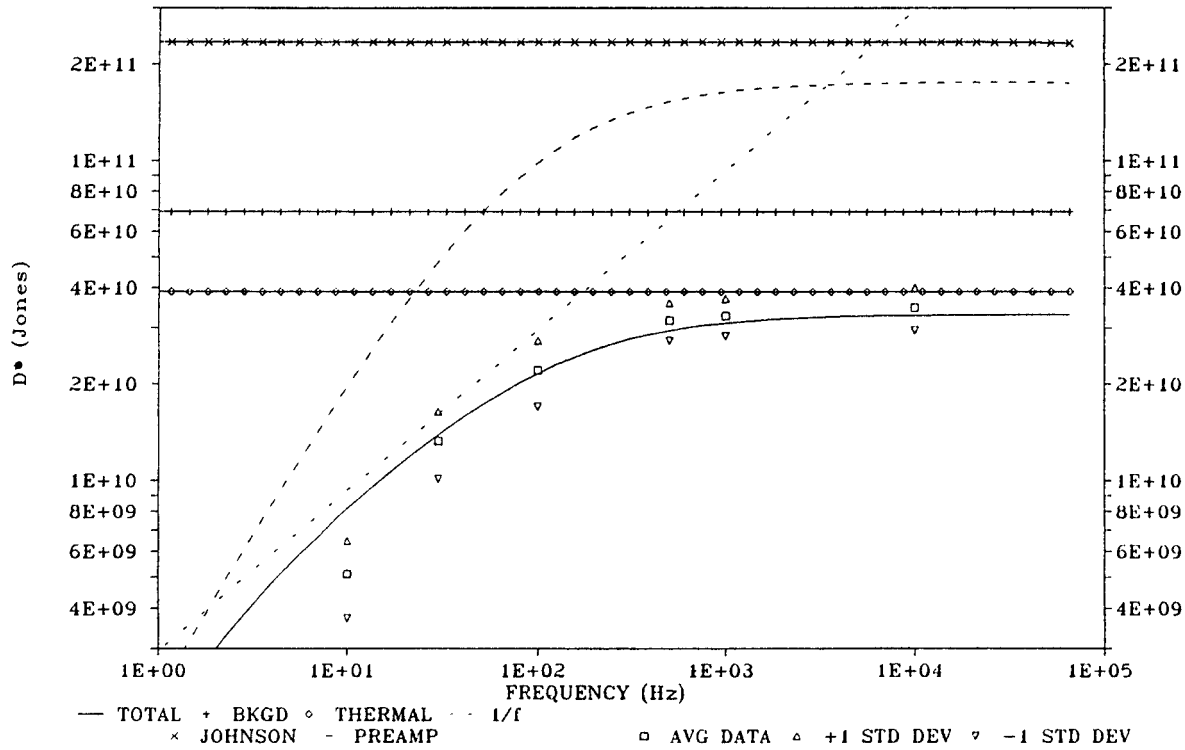

FIGURE 2.6. D* vs. FREQUENCY FOR 13 MICRON CUTOFF DETECTORS @ 0.5 mW BIAS POWER

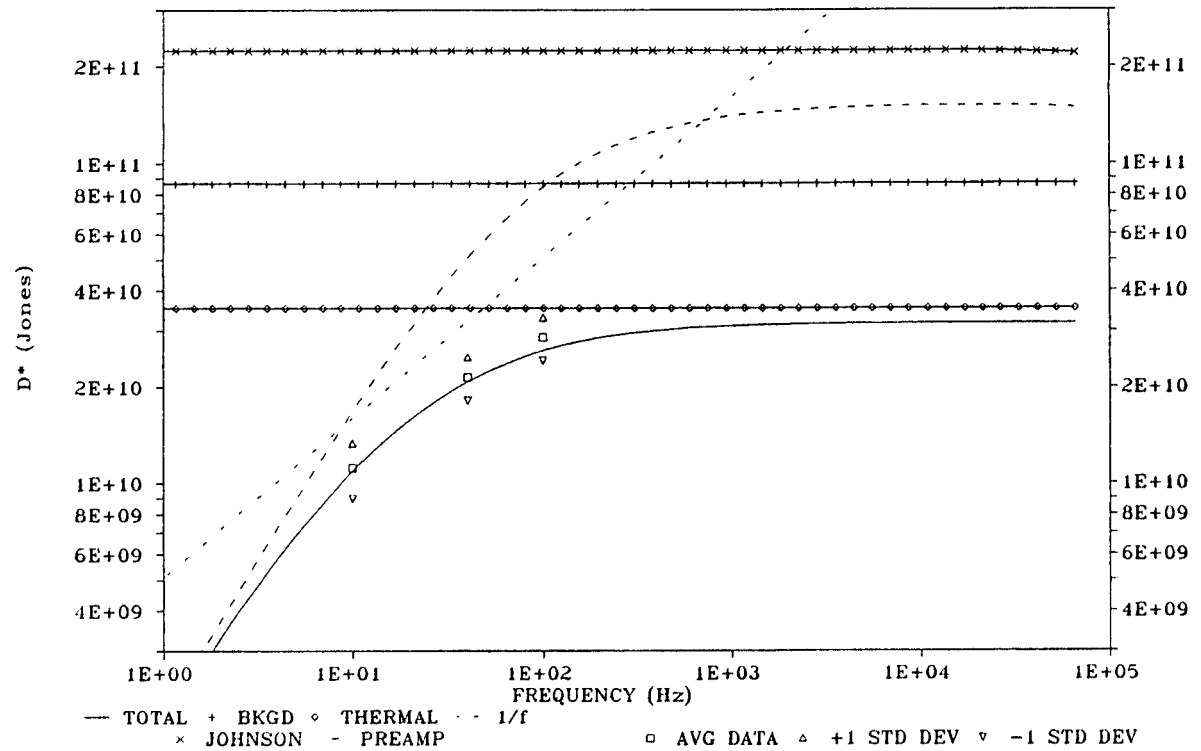

FIGURE 2.7. D* vs. FREQUENCY FOR 15 MICRON CUTOFF DETECTORS @ 1mA BIAS CURRENT

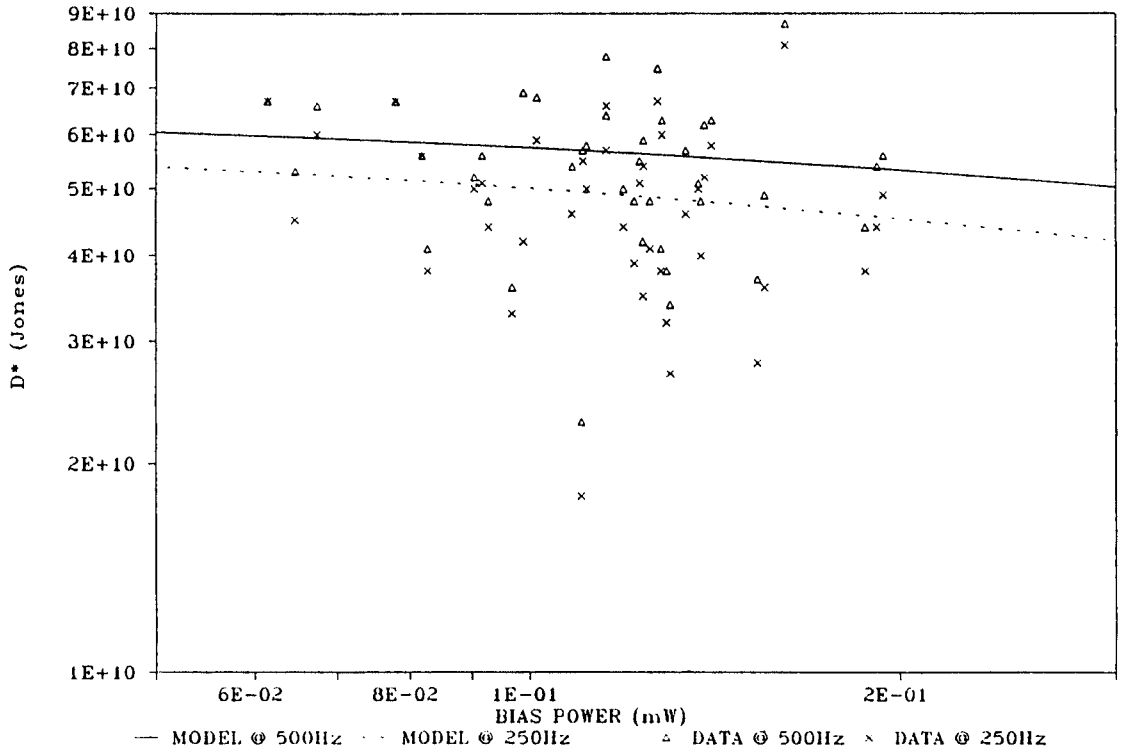

FIGURE 2.8. D* vs. BIAS POWER FOR 13 MICRON CUTOFF DETECTORS

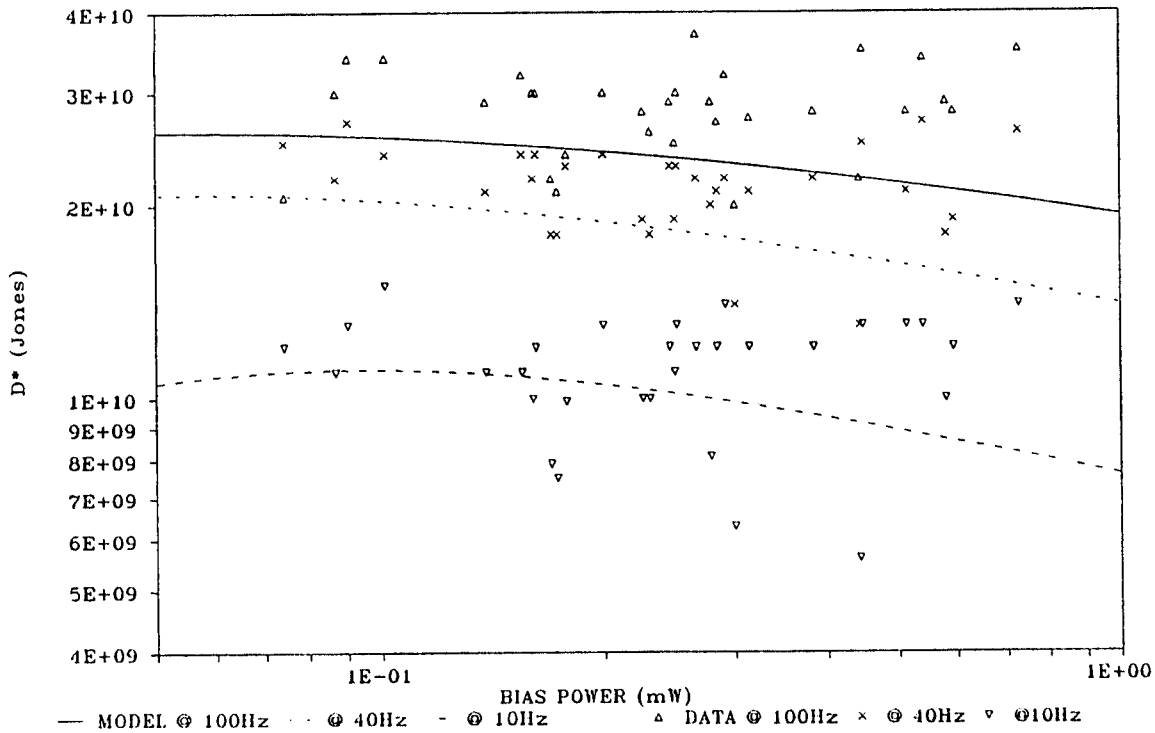

FIGURE 2.9. D* vs. BIAS POWER FOR 15 MICRON CUTOFF DETECTORS

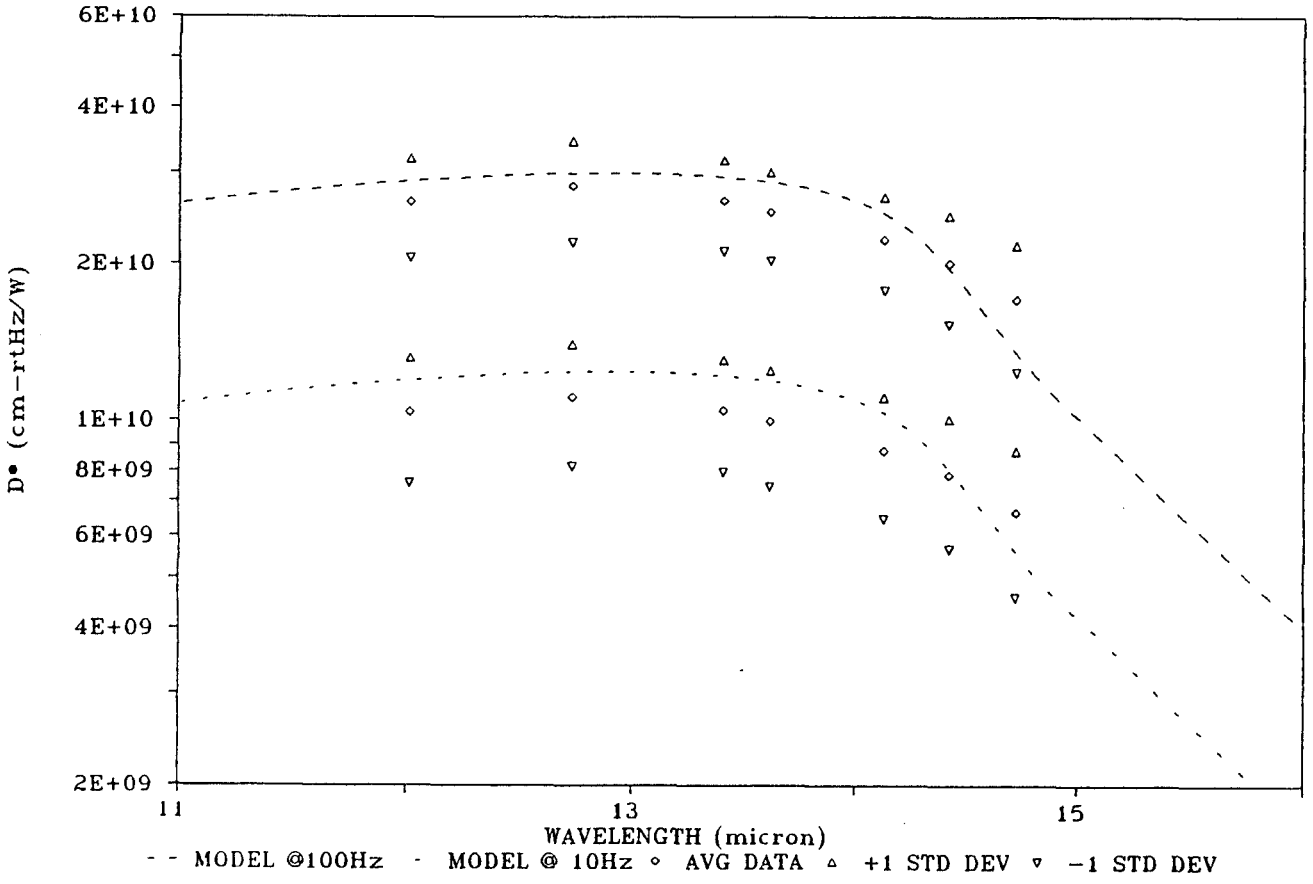

FIGURE 2.10. D* vs. WAVELENGTH FOR 15 MICRON CUTOFF DETECTORS

In addition to high D* performance, EG&G Judson also developed materials/processing technology which drastically improves spatial uniformity of HgCdTe photoconductors. Figure 2.11 shows the spatial uniformity achieved on a large area (1.6 x 1.6 mm), three cut-line detector with a cutoff wavelength of 17 microns at 95K. This data was taken with 8-12 micron radiation focussed into a 30 micron diameter spot with response measured on 100 micron steps across the entire detector. Over 40% of the active area is responsive within 10% of the maximum response point on the detector, remarkable for this long wavelength material.

In conclusion, HgCdTe photoconductors fabricated at EG&G Judson have achieved the ultimate performance limits of thermal gr noise limited D* at above 100K. In addition, detectors with excellent 1/f noise of less than 60 Hz knee frequencies have been demonstrated. A computer aided analytical capability has also been established which will enable us to conduct detector design optimization and systems performance tradeoff analyses. Process and material controls are in place that yield detectors with exceptional spatial uniformity of response across the active areas as large as 2.2 x 2.2 mm.

3. RELIABILITY

Quality performance not only demands optimum sensitivity, it also mandates product reliability. The stability of the HgCdTe detector is affected by at least three factors in the fabrication process. The first one is surface passivation/encapsulation. Because of the high mercury vapor pressure and the weak molecular bonding energy associated with HgCdTe, the detector surface can decompose with time even at room temperature. EG&G Judson has developed a surface treatment coupled with a stoichiometric anneal resulting in a process which not only passivates the detector surface, reduces 1/f noise and preserves the detector bulk lifetime, but also encapsulates the ternary alloy material which prevents decomposition and protects the device from external contamination.

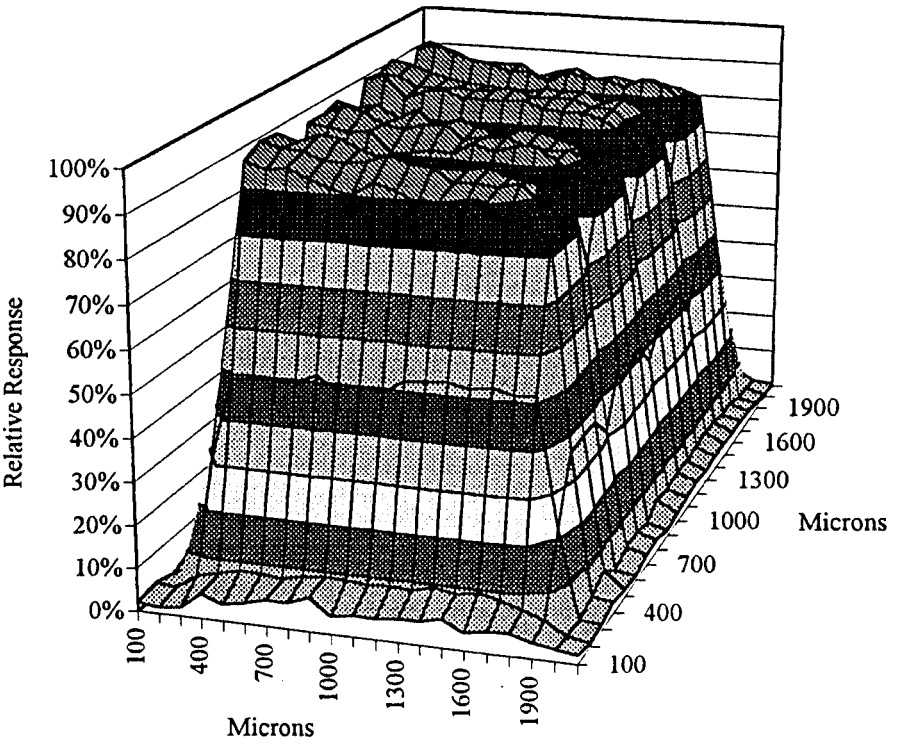

FIGURE 2.11. 3D PROFILE OF SPATIAL UNIFORMITY OF A LWIR HgCdTe 1.6 x 1.6 mm DETECTOR

The second critical detector fabrication process affecting device reliability is the contact metals used. NASA discovered in 1981 a serious satellite sensor reliability problem traceable to HgCdTe detector failures (Final Report of the HgCdTe Intermetallic Growth, July 1981, NASA Goddard). Detector impedances signal and noise were found to have changed with time. The NASA Study Team conducted a thorough investigation on all of the failed HgCdTe detectors and found one common trait: all the failed detectors had indium contacts with gold wire bonds. Gold and indium formed an intermetallic compound which modified the contact resistance to the extent that the total detector/contact impedance became unstable with time. EG&G Judson recognizes the importance of long-term device stability and has developed a double-beveled, non-indium based tri-metal contact technology with proven ohmic characteristics and long-term reliability.

The third process element which could affect detector reliability is wire bonding. If the contact pads are formed on top of the HgCdTe material adjacent to the active area, the wire bonding operation has to be performed on the HgCdTe material. A high quality bond requires the application of a substantial amount of physical force such as ultrasonic energy and/or elevated temperature or else the bond might weaken upon thermal cycling. Such physical forces, if not managed properly, could produce mechanical damage and microfractures which will slowly propagate into the active region of the detector and degrade its performance with time. For this reason, EG&G Judson has developed off-material bonding metallizations which connect the contact pads on top of the HgCdTe detector to the bonding pads down on the ceramic substrate. A high quality, mechanically strong wire bond operation, similar to that used in silicon IC industry, can now be performed on the bonding pads far from the HgCdTe material.

To demonstrate the stability of EG&G Judson's detectors, Table 3.1 shows an extremely severe stress test conducted where 784 temperature cycles were performed by our customer on 16 GOES detectors[1]. Detector parameters including resistance, signal, gr noise and 1/f noise were measured several times during temperature cycling. The worst case deviations (largest increases and decreases, not just standard deviations) were recorded on all these detectors parameters. The results shown in Table 3.1 fully demonstrate the reliability of EG&G Judson's HgCdTe photoconductor technologies.

The quality of flight worthy detector product depends not only on the stability of the detector but also on the reliability of the assembly housing which contains the detector arrays.

GOES HgCdTe DETECTOR STABILITY DEMONSTRATION					
# of Temp Cycles: 784 Temp Extremes: 90°K to 340°K					
% Change	Imager 5 (11 detectors)		Sounder Longwave (5 detectors)		GOES Acceptance Criteria
	Largest Increase	Largest Decrease	Largest Increase	Largest Decrease	
Resistance	0.3%	-0.2%	0.3%	-0.3%	±2.5%
Signal	1.9%	-0.7%	3.0%	0%	±5.0%
Noise @ 10KHz	3.2%	-4.8%	4.8%	0%	±15.0%
Noise @ 10Hz	12.3%	-19.4%	18.1%	-11.9%	±20.0%

TABLE 3.1 TEMPERATURE CYCLING (784 CYCLES) RESULTS

EG&G Judson has performed extensive environmental tests on space-qual focal plane array assemblies. Table 3.2 shows a summary of typical qualification tests conducted on each of the space programs listed. Although the pass-fail criteria are different due to different environmental conditions anticipated for the various missions, the focal plane assemblies produced by EG&G Judson passed all these tests. In many occasions, the qualification units have undergone tests exceeding the listed conditions by ten-fold and are still operating reproducibly.

PROGRAM	HALOE	INSAT II	DMSP	GOES	ADEOS-IMG	TIROS
PACKAGE TYPE	HERMETIC WITH TE COOLER	APLANAT LENS COLD FILTER	HERMETIC COLD FILTER	APLANAT LENS	HERMETIC COLD FILTER	APLANAT LENS
DETECTOR TYPE	InAs , 1 ELEMENT	MCT, 2 TO 4 ELEMENT	MCT, 2 ELEMENT	MCT, 1 TO 4 ELEMENT	MCT (1), InSb + FET (2), TEMP SENSORS (2)	MCT, 1 ELEMENT
THERMAL SHOCK	3X: -30C TO +60C	5X: -55C TO +85C	8X: -196C TO +20C (77K TO 293K)	3X: -183C TO +20C (90K TO 293K)	8X: -196C TO +20C (77K TO 293K)	3X: -191C TO +27C (82K TO 300K)
VIBRATION	RANDOM: 11.6g RMS 1 min/axis, 3 axes	SINE: 100-2000 Hz 20g peak, 4 min/sweep 4 sweeps/axis, 3 axes	RANDOM: .13g^2 /Hz 20-2KHz 2min/axis, 3 axes	SINE: 50-200 Hz 2-11g, 5 min. RANDOM: 33-51g RMS 1 min/axis, 3 axes	SINE: 5-100 Hz: 25g 100-2000Hz: 5g 13 min/axis, 3 axes Random: 23g RMS 2 min/axis, 3 axes	Random: 23g RMS 2 min/axis, 3 axes
TEMPERATURE CYCLING	10X: -30C TO +50C	100X: -178C TO +87C (95K TO 360K)	20X: -183C TO +27C (90K TO 300K)	35X: -183C TO +20C (90K TO 293K) 750X: -183C TO +67C (90K TO 340K)	100X: -196C TO +20C (77K TO 293K)	70X: -191C TO +27C (82K TO 300K)
POWER BURN-IN	168 hrs, 200K	-	240 hrs, 77K, Detector biased	24 hrs, 77K, Detector biased	500 hrs, 77K, Detector biased	24 hrs, 295K, Detector biased
LEAK RATE	< 1E-8 atm cc/sec	<5E-8 atm cc/sec	<1E-7 atm cc/sec	<5E-8 atm cc/sec	<5E-8 atm cc/sec	<5E-8 atm cc/sec
PIND	-	YES	YES	-	YES	-
HUMIDITY	-	95% RH, 40C 24 hours	-	-	-	-
MECHANICAL SHOCK	-	30g, 11msec 6X/axis, 3 axes	15g, 8msec 6X/axis, 3 axes	800g, 1.6 msec 1X/axis, 3axes	-	400g, 1msec
CONSTANT ACCELERATION	-	10,000g, 1 min., 1 axis	-	5000g, 1 min/axis 2 axes	5000g, 1 min/axis 2 axes	5000g, 1 min 1 axis
RADIATION	-	-	-	-	5000 Rad (Si)	50,000 Rad (Si)

TABLE 3.2. SPACE QUALIFICATION TEST SUMMARY

The qualification tests presented in Table 3.2 stress not only the detectors, but the packaging as well. We have developed a complete palette of techniques to preserve the detector performance such as hermetically scaled electrical feedthroughs, controlled expansion materials for maintaining hermeticity, completely hermetic attachment techniques for various optical components for incoming beams, and low outgassing components for maintaining transparent backfill atmospheres inside the detector assembly. These packaging techniques have passed some rather severe thermal and mechanical environmental stress tests during qualification testing.

Another area of great interest to the users of the HgCdTe photoconductor arrays is the sensitivity of small HgCdTe detectors to electrostatic discharge (ESD) damage. To determine the level of damage threshold, we conducted a small study on both MWIR and LWIR detectors using an ESD simulator to apply electrical energy discharges through these detector elements, measuring resistance and time constant after each increasing level of discharge. These detector elements were 33 x 33 microns in size and were at 80K in a test dewar throughout the testing.

First, a LWIR HgCdTe detector element was subjected to ESD screening following the guidelines in MIL-STD-883C, Method 3015.7 and subjected to functional testing (e.g.: time constant and resistance) following each pulse. As shown in Figure 3.1, the element was subjected to pulses from 10 volts to 4500 volts. At each voltage, one positive pulse and one negative pulse were delivered to the detector prior to retesting. Up to 2000V, no change was seen in the time constant of the detector. At 4500V, the time constant was reduced from its original value by 13%. Careful visual inspection at 400X after the ESD testing on this detector shows no change in appearance compared to the pre-ESD inspection. This is documented proof that ESD can induce changes in detector performance without causing any visible damage. Eight additional pulses at 5000V reduced the time constant by a total of 53%, as can be seen in the Table 3.3. At this level of ESD, the damage also caused the resistance to increase by 11%, and observable physical damage is visible under a microscope at 400X.

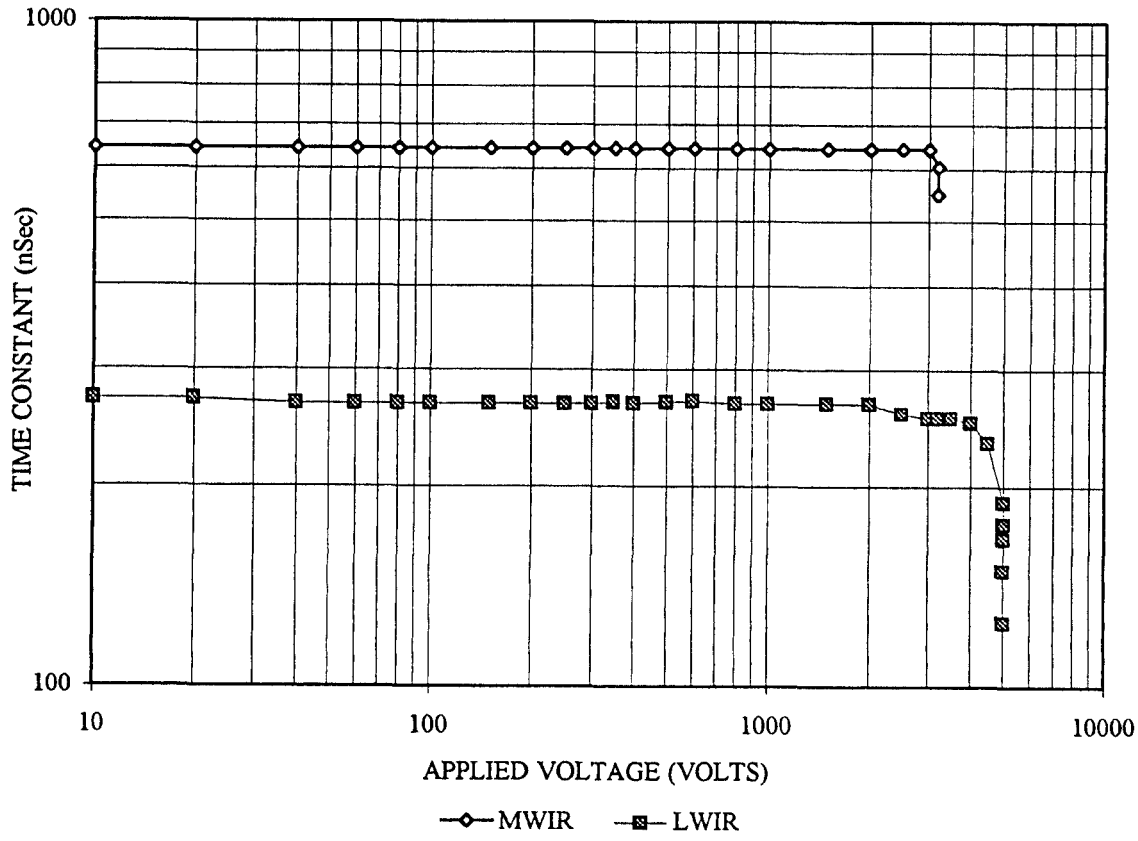

FIGURE 3.1. ESD SENSITIVITY OF HgCdTe PHOTOCONDUCTORS

The ESD screening was also performed on a MWIR detector element. Resistance and time constant were measured at 80 mV bias prior to ESD testing. The element was subjected to pulses from 10 volts to 3200 volts. Pulses were delivered the same way as for the LWIR detector. At 3200V, there was a 6% reduction in time constant and a 1.8% increase in resistance. Repeating this pulse pair caused the time constant to be reduced by a total of 14%, and the resistance to increase by 3%. These results are summarized in Table 3.3 and in Figure 3.1. Visual examination of this element shows no change in appearance compared to the pre-ESD inspection.

	LWIR Detector			MWIR Detector		
	Before ESD	After ESD	Change	Before ESD	After ESD	Change
Bias (mV)	50	50	-	80	80	-
Resistance (ohms)	68.9	76.5	+ 11%	163	168	+ 3%
Time Constant (nsec)	264	125	- 53%	643	550	- 14%

TABLE 3.3 EFFECTS OF ESD ON HgCdTe

This study shows that photoconductive HgCdTe is susceptible to ESD damage. Sometimes the damage is visible, other times it is not. But in all cases, ESD induced damage causes a reduction in the detector time constant indicating either bulk or surface damage. By installing standard ESD protection procedures established for the IC industry, one can easily avoid ESD accidents when handling HgCdTe detectors.

4. PACKAGING

EG&G Judson has been designing and building housings for spaceborne detector applications as indicated in Table 1 for quite some time. On these programs, we developed many packaging techniques that greatly enhance detector reliability and performance. While most detectors built have been for radiatively or closed-cycle cooling, multi-stage thermoelectric cooling was employed for one application which required the package to be evacuated. We introduced a state-of-the-art ceramic/metal housing with brazed subassemblies and welded final seals employing built-in getters resulting in unsurpassed vacuum integrity and lifetime.

For the backfilled housings radiatively or actively cooled, one piece metal housings with hermetic glass to metal electrical feedthrough pin seals and metal alloy sealed copper pinchoff tubes were developed. This is the basis for hermetic packaging of these detectors. For the assemblies requiring precise mounting of a germanium aplanat lens over the detector, epoxy was successfully qualified to maintain mechanical position and hermeticity of the assembly over the range of temperatures from 77K to 360K. We have also developed a technique for hard sealing bandpass germanium filters to a metal cap, which then is sealed to the housing body, creating a fully hermetic housing which has passed all space qualification requirements.

All of these programs required control of incident and reflected light. We have successfully developed a low outgassing light absorbing coating that when applied to selected surfaces controls scattered light inside the detector housing. Together with internal and external apertures and cold filters, the spectral fidelity of the detectors are preserved for both the in-band and for the blocked out-of-band regions.

Another area critical to the success of the performance of the detector product is the physical location of the sensitive element (s) of the detector array within the detector housing. The housing is the customer's interface to the detector, and the location of the array needs to be held very tightly with requirements of less than one thousandth of an inch commonplace. Figure 4.1 shows the distribution of the position of the detector element on a recent program for 15 assemblies with respect to the optical axis (x-y location) and position along the optical axis (z location) with respect to external package surfaces. The requirement tolerance is shown in the legend and it can be seen that not only has the requirement been met, but the majority of the detectors are within half the requirement. On another program, the assembly of 42 detectors yielded the results shown in Figure 4.2. Once again, the ability to accurately position the sensing element within the housing, especially in the x-y plane, is very evident.

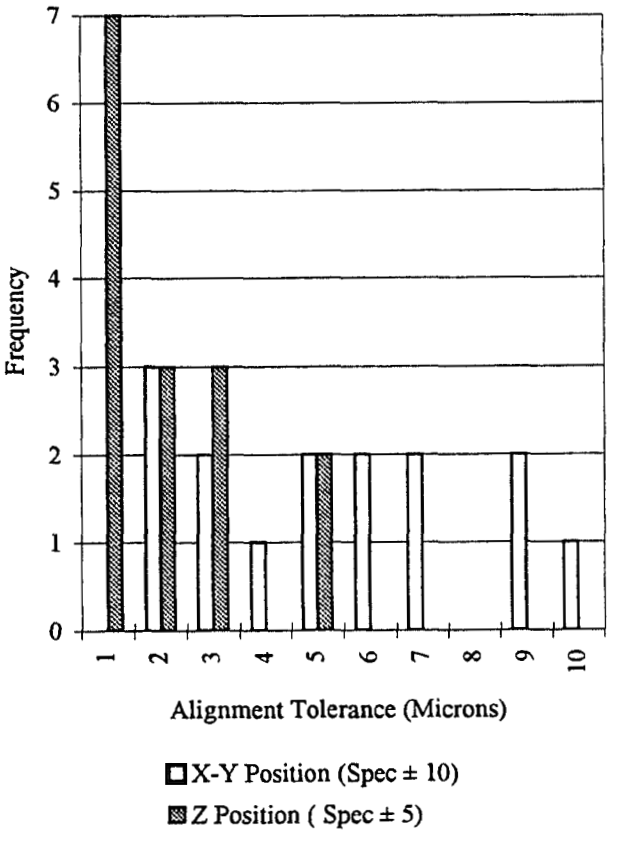

FIGURE 4.1. DETECTOR ALIGNMENT DISTRIBUTION 15 SAMPLES

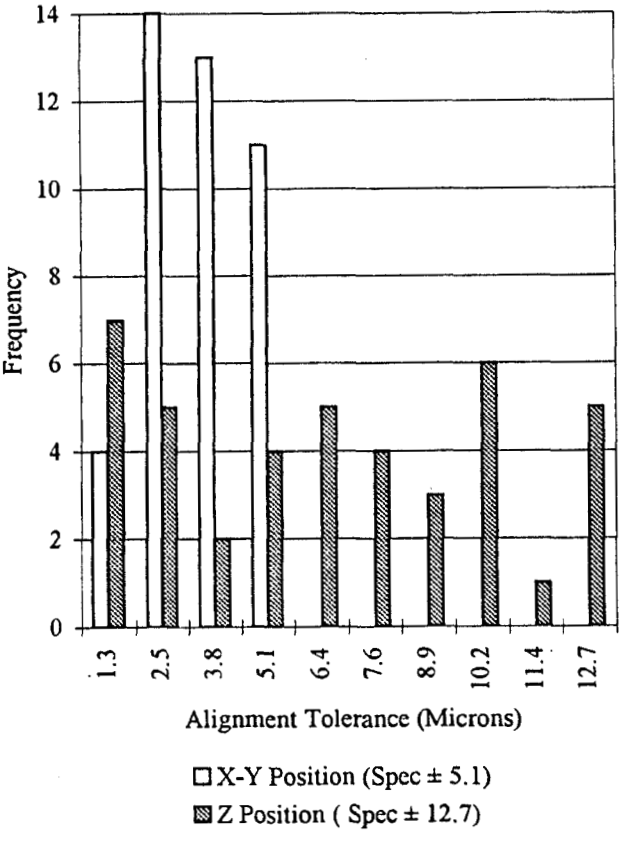

FIGURE 4.2. DETECTOR ALIGNMENT DISTRIBUTION 42 SAMPLES

In conclusion, the detector packaging developed at EG&G Judson has been demonstrated to be highly reliable, passing many demanding qualification tests. Additionally, we have shown precision alignment and measurement capabilities that exceed our customer's tight tolerance requirements.

5. SUMMARY

As the scientific community demands more from the instrument vendors, detector vendors need to be responsive in advancing their assembly and processing capabilities for producing high performance infrared detector array assemblies. In this paper we present typical performance levels achieved with photoconductive HgCdTe detector assemblies operating near 100K temperatures. Complementing the detector performance are the packaging technologies developed at EG&G Judson which provide high reliability assemblies qualified for spaceflight, and are an integral part of the weather and greenhouse monitoring satellite systems currently providing valuable information to better understand the atmosphere of planet earth.

6. ACKNOWLEDGEMENTS

The work presented in this paper was supported by EG&G Judson IR&D and the various programs listed in Table 1. In addition to the authors of this report many other employees of EG&G Judson have contributed to and supported this work. The authors would especially like to acknowledge E. Andrews and J. Derr of ITT/Fort Wayne and R. Ravella of SS/L for their technical contributions.

7. REFERENCE

1. Dr. E. Andrews, "Life Cycle Test Status," ITT-A/CD Memorandum, August 1993.

Low Frequency Noise in Photoconductive HgCdTe Detectors

Joseph Kimchi, J. Ray Frederick and Theodore T.S. Wong
EG&G Judson, Montgomeryville, PA 18936

ABSTRACT

The low frequency noise (1/f noise) characteristics of HgCdTe photoconductors are very important to the weather satellite user community because of the extremely long integration time used in these sensor applications. There are several detector technologies critical to the reduction of 1/f noise including surface passivation, bulk material selection, defect-free wafer thinning, contact metallurgy, off-HgCdTe bonding, and planar/low pressure substrate mounting. Each of these technical building blocks is discussed. When integrated to form a combined process, these critical technologies lead to a significant improvement in 1/f noise. Two widely accepted empirical models of 1/f noise are reviewed. Experimental results validate Kruse's model but repudiate Broudy's model, namely, 1/f noise is inversely proportional to the square root of the detector volume but does not depend on the gr noise of the detector. Furthermore, we find no correlations between 1/f noise and total detector surface area or the detector contact effects. A novel test structure is presented which suggests that by using innovative detector geometries, the detector designers may be able to increase D^* at low frequencies compared to the conventional square or rectangular detector structures.

Keywords: HgCdTe, Photoconductors, Infrared Detector, 1/f Noise, Excess Noise

1. INTRODUCTION

In order to fully optimize the sensitivity of HgCdTe photoconductors, one must maximize the signal response and simultaneously minimize the noise level of the detector. This requires both a firm theoretical understanding of how materials and device parameters affect detector performance as well as the realization of necessary technologies to accomplish the desired improvements. The functional dependence of the signal response and most noise mechanisms in photoconductors are well established theoretically. The only exception is the low frequency noise component which is sometimes referred to as either "1/f noise" or "excess noise". Although several theoretical and empirical models of 1/f noise mechanisms were suggested for HgCdTe photoconductors, none have been thoroughly validated experimentally. Fortunately in the past, the primary use of HgCdTe photoconductors was in scanning thermal imaging systems. They operate at frequencies above 500 Hz where 1/f noise is not the dominant noise source. In most weather satellite applications, however, the operating frequency ranges from below 0.1 Hz up to 500 Hz. The performance of the sensor instrument is almost entirely driven by the low frequency noise of the detector. It is therefore essential to identify the origin(s) of the 1/f noise and develop critical detector technologies to control, reduce, and hopefully eliminate the elements which contribute to the low frequency noise.

In this paper, we describe an on-going internally funded effort conducted at EG&G Judson aimed at minimizing 1/f noise. Several technology elements critical to 1/f noise reduction are described. These include starting material selection, off-material wire bonding, detector-substrate mechanical compatibility, surface passivation, and contact formation. Next, we present statistical correlation analyses based on a large database collected on EG&G Judson's recent space programs. The dependence of 1/f noise on the background and thermal generation-recombination (gr) noises at different biases is discussed. Several published 1/f noise models are applied to fit the data and their validities compared. Finally, a test structure designed to explore the effects of different device geometries on 1/f noise and minority carrier sweep-out is presented and experimental results summarized.

2. CRITICAL TECHNOLOGIES

In response to the needs of our customers in the space community, EG&G Judson launched a comprehensive development effort beginning in 1990 with an objective of reducing the 1/f knee frequency from close to 1000 Hz at the time to less than 100 Hz. The 1/f knee frequency is defined as the frequency at which the 1/f noise is equal to the gr noise. In order to focus our development effort only to those technology elements most relevant to controlling 1/f noise, we turned to published theories on 1/f noise for guidance. Examining the literature published for the last several decades on 1/f noise, one finds an underlying theme common to all, namely, 1/f noise is in general a result of some forms of perturbation in current flow inside a device. The McWhorter[1] model, for example, postulates that 1/f noise is a result of fluctuation in carrier mobility and/or carrier density. Armed with this simple insight, we began to bring together critical technologies with one common theme, i.e. to achieve a detector structure with the most uniform materials and device parameters in the bulk and with the least disturbing effects at the boundaries or periphery of the structure.

0-8194-2200-2/96/$6.00

First, it is decided that the starting HgCdTe material must be of the highest quality. Only single-crystal wafers are used. Poly-crystalline wafers or even wafers with low-angled grain boundaries could lead to current flow fluctuations[2] and must be rejected for low 1/f noise applications. In addition, the starting HgCdTe material should be relatively homogenous in composition, carrier density, and mobility over an area comparable to the final detector array size. These basic material selection criteria ensure uniform current flow within the bulk of the detector structure.

Not only is it sufficient that the starting HgCdTe material should be homogenous and of high quality, this quality must necessarily be preserved throughout the wafer lapping and polishing steps during which the wafer is thinned from 500 down to less than 10 microns thick. Mechanical lapping and chem-mechanical polishing with decreasing grit size are implemented followed by chemical polishing resulting in a thin HgCdTe disk with minimal damage.

Because of the very thin finished device structure and the relatively small active area sizes required in most space remote sensing applications, the bulk volume of the detector is surrounded by a relatively large total surface area including the top, side, and bottom surfaces. Considering the fact that the minority carrier diffusion length is comparable to the active area size, localized turbulence appearing at the surface due to surface defects could result in fluctuation of the current flow inside the volume. At EG&G Judson, we developed different passivation and surface treatment processes to accumulate the top, the bottom and the side surfaces of the detector in order to maintain bulk properties.

Another potential source of 1/f noise comes from the detector contacts. There are three possible contact-related noise sources. The first one is at the wire bond location. If the bond pad is positioned on top of the HgCdTe detector material (the way photoconductors were built traditionally), the heat and pressure applied to form the bond could fracture the underlying HgCdTe material. These microfractures could cause fluctuation in the current flow and therefore 1/f noise. Second, many detector manufacturers use evaporated indium to form an ohmic contact to HgCdTe. We observed experimentally at EG&G Judson, that the indium film reacts with the underlying HgCdTe and visible changes in film texture could appear over a period of months even if the device is stored at room temperature. The ohmic nature of the indium contact would also change with time which will affect both the stability of the detector and its 1/f noise behavior. Third, if the indium film is ever brought in contact with either the gold wire or other thin gold metallizations, the gold and indium will react to form an intermetallic phase[3]. As a result, the detector would exhibit instability and increase in 1/f noise.

At EG&G Judson, we have developed and qualified a non-indium based, tri-metal system to assure a stable ohmic contact. It is imperative to properly pre-treat the HgCdTe surface prior to putting down the contact metallizations. A poor metal-HgCdTe interface can give rise to barrier height inhomogeneities resulting in localized carrier injection sites. These micro-plasma sites could be another source for 1/f noise. We also employ a two-layer metal scheme where the thin metal layer is first deposited to define the active area and form the ohmic contact followed by a thicker metal layer to form electrical connections from the HgCdTe chip down over a doubly bevelled edge onto a bonding pad located on the detector substrate (see Figure 2.1). High quality wire bonds can therefore be formed on the substrate pads. Any wire bonding related material fracture is therefore completely eliminated.

Finally, there are several subtle details in the fabrication process which can also influence the 1/f noise. Most frequently used substrate materials for HgCdTe photoconductors include sapphire, alumina and zinc sulfide all of which exhibit matched thermal expansion[4] properties to HgCdTe[5]. For low 1/f noise, these substrates must be free of microscopic surface defects. Any irregularity at the substrate surface could later create localized stress to the HgCdTe[6] when it is mounted on the substrate. Although they are purchased with optical-flat-type specifications, these substrate materials often warp during detector processing. The loss of optical-flat planarity on the substrates could induce mechanical deformation on the HgCdTe wafer. At EG&G Judson, we have developed a substrate treatment process which enables the substrate to maintain optical-flat quality during the detector fabrication cycle. Finally, in order to minimize the epoxy layer between the HgCdTe and the substrate, one has to apply pressure to the HgCdTe. We discovered that the amount of pressure applied to the HgCdTe wafer during substrate mounting can affect the 1/f noise. This is supported by reports concerning the effect of dislocation on the electrical properties of semiconductors[7,8,9]. A mounting fixture was developed to assure uniform application of pressure as well as to gauge the pressure not to exceed a certain threshold above which stress induced 1/f noise may be prominent.

Each of the aforementioned technology building blocks was first individually developed and refined. They were then integrated together resulting in a reproducible detector fabrication process. The process was further qualified as a manufacturing procedure for producing flight-worthy detector arrays for space use. Today, EG&G Judson routinely produces HgCdTe photoconductors with 1/f knee frequencies less than 100 Hz. Some of the better detectors achieve 1/f knees of less than 40 Hz.

3. EXPERIMENTAL RESULTS

It has been postulated that the low frequency noise of HgCdTe photoconductors is linearly proportional to the total current flow (i.e. the bias current) inside the device. The mean square 1/f noise voltage per root Hertz can be expressed by the following equation[10]

$$V_{1/f} = \frac{K \ V_B}{\sqrt{f}} \tag{1}$$

where K is the proportionality constant; V_B is the bias voltage; and f is the frequency. Figure 3.1 shows low frequency noise data measured on a typical LWIR HgCdTe photoconductor fabricated with the technology described in Section 2. The detector has a cutoff wavelength of 17 μm at 95°K. The background is 295°K through a cold FOV of 100° full angle. Note that the low frequency noise is approximately proportional to the square root of frequency. At a frequency above 200Hz, the gr noise prevails. The knee frequency is around 35Hz.

Kruse[10] continues to argue that the proportionality constant K in equation (1) is inversely proportional to the detector volume, namely

$$K = \frac{C}{\sqrt{w \ d \ l}} \tag{2}$$

where w, d, l are detector width, thickness, and length respectively, and C is a factor dependent upon material/processing but independent of dimensions. Substituting Equation (2) into Equation (1), one obtains

$$V_{1/f} = \frac{C}{\sqrt{w \ d \ l}} \ \frac{V_B}{\sqrt{f}} \tag{3}$$

We set out to test Kruse's hypothesis that 1/f noise is inversely proportional to the square root of the detector volume, i.e. Equation (2). Figure 3.2 shows normalized 1/f noise (i.e. noise at 40Hz divided by the bias voltage) versus detector volume measured on a large number of detectors. Note that over five decades of volumes studied, the normalized 1/f noise clearly shows an inverse square root relationship with detector volume. Therefore Equation (3) is experimentally validated and the excess noise factor C can be quantified using the data shown in Figure 3.2.

As mentioned previously, it is assumed that C is a factor dependent upon material/processing technology but independent of physical dimensions. But if one postulates that 1/f noise originates at the detector surface, then one would expect C to scale with detector total surface area. Figure 3.3 shows C versus detector surface area which includes top, bottom, and side surfaces. In this case, C is simply the noise measured at 40Hz times the square root of the detector volume divided by the bias voltage using Equation (3). From Figure 3.3, one cannot definitively conclude that 1/f scales with detector surface area. If anything, Figure 3.3 seems to suggest that 1/f noise is independent of detector surface area.

In 1981, Broudy[11] reviewed various so-called "classical" theories on 1/f noise in photoconductors. He further introduced a new phenomenological model to describe 1/f noise in HgCdTe detector by postulating that 1/f noise is proportional to the gr noise raised to a power of 3/2. This power law dependence assumption dictates certain material selection criteria for 1/f noise reduction. For example, in order to reduce 1/f noise, everything else being equal, material with low gr noise should be selected. This conclusion is a new consequence of Broudy's empirical theory which does not appear in the classical theory where the 1/f noise and the gr noise are basically independent and are related solely through their bias dependencies.

We searched our vast database for possible inter-dependencies between the 1/f noise and the gr noise. If Broudy's model is valid, one would expect to see a power law dependence when plotting 1/f noise versus gr noise in a log-log graph. On the other hand, if the 1/f noise does not depend on the gr noise, then one may still see a linear dependence. It is because both the 1/f noise and the gr noise are proportional to the bias and therefore high 1/f noise data tends to associate with high gr noise data simply because they are both biased at high bias.

Figure 3.4 shows noise at 40Hz versus noise at 10KHz measured on a large number of LWIR HgCdTe detectors at 102°K. From Figure 3.4, it is not clear as to what power law dependence, if any, one can conclude. Figure 3.4 seems to suggest that there may be multiple dependencies. The relationship at higher noise levels, i.e. more than 10 nV/rtHz, seems to be more super-linear than that at lower noise levels. But the scatter is too wide to make any definitive conclusion about any power law dependence.

One possible explanation about the apparent exponential dependence of 1/f noise on gr noise at high noise levels observed in Figure 3.4 is the presence of minority carrier sweep-out and its effects on the gr noise. Figure 3.5 shows 1/f noise and gr noise versus electric field at 80°K with a cold FOV of 40°. It is quite clear that the electric field dependency of 1/f noise is different from that of the gr noise. The 1/f noise seems to vary linearly on the bias field as indicated by Equation (1) while the gr noise first shows linear relationship but then saturates at higher bias field due to minority carrier sweep-out effect. As the bias field is increased, the effective carrier lifetime is reduced because an increasing number of minority carriers is being swept to the cathode and recombine there. If one plots 1/f noise against the gr noise at various electric fields, one would observe a super-linear dependence similar to that shown in Figure 3.4.

Figure 3.6 shows a more complete picture in that it plots the electric field dependent lifetime, 1/f noise at both 10Hz and 40Hz, and gr noise at 10KHz on the same graph. The test temperature is 80°K and the FOV is at 40°. The sizes of the detectors range from 25μm to 60μm. Figure 3.6 clearly shows that the lifetime decreases with increasing electric field and the gr noise saturates as the lifetime decreases. But the low frequency noise at 10Hz and 40Hz shows no signs of saturation. Figure 3.7 shows similar plots but measured at 105°K representing the thermal gr noise regime. Again, the minority carrier sweep-out does not seem to have any effect on the 1/f noise and 1/f noise behaves linearly with the electric field according to Equation (1).

Based on the data presented in Figures 3.5 to 3.7, one can generally conclude that there is no evidence to support Broudy's empirical model which suggests that 1/f noise is proportional to the gr noise raised to a power of 3/2. On the contrary, at least in the case of sweep-out, 1/f noise has a totally different bias dependency from that of the gr noise, both in the background and thermal-limited cases. Furthermore, from Figures 3.6 and 3.7, one observes that 1/f noise also shows a temperature dependency different from that of the gr noise. Note that the electric field dependent noise at both 10Hz and 40Hz increases when the temperature is raised from 80°K to 105°K while the gr noise hardly changes. Consequently, we conclude that there is no experimental proof of any functional dependence of 1/f noise on the gr noise.

Finally, there is one other possible origin of 1/f noise proposed previously by others, namely, 1/f noise is caused by non-uniform injection of carriers at the contacts of the detector[12]. To verify this hypothesis, we designed a detector in a shape of a trapezoid where the length of the detector is 60μm, the width of one end is 25μm, and the other end, 50μm wide (designated as Element No. 4 in Figure 3.8). The different widths allow for different localized potential flow lines at the opposite contact regions. For example, for a given external bias, one would expect the local electrical field near the narrow width region (25μm) to be almost 2X higher than that near the wider end (50μm). Low frequency noise data were taken at 3 different external biases, each at forward (electric field from the narrow to the wide end) and reverse directions and the results are shown in Figure 3.9. Note that there is no discernible difference in the 1/f noise between the forward and reverse bias directions at all three bias levels. This seems to suggest that localized injection of majority carrier at the contact has no effect on the 1/f noise. In addition, we have examined low frequency noise data taken on detectors with various contact areas and structures. There is no correlation between 1/f noise and contact size. Therefore we can conclude that 1/f noise does not seem to relate to the contacts of the detector at least with the detectors fabricated at EG&G Judson.

Before coming to closure in this section, there is one more observation worth noting regarding the trapezoidal configuration. Although we report that there is no difference in the 1/f noise with respect to the direction of the bias field (see Figure 3.8), there is a difference when we examine the responsivity data. Figure 3.10 shows the responsivity versus electric field for the forward and reverse bias direction. Once again, we define the bias directions in the "forward" directions when the electric field is from the narrow width (25μm) to the wide end (50μm). The responsivity is clearly higher in the "reverse" direction. If the responsivity is higher at "reverse" bias and the 1/f noise is indifferent to the bias direction, then there is a distinct advantage in D^* at reverse bias at low frequencies. Figure 3.11 shows frequency dependent D^* at forward and reverse bias direction at a bias of 40V/cm. The reverse bias is clearly preferred. Referring to Figure 3.8, the test structure masks were designed to study the effects of different detector geometries and therefore different bias field strengths on detector performance. Four different geometric structures are positioned in close proximity to each other within a piece of HgCdTe material to minimize any material non-uniformity effects. All 4 devices were measured and D^*s are plotted in Figure 3.12. The trapezoidal structure at "reverse" bias shows the highest D^* at low frequencies. In Dean, Elliot and White's paper[13] on optically induced non-linearity, they discussed a similar detector structure which allowed for different forward and reverse bias fields. They concurred with our finding that the responsivity should be higher for a device structure where the minority carriers are swept towards the regions of higher local field. The high field region is always the narrow end, irrespective of the bias direction. Therefore, they stated that the responsivity to a "reverse" field (from wide to narrow end) is always higher than that for the same value but "forward" field. Since the low frequency noise is the same irrespective of the bias direction, the D^* has a clear preferred bias direction. Although the field dependent D^* topic is outside the scope of this paper, the results of the trapezoid structure offer the detector design engineers an extra degree of freedom in optimizing the sensitivity of the device, especially at low frequencies.

4. CONCLUSIONS

In this paper, we present several critical detector technologies developed at EG&G Judson which have direct impacts on the significant improvements on 1/f noise achieved to date. These technical building blocks include uniform starting HgCdTe material, defect-free polishing, surface passivation processes, contact metallurgy, off-HgCdTe wire bonding, and planar and low-pressure substrate mounting techniques. A couple of published empirical models on 1/f noise are reviewed and they are either verified or repudiated based on experimental results taken on a large number of detectors fabricated with the advanced technology described above. Several conclusions emerge as a result of our investigations on 1/f noise and they are summarized as follows:

- ✔ 1/f noise is unrelated to kinetics associated with generation-recombination noise mechanisms, both background and thermal limited cases.
- ✔ 1/f noise does not scale with total detector surface area.
- ✔ 1/f noise does not depend on detector contact or the direction of local field.
- ✔ 1/f noise is inversely proportional to the square root of the detector volume.
- ✔ 1/f noise varies slowly with temperature.

In addition, we present the results taken on various novel test geometries. We believe that by using innovative detector shapes and bias field design options, one could increase D^* at low frequencies compared to the conventional square or rectangular structures.

5. ACKNOWLEDGEMENTS

The authors of this report wish to thank many colleagues at EG&G Judson for their contributions and support during this work. The authors would especially like to acknowledge Dr. Ed Andrews of ITT/Fort Wayne for his technical guidance.

6. REFERENCES

1. A.L. McWhorter, "1/f Noise and Germanium Surface Properties", *Semiconductor Surface Physics*, p. 207-228, Univ. of Pennsylvania Press, Philadelphia, (1957).
2. H.F. Schaake, J.H. Tregilgas, A.J. Lewis, P.M. Everett, "Lattice defects in (Hg,Cd)Te: Investigations of their natrue and evolution", *J. Vac. Sci. Technol.* A, Vol. 1, No. 3, pp. 1625-1630, July-Sept. 1983.
3. "Final Report of the HgCdTe Intermetallic Growth", July 1981, NASA-GFSC.
4. J. Malamas, R. Bambha, "A New Approach For Solving Thermal Expansion Mismatch Problem", *Proc. IRIS Materials*, pp. 179-190, August 1990.
5. O. Caporaletti, G.M. Graham, "The low-temperature thermal expansion of $Hg_{1-x}Cd_xTe$ alloys", *Appl. Phys. Lett.*, Vol. 39, No. 4, 15, pp. 338-339, August 1981.
6. P. Raccah, U. Lee, J. Silberman, W. Spicer, and J. Wilson, "Evidence of stress-mediated Hg migration in $Hg_{1-x}Cd_x$ Te", *Applied Phys. Lett.* 42, 4, pp. 374-376, Feb. (1983).
7. K.K. Yu, A.G. Jordan and R.L. Longini, "Relations between Electrical Noise and Dislocations in Silicon", *J. Appl. Phys.* 38, pp. 572-583 (1967).
8. H. F. Matare, *Defect Electronics in Semiconductors*, pp. 173-249, Wiley-Interscience, 1971.
9. W.T. Read Jr., "Theory of Dislocations in Germanium", *Phil. Mag.*, 45, 775 (1954).
10. P. Kruse, L.D. McGlauchlin, R.B. McQuistan, *Elements of Infrared Technology*, p. 253, John Wiley & Sons, Inc., 1962.
11. R.M. Broudy, V.J. Mazurczyk, *Seminconductors and Semimetals*, Vol. 18, p. 175, Academic Press, 1981.
12. M.A. Lampert and A. Rose, *Phys. Rev.*, Vol. 121, No. 1, p. 26 (1961).
13. A.B. Dean, C.T. Elliot and A.M. White, "Photoconductive detectors emplying an optically induced non-linearity", *SPIE* Vol. 510 Infrared TechnologyX, pp. 149-153, 1984.

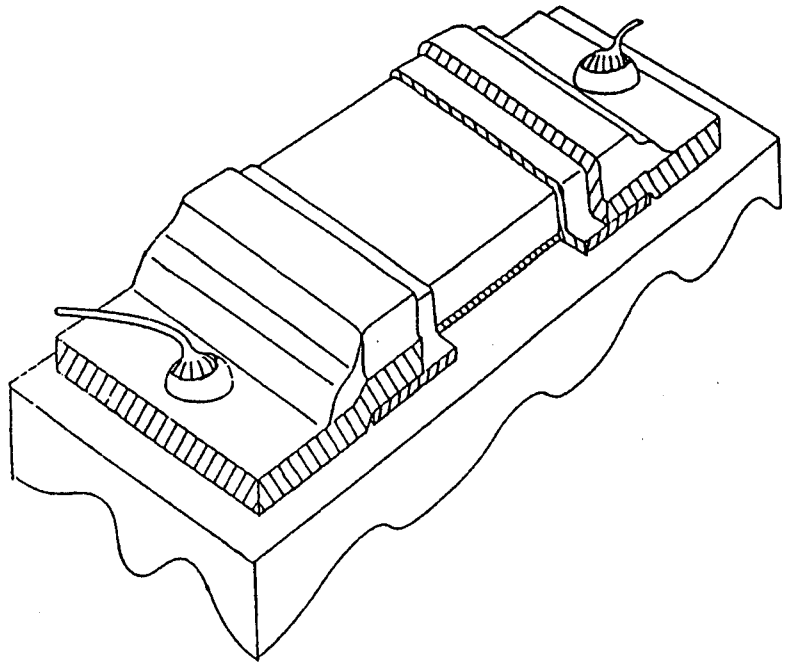

FIGURE 2.1. EG&G JUDSON'S HgCdTe STRUCTURE

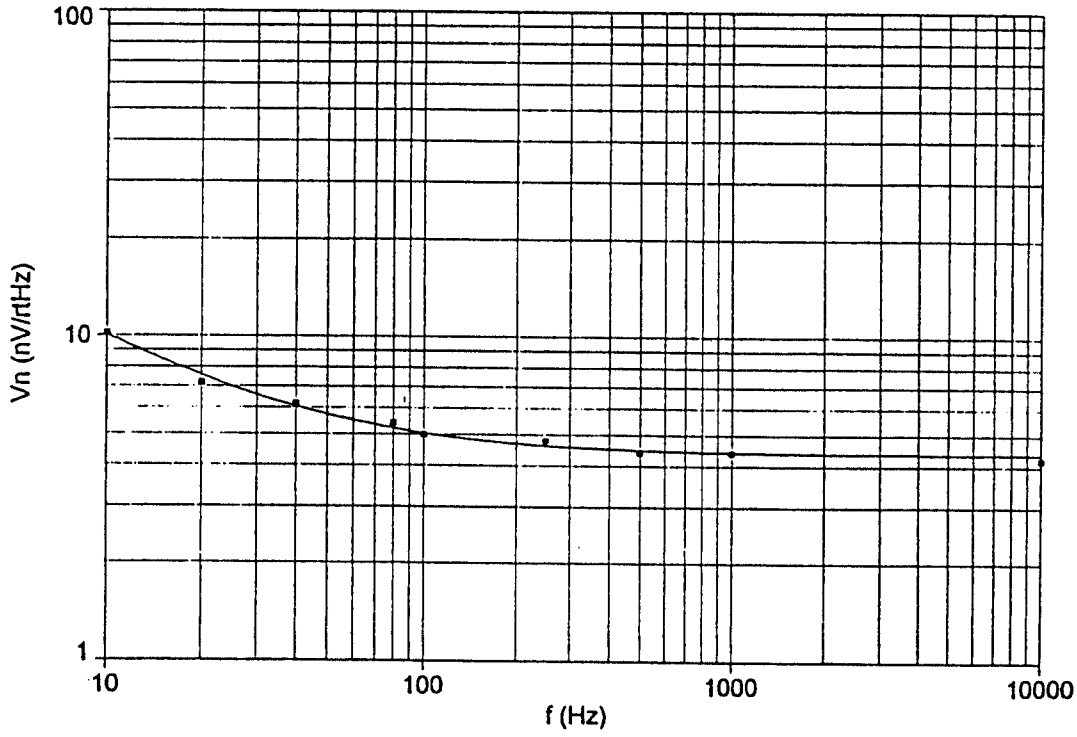

FIGURE 3.1. TYPICAL NOISE FREQUENCY SPECTRUM OF A HgCdTe PHOTOCONDUCTOR

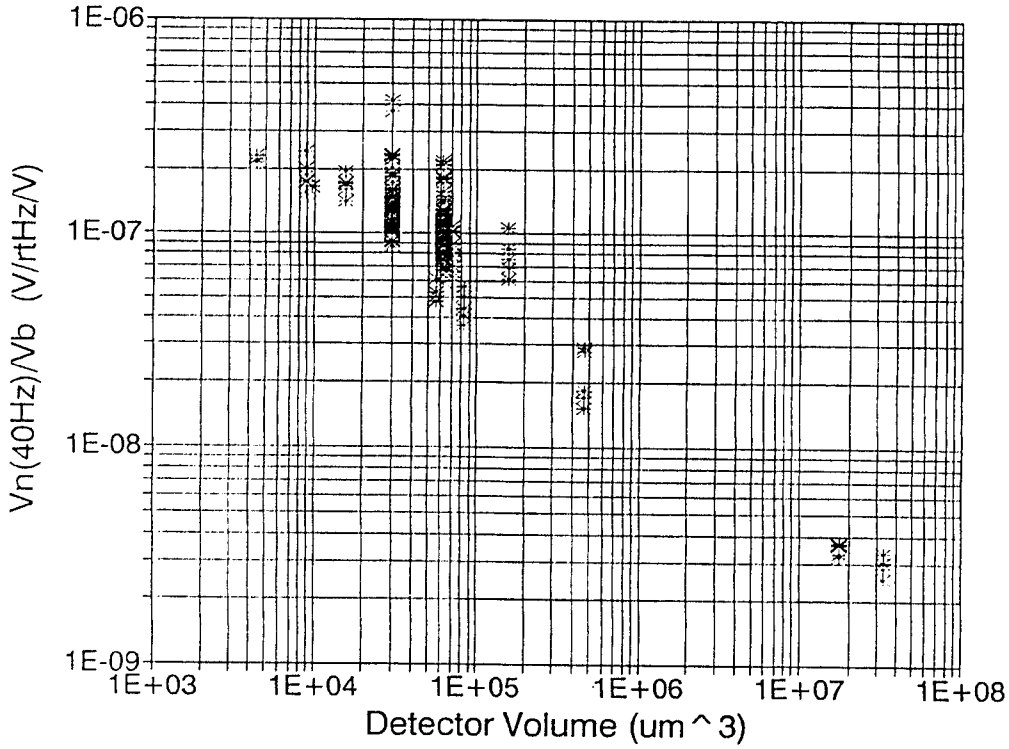

FIGUE 3.2. 1/f NOISE vs. DETECTOR VOLUME

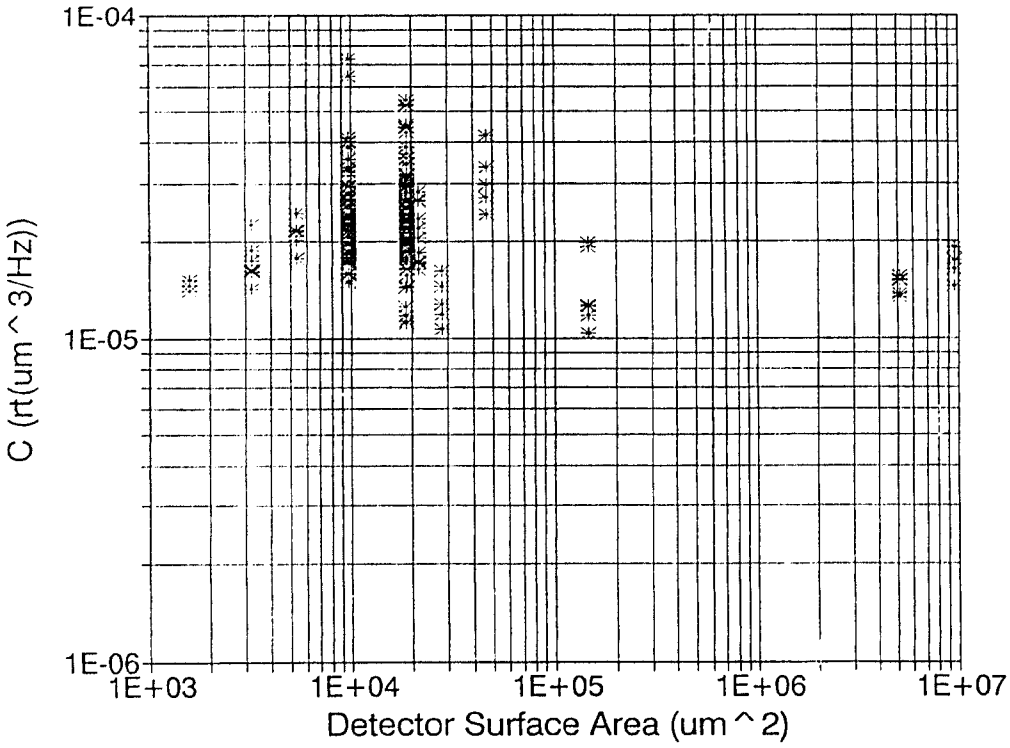

FIGURE 3.3. EXCESS NOISE FACTOR (C) vs. DETECTOR SURFACE AREA

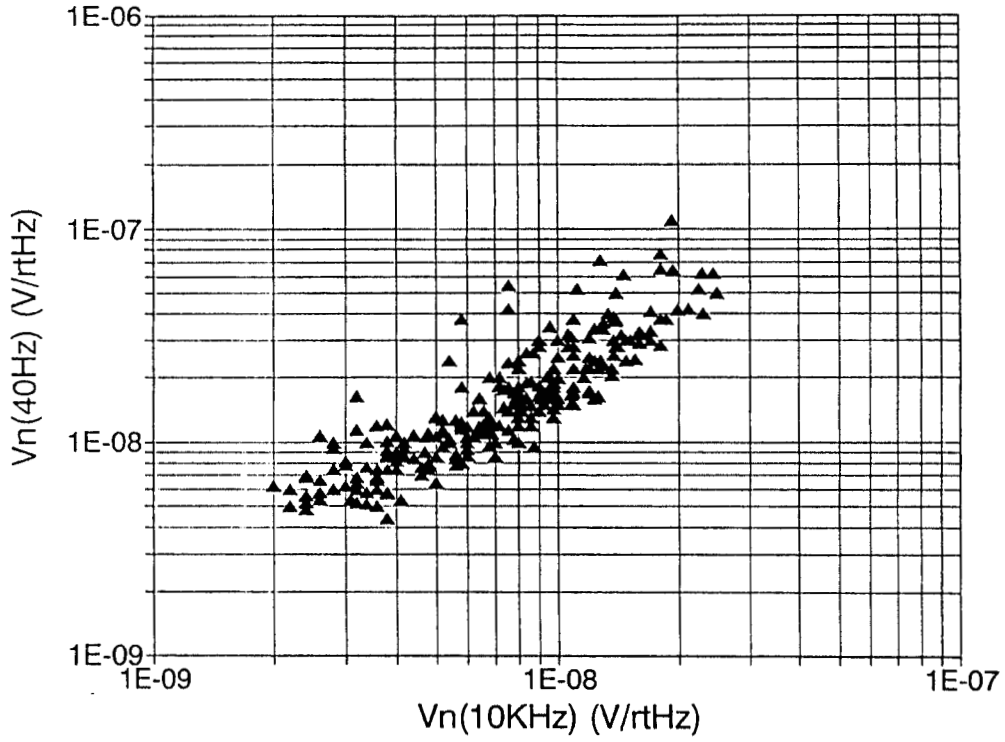

FIGURE 3.4. 1/f NOISE (40Hz) vs. GR NOISE (10KHz)

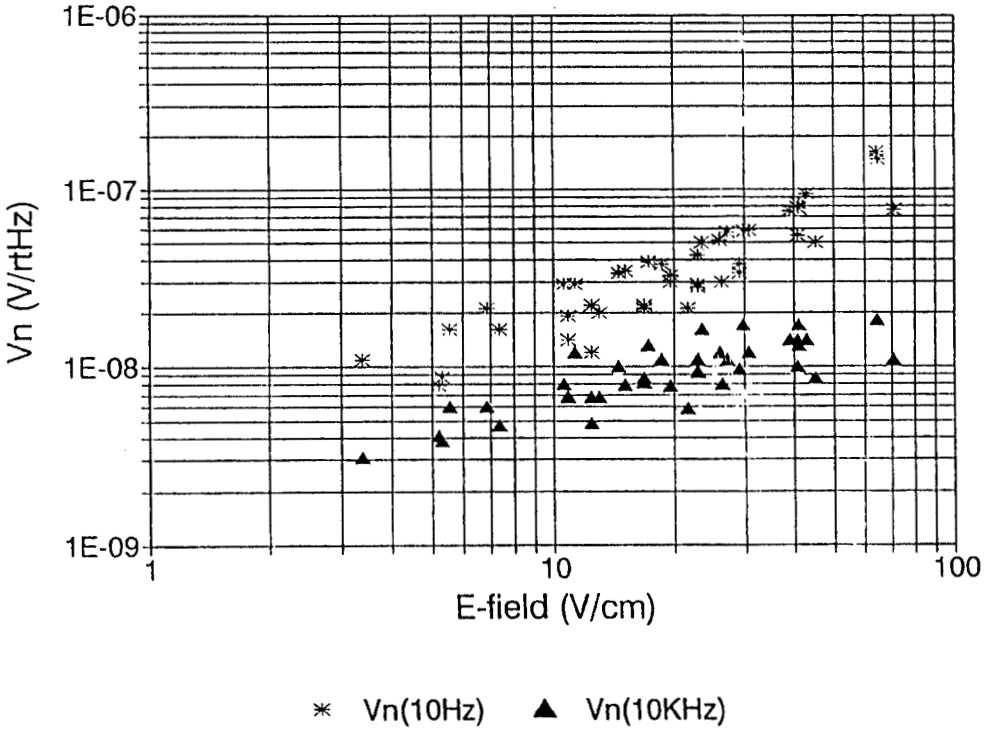

FIGURE 3.5. ELECTRIC FIELD DEPENDENT 1/f NOISE AND GR NOISE

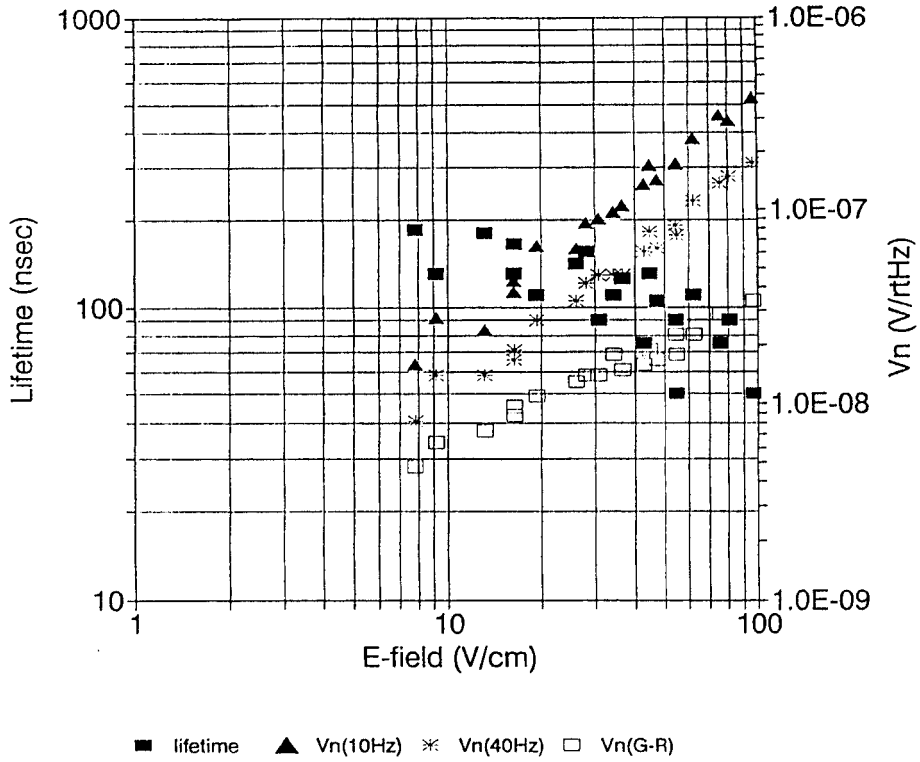

FIGURE 3.6. CARRIER LIFETIME, 1/f NOISE, AND GR NOISE vs. BIAS FIELD AT 80°K

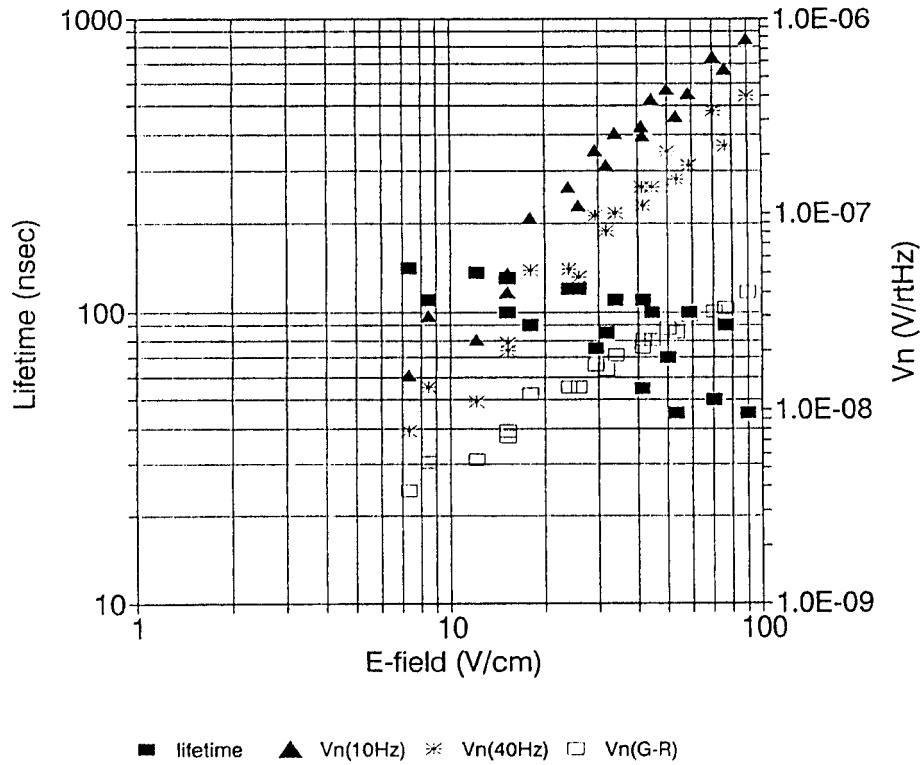

FIGURE 3.7. CARRIER LIFETIME, 1/f NOISE AND GR NOISE vs. BIAS FIELD AT 105°K

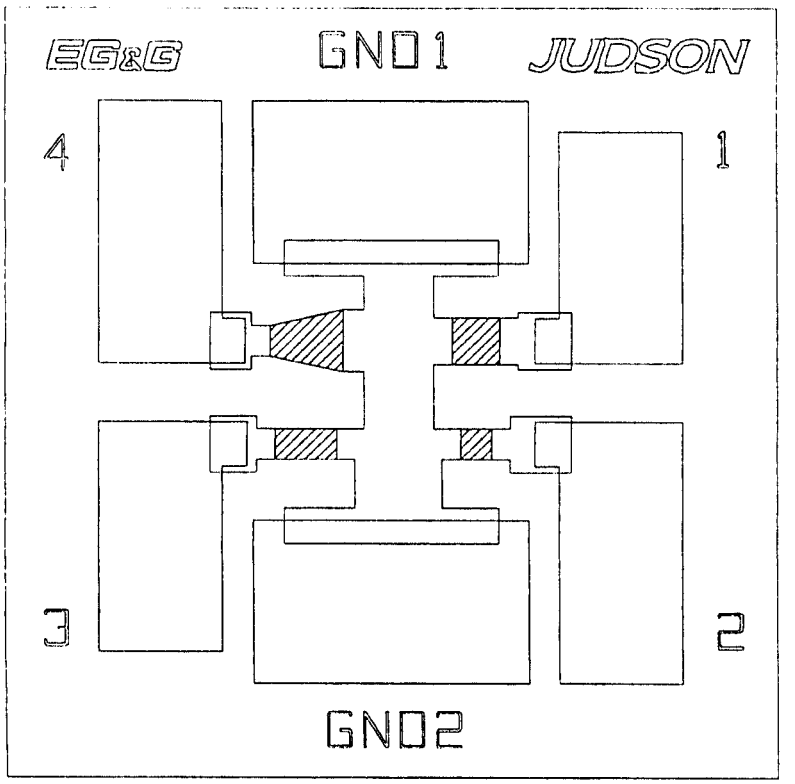

FIGURE 3.8. TEST STRUCTURE SHOWING 4 DIFFERENT CONFIGURATIONS

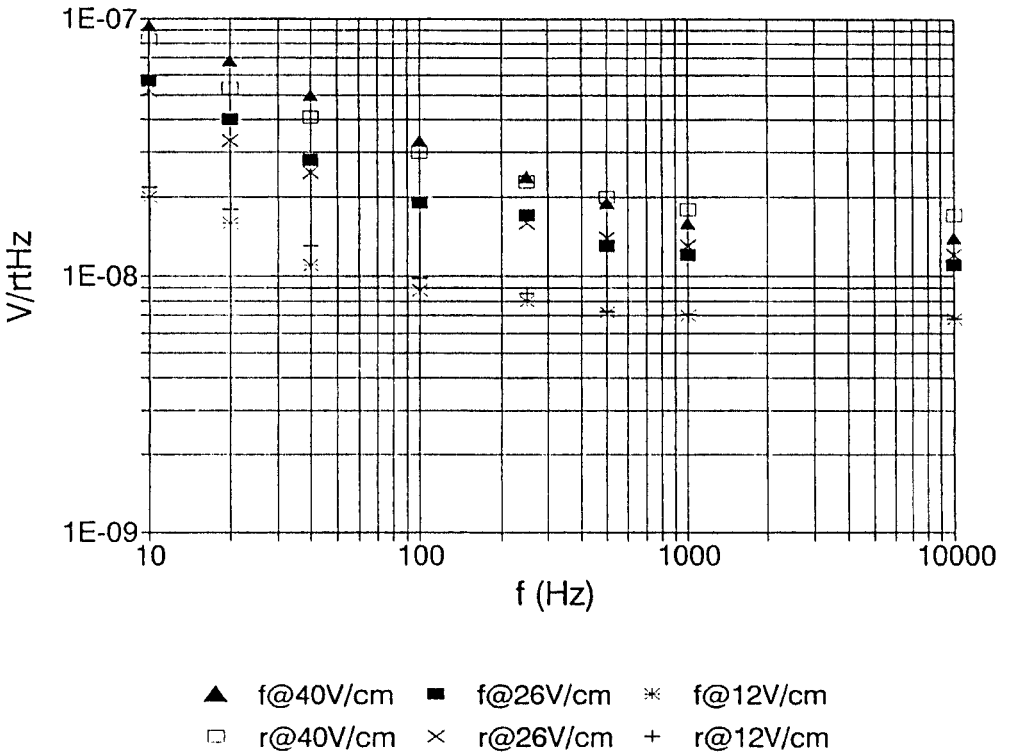

FIGURE 3.9. LOW FREQUENCY DATA WITH OPPOSITE BIASES TAKEN ON A TRAPEZOIDAL DETECTOR

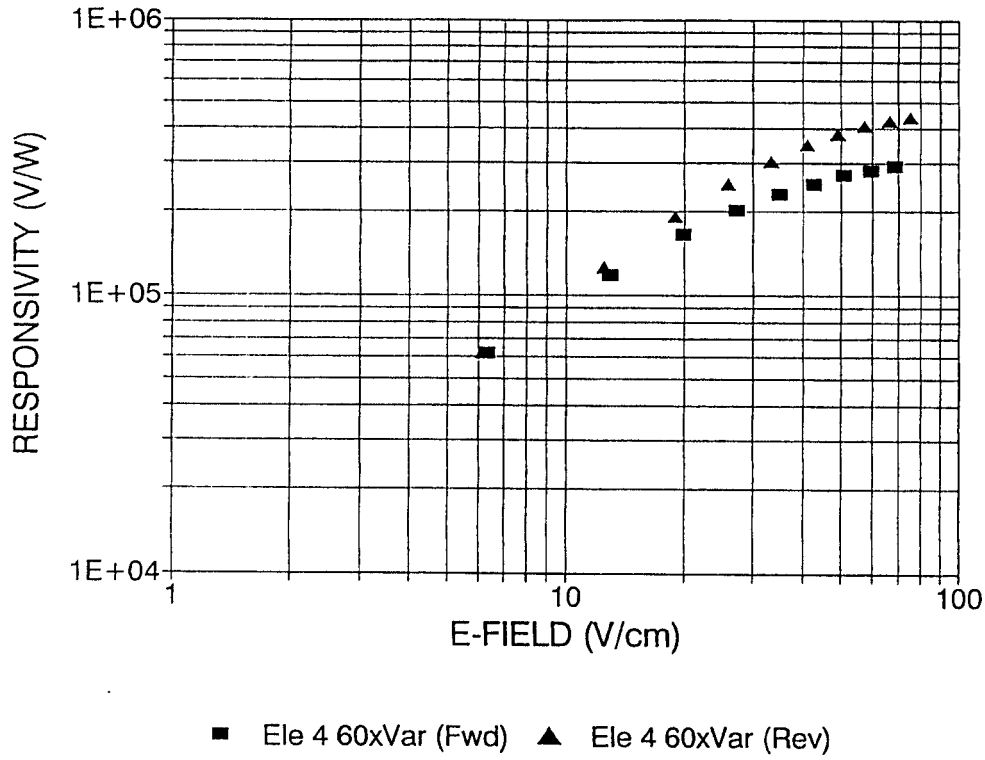

FIGURE 3.10. ELECTRIC FIELD DEPENDENT R_v AT FORWARD AND REVERSE BIAS

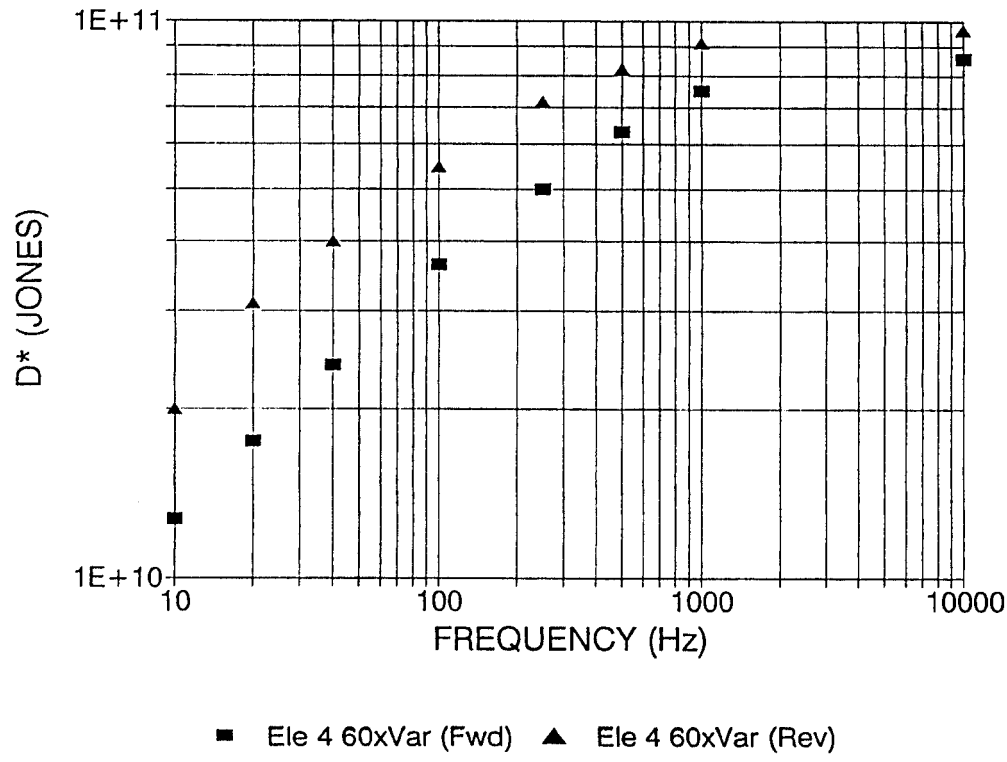

FIGURE 3.11. FREQUENCY DEPENDENT D* AT FORWARD AND REVERSE BIAS

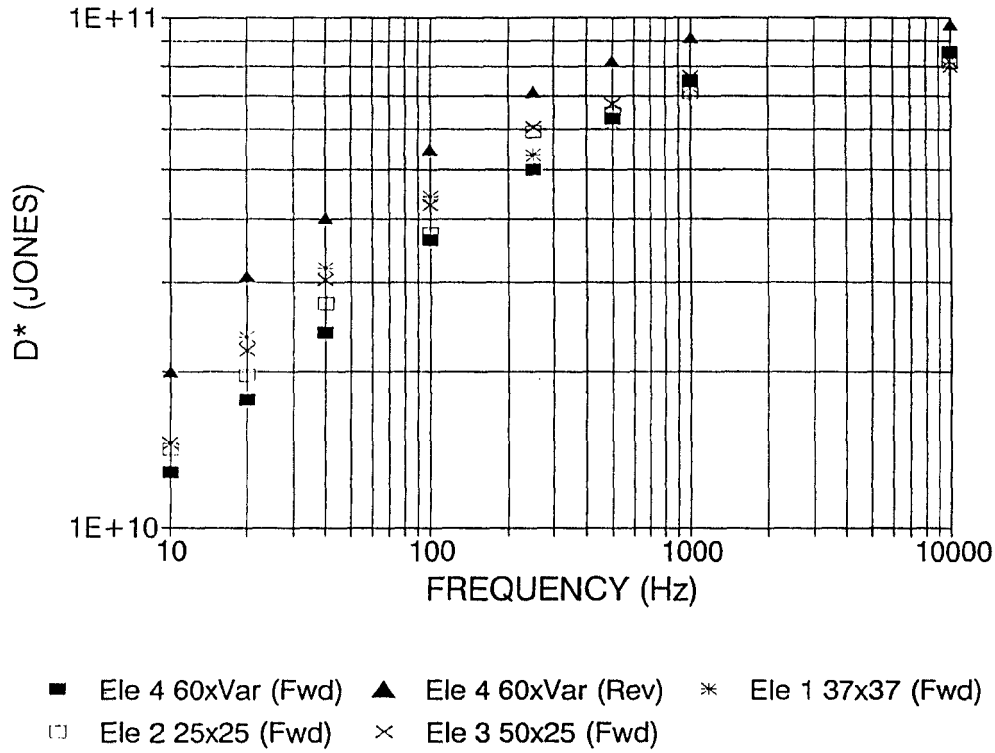

FIGURE 3.12. FREQUENCY DEPENDENT D* TAKEN ON THE TEST STRUCTURE SHOWN IN FIGURE 3.8

Improving the performance of the GOES Solar X-ray Imager (SXI) with a back-illuminated X-ray sensitive CCD

G. D. Berthiaume, B. E. Burke and J. A. Gregory

Lincoln Laboratory, Massachusetts Institute of Technology
244 Wood Street, Lexington, MA 02173

P. L. Bornmann

NOAA Space Environment Center
325 Broadway, Boulder, CO 80303

ABSTRACT

NOAA has commissioned a Solar X-ray Imager to be built for use on the GOES spacecraft. The mission of the SXI is to provide soft X-ray (6-60 Å) imagery of the Sun. The current instrument design employs a microchannel plate detector stack to convert the incident X-rays to an electrically detectable signal. In this paper, we discuss the SXI performance improvements possible by replacing the detector with a back-illuminated, X-ray sensitive CCD fabricated using technology developed at MIT/LL. In addition to a description of the X-ray sensitive CCD, we discuss possible improvements in data quality, reduction in instrument mass and power requirements, and simplified instrument handling.

Keywords: GOES, X-ray, Solar, CCD

1. INTRODUCTION

The SXI is an instrument designed to observe the Sun in the soft X-ray region (6-60 Å), providing full disk Solar imagery with an update rate of 1/min or better. A filter wheel is provided to permit images of different X-ray bandpasses to be acquired to facilitate viewing of various Solar features. Ratios of images taken through different filters can also be used to determine temperatures and emission measures of the Solar features that are listed in Table 1.

Table 1. Parameters of Solar Features

Feature	Temperature 10^6 K	Log Emission Measure cm^{-3}
Coronal Holes	1.3-2.1	42.3-43.3
Active Regions	2.5-6	43-44.6
Flares	7-20	48-49

The design of the GOES-M SXI employs a microchannel plate detector to convert the incoming X-ray flux into an electronically detectable signal. This approach was selected several years ago as the quickest, most cost effective method of meeting the SXI requirements. At the time, X-ray sensitive CCDs were difficult to find and had unacceptably low quantum efficiency (QE) at the long wavelength (low energy) end of the SXI wavelength band.

Over the past several years, Lincoln Laboratory has undertaken a program to develop X-ray sensitive CCDs with high QE in this energy range. In addition to high QE, high Charge Transfer Efficiency (CTE), low dark current, low noise, and highly uniform performance are also required in these devices.

 0-8194-2200-2/96/$6.00

This work has been undertaken in part to support the astronomical community. Lincoln CCDs are being used on the AXAF CCD Imaging Spectrometer (ACIS) onboard the AXAF satellite and the CCD Imaging Spectrometer (CIS) onboard the Japanese ASTRO-D (ASCA) satellite, in addition to other visible wavelength instruments requiring high QE in the blue and UV.

In this paper, we briefly describe the state of the art in X-ray sensitive CCDs, followed by the SXI performance improvement that could be expected should one of these arrays be used on that instrument. A detailed description of the use of CCDs as X-ray detectors may be found in Lumb *et al.* 1991[1].

2. CCD PERFORMANCE

2.1 Quantum efficiency of x-ray sensitive CCDs

The QE of an X-ray sensitive CCD is determined by two principal factors: the thickness of the active region of the device and the thickness of the dead layer on the light sensitive surface. The device thickness is principally involved in determining the QE at energies greater than ~ 1 keV (12.4 Å), while the dead layer thickness is most important at lower energies.

The devices built for use at low X-ray energies are generally of two types: back-illuminated arrays and arrays with thinned (or virtual) gates. The back-illuminated variety has the highest QE at low energy, and is described here.

For back-illuminated CCDs, X-ray photons are incident upon the side of the array that does not contain gate structures. (On front-illuminated devices, the gate structure absorbs low energy photons before they reach the active area of the array, thereby reducing the QE.) The back-illuminated array must be thinned to allow the incident photons to penetrate to the active area of the array. (Mechanical integrity is preserved by bonding the thinned device to an unthinned wafer.) The back surface of the array is then treated to eliminate traps, control dark current, and ensure that the device is fully depleted. There are several methods of treating the back surface, all of them capable of providing a dead layer of about 100 Å. Photons absorbed in the dead layer do not produce detectable charge, thereby limiting the low energy response of the array.

Figure 1 is a plot of the theoretical QE for back-illuminated X-ray sensitive CCDs of two thicknesses. The absorption cross sections used may be found in [2]. The crosses on the figure represent measured data points for a back-illuminated device manufactured here at the Laboratory similar to one that would be useful for the SXI. Shown for reference is the QE for an uncoated microchannel plate detector.[3] Note that the CCDs have nearly a factor of 10 greater QE than the microchannel plate over the range of interest of the SXI.

3. INSTRUMENT CONFIGURATION

In this section, we describe a possible modification of the GOES-M SXI design to include a custom X-ray sensitive CCD. In the next section we describe the corresponding impact on the performance of the SXI. A summary of this discussion is presented in Table 2.

3.1 Custom CCD

The option we consider is to fabricate an X-ray sensitive CCD specifically for use with the SXI. This proposed device would be a 512 × 512 array of 16 μm pixels with an equivalent framestore region. The framestore region should be split into two sections as shown in Figure 2 in order to speed frame transfer. In addition, there should be a blooming drain added to the structure to permit long integration times without fear of blooming from regions of high signal to regions of low signal (Solar flare radiation can be 10^6 times brighter than some of the faint features to be observed). Back-illumination permits inclusion of anti-blooming technology with no reduction in fill factor.

Table 2. System Configuration

Parameter	Current SXI	Proposed System
Detector	MCP/CCD	CCD
Detector Format	512 × 512	512 × 512
Pixel Size	Effectively 16 μm	16 μm
Spatial Resolution	> 5″	5″
Dark Current @ -20 C (e-/pix/sec)	~250	~250
QE (%)	~10	~95
Full Well (e-)	~200,000	~200,000
Blooming Control	No	Yes
Electronic Shuttering	Yes	Yes
Instrument Mass	34 lbs.	31 lbs.
Instrument Power	~42 Watts	~38 Watts
Radiation Tolerance	?	> 5 krad

3.2 Back-illumination parameters

The device we propose for SXI will be a thinned (~ 20 μm thick), back-illuminated device with an approximately 200 Å SiO_2 deadlayer. The device would be fabricated using proprietary Lincoln Laboratory back-side stabilization technology. The predicted QE of such a device is shown as the solid line in Figure 1.

4. SXI IMPACT

4.1 Integration time

Because the QE of the back-illuminated X-ray sensitive CCD is about 10 times greater than the QE of the microchannel plate detector, the relative integration time for the proposed system is reduced by a factor of 10 over that of the GOES-M SXI. This means that a CCD version of the SXI could obtain in 100 msec the same S/N image as the current SXI can in 1 second. This significantly improves the ability to observe faint Solar features and should improve image quality that is degraded by spacecraft pointing jitter by reducing exposure times.

In light of the vibration environment for the SXI, this is an enormous advantage. Using the onboard High Accuracy Sun Sensor (HASS), it is possible to collect a number of short exposures and coregister and add the images via postprocessing. This technique is available for the existing SXI as well as for a bare CCD version of the instrument; however, the X-ray sensitive CCD will provide a higher S/N image as the S/N for each individual image is $\sim\sqrt{10}$ times greater than that in the current SXI.

4.2 Power/weight requirements

An X-ray sensitive CCD requires no more power to operate than does a visible CCD; therefore, replacing the microchannel plate/visible CCD combination with a bare CCD will save all of the power required for operation of the high voltage supply necessary to operate the microchannel plate.

Thus, the mass of the HV supply, microchannel plate, and fiber optic coupler will be eliminated.

4.3 Storage requirements

The X-ray sensitive CCD instrument must be kept in a clean area and protected from electrostatic discharge at all times. There are no vacuum requirements for an X-ray sensitive CCD, which is required for the GOES-M microchannel plate version of SXI. Moreover, there is no evidence for any performance degradation in a CCD stored for several years on the ground.

4.4 Electronics modifications

The SXI CCD drive electronics will need to be modified from the current design to operate a three phase CCD with electronic shuttering. The analog processing may have to be altered to accept the larger output signal amplitude of a Lincoln CCD.

4.5 Mechanical modifications

The proposed CCD with electronic shuttering will require a slightly different mounting scheme than used with the microchannel plate system. In particular, the framestore area of the array must be completely shielded from all incoming illumination in order to preserve the instrument performance.

The CCD array would need to be moved forward along the optical axis of the telescope to the focal plane where the microchannel plate is located on the GOES-M SXI. A CCD is much thinner than the current detector stack.

4.6 Optical baffling

An X-ray sensitive CCD is, unlike a microchannel plate, extremely sensitive to visible light. Therefore, the prefilter/filter wheel combination must be impervious to visible light for the entire mission. The filter design must prevent visible light from impinging on the focal plane even in the presence of pinholes in either the prefilter or filter wheel.

4.7 Radiation tolerance

There are two types of radiation tolerance that need to be addressed. First is tolerance to damage caused by radiation, second is insensitivity to the false signal generated by incident radiation.

4.7.1 Damage tolerance

All CCDs are subject to performance degradation in a radiation environment. X-ray sensitive CCDs in general are neither better nor worse than standard CCDs. However, techniques have been developed at the Lab that enable our devices to be more tolerant than commercial devices to radiation damage, including damage from protons, electrons and X-rays. These techniques may be implemented on any X-ray sensitive device.

4.7.2 False signal generation

A thinned, back-illuminated CCD will generate less charge per ion for heavy ion interactions than the current SXI design. A heavy ion will deposit energy in the microchannel plate as it passes through the microchannel plate, in addition to the energy deposited directly in the CCD. By thinning the X-ray sensitive CCD to 20 μm, the amount of energy deposited in the array can be reduced. Charge generated in the substrate below the CCD may not propagate back to the active area of the CCD.

For high energy electrons, the signal in the X-ray sensitive CCD would be similar to that in the current SXI. The same is likely for γ-rays. The only advantage in the proposed system is that the bare CCD has a smaller cross section than the microchannel plate detector.

5. CONCLUSION

An X-ray sensitive CCD is an ideal replacement for the existing focal plane detector on the follow-on versions of the SXI. This modification requires minor changes to the existing SXI electronics and a different mechanical mounting scheme; however, the overall performance of the instrument is improved while reducing both weight and power consumption.

6. ACKNOWLEDGMENTS

This work was sponsored by the National Oceanic and Atmospheric Administration under Air Force Contract No. F19628-95-C-0002.

7. REFERENCES

1. Lumb, D.H., Berthiaume, G.D., Burrows, D.N., Garmire, G.P., and Nousek, J.A., *Exp. Astron.*, **2**, 179,1991.

2. Henke, B.L., Lu, P., Tanaka, T.J., Shimabukuro, R.L. and Fujikawa, B.K., *Atomic Data and Nuclear Data Tables*, 27,1-54, 1982

3. Fraser, G.W. in *X-Ray Detectors in Astronomy*, 143, Cambridge University Press, Cambridge 1989.

Figure 1: Quantum Efficiency vs Wavelength for 2 Back-Illuminated Configurations

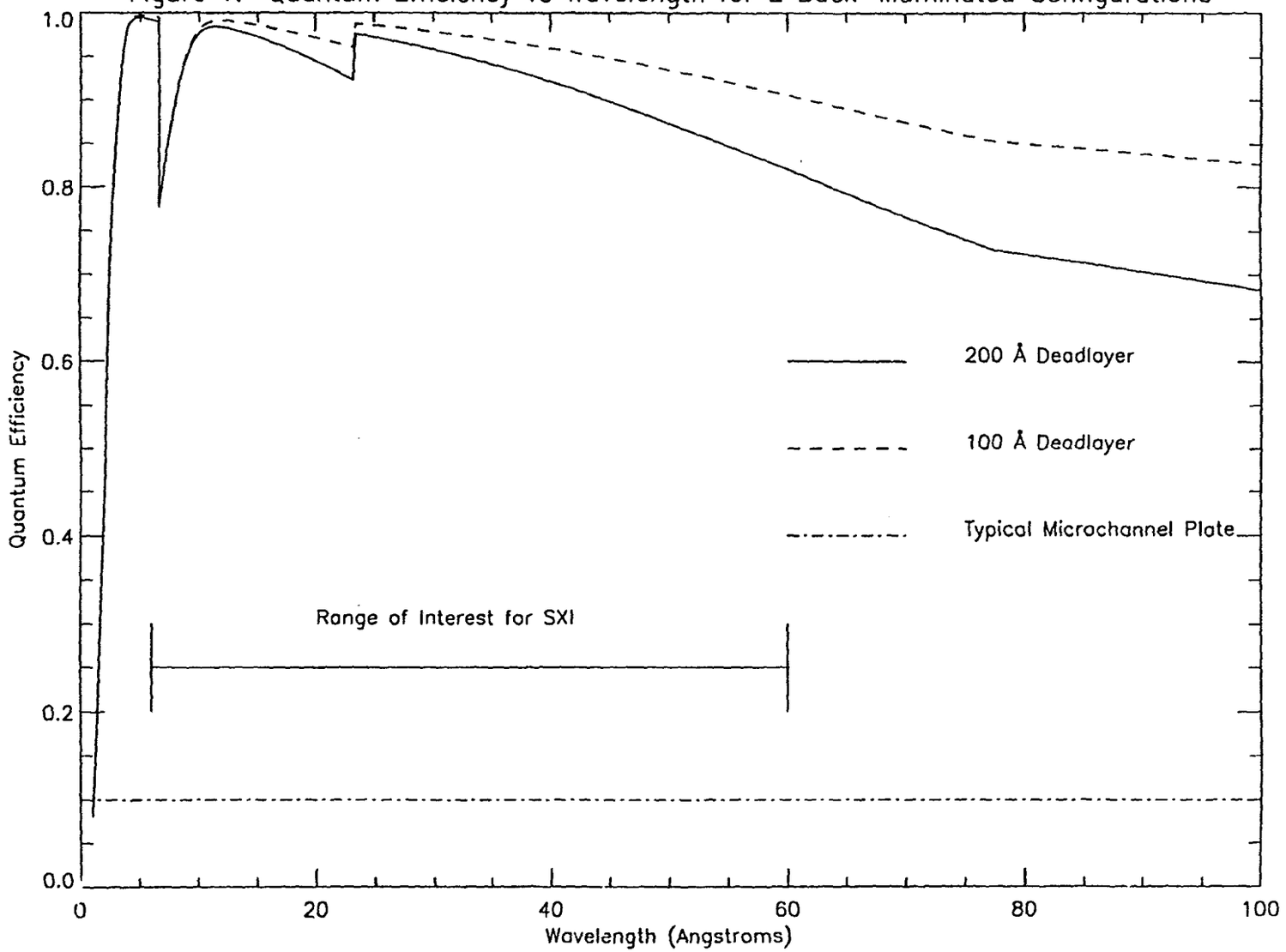

Figure 2: Proposed CCD Layout

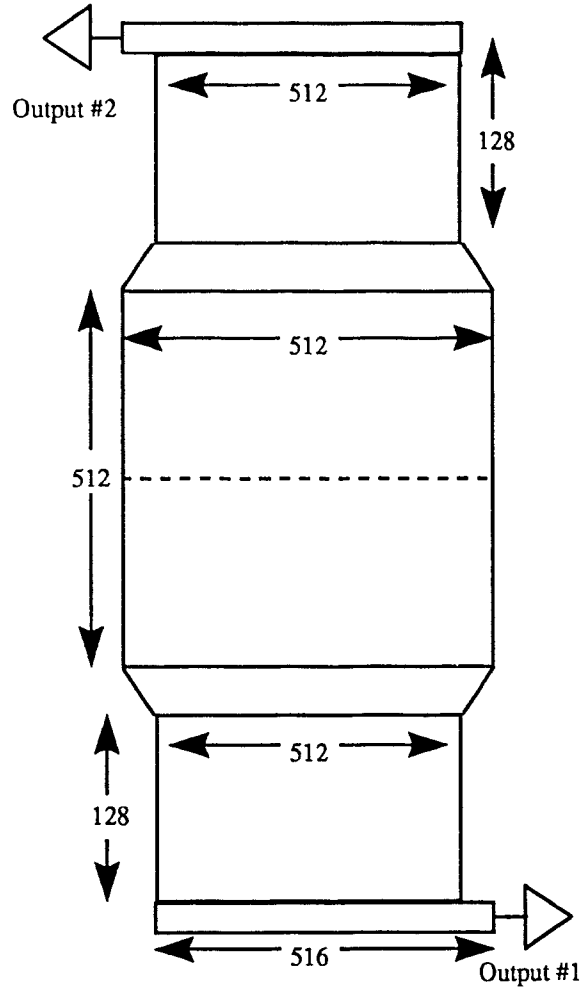

Impact of the visible detector on GOES Imager and Sounder MTF

Frederick L. Williams, David R. Wickholm, John C. Ehlert

ITT Industries, Aerospace Communications Division
1919 West Cook Road, Fort Wayne, Indiana

ABSTRACT

The modulation transfer function (MTF) is one of the Goes Imager and Sounder system's key optical performance indicators. Though the visible images from GOES-8 and GOES-9 are excellent, the MTF values measured during ground tests are below expectations. The 4490 cycle per radian frequency MTF is particularly interesting because it is not significantly affected by small changes in focus or aberrations of the optical system. The primary contributors to the low MTF values which are within the instrument are the ghost reflections from the transmissive components and the detector and its package. The ghost reflections that exist are certainly a factor in the stray light. An estimate of each ghost's intensity produces a worst case effect on MTF of approximately 2.5%. The detector itself appears to be the largest contributor to the stray light. There are several ways that the detector and its package contribute to the stray light. The most prominent among them is the reflection from the aluminum coated substrate combined with the closeness of the detector window. The stray light from the detector reduces the MTF by approximately 4%. Instantaneous geometric field of view (IGFOV) curves verify the existence of the stray light and calculations show approximately the magnitude of difference between measured and expected MTF data. A new detector design appropriate for the Imager visible channel or the Sounder star sense channel incorporates the changes recommended to reduce stray light within the detector. The first of the new detectors qualifies for the Sounder star sense detector. IGFOV curves show the reduction in stray light levels by about a factor of 2 to 4. Sounder star sense optical MTF data shows approximately 8% increase in the MTF at 4490 cycles per radian compared to SN05 Sounder.

KEYWORDS: GOES, Imager, system mtf, visible detector, Sounder, star sense MTF

1. INTRODUCTION

The GOES Imager visible channel[1,2] provides some of the most important images that serve a variety of purposes. Among them is the tracking of severe storms and hurricanes. The sharpness of these images helps greatly in the ability of the meteorologists to identify and track the motions of these storms. In addition to creating useful images the visible channel is the star sensor for the Imager's tracking and pointing system. The modulation transfer function (MTF) of the visible channel is the performance parameter that measures the image sharpness and validates the visible imaging quality. GOES-8 and GOES-9 visible images are excellent images and are satisfying the needs of the user community. However, the MTF measurements indicate lower than expected values for the Imager visible channel system MTF and the Sounder star sense channel optical MTF.

The most interesting of the frequencies is the 4490 cycle per radian spatial frequency. At this frequency the effects of focus and slight aberrations should not significantly affect the MTF. It is more likely that stray light or other unwanted light is causing the reduction in MTF. The stray and unwanted light that reduce MTF are the subjects of this discussion.

2. SYSTEM DESCRIPTION

The Imager visible optical system consists of the scan mirror, telescope primary and secondary mirrors, the visible-infrared beamsplitter, depolarizer, spectral balance filter, spectral bandpass filter, detector window and detector. Figure 1 shows an optical schematic of the visible optics. The telescope is a Cassegrain design with a 30.5 cm diameter primary mirror and a 3.8 cm diameter secondary mirror. The scan mirror is a nickel plated beryllium mirror with an aluminum coating on top of the nickel. The visible-infrared beamsplitter and depolarizer are each tilted at 45° relative to the optical axis and tilted about axes orthogonal to each other to correct for polarization effects and to balance astigmatism. The spectral filters limit the wavelengths of light reaching the detector to 0.55 +/- 0.025 μm to 0.75 +/- 0.025 μm. The two filters are both normal to the

optical axis as are the detector window and detector. The detector for the Imager visible channel and the Sounder star sense channel is the same detector.

FIGURE 1
GOES IMAGER VISIBLE OPTICAL SYSTEM

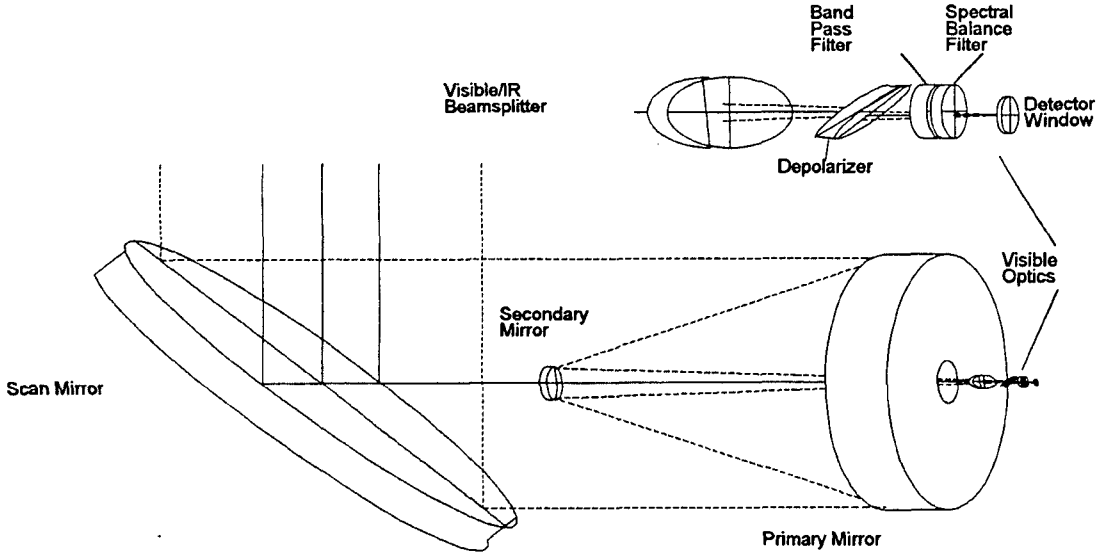

3. IMAGER MTF DATA - EXPECTED AND MEASURED

Table I shows the current GOES Imager system MTF minimum requirements for the visible channel at specified spatial frequencies.

TABLE I

SPATIAL FREQUENCY (cycles per radian)	SYSTEM MTF MINIMUM
18,000	0.32
13,500	0.53
9,000	0.72
4,490	0.92

The frequencies above are very low relative to the cutoff frequency of the telescope. For an F/12.25 system the cutoff frequency, ~1/λF#, equals ~125 line pairs per mm. For the 150 inch focal length of the Imager the 18,000 cycles per radian target corresponds to 4.72 line pairs per mm or less than 4% of the telescope's cutoff frequency. Likewise the 4490 cycles per radian is less than 1% of the telescope's cutoff frequency. It is important to note that these frequencies are far enough from the telescope limiting frequency so that very slight changes in wavefront and focus do not significantly affect the MTF of the system under ambient conditions.

The system MTF measurements will include the effects of the optics, electronics and the detector. Table II lists the expected contribution from each of these subsystems at ambient conditions. It is not necessary to include thermal effects since the measurements at room temperature are indicating a lower than expected value.

TABLE II						
VISIBLE SYSTEM MTF PREDICTIONS FOR SN06 AND SN05						
FREQUENCY	OPTICS		DETECTOR	ELECTRONICS	EXPECTED SYSTEM MTF	
cycles/radian	SN06	SN05	26.3 microrad		SN06	SN05
18000	0.908	0.905	0.662	0.878	0.528	0.526
13500	0.927	0.925	0.8	0.953	0.707	0.705
9000	0.948	0.947	0.908	0.983	0.846	0.845
4490	0.974	0.974	0.977	0.992	0.944	0.944

The "OPTICS" column includes the geometric MTF of the telescope and secondary obscuration, the effect of diffraction from the spider vanes, and the MTF of the wavefront using SN06 Zernike coefficients as modeled using CODE V software. The "DETECTOR" values are correct for a nominal size field of view of 26.3 microradians. The "ELECTRONICS" column lists the SN05 Imager measured values for the attenuation at the electrical frequencies that correspond to the spatial frequency. The "EXPECTED MTF" does not include any term for stray light.

The system MTF measurement records visible or infrared detector data with the scan mirror moving east to west and west to east at 20°/second since this is the normal mode of operation for the instrument. The instrument alignment is coincident with the test collimator, a 300 inch focal length Cassegrain telescope having a square-wave metal-mask bar target with the appropriate spatial frequency located at its focal plane. The motion of the scan mirror then sweeps the image of the bar pattern across the detectors. The detector output signal is the total system response to the square wave input and thus must be Fourier decomposed in order to find the sinusoidal MTF.

Table III shows the performance of the GOES Imager visible system MTF for SN05 and SN06:

TABLE III								
Visible SYSTEM MTF Results from Imager Preliminary Bench Testing								
	Prelimnary Bench Testing		Prelimnary Bench Testing		Prelimnary Bench Testing		Prelimnary Bench Testing	
	MTF @ 4490 cycles/radian		MTF @ 9000 cycles/radian		MTF @ 13500 cycles/radian		MTF @ 18000 cycles/radian	
	(Spec =0.92)		(Spec =0.73)		(Spec =0.53)		(Spec =0.32)	
IDE 1 E/	SN 06	SN 05	SN 06	SN 05	SN 06	SN 05	SN 06	SN 05
VIS 1	0.87	0.84	0.80	0.76	0.65	0.63	0.49	0.48
VIS 2	0.87	0.83	0.80	0.76	0.64	0.62	0.48	0.46
VIS 3	0.87	0.83	0.80	0.75	0.64	0.62	0.49	0.46
VIS 4	0.87	0.83	0.80	0.75	0.64	0.62	0.48	0.46
VIS 5	0.87	0.83	0.79	0.75	0.64	0.62	0.48	0.47
VIS 6	0.88	0.82	0.80	0.75	0.65	0.63	0.49	0.47
VIS 7	0.88	0.82	0.79	0.74	0.64	0.62	0.48	0.46
VIS 8	0.88	0.81	0.79	0.74	0.64	0.62	0.49	0.46

The system MTF results for SN06 Imager are 6% to 8% below the expected values given in Table II for each frequency. The SN05 Imager system MTF results indicate performance 11% to 12 % below expected values given in Table II. The SN06 values are the best MTF values to date. The fact that all the frequencies' MTF values for each instrument are low by nearly the same percentage suggests that the mechanism lowering this instrument's MTF may be the same for all frequencies.

4. MTF AT 4490 CYCLES PER RADIAN DISCUSSION

As Table III above shows, the results to date for the visible system MTF values are lower than the "expected MTF values" in Table II at all frequencies. However, the 4490 cycles per radian MTF is the only frequency consistently not meeting the specification requirement. It is appropriate then to consider and understand why this frequency is below specification.

The process of understanding why the visible detector MTF is below specification as 4490 cycles per radian begins by listing all the possible contributors to a lower than expected MTF at 4490 cycles per radian. The most probable sources of error to cause the low MTF at 4490 cycles per radian are:

- •poor image quality - low telescope MTF or distorted scan mirror
- •ghost reflections from optical components
- •light scattering in and around detector
- •poorly defined detector field of view - out of active area response or carrier diffusion within substrate
- •test equipment MTF - MTF of collimator, bar target MTF
- •test setup - alignment of collimator to Imager or light source to collimator

When low spatial frequencies, such as the case for the GOES Imager and Sounder, are yielding lower than expected MTF, it is usually, though not always, the result of stray or unwanted light reaching the detector. At low spatial frequencies the modulation is near unity and the minimum level is near zero. The stray light effect for low spatial frequencies reduces the modulation by approximately twice the stray light percentage, as the equation for modulation illustrates:

$$\frac{(MAX+\varepsilon)-(MIN+\varepsilon)}{(MAX+\varepsilon)+(MIN+\varepsilon)}=\frac{(MAX-MIN)}{(MAX+MIN+2\varepsilon)}=MODULATION \qquad (1)$$

where ε represents the stray light level. As the *MIN* value approaches zero the small amount of stray light has its effect doubled. Therefore a 2% stray light level will reduce the MTF by about 4%. This substantially increases the difficulty for designing systems that meet low frequency MTF requirements and for making accurate low frequency MTF measurements.

Let us address each of the instrument-related possible contributors to the low MTF. A discussion of the test equipment and test setup issues is the topic for another paper[3].

4.1 Poor Image Quality

For the Imager or Sounder sensor module the wavefront measurement of the scan mirror and telescope is the means for evaluating the quality of each subsystem prior to measuring MTF. Separate subsystem measurements of the scan mirror and the telescope verify the wavefront errors for each one. A combined wavefront measurement verifies acceptable wavefront error of the two subsystems together on the baseplate. For SN05 and SN06 Imager and Sounder the wavefront errors measure from 0.5 to 1.0 wave peak to valley. The wavefront data for SN05 telescope and scan mirror indicates 0.832 waves peak to valley or 0.121 waves rms. For SN06 Imager the wavefront data measures 0.679 waves peak to valley or 0.099 waves RMS wavefront error. With these values of wavefront error there is only a slight degradation in MTF at the 4490 cycles per radian frequency. If the scan mirror and telescope wavefront errors degrade the low frequency MTF, then the degradation at higher spatial frequencies will be even greater. Table II and III show that the MTF values are low by approximately the same percentage for all frequencies. Thus the conclusion is that the wavefront error is not degrading the low spatial frequency MTF.

4.2 Ghost Reflections

For the Imager (or Sounder) optical path there will be ghost reflections from each of the transmissive components: the visible-infrared beamsplitter, depolarizer, spectral bandpass, spectral balance filter and detector window. The visible-infrared beamsplitter and depolarizer (visible and star beamsplitter) both create a double internal reflection ghost. Each ghost will move away from the optical axis but in different directions since their tilts are in different planes. For these two components each ghost appears approximately 500 microradians off axis with an intensity of approximately 0.5%. The value of 0.5% for the visible-infrared beamsplitter is the result assuming a 2% reflectance of the MgFl coating on the back surface and assuming the reflectance is equal to 1 - transmittance for the front surface. The transmittance of the front surface is ~75% for the visible light therefore creating a reflectance of 25%. These ghosts are particularly important in the case of an extended field of view, such as the Imager has, as the ghosts can fill in dark areas or make lighter areas seem brighter. The spectral bandpass filter is normal to the incident light and has each surface anti-reflection coated which produces a double internal reflection ghost with a relative ghost intensity of ~0.04% (2% * 2%). The spectral balance filter

(not in Sounder) is a color glass filter, is normal to the incident light and has no anti-reflection coating. The approximate surface reflectance of 4% for each surface produces a double internal reflection ghost with an intensity of ~0.16%. In addition there will be a ghost reflection resulting from the facing surfaces of the two filters. This ghost will have a relative intensity of ~0.08% (also not in Sounder). The detector window is flat and normal to the incident beam with an anti-reflection coating on both surfaces producing surface reflectance of less than 1% over the spectral band of interest. A double internal ghost reflection and an external ghost reflection between the window and the spectral balance filter will result from this window with intensities of ~ 0.01% and ~0.04% respectively. These ghosts will fall very close to the optical axis as nothing is controlling the pointing of these reflections directly. For the MTF bar targets, the exact phasing of the reflections with the bar pattern will affect the level of unwanted light. The best case is when the reflections align with the bars and the worst case is when the reflection is 180 degrees out of phase with the bar pattern, i.e., a bright bar ghost image aligns with the dark bar of the primary image. The estimate of the total intensity of these ghost reflections is 1.25%. This 1.25% unwanted light level may produce a 2.5% degradation in MTF.

4.3 Visible Detector Configuration

The Imager visible detector is an 8 element array of discrete photodiodes on the same substrate. Each element of the array is approximately 0.004 inch or 100 μm square. Figure 2 shows a diagram of the detector package. The substrate bonds onto the header in the center of the TO-5 can. The window for the detector attaches to the cap. The distance from the detector substrate to the window is 0.030 inch. The detector window is 0.020 inch thick. The detector substrate has a coating of aluminum that exists everywhere except over the active area of the detectors to prevent any out of active area response from within the substrate. The estimated aluminum reflectivity within the bandpass is 80% to 90%. The detector window material is BK-7 G-18 glass and it has an anti-reflective coating with reflectance less than 1% for each surface. The kovar cap has the window bonded to the underside of it. A welding process joins the kovar cap to the header. The inside of the kovar cap is gold coated which is also very reflective -- estimated average reflectivity of gold at 0.55 to 0.75 μm is ~90%. The cap also has an oval aperture for the incident light of dimensions 0.047 by 0.080 inch. The aperture in the cap has a rolled edge of 0.005 inch thickness or greater. From this edge the detector receives a glint during slit scans of the visible field of view. Placing a 0.001 inch thick stainless steel aperture mask over the cap significantly reduces the glint. The aperture in the mask has dimensions of 0.036 by 0.065 inch. The stainless steel mask is very reflective with an estimated reflectance of ~60% to 70% at 0.5 to 0.75 μm. However only a very small rim of it is directly visible to the detector. On the telescope side the mask will reflect a significant amount of incident light back toward the filters - both specular and diffuse reflection. High reflectivity on the outside of the detector package and mask keeps the temperature of the mask, detector and detector package from increasing too much if the sun happens to walk across the image plane.

FIGURE 2
IMAGER VISIBLE DETECTOR

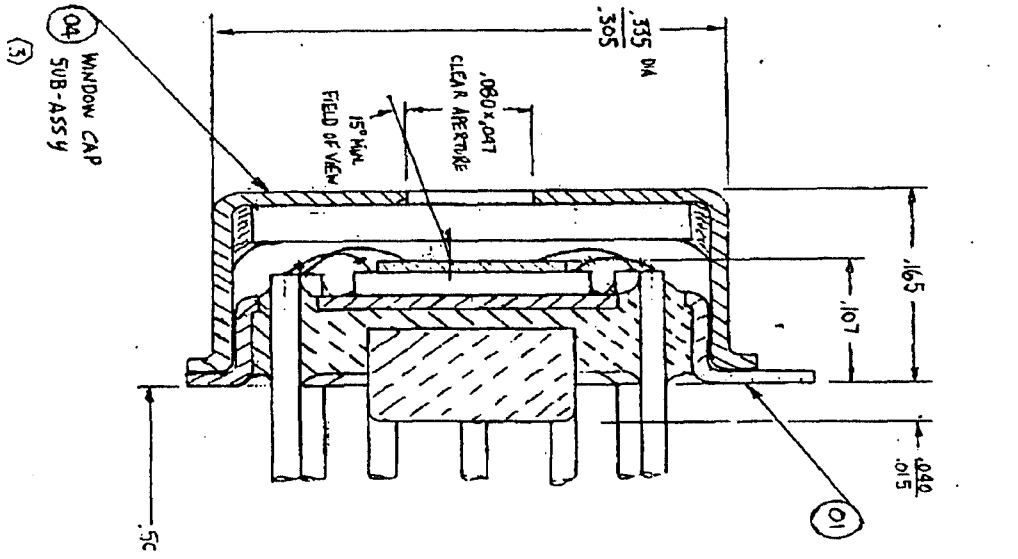

4.4 Detector Contribution to Stray Light

The visible optical path has no field stop other than the detector itself and the telescope. Therefore the full field of view of the telescope which is approximately 2 milliradians focuses onto the detector assembly. This is a circular image of nearly 0.3 inch in diameter. The light incident on the detector passes through the detector's aperture and reflects off the aluminum coated substrate back to the window and filters. Since the window is only 0.030 inches from the detector, the light will reflect from the aluminum coated surface to the window and back to the detector. Each surface of the window reflects approximately 1% of the light reflected from the aluminum which reflects 80% of the light incident on it. The intensity of the reflections at the detector will then be approximately 0.8% from each surface for a total of 1.6%. The maximum reduction in MTF would then be approximately 3.2%.

This level of stray light assumes that the reflection is all specular. The appearance of the aluminum coating on the substrate surface indicates that at least some of it may be a diffuse reflectance. Although not accurate, if one assumes that the substrate reflects diffusely, it is possible to make an estimate of the contribution to the stray light level based upon a diffuse reflection and the additional assumption that the detector package is an integrating sphere. While not an accurate model, the technique is useful to bound the situation. For an integrating sphere the ratio of output power to input power[4] or 'thruput' is:

$$thruput = \frac{R * F_e}{1 - R*\left(1 - F_j\right)} \tag{2}$$

where R is the reflectance of the interior wall, F_e is the ratio of the areas of the exit port (in this case the detector area) to the total surface area of the sphere, and F_j is the ratio of the area of all ports input aperture plus detectors to the total surface area of sphere. This formula is not strictly accurate in this case, however does produce a stray light level onto the detector which is useful for comparison. Table IV lists the appropriate values and calculation results. The resultant stray light level relative to the scene is then 1.2%. This stray light causes a possible 2.4% reduction in MTF.

TABLE IV

entrance port area	0.002062 in^2		
detector area	0.000133 in^2		0.00394 x 0.03334 (8 element array)
total surface area	0.180019 in^2		cyl. 0.30 dia. x 0.0433 long minus ports (API)
F_e	0.000739		
F_j	0.012193		
average R	0.90		API is conservative average of aluminum & gold
"thruput"	0.005993		
stray light level relative to scene	0.0116 (1.2%)		thruput * entrance port area/detector area/8

There is another source of stray light due to the detector assembly. The stainless mask which is ~60% reflective creates a significant amount of scattered light. The detector sees the mask in reflection off of the spectral balance filter and the spectral bandpass filter. The area that the detector sees has a diameter of about 0.3 inches compared to the mask aperture dimensions of 0.036 by 0.065 inch. The level of this scattered light is approximately 0.5%. This brings the worst case stray light level to a possible 2.1% from the detector and its package. The corresponding maximum effect on MTF is 4.2%.

For either specular or diffuse reflectance from the detector substrate and its package it is clear that the potential for stray light levels of 1% to 3% is high. Thus the recommendation is to reduce the reflectivities of all the surfaces near the visible detector as much as possible to minimize stray light and improve MTF performance.

If darkening the detector and its package, the potential exists for the detector to reach a higher temperature, assuming a direct viewing of the sun.. Thermal analysis shows that an exposure to the sun's image on the detector could cause the detector's temperature to reach 120 centigrade using a 10% reflectance and a 2 minute exposure to the sun's image. This is

an issue with the present detectors due to a bond which was made at 90 centigrade. Making the detector less reflective means that more of the incident light is absorbed and will cause an increase in temperature that the detector must survive.

To summarize the discussion up to this point, the image quality of the optical system is not responsible for measurable degradation of the MTF at 4490 cycles per radian, ghost reflections cause at most a 2.5% reduction in MTF at 4490 cycles per radian and the detector and its package produce as much as 4.2% reduction in MTF at 4490 cycles per radian. Assuming these effects are multiplicative then the MTF resulting from ghosts and detector stray light is 0.975*0.958 = 0.933. This reduction in MTF is again a worst case condition and is not necessarily expected for each instrument.

The worst case reduction in MTF of 6.7% is comparable to the levels by which the MTF at 4490 cycles per radian is below spec for SN06 Imager. The reduction explains SN06 MTF values but falls somewhat short for explaining SN05 MTF values at 4490 cycles per radian. The difference between SN05 and SN06 Imager instruments may be the result of component differences such as reflectivity, wedge and tilt, as well as the relative alignment between each of the components in the optical path. The instrument differences are the subject for another discussion.

5. IGFOV DATA

Assuming that the detector and its package create a significant level of stray light, the Instantaneous geometric field of view (IGFOV) curves generated by slit scans that map out each detector 's field of view will show the stray light. Figures 3 and 4 are the IGFOV curves from Imager SN06 subsystem testing of the **detector by itself** to verify the proper placement of the mask on the detector. In this test the image of a 5.2 microradian slit moves in steps of 10 μm across the detector plane. At each step the data acquisition system collects 8 values of each visible detector output signal, averages the values and stores the average value to disk. In particular the EW plot shows a low level, slightly less than 1% of the peak intensity, extending 0.018 inches either side of the detector which corresponds to the edge of the mask aperture. The mask aperture is 0.036 inches wide in this dimension compared to the 0.004 inch detector width.

FIGURE 3
SN06 IMAGER VISIBLE DETECTOR NS SLIT SCAN
ELEMENTS 1, 2, 4, 7 AND 8

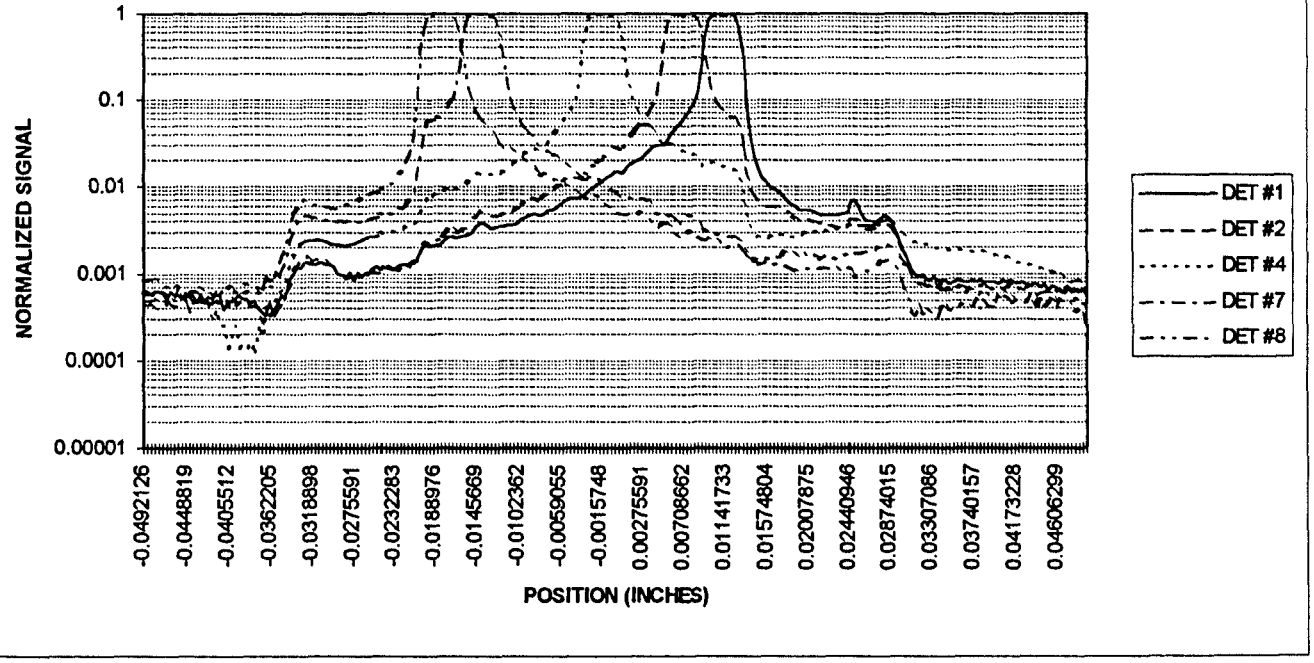

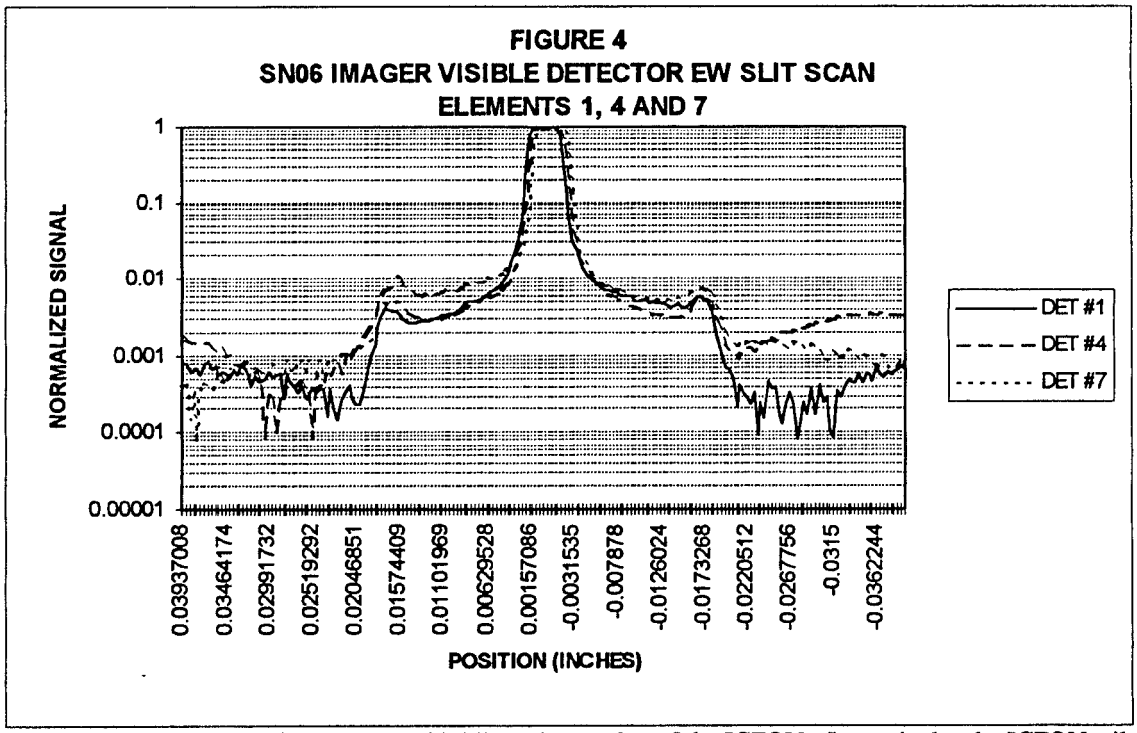

For the NS slit scan the detector IGFOV curves highlight the overlap of the IGFOVs. In particular the IGFOV tails extend out across several neighboring detector elements until about the 1% level is reached. The edges of the mask aperture are noticeable as they occur approximately 0.032 inch from the center of the detector array with a relative signal level of ~0.5%.

In order to estimate quantitatively the level of stray light present one needs to determine the detector signal coming from outside the "normal detector response" and compare that with the primary response of the detector. The exact point to separate the two regions is not obvious. The slit image has its 5.2 microradian width but extends beyond that due to diffraction. For this reason the stray light level is calculated two ways. The first method uses only the signal outside of the 1% amplitude points. The second method uses the signal outside of a 150 μm width centered about the peak response. The ratio of the integrated signal outside the detector to the integrated signal for the detector is the estimate of stray light.

For the slit scans the slit is much longer than the total field of view and therefore performs the integration in one dimension. The integration over the scan direction, the area under the IGFOV curve, then yields the desired total integrated response. Since the ratio of the areas is the value of interest and since the points have equal spacing, the sum of the signal values will be equivalent to the area. The area under the curve outside the detector is then the sum of all signal values in a specified range minus the detector signal sum. The stray light percentage is then the ratio of the outside sum to the detector sum. Table VI shows these results for the SN06 Imager for both NS and EW axes. In Table V the column heading "1% amplitude ratio" is the stay light level for the 1% amplitude criterion and the column heading "150 micron ratio" is the stray light level for the 150 μm width criterion.

The results for the EW or vertical scan show 4% to 6% of the detector output signal coming from regions outside the 1% amplitude points. The width between the 1% amplitude points is ~2.4 times the detector diameter. Using the 150 μm detector width , the results show that 5% to 8% of the detector's output signal comes from outside the detector. Whether choosing the 1% amplitude or the 150 μm width the results indicate a significant signal approximately 5% coming from outside the detector area. The 5% stray light level will cause a 10% reduction in MTF.

In the NS axis the 1% amplitude width produces results of 3% to 5% for the part of the detector output signal coming from regions outside the detector. This stray light level is slightly lower than EW primarily because the average 1% amplitude width is 6 times the detector diameter for the SN06 Imager. For the 150 μm detector width these percentages of signal

coming from outside the detector become much larger because of the broad tails on the curves. The stray light level percentages range from 14% to 21% in the NS direction.

			TABLE V				
		SN06 IMAGER VISIBLE DETECTOR					
EW STRAY LIGHT ESTIMATES					NS STRAY LIGHT ESTIMATES		
detector	1% amplitude	1% width	150 micron	detector	1% amplitude	1% width	150 micron
	ratio	inches	ratio		ratio	inches	ratio
1	0.0379	0.0094	0.0558	1	0.0464	0.0181	0.1552
2	0.0453	0.0094	0.0630	2	0.0386	0.0201	0.1825
3	0.0668	0.0094	0.0841	3	0.0463	0.0240	0.2086
4	0.0584	0.0102	0.0793	4	0.0354	0.0291	0.2143
5	0.0552	0.0094	0.0735	5	0.0325	0.0287	0.2042
6	0.0434	0.0091	0.0591	6	0.0309	0.0244	0.1873
7	0.0480	0.0091	0.0633	7	0.0384	0.0201	0.1743
8	0.0572	0.0094	0.0748	8	0.0460	0.0189	0.1398

The different character of the NS scan from the NS scan points to the possibility of another phenomenon which could be happening. The diffusion of carriers within the substrate occurs once photons penetrate far enough into the substrate. The longer wavelengths of light, greater than 0.7 μm, penetrate the substrate to depths where diffusion can occur. This effect is a concern primarily in the NS axis as there is nothing else in the EW axis to attract the carriers. So there is probably carrier diffusion occurring within the detector substrate in addition to the detector stray light that causes the IGFOV tails in the NS slit scan data of figure 3.

6. PROPOSED CHANGES TO IMPROVE LOW FREQUENCY MTF OF THE DETECTOR

After giving some rationale for the existence of stray light at the detector and showing some results which indicate the extent to which stray light may impact the MTF at 4490 cycles per radian, it is appropriate to address the particular changes that could improve or reduce the stray light within the detector package. Based upon the discussions above, the recommendations for improving the MTF at 4490 cycles per radian include the following changes:

1. Deposit a non-reflective coating on the substrate around the detector active area.
2. Improve the anti-reflection coating on the window to be <1% in the 0.55 to 0.75 μm band.
3. Place the window farther from the detector substrate at least .040 inch away.
4. Reduce the reflectivity of the inside and outside of the detector cap including the aperture mask to <50%.
5. Modify device internal structure changes to better define the active areas and reduce crosstalk in the along -the array dimension.

These changes to the detector and its package will decrease the stray light levels at the detector and thus increase the MTF at the very low frequencies.

7. THE NEW DETECTOR

Figure 5 shows a drawing of the new detector configuration. It is very similar to the old detector with the exception of the changes listed above. In the new detector the black polyimide coating will cover the aluminum coating on the substrate. The spectral curve shows that for the Imager bandpass the reflectance is approximately 5%! This is significantly lower than the 80% to 90% aluminum reflectance. The window has an anti-reflective coating with the reflectance from each surface less than 0.5% over the 0.55 to 0.75 μm wavelength band. Also the window for the new detector is now 0.048 +/- 0.008 inch away from the detector substrate. The only item in the list not included in the changes is #4, reducing the reflectivity of the cap and mask and housing. The darkening of the cap, aperture mask and housing will be forthcoming in later devices and could show a slight improvement in low frequency MTF's over the devices now in process.

FIGURE 5
THE NEW DARKENED SUBSTRATE DETECTOR

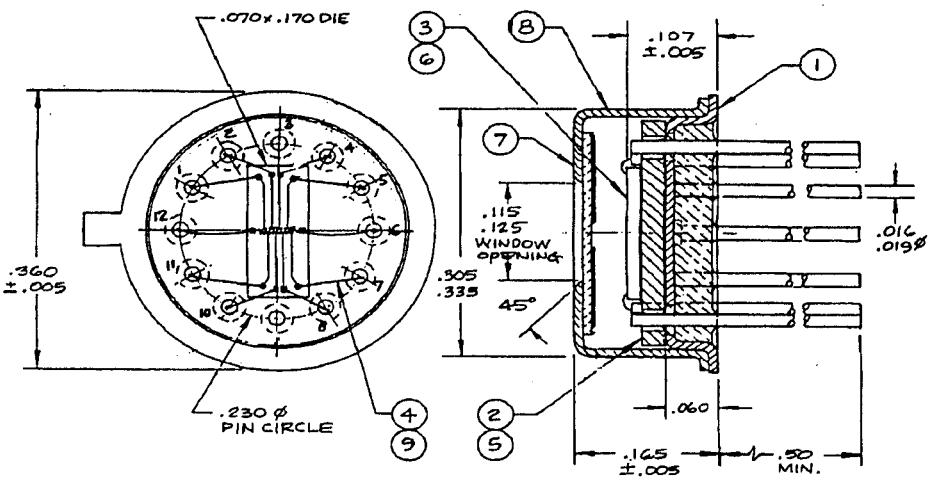

7.1 Results Of New Visible Detector MTF Tests

The SN06 sounder star sense channel will be the first opportunity to install the new device in a flight instrument. The Sounder star sense optical system is essentially the same as the Imager visible optical system with the exception that the telescope has a focal length of 145.8 inches, the spectral bandpass extends from 0.4 to 1.0 μm and the spectral balance filter is not present. The element sizes of this specific detector are slightly small in the EW and slightly large in the NS and would not meet the Imager IGFOV requirement. It is important to note that the aperture in the stainless steel mask for this device is different. The aperture is now circular rather than oblong and has a diameter of 0.058 inches. The mask is not black.

FIGURE 6
SN06 SOUNDER STAR (DARKENED SUBSTRATE) DETECTOR EW SLIT SCAN ELEMENTS 1, 4 AND 7

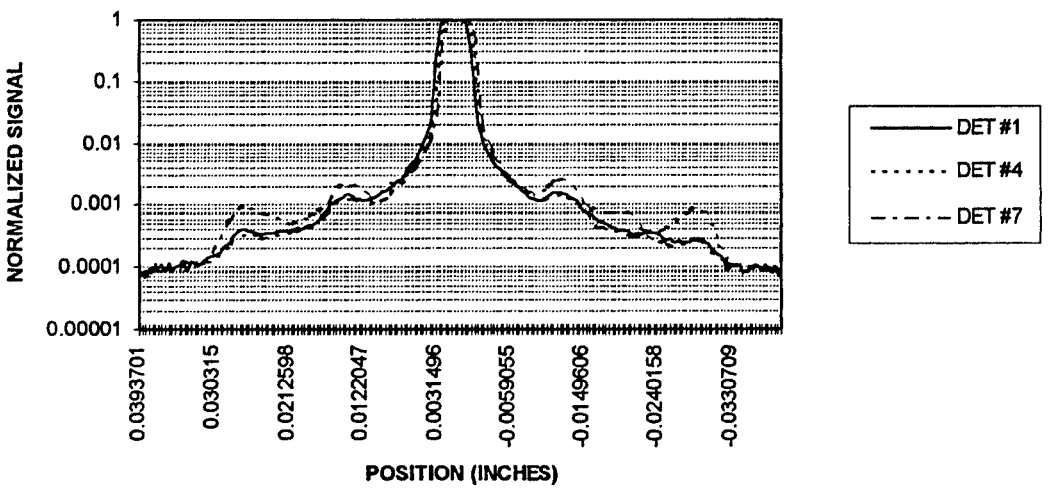

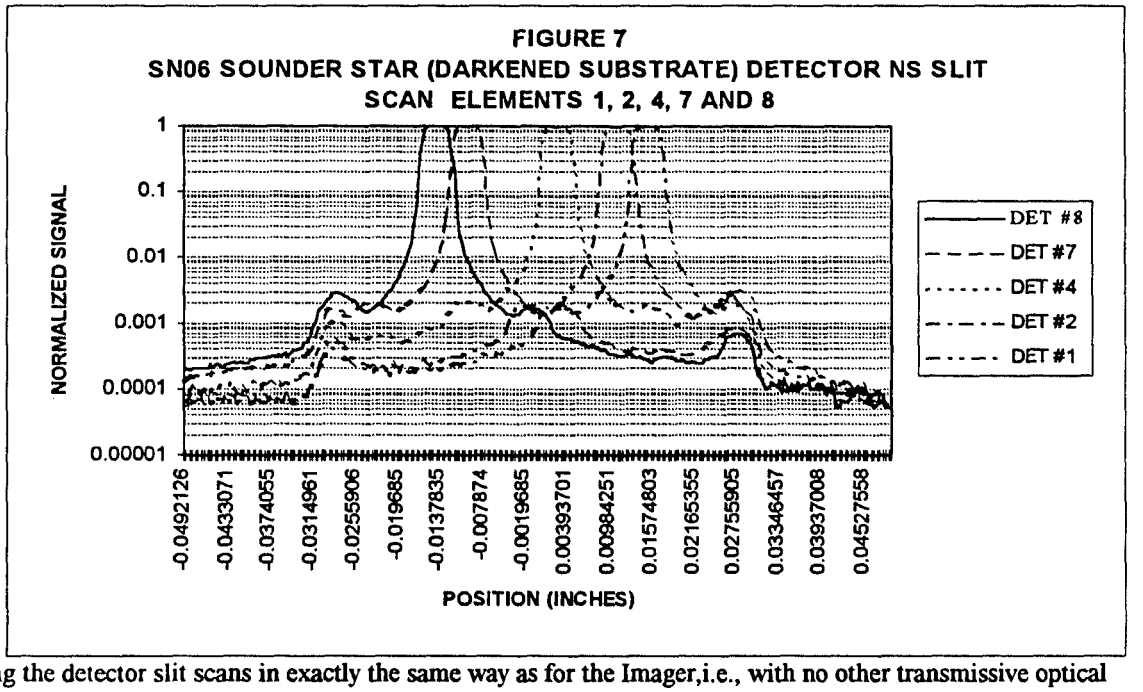

Repeating the detector slit scans in exactly the same way as for the Imager,i.e., with no other transmissive optical components in the path, will demonstrate whether the stray light levels are actually lower for the new darkened substrate detector. Figures 6 and 7 show the IGFOV scans for the darkened substrate detector. For the EW slit scans the plots show a reduction in the signal to lower levels outside the detector. This is true for the NS IGFOV scans as well. Comparing signal levels to the SN06 Imager Figures 3 and 4 the curves in figures 6 and 7 show factors of 2 to 3 reduction in the signal levels for regions just outside the detector. The reduced stray light levels should impact the MTF values for the lower spatial frequencies.

In order to compare the stray light levels between the instruments, it is necessary to repeat the same calculations or integrations performed and reported above. Table VI shows the results of the integration process for the new darkened substrate detector. In the EW axis the 1% amplitude criterion gives a detector signal outside the detector of 1.5% to 2.5%. This level is only 40% that of the SN06 Imager 4% to 6%. For the NS axis the results are similar, 1.6% to 2.5% for the new detector compared to 3% to 5% for the old detector. For the 150 μm criteria in the EW axis the new detector shows a significant reduction in the detector signal coming from outside the detector - 2% to 3% - whereas the Imager SN06 gave 5.5% to 8%. The biggest difference is for the 150 μm detector width in the NS where the new detector gives only a 2.8% to 3.7% signal level outside the detector where the SN06 Imager had a 14% to 21% signal level. The striking difference in the NS IGFOV curves is probably the result of a reduction of carrier diffusion within the substrate. Using a 2.5% stray light level for the Sounder SN06 detector will cause a reduction in MTF of 5% or about half the effect of stray light on MTF within the SN06 Imager detector. This accounts for the majority of difference between the measured and predicted MTF at 4490 cycles per radian for SN06 Imager.

TABLE VI

SN06 SOUNDER STAR (DARKENED SUBSTRATE) DETECTOR

EW STRAY LIGHT ESTIMATES					NS STRAY LIGHT ESTIMATES			
detector	1% amplitude ratio	1% width inches	150 micron ratio		detector	1% amplitude ratio	1% width inches	150 micron ratio
1.0000	0.0177	0.0067	0.0226		1.0000	0.0192	0.0079	0.0299
2.0000	0.0168	0.0075	0.0236		2.0000	0.0184	0.0083	0.0301
3.0000	0.0207	0.0071	0.0261		3.0000	0.0207	0.0083	0.0321
4.0000	0.0250	0.0071	0.0322		4.0000	0.0254	0.0083	0.0369
5.0000	0.0217	0.0071	0.0272		5.0000	0.0220	0.0083	0.0336
6.0000	0.0161	0.0075	0.0226		6.0000	0.0184	0.0083	0.0293
7.0000	0.0159	0.0071	0.0211		7.0000	0.0178	0.0079	0.0282
8.0000	0.0168	0.0071	0.0233		8.0000	0.0165	0.0083	0.0278

Table VII shows the Sounder optical MTF results using the new darkened substrate detector and also shows the SN05 Sounder optical MTF data. At 4490 cycles per radian the MTF is indeed higher than the previous instrument by ~8%. Values of 0.92 have previously never been measured on the Sounder or Imager at 4490 cycles per radian. The improvement in MTF is close to the predictions stated above. It is true also that the optical MTF values with the new detector are still a few percent below expectations leaving room for further improvement in MTF with the incorporation of a darkened cap, mask and housing.

TABLE VII
SOUNDER STAR MTF DATA

	Preliminary Bench Data MTF @ 4490 cycles/radian		Preliminary Bench Data MTF @ 9000 cycles/radian		Preliminary Bench Data MTF @ 13,500 cycles/radian		Preliminary Bench Data MTF @ 18,000 cycles/radian	
EW	SN06	SN05	SN06	SN05	SN06	SN05	SN06	SN05
SS 1	0.92	0.84	0.81	0.74	0.67	0.57	0.52	0.46
SS 2	0.91	0.83	0.81	0.74	0.67	0.57	0.52	0.46
SS 3	0.91	0.84	0.81	0.74	0.67	0.57	0.52	0.45
SS 4	0.91	0.83	0.80	0.74	0.66	0.57	0.52	0.45
SS 5	0.92	0.84	0.81	0.75	0.67	0.58	0.52	0.46
SS 6	0.92	0.84	0.81	0.75	0.67	0.58	0.53	0.47
SS 7	0.93	0.84	0.81	0.74	0.67	0.58	0.53	0.47
SS 8	0.93	0.84	0.81	0.74	0.68	0.58	0.53	0.46
NS	4490 c/r	4490 c/r	9000 c/r	9000 c/r	13500 c/r	13500 c/r	18000 c/r	18000 c/r
SS 1	0.91	0.80	0.79	0.72	0.65	0.54	0.48	0.47
SS 2	0.91	0.80	0.80	0.72	0.65	0.54	0.49	0.47
SS 3	0.90	0.82	0.81	0.72	0.64	0.55	0.49	0.47
SS 4	0.91	0.82	0.81	0.70	0.65	0.55	0.48	0.47
SS 5	0.91	0.82	0.79	0.73	0.65	0.55	0.49	0.47
SS 6	0.91	0.82	0.81	0.73	0.65	0.55	0.49	0.47
SS 7	0.91	0.82	0.82	0.71	0.65	0.54	0.49	0.47
SS 8	0.91	0.82	0.80	0.70	0.65	0.54	0.49	0.48

8. CONCLUSIONS

The results of the IGFOV and the MTF measurements with the new darkened substrate detector verify the theory that stray light has been a major contributor to the MTF at 4490 cycles per radian being below specification. The data also validates the detector as a source of a significant portion of the stray light. Further the analysis indicates that the high reflectivity of the substrate is the primary source of the stray light at the detector.

9. ACKNOWLEDGEMENTS

The authors would like to thank Ed Andrews for helping with the detector device developement. The GOES program is funded by NOAA to Space Systems Loral (SSL) who is the primary contractor for the GOES spacecraft. ITT Aerospace Communications Division is a subcontractor to SSL.

10. REFERENCES

1. ITT Aerospace/Communications Division, Imager Operational Reference Manual, 6281320-1D, 1993.
2. K. A. Hursen and R. W. Ross, "The GOES Imager: an overview and evolutionary development," in *GOES-8 and Beyond*, Edward R. Washwell, editor, Proc. SPIE 2812, to be published, 1996.
3. F. L. Williams, D. R. Wickholm and J. C. Ehlert, "Comparison between subsystem and system optical MTF for GOES Imager," in *GOES-8 and Beyond*, Edward R. Washwell, editor, Proc. SPIE 2812, to be published, 1996.
4. D. J. Lovell, "Theory and Applications of Integrating Sphere Technology," *Laser Focus/Electro-Optics*, p. 86, May 1984.

SESSION 7

Calibration

Real-world calibration of GOES -8 and -9 sensors

Michael Weinreb

Satellite Research Laboratory
NOAA/NESDIS
Washington, DC 20233

ABSTRACT

The calibration processing algorithms currently in effect for the GOES-8 and -9 imagers and sounders are described. The algorithms have been changed since the launch of GOES-8. Smoothing of the calibration slopes has been instituted to suppress the effects of noise in the blackbody sequences. In the visible channels, the signal, originally transmitted to users in absolute counts, is now provided relative to the signal from space. The operational calibration equations were generalized to eliminate errors caused by the variation of the reflectances of the instruments' scan mirrors with east-west scan position, which was discovered after the launch of GOES-8. We are in the process of developing processing changes to mitigate the effects of two other anomalies--the appearance of east-west stripes in the infrared images from the imagers; and erroneous calibrations around midnight during six months of the year, caused by the presence of unwanted radiation from hot components of the imagers' and sounders' telescopes during the calibration sequences. Instructions are given on how to convert the counts in the GVAR (GOES VARiable format) data stream to radiances, temperatures, and mode-A counts.

Keywords: calibration, infrared radiation, visible radiation, radiometers, meteorological satellite sensors

1. INTRODUCTION

The GOES-8 and -9 satellites, launched into geostationary orbit on April 13, 1994, and May 23, 1995, respectively, each carry an Earth-atmosphere imager and an atmospheric sounder.[1-3] These instruments observe the Earth in a total of 24 spectral intervals ("channels") at wavelengths between 0.6 μm and 14.7 μm. Each imager has five spectral intervals, which are isolated by stationary filters in its optical chain. There is a separate linear north-south array of detectors for each channel--eight detectors in channel 1 (visible), two in channels 2 (3.9 μm), 4 (10.7 μm) and 5 (12 μm), and one in channel 3 (6.7 μm). Each sounder has 19 spectral intervals, one in the visible and 18 in the infrared. The spectral intervals in the infrared are isolated by a rotating filter wheel. There are three sets of four detectors in the infrared, one set for all the channels in each of three infrared spectral regions--shortwave (six channels between 3.7 and 4.6 μm), midwave (five channels between 6.5 and 11 μm, and longwave (six channels between 12 and 15 μm). The visible channel is isolated with a separate optical chain and set of four detectors.

Imager outputs are transmitted to the ground station as 10-bit words, sounder outputs as 13-bit words.

The characterization of the radiometric performance of each instrument begins with an extensive program of pre-launch tests conducted by its manufacturer (ITT, Ft. Wayne, IN) and by the GOES I-M prime contractor (Space Systems/Loral, Palo Alto, CA). The tests before the launch of GOES-8 were notable for revealing performance anomalies. The most serious of these, 1/f-noise and temperature-related drifts in imager output, actually necessitated hardware changes in the instruments. In addition, modifications to the calibration processing were required, which the ground-system contractor (Integral Systems, Inc., Lanham, MD) completed shortly after the launch of GOES-8 (but before the GOES-8 instruments became operational). Despite the extensive testing before launch, the data received from space after launch revealed some additional, relatively subtle anomalies.

The purpose of this paper is to present the current status of the calibration processing, including modifications to mitigate effects of anomalies discovered when the instruments were in space. We begin by describing the calibration data produced by the instruments during normal operations. A summary of the infrared-channel calibration equations in place at the launch of GOES-8 follows. Post-launch changes to the calibration equations to correct an east-west variation in the reflectances of the scan mirrors are described, as is the technique for suppressing effects of noise in the blackbody sequences. Two remaining problems affecting the infrared channels are mentioned, for which remedies are

under development. Processing of the data in the visible channels is summarized. Although the visible channels are not calibrated in orbit, their data are normalized, and, beginning recently, relativized. Finally, instructions on how to convert the GOES VARiable format (GVAR) data--the data transmitted to users--to radiances, brightness temperatures, and mode-A counts are provided (for the infrared channels only).

2. INFRARED CALIBRATION DATA

In orbit, the imagers and sounders periodically view space and their on-board warm blackbodies to acquire data for calibrating their infrared channels. Each instrument's blackbody is in front of its entire optical chain and fills its optical aperture, providing a full-system calibration. The data acquired at the blackbody looks (and associated space looks) are used for inferring the instruments' calibration slopes (radiance increment per output count), which are the reciprocals of the responsivities. The data from the space looks, which, as we will see below, occur more frequently than the blackbody looks, allow us to infer the calibration intercepts (radiance at zero counts).

To preserve the precision of the measurements, the instruments must be calibrated often, because temperatures on a three-axis stabilized satellite such as GOES vary diurnally and rapidly by tens of Kelvins. Space looks must occur more frequently than blackbody looks, since temperature changes affect the calibration intercepts more than the slopes. Also, the imagers must view space as frequently as possible to control the effects of 1/f noise in the channels that use photoconductive HgCdTe detectors. While viewing space, the imagers execute their DC signal restores ("space clamps"). The 1/f noise manifests itself as a drift in the imager's output in the time between the space clamps. The more frequent the clamps, then, the less severe the drifts. The sounders execute DC restores while viewing their filter wheels (instead of space) at a frequency of approximately 50Hz, which essentially eliminates drifts caused by 1/f noise.

The intervals between calibration measurements are listed in Table 1. For the imager, the space looks for calibration all involve space clamps. Current calibration operations use the 2.2-sec space-look interval for imaging the full Earth and the 36.6-sec interval for imaging smaller sectors. The 9.2-sec interval is not used for routine imaging. This selection of intervals represents a compromise between radiometric precision and Weather-Service schedules.

TABLE 1: Intervals between calibration measurements

Measurement type	Imager	Sounder
Space	2.2, 9.2, or 36.6 sec	2 min
Blackbody	30 min	20 min

The following is the sequence of events at each calibration: For a sounder, a space look may interrupt a scan line in progress. It consists of the acquisition of 40 samples of data at a location at least 0.5 degrees away from the Earth. Typically, this requires a total of approximately 8 sec, of which 4 sec is devoted to taking the data and the rest to slewing and settling of the scan mirror. A blackbody sequence, which may interrupt a frame in progress, consists of acquisition of 40 samples from a view of space (4 sec), data for a check of the linearity of the electronics (1.6 sec), and 40 samples during the view of the blackbody (4 sec). The entire sequence requires approximately 55 sec, of which approximately 45 sec are devoted to slewing and settling of the scan mirror. The view of the blackbody follows that of space by approximately 23 sec.

For an imager, a space look occurs at a scan reversal--the end of an east-to-west or west-to-east scan, as the direction of the scan mirror's motion reverses in preparation for a scan in the opposite direction. The location is at least 0.5 degrees from the edge of the Earth. The sequence of events at the reversal is acquisition of 400 (nominally) samples from a view of space, the DC restore (clamp), and another acquisition of 400 samples of data from a view of space immediately following the clamp. These two views of space are called the "pre-clamp" and "post-clamp" views, respectively. Acquisition of 400 samples requires approximately 73 msec, and an entire scan reversal, including the clamp and the two space views requires 200 msec. The purpose of acquiring two sets of data at each space look is to

combat the effect of drifts during the period of data-taking on the Earth that occurs between any two spacelooks. We interpolate the calibration intercepts (see below) in time from the post-clamp of the first space look to the pre-clamp of the second. This accounts for the linear (in time) component of the drift, but it does not correct for any of the higher-order components.[4]

Imager blackbody sequences occur every half hour between frames. A sequence consists of acquisition of 400 samples from the post-clamp phase of a space look (73 msec), 1000 samples during the view of the blackbody (183 msec), and 400 samples (73 msec) from the pre-clamp phase of the space look following the blackbody. The entire sequence requires approximately 44 sec, and almost all of that is dedicated to the slewing and settling of the scan mirror. The blackbody observations take place approximately 18 seconds after the first space look and 18 seconds before the second. To minimize the effect of drifts that will almost certainly affect the instrument outputs in the intervals between the views of the blackbody and space, we interpolate the outputs from the two space looks to the time of the blackbody look. This accounts for the linear component of the drift but does nothing to correct for higher-order components.[4]

3. ORIGINAL INFRARED CALIBRATION EQUATIONS

The original basic calibration equation, in place at the launches of both GOES-8 and GOES-9, relates sensor output X (in digital counts) to scene radiance R, in $mW/(m^2\text{-}sr\text{-}cm^{-1})$, by

$$R = qX^2 + mX + b \tag{1}$$

The value of q, the coefficient of the quadratic term, was (and is) known *a priori*, having been determined from measurements made by ITT before launch.[5] The quadratic term allows for possible non-linearities in sensor response.

The coefficients m and b, termed the slope and intercept, respectively, were determined during in-orbit operations as follows: From the data in each blackbody sequence, m was given by

$$m = [R_{bb} - q\,(X_{bb}^2 - X_{sp}^2)]/(X_{bb} - X_{sp}) \tag{2}$$

where subscripts bb and sp refer to data taken from views of the blackbody and space, respectively. The blackbody's radiance R_{bb} is computed from its temperature and the spectral response function of the channel. For both the sounder and the imager, the blackbody's temperature is measured by eight thermistors. In the computations, we average nine samples from each thermistor and average over the eight thermistors. For efficiency in the real-time computation, the radiance values are computed from cubic polynomials in temperature. The polynomial coefficients were derived before launch from a fit of a cubic to a table of temperatures vs radiance evaluated at every 0.1K between 270K and 310K. This range includes every temperature the blackbodies are expected to assume in normal operations in orbit. In the table, each radiance value for each channel and detector was computed by the "exact" method: as a weighted mean over the spectral response function for that detector and channel. The errors due to use of the polynomial approximation are at least an order of magnitude less than the expected noise in each channel.

The values of X_{sp} and X_{bb} require elaboration. For the sounder, X_{sp} is the average of the 40 samples at the space look preceding the blackbody look. For the imager, X_{sp} is determined as follows: First, the 400-sample averages are computed separately for the space looks preceding and following the blackbody look. The value at the time of the blackbody look is then estimated by interpolation on time between the two space looks. The interpolation reduces the effect of drifts over the period of the blackbody sequence.[4] The values of X_{bb} are the averages of the 40 samples (sounder) or 1000 samples (imager) acquired at the blackbody view.

At each space look, b was determined from the equation,

$$b = -m\,X_{sp} - q\,X_{sp}^2 \tag{3}$$

The value of X_{sp} is the average of the 40 samples (sounder) or 400 samples (imager) acquired at the space view. For the imager, the intercepts are computed and saved for both the pre- and post-clamp views. As Table 1 indicates, space looks occur far more frequently than the blackbody looks, so the intercepts are updated more often than the slopes.

For each pixel, the radiances were computed from eq. (1) with the values of m and b from eqs. (2) and (3). For the imager, to remove the effects of drift between the space looks, we update the value of b at each pixel by interpolating between the post-clamp view at the preceding space look and the pre-clamp view at the following space look, as was described previously.

4. REVISIONS FOR VARIATION IN SCAN MIRROR EMISSIVITY

Shortly after the GOES-8 instruments began operating, we observed that the outputs of the imager and sounder channels at wavelengths between 6 and 14 μm varied with the east-west position of the field of view. This was most apparent when the scene was space. An example is in Fig. 1, which shows raw imager data from east-west scans of space above the north pole at three different times of day. Although the scans of space extend approximately 19° in the east-west direction (which slightly exceeds the 17.4° width of the Earth), they correspond to a mechanical scan-mirror rotation of half that, or 9.5°. (In Fig. 1, the abscissa is mechanical scan mirror angle.) An angle of 45° represents the meridian directly below the satellite, and the angles of 40° and 50° are located in space beyond the east and west sides of the Earth, respectively. The differences in output between the east and west sides of the scans correspond to an artificial temperature difference of approximately 150K. More to the point, there were also radiometric errors--as large as several Kelvins--in observations of the Earth, although they were masked by the variability in the scene. Similar angle dependences and radiometric errors were also observed later in data from the GOES-9 instruments. The cause of this behavior is believed to be an absorption feature of the instruments' scan mirrors' silicon oxide coatings, which causes the mirrors' emissivities to vary with the incidence angle of the incoming radiation. The processing changes[6] required to eliminate these radiometric errors will be summarized here. These changes were made operational in April 1995 and August 1995 for the GOES-8 and GOES-9 imagers, respectively. For the GOES-8 and GOES-9 sounders, they were made operational in June and April 1996, respectively.

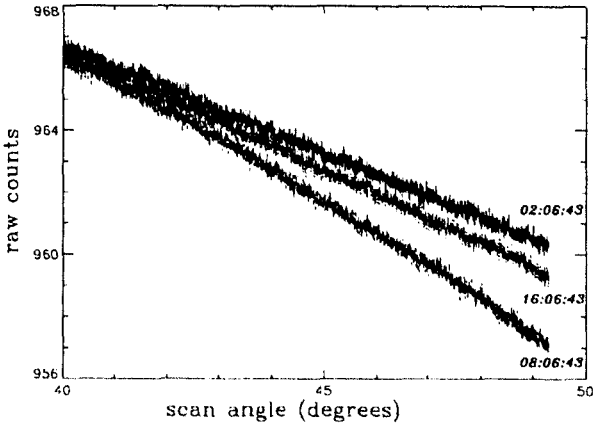

Fig. 1. Raw output on space, GOES-9 imager, channel 5 (12 μm)

4.1 Generalized infrared calibration equations

The processing changes are a generalization of the calibration equations to include the radiative transfer at the scan mirror. The generalized calibration equation is

$$(1 - \epsilon[\theta])\, R + \epsilon[\theta]\, R_M = qX^2 + mX + b \qquad (4)$$

where R, X, q, m, and b are defined as in eq. (1). The quantity ϵ is the emissivity of the scan mirror, and it is a function of scan angle θ. The procedure for obtaining the values of ϵ is described in the next section. R_M is the radiance of the scan mirror, which can be computed from its temperature and the spectral response function. On the left side of this equation, the scene radiance R is now multiplied by 1 - ϵ instead of 1; this represents the loss in radiance caused by the reflectance of the mirror now being 1 - ϵ instead of 1. The second term on the left is the radiation emitted by the scan mirror.

In orbit, the processing goes as follows: At each blackbody look, m is determined from

$$m = [r_{bb} - q (X_{bb}^2 - X_{sp}^2)]/(X_{bb} - X_{sp}) \quad (5)$$

In eq. (5), the definitions of all the variables are the same as in eq. (2). However, r_{bb} is not simply the radiance of the blackbody R_{bb}, but is related to it by

$$r_{bb} = (1 - \epsilon[45]) R_{bb} + (\epsilon[45] - \epsilon[sp])R_{M,bb} \quad (6)$$

where $R_{M,bb}$ is the radiance of the scan mirror computed from its temperature at the time of the blackbody sequence. The quantity $\epsilon[45]$ is the scan mirror's emissivity when it is at the blackbody position, for which the angle of incidence of the incoming radiation is 45°. Similarly, $\epsilon[sp]$ is the emissivity at the space look position, which will have an incidence angle of either 40° or 50°, depending upon which side of the Earth the space look occurs. (For the imager, 40° is on the west, while for the sounder it is on the east.)

Although m as defined in eqs. (5) and (6) appears to depend on the side of Earth on which the space view occurs, it is, in fact, a property of the instrument only. It is essentially the reciprocal of the responsivity of the radiometer downstream of the scan mirror and does not depend on space-view side.

At each space look, b is determined from the equation,

$$b = -m X_{sp} - q X_{sp}^2 \quad (7)$$

The value of b may depend on space-clamp side.

For each pixel, the radiances are computed from

$$R = \{qX^2 + mX + b - (\epsilon[\theta] - \epsilon[sp])R_{M,sp}\}/(1 - \epsilon[\theta]) \quad (8)$$

where m and b are the values computed in eqs. (5) and (7), $R_{M,sp}$ is the mirror radiance at the time of the space look, and $\epsilon(\theta)$ is ϵ evaluated at the scan angle (pixel position) θ.

For the imager, the interpolation of space-look counts within the blackbody sequences, and the interpolation of the intercepts between space looks, are still carried out, as described previously.

4.2 Derivation of emissivities

The scan-mirror emissivity values were determined soon after launch from in-orbit measurements of the instruments' outputs as they scanned space from the extreme west to the extreme east. Data for a number of scans were averaged to reduce random noise. For the sounders, the output varies not only with scan position, but with time, as the temperature of the instrument changes over the minute or so required for each scan. (This is not a problem for the imagers, which clamp on space every few seconds and anyway require only one second per scan.) We removed the temperature-driven drifts from the sounder data after estimating them by regression on the optics temperatures.

Emissivities were derived separately for each detector in each channel of each instrument. In the following, we suppress reference to instrument, channel, and detector, since the procedure was the same for all of them. Since we

had measurements on space at all values of θ, we simplified the definition of the calibration slope in equations (5) and (6), obtaining

$$m = \{[1 - \epsilon(45)]R_{bb} - q[X_{bb}^2 - X_{sp}^2(45)]\}/\{X_{bb} - X_{sp}(45)\}$$

where $X_{sp}(45)$ is the instrument output in counts when it views space at a scan angle of 45°. The emissivity was given by

$$\epsilon(\theta) = \epsilon(45) + \{m[X_{sp}(\theta) - X_{sp}(45)] + q[X_{sp}^2(\theta) - X_{sp}^2(45)]\}/R_M$$

where R_M is the radiance of the mirror computed from its temperature during the scans, and $X_{sp}(\theta)$ is the instrument's output in counts when it views space at scan angle θ.

The emissivities at 45° in all imager and sounder channels were provided from laboratory measurements of witness samples.[7]

The entire process was carried out for data collected approximately once an hour for 24 hours. A daily-average profile of ϵ vs θ was then computed as the average over all hours.

For each channel, we fitted a quadratic polynomial, i.e.,

$$\epsilon(\theta) = a_0 + a_1\theta + a_2\theta^2$$

to the profiles of emissivity vs θ. (Also, the variable θ was transformed to become the east-west position of the scan mirror expressed in inductosyn increment numbers, which is uniquely related to scan angle.) This produced the coefficients a_0, a_1, and a_2. They are stored in a database in the ground-system computer and are used in the processing to generate the emissivities vs angle.

Approximately once every three months we generate new emissivity-vs-angle profiles using east-west scans, as described above. Thus far, we have found no significant change in the values since the launches of the GOES-8 and -9 satellites, and so we continue to use the original values.

Figure 2 attests to the success of the generalized calibration equations. It shows the radiances of space vs scan angle derived from the original calibration equations ("before") and the generalized ones ("after") in channels 4 (10.7 μm) and 5 (12 μm) of the GOES-8 imager. The generalized equations removed apparent east-west radiance differences of 1 mW/(m²-sr-cm⁻¹) and 2 mW/(m²-sr-cm⁻¹) in channels 4 and 5, respectively.

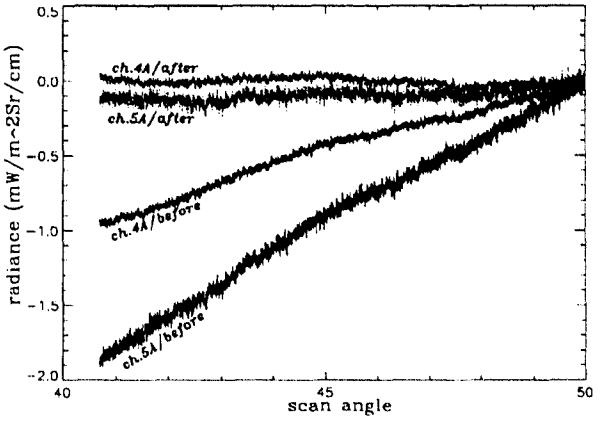

Fig. 2. Radiances of space vs angle in channels 4 and 5 of GOES-8 imager, 10/11/94.

5. NOISE SUPPRESSION IN BLACKBODY CALIBRATIONS

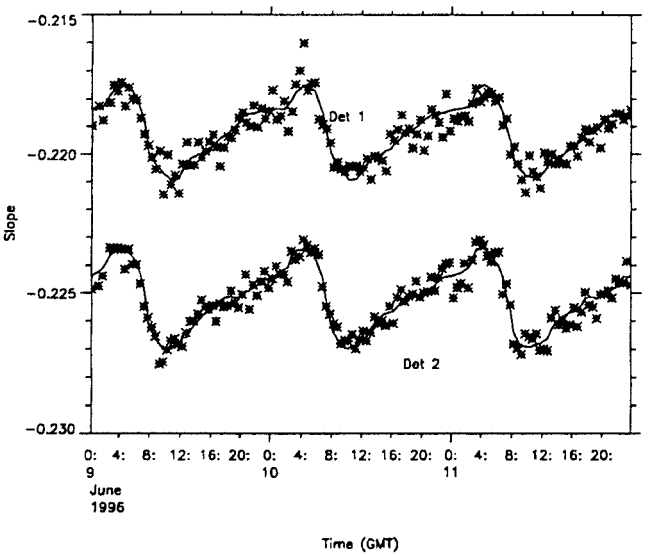

Fig. 3. Time series of slopes for detectors 1 and 2 of channel 4 of the GOES-8 imager.

Although the effects of drift and 1/f noise in the blackbody sequences are reduced by the interpolation of the space-count value to the time of the blackbody view, a significant amount of "noise" survives in the computed calibration slopes. The asterisks in Figure 3 delineate the time series of slopes, computed every 30 min, from the two detectors in channel 4 of the GOES-8 imager. Apart from the noise, these plots exhibit a repeated diurnal variation in the slopes with peak-to-peak amplitude slightly less than 2%. This is a true variation in instrument responsivity, caused primarily by temperature-driven variations in the background radiation on the detectors. This is expected, causes no errors, and will not be discussed further. However, the noise is a problem. Its primary effect is to induce errors in the radiances. It also has the effect of introducing systematic striping in the images, which is more noticeable. The reader is reminded that each of the two detectors in this channel generate alternate lines of each image. The slope error for either detector induces a systematic error in the radiance at every scene (pixel) observed by that detector for the 30 min following the calibration. Since these errors are, to a large extent, uncorrelated between the two detectors, the systematic errors in the radiances will usually be different for the two detectors, and the image will appear striped. The characteristics of the striping will change every 30 minutes, as the errors vary from one blackbody sequence to the next. The magnitude of the striping in images from channel 4 of the GOES-8 imager is typically of the order of 0.1K, for a scene at 300K, and 0.4K, for a scene at 200K. The subject of striping in images will be discussed in detail later in this session.[8,9]

The calibration processing in the ground system applies an averaging technique to smooth out the slope noise. It would not be desirable to average over a significant fraction of a day, since that would introduce errors by removing true diurnal variation. Instead, we use a two-hour running window. However, to achieve enough smoothing, we need more data than can be obtained in two hours. Therefore, we include data from the same two-hour interval from each of the previous nine days. Nine is not so many that seasonal slope changes would be significant. The averaging includes today's data--for which we have the current slope and the slopes from the previous hour, the data from the previous eight days--for which we have slopes from five blackbody sequences in the full two-hour window centered on the current time, and, finally, the data for the ninth day before the current day--for which we use the slopes for the current time and one hour afterwards. In the averaging, the slopes are weighted inversely according to their displacement in time, both in days and in minutes within the two-hour window, from the current blackbody sequence.

This averaging technique is incorporated in the calibration contingency path referred to as calibration "mode 3." Currently, it is the only one of the several contingency paths available in the ground system that is in routine use. ("Mode 1" refers to the basic calibration algorithm, including the correction for the east-west variation in scan-mirror emissivity, described in the previous sections.) The averaged (mode-3) slopes, plotted in Fig. 3 as the solid lines, reduce the scatter exhibited by the mode-1 slopes. The averaging is also effective in reducing the frame-to-frame variation in striping, as will be shown later in this session.[8]

6. INFRARED ANOMALIES YET TO BE ACCOUNTED FOR

We are currently developing new software modifications to mitigate the effects of two other performance problems--striping in infrared images from the imagers, and calibration errors due to solar heating of the imagers and sounders near satellite midnight.

6.1 Striping in infrared images

East-west stripes are observed in the Earth images produced from data in channels 4 (10.7 μm) and 5 (12 μm) of the imagers. Both of these channels use two detectors, and each detector generates every other line of the image. Quantitatively, striping is given by the mean difference between the radiances or temperatures measured by the two detectors when they view a uniform scene. Typically, its magnitude, in an rms sense, is of the order of 0.1K for scenes at 300K, and 0.4K for scenes at 200K. That the striping expressed in temperature units is relatively severe on cold scenes (a direct consequence of the Planck relationship between temperature and radiance) is unfortunate, because of its effect on data products, such as precipitation estimates, that are based on observations of high clouds.

The striping is primarily caused by 1/f noise from the detectors. In the previous section we discussed how the 1/f noise in the blackbody sequences propagates systematic striping into the images. In addition, 1/f noise in the scans themselves and in the space looks causes striping that varies randomly throughout images. Finally, there is another component of the striping, apparently constant or slowly varying over months, whose source is unknown. Striping will be described more fully later in this session.[8,9]

6.2 Calibration errors caused by solar heating near satellite midnight

Between the months of April and October, the magnitudes of the calibration slopes computed during the approximately eight hours around satellite midnight become smaller than expected. This is especially discernable in the channels at wavelengths below 10 μm. There is some evidence that, in the imager, this phenomenon is correlated with errors--of the order of 1K--in measured ocean-surface temperatures. Such behavior was predicted before launch by ITT. However, only after it was confirmed in orbit did we characterize the phenomenon and develop a correction for it. The correction will be incorporated in the ground-system software in the future. Details on this subject are presented later in this session.[10]

7. PROCESSING OF VISIBLE-CHANNEL DATA

The imager uses a north-south array of eight silicon diode detectors to image the earth, and the sounder uses an array of four similar detectors, primarily for cloud detection. With each rotation of the scan mirror, the imager thus produces eight adjacent east-west lines and the sounder, four. These detectors are not calibrated on orbit.

7.1 Normalization (destriping)

Without in-orbit calibration, the visible-channel images are susceptible to striping. Striping is reduced by the normalization of each detector's output to the output of a stable reference detector. The normalization is applied in real time at the Command and Data Acquisition (CDA) station at Wallops, VA, through application of normalization look-up tables (NLUTs) to the raw scene data.

The technique for generating NLUTs is carried out off-line and involves matching the empirical distribution functions (EDFs) of the raw data from each detector to that of the reference detector.[11] The reference detectors were chosen from considerations of long-term stability and maximal usage of the count range of the data system without clipping at the upper and lower limits.

Image striping is monitored daily at NOAA. Striping in images from the GOES-8 imager has been minimal, even without normalization. Since April 1995, the data have been normalized to remove a small amount of striping, but the detectors have been so stable that there had been no need to update the NLUT until a year later, when relativization (see below), which modifies the data slightly, was introduced. At that time a new NLUT was made operational, and we expect that it will not need to be updated for a long time. A similar statement can be made for the visible channel of the GOES-9 imager. We began normalizing in July 1995, but there was never a need to change the original NLUT until the spring of 1996, when relativization was introduced.

7.2 Relativization

The signal from any scene is the instrument's output while viewing the scene, minus its output when viewing space. Until the spring of 1996, however, the data in the visible channels of the GOES-8 and GOES-9 sensors were transmitted to users in absolute counts, i.e., scene counts without the signal from space subtracted out. In this form, the data were consistent with the visible-channel data from other NOAA satellites past and present.

We call the process of differencing the signals from the scene and space "relativization," because it produces a signal relative to space. Relativization removes effects of long-term drifts and detector-to-detector differences in offset. For the imagers, relativizing the signals is usually not important under normal conditions. The outputs of the photo-diode detectors are relatively stable in time and consistent among detectors. The space clamps continually set the count level from space to approximately 29 counts, thereby preventing significant drifts caused by temperature changes. And there are no drifts from 1/f noise in the visible channels. For a single detector, the rms variation in space-clamp levels ("clamp noise") is less than one count (out of 1024), and the variability in the space-clamp level among detectors is of the order of one count.

However, some relatively rare performance anomalies in the imagers do provide a reason to relativize. Before the spring of 1996, the visible imagery from both imagers experienced occasional incidents of severe striping, which consisted of positive or negative offsets, between 10 and 30 counts in magnitude, in the outputs of one of the eight detectors. The cause is believed to be noise spikes in the space clamps of the offending detector. Furthermore, for a few days around the equinoxes, the space clamp level of (logical) detector 6 of the GOES-9 imager's visible-channel array was observed to increase by approximately five counts for a few hours of the day, which also caused image striping. Relativization should prevent such anomalies from causing stripes in the images.

Relativization would also be of benefit for the sounders. Because they do not clamp on space, they show diurnal and seasonal drifts and detector-to-detector variations, which are tens of counts (out of 8192) in magnitude.

Therefore, in the spring of 1996 we began to relativize the visible-channel imagery from the imagers and sounders. The data are relativized before being normalized. Relativization requires two steps. First, the mean count value from the most recent space look is subtracted from the pixel counts. (For the imager, the space-look data are from the post-clamp following the preceding space look.) Second, a constant, "BOOST," is added back in. Without the second step, relativization would have two undesirable consequences. First, when space itself is the target, the distribution of the data would be approximately Gaussian with a mean of zero. Half of the distribution would have count values less than zero and would be lost, since GVAR (the GOES VARiable format data stream, which users receive) will not accommodate negative integers. Second, the overall brightness of the image would change significantly between the "relativization off" and "relativization on" states.

For all eight visible-channel detectors of all imagers, the value of BOOST is 29. For all four visible-channel detectors of all sounders, the value of BOOST is 920. Since these are the nominal values for the space-count levels in the absence of relativization, there is hardly any change in overall image brightness between the "relativization off" and "relativization on" states.

At first glance, it may seem that the two steps of relativization would cancel each other out. This not the case, however, because the mean space value and BOOST are not necessarily equal. The mean space-count level varies from space look to space look, as it is affected by noise (imager) or noise and drift (sounder), whereas BOOST is invariant.

Table 2 lists the dates that relativization was first applied to the visible-channel data from each instrument.

TABLE 2: Dates relativization began

Instrument		Date
GOES-8	Imager	5/23/96
	Sounder	6/19/96
GOES-9	Imager	4/16/96
	Sounder	4/16/96

7.3 Calibration

The visible detector-channels are not calibrated in orbit. However, calibration coefficients are measured by ITT before launch and are included in the data transmitted to users in the GVAR data stream. A factor that converts radiance to reflectance factor or albedo (on a scale of 0-1) is included as well. Since detector responsivities can vary unpredictably, the pre-launch calibration may not be valid after launch.

The calibration equation is either

$$R = mX + b \tag{9}$$

or

$$R = m(X - X_{sp}) \tag{10}$$

where R is radiance in W/(m^2-sr-μm), X is the instrument output in counts, the subscript sp refers to the view of space, and m and b are the calibration coefficients.

The value of b in eq. (9) depends on the electronic zero level, which is set at each space clamp. As was discussed in the preceding section, this level varies by approximately one count for the imagers and tens of counts for the sounder. Therefore, when the satellite is in orbit, the value of b determined in the laboratory (or at any other earlier time) may not be valid. Equation (10) is preferred.

Furthermore, relativization and normalization affect the calibration. Since normalization makes the responses from all eight detectors the same as that of the reference detector, users of the pre-launch calibration should apply the calibration coefficients for the reference detector (see Table 3) to the data from all detectors.

With relativization enabled, an instrument's output at the view of space is modified slightly, and the value of b in the calibration equation (eq. [9]) needs to be modified accordingly. For this reason also, the best approach is to use eq. (10). If eq. (9) must be used, then the value of b should be determined from the equation

$$b = -m*BOOST$$

in which m is the slope for the reference detector. Values of b determined in this way for the two imagers, as well as the values of m and BOOST, are tabulated below.

TABLE 3: Visible-channel calibration coefficients for imagers

Satellite	No. of reference detector (in physical array)	m (ref. det.)	BOOST	b
GOES-8	6	0.5521899	29	-16.014
GOES-9	7	0.5560950	29	-16.127

8. RETRANSMITTED (GVAR) DATA

Raw imager and sounder data are transmitted to the Command and Data Acquisition Station (CDA) at Wallops, VA, continuously in real time. Raw imager data are in 10-bit words, raw sounder data in 13-bit words. This section describes the subsequent data flow at the CDA, culminating in the retransmission of processed data to users.

8.1 Infrared-channel data

Calibration processing for the infrared channels, culminating in the retransmission of the data to users in the GVAR data stream, takes place at the CDA in real time. In the processing, the calibration coefficients are computed and are applied to the raw data, converting them to radiances, as previously discussed. The radiances are scaled linearly so that they utilize the full 10-bit (imager) or 16-bit (sounder) word length of the GVAR. The calibration coefficients (three per channel/detector) and the scaling coefficients (two per channel) are also transmitted in the GVAR. Users can derive the radiances from GVAR counts by inverting the scaling operation. The procedure for converting GVAR counts to radiances, temperatures, and "mode-A" counts[12] for the imagers is described in detail in the Appendix. For the sounders, the GVAR will contain both radiances and raw data. For the imagers, it will only contain the radiances, because the GVAR does not have enough bandwidth for both. The GVAR also contains statistical data and telemetry information for monitoring the calibration and instrument performance.

8.2 Visible-channel data

The raw data in the visible channels are relativized and normalized at the CDA, but no calibration is applied. The GVAR stream contains the relativized, normalized data in 10-bit words (imager) and 16-bit words (sounder). The GVAR also carries on/off flags for the status of relativization and normalization, the values of BOOST, the normalization look-up tables, the identity of the reference detector, and the ID (including the creation date) of the normalization look-up tables. In addition, it contains the visible-channel pre-launch calibration coefficients (three per detector, but with the quadratic coefficients identically zero) and the factor that converts radiance to reflectance factor.

9. CONCLUSION

This paper provides a snapshot of the calibration processing in the GOES I-M ground system as of the summer of '96. Two years ago, when the GOES-8 satellite was launched, the processing utilized only the basic algorithm. Contingency paths were available in the software to deal with likely data irregularities, but they were not being used. Now, the processing has been changed, incorporating contingency paths and recently-developed software modifications to overcome the effects of instrument problems, some anticipated and some not, that were revealed in orbit. As continued monitoring of the data exposes more subtle performance anomalies, and as aging hardware presents new problems, the processing will probably continue to evolve.

10. ACKNOWLEDGEMENTS

Development of the calibration processing in the GOES I-M ground system was a team effort involving people from NOAA, NASA/Goddard Space Flight Center, Space Systems/Loral, ITT, Integral Systems, Inc., Swales and Associates, Inc., and MIT/Lincoln Laboratory. Special mention should go to Michael Jamieson, Nancy Fulton, Carl Smith, Yen Chen, and Donald Mack of Integral Systems, Inc., who incorporated most of the algorithms in operational code; Joy Xie Johnson of Integral Systems, Inc. (formerly at SM Systems and Research Corporation) and Jeanette Baucom of Swales & Associates, Inc., for assisting in algorithm development and problem solving; Edward Wack of MIT/Lincoln Laboratory, for analyses of test data; Brent Goddard of NOAA/NESDIS for help in solving problems during check out and routine operations; James Bremer of Swales and Associates, Inc., for analyses of effects of 1/f noise and the scan-mirror emissivity variation; and Marvin Maxwell and William Bryant, Jr. of Swales and Associates, Inc. for good ideas and good advice.

11. APPENDIX

INTERPRETATION OF INFRARED IMAGER DATA IN GVAR

In the GVAR data stream, the data from the infrared channels of the imagers are scaled radiances packaged in 10-bit words. The conversion of the raw data from the instruments to 10-bit scaled radiances is carried out in real time in the Sensor Processing System computers at the Command and Data Acquisition facility at Wallops, VA, and is described in the body of this paper. This Appendix is for the GVAR user who needs to convert a 10-bit GVAR count value (0-1023) in channels 2 - 5 of the GOES-8 or -9 imager to a scene radiance, temperature, or mode-A (8-bit) count[12].

Whether the objective is to obtain radiances, temperatures, or mode-A counts, the GVAR count value must first be converted to a radiance. This is done with the following equation:

$$R = (X_G - B)/M,$$

where R is radiance in $mW/(m^2\text{-}sr\text{-}cm^{-1})$ and X_G is the GVAR count value. The coefficients M and B are the "scaling" slope and intercept, respectively, and are tabulated below. The units of M are $counts/(mW/[m^2\text{-}sr\text{-}cm^{-1}])$. Their values depend on channel, but for a given channel we expect them to be constant for all time and to be the same for each satellite of the series.

TABLE A1: GOES imager scaling coefficients

Channel	M	B
2	227.3889	68.2167
3	38.8383	29.1287
4	5.2285	15.6854
5	5.0273	16.3332

To convert radiance to temperature, one first uses the following formula (the inverse of the Planck function) to derive "effective" temperature:

$$T_{eff} = (c_2\nu)/\ln(1 + [c_1\nu^3]/R)$$

where T_{eff} is effective temperature (K), "ln" stands for natural logarithm, and R is radiance. The coefficients c_1 and c_2 are the two radiation constants, given by

$$c_1 = 1.191066\times10^{-5}\ mW/(m^2\text{-}sr\text{-}cm^{-4})$$
$$c_2 = 1.438833\ K/cm^{-1}.$$

The quantity ν is the central wavenumber of the channel. For a given channel it will vary slightly from instrument to instrument. The values of ν appear in tables A2 and A3.

To convert effective temperature T_{eff} to actual temperature T (K), one uses the following formula:

$$T = \beta T_{eff} + \alpha$$

The constants ν, α, and β depend on channel and instrument and appear in Tables A2 and A3.

TABLE A2: Constants for GOES-8 imager (side 1)

Channel	Detector	ν (cm^{-1})	α (K)	β
2	1	2556.65	-0.575836	1.00152
2	2	2557.15	-0.580028	1.00152
3	1	1481.85	-0.588961	1.00143
4	1	934.25	-0.313687	1.00126
4	2	934.35	-0.296247	1.00122
5	1	837.05	-0.420806	1.00117
5	2	836.15	-0.341538	1.00102

TABLE A3: Constants for GOES-9 imager (side 1)

Channel	Detector	ν (cm^{-1})	α (K)	β
2	1	2555.15	-0.580725	1.000955
2	2	2555.15	-0.580725	1.000955
3	1	1481.75	-0.489100	1.001092
4	1	934.55	-0.377608	1.001284
4	2	934.25	-0.358734	1.001264
5	1	833.95	-0.288899	1.000914
5	2	834.05	-0.296517	1.000926

The term "side 1" in the table headings indicates that the first of the two redundant sets of detectors and electronics is operating on each imager. The coefficients ν, α, and β depend on the choice of side. The GOES-8 and -9 imagers have always operated on side 1. We will provide the coefficients for side 2 if and when they are needed.

The use of T_{eff} accounts for the variation of the Planck function across the spectral passband of the channel. The differences between the values of T and T_{eff} increase with decreasing temperature. They are usually of the order of 0.1K. In the worst case, near 180K, they are approximately 0.3K.

A word on precision: For a scene at 300K, an increment of one GVAR count is equivalent to a temperature increment of approximately 0.11K in channels 2, 4, and 5, and approximately 0.35K in channel 3.

The mode-A count value X_A is derived from the temperature with the following equations[12]:

For $163K \le T \le 242K$ $\quad X_A = 418 - T$

For $242K \le T \le 330K$ $\quad X_A = 660 - 2T$

Mode-A count values are on an eight-bit scale and range in value from 0 to 255, with high counts representative of low temperatures. Beyond the difference in precision, there is a fundamental difference between GVAR counts and mode-A counts: their units. GVAR counts are scaled radiances, whereas mode-A counts are temperatures.

Tables of GVAR counts, radiances, temperatures, and mode-A counts will be provided by the author on request.

12. REFERENCES

1. Bradley, C. (ed.), "The GOES I-M system functional description," *NOAA Technical Report NESDIS 40*, U.S. Dep't. Commerce, National Oceanic and Atmospheric Administration, Washington, D.C., 126 pp., 1988.

2. Space Systems/Loral, *GOES I-M Data Book*, prepared for NASA/GSFC under contract NAS5-29500, 184 pp, 1994.

3. Menzel, W.P. and J. F.W. Purdom, "Introducing GOES-I: The first of a new generation of geostationary operational environmental satellites," *Bull. Amer. Meteorol. Soc.*, **75**, pp. 757-781, 1994.

4. Bremer, J.C. and G.J. Comeyne, "Optimization of the GOES-I imager's radiometric accuracy: drift and 1/f noise suppression," *Optical Engineering*, **33** (10), pp. 3324-3333, 1994.

5. Weinreb, M.P., W.C. Bryant, Jr., M. S. Maxwell, and J.C. Bremer, "Operational in-orbit calibration of the GOES-I Imager and Sounder," preprint volume, *Seventh Conf. on Satellite Meteorol. and Oceanography*, Monterey, CA, 1994 (Amer. Meteorol. Soc., Boston, MA 02108-3693), pp.473-476, June 6-10, 1994.

6. Weinreb, M.P., J.X. Johnson, J.C. Bremer, E.C. Wack, and O. Chen, "Algorithm to compensate for variation of reflectance of GOES-8 and -9 scan mirrors with scan angle," preprint volume, *Eighth Conf. on Satellite Meteorol. and Oceanography*, Atlanta, GA, (Amer. Meteorol. Soc., Boston, MA), pp. 110-114, Jan. 28-Feb. 2, 1996.

7. Cafferty, M., "Reflectance measurements of the SN03 scan mirror witness sample," MIT/Lincoln Laboratory internal memo, 8 pp., 15 Aug. 1994.

8. Baucom, J. and M. Weinreb, "Characteristics of E/W stripes in infrared images from the GOES-8 imager," to appear in the *Proceedings of the SPIE Intl. Symposium on Optical Science, Engineering, and Instrumentation; Conference on GOES-8 and Beyond*, Denver, CO, 4-9 Aug. 1996.

9. Wack, E.C. and L.M. Candell, "Simulation of GOES-8 imager striping due to 1/f noise," to appear in the *Proceedings of the SPIE Intl. Symposium on Optical Science, Engineering, and Instrumentation; Conference on GOES-8 and Beyond*, Denver, CO, 4-9 Aug. 1996.

10. Johnson, R.X. and M. Weinreb, "GOES-8 imager midnight effects and slope correction," to appear in the *Proceedings of the SPIE Intl. Symposium on Optical Science, Engineering, and Instrumentation; Conference on GOES-8 and Beyond*, Denver, CO., 4-9 Aug. 1996.

11. Weinreb, M.P., J.X. Johnson (nee R. Xie), J.H. Lienesch, and D.S Crosby, "Destriping GOES images by matching empirical distribution functions," *Remote Sens. Environ.*, **29**, pp. 185-195, 1989.

12. Bristor, C.L. (ed.), "Central processing and analysis of geostationary satellite data," *NOAA Tech. Memo. NESS 64*, U.S. Dep't. Commerce, National Oceanic and Atmospheric Administration, Washington, DC, 155 pp., 1975.

Characteristics of E/W stripes in infrared images from the GOES-8 imager

Jeanette G. Baucom

Swales and Associates, Inc.
5050 Powder Mill Road
Beltsville, Maryland 20705

Michael Weinreb

Satellite Research Laboratory
NOAA/NESDIS
Washington, DC 20233

ABSTRACT

East-west stripes are observed in images in channels 4 (10.7 μm) and 5 (12 μm) of the GOES-8 imager. These channels use two detectors arranged in a north-south array to sweep out alternate lines of an image. The stripes are caused by differences in the outputs of the two detectors. There is a clear correlation between scene temperature and the magnitude of the striping. Measured in temperature units, the striping is more severe at the cold end of the spectrum, and therefore affects meteorological products which depend on observations of cold targets. The striping can be divided into three components: 1) within-frame random, 2) systematic within-frame but random from frame-to-frame, and 3) systematic over many frames. The first two components are caused by 1/f noise during data-taking and calibrations. The cause of the third component of the striping is not known. Examples of each striping element are presented and discussed. A brief comparison of GOES-8 and GOES-9 imager striping is made.

KEYWORDS: Calibration, Infrared, Imagery, Striping, Noise

1. INTRODUCTION

The GOES-8 imager observes the Earth in five spectral intervals ("channels") at wavelengths between 0.6 μm and 14.7 μm. Channels 4 (10.7 μm) and 5 (12 μm) each consist of two detectors in a north-south array that scan the Earth in the west-east and east-west directions via an oscillating "scan" mirror. With sufficient contrast enhancement, one can see east-west stripes in the images made from data in these channels. The striping on uniform scenes is caused by differences in the outputs of the two detectors in a channel, since alternating lines in an image are observed by different detectors. The striping can be quantified as the difference between the average outputs of the two detectors. Striping magnitudes of several tenths of a Kelvin on a 290 K scene are common. The factors that contribute to such striping include the following: Each detector-channel operates independently and is calibrated independently. The signals are unchopped. The detectors, photoconductive HgCdTe, have substantial 1/f noise, with knee frequencies between 75 and 375 Hz. The electronic zeroes are restored at views of space that occur infrequently--every 2.2, 9.2, or 36.6 seconds. Blackbody calibrations, which occur every 30 minutes, involve a spacelook, a blackbody view, and a second spacelook, with the three observations separated by two 18-second slews of the scan mirror. The 1/f noise causes the outputs of the detectors to drift randomly during calibrations and imaging, and as a result, the noises in each detector-channel are uncorrelated.

Fig. 1. GOES-8 imager ch 4 (10.7 μm) image with striping

Figure 1 shows an image of the Great Lakes from channel 4 of the GOES-8 imager that contains striping. The magnitude of the striping

in channel 4 is typically 0.4 K for scenes at 200 K, but only 0.1 K for scenes at 300 K. The more severe striping at the cold end of the spectrum is due to the Planck relationship between blackbody temperature and radiance. Therefore, meteorological products such as precipitation estimates, which are based on observations of cold high clouds, are affected disproportionately by the striping.

2. BACKGROUND

2.1 GOES imager calibration

Each of the detectors in the GOES-8 imager is calibrated separately according to the equation:

$$R_i = q_i X_i^2 + m_i X_i + b_i \tag{1}$$

where i is the detector, R_i is the radiance of the scene, X_i is the instrument output in ten-bit digital counts, and q_i, m_i, and b_i are calibration coefficients. The quadratic coefficients q_i are determined from prelaunch measurements and are not altered on-orbit. The coefficients m_i and b_i are determined on-orbit from data acquired during blackbody looks and spacelooks[1].

At each blackbody look, the slopes m_i are determined from the equation:

$$m_i = \frac{R_{bb} - q_i (X_{bb_i}^2 - X_{sp_i}^2)}{X_{bb_i} - X_{sp_i}} \tag{2}$$

where i is the detector and subscripts bb and sp refer to data taken from views of the blackbody and space, respectively. The blackbody radiance is computed from its temperature and the spectral response function of the channel. Blackbody looks occur every 30 minutes and always take place between images, so the slope is constant within any given image.

At each spacelook, the intercepts b_i are determined from the equation:

$$b_i = -m_i X_{sp_i} - q_i X_{sp_i}^2 \tag{3}$$

Spacelooks occur much more frequently than blackbody looks. For the imager, spacelooks occur every 2.2, 9.2, or 36.6 seconds. This means that the intercepts are updated far more frequently than the slopes. For each scene pixel, the radiances are computed from equation 1 with the values of m and b from equations 2 and 3.

The resetting of the electronic zero is referred to as a space clamp; the intercept is also calculated at a space clamp. Currently, imaging is only performed at 2.2 second and 36.6 second clamp intervals. Full earth images (full disks) are imaged with 2.2 second clamp intervals, and all other frames are imaged with 36.6 second clamp intervals. Equations 1-3 are simplified versions of the actual calibration equations applied on-orbit; however, all of the information pertinent to the striping is accounted for in the simplified equations. The full on-orbit calibration equations are derived and explained in Reference 2.

2.2 1/f noise

Photoconductive HgCdTe detectors are subject to 1/f noise[3]. This noise has an amplitude which is inversely proportional to its frequency, and its mechanism is not well understood. The 1/f noise causes the output of the instrument to drift in an unknown, random manner over time. In addition, the 1/f noise is not correlated between detectors, so the drift in each detector is unrelated to drift in other detectors. Knee frequency is a parameter describing 1/f noise; it is the highest frequency at which the detector noise is dominated by 1/f noise. Above the knee frequency, "white" noise is the primary noise component; below the knee frequency, 1/f noise prevails. A desirable detector has a knee frequency as low as possible and below the clamping frequency of the electronics. Unfortunately, the latter criterion is not met for the detectors of the GOES-8 imager which have knee frequencies between 75 and 375 Hz. As described in the last section, the clamping frequencies for the imager are 0.45 Hz (2.2 sec clamp interval), 0.11 Hz (9.2 sec clamp interval), and 0.03 Hz (36.6 sec clamp interval), so 1/f noise is a predominant source of noise.

As seen in equations 1-3, each detector in a channel is calibrated independently of the other. Theoretically, both detectors should provide the same scene radiances when they view the same scene, because they are viewing identical references (space and blackbody). During calibrations (blackbody looks and spacelooks), the references drift because of 1/f noise, and the drifting is completely uncorrelated between the two detectors in a channel. Therefore the slopes and intercepts of the two detectors can vary randomly. The 1/f noise does not only affect the instrument during calibration, but also during imaging. Individual pixel radiances change unpredictably throughout an image causing further differences in detector output. The more time that passes between calibrations, the further apart the detectors can wander, and the more severe the striping.

3. NUMERICAL DEFINITION OF STRIPING

For the analysis presented here, frames from the GOES-8 imager were searched for 7 pixel x 4 line uniform scenes. This is equivalent to a square approximately 16 km on a side on the Earth. (Seven pixels are required to cover the same distance as four lines, because the GOES imagers over-sample in the E/W direction.) Beginning in the northwest corner, all 7x4 areas are examined for uniformity according to the criterion that the standard deviation of the pixels in each detector must be near the noise level for that channel. The GOES satellites retransmit image data and telemetry to users in GVAR (GOES VARiable) format. For images, GVAR counts are radiances which have been linearly scaled to fill up the dynamic range of the GVAR data stream (10 bits). All results in this paper are presented in GVAR counts. Only data from channel 4 (10.7 μm) are presented. The noise level in channel 4 of the GOES-8 imager is typically 0.9 GVAR counts; therefore, the chosen uniformity criteria is $\sigma_i \leq 1$ GVAR count, where i is the detector number. GVAR counts are nonlinear on a temperature scale with an increment of 1 GVAR count corresponding to an increment of ~0.4 K at 200 K and ~0.1 K at 300 K. In absolute terms, 15-20 GVAR counts represent the 3 K of cold space, 70-80 GVAR counts represent approximately 195-200 K, and 550-600 GVAR counts represent 295-300 K.

Striping is defined as the difference between what different detectors in the same channel measure when viewing the same scene. When the uniformity criteria are met, striping is calculated as the difference in the average measurement from each detector:

$$Striping = C_1 - C_2 \qquad (4)$$

C_1 is the north detector and C_2 is the south detector. Figure 2 shows a plot of the striping (in GVAR counts) versus GVAR counts (scaled radiances) of the scene, for one frame. Each point represents the striping in one uniform scene within that frame. The x-axis is the average GVAR count level for both detectors (the average of all 28 pixels in the uniform scene). In equation 4, the C_i are each an average of 14 integer numbers. For easier viewing, the data in Figure 2 were divided into bins fifty GVAR counts in width, and statistics were calculated. Figures 3 and 4 show the mean and standard deviation within each bin for the frame of Figure 2. The data are plotted at the highest value in that bin, i.e., statistics for the

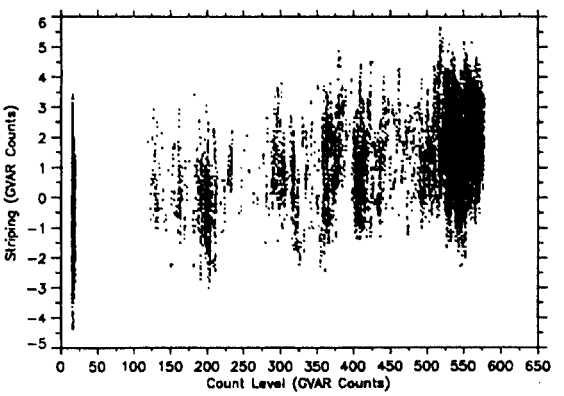

Fig. 2. GOES-8 Imager ch 4 striping on 1/17/96 at 08:00 GMT

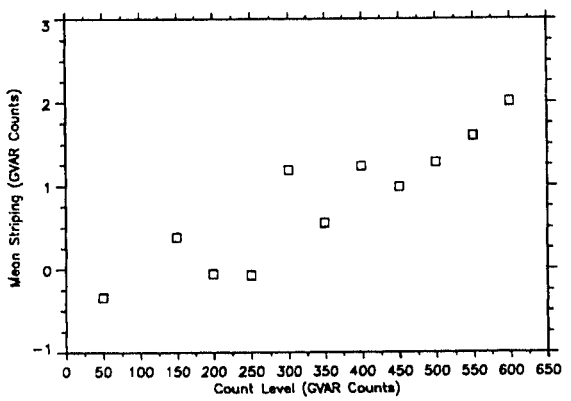

Fig. 3. Imager ch 4 mean striping on 1/17/96 at 08:00 GMT

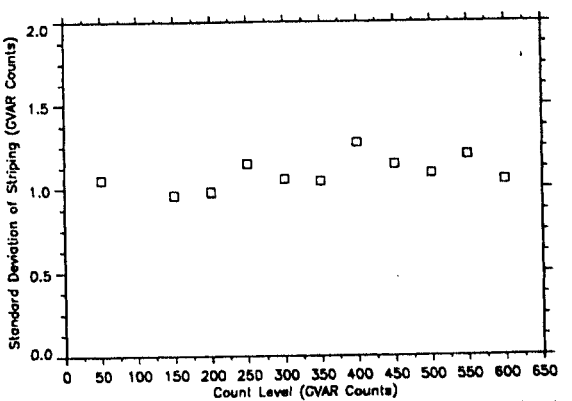

Fig. 4. Standard deviation of striping in each bin on 1/17/96 at 08:00 GMT

0-50 count bin are plotted versus 50 counts in the figures. The mean striping shown in Figure 3 illustrates the systematic (constant) within-frame striping. The spread of the data in Figure 2 as measured by the standard deviation in each bin is presented in Figure 4. This standard deviation measures the random within-frame striping. Further significance of these statistics will be discussed in the following section.

4. STRIPING RESULTS

4.1 Data collection

The data presented here were collected from a series of 24-hour experiments in which imagery was collected and analyzed for striping as described in Section 3. For the first tests, at least one image (and usually more) was examined for each hour of the day. As more data was acquired, though, it became apparent that one frame per hour provided ample data for the striping analysis. Most frames analyzed were imaged with a 36.6 second clamp interval, although some (~ 1/3) were imaged with a 2.2 second clamp interval. Table 1 shows the dates of the tests and the corresponding calibration modes. Calibration mode 1 is the baseline slope calculation shown by equation 2. Calibration mode 3 uses an average slope which is based on a history file of mode 1 slopes: slopes in a window around the present time are averaged over some previous number of days. The mode 3 slopes are weighted averages with the most current mode 1 slope receiving the highest weight. Mode 3 is currently the standard calibration mode for the GOES-8 imager using a window of ±1 hour from the present time and nine previous days. The effect of mode 3 on the striping will be discussed in the following sections.

Table 1. Schedule of GOES-8 Imager 24-Hour Striping Tests

Date	ID (Year/Julian Day)	Calibration Mode
September 18, 1995	95261	3
October 13, 1995	95286	3
November 9, 1995	95313	1
January 17, 1996	96017	1
February 22, 1996	96053	1 & 3
March 27, 1996	96087	3

4.2 Striping components

The striping observed on the GOES-8 imager consists of three major components:

1) Random striping within a frame, probably caused 1/f noise in scans and spacelooks. As discussed in Section 2.2, the detector outputs drift unpredictably from pixel-to-pixel within the image. Also, at each space clamp, the computed intercepts (equation 3) are subject to a random variation.
2) Systematic striping within the frame, consisting of two elements:
   A) Frame-to-frame variation, probably caused by 1/f noise in the blackbody calibration and associated spacelooks. An entire blackbody calibration, consisting of a spacelook, a blackbody look and another spacelook, takes forty-two seconds. The 1/f noise at each step of the calibration causes fluctuations in detector response which cause the slopes (equation 2) of the two detectors to be subject to random unpredictable errors.
   B) An offset in the striping, which appears after averaging many frames. The cause of this residual systematic offset is not known.

Each of these components will be illustrated and discussed in the following sections.

4.2.1 Random striping within a frame

Random striping within an image can be measured as the standard deviation of the striping in each bin within a frame as shown in Figure 4. Figure 5 shows the random striping for six hours on January 17, 1996. Each point represents the standard deviation of the striping in a fifty-count wide bin. Data between 100 and 300 GVAR counts and above 600 GVAR counts are unreliable because very few measurements exist in those regions. Where there is missing data in a certain bin, there were no uniform scenes at that count level in that image. The standard deviations in Figure 5 are constrained to a fairly narrow range of values indicating that random within-frame striping is around 1 GVAR count, which corresponds to approximately 0.11 K at 300 K.

The individual image standard deviations can be averaged over the day resulting in the average standard deviation in each bin for that day. Such daily average standard deviations for six different days can be seen in Figure 6. Figure 7 shows two sets of points from February 22, 1996 representing the two calibration modes described in Section 4.1. (The data from February 22 in Figure 6 are mode 3 results.) From these figures, it can be concluded that the random striping is approximately 1 GVAR count at all count levels, and that it does not vary seasonally. In addition, averaging the calibration slope does not affect the random within-frame striping.

These characteristics are consistent with the hypothesis that the random striping is being caused 1/f noise in the scans and spacelooks. The relationship between 1/f noise and this random component of striping has been quantified in simulations in Reference 4. Mode 3 should not change the within-frame random striping, because the slopes are constant throughout an image whether it was calculated using mode 1 or mode 3.

Since the intercept is calculated more frequently in full disk images (2.2 second clamp interval), there is less time for the detectors to drift, and the within-frame striping should be less in these images. The standard deviation of the striping in two well-populated bins is shown in Figures 8 and 9 with full disks discriminated from other images. It is obvious that the more frequent clamps reduce the random component of the striping, further supporting the assertion that 1/f noise in the scans and clamps is the major source of within-frame striping.

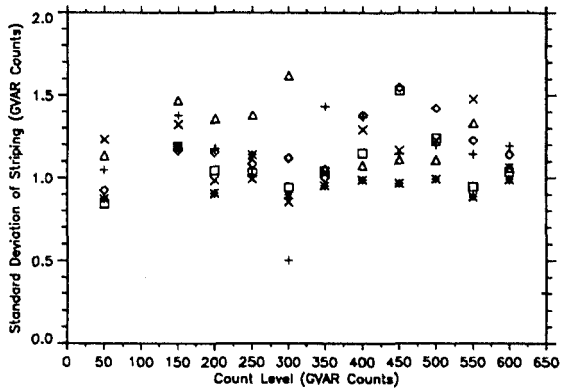

Fig. 5. Standard deviation of striping in each bin on 1/17/96 at □ 01:30, ✕ 05:30, △ 09:30, ✱ 13:30, ◇ 17:30, + 21:30 GMT

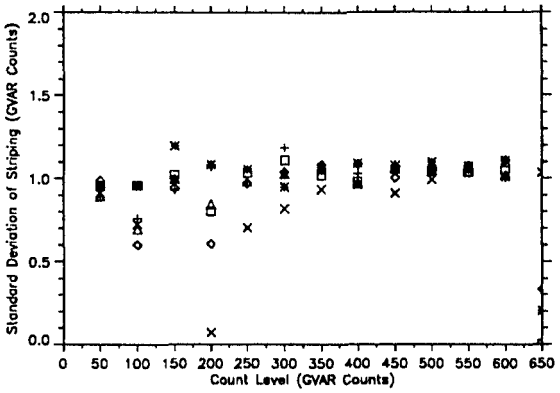

Fig. 6. Daily average standard deviation within bins: □ 95261, ✕ 95286, △ 95313, ✱ 96017, ◇ 96053, + 96087

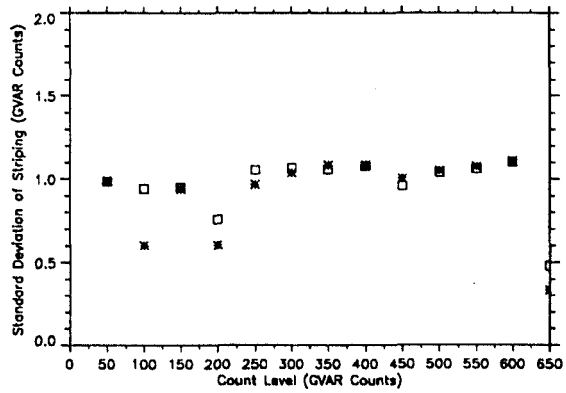

Fig. 7. Daily average standard deviation within bins on February 22, 1996: □ Mode 1, ✱ Mode 3

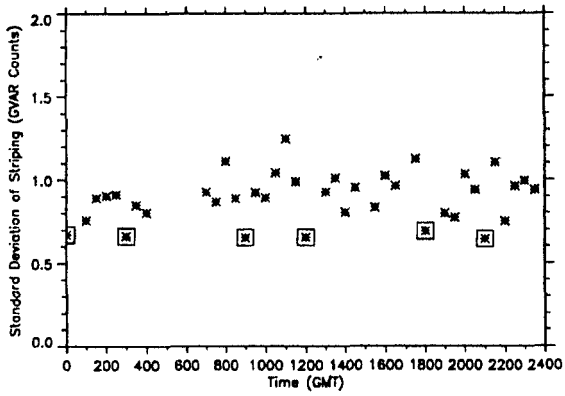

Fig. 8. Standard deviation vs. time from 0-50 GVAR counts on March 27, 1996. Squares are 2.2 sec clamp.

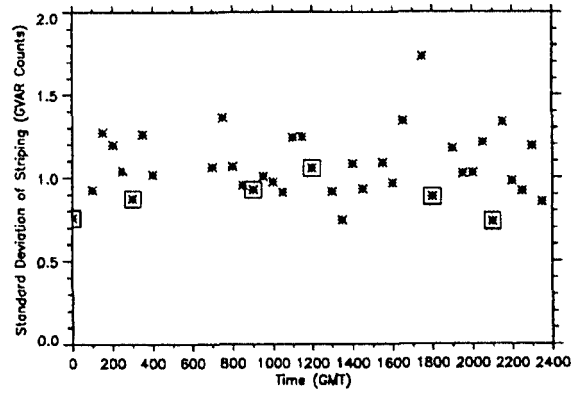

Fig. 9. Standard deviation vs. time from 400-450 GVAR counts on March 27, 1996. Squares are 2.2 sec clamp.

4.2.2 Systematic striping

Systematic striping is defined as the striping which is constant within a frame. On the GOES-8 imager, the systematic striping is divided into two components: striping due to 1/f noise in the blackbody calibration sequence and subsequent slope calculation, and an offset which remains after the striping in many images is averaged.

Systematic striping can be measured by the mean striping within a bin as shown in Figure 3. This striping in an individual image is believed to be caused by errors in the calibration slopes caused by 1/f noise in the calibration sequences. The space values measured before and after the blackbody view are interpolated linearly to determine the space value at the time of the blackbody view. Due to 1/f noise, the space values for each detector can change in a random manner over the approximately 36-second time period between the two spacelooks, causing the value of m_i to be incorrect. Striping is the result, since as stated in Section 2.2, the errors in the two detectors are unrelated.

In addition to the frame-to-frame variation in the mean, there is another feature of the systematic striping that persists after all of the individual frame means are averaged. An offset in the daily average mean striping which increases linearly with count level has been observed in each of the 24-hour tests. This is the only component of the striping which cannot be attributed to 1/f noise, and its cause is unknown.

4.2.2.1 Variation from frame-to-frame

Systematic striping in a single frame can be measured by the mean striping in each bin. Each point in Figures 10 and 11 represents the mean striping in a 50 count wide bin. Data for six different images on two different days are presented in the figures. (Once again, results from 100-300 GVAR counts and above 600 GVAR counts are unreliable due to a lack of data.) These figures show that the mean (systematic within-frame) striping varies in both magnitude and sign with count level and with time of day. (The data in Figures 10 and 11 from February 22 are mode 3 results.)

To see if the mean striping has any coherent diurnal pattern, the mean striping in each bin was plotted versus time of day. Examples of two well populated bins are shown in Figures 12 and 13 for February 22, 1996. Statistics for the data in these figures are presented in Table 2. As seen in the figures, the pattern to the variation with time of day is dominated by a random component, supporting the expectation that errors in the slopes of the two detectors vary randomly in time. There is

Table 2. Statistics of Striping on February 22, 1996: Comparison of Mode 1 and Mode 3

Calibration Mode	0-50 GVAR Counts		400-450 GVAR Counts	
	Average	Standard Deviation	Average	Standard Deviation
1	0.11	0.43	1.56	1.22
3	0.13	0.45	1.19	0.41

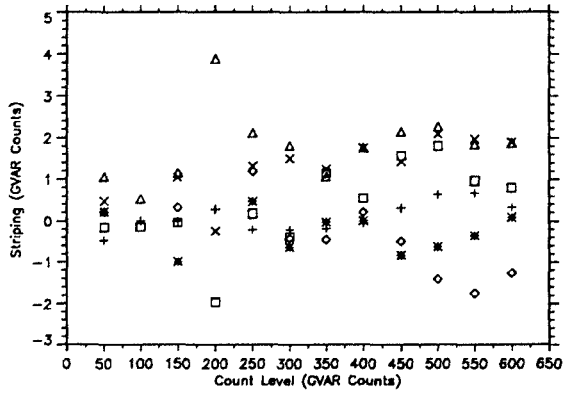

Fig. 10. Mean striping on November 9, 1995: □ 01:30, ✕ 05:30, ✱ 13:30, △ 09:30, ◇ 17:30, + 21:30 GMT

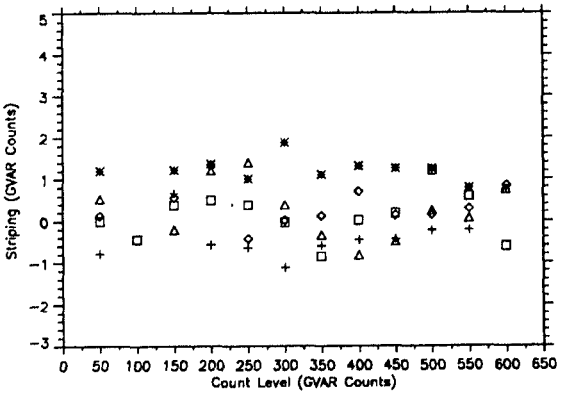

Fig. 11. Mean striping on March 27, 1996: □ 01:30, ✕ 05:30, ✱ 13:30, △ 09:30, ◇ 17:30, + 21:30 GMT

also the suggestion of a periodic variability, which will be the subject of future investigation.

The standard deviation of the data in Figures 12 and 13 is a measure of the frame-to-frame variability of the striping in two bins. Calibration mode 3 was designed to reduce the effects of noise in the calibration slopes, so it would also be expected to reduce the frame-to-frame variability of the striping. Slope errors cause larger radiance errors on warm scenes than on cold (see equation 1), so mode 3 should reduce the striping more on warm scenes (high GVAR counts). This is seen by comparing the results in Figure 12 (0-50 GVAR counts) and Figure 13 (400-450 GVAR counts) and Table 2. Mode 3 significantly reduces the frame-to-frame variation of the striping in the 400-450 GVAR count bin but not in the 0-50 GVAR count bin. This is also confirmed by Table 2 in that the standard deviation (variation) of the data in the two modes is almost identical in the 0-50 bin, but mode 3 results are a factor of three lower in the 400-450 bin. Standard deviations for *all* the bins can be seen in Figure 14. Figure 14 also shows that the frame-to-frame variation in the mean striping is reduced by the use of calibration mode 3, and that the standard deviations of the means increases with count level. All of the results presented are consistent with the hypothesis that 1/f noise is the primary mechanism causing a frame-to-frame variation in the striping.

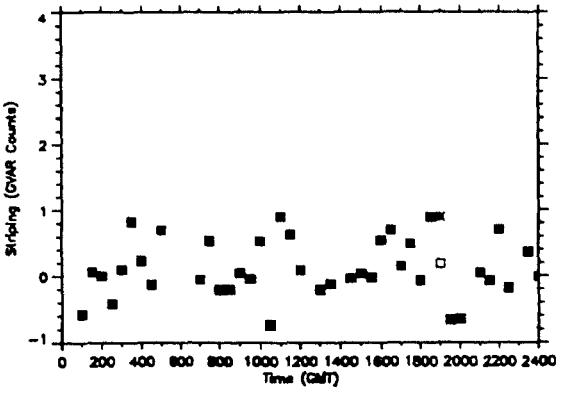

Fig. 12. Mean striping vs. time on February 22, 1996 from 0-50 GVAR counts: □ Mode 1, ✱ Mode 3

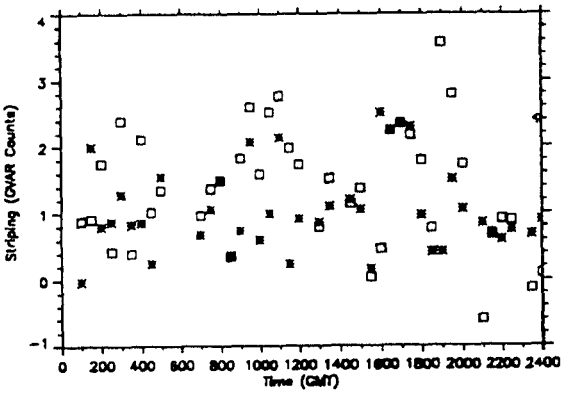

Fig. 13. Mean striping vs. time on February 22, 1996 from 400-450 GVAR counts: □ Mode 1, ✱ Mode 3

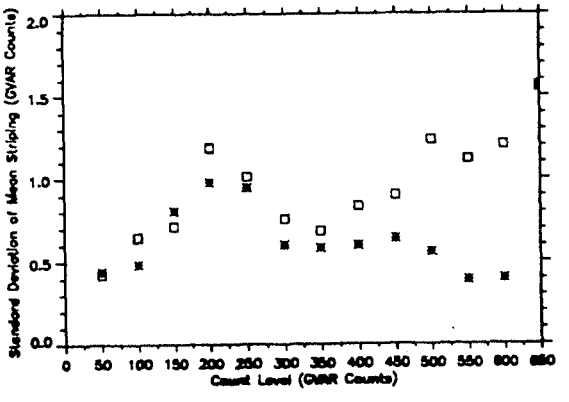

Fig. 14. Standard deviation of mean striping within bins over a day, on February 22, 1996: □ Mode 1, ✱ Mode 3

4.2.2.2 Residual offset

The average striping for a day can be calculated as the average of the means in each bin, e.g., the average of all of the data in Figure 12 is the average striping in the 0-50 GVAR count bin on February 22, 1996, and the average of all the data in Figure 13 is the average striping in the 400-450 GVAR count bin. Figure 15 shows the daily average striping for each of the 24-hour experiments (96053 is mode 3 data) plotted against count level. These figures show that the daily average striping at all count levels (with the possible exception of 0-50 GVAR counts) is significantly different from zero. The offsets are positive (detector 1 greater than detector 2) and increase with count level. At 300 K, this results in 0.11-0.18 K of striping. There seems to be some variation with time of year. Figure 16 shows data for both mode 1 and mode 3 on February 22, 1996. Mode 3 had a small effect on the offset as seen in Figure 16 and Table 2. The reason mode 3 affected the offset of the striping is not understood, so it is not known whether mode 3 would always reduce this component of the striping.

For data on a given day, the slope of a linear least squares fit to the daily average mean striping versus count level (the data in Figures 15 and 16) provides a single parameter which measures the systematic striping at all count levels for that day. Figure 17

is a plot of these slopes versus date. Interpretation of the data in Figure 17 is complicated by the possible difference in slope between mode 3 and mode 1 data. All that can be concluded from Figure 17 is that there is a variation of the striping offset with date, but no seasonal or long-term trend is currently discernable. Testing is on-going to determine any seasonal pattern to this component of striping.

The cause of the offset in the striping which persists even after averaging is not understood. It is not believed to be caused by 1/f noise, and it varies over time with no obvious pattern. If a trend is discovered, an algorithm will be developed and used to remove the systematic offset in ground system processing.

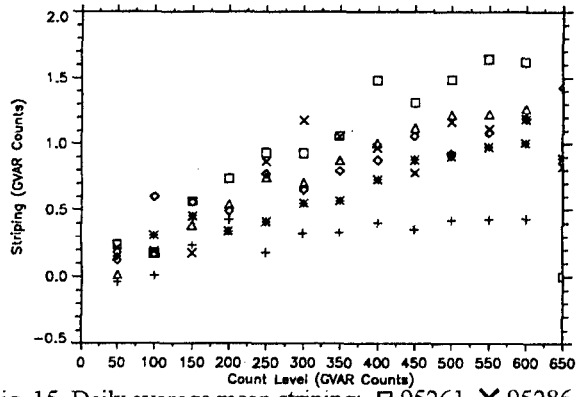

Fig. 15. Daily average mean striping: □ 95261, ✕ 95286, △ 95313, ✱ 96017, ◇ 96053, + 96087

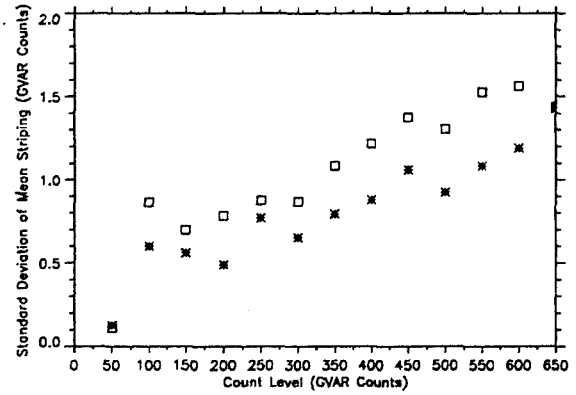

Fig. 16. Daily average mean striping on February 22, 1996: □ Mode 1, ✱ Mode 3

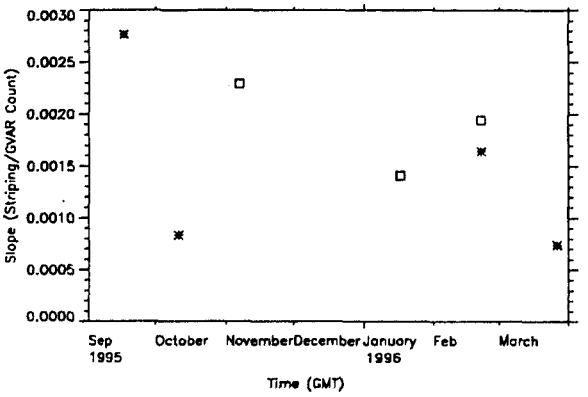

Fig. 17. Slope of linear least squares fit to average daily striping vs time: □ Mode 1, ✱ Mode 3

5. GOES-9 STRIPING

Striping on the GOES-9 imager has been studied less extensively than that on GOES-8; however, some comparisons can be made. Data from two 24-hour tests (as described in section 4.1) have been analyzed for the GOES-9 imager. In addition, MIT/Lincoln Laboratory has spot checked the GOES-9 imager channel 4 striping several times since launch in May 1995[5]. As discussed in section 4.2.1, the standard deviation of the striping in each bin within a frame measures the random within-frame striping. Averaged over a day, these standard deviations give the average random within-frame striping for that day. Figure 18 shows the average standard deviations from the two GOES-924-hour tests. From these data it has been found that the random striping in channel 4 of the GOES-9 imager is approximately 0.6 GVAR counts (or 0.07 K at 300 K) -- 40% lower than GOES-8. (Compare Figure 18 to Figure 6.) This is consistent with the properties of the 1/f noise of GOES-9 imager: the knee frequencies for GOES-9 are substantially lower than those for GOES-8 (45-50 Hz compared to 190-255 Hz in channel 4)[6].

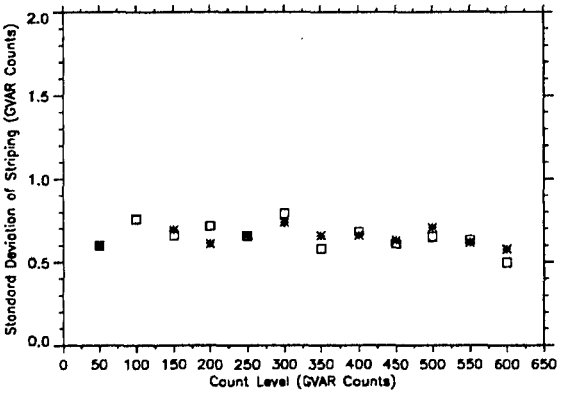

Fig. 18. GOES-9 imager daily average standard deviation: □ 96087, ✱ 96122

For a given frame, the systematic striping can be calculated as the mean striping in each bin. The average striping for a day is the average of all of the individual frame means. Data from the GOES-9 24-hour tests show daily average mean striping of ~0.2 K at 300 K (2 GVAR counts), as illustrated in Figure 19.

These results are comparable to those for GOES-8 (Figure 15) in magnitude; however, the systematic component of the GOES-9 striping is opposite in sense from GOES-8: the output of detector 2 is usually higher than that of detector 1.

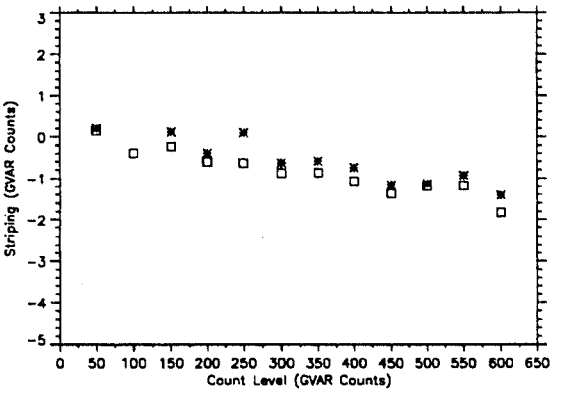

Fig. 19. GOES-9 imager average daily mean striping: □ 96087, ✱ 96122

6. SUMMARY

Striping in channel 4 of the GOES-8 imager has random and systematic components. The random component, probably due to 1/f noise in the scans and spacelooks, is approximately 1 GVAR count (0.1 K at 300 K) and does not depend on scene temperature or time. The systematic component of striping has a frame-to-frame variation and an offset. The frame-to-frame variability (~0.13 K for scenes around 300 K) is believed to be caused primarily by 1/f noise in the blackbody cycle. There is no clear diurnal pattern in this variation, and it is significantly reduced by mode 3 calibration slope smoothing. Since 1/f noise is a random phenomenon, these two components of the striping cannot be corrected in real-time in the ground system. Selection of optimal detectors to minimize 1/f noise for future instruments is the best solution, and this course is being pursued by the instrument contractor.

In channel 4 of the GOES-8 imager, the systematic offset in the striping is generally positive (detector 1 higher than detector 2) and increases with count level. For scenes at temperatures near 300 K, the magnitude of the striping lies between 0.11 and 0.18 K. The offset appears to vary with date; however, no seasonal trend has been evident. The source of the striping offset is unknown; however, it is not believed to be caused by 1/f noise. If a long-term trend is discovered, a ground system correction algorithm will be developed.

Channel 4 of the GOES-9 imager has less striping than GOES-8. This is because GOES-9 has much lower 1/f noise knee frequencies, resulting in less drift in the detectors. The imager on GOES-9 also exhibits an offset in the striping, which based on limited data, appears to be comparable to that from GOES-8. Striping on GOES-9 is opposite in sense to that on GOES-8 with detector 2 normally higher than detector 1.

7. REFERENCES

1. M. P. Weinreb, W. C. Bryant, Jr., M. S. Maxwell, and J. C. Bremer, "Operational in-orbit calibration of the GOES-I Imager and Sounder," preprint volume, *Seventh Conference on Satellite Meteorology and Oceanography*, pp. 473-476, June 6-10, 1994.

2. M. P. Weinreb, J. X. Johnson, J. C. Bremer, E. C. Wack, and O. Chen, "Algorithm to compensate for variation of reflectance of GOES-8 and GOES-9 scan mirrors with scan angle," preprint volume, *Eighth Conference on Satellite Meteorology and Oceanography*, Atlanta, GA, (American Meteorological Society, Boston, MA), pp. 110-114, January 28-February 2, 1996.

3. J. C. Bremer and G. J. Comeyne, "Optimization of the GOES-I imager's radiometric accuracy: drift and 1/f noise suppression," *Optical Engineering*, 33 (10), pp. 3324-3333, 1994.

4. E. C. Wack and L. M. Candell, "Simulation of GOES-8 imager IR striping due to 1/f noise", to appear in the proceedings of the *SPIE International Symposium on Optical Science, Engineering, and Instrumentation*; *Conference on GOES-8 and Beyond*, Denver, CO, August 4-9, 1996.

5. E. C. Wack (MIT/Lincoln Laboratory, Lexington, MA), "1/f noise and imager IR striping", GOES Monthly Data Review at ITT, October 24, 1995.

6. E. C. Wack (MIT/Lincoln Laboratory, Lexington, MA), July 31, 1995, (personal communication).

GOES-8 imager midnight effects and slope correction

Rongrong Xie Johnson

Integral Systems, Inc.
5000 Philadelphia Way, Suite A
Lanham, Maryland 20706-4417

Michael Weinreb

Satellite Research Laboratory
NOAA/NESDIS
Washington, DC 20233

ABSTRACT

Since the GOES-8 launch in 1994, unexpected values of imager calibration slopes (radiance/count) have been observed near satellite midnight, especially in the "shortwave" channels 2 (3.9 um) and 3 (6.7 um). Concurrent imager measurements of apparently decreased ocean temperatures suggest that the slope changes do not reflect actual changes in the instrument, but rather errors in the onboard calibration process. One type of error is believed to be caused by heating of the instrument surfaces around midnight when the sun is above the equator. Reflected by the onboard blackbody (which is not perfectly black), excessive radiation from these hot surfaces reaches the detectors when the blackbody look is performed during the calibration process. This decreases the magnitude of the slope, causing the earth scene to appear cooler. Another type of error is introduced by scattered solar radiation, which contaminates the instrument space-look signal around midnight during the two annual eclipse seasons. When the calibration uses the contaminated space signal, it increases the magnitude of the slope, causing the earth scene to appear warmer. Both midnight effects alter the slope by as much as 4% in the shortwave channels, thus leading to temperature errors of up to 1 K for a 300 K target.

This paper describes a study of these effects and an algorithm to correct them. The algorithm estimates the correct slope at midnight from correlations between the slope and the temperatures of optic components within the instrument. In particular, it is found that the slope can be predicted from the telescope primary-mirror temperature with an rms error of less than 1%. Our study also indicates that the effective temperature of the hot surfaces may reach 360 K in the middle of summer, and the shortwave channel space look may be contaminated with radiation from an apparent "target" with temperature as high as 250 K around the eclipse seasons.

KEYWORDS: Calibration, Infrared, Midnight, Radiometry

1. INTRODUCTION

Three-axis stabilized in geostationary orbit, the new generation GOES I-M satellites keep constant vigil on our environment, providing information about the land, ocean, and constantly changing atmosphere. Offering more rapid and flexible coverage than its predecessors, the onboard imager and sounder[1] also present challenges in calibration. On a three-axis stabilized satellite, an earth-observing instrument faces the sun during local night. In certain circumstances, excessive solar radiation can heat the instrument drastically in a very short time. During such periods, not only do the hot instrument surfaces radiate more energy, which increases the background flux on the detectors, but also rapid changes in temperature can cause significant changes in the instrument radiometric responsivities, which the current calibration procedure may not be able to follow[2].

Both the GOES imager and sounder carry a blackbody as a hot calibration source, while using space as the cold calibration source. During satellite operations, in order to accommodate the requirement of rapid coverage on earth, the imager and sounder perform blackbody looks only once every 30 and 20 minutes, respectively. Space looks are performed more

0-8194-2200-2/96/$6.00

frequently, at every 2.2, 9.2, or 36.6 seconds (imager), and every 2 minutes (sounder). When it includes averaging and/or interpolating techniques, the calibration algorithm meets the requirements of data accuracy most of the time. Around satellite midnight, however, calibration errors are expected to occur due to excessive radiation from the heated instrument surfaces, scattering off mirrors and/or being reflected off the blackbody (which is not absolutely black). Pre-launch analysis from the instrument manufacture (ITT, Ft. Wayne, IN) indicated possible temperature errors of 0.26 to 0.42 K (imager[3]) and 0.28 to 0.49 K (sounder[4]) at 300 K caused by this effect.

After the launch of GOES-8 in April 1994, instrument calibration data have been constantly monitored and studied at NOAA's Satellite Operations and Control Center (SOCC) in Suitland, Maryland. Comparisons between the in-orbit observations and pre-launch predictions of instrument radiometric performance have been made. This paper describes the in-orbit observation of the GOES-8 imager calibration midnight effects, presents a processing technique that corrects the effects, and characterizes the sources of the effects in the instrument.

2. IN-ORBIT OBSERVATIONS OF GOES-8 IMAGER SLOPES

2.1 The imager and its calibration

The GOES-8 imager possesses four IR channels with characteristics given in Table 1.

There are two detectors each (called A and B) for channels 2, 4, and 5, and one for channel 3. For each detector, instrument measurements are converted to radiance through the following basic calibration equation[5],

TABLE 1: GOES-8 imager characteristics

Channel Number	Center Wavenumber (cm^{-1})	In-orbit NEΔT(K) at 300 K
2	2557	0.22
3	1482	0.20 (at 230 K)
4	934	0.13
5	837	0.23

$$R = qX^2 + mX + b \quad (1)$$

where R is the scene radiance, X is the instrument scene output in ten-bit digital counts, and q, m, and b are the calibration coefficients. The second order gain q is determined from pre-launch measurements. The first order gain (i.e., the slope) m and intercept b are determined from in-orbit data acquired from the instrument blackbody and space looks, which are described below.

At each blackbody look, taken once every 30 minutes, m and b are determined from the pair of equations,

$$R_{bb} = qX_{bb}^2 + mX_{bb} + b \quad (2)$$

$$0 = qX_{sp}^2 + mX_{sp} + b \quad (3)$$

where X_{bb} is the instrument output counts when viewing the blackbody, and X_{sp} is the space look output counts interpolated to the time of the blackbody look from space looks occurring before and after it. The two space looks are approximately 50 seconds apart. The blackbody radiance R_{bb} is computed from its temperature, which is measured instantaneously by eight temperature sensors distributed around the blackbody.

Hence,

$$m = [R_{bb} - q(X_{bb}^2 - X_{sp}^2)]/(X_{bb} - X_{sp}) \quad (4)$$

and

$$b = - qX_{sp}^2 - mX_{sp} \quad (5)$$

At each subsequent space look once every 2.2, 9.2, or 36.6 seconds, b is computed again from Eq. (5), using the slope determined at the last blackbody look. The slope is updated less frequently than the intercept since the instrument

responsivity (which is the reciprocal of the slope) is a weaker function of the instrument background radiation than the intercept.

For measurements of the earth scenes, radiances are obtained from Eq. (1) with the most recent slope m and intercept b (1/f-noise corrected[5]). The calibration accuracy depends on the accuracies of blackbody and space measurements, and consistencies of the instrument responsivity and background radiation between these measurements.

Recently, the above equations have been modified to account for the east-west variation in reflectance of the instrument scan mirror[6]. Describing those terms are beyond the scope of this paper. However, all results presented below have been processed with the modification, which does not, in any case, have a significant effect on the phenomenon described in this paper.

2.2 In-orbit calibration slopes and midnight anomalies

Figures 1.1 and 1.2 show the GOES-8 imager calibration slopes computed at each blackbody look during a three-day period from 21 to 23 June 1995 for channels 2 and 4 respectively. (Channel 3 is similar to channel 2, both defined as shortwave channels, and channel 5 is similar to channel 4, both defined as longwave channels. Data illustrated are from detectors-A only since both A and B detectors behave similarly.) The slopes in all the channels have consistent diurnal patterns, which peak around local midnight (05 UTC). For shortwave channels, there are abrupt increases in slope shortly before midnight, which account for a major portion of their diurnal variations. Slopes of longwave channels display noticeable variations between one blackbody look and another, with no drastic increases around midnight.

Before the GOES-8 launch, Annable[3] predicted errors in the imager slope computed from Eq. (4) during the five hours centered at midnight. He indicated they would be caused primarily by the non-blackness of the onboard blackbody. When the emissivity of the blackbody is not unity, Eq. (2) should be rewritten as,

$$\epsilon_{bb}R_{bb} + (1-\epsilon_{bb})\sum F_i R_i = qX_{bb}^2 + mX_{bb} + b \qquad (6)$$

where ϵ_{bb} is emissivity of the blackbody, and $(1-\epsilon_{bb})$ is its reflectivity. The subscript i represents the i-th instrument component that is seen by the blackbody, F_i is the blackbody view factor of this component, and R_i is its effective radiance. Equation (6) states that when the imager looks at a non-ideal blackbody, the amount of radiation received not only originates from the blackbody, but also from other sources reflected by the blackbody. Pre-launch analyses by ITT have indicated that certain structural components in the vicinity of the scan mirror can become significant sources of radiation around midnight[3].

Let us now re-examine the calibration equations (2) and (3). To determine the slope m and intercept b simultaneously, certain assumptions are made. First, the instrument background flux measured at the space look is the same as at the

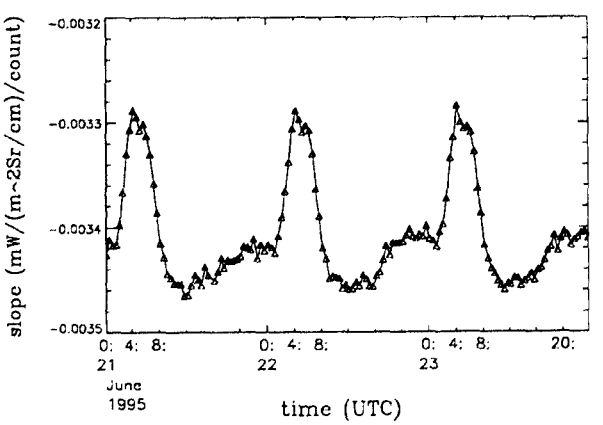

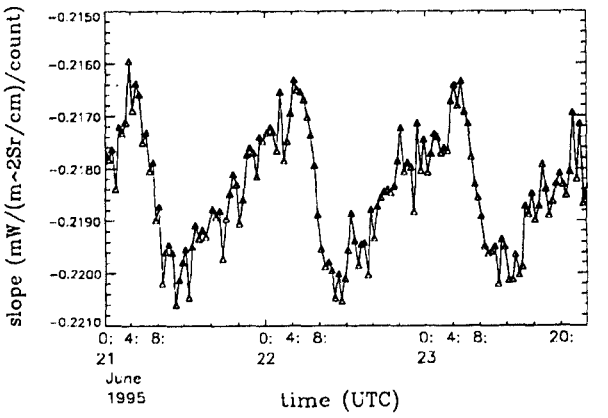

Figs. 1.1 (left) and 1.2 (right). GOES-8 Imager calibration slopes vs time for channels 2 (left) and 4 (right).

measurement of the blackbody. Second, the blackbody is ideally black, meaning it emits 100% and reflects no energy from any other source. Moreover, for accurate earth measurements from Eq. (1), the background flux must remain constant between the measurements of space and the Earth, and the instrument responsivity must also remain constant between the measurements of the blackbody and the Earth.

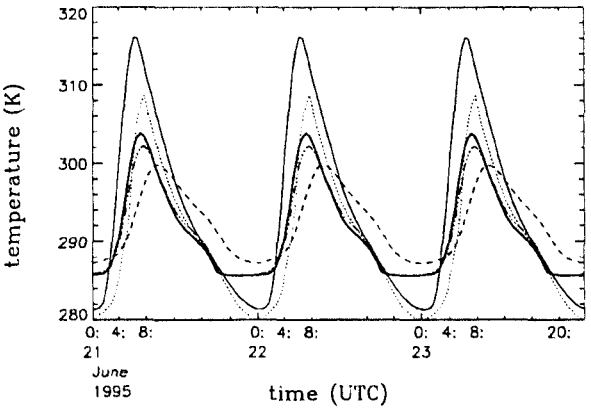

Fig. 2. GOES-8 Imager component temperatures vs time (with thin solid for scan mirror, thick solid for blackbody, dash for primary mirror, dot for secondary mirror, and dotted-dash for baseplate).

During instrument operations in orbit, the first assumption (the constant background flux) is valid when the instrument scan mirror is commanded to face far from the sun. This prevents potential solar contamination at the space looks, which usually does not affect the blackbody looks. The second assumption is approximately "true" (in spite of the non-unity blackbody emissivity) when the instrument components seen by the blackbody maintain temperatures close to the blackbody's (~ 285 to 305 K). If every R_i equals R_{bb}, then Eq. (6) becomes Eq. (2). The requirements that both the background flux and responsivity remain constant between measurements of the space/blackbody and the Earth are met when the instrument does not experience rapid changes in temperature. However, there are times when one or all of the above assumed conditions are violated in orbit. One such time is around satellite midnight, when the instrument faces the sun. During this period, the instrument undergoes heating and then cooling as shown by the temperature plot over the three-day period (same as in Figs. 1.1 and 1.2) for the scan mirror, primary and secondary telescope mirrors, baseplate, and blackbody (Fig. 2). It can be seen that as the mirrors and baseplate (and many other components as well) are heated around midnight, so is the blackbody, although to a lesser degree. This tends to minimize temperature differences between the blackbody and other instrument components seen by the blackbody. Unfortunately, there are no temperature sensors on the structural components in the vicinity of the scan mirror, which ITT predicts[3] can be heated to temperatures far excess of that of the blackbody around midnight. Under such circumstances, the slope computed from Eq. (4) would be erroneous, since the instrument responds to more radiation than would be received from the calibration target alone. Thus, a slope would be obtained with smaller magnitude from Eq. (4) than its actual value from Eq. (6). (Since the imager output counts and radiance are related inversely, we can expect a false algebraic increase in slope from Eq. (4) around midnight.) From predicted maximum instrument temperatures, Annable[3] estimated that these slope errors can cause temperature errors of up to 0.26 and 0.42 K for a 300 K earth target in channels 2 and 5 respectively.

2.3 Observed midnight calibration errors

To demonstrate that the observed slope anomalies around midnight are calibration errors, we also present evidence from observations[7] provided by the University of Wisconsin - Madison. During a number of days in June 1995, GOES-8 imager channel 2 measurements of the brightness temperature over the Gulf of Mexico were obtained at 45 minutes past each hour. The data were then processed by averaging a number of 5 x 5 clear field-of-view (FOV) boxes to produce the ocean's brightness temperature. Figure 3, as an example, displays the temperature measurements (with an asterisk for the mean and vertical line for the standard deviation) from 2345 UTC on 21 June to 1645 UTC on 22 June 1995. The ocean temperatures exhibited an approximate 1 K depression around midnight, in spite of the uncertainty caused by possible cloud contamination in some

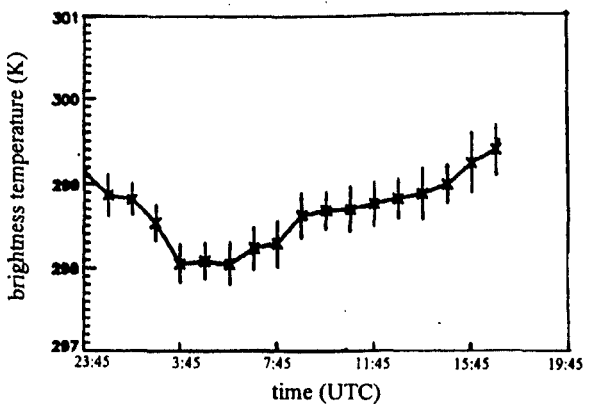

Fig. 3. Brightness temperature of scene over the Gulf of Mexico vs time on 21-22 June 1995, measured by GOES-8 imager channel 2.

measurements. The depression started about three hours before midnight, reached a maximum shortly before midnight, and then decreased during the three hours following midnight.

Generally, diurnal variations of an ocean temperature do not exceed a few tenths of a degree. From that we infer that the GOES-8 imager channel 2 measurements of the Gulf of Mexico must have been incorrect around midnight. These errors were likely introduced by errors in the calibration process. When there is a false decrease in slope magnitude, Eq. (1) will produce a scene radiance and brightness temperature smaller than reality. The in-orbit measurements, therefore, support the hypothesis that false increases in the slope around midnight lead to errors in the instrument measurements, as predicted before launch. These errors exceed the instrument noise levels and thus need to be corrected.

3. ESTIMATES OF THE CORRECT CALIBRATION SLOPE

To determine errors in the imager's rapidly changing slope around midnight, the effect of extraneous radiation from the hot instrument needs to be isolated from the effects of instrument temperature changes. The changes in instrument temperature produce real changes in instrument responsivity, and thus real changes in slope, which can be seen in Figs. 1.1and 1.2 in the periods away from satellite midnight. Analysis of the ITT pre-launch test data indicated a strong dependence of the detectors' responsivity on instrument component temperatures[8]. It was suggested that in orbit, the calibration slope could be predicted from temperature measurements of the primary telescope mirror and/or visible optics. Immediately after the GOES-8 launch, Heinrichs[9] studied the diurnal variation of the responsivities, using less than 10 days of in-orbit data. The dependence of the imager responsivity on the temperature of the primary telescope mirror agreed with that found before launch. A suggestion was made to utilize this correlation to predict the true slope in orbit around midnight.

With more than six months of in-orbit data, we carried out a thorough study of the dependence of calibration slopes on the temperature of instrument components. Our goal was to develop an Operation Ground Equipment (OGE) algorithm which would effectively correct the midnight slope errors.

3.1 Correlations between imager slopes and instrument temperatures

For the period between 5 May and 22 November 1995 (202 days; referred to as "the test period" hereafter), data were collected of slopes and concurrent temperature measurements for the scan mirror, primary telescope mirror, secondary telescope mirror, visible optics, primary mirror baffle, electronics, baseplate, patch (whose temperature is essentially that of the detectors), and the cooler radiator. To demonstrate the temperature dependence of the slope, slopes were plotted against each instrument temperature. An example for the primary mirror is displayed in Figs. 4.1 and 4.2 for channels 2 and 4. These figures include data obtained at each blackbody measurement during the first 115 days of the test period when the detector temperatures were controlled at a constant 101 K. (The detectors were later maintained at a lower temperature,

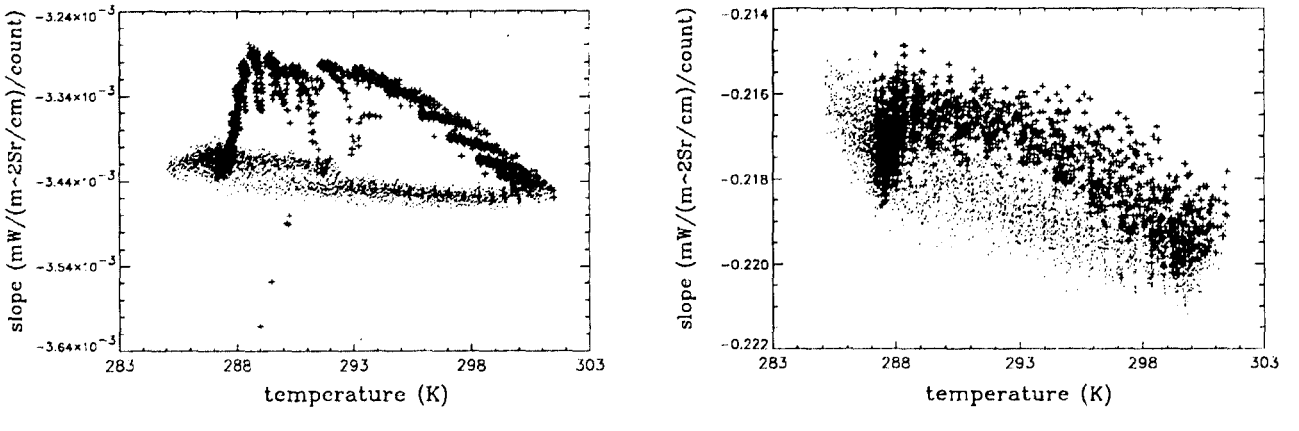

Figs. 4.1 (left) and 4.2 (right). Computed slopes vs primary-mirror temperature for GOES-8 imager channels 2 (left) and 4 (right), data from 5 May to 27 Aug. 1995. 8-hours night +; daytime •.

which greatly changed the magnitude of the slope, thus later data are not plotted here. Nevertheless, those data exhibit patterns similar to those described below.) In these figures, data obtained within four hours before and after midnight are depicted by crosses (+), while data from other times are depicted by dots (•). It can be seen that most of the slopes in channel 4 are contained within a relatively well-defined band, with night measurements located on the upper portion. Slopes in channel 2, however, fall along two bands, with most of the daytime measurements concentrated on the lower nearly-horizontal band, and most of the night measurements lying on the upper bell-shaped band.

Despite the differences in the slope-temperature patterns of these two figures, a common trait in both channels is the almost straight band formed by data that were sampled at daytime, i.e., the daytime slope (which is presumably correct and free of the midnight effect) relates to the primary-mirror temperature in a nearly linear pattern. Plots of daytime slopes vs. the temperature of other instrument components, including the scan mirror, primary mirror, secondary mirror, and aft-optics, illustrate similar patterns. Thus, statistical regressions with daytime data can be performed to determine the slope's dependence on temperatures. It should also be pointed out that in addition to measurement noise, the spread of these daytime data suggests seasonal variations in the slope-temperature relationship. In order to predict the correct slope from the instrument temperatures by regression, three factors need to be determined: first, the length of the daytime period during which the slope is correct and thus the measurements can be included in the regression (accordingly, slopes are considered erroneous during the rest of the day, which hereafter will be called the midnight-effect period) ; second, the number of days over which seasonal instrument changes are not significant, so their data can be used together as legitimate samples for the regression; third, the predictors and the regression form.

To determine the daytime period and the legitimate number of days quantitatively, the slope-temperature correlation coefficient r is used as an indicator. Since the correct slope can be correlated with the instrument temperature, the correlation is degraded when erroneous slopes at night and/or data with seasonal variations are included in the computation. Thus, the optimal correlation coefficient (i.e.,|r| nearest to 1) indicates the best selection of the daytime period and the number of days for sampling. Several midnight-effect periods (0, 2, 4, 6, 8, 10, and 12 hours centered at midnight), and the number of days

TABLE 2: Correlation coefficients relating GOES-8 imager slopes and component temperatures

Midnight effect period (hours)	Scan mirror	Primary mirror	Aft-optics	Secondary mirror	Baffle	Base-plate	Elec-tronics	Black-body	Patch	Cooler-radiator
channel 2:										
0	*0.26*	*-0.28*	*-0.14*	*-0.08*	*0.15*	*0.14*	*0.44*	*0.22*	*-0.02*	*-0.01*
4	*-0.28*	*-0.51*	*-0.40*	*-0.34*	*-0.23*	*-0.15*	*0.65*	*-0.11*	*-0.02*	*-0.01*
8	*-0.81*	*-0.80*	*-0.72*	*-0.82*	*-0.71*	*-0.60*	*0.89*	*-0.59*	*-0.10*	*-0.02*
12	*-0.89*	*-0.84*	*-0.74*	*-0.91*	*-0.75*	*-0.62*	*0.93*	*-0.72*	*-0.12*	*-0.02*
channel 3:										
0	*-0.26*	*-0.76*	*-0.63*	*-0.59*	*-0.34*	*-0.36*	*0.78*	*-0.29*	*-0.02*	*-0.01*
4	*-0.73*	*-0.88*	*-0.80*	*-0.78*	*-0.68*	*-0.63*	*0.88*	*-0.59*	*0.00*	*-0.01*
8	*-0.94*	*-0.95*	*-0.89*	*-0.96*	*-0.87*	*-0.79*	*0.92*	*-0.77*	*-0.04*	*-0.02*
12	*-0.97*	*-0.95*	*-0.88*	*-0.98*	*-0.88*	*-0.76*	*0.94*	*-0.84*	*-0.12*	*-0.02*
channel 4:										
0	*-0.36*	*-0.80*	*-0.70*	*-0.64*	*-0.44*	*-0.45*	*0.75*	*-0.38*	*-0.03*	*-0.01*
4	*-0.76*	*-0.88*	*-0.82*	*-0.79*	*-0.71*	*-0.66*	*0.80*	*-0.63*	*-0.01*	*-0.02*
8	*-0.90*	*-0.90*	*-0.86*	*-0.91*	*-0.84*	*-0.78*	*0.83*	*-0.77*	*-0.03*	*-0.02*
12	*-0.88*	*-0.87*	*-0.81*	*-0.89*	*-0.80*	*-0.71*	*0.83*	*-0.79*	*-0.10*	*-0.02*
channel 5:										
0	*-0.33*	*-0.74*	*-0.66*	*-0.56*	*-0.43*	*-0.41*	*0.64*	*-0.33*	*-0.05*	*-0.01*
4	*-0.67*	*-0.81*	*-0.77*	*-0.70*	*-0.66*	*-0.60*	*0.69*	*-0.55*	*-0.03*	*-0.01*
8	*-0.81*	*-0.85*	*-0.82*	*-0.83*	*-0.81*	*-0.73*	*0.73*	*-0.70*	*-0.05*	*-0.02*
12	*-0.79*	*-0.80*	*-0.77*	*-0.79*	*-0.77*	*-0.68*	*0.72*	*-0.72*	*-0.10*	*-0.01*

for sampling (1, 3, 5, 10, and 15 days) were tested to obtain the optimal slope-temperature correlation coefficient r. Table 2 lists the correlation coefficients between the slopes of all IR channels and a variety of temperatures with one-day sampling and the 0, 4, 8 and 12-hour midnight-effect period. The results shown are averaged over the entire test period. As expected, |r| values are relatively small when more data near midnight are included in computation, especially for channel 2. When the midnight-effect period expands from 2 to 8 hours, |r| values increase for most instrument temperatures, except for the patch and cooler-radiator temperatures which are controlled and do not vary diurnally, therefore, they are not applicable slope predictors. The improvement in these correlations with increasing length of the midnight-effect period is especially significant for channel 2. When the 12-hour midnight-effect period is selected, however, |r| values decrease for channels 4 and 5, likely due to the decrease in variability in the samples compared to their noise. Overall, for all the channels, the applicable |r| values are adequate with the 8-hour midnight-effect period, which is thus the effective length of the period during which the calibration slopes are degraded by the hot instrument components.

A similar analysis was performed to determine the number of days for regression sampling. For each day during the test period, computations were based on data from outside the midnight-effect period in the current and several previous days. The results show that the slope-temperature correlations of the one-day data are similar to those of the three- or five-days. However, the correlations become weaker when the number of days increases to more than ten. This indicates that the seasonal changes may be significant for periods of more than ten days.

Overall, our analyses with the correlation coefficients indicate that among all the instrument temperatures, that of the primary telescope mirror is by far the best single predictor for the GOES-8 imager slopes. The scan mirror, secondary mirror, and aft-optics temperatures are also effective. In fact, these temperatures are highly correlated to one another, which introduces difficulties in calculating multiple temperature regressions of the slope. Although the multiple regression technique may be more desirable for representing the detector background flux, our attempt to apply the method to determine an optimal set of independent temperature predictors was inconclusive. Nevertheless, as a single predictor, the primary-mirror temperature should be effective. Exhibited in Figs. 4.1 and 4.2, the relation between the daytime slope and primary-mirror temperature is nearly linear, with a slight curvature. Standard errors of estimate from polynomial fits with data in the test period indicate that overall, a quadratic fit produces the best results. Thus, the regression takes the form:

$$m = c_0 + c_1 T + c_2 T^2 \qquad (7)$$

where T is the primary-mirror temperature, and c_0, c_1, and c_2 are regression coefficients determined from fitting the sampling data. Examples of the predicted slope are presented in the next section.

3.2 Algorithm to correct the midnight effect

The following algorithm has been proposed, and will be implemented in the ground system in the near future:

After each instrument blackbody look, the "original" slope is computed from Eq. (4), which is then compared with the "estimated" slope from Eq. (7). In Eq. (7), T is now the concurrent value of the temperature of the optic component used as a predictor (which is likely to be the primary mirror, as discussed earlier). The coefficients for Eq. (7) are determined from fitting the predicting temperature and original slope with data obtained outside the midnight-effect period, which is between the hours H1 and H2 UTC, and within the preceding D (D≤ 10) days. Data from each day may be given different weights (the most recent data usually are weighted more than earlier data). Before the fit is performed, all the samples are quality-checked, and data whose studentized-deleted residuals exceed a certain level M1 ("M1-filter"), or whose estimated slope residuals exceed a certain multiple M2 of the standard error of the regression ("M2-filter"), are rejected.

To determine if the estimated slope is to replace the original slope for instrument calibration, an "N-filter" is applied, in which the difference between the two slopes is compared with a multiple (N) of the standard error of the regression. If the difference is within the N-filter range, the original slope is kept for the calibration. Otherwise, the estimated slope is selected.

Illustrating how the algorithm works, Figs. 5.1 and 5.2 plot the original and estimated slopes during the three-day period (same as in Figs. 1.1and 1.2) for channels 2 and 4 respectively. In these plots, crosses (x) represent the original slopes, and

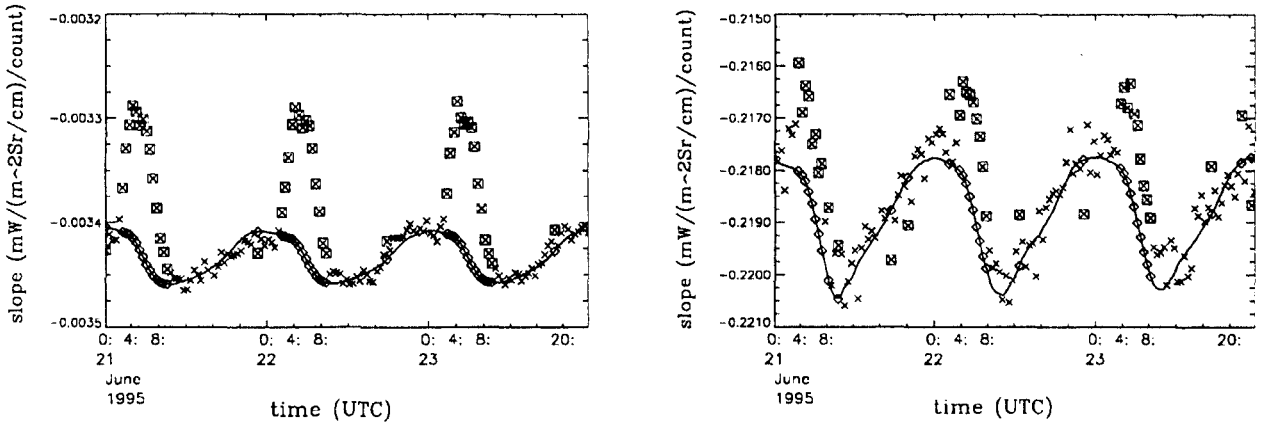

Figs. 5.1 (left) and 5.2 (right). Original (x) and estimated (curve) slopes for GOES-8 channels 2 (left) and 4 (right). Rejected original slopes (⊠) are replaced by estimates (◇).

solid lines connect the estimated slopes. To estimate the slopes, the primary-mirror temperature was used as the predictor,

and three days of data outside the 8-hours midnight-effect period (i.e., D=3, H1=1 UTC, and H2=8 UTC) and an M2-filter with M2 equal to 5 were used for the regression. An N-filter with N equal to 2 was used to select the calibration slopes. The slopes to be replaced by the estimated values are surrounded by open squares (e.g., ⊠). Their replacements are marked with diamonds (◇). It can be seen that the rejected slopes are largely within the midnight-effect period. This is especially pronounced for channel 2. Outside the midnight-effect period, there are also a number of slopes that are replaced by the estimates. This indicates that in addition, the midnight algorithm can function as a slope filter to reduce the calibration noise. Currently, a slope-averaging technique[5] is being used for this purpose.

To provide further study, the original and estimated slopes are displayed in Figs. 6.1 and 6.2 for the entire test period, with lighter and darker symbols representing the original and estimated slopes respectively. (The abrupt slope changes which occurred on 28 August were due to a detector temperature change.) The slope-temperature regressions of this period yield an averaged slope rms errors of less than 1% for all channels. The maximum amount of slope correction is about 4%, which is observed in channel 2 around midnight during the middle of summer. The size of the correction decreases significantly from summer to winter. In channel 4, however, the correction is relatively small (less than 1 or 2 %), yet has a slightly larger

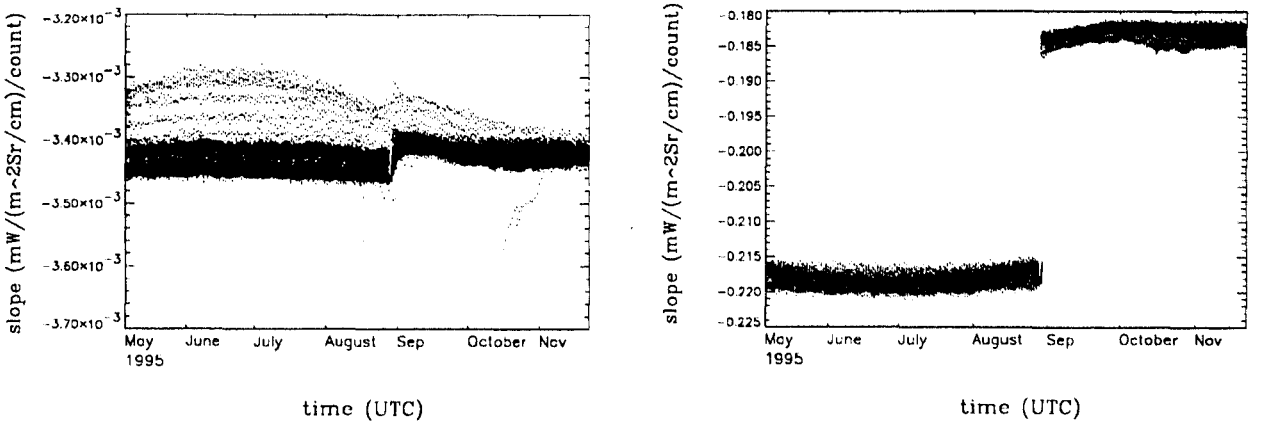

Figs. 6.1 (left) and 6.2 (right). Original (lighter dots) and estimated (darker dots) slopes for GOES-8 imager channels 2 (left) and 4 (right) between 5 May and 22 Nov. 1995.

magnitude during the middle of summer. This indicates that the midnight effect is stronger in the summer than in the winter.

In contrast to the false increases in slope values caused by the midnight effect discussed above, Fig. 6.1 also shows a few original slopes measured with extremely small values (i.e., large magnitudes) around midnight in August and October, which are the pre- and post-eclipse seasons around the equinox. (During the eclipse season itself, the instrument is turned off, so the effect is not seen.) When the instrument space look is contaminated by solar radiation, in order to calibrate the instrument correctly, the left side of Eq. (3) should include a contribution from the solar contamination in the space look. Using a zero space radiance, however, yields a slope with a larger magnitude than reality, especially for the shortwave channels, as Fig. 6.1 displays. In fact, around midnight of an eclipse season, slope errors in the shortwave channels are the result of two midnight effects, one caused by radiation from the hot instrument, and the other by the sun in the space looks. In either case, the erroneous slopes at night would be replaced by the estimates, should the slope correction algorithm be applied. It is clear that the midnight algorithm is capable of correcting slope errors of many kinds, and is not limited to those caused only by the hot instrument at night.

3.3 Calibration errors from midnight effects

Assuming the estimated slope is accurate, calibration errors from an erroneous original slope can be calculated at temperature T as,

$$\Delta T = \Delta R(dR/dT)^{-1} \tag{8}$$

where dR/dT is the derivative of the Planck function with respect to temperature, and ΔR is the radiance error for a target at this temperature, which, when caused by an erroneous slope, can be obtained from the derivative of Eq. (1),

$$\Delta R = \Delta m X \tag{9}$$

where Δm is the difference between the original and estimated slopes.

Figure 7 displays such calibration errors at 300 K on 22 June 1995. Errors of up to about -1 K and -0.6 K are found within the approximately eight hours around midnight for channels 2 and 4, respectively. For channel 2, these errors exhibit a more distinct diurnal pattern, while in channel 4, they are masked with greater noise. The errors in channel 2 correlate well with temperature depressions[7] measured by the instrument over the Gulf of Mexico, as displayed in Fig. 3. This agreement provides more evidence that the apparent ocean temperature decreases at night are indeed caused by calibration errors.

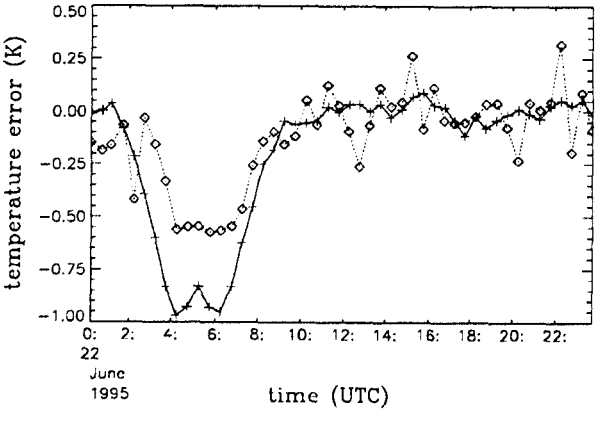

Fig. 7. Temperature errors at 300 K resulting from slope errors for GOES-8 imager channels 2 (+) and 4 (◊).

Figures 8.1 and 8.2 display the calibration errors at 300 K over the test period, for channels 2 and 4 respectively. Seasonal changes of these negative errors are apparent in channel 2, since the midnight effect is stronger in the summer and weaker in the winter. Errors in channel 4 are rather scattered, suggesting that the major error source is noise in the longwave channel slope computation. Errors in channel 2 are more pronounced at night and extremely small at daytime, indicating the greater need for midnight corrections on the shortwave channel slopes. The few large positive errors in channel 2 (up to more than 1 K) are associated with slopes that were computed with the solar-contaminated space measurements. This effect introduces positive temperature errors in calibration, which is the opposite from the midnight effect by the hot instrument.

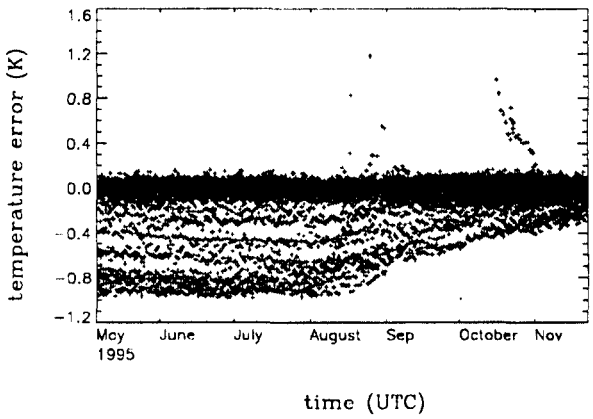

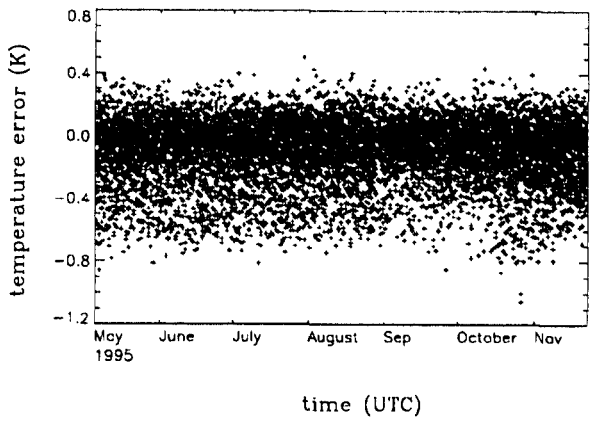

Figs. 8.1 (left) and 8.2 (right). Temperature errors at 300 K resulting from slope errors for GOES-8 imager channels 2 (left) and 4 (right) between 5 May and 22 Nov. 1995.

4. CHARACTERISTICS OF THE EFFECTIVE RADIATING SOURCE AROUND MIDNIGHT

After the correct slope is estimated from the temperature prediction, we can go back to investigate the sources of the midnight effects and determine their radiometric characteristics.

As mentioned in section 2.2, the midnight slope errors introduced by the hot instrument are believed to be caused by the non-blackness of the blackbody. When the instrument looks at the blackbody, the measured radiation includes both emitted and reflected energy from the blackbody. The amount of reflected radiation, expressed by $(1-\epsilon_{bb})\sum F_i R_i$, can be computed from Eq. (6) with the correct slope value m. To characterize the source(s) of this radiation, we simplify the problem by assuming that the reflected radiation originates from one source at an effective temperature T_{eff}, radiance R_{eff}, and view factor F_v at the blackbody. Then, for each channel, the reflected radiance can be computed as,

$$(1-\epsilon_{bb})F_v R_{eff} = q(X_{bb}^2 - X_{sp}^2) + m(X_{bb} - X_{sp}) - \epsilon_{bb} R_{bb} \qquad (10)$$

(Eq. (5) was used to replace the intercept b in Eq. (6), and the term $\epsilon_{bb}R_{bb}$ also includes self-reflected blackbody radiation in the actual computations.) The blackbody emissivity ϵ_{bb} is assumed[3] to be 0.98. Assuming that all the channels possess the same view factor F_v, one can infer the values of F_v and T_{eff} by iterating over different temperature values to find the best fit of a Planck curve to the computed R_{eff} in all the channels. Figure 9 illustrates, as an example, the results of such a computation for the blackbody look at 0514 UTC 21 June 1995. The derived value of the effective view factor is 0.59, and the derived effective radiances in all four channels (pluses in the figure) fit well to the Planck curve of 344 K (the solid line). Hence, the effective temperature of the source is approximately 344 K at the time of this blackbody look.

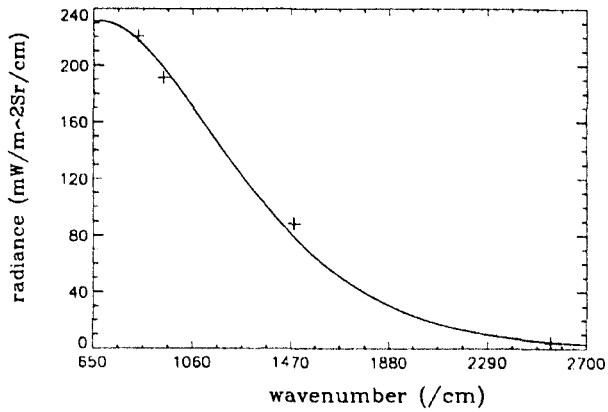

Fig. 9. Fit of Planck curve for 344 K to GOES-8 imager radiances (+) for hot source, data from 0514 UTC 21 June 1995.

Figure 10 displays the effective temperature of the hot source during the three-day period (same as in Figs. 1.1 and 1.2),

computed with an effective view factor averaged over the entire test period, which is 0.54. It can be seen that around midnight, the source heats up rapidly from the blackbody temperature level (~ 290 K) to about 360 K, and then cools down to the blackbody temperature level. It is during this period that the source's extraneous radiation contaminates the blackbody measurements and causes significant errors in the calibration, especially for the shortwave channels. The computation results completed over the test period indicate that the peak temperature of the hot source at night falls from about 360 K in June to about 310 K in November, which is in agreement with the midnight effect reduction from summer to winter observed in section 3.2. This seasonal variation is likely caused by the seasonal change in the amount of sunlight on the components seen by the blackbody. The temperature values computed above are not necessarily actual representations for any particular component, but rather a measure of the midnight effect from the collective sources. The actual temperatures are uncertain, since they depend on the view factors of each individual component and the correct measurement of the blackbody emissivity. Furthermore, our analysis may have neglected other potential error sources, such as a differential in the intensities of the scattered radiation from the scan mirror between the views of space and the blackbody. This could become significant when the instrument is hot[10]. If such sources were included, it might change the values we compute for the effective temperature.

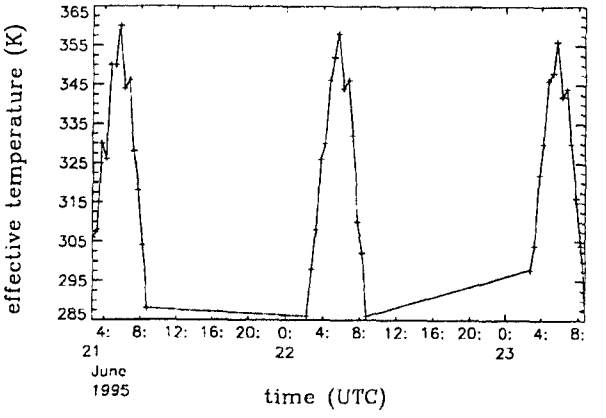

Fig. 10. Effective temperature of GOES-8 imager hot source vs time.

For the solar contaminations in the space looks around the eclipse season, computations indicate that the excess energy in channel 2 corresponds to a "target" whose temperature may be as warm as 250 K.

5. CONCLUSIONS

This study of the midnight effect provides information on the GOES-8 imager calibration errors and guidelines for the correction algorithm. Characterizations of the error source can help point to future improvements in instrument design and the pre-launch tests. The GOES-9 imager displays the same midnight effects as the GOES-8, but to a lesser degree. This improvement has been credited primarily to the extensive cleaning of the instrument's mirrors before launch[10]. This helped reduce the excess radiation scattered from the scan mirror, but not the extraneous radiation from the hot instrument reflected by the blackbody. (Regardless of the sources of the midnight effect, however, the correction algorithm will still be effective.) The midnight calibration effects described in this paper have also been observed in the sounders of both GOES-8 and -9, and are expected to affect the later instruments of the current generation of GOES satellites. Unless and until major instrument design changes can be implemented to improve the in-orbit calibration, the algorithm proposed in this paper will be utilized in ground data-processing to ensure the accuracies of the imager measurements. This is especially pertinent for the shortwave IR channels around satellite midnight and during eclipse seasons. Studies of midnight effects in the sounders are currently underway.

6. REFERENCES

1. Menzel, W.P. and J.F.W. Purdom, "Introducing GOES-I: The first of a new generation of geostationary operational environmental satellites," *Bull. Amer. Meteorol. Soc.*, **75**, pp. 757-781, 1994.

2. Annable, R., "GOES sunshields: Degradation of in-flight calibration accuracy," ITT internal memo, 1 p., 24 Feb. 1988.

3. Annable, R., "In-Flight calibration errors from the INR sunshields: Reduction in shield temperature (imager)," ITT internal memo, 4 pp., 12 Apr. 1988.

4. Annable, R., "In-flight calibration errors from the redesigned INR sunshields (sounder)," ITT internal memo, 7 pp., 22 Apr. 1988.

5. Weinreb, M.P., "Real-world calibration of GOES-8 and -9 sensors," to appear in the proceedings of the *SPIE Intl. Symposium on Optical Science, Engineering, and Instrumentation: Conference on GOES-8 and beyond*, Denver, CO, 4-9 Aug. 1996.

6. Weinreb, M.P., J.X. Johnson, J.C. Bremer, E.C. Wack, and O. Chen, " Algorithm to compensate for variation of reflectance of GOES-8 and -9 scan mirrors with scan angle," preprint volume, *Eighth Conf. on satellite Meteorol. and Oceanography*, Atlanta, GA, (Amer. Meteorol. Soc., Boston, MA), pp. 110-114, 28 Jan. - 2 Feb. 1996.

7. Paul van Delst, Space Science and Engineering Center (SSEC), University of Wisconsin - Madison, private communication, 5 July 1995.

8. Consins, D., E.C. Wack, and R.M. Heinrichs, "GOES SN03 imager final thermal vacuum IR calibration results," MIT/LL NOAA-5 Project Report, 163pp., 1 Sept. 1993.

9. Heinrichs, R.M., "GOES 8 imager diurnal responsivity variation," MIT/LL internal memo, 18pp., 22 Aug. 1994.

10. Annable, R., "GOES-9 imager : Responsivity Anomaly Near Midnight," ITT internal memo, 4 pp., 2 Oct. 1995.

Simulation of GOES 8 Imager IR striping due to 1/f noise[1]

Edward C. Wack and Lawrence M. Candell

Lincoln Laboratory, Massachusetts Institute of Technology
244 Wood St., Lexington, MA 02173

ABSTRACT

The present GOES Imager exhibits East-West stripes in IR images due to low frequency errors in the calibration of the adjacent North-South detectors. Striping makes delineating boundaries of structures in images difficult, especially in the case of cold scenes. A computer program has been developed that generates simulated (CONUS size, constant temperature scene) IR images using detector noise (Gaussian and 1/f) parameters as inputs. The simulation includes errors due to background drift between space clamps, drift during a space clamp, and errors determining the first order gain during the internal blackbody calibration. The results of the simulation agree well with on orbit measurements of GOES 8 and 9 striping in channels 4 and 5. These simulations can also predict striping performance of future GOES Imagers from detector noise parameters allowing for improved detector selection constraints.

Keywords : GOES, 1/f noise, calibration

1. INTRODUCTION

The GOES 8 and 9 Imagers have suffered from striping in the LW IR channels (4 and 5) since becoming operational. These channels consist of two HCT detectors adjacent in the North-South direction which are then scanned East-West[1]. Striping occurs when errors in calibration cause the output of each detector to be in error with respect to its neighbor. This leads to East-West stripes which are most visible in constant radiance scenes. When the relative calibration error between the two detectors exceeds the white noise level, or NEDT, striping becomes apparent. This introduces a qualitative error in the images which makes delineating boundaries of structures difficult. Figure 1 shows a magnified, contrast enhanced image from GOES 8 channel 4 of the Gulf of Mexico. Striping is clearly evident in the warm water scene. There is a quantitative error, as well, since it is not known which detector is the most accurately calibrated.

HCT detectors are known to have excessive low frequency, or 1/f, noise. It has been hypothesized that this is a leading cause of the striping in channels 4 and 5. This paper presents a model of the GOES Imager calibration process, using detector noise parameters, to simulate image striping. Laboratory measurements were made during instrument calibration that have determined the 1/f noise parameters of the Imager detectors. These are used as inputs to the simulation and output striping statistics are computed. Striping is evaluated as a function of 1/f noise. Measured detector 1/f noise parameters are input and striping statistics compared to those from images collected on orbit.

Not including systematic bias between detectors, which is not related to 1/f noise, both channels 4 and 5 of GOES 9 have less striping than GOES 8. The GOES 9 detectors also have less 1/f noise than GOES 8. Since striping becomes apparent when errors in the calibration from low frequency noise are larger than the

[1]This work was sponsered by the National Oceanic and Atmospheric Administration under Air Force Contract F19628-95-C-0002

0-8194-2200-2/96/$6.00

NEDT, it is possible to determine from simulation whether a given detector's 1/f noise will cause visible striping. Table 1 lists the GOES 8 and 9 1/f noise knee frequencies, NEDT, and RMS striping. Each of the two detectors for a given channel have slightly different knee frequencies, but similar NEDT. These parameters will be discussed in further detail later.

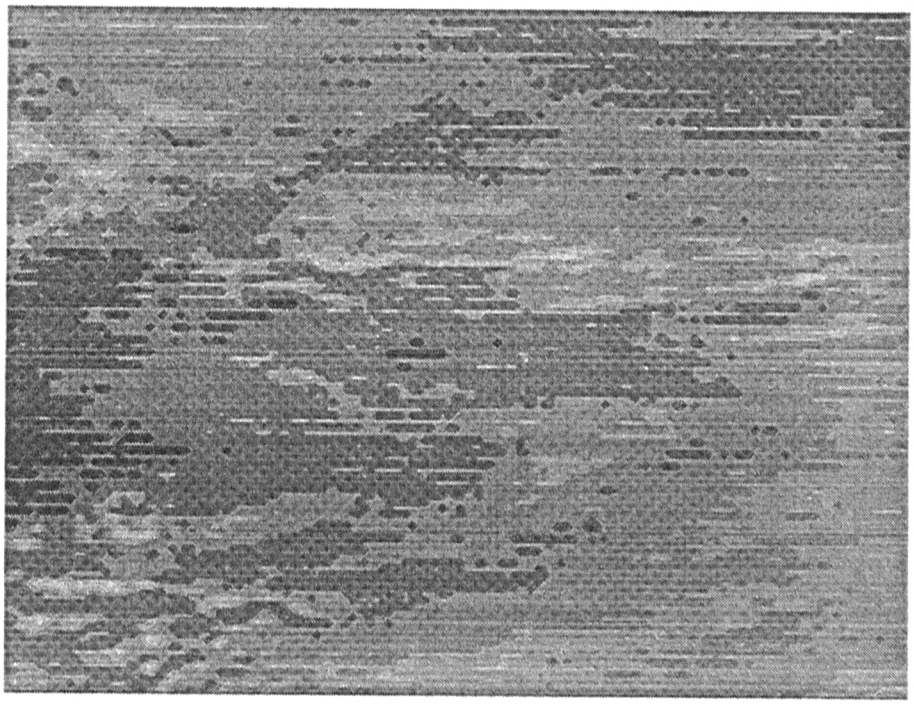

Figure 1. GOES 8 Channel 4 image of the Gulf of Mexico with striping

TABLE 1. GOES 8 AND 9 KNEE FREQUENCY, NEDT AND RMS STRIPING

	GOES 8 Ch 4	GOES 9 Ch 4	GOES 8 Ch 5	GOES 9 Ch 5
Knee Frequency	280, 210 Hz	45, 50 Hz	210, 100 Hz	90, 100 Hz
NEDT	0.09 K	0.06 K	0.14 K	0.11 K
RMS Striping	0.14 K	0.08 K	0.21 K	0.14 K

2. 1/f NOISE GENERATOR

1/f noise is present in many physical systems, including HCT detectors[2]. Measurements of 1/f noise were made for the Imager detectors at the instrument vendor during T/V calibration. For a more thorough discussion on GOES Imager noise model, see reference 3. Figure 2 shows the noise power spectrum of the GOES 8 channel 4 detector A. There are three parameters that are used to describe the noise power spectrum; the white noise level, the knee frequency, and the slope of the low frequency noise. The following function was

fit to the detector noise power spectrum, and the three parameters determined[4].

$P(f) = wn * (1.0+(kn/f))^{sl}$ where

wn = white noise level
kn = knee frequency
f = frequency
sl = slope of the low frequency noise
P(f)= noise power at frequency f

A computer program has been developed to generate a digital signal with known 1/f and white noise parameters[5]. Figure 3 shows the noise power spectrum of a synthetic signal created to simulate the detector noise in Figure 2. This signal can be generated with different lengths (time) and used to simulate GOES detector outputs.

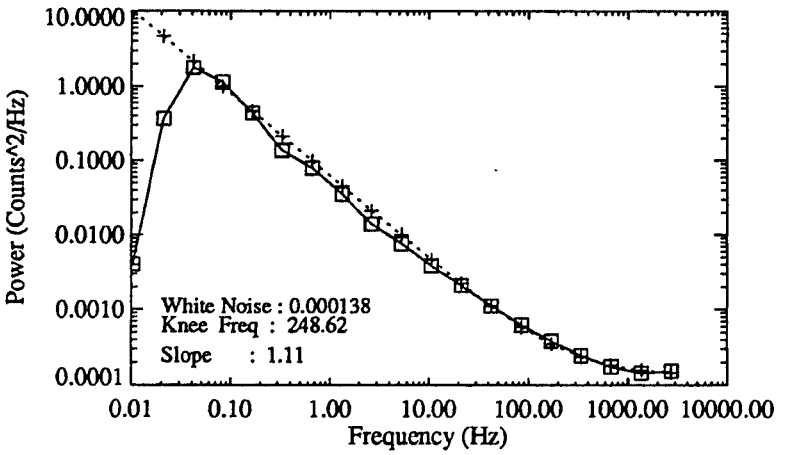

Figure 2. Noise Power Spectrum of GOES 8, Ch 4a

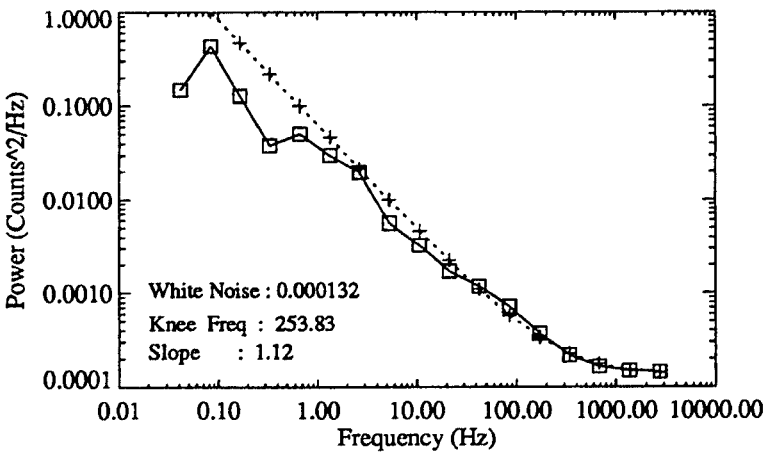

Figure 3. Noise Power Spectrum of Simulated Signal

3. ON ORBIT STRIPING

To quantify the magnitude of striping on orbit, Mike Weinreb of NOAA devised the following algorithm[6]. A given calibrated image is searched for groups of pixels of dimension 7x4 (16km x 16km) in which the standard deviation of each detector is less than 1. This filters the image for sections which have near constant scene brightness where detector to detector comparisons can be made. The 14 pixels for each detector are averaged, then subtracted to arrive at a difference between the two detectors. These differences are accumulated over one and/or many images. The metric I use in this paper is the RMS total of these differences over an image. Over many images, the RMS error is averaged. Weinreb and Tina Baucom (Swales) have done extensive analysis of on orbit striping and present their results in paper 2812-53 at this conference[7]. They also provide the equations for computing further statistics (means and standard deviations over many images).

4. CONUS IMAGE SIMULATION

A software program was written to model the calibration process and image generation of the GOES Imager for a CONUS type image. The model includes the internal blackbody calibrations, space clamps, and CONUS image line length and number of lines. The image scene is a constant 600 counts. The internal blackbody temperature is fixed at 300K. Each event (clamp, scan line, blackbody calibration) has a well defined time extent which includes mirror slew times and the number of samples measured. The signal generator described in section 2, with a given noise parameter input, outputs raw counts for each of the two detectors for a given channel. These signals are generated for a given time period depending on the event. An internal blackbody calibration takes approximately 40 seconds. The time between space clamps is 36.6 seconds. The scene counts are calibrated using coefficients computed from the model process. The calibrated radiance is then converted to GVAR counts and striping statistics computed.

5. STRIPING SIMULATION RESULTS

To determine that increased 1/f noise causes increased striping, I ran several simulations. Figure 4 shows the result of increasing the 1/f noise for a fixed white noise level and the resulting RMS striping. The white noise is denoted here as NEDT. The values shown are typical of the Imager channel 4. The 1/f noise is represented by the knee frequency. A higher knee frequency means more 1/f noise relative to white noise. Each point on the plot is the total RMS striping computed over 20 simulated CONUS size images with a given noise level. Above 30Hz, striping increases linearly with knee frequency. Above 100 Hz, striping becomes significantly larger than the NEDT and would be apparent in images.

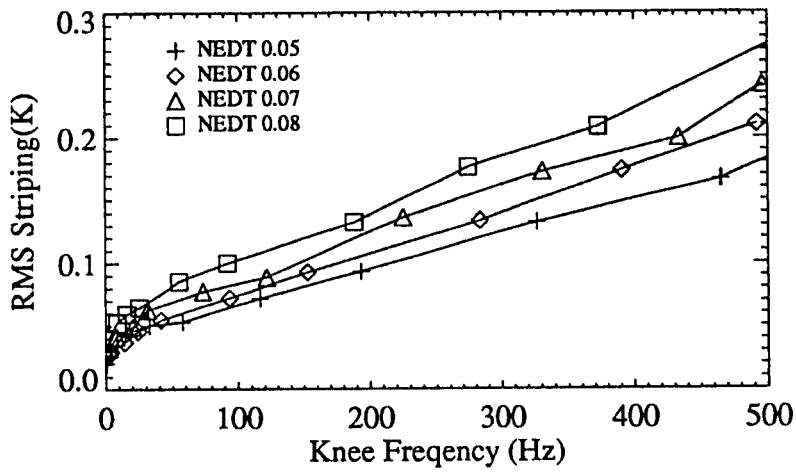

Figure 4. Simulated Channel 4 Striping Vs. Knee Frequency

To see how the simulation agrees with on orbit striping measurements, I input the actual GOES detector noise parameters measured on the ground. Again, 20 CONUS size images were generated and striping statistics computed. Figure 5 shows the results. On orbit data includes GOES 8 and 9, channels 4 and 5. Simulated data, using ground measurements of noise, includes both channels 4 and 5 for GOES 8 and 9 as well as SN05 and SN06 Imagers which are scheduled to fly on GOES 10 and 11. The GOES 9 simulated data is less than the on orbit data for two reasons. First, the 12/08/95 data point was using OGE Mode 1 calibration, where blackbody slopes are not averaged to reduce noise. The simulation uses the average of 40 calibrations, OGE Mode 3. Second, the 02/26/96 data point has a systematic component to the striping which is not accounted for in the simulation. The GOES 8 data agrees well, with the simulation slightly over-predicting channel 4 and under-predicting channel 5. The channel 4 striping for GOES 10 and 11 are similar to GOES 9 without the systematic striping component. That is good. Channel 5 striping for GOES 10 and 11 will be more like GOES 8 than GOES 9, which is not good. As stated earlier, striping becomes more apparent when it is significantly larger than the NEDT. This is the case for GOES 8 and GOES 9 channel 4 including the systematic component of striping.

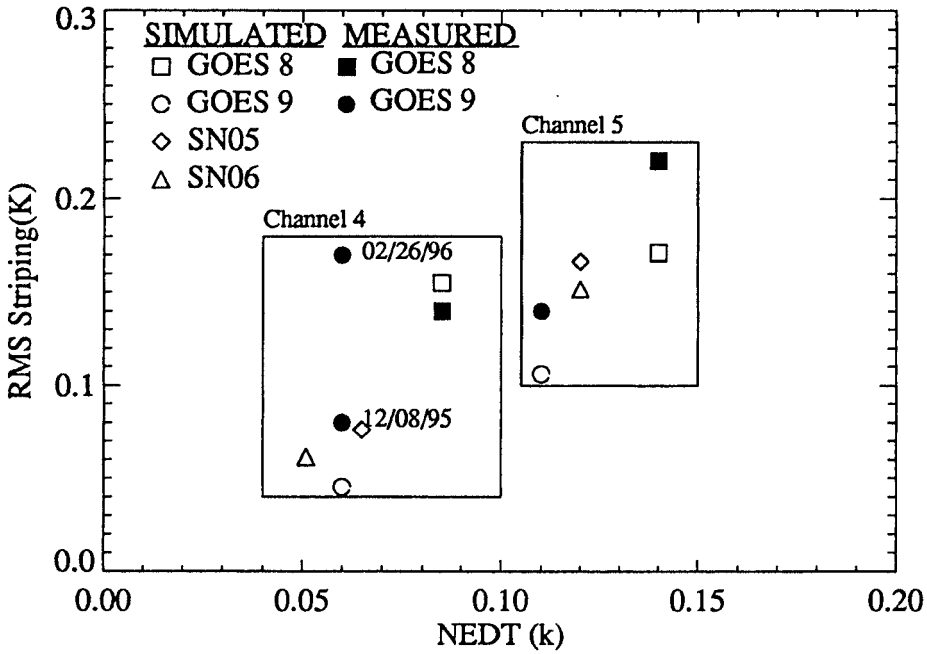

Figure 5. Simulated and Measured Striping vs. NEDT

6. CONCLUSION

The results of the simulation show that 1/f noise is a source of error in the calibration that leads to striping. The error is introduced into the blackbody calibration, the space clamp, and drift in the detector signal between space clamps. Striping becomes problematic when it is larger than the NEDT. Knee frequencies above

100 Hz cause problematic striping. The simulation agrees well with on orbit measurements. It can also predict future instruments' on orbit striping performance based on ground measurements. Based on this simulation, channel 4 in GOES 10 and 11 will have striping similar to GOES 9. Channel 5 will be similar to GOES 8. This type of simulation can be used for providing constraints on detector selection for improved performance.

7. ACKNOWLEDGEMENTS

The authors would like to thank Mike Weinreb of NOAA and Tina Baucom of Swales for their work characterizing GOES 8 and 9 striping. We also would like to thank ITT A/CD for providing access to instrument level test data used in determining detector 1/f noise.

8. REFERENCES

1. J. Savides, "Geostationary Operational Environmental Satellite, GOES I-M", December, 1992, Space Systems Loral

2. M. S. Keshner, "1/f Noise", Proceedings of the IEEE, Vol. 70, No. 3, pp. 212-218, March, 1982

3. J. C. Bremer, G. J. Comeyne, "Optimization of the GOES-I Imager's radiometric accuracy: drift and 1/f noise suppression", Optical Engineering, Vol. 33, No. 10, pp. 3324-3333, October, 1994

4. G. Wornell, A.V. Oppenheim, "Estimation of Fractal Signals from Noisy Measurements Using Wavelets', IEEE Transactions on Signal Processing, Vol 40, No. 3, pp. 611-623, March, 1992

5. G. Corsini, R. Saletti, "$1/f^{\gamma}$ Power Spectrum Noise Generator", IEEE Transactions on Instrumentation and Measurement, Vol. 37, No. 4, pp. 615-619, December, 1988

6. M. Weinreb, private communication on striping algorithm.

7. J. Baucom, M. P. Weinreb, "Characteristics of E/W Stripes in infrared images from the GOES-8 Imager", SPIE Optical Science, Engineering and Instrumentation, GOES 8 and Beyond, paper 2812-52, August, 1996

Statistical properties of inter-calibration techniques which use empirical distribution functions

David S Crosby

National Environmental Satellite, Data, and Information Service, Washington DC 20233

Elena Randou

The Department of Mathematics and Statistics, American University, Washington DC 20016

ABSTRACT

Techniques which use empirical distribution functions have been used successfully to intercalibrate detectors on the same instrument or channels on different instruments. In this paper the procedure is developed as a statistical technique for estimating a function. Since it is a statistical procedure, it is possible to use classical statistical techniques to evaluate the accuracy of the results. Confidence regions can be constructed for the estimated parameters. Given a required degree of accuracy it is possible to estimate the required sample sizes. Using hypotheses testing techniques questions about possible changes in the inter-calibration functions can be answered. The theory, which uses quantiles from the distributions of random variables, is outlined. The large-sample properties of the estimators of these quantiles are presented. The theory requires that the data be continuous. However, it is discrete. Preliminary simulation results indicate that the theory for continuous data can be applied to the discrete data with little loss of accuracy.

KEY WORDS

Intercalibration, empirical distribution function, estimation, quantiles, hypothesis testing, confidence intervals.

1. INTRODUCTION

A technique which uses empirical distribution functions (EDF's) has been used successfully to intercalibrate similar detectors on the same instrument [1, 2] and channels on successive satellites [3]. These procedures which have been referred to by various names such as histogram modification, normalized look-up tables, or EDF techniques all use the same assumptions. The paper by Weinreb et al. [2] discusses some of the mathematical properties of the technique and gives an application to the destriping of the imager on GOES. Even though the technique is fundamentally a statistical one there has been little discussion in the literature of the statistical properties of the procedure. In this paper some of the statistical properties are outlined. If the model is specified in the proper way and a number of assumptions are made about the data, then it is possible to treat the problem using classical statistical techniques. The model is written in terms of the distribution functions and the quantiles of the distribution functions. By formulating the problem in this manner, the EDF techniques becomes equivalent to a procedure for estimating the difference between the quantiles of distribution functions. The large-sample properties of these estimators which use the order statistics is well known. This will allow the construction of confidence intervals and hypothesis testing. This means that not only can the intercalibration functions be given, but that error estimates can be provided. It also means that an objective criterion for testing if there has been a change in the intercalibration function can be developed. If a fixed degree of accuracy is required at a particular quantile then the necessary sample size can be specified.

2. DEFINITION AND MODEL

For simplicity, it will be assumed that all the measurements are continuous. They are, of course, actually discrete. However, treating them as discrete complicates both the notation and the theory. The fundamental results will still hold to a reasonable degree of accuracy. The convention of using X to represent a random variable and x to be a particular realization of the random variable will be followed in this paper.

 0-8194-2200-2/96/$6.00

Given a random variable X the function

$$F_x(x) = P(X<x) \tag{1}$$

is the theoretical distribution function of X. Since $F_x(x)$ is a probability it takes on values between 0.0 and 1.0. It is defined for all real values of x and is monotonic. In this paper it will be assumed for all random variables that for all x, $0.0 < x < 1.0$, the distribution function is strictly monotonic. This means that for a given p, where $0.0 < p < 1.0$, there is a unique solution to the equation

$$F_x(x) = p. \tag{2}$$

The solution to this equation is X_p and is called the pth quantile of the random variable X or the distribution function $F_x(x)$.

Let T represent some geophysical parameter measured by the satellite, which will be treated as a random variable.. Let X(t) and Y(t) be measurements of this parameter by different detectors and the same instrument or channels on different satellites. If the instruments were the same and if there were no noise, then for the same t, it would follow that

$$X(t) = Y(t). \tag{3}$$

This is often not the case. The problem then becomes to modify one or both of the functions, X(t) and Y(t), so that for the same observed value of T, to within the limits of noise, the instruments or X(t) and Y(t) will produce the same measured value. The usual approach is to select one of the instruments as the reference, say X(t), and modify the second, Y(t), so that they are the same for identical t's. That is, it is necessary to find a function H(y) such that

$$X(t)= H(y(t)) \tag{4}$$

for all possible values of t. If both instruments viewed the same area, at the same time, under the same conditions (same view angle etc.) then this problem could be easily solved. However, this is frequently not the case.

In order to estimate H(y) using the EDF technique, a number of assumptions are required. These are as follows:

1. Both X(t) and Y(t) are strictly monotonic functions of t. That is, both dX/dt and dY/dt are positive (or both negative) for all values of t.

2. There is a large sample from the random variable T which cover the most of the possible range of T.

3. The probability distribution of T is the same for both detectors or instruments.

From assumption (1) and the chain rule , it follows that dx/dy is positive. Since T is assumed to be random, it follows that X(t) and Y(t) are random variables. If the instruments were identical, then X(t) and Y(t) would have the same distribution function. The EDF technique is equivalent to finding a transformation of Y(t), H(y), so that H(Y(t)) has the same distribution function as X(t).

Since the function H(t) should be very close to the identity, it will be represented by

$$H(y) = y + \delta(y), \tag{5}$$

where $\delta(y)$ is small. The problem then becomes the determination of $\delta(y)$. Let p be a number between 0.0 and 1.0. Let

$F_y(y)$ be the distribution function of Y. Then the unique solution to the equation

$$F_y(y) = p, \tag{6}$$

Y_p ,is the pth quantile of the random variable Y. Let X_p be the pth quantile of the random variable X. Two distributions are the same if they have the same quantiles for all values of p. From this fact and simple algebra, it follows that

$$\delta(Y_p) = X_p - Y_p. \tag{7}$$

for all p between 0.0 and 1.0. Note that under the assumptions given above set of values of the Y_p's will cover the entire domain of the Y's. Given the distribution function of the random variables X and Y, it is possible to compute the $\delta(y)$ and hence the H(y).

4.STATISTICAL PROPERTIES

The results given in section 3 assumes that the true distribution functions $F_X(x)$, $F_Y(y)$ and hence the true p^{th} quantiles are known. This is not the case and it is necessary to estimate these functions and parameters from the data.

Let $x_1, x_2,...,x_n$ be a random sample from the distribution of X. Let $x_1^* \leq x_2^* \leq ... \leq x_n^*$ be the order statistics for this sample. Then the EDF of this sample is defined as

$$\begin{aligned} F_x^*(x) &= 0 \qquad x < x_1^* \\ F_x^*(x) &= k/n \qquad x_k^* \leq x < x_{k+1}^* \\ F_x^*(x) &= 1 \qquad x_n^* \leq x. \end{aligned} \tag{8}$$

Given a random sample from the random variable Y the EDF of this sample is defined in a similar fashion. From these EDF's it is possible to obtain the sample quantiles. Note that since the EDF's are step functions there will be p values for which there is no Y_p value and p values for which there are an interval of y values. These cause minor technical problems, which can be solved in a number of ways [2].

Given the sample estimate of the quantiles, X_p^* and Y_p^*, the estimate of $\delta(Y_p^*)$, is given by

$$\delta^*(Y_p^*) = X_p^* - Y_p^*. \tag{9}$$

The variables δ^*, X_p^*, Y_p^* are all random variables or statistics whose values depend on the sample values $x_1, x_2,..x_n$, $y_1, y_2,..., y_m$. The large-sample behavior of the sample quantiles is well known. If the random variable X has a density, $f_x(x)$, with a derivative at point X_p then the sample quantile will for large n have approximately a normal distribution with mean X_p and variance $(p(1-p))/(n(f_x(X_p)^2)$ [4]. Given the large sample sizes it is possible to estimate the density and hence the distribution of the statistic X_p^*. If the samples for X and Y are assumed to be independent then it is possible to obtain the asymptotic density of δ_p^*. That is, δ_p^* will be approximately normal with mean, δ_p, and variance $(p(1-p)/n(1/(f_x(X_p)^2)+(1/(f_y(Y_p)^2)))$.

The above results allow the construction of approximate confidence intervals for δ_p and the testing of hypotheses about the value of δ_p. The construction of confidence intervals for a particular δ_p is not of great interest unless it is a special case such as p =0.5. That is, how the medians of the two distributions differ. However, by using a Bonferroni approach it is possible to construct a confidence region and hence test hypotheses about any finite number of the δ_p's. A discussion of the Bonferroni approach in a multivariate regression problem is included in a number of standard texts[5]. Using the confidence region for a fixed number of quantiles, say, p= .05, .10,..., .90, .95, it is possible to obtain simultaneous confidence bounds on the difference between the true δ_p 's and the estimated δ_p^*'s. Using the relationship between confidence regions and hypothesis testing, it is possible to use this technique to test if the δ_p's have changed and hence if the relationships between the measured values on the two instruments have changed.

An application of this statistical approach is in the understanding of why the EDF technique works poorly in some cases, for the extreme values of X(t) and Y(t). An examination of the limiting distribution of the density of δ_p^* for small values of p or for values of p close to 1.0 gives a clear indication of the reason that the EDF technique does not work well in the ends of the distribution when there are long tails. In This case the density functions will be very small and the standard deviation of the δ_p^* will be large. This may give estimates, δ_p^*, which may be very far from the true value ,δ_p .

It is also possible to use the limiting distribution of δ_p^* to estimate the sample sizes need to obtain a specified degree of accuracy for the estimates of δ_p. For example, in the case for the 53.7 GHz microwave channels on NOAA-10 and NOAA-12, it is necessary to have samples of the order of 500,000 to insure that with a probability of 0.99 that the estimated δ_p^* is within 0.10 degree C^0 of the true δ_p over a wide range of p values.

Many simulation of the technique have been carried out using microwave data from NOAA-10 and NOAA-12. This data is discrete as is the data from GOES. The simulations indicate that the theory , which assumes continuous data, gives reasonable results when applied to discrete data. For example, if theoretical confidence regions are constructed, and simulated confidence regions computed the results are similar. For a 78 percent theoretical confidence region about 85 percent of the regions actually contained the true values of the parameters. This is based on 1000 simulations. Note that these results are conservative. This is to be expected with the Bonferroni approach.

5. SUMMARY.

In this paper a standard technique has been examined from a different point of view. The EDF technique for inter-calibrating two detectors on the same instrument or two channels on different instruments is a statistical technique for estimating a function. It has large-sample properties which can be used to investigate the accuracy of this estimation procedure. It is possible to construct a confidence region for the value of the functions at a finite number of points in its range. It is also possible to test hypotheses about this function. Hence, using the EDF technique it is possible to test if the relationship between two detectors has changed. Once the problem is formulated in the proper way, it is possible to use standard techniques which can be found in many mid-level statistical texts. The technique requires, except for the large sample sizes , minimal assumptions. For the problem of adjusting two channels or two detectors it has many advantages.

6. ACKNOWLEDGMENTS

A portion of this work was supported by the TOVS Pathfinder Project and EPA grant CR 822636-01-0.

7.REFERENCES

1. B.K. Horn and R.J. Woodham, "Destriping LANDSAT MSS images by histogram modification," Comput. Graphics Image Process. 10:69-83 (1979)

2. M.P. Weinreb, R. Xie, J.H. Lienesh, and D.S Crosby, "Destriping GOES Images by Matching Empirical Distribution Functions," Remote Sens. Environ. 29:185-195(1989)

3. D.S Crosby, M.D. Goldberg, and W. Chung, "Inter-Satellite calibration using empirical distribution functions," Preprints of *Eighth Conference on Satellite Meteorology and Oceanography,* pp. 188-190, American Meteorological Society, Boston MA 1996.

4. C.R. Rao, *Linear Statistical Inference and its Applications,* John Wiley & Sons, Inc., New York, 1965.

5. J. Neter, W. Wasserman, M.K. Kutner, *Applied Linear Regression Models,* Second Edition, Irwin, Homewood, IL 1989.

Technique for visible calibration of future GOES sensors by solar viewing through a perforated screen

James C. Bremer and Guojun Si
Swales and Associates, Inc.
5050 Powder Mill Rd.
Beltsville, MD, 20705
E-mail: j_bremer@swales.com g_si@swales.com

ABSTRACT

Future GOES missions, augmented by the addition of very stable visible calibration, could measure long-term changes in the earth's albedo. Direct sunlight can be viewed through a plate perforated by small holes, attenuating the radiance at the center of the solar image by both blockage and diffraction. Attenuation by a factor of 50,000 produces a full-aperture, end-to-end calibration source with radiance comparable to a high-albedo target. Since its radiance depends only upon geometry, the perforated plate technique avoids the materials degradation problems inherent to calibration techniques based on reflection or refraction. Our analysis indicates that a plate with 50 μm holes spaced 4.9 mm apart in a hexagonal array has the potential to satisfy the requirement for a source stable to < 1% over a 5-year GOES mission. Some randomization of the hole positions may be desirable to suppress interference effects. We have made preliminary measurements of the large-scale angular structure of a simulated solar image viewed through a perforated screen, and have demonstrated their agreement with our theoretical predictions.

Keywords: calibration, visible, solar, albedo, radiance, GOES

1. VISIBLE ALBEDO MONITORING

A secondary, but nevertheless important, goal for augmentation of future GOES missions is to support global climatic change research. One requirement is to measure long-term changes in the earth's visible albedo to a precision of about 2%. The GOES mission has a number of attributes which make it well-suited to monitor long-term changes in the earth's visible albedo. Because the GOES satellites are in geostationary orbit, they view a large portion of the earth's surface. The "full-disk" of useful coverage extends approximately 60° from nadir in latitude and longitude. Each satellite in the GOES I-M series, including the GOES 8 and 9 satellites that are now operational, has an Imager and a Sounder. Channel 1 of the Imager has a central wavelength of 650 nm and a full-width, half-maximum (FWHM) of 200 nm. Its dynamic range extends from 0.1% to 100% albedo, with a resolution of 0.1%. It has a 1x8 detector array, in which each pixel subtends a 28 μrad square instantaneous-field-of-view (IFOV). Channel 19 of the Sounder has 4 detectors with a central wavelength of 700 nm and a circular IFOV 242 μrad in diameter.[1]

The presence of both the Imager and the Sounder on a single satellite provides an opportunity to cross-calibrate the two sensors by simultaneously viewing the same area on the earth's surface. There is a substantial area in the Pacific Ocean which is visible to both the GOES-East and GOES-West satellites, permitting their sensors to be cross-calibrated. Such cross-calibration has determined that the average throughput of the eight visible channels on the GOES-9 spacecraft is at least 15% greater than that of the corresponding channels on the GOES-8 spacecraft.[2] Furthermore, GOES is an on-going mission in which new satellites are checked out on orbit before old satellites are de-commissioned, providing a time interval for calibration transfer from the old sensors to the new ones.

Long-term visible albedo monitoring to a precision of 2% requires that changes in the throughput of the Imager's and Sounder's visible channels be measured to a precision < 1% over the nominal five-year lifetime of each satellite. The raw throughput of the visible channels is expected to decrease with time due to effects such as degradation of optical surfaces and radiation damage to detectors. A very stable calibration source is essential to quantify this decrease in throughput.

2. CALIBRATION SOURCE REQUIREMENTS

It is highly desirable to perform a full aperture, end-to-end calibration of the system using a known, stable source of visible light. The end-to-end requirement is driven by the fact that the scan mirror, at the front end of the optical train,

 0-8194-2200-2/96/$6.00

is the optical element most highly exposed to contamination, micro-meteoroids, and solar vacuum ultraviolet (VUV) radiation. The full-aperture requirement stems from the fact that contamination, coating delamination, or other degradations may not be uniformly distributed on the surface of a mirror. Also, only a full-aperture calibration can respond accurately to changes in vignetting if the telescope's alignment shifts.

The Imager and Sounder both use scan mirrors with an angle of incidence that varies from 40° to 50°. The reflectivity and polarization of the reflected optical beam tends to vary with incidence angle, particularly if the scan mirror becomes contaminated. Therefore, it is preferable to have a calibration source with minimal polarization, that can be viewed at several different scan mirror incidence angles within the field-of-view (FOV) of the sensor.

By viewing dark space, we can obtain an accurate measurement of the dark current associated with each visible channel. To determine the gain of each channel accurately, it is also necessary to measure its response to a known radiance, preferably near the top of its dynamic range, which extends from 0.1% to 100% albedo. A 100% albedo corresponds to an ideal Lambertian (diffuse) reflector illuminated by the sun at the normal angle of incidence. When viewed from earth, the sun subtends an angular diameter, θ, of 0.0093 radian, corresponding to a solid angle of 68×10^{-6} steradian. Therefore, 100% albedo is equivalent to direct sunlight attenuated by a factor of $\pi/(68 \times 10^{-6})$, or about 46,000. Although the main goal is to measure changes in albedo, it would also be beneficial to measure the absolute value of the albedo as accurately as possible.

A good radiometric calibration source should have as little angular structure as possible. Its radiance, as a function of angle, should have a broad, flat maximum that is large in comparison to the instantaneous-field-of view (IFOV) of a pixel. The variation in radiance should be << 1% (the desired accuracy of the measurement) over the solid angle used for calibration, allowing for both angular structure in the calibration source's radiance and uncertainty in the measurement geometry.

Any calibration subsystem which is deployed only for calibration and is stowed during normal data-taking operations must be relatively insensitive to positional and rotational changes. It is not practical to require that the mechanism which implements this deployment be reproducible to high levels of precision. It is also imperative that any such mechanism have a redundant retraction mechanism, to insure that a single failure does not lead to a loss of the sensor's data-taking capability. These requirements for a visible calibration source are summarized in Table 1.

Table 1. Requirements for long-term visible calibration source

OBJECTIVE	RATIONALE
1% Radiometric precision	•Track long-term albedo changes of 2%
End-to-end	•Scan mirror most exposed to degradation
Full aperture	•Throughput may vary over pupil •Optical surface degradation may not be uniform •Necessary to quantify changes due to alignment shifts
Multiple scan mirror incidence angles	•Throughput varies over 40°-50° incidence angle range
Minimal source polarization	•Scan mirror & beamsplitter cause polarization sensitivity
Maximum radiance near full albedo level (1/46,000 direct solar radiance)	•Cover dynamic range of visible channel (with dark current measurement)
Absolute radiance level	•Determine absolute albedo irradiance •Support sensor-to-sensor calibration transfer
Radiance variation < 1% over solid angle used for calibration	•Reduce sensitivity to geometric uncertainty •Simplify characterization of irradiance input to detectors
Redundant retraction mechanism	•Eliminate critical single-point failure

3. OVERVIEW OF POTENTIAL CALIBRATION TECHNIQUES

Either internal or external sources of visible light may be used for calibration. Internal calibration lamps may be used to perform periodic measurements of the short-term stability of detectors, but cannot practically generate a full-aperture beam of with the radiance level of a high-albedo target. In addition, calibration lamps are not stable enough to provide the required precision over the life of the mission.

The preferred approach is to use indirect solar flux for a full aperture, end-to-end calibration. The moon is a potential calibration target, since its radiance level lies within the dynamic range of GOES visible channels and since it subtends a solid angle much larger than the IFOV's of both sensors. Alternative approaches involve reducing the radiance of direct sunlight to a level within the dynamic range of the sensor, either by diffuse reflection or by transmission through holes in an opaque material. (Transmission through a refractive material, which is sensitive to both surface and bulk degradation of the refractive material, is not an attractive attenuation technique.)

Calibration techniques which use direct sunlight also have the potential to measure the absolute radiance level of the albedo. The total solar irradiance has been tracked by Active Cavity Radiometer Irradiance Monitor (ACRIM) sensors, starting in 1980 with the Solar Maximum Mission (SMM), and continuing in 1991 with the Upper Atmospheric Research Satellite (UARS), which is still operational. Launch of a third ACRIM is planned for December, 1998. The total irradiance is measured to an accuracy of about ±0.2% and a precision of about 0.005% by ACRIM sensors. The short-term variation in the visible solar radiance is about 0.3%.[3]

3.1. Lunar calibration

The moon is a far-field, extended target with stable surface reflectance properties. The lunar albedo values lie within the dynamic range of the GOES visible channels, with typical values of 0.07-0.13 and extreme values ranging from 0.05 to 0.18.[4] The edge of the lunar image is well-defined throughout the visible and infrared spectrum of the GOES sensors, and is now being used as a target to measure the registration errors among the channels of both the Imager and the Sounder. It could also be used to characterize other geometric parameters of each channel, such as the modulation transfer function (MTF) and the off-axis rejection.

The lunar image could potentially be used for radiometric calibration of the GOES sensors, but has some problems which limit its utility. The reflected lunar light is more difficult to characterize than direct solar radiation, and present models of the lunar radiance have errors of about 15%, making them inadequate to support the GOES calibration process. A dedicated observatory is now measuring the moon every night during the bright half of its cycle. The lunar surface is being imaged onto a CCD array, with an angular resolution of 21 μrad in several spectral bands from 0.4 μm to 1.0 μm. This array also measures stars of known magnitude and color to correct for atmospheric extinction, with an absolute accuracy goal of about 2%. Measurements with an angular resolution of 42 μrad are also planned for the spectral region from 1.0 μm to 2.5 μm. At least 4.5 years of observation will be required to characterize the variation of the lunar radiance with phase and libration.[5] When the completed lunar reflectivity maps become available, it will be necessary to derive the lunar radiance from a complex algorithm which compensates for sun/moon distance, solar incidence angle, the roughness of the lunar surface and its non-Lambertian reflectivity. The reflected radiation may be polarized up to 8%.[6] Also, the moon's visible radiance is several times smaller than that of a high albedo target, so data taken at the lunar radiance level must be extrapolated to calibrate the visible channels at the high end of their dynamic range. Due to this combination of factors, the use of the moon as a radiometric calibration source may not be straightforward, even when the lunar mapping effort has been completed.

3.2 Diffuse reflection

Some spaceborne earth-viewing sensors perform radiometric calibration with a diffuser plate, which attenuates direct sunlight by Lambertian scattering. When an ideal Lambertian reflector overfills the aperture of a sensor, then the radiance observed by that sensor is independent of the angle of observation. If the line-of-sight (LOS) to the sun is normal to the surface of the diffuser plate, then the radiance is also insensitive to first-order tilt. No surface is perfectly Lambertian, however. Characterization of and compensation for the non-ideal bi-directional reflectance distribution function (BRDF) of the surface, including polarization, is required. Also, a diffuser plate must usually be deployed in a geometry which exposes it to sun glints reflected off the body of the spacecraft as well as to direct sunlight.

The main problem with a diffuser plate is the progressive degradation of its diffusely reflective surface. Contaminants, either particulates or molecular films, can accumulate on the surface. In addition, many materials are unstable when exposed to VUV radiation. Some hydrocarbon contaminants are transparent in the visible and the near IR under normal conditions, but become strong absorbers after they react in the presence of VUV radiation. Even a molecular monolayer, less than a nanometer thick, can produce a significant change in the reflectivity of an optical surface.[7,8] Contaminants which exhibit in-band luminescence when exposed to UV radiation are another potential problem.

An integrating sphere may be used to create a uniform, diffuse source whose radiance level may be varied easily by changing the dimensions of its input aperture. In an integrating sphere, however, surface degradation is even more critical than it is for a diffuser plate, due to the fact that the average ray undergoes several diffuse reflections in the sphere. Furthermore, the diameter of the integrating sphere must be significantly larger than the 311 mm aperture of the Imager's and Sounder's telescopes, so an integrating sphere is not a practical option.

3.3. Perforated plate technique

Transmission through small holes in an opaque material can provide attenuation without being sensitive to the surface properties of that material. A plate perforated with small holes can be designed to produce nearly uniform illumination over the full aperture with greatly attenuated sunlight. If the holes are sufficiently small, then diffraction will broaden the solar image, attenuating the peak radiance by a factor greater than the ratio of the area of the holes to the area of the plate. Diffraction will also smear out any structure in the solar image due to sunspots, limb darkening, or flares. If the LOS to the sun is close to the normal to the plate and the diameter of the holes is many times greater than the wavelength, then the plate will not induce any significant polarization.

Since the perforated plate is used in transmission, its utility is restricted to windows of availability during which the sun lies within the 21° by 23° rectangular FOV of the sensor, centered about nadir. If the spacecraft's attitude is maintained, then solar calibration will only be possible during daily time intervals of 1.5 hours, around local midnight, during the seasons of eclipses: periods of 52 days around each equinox. The interruption of normal data-taking to perform calibration will have minimal impact near local midnight, since visible images can not be taken and since the IR frames are restricted by solar avoidance constraints. The 131 day gaps between periods of availability are undesirable, but it is still possible to measure the long-term changes in the throughput with the perforated plate calibration, particularly if these measurements are augmented by lunar calibration and by short-term stability measurements.

The optimal geometry for calibration is one in which the LOS to the sun is about 9.5°-10° from nadir: far enough from the earth's limb (8.7° off-nadir) to avoid atmospheric extinction, yet close enough that only a narrow, crescent shaped "new earth" is both illuminated by the sun and visible to the spacecraft. In this viewing geometry, the earthshine which reaches a spacecraft at geostationary altitude is less than 0.01% of the direct sunlight. It is possible to configure a perforated plate with a redundant retraction mechanism which covers the outer aperture of the sunshades of both the Imager and Sounder during calibration. In this geometry, the outer surface of the plate is not exposed to sun glints from the body of the spacecraft and the only light which enters the either sensor's optical cavity is that transmitted through the holes in the plate. Therefore, the effects of indirect sunlight should be far lower for a perforated plate than for a diffuser plate.

A perforated plate is a promising method for calibration of long-term changes in the throughput of the channels on the GOES sensors, and the visible and near infrared channels on spaceborne sensors, in general. To determine the practicality of this approach, it is necessary to derive quantitative values for all significant plate parameters, to demonstrate theoretically that a plate constructed with these parameters is capable of satisfying the requirements listed in Table 1. Then, it is necessary to fabricate a plate with the specified parameters and verify its performance experimentally.

4. PERFORATED PLATE ANALYSIS

A trade analysis is required to obtain the appropriate values of the diameter of the holes, D, and the separation between adjacent holes, S. The configuration of holes in an array is also a trade issue. A periodic array has the advantage of providing a uniform level of illumination, but produces an interference pattern which may be partially suppressed by some type of randomization in the configuration of the array of holes.

The Imager's Channel 1 defines the baseline for this analysis. It has a central wavelength of λ = 650 nm, a FWHM of 200 nm, a minimum signal-to-noise ratio (SNR) of 150 at full albedo, and a 1x8 array which subtends 28x244 μrad. The solar radiance as a function of angle is approximated as constant inside a disk of diameter θ = 0.0093, and zero outside this diameter. The required attenuation is a factor of 50,000 (throughput of $2x10^{-5}$), which corresponds to 92% albedo.

4.1 Uniform full-aperture illumination

Any pair of values for D and S must yield a total throughput of $2x10^{-5}$ at the peak of the radiance distribution. A single hole, 1.4 mm in diameter, could provide the required level of attenuation for the 311 mm Imager and Sounder apertures, but could not approach satisfying the full-aperture requirement for any practical separation between the hole and the scan mirror, Z. It is necessary to have an array of sub-millimeter holes in the perforated plate. Assuming that the value of D is small enough so that diffraction is the dominant cause of solar image broadening, we may use the Rayleigh criterion to find a maximum value of S for which the individual holes will be unresolved at the mirror:

$$S < (1.22\lambda/D)Z \quad (1)$$

It would be beneficial to deploy the perforated plate on the Imager's sunshade, which would not only minimize its size and weight, but would also avoid the stray light problems inherent to an external boom. The maximum distance above the optical port where the perforated plate can be deployed without interfering with an antenna results in a value of Z = 600 mm for the Imager.[9] Eq. (1) leads a constraint of the product of D and S:

$$DS < 0.48 \text{ mm}^2 \quad (2)$$

The diffraction of light by a hole increases as a function of the ratio of the wavelength of the light to the diameter of the hole. Thus, the solar image will appear "blue" in its center and "red" around its circumference when viewed through a plate containing small holes. This effect will be more pronounced for smaller values of D.

4.2 Uniform high-albedo radiance

The peak of the solar radiance distribution, as viewed through the perforated plate, must be broad and flat, so two conditions must be satisfied. First, the radiance as a function of angle due to a single pinhole of diameter D must have a maximum in which the radiance is constant to << 1% over a solid angle greater than the IFOV of the detector array. It is also necessary that any modulation of the detected radiance due to interference among the holes of the array be << 1%. (Scanning the array over the center of the solar image may be required to average radiance variations due to interference.) The throughput at the center of the solar radiance distribution produced by a single pinhole is the product of two factors: a geometric throughput, τ_g, and a diffraction throughput, τ_d. In this trade, we have assumed that the holes are oriented in a regular hexagonal array, so the plate area per hole is $0.866S^2$. The area of a hole of diameter D is $(\pi/4)D^2$, so τ_g becomes:

$$\tau_g = (\pi D^2/4)/(0.866S^2) = 0.907(D/S)^2. \quad (3)$$

τ_d is the ratio of the radiance at the center of the actual solar image to the radiance which would be present in the absence of diffraction. The solar image viewed through the pinhole is the convolution of the geometric solar disk (without diffraction) with the Airy diffraction pattern of the pinhole. To determine τ_d, the convolution is normalized with respect to the geometric solar disk.

Fig 1 shows the convolutions of the solar disk with the Airy diffraction patterns produced at a wavelength of λ = 650 nm by pinhole diameters of 20, 50, 100, 200, and 500 μm. Table 2 presents the results of this convolution analysis within one mrad of the center of the image. The top numbers in the matrix are normalized to the unity with respect to the geometric solar disk; the numbers in parentheses are normalized with respect to the radiance at the center of the image for the pinhole diameter of that row in the matrix, i.e., that row's value of τ_d. The convolutions of the 20 and 50 μm pinholes are dominated by diffraction, closely resembling Airy patterns. The convolutions of the 200 and 500 μm pinholes are dominated by the geometry of the 9.3 mrad diameter solar image. Note that the radiance has a minimum at the center of the image formed by the 200 μm pinhole, and that it increases between 750 μrad and 1000 μrad off-center in the image formed by the 500 μm pinhole. This behavior is caused by the side-lobe structure of the Airy diffraction pattern, and is not

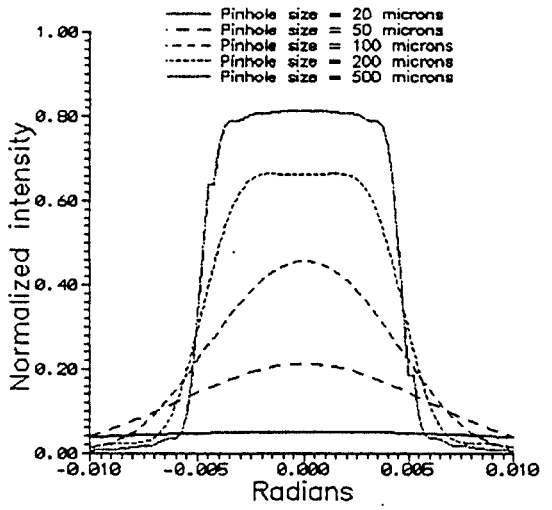

Fig.1 Normalized radiance at λ = 650 nm as a function of angle for several pinhole diameters

anticipated for a broad spectral band, such as the Imager's Band 1. The convolution of the 100 μm pinhole has an intermediate shape that is undesirable because the solar image has a peak with a sharp fall-off in its central region.

Since the desired accuracy is << 1%, and the detector array subtends 28x244 μrad, it is reasonable to require that the radiance vary by no more than 0.1% over a solid angle 500 μrad in diameter. This requirement can be met either by an array of closely-spaced small holes (D = 20 or 50 μm) or by a more widely spaced array of large holes (D = 200 or 500 μm), but not by an array of 100 μm holes.

Values of D and S that are large enough to produce a geometric solar image with the required radiance level violate Eq (2), i.e., they can not illuminate the scan mirror uniformly. Other considerations make in beneficial to avoid small values of D and S. Therefore, a hole diameter of D = 50 μm appears to be a reasonable choice. The value of τ_d is 0.2123 for a 50 μm hole. (Refer to Table 2) For a throughput of $2x10^{-5}$, τ_g = $9.7x10^{-5}$, so Eq (3) leads to a spacing of S = 4.9 mm between adjacent holes. The product DS equals 0.245 mm^2, satisfying Eq (2). The following analysis demonstrates that this pair of values, D = 50 μm and S = 4.9 mm, satisfies the remaining requirements. Approximately 3650 holes are required to cover the Imager's aperture (311 mm in diameter).

Table 2. Normalized radiance at λ = 650 nm for several pinhole diameters as a function of angle from image center

ANGLE FROM IMAGE CENTER (in μrad) ⇒ PINHOLE DIAMETER (in μm) ⇓	0 [τ_d]	250	500	750	1000
20	0.050793 (1.0000)	0.050784 (0.9998)	0.050756 (0.9993)	0.050710 (0.9983)	0.050645 (0.9971)
50	0.21231 (1.0000)	0.21211 (0.9991)	0.21149 (0.9961)	0.21048 (0.9914)	0.20906 (0.9847)
100	0.45521 (1.0000)	0.45451 (0.9985)	0.45239 (0.9938)	0.44886 (0.9861)	0.44395 (0.9753)
200	0.66224 (1.0000)	0.66226 (1.0000)	0.66237 (1.0002)	0.66260 (1.0005)	0.66298 (1.0011)
500	0.81200 (1.0000)	0.81163 (0.9995)	0.81103 (0.9988)	0.81095 (0.9987)	0.81110 (0.9989)

4.3 Interference

When the sun is viewed through multiple holes, interference must be considered. Even though the sun is an incoherent source of light, closely-space holes illuminated by sunlight can produce interference effects. This problem is aggravated in narrow spectral bands. The interference effect is suppressed when the spacing between adjacent lines of holes (0.866S in the hexagonal array) becomes much greater than the spatial coherence interval of the source, defined as λ/θ.[10]

$$0.866S >> \lambda/\theta \quad (4)$$

For Band 1 of the Imager, the solar coherence interval is 70 μm, leading to the requirement that the separation S >> 81 μm. The proposed value of S = 4.9 mm, 60 times greater, appears to be satisfactory.

The FWHM of 200 nm also helps to suppress interference effects, restricting modulation of the total in-band irradiance to the first few diffraction orders. To obtain a quantitative estimate of the angular extent of structure in the diffraction pattern, we may approximate the spectral dependence of the channel's throughput by a Gaussian function, for which a FWHM of 200 nm corresponds to a standard deviation, σ, of 85 nm. Two Gaussian functions which are separated by less than 2σ merge into a smooth curve with a single maximum. The overlap of adjacent orders will wipe out structure in the diffraction pattern whenever N, the order of the diffraction maximum, satisfies the inequality:

$$N > \lambda/2\sigma \tag{5}$$

Modulation at the center of the solar image should be suppressed if the interference order at the circumference of the solar disk is large enough to produce overlap. As stated above, the angular separation between adjacent diffraction orders is $\lambda/(0.866S)$. The interference order, N, on the circumference of the solar disk is:

$$N = (\theta/2)/(\lambda/0.866S) = 0.433S\theta/\lambda \tag{6}$$

Combining Eqs. (5) and (6), we obtain a constraint on the minimum value of S:

$$S > 1.155\lambda^2/\theta\sigma \tag{7}$$

Eq. (5) is satisfied by the 4th and higher interference orders, and Eq. (7) is satisfied whenever S > 0.62 mm.

4.4 Array Randomization

To minimize interference effects, it is desirable to randomize the spacing of the holes so that they do not form a periodic array. A pseudo-random array of holes may be able to minimize both the interference effects inherent in a perfectly ordered array and the fluctuations in illumination inherent in a perfectly random array. Since the proposed values of D and S exceed the requirements of Eq. (2) by a factor of 2, there is a comfortable margin, for deviation from a periodic array of holes. For example, the plate could be configured in a grid of hexagonal cells, with each cell containing one hole located at a random point within the hexagon. This pattern will exhibit some interference maxima, but the modulation of intensity will be much lower than that produced by an array of uniformly spaced points.

Due to the variable angle of incident sunlight and to any non-uniformities in the deployment mechanism of the perforated plate, the portion of the plate's cross-section which lies in front of the aperture will probably vary. Since the holes in the pseudo-random array are not perfectly ordered, there will be some variability from measurement to measurement in the total number of holes through which the sun is viewed. To obtain a pessimistic estimate of the uncertainty in the irradiance, we may use a geometric model and find the standard deviation in the number of holes within the Imager's aperture. The diameter of the aperture is 311 mm, so its area is 7.60×10^4 mm^2, while each hole occupies a hexagon of area 20.8 mm^2. The average number of holes in this area is 3652. Because each hole is situated in a random position within its hexagonal cell, the number of holes in front of the aperture will not remain fixed if the plate is translated. The presence or absence of a hole in a cell along the circumference of the aperture may be treated as a random event. If there are n hexagonal cells along the circumference and if one-half of them contain holes, then the average of holes is n/2 and $n^{1/2}/2$ is the standard deviation in the number of holes.[11] An aperture 311 mm in diameter has a circumference of 977 mm. Since the grid spacing is 4.9 mm, approximately n = 199 hexagonal cells will lie on the circumference. Therefore, the average number of holes on the circumference is 100 and the standard deviation is 7, or 0.19% of the total number of holes in the aperture.

4.5 Radiometric precision

The SNR of the Imager's Channel 1 is specified at > 150/1 for a full-albedo target. Its noise is dominated by Gaussian or "white" noise, which is uncorrelated from pixel to pixel. From Table 2, we find that radiance of a single 50 μm pinhole is nearly uniform (within 0.1%) over an angle of 500 μrad which corresponds to 18 of the 28 μm pixels. By scanning the center of the solar image and averaging 18 pixels, we obtain a SNR of $150(18)^{1/2} = 636/1$. This SNR produces

an error of 0.16% in the value of the solar radiance. The scanning process also averages any residual angular variation in the radiance due to interference. Further reduction in error due to interference is possible by performing multiple scans of the solar image. The sun angle precesses at a rate of 2π radians in 24 hrs, which equals 72 μrad/sec; the angular separation between interference fringes is $\lambda/(0.866S) = 153$ μrad. Therefore, scans of the solar image performed several seconds apart will see independent interference patterns, and averaging several scans will further reduce the noise due to interference.

4.6 Fabrication and alignment

The value of τ_g, the geometric ratio of the area of the holes to the total plate area, is insensitive to uniform thermal expansion of the plate. The value of τ_d, the diffractive factor in the throughput, equals 0.2123 at D = 50 μm and increases with increasing hole diameter. Interpolation among the values of τ_d at D = 20, 50, and 100 μm, leads to an estimate of $d(\tau_d)/dD \approx 0.0051\ \mu m^{-1}$. (Refer to Table 2.) If α is the coefficient of thermal expansion of the plate, then a temperature excursion, ΔT, changes the hole's diameter by $D\alpha\Delta T$, resulting in a fractional change in diffractive throughput, $\Delta\tau_d/\tau_d$, of:

$$\Delta\tau_d/\tau_d = (d\tau_d/dD)(D\alpha\Delta T)/\tau_d = 1.20\alpha\Delta T \tag{8}$$

Thermal expansion should not be a significant source of error. For example, a plate made of aluminum has a relatively high coefficient of thermal expansion, $\alpha = 25\times10^{-6}/°C$. Even if its temperature changes by $\Delta T = 40°C$, then Eq. (8) yields $\Delta\tau_d/\tau_d = 0.12\%$.

The plate is integrated into the sunshade with its normal pointing toward nadir. As mentioned before, the LOS to the sun must lie more than 8.7° away from nadir to avoid the earth's limb. The typical angle between the solar beam and the normal to the plate is $\phi = 10°$, with various azimuth angles. The holes in the perforated plate should be tapered, with their small diameters on the sunward side of the plate. The half angle of the tapered holes, β, should be large enough to guarantee that their apertures are uniquely defined by these smaller diameters. To satisfy this requirement, β must exceed the sum of the maximum off-axis LOS to the sun (including an alignment tolerance, $\Delta\phi$), $\phi+\Delta\phi$, the geometric half-angle of the sun, $\theta/2$, and the half-angle of the Airy disk, $1.22\lambda/D$:

$$\beta > \phi + \Delta\phi + \theta/2 + 1.22\lambda/D \tag{9}$$

Assuming a relatively lax alignment tolerance of $\Delta\phi = 0.5° = 0.00873$ radian, and the previously-define values of these parameters, we obtain $\beta > 0.204$ radian (11.7°).

The solar beam that passes through each tapered hole has an elliptical cross-section, with area proportional to $\cos(\phi)$. The density of holes in the beam is inversely proportional to $\cos(\phi)$, so the value of τ_g is independent of ϕ. The value of τ_d decreases with increasing ϕ. The uncertainty in the foreshortened dimension of the holes is $-D\sin\phi\Delta\phi$. Since only one dimension of the holes is foreshortened, we may assume that the change in τ_d produced by a change in the minor axis of the hole equals $0.5[d(\tau_d)/dD]$, so that:

$$\Delta\tau_d/\tau_d = 0.5(d\tau_d/dD)(-D\sin\phi\Delta\phi)/\tau_d = -0.60\sin\phi\Delta\phi \tag{10}$$

Substitution of previously-defined parameters into Eq. (10) yields $\Delta\tau_d/\tau_d = 0.09\%$.

Tapered holes 50 μm in diameter are well within the state-of-the art. Lax tolerances are permissible on the diameters of individual holes and on their approximations to circular cross-sections. However, they must have good geometric stability, a minimal amount of kerf, and be free of any burrs that could become detached during the mission. Laser drilling is probably the best fabrication method. Since the perforated plate introduces diffraction into the solar image, it must be oversized with respect to the aperture to avoid fall-off of intensity at the edge of the beam. It should be straightforward to implement a redundant retraction mechanism for the plate, and to blacken the side of the plate that faces the scan mirror.

4.7 Contamination

To maintain stable calibration, D must be much larger than any molecular films or particulates which are likely to accumulate on the holes during the lifetime of the mission. It is possible to quantify the maximum allowable thickness of

opaque contaminant film, Δt, on the holes that will change the throughput by -0.2%. A contaminant build-up of thickness, Δt, will decrease the diameter of the holes by $\Delta D = -2\Delta t$. Since the total throughput is equal to $\tau_g\tau_d$, the requirement that the fractional decrease in throughput due to a change in t be < 0.2% may be written as:

$$[(1/\tau_g)d\tau_g/dD + (1/\tau_d)d\tau_d/dD](2\Delta t) < 0.002 \quad (11)$$

The fractional change in τ_g follows directly from geometry. The fractional change in τ_d was derived in Section 4.6. For circles of diameter D = 50 μm:

$$(1/\tau_g)d\tau_g/dD = 2/D = 0.04\ \mu m^{-1} \quad (12)$$

$$(1/\tau_d)d\tau_d/dD = 0.024\ \mu m^{-1} \quad (13)$$

Combining Eqs. (11), (12), and (13), we obtain:

$$\Delta t < 0.001/(0.064\ \mu m^{-1}) = 0.0156\ \mu m \quad (14)$$

The single most important advantage of a perforated plate over a diffuser plate is the perforated plate's relative insensitivity to surface degradations. For example, a monolayer of hydrocarbon contaminant film, $<10^{-3}$ μm in thickness, can decrease the reflectivity of a surface by much more than 0.2%, particularly if it is chemically altered by VUV radiation. On the other hand, a monolayer will have a negligible effect upon a hole 50 μm in diameter. Likewise, VUV radiation, atomic oxygen, and charged particle bombardment may effect the reflectivity of a surface, but will not change the area of a hole. A micrometeoroid bombardment will degrade a perforated plate only if creates a hole in the plate or causes significant warpage. It is necessary, of course, to use reasonable care in avoiding contamination of the plate. The plate should be handled in a clean room environment on the ground, and should be stowed when not in use in space.

4.8 Preliminary Radiometric Error Budget

Table 3. presents a preliminary error budget for the radiometric precision of the perforated plate on a single scan through the sun. The third column of Table 3 refers to the preceding sections of this paper in which the error estimates were derived. Since the individual errors tend to originate from independent sources, they are assumed to be uncorrelated and the total error estimate is their root-sum-square. Lax tolerances and pessimistic values have been assumed. The offset produced by the relative enhancement of short wavelength irradiance at the center of the image remains constant over the life of the mission, so it is not been included in the error budget for measurement precision. Interference effects have not yet been quantified, and are assigned an error of 0.2%.

Even with these moderately pessimistic assumptions, the predicted worst-case error in a single scan is only 0.51%: less than twice the intrinsic limit of 0.3% due to short term variance in the solar flux. Since errors due to interference, the pseudo-random hole pattern, and SNR will be random from scan to scan, they can be reduced by averaging measurements. The precision of the perforated plate technique is well within the scientific requirements for long term stability monitoring, and represents a significant improvement over the performance of other candidate calibration techniques.

Table 3. Radiometric precision of the perforated plate technique: Preliminary error budget

ERROR SOURCE	ESTIMATED MAGNITUDE	REFERENCE SECTION
Solar flux variance	0.30%	3.
Earthshine	0.01%	3.3
Radiance vs. angle	0.10%	4.2
Interference	0.20%	4.2-4.3
Pseudo-random hole pattern	0.19%	4.4
SNR	0.16%	4.5
Thermal expansion (diffraction)	0.12%	4.6
Alignment	0.09%	4.6
Contamination	0.20%	4.7
RSS	0.51%	—

5. EXPERIMENTAL INVESTIGATION

We performed some preliminary experiments to characterize a simulated solar image as viewed through an array of small holes. We used a commercially-available sieve, a sheet metal screen with holes of diameter D = 22 μm in a hexagonal array at a spacing of S = 200 μm between adjacent holes. From Eq. (3), τ_g = 0.0110; interpolation from Table 2 yields, τ_d = 0.0616. Thus, the theoretical prediction for the total throughput at the center of the solar disk is 6.8×10^{-4}, 34 times greater than the baseline for GOES, but adequate for a proof-of-principle experiment.

Fig. 2 illustrates the setup for the perforated screen experiment. We illuminated the perforated screen with a 150 Watt xenon arc lamp that was nearly collimated to simulate the 0.0093 mrad solar disk. A filter holder behind the perforated screen held bandpass filters at different central wavelengths. The image of the source generated by the perforated screen was focused by a convex lens (focal length 310mm, f/6.1) onto the silicon detector. There was a 40 μm pinhole in front of the silicon detector, corresponding to a 130 μrad circular IFOV. The detector was attached to a linear translation stage which scanned continuously across the focal plane of the lens, under the control of a stepping motor. A map of radiance as a function of field angle was recorded by the computer.

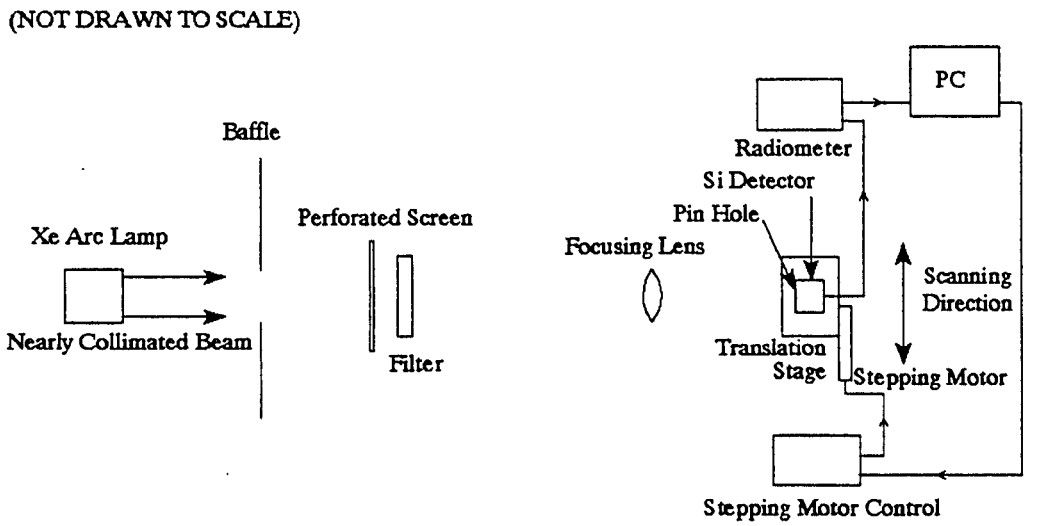

Fig. 2 Perforated Screen Experiment Setup

We measured the radiance as a function of angle in the focal plane using three narrow bandpass filters with central wavelengths of 482nm, 575nm, and 670nm and FWHM's of 8-10 nm. We also performed a wide bandwidth measurement, using the silicon detector without a spectral filter. We found short-term fluctuations of about 2% in our detector's output when scanning the solar image through the narrow-band filters and about 1% when no filter was used. Due to the averaging effects of the scan motion, we are unable to reconstruct the angular structure of the image at the resolution level of the 130 μrad IFOV of our experiment. We were also unable to determine what fractions of this fluctuation were due optical interference and to electronic noise. We calculated the convolution integrals for D = 22 μm and the three filter wavelengths, using the procedure discussed in Section 4.2. We were able to verify that the large-scale structure of radiance as a function of angle is predicted correctly by the convolution analysis. Table 4. compares the experimental and theoretical values of the widths of the radiance profiles at 85% of maximum.

Table 4. Comparison of experimental and theoretical radiance profile widths at 85% maximum

WAVELENGTH (in nm)	482	575	670
Experimental Result	10.6 mrad	11.8 mrad	15.0 mrad
Theoretical calculation	11.0 mrad	13.0 mrad	15.0 mrad

We have also observed the sun through the perforated screen, with each of the three narrow band filters discussed above, and with a neutral density filter. When viewed by eye through the perforated screen and a broadband neutral density filter, no interference structure is visible in the center of the solar disk. There are some colored rings with a slight hexagonal structure on the edge of the solar image, well outside the 9.3 mrad disk. When the sun is viewed through the narrow bandpass filters, a hexagonal interference pattern is clearly present, even in the center of its image. Table 5. compares the combination of the perforated screen with S = 200 μm and three narrow bandpass filters used in the experiment with the proposed perforated plate with S = 4900 μm in conjunction with the wavelength and bandpass of the Imager's Channel 1. The value of S is about three times greater than the coherence interval for the experimental parameters, but about 60 times greater for the proposed GOES calibration. [Refer to Eq. (4)] There is an extreme difference in the overlap of diffraction orders. The experimental parameters fail to satisfy Eq. (7) by factors greater than 100, but the proposed Channel 1 calibration satisfies it with a factor of 7.7 margin.

Table 5. Comparison of experiment and proposed GOES calibration with interference constraints (all dimensions in μm)

λ	FWHM	σ	S	Coherence interval S >>	Order overlap S >
0.482	0.010	0.00425	200	60	6790
0.575	0.008	0.0034	200	71	12100
0.670	0.010	0.00425	200	83	13100
0.650	0.200	0.085	4900	81	620

It appears that values of S about of 3 times greater than the coherence interval is insufficient to suppress the interference pattern when the diffraction orders do not overlap. Further experimentation will be required to quantify the interference patterns as functions of the parameters D, S, λ, and Δλ, for a regular hexagonal array, as well as to investigate the suppression of interference by randomization of the hole pattern.

6. CONCLUSIONS

Long term changes in the throughput of GOES-Next visible channels should be monitored by full aperture, end-to-end calibration. Lunar calibration should play a role in this process, due to its minimal requirement for spaceborne hardware, minimal impact on spacecraft operations, and frequent windows of availability. Characterization of the lunar albedo, polarization of the lunar radiation, and the low level of the lunar albedo all limit the precision of lunar calibration, however. A high intensity source of indirect sunlight should also be used.

There are two potential techniques for reducing the radiance of the sun to an appropriate level: a reflective diffuser plate or a transmissive perforated plate. The perforated plate technique has several significant advantages over the diffuser plate technique, and should be studied further. The most obvious advantage is that the transmissivity of a perforated plate depends upon geometry only, and is independent of surface conditions, while the reflectivity of a diffuser plate is subject to degrade when exposed to the space environment. The primary problems of the perforated plate are interference and diffraction. Excessive structure in the interference pattern would make the plate too difficult to characterize. Factors that tend to wipe out this structure include the randomization of the hole locations within the hexagonal grid, the overlap of higher-order diffraction peaks due to the broad bandwidth of Channel 1, and the convolution of the diffraction pattern over the 9.3 mrad diameter solar disk. When viewed through the perforated plate, the solar image will be blurred by diffraction and will be

biased toward short wavelengths in its center and toward long wavelengths around its circumference. The wavelength-dependent blurring of the solar image should remain stable throughout the mission and be straightforward to characterize.

The perforated plate calibration will be restricted to two windows of availability per year, around the equinoxes. These solar calibration measurements, in conjunction with the other, more frequent calibration measurements, should improve the precision to which the Imager's throughput can be characterized over the lifetime of the mission. The perforated plate approach has the potential to achieve a precision of better than 1% between beginning and end of life, which is better than any alternative approach can achieve. The feasibility of the perforated plate approach appears promising, based upon this preliminary investigation.

Further analysis is required to optimize the plate parameters and to address fabrication and deployment issues. Plans are now being made to fabricate several prototype perforated plates and to map their irradiance profiles with a telescope capable of 10-20 μrad angular resolution and a step-and-stare scanner to translate the detector across the focal plane.

7. ACKNOWLEDGEMENTS

The initial concept study and the preliminary laboratory measurements were performed under contract NAS-30375 for NASA's Goddard Space Flight Center (GSFC). Mr. Les Thompson was the technical monitor for the study and Dr. James Butler was the technical monitor for the preliminary laboratory measurements. Investigation of this concept is continuing under contract NAS5-32650. The authors are pleased to acknowledge the assistance of Dr. Qian Gong of Swales & Associates, Inc., who performed the convolution integrals. Messrs. James Heaney, and Sanford Hinkal, and Dr. Del Jenstrom of GSFC, and Ms. Jeannette Baucom and Dr. Harry Farthing of Swales and Associates, Inc. also provided information and assistance.

8. REFERENCES

1. GOES I-M Data Book, Space Systems/Loral, Palo Alto, CA, pp. 19-56.

2. Weinreb, M., NOAA/NESDIS, D. Chesters, NASA/GSFC, private communications.

3. Solar Influences on Global Change, National Academy of Sciences, National Academy Press, pp. 113-114, 1994.

4. Minnaert, M., "Chapter 6, Photometry of the Moon", in Planets and Satellites, edited by G. P. Kuiper and B. M. Middlehurst, University of Chicago Press, Chicago, pp. 213-247.

5. Wildey, R. L. and H.H. Kiefer, "A New Facility for Absolute Photometric Imaging of the Moon", Bulletin of the American Astronomical Society, 25, p. 1089, 1993.

6. Kieffer, H., and R. Wildey, "Use of the Moon for Calibration", Committee on Earth Observation Satellites Cal/Val Newsletter, April 1995.

7. Hass, G., W. R. Hunter, "Laboratory Experiments to Study Surface Contamination and Degradation of Optical Coatings and Materials in Simulated Space Environments," Applied Optics, Vol. 9, No. 9, pp. 2101-10, 1970.

8. Heaney, J. B., H. Herzig, and J. F. Ozantowski, "Auger Spectroscopic Examination of MgF_2-Coated Al Mirrors Before and After UV Irradiation," Applied Optics, Vol. 16, No. 7, pp. 1886-9, 1977.

9. ITT personnel, private communication, ITT Aerospace and Communications Division, Ft. Wayne, IN,

10. Reynolds, G. O., J. B. DeVellis, G. B. Parrent, Jr., and B. J. Thompson, Physical Optics Notebook, Tutorials in Fourier Optics, SPIE Optical Engineering Press, Bellingham, WA, pp 71-93, 1989.

11. Kittel, C. and H. Kroemer, Thermal Physics, 2nd Ed., W. H. Freeman and Co., New York, pp 18-23, 1980.

Sounder bias correction of the east-west radiance gradient

Timothy J. Schmit

NOAA National Environmental Satellite Data and Information Service
Office of Research and Application
Advanced Satellite Products Team
1225 West Dayton Street, Madison WI 53706

ABSTRACT

As reported by Weinreb et. al. (1996)[1], both the imager and sounder exhibit an east-west radiance gradient due to reflection off the coating of the scan mirrors. While this problem was basically eliminated with ground processing in the imagers as of the spring and summer of 1995, the sounder instruments were corrected on March 26, 1996 and June 19, 1996 for the GOES-9 and GOES-8, respectively. This paper will investigate the process of minimizing the sounder east-west radiance variation by a radiance bias adjustment (shrinkage estimation) prior to the use of radiances in product generation. The sounder ground-corrected data show that the radiance bias adjustment does not change as much as a function of longitude, and that the biases between those observed from the sounder and those calculated from the 'truth' profiles are reduced. The artificial east-west gradient across the earth is difficult to observe due to several affects, including clouds, land/sea differences, topography and natural variations. Reducing/eliminating the artificial east-west gradient helps the retrieving of atmospheric parameters, like moisture. The second part of this paper presents the verification of satellite derived moisture profiles. Even before the ground correction of the east-west gradient, atmospheric moisture retrievals have been shown to improve upon the 'first guess' profile.

Keywords: infrared calibration, radiance tuning, atmospheric retrievals, retrieval verification

2. INTRODUCTION TO GOES SOUNDERS

With the launch of sounders on the GOES-8 and -9 satellites, operational hourly atmospheric temperature/moisture profiles have become a reality. This new set of sounders offer many advantages over the earlier system (Menzel and Purdom, 1994)[2] including more frequent viewing, more continuous viewing, additional channels, channels with better signal-to-noise and a more complete calibration. A disadvantage is the artificial east-west gradient introduced due to the scan mirror coating (Weinreb et. al., 1996)[1]. A radiance bias adjustment is used in the GOES algorithm to correct uncertainties associated with calibration and forward modeling. This correction is usually referred to as radiance "tuning". Some form of tuning has been applied with all successful physical retrieval schemes in the past. (An evaluation of the result of not including tuning is given in Eyre, 1989)[3]. Invariably, tuning involves a sample of collocated measured and calculated radiances; the calculated radiances are generated from some "true" profile of temperature and moisture of the atmosphere. Early work defined a mean (bias) difference and an exponential adjustment to the transmittance function for non-linear effects (Smith et al., 1974[4], Weinreb, 1979[5], Susskind, 1983[6]). More recent methods have recognized that tuning requirements

 0-8194-2200-2/96/$6.00

are airmass dependent, and use regression techniques whereby the measurements themselves are used to specify the tuning adjustments (Eyre, 1992)[7]. Most recently, some variant of "ridge" regression (e.g. McMillin et al., 1989[8], Fleming et al., 1991[9]) has been used to ensure that each band be the principal predictor of itself. Without such constraint the naturally occurring vertical correlation of atmospheric structure will lead to illogical results whereby a measurement emanating from the stratosphere is the dominant predictor of a measurement representative of near surface layers. Also, coefficients with large magnitude and alternating sign can result, and these serve to amplify noise.

3. EAST-WEST RADIANCE GRADIENT

The scan mirror induced east-west radiance gradient is often masked by clouds and surface variations. The gradient is most readily seen in the longest wave sounder channel, which peaks above the clouds. Figure 1a is an example of GOES-8 channel 1 (14.7 microns) contrast-stretched image before the east-west correction was implemented. The natural variation from east-to-west across the image is fairly small, but a gradient can be seen. A difference of 0.4K exists between the east and west sides of the image. The gradient was also evident in preceding days (not shown). Figure 1b is the same channel 1 hour later, after the ground processing was initiated to remove the east-west gradient. Two effects can be seen. First, the overall image became warmer (darker). The mean brightness temperature increased 0.7K degrees. By looking at the preceding and subsequent days, its possible to infer that 0.5K of the increase was solely due to the calibration algorithm enhancement). This warming reduces the difference of measured and calculated radiances (i.e. the warming is an improvement). The second affect is a reduction in the east-west gradient. Now the east and west regions have approximately equal temperatures. To bolster the argument that this is not an anomaly, the subsequent days also show relatively equal temperature values.

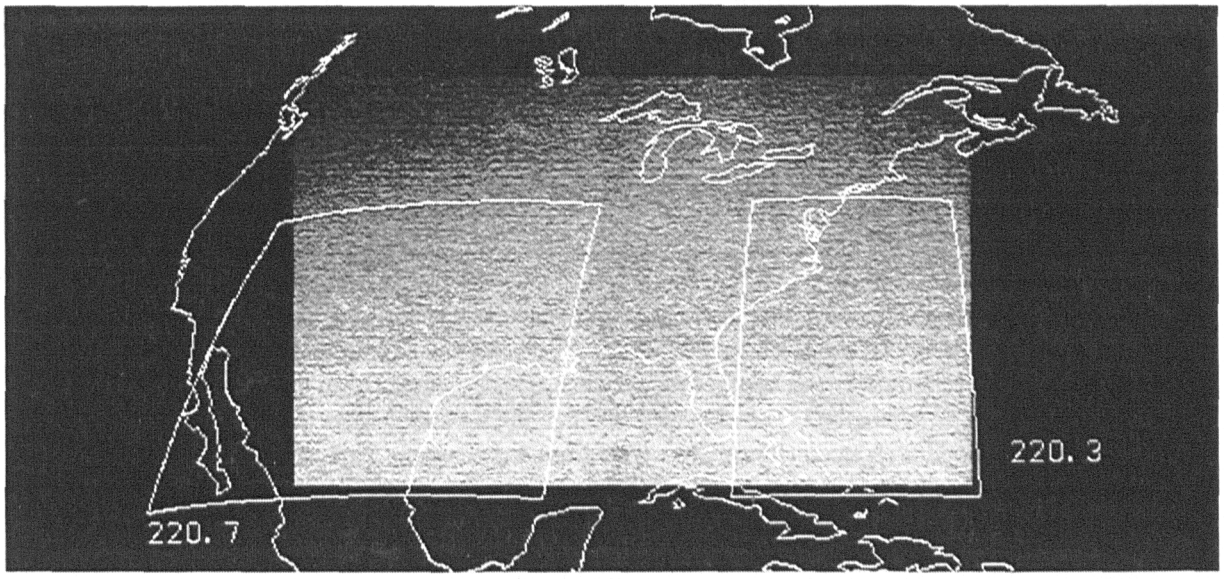

Figure 1a. Before the east-west correction. GOES-8 Sounder. June 19, 1996. 11:46 UTC. Enhanced channel 1.

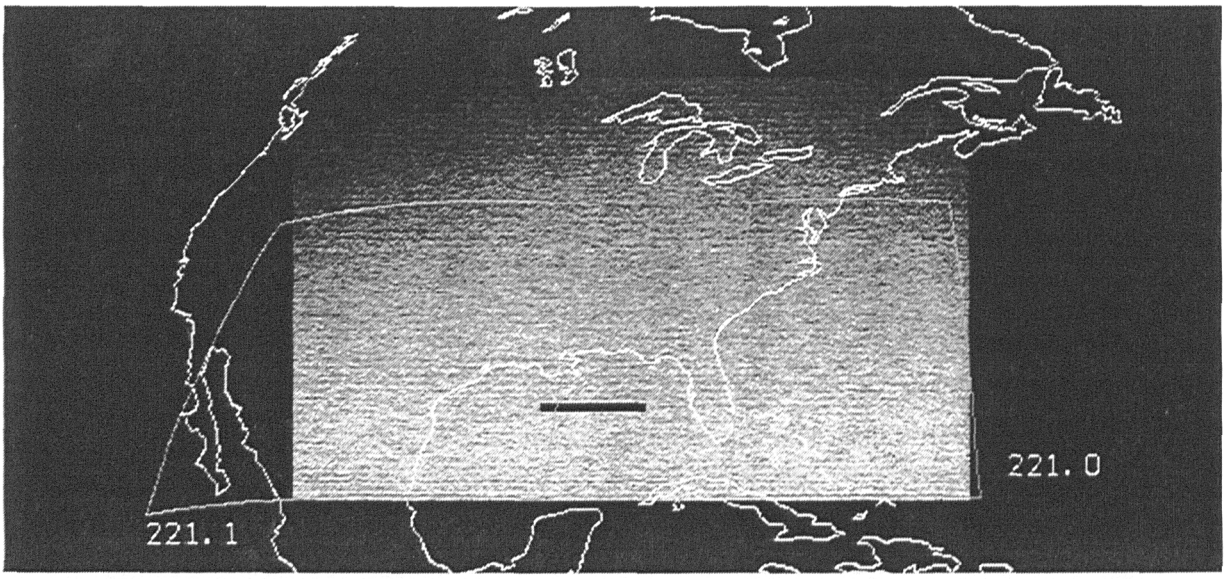

Figure 1b. After the east-west correction. GOES-8 Sounder. June 19, 1996. 12:46 UTC. Enhanced channel 1.

The method of the bias "tuning" used here follows the lead of Fleming et al. (loc. cit.) who have applied "shrinkage estimation" (Oman, 1982)[10] as the correction scheme for interactive TOVS retrievals currently operational at the National Center for Environmental Prediction (NCEP). In shrinkage estimation, one "shrinks" the estimator towards prior knowledge. Prior knowledge comes from the probable measurement error of the various bands or the anticipated accuracy of the transmittance model at each spectral frequency. This information can be accommodated in the shrinkage technique. Since the GOES retrieval is an iterative technique (Hayden, 1994)[11] , the correction is made to the observed rather than the calculated radiance temperatures, since this needs be done only once per retrieval. The current "tuning" predictors are the measurements (averaged, cloud-cleared), plus latitude, longitude, solar and local zenith angles and skin temperature. The time-interpolated numerical model temperature/moisture profile is used as the 'truth', because it has better time continuity compared to radiosondes. Investigations remain if an hourly application of the radiance bias adjustments are still necessary (after the ground correction).

All the sounder channels, except for channel 1, are sensitive to cloud. Investigation of the east-west bias in those channels over the regular (non-space) viewing area, must be with 'cloud-cleared' data. Figure 2a shows a scatter plot of the averaged, cloud-cleared channel 2 (14.4 microns) brightness temperatures versus longitude for 12 UTC cases (from 96123 to 96171) before the correction was implemented. The east-west slope is clearly seen. After the radiance bias adjustment, the slope is reduced (figure 2b). The ground processing correction (without radiance bias adjustment) is shown in figure 2c (for the six days (96172 to 96177) following the correction). The slope may not be flat due to natural variations, or possibly more data is needed to smooth out daily changes.

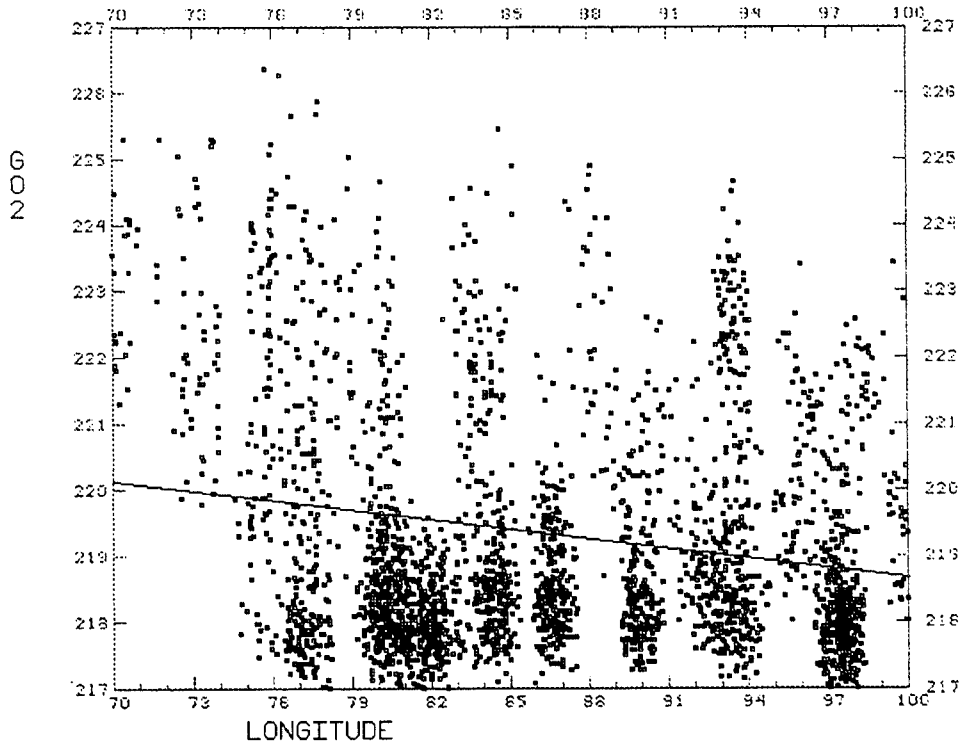

Figure 2a. The GOES sounder channel 2 brightness temperature observations versus longitude at 12 UTC between May 2 and June 19, 1996--before the ground correction.

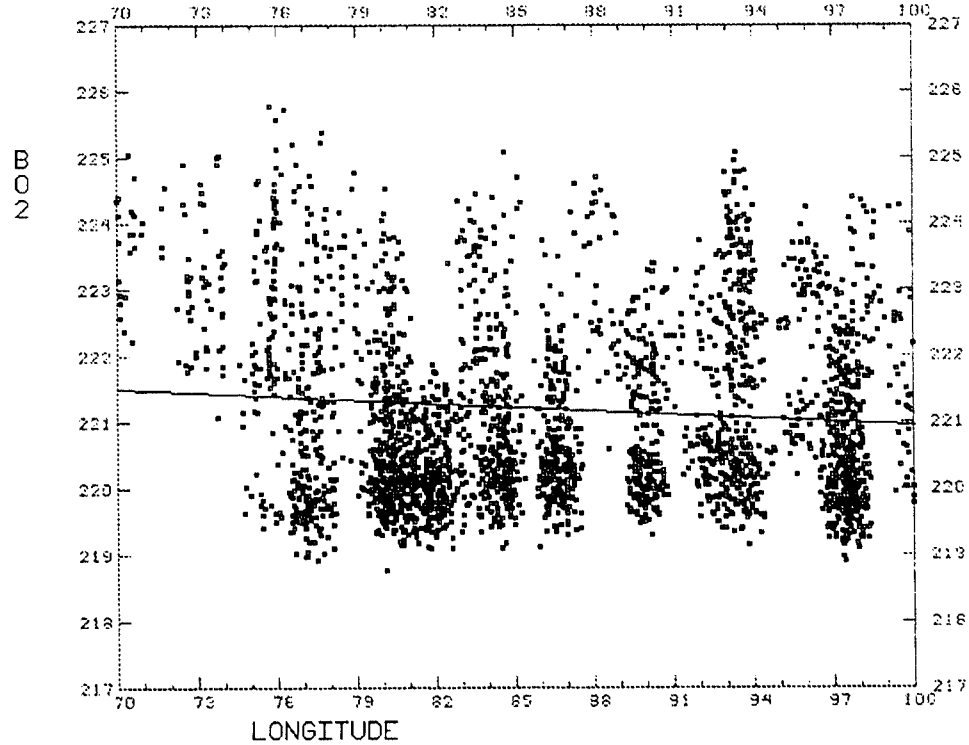

Figure 2b. The bias-corrected GOES sounder channel 2 brightness temperature observations versus longitude at 12 UTC between May 2 and June 19, 1996--before the ground correction.

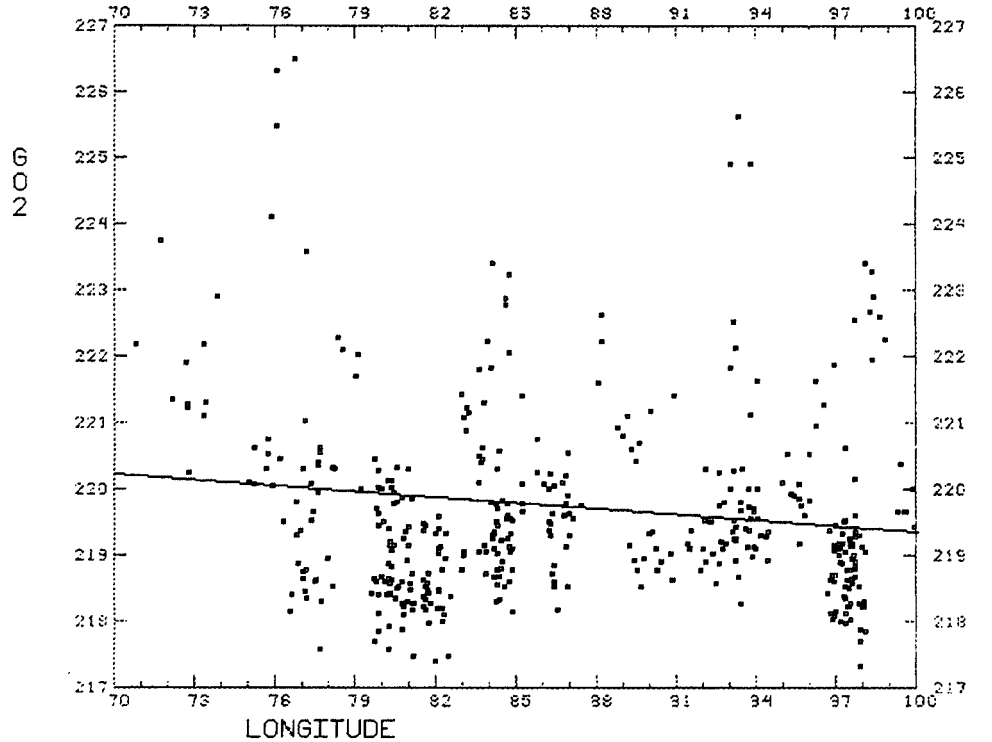

Figure 2c. The GOES sounder channel 2 brightness temperature observations versus longitude at 12 UTC between June 20 and June 25, 1996--after the ground correction.

4. GOES RETRIEVAL VERIFICATION

This section discusses the validation of the GOES-8 retrievals (Hayden and Schmit, 1994)[11] versus co-located radiosondes. The 00 UTC moisture retrievals produced at the Cooperative Institute for Meteorological Satellite Studies (CIMSS) from August 1995 to the end-of-May 1996 are considered. Each retrieval represents 5 x 5 fields of view (fov) or approximately a 50 km resolution. Retrievals can not be made in cloudy regions. Retrievals are produced only where at least 9 of the 25 fov are believed to be clear. Typically between 800 and 1500 retrievals for each satellite, depending on cloud cover, are made each hour. For this dataset there are over one thousand matches (1176) at a match distance of 0.25 degrees. The GOES-8 soundings were obtained from 23:46 to approximately half past the hour. For this ten month range, the retrieved total water vapor improved the guess from 3.5 to 2.8 mm RMSE (table 1). As can be seen, the retrievals are improving over the time-interpolated (Nested Grid Model) first guess for all moisture layers. Total water vapor is improved on the order of 20%, in a root-mean-square error sense. This moisture improvement over the NCEP short-term, regional forecasts, occurs in the vicinity of the radiosonde where they must necessarily be verified (and the quality of the first guess is higher). It should be noted that the forecast ('Guess') has been modified to include the surface air temperature and mixing ratio measurements (Hayden, 1988)[12], so little improvement should be anticipated near the lowest layer. Layered precipitable water was used because it is the quantity which has been first introduced into the NEMC regional forecast (Lin et al., 1996)[13].

Quality control of the radiosonde includes the following:

1. Radiosondes are required to reach 100 hPa.
2. Radiosondes must report at least 15 levels.
3. Station pressure for radiosonde must be greater than 700 hPa.
4. Station pressure and retrieval surface pressure must be within 25 hPa.
5. Radiance temperatures computed from radiosonde must be within 3 K measurement for longwave bands 3 through 7 (13.4 to 14.4 microns).

In making the fifth quality control check, the radiosonde profile is given the surface temperature and mixing ratio of the satellite retrieval, and the integration is made to the satellite surface pressure. Also, radiosonde reported mixing ratios above 100 hPa are set to .003 g/kg, and levels above the reported top are filled with values from the satellite retrieval. In collocating the sample we have permitted spatial differences as much as 0.25 degrees. Only clear (i.e., non-cloud corrected) and successful (passing the retrievals passing internal radiance checks) are included in this sample.

Table 1. GOES-8 retrieval moisture verification. The dates range from 95214 (August 2,1995) to 96151 (May 30, 1996). Only 00 UTC retrievals are included. Match distance of 0.25 degree. RMSE compared to radiosondes (in mm). sigma is the ratio of the pressure over the surface pressure. Sample size is 1176.

	Guess			Retrieval		
	BIAS	RMS	RMSE	BIAS	RMS	RMSE
Total Water Vapor	**-0.3**	**3.5**	**3.5**	**0.3**	**2.8**	**2.8**
WV1 (Surface to .9 sigma)	**-0.7**	**1.5**	**1.7**	**-0.3**	**1.3**	**1.4**
WV2 (0.9 to 0.7 sigma)	**0.2**	**2.1**	**2.2**	**0.5**	**1.8**	**1.8**
WV3 (0.7 to 0.3 sigma)	**0.2**	**1.3**	**1.4**	**0.1**	**1.0**	**1.0**

The above table shows how integrated quantities derived from the sounder data improve upon the first guess information. Early results from simulation (Hayden and Schmit, 1991)[14] suggest one should only reply on the integrated moisture quantities, yet figure 3 shows the dewpoint level verifications versus radiosonde data for the same data set used above. One can see that there is improvement at all levels, with the exception of some "ties" near 900 hPa.

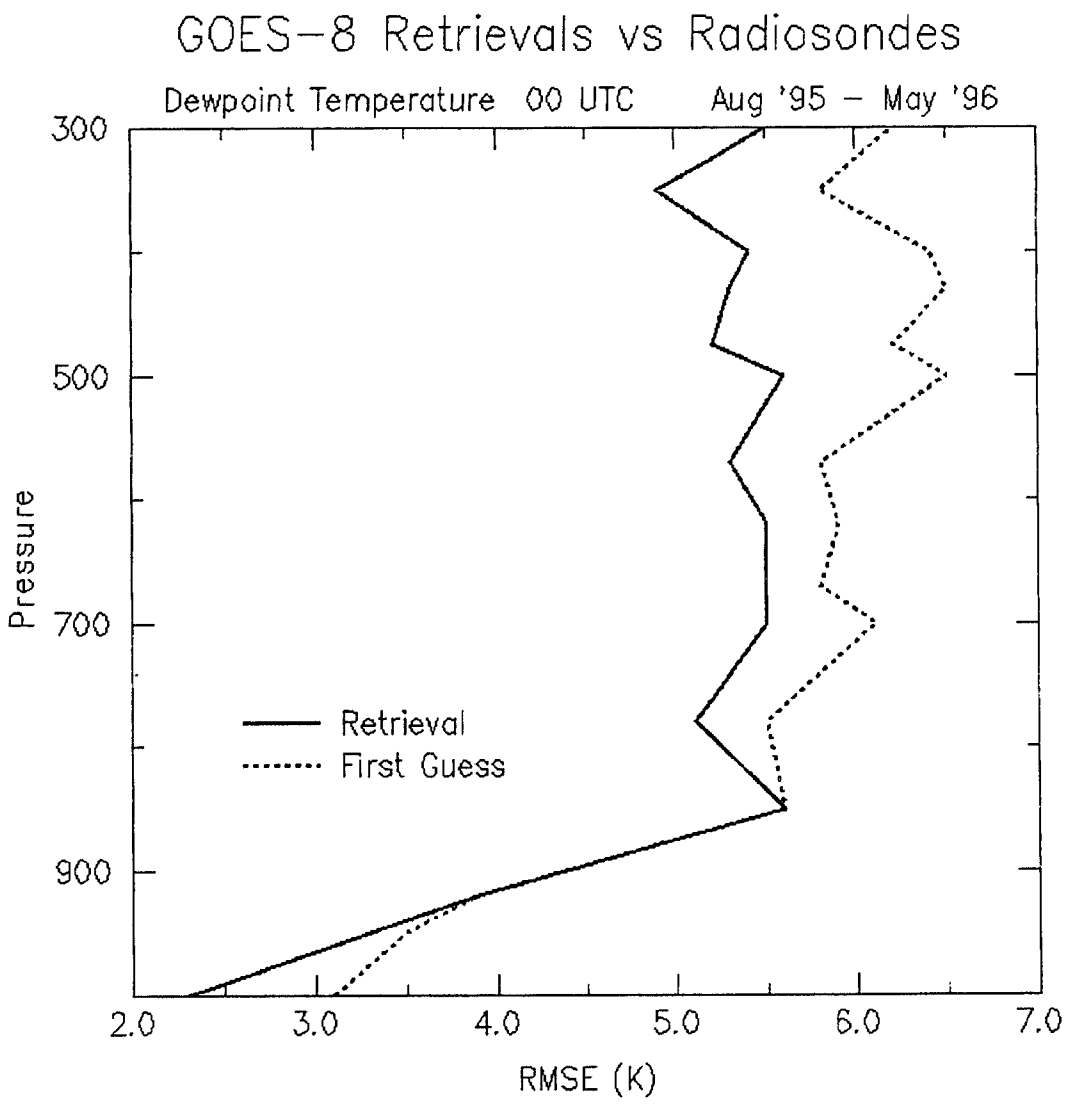

Figure 3. Level dewpoint retrieval comparisons versus co-located radiosondes.

5. SUMMARY

The east-west radiance gradient was somewhat mitigated via a radiance bias adjustment (at least for the highest sounder channels) before the ground correction. The artificial gradient was largely eliminated due to the ground correction algorithm. This correction is much superior to the radiance bias method in that its valid for all channels, no assumptions need to be made about the behavior of channels and the users do not need to do any additional pre-processing. The near elimination of the artificial gradient helps in producing more accurate GOES retrievals. Verification of the GOES sounder moisture retrievals, both before and after the ground correction, show significant improvement over the forecast model first guess with respect to radiosondes.

6. REFERENCES

1. Weinreb, M. P. J. X. Johnson, J. C. Brener, E. C. Wack, and O. Chen, 1996: Algorithm to compensate for variation of reflectance of GOES-8 & 9 scan mirror with scan angle. Preprint volume, AMS Eighth Conference on Satellite Meteorology, 28 Jan - 2 Feb., 1996, Atlanta, GA.

2. Menzel, W. P. and J. F. W. Purdom, 1994: Introducing GOES-I: The first of a new generation of geostationary operation environmental satellites. *Bull. Amer. Meteor. Soc.*, **75**, 757-781.

3. Eyre, J. R., 1989: Inversion of cloudy satellite sounding radiances by nonlinear optimal estimation: theory and simulation for TOVS. *Q. J. R. Meteorol. Soc.*, **115**, 1001-1026.

4. Smith, W. L., H. M. Woolf, P. G. Abel, C. M. Hayden, M. Chalfant and N. Grody, 1974: NIMBUS-5 sounder data processing system. Part I: Measurement characteristics and data reduction procedures. NOAA Tech. Memo. NESS 57, Washington D.C., 99 pp.

5. Weinreb, M. P., 1979: Atmospheric transmission for remote temperature sounding. *Proc. Soc. Photo-Optical Instrumentation Engineers*, **195**, 22-30.

6. Susskind, J, J Rosenfield and D. Reuter, 1983. An accurate radiative transfer model for use in the direct physical inversion of HIRS-2 and MSU temperature sounding data. *J Geophys. Res.*, **88**, 8550-8568

7. Eyre, J. R., 1992: A bias correction scheme for simulated TOVS brightness temperatures. *ECMWF Tech Memorandum* 186.

8. McMillin, L. M., L. J. Crone, and D. S. Crosby, 1989: Adjusting satellite radiances by regression with an orthogonal transformation to a prior estimate. *J. Appl. Meteor.*, **28**, 969 975.

9. Fleming, H. E., N. C. Grody, and E. J. Kratz, 1991: The forward problem and corrections for the SSM/T satellite microwave temperature sounder. *IEEE Transactions on geoscience and remote sensing*. **29**, 571-583

10. Oman, S. D., 1982: Shrinking towards subspaces in multiple linear regression. *Technometrics*, **24**, 307-311.

11. Hayden, C. M. and Timothy J. Schmit, 1994: GOES-I temperature moisture retrievals and associated gradient wind estimates. Preprint volume, Seventh Conference on Satellite Meteorology and Oceanography. June 6-10, 1994, Monterey CA. 477-480

12. Hayden, C. M., 1988: GOES VAS simultaneous temperature moisture retrieval algorithm, *J. Appl. Meteor.*, 27, 705-733.

13. Lin, Y., E. Rogers, G. J. DiMego, K.E. Mitchell and R. M. Aune, 1996: Assimilation of GOES moisture data into NMC's ETA model. Preprint volume, AMS Eighth Conference on Satellite Meteorology, 28 Jan - 2 Feb., 1996, Atlanta, GA.

14. Hayden, C. M. and Timothy J. Schmit, 1991: The sounding capabilities of GOES-I and beyond. *Bull. Amer. Meteor. Soc.*, **72**, 1835-1846.

The Solar X-ray Imager (SXI) Detector Calibration and Characterization

K. Russell, J. Briscoe, E. Corder, and S. Wallace
NASA-Marshall Space Flight Center, EB-53
Huntsville, AL 35812

J.H. Chappell
New England Advanced Research Laboratories
Lee, NH 03824

ABSTRACT

The SXI detector is designed to cover the 6Å-60Å soft X-ray band and operate in a single photon or integrating camera mode. The detector is based upon a MCP intensifier/converter coupled to a CCD via phosphor coated fiber optic. This paper discusses the detector characterization and calibration to date.

1 Introduction

1.1 Instrument Design and Operation

The *Solar X-ray Imager* (SXI)[1] is designed to image the full solar disk in the soft X-ray band at a frequency of one image per minute. The SXI is designed to be flown on board a NOAA GOES-L spacecraft.

To meet the imaging requirements (5x5 arc sec pixels) and the energy bandwidth (6 to 60 Å), an intensified CCD design imaging detector was adopted. The micro channel plate (MCP) intensified CCD detector consists of three major components: MCP,[2] phosphor coated fiber optic taper, and the CCD.

When an x-ray photon is photoelectrically absorbed in the top MCP pore wall, a fraction of the secondary electrons produced in the glass will escape into the pore vacuum. The number of secondary photoelectrons that escape into the pore is a function of the intrinsic MCP soft x-ray absorption properties and the electron range in the bulk MCP glass material. These vacuum electrons are accelerated down the pore and will generate additional electrons at each collision with the MCP wall. Typically 1-4 electrons are produced with each collision. The electron gain of the MCP is a function of the plate length to pore diameter (L/D) ratio and the operating voltage. The electron gain can vary from 10^3 to 10^5 electrons per x-ray event.

The exiting electrons are proximity focused onto a fiber optic taper coated with a rare earth phosphor screen by a $\approx$ 4KV electric field. Visible light photons are produced as the electrons lose energy via a

0-8194-2200-2/96/$6.00

bremsstrahlung process in the phosphor grains. The isotropically produced visible light photons diffuse to the rear of the phosphor screen where a certain fraction will exit through the fiber optic expander (1:1.2) which is coupled to the CCD.

1.2 Characterization Objectives

The calibration tasks can be divided into two groups, x-ray sensitivity and spatial characterization. The camera sensitivity characterization has two primary goals:

1. Derive a relationship between the incident x-ray flux Io, $(photons\ pixel^{-1})$, MCP voltage V, and the recorded CCD average digital number $(< DN >)$.
2. Determine the single photon detection quantum efficiency as a function of MCP voltage.

The camera spatial characterization has three primary goals:

1. Derive the effective point spread function (PSF).
2. Determine the focal plane plate scale.
3. Characterize any spatial non-linearities in the imaging system.
4. Characterize the flat field response (work in progress - not presented in this paper).

2 Calibration Facility

2.1 Vacuum System

The instrument calibration was conducted at the MSFC SXI laboratory calibration vacuum test facility. The vacuum facility consists of a 2.4m pipe, a x-ray generator, and beam monitoring flow proportional counters. Vacuum pressure during the calibration was maintained at $3.0\ 10^{-6} torr$ or below. The 0-degree biased MCP was oriented relative to the incident radiation at a fixed 7° incident angle.

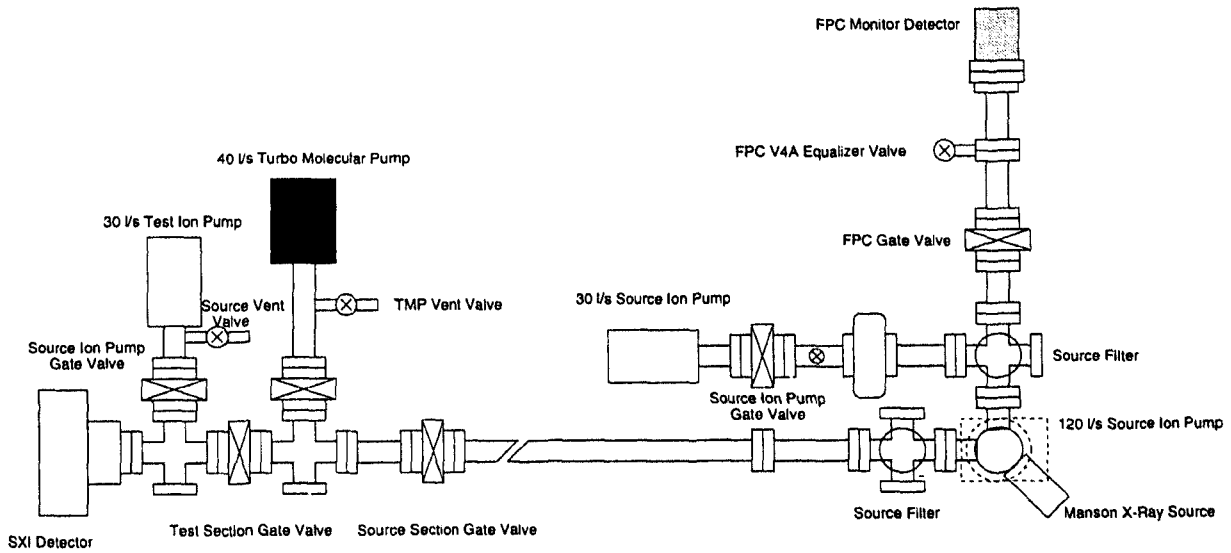

Figure 1: SXI detector characterization facility

X-rays are generated by an electron impact source (Manson Source Model-2 from Austin Instruments[3]). The detector is calibrated at two energies, 0.277 keV and 1.49 keV. A secondary source filter assembly[4] was used in conjunction with the source to filter the low energy continuum. The aluminum secondary source filter was a 25.4 μm thick aluminum filter. The carbon secondary source filter was a 25.4 μm thick polypropleyene filter.

The x-ray flux was obtained by an orthogonally mounted flow proportional counter (FPC) provided by Austin Instruments . The FPC body has an effective body thickness of 2.02 cm. The FPC window material consisted of 1942$\AA$ thick VYNS window supported by a 60% transmitting nickel mesh. The nickel strong back mesh was 6 μm thick. The x-ray flux monitor was cross calibrated with two FPC's. For the aluminum energies, P10 gas was used for the absorber gas. For the 0.277 keV x-rays, a methane absorber gas was used. Nominal pressures for the counter was set for 220 mm-Hg for both absorber.

2.2 Data Acquisition Scenario

To characterize the sensitivity and spatial resolution, images were acquired at a constant flux setting on the x-ray generator, phosphor voltages (V_{phos}), x-ray angle of incidence, and CCD temperature (T). The MCP integration time was used to vary the total number of acquired photons. The nominal integration exposures varied from 0 to 60 sec. MCP voltages ranged from 750 to 1100V.

3 X-ray Sensitivity

3.1 Photon Integration Mode

In the photon integration counting mode, the light collected in individual CCD pixels is the result of light produced by several photons distributed spatially and temporally during the selected integration period. For this condition, we define the camera sensitivity $S_{integrated}$ as:

$$S_{integrated}(I_o, V_{mcp}, \tau, T) = \frac{< DN_{s+b} > - < DN_b >}{I_o \, \tau \, A} \tag{1}$$

where $< DN_{s+b} >$ represents the average DN value (signal + background) for a single pixel $p_{i,j}$ integrated over n images. For this test, we assume that the single pixel averaged over n images is equivalent to the average digital value of n pixels summed over a specified ROI in a single image. $< DN_b >$ is the average DN values produced by the total camera system integrated over the same spatial and temporal period, τ is the integration time (sec), A is the active CCD ROI detection area (cm^2), and I_o is the incident x-ray flux ($photons\ pixel^{-1}$). $S_{integrated}$ has units if $< DN > /photon$.

3.1.1 Lower Sensitivity Limits

In every conversion process, statistical fluctuations introduce uncertainty in the final recorded digital value. Statistical variations occur in the photon-electron interactions in the MCP, electron-photon conversion in the phosphor, and light transfer from the phosphor into the fiber optic taper. In the CCD the photoelectron production, electron transport, amplification, and digitization effects all add noise to the final recorded digital value. The camera background can be defined in terms of the of the average DN's produced by these noise sources plus any DC offsets in the signal. With the assumption that the components are uncorrelated, we can compute the total camera *noise* N in terms of the standard deviation about the mean background value σ_b.

$$N = \sigma_b \tag{2}$$

The lower sensitivity limit of the camera will be dominated by the statistical fluctuations about the average background level. The minimum camera sensitivity, S_{min} is defined in terms of the camera noise

characteristics at $-20°C$ and an exposure time of $100ms$.

$$S_{min}(\tau, T) = 3N = 3\sigma_b \tag{3}$$

3.1.2 Upper Sensitivity Limits

The upper sensitivity limit of the camera will be dominated by saturation in the CCD *and/or* the MCP depending upon the operating conditions. CCD saturation occurs when sufficient light is generated in the phosphor to saturate the individual pixel to its full well depth capacity. MCP count rate saturation occurs when the count rate per pore exceeds a critical value. Count rate saturation will vary with bulk MCP plate resistance. The gain of the MCP begins to drop when the plate resistance dominates the electron recharge time.

3.2 Single Photon Detection Mode

The 'single photon counting' sensitivity mode occurs where the incident flux and the camera integration time are such that single x-ray events can be detected above the CCD noise floor. In this case, the light produced by a single photon event will be collected in several adjacent CCD pixels. In the single photon counting mode, it is more appropriate to work with a Detection Quantum Efficiency (DQE) defined by:

$$DQE(V_{mcp}, T, E_x) = \frac{< N_{det} >}{I_o \ \tau \ A} \tag{4}$$

Where $< N_{det} >$ represents the average number of *detected* single photon events. In this mode, the light collected from multiple pixels and are summed to give a average DN for each event.

3.2.1 Lower Sensitivity Limits

As above, there are several ways to define a detected event. Since the event is distributed over several pixels, event recognition can be accomplished by a 'double sliding' box technique to compute the event S/N ratio. The detection S/N ratio is defined in terms of the summed DN values associated with an event above a local DN background value. A valid detection occurs when the summed event pixels exceed the local background by a specified amount (ie. 3σ).

3.2.2 Upper Sensitivity Limits

In both operational modes, the upper dynamic range of the camera will be dominated by saturation in the CCD *and/or* the MCP depending upon the operating conditions. The characterization of the upper sensitivity limits are still under study.

3.3 Observations

A total of 1100 images were acquired at Al(1.49 keV) and C (0.277 keV) energies. The preliminary Al results are presented here, the C data set is still under analysis. The Al x-ray sensitivity plot is shown in Figure 2. This plot shows the CCD response as a function of the number of incident 1.49 keV photons per pixel. Incident radiation varying from 0.1 to 50 photons per pixel can readily be observed depending upon the MCP voltage. The x-ray sensitivity can be varied as a function of the MCP voltage. For example, at 840V, the camera sensitivity is $\approx$ 1.4 DN/photon. This increases to a maximum of $\approx$ 24.7 DN/photon at 1100V.

Figure 3 shows the single photon detection quantum efficiency as a function of MCP voltage. This plot describes the DQE to detect *single photon events*. Below 850V, the single photon DQE approaches 0. This does not imply that the camera is not sensitive to incident radiation when the camera is operated below this MCP voltage. At these energies, the probability of a x-ray initiating a electron avalanche is $\approx$ 8

%, independent of the MCP voltage. Light generated from these low gain electron clouds are recorded in the CCD and contribute to a increased DN level proportional to the incident flux similar to photographic film. Above 850V, the electron gain is sufficiently high to generate charge clouds that can be identified above the CCD background. With short exposures (and/or low fluxes), the camera can be operated as a single photon detector.

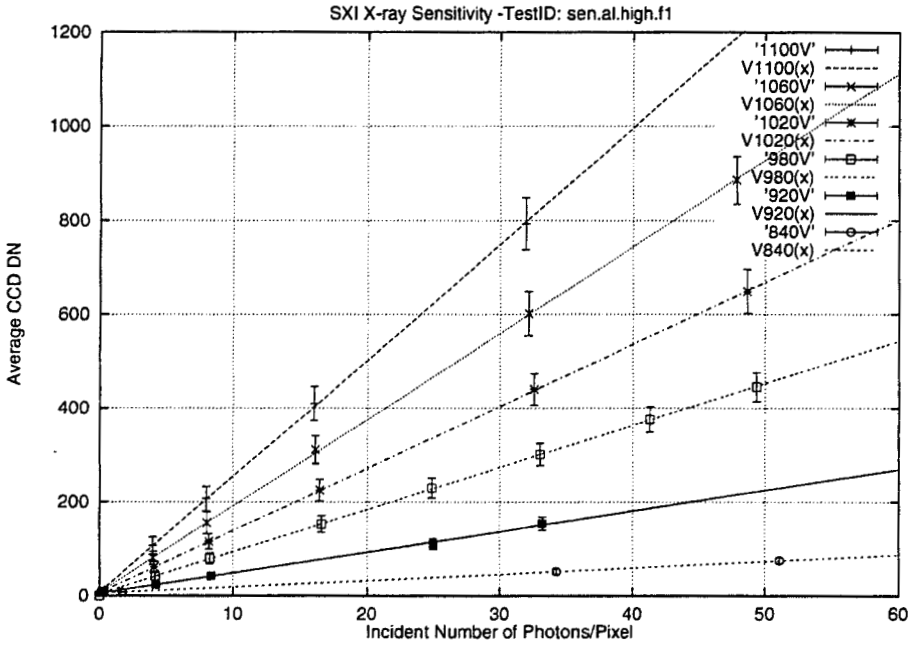

Figure 2: Preliminary Sensitivity Plots as a function of MCP voltage in response to 1.49 keV photons. The straight lines represent a linear least square fit to the measured data points.

4 Spatial Resolution

4.1 Objective

The primary goal of this report is to characterize the spatial resolution, focal plane plate scales, and their respective errors with the flight SXI detector. There are a number of fundamental questions that need to be addressed now that the instrument is in the final flight configuration:

1. How does the spatial resolution vary as a function of MCP voltage?
2. Does the spatial resolution vary in the horizontal or vertical directions with respect to the CCD?
3. Does the spatial resolution vary with exposure time ?
4. Does the spatial resolution depend on the spectral content of the incident radiation?

4.2 Resolution Mask

An etched nickel spatial resolution mask is placed in direct contact with the input MCP surface. This USAF resolution chart consists of a series of closely spaced slit patterns. The pattern consists of three

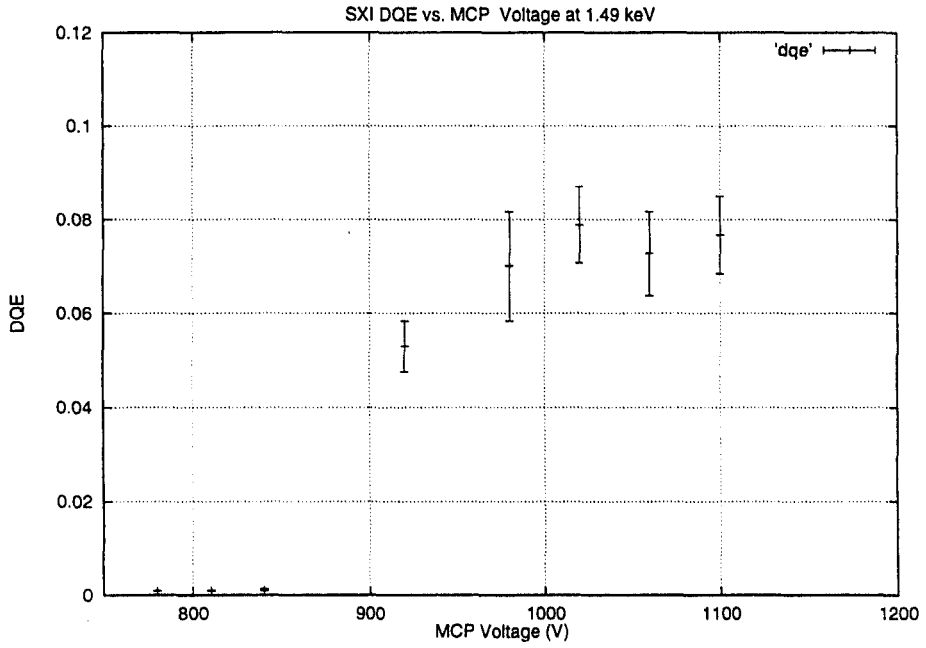

Figure 3: Preliminary single photon detection DQE plots as a function of MCP voltage at 1.49 keV

lines and two spaces of equal width and a length five times the width. The center to center spacing (D) is designed to be $\approx$ twice the slit width (W). However, due to the lithographic errors in the fabrication process, every mask must be measured and verified.

4.3 Analysis Overview

By placing a series of known slit patterns in contact with the MCP focal plane surface and exposing the camera to a near parallel beam of x-rays, the instrument point response function (PSF) can be determined. The PSF describes the how the instrument responds to a point source. The resolution pattern is characterized by the width of the slits (W) and the center-to-center separation distance (D). The separation distance between the slits provides an absolute calibration of the instrument focal plane scale (FPS).

Measuring the intensity modulation response (MOD) to the resolution bars enables the user to model/estimate the instrument PSF. The instrument response due to decreasing spatial resolution is plotted Figure 4. The intensity modulation is determined by measuring the 'peak' and 'valley' (open and closed) instrument response to the mask patterns.

$$P(y_{max}, \sigma, w, d) = I(y = y_o + d/2, \sigma, w, d) \quad (5)$$

$$V(y_{min}, \sigma, w, d) = I(y = y_o, \sigma, w, d) \quad (6)$$

$$MOD(P,V) = \frac{(P-V)}{(P+V)} \quad (7)$$

Figure 5 shows the predicted MOD vs. the σ/w for a Gaussian PSF function.

The analysis technique is complicated by additional instrumental effects such as the digitization of the incident photons by the MCP, phosphor light spread, and the finite size of the CCD pixels. Ideally,

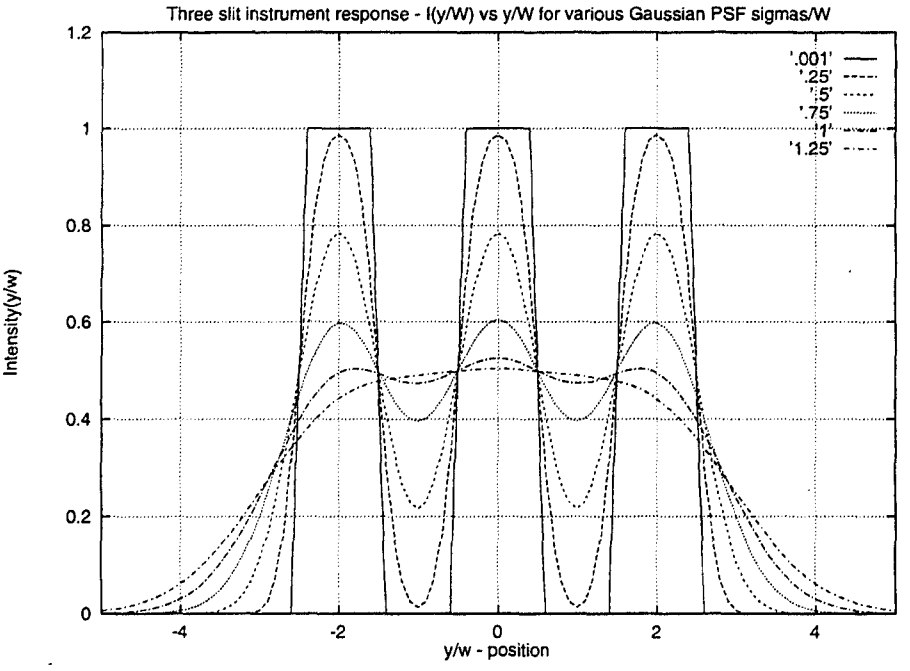

Figure 4: The modeled spatial response to a parallel incident beam passing through a three slit pattern of width w and $d/w = 2$. The different curves represent various detector response σ's

one would choose a resolution pattern that has a modulation of 0.1 and 0.4. Outside these values the deconvolution becomes more sensitive to measurement error and background subtraction. The resolution pattern selected typically covers 3-4 CCD pixels. As a result, the division of light into the pixels can yield slightly non symmetric peaks. For this reason, we have averaged the outer and inner modulations and their respective σ's to determine average instrument response.

Other complicating issues arise when the mask pattern is not aligned with the CCD pixel axis. The image must be rotated to acquire the correct projection data. As a result of the rotation, a certain amount of aliasing occurs, leading to a slightly broader projection. For these tests, the rotation angle is $\approx 0°$.

The projection regions of interest (ROI) have been selected to minimize the rotation aliasing effects and edge effects of the top and bottom aperture slit. The USAF 3-5 resolution bar pattern was used in the analysis.

The background subtraction also contains sources of error. A constant background value was subtracted from each image. This background value was determined by averaging the non-exposed areas of the CCD.

The next area that leads to error in the modulation measurement is the determination of the peak and valley positions and heights. Since each open area exposes 3-4 pixels, determining the peak centroid and height becomes a significant problem. In an attempt to have a consistent method to determine these values, automatic fitting software was developed. This software uses a combination of first and second derivatives to determine the coarse center position of each peak and valley. Once the coarse positions have been located, a least square Gaussian fit program was developed to determine the centroid X and Y positions of the peaks and valleys.

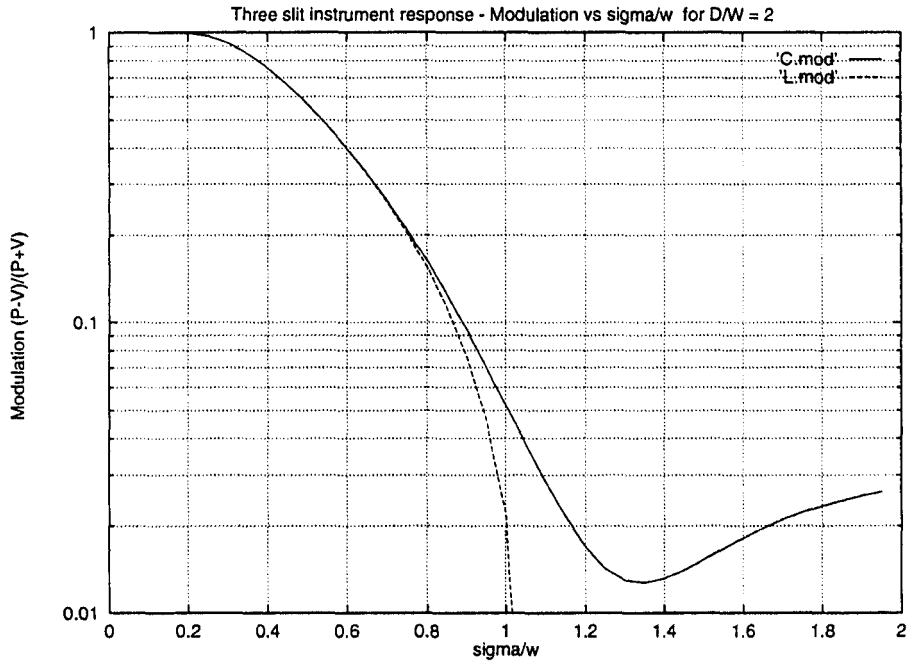

Figure 5: The double slit response showing the calculated modulation (MOD) vs. the σ/w of the Gaussian PSF. The left most curve is the modulation calculated using the left or right peak ratioed to the adjacent valley. The right most peak is the modulation calculated using the center peak ratioed to its nearest valley.

4.4 Sample Input Data and Generated Data Products

Figure 6 shows a typical input image. The image on the left is the full field image. The image on the right shows an expanded region of interest centered on the selected three slit pattern (USAF Group 3-5). Figure 7 shows the instrument response to a three slit pattern in 3-D perspective. The projection and respective Gaussian fits are shown in Figure 8. The peak and valley positions are extracted from the image. There are a number of analysis options that can used to extract the modulation parameters. Due to rotation aliasing and the finite CCD pixel sampling size, a simple Gaussian fit was applied to find the peak and valley position

4.5 Observations and Conclusions

A total of 46 images were acquired for the spatial resolution analysis. As enumerated in the Introduction, there are a number of fundamental questions that need to be verified with regard to the spatial characteristics of the flight instrument: The '750V' and '800V' data sets varied the exposure time (16 - 60 sec) to investigate any temporal variations and confirm past results. For all other MCP voltages the exposure time was 60 seconds. Taken over *all MCP voltages and exposure times*, the average Gaussian PSF (σ) is $22.68\mu m \pm 1.97$.

As expected, the spatial resolution is MCP voltage dependent. At *fixed* voltage, the σ_{PSF} varies from $20.5\mu m$ at 750V to $26.5\mu m$ at 1000V. The PSF vs. MCP voltage is plotted in Figure 9. As the MCP voltage is reduced, the electron gain is decreased thereby producing a smaller charge cloud resulting in a smaller PSF. As observed in past measurements, the single photon encircled energy distributions are correspondingly reduced as a function of voltage. The σ_{PSF} varies from $20.5\mu m$ at 750V to $26.5\mu m$ at

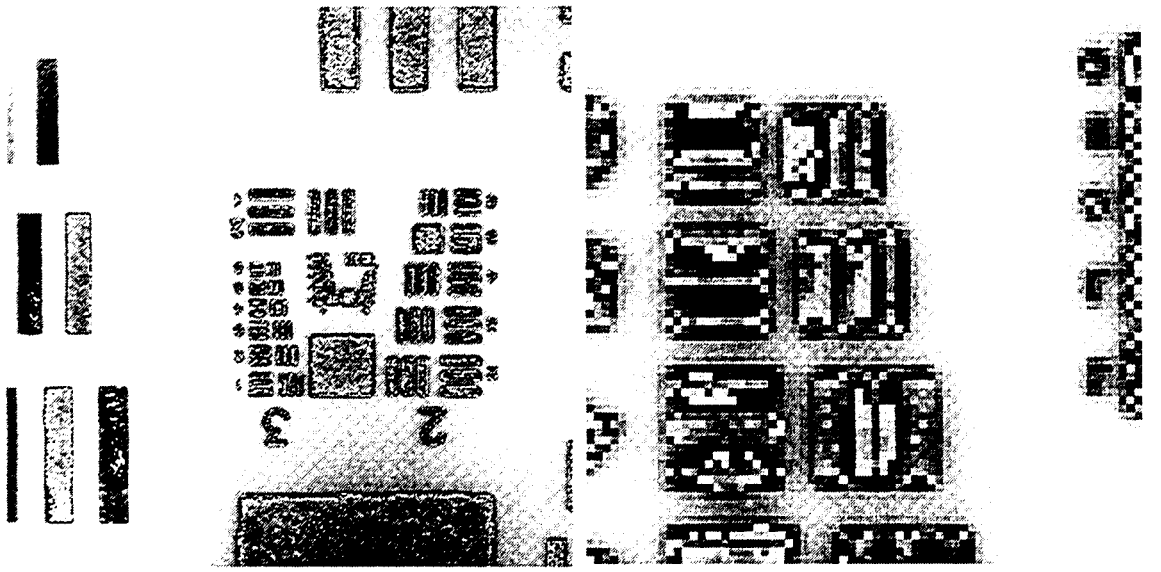

Figure 6: Sample Image file 960423.659.img showing the three slit instrumental response . The full field is shown on the left and the expanded analysis ROI is on the the left.

1000V. At a fixed voltage, the uncertainty in the σ_{PSF} is $\approx$ $0.5\mu m$. A linear relationship can be derived between the σ_{PSF} and the MCP voltage.

$$\sigma_{PSF}(V_{mcp}) = 5.073 + 0.020\, V_{mcp} \tag{8}$$

This relationship was derived using the entire data set.

Resolution analysis was performed with the vertical and horizontal resolution bars for all MCP voltages and exposures. No statistical difference was observed between the two patterns.

No statistical difference was observed in the σ_{PSF} as a function of exposure time. The calculated σ_{PSF}'s are plotted in Figure 10. This plot contains the estimated σ_{PSF} as a function of integration time.

To verify that the spatial resolution is independent of the input spectrum, several images were acquired with and without the secondary source filter. No measurable differences in the PSF could be seen with the two input spectrums.

The calculated Focal Plate Scale (FPS) for the horizontal dimension is $16.49\mu m/pixel$ $\pm$ 0.20. The FPS for the vertical dimension is $16.47\mu m/pixel$ ± 0.29. In this flight configuration, for all MCP voltages, exposure times, and CCD axis the FPS's are statistically identical. The PSF vs. camera exposure time is plotted in Figure 10.

5 Spatial Linearity

The spatial linearity characterization test uses a uniformly spaced pinhole array mask to measure any spatial distortion and to verify the plate scale over the focal plane surface of the camera system. The mask is composed of 0.001" nickel. The open areas have been chemically etched using a photolithographic technique. The multiple pinhole aperture mask consists of a uniform nickel mask with $100\mu m$ diameter

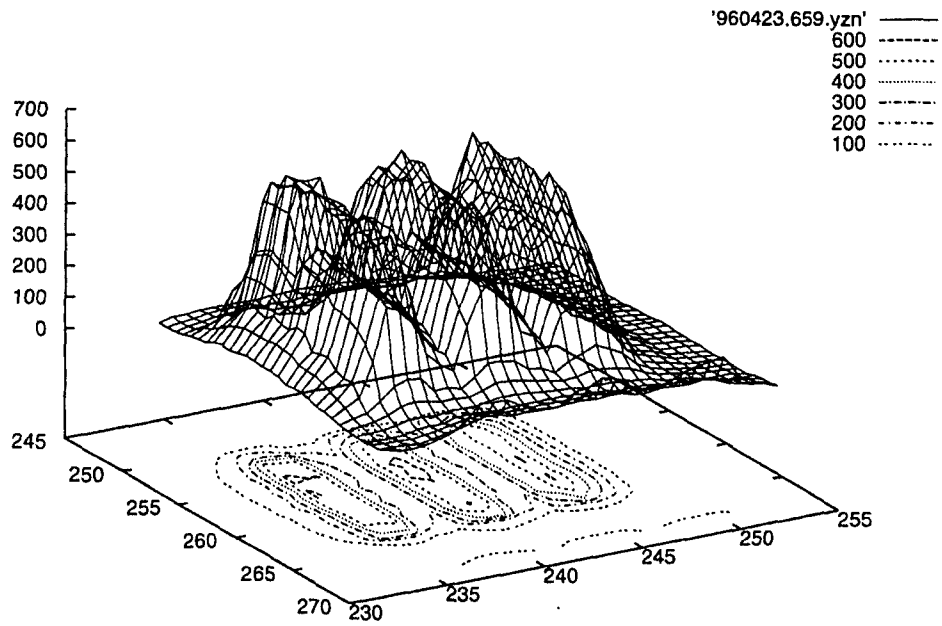

Figure 7: The instrument response to a three slit pattern (960423.659.img)

holes placed on 254.0μm centers. Since the actual center to center spacing of the mask is well known, the focal plane plate scale can be determined. Any gross or shear distortion effects of the fiber optic expander can be identified in this test.

5.1 Observations

Figure 11 shows the camera response to the 1.49keV combined with the uniform pinhole mask. Figure 12 shows a selected region of interest in a contoured 3-D perspective. The differences between the expected vs. the measured centroid positions is less than 2% over the full field.

6 REFERENCES

[1] J.Davis, D.Bagdidian, S.Bushmann, G.Crag, J. Russell, and K.Wallace. *AIAA Space Programs and Technologies Conference*, AIAA 93-4204:687, 1993.

[2] 0-degree biased; 60:1, 8 μm pore diameters. Supplier: Galileo Electo-Optics Corp. Sturbridge MA, 01566, 508 347 9191.

[3] Austin Instruments Inc. Reading MA, 01867, (800) 818 7403.

[4] New England Advanced Research Laboratories, Lee NH, 03824, (603) 659 6562.

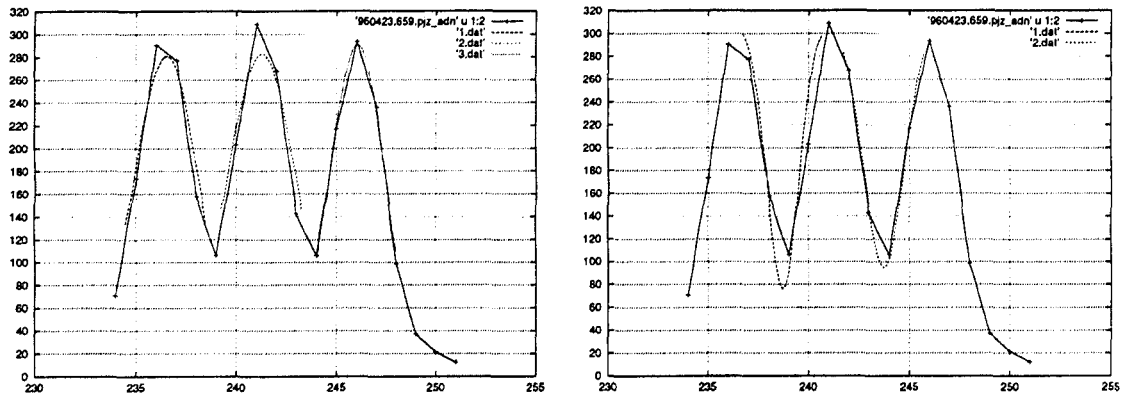

Figure 8: A) (Bottom Left) Gaussian fits for the peaks overlaid with the projection data. B) (Bottom Right) Gaussian fits for the valleys overlaid with the projection data.

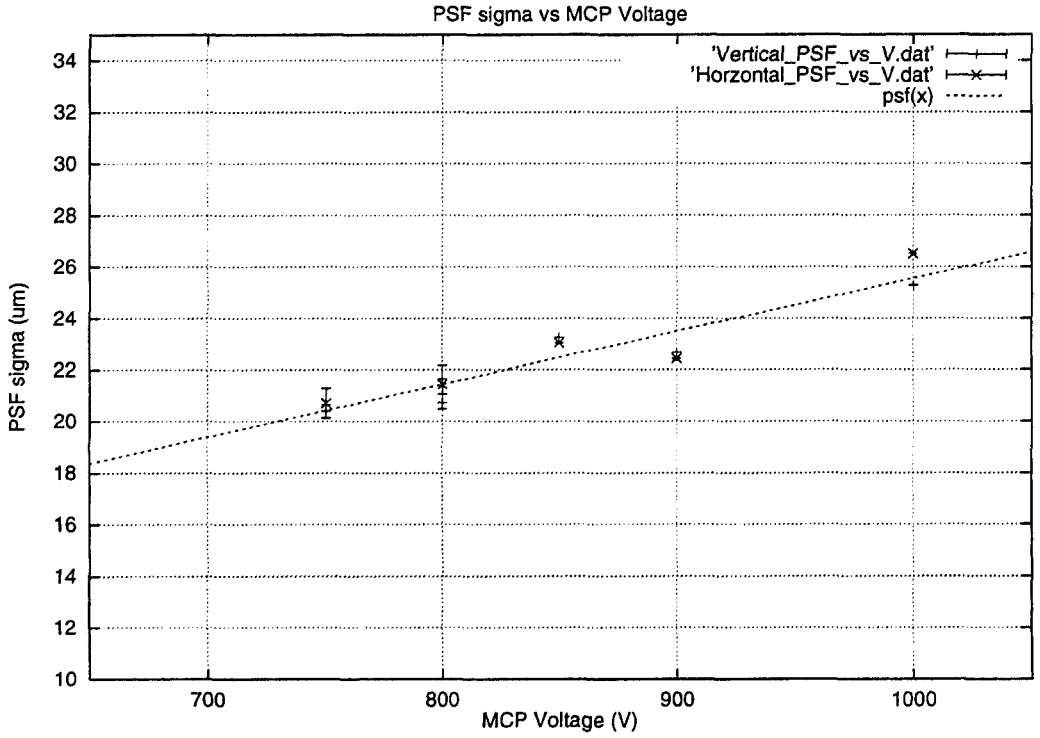

Figure 9: Gaussian PSF σ plotted as a function of MCP voltage.

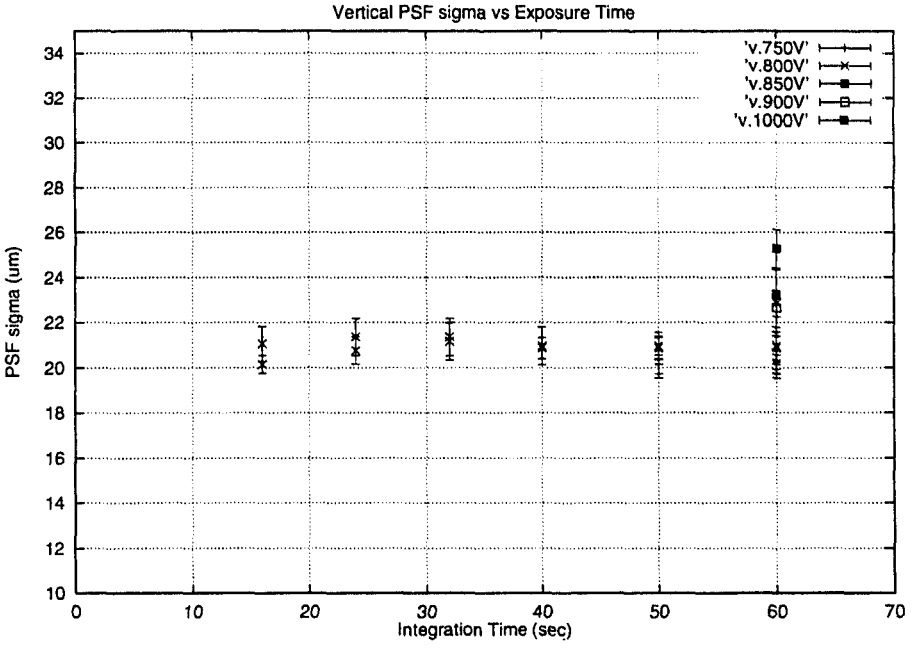

Figure 10: Gaussian PSF σ plotted as a function of exposure time.

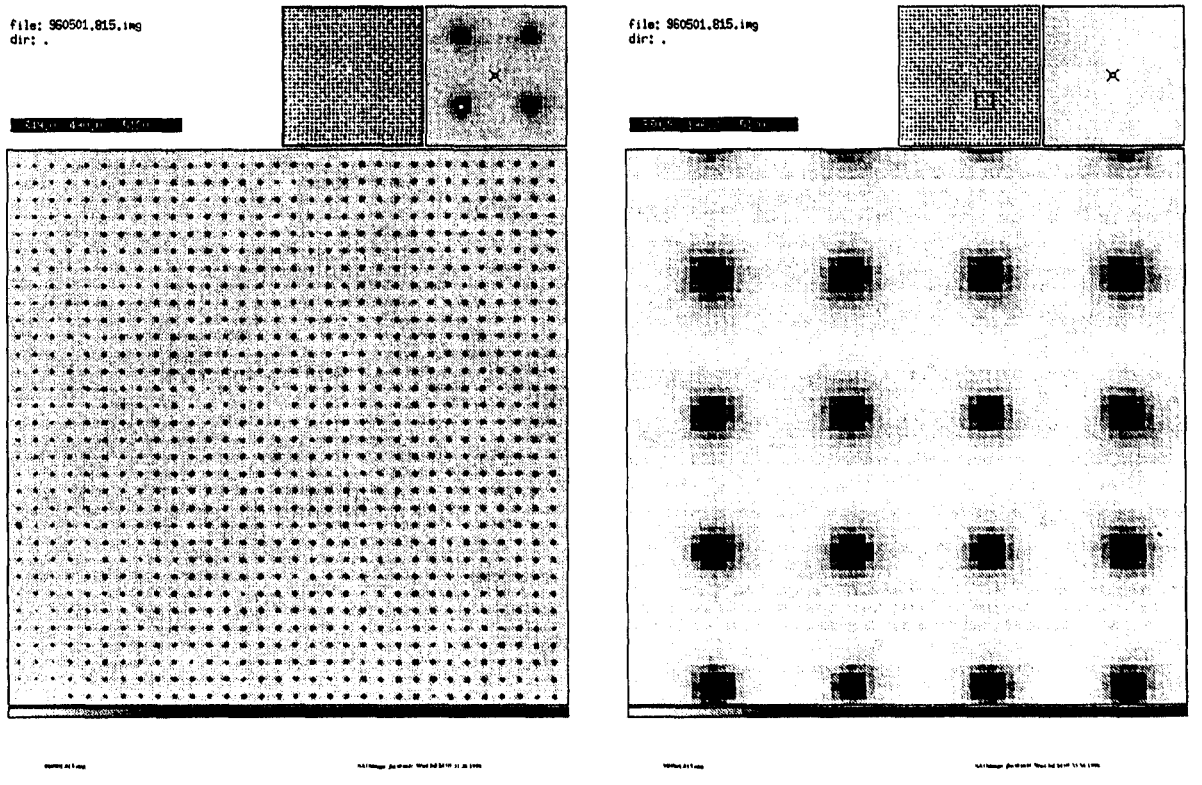

Figure 11: (Left) Full field view of the pinhole mask. (Right) An expanded view of the pinhole mask.

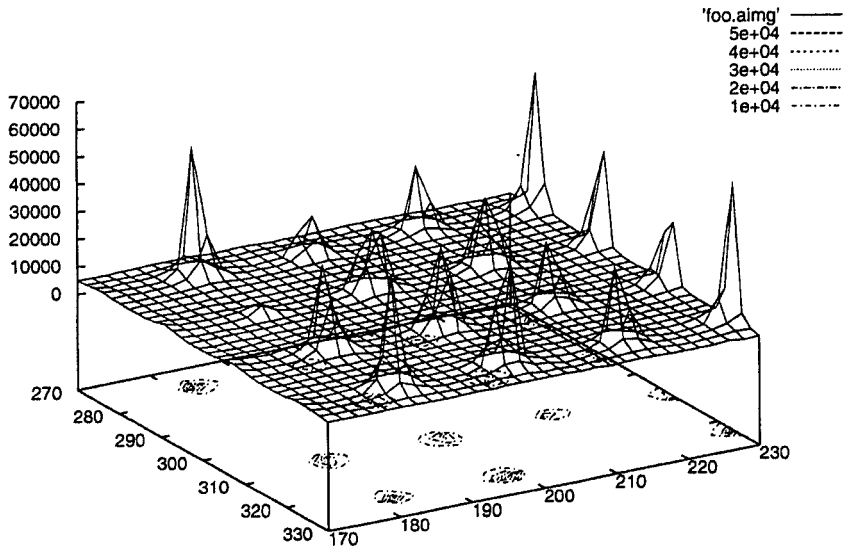

Figure 12: Spatial linearity ROI image shown in a contoured 3-D perspective.

SESSION 8

Attitude Control

GOES orbit and attitude determination – theory, implementation, and recent results

Kwok M. Ong and Steve Lutz

Space Systems/Loral, Palo Alto, California 94303

ABSTRACT

This paper presents the mathematical formulation and implementation techniques used in the GOES orbit and attitude determination (OAD) software. Also presented are some recent results obtained by analyzing data from the operational GOES. The OAD software, a key component of the Orbit and Attitude Tracking Subsystem (OATS), has been in use for operating the GOES spacecraft successfully since the beginning. Three kinds of observables are ingested by OAD: range, star line-of-sight direction, and landmark line-of-sight direction. Raw observations are preprocessed to rid of known systematic errors. Among the solve-for parameters are six (6) orbital elements, dynamic model constants, range bias, and a number of instrument attitude coefficients. The attitude of either the imager or the sounder instrument is characterized by five (5) angles: roll, pitch, yaw plus two rotation angles specifying the misalignment of the optical axis of the instrument. Each attitude angle is modeled as the sum of Fourier terms and optional polynomial and exponential terms. The original version of the software was implemented as a least squares batch filter, ingesting observations in batches of one to two days at a time. A recent enhancement to the software to include a priori knowledge of the orbit and attitude solution and their statistical properties (sequential batch filter) has been implemented. By reprocessing operational data using this new software, it is shown that the sequential batch solution obtained exhibits better daily stability as well as providing a better model for next day predictions compared to the batch solution.

Keywords: orbit and attitude determination, navigation, a priori, estimation, sequential batch filter

1. INTRODUCTION

The success of the GOES-8 Image Navigation and Registration (INR) system [1] is critically dependent on the availability of accurate spacecraft orbit and instrument attitude information. Such information is provided by the Orbit and Attitude Determination (OAD) software of the Orbit and Attitude Tracking Subsystem (OATS), one of the components of the Operational Ground Equipment (OGE).

The OAD software is designed to process range, star, and landmark data and solve for the dynamically varying spacecraft orbit and instrument attitude simultaneously. A detailed mathematical model has been developed for each type of observable in terms of the orbital and attitude states. Because the GOES operational concept called for a daily OAD solution, it was originally felt that a batch least squares procedure, ingesting 24 hours of observations, would yield sufficiently accurate and stable solution for use in the INR system.

The first year of GOES operational experience showed that the batch solution is generally quite adequate. However, when large data gaps existed or when star observations were not well distributed (as during single-chord operations or eclipse), the batch solution could become quite poor. High correlations among solve-for parameters leading to large estimated errors were the inevitable consequences in such cases. To circumvent these problems, the OAD software has recently been enhanced to include the option of *a priori* processing making it a *sequential batch filter*. Underlying this optional processing mode is the assumption that the spacecraft orbital elements and the instrument attitude behavior are inherently repeatable from day to day; therefore, the knowledge already obtained for the solution based on prior data could and should be carried over into the current solution. This *a priori* knowledge should help stabilize the current

 0-8194-2200-2/96/$6.00

solution should the current span of data be inadequate for the above-stated reasons. This paper describes the algorithm and implementation techniques used for this software enhancement.

In the batch processing mode, a brand new solution is obtained by processing the data presented. Any prior knowledge of the orbit and attitude has no impact on the new solution. The current solution (as stored in the data base) is used only as an initial guess, or a "nominal solution" to start the differential correction process. One could equally well use any reasonable guess, totally unrelated to the current solution, to start the iterations and would still come up with essentially the same final solution in batch processing.

In the sequential batch processing mode, the prior (existing) solution and its covariance matrix are treated as *a priori* information and not merely used as a guess. *A priori* information can be thought of as additional data weighted by the *a priori* covariance matrix. It can be used in conjunction with the new observational data for determining the new solution. The new solution would minimize a combined "cost function" based not only on the new observations, but also on the *a priori* knowledge of the solution. The (sequential) process can be continued indefinitely using the current solution as *a priori* to process the next batch of data. Thus, at any point in time, the resulting *a priori* solution embodies, in some sense, the contribution of all previous data.

2. MATHEMATICAL FORMULATION OF OAD

The OAD mathematical model is briefly described in this section. The model consists of the *observation model* which relates the three types of observbables to the (orbit and attitude) state vector, and the *state model* which describes how the state vector propagates in time.

2.1 Coordinate Systems

The primary inertial reference system for OAD is the *Earth's Mean Equator and Mean Equinox of B1950.0 ("EME 1950")* Coordinate System. In this reference frame, the origin is at the center of the Earth, the fundamental XY-plane coincides with the mean equatorial plane of the Earth at epoch of 0 hr UT on 1 January 1950, and the X-axis is in the direction of the mean equinox at epoch. The Y-axis is 90 degrees counterclockwise from the X-axis on the equatorial plane, and the Z-axis points toward the north pole. To describe observables at any instant of time, the reference frame called the *True Equator and True Equinox of Date ("True-of-Date")* is used. In this system, the fundamental plane coincides with the *instantaneous* equator of the Earth and the X-axis is aligned with the true direction of the Vernal Equinox. Precession, nutation, and polar motion account for the differences between the two frames.

To describe observations made by the on-board instrument, it is convenient to introduce a moving coordinate system with origin at the center-of-mass of the spacecraft, z-axis directed toward the geocenter, y-axis in the negative angular momentum vector direction, and x-axis completing the right-handed orthonormal triad x_s, y_s, z_s. We call this frame of reference the *Orbital Coordinate System (OCS)*. Furthermore, to study attitude variations of the spacecraft and its onboard instruments, we also need the *Instrument Coordinate System (ICS)*, also known as the Instrument Body Frame. The origin of the ICS is the center of the scan mirror of the instrument while its axes (x_b, y_b, z_b) are derived from the OCS frame by rotating each of the 3 OCS coordinate axes (x_s, y_s, z_s) repsectively by the attitude angles called *roll* (ϕ), *pitch* (θ), and *yaw* (ψ) in that order.

2.2 Observation Model

Three types of observables are processed by OAD: range, star scan angles, and landmark scan angles.

The range observable is derived by measuring the time delay between the uplink (modulator input) retransmitted signal and the downlink (splitter output) retransmitted signal. The time delay is transformed into a distance (range) by multiplying with the speed of light. Because of the relative motion of the spacecraft and the tracking station and the finiteness of the speed of light, the time-delay derived quantity is not exactly equal to the geometric range. Furthermore, corrections need to be made for the propagation delays due to the troposphere and the ionosphere. Any known electronic delays must also be taken out. The unknown delays are modeled by means of a solve-for "range bias" constant. Thus, the mathematical model of the range observable is:

$$\rho = |\vec{r} - \vec{R}| + \rho_b \tag{1}$$

where $\vec{r}$ is the position vector of the spacecraft at the observation time, $\vec{R}$ is the position vector of the ground station, and ρ_b is the range bias. The range bias term, ρ_b, is peculiar to the particular tracking station due to inherent clock synchronization errors, cable delays, and other unknown effects. It is assumed that the range bias is a slowly varying function in time. In the OAD, the range bias is assumed to be a constant and will be estimated along with other adjustable parameters.

Both star and landmark observables are derived by measuring the line-of-sight (LOS) direction of the instrument (Imager or Sounder) during star sensing or imaging/sounding. The LOS in any coordinate system is specified by two angles of rotation. For the GOES instrument, these angles are called the East-West scan angle, E, and the North-South scan angle N. The star line-of-sight direction is subject to errors due to proper motion, parallax, and both annual and planetary aberration. These effects must be removed by preprocessing the star scan angle data. Landmark scan angles must be compensated for INR errors and for aberration. Once these errors are removed, the star and landmark scan angle can be treated as geometric quantities and modeled accordingly.

Ideally, the outer gimbal axis, or the optical axis of the instrument, is aligned with the $-x_b$-axis of the ICS. However, because of mechanical imprecision and thermal distortion effects, such may not be the case in reality. As a result, to completely define the state of the instrument relative to the spacecraft roll-pitch-yaw state, two additional parameters are needed for specifying the misalignment of the optical axis: the roll misalignment(ϕ_{ma}) and pitch misalignment (θ_{ma}). The five attitude angles are collectively referred to as the attitude state vector β.

The scan angle observables are functions of the orbital state vector and the instrument attitude state vector. The following mathematical model has been developed for the scan angle observables, for landmarks and stars alike:

$$E = \sin^{-1}(\hat{s} \cdot \hat{x}_b) + \delta E_{ma} \tag{2}$$

$$N = \tan^{-1}[-(\hat{s} \cdot \hat{y}_b)/(\hat{s} \cdot \hat{z}_b)] + \delta N_{ma} \tag{3}$$

where $\hat{s}$ is the line-of-sight unit vector from the S/C to the landmark or star, $\hat{x}_b, \hat{y}_b, \hat{z}_b$ are the unit vectors of the ICS, and $\delta E_{ma}, \delta N_{ma}$ are corrections to the respective scan angles due to the optical axis misalignment effect. By considering the geometry of the mirror and detector subsystem of the instrument, the following equations for the misalignment effect has been derived:

$$\delta E_{ma} = -\phi_{ma} \sin N - \theta_{ma} \cos N \tag{4}$$
$$\delta N_{ma} = (-\phi_{ma} \sin N + \theta_{ma} \cos N)/\cos E \tag{5}$$

The components of the line-of-sight vector in the ICS are related to the components in the OCS by a rotation:

$$\hat{s}_b = M_E \hat{s}_s \tag{6}$$

where

$$\hat{s}_b = (\hat{s} \cdot \hat{x}_b, \hat{s} \cdot \hat{y}_b, \hat{s} \cdot \hat{z}_b) \tag{7}$$
$$\hat{s}_s = (\hat{s} \cdot \hat{x}_s, \hat{s} \cdot \hat{y}_s, \hat{s} \cdot \hat{z}_s) \tag{8}$$

and M_E is a rotation matrix commonly referred to as the Euler Matrix. It can be thought of as the product of three successive rotations about the roll, pitch, and yaw axes. If these rotations are performed in the "1-2-3" order; i.e., first a rotation by ϕ about the x-direction, followed by a rotation by θ about the new (body) y-direction, and finally followed by a rotation by ψ about the new z-direction, then the Euler Matrix takes the following form:

$$M_E = \begin{pmatrix} C_\theta C_\psi & S_\phi S_\theta C_\psi + S_\psi C_\phi & -C_\phi S_\theta C_\psi + S_\psi S_\phi \\ -C_\theta S_\psi & -S_\phi S_\theta S_\psi + C_\psi C_\phi & C_\phi S_\theta S_\psi + C_\psi S_\phi \\ S_\theta & -S_\phi C_\theta & C_\phi C_\theta \end{pmatrix} \tag{9}$$

The unit vectors in the OCS are given in terms of the S/C position and velocity vector:

$$\begin{aligned} \hat{z}_s &= -\vec{r}/r \\ \hat{y}_s &= -\frac{\vec{r} \times \vec{v}}{|\vec{r} \times \vec{v}|} \\ \hat{x}_s &= \hat{y}_s \times \hat{z}_s \end{aligned} \tag{10}$$

Note that the entire attitude dependency of the scan angle observables is contained in the matrix elements of M_E .

2.3 State Model

To estimate ever-changing orbit and attitude states from measurements of state-dependent observables, one must be able to parametrize the states in terms of constant parameters. In the case of the orbital state, the constant parameters can be taken to be the orbital elements at a particular epoch, plus a number of constant parameters that characterize the dynamics of the spacecraft such as the solar radiation constant and the thrust parameters. The orbital model used in OAD is based on the proven Air Force AOES formalism [2] and will not be detailed here.

Each component of the attitude state vector $\vec{\beta} = (\phi, \theta, \psi, \phi_{ma}, \theta_{ma})$ is modeled mathematically as a time series composing of a finite Fourier series, a polynomial, and an exponential:

$$\beta_i = \sum_{n=1}^{n_f} [c_n \cos n\omega t + s_n \sin n\omega t] + \sum_{j=0}^{n_p} a_j (\omega t)^j + \sum_{k=1}^{n_e} \epsilon_k e^{-(t-\tau_o)/\tau_k} \tag{11}$$

In this equation, $\beta_i, i = 1, \ldots, 5$ is the ith attitude angle, n_f, n_p are the maximum orders of the Fourier and polynomial terms, c_n, s_n are the cosine and sine coefficients, a_j are the polynomial coefficients, n_e is the number of exponential terms, $\epsilon_k, k = 1, \ldots, n_e$ are the exponential coefficients, τ_k are pre-determined constants, and ω is the daily solar rate. It is understood that the subscript i which should be attached to each of the coefficients in order to distinguish a particular attitude angle has been suppressed for notational simplicity.

The Fourier terms are chosen because the Sun's apparent movement about the Spacecraft in the course of a day would cause near-periodic thermal distortions of the attitude and misalignment angles, whereas the polynomial terms are chosen to model the nonrepeatable behavior in attitude caused by such phenomena as Earth sensor radiance gradient, clouds, and Earth's magnetic field variation effects on spacecraft yaw. Exponentials are intended for use to model rapid attitude change upon entering and exiting eclipses. In practice, polynomials only up to quadratic have proven to be sufficient to model the daily nonrepeatable attitude behavior and exponentials have not been required.

3. THE SEQUENTIAL BATCH FILTER

Range, landmark, and star measurements can be fitted to the mathematical model described in Section 2 to determine the orbital elements, dynamics modeling parameters, range bias, and an appropriate number of attitude coefficients via the method of least squares. The original OAD software was developed as a least squares batch filter and has been used to operate the GOES spacecraft successfully since the beginning. However, occasionally, it was found that the daily attitude solution obtained via the batch filter lacked the anticipated stability required to register quality images. The problems are most noticeable when there exist sizeable data gaps in the input observation span, and when star distributions are scarce and poor. It was then suggested that the solution can be stabilized by means of a "sequential batch filter," with the capability of processing *a priori* information.

The basic premises for *a priori* processing are the presumed stability of a subset of the parameters in the solve-for parameters space. For the current OAD software enhancement, the subset of parameters considered to exhibit stability are the six orbital elements and the Fourier attitude coefficients. It is recognized that the ramp and the quadratic coefficients used for modeling the nonrepeatable daily variations of the attitude angles are inherently nonrepeatable, and thus are not treated as *a priori* parameters.

3.1 A Simple Illustration of the *A Priori* Concept

The concept of *a priori* (sequential batch) processing can be illustrated by means of a simple example. Consider the problem of estimating the length of a rod by making repeated measurements with a meter stick. Let us say we have taken n_a measurements of the rod length, $y_i, i = 1, 2, \ldots, n_a$ with the 1-σ error on each measurement estimated as $\sigma_i, i = 1, 2, \ldots, n_a$. From these measurements, we can obtain a pretty good estimate of the rod length and its standard deviation using the "weighted average" formulas:

$$y_a = \sum_{i=1}^{n_a} \frac{y_i}{\sigma_i^2} \Bigg/ \sum_{i=1}^{n_a} \frac{1}{\sigma_i^2} \tag{12}$$

$$\sigma_a^2 = 1 \Bigg/ \sum_{i=1}^{n_a} \frac{1}{\sigma_i^2} \tag{13}$$

Suppose at a certain time later, it is decided to re-determine the rod length again by making, say, another n_b measurements $y_i, i = n_a + 1, \ldots, n_a + n_b$. With a "batch philosophy," we would ignore the previous estimate y_a and re-estimate the rod length and its error solely from the new data. For the sake of

argument, let the standard deviation of the latter estimate be larger than the standard deviation of the earlier estimate. Since the two solutions are completely unrelated, should one believe the more recent estimate with higher error or should one believe the earlier estimate with lower error?

Common sense, however, tells us that we should be able to get a better estimate of the rod length and its error by combining all n_a+n_b measurements and taking an overall weighted average. This is a consequence of the fact that the length of the rod is not expected to change between the two batches of measurements. Alternatively, we can adopt the "sequential processing philosophy" by treating the previously obtained solution (y_a, σ_a) as an additional piece of (highly precise) data. A new estimate $(\tilde{y}, \tilde{\sigma})$ can be obtained by taking the weighted average of the new ("batch b") data **and** this additional data. The reader can easily verify that the sequential batch solution $(\tilde{y}, \tilde{\sigma})$ is indeed equal to the overall solution $(\bar{y}, \bar{\sigma})$. This is the beauty of sequential processing: knowledge gained from processing previous data is not lost, it is used in a statistically correct way together with the new data to determine new solutions.

3.2 Least Squares Formulation with *A Priori*

Since the observation equations for OAD is inherently nonlinear, it is necessary to formulate the *a priori* processing algorithm as a nonlinear estimator. The corresponding theory for a *linear* sequential estimator is well developed in the estimation theory literature [3].

The nonlinear observation model can be written generically as follows:

$$y = y_c(x) + \epsilon \tag{14}$$

where y is the observation vector, x is the solve-for parameters vector, $y_c(x)$ is the (nonlinear) model function, and ϵ the noise vector. The covariance of the noise vector, Γ_ϵ and the data weight matrix W are defined as in the linear model.

Let an *a priori* solution vector x_a and the corresponding *a priori* covariance matrix Γ_a be given. The *a priori* information matrix Λ_a is defined to be the inverse of the *a priori* covariance matrix. The sequential estimation problem with *a priori* is to determine a solution $\hat{x}$ which minimizes the following total chi-square:

$$\chi^2_{tot} = \chi^2_{newdata} + \chi^2_{apriori} \tag{15}$$

with respect to all candidate solutions x where

$$\chi^2_{newdata} = [y_o - y_c(x)]^T W [y_o - y_c(x)] \tag{16}$$

$$\chi^2_{apriori} = f_a (x - x_a)^T \Lambda_a (x - x_a) \tag{17}$$

and f_a is a so-called "*a priori* retention factor" (formerly known as the "forgetting factor") used for tuning the relative strengths of the *a priori* information matrix relative to the new data information.

The solution that minimizes the above total chi-square can be developed using the "differential corrections" approach. In general, several iterations are needed before convergence can be achieved. For each iteration, we start with a *nominal* solution x_0. The nominal solution for the first iteration may conveniently be equated to the *a priori* solution x_a, but that is not necessary. Any good guess will do. The nominal solution for successive iterations are determined from the previous iteration's corrected solution whereas the *a priori* solution remains unchanged throughout the differential correction process.

Once a nominal solution, x_0 has been established, the observation model can be expanded about it and the nonlinear estimation problem is effectively linearized. The linear estimation equations can be solved via standard techniques, giving the following expression for the differential correction vector δx:

$$\delta x = (A^T W A + f_a \Lambda_a)^{-1} [A^T W \delta y + f_a \Lambda_a \delta (x_a - x_0)] \tag{18}$$

and the covariance matrix of the new nominal solution is given by

$$\tilde{\Gamma} = (A^T W A + f_a \Lambda_a)^{-1} \tag{19}$$

Here,

A is the matrix of partial derivatives of the components of the observation vector with respect to each of the solve-for parameters, evaluated at the nominal solution,

W is the data weight matrix,

f_a is an a priori tuning factor. (Value 1 means a priori data receives full weight as current data),

Λ_a is the a priori information matrix (inverse of the a priori covariance matrix), and

The differential correction obtained from the linear estimator is added back to the nominal solution to get an improved solution which is then used as the new nominal solution to start the next iteration. This process is repeated until convergence is established based on the behavior of the actual and predicted RMS residuals satisfying either one of the following criteria:

a) The actual RMS residual for each data type falls below a pre-specified level;

b) The percentage change of the predicted total RMS residual for the next iteration from the actual total RMS residual for the current iteration is less than a specified level.

The solution may also be accepted or rejected manually by opeator action.

4. IMPLEMENTATION

The original OAD software is implemented in FORTRAN for the Encore MPX-32 multitasking computer system and later ported to the Digital Equipment Alpha workstation. The sequential batch enhancement is implemented for the workstation. A number of improvements and bug fixes to the original OAD were accomplished during the course of the software enhancement.

Some highlights of the OAD implementation and enhancement are as follows:

a) The equinoctial orbital elements are used internally to avoid any singularities due to zero inclination and eccentricity.

b) All partial derivatives are analytically evaluated with the exception of certain perturbative partials which are obtained semi-analytically during ephemeris generation.

c) The spacecraft roll and pitch attitude angles are highly correlated with the instrument misalignment angles. To minimize the correlations, the following modified variables ϕ_n, θ_n are solved in place of spacecraft roll (ϕ) and pitch (θ):

$$\phi_n = \phi + \phi_{ma} \tag{20}$$

$$\theta_n = \theta + \theta_{ma} \tag{21}$$

These modified roll and pitch can be determined to much higher precision than the spacecraft roll and pitch from the scan angle observables.

d) The normal equation is sequentially accumulated and symmetric matrices are stored linearly to conserve storage. Solution of the normal equation is via the numerically stable technique of Cholesky decomposition.

A block diagram of the OAD process flow is presented in Figure 1.

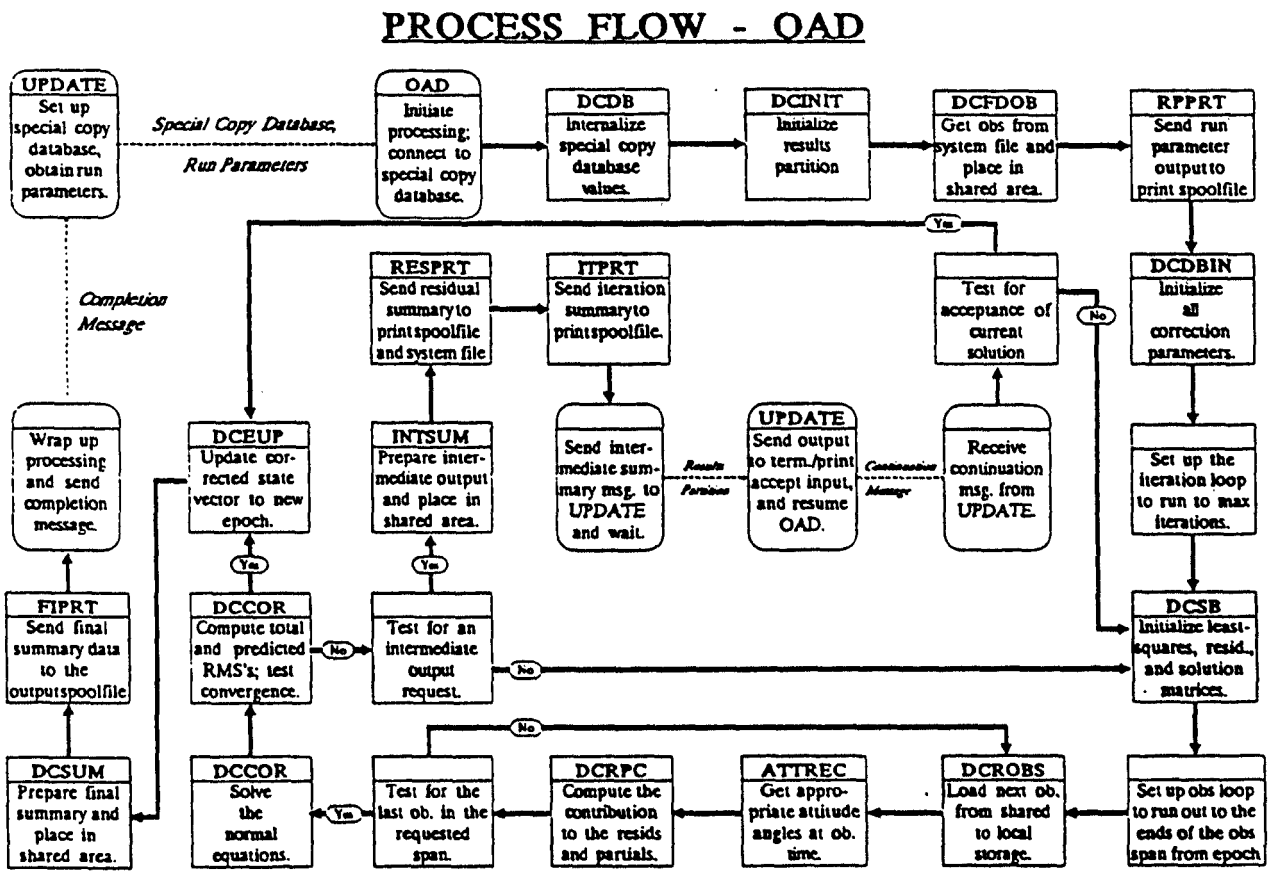

Figure 1. OAD Process Flow Diagram

5. TESTING

The *a priori*-enhanced OAD software has been extensively tested for its intended purpose and for robustness against inadvertent user errors. The following spans of data, from three separate periods, have been examined and used in these tests:

Set 1. Processed observations from 1995 Day 257 through Day 272 (Eclipse data).
Set 2. Processed observations from 1995 Day 297 through Day 312
Set 3. Processed observations from 1995 Day 358 through 1996 Day 3.

Of the multitude of tests conducted, the following ones are of particular interest:

• *Theory Test: Multi-Day vs Sequential Batch Solutions.* According to theory, if the model parameters are stable, then the "last" sequential batch solution should be equivalent to the "overall" solution provided that the *a priori* information is considered at full strength. A simple example illustrating this result has been given in Sec 3.1. In the context of OAD, a "two day non *a priori*" solution (Solution A) is shown to be substantially equivalent to the "second-day sequential batch solution" (Solution B) having the first day's non *a priori* solution as fully-weighted ($f_a = 1$) *a priori* information. Figure 2 shows results of comparing the two solutions. The difference between the solutions are plotted. The agreement between the two solutions in roll, pitch, and yaw are seen to be excellent, with maximum difference less than 10 μrad. The larger (maximum 100 μrad) discrepancy between the two misalignment solutions are probably due to the instability of misalignment during the two day span.

• *Stability Tests.* The *a priori* solution produces more stable attitude profiles than the non-*a priori*, two-day thinned solutions. This can be seen by examining Figure 3 shows attitude profiles for multiple days on the same plot: 3a for *a priori* solutions and 3b for batch solutions. It is seen that the a priori solutions are considerably more stable in terms of day to day variations than the batch solutions.

• *Gap Test.* The *a priori* solution is stable across large gaps of data. The software performs a check on the sufficiency of the number of "relevant data points" in relation to the number of *non-aprioried* solve-for parameters. There is therefore no need to pay special attention to gap lengths, as is necessary in a batch solution where the gap length dictates the maximum Fourier order that can be used. In the Gap Test, a large, 5-hour gap is created by manually deleting a span of observations (in Day 311) in the Processed Obs File, thereby simulating the entrance to an eclipse. Comparison of the "two day batch" solution with the "2nd day *a priori*" solution shows better agreement than the comparison between two successive batch solutions. This is due to the fact that the second batch solution has to fit across the long gap.

• *Prediction Residuals Tests.* The *a priori* solution generally leads to prediction residuals that are less jumpy at the start and the standard deviations of the prediction residuals are generally smaller than its non *a priori* counterparts. Figure 4 shows 24-hour prediction residuals starting at 1996/003/2100, based on the regular "2-day batch" solution and on the "1-day *a priori*" solution. The quality of the two predictions are quite comparable, with a slight edge given to the *a priori* solution.

6. CONCLUSIONS

The sequential batch enhancement has been successfully implemented into the operational OAD software. Based on comparison of results of reprocessed data with and without the use of *a priori*, use of the enhanced OAD could result in the following benefits:

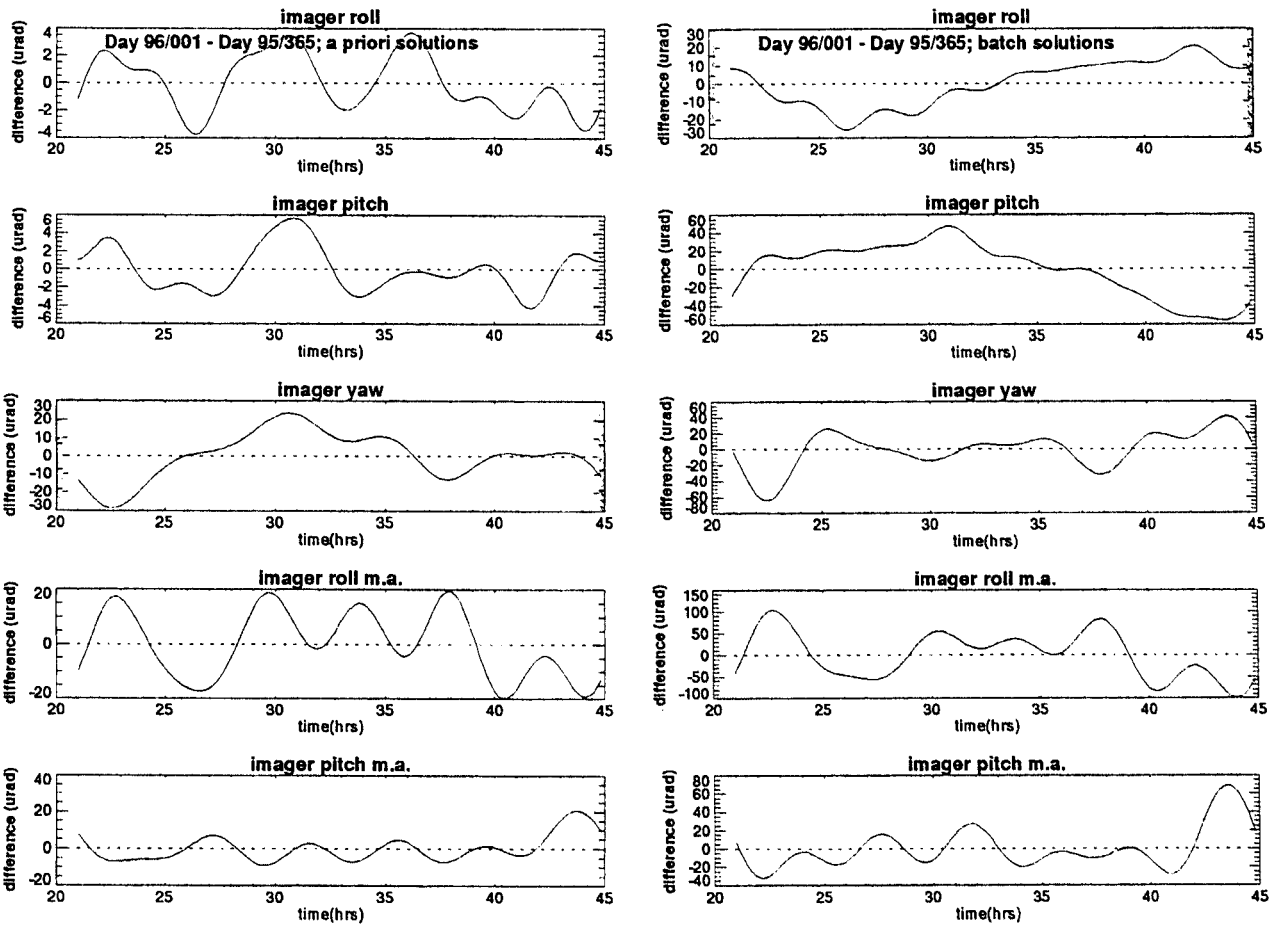

Figure 2. Theory Test: Multi-day vs. Sequential Batch Solutions

a) The day-to-day variation of orbit and attitude would be more gradual for successive *a priori* solutions than for batch solutions;

b) The *a priori* solution should be able to handle scarce data sets, or very short data spans, without causing the least squares process to become singular;

c) The *a priori* solution should be insensitive to long data gaps. In ordinary batch solution, long data gaps typically cause very high correlations among solve-for parameters and often lead to spurious oscillatory attitude behavior. "Stop gap measures" have been suggested to lower the orders of the Fourier fits to cut down the oscillations, but at the sacrifice of modeling accuracies. With the use of *a priori*, the solution across long gaps should be stable and the nominal Fourier orders in use need not be tampered with.

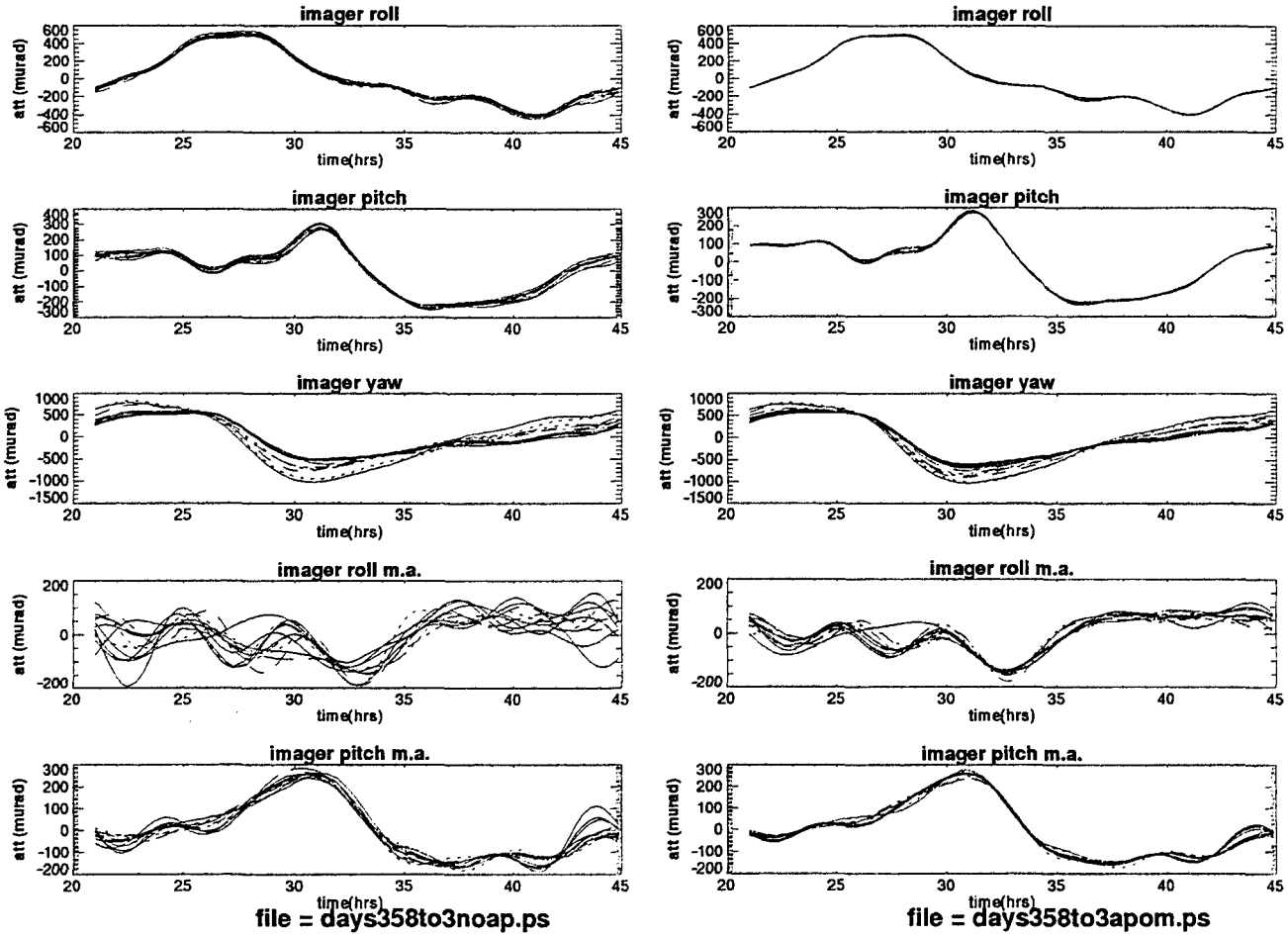

(a) Batch Solutions

(b) A Priori Solutions

Figure 3. Stability Test: Overplot of Multiple Day Profiles

d) It is not necessary to process very long spans of data at one time to get a good solution, as the *a priori* process actually retains the knowledge accumulated.

e) The *a priori* solution is a better solution than an *averaged* batch solution over multiple successive spans, since the correct statistical properties are taken into account in the *a priori* solution but not in the averaged solution. In an averaging scheme, the correlations among solve-for parameters are completely ignored.

7. ACKNOWLEDGMENTS

The authors would like to acknowledge the contributions of J. Goddard and M. Veneroso to the implementation of the original version of OAD and thank Mr. Veneroso for capably implementing the user

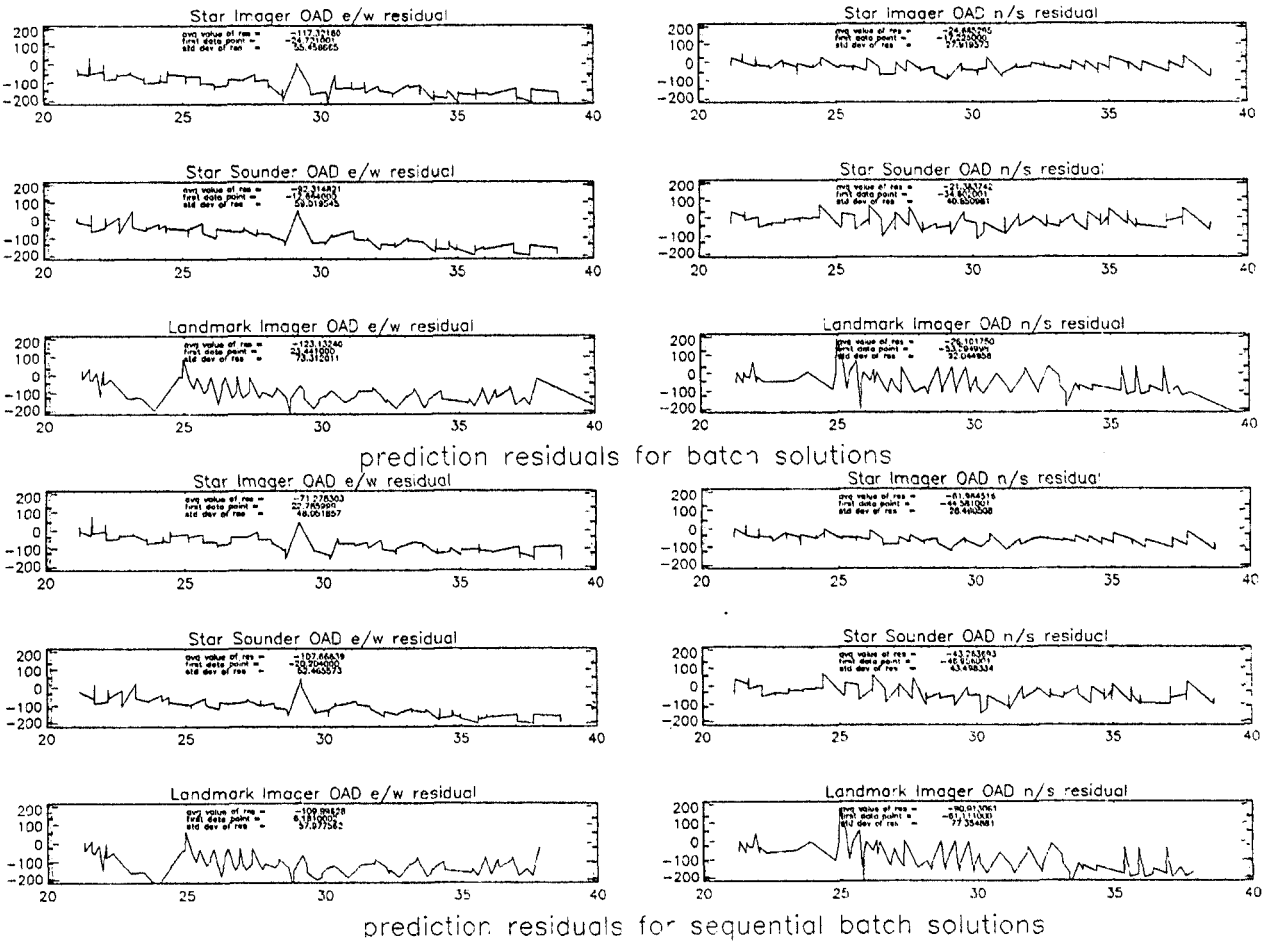

Figure 4. Prediction Residuals Test

interface for the enhanced software. Constant encouragement from Dr. A. A. Kamel and from S. R. Reyes has made this project possible.

8. REFERENCES

1. A. A. Kamel, "GOES Image Navigation and Registration System," GOES-8 and beyond SPIE proceedings Vol. 2812, August 1996.

2. P.E. Koskela, "Astrodynamic analysis for the Advanced Orbit/Ephemeris Subsystem," Aeronutronic Publication No. U-4180, Philco-Ford Corporation, Newport Beach, CA, 1 September 1967.

3. H. W. Sorenson, "Parameter Estimation," Marcel Dekker, Inc., 1980.

On-Orbit Jitter Performance of the GOES Spacecraft and Instruments

John Sudey, Jr.
Wayne Dellinger

Swales and Associates, Inc.
Beltsville, Maryland 20705

Mike Hagopian

NASA Goddard Space Flight Center, Code 723
Greenbelt, Maryland 20771

ABSTRACT

This paper presents jitter performance of the Geostationary Operational Environmental Satellite (GOES) spacecraft and instruments. Of primary interest is the validation of design and ground test procedures with on-orbit data. System requirements, spacecraft and instrument disturbances, ground testing techniques, and on-orbit testing are discussed. Dynamic spacecraft signatures during appendage deployment are illustrated and used to determine spacecraft modal response frequency and damping. Specific analysis results from Angular Displacement Sensor (ADS) data, used to measure jitter dynamics from 0.2 to 160 Hertz, and Digital Integrating Rate Assemblies (DIRAs), used to measure low frequency, are detailed with regard to solar array, momentum wheel, and other spacecraft disturbances including those generated by instruments during scanning and slewing. Emphasis is also given to feed-forward pointing compensation and optimization of the solar array stepping. This optimization reduces pointing errors, improves image registration, and reduces pixel smear. Performance is illustrated with sensor statistics, Fast Fourier Transforms (FFTs), and Earth images. Both long term as well as short term evaluations are presented.

Keywords: GOES, Jitter, FFT, On-Orbit Measurement, Disturbances, Dynamics, Damping

1. INTRODUCTION

Earth viewing instruments with requirements for highly accurate co-registered images are being proposed and developed as integral components of present and future spaceflight missions. These instruments are highly sensitive to angular displacements caused by wide bandwidth disturbance torques which often excite relatively low frequency bending and torsional modes. While the engineering community is required to make early performance predictions of these precision pointing instruments, accurate pre-launch predictions are difficult to obtain due to a limited ability to test large flexible structures in a gravitational environment. Even once in orbit, pointing performance is often difficult to ascertain due to limited instrumentation. An understanding of these limitations by the Geostationary Operational Environmental Satellite (GOES) Project and the National Oceanographic and Atmospheric Administration (NOAA) resulted in the latest generation of GOES spacecraft being designed with increased instrumentation. The impetus for this was the potential improvement of the follow-on spacecraft. In addition, a series of on-orbit tests and measurements to evaluate spacecraft jitter are performed. Jitter is any undesired motion that leads to error in the optical line of sight and is principally evaluated in this paper through spectral analysis of sensor measurements. The goal of these tests is to characterize the spacecraft dynamics and improve performance wherever possible by appropriate selection of operational modes and ground processing. Moreover, large amounts of data are collected as part of normal trending operations with which spacecraft dynamics can be evaluated.

1.1 Spacecraft Description

These new GOES spacecraft are designed and built by Space Systems/Loral (SS/L) and consist of five satellites, GOES I-M (renamed GOES 8-12 after obtaining operational status). Each spacecraft provides a continuous earth pointing platform from the Geostationary orbit for two primary radiometric weather instruments, the Imager and Sounder, built by ITT. Figure 1 shows the layout of the spacecraft in the deployed orbital configuration with the Imager and Sounder mounted close to each other on the earth facing panel of the spacecraft main body. The spacecraft employs a solar array for power, solar sail to balance the solar

 0-8194-2200-2/96/$6.00

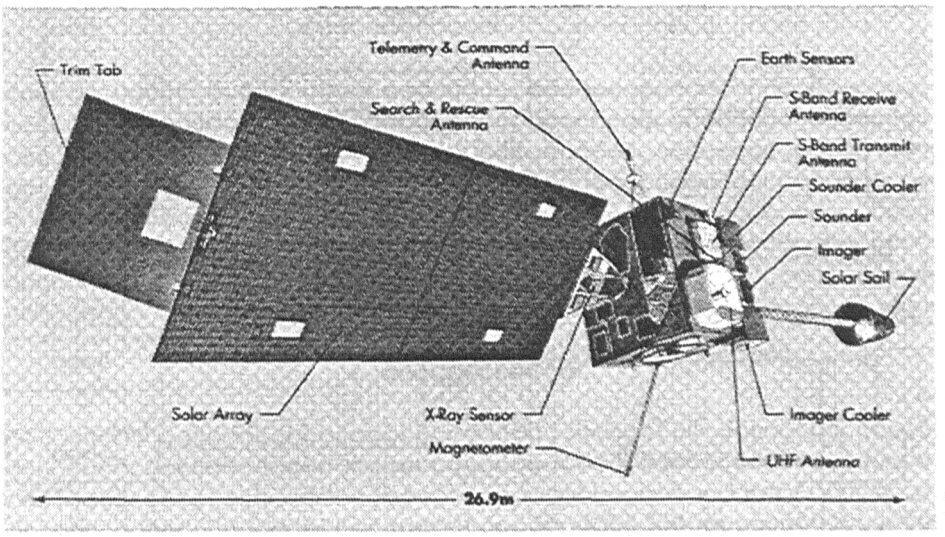

Figure 1. The GOES Spacecraft

torque on the array, and a trim tab to fine tune the balancing. In addition to the Imager and Sounder, there are five other instruments on board, the magnetometer, the X-Ray Sensor (XRS), the Energetic Particles Sensor (EPS), the High Energy Proton and Alpha Detector (HEPAD), and the Search and Rescue (SAR). The communication system utilizes two S-Band antennae, one to transmit and the other to receive. A separate antenna is used for telemetry and commanding. These antennae have a fixed orientation with respect to the spacecraft body.

Magnetic torquers provide momentum management and earth sensors provide two-axis pitch and roll information. Earth pointing roll and pitch attitude control is provided by a momentum bias system in which two momentum wheels are used in a "V" configuration. There is also a back-up mode referred to as L-1 Mode in which a reaction wheel is used in conjunction with a single momentum wheel. Yaw is not directly sensed by the attitude control system, however yaw error is derived from and controlled by roll-yaw coupling. A simple block diagram of the spacecraft control system is shown above the dotted line in Figure 2.

Digital Integrating Rate Assemblies (DIRAs) are used to control the spacecraft during all initial orbit and stationkeeping maneuvers, and occasionally to measure jitter. The DIRAs are not required for all aspects of the mission and were only designed for a limited life (2000 hours), thus they are used sparingly. In addition, DIRA data are only marginally useful due to a triangular error of 112 microradians caused by non-synchronization of the DIRA and Attitude and Orbit Control Electronics (AOCE) clocks.

Two of the GOES spacecraft include a set of orthogonally mounted Angular Displacement Sensors (ADSs) sensitive to sub-microradian levels of angular displacement. This set is located on the Imager mounting plate and oriented to measure roll, pitch, and yaw. While the ADS measurements are attenuated below 2.0 Hertz, knowledge of the transfer function allows data manipulation such that frequencies as low as 0.2 Hertz can be resolved.

A Multi-use Data Link (MDL) telemetry channel provides wide-bandwidth ADS and DIRA measurements in three modes of operation. Mode 1 provides ADS and DIRA roll, pitch, and yaw data, Mode 2 provides ADS roll, pitch, and yaw data and Imager East/West (E/W) and North/South (N/S) servo errors, and Mode 3 provides ADS roll, pitch, and yaw data and Sounder E/W and N/S servo errors. These telemetry modes can be selected by on-orbit commands.

1.2 Imager/Sounder Description

The Imager and Sounder are the primary instruments on the GOES spacecraft and have many similarities. Physically, they are mirror images of each other with their aperture openings side-by-side, as shown in Figure 1. Both instruments contain a two-axis

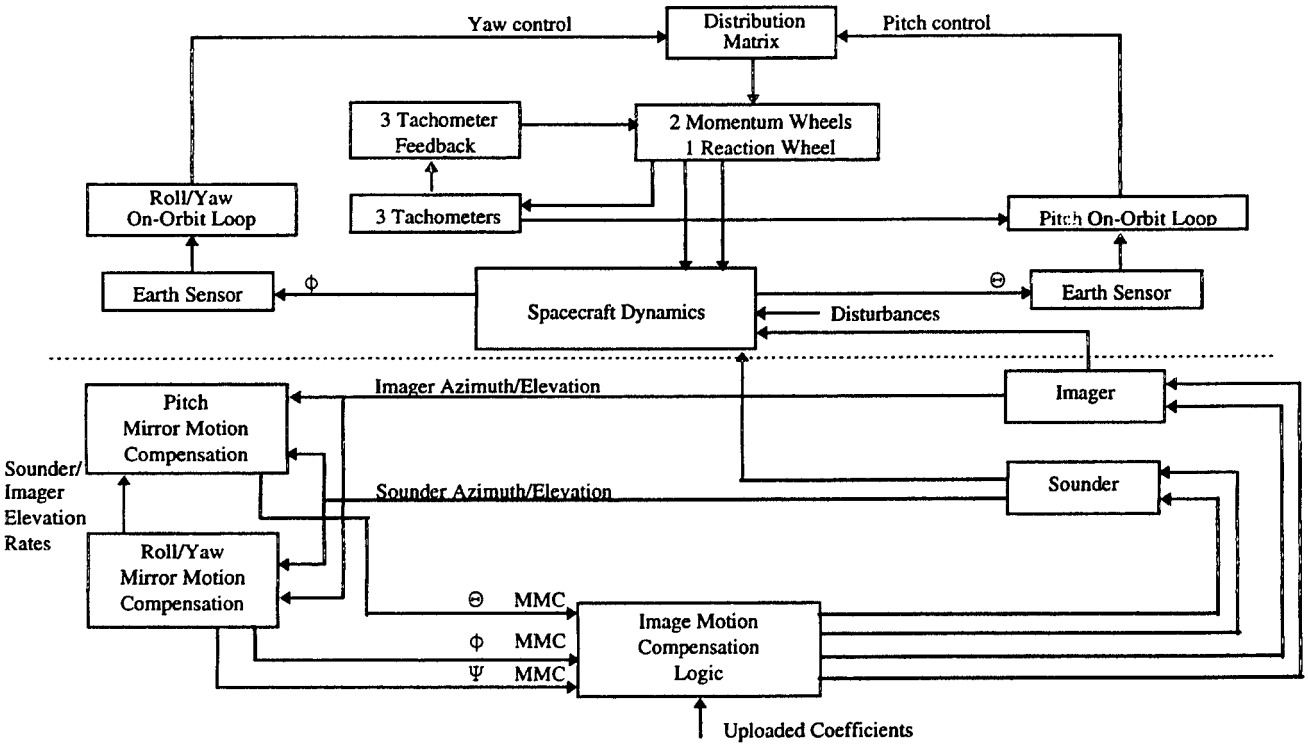

Figure 2. Spacecraft/Instrument Interface

gimbaled scan mirror system with inductosyns as control sensors and brushless DC torquers as actuators. This system allows independent motion in the N/S and E/W directions. Basic inductosyn resolution is seven bits but is electronically interpolated to twenty-one bits using a sin/cos modulation technique. Digital addressing is used to position the mirrors in the E/W and N/S directions making the instruments independently commandable to any set of coordinates within their respective field-of-view. Open-loop bandwidth of each instrument control system is 30 Hertz. Each instrument provides the capability for blackbody and spacelook calibration maneuvers. Blackbody calibrations consist of slewing the N/S axis 180 degrees from the nadir pointing position to a blackbody target while spacelooks involve slewing E/W to space. Each instrument is also capable of sensing star locations. These star data are not actively used by the attitude control system but are used by the ground software to improve Image Navigation and Registration (INR). When slewing from one location to another, the slew rate is a constant 10 mechanical degrees per second.

Imaging performed by the Imager is accomplished by scanning (slewing) from east to west or west to east. At the end of a scan line, the N/S axis steps South by 224 optical microradians, a 200 millisecond E/W turn-around profile is executed, and scanning is resumed in the opposite direction. This rastor scan format is continued until the end of the frame is reached. The Sounder differs from the Imager in that the mirror is stepped across the field-of-view by taking 100 millisecond steps. Each step moves the mirror 280 optical microradians and is required to give a nominal quiescent dwell period of 76.5 milliseconds. At the end of a line the N/S axis steps South by 1120 optical microradians and a 200 millisecond E/W turn-around profile is executed. Stepping is then resumed in the opposite direction. Timing and sampling of the various detectors is accomplished with the aid of a filter wheel spinning at 600 revolutions per minute, thus providing a sampling of all detectors with a single filter wheel revolution in 100 milliseconds.

Due to the independent operation of the instruments, the pointing of one instrument (specified to be accurate to 22 microradians zero-to-peak) is disturbed by the relatively large spacecraft motion (>150 microradians zero-to-peak) resulting from the blackbody calibration of the other. For this reason a Mirror Motion Compensation (MMC) algorithm has been implemented. MMC models the spacecraft dynamics and alters the commanded gimbal angles of the affected instrument to account for the predicted spacecraft motion. Tuning of the MMC model requires Imager, Sounder, and spacecraft telemetry (wheel speed, DIRA

data, etc.) and is performed during initial on-orbit startup operations and updated yearly to account for spacecraft mass changes due to fuel usage.

Instrument pointing errors also result from daily variations in orbit, attitude, and spacecraft thermal distortion as measured by star senses and ground landmark measurements. Ground software models these variations with a set of Fourier coefficients which in turn are used to generate Image Motion Compensation (IMC) to the instruments. Measurements from day n are used to predict the variations of day $n+1$. The AOCE uses these coefficients, along with scan synchronization signals, to generate compensation signals. These signals are then converted to the proper scan adjustments by the Imager and Sounder. Calculation of the IMC in the AOCE also provides the ability to add additional compensation to correct for unexpected disturbances. Currently, corrections are generated to compensate for unanticipated earth sensor stray light effects. Figure 2, below the dotted line, shows the spacecraft control system interface to the instruments. It should be noted that IMC only corrects slowly varying disturbances.

2. REQUIREMENTS

The GOES I-M system is required to provide and maintain line-of-sight pointing of the geographical locations of the Imager and Sounder picture elements (pixels) to a high accuracy in almost real-time. These requirements are specified in terms of INR which involves determining the location of a pixel in terms of its earth latitude and longitude and maintaining the navigation solution of a pixel within tolerable limits in time. The key pointing requirements for GOES I-M are summarized in Table 1. Derived jitter requirements include allocations of 3.5 and 3.2 microradians 1 sigma for the momentum wheels and solar array drive, respectively. More detailed navigation and registration requirements can be found in the literature.[1-4]

Navigation Accuracy	4 kilometers (3 sigma)
Registration Accuracy	42 microradians (3 sigma), within the image, 27 minutes
Co-Registration Accuracy	42 microradians (3 sigma), between the pixel in successive images of the same earth region taken within a 15 minute frame
Channel-to-channel Registration	28 microradians (3 sigma)
Derived Jitter Requirements	less than 5 microradians (1 sigma)

Table 1. Key Pointing Requirements

3. DESIGN AND TEST METHODOLOGY

The GOES I-M spacecraft have several moving and/or flexible subsystems which in combination produce disturbance torques. These include the solar array drive, momentum and reaction wheels, Imager and Sounder gimbals, Sounder filter wheel, and the flexible modes of the solar array, solar sail, and magnetometer boom. Most of the disturbances created by these subsystems are insignificant or were minimized by design. However, in critical areas they were allocated a portion of the INR error budget.

At each stage of the design and build, analyses and tests are performed to quantify instrument disturbance rejection and the levels of disturbances generated by instrument operations. Instrument disturbance susceptibility was evaluated by modeling the instrument control systems in SIMULINK. Analysis and evaluation of the Imager and Sounder disturbance effects on the spacecraft are modeled using the Fourier series representation of the periodic scan motion.[5] Of primary concern is the multitude of scan frequencies, and their harmonics, which can be generated by the many commandable image frame sizes, thus providing the opportunity to excite the various spacecraft modes throughout the mission.

Dynamic interaction between the various subsystems is monitored throughout the build. Instrument level tests are performed at ITT in which each instrument is subjected to the anticipated levels of momentum wheel disturbance for the expected wheel speed frequency range of 40 to 80 Hertz. This provides the spacecraft engineers with measured instrument sensitivities prior to instrument delivery. Once the instruments are received and mated with the spacecraft, specific interaction tests are performed in which servo errors are examined while the momentum wheel speed is varied. Wheel speed constraints are then set based upon instrument and various subsystem sensitivities. Spacecraft level testing also verifies the IMC/MMC interface with the instruments. Synchronization of the IMC with the instruments is critical to achieving minimum disturbance from this compensation signal.

Once in orbit, prior to spacecraft operational status, Post Launch Tests (PLTs) are performed to evaluate on-orbit spacecraft performance. A subset of these tests includes IMC and MMC check-out and dynamic interaction between subsystems. ADS, DIRA, instrument servo error and detector signals, and ground landmarks are analyzed to determine interaction between the instruments and between the instruments and the earth sensor. The PLT phase provides an opportunity for adjusting operational constraints with on-orbit data. Additionally, this phase offers the possibility of comparing on-orbit data with ground data with emphasis toward improving tests for subsequent builds.

4. ON-ORBIT RESULTS

4.1 Appendage Deployment

The GOES spacecraft has several appendages that are stowed for launch and are deployed during the orbit raising mission phase. Ninety minutes after launch of GOES-8 the outer solar array panel was deployed to 90 degrees from its stowed position. Its solar cells were exposed to the Sun and power was provided to the spacecraft during the transfer-orbit phase of the mission. When it was determined that sufficient power was available with adequate margin, the MDL was activated and used to transmit ADS and DIRA data during the remaining deployment operations. Initial GOES-8 ADS data showed the capture of a thruster firing transient response during orbit raising operations. The data revealed frequencies (6.8 Hertz) higher than expected.

After completion of all the orbit raising main thruster firings, when the spacecraft was near its geosynchronous orbit, the magnetometer boom was deployed. The signature of the ADS roll axis during this deployment is shown in Figure 3. Note that the ADS collection is highly sensitive and of sufficient duration to allow the determination of the boom's modal frequency and damping. The presence of a nonlinear interaction of energy transfer from higher to lower frequencies, and possibly of boundary condition changes, is apparent as demonstrated by frequency and damping variations occurring as a function of time. On-orbit measured and predicted frequencies and damping for all three axes are shown in Table 2. On-orbit data was analyzed 5 seconds after the magnetometer was locked in position. The frequency indicated is very likely the first bending mode of the magnetometer boom.

	Roll	Pitch	Yaw	Predicted/Simulated
Frequency (Hertz)	3.1	3.1	3.1	4.62
Damping (zeta)	0.0077	0.0128	0.008-0.012	0.01

Table 2. Magnetometer Modal Frequencies

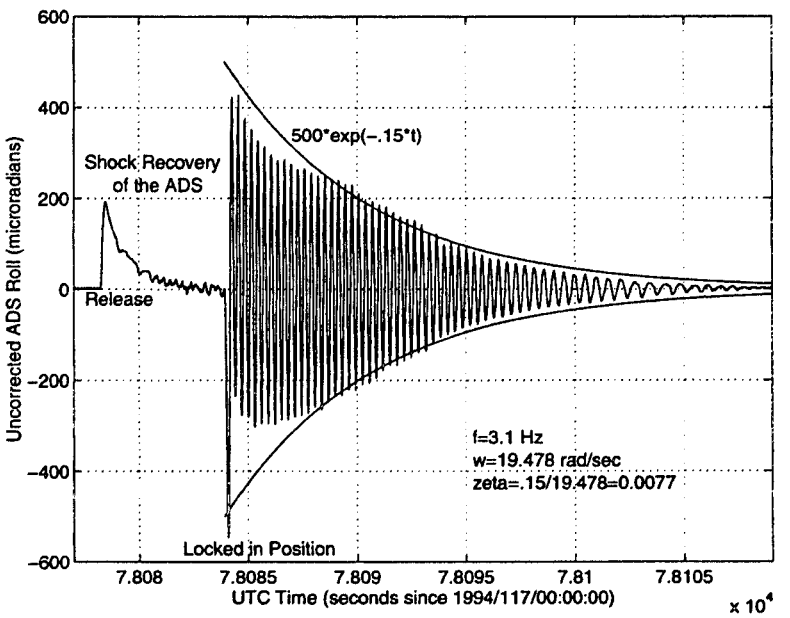

Figure 3. Magnetic Boom Deployment

Next, at the conclusion of orbit raising maneuvers, the final phases of solar array deployment were completed using the DIRA for attitude reference control. Once again a nonlinearity was apparent. Discernible frequencies were: 0.92 Hertz and 3.1 Hertz in roll; 0.92 Hertz and 1.8 Hertz in pitch; and 0.92 Hertz in yaw. The yaw damping was 0.0275; roll and pitch damping was not readily measurable due to the significant contribution of multiple frequencies. It is important to note that 1.8 Hertz was excited during solar deployment and, as will be discussed later, this disturbance frequency is one of the main contributors to spacecraft jitter.

After the spacecraft was commanded to V-mode wheel control, the solar sail and boom were extended. Again, ADS data showed a nonstationary characteristic during this deployment. Results of power spectral analysis are summarized in Table 3. Note that the 0.525 Hertz mode was not predicted but is not problematic to overall spacecraft jitter. This mode changes frequency slightly and its excitation varies throughout the orbit.

	Measured On-orbit Frequency (Hertz)			Predicted/Simulated Frequency (Hertz)		
	Roll	Pitch	Yaw	Roll	Pitch	Yaw
1st Bending	0.31	0.31	0.285	0.316	0.316	0.256
Unknown	0.525	0.525	0.525	N/A		
Solar Array	1.09	1.10	----	1.048	1.048	1.048
Solar Array	2.60	2.75	2.75	2.709	2.709	2.709

Table 3. Observed Modal Frequencies

4.2 Momentum Wheels

Extensive testing was performed on the ground to determine Imager, Sounder, and earth sensor dynamic interaction with the momentum wheels. The wheels are a major source of disturbance, mostly due to wheel imbalance, at the fundamental and associated harmonics of the wheel speed. At speeds of 4500 revolutions per minute (rpm) and above, bearing related frequencies also begin to appear, but at low levels. Momentum wheel induced disturbances are analyzed by viewing servo error and ADS data, detector images, and FFT/3D-AFT images of servo error spectra. The FFT/3D-AFT is a Fast Fourier Transform in a 3-dimensional format, relating Amplitude, Frequency, and Time and is essentially a 3-dimensional spectrogram. Amplitude is specified as the root-mean-squared value.

A test was run on GOES-8 to assess INR performance at increased momentum wheel speeds which would provide stiffer spacecraft control. This test provided a unique opportunity to correlate on-orbit wheel to instrument interaction responses to ground test data. In this test the momentum wheel speeds were increased from the nominal 2900 rpm to 4500 rpm while Imager servo error data was collected. This differs from similar ground tests in which the wheels are ramped up in unison or individually. However, assuming a linear response, the disturbance signature of each individual wheel can be separated out of the flight data to allow direct comparison. Servo error spectral variations as a function of momentum wheel speed for GOES-9 ground testing are shown in Figure 4. Results from the high-speed wheel test are shown in Figure 5. As can been seen, the signatures of servo error spectra are very similar between the two tests. One can also see the sensitivity of the Imager to the excited resonance around 60 Hertz. In both cases, the contribution of momentum wheel disturbance to Imager servo error at 2900 rpm (48.3 Hertz) is below 1.0 microradians. Overall, very good correlation between ground and on-orbit tests was found even with the testing procedure difference.

The momentum wheels can cause more severe interaction with the earth sensor. When earth sensor resonances are excited, the earth sensor response can change by as much as 0.2 degrees. This is because the earth sensor contains a galvanometer-type scanner that has a very high Q (approximately 2000). Once the critical earth sensor resonant frequencies are found through ground testing they are avoided on-orbit by constraint. The effectiveness of these keep-out zones is then verified after launch.

4.3 Short Term Performance Evaluation

Short term performance, defined here as error within a frame, can be evaluated using ADS, servo error, and IMC/MMC compensation data during imaging and sounding frames and is performed frequently. For example, E/W servo error statistics for a GOES-9 Imager full earth image on day 103 of 1996 were: mean=5.56, standard deviation=3.77, minimum=-15.96, and

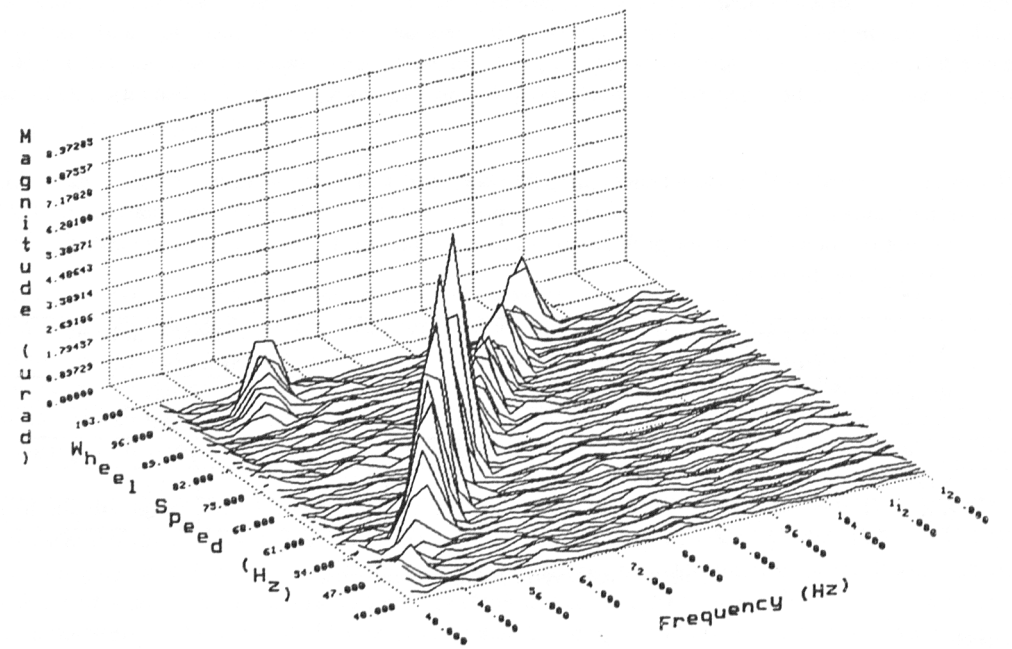

Figure 4. Momentum Wheel Disturbance - Ground Test

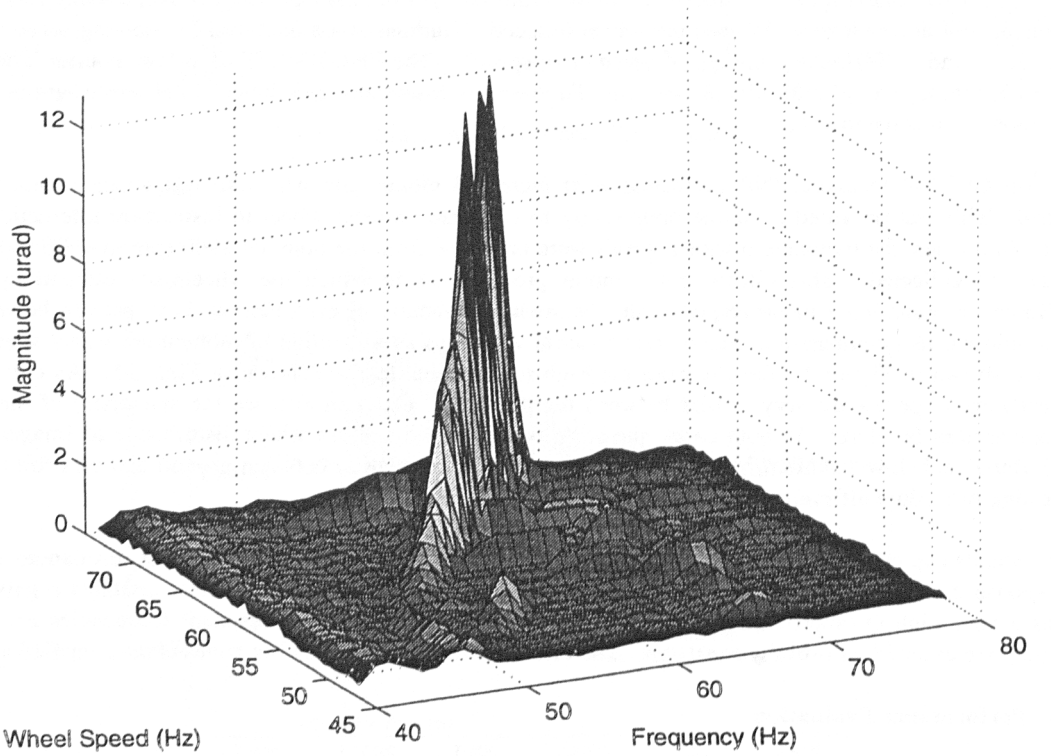

Figure 5. Momentum Wheel Disturbance - On-orbit

maximum=25.64 (all values in microradians). N/S servo error statistics were: mean=0.56, standard deviation=1.03, minimum=-7.47, and maximum=8.64. These statistics did not exceed the allocated standard deviation budget of 5 microradians one sigma despite the large MMC signal resulting from two Sounder blackbody calibrations.

Figure 6 shows the image of the N/S IMC/MMC compensation for the frame from which the above statistics were drawn. Sample number (0-5207 left to right) is along the horizontal axis and scan line number (0-1353 top to bottom) is along the vertical axis. The two light colored lines across the image are the result of an MMC correction; while the Imager was imaging the full earth, the Sounder performed two blackbody calibrations. The actual MMC correction to the N/S servo was 155 microradians, which compares favorably with the predicted value of 148 microradians.

The Imager's short term performance can be observed qualitatively in Figure 7. The moon was scanned with 38 short scans each lasting only 0.085 seconds. The widest moon scene was only 484 visible data samples and yet the image is quite crisp with only a small amount of shear visible.

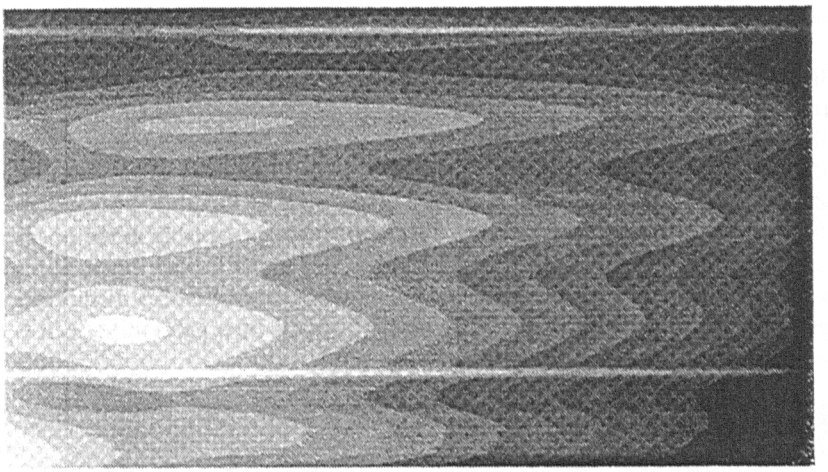

Figure 6. N/S IMC/MMC Compensation Image

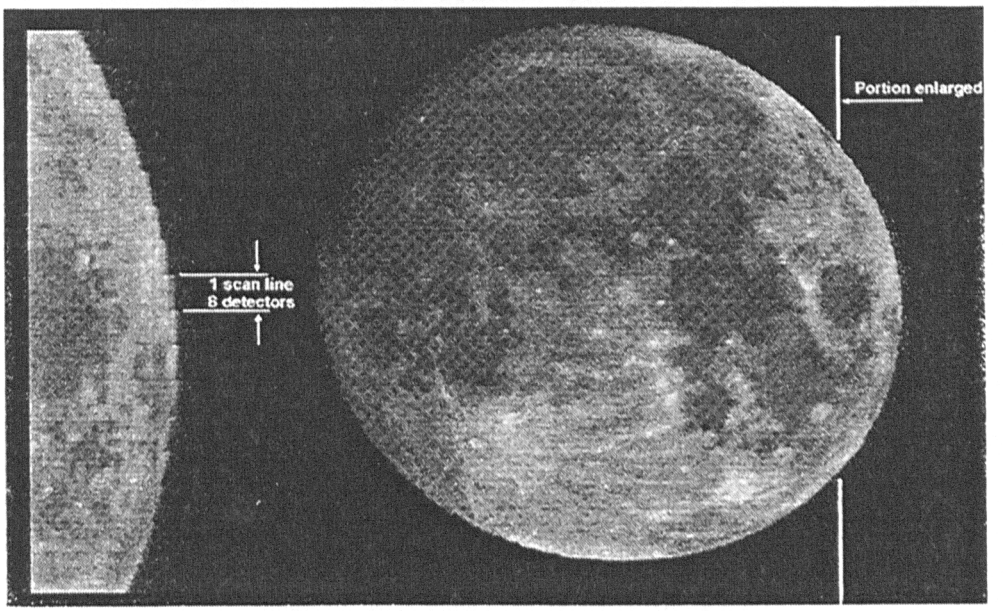

Figure 7. Moon Image

4.4 Solar Array Stepping

Early analysis and simulation of array stepping dynamics by SS/L led to a design which incorporates three on-orbit selectable stepping profiles to accommodate modal frequency uncertainty and reduce spacecraft jitter. These profiles are illustrated in Figure 8. The value of τ is 0.24 seconds for Profile 1 and 0.28 seconds for Profile 2. Note that even though the magnitudes are identical, the harmonic content is quite different between the Baseline and the other two profiles. Of even greater significance are the null frequencies, which can be moved by varying the delay between pulses. The desire is to have the most severe structural resonances occur at the solar array drive disturbance spectrum nulls.

To determine and evaluate GOES-8 jitter due to these stepping profiles, a three-day test was performed on days 100, 102, and 103 of 1995 using ADSs as the primary sensors. Results of this test are shown in Figures 9 through 12. Valid results are in the 0.3 to 2.0 Hertz range. As can be seen in these figures, the magnitude at 1.78 Hertz varies during the orbit and reaches a maximum of approximately 14 microradians peak-to-peak in pitch during the Baseline stepping. Worst case roll, pitch, and yaw disturbances for Profile #1 were approximately 60% of those measured during the Baseline stepping. Profile #2 exhibited the lowest jitter with pitch disturbances very close to 40% of Baseline and roll and yaw 30% of Baseline.

Figure 9 shows the FFT/3D-AFT of the ADS pitch axis for Baseline stepping of day 103. Note the dynamic behavior of the response. This type of graphic representation gives an excellent depiction of the spacecraft environment during normal daily operations. Amplitude nulling occurs throughout the orbit at 1.78 Hertz and some frequencies appear and disappear. The highest jitter occurs in the area of 0.3 to 0.6 Hertz because the Baseline stepping frequency is at 0.592 Hertz and Imager scanning frequencies (due to the width of the scan frames) are in this area. A top view of Figure 9 is shown in Figure 10. Jitter at 0.592 Hertz and its second and third harmonics are clearly evident. The jitter is also observable at the Imager scanning frequencies of 0.43 Hertz (full frame occurring every three hours) and 0.848 Hertz (Continental United States frame occurring every quarter-hour). The solar sail first bending frequency is evident at 0.31 Hertz. The varying frequency disturbance in the area of 1.15 Hertz is interesting because it signifies an unknown nonlinearity. However, from the jitter point of view, it is not significant because it represents only a small fraction of a microradian.

Figures 11 and 12 represent the same scenario as Figures 9 and 10 except the solar array is stepped at 0.296 Hertz by Profile #2. Here the magnitude at 1.78 Hertz is considerably smaller because of the nulling caused by this profile. Note that with this stepping frequency there is greater opportunity to excite structural resonances due to an increased number of harmonics. While this is true, it should be realized that the line spectra of these harmonics have very narrow band and thus the probability of hitting a resonance is reduced. The overall jitter is lower using Profile #2 and, based on these results, both GOES-8 and 9 now use Profile #2.

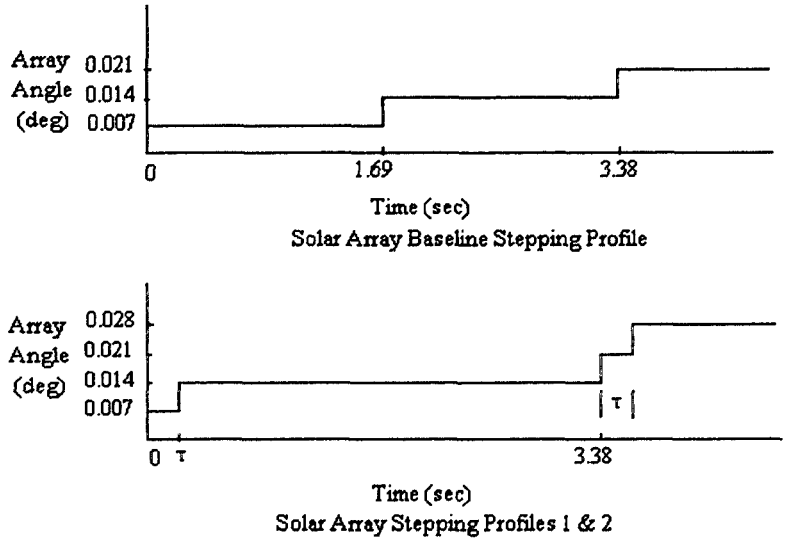

Figure 8. Solar Array Stepping Profiles

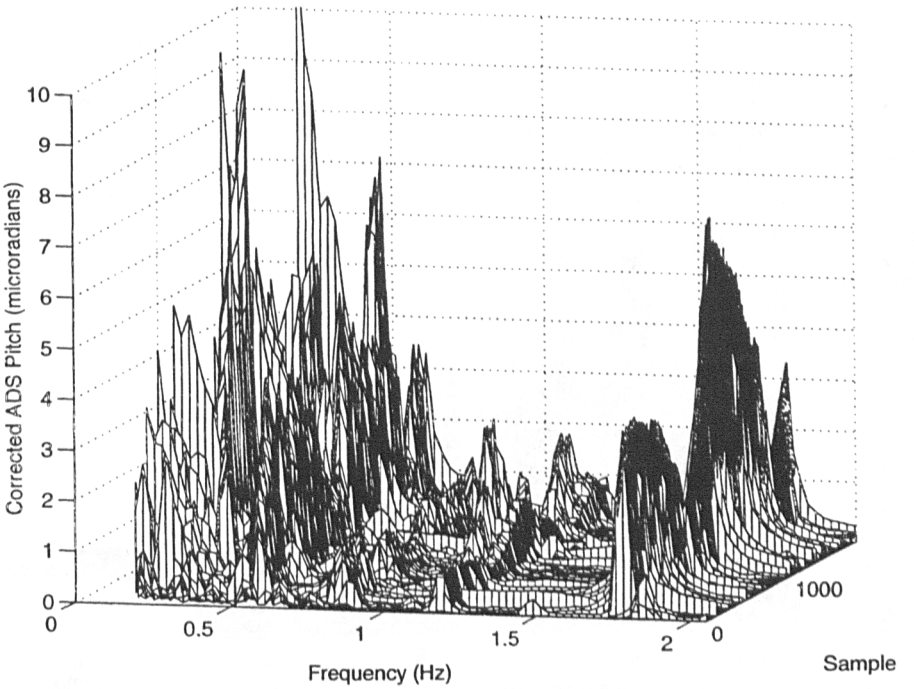

Figure 9. ADS Pitch Data, Day 103, Baseline Profile

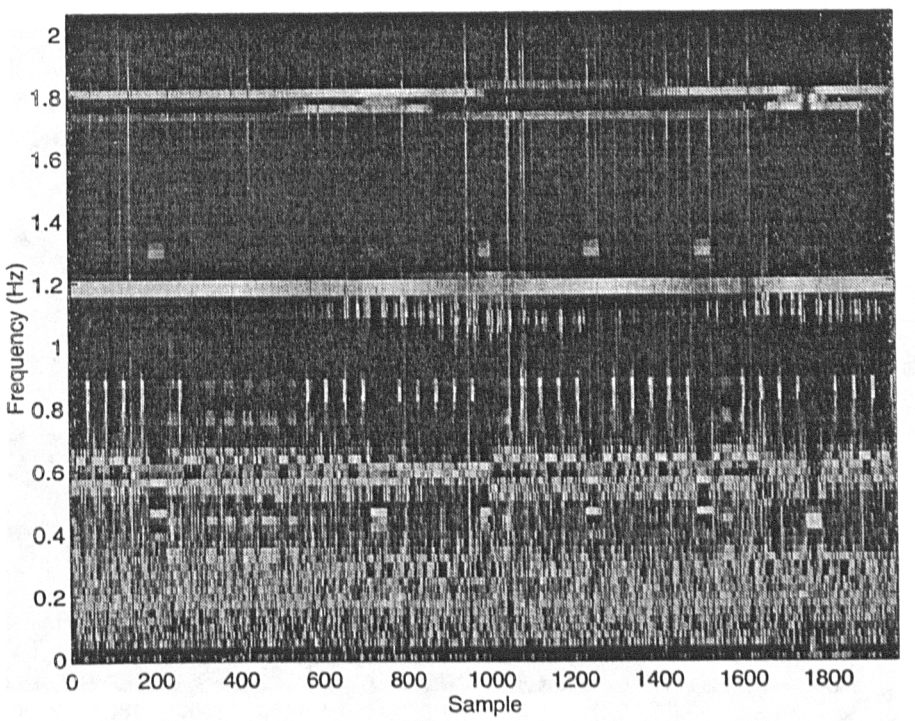

Figure 10. ADS Pitch Data, Day 103, Top View

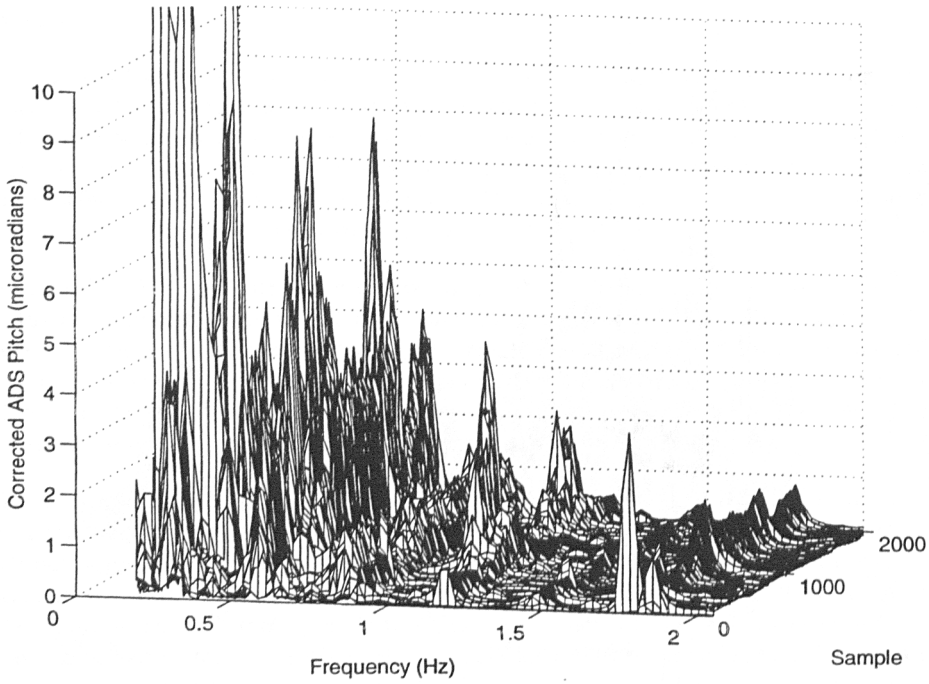

Figure 11. ADS Pitch Data, Day 102, Profile 2

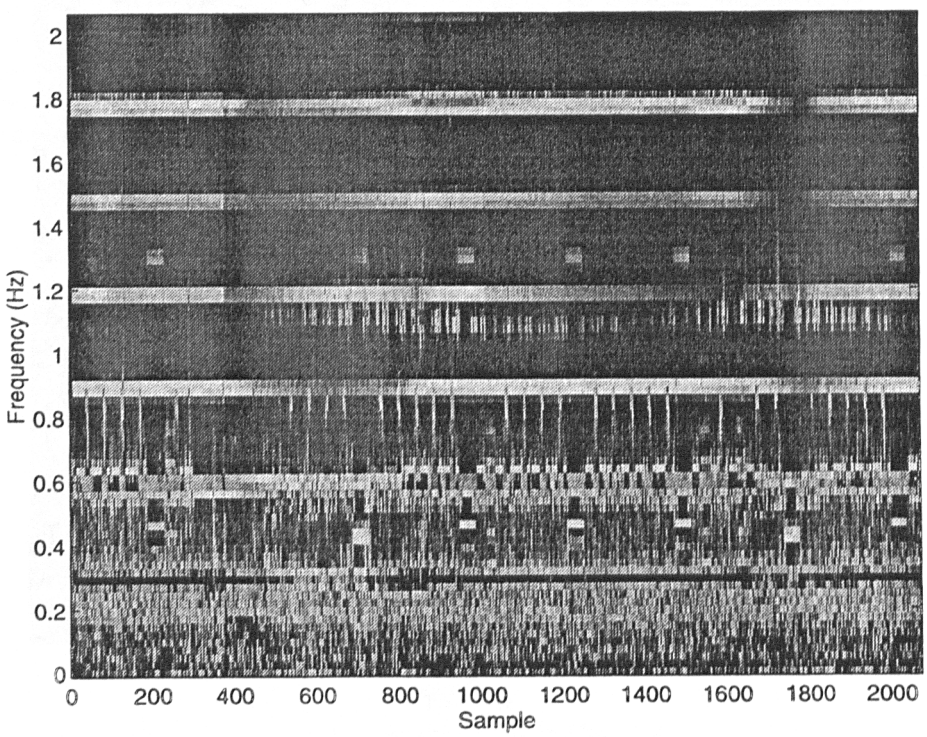

Figure 12. ADS Pitch Data, Day 102, Top View

4.5 Long Term Performance Evaluation

Long term performance is defined here in terms of performance evaluation over weeks and months. Imager and Sounder motor current and servo error, and ADS data, are collected every two weeks as part of trending activities. These data are analyzed to determine if, or how, the performance is changing. Attention is paid to collecting the same data at identical time periods so as to minimize variations due to temperature and scheduled operations.

Items for trending include motor running torque, flex-lead torque, Sounder coregistration, lubricant hilling effects, and spacecraft jitter as measured by 24 hour ADS collections. Comparisons are made between the most recent data and all previous data. Anomalies, should they exist at this level, are investigated with further analysis. Figures 9-12 are examples of the ADS analysis performed.

To date two anomalies have been discovered. These involve changes in motor current resulting from GOES-8 Sounder and GOES-9 Imager E/W motor winding failures. All other data have been nominal.

5. UNRESOLVED ANOMALY

There is one unresolved anomaly possibly related to jitter, image shearing. Partial GOES-8 earth images taken in October 1995 at 08:45 Universal Time are shown in Figure 13. These images show the east limb exhibiting considerable image shear. The shearing occurs on alternate scan lines with varying amplitude and at times extends into the earth image. The GOES-8 Imager does have known servo errors as large as 64 microradians at the end of a west going scan (at 8.5 degrees), but these errors by nature occur off the image and do not account for the shear. Shear is also present on GOES-9, but to a lesser extent both in amplitude and frequency of occurrence. Attempts have been made to correlate image shear to data indicative of spacecraft motion. ADS, DIRA, and earth sensor data collected during image shear events have not shown spacecraft motions of the levels required to cause the shear. Other tests, especially data collected during Wide Field Collimator (WFC) testing on the ground, indicate that the IMC can cause shear even when it is tuned and synchronized with Imager scanning. However, the magnitude of these errors are also too small to account for shear in Figure 13. This issue is still being investigated on-orbit, and GOES-K final performance tests will be judiciously tailored to identify and possibly correct the problem.

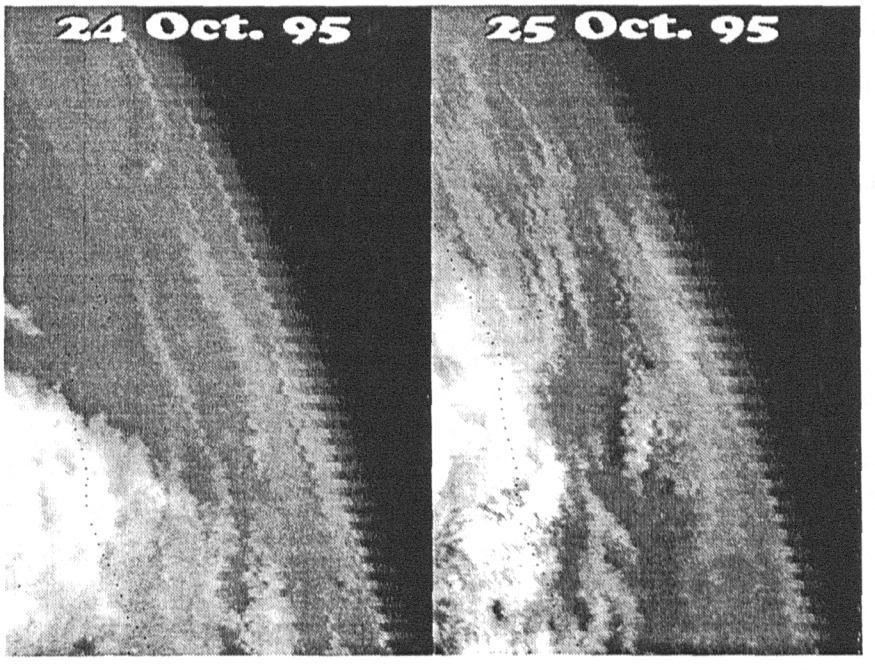

Figure 13. GOES-8 Imager Shear

6. CONCLUSION

Jitter performance of the latest generation of GOES spacecraft, and the Imager and Sounder instruments, has been presented. This performance has been characterized with on-orbit measurements as well as with the ground test data. The evaluation methods of using the FFT/3D-AFT of servo error spectra and compensation signal images has been shown to simplify and reduce the jitter evaluation process.

The optimum of three solar array stepping profiles has been selected based on jitter performance, and new knowledge of spacecraft structural modes has been obtained. It was shown that momentum wheel disturbance is well below the assigned budget at 2900 rpm. Low frequency disturbance effects were not evaluated due to poor DIRA data, however manipulation of ADS data allowed reasonable confidence down to the 0.2 Hertz range. Additional confidence in instrument and spacecraft level testing has been gained by demonstrating that on-orbit data correlate well with ground test data. Although image shearing remains as an unresolved issue, the data demonstrate that it is not caused by large spacecraft jitter above 0.2 Hertz.

7. ACKNOWLEDGMENTS

The authors would like to thank the GOES Project and NOAA for making these on-orbit measurements possible. The process of testing and obtaining flight data was a collective effort of many individuals at SS/L, GSFC, NOAA, and their contractors. All of their contributions, and those of the Mission Operations Support Team, are greatly appreciated.

8. REFERENCES

1. M.K.P. Bhat and A. Kamel, "GOES I-M Image Navigation and Registration System," MSC World User's Conference, Universal City, California, March 23-25, 1988.

2. D. Jaures and E. Koeing, "Infrared Imaging and Sounding from a Geostationary Body- stabilized Spacecraft," Twenty First International Symposium on Remote Sensing of Environmental, Ann Arbor, Michigan, October 26-30, 1987.

3. W. C. Bryant, Jr., S. Ashton, Gus Comeyne III, and Douglas A. Ditillo, "GOES Image Navigation and Navigation and Registration On-Orbit Performance," SPIE Proceedings, Vol. 2812, (GOES-8 and Beyond Conference), August 1996.

4. A. Kamel, "Image Navigation and Registration System," SPIE Proceedings, Vol. 2812, (GOES-8 and Beyond Conference), August 1996.

5. J. Sudey, Jr., and J. R. Schulman, "In-Orbit Measurements of Landsat-4 Thematic Mapper Dynamic Disturbances," Acta Astronautica, Vol. 12, No. 718, pp. 485-502, 1985, Printed in Great Britain.

Effect of the magnetometer boom shadow on the attitude pointing and control of the GOES-8 and GOES-9 spacecraft

Andre' Dress

Computer Sciences Corporation
Seabrook, Maryland 20706

Keiko Chevray

Space Systems / Loral
Palo Alto, California 94303

ABSTRACT

Following the successful transition of GOES-8 to the on-orbit mode, small disturbances were observed at approximately 14:30 SLT. Further analysis has shown that the disturbance is caused by shadowing of the solar sail by the magnetometer boom. The disturbance is most prominent when the sun is at lower declinations causing the shadow to rise higher along the sail boom. Data for the solar sail snap caused by the magnetometer boom shadow is analyzed, showing the time dependence of the attitude motion in the wheel angular momentum data and earth sensor data. Additional data is presented showing the profile of the shadow as viewed through the Imager and Sounder cooler radiator patch heater control voltage data. The presentation will demonstrate the following: 1) The attitude variation is caused by the magnetometer boom shadow as it is correlated with the true position of the sun, 2) The magnitude of the spacecraft motion for GOES-8 and GOES-9 is measured and compared over the seasonal duration of the effect, 3) The amount of deflection of the sail boom required to cause the observed attitude motion is estimated, 4) The dependence of the magnitude of the attitude motion is compared with sun angle subtended by the spacecraft north panel at the shadow point on the sail boom, and 5) Use of the onboard computer's reprogrammability function has provided a mechanism of compensating for the disturbance.

Keywords: GOES, magnetometer boom, solar sail, attitude and control, shadow, image compensation.

1. INTRODUCTION

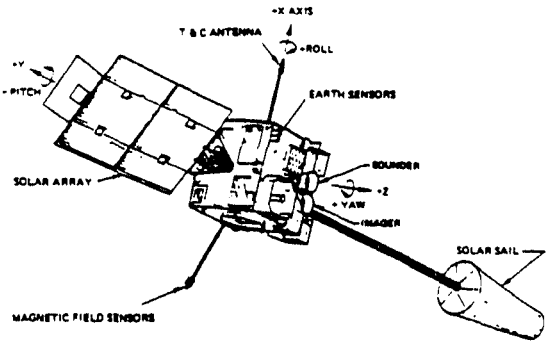

Figure 1-1: GOES Spacecraft

The GOES I through M series spacecraft is a three axis stabilized geosynchronous weather satellite, which provides near real-time visible and infrared images of the Earth. The attitude control system utilizes an earth sensor and a momentum biased V shaped wheel configuration. The power subsystem is sustained by one solar array aligned parallel to the positive pitch axis, mounted on the south panel. Figure 1-1 provides an illustration of the spacecraft layout.

The lack of a solar array on the north panel (-Y axis) was necessary to maintain thermal stability for the Imager and Sounder. Solar reflections or radiative heat originating from sizable appendages closely mounted along the north panel degrade instrument performance. However, the absence of a complementary solar array would produce solar disturbance

torques larger than those sustainable with the attitude control system design. The compromise was to mount a long slender solar mast and sail, thus, reducing heat input into the instrument radiative coolers and providing sufficient surface area to balance solar torques. The solar sail is comprised of a 14.4 meter mast and a 3.3 meter conical shaped sail. In addition to the solar sail, a trim tab, mounted at the south end of the solar array, provides a mechanism for fine adjustments of roll/yaw torque disturbance variations. Daily adjustments to the trim tab compensate for changes in solar declination and residual roll/yaw torques.

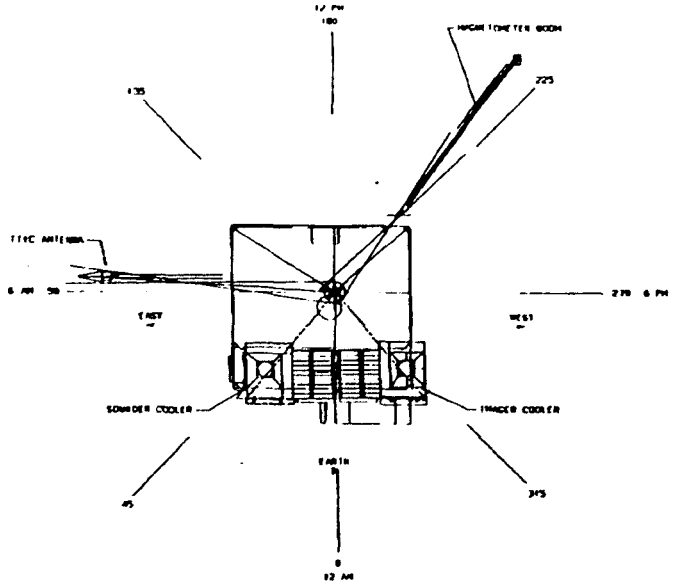

Figure 1-2: GOES Spacecraft (North Face)

Other prominent appendages on the GOES spacecraft are the telemetry and command antenna and the magnetometer boom. Prior to launch, the magnetometer boom is stowed along the anti earth face (-Z axis). Deployment motion rotates the boom 135° and positions it as depicted in Figures 1-1 and 1-2. The base of the boom is attached in close proximity to north-west (-Y to -X axis) corner of the anti earth panel.

One week following the beginning of the spacecraft autumnal eclipse season, a disturbance in earth sensor roll data and stored yaw momentum became prominent. The anomaly was also correlated to uncharacteristic changes in the Imager and Sounder heater patch control voltages. Further analysis demonstrated the anomaly's dependence on spacecraft local time. Time correlation provided the basis for the hypothesis, that the magnetometer boom was projecting a shadow on to the solar sail mast. The projected shadow results in radiative cooling of the shadowed portion of the solar mast. Ultimately, flexing of the solar mast results in a spacecraft disturbance. The anomalous responses in the Imager and Sounder patch heater control voltages supports the hypothesis that solar mast shadowing disrupts thermal coupling between the solar mast and the Imager and Sounder radiative coolers.

The spacecraft motion caused by the disturbance affects the Image Navigation and Registration (INR) performance. In the baseline configuration, registration is degraded because the characteristics of the disturbance do not allow for corrections by real-time methods. The use of reprogramming has provided a mechanism for autonomous correction at the instrument level to improve INR performance.

2. ON-ORBIT DATA

Disturbances caused by the projection of the magnetometer boom shadow on the solar mast are predominantly observable in the spacecraft yaw momentum and earth sensor roll data. Pitch disturbances are not readily observable in the earth sensor or wheel speed data. The control system's slow roll/yaw response and wheel configuration provides a reliable method for monitoring the disturbance. A combination of earth sensor data, wheel speed data, and controller logic is required to predict true disturbance magnitude. Figure 2-1 provides an unfiltered sample of flight data observed on day-of-year (DOY) 343 for GOES-8. During this time frame the shadow's projection onto the solar mast is near its maximum height of approximately 2.8 meters. Note that the earth sensor pitch data does not provide any conclusive indication of the disturbance. However, roll data, yaw momentum and patch control voltages furnish adequate indication of a disturbance.

A typical roll attitude for DOY 41 is shown in Figure 2-2 and 2-3 for GOES-8 and GOES-9, respectively. There is no observed pitch transients, most likely because the pitch control loop has enough bandwidth to eliminate the disturbance. The roll attitude is determined by taking the earth sensor data, subtracting known roll motion caused by the instrument mirror slews, and passing the data through a low pass filter to reduce noise. It should be noted that GOES-8 and GOES-9

are flown at two different roll/yaw control loop gain sets, therefore, the controller responses are expected to be different, even if the disturbances are the same.

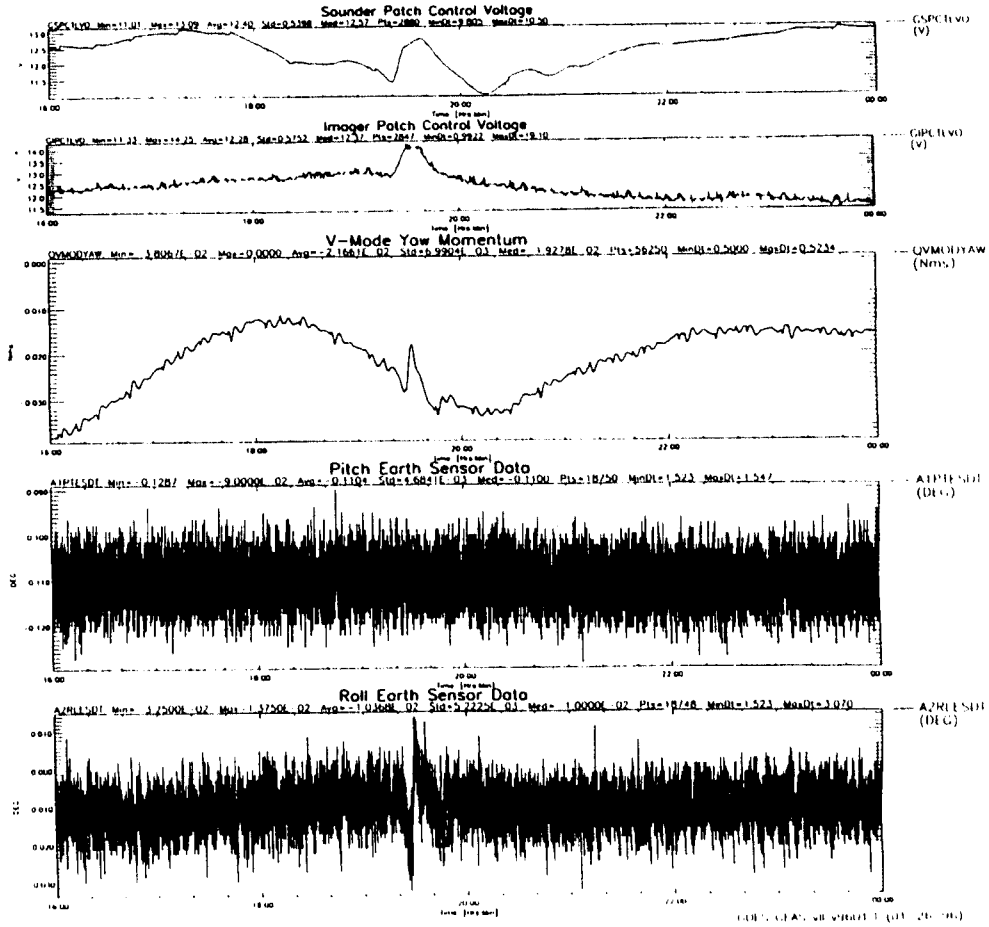

Figure 2-1: GOES-8 data

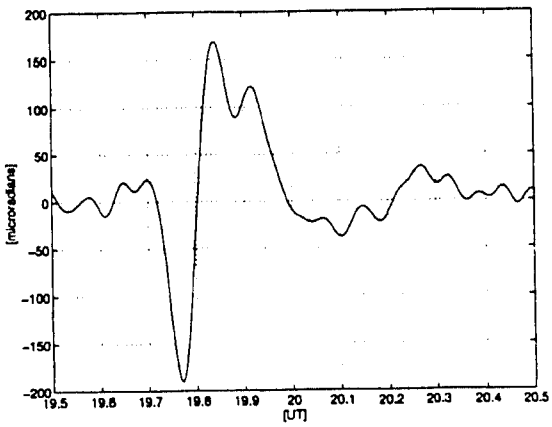

Figure 2-2: GOES-8 roll attitude

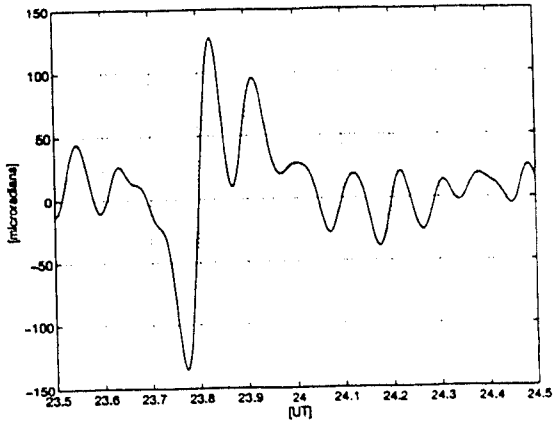

Figure 2-3: GOES-9 roll attitude

3. SEASONAL CHARACTERISTICS

The disturbance is observed on both GOES-8 and 9 for approximately 210 days per year, from September 7 through April 4. The disturbance is most prominent when the sun is at lower declinations, when the shadow is higher along the sail boom. The correlation between the disturbance and sun angles are described below.

The disturbances are observed at slightly different times each day, as shown in Figure 3-1 for GOES-8. The data shown in this figure covers a 2 months period from early 1996. Figure 3-2 provides a 1.5 hour time span of yaw momentum data sampled every two weeks (from DOY 245 to 357) and plotted as a function of UTC. The plotted yaw momentum data has been modified by removing the diurnal signature with a fifth order polynomial fit. The data set was then consecutively incremented with an 0.01 Nms bias to visually emphasize the disturbance increase and its time dependence. Note that the magnitude of the disturbance with respect to the bias remains unchanged. The smaller oscillations are caused by movements of the Imager and Sounder. The larger disturbance starting around 19:30z is the consequence of boom shadowing.

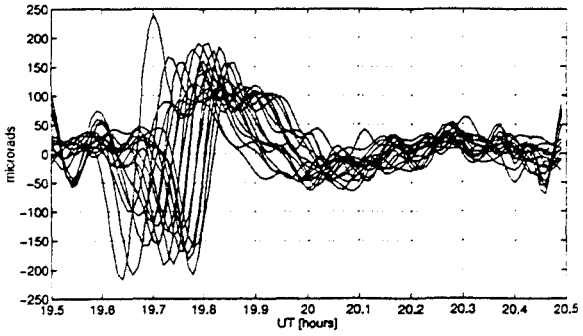

Figure 3-1: Seasonal trending of GOES-8 roll attitude as a function of UT

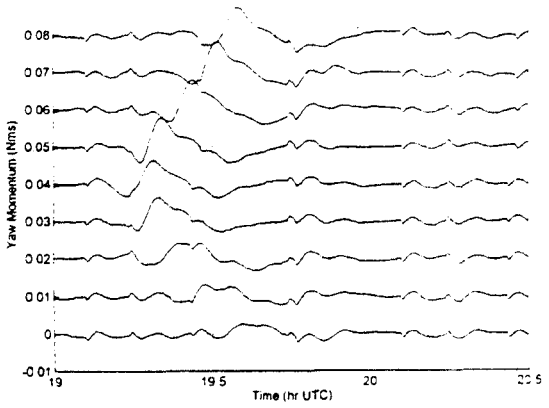

Figure 3-2: Seasonal trending of GOES-8 yaw momentum as a function of UT

Data supporting the dependence on spacecraft local time is observed in the trending of flight data. The analysis of the data indicates that the phenomena occurs at the same east-west sun angle each day, as shown in Figure 3-3, which corresponds to a satellite local time of 14:30.

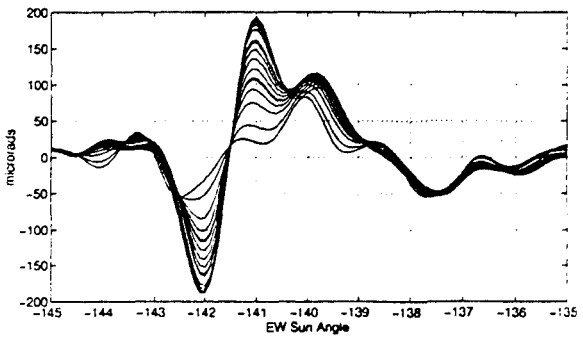

Figure 3-3: Seasonal trending of GOES-8 roll attitude as a function of sun angle

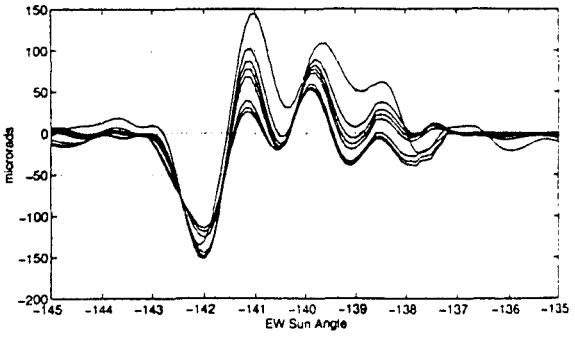

Figure 3-4: Seasonal trending of GOES-9 roll attitude as a function of sun angle

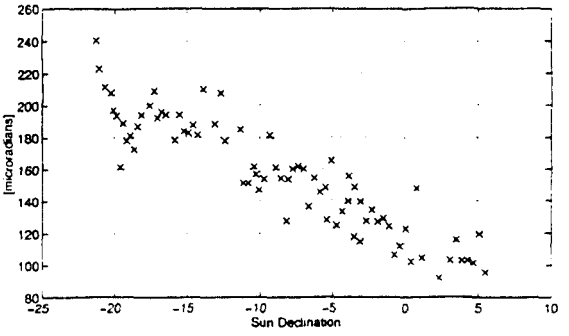

Figure 3-5: Seasonal trending of GOES-8 roll peak magnitude as a function of sun angle

GOES-9 roll attitude is slightly more difficult to trend, due to lower control loop gain, however, it also indicates that the phenomenon occurs at the same east-west sun angle each day, as shown in Figure 3-4. In addition, it should be noted that the sun angle at which this phenomenon takes place is the same for both GOES-8 and 9.

The peak magnitude as a function of sun declination is shown in Figure 3-5 for GOES-8. The peak transients are observed when the sun declination is the highest. The phenomena is observed for sun declinations of approximately 5 degrees or lower, which corresponds to the thermal snap season starting around September 7 and ending around April 4, for total of 210 days per year.

4. SUN REFLECTIONS INTO IMAGER AND SOUNDER

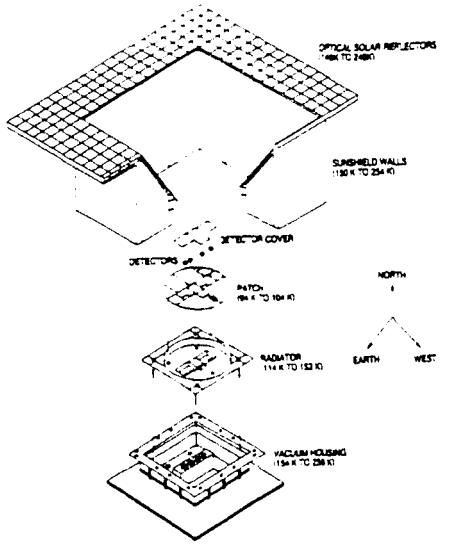

Figure 4-1: Radiant Cooler Expanded View

As described in section 1, the absence of a solar array on the north panel (-Y axis) was necessary to reduce solar reflections and radiative heat into the Imager and Sounder radiative coolers. The radiative coolers are mounted on the north panel (-Y axis) as depicted in Figure 1-1 and are shielded from direct sunlight for angles up to a maximum of 23.5° elevation. Figure 4-1 provides an expanded view of the radiant coolers and the relative placement of the detectors. Power required to maintain detector thermal stability is monitored via the Imager and Sounder patch heater control voltage. The patch is an emitter on which the detectors are mounted and provides passive radiation cooling through direct space viewing. The patch is entirely shaded from direct sunlight for angles up to 26.1° elevation. The heater control voltage drives a proportional heater (maximum 0.4W at 42 volts) to maintain the detectors at a constant temperature. The diurnal and seasonal variation of the control voltage is driven predominately by solar input. In general, as the external environment temperature decreases, the heater control voltage increases proportionally.

During the time frame in which the solar mast is shadowed by the magnetometer boom, an uncharacteristic short term rise in the patch heater control voltage is observed. This higher frequency signature gives indication of an local environmental reduction of thermal energy into the radiative coolers. The increase in heater control voltage is present in both Imager and Sounder patch heaters and is approximately the same magnitude. The coincidentally occurring anomalies and relative local time corroborated the evidence that the rise in heater current could not be a result of a direct projection of the magnetometer boom shadow on the radiator coolers. Instead, the data suggests that the reduction of thermal input was the result of an independent heating mechanism. Given the relative alignment of the magnetometer boom with the solar mast and the relative local time, it was concluded the that projected shadow resulted in a reduction in the immediate thermal environment.

The relative increase in the heater control voltage is shown to be dependent on solar declination. Figures 4-2 and 4-3 provide a 1.5 hour time span worth of Imager and Sounder heater control voltage data, sampled every two weeks from DOY 245 to 357. The presented data was modified by subtracting the first data point to remove the relative bias while preserving the magnitude of the disturbance. The heater control voltage data, as did the yaw momentum data, demonstrates its dependence on spacecraft local time and solar declination.

Figure 4-4 shows the predicted magnitude of the boom projection on to the solar mast as a function of DOY (solar declination). Analysis as described in Reference 1 has shown that by repositioning the magnetometer boom, the effects of shadow can be reduced or eliminated. Given the relative change in control voltage, height of the projected shadow, and power required to operate the proportional heater, a direct association with the radiative power of the solar mast can be assumed. At the maximum shadow projection, the decrease in radiative power onto each radiator cooler has been calculated to be approximately 0.014 Watts.

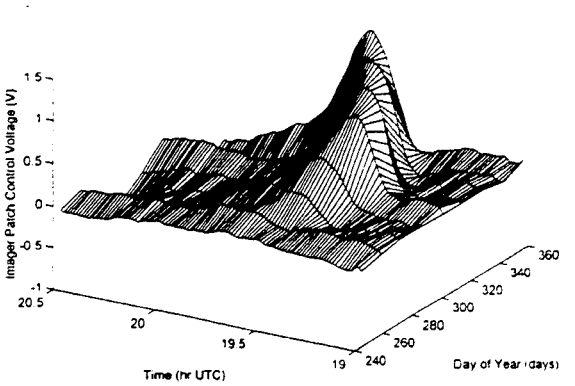

Figure 4-2: Imager patch control voltage

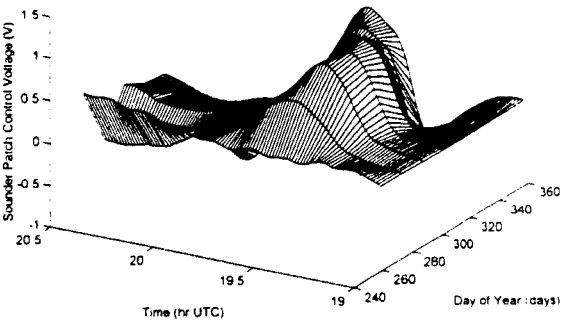

Figure 4-3: Sounder patch control voltage

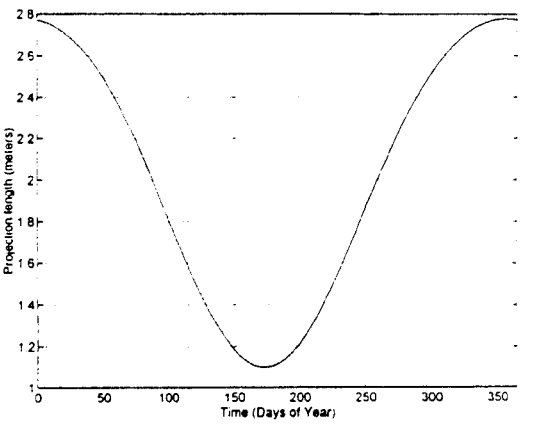

Figure 4-4: Magnetometer boom projection on solar sail

5. CORRELATION OF EXPECTED DEFLECTIONS WITH ACTUAL DATA

The flight data and error estimates were utilized to predict, with reasonable certainty, the angle and tip displacement of the solar mast. This was accomplished by utilizing the calculated shadow projection on to the solar mast shown in Figure 4-4, the observed momentum exchange, and the moments of inertia and mass for the spacecraft and solar sail.

Using the observed flight data and spacecraft geometry, the disturbance duration is calculated to be approximately 1400 seconds. The maximum integrated magnitude of the disturbance, in terms of momentum, was observed to be approximately 0.011 Nms. Conservation of momentum states that the relative movements be proportional to the moment of inertia of the spacecraft and solar sail. Given the observed data points, a deflection angle and sail displacement for the maximum disturbance was determined to be 1.4° and 0.4 meters respectively. This calculation assumes the solar mast flex point is at the center of the projected shadow area.

6. CORRECTIONS USING REPROGRAMMING CAPABILITY

A capability exists for both GOES-8 and GOES-9 to reprogram the existing flight software. One of the reprogramming elements is called the Spacecraft Motion Compensation (SMC). SMC utilizes a set of coefficients that can be loaded to the spacecraft and applies a correction to the instrument mirrors. Although this capability was developed specifically for an earth sensor stray light problem, it has the capability to compensate for any anomalous spacecraft motion at the instrument level. A set of coefficients for roll and pitch attitude profiles, as a function of Attitude and Orbit Control Electronics (AOCE) clock time, is loaded to the spacecraft each day. When this function is enabled, the AOCE will automatically compute a smooth profile from the uploaded coefficients and apply the compensation to the instruments at the specified time.

A prototype of the SMC correction to compensate for the roll attitude caused by the boom shadow was tested on GOES-8. An engineering model of a ground software to generate SMC coefficients was developed. The ground software calculates the roll profile from filtered earth sensor data and maps the profile to the sun azimuth. The pitch profile is assumed to be zero. Then, the predicted orbit data is used to calculate the sun position for the following day, which in turn determines the appropriate AOCE clock time to apply the correction.

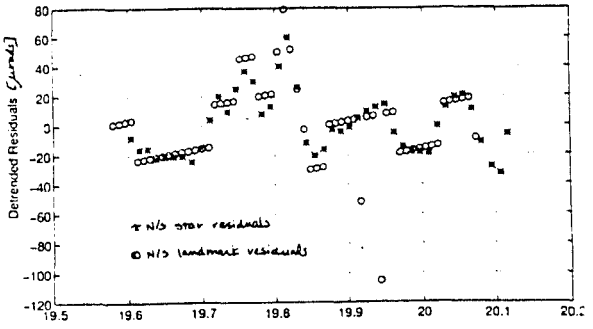

Figure 6-1: Residual data during SMC test

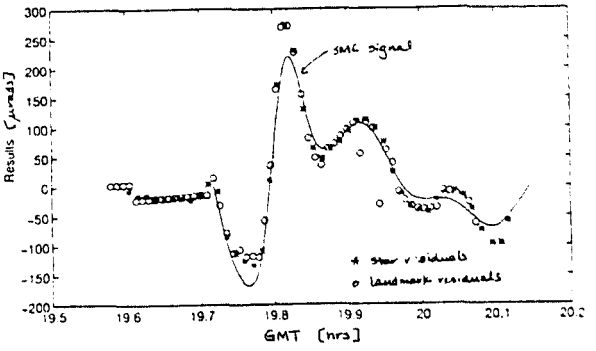

Figure 6-2: Comparison of roll transient and residual data during SMC test

A special test was performed on 5 Feb 1996, where line-of-sight stars and short frame landmark measurements from Imager and Sounder were used to measure the image navigation and registration performance using SMC. The results are shown in Figures 6-1 and 6-2. Figure 6-1 shows the residual error observed by the star and landmark residuals. Figure 6-2 shows the comparison of the roll transients as observed by the star and landmark residuals and the SMC signal used to compensate for the error. The error was reduced from 200 microradians to less than 50 microradians.

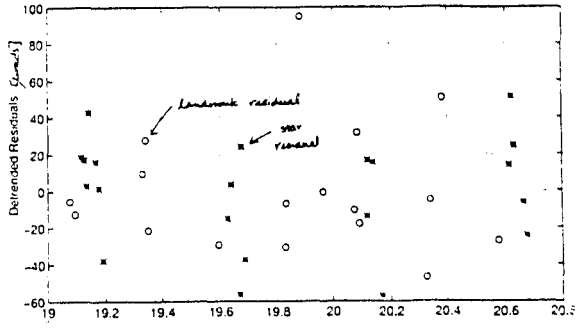

Figure 6-3: Residual data during SMC test (2)

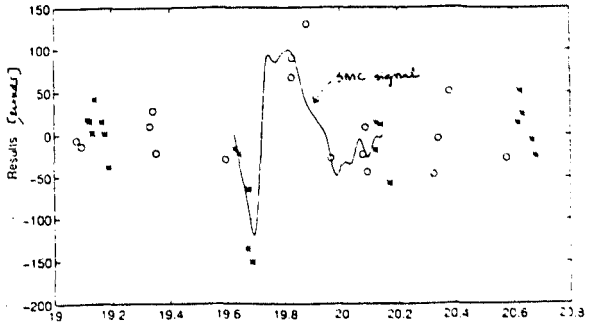

Figure 6-4: Comparison of roll transient and residual data during SMC test (2)

In addition, the use of SMC was again tested in March 1996 during normal operations. The results are shown in Figures 6-3 through 6-6. On both days of the test, the error was reduced from 125 microradians (zero-to-peak) to 50 microradians. 50 microradians zero-to-peak is within the normal scatter observed in the data.

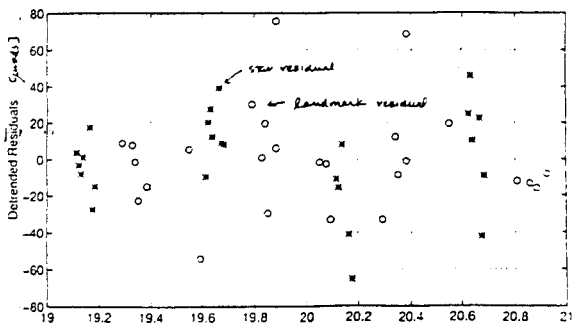

Figure 6-5: Residual data during SMC test (3)

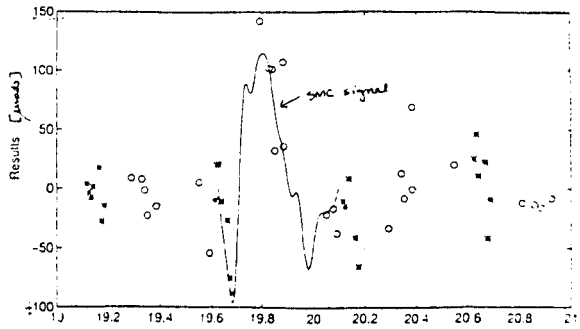

Figure 6-6: Comparison of roll transient and residual data during SMC test (3)

A proposal has been submitted to incorporate the SMC coefficient generation into operational ground equipment available at SOCC and incorporate the use of SMC for correction into normal operations. The ground software modifications are expected to be complete by the start of next boom shadow season in the fall of 1996.

7. SUMMARY

The disturbance observed around 14:30 SLT on both GOES 8 and 9 has been determined to be caused by the projected shadow of the magnetometer boom onto the solar sail. The thermal discontinuity on the solar mast results in the deflection of the sail and an exchange of momentum with the spacecraft. This disturbance impacts the Image Navigation and Registration. The calculated spacecraft motion, caused by the disturbance, has been characterized over a season and has been correlated to the relative position of the sun to the spacecraft. Coupling with the solar mast's reflected thermal energy onto the radiative coolers has been demonstrated. The rise in patch heater control voltage maintains the patch temperature at the commanded setting which prevents degradation of the products.

Reprogrammability has provided a mechanism for autonomous corrections by steering the mirrors appropriately. On orbit tests have successfully demonstrated that the spacecraft motion can be compensated by using the Spacecraft Motion Compensation function.

8. ACKNOWLEDGMENTS

The authors are pleased to acknowledge the contributions of Dr. Milton Phenneger of Computer Sciences Corporation for his insights and analysis in correlating the anomaly to the boom shadow. The results presented in this paper made extensive use of analysis software developed by Xen Price of Space Systems / Loral which filters the earth sensor data to determine roll attitude.

9. REFERENCE

1. Task Assignment #42 (Magnetometer Boom Relocation) Final Briefing, Space Systems / Loral, February 8, 1996.

2. GOES Program Spacecraft Operations Handbook, DRL 503-02, SS/L-TR00570, Space Systems / Loral, August 31, 1995.

Improved GOES Earth Sensor Performance

Edward R. Washwell, Keiko Chevray, Ahmed Kamel
Space Systems/Loral, Palo Alto, California 94303

Andre Dress
Computer Sciences Corp, Seabrook, Maryland 20706

Timothy Walsh
National Oceanic and Atmospheric Administration
Suitland, Maryland 20746

ABSTRACT

The Earth Sensors on GOES-8 exhibit seasonal pointing errors in both the dual and single chord operating modes of the sensors. The errors were largely compensated for by a software patch uploaded to the satellite. The combination of detailed analyses and laboratory test results established that the observed error signatures are the result of stray solar radiation. The nature of the stray radiation paths giving rise to the seasonal errors is such that only the most significant stray path was eliminated in the GOES-9 hardware. The Earth Sensors on GOES-9 show significantly improved pointing performance over GOES-8, validating the origin of the most significant error source in the GOES-8 Earth Sensors. Low level seasonal pointing errors are observed, as expected, in the GOES-9 Earth Sensors. These errors again are effectively compensated for by an additional software patch developed to permit satisfactory single chord Earth Sensor operation. The operating principles of the Earth Sensor are described. On-orbit data of the seasonal anomalies are presented for both the uncompensated and compensated hardware and operating modes.

Keywords: earth sensors, stray light, GOES, single chord, dual chord

1. INTRODUCTION

The earth sensors (ESs) on GOES provide attitude reference in two axes (pitch and roll) for both transfer orbit and synchronous orbit operations. Two ESs are provided per spacecraft for redundancy. Each sensor is oriented toward the earth such that its mirror scans East-West (E-W) about the spacecraft pitch axis and the earth radiance is reflected onto two detectors A and B, where the two fields of view (FOV) are shown as scan A and B in Figure 1-1.

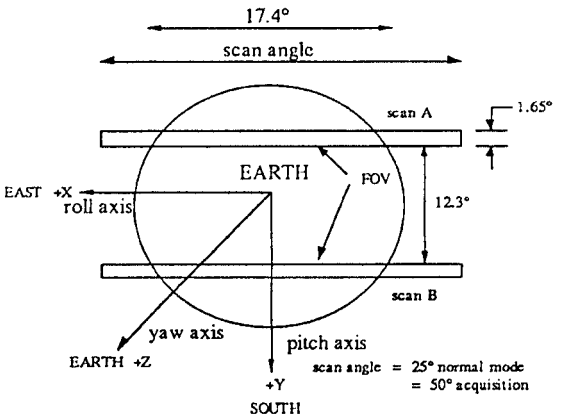

Figure 1-1. Earth Sensor Scan Geometry Relative to Spacecraft and Earth

The sensor is comprised of an optical assembly and an electronics assembly. These assemblies are housed in a single package separated by a thermal control plate which maintains the detectors at a fixed temperature and minimizes thermal structural distortions. An alignment cube mounted on the housing (and flown with the spacecraft) provides an accurate and repeatable alignment reference during installation and test. The optical assembly includes the scan mirror assembly and the telescope assembly.

The telescope assembly consists of an objective lens, a bandpass filter, two detectors, and preamplifiers. The detectors are thermistor bolometers bonded to a thin immersion lens. The detectors are oriented such that their fields are coincident in the E-W direction and are separated by 12.3° in the N-S direction. The sensor detectors have an instantaneous FOV (nominally) of 1.65° square. The sensor responds to the 14 to 16 micrometer CO_2 absorption band of the earth. This band of wavelengths ensures minimal effect on sensor signals due to radiance variations of the atmosphere.

The signal from each thermistor bolometer detector is differentiated, amplified, and then threshold detected. The threshold detection method uses an adaptive slope threshold technique in order to reduce the error caused by the radiance gradient across the earth. This technique uses only the space to earth crossing of the detector outputs. By adding optical encoder pulses from the space-to-earth crossing to mirror center and subtracting those from mirror center to the earth-to-space crossing, a signal proportional to the attitude error in pitch is obtained. By averaging output signals from two complete cycles, noise errors and the errors due to radiance variation, gain changes, bandwidth changes, and threshold drifts are reduced. For the roll axis, pulse trains between space-to-earth and earth-to-space crossings are combined for both detector circuits and the roll error calculated from the difference in these pulse trains.

Each ES has two commandable operating modes, normal mode and acquisition mode, which determine the scan width of the sensor. Normal mode provides low noise for an on-orbit and station keeping modes. The scan mirror scan amplitude is $\pm 12.5°$ in normal mode. In acquisition mode, the scan amplitude is $\pm 25°$.

The ES has the ability to collect data from a single detector, in what is known as single chord operation, in order to reduce errors due to intrusion of a sun/moon target upon one of the sensor scans. Single chord operation is brought about either by automatic inhibition or by manually commanded inhibition of the scan which has been corrupted by a sun/moon target. Automatic scan inhibition is provided by internal ES logic; no operator input is required. If neither ES scan is inhibited and the sun/moon enters a detector scan FOV, a target check circuit detects an additional space-object crossing and the appropriate detector will automatically be inhibited. This causes the affected detector data to be rejected and replaced by a standard chord. Pitch information is then calculated from the unaffected, "active" detector, and roll information is calculated by comparing the usable detector signal to the standard chord. Automatic inhibition of ES scans may occur while the sensor is in either normal mode or acquisition mode. Upon exit of the sun/moon target from the ES FOV the sensor will revert to the previous dual chord operation.

The ESs on GOES-8 exhibit seasonal pointing errors characterized by similar response in both the dual (normal) and single chord operating modes of the sensors. The ESs on GOES-9 show significantly improved performance over GOES-8, largely as a result of hardware modification. Software patches uploaded to both spacecraft also significantly contribute to improved performance. The following sections describe the anomalies and their resolution. It should be pointed out that the principal historical application of the type of Earth Sensors used on GOES was for communication satellites which have relatively modest requirements as opposed to GOES which is a demanding application.

2. GOES-8/9 EARTH SENSOR CHARACTERISTICS

As discussed in Section 1, the GOES earth sensors exhibit errors that have been attributed to thermal, stray light and dual-to-single chord transition sensor characteristics. Over the past two years, these error sources have been comprehensively characterized for both GOES spacecraft in order to develop effective error compensation techniques. Figure 2-1 shows the maximum observed magnitudes for repeatable known earth sensor error sources. While the thermal and single chord transition errors appear to be diurnal characteristics, the stray light errors such as the batwing/winglet and the bevel have a direct correlation to sun declination. The occurrence of specific stray light effects is shown as a function of sun declination in Figure 2-2.

2.1 Typical ES Dual and Single Chord Signatures

Normal on-orbit operations are conducted with the earth sensor configured in dual scan mode. An example of 24 hours of dual scan earth sensor data is shown in Figure 2.1-1. Most of the lower frequency movements shown in the figure (primarily in roll) result from instrument mirror movements and housekeeping activities. In the dual scan configuration, the high frequency RMS noise of the normal earth sensor telemetry has been measured at approximately 0.005° for GOES-8 and about 20% higher on GOES-9. A comparison of GOES-8 and GOES-9 noise characteristics for a selection of earth sensor modes are shown in Table 2.1-1 (ES 2 is currently selected for control for both GOES-8 and GOES-9).

Table 2.1-1 ES RMS Noise Characteristics

Sensor	Mode	Standard Deviation (degrees), 1 σ	
		Roll	Pitch
GOES-8 ES 1	Normal Dual Scan	0.00523	0.00564
GOES-8 ES 2	Normal Dual Scan	0.00436	0.00455
	North Scan Inhibit	0.00573	0.00621
	South Scan Inhibit	0.00657	0.00707
GOES-9 ES 1	Normal Dual Scan	0.00564	0.00520
GOES-9 ES 2	Normal Dual Scan	0.00539	0.00557
	North Scan Inhibit	0.00800	0.00740
	South Scan Inhibit	0.00770	0.00723
	Acquisition	0.00920	0.00842

During lunar and solar scan intrusions, the affected Earth Sensor (ES) scan is disabled for the duration of the intrusion. During the transition from the dual to single chord, a step offset is observed in pitch earth sensor telemetry. The offset biases used for dual and single chord operations were fully characterized during the post-launch test periods for both spacecraft and are summarized in Table 2.1-2.

Table 2.1-2 Measured ES Mode Biases (for the Controlling ES)

Sensor	Mode	Offset Bias (degrees)	
		Roll	Pitch
GOES-9 ES 2	Normal Dual Scan	-0.010	-0.110
	North Scan Inhibit	-0.010	-0.087
	South Scan Inhibit	-0.010	-0.133
GOES-9 ES 2	Normal Dual Scan	-0.065	-0.050
	North Scan Inhibit	-0.065	-0.045
	South Scan Inhibit	-0.065	-0.055

The dual scan pitch biases shown in Table 2.1-2 represent required pitch offsets to align instrument nadir. The step offsets to compensate for the transition errors are represented by the differences between the dual and single chord pitch biases. The roll biases, unaffected by ES mode changes, are used to align the spacecraft momentum vector to a position normal to the ES pointing vector.

2.2 Thermal Distortion

Post launch testing concluded that GOES-8 and GOES-9 earth sensors experience pointing errors in both the roll and pitch axes. These pointing errors, specifically those induced by single chord operations, disturb Image Navigation and Registration (INR) (Ref. 1) long term and short term performance. Software and operational modifications to alleviate the impact of these disturbances have been successfully implemented and have virtually eliminated the repeatable error. Non-repeatable components, manifested in the Earth's atmosphere, such as clouds and radiance gradients remain uncorrectable via autonomous methods. Real-time adjustments, uplinked to the spacecraft, maintain the system level pointing requirement.

Structural distortion results in a diurnal migration of the earth sensor-to-momentum wheel alignment. This type of thermal distortion is not perceived as a system level pointing problem since the disturbance is slow and repeatable, and is easily compensated for with on-board mirror correction, namely Image Motion Compensation (IMC). The structural distortion has been analyzed with respect to different on board sensors, mainly the Imager, Sounder and redundant earth sensor. Figure 2.2-1 shows the Imager diurnal roll profile for two separate days. The data represents diurnal spacecraft motion with respect to the Imager. The two profiles were obtained using different earth sensors for control. Figure 2.2-2 shows the Imager diurnal pitch profiles for the corresponding days. The plot shows a significant change in pitch profile centered around spacecraft midnight. This variation is likely the result of thermal distortion in the earth sensor, which translates to pointing errors. Figures 2.2-3 and 2.2-4 represent the difference between the two Imager roll and pitch profiles, respectively. The diurnal variation, as seen by the Imager, is corroborated by observations with the redundant earth sensor. Figure 2.2-5 shows telemetered dual chord data from the redundant earth sensor with the controlling earth sensor also in dual chord. This plot, which represents distortion difference between the two earth sensors, shows that the thermal distortion along the roll axis are similar, while pitch distortion is different. The magnitude of the pitch difference as seen by the earth sensor ($\cong$ 0.03°)

correlates well with the Imager pitch profile difference. Since these two difference plots agree, it can be reasonably assumed that pitch error as seen by the Imager is not a thermal distortion of the Imager but rather that of the earth sensor.

Earth sensor thermal distortion and non repeatable error sources produce attitude pointing errors. These error sources are magnified during single chord operations. The standard chord variations created unacceptable pointing errors incurred by scan inhibit (single chord) operations. Operational and flight software changes virtually eliminated the repeatable error sources and have diminish the impact of the non-repeatable portions. While the impacts of thermal distortion has been reduced, indisputable evidence, pinpointing the individual error sources and its components have not been accomplished. The spacecraft's baseline configuration required frequent mirror adjustments to maintain pointing within INR specification. Figure 2.2-6 provides the measured profiles for the repeatable error sources contributed by eccentricity and system thermal distortion. Non-repeatable error sources remain unpredictable and are largely a function of cloud and radiance variations resident in the Earth's upper atmosphere. Repeatable contributions are compensated for, via reprogramability, using the profiles provided in Figure 2.2-6. The summation of these profiles is applied in the roll direction, with the sign reversed for the north and south chord inhibit modes. Thermal and eccentricity corrections are uplinked to the spacecraft in the form of Fourier and orbit coefficients respectively. Autonomous reprogram logic allows the compensation to be applied, to the mirrors, at the appropriate time. Thermal and eccentricity error sources mainly affect the roll component and are coincidentally compensated. Performance is provided via the landmark and star residuals.

Non-repeatable error sources present in both the roll and pitch axes are compensated for with two different methods. Pitch errors are observable, in earth sensor data, immediately following switch to single chord mode. A real time estimator, implemented in reprogram, estimates the pitch error and provides an autonomous signal for mirror compensation. Roll and yaw errors are detectable, on the ground, via landmark and star sense residuals, and are compensated via additional IMC set uplink. Roll and yaw non-repeatable error sources are autonomous via ground detection but require user intervention for correction. Reprogramability of the flight software has provided a method for autonomous corrections. Error correction is measured via Imager and Sounder observations and onboard compensation signals. The observed residuals indicate good correlation between the two signatures. The implementation of the reprogram single chord correction has increased the quality of the products and reduced the burden on operations. Only the non-repeatable roll contributions restrain total corrections.

2.3 Batwing / Winglet

On GOES-8, an earth sensor anomaly was observed around summer solstice, which later was named "batwing" anomaly. The origin of the batwing has been shown by analysis to be due to out of field stray solar radiation which has a sneak path to the detector. A typical spacecraft response to the batwing is shown in Figure 2.3-1. The main difference in roll and pitch attitude is due to the different control loop bandwidth of the roll/yaw and pitch loops. The pitch attitude transients are typically twice that of roll transients, where the peak attitude transients during the summer batwing season are 650 microradians in roll and 1400 microradians in pitch. In addition, similar but attenuated attitude transients are observed around winter solstice. The peak transients during this period are 400 microradians in roll and 650 microradians in pitch. An analysis of the flight data indicates that the batwing is a function of the sun position with respect to the earth sensor. Therefore, the spacecraft attitude can be determined given the sun position. The estimated spacecraft attitude as a function of the sun angle is summarized in Figure 2.3-2. The summer batwing is observed for north-south sun angles greater than 17.1 degrees and winter batwing is observed for angles less than -19.9 degrees. Therefore, summer batwing is in effect for approximately 85 days per year and the winter batwing is in effect for approximately 65 days per year. The winter batwing is believed to be caused by an indirect reflected stray light resulting in attitude transients approximately one half those of the summer batwing.

For GOES-9, the sneak path of the stray light was largely eliminated by a hardware fix. The residual error was named "winglet" anomaly. The attitude transients are on the order of 50 microradians in roll and 100 microradians in pitch during this phenomena, which occurs around the same time GOES-8 summer batwing is observed. This effect is not observed during the GOES-8 winter batwing periods on GOES-9 and is expected to be completely eliminated by a hardware fix in the subsequent satellites in the series (GOES-K, L, M).

For GOES-8 batwing, the reprogramming function of the Attitude and Orbit Control Electronics (AOCE) was used to provide Spacecraft Motion Compensation (SMC), which corrects for the spacecraft motion at the instrument mirrors. The SMC provides the correction to the mirrors from a set of uploadable coefficients, from which roll and

pitch compensation profiles are calculated as a function of the AOCE clock time. The SMC coefficients, which are uploaded daily during the batwing seasons, are determined on the ground from a table of spacecraft attitude as a function of the sun angle and sun angle position for that day. Typical SMC performance, as measured by the star and landmark residuals, is that (uncorrected) attitude errors of 650 microradians in roll and 1100 microradians in pitch are reduced to less than 100 microradians.

2.4 Bevel

The bevel effects are observed on both GOES-8 and 9 two seasons per year, for total of approximately 100 days. There is a strong evidence that the origin of the anomaly is the result of solar radiation reflecting off a beveled surface in the earth sensor. A typical earth sensor and momentum telemetry during the bevel is shown for GOES-9 from day 306 in Figure 2.4-1 and typical roll attitude transients are shown in Figures 2.4-2 and 2.4-3 for GOES-8 and 9, respectively. As the figures indicate, the resulting attitude transients during the bevel are similar in magnitude and frequency content for GOES-8 and 9. The peak transients observed during the bevel seasons are 100 microradians in roll and 200 microradians in pitch. An analysis indicates that the bevel phenomena affects only one of the two chords of the earth sensor, therefore, this effect can be eliminated by commanding the earth sensor into single chord. This concept is used operationally on both GOES-8 and 9 during the bevel seasons and has shown to totally eliminate the effect, as shown in Figure 2.4-4 for GOES-9 on day 307.

3. ANOMALY INVESTIGATIONS - RAY TRACING AND LABORATORY TESTS

The on-orbit anomalies described above were unexpected because performance analyses had put limits on the amount of stray (out-of-field) radiation that would adversely affect Earth Sensor pointing performance. The laboratory acceptance test levels were established based on these predictions.

The seasonal nature of the Earth Sensor anomalies on GOES-8 suggested a strong correlation with sun declination. Two parallel paths were taken to uncover possible contributors to the anomalies. Historical FOV mapping data was processed (summed) to enhance any signatures that might have been below the detection (acceptance) level. These analyses did indeed show the presence of two stray radiation signatures, referred to as the batwing and bevel effects, respectively, which could be associated with specific sun declinations. Figure 3-1 shows an example of FOV data processed to enhance any stray radiation signatures. The horizontal axis corresponds to sun declination (north-south, degrees) and the vertical axis to its east-west motion(degrees). The contour lines represent signal level normalized to the bolometer signal (channel 1 shown at 0° N-S and 6° E-W. The summer batwing signature is shown at approximately 21° N-S and 16° E-W, the winter batwing at -23° N-S and 14° E-W, and the bevel signature at 17 N-S (extending over a range of approximately 18° E-W).

In parallel, a detailed ray trace analysis was performed to uncover possible stray radiation paths which had the key characteristics of the anomalies, viz., signals present on both bolometers for the batwing effect but present only on one detector (and on a different detector depending on the sun declination) for the bevel effect. The ray trace analyses were successful in uncovering indirect stray radiation paths responsible for both anomalies and, additionally, put a bound on the duration of the respective seasonal occurrences. Figures 3-2 and 3-3 show the ray trace spot diagrams of the stray radiation paths projected into external space for the winter and summer batwing effects, respectively. Figure 3-4 shows a representative ray trace spot diagram for the bevel effect (positive sun declination). These angles correspond to the sun's position; the seasonal predictions are in excellent agreement with the on-orbit data shown in Fig. 2-2. As a result of these studies and additional radiometric analyses, the requirements on the FOV mapping test were modified and the sensitivity of subsequent FOV mapping tests was improved.
The batwing effect observed on GOES-8 was largely eliminated for GOES-9 by a hardware modification before launch, as determined from GOES-9 on-orbit performance, validating the origin of the effect. The residual batwing effect (winglet) noted on GOES-9 is not expected on subsequent satellites as a result of improvements made in the design and implementation of the retrofit hardware since GOES-9.

A hardware modification to eliminate the bevel effect was not attempted for GOES-9. Efforts on a hardware retrofit to eliminate the bevel effect using the Engineering Model were not completely successful. The approach taken was based on ray trace analyses, hardware modification and testing. Residual signatures were observed which could be explained by stray paths and diffraction effects introduced by the hardware modification. These results, coupled with the success of the single chord patch and the consistent signature of the bevel effect led to the decision to discontinue the hardware retrofit activities and to rely on the software patch solution.

The origin of the single chord/thermal anomaly is still unknown. As of this writing, diagnostic Thermal/Vacuum tests are planned on GOES-K in order to gain insight into the mechanism responsible for the effect. It should be pointed out that, as a result of its thorough characterization and repeatable nature, the effect is satisfactorily compensated by a software patch.

4. SUMMARY

The origin of seasonal pointing errors in the GOES -8 and -9 Earth Sensors have been characterized and effectively eliminated by a combination of software and hardware fixes. The origin of a diurnal anomaly has not been identified. This anomaly is effectively accommodated by a software solution. These solutions have resulted in considerably improved ES performance.

5.ACKNOWLEDGMENTS

The authors are pleased to acknowledge the contributions of Lockheed Martin Missiles and Space to the resolution of the anomalies. In particular, Jeff Green, Bill Krigbaum and Dr. Paul Lee for their insights and analysis of the hardware and its operation, and Alice Palmer for the ray trace analysis detective work. Dr. John Scholtz of SS/L was the principal architect of the software patches and showed exceptional ability to insert the patches into the on-board processor. The results reported here made extensive use of the analyses performed by Edwin Harvie (Computer Sciences Corp.) for the Mission Operations Support Team during the Post Launch Tests.

6. REFERENCE

1. A. Kamel, "Image navigation and registration system", SPIE Proceedings, Vol.2812 (GOES-8 and Beyond), August 1996.

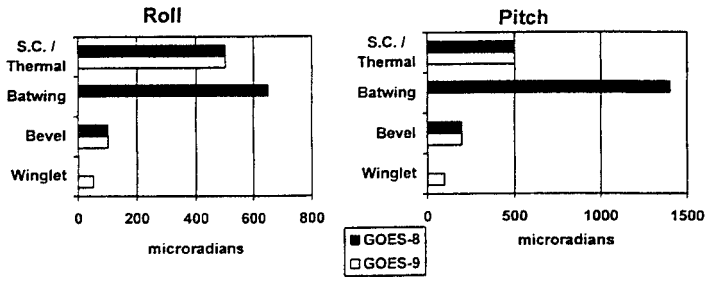

Fig. 2-1. Earth Sensor Error Sources

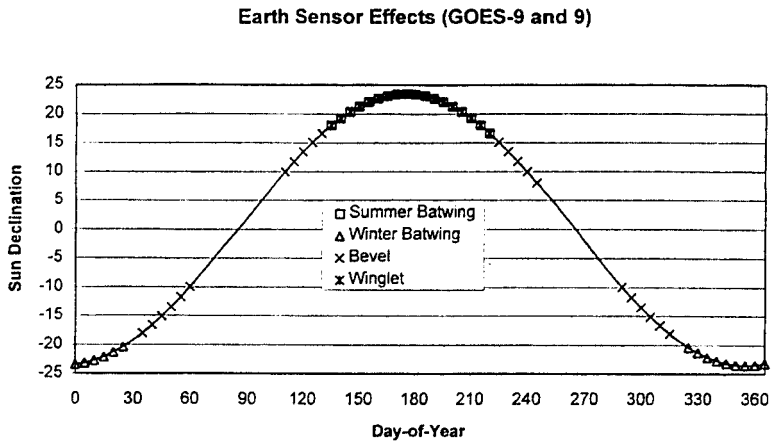

Fig. 2-2. Earth Sensor Seasonal Effects

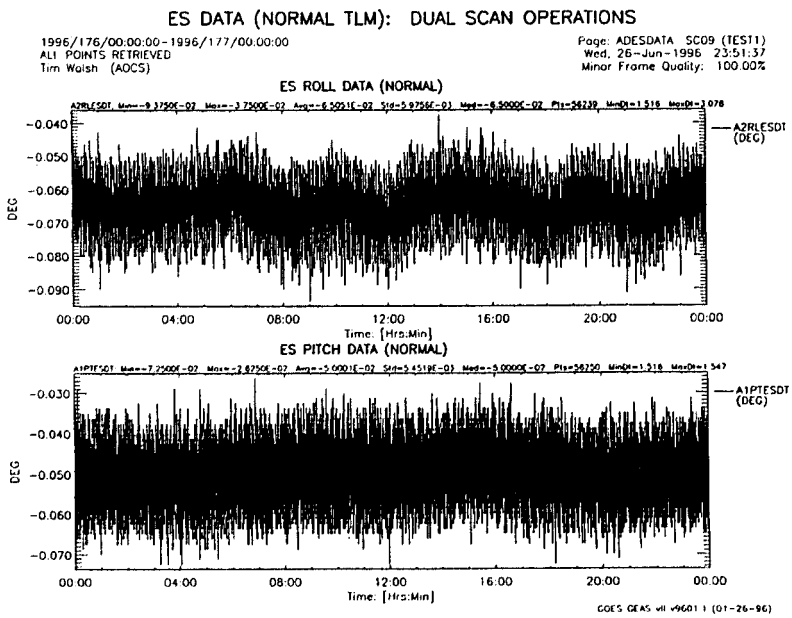

Fig. 2.1-1. Earth Sensor Telemetry during Dual Scan Operations

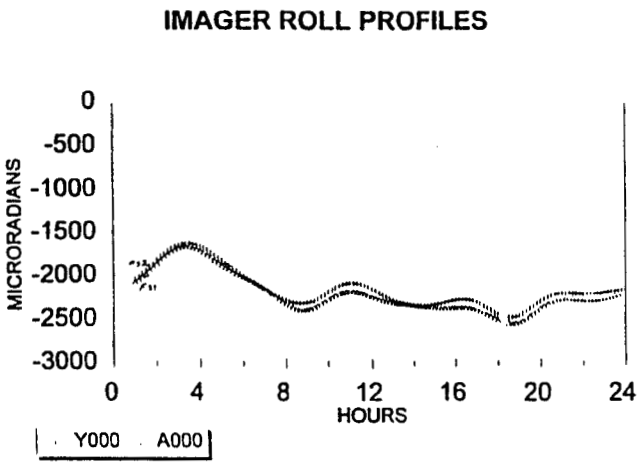

Fig. 2.2-1. Imager Roll Profile

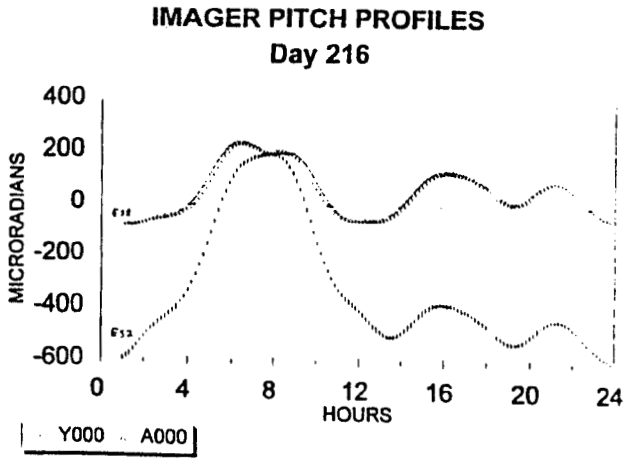

Fig. 2.2-2. Imager Pitch Profile

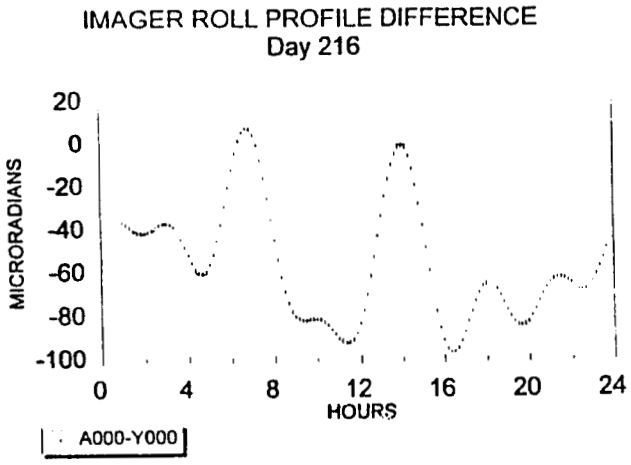

Fig. 2.2-3. Imager Roll Profile Difference

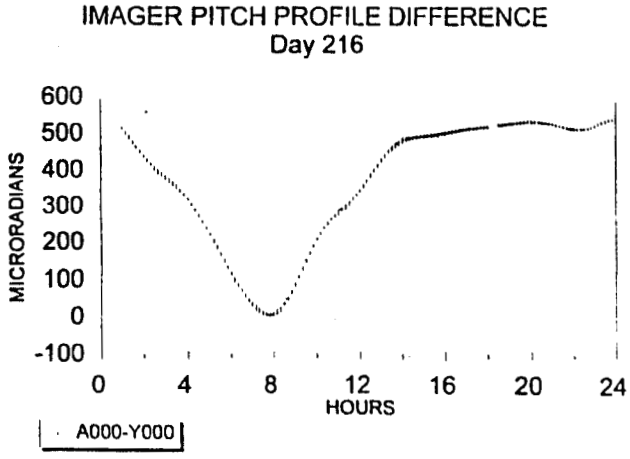

Fig. 2.2-4. Imager Pitch Profile Difference

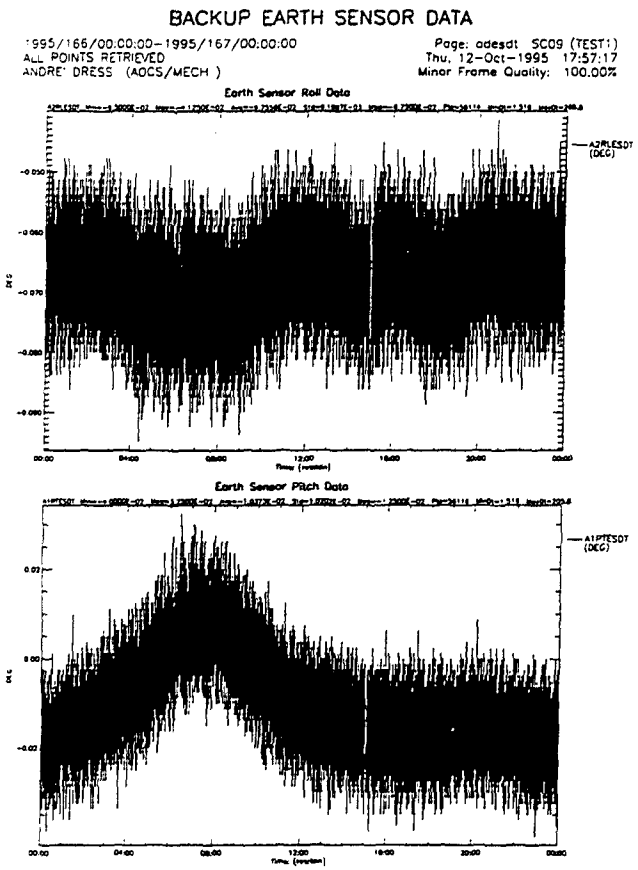

Fig. 2.2-5. Backup Earth Sensor Data (Dual Chord)

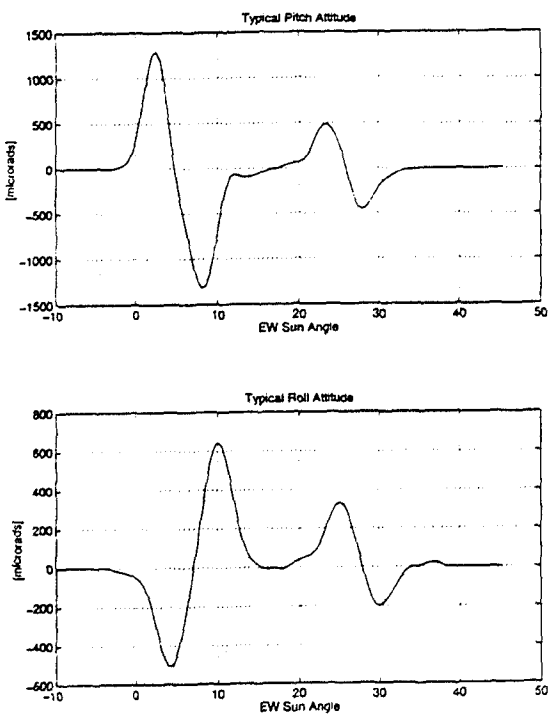

Fig. 2.3-1. Typical Spacecraft Response to Summer Batwing

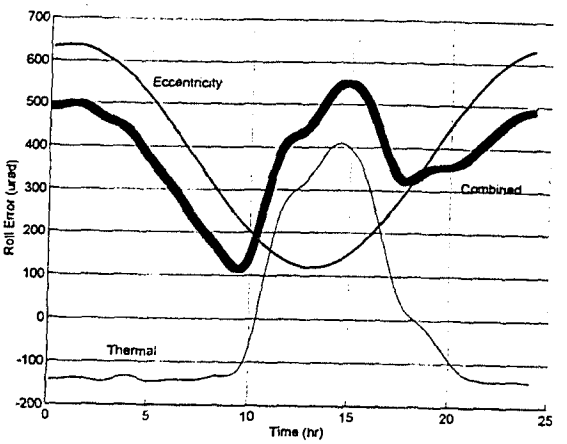

Fig. 2.2-6. Roll Repeatable Error

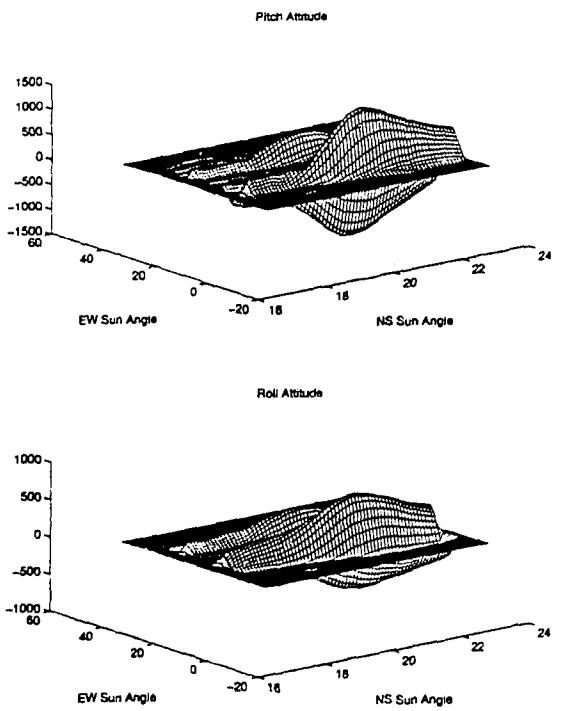

Fig. 2.3-2. Spacecraft Attitude during Summer Batwing Season

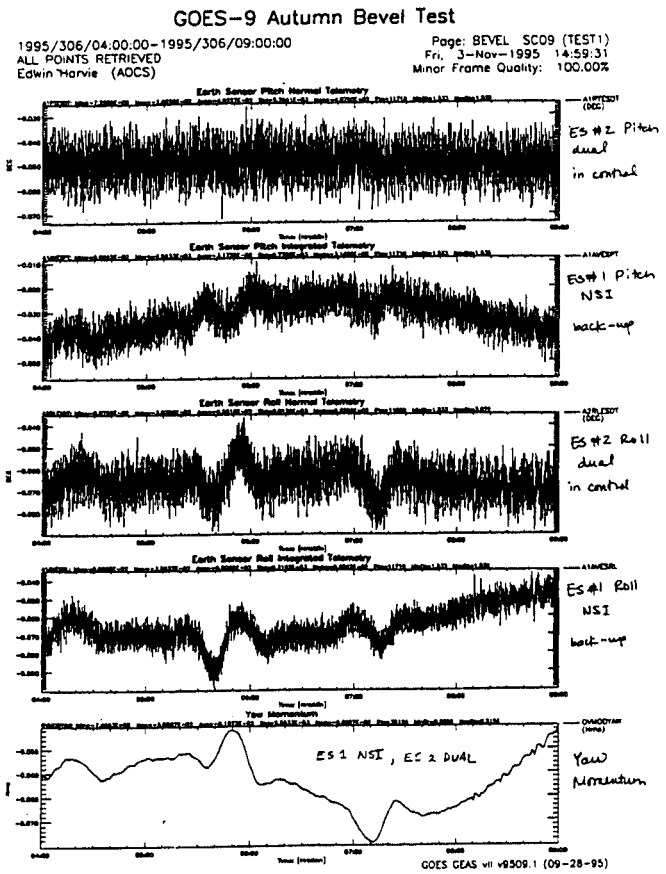

Fig. 2.4-1. GOES-9 Telemetry during Bevel

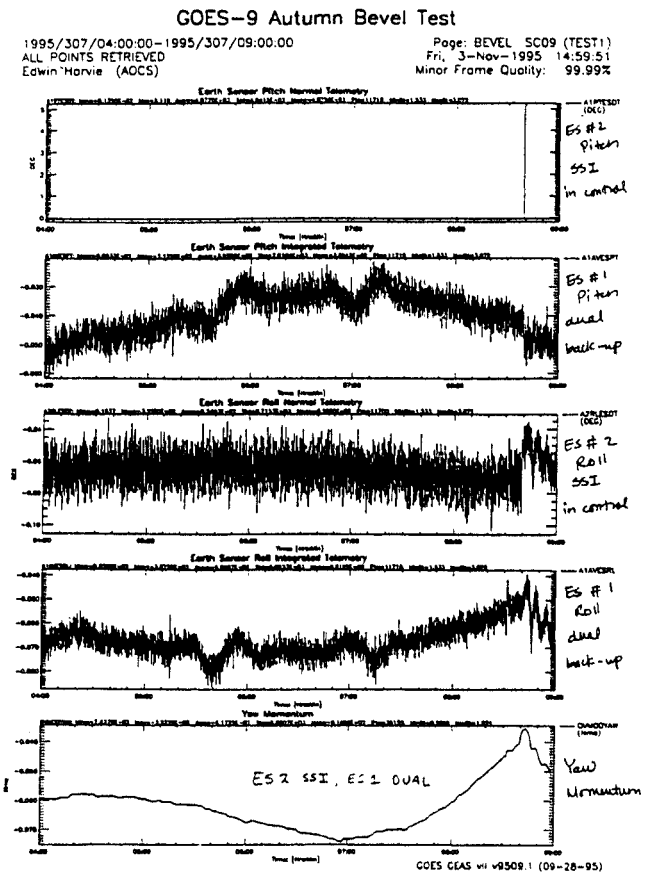

Fig. 2.4-4. GOES-9 Telemetry during Bevel with Controlling ES in SSI

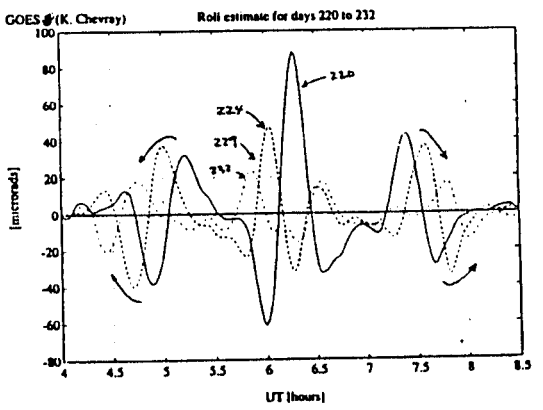

Fig. 2.4-2. GOES-8 Roll Attitude during Bevel

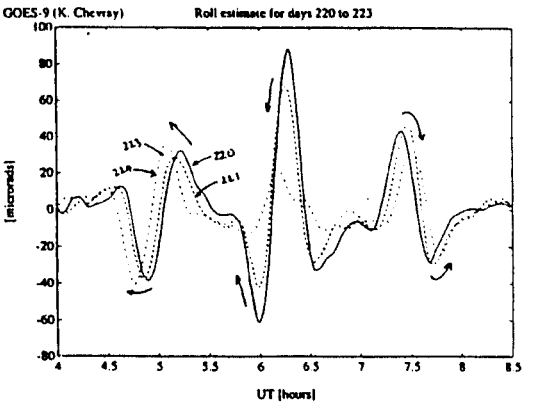

Fig. 2.4-3. GOES-9 Roll Attitude during Bevel

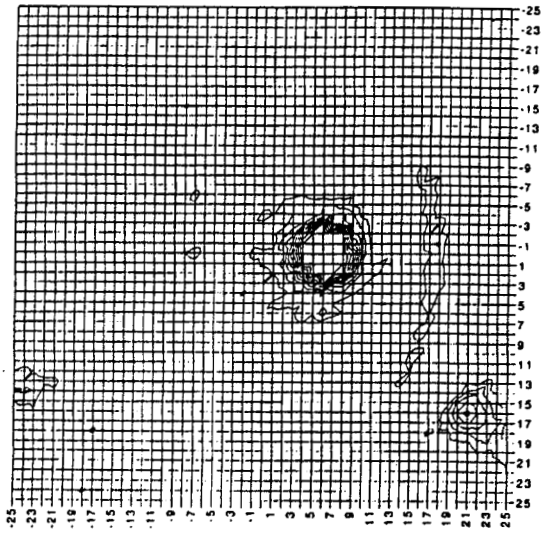

Fig. 3-1. Processed FOV Mapping Data

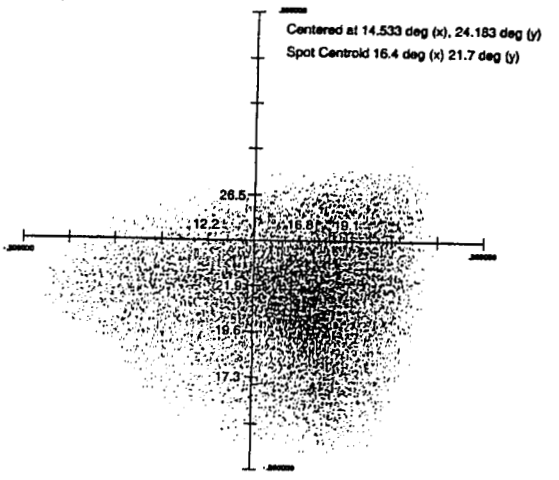

Fig. 3-2. Projected Spot Diagram for Summer Batwing

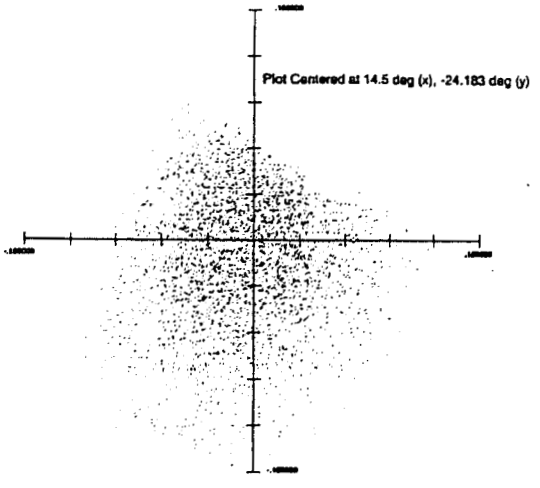

Fig. 3-3. Projected Spot Diagram for Winter Batwing

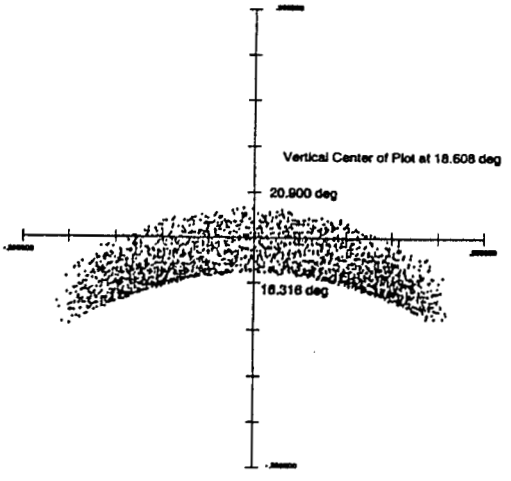

Fig. 3-4. Representative Projected Spot Diagram for Bevel Effect

Understanding GOES-8 dynamics

Sivakumar S.K. Tadikonda[1]

McDonnell Douglas Aerospace
Seabrook, MD 20706

and

Sandra A. Cauffman[2]

NASA Goddard Space Flight Center
Greenbelt, MD 20771

ABSTRACT

The dynamics of Geostationary Environmental Operational Satellite-8 is simulated using an articulated, flexible, multibody dynamics model. The solar array on this spacecraft is flexible, and is articulated with a stepper motor. Three stepping configurations are available: a 0.007° single step every 1.69 seconds, and two double stepping options that were provided in order to deadbeat the solar array oscillations. In this paper, models that are commonly employed for simulating the dynamics of spacecraft with flexible appendages are reviewed and the advantages of the present model over other methods are emphasized. Simulation results show good agreement with the flight data when orbital environmental effects are accounted for. This study has significant implications for both the design and dynamic modeling of articulating, flexible solar arrays attached to the spacecraft, especially when payloads such as the Solar X-ray Imager with tight pointing requirements are to be located on the solar array. The implications are: i) appropriate dynamic models must be employed, ii) the solar array actuating device must be such that vibrational modes of the array are not excited, and iii) conservative damping estimates must be used when empirical values are not available.

1. INTRODUCTION

Geostationary Environmental Operational Satellite-8 (GOES-8) was launched on April 13, 1994. The GOES-8 is a spacecraft in the GOES/I-M series, with all the spacecraft having the same kinematic structure and possessing similar mass properties. GOES-I was renamed GOES-8 after launch. The spacecraft, shown in Figure 1, has an articulating solar array that is driven by a stepper motor, with a single step corresponding to a 0.007 degree rotation, occurring every 1.69 seconds. Two double stepping profiles, described in Section 4, are also available. The double stepping profiles are selected with the objective of deadbeating the solar array oscillations.

A Solar X-ray Imager (SXI) is to be flown on GOES-M scheduled for launch in 1999. The SXI is currently being accommodated on the yoke of the solar array. The solar array has four component fixed-free vibrational modes with frequencies below 2 Hz. Of these, the first torsional mode is the one that is expected to be excited most by the constant stepping of the solar array drive motor, thus affecting the SXI's performance. This necessitated the development of an appropriate model to characterize the dynamic environment under which the SXI must operate. Consequently, a model is developed for predicting the SXI jitter, and is validated by comparison with the flight data of GOES-8, one of the predecessors to GOES-M. In addition to a flexible solar array, GOES/I-M spacecraft also consist of a flexible solar sail that is rigidly attached to the north side of the spacecraft, and a magnetometer boom. The solar sail has five component fixed-free vibrational modes below 2 Hz.

Simulation results obtained using the articulated multi-flexible-body dynamic approach are presented in this paper. This approach is reviewed in this paper and is contrasted with other dynamic models that are routinely employed in the space industry. The salient feature of the present approach is that it enables the correct modeling of an articulating flexible solar array as well as a non-articulating flexible solar sail, and a rigid spacecraft bus. The spacecraft system is assembled from component body models which are obtained using a finite element approach. The

[1] Senior Principal Engineer
[2] SEM Instrument Manager

effects of the baseline single stepping profile and that of one of the two double stepping profiles described in Section 4, were investigated. Simulation results were compared with the flight data for day 103 of 1995 for the single stepping case, and for day 102 of 1995 for the double stepping case. The results of this study provide an understanding of the jitter environment the Solar X-ray Imager on GOES-M is expected to experience.

After a successful comparison of the simulation results with the flight data, a design issue and an analysis issue are addressed. The design issue corresponds to the selection of an actuating device for the articulation of the solar array. The analysis issue concerns what levels of damping must be employed in analyses for the GOES/I-M

2. SPACECRAFT DYNAMIC MODELS

The spacecraft dynamic models employed in the space industry can essentially be divided into four types. They are: i) a decoupled rigid body and flexible body model set, shown in Figure 2a, ii) a one-way coupled model in which only the rigid body (attitude) dynamics affects the flexible body dynamics, as shown in Figure 2b, iii) a completely coupled model in which the attitude dynamics and the flexible body dynamics interact with each other, as shown in Figure 2c, and iv) a coupled model for spacecraft with articulated flexible appendages, with a block diagram similar to that in Figure 2c. Note that the first three models require a flexible body model for the entire spacecraft, not just for the flexible appendages, where as the last model requires flexible body models only for those bodies that are considered to be more flexible compared to other bodies. The salient features of these dynamic models are described next.

Model I: The uncoupled one body model: In this model, the attitude and vibrational dynamics are simulated separately, and the results are simply superimposed. Using the following definitions,

$\mathbf{M}_{RR}$ Rigid body mass matrix,
$\mathbf{M}_{FF}$ Mass matrix corresponding to flexible motion,
$\mathbf{q}_R$ A column matrix of generalized coordinates representing rigid body degrees of freedom,
$\mathbf{q}_F$ A column matrix of generalized coordinates representing vibrational degrees of freedom,
$\mathbf{G}_R$ A column matrix representing linear and nonlinear terms in rigid body generalized coordinates and their time derivatives,
$\mathbf{G}_F$ A column matrix representing linear and nonlinear terms in generalized coordinates and their time derivatives associated with the vibrational degrees of freedom,
$\mathbf{u}_R$ External excitations to rigid body motions,
$\mathbf{u}_F$ Inputs exciting the vibrational motion,
$\mathbf{0}$ A null matrix of appropriate dimension,

with a solid dot over a variable denoting differentiation with respect to time in the inertial frame, this model can be expressed mathematically as:

$$\begin{bmatrix} \mathbf{M}_{RR} & 0 \\ 0 & \mathbf{M}_{FF} \end{bmatrix} \begin{Bmatrix} \ddot{\mathbf{q}}_R \\ \ddot{\mathbf{q}}_F \end{Bmatrix} + \begin{Bmatrix} \mathbf{G}_R(\mathbf{q}_R, \dot{\mathbf{q}}_R) \\ \mathbf{G}_F(\mathbf{q}_F, \dot{\mathbf{q}}_F) \end{Bmatrix} = \begin{Bmatrix} \mathbf{u}_R \\ \mathbf{u}_F \end{Bmatrix} \tag{1}$$

Note that a coupling between the two sets of equations does not exist either through the mass matrix or through the nonlinear terms. The simulations can occur sequentially, and not necessarily on the same computer either. There are conditions under which this model is valid. A spacecraft with fixed-wing solar arrays or solar sails and modeled with free-free modes belongs to this category. In such a system, due to the orthogonality of the system free-free flexible modes to the rigid body modes, no coupling exists between the rigid body and vibrational motions in a linear system model[1]. If fixed-free flexible modes are used, however, Models II or III must be employed.; otherwise an incorrect model will result. Rigid body attitude dynamics models alone are employed for analyzing Attitude Control System (ACS) designs where the objective is to study long term effects. In fact, ACS studies often ignore the vibrational dynamics altogether because 24 hour simulation runs with included flexible body dynamics would require long simulation times. In addition, the ACS bandwidth is typically much smaller than the lowest natural frequency.

Model II: One body model with one way coupling: In this model, only the rigid body dynamics affects the vibrational dynamics. However, in contrast to Model I, the dynamic equations must be solved together with the flexible body equations. The final results are superimposed to obtain the jitter in spacecraft attitude. The mathematical model for this case is:

$$\begin{bmatrix} M_{RR} & 0 \\ M_{FR} & M_{FF} \end{bmatrix} \begin{Bmatrix} \ddot{q}_R \\ \ddot{q}_F \end{Bmatrix} + \begin{Bmatrix} G_R(q_R, \dot{q}_R) \\ G_F(q, \dot{q}) \end{Bmatrix} = \begin{Bmatrix} u_R \\ u_F \end{Bmatrix} \tag{2}$$

where M_{FR} denotes the coupling in the mass matrix between the rigid body and elastic motion variables, $q = [q_R^T \; q_F^T]^T$ and T denotes transpose. This case arises when fixed-free modes are employed for modeling the flexibility, but the attitude motions are solved independent of the vibrational dynamics. Numerical simulations using this model will require considerably longer times than Model I. Although some interaction is considered between attitude and vibrational dynamics, this interaction will vanish when free-free flexible modes for the entire system are employed.

Model III: One body model with complete coupling: This model considers the complete interaction between the fast (vibrational) and the slow (rigid body) dynamics. Once again, this model will be identical to that in the previous two cases for the linear case when free-free flexible modes for the entire system are employed. Mathematically,

$$\begin{bmatrix} M_{RR} & M_{RF} \\ M_{FR} & M_{FF} \end{bmatrix} \begin{Bmatrix} \ddot{q}_R \\ \ddot{q}_F \end{Bmatrix} + \begin{Bmatrix} G_R(q, \dot{q}) \\ G_F(q, \dot{q}) \end{Bmatrix} = \begin{Bmatrix} u_R \\ u_F \end{Bmatrix} \tag{3}$$

where $M_{RF} = M_{FR}^T$. Note that G_R and G_F can now contain both linear and nonlinear terms, and can include rigid body as well as elastic displacements and velocities. Thus, the coupling is not only through the mass matrix but also through the remaining terms in Eq. (3).

Three points must be noted with respect to the three models described above: i) A one-body model for the entire spacecraft, including all the rigid and flexible appendages, is needed for analyses in each case. This is typically a finite element model set up in finite element software such as NASTRAN. For the case of free-free component modes, the numerical simulations (transient analyses in NASTRAN parlance) can even be run using NASTRAN, although it is cumbersome to do so. ii) The types of flexible modes (with free-free or fixed-free end conditions, for example) to use for modeling flexible body dynamics is an issue that has undergone much discussion in the literature and has been again addressed recently[2]. iii) The discussion thus far has been limited to fixed-wing spacecraft (no articulation of appendages, rigid or flexible).

Model IV: A coupled model for spacecraft with articulated flexible appendages: Earth-pointing spacecraft typically have articulating solar arrays. These solar arrays are flexible, and articulation of these appendages excites the solar array vibrational dynamics resulting in jitter in spacecraft attitude. Articulated, flexible body systems can also be found in manipulators, robots, space station, machinery, and so on. These systems cannot be modeled using the techniques presented in Models I - III and require special methods such as those presented in References 3-5. The main reason is that different articulation angles between adjoining bodies result in different vibrational frequencies and mode shapes. For example, in the case of GOES-8, as will be shown in the numerical examples section, the jitter pattern in the roll and yaw of the spacecraft switch every quarter orbit due to the fact that the solar array undergoes a full rotation every orbit. In addition, if the rigid body velocities are significantly large, the nonlinear Coriolis and centrifugal forces arising due to these fast and large overall motions can be modeled using only this approach.

In the multibody approaches[3-5], component flexible body models are employed to synthesize the system dynamics model. The advantage of this approach is that the analyst can determine which component body needs to be modeled as a flexible body. For example, in the case of GOES-8, the bus can be modeled as a rigid body while the solar array and the solar array must be modeled as flexible bodies. The mathematical model for this case is similar to that in Eq. (3), with the equations for the articulating degrees of freedom also appearing.

Recognizing that the applicability of the first three models is limited to spacecraft that contain only non-articulating appendages, in the case of spacecraft such as GOES-8 with articulating flexible solar arrays, dynamic analyses are performed typically for a few different but fixed orientations of the solar array. Consequently, in the articulating appendage cases such analyses omit the transition between those orientations. Note that the underlying assumptions behind dynamic models are often not stated explicitly and this can indeed lead to confusion regarding who has a better model or which results are more believable when comparing results from different models.

It will be shown using the flight data that in the case of GOES-8, the persistent disturbance on the spacecraft is due to the articulation of the solar array, and in particular due to the stepping process. As a result, modeling the transition between different solar array orientations, even if they are only 0.007 degrees (one single step for the stepper motor) apart, and its effect on the spacecraft attitude, is paramount for any model validation. An articulated, flexible multibody dynamic model that also models the stepping process so that the effect of stepping can be studied was

developed and presented in Ref. 6. A brief description of the dynamic model for the GOES-8 spacecraft is presented below. The details for larger systems can be found in References 3-5.

3. GOES-8 DYNAMIC MODEL

As stated earlier, there are two main reasons due to which the first three dynamic models described in Section 2 are not suitable for predicting the jitter in the spacecraft attitude. The first one is the fact that the solar array is indeed not rigidly fixed to the spacecraft but is articulating at an average rate of 360° every 24 hours. The second one is that a single flexible body model for the whole spacecraft in an on-orbit, deployed configuration and for any fixed orientation of the solar array, is not available in the entire GOES program. The spacecraft bus is modeled as rigid in analyses involving deployed configurations.

The GOES-8 dynamic model presented in Ref. 6 and reviewed here belongs to the Model IV category and can be derived using any of the approaches in Refs. 3-5. The salient features of this model are: i) the spacecraft bus is modeled as rigid, ii) the solar sail is modeled as a flexible body that is rigidly attached to the spacecraft bus, iii) the solar array is modeled as a flexible body that can articulate with respect to the spacecraft bus, iv) finite element descriptions of component body fixed-free modes are used for modeling the flexibility of the solar array as well as the solar sail, v) the first seven modes are used for the solar array and the first five modes are used for the solar sail, and vi) the magnetometer, owing to the fact that its first natural frequency is larger than twice the largest of the above modeled component frequencies, is modeled as rigid and as rigidly attached to the spacecraft bus. The actuation of the stepper motor is modeled by a PD controller:

$$u = -\left[\Omega^2\left(\theta - \hat{\theta}\right) + 2\zeta\Omega\,\dot{\theta}\right] \mathbf{I}_1(2,2) \tag{4}$$

where u is input to the solar array articulation degree of freedom, $\mathbf{I}_1(2,2)$ is the (2,2) element of the inertia tensor $\mathbf{I}_1$ for the solar array in its own body frame, Ω is the natural frequency in radians/second, ζ is the damping ratio, θ is the angle between the solar array and the spacecraft body frames about the spacecraft pitch axis, $\hat{\Theta}$ is the desired angle which is stepped up 0.007 degrees every 1.69 seconds, and $\dot{\Theta}$ represents the articulation rate.

A result of employing component body models for modeling the flexible body dynamics is the need to compute the modal coupling terms[1]. These terms describe how the rigid body and flexible motions are coupled in the model. Let the elastic displacement of the solar array be modeled using the assumed modes method[7] as:

$$\underline{U}(\underline{r},t) = \sum_{i=1}^{N} \underline{\phi}_i(\underline{r})\,\eta_i(t) \tag{5}$$

where $\underline{r}$ represents the location of a generic point on the solar array with respect to a selected coordinate system, $\underline{U}(\underline{r},t)$ represents the spatial as well as time dependent elastic displacement having x, y and z components, t denotes time, $\underline{\phi}_i$ represent the spatial dependent mode shapes, $\eta_i(t)$ denote their time dependent amplitudes and N denotes the number of modes used. The modal integrals to be computed are:

$$\underline{\alpha}_i = \int \underline{\phi}_i(\underline{r})\,dm, \quad i = 1, 2,..., N \tag{6}$$

representing the modal linear momentum coefficients, and

$$\underline{h}_i = \int \underline{r} \times \underline{\phi}_i(\underline{r})\,dm \quad i = 1, 2,..., N \tag{7}$$

representing the modal angular momentum coefficients. These coefficients denote how rigid body motion and elastic motions affect each other, and are computed for each elastic body in its own body frame. Note that each of the coefficients in Eqs. (6) and (7) have x, y, and z spatial dependence and in addition are associated with each of the flexible modes. These coefficients can be calculated via NASTRAN DMAP sequences[8] or by using other algorithms outside NASTRAN[9]. The modal mass and stiffness matrices complete the flexible body modeling. The complete component body data for the solar array, solar sail, and the spacecraft bus are given in Ref. 6.

The model thus set up is of the form shown in Eq. (3). The model in Eq. (3) can be numerically integrated to obtain time histories of various variables. The eigenvalue problem for a linearized version of the system in Eq. (3) can

also be solved to obtain the system frequencies. It must be emphasized that although component flexible body data is used, the synthesized GOES-8 model may have system characteristics that are entirely different from component body characteristics. One may find that some or all of the component frequencies have undergone significant changes. Let us refer to the results for GOES-8 summarized in Table 1[6].

The first column in Table 1 lists the component flexible body. The second column characterizes the modes as Out-of-Plane (OP) bending, In-Plane (IP) bending, or Torsion (T). (Plane refers to the plane of the undeformed solar array.) The component frequencies for the first seven modes for the solar array and the first five modes for the solar sail are shown in the third column. The frequencies obtained from the synthesized model for GOES-8 for a particular orientation of the solar array are shown in the fourth column. Finally, the system frequencies obtained from a one-body finite element analysis in NASTRAN for the same fixed orientation are tabulated in the last column.

We observe from Table 1 that the system frequencies are higher than component body frequencies. This is due to the fact that the component body models consider a fixed-end condition at the interface between the flexible body and the spacecraft. However, that interface is fixed only with respect to the bus and moves with the bus. This represents a relaxation of a constraint and thus the frequencies increase[7]. However, the percentage change in a frequency depends on how much such a relaxation will affect the end condition. For example, the IP1 frequency is affected much more than any other component body frequency for the solar array. In fact, it will be shown in the next section that this IP1 mode of the solar array plays a pivotal role in GOES-8 vibrational dynamics. The torsional mode T1 is not affected because the spacecraft inertia about the pitch axis is so large that the interface between the solar array and the bus represents almost an inertially fixed end condition.

We also observe from Table 1 that the same solar sail component frequencies get transformed into different system frequencies. The percentage increases in OP2 and OP4 modal frequencies at the system level are higher than those for the OP1 and OP3 frequencies, respectively, for the solar sail. This is due to the fact that the spacecraft inertias for the direction affecting the OP2 and OP4 modes are lower than those for the direction affecting the OP1 and OP3 modes. The torsional mode T1 for the sail is not affected for the same reason given in the previous paragraph.

Note that as the orientation of the solar array with respect to the spacecraft bus changes the system frequencies shown in the fourth and last columns also change. The results in the last column are for a one-body model, presented in order to provide a measure of authenticity for the results of the articulated, flexible multibody dynamics model.

4. SIMULATION RESULTS VS. FLIGHT DATA

The solar array on GOES-8 can be articulated using one of the two stepping scenarios shown in Figures 3a and 3b. A 0.007^{o} articulation every 1.69 seconds forms the baseline stepping case shown in Figure 3a. The profile stepping (also called double stepping) case in Figure 3b is provided with the objective of deadbeating the solar array torsional mode. Two ΔT options of 0.241 and 0.28 seconds are available for the double stepping case.

The flight data is provided by the Angular Displacement Sensors (ADS), one for each axis, located on the spacecraft. The ADS works as a high pass filter with a cut off frequency near 2 Hz. However, the ADS transfer function is known with sufficient accuracy so that the response below 2 Hz can be obtained by passing the flight data through an inverse transfer function of the ADS. The sampling rate of ADS is 800 Hz (400 Hz Nyquist frequency) and a 2^{17} point Discrete Fast Fourier Transform (DFFT) must be employed in order to obtain a resolution of 0.003 Hz. Thus, the flight data for comparison is at least over 5 minutes and 28 seconds in each case described below.

Numerical simulations are performed using Model IV described in Section 2. Simulation results using the nominal model data and the corresponding flight data for Day 103 of 1995 are shown in Figure 4, for the single stepping case. The flight data is for near the top of the hour at 11:00 hrs. GMT. We observe that the simulated pitch has larger amplitudes than the flight pitch and that simulated roll is much smaller than and clearly has a different frequency content from the flight data. The reason for this difference becomes clear when we look at the Power Spectral Density (PSD) plots for two cases in Figure 4. The peaks in the PSD plots in Figure 5 for the flight data correspond to the harmonics of the 1/1.69 (= 0.592) Hz stepping. The reason the second and third harmonics of this stepping appear to contribute significantly to the spacecraft jitter is that these harmonics are close to certain frequencies of the spacecraft, and in particular to certain frequencies of the solar array.

It is easy to conclude that the third harmonic of the stepping is close enough to the T1 mode of the solar array to excite it. But, what about the second harmonic? We observe from Table 1 that two system modes - IP1 and OP2 - arising from solar array vibrations are close to the second harmonic of stepping. In fact, the system frequency of 1.14 Hz due to the solar array IP1 mode is closest to the (2*0.592 =)1.184 Hz stepping harmonic. Further analyses showed that it is indeed the IP1 mode that was getting excited by the second harmonic of stepping.

With the understanding that the IP1 and T1 modes are getting excited due to the stepping we now observe from Figure 5 that the simulated roll and yaw have an almost missing T1 mode of the solar array, a simulated roll that has a much larger IP1 peak than the flight data, and a simulated pitch that has a larger T1 peak than the corresponding flight data. Parametric studies were then conducted in order to obtain a good agreement with the flight data. Since it is the IP1 and the T1 modes that have a significant participation in the flight data, the parametric study is limited to studying the effects of these two modes. In particular, the linear and angular momentum coefficients associated with these modes of vibration as well as their component natural frequencies are the parameters. These studies conclusively proved that it is the IP1 mode that is present in the flight data in Figures 4 and 5. The parametric set resulting in a good agreement between flight data and simulation results is shown in Table 2[6]. Simulation results shown in Figure 6 indeed compare well with the flight data shown in Figure 4.

Similar modifications were needed for other configurations of the solar array and the parameters are again shown in Table 2[6]. Figure 7 shows the simulation results for the time period around 17:00 hrs. GMT, with the modified parameter set. These results are in good agreement with the flight data (not shown). The modifications implied that the solar array bends as twists, and twists as it bends in-plane. The reason for such modifications is the fact that the orbital thermal environment is not modeled in this study. This thermal environment was also not a part of the structural model that was provided for this study. Separate thermal analyses yielded results that indicate that the solar array bends out-of-plane due to thermal distortions, thus causing a coupling between torsion and bending.

It is clear from the flight data that the spacecraft jitter is due to the vibration of the solar array excited by the stepping action of the actuator. This clearly represents the interaction between the rigid body and vibrational motion of the solar array and only Model IV from Section 2 is capable of simulating such an interaction.

4.1 Effect of Damping

Although viscous damping models are routinely employed in structural and multibody dynamics simulations, including the present one, what damping ratios should one use in analyses remains an open question in the absence of any empirical data. The issue of damping is clearly both an analysis and a design issue. Although it is immaterial what value is used in the analyses, the results will have a significant impact on the design of specific components.

The simulations results in Figures 4 and 6 were generated with a 2% modal damping for the T1 mode of the solar array. This appears appropriate because the flight data does not show significant attenuation. What about higher modal damping values? Simulation results generated with the successful parameter set for the results shown in Figure 6, but now with a 5% damping for the T1 mode of the solar array, are shown in Figure 8. The attenuation is significant and now the simulation results do not agree well with the flight data shown in Figure 4. In addition, results similar to those in Figure 8 may point to the wrong conclusion regarding the amplitude of the spacecraft jitter, especially at locations on the solar array where the jitter increases by at least an order of magnitude (due to the conservation of momenta).

4.2 Alternate Baseline Stepping

All the spacecraft in the GOES/I-M series have the same baseline stepping for the articulation of the solar array. Images from the Imager and the Sounder on GOES-8 indicate that the fact that the harmonics of baseline stepping excite the vibrational motion of the solar array has no significant impact on their performance. However, the Solar X-ray Imager is being located on the solar array yoke on GOES-M. Analysis results indicate that the SXI will experience jitter that is about 10 to 25 times that on the spacecraft side. In addition, the PSD plots shown in Figure 9 for day 102 of 1995 for the double stepping case with $\Delta T = 0.28$ sec. indicate that the contribution from the torsional mode is second only to that of the double stepping mode. Recalling that in this mode the double steps are executed every 3.38 seconds (~0.3 Hz), we note that the fourth and sixth harmonics of this profile are close to the IP1 and T1 modes of the solar array, respectively. With such profiles, one ΔT cannot be expected to provide the desired deadbeating. Thus, it necessitates the exploration of alternate methods for jitter mitigation within the constraints of stepping.

Assuming that we are restricted to the use of a stepper motor for an actuating device for the solar array, we investigate the following alternate baseline stepping profiles: i) a 0.008° step every 1.92 seconds (stepping harmonics: 0.52, 1.04, 1.56 and 2.08 Hz) and ii) a 0.006° step every 1.44 seconds (stepping harmonics: 0.69, 1.38, and 2.07 Hz). By comparing these harmonics with the GOES-8 natural frequencies in Table 1 we observe that the 0.008° step case should perform the worst among the 0.006°, 0.007° and 0.008° step cases because of the closeness of the second harmonic to the IP1 and OP2 modes. This indeed is the case as can be seen from the roll, pitch and yaw plots shown in Figure 10. Similarly, we expect the second alternate baseline profile to perform even better than the 0.007°/1.69 sec profile because the stepping harmonics are far removed from the GOES-8 natural frequencies. We observe from Figure 11 that this indeed is the case.

We conclude that there are better and worse baseline stepping profiles than the one that has been implemented on GOES-8 and GOES-9, and is being implemented on GOES/K-M, even when one is constrained to use a stepper motor.

5. CONCLUSIONS

GOES-8 dynamics has been simulated using an articulated, flexible multibody dynamic model. This model and three other models that are commonly employed for simulating the dynamics of a system consisting of flexible bodies are reviewed. The solar array articulation on this spacecraft is via a stepper motor and both the flight data and simulation results demonstrated that this stepping excites the vibrational dynamics of the solar array. Numerical simulation results showed good agreement with flight data. Two design and analysis issues are investigated.

The important conclusions of this study are:

i) Selection of an appropriate mathematical model and consideration of all the limitations of such a model are essential for correctly simulating and understanding the microradian level response of GOES-8 spacecraft.

ii) On-orbital vibrational dynamics of flexible bodies such as the solar array may be significantly different from the analytical predictions due to the effects of the orbital environments.

iii) Solar array stepping causes significant jitter. Selection of the actuating device for the solar array articulation must be done in conjunction with a detailed structural analysis of the solar array. In particular, one must avoid any actuating devices (steppers or servos) with frequencies or their harmonics that are close to the natural frequencies of the solar array.

iv) When empirical values are not available for damping conservative estimates must be used.

ACKNOWLEDGMENT

The first author's part of this work was performed under contact to NASA Goddard Space Flight Center (GSFC), Contract No. NAS5-32590. The authors thank Mr. Mike Hagopian of NASA and Dr. Wayne Dellinger of Swales & Associates, Inc. for providing the GOES-8 flight data, and Mr. Sharad Mehta of Space Systems/Loral for providing the component modal data from NASTRAN analyses.

REFERENCES

1. Tadikonda, S.S.K., Mordfin, T.G., and Hu, T.G., "Assumed Modes Method and Articulated Flexible Multibody Dynamics," Presented at the 1993 AIAA Guidance, Navigation, and Control Conference, Monterey, CA. Also, Journal of Guidance, Control, and Dynamics, May-June, 1995, pp. 404-410.

2. Mordfin, T.G., and Tadikonda, S.S.K., "Truth Models for Articulated Flexible Multibody Dynamics," To be presented at the 1996 AIAA Guidance, Navigation, and Control Conference, San Diego, CA, July 29-31.

3. Hooker, W.W., "Equations of Motion for Interconnected Rigid and Elastic Bodies: A Derivation Independent of Angular Momentum," Celestial Mechanics, Vol. 11, 1975, pp. 337-359.

4. Singh, R.P., VanderVoort, R.J., and Likins, P.W. "Dynamics of Flexible Bodies in Tree Topology - A Computer-Oriented Approach", Journal of Guidance, Control and Dynamics, Vol. 8, No. 5, 1985, pp.584-590.

5. Bodley, C., Devers, A., Park, A., and Frisch, H. "A Digital Computer Program for Dynamic Interaction and Simulation of Controls and Structures (DISCOS)," NASA Tech. Paper 1219, May 1978.
6. Tadikonda, S.S.K., "Articulated, Flexible Multibody Dynamics Modeling: A GOES-8 Case Study," To be presented at the 1996 AIAA Guidance, Navigation, and Control Conference, San Diego, CA, July 29-31.

7. Meirovitch, L., "Computational Methods in Structural Dynamics," Sijthoff - Noordhof, Alphan aan den Rijn, The Netherlands, 1980.

8. Messac, A., and Storch, J., "Evaluation of Inertial Integrals for Multibody Dynamics," Journal of Guidance, Control, and Dynamics, May-June, 1994, pp. 624-626.

9. TREEFLX Theory Manual, Dynacs Engineering Co. Inc., Clearwater, FL.

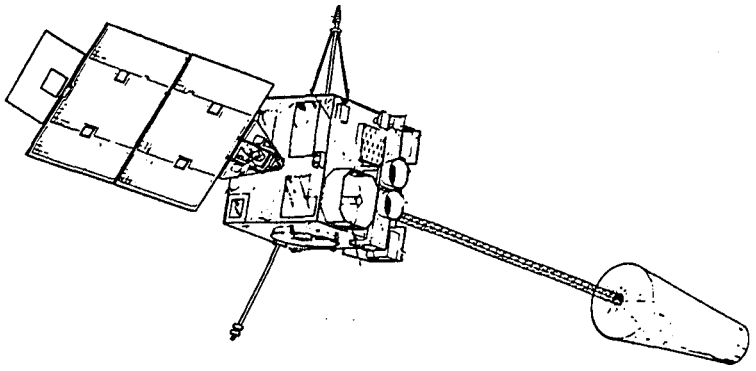

Figure 1: GOES-8 Spacecraft

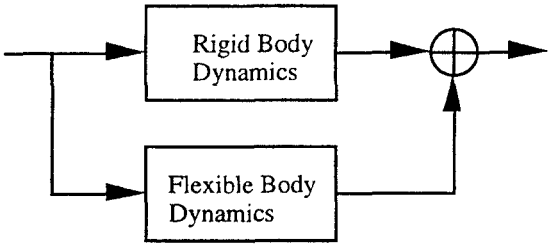

Figure 2a: A Decoupled Model

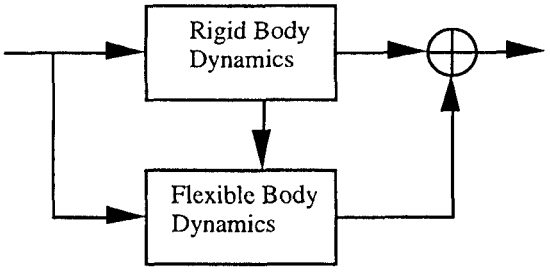

Figure 2b: A One-way Coupled Model

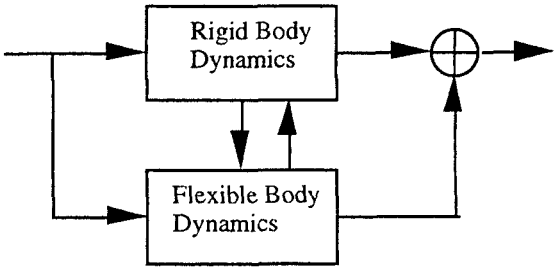

Figure 2c: A Completely Coupled Model

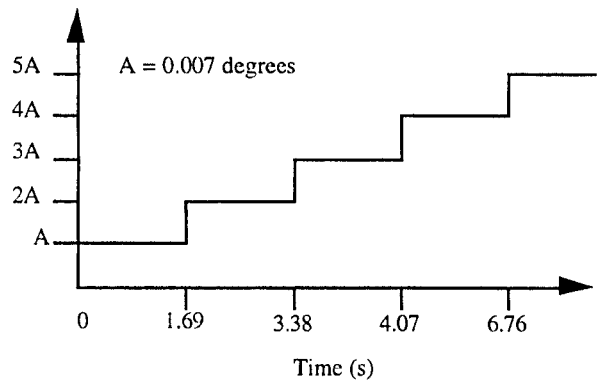

Figure 3a: GOES-8 Single (Baseline) Stepping

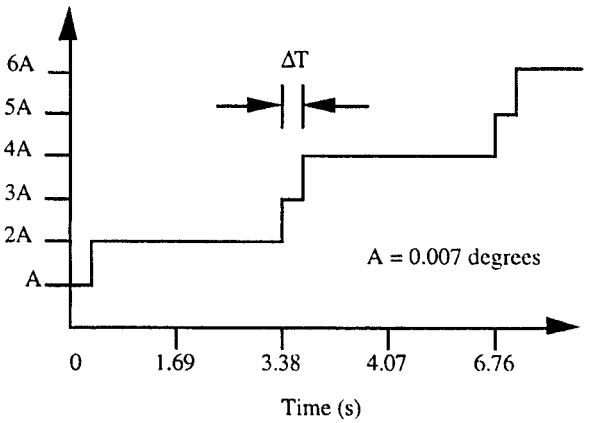

Figure 3b: GOES-8 Double (Profile) Stepping

Table 1: Component and System Frequencies

Component	Component Mode Characterization	Component frequencies (Hz)	System frequencies obtained using the present method (Hz)	System frequencies obtained from a one body NASTRAN analysis
Solar Array	Out-of-Plane (OP) 1	0.17262	0.19950	0.19960
	In-Plane (IP) 1	0.69255	1.14354	1.12163
	OP2	1.07264	1.11905	1.11077
	Torsion (T) 1	1.83254	1.85410	1.85243
	OP3	2.50776	2.59547	2.57851
	OP4	2.81275	2.90904	2.91283
	OP5	3.26070	3.26193	3.26067
Solar Sail	OP1	0.22501	0.25791	0.25682
	OP2	0.22501	0.33056	0.33677
	T1	0.97909	0.97920	0.97882
	OP3	1.79672	1.81379	1.81375
	OP4	1.79672	1.82298	1.81908

Table 2: Parameter modifications needed for matching flight data

Solar Array Configuration	Spacecraft Attitude Degree of Freedom	Linear momentum coefficients $\alpha^{(1)}$ for		Angular momentum coefficients $\mathbf{h}^{(1)}$ for		Component T1 modal frequency (Hz)
		IP1 ($\sqrt{Kg}$)	T1 ($\sqrt{Kg}$)	IP1 ($\sqrt{Kg}.m$)	T1 ($\sqrt{Kg}.m$)	
05:00 hrs. GMT and 11:00 hrs. GMT	Roll (x)	-0.0004	-0.3970	30.2520	-1.8487	1.8325
	Pitch (y)	0.0611	-0.0079	0.6723	4.3697	
	Yaw (z)	7.5194	-0.3308	1.3916	1.6807	
14:00 hrs. GMT	Roll (x)	-0.0004	-0.2647	26.8907	-1.8487	1.79
	Pitch (y)	0.0609	-0.0079	0.6723	4.3697	
	Yaw (z)	5.2934	-1.0587	-1.3916	-0.8403	
17:00 hrs. GMT	Roll (x)	-0.0004	-0.7940	26.8907	-1.1765	1.79
	Pitch (y)	0.0609	-0.0079	0.6723	4.3697	
	Yaw (z)	6.6168	-0.2647	-1.3916	1.6807	

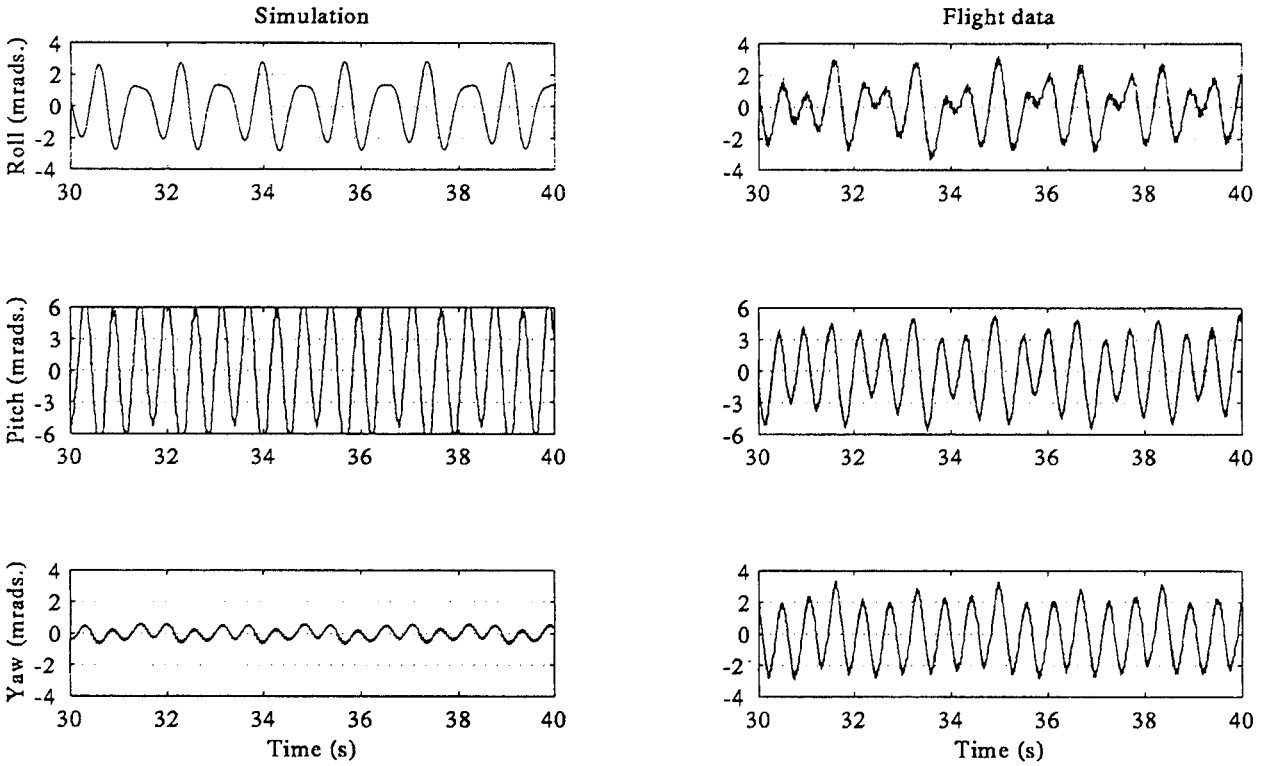

Figure 4: Comparison of simulation results with GOES-8 nominal parameters and flight data around 11:00:00 hrs. GMT

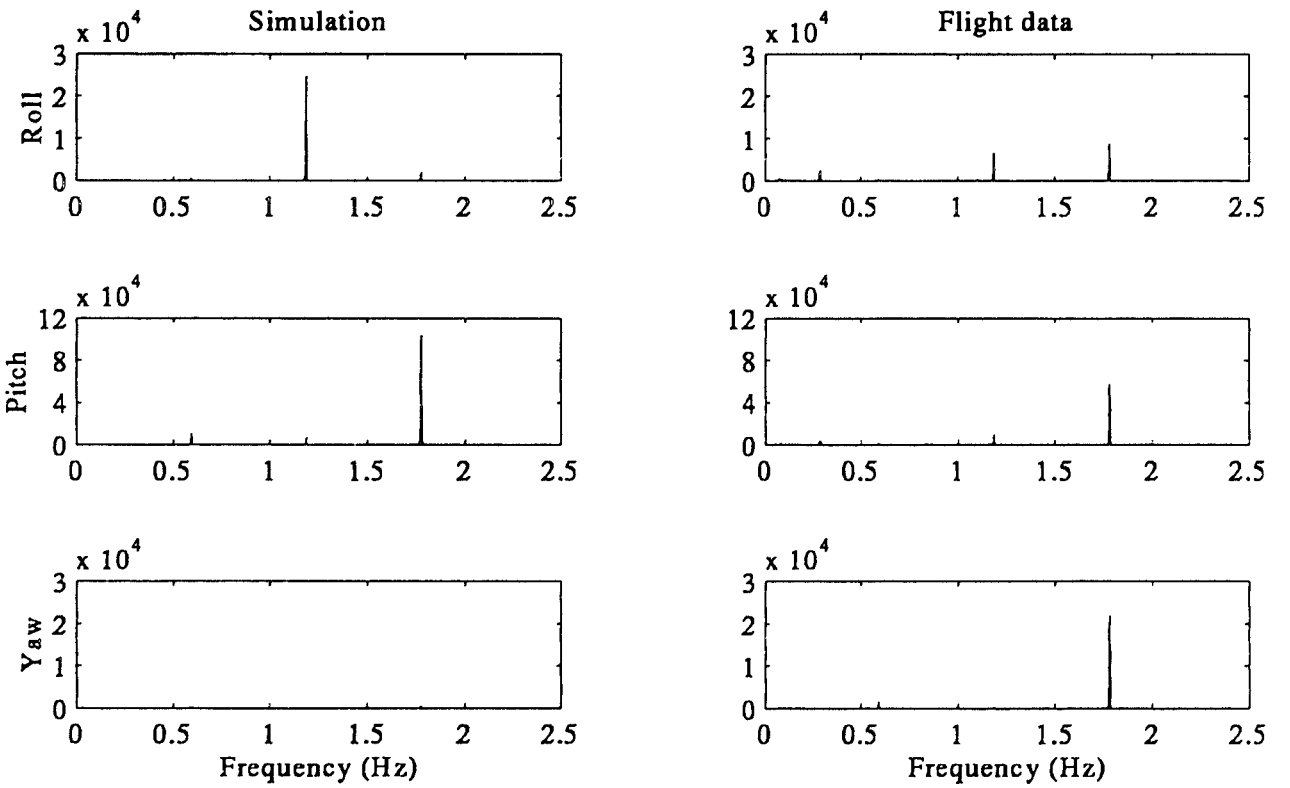

Figure 5: Power Spectral Density (PSD) plots for the data shown in Figure 4.

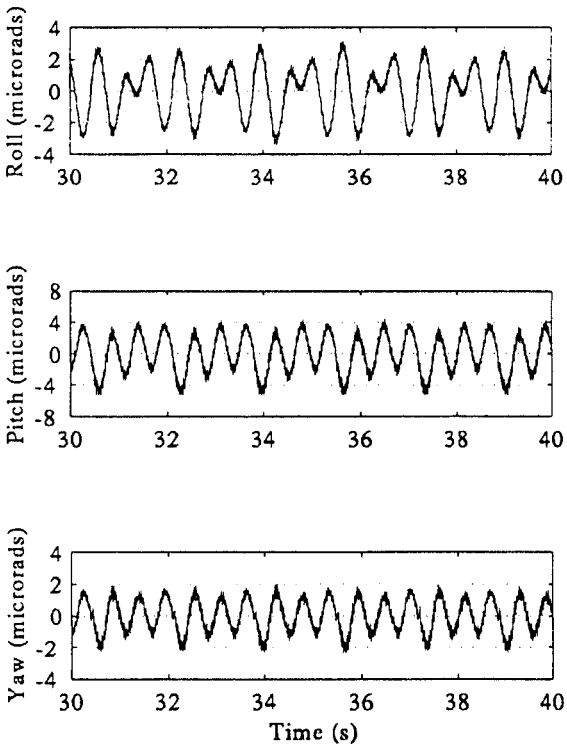

Figure 6: Simulation results with modified data for the case in Figures 4 and 5

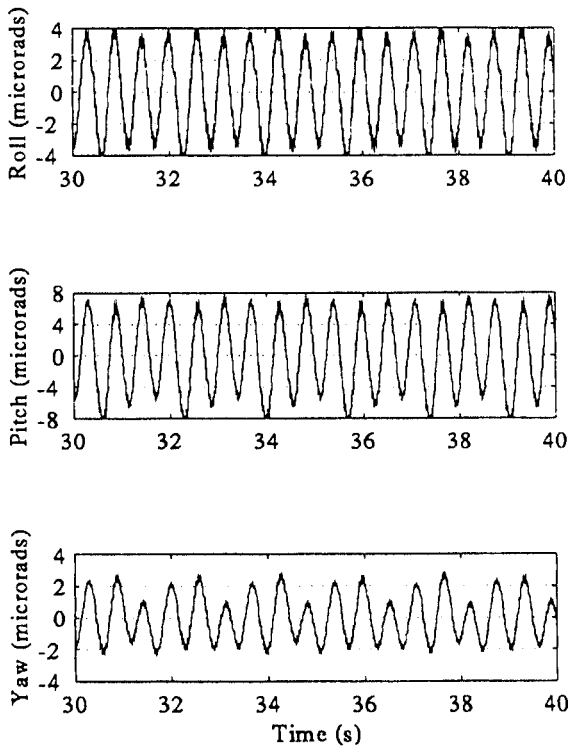

Figure 7: Spacecraft dynamics simulation results for the 17:00:00 hrs. GMT configuration

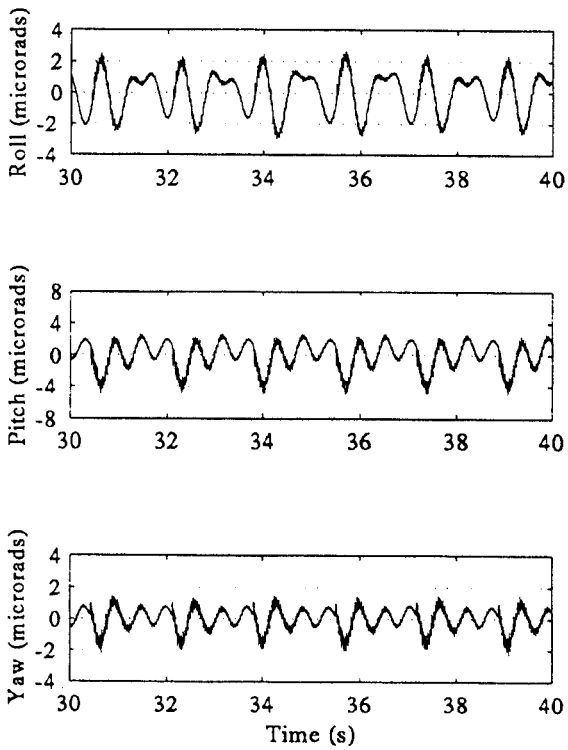

Figure 8: Simulation results for the case in Figure 6, with increased (5%) damping for the T1 mode

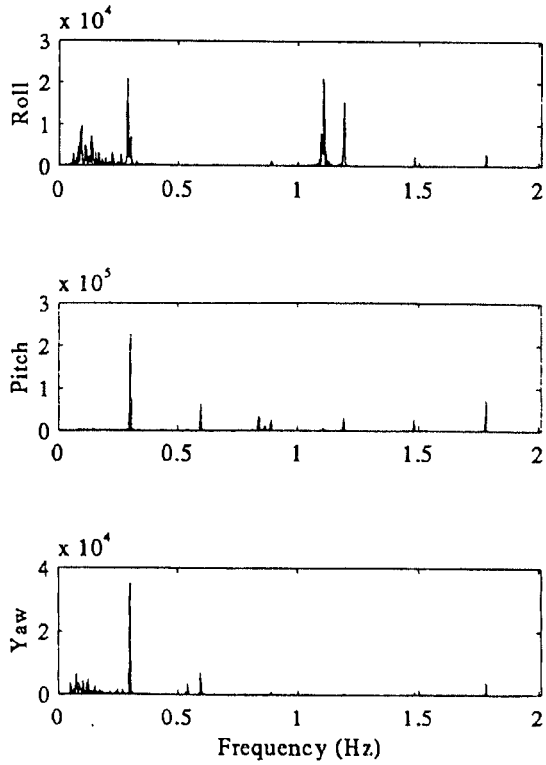

Figure 9: PSD plots of the flight data for the double stepping case and with DT = 0.28 seconds

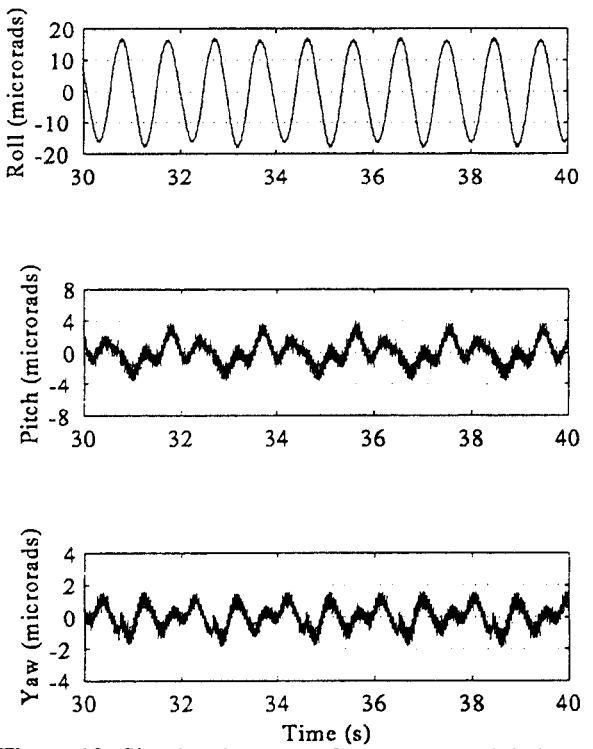

Figure 10: Simulated spacecraft response to 0.008°/1.92 second baseline solar array stepping

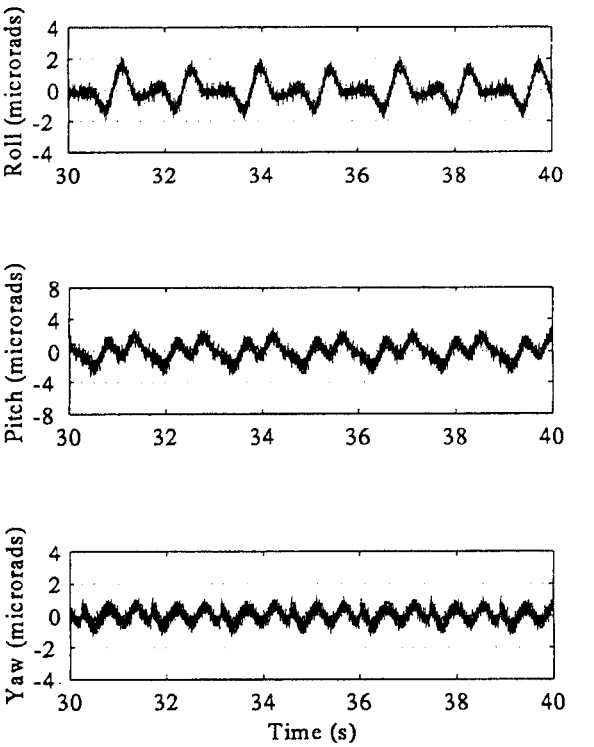

Figure 11: Simulated spacecraft response to 0.006°/1.44 second baseline solar array stepping

Long-Term Stability of GOES-8 and 9 Attitude Control

James L. Carr

Carr Astronautics Corporation
1509 Corcoran St. NW
Washington, DC 20009 USA

e-mail: 100022.3043@compuserve.com

ABSTRACT

An independent audit of the in-orbit behavior of the GOES-8 and GOES-9 satellites has been conducted for the NASA/GSFC. This audit utilized star and landmark observations from the GOES Imager to determine long-term histories for spacecraft attitude, orbital position, and instrument internal misalignments. The paper presents results from this audit. Long-term drifts are found in the attitude histories, whereas the misalignment histories are shown to be diurnally stable. The GOES Image Navigation and Registration (INR) system is designed to compensate for instrument internal misalignments, and both the diurnally repeatable and drift components of the attitude. Correlations between GOES-8 and GOES-9 long-term roll and pitch drifts implicate the Earth sensor as the origin of these observed drifts. This result clearly demonstrates the enhanced registration stability to be obtained with stellar inertial attitude determination replacing or supplementing Earth sensor control on future GOES missions.

Keywords: Image Navigation and Registration, Star Sensing, Attitude and Orbit Determination, Star Trackers, Earth Sensors

1. INTRODUCTION

The GOES-8 and GOES-9 spacecraft are the first of America's 3-axis stabilized geostationary meteorological satellites[1]. Three-axis stabilization presents challenges in providing an accurate and stable remote sensing platform which are not present in spin-stabilized designs. In particular, the diurnal variation in spacecraft-sun geometry leads to thermal deformations which alter the instrument lines-of-sight relative to the IR Earth sensor boresight used by the attitude control system to orient the satellite, and additionally, cause instrument internal misalignments (seen in the images as scan-angle dependent deformations). The Image Navigation and Registration (INR) system has been designed to compensate for these and other dynamic effects[2]. The INR system provides a model for the deformations, as a function of time of day, which is used on-board to adjust the instrument scan patterns. Instrument star and landmark observations, plus satellite-to-CDA ground station ranges, are processed on the ground by the Orbit and Attitude Determination (OAD) process of the Orbit and Attitude Tracking System (OATS) to determine the corrections to be applied during the following day.

Ideally the compensation provided by the INR model should be nearly perfect; however, meteorological effects, in particular, can alter the radiance of the Earth and cause the IR Earth sensor to mispoint the satellite in a nonrepeatable and not easily predicted manner. Therefore, it is necessary to frequently readjust the OAD solutions during daily operations. Such readjustments, called Short Span Attitude Adjustments (SSAA's), reestablish the accurate pointing of the instruments towards the nadir. The primary purpose of the work reported in this paper is to describe the long-term in-orbit behavior of the GOES satellites, and to verify that the Earth sensor is a significant contributor to the need for SSAA operations. In the latter case, significant operational simplification and product improvement may be anticipated if the present Earth sensor control is replaced or supplemented by stellar inertial control on later GOES satellites.

The analysis begins with a determination of the attitude and instrument internal misalignments from Imager star sensing data. The orbit is then determined using Imager VIS landmark data. Finally, the attitude with respect to the true orbit plane is decomposed into diurnally repeatable and nonrepeatable components. The latter component requires SSAA operations for correction.

2. PROCESSED STAR, LANDMARK, AND RANGE DATA

The GOES Imager star and landmark data are preprocessed on the ground before being used by the OAD process. This preprocessing consists of assigning Ephemeris Time (ET) time tags, and calculating gimbal angles and inertial position vectors for objects. These data are archived and available for analysis in processed observations (PROCOBS) files. For the purposes of this study, it was decided to use the PROCOBS data instead of the raw observations since a significant amount of processing is required before the more voluminous raw data may be interpreted.

Satellite-to-CDA ground station range is also recorded in the PROCOBS files, and is used as an aide in orbit determination.

In this analysis, no use is made of other OATS products, with the exception of the OAD orbit solutions. However, the OAD orbit solutions are used only to rotate the star observations into an approximate orbit-frame (quasi-orbit frame; relative to which, roll, pitch and yaw angles are numerically small). Linearized estimation theory is applied to find the attitude with respect to the quasi-orbit frame. Once the attitude is known in the quasi-orbit frame, it can then be transformed into any well-defined reference frame (*e.g.*, inertial, or true orbit plane). In this way, the OAD orbit solutions are used only in a formal sense which does not affect the inertial attitude estimates.

3. ATTITUDE AND INSTRUMENT INTERNAL MISALIGNMENT FILTER

Attitude and instrument internal misalignments are determined from the star data. In general, the Imager acquires 4 star observations within a narrow time window (<5 min.) every half-hour.

The Imager state may be described by a state vector

$$p = \begin{pmatrix} \text{roll} \\ \text{pitch} \\ \text{yaw} \\ \text{misalignment \#1} \\ \text{misalignment \#2} \end{pmatrix} \tag{1}$$

The techniques of linear estimation theory are used to solve for each state vector using star data acquired during time windows of duration not exceeding 5 minutes (during which we assume the state is invariant) and which contain at least 3 stars. The sensitivity matrix expresses the model for the data according to $\zeta = H \cdot p$ where

$$H = \begin{pmatrix} 0 & C\alpha C\varepsilon & C\alpha S\varepsilon & \mp S\varepsilon C\alpha & 0 \\ -C\alpha C\varepsilon & 0 & S\alpha & 1-C\varepsilon C\alpha-S\varepsilon^2(1\pm S\alpha) & \pm S\varepsilon C\varepsilon(1\pm S\alpha) \end{pmatrix} \tag{2}$$

with the upper (lower) sign chosen for the Imager (Sounder)[3]. The "C" and "S" notations are abbreviations for cosine and sine respectively. The residual ζ is formed from the quasi-orbit frame components of the star direction vector

$$\zeta = \begin{pmatrix} \text{x-star} \\ \text{y-star} \end{pmatrix} - \begin{pmatrix} \sin\alpha \\ -\cos\alpha\ \sin\varepsilon \end{pmatrix} \tag{3}$$

where α is the EW (optical) gimbal angle and ε is the NS gimbal angle. We note that typically $|\zeta|$ is of the order 10^{-3}, meaning that the errors introduced by linearization are of the order 10^{-6}.

Each state vector solution presents a snapshot of the attitude and internal misalignment state of the Imager at an instant in time.

4. LANDMARK ORBIT DETERMINATION

We accomplish an independent determination of the satellite orbit using landmarks found in the GOES images and satellite-to-CDA ground station ranges. Imager landmarks are acquired in both the VIS and IR channels as part of routine ground system operations. During daylight hours, the emphasis is on VIS landmark acquisition. We decided to use only the VIS landmark data for this study, since the star data is also from the VIS channel.

Our orbit determination process consists of first computing a satellite position fix for each landmark, and then developing an orbit solution which best fits these fixes and respects the laws of celestial mechanics. To fix the position of the satellite, the measured gimbal angles for each landmark are corrected using the estimated attitude and internal misalignment solution $\hat{p}$ interpolated to the landmark time tag. The transverse components of the Imager line-of-sight in the quasi-orbit frame are given by

$$l_\perp = \begin{pmatrix} \sin\alpha \\ -\cos\alpha\ \sin\varepsilon \end{pmatrix} - H \cdot \hat{p} \tag{4}$$

The satellite position fix is calculated from the line-of-sight transformed into the inertial frame:

$$R_{FIX} = r_{LMK} - s\,\hat{1} \qquad (5)$$

where r_{LMK} is the position vector of the landmark. The unknown slant range s is calculated by constraining $|R_{FIX}-r_{CDA}|$ to equal the satellite-to-CDA ground station range interpolated from the range data at the time tag for the landmark.

A long arc of position fixes is used as input for an orbit determination program based on the European Space Agency (ESA) PEPSOC program which is particularly adapted to geostationary satellites. The PEPSOC orbital integrator models the Earth gravity, lunar and solar point masses, and solar pressure. The orbit determination program finds the satellite position, velocity, and optionally an effective area-to-mass ratio so that the weighted sum of the squares of the differences between the satellite position fixes and the integrated orbit is minimized.

In general, it was found that better solutions for long arcs were obtained when the radial components of the position fixes were down weighted (effectively down weighting the range data). This is probably due to the fact that systematic errors even as small as 1 m (due to ionospheric, station location, and electronic delay uncertainties) can result in errors as large as 250 m in-track after 24 days of integration.

Figure 1 shows a 24-day orbit solution for GOES-8 where the satellite position is described in an Earth fixed frame with the x-axis at the nominal satellite station of -75° longitude.

5. LONG-TERM ATTITUDE CONTROL STABILITY

With the attitude and orbit solutions, we finally transform the attitude description such that it defines the attitude with respect to the true orbit plane. The on-board attitude control system is designed to control the satellite so that the orbit-plane roll, pitch and yaw angles are zero. In reality this is not the case due to thermal deformations between the Earth sensor and the Imager, solar torque imbalance, noise, and systematic errors in the Earth sensor roll and pitch measurements.

Thermal deformations are very repeatable day-to-day and are well corrected by the operational INR system. In analyzing times series of roll, pitch, and yaw solutions, we have decomposed the time series into repeatable and nonrepeatable parts using a periodigram method. It was found that the internal misalignments are indeed very repeatable, which is not surprising since they are purely thermo-elastic in nature. Figure 2 shows the GOES-8 Imager misalignments around the 1995 summer solstice as a function of time of day. Each of the four data arcs shown are 24 days long beginning on the 116-th day of the year. There is a slow evolution from one arc to the next due to the changing solar declination.

Figure 1. GOES-8 Earth-Fixed Ephemeris

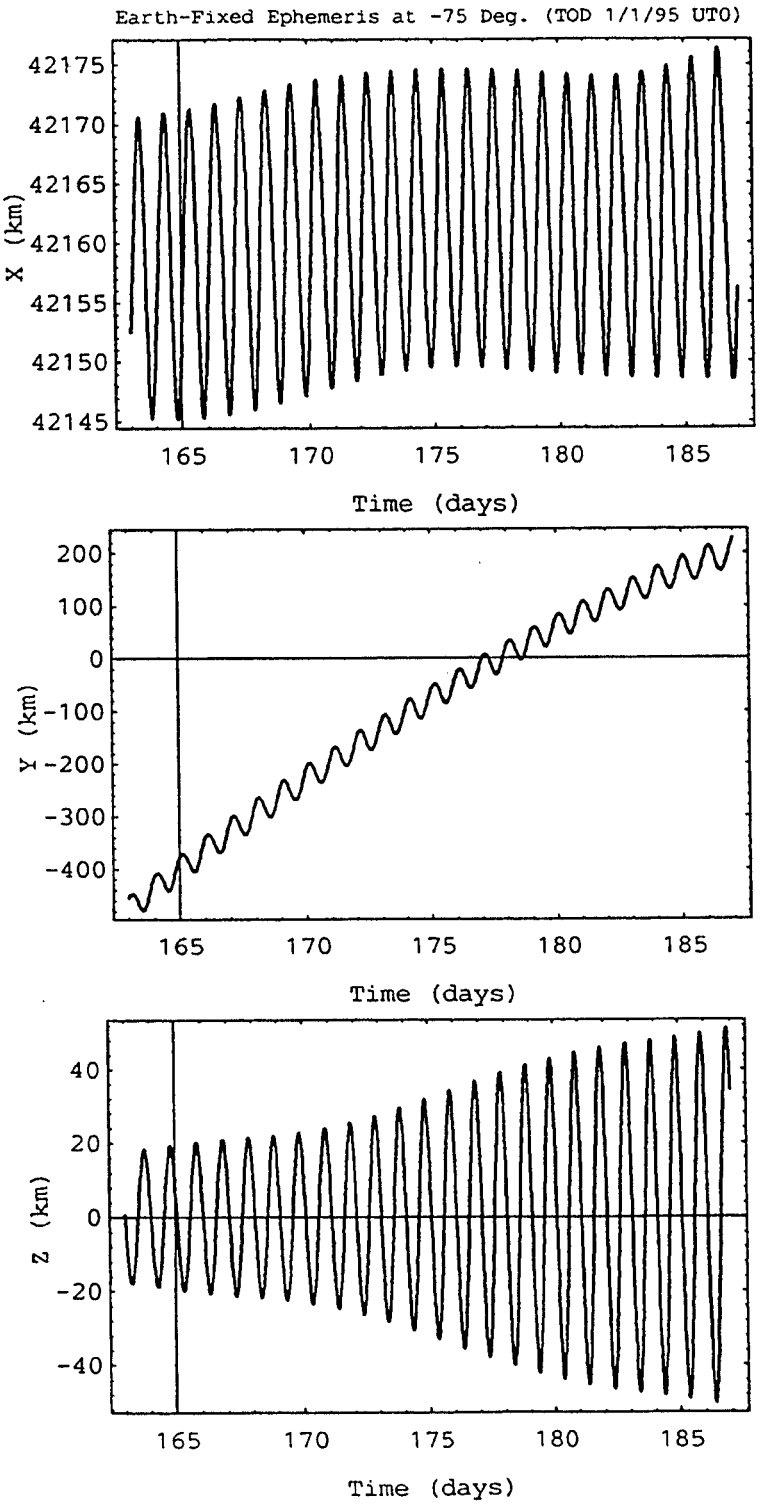

Figure 2. GOES-8 Imager Summer Internal Misalignments

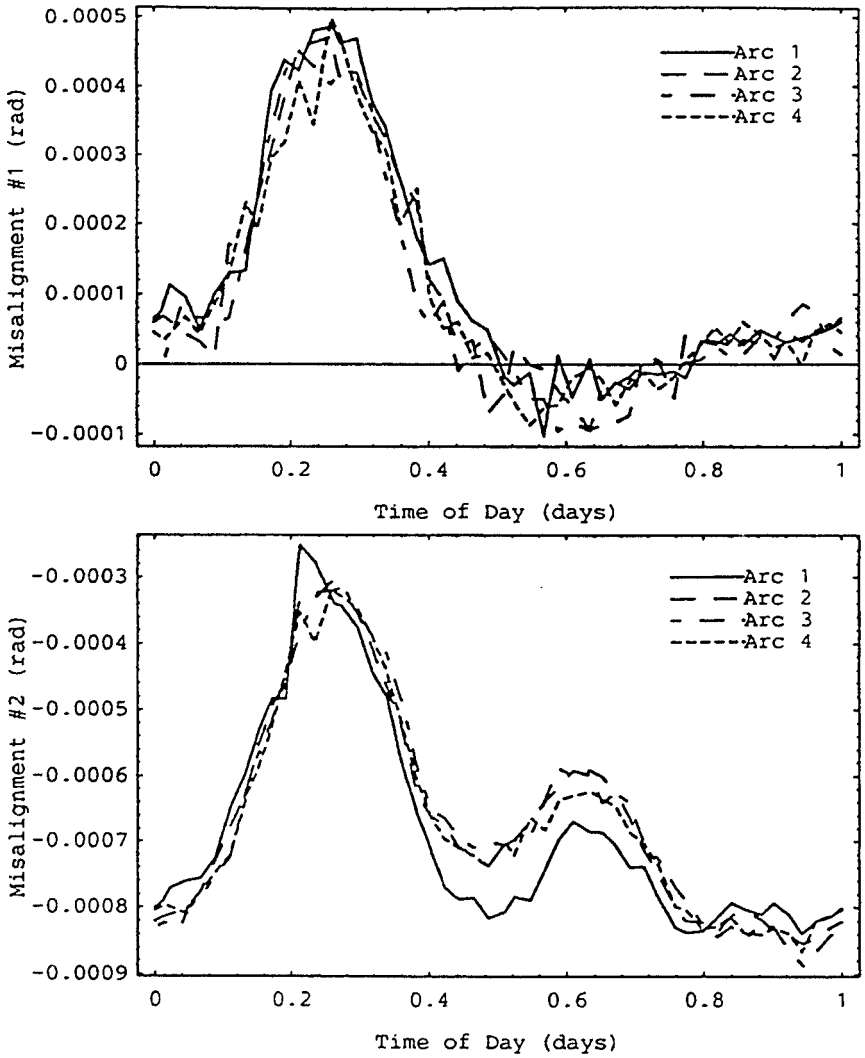

Figure 3 shows the repeatable parts of the GOES-8 attitude angles for the same four data arcs. Note that the mean values of the repeatable roll and pitch profiles evolve with time. Some of this evolution is likely to be due to seasonal changes in the IR emissions of the Earth which lead the Earth sensor to mispoint the spacecraft.

The nonrepeatable parts of the attitude time series have been found concurrently for GOES-8 and GOES-9 during the 1995 autumn eclipse season, and are shown in Figure 4. Both time series show a low-frequency random-walk behavior which is characteristic of what one would expect from the influence of meteorological phenomena upon the IR Earth sensor. The noise-like scatter in the nonrepeatable attitude time series about the apparent random walk is the result of a combination of jitter in the attitude control and noise in the star observations used in this analysis.

Figure 3. GOES-8 Imager Summer Repeatable Attitude

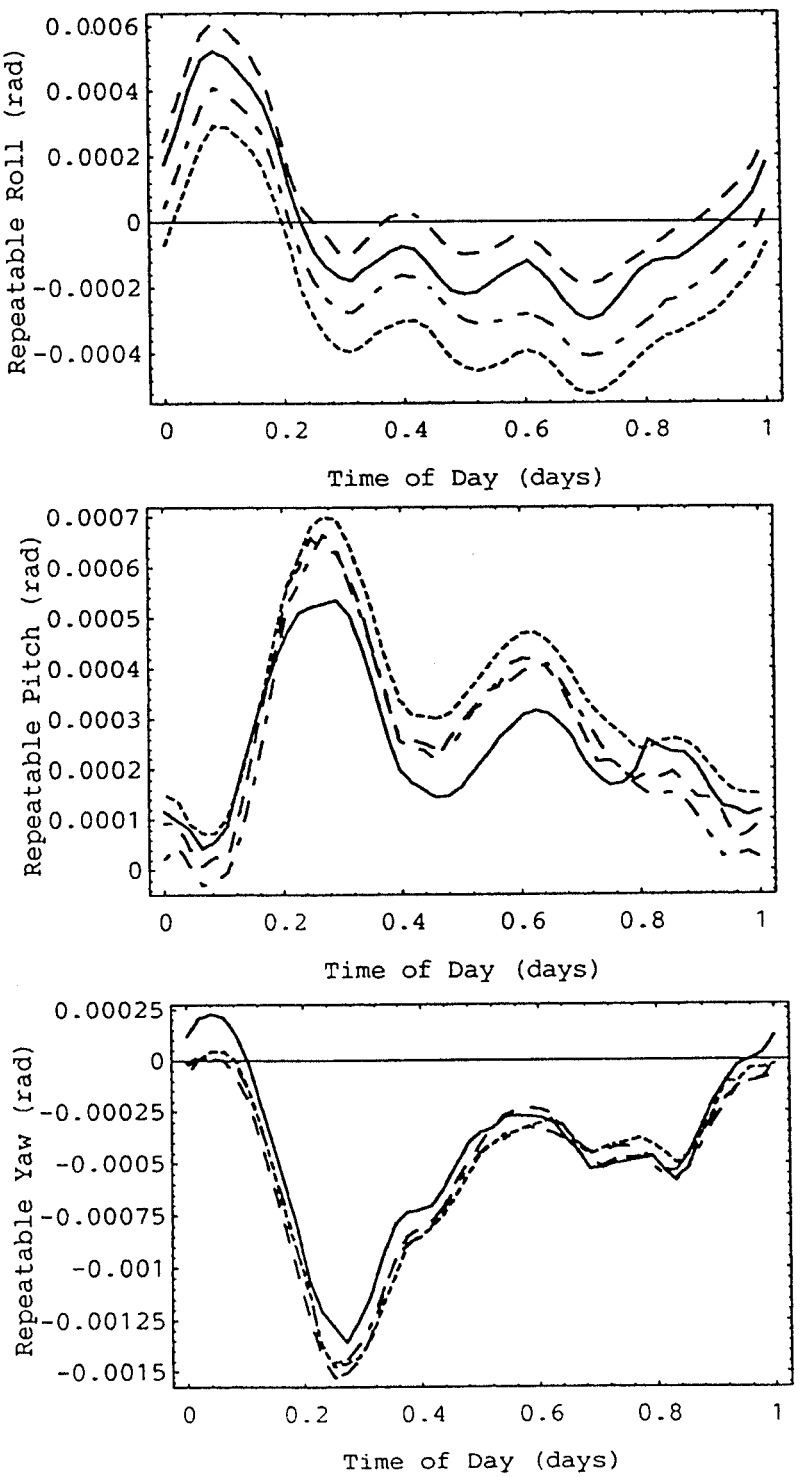

Figure 4. GOES-8 & 9 Nonrepeatable Attitude

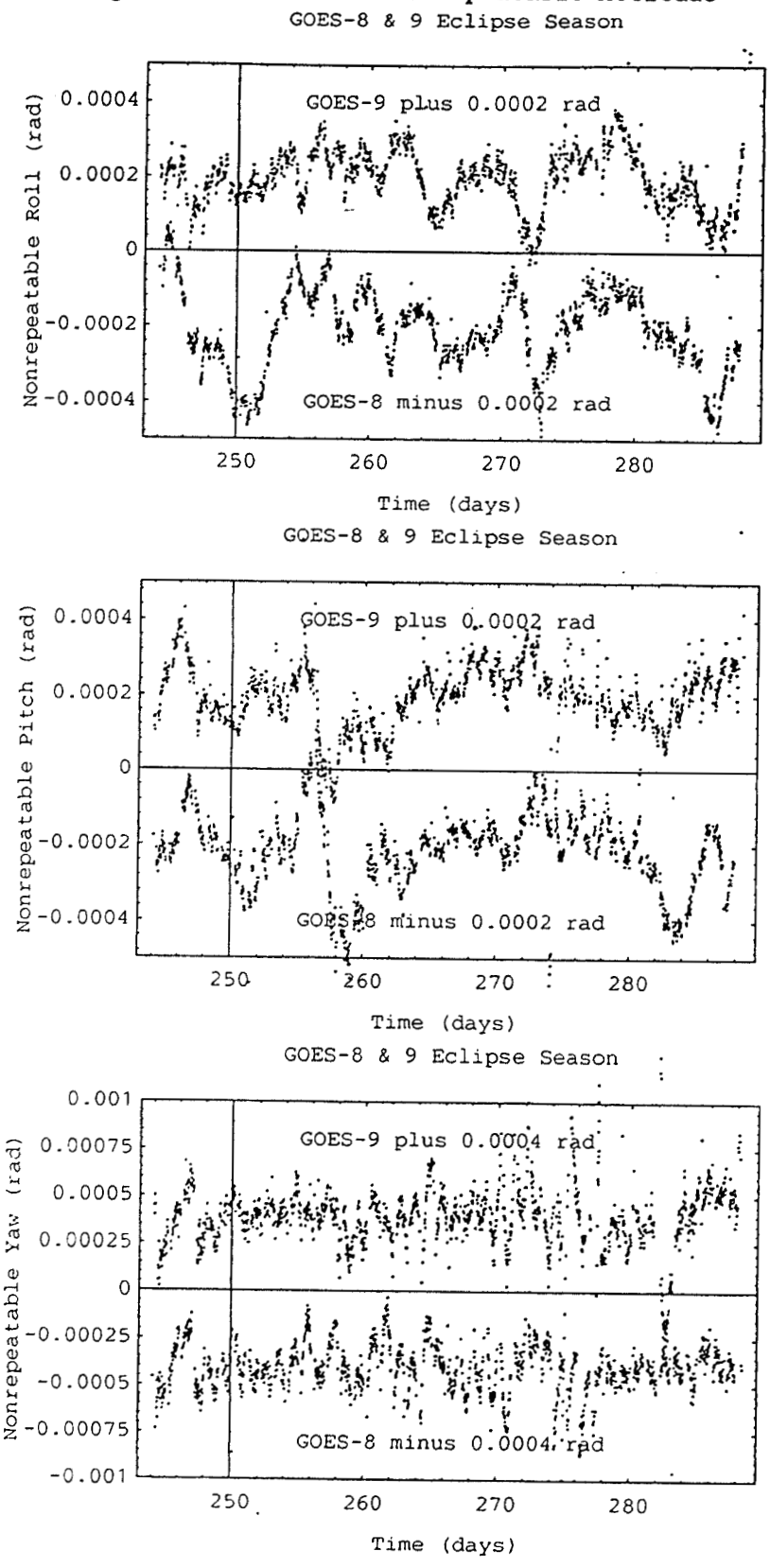

The degree of similarity between the behaviors of the two satellites (as shown in Figure 4) may be quantified by computing a cross-correlation coefficient between the nonrepeatable attitude components of the two satellites. As shown in Figure 5, there is a high (with nearly identical maxima) correlation between the nonrepeatable rolls and pitches of the two satellites, but not between the nonrepeatable yaws. Moreover, disturbances are seen by GOES-9 before being seen by GOES-8. At this time GOES-9 was stationed at -90° longitude and GOES-8 was stationed at -75° longitude. The nearly identical maximum correlation values can be understood as following directly from the Earth sensor roll and pitch calculations

$$\begin{aligned} \text{roll} &= (NE + NW - SE - SW)/4 \\ \text{pitch} &= (NE - NW + SE - SW)/4 \end{aligned} \tag{6}$$

Figure 5. GOES-8 & 9 Nonrepeatable Attitude Correlation

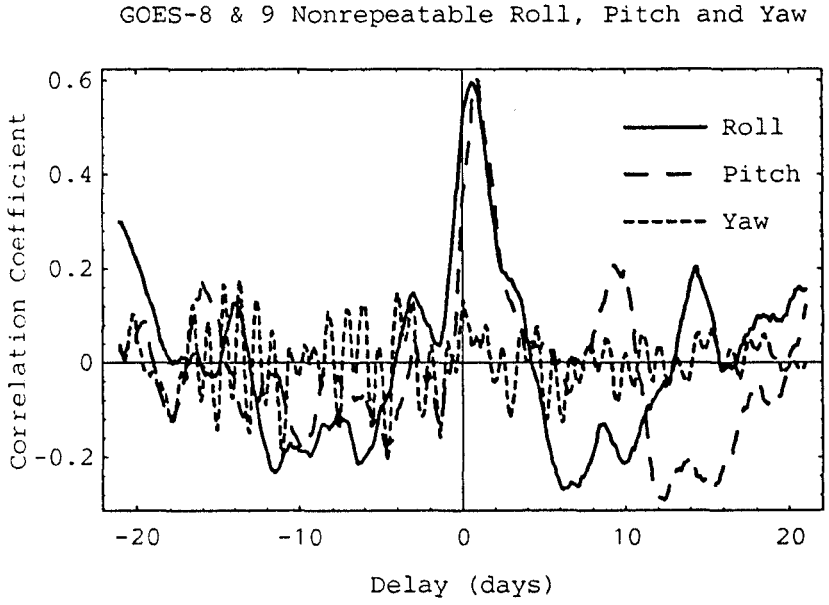

where NE, NW, SE, and SW are the four Earth sensor semichords. These behaviors support the hypothesis that the Earth sensor response to radiance changes induced by meteorological phenomena is a large contributor to nonrepeatable roll and pitch.

It is also interesting to compare the GOES-8 and GOES-9 instrument internal misalignments and repeatable attitude components, as shown in Figures 6 and 7 (Note that the gaps straddle the eclipse during which little or no data is available). Figures 6 and 7 show similar morphologies for the instrument internal misalignments of the two satellites, with a phase shift characteristic of their differing longitudes.

Figure 6. GOES-8 & 9 Autumn Eclipse Internal Misalignment

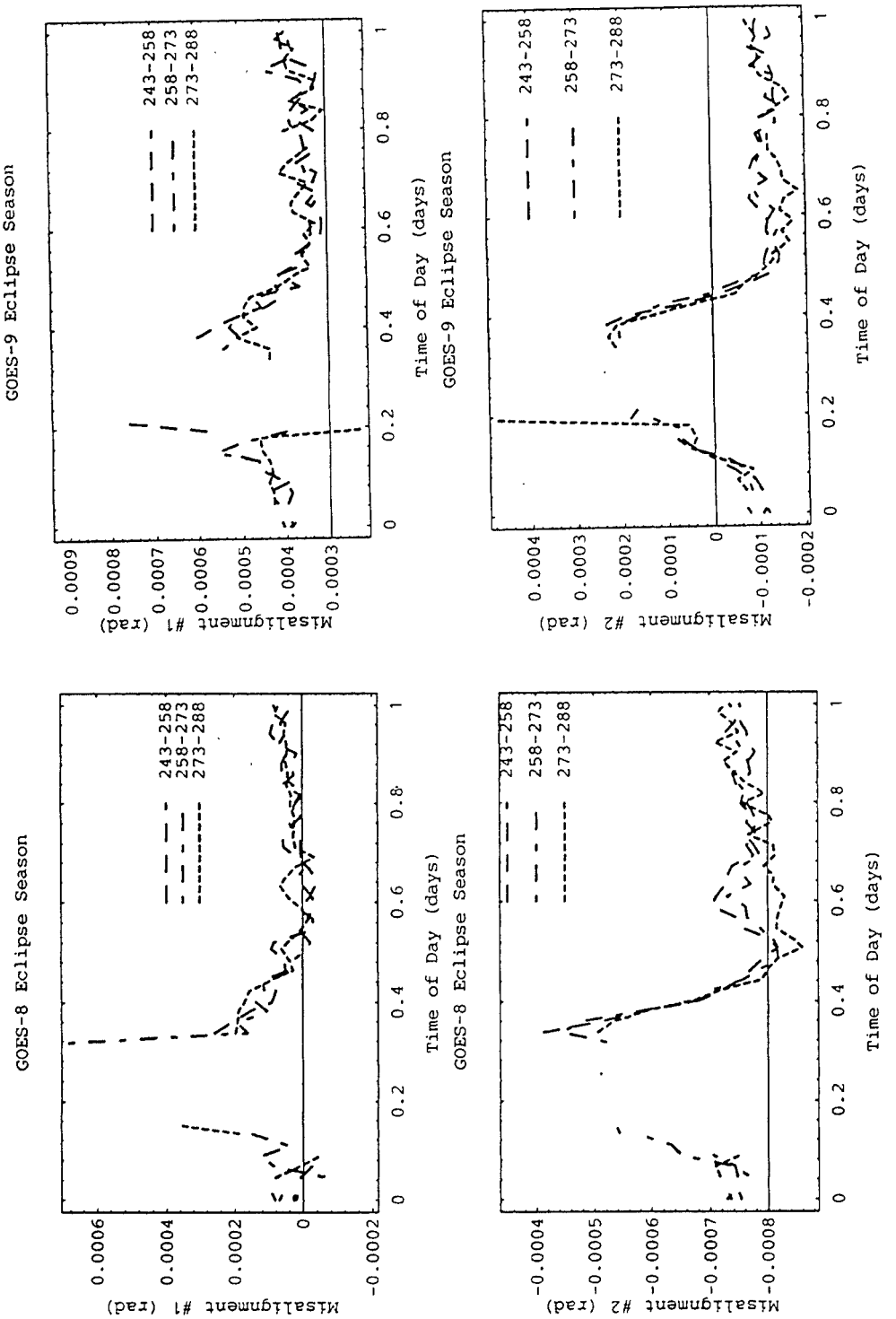

Figure 7. GOES-8 & 9 Autumn Eclipse Repeatable Attitude

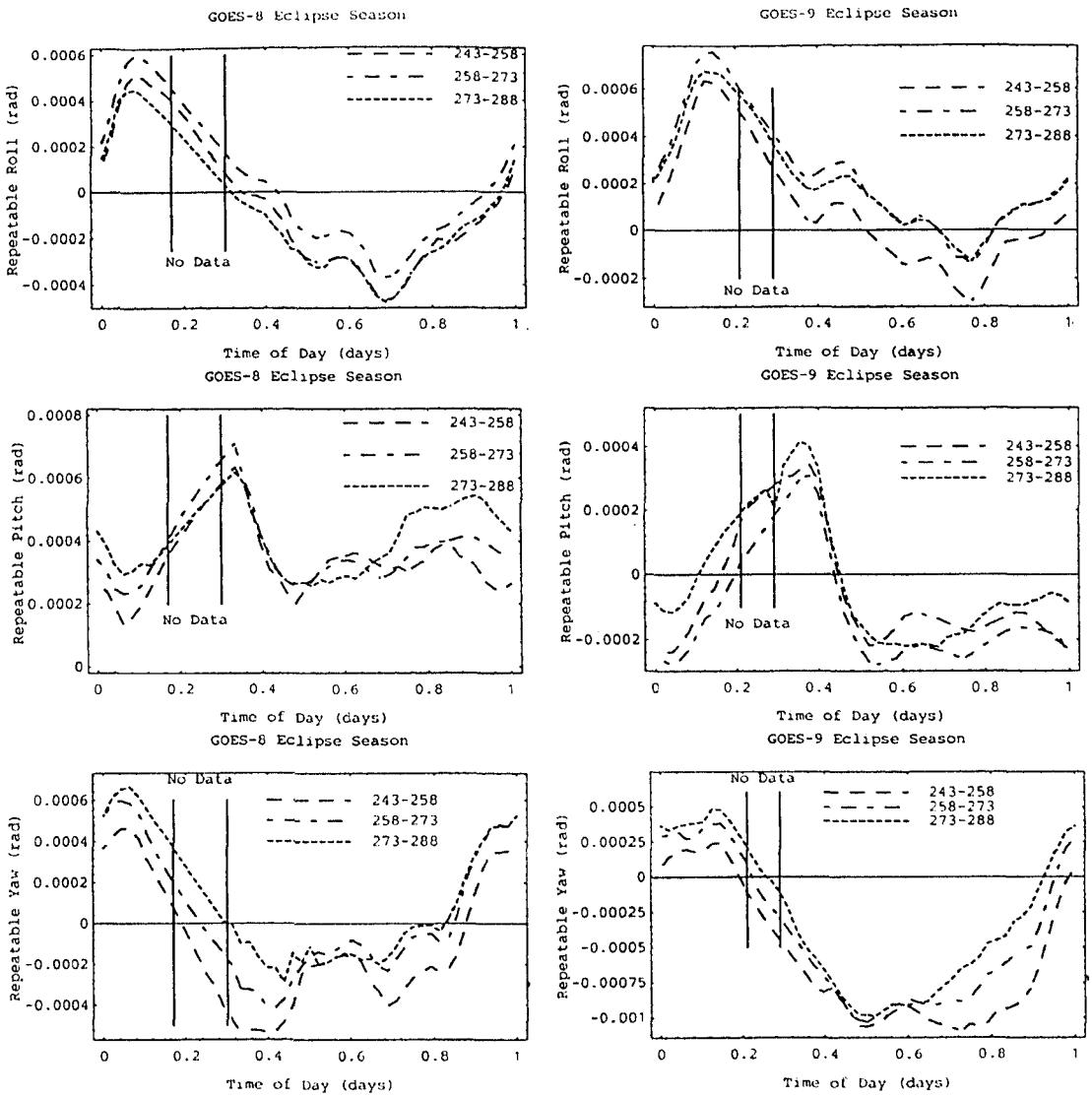

6. CONCLUSIONS

Despite the large nonrepeatabilites found in the attitude profiles, the INR system has been largely successful in delivering accurate and stable images. The success of the INR system is mainly due the large number of SSAA operations performed daily.

This paper has presented evidence which shows that the Earth sensor is a likely source of a significant component of the nonrepeatable roll and pitch. As such, replacing or supplementing Earth sensor attitude determination on later GOES spacecraft by stellar inertial determination (unaffected by Earth IR radiance changes, and extremely stable) has the potential to greatly simplify satellite operations and to further improve the quality of the GOES image products.

Stellar inertial measurements can either directly replace the Earth sensor measurements in the satellite attitude control system, or be used to provide a compensation to be applied while controlling the pointing of the instrument mirrors. In both cases, accurate orbit determination is essential, since the instrument lines-of-sight must be targeted with respect to the Earth. However, orbit determination (*e.g.*, with landmarks, or multiple station ranging) and prediction are problems for which all of the influences can be very well modeled, unlike that of predicting the Earth sensor pointing disturbances.

7. ACKNOWLEDGEMENT

This work was performed for Swales & Assoc. Inc., 5050 Powder Mill Rd., Beltsville, MD 20705, under contract NAS5-32650 for NASA/GSFC.

8. REFERENCES

[1]Savides, J. and K.G. Reseck, "GOES I-M System Characteristics", GOES I-M Operational Satellite Conference, Arlington, VA, April 3-6, 1989.

[2]Carr, J., H.W. Dunhill, D. Gamble, and A. Kamel, "Simulation Studies of the GOES-I Image Navigation and Registration (INR) System", *Advances in the Astronautical Sciences*, Vol. 72, 1990.

[3]Carr, J., "Image Navigation for Geostationary Weather Satellites", *Advances in the Astronautical Sciences*, Vol. 77, 1992.

Evaluating the GOES-8 & -9 Earth IR horizon sensor error response using the GOES-9 Sounder IR channel 1 thru 4 data.

Milton Phenneger

Computer Sciences Corporation
7404 Executive Place
Seabrook MD, 20706-0001

William C. Bryant, Jr.

Swales & Associates Inc.
5050 Powder Mill Rd.
Beltsville MD 20705

Jeanette Baucom

Swales & Associates Inc.
5050 Powder Mill Rd.
Beltsville MD 20705

Kurt Woodham

McDonnell Douglas Aerospace
7404 Executive Place
Seabrook, MD 20706-0001

ABSTRACT

Fourteen days of Sounder observations were scheduled during the GOES-9 Post Launch Test to perform an inflight measurement of the effects of Infrared(IR) Radiance variations in the stratosphere on attitude control using the GOES Type II IR Earth Sensor. Two 16.33° by 1.65° scenes corresponding to the Earth sensor north and south chords were scheduled every four hours for the 14 days from July 19, 1995 until August 2, 1995. The data from IR Channels 1 thru 4(14.7, 14.3, 13.9, and 13.6 microns respectively) are integrated over a 1.65° square FOV and weighted to synthesize the GOES ES medium passband IR filter and a narrow IR passband filter. The integrated scenes were converted to time dependent Earth sensor radiance input pulses for each passband, north and south chord, for six times per day over the 14-day interval. The qualitative features of these synthesized Earth Sensor IR input pulses are compared graphically and correlated with Image Navigation Registration(INR) star residuals for the operational GOES-8 spacecraft. Comparisons of the altitude of the IR horizon on the raw Sounder scans in channel 1 with channel 7(the 12.0 micron window channel) are proposed to detect variations the 14.7 micron horizon altitude. Schemes for removing the effects of attitude motion from the Sounder scenes are discussed and the Earth sensor pulses are processed through a linear model of the Earth sensor electronics to evaluate the relative error response to the synthesized IR input pulse shapes. These results appear to be influenced by thermal mechanical distortion of the spacecraft. Correlation analysis shows that the GOES Earth sensors are responding to nonrepeatable and therefore unpredictable variations in stratospheric radiance and that the time evolution of these variations is consistent with the INR star residual data from GOES-8. Geometric and time adjustments are made for the stratospheric rotation rate and the 15 degree eastward displacement of GOES-8 relative to GOES-9. The performance of the narrow and wide passband filters shows no difference for the pitch androll errors computed at this level of accuracy. Finally, based on this work methods of implementing sounder data from the Earth IR limbs scenes into the daily INR process to improve image registration accuracy may be developed.

KEY WORDS: earth sensors, infrared, stratosphere, GOES, atmospheric sounding

2. Introduction

The GOES-8 and -9 spacecraft attitude pointing requirements are driven primarily by the Imager and Sounder payloads. The Imager visual and IR registration performance between repeated images is the most demanding. Navigation, or the determination of the latitude and longitude of a visual or IR pixel, is accomplished with star and landmark measurement for spacecraft attitude determination and by ranging and landmark for orbit determination. The 3σ requirements for registration (assuring that a pixel is located within an error circle centered at the same longitude for two scenes separated by a given time are[1]: 42μradians($\approx 0.0024°$, $0.001° = 17.45\,\mu$rad.) for 15 minute up to 210 μrad. for 48 hours 16 hours centered on a spacecraft local time(SLT) of 12:00. The 3σ requirement for within frame(25 minutes) registration is that two pixels must maintain the same separation within 42 μrad. The registration requirement can be met either by controlling the spacecraft attitude and instrument alignments or by having repeatable attitude and alignment motion that is measurable using the stars and applying the correction to the Imager scan mirror. The latter approach, called, Image Motion Compensation(IMC), therefore does not tolerate a significant nonrepeatable attitude or structural distortion on time frames of 24 and 48 hours. This work is to determine if variations in the Earth stratosphere IR radiance is a source of nonrepeatable attitude motion and to characterize the amplitude and timing of variations in the IR image of the Earth wavelengths common to those used in the GOES Earth sensor. This work is based upon a special set of GOES-9 sounder scenes taken between DOY 200(July 19th) and DOY 214(August 2) 1995. The scenes were designed to map the Earth coincident with the north and south chords of the GOES type II IR Earth sensor which provides the pitch and roll error input to the GOES attitude control loop. The scenes were 16.33° long and 1.65° wide, which is 8° short of a full east/west chord. Figure 1 illustrates the sounder test scenes and the Earth sensor scan chord geometry. The compromise was made to limit the total time it takes to complete one scene to assure near simultaneous north and south scenes. The sounder dwells 0.1 seconds on each pixel, taking 101.8 seconds per 16.33° line and 45 minutes to map the portion of one chord as specified above. Two scenes were scheduled every 4 hours for the duration of the test, starting at 03:15 UTC for the north chord scene and ending at 04:45 for the corresponding south chord scene. Each sounder scene contains 18 IR channels between 14.7 μ and 3.7 μ and 1 visible channel. To create an Earth sensor pulse, channels 1(14.71μ), 2(14.37μ), 3(14.06μ), and 4(13.64μ) were weighted to represent a medium and narrow IR passband and integrated at each scan point over a square field of view(FOV) as illustrated in Figure 1. The IR passband filters and the integration weights[2] for them are illustrated in Figure 2.

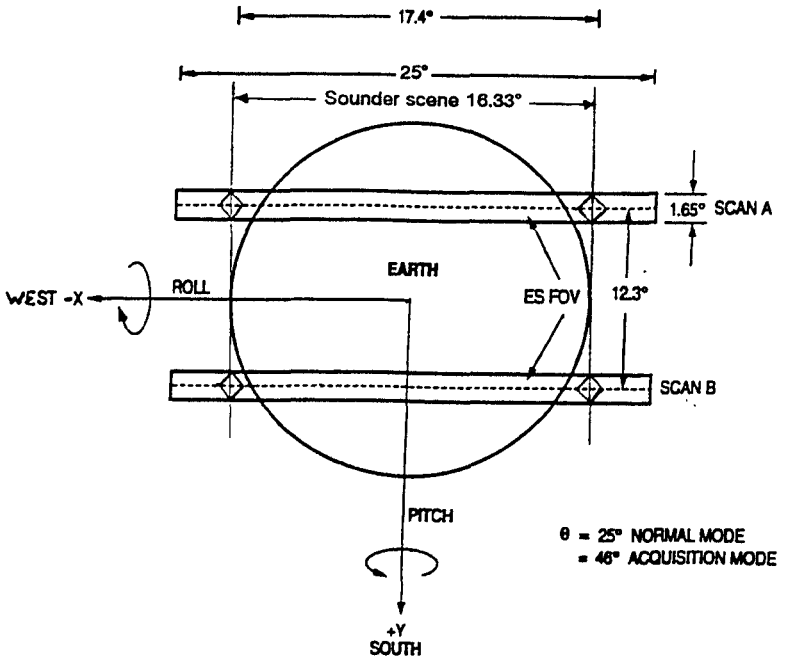

Figure 1. GOES-9 Earth Sensor Chords and Sounder Scene Geometry

Figure 2. Approximate IR Passbands
Sounder Channel Integration Weights

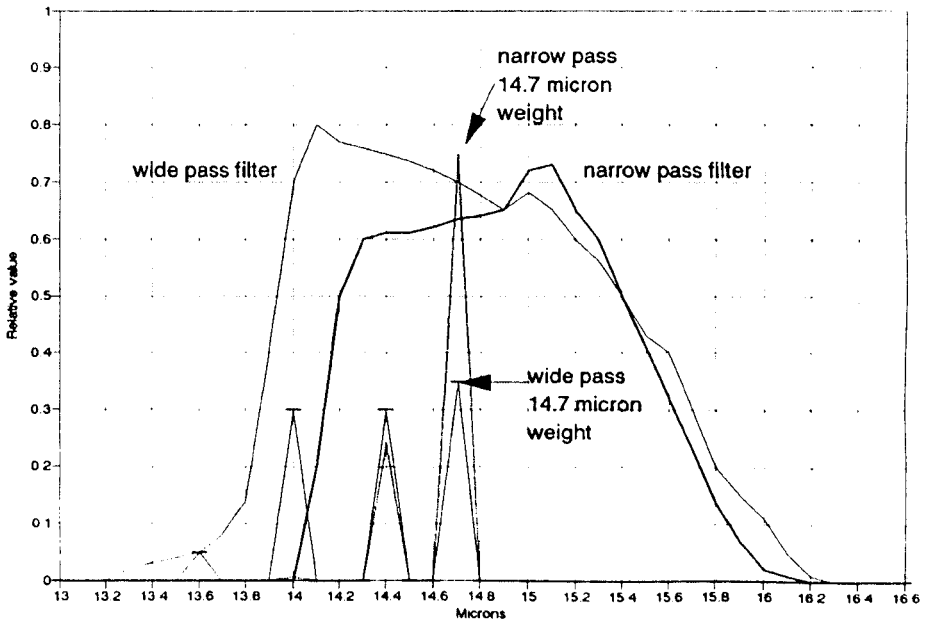

The processing of the sounder data included the application of the IR calibration constants for each of the 4 long wave detectors involved in the integration to generate the synthetic Earth sensor input pulse for this work. However, the sounder was not completely operational at the time these data were accumulated so that two aspects of the sounder data stream are not available. One of these, IR detector optical coallignment is minor and the other, sounder star measurements is significant. Had Sounder star sensing been operational at the time of the Earth sensor scenes, a reference attitude offset before and after each scene would have been available. This would have allowed accurate renormalization of the Earth chord pulse shapes which are the input in this analysis to the linear laplace transform function and IR horizon locator logic. Finally, the IMC function, which is determined from the landmark and star measurements of the previous day and applied to the Imager, is not routinely enabled on the Sounder. Thus removing the effects of spacecraft attitude motion from the scenes is a major challenge of this work and it is essential to meet one of the goals to measure the amplitude of the nonrepeatability effects caused by IR variability of the stratosphere. In section 3 the Earth sensor input pulses generated by integrating the sounder scenes are presented showing the variability of these pulses. Section 4 describes the processing of the synthetic Earth chord pulses in a linear representation of the Earth sensor electronics. Section 5 describes preliminary efforts to detect secular random changes in the altitude of the 14 micron horizon using the 12 micron channel as a reference for the Earth limb when clouds are not present on the limb. Section 6 summarizes the results of this work, and proposes modifications to the method of sounder scene definition and collection, to remove uncertainties caused by attitude motion between corresponding north and south chord measurements.

3. Earth sensor synthesized input pulse from the sounder

Figure 3 illustrates the detail for DOY 201, comparing the six Earth chord pulses obtained for the narrow and medium IR passband filters. This data shows the southern stratosphere radiance with a significant west to east radiance gradient. The north(summer) profiles show significant limb brightening and lower percentage variation of limb brightness over the day. Comparing the southwest limb in the medium(wide) band to the northeast narrow band profiles, the variation was double. Also both narrow and wide southern profiles have the same east west variation while the north profiles have almost none. Note that no significant diurnal variation is apparent, although an obvious temperature wave appear to be evolving westward in the south profile. Figure 4 shows 12 days

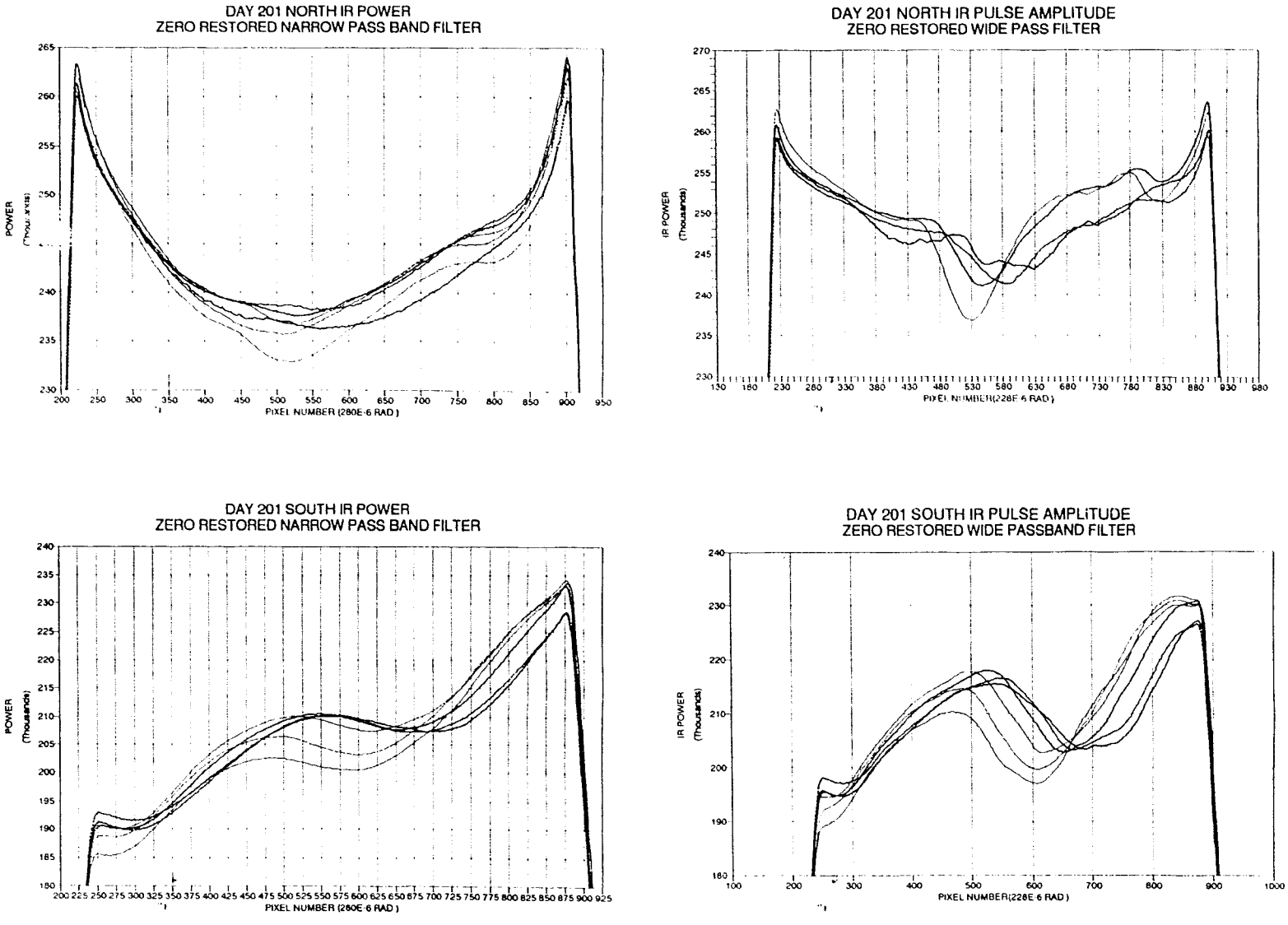

Figure 3. DOY 201 North/South Profiles for the Narrow and Wide Passbands

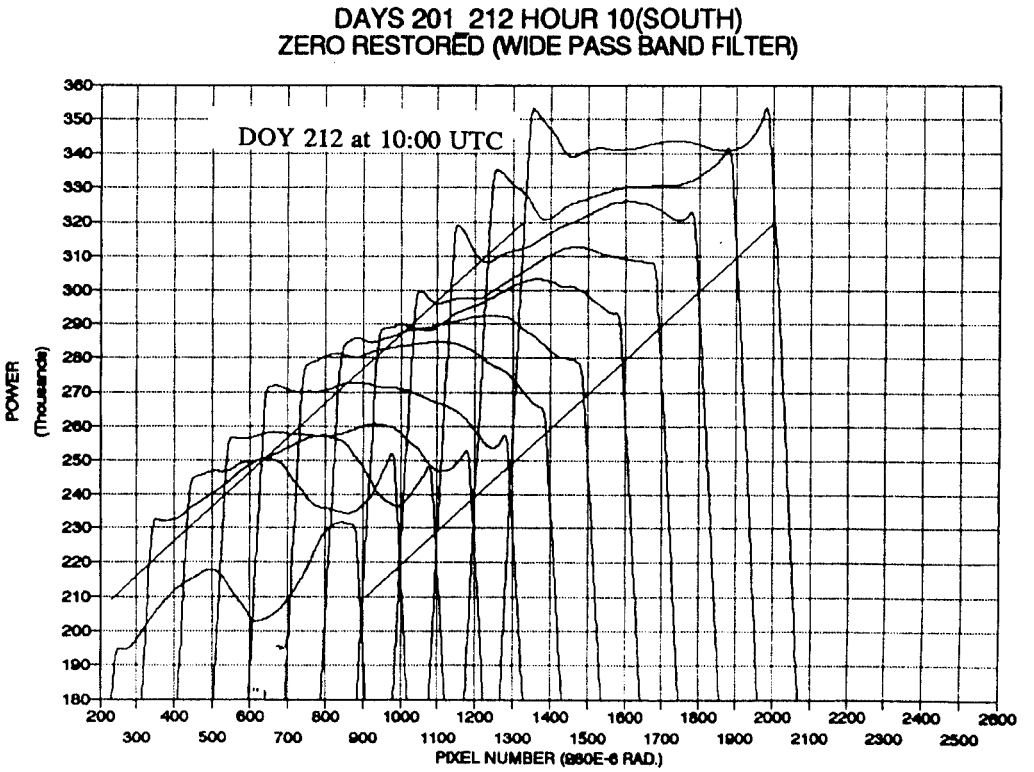

FIGURE 4.

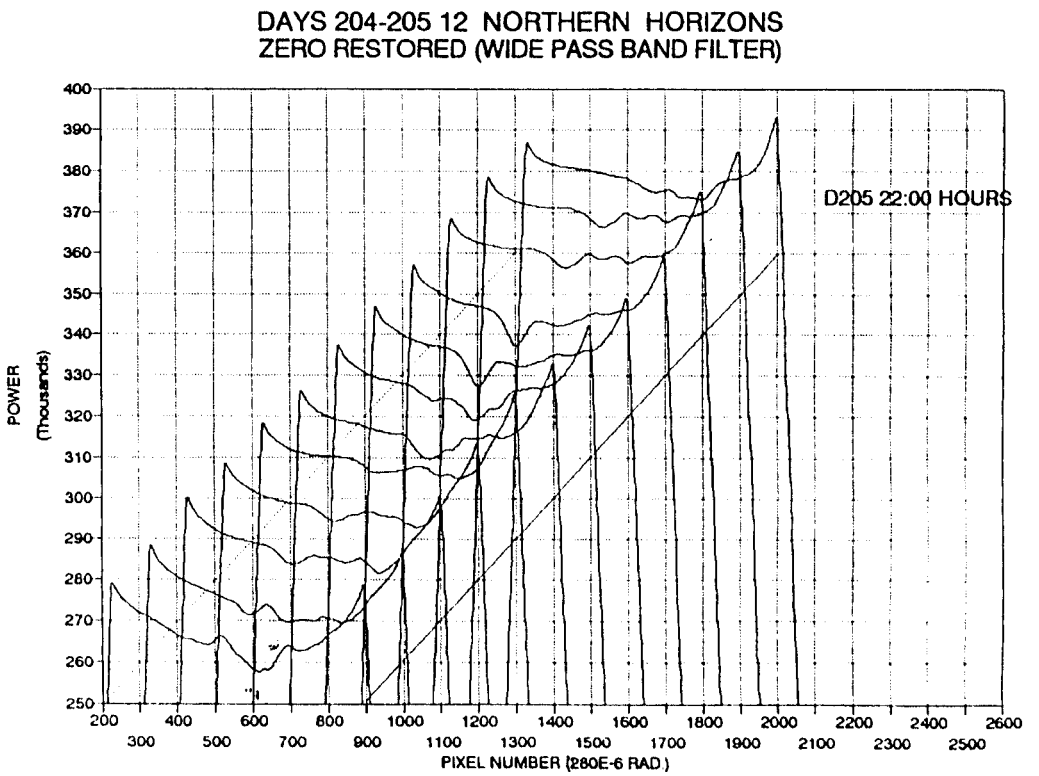

FIGURE 5.

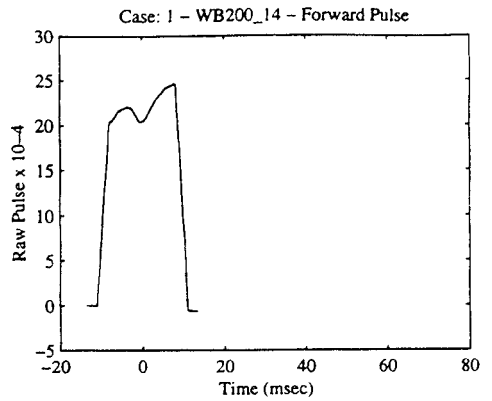
Case: 1 – WB200_14 – Forward Pulse
Raw Pulse x 10–4
Time (msec)

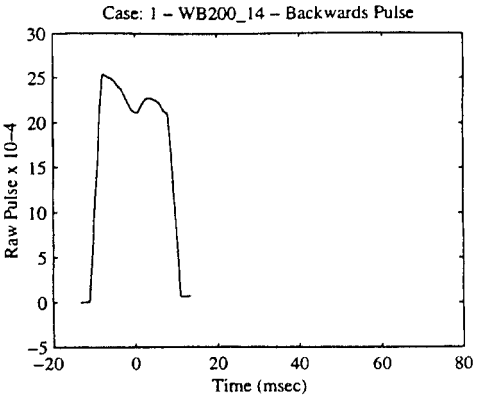
Case: 1 – WB200_14 – Backwards Pulse
Raw Pulse x 10–4
Time (msec)

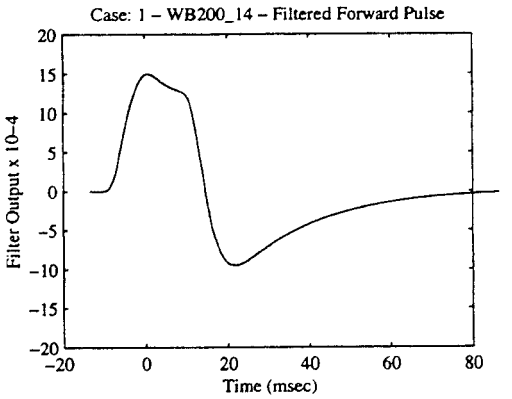
Case: 1 – WB200_14 – Filtered Forward Pulse
Filter Output x 10–4
Time (msec)

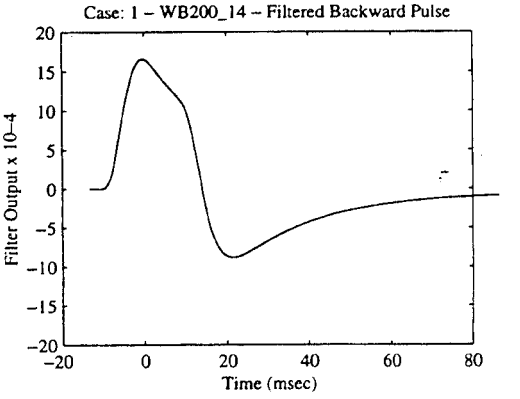
Case: 1 – WB200_14 – Filtered Backward Pulse
Filter Output x 10–4
Time (msec)

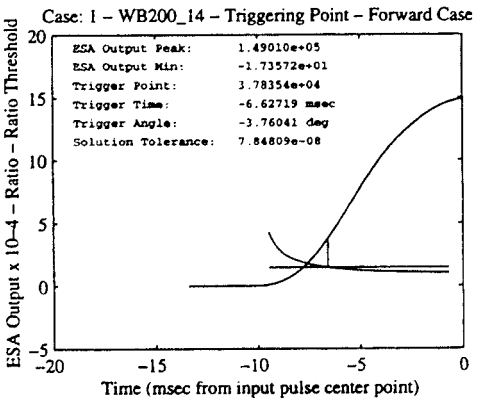
Case: 1 – WB200_14 – Triggering Point – Forward Case
ESA Output Peak: 1.49010e+05
ESA Output Min: -1.73572e+01
Trigger Point: 3.78354e+04
Trigger Time: -6.62719 msec
Trigger Angle: -3.76041 deg
Solution Tolerance: 7.84809e-08
ESA Output x 10–4 – Ratio – Ratio Threshold
Time (msec from input pulse center point)

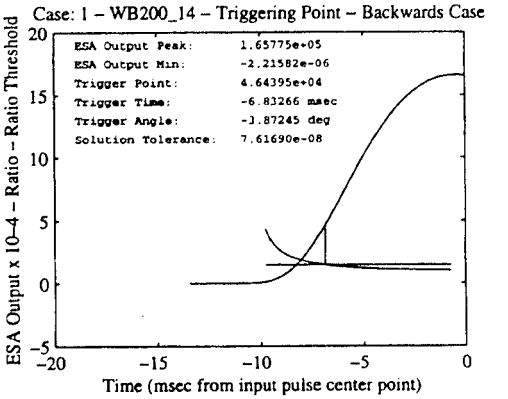
Case: 1 – WB200_14 – Triggering Point – Backwards Case
ESA Output Peak: 1.65775e+05
ESA Output Min: -2.21582e-06
Trigger Point: 4.64395e+04
Trigger Time: -6.83266 msec
Trigger Angle: -1.87245 deg
Solution Tolerance: 7.61690e-08
ESA Output x 10–4 – Ratio – Ratio Threshold
Time (msec from input pulse center point)

FIGURE 6

of profiles offset by one decade per day to illustrate the time evolution of the feature in the south profile of DOY 201, which eventually suppresses the limb brightness on DOY 206, while the west limb has significantly increased its brightness from 190,000 to 220,000 units of power. The power amplitude is a result of integrating the radiance calibrated signal from all four sounder long wave detectors at each 280 μrad step in the scene, over an analytical FOV for the Earth sensor which is a 1.65° square, rotated in space as illustrated in Figure 1. Figure 5 shows two days for the northern hemisphere with much less variability. To summarize the whole data set, the northern profile limb brightness varied between 275,000 and 285,000 and east west gradients(the difference in the peak brightness at each limb) were frequently less than the observed limb variation. The southern profiles appeared to have waves in them which cause the limb brightness to vary from minimum to maximum in 4 days to 7 days as illustrated on the east limb of the data in figure 4. The reason for drawing attention to this is that the GOES Earth sensor is designed to be insensitive to the radiance variations that are occurring near the center of the Earth disk and also to variations in the slope of the rising edge of the Earth pulse. However, it cannot compensate for an apparent shrinking(cooled stratosphere) or expanding(warm stratosphere) of the sensed IR limb. If the slope and peak brightness of the Earth pulse stays constant but the scan angle at which it rises changes relative to the nadir crossing point of the scan, an error will be sensed.

4. Processing the synthesized earth pulses in a linear model of the earth sensor electronics

The synthesized Earth sensor input pulses were processed as input to a linear laplace transform representation of the GOES type II Earth sensor electronics[3] and the horizon detection method was applied to the output pulse, similar to methods previously reported[4]. The Earth sensor uses an adaptive slope thresholding method[3,2] as it scans the Earth. The scan period is 8 Hz from west to east and return, and the rising edge of space reference zero restored Earth pulse is detected at 80% of a reference voltage that is 7 milliseconds later in the scan than the threshold of the previous scan in the same direction. The pulse processing method is illustrated in Figure 6. Since in this analysis there is no 8 Hz pulse stream, one pulse is analyzed. For this one pulse locator the horizon threshold is a point where, 1.25 times the value at the threshold is equal to the pulse level 0.007 sec later. The difference function for this search intercepts zero at the vertical line in the lower two graphs of Figure 6. The north and south earth chords generated by the mathematical process were converted to pitch and roll error for the test interval. These data are shown for pitch error in Figure 7.

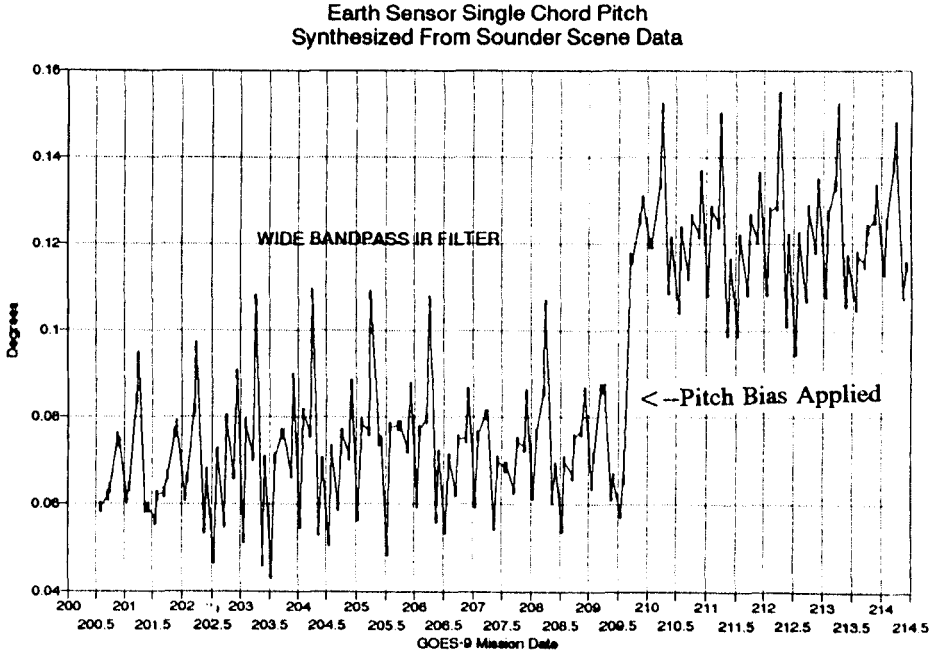

FIGURE 7

The north and south chord pitch is graphed as a single timed series to show the detailed features of these data. When one chord was missing, it's value was set equal to its counter part. The pitch data illustrates a challenge to one . goal: of this analysis. The data is dominated by diurnal attitude motion which more or less repeats. The pitch measurements from the associated north and south chord can be seen as grouped pairs. Looking closely at the data near 202.5, the north chord pitch is about 0.02° lower than the south chord pitch and the difference changes over the span of the data. The peak pitch error occurs at spacecraft midnight. Also in the data a pitch bias was applied to the Earth sensor shortly after 12:00 UTC on DOY 209. The source of the diurnal variation is probably a thermal distortion phenomena, as the eccentricity of the orbit on these days was to low to cause errors of this magnitude. The roll data generated by the dual chord method shows a similar diurnal variation of 0.05° peak to peak, and the narrow and wide passband data are the same at this level or accuracy in the analysis. Thus the second step in the process to use sounder synthesized Earth sensor input pulses to evaluate the effects of variations in the stratosphere is not yet achievable. To do this a method has to be developed to remove the effects of spacecraft attitude motion from the sounder scenes. This could have been done with sounder star measurements had this function been operational at the time.

5. Methods of removing attitude variation from the synthesized sounder Earth chord data

Three methods are discussed to measure the effects of stratospheric radiance variations on the GOES Earth sensor. 1) Determine the sounder attitude from detailed analysis of the scene data and renormalize the input pulse widths to remove north/south and east/west pointing errors that were occurring in the instrument while the chord scenes were being taken. Then reprocess these scenes to see if the Earth sensor electronics detects nonzero error. An example of this is illustrated in Figure 8 where the individual detectors lines prior to the integration over the mathematical ES FOV have been used to create a high resolution look at the 14.7 Micron horizons. This picture has been geometrically compressed to show details of the Earth limbs in the north and south chord scenes.

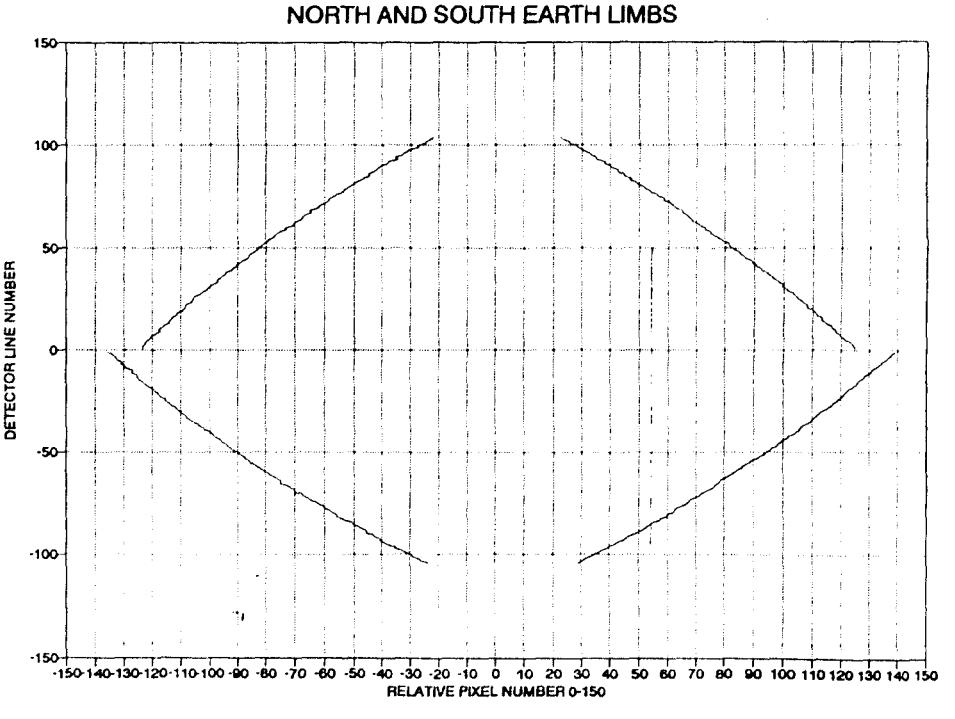

FIGURE 8 Using Raw 14.7 Micron Data to Measure the IR Horizon and Correct for Attitude Error

2) Measure the altitude of the 14.7, 14.4, and 14.07 micron IR horizons relative to the 12 micron IR channel horizon when there are clear east west 12 micron horizons(no clouds) and demonstrate the effects of the cooling and warming events that are seen in the profiles presented section 3. An example of this method is illustrated in Figure 9[4] where the NIMBUS-6 LRIR HNO_3 channel was used as a reference for the location of the Earth's surface. The clear days can easily be seen in these data. 3) Use coarse information in the Earth pulse data such as the correlated motion and uncorrelated motion measured by the location of the east and west limbs of the north and south chords and develop a renormalization scheme based upon the assumption that significant attitude motion is not occurring during the individual scenes, and that adjustment of the pulse data is for a constant or average attitude. This method requires less analysis than the first two methods.

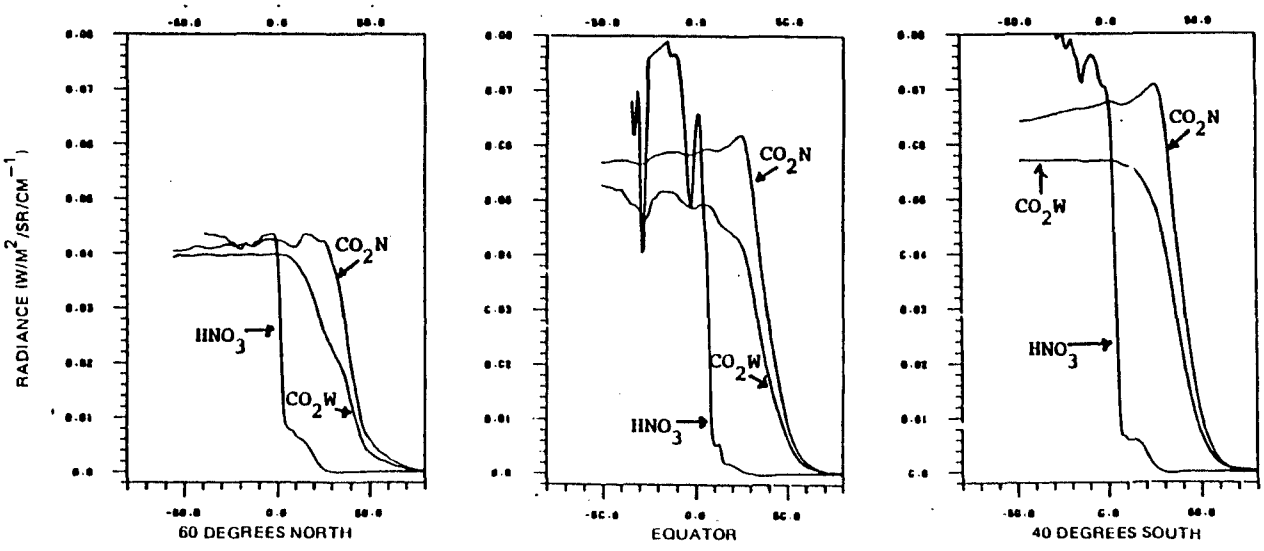

FIGURE 9. Nimbus-6 LIMS Profiles as References for Tangent Heights

6. Discussion of Results

When the idea to use the sounder data as a method of validating Earth sensor performance was first presented, it was to be a correlation experiment with hopes of observing extreme events such as a sudden stratospheric warming event[6] in the southern winter. If the spacecraft showed attitude errors with a time history similar to the time history of the sounder synthesized input IR pulses, then the objective would be met. Simultaneous measurement of attitude and IR pulse variations on the same GOES spacecraft is unnecessary. It would be unlikely that a test of this nature could be run on a fully operational spacecraft. The extension of this work to a direct measurement of Earth sensor response using the sounder profiles is not completed. However, the first objective to show a time correlation appears to have been met. The GOES-8 spacecraft, 15° east of GOES-9 at the time of the test, was in the operational mode of Imaging. In addition to this, extensive analysis was being performed[7] to understand the source of nonrepeatable attitude errors in the INR function. Figure 10[7] illustrates east/west and north/south star data residuals on GOES-8 for a time period that overlaps the test interval DOY 200 to DOY 211. The cooling anomaly illustrated in the DOY 201 data of Figure 3 rotated into the GOES-9 Earth limb on DOY 202(7/21) to DOY 206(7/25), and the warming of the west limb(i. e. a cold wave moving into the GOES-8 west limb) on DOY 202 can be seen to precede the 300 microradian jump in the north/south star residuals in GOES-8. A reduction in the south chord width(by limb cooling) causes a positive north/south star residual. Also, the time history of the Fig. 10 data resembles the time history of the amplitudes of the southern hemisphere profiles. There is strong evidence for the correlation. The more difficult challenge to show mathematically that the stratosphere is causing the residuals of Figure 10, remains. Part of the solution to this is to schedule sounder scenes to measure the limb radiance at intervals of a few minutes to limit attitude motion effects.

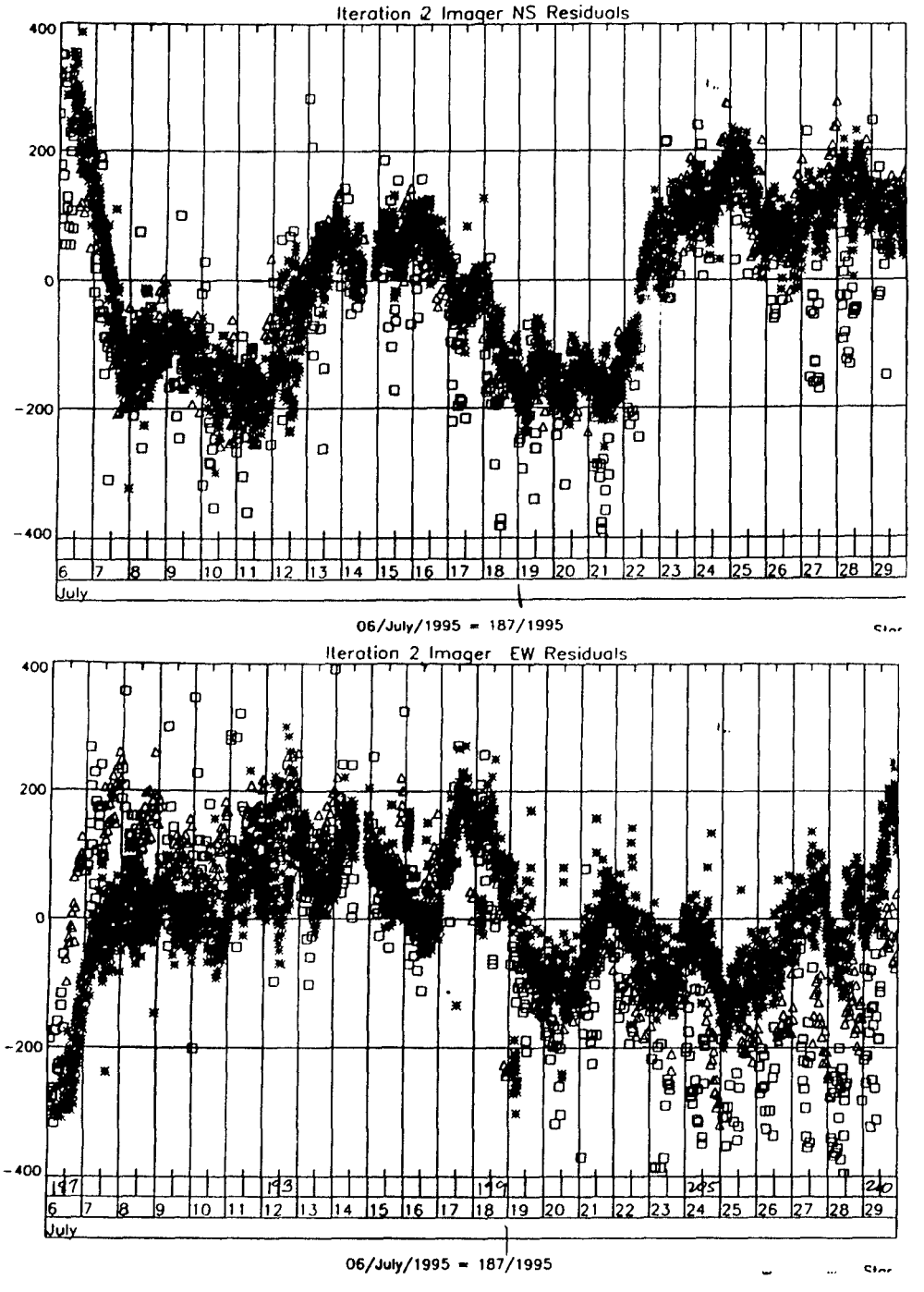
Iteration 2 Imager NS Residuals
400
200
0
-200
-400
6 7 8 9 10 11 12 13 14 15 16 17 18 19 20 21 22 23 24 25 26 27 28 29
July
06/July/1995 = 187/1995
Iteration 2 Imager EW Residuals
400
200
0
-200
-400
6 7 8 9 10 11 12 13 14 15 16 17 18 19 20 21 22 23 24 25 26 27 28 29
July
06/July/1995 = 187/1995

FIGURE 10

7. ACKNOWLEDGMENTS

The authors would like to thank Gus Comeyne for his assistance in the capturing and processing of the Sounder data during and after it was being taken and John Fiorello for his support in the designing the Sounder scenes to a specification, for building the Spacecraft Command Schedule that commanded the Sounder on a regular basis to make these measurements and for assisting in the operational support of the post launch test activities during the test, and Eric Chipman as the postlaunch test director and the mission operations controllers and on-line engineers for their support and to Ed Harvie for his technical review of this document.

8. REFERENCES

1) GOES Program, Spacecraft Operations Handbook, DRL 503-02, Vol III., Spacecraft Description GOES I-M, SS/L-TR00570 Rev. G, August 31, 1995.

2) Transcribe from Figure 4 LMSC/F023696, received from E. Washwell (private communications)

3) GOES IJK/LM Earth Sensor Technical Review Meeting at GSFC, (meeting notes), Ford Aerospace Corporation/Space Systems Division, April 28, 1988.

4) "Infrared Horizon Radiance Modeling for Attitude Determination and Control: Analysis and Mission Experience", M.C. Phenneger, S. P. Singhal, T. H. Lee, and T. H. Stengle, NASA TM 86181, March 1985.

5) "In-Flight Measurement of the National Oceanic and Atmospheric Administration(NOAA)-10 Static Earth Sensor Error", E. Harvie, O. Filla, and D. Baker; AAS/AIAA Spaceflight Mechanics Meeting, Pasadena, California, Feb 22-24, 1993; Paper No. AAS 93-101.

6) S. Fritz and S. D Soules, "Planetary Variations of Stratospheric Temperatures", Monthly Weather Reviews, vol. 100, no. 7, July 1972.

7) W. Bryant, From personal Image Navigation and Registration analysis notes.

Numerical Filter equalization of spacecraft parameters telemetered in disparate bandwidths

Winfield H. Farthing

Swales and Associates, Incorporated
5050 Powder Mill Road, Beltsville, Maryland 20705

Sandra Cauffman

Goddard Space Flight Center
Greenbelt, Maryland, 20701

Eric G. Chipman
Computer Sciences Corp.
Seabrook, Maryland, 20706

ABSTRACT

The magnetic field data from the GOES Satellite must be corrected on the ground for the contribution from the roll and yaw torquer coils which comprise important elements of the spacecraft Attitude and Orbit Control System (AOCS). The correction may be calculated from measurements of the torquer currents which are telemetered at the same rate as the magnetic field data or from torquer input command data. The baseline plan was to allow torquer current changes only at infrequent intervals of once per 20 minutes since it was suspected that torquer switching noise might be a problem. However, for improved navigation and registration performance in the radiometric instruments, the actual mode of operation has been to calculate the torquer current drive more frequently and to rate limit the current changes to one commanded increment (about 3.2 ma) per step.

The magnetic signature of the 3.2 ma step is as much as 1.2 nanoTeslas. Both the current level and the telemetered value change essentially instantaneously when compared to the frequency response of the magnetometer, which incorporates a 0.5 Hz bandwidth five-pole Butterworth anti-aliasing filter in each data channel. Straightforward correction of the data using the current telemetry therefore results in objectionable noise spikes in the derived bandwidth-limited output data. The problem is complicated by the fact that the clock which governs the AOCS current commands to the torquers is not synchronized with the telemetry unit clock which governs magnetometer data sampling. Fortunately, it has been possible to incorporate data in the spacecraft telemetry which provides improved information for determining the time of a current step in the telemetry unit time base as well as the torquer input command data mentioned as one method of compensation.

This paper describes the development of a numerical filter used in ground processing of the telemetered current to simulate the five-pole Butterworth response of the magnetometer output filter. Since the timing information is determined to an accuracy of 1 part in 8, one of eight sets of filter weights is selected based on the telemetered timing information. Examples are given of the improvement in output data quality resulting from the technique.

1. INTRODUCTION

The Space Environment Monitor (SEM) has been part of the GOES payload complement since the formative days of the predecessor Synchronous Meteorological Satellite program. The Solar X-Ray Sensor, Energetic Particles Sensor, and Magnetometer which comprise the SEM provide a significant portion of the total data base used by NOAA's Space Environment Center (SEC) to monitor and forecast the terrestrial effects of solar activity. Magnetometers for space flight are notoriously susceptible to interference from spacecraft mechanisms and electrical systems, so there was concern when Ford Aerospace and Communications Corporation (now Space Systems Loral) proposed to use magnetic torquers as essential components of their control system for the GOES I/M program. Magnetic torquers had been used successfully on their heritage INSAT program, but INSAT had no requirement for magnetic field measurement. However, the torquer design used large area, vacuum-cored, dimensionally stable coils, with only incidental permeable spacecraft magnetic material present, so the magnetic

 0-8194-2200-2/96/$6.00

signature was expected to be very stable. Thus an accurate current monitor was proposed to monitor the coil currents, and the update rate of the torquers was limited to once each 20 minutes to avoid noise and transient effects which would be associated with current switching.

A number of problems were experienced during the in-orbit evaluation of GOES-8 which resulted in compromising the magnetometer data and required corrective action on GOES-8 and later spacecraft. The fundamental problem was that achieving good Image Navigation and Registration performance for the prime Imager and Sounder instruments was not compatible with the infrequent updates of the torquer coil currents. Unfortunately, when the torquers were operated in a more frequent update mode, the corrected magnetometer data was degraded from three separate effects:

a. Different measurement bandwidths applied for the magnetometer and torquer current parameters

b. Different time bases governed sampling of magnetometer data (sampled by the telemetry unit) and control of the torquer currents (digitally controlled and encoded by the Attitude and Orbit Control Electronics, or AOCE)

c. There was telemetry read-out noise associated with the current telemetry monitors, at times as much as 10 counts, peak-to-peak. For the most sensitive magnetometer axis, 3.5 nT peak-to-peak noise is introduced.

In order to satisfactorily recover the magnetometer data on GOES-8 and later spacecraft, all of these effects have had to be addressed.

2. ANALYSIS

2.1 Bandwidth induced errors

Let the time variation of the ith component of the ambient field vector at the spacecraft be given by $B_{ia}(t)$ and the impulse response of the pre-sampling filter, matched for each axis, be given by h(t), Then the desired output for the ith component at time t_1 is the convolution of the ambient field with the filter impulse response, evaluated at $t = t_1$.

$$B_{io}(t_1)=\int_{-\infty}^{\infty} B_{ia}(\tau)h(t-\tau)d\tau, \quad t = t_1 \tag{1}$$

In order to strongly discriminate against aliasing of either ambient or spacecraft time varying fields, the magnetometers on GOES have always incorporated a pre-sampling filter with high attenuation at or above the Nyquist frequency. For GOES I/M, the filter is a five pole Butterworth type with 3dB frequency at 0.5 Hz, approximately half the Nyquist frequency, providing >29dB discrimination against frequencies higher than Nyquist. The impulse response for this fifth order Butterworth filter is shown in Figure 1, and is given analytically by:

$$h(t)=\pi[1.8942e^{-\pi t}+2.7524e^{-0.809\pi t}\cos(.587\pi t+1.3\pi)+0.8943e^{-0.309\pi t}\cos(.951\pi t+0.6\pi)] \tag{2}$$

The convolution integral (1) calculates the output of the linear filter at time t_1 by reflecting $h(t_1)$ about the origin and treating it as a temporal weighting function for the input signal. This is illustrated by Figure 2.

The actual field at the magnetometer sensor is the sum of the ambient and spacecraft field. For the purposes of this analysis, the spacecraft field at the sensors is a linear combination of the roll and yaw torquer currents, I_r and I_y, with coefficients α_{ir} and α_{iy} determined by in-orbit magnetometer sensitivity tests. Thus the field sensed in the ith vector component is:

$$B_i(t)=B_{ia}(t)+ \alpha_{ir}I_r(t)+ \alpha_{iy}I_y(t) \tag{3}$$

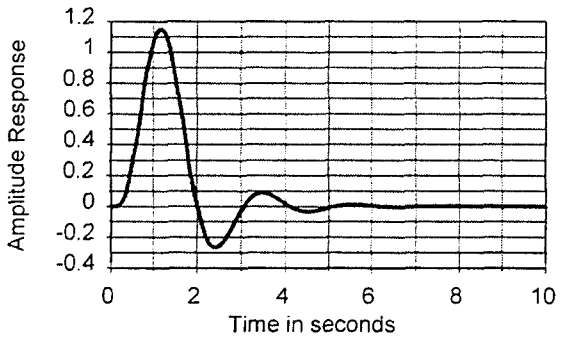

Figure 1
GOES Magnetometer impulse response

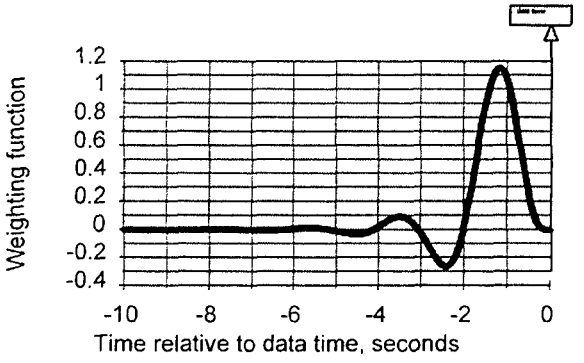

Figure 2
GOES Magnetometer temporal weighting function

and the field measurement obtained at the magnetometer output is:

$$B_{io}(t_l)=\int_{-\infty}^{\infty}[B_{ia}(\tau)+ \alpha_{ir}I_r(\tau)+ \alpha_{iy}I_y(\tau)]h(t-\tau)d\tau, \quad t=t_l \tag{4}$$

The error $B_{\epsilon i}(t)$ to be computed on the ground and subtracted from the measured data is the difference between (4) and (1):

$$B_{\epsilon i}(t_l)=\int_{-\infty}^{\infty}[\alpha_{ir}I_r(\tau)+ \alpha_{iy}I_y(\tau)]h(t-\tau)d\tau, \quad t=t_l \tag{5}$$

The torquer coils on the spacecraft respond to commanded currents with negligible bandwidth limitation relative to the magnetometer response function, so the filter function h(t) given by (2) must be approximated in ground processing through use of a numerical filter. However, there is an additional complication in that the time base for magnetometer sampling is not synchronous with the timebase controlling the torquer current generators, and the telemetry functions are not simultaneously sampled by the telemetry unit.

2.2 Timebase induced error

Each telemetry frame transmitted from the GOES spacecraft provides a measurement of the three components of the vector field and each of the torquer current magnitudes. The absolute time of a sample is not as important as the relative time between changes in the torquer current and the magnetometer samples. The Magnetometer incorporates an internal 16 bit dual slope A/D converter which sequentially converts the X, Y, and Z magnetometer data in synchronism with the spacecraft telemetry frame. The X axis conversion interval is centered at 64 milliseconds after the trailing edge of the read gate which transfers the previous 48 bit vector sample to the spacecraft telemetry unit, with the Y and Z axes occurring at 128 and 192 milliseconds respectively. Taking the frame time assigned to telemetry data as a reference, then real time of the X, Y, and Z data reported in the frame lags (is older than) the reference by approximately τ_i = 384, 320, and 256 milliseconds respectively.

The torquer current magnitudes are sampled by the spacecraft telemetry unit at word times 120 and 122 of the 128 word telemetry frame. The time base error caused by assuming a common conversion time at word 121 is negligible compared to the time resolution of the bandwidth under consideration. The time of conversion therefore leads (is later than) the reference by approximately 121/128 of the 512 milliseconds frame time, or 484 milliseconds. However, because the AOCE which controls the torquers operates on its own clock independent of the telemetry unit, there is an ambiguity in the effective time

of the reported data. While the AOCE clock is independent of the Telemetry Unit clock, the processor cycle is 256 milliseconds long and consists of four 64 millisecond subcycles. The processor and telemetry cycles are then commensurate, and drift relative to each other because of the slight difference in frequencies. To address the resulting time ambiguity of the torquer control, SS/L devised software for the reprogrammable AOCE processor which provides telemetry capable of resolving the time ambiguity to within 64 milliseconds, as well as determining the command state for the torquers.[1] These changes, along with others designed to improve Image Navigation and Registration subsystem performance, were uploaded to the AOCE software in the "AOCE2 R2 patch". The revised telemetry is substituted by the AOCE for gyro data when the rarely used gyros are "off". Normally these data are sub-multiplexed by the AOCE and ingested at word time 24 of every third frame of the Telemetry Unit as "Format 1" data . Word 24, bits 4 and 5 {0,1,2} for Format 1 contain the value of the TLMSEQ counter that was valid when a current transition occurred, resolving the major frame ambiguity. Word 24, bits 6 and 7 {0,1,2,3) make up the FLAG64 parameter which identifies the current 64 millisecond subcycle of the 256 millisecond AOCE computation cycle. Torquer current transitions can only occur when FLAG64 is 1, and the actual switching time is near the beginning of that 64 millisecond subcycle. Finally word 24, bit 8 (MAGUPD) is the least significant bit of the AOCE cycle counter used to rate limit the torquer current steps. If MAGUPD is "0", then the event, if it occurred, happened during the current AOCE cycle, while a "1" indicates the previous AOCE cycle. Words 26 and 27 of format 1 contain the commanded values for the roll and yaw torquer currents, respectively.

In order to calculate the torquer corrections to the magnetometer data, we may either use the command data of words 26 and 27 of Format 1 or the measured values obtained by analog telemetry at telemetry word times 120 and 122. If the measured torquer currents are used, as is the case addressed here, then the torquer command states are not required nor is it required to resolve the telemetry frame ambiguity. In this case only the FLAG64 and MAGUPD parameters are required to resolve the time ambiguity. Table 1 shows the expected value of the resulting data time for the torquer currents, given the 64 millisecond ambiguity and assuming the current transition to be at the beginning of the AOCE subcycle. The current data time is relative to the nominal frame time. Also listed are the corresponding time delays for each axis of the magnetometer between its respective sample time and the current data time. There is a small but finite possibility of a one frame error in time tagging the data when FLAG64=2 and MAGUPD=0 for torquer 2, which could be resolved by using the commanded data rather than measured.

TABLE 1

Word 24 bit 6-7 (FLAG64)	Word 24 bit 8 (MAGUPD)	Update Interval (Prior to WD 24)	Current Data time (Relative to nominal.)	Relative delay, milliseconds MAG X	MAG Y	MAG Z
1	0	0	τ_{10} = +64ms	448	384	320
2	0	1	τ_{20} = +00 ms	384	320	256
3	0	2	τ_{30} = +448 ms	832	768	704
0	0	3	τ_{00} = +384 ms	768	704	640
1	1	4	τ_{11} = +320 ms	704	640	576
2	1	5	τ_{21} = +296 ms	640	576	512
3	1	6	τ_{31} = +192 ms	576	512	448
0	1	7	τ_{01} = +128 ms	512	448	384

Equation (5) must therefore be corrected by the proper delay time τ_{jk} to put the current measurement in the same time reference as the magnetometer data, as shown in equation (6).

$$B_{ei}(t_l)=\int_{-\infty}^{\infty}[\alpha_{ix}I_x(\tau+\tau_{jk})+\alpha_{iy}I_y(\tau+\tau_{jk})]h(t-\tau-\tau_i)d\tau, \quad t=t_l \tag{6}$$

Figure 3 shows, for instance, the weighting function for calculating the correction to the magnetometer X axis and the current profile when FLAG64 is "1" and MAGUPD is "0". Note that time divisions on the horizontal axis correspond to sample intervals of 512 milliseconds relative to the reference time for frame n.

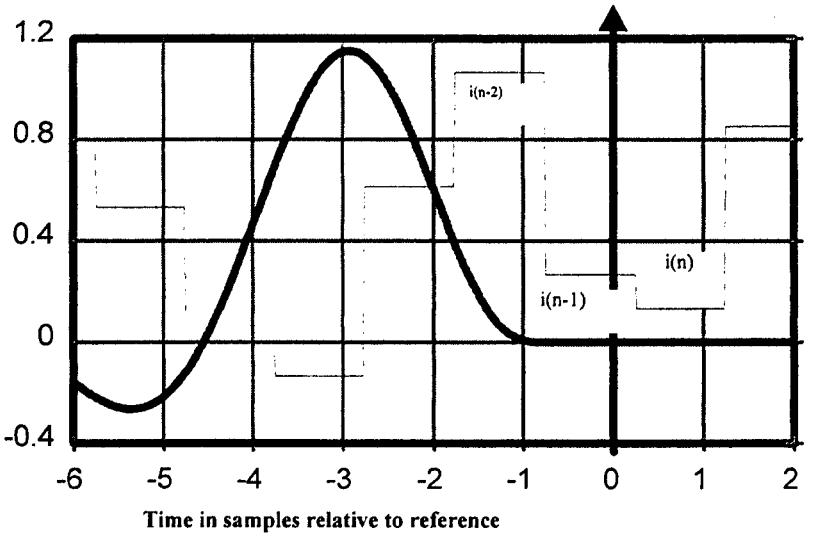

Figure 3
X-Axis Temporal weighting function, MAGUPD=0, FLAG64=1

Note that the value of current read in frame n extends into frame n+1, depending on the phasing of the AOCE clock. The numerical filter weight for each current value is the integral under the weighting function curve for the duration of that value. For this instance, the first two filter weights are zero. Note that the AOCE R2 patch rate limits the current steps to one least significant bit per step. Large steps are shown on this torquer current example for clarity.

2.3 Telemetry noise correction

For GOES-8, excessive high frequency noise was observed on the current telemetry from the spacecraft. This noise had been observed at lower levels during ground test, but it was thought to be 60 Hz noise which would disappear in orbit. After GOES-8 in-orbit test, tests on the GOES-J spacecraft also showed the noise to be present on the telemetry, but caused by unfiltered power converter switching noise on the spacecraft power bus. There was also AOCE digital switching noise present which drifted slowly through the asynchronous telemetry sampling and was aliased at times to low frequency noise referred to as "blooming". For a discussion of the noise problems and remedial actions taken, see the separate paper published as part of this Conference.[2] For GOES-J and later, a passive filter has been added to the telemetry point in the spacecraft, which removes much of the current telemetry noise. However, for GOES-8 the use of current telemetry for torquer correction introduces artificial noise into the magnetometer data product. This is not a problem for time averaged data used extensively by SEC, but would be a significant problem for high time resolution data products. While the approach used in this paper utilizes the measured current data, processing high time resolution data for GOES 8 will be addressed by using the TLMSEQ and other parameters introduced by SS/L in the AOCE2R2 patch to reconstruct the sequence of command states.

3. NUMERICAL FILTER FORM

Since we are here dealing with sampled data, we must convert the analog form of (6) to a discrete calculation:

$$B_{\varepsilon i}(n)=\sum_{k=0}^{k=m}[\alpha_{ir}I_r(n-k)+\alpha_{iy}I_y(n-k)]a_{ki} \qquad (7)$$

where the numerical filter weights are given by:

$$a_{ki} = \int_{-(k+1)\Delta t}^{-k\Delta t} h(-\tau-\tau_i)d\tau = \int_{k\Delta t}^{(k+1)\Delta t} h(\tau+\tau_i)d\tau \qquad (8)$$

In Figure 3, the weights for each sample are the integrals over that sample interval of the properly delayed temporal weighting function. Table 2 shows filter weights calculated for k equal 0 through 10, covering the impulse response function through the second positive lobe. Because of the common 64 millisecond separation in magnetometer component sample times and 64 millisecond granularity of the time base correction, the coefficient sets are cyclic.

4. RESULTS

Figure 4 shows the results for GOES-9 data of applying the filter weights to the compensation algorithm at a time when the phasing between the AOCE and telemetry clocks was such that FLAG64=2 and MAGUPD=0. Figure 5 shows the sensitivity of the compensation by comparing the transient response with the nominal filter to nearest neighbors at the 64 millisecond interval. By contrast, Figure 6 shows the response when the phasing is in error by a full telemetry frame.. Using the proper phasing for the compensation results in limiting the transient error to less than 0.1 nT. Note that the X axis was chosen for the demonstration because it has the largest sensitivity to any single coil current, in this case torquer 1, but also has a reasonable sensitivity to torquer 2.

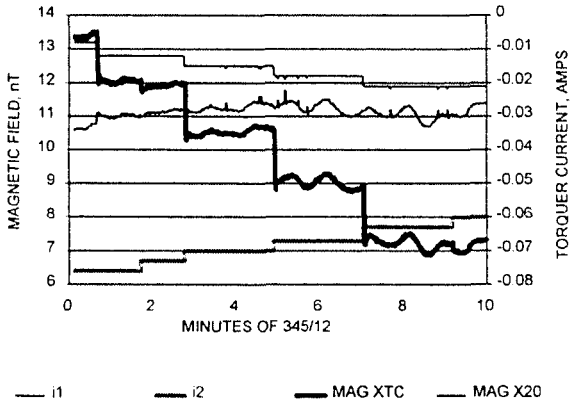

Figure 4
Raw and corrected X axis magnetic field for FLAG64=2, MAGUPD=0, Filter X20. MAGXTC is corrected for for measured temperature only. MAGX20 is corrected for S/C field using filter X20. GOES-9 data from 1995, day 345.

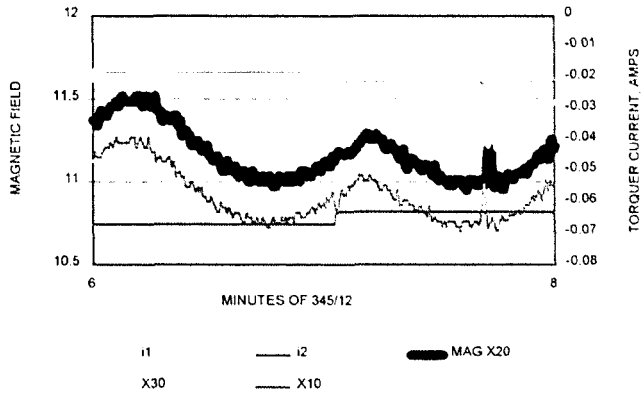

Figure 5
Comparison of corrected data with that using nearest neighbor filters. The telemetry quantization noise spike at about 7.5 minutes is not removed by the filters. X20 and X10 are data processed with ±64 millisecond delays. Expanded from Figure 4.

Figure 5 shows that the correction for a true change of state of the torquer currents is compensated to less than 0.1 nT by application of the telemetry filter. It also shows that by comparison to the large amount of noise introduced into the GOES-8 data by the noise on current telemetry, this source of noise has been greatly reduced on the GOES-9 data by virtue of the filter added to the telemetry point. Nonetheless, the residual noise still triggers quantization steps in the telemetry unit A/D converter. While true steps commanded in the torquer current by the AOCE are measured at about 4 LSB's in the A/D converter, the converter resolution, about 0.8 milliamps per LSB, still results in the introduction of noise into the processed data which is not compensated for by the filter. Introduction of this noise can be avoided by using the command telemetry, but there has been concern that stability with life and temperature of the analog current source controlled by the AOCE would lead to uncertainty in the compensation. Observations thus far on GOES-8 and GOES-9 indicate however that the torquer signatures are quite

stable, so optimum performance may well be obtained by using the commanded current values. Another option for improving the performance of future spacecraft is to improve the quantization noise for the torquer current monitors by increasing the A/D converter resolution, which was originally meant to be better than the current design by a factor of two. Other options for dealing with the residual telemetry noise are discussed in Reference 2.

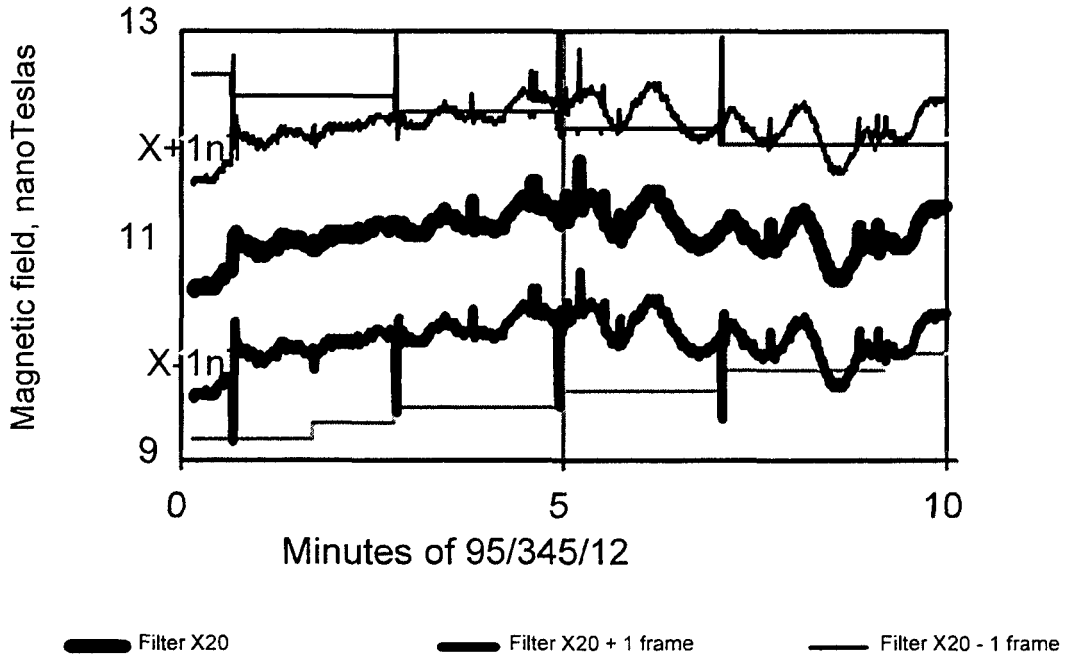

Figure 6
Magnetometer data processed with +/- 1 frame filter delay

5. DISCUSSION

The particular GOES magnetometer problem addressed here is mostly caused by the asynchronous clocks in a digitally controlled subsystem and its telemetry monitor which leads to ambiguity in determining the state of the subsystem as a function of time. As more and more digitally controlled subsystem design becomes the practice, this particular problem is likely to proliferate. Even on GOES, similar complications are caused by asynchronous operation of the DIRA and its Telemetry Unit monitor. It would behoove designers to establish a general design rule that digitally controlled subsystems and their state monitors should be synchronous, and that departures from this practice must be justified.

The second problem addressed here is the error associated with the calculation of a quantity derived from two spacecraft parameters measured in disparate information bandwidths. In this instance, the wider bandwidth (the current telemetry) was so disparate that the solution was to reconstruct the time history of the function and pass it through a digital approximation to the narrower bandwidth parameter (Magnetometer data). Formulating the more general problem of two analog functions, say g_1 (t) and g_2(t), which are properly sampled in accordance with sampling theory, but have disparate information bandwidths characterized by impulse response functions $h_1(t)$ and $h_2(t)$, producing time series say $f_1(t)$ and $f_2(t)$, such that:

$$f_1(t) = \int_{-\infty}^{\infty} g_1(\tau)\, h_1(t-\tau)\, d\tau \quad : \quad F_1(s) = G_1(s) H_1(s) \tag{9}$$

$$f_2(t) = \int_{-\infty}^{\infty} g_2(\tau) h_2(t-\tau)\, d\tau \quad : \quad F_2(s) = G_2(s) H_2(s) \tag{10}$$

then the function g_2 measured in bandwidth h_1, call it f_2', is expressed by:

$$f_2'(t) = \int_{-\infty}^{\infty} g_2(\tau) h_1(t-\tau)\, d\tau \quad : \quad F_2'(s) = G_2(s) H_1(s) = F_2(s) H_1(s)/H_2(s) \tag{11}$$

i.e., $f_2'(t)$ can be recovered by convolving $f_2(t)$ with a time domain function whose Laplace transform is $H_1(s)/H_2(s)$ if the inverse transform of $H_1(s)/H_2(s)$ exists. Practically this means that one or both time functions may be re-sampled to lower bandwidths.

In general, if a situation arises where calculations of derived parameters is necessary, the existence of the error source described by equation 5 should not be overlooked. Where possible, identical response functions should be designed into pre-sampling filters where derived parameters are expected. Where that is impractical, equalization in ground processing must be provided.

1. John Scholtz, "Re-definitions and additions to GOES 8 telemetry by the AOCE 2 reprogramming release," Space Systems Loral internal technical memorandum GOES-PCC-TM-6842, March 10, 1995.

2. F. Zimmerman, S. Cauffman, and R. Hooker, Compensating GOES-8 and -9 magnetometer data for spacecraft induced errors," (paper 2812-31 of this conference), *GOES-8 and Beyon*d, Edward R. Washwell, SPIE, 1996 (in press).

TABLE 2
FILTER WEIGHTS

(a) FILTER WEIGHTS FOR FLAG64=1, MAGUPD=0

SAMPLE =	MAG X	MAG Y	MAG Z
n	0.00000	0.0000	0.0000
n-1	0.00002	0.00007	0.00049
n-2	0.05671	0.08462	0.11957
n-3	0.41507	0.46023	0.49849
n-4	0.51988	0.48773	.44757
n-5	0.12968	0.07923	0.03518
n-6	-0.11748	-0.12110	-0.11962
n-7	-0.04610	-0.03028	-0.01523
n-8	0.03958	0.04163	0.04135
n-9	0.01815	0.01254	.00710
n-10	-0.01549	-.01467	-.01340

(b) FILTER WEIGHTS FOR FLAG64=2, MAGUPD=0

SAMPLE =	MAG X	MAG Y	MAG Z
n	0.00000	0.00000	0.00000
n-1	0.00007	0.00043	0.00179
n-2	0.05462	.11957	.16114
n-3	0.46023	.49849	.52816
n-4	.48773	.44757	.40091
n-5	.07923	.03518	-.00757
n-6	-.12110	-.11962	-.11374
n-7	-.03028	-.01523	-.00142
n-8	0.04163	0.04135	0.04044
n-9	..01254	.00710	0.00204
n-10	-.01467	-.01340	-.01175

(c) FILTER WEIGHTS FOR FLAG64=3, MAGUPD=0

SAMPLE =	MAG X	MAG Y	MAG Z
n	0.0000	0.0000	0.0000
n-1	0.0000	0.0000	0.0000
n-2	.00043	.00179	.00487
n-3	.11957	.16114	.20825
n-4	.49849	..52816	..54799
n-5	.44757	.40091	.34942
n-6	.03518	-.00757	-.04235
n-7	-.11962	-.11374	-.10424
n-8	-.01523	-.00142	.01078
n-9	..04135	.04044	.03765
n-10	-.00629	-.00971	-.01237

(d) FILTER WEIGHTS, FLAG64=0, MAGUPD=0

SAMPLE =	MAG X	MAG Y	MAG Z
n	0.00000	0.00000	0.00000
n-1	0.00000	0.00000	0.00000
n-2	.00179	.00487	.01077
n-3	.16114	.20825	.25932
n-4	.52816	.54799	.55716
n-5	.40091	.34942	.29485
n-6	-.00757	-.04235	-.07078
n-7	-.11374	-.10424	-.09193
n-8	-.00142	.01078	.02110
n-9	.04044	.03765	..03374
n-10	-.00971	-0.01237	-.01423

(e) FILTER WEIGHTS FOR FLAG64=1 MAGUPD=1

SAMPLE =	MAG X	MAG Y	MAG Z
n	0.0000	0.0000	0.0000
n-1	0.0000	0.0000	0.0000
n-2	00487	.01077	.02064
n-3	.20825	.25932	.31233
n-4	.54799	.55716	.55537
n-5	.34942	.29485	.23894
n-6	-.04235	-.070787	-.09269
n-7	-.10424	-.09193	-.07762
n-8	01078	.02110	.02937
n-9	..03765	03374	.02901
n-10	-.01237	-.01423	-.01535

(f) FILTER WEIGHTS FOR FLAG64=2, MAGUPD=1

SAMPLE =	MAG X	MAG Y	MAG Z
n	0.0000	0.0000	0.0000
n-1	0.0000	0.0000	0.0000
n-2	.01077	.02064	.03562
n-3	.25932	.31233	.36502
n-4	.55716	.55537	.54274
n-5	.29485	.23894	.18337
n-6	-.07078	-.09269	-.10816
n-7	-.09193	-.07762	-.06210
n-8	.02110	.02937	.03552
n-9	..03374	.02901	.02372
n-10	-.01423	-.01535	-.01

(g) FILTER WEIGHTS FOR FLAG64=3, MAGUPD=1

SAMPLE =	MAG X	MAG Y	MAG Z
n	0.0000	0.0000	0.0000
n-1	0.0000	0.0000	0.0000
n-2	.02064	.03562	.05671
n-3	.31233	.36502	.41507
n-4	.55537	.54274	.51988
n-5	.23894	.18337	.12968
n-6	-.09269	-.10816	-.11748
n-7	-.07762	-.06210	-.04610
n-8	.02937	.03552	.03958
n-9	.02901	.02372	.01815
n-10	-.01535	.01573	-.01549

(h) FILTER WEIGHTS, FAG64=0, MAGUPD=1

SAMPLE =	MAG X	MAG Y	MAG Z
n	0.00000	0.00000	0
n-1	0.00000	0.00002	0.00007
n-2	.03562	.05671	08462
n-3	.36502	.41507	..46023
n-4	.54274	.51988	.48773
n-5	.18337	.12968	.07923
n-6	-.10816	-.11748	-.12110
n-7	-.06210	-.04610	-.03028
n-8	.03552	.03958	.04163
n-9	.02372	.01815	.01254
n-10	-.01573	-.01551	-.01467

Performance Analysis of the GOES Trim Tab Solar Pressure Torque Angular Momentum Control

Edwin Harvie
Computer Sciences Corporation, Seabrook, MD 20706

John Rowe
Computer Sciences Corporation, Seabrook, MD 20706

Yo-Kung J. Tsui
Lockheed Martin, Seabrook, MD 20706

ABSTRACT

The GOES I/M series of geostationary weather satellites are 3-axis stabilized and incorporate an optical trim surface, or "trim tab", to balance solar radiation pressure torque between the south moment arm, formed by a single solar array, and the north moment arm, formed by a solar sail on an extended boom. This design minimizes the need for active roll/yaw momentum management from thrusters or magnetic dipoles and provides margin for uncertainties and changes such as center of mass shift and degradation of surface optical properties. The trim tab has one rotational degree of freedom and is actuated via open loop ground command to a motor on the rotation axis. Normal operational procedure is to command a small incremental trim tab slew daily to track the change in north/south solar radiation pressure torque with Sun declination. Proper management of the trim tab is critical to spacecraft roll/yaw pointing performance and the open loop design of the system requires sophisticated ground based algorithms to determine trim tab position error and develop a daily commanding profile. Flight experience with the GOES-8 and GOES-9 spacecraft has proven the feasibility of the trim tab design and has led to refinement of the ground based trim tab analysis algorithms. This paper summarizes the performance of the trim tab roll/yaw momentum control system and describes analysis methods developed by the GOES mission operations team to support trim tab operations.

KEYWORDS: GOES, trim tab, solar pressure torque, momentum management

INTRODUCTION

The GOES-I/M spacecraft are 3-axis stabilized geostationary platforms to permit continuous imaging and sounding of the Earth. GOES-I (designated as GOES-8 on orbit) was launched on April 13, 1994 and GOES-J (designated as GOES-9 on orbit) was launched on May 23, 1995. The attitude control system is a bias momentum design with two canted momentum wheels (V-mode) providing torque components in pitch and yaw, with roll controlled through gyroscopic coupling. A smaller reaction wheel mounted on the z-axis provides backup yaw torque using only one momentum wheel (L-mode). Two 100 Ampere-Turn-meter^2 magnetic dipole coils are located on the roll and yaw axes for roll/yaw momentum management. Attitude is referenced to the Orbit Coordinate System (OCS): z-axis (yaw) aligned with geocentric nadir, y-axis (pitch) aligned with negative orbit normal, and x-axis (roll) approximately along the velocity vector. Figure 1 shows the GOES satellite and Figure 2 is a simplified representation of the attitude control system.

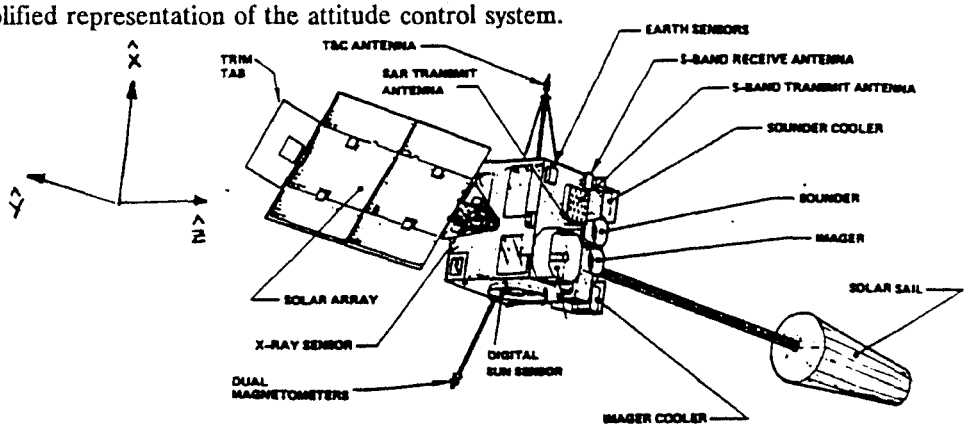

Figure 1. GOES I/M Spacecraft

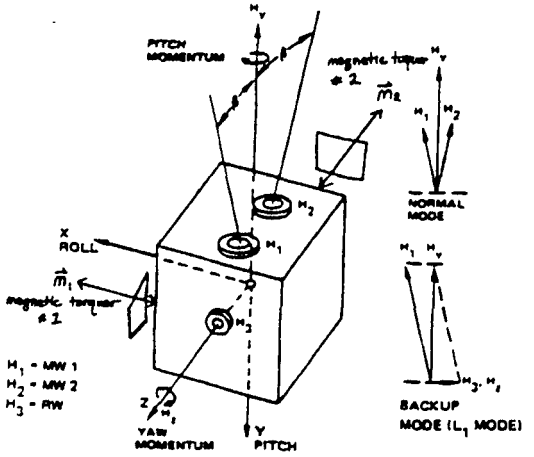

Figure 2. GOES I/M Simplified Attitude Control System

To facilitate radiative cooling of the instruments, a large solid angle of cold space is required in the spacecraft northern hemisphere. This requirement prohibits symmetric solar arrays on the north and south faces, so that a single large array is mounted on the south panel. To compensate for the north/south solar pressure torque imbalance, a solar sail of aluminized Kapton is mounted on the north panel at the end of a 58 foot deployed boom. The solar sail provides an area moment arm sufficient to offset the south solar array moment arm, and is located a sufficient distance from the north panel so that minimal infrared is reflected or re-radiated down into the instrument cooler housings.

After the solar sail parameters are chosen to minimize the average north/south solar radiation pressure torque, a seasonal variation remains as the torque profile changes with changing body frame Sun declination. The resulting solar pressure torque imbalance would require large magnetic dipole coils for momentum management, increasing weight, power requirements, stray magnetic effects and magnetic storm effects (the magnetic control law uses a modeled magnetic field). Yaw thruster momentum unloads, although available for contingencies, cause unacceptable disturbances for imaging. To minimize the size of the magnetic dipole coils, a motorized trim tab with a single rotation axis is placed at the end of the Solar array to vary the effective area of the south solar pressure moment arm. The aluminized trim tab surface is highly reflective to increase its efficiency. A precision stepping motor on the rotation axis positions the trim tab via ground command, with a quantization of less than 0.001 deg. Redundant potentiometers indicate coarse position to approximately 1.0 deg and fine position to 0.1 deg. Trim tab position is defined as 0 deg coplanar with the solar array and -180 deg stowed against the solar array anti-Sun side. Figure 3 shows the approximate seasonal trim tab range (Reference 1). Normal procedure is to command a small incremental trim tab slew each day to track the change in north/south solar pressure torque with changing Sun declination.

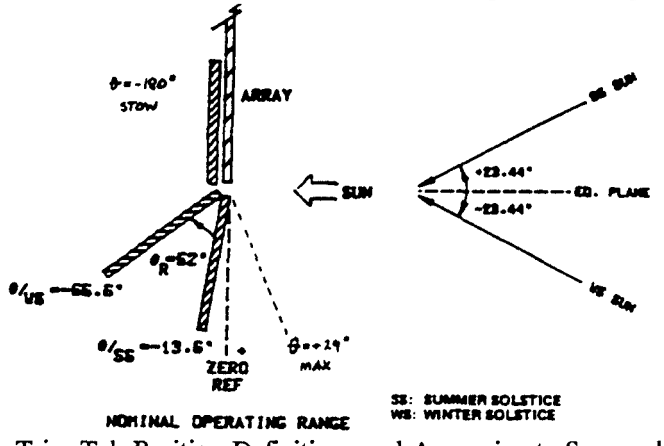

Figure 3. Trim Tab Position Definitions and Approximate Seasonal Range

The open loop design of the trim tab system requires sophisticated ground based algorithms to determine trim tab error and generate uplink commands. The Orbit and Attitude Tracking System (OATS) was intended to fill this role. Early GOES-8 flight experience proved that the original OATS algorithm was unsatisfactory. An independent trim tab program developed

as an off-line analysis tool by the Goddard Flight Dynamics Facility (FDF) was used to evaluate trim tab error during the first phases of the GOES mission. Several months after the GOES-8 launch, the OATS trim tab process was extensively modified and has since performed satisfactorily, although a long lead time (2 months) is required for the initial convergence. Prior to the GOES-9 launch, another more rigorous trim tab analysis utility was developed by the GOES Mission Operations Support Team (MOST) for use during initial on-orbit tuning and to supplement the OATS and FDF results.

FDF TRIM TAB ANALYSIS

The approach used by the FDF to manage the trim tab is to calculate the residual disturbance torque using telemetry data from the magnetic dipole coils, momentum wheels, and thrusters and use a theoretical rate of change of torque with trim tab angle (at constant Sun angle) to calculate the trim tab angle change necessary to balance the residual torque. The trim tab angle change to be commanded is then obtained by adding the change from the computed residual torque to the change necessary to track the Sun from the current day to the next.

The residual torque acting on the spacecraft can be estimated from the change in angular momentum over a period of time. Calculation of angular momentum change from wheels and thrusters is straightforward. The magnetic torque calculation is based on the magnetic dipole telemetry, estimated spacecraft residual dipole, measured magnetic field from magnetometer telemetry, and correction for coupling of the dipoles to the magnetometers. In the FDF trim tab analysis utility, momentum wheel speeds are sampled at 6 PM satellite local time (SLT), where the north/south solar torque imbalance is absorbed purely in the yaw component of the wheel momentum, and subtracted from the wheel speed sample 24 hours earlier at 6 PM SLT. The difference in wheel momenta is attributed to the residual solar torque stored in the momentum wheels over 24 hours. Magnetic torques and torques from any thruster unload that may have occurred are computed through the 24 hour period. The 24 hour averaged torques are converted to the Sun Pointing System (SPS) coordinate frame: the y-axis is aligned with negative orbit normal, the z-axis is the projection of the Sun line onto the orbit plane, and the x-axis completes the right-handed orthogonal triad (Figure 4). In the SPS frame, the x-component of the net residual disturbance torque is always aligned with the trim tab axis of rotation, since the solar array always tracks the Sun. The 24 hour average SPS x-component torque is thus used to compute trim tab error.

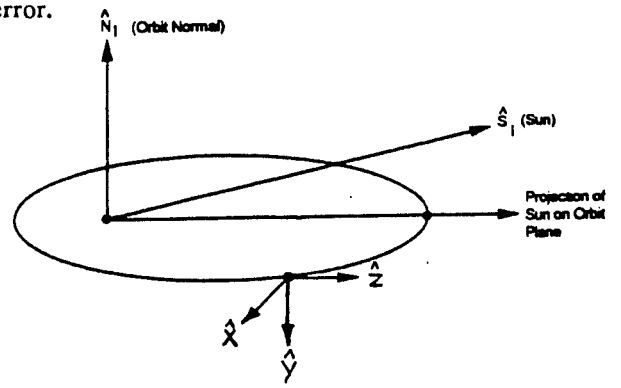

Figure 4. Sun Pointing System (SPS) Coordinate Frame

The theoretical rate of change of torque with trim tab angle and the day-to-day change in the trim tab angle are calculated from a simple surface decomposition of the spacecraft. The principal torques are due to solar radiation pressure acting on the solar array and solar sail, with a much smaller contribution from the main body. The solar array and trim tab are modeled as plates. The top of the solar sail is modeled as a plate, while the middle and bottom surfaces are modeled as truncated cones.

MOST TRIM TAB ANALYSIS UTILITY

Prior to the GOES-9 launch, an independent trim tab analysis utility was developed by the GOES MOST for tuning the trim tab during initial on orbit operations, and to supplement the OATS process since a long convergence time was anticipated for the OATS algorithm. To compute the trim tab roll/yaw torque, Euler's equation is solved for a net residual disturbance

torque, including the effects of all control torques (wheels and magnetic dipoles) and gyroscopic torques. Thruster momentum management torques are also included, based on user input times, duration, and thruster selection. All input data are smoothed to reduce the effect of telemetry quantization. Discontinuities in the dipole-corrected magnetometer telemetry that arise from slight asynchronization between the magnetometer and magnetic dipole telemetry are filtered as well. The equation of motion is evaluated using control actuator and corrected magnetometer telemetry data explicitly at each data sampling interval through the orbit. At each interval, the net residual disturbance torque is transformed in to the SPS frame. Each component of the SPS residual torque is then averaged over the 24-hour period. The 24-hour average x-component SPS residual torque is attributed solely to solar torque imbalance and is related to trim tab angle error through the torque-to-angle partial derivative. The torque-to-angle partial, approximately 2.3×10^{-6} Nm/deg, is computed analytically and changes only slightly from the winter to summer solstice positions. In practice, trim tab error is evaluated over several days to establish a consistent trend before making a large correction. Uncertainty in the solution can be 0.1 deg, but is usually better.

In addition to displaying the actuator and magnetometer data used in the computation, the MOST utility displays the 3 torque components as a function of time in the spacecraft body frame as well as in the SPS frame. These data are useful for evaluating the nature of the net residual disturbance torque. When transformed into the SPS frame, a constant body frame torque will vary sinusoidally at the orbit period over 24 hours. Similarly, a constant torque in the SPS frame will vary sinusoidally in the body frame. Non-constant torques will lead to terms that vary faster than the orbital period.

OATS TRIM TAB PROCESS

The trim tab angle determination function of the OATS was developed as the primary ground support element for trim tab operations. The OATS was intended to provide both start-up and routine trim tab angle determination. Requirements for OATS trim tab residual torque management were separated into start-up operations (10×10^{-7} Nm, or 0.43 deg) and normal on orbit operations ($\leq 1.5 \times 10^{-7}$ Nm, or 0.07 deg). In the original OATS algorithm, the telemetered trim tab position and Sun declination were used to calculate the solar torque provided by the trim tab from an analytic solar torque model. The 24 hour average torque applied by the control system was computed using spacecraft actuator and magnetometer data, similar to the FDF and MOST algorithms. The net torque needed to be compensated by an adjustment of the trim tab was then calculated from the torque from telemetry data, the adjusted solar torque profile, and the change in torque required to track the Sun from one day to the next. Once the net change in torque was calculated, the trim tab angle adjustment was obtained through an iterative process. From the set of equations defining the trim tab inertial torque, the partials of the torque with respect to trim tab angle were derived. The first estimate of the change in angle was obtained using the Newton-Raphson method. The modified trim tab angle was then used to re-compute the trim tab solar torque, and the iteration process continued until convergence was reached.

Over the first several months of GOES-8 launch support, the original OATS trim tab algorithm did not converge on a consistent trim tab angle. Problems arose in part from the discrete day-to-day nature of the solutions, which made the commanded angles more susceptible to solution error, and also from the dependence on trim tab position telemetry, which was subject to noise and potentiometer calibration error. Also, the magnetometer telemetry used for computing the magnetic control torque was not properly corrected for dipole coupling. The OATS trim tab algorithm was therefore extensively redesigned (Reference 2).

The redesigned OATS algorithm still requires calculation of the net residual torque from telemetry over past 24 hours. A history file containing 60 records (one per day) of the trim tab angle from telemetry, Sun declination, and residual torque is updated at the end of the daily analysis process. A linear least squires fit program (LSQ) then uses trim tab position telemetry data over the last 2 month period to generate a 3rd order polynomial fit to predict the trim tab angle for next 10 days. (Telemetered trim tab position is not corrected for computed error before the fit is applied.) The daily commanded slew angle is simply the difference of the predicted trim tab angle for next day to the current day. The OATS automatically collects telemetry data from the GOES-I/M Telemetry and Command System (GIMTACS), processes the telemetry data, computes the residual torque and daily trim tab slew angle, and then sends the slew command information to GIMTACS. In the current operation, telemetry collection and processing is activated by a timer in OATS and the trim tab history file is updated daily. The LSQ function is performed every 2 to 3 days. The daily slew command to GIMTACS is also activated by the timer. The OATS also provides the capability to perform manual adjustment of the trim tab angle to correct accumulated error. The accumulated trim tab error is normally removed manually when the residual torque reaches 1.0×10^{-6} NM.

GOES-8 TRIM TAB OPERATIONS

During the initial weeks of the GOES-8 launch, the FDF trim tab analysis utility was used exclusively to determine trim tab error due to lack of convergence of the OATS results. The initial setting of -22.2 deg on Day 122, 1994 was selected by Space Systems/Loral (SS/L) based on a detailed analytic solar torque model. GOES-8 was in the L-1 control mode at this time, and Figure 5 shows the resulting yaw momentum for the first 24 hours, which quickly exceeded the 0.4 Nm-sec desaturation limit. The spikes are thruster firings unloading yaw momentum. Figure 5 demonstrates the sensitivity of the GOES roll/yaw control to error in the solar array/trim tab system.

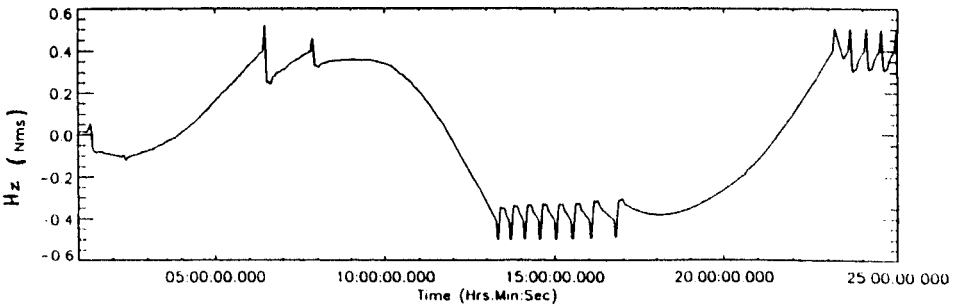

Figure 5. GOES-8 Yaw Momentum During the Initial 24 Hours of L-mode Operations

The inertial torque imparted to the spacecraft by these firings was calculated by FDF as -2.0×10^{-5} Nm, which suggested that the trim tab angle should be changed by +8 deg. SS/L engineers computed a similar estimate, and so on Day 123 the trim tab angle was increased by half this amount (+4 deg) as a test. A further +2 deg change was performed later on Day 123, because the first adjustment appeared to be in the correct direction. Another calculation showed that the thruster torque had been reduced by about an order of magnitude as a result of the +6 deg change, and on Day 124 the magnetic dipoles were turned on. Figure 6 shows trim tab fine position telemetry for the first 45 days of normal on orbit control.

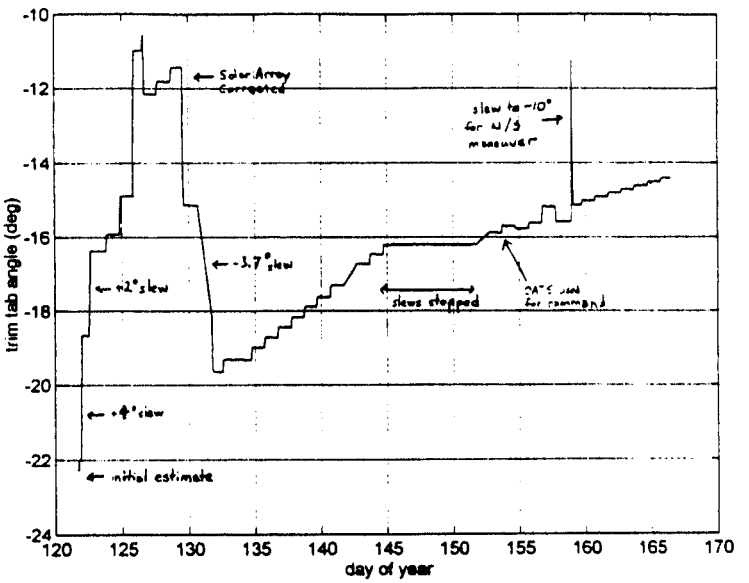

Figure 6. GOES-8 Initial Trim Tab Tuning

This procedure of trying trim tab settings continued for several days with no real reduction in the number of thruster firings until two steps were taken. On Day 130, a -0.05 deg Earth sensor roll bias was applied to center the yaw momentum and reduce the tendency of most of the firings to occur on one side of the orbit. Also, at about this time it was discovered that an incorrect calibration curve for the solar array position potentiometer had caused a solar array offset of 8 deg, greatly reducing the south area moment arm and biasing the solar torque. After the array was re-pointed, the torque calculations indicated that the trim tab angle was too positive. The trim tab angle was moved a total of -3.7 deg by Day 133, after which no more yaw thruster firings were observed. By Day 135, the spacecraft was in the V-2 control mode.

From Day 135 to Day 146 the trim tab was slewed each day according to the SS/L theoretical value. The trim tab angle was following the theoretical curve with an offset of about -1.0 deg. The torque from the magnetic dipoles as calculated by FDF and OATS indicated that the trim tab was still too far in the positive direction by 1.0 to 1.5 deg. A critical piece of information, the coupling between the dipoles and magnetometers, was not available. Inspection of the magnetometer and dipole data plots showed that the magnetometer output is dominated by the magnetic dipoles; thus it was felt that the torque calculation might be unreliable. However, by Day 145 it was felt that the sign of the trim tab error was probably correct, so the routine daily adjustments were stopped at that time.

The magnetic dipole-to-magnetometer coupling matrix was obtained on Day 147, and the magnetometer data were properly corrected. The general approach used by FDF at this point in the GOES-8 support was to step the trim tab at the theoretical rate for several days while observing the magnetic torques. A change in angle was then commanded to reduce the magnetic torque level. This worked essentially because the torquers were acting to minimize the wheel speed changes and the trim tab setting was close enough to eliminate yaw thruster firings. Figure 7 shows the magnetic torque as a function of day of year with the dipole correction applied along with the torque being absorbed by the wheels. The daily updates were omitted until Day 153, at which time the magnetic torque had passed through zero. At this point the actual trim tab angle was about 2.5 deg more negative than the theoretical value.

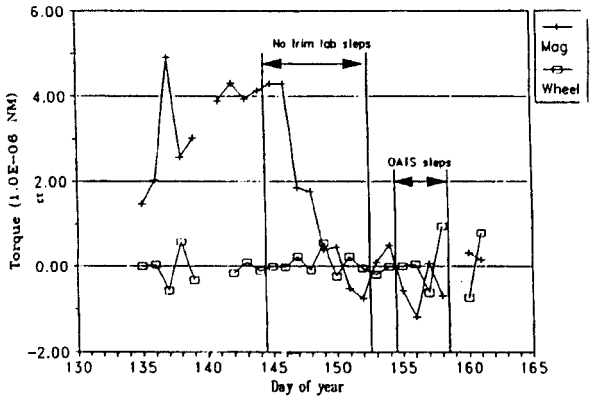

Figure 7. Magnetic and Wheel Torque Components - GOES-8 Initial On Orbit Operations

Starting Day 154, the value computed by the original OATS algorithm was used for adjusting the trim tab. The OATS calculated the following trim tab slews:

Day of Year of Command	OATS Recommended Slew (deg)	Slew Actually Commanded (deg)	Remarks
154	-0.075	-0.075	
155	0.43	0.1	Solar Array had been depointed, OATS thought to be incorrect.
156	0.47	0.47	
157	-0.47	-0.47	
158	1.0	Angle of -15.5	
159	--	0.10	N/S Stationkeeping, day 159. OATS was not run.
160	-0.525	0.098	
161	0.581	0.098	

This history is based on a combination of adding up the daily slews and averaging telemetry from the redundant fine potentiometers (which can differ by up to 0.5 deg). Note that the OATS develops a pattern of requesting large alternate sign slews on alternate days. The resulting trim tab error caused the magnetic dipoles to saturate the 0.075 A dipole current limit and forced a switch to the 0.4 A maximum current limit. The OATS recommended slew angle was incorrect for several reasons. Several polarity and coefficient errors were found in the solar torque calculation. Errors in the computed magnetic torque, noisy potentiometer data, and a data collection interval not beginning at 6 PM SLT also contributed to the OATS problems. FDF predictions were therefore used routinely until mid November, when the redesigned OATS algorithm was implemented. The improved OATS algorithm proved capable of managing trim tab error to within ±0.5 deg. Figure 8 shows good agreement between the FDF and improved OATS solutions (OATS is online at Day 322). Shortly after the improved OATS algorithm was implemented, the normal on orbit mode roll/yaw controller was replaced with the reprogrammed HZC algorithm to improve roll/yaw pointing performance. The HZC controller rejects roll/yaw disturbances more efficiently than the original controller and so provides a greater margin for trim tab error.

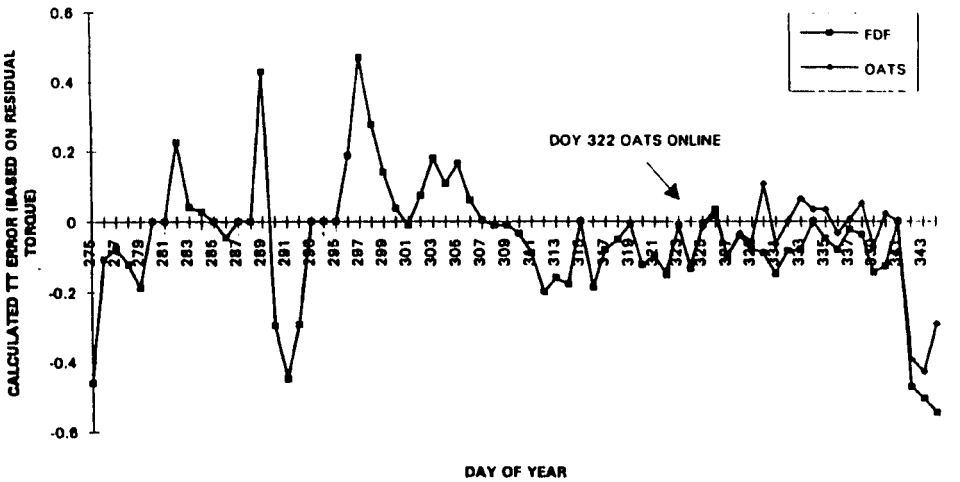

Figure 8. Trim Tab Error - FDF vs. Redesigned OATS

Long term trends can be evaluated for GOES-8, since over 2 years of flight data is available. Figure 9 shows the complete history of GOES-8 trim tab position (from hourly averaged fine potentiometer 2 telemetry) from initial on orbit operations in May 1994 through the 1996 summer solstice. After approximately Day 160, 1994, the trim tab has been well tuned (with a one-sigma error of ~0.2 deg) so figure 9 represents the optimum seasonal trim tab angle profile. The GOES-8 seasonal trim tab range has been approximately -68 deg to -14 deg. Figure 9 shows that the estimate of -22.2 deg at the initial transition to on orbit mode (May 1, 1994) is within 2 deg of the nominal position for May 1, 1995. The clearest trend from Figure 9 is the offset between 1995 and 1996 positions at the solstices. Trim tab position is less negative over time (i.e. more trim tab area must be presented to balance the torque), indicating a net decrease in the effective south moment arm over time. This decrease is attributed to a migration of the center of mass southward (towards +y) due to propellant depletion from the inclination adjust maneuvers, performed near the winter solstice. The other possible cause of the trend would be changes in the optical properties of the principal north/south solar torque components, the solar array and solar sail. Since the solar sail becomes 20% more absorptive from beginning-of-life to end-of-life and the solar array properties change very little (Reference 3), the trend, assuming no center of mass change, would favor an increased effective south moment arm. Degradation of the trim tab surface, which becomes only 3% more absorptive beginning-to-end of life, will decrease the south moment arm only slightly. Thus, degradation in the solar sail material over time may help to offset the change in solar torque profile from center of mass migration.

Figure 10 shows the relationship between trim tab position as shown in Figure 9 and Sun declination, from summer solstice 1995 to summer solstice 1996. The relationship is approximately linear, except for a slight deviation near winter solstice, which indicates that the trim tab angle to solar torque partial is also approximately linear over the full seasonal range. The offset between the two functions for increasing and decreasing Sun angle is due to the center of mass shift following the December 1995 inclination adjustment maneuver.

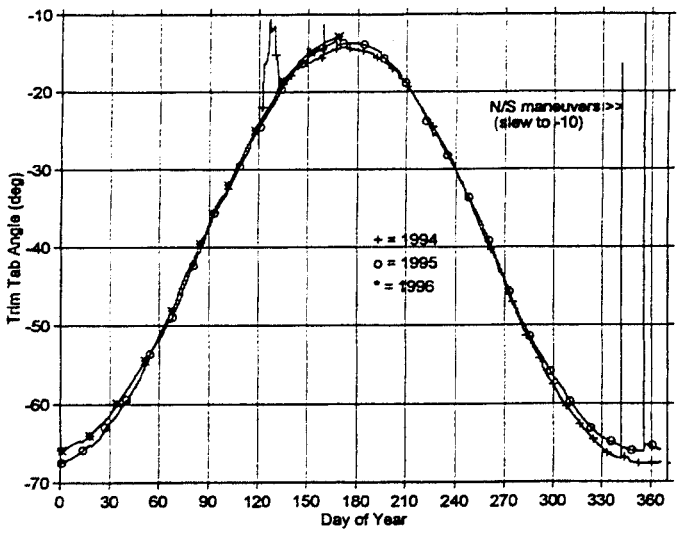

Figure 9. GOES-8 Trim Tab History, May 1994 through June 1996

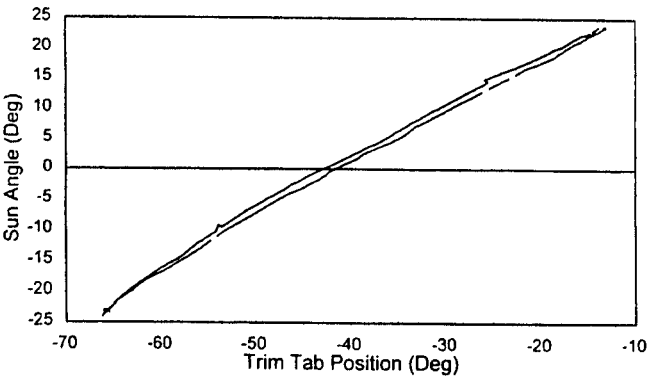

Figure 10. GOES-8 Trim Tab Position vs. Sun Declination, June 1995 to June 1996

The OATS residual solar torque from Day 34, 1995 through the 1996 summer solstice is shown in Figure 11. The residual torque is controlled mostly to under ± 1.0×10^{-6} Nm (± 0.4 deg trim tab angle error). For a residual torque greater than approximately 2.0×10^{-6} Nm, spacecraft yaw pointing error is observable in the Image Navigation and Registration (INR) process. Near Day 226 in Figure 11, a trim tab error of 1.0 deg caused a yaw error of 100 μrad as determined from INR star observations. Since the daily commanded slews are the difference of predicted angles over two consecutive days, it is difficult to control residual torque to within 0.5×10^{-6} Nm (0.2 deg angle) consistently. Error caused by quantization in the stepping motor duration command and by calibration error in the fine position potentiometers eventually causes trim tab error to exceed 0.2 deg. Figure 12 shows the difference between the commanded trim tab slew angle and the fine position telemetry, which integrates into a net residual torque offset that must be removed by manual correction. Manual corrections are performed more often around the solstices when the stepping error may be larger than the daily commanded slew angle.

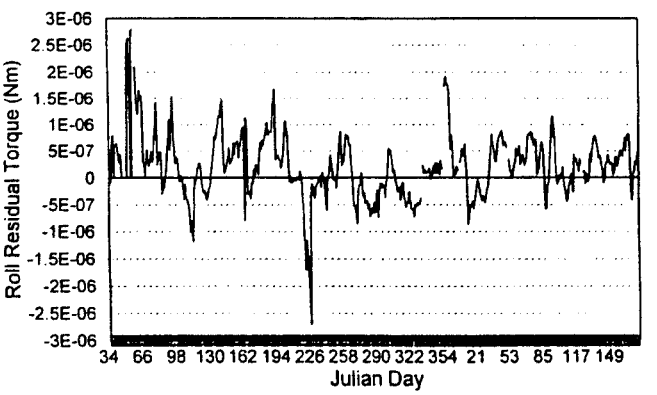

Figure 11. GOES-8 Residual Torque History From OATS, 95/034 - 96/177

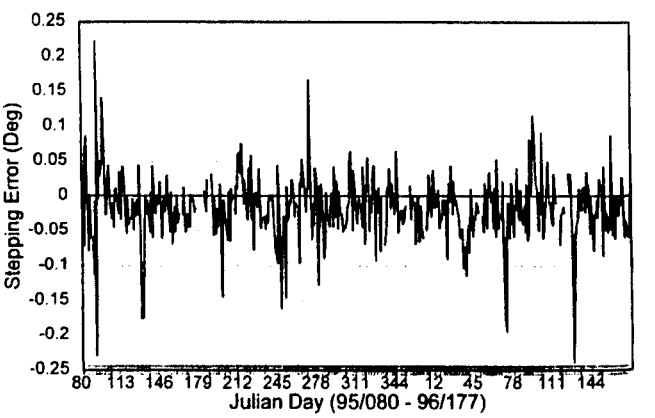

Figure 12. GOES-8 Trim Tab Stepping Error

GOES-9 TRIM TAB OPERATIONS

Based on GOES-8 experience, a consistent and well-defined plan was developed by the mission operations team for the GOES-9 initial on orbit operations and trim tab tuning. At the initial transition to on orbit mode, the trim tab was slewed to the current GOES-8 position for that day. The actual GOES-8 trim tab position from telemetry was considered to be a better *a priori* estimate than an analytic model, neglecting subtle differences between the two spacecraft in mass and surface properties. The solar array was then slewed ±10 deg about the expected Sun position to locate the east/west Sun Analog Sensor null and validate the solar array potentiometer telemetry. After the solar array was verified to be precisely normal to the Sun, on orbit control using the reaction wheel (L-1 mode) was enabled for a period of 48 hours without the magnetic dipoles. Yaw momentum was allowed to accumulate up to the reaction wheel maximum limit before a thruster unload would be allowed (the reaction wheel control mode has a much greater margin for storing yaw momentum than the dual momentum wheel V-mode). This technique has the advantage that the solar torque imbalance is absorbed purely in the reaction wheel, eliminating uncertainty in the residual solar torque calculation caused by yaw thruster unloads and magnetic dipole activity. Figure 13 shows the trim tab position telemetry from fine potentiometer 2 during the initial on orbit tuning process. Corruption of certain segments of the fine potentiometer 1 has caused fine potentiometer 2 to be used exclusively as the true trim tab measurement.

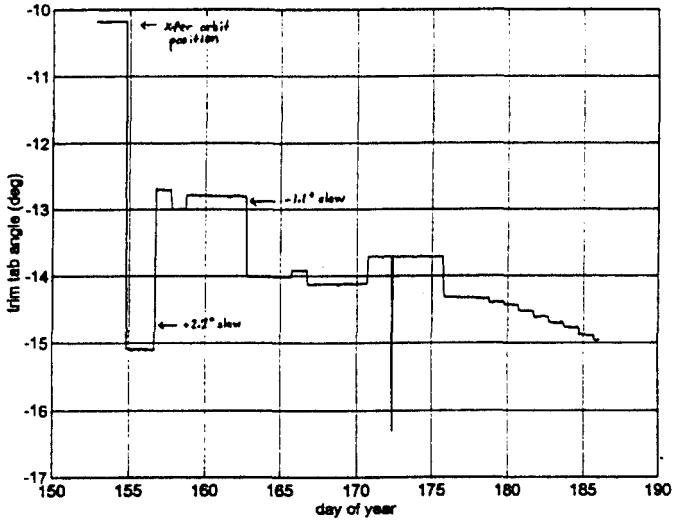

Figure 13. GOES-9 Trim Tab Initialization

During the initial 24 hours of L-mode operations, a large yaw momentum excursion occurred that was attributed to trim tab error. No yaw thruster unload was allowed. On day 157, the trim tab was slewed +2.29 deg to correct for the roll/yaw disturbance. After 4 days, solutions from the MOST trim tab analysis utility indicated that the Day 157 slew had over-compensated for the L-mode momentum accumulation and that a -1.1 deg correction was required, which brought the trim tab closer to the initial position estimate. Subsequently, the roll/yaw disturbance was correlated with a large outgassing torque observed in pitch during the first two days of normal Sun angle geometries. By Day 164, a consistent residual torque profile was reached, with a difference between GOES-8 and GOES-9 of only 1.0 deg (a 0.5 deg error was injected purposely on Day 171 to test a shift in residual solar torque polarity through the solstice).

The MOST trim tab analysis utility was used for error determination and commanding until Day 205, 1995, when the OATS algorithm became primary for routine trim tab operations. For the initial 20 days of GOES-9 trim tab operations using the MOST utility, the daily trim tab commands were generated from a sinusoidal fit to one year of GOES-8 fine trim tab position data. Day-to-day differences in the analytic fit were used for the predictive daily adjustments. After 20 days of data were collected, a new method of daily slew predictions was used. A profile of corrected trim tab angles was generated by applying the computed trim tab error to the daily average fine potentiometer data. The resulting function is the best estimate of the actual trim tab position required to balance the residual solar torque. That the corrected daily position is a relatively smooth function implies that an extrapolation may be used to predict trim tab position several days in advance. Figure 14 gives the corrected trim tab position data together with a 4th order polynomial fit, extrapolated for 10 days. Polynomial fits greater than 4th order extrapolated 10 days tend to diverge from the optimum angle profile, while lesser order fits do not track the profile

as well. The difference between the corrected trim tab position and the 4th order fit, shown in figure 15, together with the computed error, is less than 0.2 deg over the entire 50 day span. The close match of the 4th order fit indicates that a predictive error of less than 0.2 deg is possible by extrapolating a polynomial fit to the *corrected* trim tab position several days in advance. This technique is different from the OATS algorithm, which uses uncorrected trim tab position telemetry in the least squares fit to generate the angle predictions.

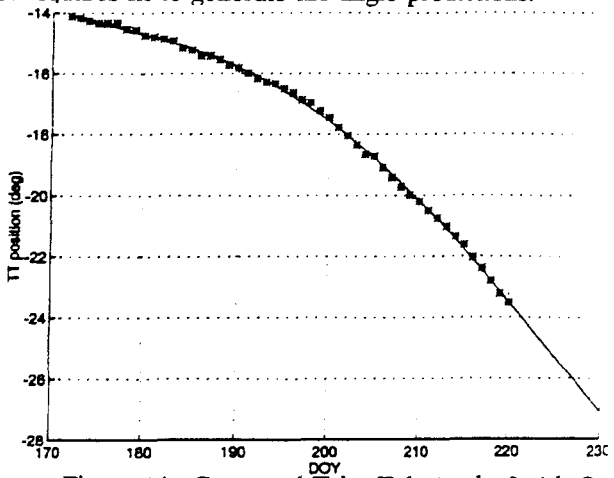

Figure 14. Corrected Trim Tab Angle & 4th Order Fit Extrapolated 10 Days

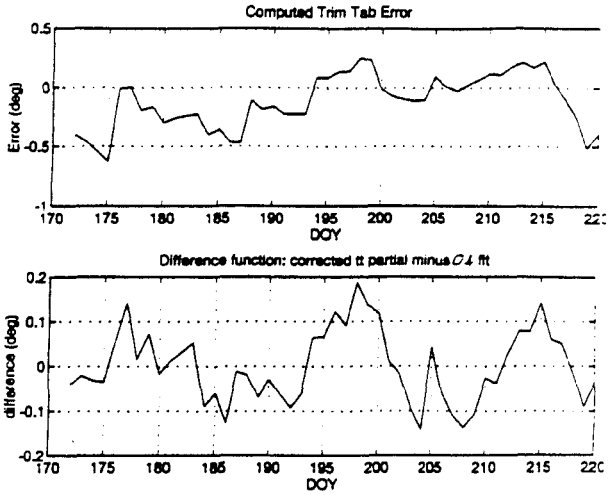

Figure 15. Computed Trim Tab Error and Corrected Angle minus 4th Order Fit

Trim tab fine potentiometer 2 data from initial on orbit operations in June 1995 through the 1996 summer solstice are plotted in Figure 16. Minimum trim tab angle at the winter solstice is -70 deg. The GOES-9 angles are consistently 1 to 2 deg more negative than GOES-8. This discrepancy may reflect spacecraft center of gravity differences as well as small differences in optical surface properties and potentiometer calibration. Figure 17 shows trim tab position as a function of Sun declination between the 1995 and 1996 summer solstices. As for GOES-8, the relationship is approximately linear, with a slight divergence near winter solstice. The close correspondence between the increasing and decreasing Sun declinations is because the GOES-9 inclination maneuver performed on Day 187, 1995 was small and did not significantly affect center of mass. Figure 18 shows the OATS calculated residual torque for GOES-9 over the same period. On Day 170, 1996, another inclination maneuver was performed and the trim tab was slewed -0.53 deg to accommodate the 0.6 deg inclination change. However, on Day 171, the OATS calculated a large residual torque of -1.5×10^{-6} Nm. A manual adjustment of +0.5 deg was then made. This shows that correction for Sun declination change after inclination maneuvers is not sufficient for post-maneuver trim tab prediction and that center of mass relocation effects must also be accounted for.

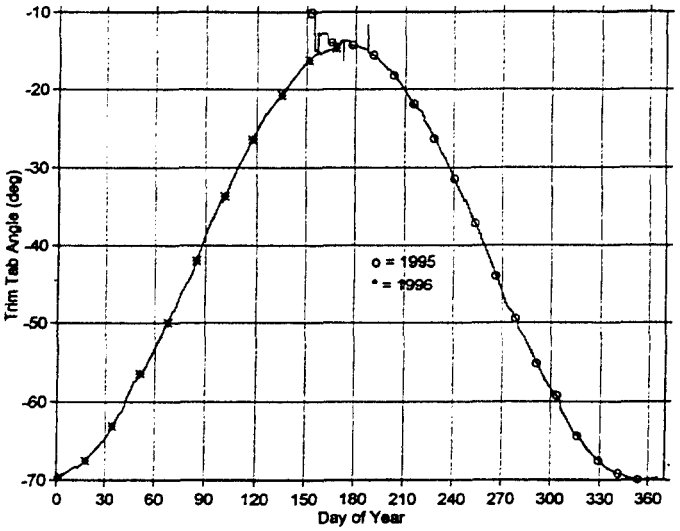

Figure 16. GOES-9 Trim Tab History, June 1995 - June 1996

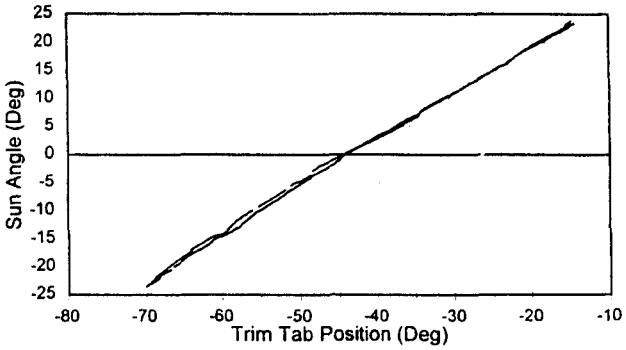

Figure 17. GOES-9 Trim Tab Position vs. Sun Declination

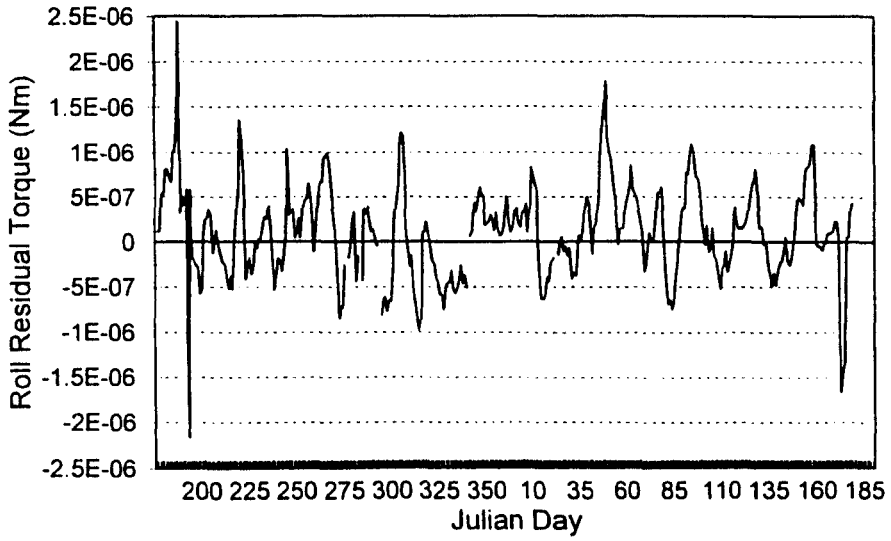

Figure 18. GOES-9 Residual Torque History From OATS, 95/176 - 96/177

To illustrate the effectiveness of the trim tab roll/yaw torque management, the x- and z-axis residual solar torque for a typical day (Day 345, 1995) computed using the MOST trim tab analysis utility is plotted in the body frame in figures 19 and 20. For a significant trim tab error, the inertial residual solar torque would be sinusoidal in the body frame, with a 24 hour period. The body frame x- and z-axis residual torques for this day vary at approximately 4 times the orbit period, indicating a higher order roll/yaw disturbance than the 24 hour period trim tab solar torque imbalance.

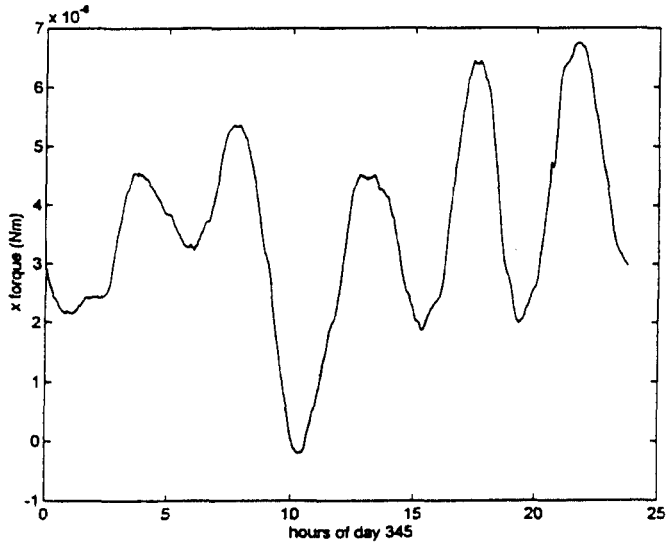

Figure 19. Body Frame X-Axis Residual Torque GOES-9, Day 95/345

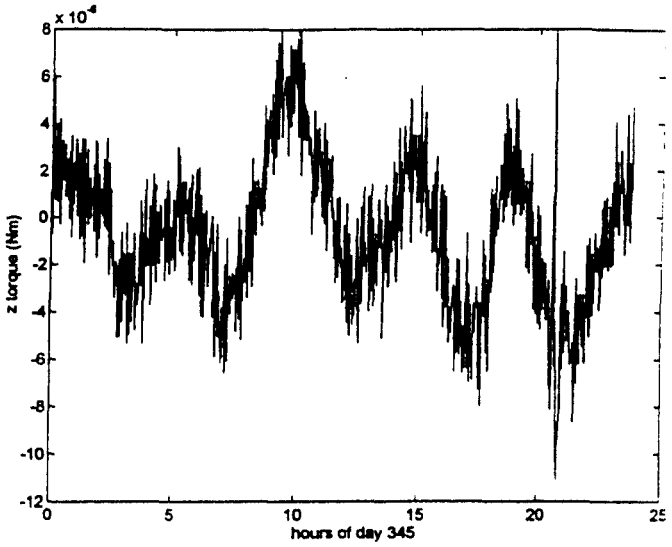

Figure 20. Body Frame Z-Axis Residual Torque GOES-9, Day 95/234

Figure 21 shows the x-component of the SPS residual torque, which is parallel to the trim tab axis of rotation. A trim tab imbalance would result in a constant offset from zero of the SPS x-axis torque component over one day. Variation in the SPS x-axis torque in figure 21 indicates a higher order inertial roll disturbance. The 24 hour average SPS x-axis torque indicates that trim tab error for this day was approximately 0.25 deg. The maximum magnitude of the inertial roll torque, approximately 7 x 10-6 Nm, is well within the capacity of the magnetic dipoles. Maximum magnetic dipole current for this day was less than 0.2 A. Figure 22 shows the corresponding momentum wheel yaw momentum for Day 345.

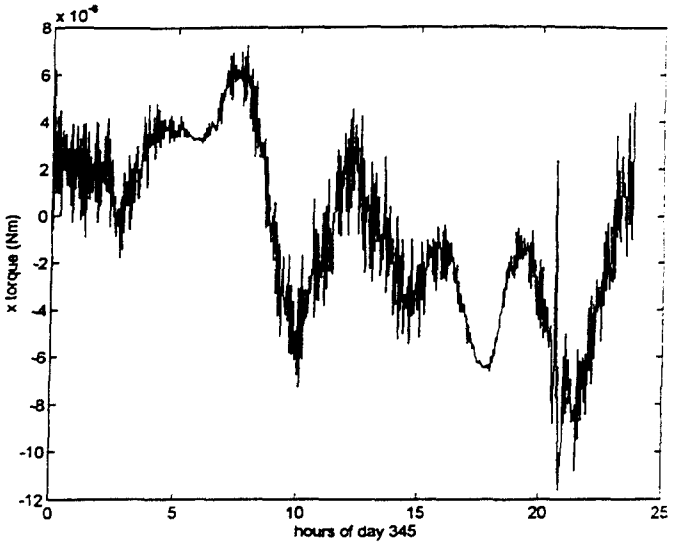

Figure 21. SPS X-Axis Residual Torque, GOES-9 Day 95/345

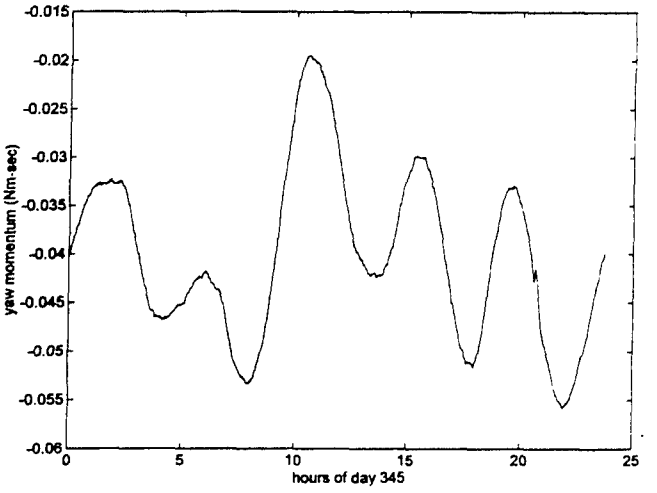

Figure 22. Yaw Momentum, GOES-9 Day 95/345

CONCLUSIONS

Flight experience has validated the GOES trim tab design as an effective system of semi-passive angular momentum control. The GOES missions have also shown that the rigorous solar torque model developed by SS/L was very effective in the trim tab design and predictions generated using the model matched flight data to within 2.0 deg. Incorrect telemetry calibration of the solar array position potentiometers and unknown magnetic dipole/magnetometer coupling effects hampered early efforts to tune the trim tab during GOES-8 launch support. The original OATS trim tab algorithm did not provide consistent results during early GOES-8 operations. Experience gained from the GOES-8 launch was used to refine GOES-9 launch support trim tab procedures and resulted in a rapid tuning process and smooth transition to routine on-orbit operations. A similar plan will be used for the GOES-K launch support. Flight experience has also proven the advantage of having different analysis algorithms in place to provide independent validation of results and as a backup method for trim tab commanding in case of problems with the primary algorithm.

Following extensive redesign, the OATS trim tab determination system has proven effective in maintaining trim tab error to within 0.4 deg, which is sufficient to meet INR yaw pointing and day-to-day yaw repeatability requirements. The original goal to manage trim tab error to 0.1 deg has proven impractical. A possible improvement to the OATS algorithm would be to apply the least squares fit to trim tab position data that has been corrected using the daily residual torque solutions instead of to uncorrected trim tab position telemetry. Several incidents in which trim tab error has approached 1 deg have permitted trim tab error to be correlated with spacecraft yaw pointing performance through INR measurements, with typical daily trim tab errors producing roll/yaw pointing variation at the limit of INR observability.

REFERENCES

1. GOES Program Spacecraft Operations Handbook, DRL 503-02, vol. III, revision G - Spacecraft Description, Space Systems/Loral, August 31, 1995.

2. GOES IJK/LM Operations Ground Equipment Operations and Maintenance Manuals, DRL 504-06, Space Systems/Loral, August 24, 1995.

3. GOES IJK/LM Attitude/Orbit Control Analysis Critical Design Review, vol. II, SSD-TR10816A, Ford Aerospace Corporation/Space Systems Division, March, 1988.

Using the Sun Analog Sensor(SAS) data to investigate solar array yoke motion on the GOES-8 and -9 spacecraft

Milton C. Phenneger

Computer Sciences Corporation

Jenifer L. Knack

Computer Sciences Corporation

ABSTRACT

The GOES-8 and -9 Sun Analog Sensor(SAS) flight data is analyzed to evaluate the attitude motion environment of payloads mounted on the solar array. The work was performed in part to extend analysis in progress to support the Solar X-Ray Imager(SXI) to be flown on the GOES-M. The SAS is a two axis sensor mounted on the X-Ray Sensor Pointing(XRP) module to measure the east/west error angle between the Sun and the solar array normal and to provide a north south error angle for automatic solar pointing of the X-Ray Sensor(XRS) by the XRP. The goal was to search for evidence of solar array vibrational modes in the 2 Hz and 0.5 Hz range and to test the predicted amplitudes. The results show that the solar array rotates at the rate of the mean Sun with unexpected oscillation periods of 5.6 minutes, 90 minutes, and 1440 minutes originating from the two 16:1 gear drive train stages between the solar array drive stepper motor and the solar array yoke. The higher frequency oscillations are detected as random noise at the 1/16 Hz telemetry sampling rate of the SAS. This supports the preflight predictions[1,2] for the high frequency modes but provides no detailed measurement of the frequency as expected for this data period. In addition to this the data indicates that the solar array is responding unexpectedly to GOES Imager instrument blackbody calibration events.

KEY WORDS: GOES-9, geosynchronous, solar array, sun sensor, flight experience, Solar X-Ray Imager

2. INTRODUCTION AND BACKGROUND

The GOES-9 Sun Analog Sensor(SAS) is a component of the X-Ray Sensor(XRS) payload on the GOES spacecraft and is illustrated in Figure 1[3]. The SAS in mounted on the yoke of the solar array assembly and provides two axis Sun angle measurements to monitor the East/West error in the XRS field of view(FOV) and North/South error for input to the X-Ray Positioner Electronics(XRPE) for automatic tracking of the Sun as its declination changes with the seasons. The East/West error sensed by the SAS is a result of solar array run rate variations and vibrations, spacecraft attitude(driven by orbital eccentricity on the pitch axis), and true solar motion along the ecliptic. The solar array runs in an open loop mode at the mean solar rate of 360° in 24 hours in the body frame, and it is reset every day to remove the accumulated east/west error at 06:00 spacecraft local time(SLT). These offset errors are caused by periodic planned interruptions of the solar array drive to adjust the angle of the trim tab solar pressure torque[4] balance area and by daily changes in the true rate of the Sun on the ecliptic.

The goal of this work was to determine solar array vibrational modes[1] were measurable in the SAS data. This analysis is to provide flight data to complement the work in reference 1 for the Solar X-Ray Imager(SXI). The SAS data period is 16 seconds with a resolution of 0.016°. SAS data sensitivity is dependent upon the following conditions; if amplitudes of the 5 solar array modes between 0.17 Hz and 2.5 Hz, amplitudes are in the range of 50 μradians($\approx$0.003°), if the SAS analog noise is low relative to the 0.016° least significant bit(lsb), and array vibrations are not highly correlated with the SAS telemetry sampling. The array torsional(east/west) mode amplitudes will be revealed as noise in the SAS data. If noise transitions in the SAS data are more frequent near the thresholds of the telemetry steps, some information about the vibration amplitude may be obtained from SAS flight data. If actual amplitudes are greater than predicted[1], it will be more obvious in the SAS data.

Section 3 describes the analysis method and results with illustrations comparing modelled and flight data. Section 4 presents details of the SAS telemetry data model. Section 5 is a short discussion of the results.

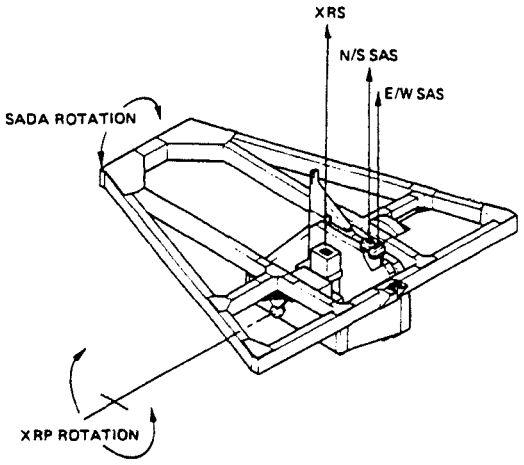

Figure 1. Solar Array Yoke Assembly With XRS Subsystem[3]

3. ANALYSIS METHOD AND RESULTS

The 16 sec SAS telemetry data was filtered in a 7 point running average to provide visual enhancement of the features in this data. To understand these features a model of the SAS east/west errors was developed including the effects of true solar motion, spacecraft orbital motion, and presumed solar array drive gear train effects. The analog model data is digitized and averaged for visual comparison with the flight data. Conclusions about the features in the flight data are made after good visual similarity with the model is obtained. Figure 2. illustrates the effect of a running average on the raw data. The average function converts the discrete two level data into an analog counterpart. The figure reveals three unexpected features; 1) the 5.6 minute oscillations, 2) the 90 minute oscillations, and 3) 1 lsb transitions in the average are correlated with the Blackbody calibration(BB Cal) nutation indicated by the earth sensor roll data. This is unexpected, as the BB Cal response is primarily a roll/yaw nutation at a period near 5.6 minutes, not on the pitch axis. The data shows that there is a significant east/west response at the array yoke to the BB Cal. One transition in the average is equivalent to 9 consecutive samples offset in the negative direction of the raw data. Comparisons between the model and the averaged flight data for GOES-9 on days of year(DOY) 173, 184, and 228 (1995) are illustrated in figures 3, 4, and 5. The model results are biased upward in these figures to allow comparison. Figure 6 is a detailed look at the averaged data for DOY 184 showing phase agreement in the 5.6 and 90 minute oscillations and slightly higher noise effects in the flight data(i.e. the sample to sample ripples on the 5.6 minute oscillations at 04:40 UTC). The observations of this analysis are summarized as follows:

1) The 5.6 minute oscillation and the 90 minute oscillations are caused by the solar array gear drive. The amplitude of the oscillation from this analysis is near 0.003° for the 5.6 minute period and 0.005° for the 90 minute oscillation. The drive has two gear stages, 16:1 each with an outer gear rate of 360° per 1440 minutes in the body frame. The corresponding inner gear periods are 90 and 5.6 minutes respectively. The model assumes that the gear teeth have a sinusoidal error over one rotation and matches all maxima detected in the data for each day analyzed. No phase deviations are observed throughout the day as expected for spacecraft nutation. Also, Figure 7 shows data from DOY 275(wheels at 2900 RPM) & 276(wheels 4500 RPM), when the nutation period should have been different, has close correspondence of the maxima on both days. The differences in amplitude of the maxima are primarily due to the differences in the location of the Sun between the SAS digital levels at the same time on each day.

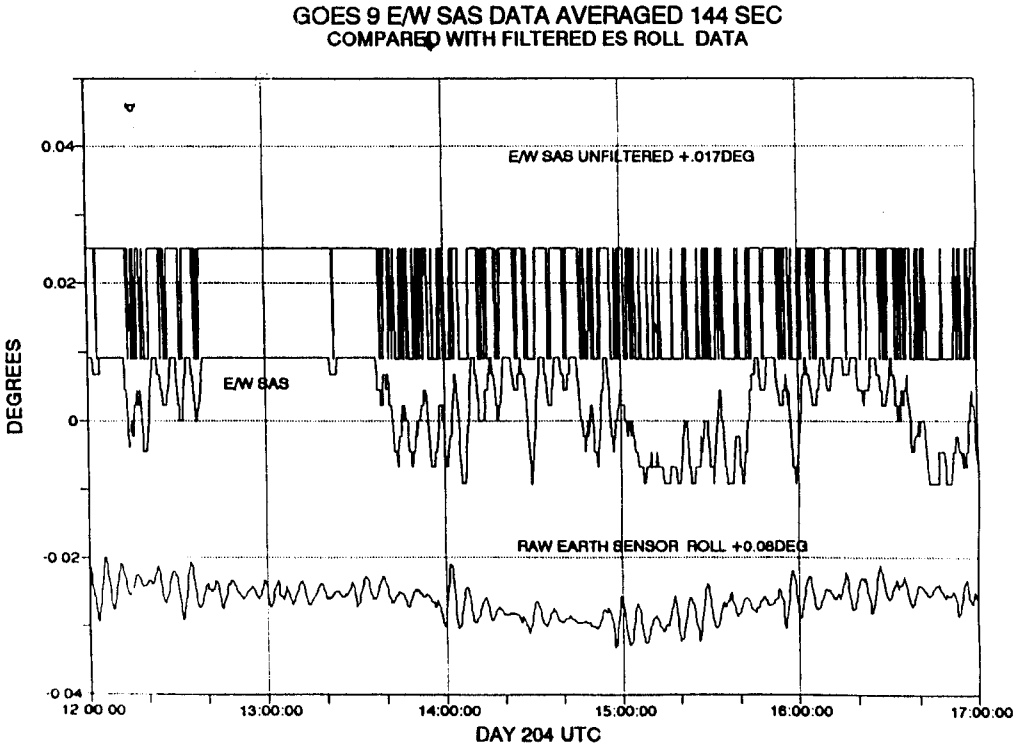

FIGURE 2

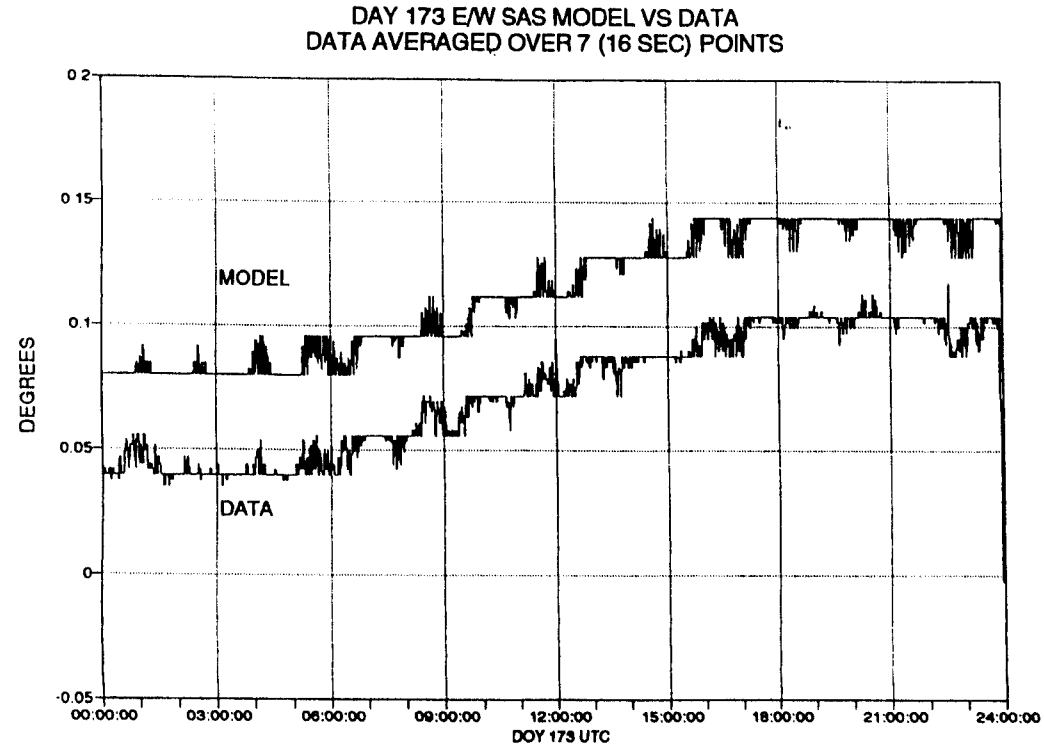

FIGURE 3

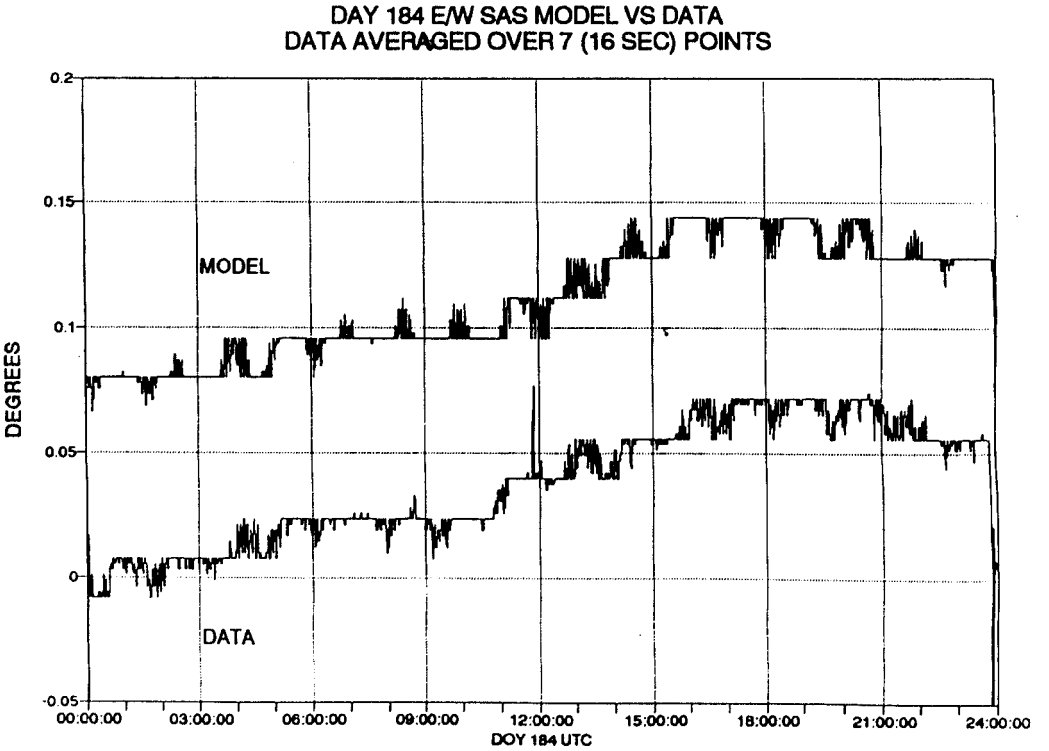

FIGURE 4

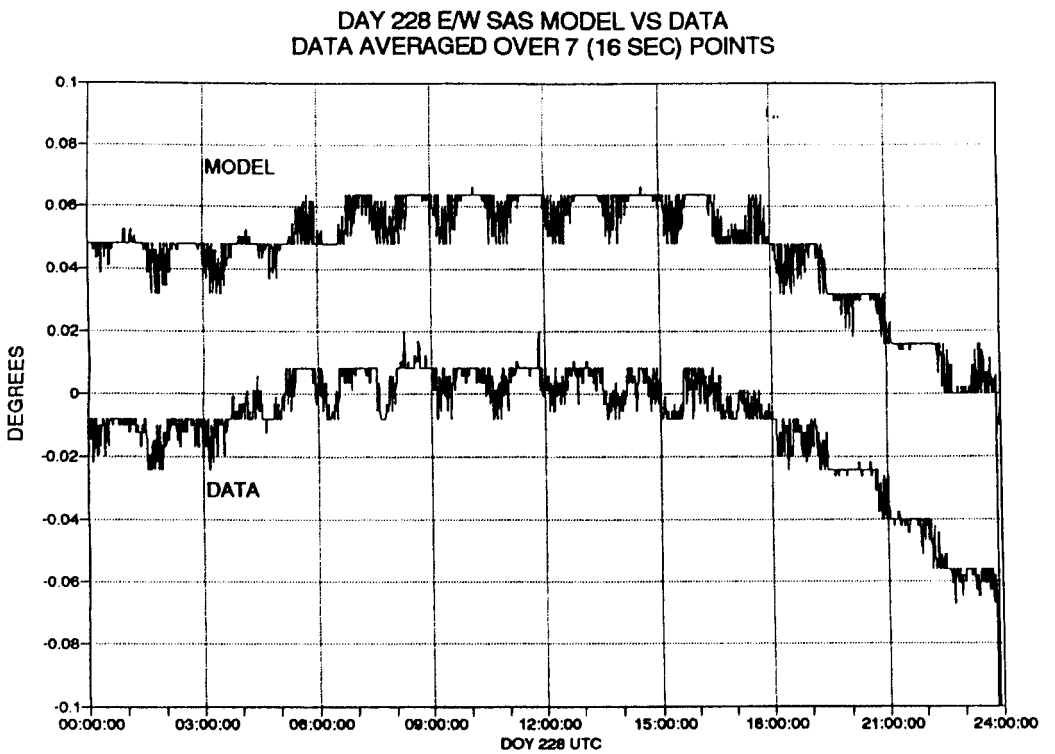

FIGURE 5

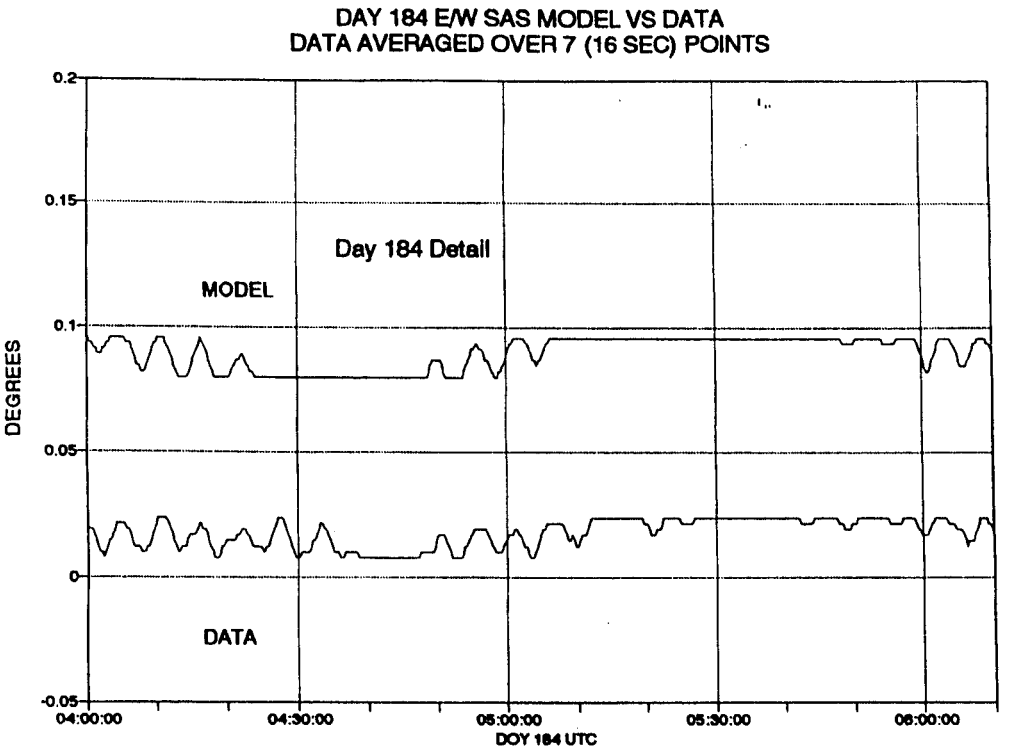

FIGURE 6

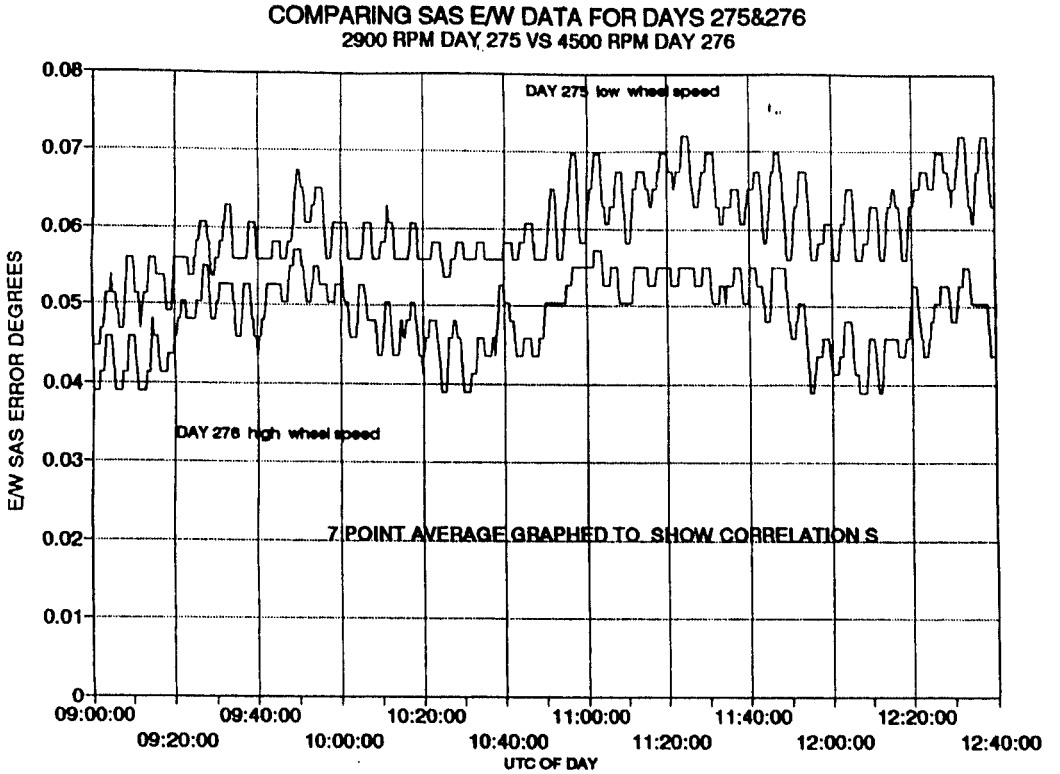

FIGURE 7

2) A one day sinusoid or gaussian shaped outer gear error centered at 12:00 UTC worked to match the data. The amplitude of this error is between 0.02° and 0.03° and it was necessary in the model.

3) A constant run rate error which causes a linear growth in the Sun angle error throughout the day was not resolved. This error is linear in time and is added to the effect of the true solar motion and the spacecraft longitude drift. The accuracy of matching these linear terms is about $\pm 0.008°$. The model matched the data without explicit compensation for the longitude drift. A run rate error of $+0.016°$ per day is consistent with DOY 173 and DOY 184 but not DOY 228. If the array occasionally adds or skips step a run rate error measurement could not be made with this three day sample.

4) The pitch thermal error, which is about 0.024°, a known feature of the earth sensor pitch control[4], centered at spacecraft midnight was not clearly visible in the data. Attempts to insert it were not successful. This inconsistency could be caused by perigee and outer gear effects of similar amplitude masking the Earth sensor pitch error. For the most part the pitch thermal offset should be detectable in this SAS data model and it is not. This is an analysis result that requires further work.

5) The BB Cal couples into the east/west motion of the array for a much longer time than expected from the Mirror Motion Compensation(MMC) signals that are accurately correcting the mirrors of the scanning instrument while the non-scanning instrument is executing the calibration slew that stimulate spacecraft nutation. The data of Figure 2. indicate that at 13:30, 14:30, and 16:00 there are transitions in the SAS data that are out of family with surrounding data. The 14:30 and 16:00 spikes are sustained pitch excursion of 9 raw samples in length(144 sec) whereas the pitch MMC for the sounder is only a 25 seconds long and 30 microradians. The data indicates that the array appears to slip west toward negative angles at the beginning of the BB-Cal, returning east by the same amount($\approx 0.016°$) 144 seconds later. This is not visible at every BB Cal because the alignment of the Sun between the transition thresholds can position the analog values of the starting Sun angles such that only one raw sample exceeds the 0.016° transition threshold. This is apparent when the Sun is centered in the digitization bin at 13:30 UTC causing the BB Cal to stimulate a 1/9th pulse on the averaged output. Finally, Earth sensor pitch data is less informative as the pitch loop acts fast to null it.

6) The amplitude of the random noise component of the model was between $\pm 0.004°$ and $\pm 0.007°$ and is consistent with the predictions[1]. If the high frequency (0.5 Hz - 2.0 Hz) motion is small relative to the digitization bin size it will stimulate random looking transitions when Sun angles approach an A-to-D threshold from above and below. The prediction[1] for the amplitude was near ± 50 μradians or 0.003°.

7) Fast Fourier Transforms performed on one day intervals of the SAS east/west data to verify the frequencies in the data model showed that GOES-8 has a lower amplitude 5.6 minute oscillation than GOES-9. Figure 8 illustrates this comparing one orbit of GOES-9 and GOES-8(with a higher eccentricity). The FFT results illustrated in Figure 9 also detect frequencies not observed in this analysis.

4. DATA ANALYSIS AND MODEL

The SAS telemetry data is subcommutated at 1/32nd the GOES telemetry period of 0.512 sec to produce a 16 second data period. In addition to this the resolution of 0.016° is large relative to the amplitude of the diurnal variations in the east/west Sun angle. On occasion the orbital eccentricity combined with zeros in the daily rate of change of the sundial correction can limit 24 hours of telemetry data to two or three telemetry values. To recover the analog information from this highly digitized data, a running average is performed which converts data toggling frequency at the lsb transition points into analog levels which are easier to interpret visually. The choice of the averaging period of seven samples or 1.87 minutes was made to avoid removing attitude information at the spacecraft nutation period which is near 6 minutes. Figure 2 shows how a nine point running average reveals the east/west motion. Note that an isolated transition of 0.016° is reduced in amplitude to 1/9th.(e.g. at 13:20 UTC). Conversely when one point in the averaged data reaches 0.016° it is equivalent to nine consecutive points in the raw data at a level different by 1 lsb(e.g. near 14:30 UTC and 16:00 UTC).

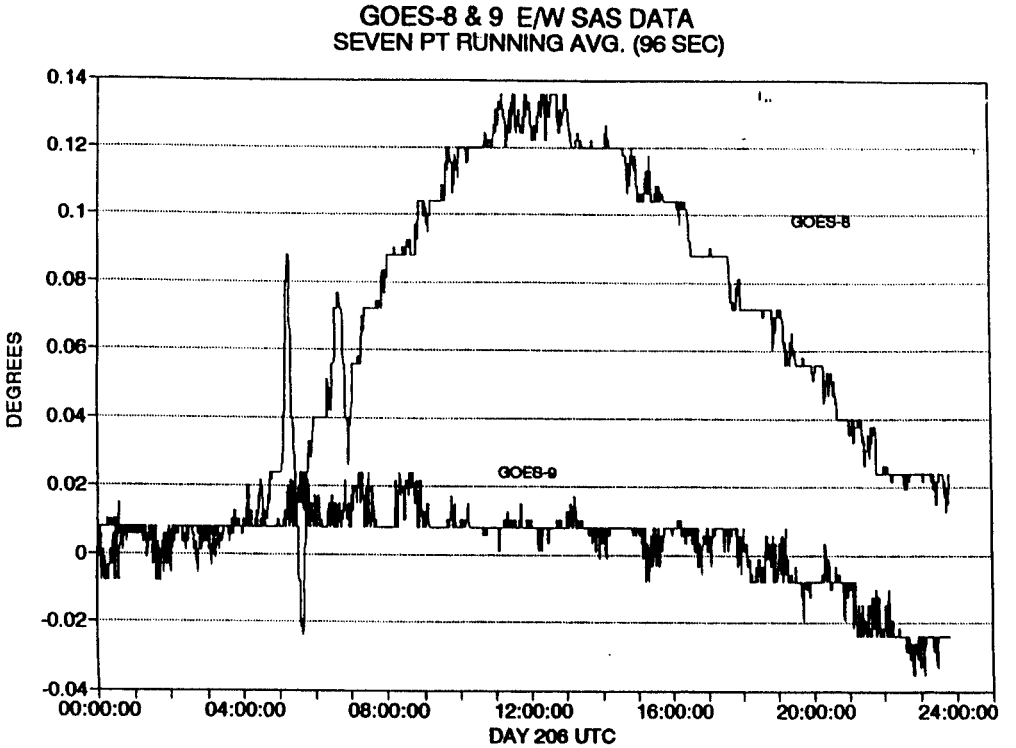

FIGURE 8.

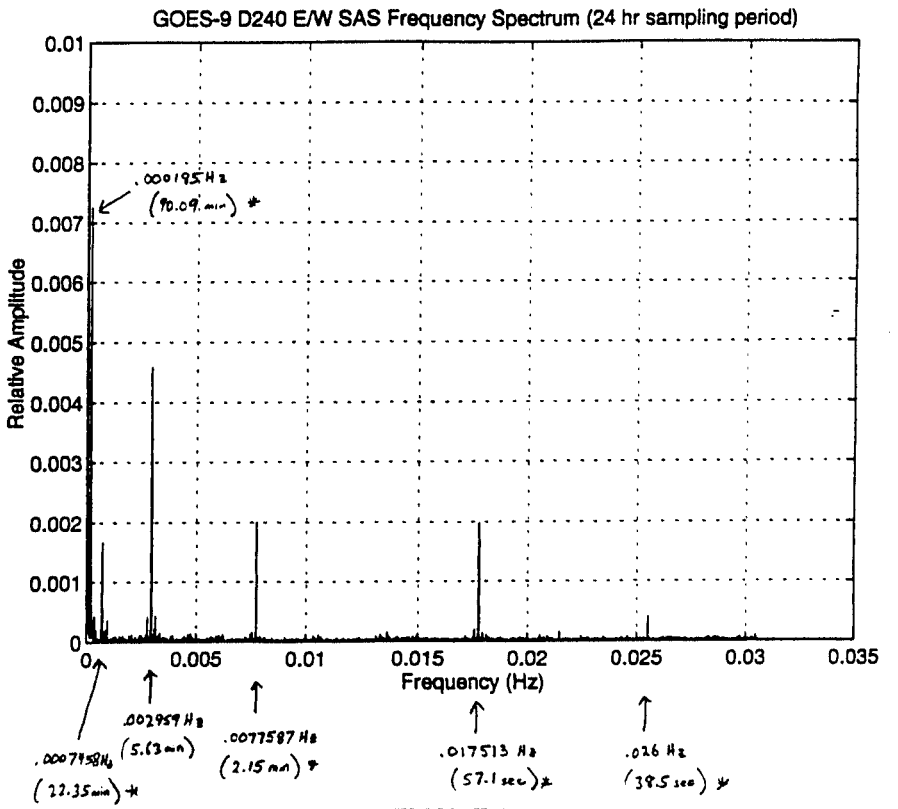

FIGURE 9.

4.2 Model Description

The result of the first step in the analysis of the running average revealed unexpected 5.6 minute and 90 minute oscillations in the SAS data. To understand the Sun angle variations caused by solar array motion a SAS data model was developed which applied all of the known deterministic effects such as orbit eccentricity, spacecraft longitude drift, the sundial correction, and solar parallax at the geosynchronous orbit radius. The other effects such as the newly revealed 5.6 minute and 90 minute motion were modelled as sinusoidal with adjustable phase and amplitude. High frequency modes in the array were accounted for as a feature in the data using a random noise function with an adjustable amplitude, which for the low sampling rate of the SAS was thought sufficient to simulate the effect of the superposition of uncorrelated(with the telemetry sampling process) five higher frequency modes analyzed in reference 1.

Additional features of the solar array motion to be revealed in the data were then left to be developed and explained. Thus there are three categories of information in the model; the known deterministic angle errors, the obvious periodic functions with amplitudes, frequencies, and phases to be determined, and the remaining "to be developed features" which would be revealed as unresolved differences after the periodic and random components parameters are optimized. The parameters of the model for each of the days analyzed in this work are presented in Table 1.

TABLE 1.0 PARAMETERS OF THE SAS E/W DATA MODEL

PARAMETER DESCRIPTION	DOY 173	DOY 184	DOY 228
PARALLAX	2*0.016°	2*0.016°	2*0.016°
RANDOM NOISE	±0.004°	±0.004°	±0.007°
90 MIN GEAR	0.004°	0.005°	0.006°
5.6 MIN GEAR	0.003°	0.003°	0.003°
1440 MIN GEAR τ=(1/e half width)	0.023° 7.2 hours	.030° 4.15 hours	0.019° 4.15 hours
ECCENTRICITY[1] (ERROR EST.) (ERROR USED)	.00007 (.008°) (0.015°)	0.00014 (.013°) (0.0125°)	0.000121° (0.011°) (0.015°)
SUNDIAL ERROR USED S/C LON. DRIFT[2]	0.053° (0.055°) -0.0066°/DAY	0.046° (0.046°) -0.0134°/DAY	-0.051 (-.051°) +0.0169°/DAY

1 Differences in the actual(from osculating elements) and "used" are in part caused by variations in the osculating value around an orbit, a mean of the osculating elements would have been better. Also this may reflect the intrinsic accuracy limitations of the method.

2 (Not used) If drift rate is positive(eastward) Sun error is a negative pitch and SAS error. Therefore, if used the longitudinal drift rates listed would increase the calculated model value to exceed the value used for all cases. This difference could be solar array run rate error.

4.2.1 Deterministic ephemeris errors

There are four errors in this category; parallax, GOES orbital eccentricity, the daily variation true solar motion, and the GOES longitude drift. The parallax error is a maximum at 06:00 am SLT because the solar array is reset manually at 06:00 pm SLT. The amplitude of this error, 0.032° zero to peak, is not dependent on solar declination and is sinusoidal. The orbital eccentricity error effects the spacecraft pitch control loop which tracks the Earth nadir vector at the orbit rate causing a diurnal variation in the Sun angle. The resultant pitch error relative to pitch from a perfect zero eccentricity orbit(Mean anomaly minus true anomaly) is projected onto the SAS sensitive axis by the cosine of the solar declination. The change in the true solar rate is the derivative of the sundial correction(the derivative of equation of time, since the solar array is recentered every day) and it is projected from an equatorial longitude reference to the SAS east/west axis by the solar declination. The spacecraft longitude drift is linear with time of day and is projected onto the SAS east/west axis by the solar declination. The model terms applied used the operational osculating elements for, orbital eccentricity, argument of perigee, ascending node right ascension, and longitudinal drift rate(orbital period sideral period error). However the terms that produce a linear growth in the east/west error with time such as orbit period, are equivalent in the model to the correction for true solar motion, solar array run rate error and solar array step errors such as stepper motor skipping and backlash in the gears. The linear terms used do not agree with the values one would obtain by adding all known linear effects such as the sundial and the longitude drift. Run rate error may not be measurable in this 3 day sample if the array occasionally adds or skips steps in response the spacecraft pitch control jerks at the times of BB Cal.

4.2.2 Periodic and random effects with amplitude, periods, and phase to be determined.

The 5.6 minute oscillation and the 90 minute oscillation discovered immediately after the first sample of GOES-9 data was averaged, were determined to be from the solar array gear drive and stepper motor. Two 16:1 gear stages result in one rotation in the spacecraft body frame every 1440 minutes. The following gear periods result; 1440 minutes for the outer gear on the array yoke, 90 minutes for the gear that drives it, and 5.6 minutes for the 1st stage gear. Initial suggestions that the 5.6 minute period was spacecraft roll/yaw nutation were discounted by observations that the phase angle once determined is good for a whole days data. Spacecraft nutation which is driven primarily be Imager/Sounder BB Cal mirror motion would not maintain phase consistency throughout one day. Thus the inner and outer gear rate variations were modelled as though the error were sinusoidal with a period of 5.6 and 90 minutes determined by obtaining phase consistency between the model and flight data over 24 hours. A random noise function with an adjustable amplitude was use to match the random noise visible in the flight data processed in the running average.

4.2.3 Additional effect to determined in the analysis

The failure to accommodate the Earth sensor pitch thermal offset at 00:00 SLT can be considered a discovery of this work. However; no explanation is offered, except that perigee effects near this time masked it. A pitch offset of 0.024° centered at spacecraft midnight should have been detectable in this analysis. Instead it was absolutely necessary to include a gradual pitch offset and return, centered at 12:00 UTC which was 06:00 am SLT. The amplitude of the offset was 0.022° the error function was gaussian with width between 4.15 hours and 7.2 hours on the days analyzed. The most obvious explanation of this error is the solar array outer gear. Although the time of the maximum offset occurs when the pitch torque reverses sign and the wheels reverse their acceleration. It is possible that the Earth sensor pitch thermal effect is also canceling a component of the outer gear error and the outer gear model produced here is the sum of the two effects.

4.2.4 Mathematical summary of the model

The model can be written mathematically as follows:

4.2.4.1 Parallax:

$$P=0.016(1-\cos(2*\pi*t/T)$$

Where: t is the time in UTC
T is the orbit period
0.016° is (42,164/ 1AU)*57.3

4.2.4.2 Orbital eccentricity:

$$E=-0.0115*\sin(n)*\cos(\delta)$$

Where: -0.0115° is a model parameter for eccentricity 0.0001(for example)
n is the mean anomaly
δ is the declination of the Sun required to project the pitch motion onto the SAS east/west rotation axis.

4.2.4.3 True solar motion:
Solar array run rate error:
Spacecraft longitude drift:

$$L=\alpha*t$$

Where: α is the sum of the three effects per day
t is the time of day since solar array reset which was at 00:00 UTC

4.2.4.4 Stepper Motor and Second Gear:

$$G1=0.004°*\sin((t/5.6)*2*\pi+\phi)$$
$$G2=0.004°*\sin((t/90)*2*\pi+\psi)$$

Where: 0.004° is the observed amplitude for this effect
t is the time of day UTC in minutes
ϕ is the phase of the stepper motor gear at the 0 minute UTC
ψ is the phase of the second gear at 0.0 minutes UTC

4.2.4.5 Outer Gear(Pitch deadband):

$$OG=0.022*\exp((t-.5)/\tau)^{*2}$$

Where: 0.022° is the observed amplitude from the data.
τ is 0.09 day for DOY 173 is the gaussian width duration of error effect.

The total error is:

$$E_{total}= P +E +L + G1 + G2 + OG$$

The digitized telemetry is:

$$DE=(INT(E_{total}/0.016))*0.016°$$

The digitized samples at the 16 sec computation period are then averaged to compare with flight data.

5.0 Discussion of results

The method of analysis presented is preliminary and simplified relative to what could be done with more resources and time. However the limitations of the SAS data may not yield an increase in the understanding proportional to the effort to implement more complex methods such as a least squares estimation. The input data for the model presented in this work was approximate as the osculating orbital elements were used to represent the argument of perigee of a near circular orbit. Thus some flexibility was allowed in the matching process as indicated in Table 1. Improvement of this qualitative comparison method can be made by forcing the linear term for the sundial effect, and longitudinal drift effect to estimate the value for the daily array drive run rate error. If so added precision in the determination of the longitudinal drift would be required and an orbit represented by the average of the osculating elements would be necessary. In addition to this precise measurement of the array initial location after the daily operational reset would have to be made. The results obtained are presented to stimulate thought about the nature of attitude pointing for payloads attached the solar array yoke such as the SXI. Significant results were obtained with minimal analysis effort and limited accuracy. This shows that if a 0.5 sec sample rate and 50 % higher precision were available a more direct measurements of transient phenomena such as the BB Cal response and stepper motor increments.

6. ACKNOWLEDGMENTS

The authors would like to thank Edwin Harvie and Tim Walsh for their assistance in the Fourier Transform analysis of these data.

7. REFERENCES

1. Sivakumar Tadikonda. "GOES-8 Dynamic Model Validation and Implications for SXI" McDonnell Douglas Aerospace, Tech Memo TM-415-95-005 to S. Cauffman, Code 415, Goddard Space Flight Center, Greenbelt, MD.

2. Sivakumar Tadikonda and Sandra Cauffman, "Understanding GOES-8 Dynamics", SPIE, Denver, CO Aug 6-9, 1996 SPIE Conference "GOES-8 and Beyond" Paper No. 2812-64.

3. GOES Program Spacecraft Operations Handbook, DRL 503-02, Vol. III - Spacecraft Description GOES I-M; August 31 1995, SS/L-TR00570, Revision G, Space Systems/Loral, Palo Alto, CA

4. Edwin Harvie and John Rowe. "Performance Analysis of the GOES Trim Tab Solar Pressure Torque Angular Momentum Control", SPIE, Denver, CO Aug 6-9, 1996 SPIE Conference "GOES-8 and Beyond" Paper No. 2812-68.

5. E. R Washwell, K. Chevray, A. Kamel, A. Dress, and T. Walsh. "Improved GOES Earth Sensor Performance", SPIE, Denver, CO Aug 6-9, 1996 SPIE Conference "GOES-8 and Beyond" Paper No. 2812-63.

Blank page retained for pagination

SESSION 9

Image Navigation and Registration

GOES Image Navigation and Registration System

Ahmed A. Kamel

Space Systems/Loral, Palo Alto, California 94303

ABSTRACT

The GOES I-M Image Navigation & Registration (INR) system was developed and patented by Space Systems/Loral (SS/L) in response to NASA/NOAA pointing requirements of Imager and Sounder payloads. This INR system is divided into space segment and ground segment. The space segment consists of Image Motion Compensation (IMC) system that compensate for deterministic errors caused by orbit and attitude motions and Mirror Motion Compensation (MMC) system that compensate for spacecraft attitude motion caused by Imager and Sounder scanner mirror motion. The ground segment consists mainly of Orbit & Attitude Tracking System (OATS) that determines the IMC orbit and attitude coefficients from star, landmark, and range measurements.

Keywords: image navigation, image registration, orbit determination, attitude determination, attitude control

1. INTRODUCTION

GOES I-M satellites are designed and built by SS/L for NASA/NOAA. These satellites have considerably enhanced capabilities in terms of flexibility and quantitative data. GOES I-M satellites provide a three-axis, body-stabilized platform with independently operating Imager and Sounder Instruments built by ITT Aerospace/Communications Division. These Instruments offer improved sensitivity, spatial resolution, scan flexibility, and pointing accuracy compared to the previous GOES instruments. In addition, the GOES I-M system provides the end users with radiometrically calibrated Imager and Sounder data and complete navigation information in near-real time. Furthermore, the Imager data is also registered with reference to a grid that remains unchanged (fixed) over the satellite orbital lifetime. The IMC/MMC systems are the key to providing end users with products that are preregistered with respect to a fixed grid in near-real time.

1.1 GOES I-M System

Figure 1 is a schematic of the GOES I-M system, which comprise two orbital satellites (GOES East and GOES West) and an

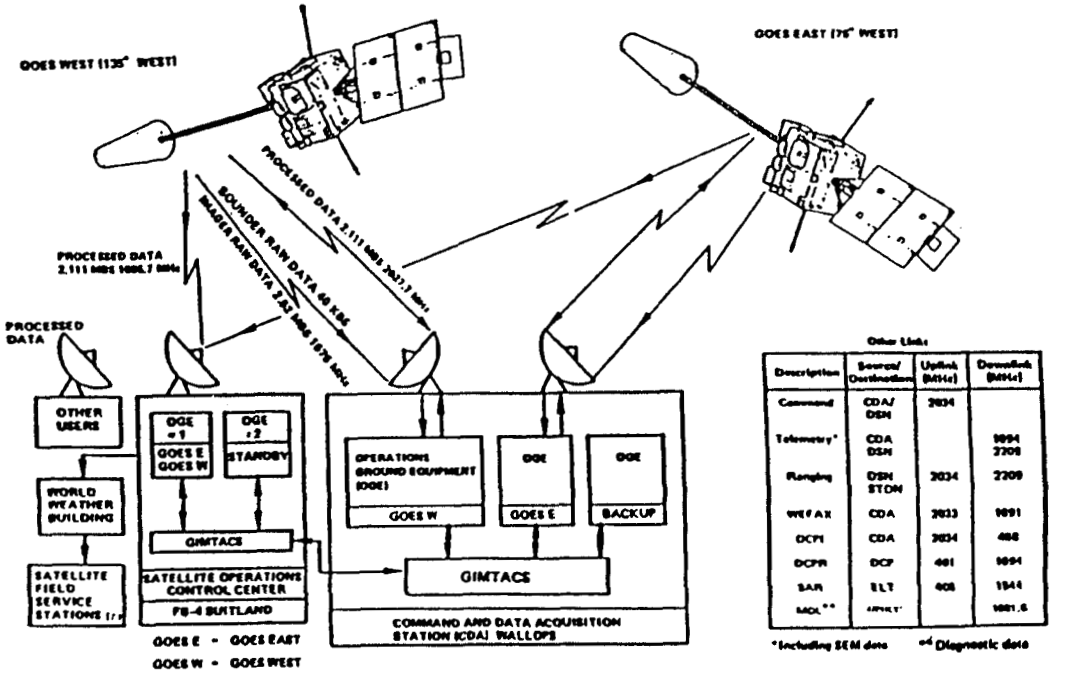

Figure 1 GOES I-M System

0-8194-2200-2/96/$6.00

operational ground system consists of Operations Ground Equipment (OGE) and GOES I-M Telemetry and Command System (GIMTACS). Radiometric data transmitted by each of the two Instruments (Imager and Sounder) from both satellites are simultaneously received at the OGE where they are reformatted and corrected for radiometric calibrations and are then retransmitted to the satellite in final form via GIMTACS for reception by the user community. The data, containing image navigation information for retransmission, is generated in near-real time (within a few seconds). The OGE also generates all necessary IMC coefficients using star measurements taken by the Imager and Sounder, Earth landmarks from images, and ranging data. These coefficients are transmitted to the satellite, typically once a day, for on-board generation of correction signals that continuously adjust the Instrument mirror position to nullify the orbit and attitude effects so that all pixels (picture elements) will be registered relative to a fixed grid as will be explained below.

1.2 GOES I-M Satellite

GOES I-M is a three-axis-stabilized satellite using the momentum bias principle to maintain pointing the Imager and Sounder optical line of sight to the Earth. Figure 2 shows the satellite in the deployed orbital configuration.

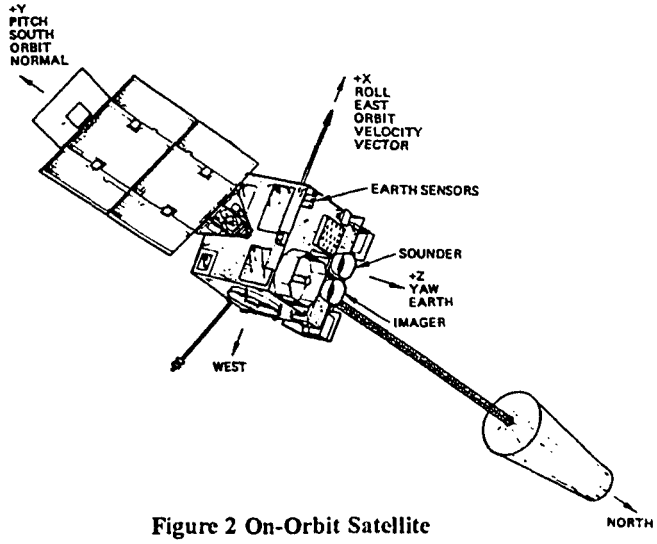

Figure 2 On-Orbit Satellite

The satellite consists of a central body containing all the propulsion and electronic equipment and provides the platform on which the Imager and Sounder are mounted. A solar array continuously rotates about the satellite pitch axis to track the Sun during the orbital motion, generating the required power of approximately 1100 watts. An unobstructed view of the detector coolers to space is required to maintain the temperature of the infrared detectors at near 100 K. An unsymmetric solar array configuration that avoids solar input into the passive coolers was selected to fulfill this requirement. The result is a conical shaped solar sail on top of a 16-meter boom on the north side to balance the torque caused by solar radiation pressure. A trim tab panel at the tip of the solar array is used to fine balance the solar radiation pressure torque on the satellite by adjusting the tilt angle of the trim tab daily to account for varying Sun declination effects. Two other smaller booms on the east and anti-Earth side of the satellite hold the telemetry and command antenna and the magnetometer assembly. Redundant Earth Sensors and various communications antennas are mounted on the Earth-facing panel of the central body.

The satellite attitude control uses a momentum bias concept with two skewed momentum wheels that provide pitch and roll control. The Earth Sensor provides pitch and roll information that is used to maintain Earth pointing. Two magnetic torquers are used to absorb gradual buildup of roll and yaw momentum from the solar radiation pressure torques, eliminating the need to unload the wheels by firing thrusters.

The Imager and Sounder are shown in Figure 3 and they consist of Earth pointing optical ports, coolers looking north, scan mechanisms, and optical systems (including the telescope) that collect the incident radiation energy in different spectral bands onto the respective detectors. The scan mirror is mounted on a two-axis gimbals with orthogonal scan axes along the east/west and north/south directions. The scan is servo controlled through a high bandwidth precision servomechanism.

The Imager has five spectral channels, four infrared and one visible. It sweeps an 8 km longitudinal swath along the east/west path on the Earth, providing simultaneous data on all channels for the viewed scene. The scan system provides complete flexibility in terms of the size and area to be scanned. The visible channel has a pixel size of 1 km (equivalent to 28 microradian field of view) at the subsatellite point. A full Earth scan can be accomplished in about 26 minutes.

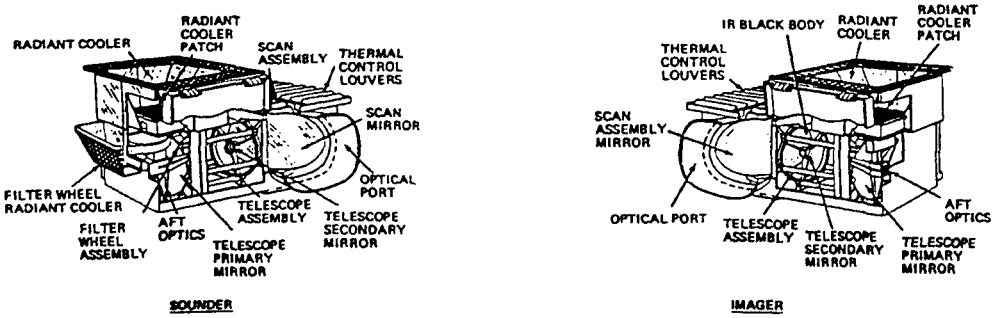

Figure 3 Expanded View Of Image and Sounder

The Sounder provides simultaneous coregistered data in 1 visible and 18 infrared channels through a filter wheel assembly. The scan mirror in the Sounder step-scans a 40 km longitudinal swath across an east/west path in 10 km increments.
Detailed descriptions of the Imager and Sounder can be found in references 1 and 2.

2. IMAGE NAVIGATION AND REGISTRATION

2.1 Definitions

Image navigation is the process of determining the location of any pixel within an image in terms of Earth longitude and latitude. Image navigation is, therefore, a measure of absolute pointing accuracy.
Image registration refers to the process of keeping any pixel within an image pointed to its nominal Earth location within specified accuracy. Image registration is, therefore, a measure of pointing stability.
Gridding refers to the assignment of political and geographic boundaries to pixels. The GOES I-M IMC system provides a fixed gridding capability, meaning that the pixel assignments of grid points are invariant over the satellite orbital lifetime.

2.2 GOES I-M INR Requirements

The most significant requirements are that:
o Imager absolute line of sight pointing should be within 112 microradians (3 sigma). This is equivalent to 4 km at subsatellite point.
o Pixels within an image should mutually be registered with respect to each other within 42 microradians (3 sigma) of their nominal separation.
o Corresponding pixels of successive images of the same Earth region taken within a 15 minute interval should be registered within 42 microradians (3 sigma).
o Corresponding pixels of successive images of the same Earth region taken within a 90 minute interval should be registered within 84 microradians (3 sigma).
The INR system requirements and GOES 8 & 9 on-orbit performance can be found in reference 3.

2.3 INR System Description

Figure 4 shows the various elements of the INR system. The system forms a closed loop connecting the space and ground segments that is essentially a control loop for the compensation of diurnal orbit and attitude errors whose amplitudes are slowly varying over time. The space segment consists mainly of the IMC/MMC software in the Attitude & Orbit Control Electronics (AOCE), AOCE interface hardware with Imager and Sounder, and scanner position adjustment circuits in Imager and Sounder. In addition, the space segment contains the Attitude Data Multiplexer/Multi-use Data Link (ADM/MDL) for INR Dynamic Interaction Diagnostic (DID) using solar array step/no step status, mirror slew/no slew status, Instrument servo error, Angular Displacement Sensor (ADS), and Digital Integrated Rate Assembly (DIRA) data. The navigation parameters are included in the GOES Variable retransmitted data format (GVAR) which is sent to the users via the Processed Data Relay (PDR) link. The ground segment consists mainly of the OATS system and the INR portions of OGE, Sensor Processing System (SPS), Product Monitor (PM), and GIMTACS.

The INR system operation is shown in Figure 5. The INR system operates by collecting navigation observations from the Instruments in the form of star positions and landmark positions, plus two-way ranges through the PDR transponder. These are processed in the OGE to generate coefficients of a model for the orbital and attitude errors corrupting the INR. These coefficients are uploaded to the spacecraft and are used by the AOCE to generate IMC signals based on the orbit and attitude model in the

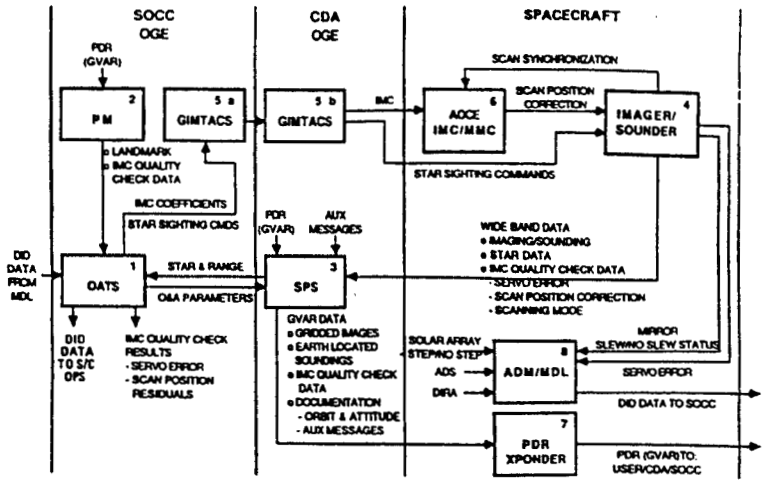

Figure 4 INR System Conceptual Design

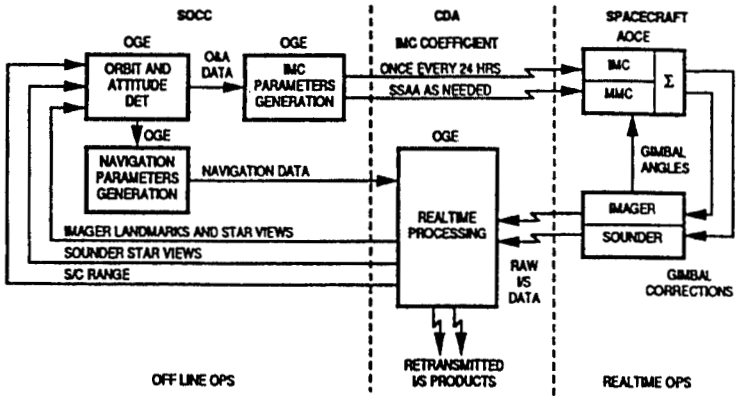

Figure 5 INR System Operation

AOCE and the scan mirror position sent by the Instrument to the AOCE. The net result is compensation for the pointing errors caused by the orbital and attitude variations.

In general the navigation observations collected for day N are used to generate the IMC model for day N+1. Thus a fundamental feature of the INR system is to compensate for attitude errors caused by the Sun apparent diurnal motion about the satellite such as line of sight deflections induced by thermal distortions and/or solar radiation pressure effect on spacecraft yaw attitude. Other errors which are not diurnal in nature are minimized by design; however, the INR system has been equipped with the capability to detect and compensate errors which are non-diurnal but slowly varying such as drifts in the Earth Sensor boresight caused by meteorological effects, and station-keeping disturbances. In this case, the star and landmark observations are compared to their expected values when processed in OATS. When OATS detects a trend in the star and landmark residuals indicating that the on-board IMC model is not adequately compensating for some non-diurnal effects, a Short Span Attitude Adjustment (SSAA) coefficients or Short Span Orbit And Attitude Adjustment (SSOAA) coefficients are generated by OATS and transmitted to GIMTACS. These coefficients are then uploaded to the satellite to adjust the on-board IMC attitude and orbit models. The net result is compensation for these slowly varying non-diurnal errors.

In addition to the IMC, there is MMC which is designed to compensate for disturbances caused by slewing the Imager and Sounder mirrors. This is described in details below.

Simulation studies of the INR system can be found in reference 4.

3. MAJOR SOURCES OF ERROR

Ideally, if the satellite was to be geostationary and the optical axes of the imaging Instrument were to be held fixed relative to a geocentric coordinate frame, all images would have the same navigation solution, i.e., corresponding pixels of successive images would have the same earth longitude and latitude; the objective of fixed gridding would thus be achieved. In reality, however, the orbital motion of the satellite as well as perturbations in the attitude of the optical axes cause varying motions of images over time. The purpose of the IMC system is to correct for such motions at the source, i.e., adjust the scan mirror, such that the apparent pixel shift due to these effects is "zeroed" out and the resulting image remains fixed in the scan coordinate frame. The sources of disturbances that cause the pixel shift can be classified under two categories: 1) satellite orbital effects and 2) attitude variations of optical axes of the Imager and Sounder. In this section we shall discuss the nature of these disturbances and their effect on pixel motion.

3.1 Orbital Effects

A geostationary satellite in a circular orbit with small inclination and no east/west drift subtend the well known figure eight pattern at its ground track. Figure 6 shows such a ground track for an inclination of 0.1 degree.

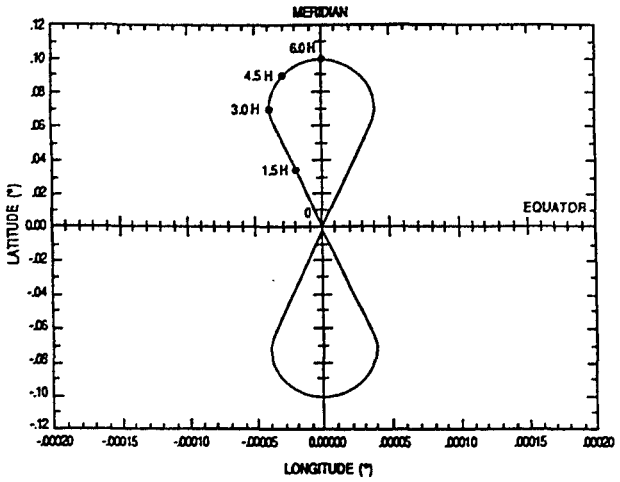

Figure 6 Satellite Ground Track, 0.1 degree Inclination

Figure 7 shows the pixel shift along an east/west scan line with zero scan elevation (i.e., nominally equatorial scan) as a function of scan azimuth for various satellite positions in orbit. The orbital positions are identified by the parameter T with T = 0 corresponding to northerly nodal crossing and T = 6 corresponding to 6 hours later. As may be seen, the maximum pixel shift of 312 microradians occurs at T = 6.

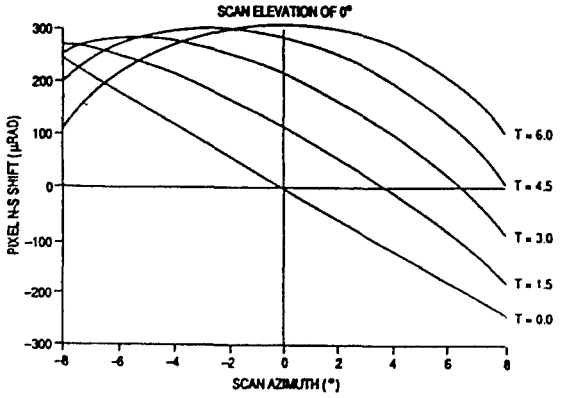

Figure 7 Pixel Shift Growth in Time as Function of Scan Azimuth (east/west) and Elevation (north/south)

In the case of an orbit with finite eccentricity and east/west drift in addition to inclination, the ground track would be more complicated than that shown in Figure 6. However, the pixel shift caused by such orbit motion can be accurately computed once the orbit parameters are known. Knowledge of the satellite orbit, therefore, enables prediction in advance of pixel shifts as a function of time. Further, the day-to-day variations in orbital parameters can also be accurately predicted using standard orbit models.

3.2 Attitude Motions

The pointing of the satellite to Earth is maintained and controlled by the attitude control system using an infrared Earth horizon sensor as reference. The Earth Sensor provides pitch (rotation about the north/south axis) and roll (rotation about east/west axis) information which are maintained at zero by means of control torques developed by two skewed momentum wheels driven by control signals developed in the AOCE using the Earth Sensor data. The satellite yaw (rotation about the Earth pointing axis) is not actively controlled but is maintained small due to the fine balancing of solar torques. In addition, long term accumulation of yaw is controlled by means of two magnetic torquers that develop roll and yaw torques by interacting with Earth's ambient magnetic field. Deviations from the ideal attitude can be caused by the following disturbances:

o Non ideal response of the Earth Sensor caused by noise, sensitivity to stray light, thermal variation, aging, and atmospheric conditions such as cloud motion.
o Unpredictable diurnal variations in Earth's magnetic field including disturbance fields such as magnetic storms
o Moving elements in the satellite such as momentum wheels, Imager and Sounder scan mirrors, and solar array which is stepped at regular intervals to track the sun.
o Structural vibrations of flexible satellite components such as solar array, solar sail and other booms caused by excitations from the moving elements.

Furthermore, the optical axes of the Imager and Sounder could have relative motion with respect to the satellite attitude control axes due to thermally induced structural distortions caused by varying temperature on the satellite and on the Imager and Sounder during the diurnal cycle. Such thermal distortions are, therefore, yet another source of pixel shifts that need to be compensated for.

The INR approach to correct for attitude motion is based on the following:

o Use IMC system to compensate for repeatable diurnal variations such as thermal distortion and spacecraft yaw. IMC also compensate for slowly nonrepeatable attitude variations such as spacecraft response to cloud motion.
o Use MMC system to compensate for spacecraft attitude variation due to Imager and Sounder mirror motion.
o Minimize by design the effect of high frequency disturbances such as Earth Sensor noise and structural vibration due to solar array stepping and momentum wheel imbalance.
o Use AOCE RAM reprogramming capability to compensate for effects that are not known before launch.

It should be pointed out that after launch of GOES I (Called GOES 8 in orbit), two more compensation schemes were developed, using the reprogramming capability, to compensate for effects that were not known before launch. The first compensation scheme is called Spacecraft Motion Compensation (SMC) that was required to compensate for spacecraft attitude motion due to stray light effect on Earth Sensor (See references 5,6,7 for more details) and for the effect of solar sail boom thermal snapping due to magnetometer boom shadowing. The second compensation scheme is called Single Chord Reprogramming Element (SCRE) that was required to compensate for the difference between spacecraft attitude during Earth Sensor dual chord operation vs. single chord operation.

4. IMAGE MOTION COMPENSATION

4.1 IMC Concept

The on-board IMC corrects for pixel shift at the source. Compensation of the deterministic orbital and attitude motion effects on pixel shifts is generated in the AOCE to apply simultaneous east/west (azimuth) and north/south (elevation) corrections.
Figure 8 shows the scanlines traced by the Imager and Sounder with and without pixel shift due to orbit and attitude motion. The effect has been exaggerated in the figure for visibility. This shift is predicted using the equations in section 4.2 below. The on-board compensation method involves a sequence of incremental adjustments that are applied to the azimuth and elevation drives of the Imager and Sounder while the Instrument is generating scan lines. In the example shown in Figure 8 the correction (Az,El) is applied in an east-south direction to compensate for satellite oppsite motion in the west-north direction. When this line is seen by the users, it will be similar to scan lines with no satellite motions as shown in Figures 8, 9 , and 10.

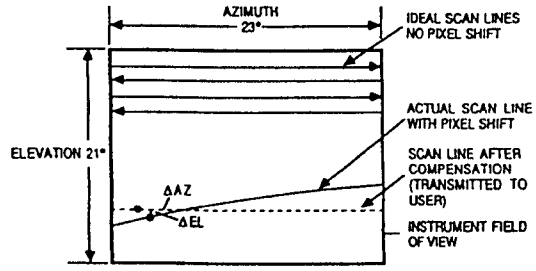

Figure 8 Image Motion Compensation at Source

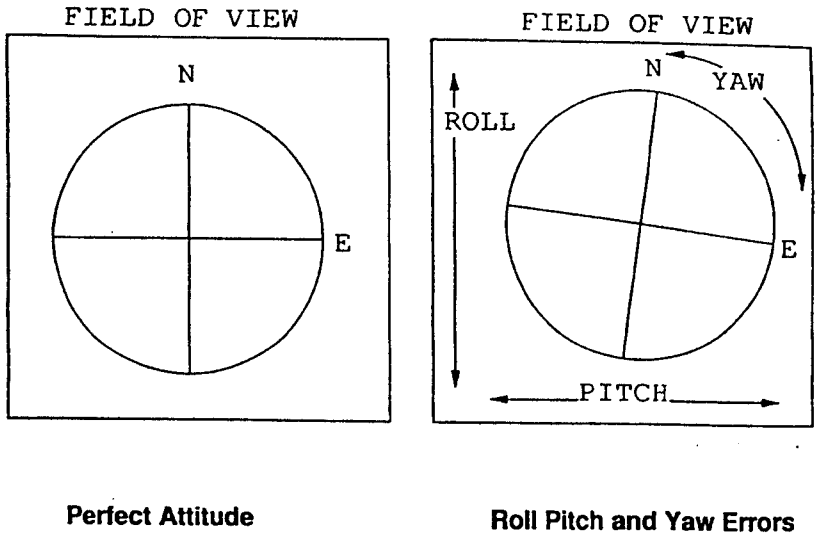

Figure 9 Attitude Effects on Earth Perspective

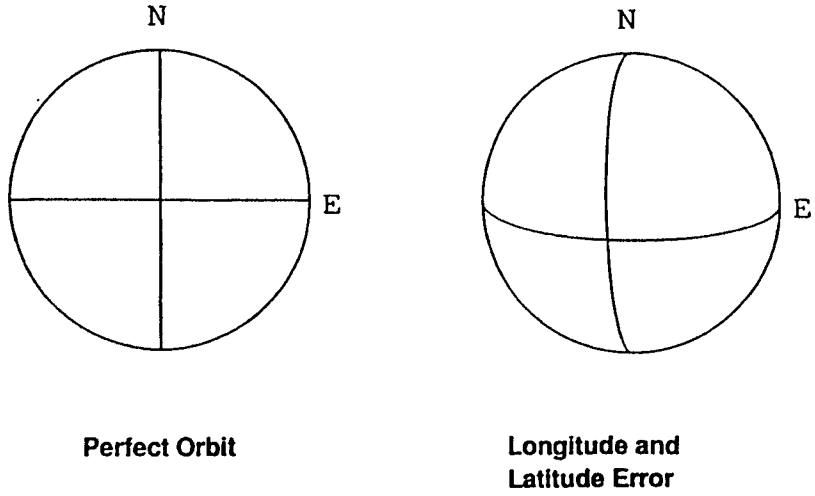

Figure 10 Orbit Effects on Earth Perspective

4.2 IMC Algorithm

The effect of pitch and roll attitude motions is to produce a corresponding east/west or north/south pixel shift of equal amount. The yaw attitude motion results only in pixel rotation at the nadir and rotation combined with east/west and/or north/south shift at other points on Earth. The combined effects of orbit and attitude motions on pixel shifts are given by:

$$\Delta AZ = -A(\alpha)*AZ*\Delta R_S - B(\alpha)*\Delta\lambda_S - EL*(\psi-\psi_S) - \theta$$
$$\Delta EL = -A(\alpha)*EL*\Delta R_S - B(\alpha)*L_S + AZ*(\psi-\psi_S) - \varphi$$

where

ΔAZ, ΔEL	= Azimuth, elevation IMC compensation
AZ, EL	= Instrument mirror position
$A(\alpha)$	$= [\cos(\alpha) - C(\alpha)]^{-1}$
$B(\alpha)$	$= A(\alpha)*C(\alpha)$
$C(\alpha)$	$= [\cos^2(\alpha) - 1 + (R_e/R_S)^2]^{1/2}$
$\cos(\alpha)$	$= \cos(AZ)*\cos(EL)$
ΔR_S	= Normalized radius deviation from synchronous radius
R_e	= Earth's radius = 6378 km
R_S	= Synchronous radius = 42164 km
$\Delta\lambda_S$	= Satellite longitude deviation
L_S	= Satellite latitude
ψ_S	= Satellite orbital yaw *
φ, θ, ψ	= Satellite roll, pitch, yaw

note: the quantities φ, θ, ψ, $\Delta\lambda_S$, L_S, ΔR_S, ψ_S , are calculated as a function of time from ground supplied coefficients.

* varies between orbit inclination (when satellite crosses the equator) and zero (when satellite is at maximum latitude).

The above equations are a simplified version of the IMC algorithm; the actual algorithm implemented on-board is more complicated, e.g., nonlinear terms in orbit and attitude and Instrument misalignment angles are included.

4.3 Orbit/Attitude Determination

The orbit/attitude determination software uses least squares fit, NASA standard gravitational models for orbit, and trigonometric series in time with slowly varying coefficients and an exponential term for Imager and Sounder optical line of sight attitude and misalignments. These coefficients are determined by OATS. They represent initial alignments and every type of attitude variations including thermal distortion, sensor drift, aging and effects of solar radiation pressure. The OATS compares star, landmark, and range measurements with predicted values. The reference optical axis attitude and orbit are updated on the basis of this comparison using the least squares fit.

4.4 Measurement Method

Stars The star measurement method is unique to the 3 axis stabilized satellite because of its quiet environment. Star measurement utilizes the drift of the stars across the field of view of the Instrument's visible detectors which is produced by the pitch rate caused by the satellite orbital motion (0.25 deg/min). A star measurement is initiated by ground command which slews the scan mirror to a predetermined position (or positions for multiple star looks) corresponding to the east of the star location. The star moving across the detector stack at the rate of 0.25 deg/min crosses the stationary detector array in 0.3 second. After the

measurement, the mirror is slewed back to its original position. Separate and independent star sensing capability for the Imager and Sounder enable accurate attitude determination of the optical axes of each Instrument.

Landmarks Landmark identification is performed on ground and consists of retrieving the Imager data for landmark area and comparing the coordinates of the landmark with its known geographic location.
Reference 8 describes in details the GOES landmarking measurement technique and methods to improve it.

Range Is computed by measuring the elapsed time between PDR transmitted and received signal at CDA. After correcting for the fixed and measurable satellite and ground system delays, the remaining time is two-way transmit time, which is directly proportional to the range.

4.5 Orbit Model

The OATS orbit determination model is based on well-known NASA models. The total acceleration on the satellite includes perturbing effects due to the asphericity of the geopotential field up to 12th order harmonics, gravitational attractions of Sun and Moon, direct solar radiation pressure on the satellite, along-track empirical accelerations and range bias.
The IMC orbit model is based on an empirical representation of the 4 orbital elements (known as Kamel's elements) used in the equations of section 4.2 above. This model is a combination of second order power series and trigonometric series in time with 24 coefficients (known as Kamel's coefficients). These coefficients are obtained by least squares fit of the Kamel's elements to the orbital ephemeris over a few days time span.

4.6 Attitude Model

The OATS and IMC attitude models are identical and they are based on empirical representation using trigonometric series in time. The fundamental period is selected, as mentioned above, to be the time taken by the Sun to complete one revolution about the satellite thus corresponding to a daily cycle when the satellite is on station. The number of harmonics to be used is selectable to obtain the best fit. In addition to these harmonic series a number of exponentials are selectable for possible use during eclipse season.

4.7 Coefficient Update

The orbit and attitude data obtained as described above is used to calculate roll, pitch, and yaw attitude, Instrument roll and pitch misalignments and orbital elements using a least squares fitting. The best fit attitude and misalignment coefficients and the 24 orbital coefficients mentioned above are uploaded to the satellite typically once a day. These coefficients are then used by the AOCE to compute in real time east/west and north/south correction signals for the Instruments.
Description of the IMC system development and test can be found in reference 9.

5. MIRROR MOTION COMPENSATION

The normal scan and slew motions of the scan mirror cause a satellite attitude motion that can be excessive for accurate image registration. Since the two Instruments on-board the same satellite must operate independently of one another, disturbances such as that caused by large mirror motion (needed for black body calibration) must be corrected. The attitude disturbance resulting from mirror motion is deterministic and can be computed accurately on-board. This computation, along with the IMC computations detailed above, is carried out in the AOCE. Figure 11 demonstrates the concept of the mirror motion compensation. The AOCE monitors the position of each mirror in east/west and north/south direction, and computes the satellite attitude (pitch, roll, and yaw) motions resulting from the mirror motion. These attitudes are combined with the attitudes computed by the IMC algorithms before the final correction signal is applied to the Imager/Sounder scan drive circuitry.

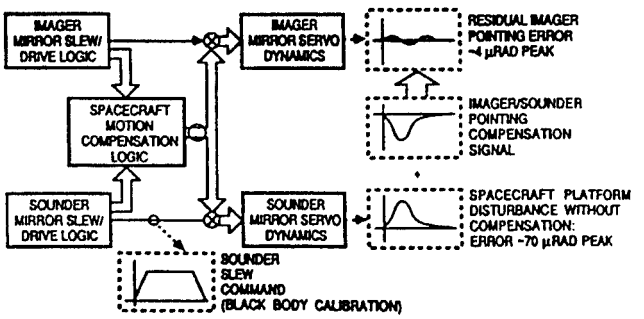

Figure 11 Mirror Motion Compensation Concept

6. CONCLUSION

This paper summarizes the image navigation and registration technique used in the GOES I-M satellite system to provide near-real-time radiometric data that are accurately registered relative to a fixed grid valid for the satellite orbital lifetime. These features, coupled with other enhancements of the GOES I-M radiometers such as improved spacial resolution, scan flexibility, and pointing accuracy, provide the end user with improved meteorological data utilization for weather forecasting during the 1990's and beyond. Further INR performance improvements can be achieved using star trackers as shown in reference 10.

7. ACKNOWLEDGMENTS

The author wish to acknowledge the effort of the INR team (See Appendix). The author had the honor to receive on May 9, 1996 the GSFC group achievement award on behalf of the team in recognition of their dedication, ingenuity, and sustained technical excellence in the design, development, test, and implementation of the GOES INR system.

8. APPENDIX

National Aeronautics and
Space Administration
Goddard Space Flight Center
Greenbelt, MD 20771

415 May 6, 1996

TO: Distribution

FROM; 415/GOES Project Manager

SUBJECT: INR Team Award

Congratulations! You have been selected as part of the GOES INR Team to receive a GSFC Group Award at the Awards Ceremony on May 9, 2 p.m., in the Building 8 Auditorium.

Martin A. Davis

INR GROUP AWARD LIST

SS/L

Ahmed Kamel
Xen Price
Kam Chan
KP Bhat
Tom Henthorn
Donald Gamble
Peter Chu
Subhash Garg
John Gaiser
Keiko Chevray
John Scholtz
P Jayachandran
Rudolph Reyes
Steve Lutz
Shu-shih Butt
Kwok Ong
James Goddard
Belinda Wheeler
Don Davalle
Scott Sawyer

Integral Systems, Inc
Mike Jameison
George Scott
Donald Mack

ITT

Joseph Predina
Ramu Krishna

GSFC

Michael Hagopian
Pamela Sullivan

Swales & Assoc

John Sudey
Sanford Ashton
Gustave Comeyne III
Douglas Ditillo
Timothy Cole
William Bryant
Wayne Dellinger
Marvin Maxwell
Daniel Hubscher
James Carr

NOAA

Kathy Kelly
James Hudson

Loral Aerosys

Nick Pinkine
John Tsui

Computer Sciences Corp

John Fiorello

9. REFERENCES

1. K. A. Hursen, R. Ross, "GOES Imager: overview and evolutionary advancements in geostationary orbital imaging instruments", GOES-8 and beyond SPIE proceedings Vol. 2812, August 1996.

2. J. E. Murphy, S. W. Hinkal, "GOES Sounder:an overview", GOES-8 and beyond SPIE proceedings Vol. 2812, August 1996.

3. W. C. Bryant, Jr., "GOES on-orbit INR system performance", GOES-8 and beyond SPIE proceedings Vol. 2812, August 1996.

4. J. L. Carr, H. W. Dunhill, D. W. Gamble, A. A. Kamel, "Simulation Studies of the GOES-I Image Navigation and Registration (INR) System", 13th annual AAS guidance and control conference, February 1990.

5. E. R. Washwell, K. Chevray, A. Kamel, A. Dress, T. Walsh, "Improved GOES earth sensor performance", GOES-8 and beyond SPIE proceedings Vol. 2812, August 1996.

6. K. A. Kelly, J. F. Hudson, N. Pinkine, "GOES-8/9 image navigation and registration operations", GOES-8 and beyond SPIE Proceedings Vol. 2812, August 1996.

7. M. Phenneger, W. C. Bryant, Jr., J. Baucom, K. Woodham, "Evaluating the GOES-8 and-9 earth IR horizon sensor error response using the GOES-9 sounder IR channel 1 thru 4 data", GOES-8 and beyond SPIE proceedings Vol. 2812, August 1996.

8. W. G. Eppler, D. W. Paglieroni, M. Louie, J. Hanson, "GOES landmarking positioning system", GOES-8 and beyond SPIE proceedings Vol. 2812, August 1996.

9. A. A. Kamel, M. K. P. Bhat, D. Gamble, J. H. Scholtz, "GOES I-M Image Motion Compensation System", AIAA Aerospace Design Conference, Irvine, CA., February 1992.

10. S. H. Hur-Diaz, A. Kamel, "Image navigation improvement using star trackers", GOES-8 and beyond SPIE proceedings Vol. 2812, August 1996.

GOES 8/9 Image Navigation and Registration Operations

Kathleen A. Kelly
James F. Hudson
National Environmental Satellite, Data, and Information Service
National Oceanic and Atmospheric Administration
Washington, DC 20233

Nickalaus Pinkine
Lockheed Martin
Space Missions Systems
Bethesda, MD 20817

ABSTRACT

GOES 8/9 presents a new challenge to the National Environmental Satellite, Data, and Information Service's (NESDIS) Office of Satellite Operations. In the previous series of spin stabilized GOES satellites, the image navigation was performed off-line with little operator intervention or oversight. This system provided accuracy to 10 KM. However, the more stringent 4 KM navigation requirements of the new generation of three axis stabilized GOES satellites has resulted in a far more demanding Image Navigation and Registration (INR) operation. The new system requires continuous observation gathering and monitoring of performance along with commanding real time corrections to the on-board Image Motion Compensation (IMC) system to maintain accuracy. All this must be accomplished while providing images as frequently as every 7.5 minutes in rapid scan mode and operating the independent sounder.

Once the GOES 8/9 navigation system was operational, it became apparent that there were several sources of pointing error which were not anticipated prior to launch. Most of these problems are related to special operational modes of the Earth sensor. It became necessary to devise new operational work-arounds for these problems to minimize the impact on the user community and continue to provide within specification INR performance.

This paper will describe the GOES 8/9 INR operation and how it is integrated into the instrument and spacecraft command schedules. It will also describe the various operational solutions which NESDIS devised to overcome INR errors.

Keywords: image navigation and registration, operations, operational techniques, orbit and attitude

1. INTRODUCTION

In 1994, NOAA/NASA launched into orbit GOES-8, the first in the series of advanced geostationary weather satellites followed closely by GOES-9 in May of 1995. These new three-axis stabilized satellites represented a complete change to NOAA's geostationary satellite operational concept, especially in the area of INR. The National Weather Service (NWS) requirement of accurately navigated and registered imagery being available within 3 minutes of its sensing by the instruments without ground remapping, dictated a ground operation at a much higher level of complexity than the previous GOES system. The 24-hour Fourier model of the attitude profile for both instruments requires continuous star and landmark observations to provide the required accuracy. The fourth order geopotential orbit model requires frequent landmark and range observations. The on-board IMC system remaps each image to a "perfect GOES projection". Every image received by the user is corrected for orbit, attitude, and spacecraft effects at the instrument during the scanning process. This process requires a daily upload to the satellite of spacecraft motion corrections, the orbit and attitude solution, and periodic updates to those parameters to maintain accuracy.

Several years of pre-launch design and simulation activity provided the basis for the INR operational concept. Yet once GOES-8 was placed into operation, we found that pointing impacts caused by certain components of the spacecraft hardware, especially the Earth sensor, were effecting our ability to achieve consistent within specification performance. A team of engineers from Space Systems/Loral, NASA, and NOAA spent the next 2 years devising a series of ground system and spacecraft software fixes to correct these performance problems.

This paper will focus on the ground operation of the GOES 8/9 INR system and the special operations necessary to provide in-specification performance on a day-to-day basis.

2. PREVIOUS GOES NAVIGATION OPERATION

From the late seventies to January, 1996, the GOES image navigation information for the spinning series of satellites (through GOES-7) was generated on an off-line system called the VISSR Image Registration and Gridding System. This system provided the first capability in NESDIS to work interactively with the GOES images in a quantitative manner. Geographic features of known latitude and longitude, called landmarks, were obtained from images every 2 hours during the visible part of the day. At the end of the data collection period, the landmarks (10 to 15 observations total) were input into a two body orbit model and simple attitude estimation model. Since the system could not handle nighttime infrared data, the attitude solution was propagated forward using a linear model. Star information gathered as part of the overscan at the Earth limb was used periodically to separate orbit and attitude effects. Chebsychev coefficients describing the predicted orbit and sun position were incorporated into the processed imager data stream and served as input to user Earth location programs. Gridding information was generated in the ground system for each image. Differences in grid position versus land boundary were measured every 2 hours, and adjusted if necessary, to maintain accuracy. Updates to navigation parameters were provided twice per day, at 1800Z and 0000Z.

This system provided navigation accuracy to approximately 10 KM worst case. Registration and within frame performance was provided by the inherent stability of the spin stabilized platform. Frame-to-frame variation each half hour was extremely small, the main contributor being variations in Earth pointing due to orbital inclination. This was maintained at .1° or less through bi-monthly stationkeeping maneuvers.

3. GOES 8/9 INR OPERATION

3.1. Overview of Daily Operation

Satellite operation is conducted by timed activities continuously commanded from the ground in real time from the Satellite Operations Control Center (SOCC) located in Suitland, Maryland. All commands are scheduled and executed by time tag via the GOES I-M Telemetry and Command System (GIMTACS). Two types of imaging and sounding schedules are prepared each day for satellite and instrument commanding. The "routine" schedule is used for normal instrument scan operations and provides four looks at the continental United States (U.S.) each hour. The "rapid" schedule is used for severe weather monitoring and provides eight looks at the continental U.S. each hour. A weather forecast research schedule consisting of periods of 1 minute repeated imaging over severe storm areas in the U.S. is also available on a 24-hour notice. The NWS has the option of calling up the storm schedules through an interagency coordination process to monitor severe weather and hurricanes.

Each command schedule consists of imaging, sounding and star sensing activities providing the necessary observations to support orbit and attitude determination. Images and soundings are obtained by loading the selected frame start and stop coordinates to the instrument and executing the frame at the scheduled time. The scan mirror slews to the commanded northwest corner of an image/sounding sector and begins the scan process. The mirror moves north to south while scanning west to east and east to west in a bi-directional fashion until it reaches the end-of-frame coordinates. The image is corrected during the scanning process for orbit and attitude effects and spacecraft nutation due to instrument operation using the compensation signals sent through the instrument electronics from the spacecraft attitude control computer at a rate of 64 times per second. The raw instrument data are received in real time at the NESDIS Command and Data Acquisition Station (CDA) at Wallops Island, Virginia. The data are input to the Sensor Processing System (SPS) where navigation, calibration and other documentation parameters are appended. It is then reformatted into the GOES Variable (GVAR) data stream and retransmitted via the satellite to the user receive stations, at the SOCC and other locations across the U.S., South America and Europe. Each image and sounding is ingested and monitored at the SOCC in the Product Monitor (PM) to ensure quality control.

In addition to the image and sounding scan operations, 2.5 minute star windows are scheduled every half hour for each instrument, providing a dedicated period to view stars. These windows are updated once each day from the Orbit and Attitude Tracking System (OATS) using the daily orbit and attitude prediction and a customized star catalog. The catalog contains those stars whose signal is strong enough to be detected against the background noise of space by the instruments' visible detectors. The OATS determines which stars are viewable at the particular window time and then selects those which provide the best geometric

separation for attitude determination. OATS calculates the instrument scan position for viewing the stars selected for that window and sends that information to GIMTACS for incorporation into the command schedule. At the scheduled time, the instrument is commanded to slew to the predicted star position and stares at that position while the star passes through the field of view. The star data are received at the SPS where the star crossing event is determined and sent to OATS. Each star is viewed twice. Four imager or three sounder stars can be viewed in one star window.

Also included in the command schedule are four 10 minute periods reserved for satellite housekeeping activities. Included in these periods are attitude thruster firings for momentum unloads, commanding and activation of IMC and Spacecraft Motion Compensation (SMC) coefficients and positioning of the solar array and trim tab.

Finally single station ranging is performed every 15 minutes at the SPS. The range is determined by measuring the time delay between the transmission and receipt of the GVAR data at the CDA. The range measurements are averaged and error checked, and then sent to the OATS for inclusion in the daily orbit determination process.

3.2 Landmark Measurement and Processing

Landmark measurements are obtained from each image at the PM. The PM operators select cloud-free landmarks for daily ingest from a pre-defined data base. The data base consists of unique geographic features of known latitude and longitude viewable by a satellite at its particular station location. Latitude and longitude coordinates are obtained from a separate mapping software system whose inputs are derived from the "Digital Chart of the World".

An image sector containing the selected landmark is ingested and displayed at the PM. The operator locates the landmark in the imagery and obtains a line/pixel location of that feature from the image. The measured position versus the predicted position are evaluated and residuals calculated and displayed. The measured line/pixel position, the associated latitude and longitude of that position, landmark altitude and scan time are sent to the OATS for use in the orbit and attitude determination process. Three to four landmarks are measured from each image providing a continuous monitor of the current Earth location accuracy. Both visible and infrared data are used to provide a 24-hour data set. While a semi-automatic correlation measurement process was delivered with the system, inconsistencies in its performance were uncovered during post launch testing. The process is currently performed manually while an alternative autocorrelation measurement scheme is under development. While landmarking from the sounder visible channel is possible, this data type is only used during post launch INR start up due to the reduced resolution of the observation.

At the OATS, the landmark is converted to a scan angle in instrument space for use in the orbit and attitude determination process. The IMC correction is removed in order to compute the actual observed scan position of the landmark by the instrument. The scan angle for the predicted landmark position based on the orbit and attitude solution is calculated and a residual is formed. This residual is displayed for real time navigation accuracy trending.

3.3 Star Observation Processing

GIMTACS executes star commands with a Command Procedure (CP) that is automatically included into the command schedule during the OATS update. The CP first checks to make sure the instrument can safely command stars and then continues to upload the parameters for the star sense. These parameters include mode of star sensing, time of dwell, and start coordinates for the dwell in cycles and increments. GIMTACS is given the time to start the dwell by OATS, and that time is used to tag the star frame start command. The ground system is capable of using multiple looks to find stars. A single look is defined as one stare for a period of time covering at least 224 μradian (μr) square. The north/south field of view of the detector arrays (eight detectors) of both the imager and sounder is 8 x 28 μr or 224 μr. Since the motion of the stars relative to the spacecraft is 72 μr/sec, 7 second dwells are used for double looks. OATS also has the capability to change the number of looks used to sight stars based on special spacecraft states. These states include post-maneuver, post-eclipse, and single chord operations. When the instrument enters star mode, the SPS analyzes the star sense data in real time. The background signal of each detector is evaluated and spikes of specified widths which reach a specified threshold are tagged as stars. The SPS then builds the star message which is sent to GIMTACS. This message contains the dwell start time, the mirror position at the dwell time, the dwell duration, the background level of each detector and a sequential list of events found in each detector with the center time and threshold of each event. GIMTACS takes the dwell start time and matches that with the star identification (ID) which was commanded at that time. All of the information in

the SPS star message, along with the star ID is passed on to OATS. When OATS receives the message, PREOBS (Observation Preprocessing) puts all the information into the raw star file. PREOBS then takes the raw data and converts it into a measurement in the scan angle space for a particular time. Based on the event time, the dwell mirror position, and the look and detector in which the star was seen, a north/south and east/west scan angle to the star from the boresight of the instrument is calculated. PREOBS verifies the star with a signal to noise check using values stored in the star catalog. If there are multiple events in the star sense, PREOBS uses the signal to noise check to pick the best candidate star. After PREOBS determines the measured scan angle it computes an ideal scan angle to the star correcting the right ascension and declination from the catalog for parallax, proper motion, and aberration. The look angle is determined from the corrected right ascension and declination of the star along with the observation time and current orbit and attitude. PREOBS calculates an observation residual by subtracting the measured from the computed scan angle.

3.4 OAD/IMCGEN

Utilizing range, star and landmark observational data as input, the Orbit and Attitude Determination (OAD) process is executed daily, using the OATS, to update the spacecraft orbit and imager/sounder attitude solutions. The Image Motion Compensation and Generation (IMCGEN) process transforms the OAD solution into a set of coefficients used by the spacecraft Attitude and Orbit Control Electronics (AOCE), called the "parent" IMC set, which uses the coefficients to compute near real-time corrections applied to the imager and sounder scanning mirrors. These coefficients are transmitted via ground command to the GIMTACS where they are uplinked to the spacecraft AOCE. The coefficients are valid for a 24-hour "registration period" and are updated by the OATS on a daily basis.

During the INR characterization phase, various combinations of OAD input parameters were tested. Extensive numerical and graphical analysis was performed to determine which combination of OAD inputs provided optimal navigation and registration performance. Using this type of analysis the INR team has formulated a set of OAD inputs which best predicts spacecraft orbit and instrument attitude behavior for the next "registration period". These inputs reside in a run parameter file named "DAILY.UPR" which is used by OAD during daily execution. Presently, OAD execution is performed by an OATS controller, the individual responsible for monitoring the OATS and generating OATS derived INR products. Under normal circumstances, at a set time each day, the OATS controller will manually execute OAD using the aforementioned run parameter file, "DAILY.UPR". Special circumstances, such as observational data drop-outs, spacecraft maneuvers, eclipse periods, and spacecraft/ground system anomalies may dictate that the inputs be modified or that an alternative operational mode of OAD be implemented.

The OAD orbit model consists of six equinoctial elements describing the spacecraft orbit. The attitude model for each instrument (imager and sounder) and each attitude angle (roll, pitch, yaw, roll misalignment and pitch misalignment) consists of the sum of three functions: a Fourier series, an exponential function, and a ramp function. The Fourier series is used to approximate those aspects of the thermal profile which are periodic over one solar day. The exponential and ramp functions are not used operationally. The operational Fourier orders are as follows and are the same for each instrument: Roll - 8, Pitch - 8, Yaw - 6, Roll Misalignment - 6, and Pitch Misalignment - 6. An observation span of 48 hours is used in our daily solution to cover any possible data gaps accrued during the past 24 hours. After OAD converges on a final solution, the ephemeris generation (EPHGEN) process is called to propagate an orbital ephemeris over the 24-hour registration period. Following EPHGEN execution the EVENTS process is run to predict instrument and Earth sensor intrusions and tabulate spacecraft events such as nodal crossing times and eclipse entrance and exit periods.

Following EVENTS the IMCGEN process is executed automatically. IMCGEN transforms the six orbital elements into a set of 24 Kamel coefficients which represent the orbit as a time varying function. The attitude Fourier coefficients are represented by a magnitude and a phase angle, as well as one constant order term for each instrument. The combined number of orbit and attitude coefficients totals 178 for both instruments. Upon IMCGEN completion, the computed coefficients are automatically transmitted to GIMTACS in the form of an external message, where they can be integrated into a command schedule and uplinked to the spacecraft. Simultaneously, a second message containing the coefficients is transmitted to the SPS which utilizes the coefficients for image gridding. Although the coefficients have been disseminated throughout the ground system, they are only utilized by IMC upon "activation". The "activation" process can take on two forms determined by the type of IMC operation the INR system is using, namely "IMC ON" or "IMC OFF".

For "IMC ON" mode, our typical mode of operation, the coefficients will be loaded to the spacecraft at the same time each day. The coefficients will be enabled (transmitted to active spacecraft computer memory) during the next spacecraft housekeeping period. At this time the coefficients will be automatically activated throughout the ground system prior to the next spacecraft image. Although "IMC ON" operation provides improved registration performance over "IMC OFF" operation, it requires more intensive operations support since the coefficients need to be transmitted to the spacecraft on a regular basis.

"IMC OFF" is only used during special circumstances, such as, spacecraft longitude repositioning or an IMC subsystem anomaly. On-board IMC is not applied and uplink of the coefficients to the spacecraft is not necessary. The SPS will set a flag in the GVAR data stream indicating that IMC is disabled. Users of the GVAR data will key off this flag to determine what type of Earth location scheme to implement. If the flag indicates that IMC is off, Earth location is performed using the time-varying IMC coefficients. In this mode of operation, IMC activation is achieved by transmitting a GIMTACS directive to the OATS and SPS. Upon receipt of this directive the IMC coefficients will be activated throughout the ground system and utilized in the next available image. This mode of operation has been implemented successfully and has the advantage of allowing the INR team to activate a new set of IMC coefficients at any time.

3.5 Trending and SSAA Operations

PREOBS has the capability to exclude star observations based on the residual using outlier and sigma edit algorithms. PREOBS also takes accepted residuals and performs trending on the data. Data base items control trending window size and population. When a set number of consecutive observations has caused the average in the window to go above a set threshold limit, PREOBS will trigger OAD to make an adjustment to the current orbit and attitude based on a run parameter file named in the database. Additionally, PREOBS outputs residual files on a timer. This function is used in coordination with a PC workstation to provide real time plots of residual performance. A PC macro retrieves, parses, and inserts the data into a spreadsheet which incorporates the data into various plots. The plots consist of north/south and east/west residuals against time, where time is set to the last 24 hours. Figure 3.5.1 is an example of one of the plots:

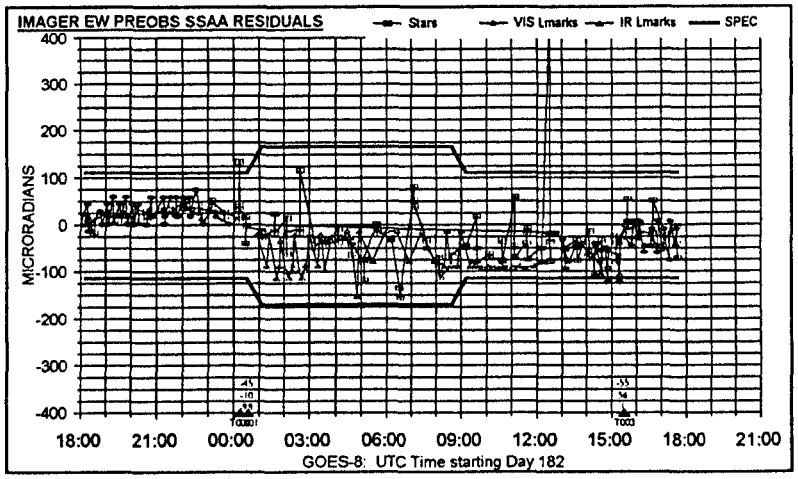

Figure 3.5.1 Real Time Trending Plot

Operationally, adjustments or SSAA's (Short Span Attitude Adjustments) are made to the imager roll, pitch, and yaw constant order terms with imager stars and visible landmarks and to the sounder roll, pitch, and yaw constant order terms with sounder stars. OAD currently uses the last 75 minutes of data which assures two star windows per instrument being included in the OAD fit. When the SSAA IMC set has been made on the OATS, GIMTACS is notified that the set is ready via an alarm. This prompts the operator to type in a directive to create an upload schedule. GIMTACS builds the upload schedule with data contained in a message sent from OATS. When at least 2 minutes of command free time is found in the operational schedule, the schedule is suspended and the IMC load schedule is run. This load schedule will put 13 coefficients, which are the constant terms in Fourier attitude representation, in the buffer memory of the AOCE. After the load has completed successfully, the operator commands the buffer memory to the active memory. The imager must be idle when this CP is run so that there are no instrument servo spikes during activation. Periods for SSAA commanding occur every 30 minutes in the schedule. When the set is activated on the spacecraft, GIMTACS notifies the SPS and the OATS of the activation time. The SPS will update GVAR with this information in the next frame and OATS will alter its landmark processing according to the on board orbit and attitude change. GIMTACS keeps track of which set is active and what coefficients are included in each set so that it can bias the star commanding appropriately. This operation is referred to as "Star Sense Deltas". Since the operational schedules are updated with respect to the parent IMC set, any changes in attitude are not reflected in the star commanding done to acquire star measurements. With double

looks there is an error tolerance of ~ +/- 224 μr in north/south and east/west directions. Star sense deltas convert the SSAA roll, pitch, and yaw corrections to north/south and east/west increments and applies this bias to the proportional command load in real time. Therefore the error in acquiring the star measurement is equivalent to the PREOBS star error.

4. SPECIAL OPERATIONS

4.1 Maneuvers

Operational requirements state that GOES satellites must stay in an orbital box 1° east/west by 1° north/south around its station. OATS has the capability to plan maneuvers in both the east/west and north/south directions to meet these requirements. The orbital environment causes the inclination of geosynchronous spacecraft to grow .9°/year. Since the north/south box is +/- .5°, OATS has been set up to do north/south stationkeeping (SK) once a year by achieving an orbit that lets the inclination go down from .45° to zero and grow back to .45° for the next maneuver cycle. North/south maneuvers are done at solstice due to solar array pointing constraints and are performed at the descending node, since the north/south thrusters (6 and 7 for both A and B strings) are on the south panel of the spacecraft. When the north/south SK is performed, the descending node is essentially turned into the ascending node. In terms of east/west, the GOES spacecraft naturally drift toward 105° west longitude. It follows that GOES-8 (the east satellite at 75° west) naturally drifts west and GOES-9 (the west satellite at 135° west) naturally drifts east. East/west maneuvers are designed to make the satellite drift in the opposite direction to the natural drift such that the drift changes direction at the edge of the box. Figure 4.1.1 below shows the longitude position versus time for an east/west SK scenario.

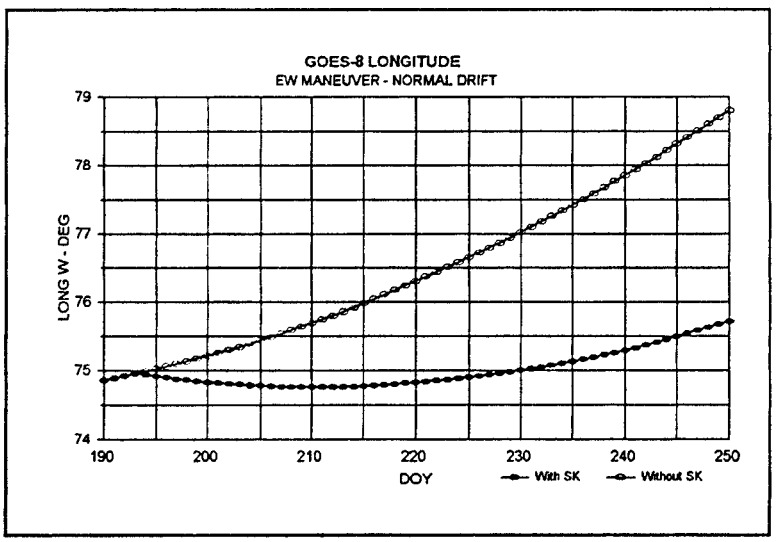

Figure 4.1.1 East/West Stationkeeping Cycle in Longitude versus Time

The GOES spacecraft has two pairs of thrusters (2,3, and 4,5 for both A and B strings) on both the east and west face of the spacecraft so that drifts can be imparted to the orbit in both east and west directions. SKPLAN (Stationkeeping Planning) is the OATS module that calculates the ΔV needed for each particular maneuver scenario. SKPLAN first gets the orbit epoch and spacecraft ephemeris from the database which are updated daily by OAD. SKPLAN takes the orbital information and solves for the ΔV using the ephemeris propagator EPHGEN and the known requirements for the SK. SKPLAN saves ΔV in the OATS data base which allows the operator to propagate a stationkeeping ephemeris to show vital orbital information resulting from the maneuver such as longitude or inclination turnaround. SKCOM (Stationkeeping Commanding) follows the completion of SKPLAN. SKCOM produces thruster firing sequences which achieve the planned ΔV. SKCOM uses thruster force models and alignment angles in the OATS database to perform this function. For north/south maneuvers SKCOM controls thruster duty cycles to optimize cross axis (east/west) ΔV components. When SKCOM has arrived at thrusters and thruster on times for the maneuver, it sends this information over to GIMTACS via the stationkeeping message. GIMTACS builds a stationkeeping command schedule, which consists of three CP's, based on this message. These procedures set up the stationkeeping submode and the thrusters to be used, the pre-maneuver yaw bias for north/south SK, the pulse width of the thruster firings, the number of pulses in the firing, and the post SK yaw bias control. The north/south SK is split up into two burns due to propellant line maintenance constraints and management of the x-axis (east/west) ΔV component. In order to adequately exercise the propellant lines, one burn is performed on the A string thrusters and the other burn is done on the B string thrusters. East/west maneuvers are commanded on thruster strings shown to have best performance. Stationkeeping schedules have to also account for pre- and post-SK spacecraft configuration as well as SK execution. For east/west SK, pre-maneuver configuration consists of DIRA (Digital Integrating Rate Assemblies or GOES gyros) turn on, DIRA calibration performed by the OATS, XRP (X-Ray Positioner) stow, and pre-SK mode setup, and post-maneuver configuration consists of transition to on-orbit mode setup and execution, DIRA turn off, XRP slew back to sun, and post maneuver IMC set enabling. The typical operational schedule interruption is 3.5 hours

for the east/west SK and configuration commanding. For north/south SK, pre-maneuver configuration consists of DIRA turn on, DIRA calibration performed by the OATS, XRP stow, pre-SK mode setup, payload configuration, and Trimtab/Solar array park, and post-maneuver configuration consists of transition to on-orbit mode setup and execution, Trimtab/Solar array slew, payload configuration, DIRA turn off, XRP slew back to sun, and post maneuver IMC set enabling. The typical operational schedule interruption is 4.5 hours for the north/south SK and configuration commanding.

When post maneuver spacecraft configuration is complete, a post maneuver operational schedule is run for 7 hours to account for attitude transients encountered from the transition to on orbit mode. The post maneuver schedule has 6.5 minute star windows every 30 minutes for both instruments. These large windows allow for commanding of four stars with four looks which gives the system an error tolerance of ~500 μr in acquiring the stars. When the first stars are measured after the burn, the star's residuals reflect a large yaw error that remains from the maneuver. SSAA's are manually created by the navigator which correct for roll, pitch, and yaw using data from just one star window if possible. Stars used in the solution must be in opposing quadrants in the field of vision to reliably solve for yaw. SSAA's are created manually at every upload opportunity until the control system has removed the yaw error. As more maneuvers are executed, the planning of the maneuvers has been refined so that orbit errors occur less frequently. When navigationally significant orbit errors occur, the navigator uses the OATS to create Short Span Orbit and Attitude Adjustments (SSOAA's). Orbit errors become apparent when star residuals diverge from landmark residuals. In the presence of orbit errors, attitude corrections cannot fit both the star and landmark observations, and poor solutions result. SSOAA's can alter the four constant terms of the orbital coefficients as well as the attitude terms so that good short term (2-3 hours) fits can be generated. Figure 4.1-2 shows how SSOAA performance compares to performance without SSOAA's.

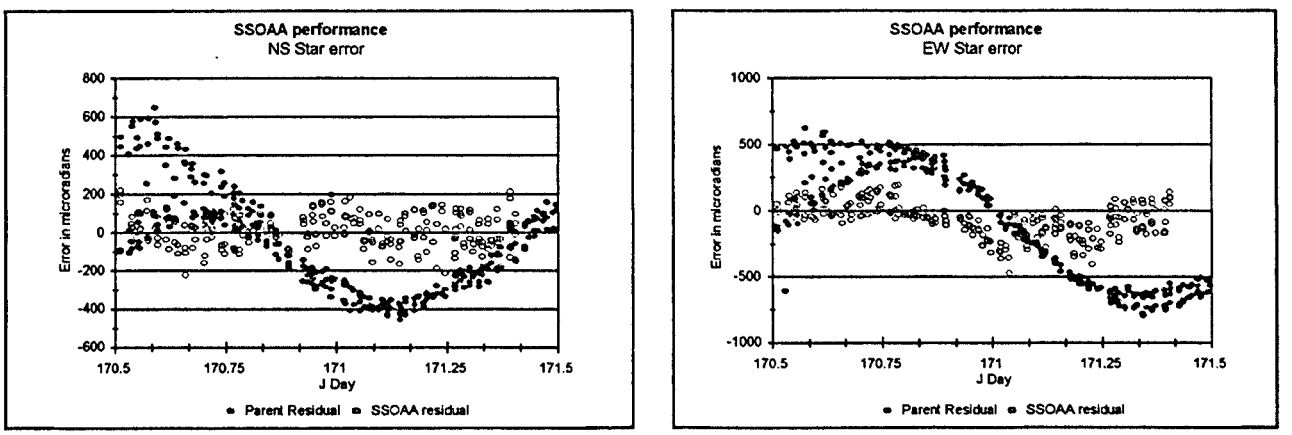

Figure 4.1.2 SSOAA Performance versus Predict Orbit Performance

4.2 Eclipse Recovery

The 24-hour attitude model is very sensitive to any periods of data loss. An example of this is during the eclipse season. At the vernal and autumnal equinox, the Earth shadows the satellite at spacecraft midnight, requiring battery operation for up to 72 minutes. Imager and sounder operations are suspended for as long as 2.5 hours while the instruments are configured to shut down, are off during the battery period and then reconfigured for operations. No observations are acquired during this period. The Fourier functions which model the attitude are not constrained in a data gap and can fluctuate unpredictably during this period. This is not an impact during eclipse itself since there are no instrument operations. The real problems begin on the first day and subsequent days following eclipse. The unconstrained attitude model of the past 45 days creates large errors when used for navigation purposes when midnight scanning operations are resumed. If normal operational schedules are used during this period, we risk losing our ability to acquire stars and our ability to accurately determine the attitude profile. This results in several days of severely degraded navigation and registration during the midnight period. Figure 4.2.1 illustrates the large midnight navigation errors experienced in the spring of 1995 during the first two days following eclipse using the routine imaging schedule for recovery.

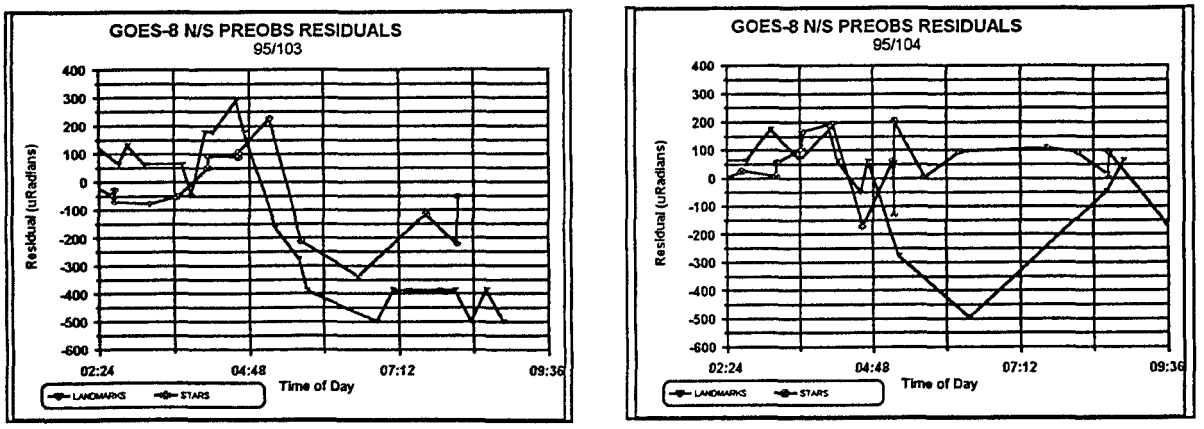

Figure 4.2.1 - Spring '95 Post Eclipse Errors

To overcome this problem, we have introduced special scanning operations during these first days of the post eclipse period. A recovery schedule consisting of abbreviated full disk images and expanded star sense windows (identical to the post maneuver recovery schedule) is inserted in the data outage period. The 6.5 minute star windows contain four looks at each star, making it possible to obtain these observations in the presence of large navigation errors. After one day of intensive data collection, we can reduce the navigation errors significantly to within specification levels. A second day of recovery operations is scheduled as a contingency, however by this time, we are back to within specification navigation. In the spring of 1996, the recovery schedule was used to regain navigation accuracy in the post eclipse period. The improved result on the second day of post-eclipse operations is illustrated in figure 4.2.2.

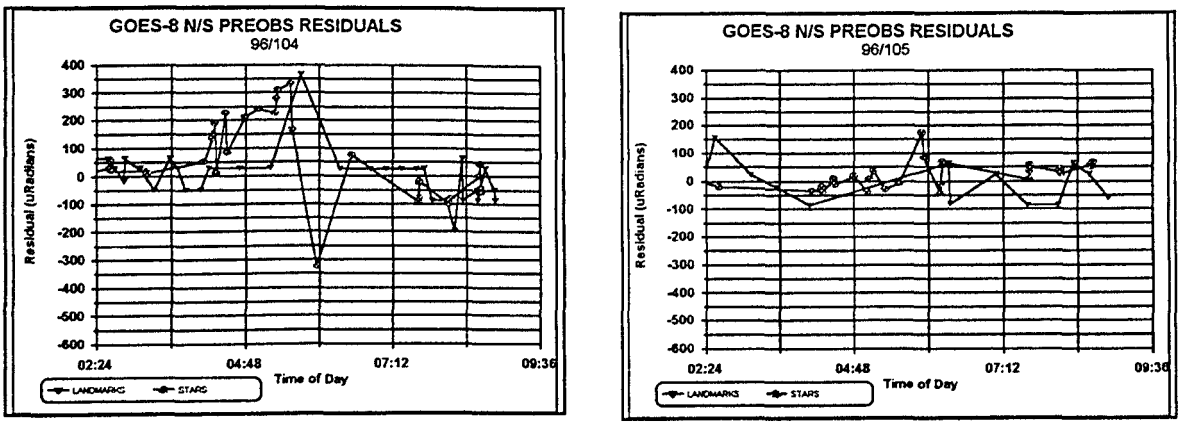

Figure 4.2.2 - Spring '96 Post Eclipse Errors

4.3 Operations to Correct the "Batwing" Phenomenon

After launch of GOES-8, it was discovered that for 12 weeks centered on summer and winter solstice, the spacecraft exhibits large deviations in pointing as high as 2000 μr peak to peak for 3 hours around satellite midnight. This phenomenon is called "batwing", so named because of the shape of the momentum plots during this period. The error is caused by sunlight entering the Earth sensor through an open alignment hole. Left uncorrected, the imagery and sounding data gathered during this period are unusable. Space Systems/Loral developed a correction scheme, SMC, utilizing both spacecraft and ground system software which eliminates the north/south error and reduces the east/west error to 200 μr peak to peak.

SMC coefficients which model the spacecraft pointing error for each day of the "batwing" season are stored in a table in the OATS. The OATS operator accesses this table once per day to generate the SMC coefficient upload for the upcoming midnight period. The correction profile is compared to the previous night's performance as a sanity check and then converted to command parameters for upload to the spacecraft along with a start time and a duration. The SMC enable commands are sent in the 0035Z housekeeping period. The on-board computer begins applying the correction to the instruments at 0445Z and continues for 3 hours. At the expiration of the uploaded duration, the function is automatically disabled on board the spacecraft. The process is repeated daily for GOES-8 operations during the "batwing" season. The "batwing" error has been eliminated on GOES-9 and future GOES spacecraft through changes to the Earth sensor hardware.

4.4 Single Chord Operations

The GOES-8 and GOES-9 satellites utilize a "dual-chord" scanning Earth sensor which provides spacecraft roll and pitch information to the onboard attitude control system. As a result of the relative satellite and lunar orbital geometries, the moon will drift into one of the Earth sensor chords several times a month. If the moon drifts into a chord of the Earth sensor, while the Earth sensor is scanning, large unpredictable attitude errors will result. In order to prevent such errors, the chord containing the intrusion will be inhibited and the Earth sensor is operated in "single-chord" mode. Single-chord mode typically lasts 3 hours to account for the intrusion duration and spacecraft configuration commanding.

Using the OATS we can precisely predict when such lunar intrusions will occur. Figure 4.4.1 is a product developed by the INR team which utilizes OATS data to visualize lunar intrusions. From this figure it is evident that a lunar intrusion will occur on Julian days 186 and 189 for the GOES-8 spacecraft. If the moon is outside the center of the Earth sensor scan region, single-chord will not be commanded in order to avoid potential navigation errors. This product is used operationally to determine when lunar intrusions will occur and if single-chord operation is necessary.

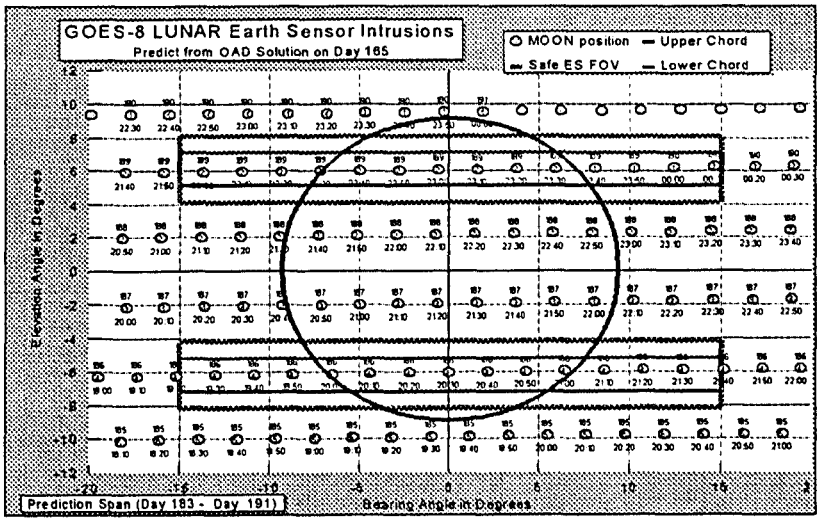

Figure 4.4.1 GOES-8 Lunar Intrusion Plot

Prior to the AOCE2R2 flight software update, which provides autonomous Earth sensor single-chord correction, navigational errors during single-chord operations were corrected using manually generated SSAA's. During the transition from dual-chord to single-chord, a step pitch error in the range of (50 - 200) μr is typically experienced. In addition, a time varying roll error, as much as 600 μr near spacecraft local midnight, can be accumulated during the single chord period. After single chord is commanded, a set of star and landmark measurements is processed by OATS and used to compute the magnitude of the resulting single-chord transition error. An SSAA is then manually generated, loaded to the spacecraft and used by the IMC system to correct

the resulting error. During the remaining single-chord period, SSAA's are automatically generated by OATS and uploaded to the spacecraft as needed to maintain navigational accuracy.

When returning to normal dual chord operations, the SSAA corrections accrued during the single-chord period need to be removed. This was achieved by "resurrecting" the IMC set that was active prior to entering single chord. This resurrected IMC set represents the state of the instrument attitude prior to single-chord activation and is our best estimate of the instrument attitude post single-chord. Although this method of single-chord navigation has been replaced by an onboard correction algorithm, it exemplifies the operational solutions used early in the GOES mission to correct sources of navigation error.

4.5 Longitudinal Repositioning (IMC Reference Updates)

Upon completion of their transfer orbits, the GOES-8 and GOES-9 spacecraft were stationed at approximately 90° west longitude. In order to provide maximum global coverage both spacecraft have been repositioned. GOES-8 is currently stationed at 75° west and GOES-9 is stationed at 135° west. During this transitional phase GOES-8 was moved at 0.5°/day over a 30 day period and GOES-9 was moved at 1.0°/day over a 45 day period. These maneuvers were achieved by adjusting the semi-major axes of the orbits to induce the desired drift rate. During the longitude repositioning phase the spacecraft drift rate was 10 to 20 times faster than the nominal rate, posing a limiting factor to the IMC operation.

Prior to the AOCE2R2 flight software update, the on-board IMC reference longitude needed to be maintained to within +/- 0.2° of the spacecraft sub-satellite point. Since the sub-satellite point was changing so rapidly during the drift period the reference longitude needed to be updated every 3 days to ensure that IMC requirements were satisfied. In order to meet these requirements the OATS was used to predict the sub-satellite point variation over the entire drift period. Using this information the INR team created a table for the OATS controller to use, listing the correct reference longitude to use for a particular day. In this manner, the OATS controller could input the correct reference longitude into IMCGEN, ensuring that the daily IMC coefficients would not violate IMC restrictions.

5. OTHER OPERATIONAL WORK-AROUNDS

5.1 Early Child Enable

During the INR characterization process it became apparent that Earth sensor performance was effecting the daily repeatability of instrument pointing. As stated in section 3.4, the OAD process is executed daily to estimate the orbit and imager/sounder attitude for the GOES-8 and GOES-9 spacecraft. Since OAD was not designed to accommodate non-repeatable phenomena, like that caused by the Earth sensor, certain image navigation and registration errors were unveiled.

In particular, consecutive daily OAD solutions exhibited a discontinuity at the end of one solution and the start of the next day's solution. This discontinuity was observed in the form of an image "jump" whenever a new IMC set was activated. The INR team attempted to correct these discontinuities by implementing the ramping capability of OAD. Although effective in some cases it was evident after thorough testing that using a ramp function in OAD would not consistently correct the discontinuity. In several cases, OAD's inability to determine the direction of the ramping function actually made the discontinuity larger. After concluding that a ramping function was not the best solution, a quadratic function was implemented with similar results.

In an attempt to minimize the magnitude of the registration error during new IMC set activation, a capability termed "IMC Matching" was added to OAD which would adjust the constant order roll, pitch, and yaw terms using data at the end of the fit span. Although this was an improvement over the ramping and quadratic functions, the constant order adjustment was based on data which were 3-hours old by the time the new IMC set was activated. This 3-hour gap exists in order to give the operations personnel enough time to create and validate the daily operational schedules and upload the coefficients after the new IMC set has been created.

Using the "IMC Matching" concept as a baseline, the INR team developed a procedure which would adjust the constant order terms of the new IMC set using data taken just 15 minutes prior to IMC set activation. This procedure, named "Early Child Enable" (ECE), utilizes a GIMTACS command directive to trick the ground system into thinking that the new IMC set has been activated onboard the spacecraft, when in actuality it has not. Once the ground system assumes that the new IMC set has been enabled on the spacecraft, the timer capability of OATS is utilized to create an SSAA relative to the new IMC set. This SSAA can

then be loaded to the spacecraft and integrated with the parent IMC set before the parent IMC set is activated during the upcoming housekeeping period. This procedure has been automated and integrated into the daily command schedules for both GOES-8 and GOES-9. As a result of this procedure the navigation and registration errors have been minimized for the first image of a given registration period. The table below lists the average registration error for the first daily image prior to and following the implementation of the ECE procedure. Approximately 1 month of data are used for both periods of interest. These results illustrate the effectiveness of the ECE procedure and the contribution that operational solutions have in improving INR performance.

SPACECRAFT	Pre-ECE Average Registration Error (microradians)		Post-ECE Average Registration Error (microradians)	
GOES-8	N/S E/W	42.0 45.0	N/S E/W	23.0 25.0
GOES-9	N/S E/W	39.0 41.0	N/S E/W	24.0 19.0

Table 5.1.1 ECE Performance Comparison

5.2 "Bevel" Correction

Another Earth sensor error which significantly impacts INR performance is known as the "bevel" error. This error is caused by sunlight reflected within the Earth sensor which corrupts one of the Earth scan chords. The error occurs for 2 weeks in early February, early May, early August, and early November when the sun is between 15° and 18° declination. The error manifests itself as a "batwing" like registration shift around spacecraft midnight, both north/south and east/west, but of much smaller magnitude. The size of the error is unique for each Earth sensor. The GOES-8 error is approximately 100 to 200 μr occurring from 0430Z to 0730Z. On GOES-9, the error is twice as large, 200 to 400 μr, occurring from 0730Z to 1030Z.

An option for correcting this error is the SMC process. However, since this effect is caused by a disturbance in one of the two Earth sensor scan chords, we have found that by inhibiting this chord from contributing to the spacecraft pointing, we will eliminate the error. Our operational work-around is then to command single chord operations (disabling the effected chord) at the first available opportunity prior to the start of the sun interference and then to remain in single chord for the duration of the error, approximately 4 hours. Figure 5.2.1 shows the performance improvement gained from the single chord operation during the "bevel" period.

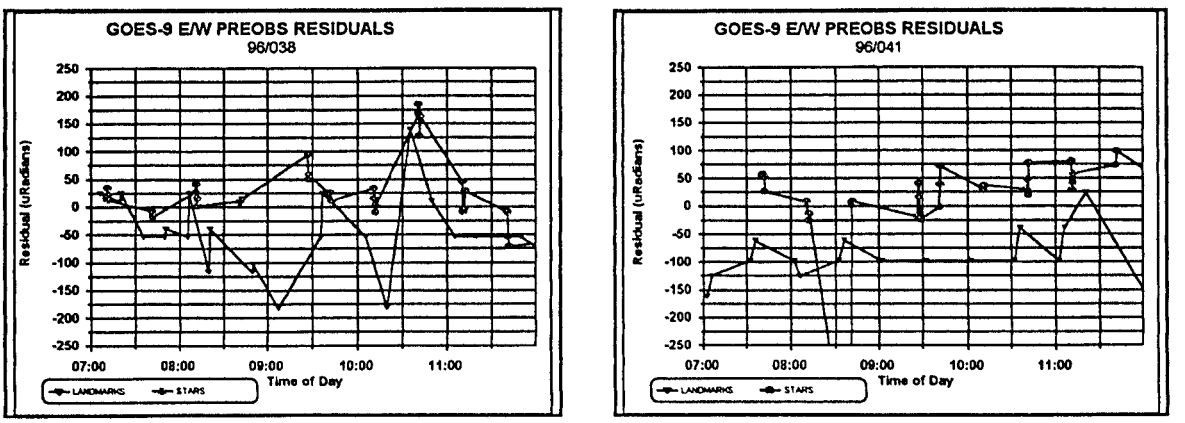

Figure 5.2.1 - Bevel Correction

There is a pointing impact from the single chord operation itself. This error, which can be as large as 600 μr, is corrected by an independent compensation process in the on-board computer, called Single Chord Compensation. The remaining impact is the loss of one image and one star window to provide time for commanding the single chord configuration and for the control system to settle after the configuration change.

6. SUMMARY

The evolution of the GOES 8/9 INR operation from its prelaunch concept to today's configuration demonstrates the importance of a flexible ground system and the ingenuity of the operations personnel in making the best use of the ground system's capabilities. We have overcome many of the performance limitations of the spacecraft and are providing accurately navigated image and sounding products to the NWS with a greater than 95% success rate. With continued work and innovative ideas, we hope to improve our performance and operational reliability in the future.

7. ACKNOWLEDGEMENTS

The authors gratefully acknowledge the contributions of Wyatt Wallace and John Tsui of the Lockheed Martin INR support team for their help in developing the data for this paper and their continued contributions to the INR operation. We also would like to thank Rose Fleming and Tim Walsh of NESDIS for their help in our final editing of this paper.

8. REFERENCES

The following publications are references for the preceding paper and should be consulted for more information on the GOES INR system.

1. Space Systems/Loral, Operations Ground Equipment Operations Maintenance Manuals, DRL 504-06, August 24, 1995.

2. Space Systems/Loral, Image Navigation and Registration, DRL 300-06, March 4, 1994.

3. Kelly, Kathleen A., GOES I-M Image Navigation and Registration and User Earth Location, April, 1989.

4. Washwell, E.R., K. Chevray, A. Kamel, A. Dress, T. Walsh, "Improved GOES Earch Sensor Performance", to appear in the Proceedings of the SPIE International Symposium Optical Science, Engineering, and Instrumentation; Conference on GOES-8 and Beyond, Denver, CO, August 4-9, 1996.

5. Ong, K.M., S.D. Lutz, "GOES Orbit and Attitude Determination: Theory, Implementation, and Recent Results", to appear in the Proceedings of the SPIE International Symposium Optical Science, Engineering, and Instrumentation; Conference on GOES-8 and Beyond, Denver, CO, August 4-9, 1996.

6. A. Kamel, "Image Navigation and Registration System", to appear in the Proceedings of the SPIE International Symposium Optical Science, Engineering, and Instrumentation; Conference on GOES-8 and Beyond, Denver, CO, August 4-9, 1996.

GOES Landmark Positioning System

Walter Eppler
David Paglieroni
Marcus Louie
Jeffery Hanson

Lockheed Martin Western Development Laboratories

ABSTRACT

This paper describes methods, algorithms, and software developed to select and represent landmarks from cartographic databases and to automatically determine the landmark position in GOES imagery. A simulation study was conducted to demonstrate that the landmark position can be measured with subpixel accuracy.

KEY WORDS

GOES; Landmarks; Imagery; Navigation; Registration; Positioning; Orbit; Attitude; Cartography; Photogrammetry

1. INTRODUCTION

To properly exploit the GOES imagery, it is important to know precisely the location on the Earth of any/all pixels in the digital image. For example, applications such as Interactive Flash Flood Analysis (IFFA) and wind velocity determination (based on tracking cloud motion) place stringent requirements on imager positional accuracy and frame-to-frame stability.

A mathematical model, described in Ref. 1, gives the geodetic latitude and longitude of any point in terms of its line and pixel address in the digital image. This model requires very accurate knowledge of spacecraft position and attitude parameters. These parameters can be derived using range measurements from known Earth locations and line-of-sight (LOS) measurements to known stars. The orbit and attitude parameters are further refined by fitting line and pixel image coordinates of salient features called landmarks to their known latitude, longitude, and height on the Earth. As described in Ref. 2, this spatial calibration of an image is performed by the Orbit and Attitude Tracking System (OATS). Once the orbit and attitude parameters have been determined, the nominal motion of the imager scan mirror can be modulated to compensate for orbit and attitude errors in order to produce a metrically correct image.

This paper describes the GOES Landmark Positioning System (GLPS), which automatically determines the line and pixel coordinates of a landmark in the GOES image. This system provides the following advantages over the present method of manual landmarking:

- It is more consistent and can measure position with subpixel accuracy. This is especially important for nighttime operations when IR channels with 4 km resolution must be used.
- It is potentially capable of autonomous operation, which will increase system reliability and reduce operating costs.

2. APPROACH

The GLPS approach is superior to the approaches used in the past in that we use landmarks in *symbolic* form (i.e., perimeters of lakes and islands) derived from precise cartographic source materials. Earlier approaches used actual GOES imagery from a previous cloud free acquisition as the landmark, which had the following disadvantages:

- Its true position (in image coordinates) was ambiguous and could not be known accurately.
- Several versions of the landmark had to be used corresponding to different acquisition conditions (e.g., different diurnal and seasonal conditions).

Our approach upsamples (i.e., *magnifies*) the GOES image prior to the matching process in order to improve the location accuracy. The validity and efficacy of this approach was proven in the subpixel accuracy investigation described in Section 8.

We developed an optional enhancement process, which is applied to the GOES sector prior to the matching process. The enhancement algorithm, described in Section 6, can use the full 10-bit precision of the original image and convert it into a likelihood ratio based on radiometric calibration. Cloud pixels are detected on the basis of their brightness and eliminated from both the radiometric calibration and the subsequent matching process. This makes it possible to use our system even when the landmark is partially obscured by cloud cover. We investigated six different matching algorithms, which are described in Section 5. The results of tests using 68 sectors including both visible and IR channels are summarized in Section 7. The best two algorithms achieved 90% and 96% correct and accurate matches.

3. CHARACTERISTICS AND ADVANTAGES OF GLPS

A number of factors make the GOES Landmark Positioning System simpler than most image matching applications described in the literature (Refs. 3–5). The first is that in GLPS the designer gets to select from a very large geographic area the best features to match; this is much easier than reconnaissance image processing in which the regions to be matched are dictated by the application. This allows the designer to select very simple features consisting of a single enclosed object embedded in an extended homogenous background (called the surround). Another simplifying characteristic is that the GOES image is almost never misregistered by more than a few pixels. This reduces the required search range, which reduces the computation time and the likelihood of a false matchpoint. Also, because of the very accurate control of the satellite and imaging sensors, the scale and orientation of the imagery is very accurately known. Eliminating scale factor and rotation errors preserves the sharpness of the correlation surface peak and improves the reliability and accuracy of image matching.

Another feature of the GLPS application is that variations in pixel gray-scale values can be reduced by a calibration process that is customized for each acquisition. This is made possible by the fact that the landmark mask provides ground truth information necessary to compute separate statistics for pixels within the landmark and the surround. This self-calibration procedure eliminates contrast reversals and other gray-scale variations caused by different acquisition conditions (e.g., different diurnal and seasonal conditions).

The proof of concept system described in this paper offers a number of important advantages over the system previously installed in the Product Monitor. It is capable of subpixel accuracy on the order of 250 m for the visible channel. It achieves this accuracy even in the presence of partial cloud cover. Furthermore, the likelihood of cloud cover is reduced by using smaller landmarks (i.e., 12 km for the visible channel) than the previous system (i.e., 64 km). As described in Section 4, we have identified nearly 170 landmarks suitable for use with visible and IR channels of GOES East and West. This greatly increases the likelihood of finding multiple cloud-free landmarks in any particular frame.

We believe the methods we have developed can be used in the future to implement a completely automatic/autonomous system that will be more reliable and cost effective than the proof-of-concept system. To develop the autonomous system, research must be carried out in two areas:

- Detection of clouds and shadows as necessary to discard landmarks that are obscured or unreliable for each particular acquisition.
- Formulating procedures for computing one or more figures of merit that predict the reliability and accuracy of the landmark position estimate.

4. LANDMARK DATABASE PREPARATION

The landmarks are represented and stored in *symbolic* form, specifically vertices representing the perimeters of islands or lakes. The first step is to screen very large geographic areas (e.g., full Earth disks) to identify islands and lakes having the proper size, shape, and orientation. This results in a list of landmarks with their corresponding parameters as shown in Table 1.

Table 1. Output of Landmark Identification Phase

	LAT	LON	ID	Type	Feature	GOES East	GOES West	Rating	Perimeter	Name
1	-16.822094	-151.446884	BEPP3310	VIS	ISLAND	4.3	62.7	A		Raiatea
2	22.049999	-159.533340	BHFH2803	I R	ISLAND	-3.6	52.2	A		Kauai, HI
3	21.466667	-158.000000	BHHG0028	I R	ISLAND	-2.2	53.8	B		Oahu, HI
4	20.766666	-156.350006	BHJF3946	I R	ISLAND	-0.6	55.7	A		Maui, HI
5	33.966667	-120.116669	DJQD5358	VIS	ISLAND	28.2	47.4	B		Santa Rosa Is., CA (SRI)*
6	39.083332	-120.050003	DJQK5705	VIS	LAKE	25.4	42.1	B	Yes	Lake Tahoe, CA
7	28.183332	-115.233330	EHEP4611	I R	ISLAND	35.2	50.5	C	Yes	Cedros, Mexico
8	29.266666	-113.383331	EHGQ3716	I R	ISLAND	36.1	48.4	B	Yes	Angel De La Guarda, Mexico (BAJ)*
9	28.983334	-112.366669	EHHP3859	I R	ISLAND	37.1	48.0	A		Tiburon, Mexico
10	24.216667	-109.866669	EHLK0813	VIS	ISLAND	42.0	50.1	B	Yes	Cerralvo, Mexico (CER)*
11	38.683334	-118.716667	EJBJ1741	I R	LAKE	26.6	42.1	B	Yes	Walker Lake, CA
12	30.250000	-90.516670	FJQA2915	VIS	LAKE	50.9	30.6	B	Yes	Lake Maurepos, LA
13	30.166666	-90.133331	FJQA5210	I R	LAKE	51.1	30.3	B	Yes	Lake Pontchartrain, LA
14	14.850000	-88.000000	GGCQ0051	VIS	LAKE	67.0	34.0	A		Lago Yojoa, El Salvador
15	20.433332	-86.916664	GHDF0526	I R	ISLAND	62.5	31.3	B		Isla de Cozumel (COZ)*
16	21.683332	-82.849998	GHHG0941	I R	ISLAND	63.1	27.0	A	Yes	Isla de Piñas

Once a feature has been selected, the exact geodetic coordinates of perimeter vertices are read out as a sequence of latitude and longitude values as an operator traces out the perimeter on an interactive softcopy map display; a typical result is shown in Table 2. The perimeter vertices are stored in the landmark database as a variable length file of floating point numbers in ASCII format. The file size is rarely greater than 125 vertices or 3,000 bytes.

Table 2. Output of Landmark Preparation Phase

Mormon Lake, AZ	Datum: WGS84	Height: 2155 m	
1. 34.964245	-111.454948	13. 34.922371	-111.443619
2. 34.965249	-111.457817	14. 34.922520	-111.437866
3. 34.964394	-111.466087	15. 34.925762	-111.434631
4. 34.962036	-111.470406	16. 34.929745	-111.434631
5. 34.953777	-111.471481	17. 34.934460	-111.436432
6. 34.950680	-111.473999	18. 34.945076	-111.438049
7. 34.946552	-111.473099	19. 34.948322	-111.437866
8. 34.940361	-111.473099	20. 34.949650	-111.439484
9. 34.939770	-111.470940	21. 34.954662	-111.439308
10. 34.932396	-111.465553	22. 34.960854	-111.442902
11. 34.928417	-111.459259	23. 34.965279	-111.446320
12. 34.923401	-111.448296	24. 34.966164	-111.450272
		25. 34.964100	-111.454765

The Common Mapping Toolkit (CMTK) was developed by the Air Force at Rome Laboratory and is available to Government organizations at no charge. It can use the majority of DMA products including Digital Chart of the World (DCW), ARC Digitized Raster Graphics (ADRG), and Digital Terrain Elevation Data (DTED). In addition, it can import and register user-digitized hardcopy maps.

Landmark selection is accomplished using the DCW with the CMTK. The DCW is a worldwide, seamless, thematic, vector map derived from hardcopy maps at a scale of 1:1,000,000. We wrote a CMTK-based application to create an icon that represents a 12-line by 21-pixel imager footprint on the ground for either visible or IR imagery from GOES East or West. This footprint is superimposed on the DCW display and allows the analyst to judge whether the candidate island or lake has the required size, shape, and orientation.

Once a feature with the proper size, shape, and orientation has been identified, the operator brings up a higher resolution display based on the DMA ARC Digitized Raster Graphics (ADRG) data made from the 1:250,000 scale Joint Operation Graphic (JOG) hardcopy maps. He uses the cursor to trace around the island or lake by clicking on vertices (i.e., where the outline changes direction). CMTK extracts and stores the latitude and longitude of all vertices. Displays formed using the JOG product are preferred for outlining because the hardcopy maps have an accuracy specification such that 90% of the points have location errors less than 250 m (i.e., one-fourth of a GOES visible line). The pixel spacing on the softcopy raster is 25 m so that the operator can trace the outline with negligible error. The landmarks need to be outlined only once because (to a first approximation) the perimeters do not change with diurnal and seasonal conditions.

The upper-left window of Fig. 1 shows a CMTK display of a DCW vector map in which the scale on the monitor was approximately 1:1,500,000. The island just South of Cuba is Isla de Piñas, and the superimposed footprint is for GOES East IR channels. The upper-right window shows a CMTK display of an ADRG JOG softcopy raster map in which the scale on the monitor was approximately 1:300,000. The GOES East IR footprint, shown as a trapezoidal outline, indicates that the size, shape, and orientation of this island make it an ideal IR landmark. The analyst traces out the perimeter of the feature in the top-right window by using the cursor to delineate a sequence of vertices that, when connected by straight lines, almost exactly match the map outline. The straight line approximation is shown in the upper-right and lower-right windows. The lower-left window shows the perimeter traced from the high-resolution JOG raster map superimposed on the DCW vector map. The fact that they match almost exactly[1] means that the DCW can be used as a backup in areas where ADRG JOG coverage is not available.

Table 2 shows the contents of the database file for a typical landmark. In this case the lake is represented by 25 vertices having specified latitude and longitude. Also specified is the height above sea level of all[2] vertices. Special care must be taken to make sure all landmark vertices are measured with respect to the same geodetic datum, as follows:

- The datum used to specify the location of the reference points from which range to the satellite is measured; see OATS description in Ref. 2.
- The datum used to specify the Earth equatorial radius and eccentricity in the imager mathematical model; see Ref. 1.

The geodetic datum used in the GLPS is WGS84.

As mentioned previously, only islands and lakes are used as landmarks. This is due to the large difference in gray-scale values between land and water. They also have the important characteristic that they are closed features embedded in a homogeneous surround.[3] It is also important that the landmark have the proper size, shape, and orientation We try to locate square or round features that span 12 lines and 21 pixels in the GOES image. This size ensures that the landmark mask will cover at least two-thirds of the feature in each direction in the GOES image even at maximum allowable misregistration (i.e., ±4 lines and ±7 pixels); this is necessary for the enhancement preprocessing described in Fig. 5.

---

[1]The degree of match can be judged by recalling that the entire island is only 12 imager lines high (i.e., 48 km).

[2]The height of the vertices is a constant because the perimeter is a land-water interface.

[3]These characteristics are very advantageous because they eliminate nonstationarity or "edge effect" in the crosscorrelation function (when the edge of a subsector passes through an extended high-contrast feature).

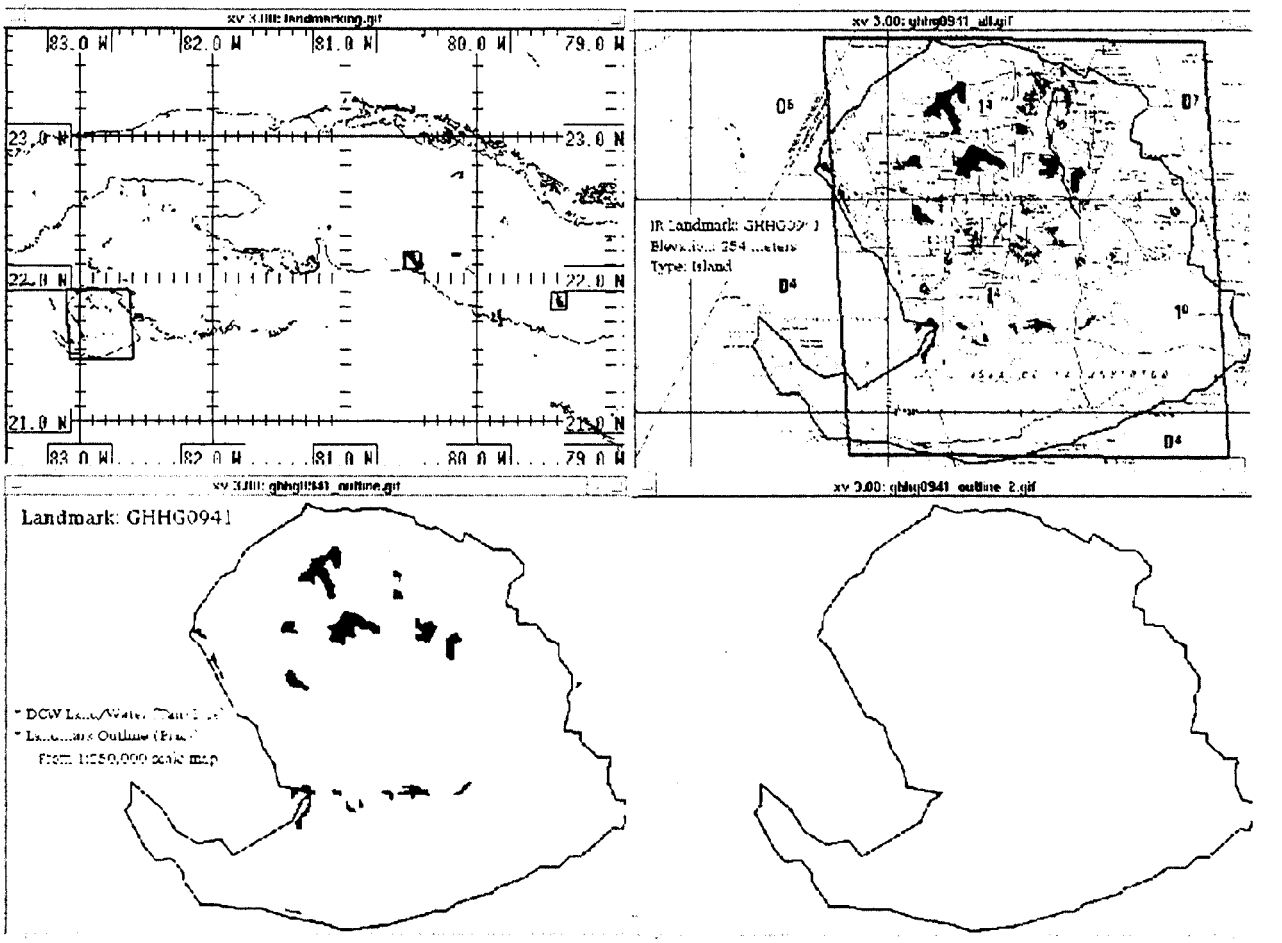

Figure 1. Example of Landmark Selection and Perimeter Tracing

Another important requirement is that the landmarks must be spatially distributed throughout the image frame. This is necessary in order to obtain a robust solution for the orbit and attitude parameters.

An additional constraint is that the elevation angle measured from horizontal of the line-of-sight (LOS) from the landmark to the satellite must be at least 30°. At lower elevation angles the spatial distortion (i.e., foreshortening along the LOS) becomes a problem. Also, the landmark perimeter will be obscured if there is significant terrain relief along the LOS.

Still another desirable attribute of a landmark is that it is cloud free a large percentage of the time. Over the course of this study we had the most success with the islands in the Gulf of California and the Greater and Lesser Antilles.

The requirement for landmarks to be distributed throughout the Earth disk must be balanced by the requirement to limit the spatial distortion of the landmark image. Figure 2 shows the outline in image coordinates (i.e., GOES East line and pixel) of circular landmarks located at different places on the Earth. The upper-left window shows the distortion for a landmark at the subsatellite point. The image is an ellipse where the ratio of semimajor to semiminor axes is 28:16, the sample interval in north-south and east-west directions, respectively; see Ref. 1. In the top-right window the aspect ratio is further exaggerated by foreshortening along the LOS, which is characteristic of oblique photography. The bottom-left window shows that there is a location on the Earth where the foreshortening cancels the 28:16 aspect ratio caused by the different sampling angles. The lower-right window shows that, in general, a circular landmark is distorted into an ellipse with the semiminor axis aligned along the LOS azimuth.

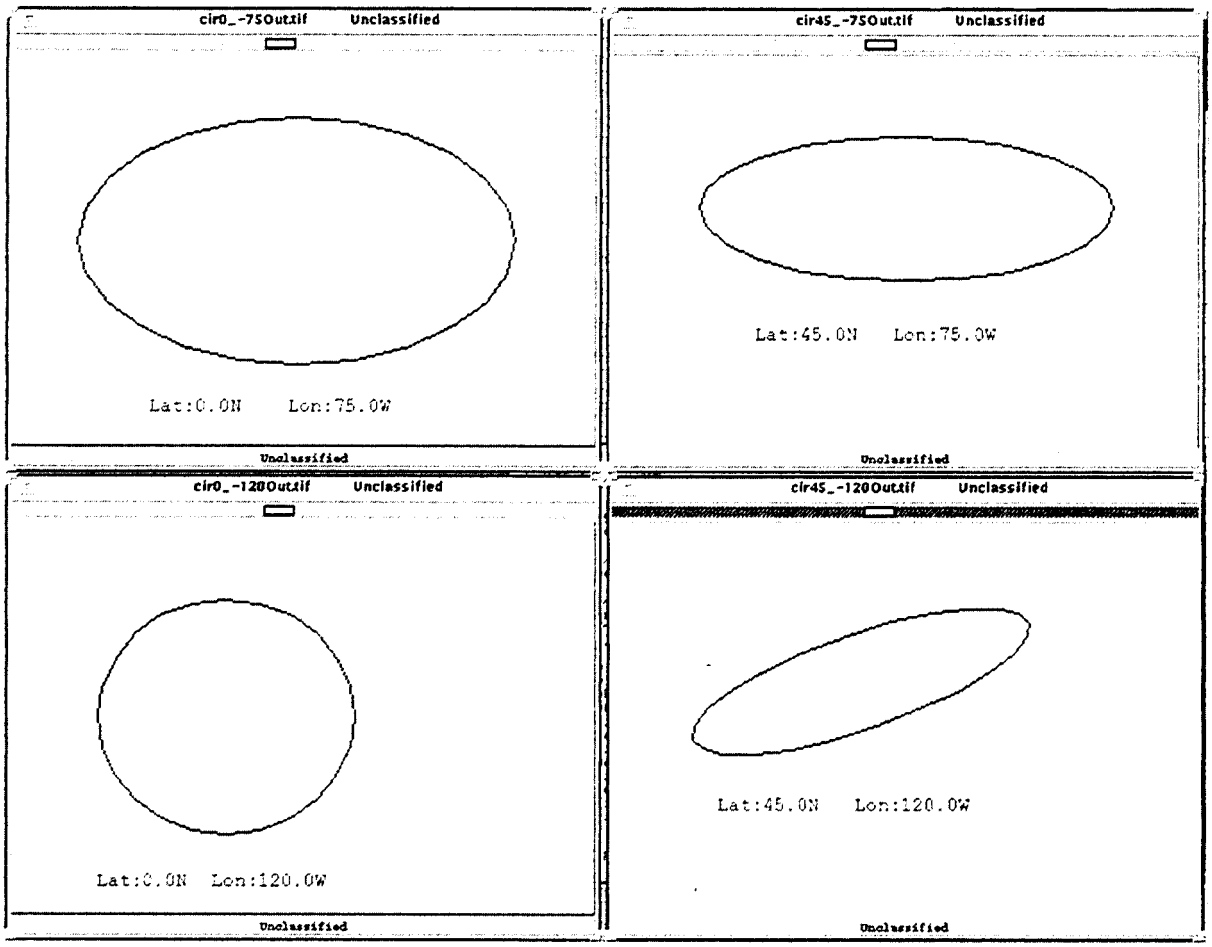

Figure 2. Spatial Distortion for Various Landmark Locations

Table 1 shows a subset of the 169 landmarks selected for visible and IR images for GOES East and West. It gives the following information about each landmark:

- Latitude and longitude of the approximate[4] center point.
- The identification designator, based on the Geographic Reference (GEOREF) coordinates of the landmark nominal center point. As shown in Figure 3 the first two letters designate a specific 15° x 15° area of the world.
- Whether the landmark is to be used for visible or IR imagery. IR landmarks are approximately four times as large as visible landmarks.
- Whether the landmark is a lake or island.
- The elevation angle of the LOS to the satellite for GOES East and West. For best performance, this angle should be greater than 30°.
- A subjective, qualitative rating intended to predict the reliability and accuracy of the line and pixel position estimate. This rating is based on the landmark size, shape, and orientation with respect to the footprint (e.g., see Fig. 1) and takes into account the complexity (i.e., jaggedness) of the perimeter.
- Whether the perimeter was digitized during the course of this study.
- The name of the landmark.
- If the landmark is currently used at the Space Operations Control Center (SOCC), its designation in the VIRGS book is given.

---

[4]It is not necessary to estimate the center point exactly. It is used only to extract the image sector in the Product Monitor. The exact landmark position is derived from the coordinates of *perimeter vertices*, which must be very accurate.

Figure 3 is a plot showing the 169 landmarks selected for visible and IR images from GOES East and West. Also shown are the estimated quality measure for each landmark and the circles of constant elevation angle.

5. IMAGE MATCHING ALGORITHMS

During the course of this study, six different image matching algorithms were investigated using a large number of visible and IR sectors from many different landmarks. The basis of operation and the characteristics of these algorithms are summarized in this section.

5.1 Centroid

In the current manual system, an operator identifies and delineates in the GOES image a single salient feature marked on a hardcopy map. Because it is difficult to program a computer to recognize salient features such as "cusp of inlet cove" etc., a simpler characterization is used; i.e., the landmark centroid. In this approach, the landmark perimeter vertices coordinates are projected onto the GOES image and used to compute the line and pixel coordinates of the centroid (i.e., center of mass) of the landmark bitmap. The GOES gray-scale image is then thresholded to form a bitmap whose centroid is computed. The offset error is the difference between the two centroid locations. The centroid approach is simple and fast, but is not accurate if there are clouds anywhere in the GOES subsector.

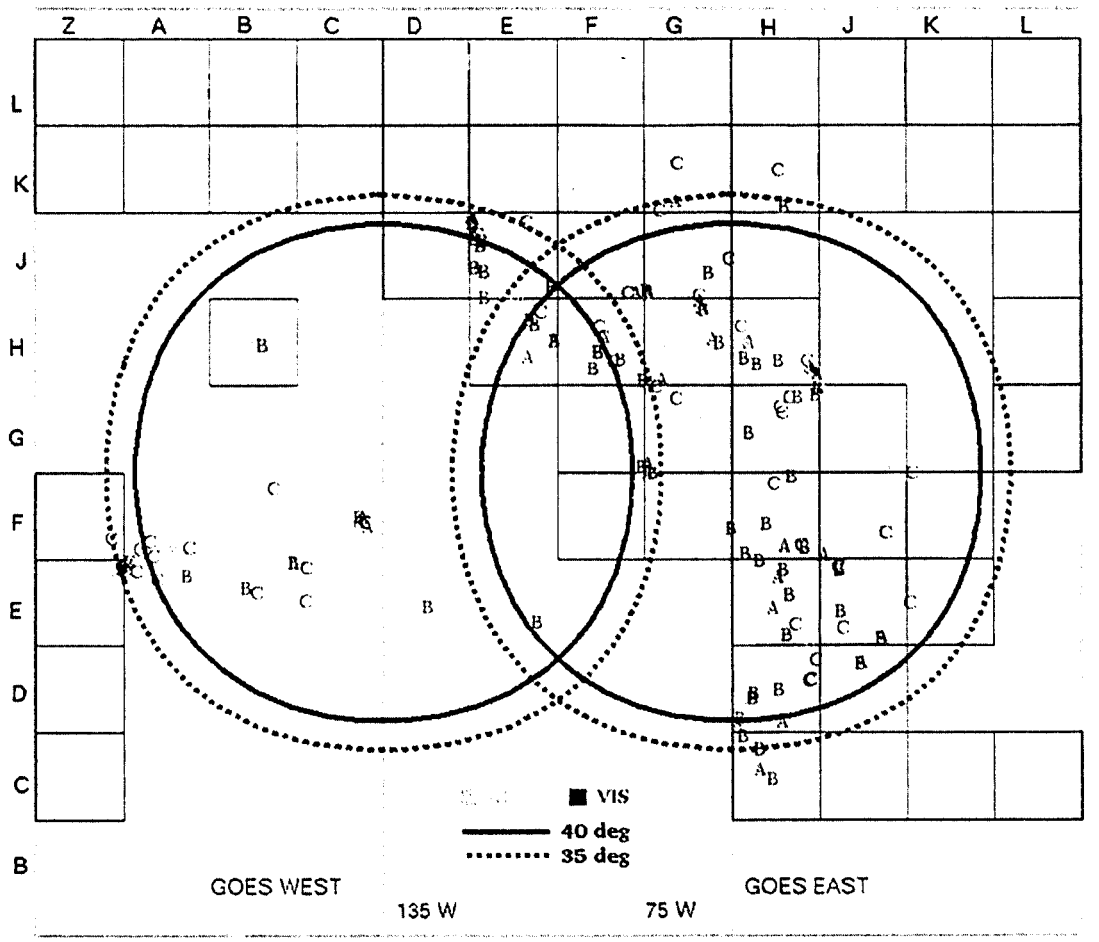

Figure 3. Landmarks Selected for GOES East and West

5.2 Edge Matcher

The edge matcher achieves location accuracy by matching a large number of edge points in the GOES image to the projected landmark perimeter. The edges are derived using the Laplacian-of-Gaussian algorithm given in Ref. 6. The edge matching is carried out using the Nearest Edge Transform described in Refs. 7 and 8. This approach is relatively insensitive to variations in gray-scale intensity and cloud cover anywhere in the GOES image subsector. However, it requires too much computer memory and speed to use in the Product Monitor.

5.3 Cluster Reward

This algorithm, described in Ref. 4, operates by forming the histogram of gray-scale intensity values of pixels inside the shifted, projected landmark perimeter. It takes as its position estimate that offset at which the histogram is most clustered (i.e., narrowest and highest peaks). This algorithm is well suited for applications in which gray-scale "contrast reversals" are a problem. However, when landmarks are small Cluster Reward can have a false match for offsets that are completely misregistered and therefore is not recommended for use in GLPS.

5.4 Minimum Variance

This algorithm, described in Ref. 5, operates by computing the variance of gray-scale intensity values of pixels inside the shifted, projected landmark perimeter. It takes as its position estimate that offset at which the variance is minimum. This algorithm is well suited for applications in which gray-scale "contrast reversals " are a problem. Like Cluster Reward, the Minimum Variance algorithm can have a false match for offsets that are completely misregistered and therefore is not recommended for use in GLPS.

5.5 Crosscorrelation

Crosscorrelation, also called the classical matched filter, is the most common technique for image matching, and Ref. 9 shows that it is the most accurate algorithm for determining the feature location. In GLPS the gray-scale image is multiplied by the shifted landmark bit mask and summed over the subsector. This amounts to computing the average value of GOES pixels within the landmark. The position estimate is taken to be that offset which maximizes[5] the average value of GOES pixels within the landmark perimeter. Crosscorrelation is sensitive to cloud cover interference only if it occurs on the landmark boundary. This algorithm was implemented on the Product Monitor at the SOCC because it is simpler than the Edge Matcher.

5.6 Normalized Crosscorrelation (NCC)

Normalized Crosscorrelation (NCC) is the same as crosscorrelation (i.e., maximum average) except that both the GOES subsector and the landmark mask are preprocessed to subtract the mean value and divide by the standard deviation for each offset. This normalization does not change the position estimate for landmarks that are enclosed and embedded in a homogenous surround: this is why the landmarks are chosen with these properties.

It should be mentioned that the last four algorithms have execution times proportional to the *area* of (i.e., number of pixels in) the landmark; this is a disadvantage compared with the Edge Matcher where the compute time is proportional to the *length* of landmark perimeters. Although it was outside the scope of this study, it is possible to reformulate the last four algorithms so that their compute time is proportional to the number of perimeter pixels as with the Edge Matcher.

6. PREPROCESSING OPERATIONS

The performance of all six matching algorithms can be improved by certain preprocessing operations on the GOES imagery. One such operation detects cloud pixels (on the basis of their brightness) and eliminates them from the matching process. A second type of preprocessing enhances the contrast between land and water and eliminates the contrast reversals (particularly in the IR imagery) that result from diurnal variations.

---

[5]This assumes that pixels from the landmark have a higher gray-scale value than pixels from the surround. If it is known that this is not the case, then the average value should be *minimized*.

In Fig. 4 all four windows show the landmark perimeter superimposed over a GOES visible image at the estimated position. The upper-left window was registered using the Edge Matcher, and the upper-right window was registered using the Maximum Average (Crosscorrelation) algorithm. It is apparent that a large position error is caused by clouds in the case of the Maximum Average algorithm, which moves the GOES image up to maximize the contribution caused by the bright clouds. The Edge Matcher was not perturbed by cloud interference.

In the bottom two windows, cloud pixels were detected on the basis of their very bright returns and eliminated from the matching computations. There was no improvement in the match quality in the Edge Matcher in the lower-left window. In the lower-right window, two preprocessing operations were performed on the GOES image prior to matching using the Maximum Average:

- The cloud pixels were eliminated; this is shown by the black areas in the image.
- The image was enhanced using a method to be described next.

The result of the preprocessing is that the Maximum Average gives the same offset position as the Edge Matcher despite severe interference by cloud cover.

The GOES Landmark Positioning System provides an option for enhancing the image in a preprocessing operation prior to matching. The purpose is to increase the contrast between landmark and surround and to eliminate contrast reversals (i.e., to ensure that the landmark is brighter than the surround). The transformation converts the radiometric value of each pixel to the *probability* that the pixel is within the landmark. This involves computing separate statistical parameters for landmark and surround pixel gray-scale values. The necessary statistics are derived using the landmark mask for extracting training samples.

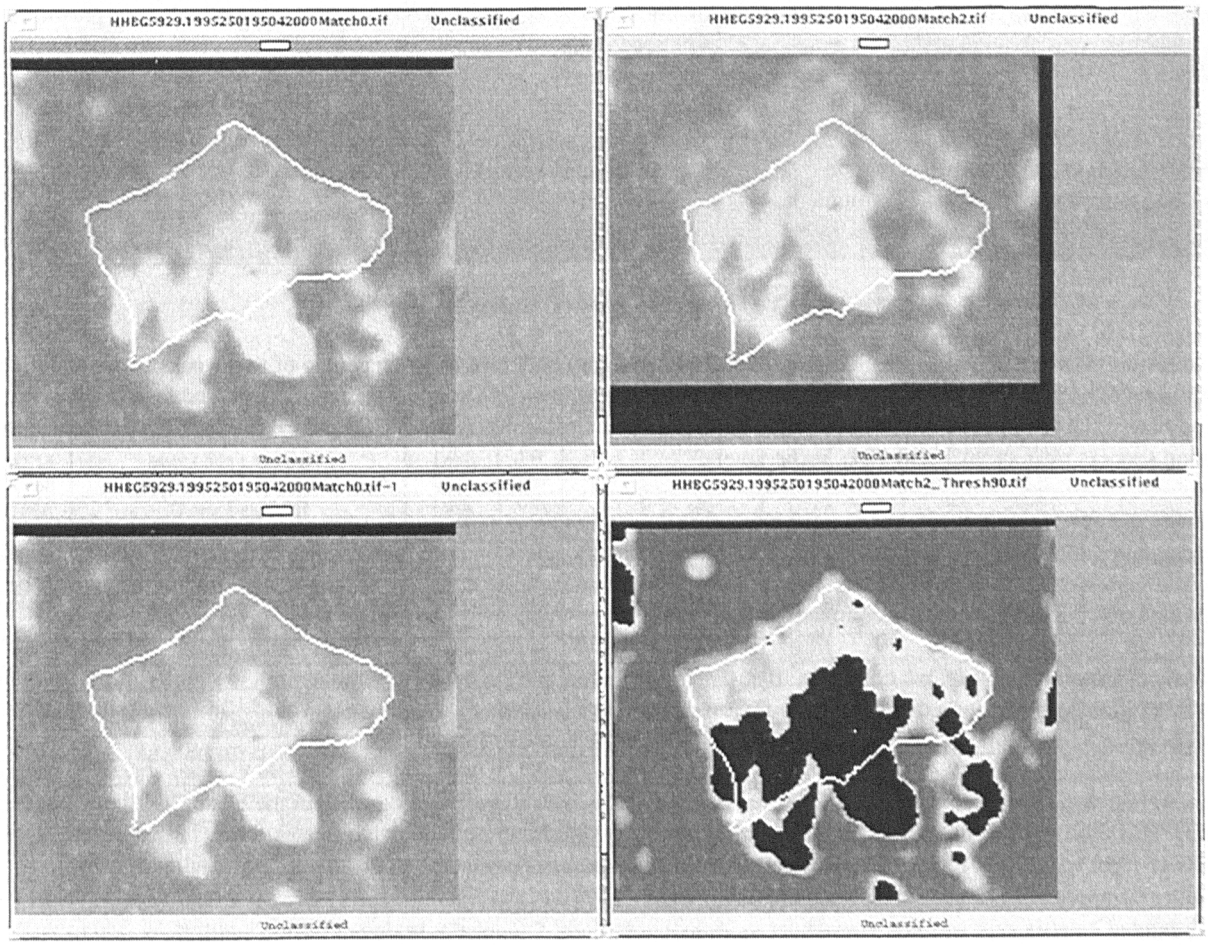

Figure 4. Sensitivity to Cloud Cover Interference

In Fig. 5 the enhancement process begins with the landmark outline shown in the upper-left window. It is obtained by connecting the vertices with straight-line segments and filling in the outline to form the landmark bitmap. If there were no orbit and attitude errors, all pixels within the outline would be landmark pixels and could be used to compute landmark statistics including a mean and standard deviation. Similarly, all pixels outside the boundary could be used to compute statistics for the surround. However, because of Image Navigation and Registration (INR) errors, pixels near the border can be either landmark or surround and must be excluded from the statistics computations. As shown in the lower-left window, the bitmap is divided into three regions:

- The center area is always aligned with landmark pixels.
- The outside area is never aligned with landmark pixels (i.e., always contains surround pixels).
- The area between can contain either type of pixels and is not used for computing statistics.

The upper-center and upper-right windows are subsectors of GOES IR imagery of an island acquired at two different times of day. Notice that the images have very low contrast and that the island changes from bright to dark over the course of 9.5 hours (i.e., there has been a contrast reversal). The bottom-center and bottom-right windows show the corresponding images after they have been enhanced. In these images, the gray-scale value of a pixel corresponds to the *likelihood* that it is a landmark pixel. Notice that the enhanced images have much higher contrast and that the contrast reversal has been corrected.

Figure 5 shows that the gray-scale values in an image change with time and are not a reliable indicator of whether the pixel is landmark or surround. The enhancement method uses "ground truth" information from the landmark bitmap to radiometrically calibrate the image to reduce these variations and make the enhanced image more robust. In the enhanced image the landmark pixels are brighter than surround pixels for all times of day, regardless of whether the landmark is an island or lake or whether the channel is visible or IR. Because this enhancement method can be extended to work with multispectral input imagery, consideration has been given to using two channels of registered imagery to improve the discrimination between landmark and surround.

The original GOES imagery is digitized to 10 bits, but the matching computations are performed using 8-bit images. Our enhancement method uses 8 bits to represent only that range of input gray-scale values needed to discriminate between landmark and surround; in this way we retain the full precision of the original 10-bit image.

7. RESULTS OF GLPS TESTING

Extensive testing was performed using GOES visible and IR imagery collected over the course of two weeks between Julian dates 248 and 262, 1995. Table 3 gives the results for $(77 - 9) = 68$ sectors[6] from 16 different island and lake landmarks. It was found that of the five matching algorithms tested, Normalized Crosscorrelation (NCC) and Edge Matching performed the best, giving success rates of 96% and 90%, respectively.

The majority of false matches were caused by the fact that the landmark was too small or too distorted by foreshortening. Experience gained from these tests caused us to change our landmark selection criteria to require larger landmarks (i.e., at least 12 lines by 21 pixels) and to require higher elevation angles (i.e., at least 30°). Of the 16 landmarks used in these tests, only seven are included in our final list of recommended landmarks.

On the basis of extensive testing, we concluded that Crosscorrelation gives a position estimate that is slightly more accurate than the Edge Matcher. This was determined by reviewing displays (such as the lower-right window in Fig. 4) showing the landmark boundary superimposed over the upsampled GOES image at the estimated offset.

As shown in Fig. 4, Edge Matching is less sensitive to disturbances caused by cloud cover than the *basic* Crosscorrelation algorithm. This motivated us to add the cloud rejection preprocessing function, which eliminates errors in Crosscorrelation; see the lower-right window in Fig. 4. Experience gained from these tests caused us to make our final landmark selection criteria more stringent with respect to size and elevation angle.

---

[6]A sector was discarded if clouds covered a majority of the image or if the contrast between the landmark and surround was inadequate.

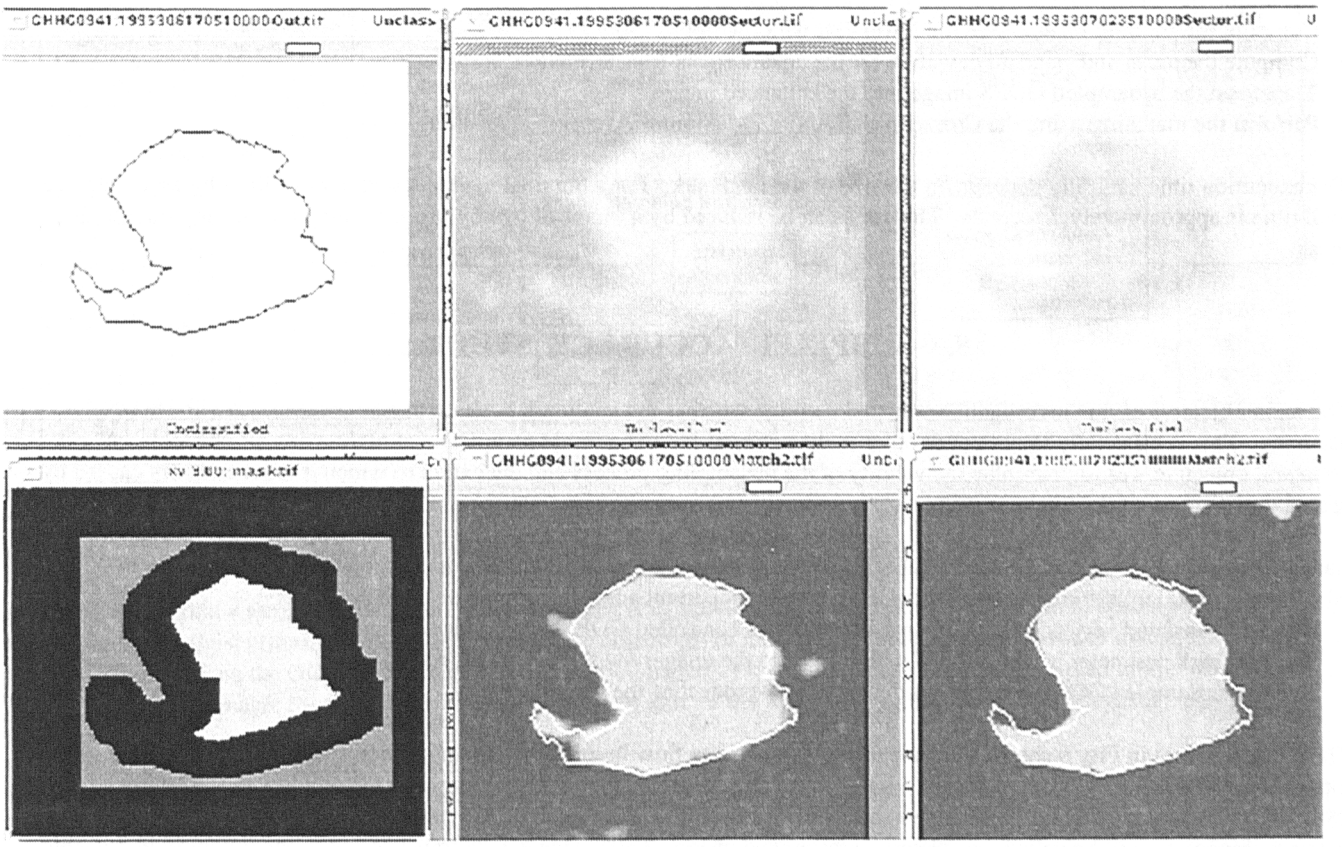

Figure 5. Explanation of Enhancement Process

Table 3. Results of GLPS Testing

ID #	Name	Type	Band	Rating	Sectors Processed	Bad Sect	Number of sectors correctly matched				
							Edge	Cluster	MinVar	NCC	Cntroid
FKMB1914	Mille Lacs Lake, MN	Lake	I R	C	7	2	5	0	0	5	0
EJHQ0758	Clark Canyon Reservoir, WY	Lake	VIS	D	1	0	1	0	1	1	0
DJNN5256	Crater Lake, OR	Lake	VIS	A	4	0	4	0	4	4	0
DJQN4639	Lake Abert, OR	Lake	I R	A	5	0	3	0	5	5	1
DJQM3456	Goose Lake, CA	Lake	I R	B	2	0	2	0	2	2	1
DJPM2854	California	Lake	VIS	A	1	0	0	0	1	1	0
GJHM2046	Pelee Island, Lake Erie	Island	VIS	A	1	0	1	0	0	1	0
GJFL2931	Grand Lake, OH	Lake	VIS	A	18	0	17	0	18	18	15
DJQK5705	Lake Tahoe, CA	Lake	I R	A	1	0	1	0	1	1	1
EJAJ5900	Mono Lake, CA	Lake	VIS	A	13	0	13	12	13	13	9
EJJE3256	Mormon Lake, AZ	Lake	VIS	A	2	0	2	0	2	2	0
FJQA5310	Lake Pontchartrain, LA	Lake	I R	B	15	5	8	9	9	9	0
GHJN3549	Lake Weohyakapka, FL	Lake	VIS	A	2	0	2	0	2	1	0
HHBG5929	Little Inagua, West Indies	Island	VIS	A	1	0	1	0	0	0	0
HHDC2934	Isla Beata, Santa Domingo	Island	VIS	A	1	0	1	0	0	1	0
GGAP2751	Lago De Coatepeque, San Salvador	Lake	VIS	A	3	2	0	0	1	1	0
				Number:	77	9	61	21	59	65	27
				Percentage:			90%	31%	87%	96%	40%

We observed that at all times during the night, Channel 2 invariably had more land-water contrast than either Channel 4 or 5. At those times when Channel 2 had inadequate contrast, Channels 4 and 5 were even worse. This causes us to question the merit of the multichannel approach.

In the course of GLPS testing, computer execution time required for position determination was measured on a Sun Sparcstation 10. This included the time required to do the following:

- Upsample the GOES image 7X in lines and 4X in pixels.
- Compute the training mask. (See the lower-left window in Fig. 5.)
- Compute the mean and standard deviation for the enhancement transformation.
- Transform the upsampled GOES image into the enhanced image.
- Perform the matching using the Crosscorrelation (i.e., Maximum Average) algorithm.

The execution time naturally depends on the size of the landmark. For a nominal visible landmark (12 lines by 21 pixels) the total time is approximately 7 seconds. This time can be reduced by a factor of two by precomputing and storing the training mask.

8. SUBPIXEL ACCURACY STUDY

The main objective of this investigation was to determine whether the landmark position can be determined with subpixel accuracy. This is especially important in order to determine orbit and attitude parameters at night using IR channels. A collateral objective was to determine the validity of the upsampling process and the extent to which it reduces errors caused by spatial quantization of the landmark bitmap.

Landsat imagery was used to simulate GOES imagery. Because Landsat resolution is much greater than GOES (25 m compared to 1,000 m) the simulated imagery offered three important advantages over real GOES imagery:

- It can be translated very accurately in both directions in controlled GOES subpixel increments.
- The landmark perimeter can be defined with respect to the imagery with very great precision.
- An ideal upsampled GOES image is produced as a by-product of the simulation.

The block diagram in Fig. 6 shows all of the processes and data flow involved in the simulation study. The dashed box at the top is the GOES simulation. First, the Landsat image is blurred with a 41 x 41 moving average window corresponding to a 28 x 28 μrad detector. The blurred image is then downsampled by a factor of 5.71 to produce an image having 4 x 4 μrad spacing; this image will be called the "Natural" upsampled image. This image can be translated very accurately in increments of 4 μrad. This image is downsampled 7X in north-south and 4X in east-west using nearest neighbor resampling to produce the simulated GOES imagery having a line spacing of 28 μrad and a pixel spacing of 16 μrad.

The lower-right dashed box corresponds to the GOES Landmark Positioning System (GLPS). The first step is to upsample the simulated GOES imagery 7X north-south and 4X east-west to form what we call the "Derived" upsampled image. As in the GLPS, we use Cubic Convolution interpolation as described in Ref. 10. Either the Derived or Natural upsampled image can be processed with any one of the five different matching algorithms to compute the position offset relative to the landmark perimeter. In addition, we added the capability to interpolate to a fractional part of the 4 μrad spacing.

The dashed box at the lower left shows how the landmark boundary is obtained. An analyst traces around the perimeter of the full resolution (i.e., 25 x 25 m ground spacing) Landsat image. The resulting vertices are downsampled by a factor of 5.71 and rasterized to form the landmark boundary or bitmap used by the matching algorithms. The resulting landmark is accurate enough that its contribution to the error in position determination is negligible.

Figure 7 shows two sections of a Landsat image covering part of Florida acquired on February 22, 1995. The left image is Lake Apopka and the right one is Lake George, both in Landsat Band 2 (Green: 0.52–0.60 μm). The size, shape, and orientation of both lakes are almost perfect for GOES East visible landmarks. The outlines were traced out by the analyst using the full resolution image. The landmark outlines should contribute negligible error to the position determination because:

- The analyst traced the high-contrast land/water boundary using the same image used in the matching process (rather than a map).
- The image resolution is high (25 m/pixel) compared to the upsampled GOES spacing (143 m/pixel).

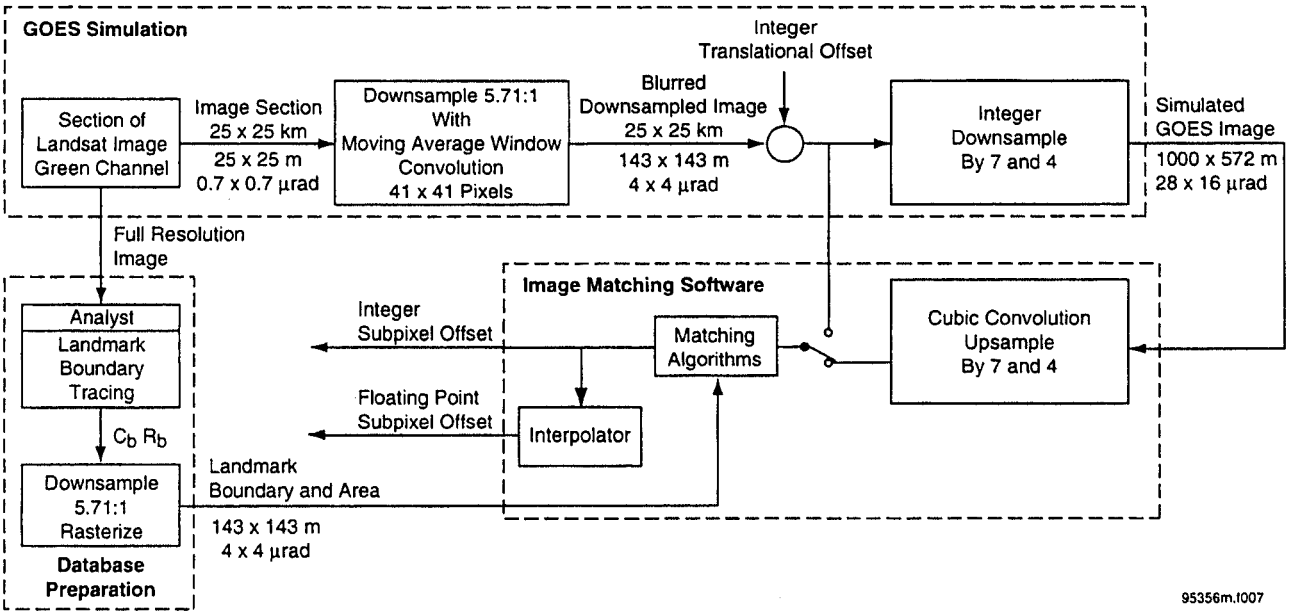

Figure 6. Block Diagram for Subpixel Accuracy Study

It is well known that a sampled signal can be reconstructed (i.e., its values computed at arbitrarily small spacing) from the samples if the Nyquist criterion[7] is satisfied. One of the objectives of the subpixel accuracy study was to investigate the validity of upsampling the GOES imagery. This was accomplished by comparing the Derived upsampled image with the Natural upsampled image; these are the two images on either side of the switch in Fig. 6. These two images are compared in two ways:

- Compare the gray-scale values on a pixel-by-pixel basis.
- Compare the position estimates obtained by processing each of them using the same matching algorithm; this is the meaning of the switch in the diagram in Fig. 6.

In Fig. 8 the upper-left window shows the Natural upsampled image for Lake George. It is a by-product of the simulation and is not available in the real GOES system. The upper-right window shows the Derived upsampled image formed by Cubic Convolution interpolation of the simulated GOES samples. A very detailed comparison of the two images is accomplished by subtracting one from the other; the lower-left window is the difference image. It can be seen that the Natural and Derived upsampled images are almost identical, differing only in regions having a lot of detail and contrast (i.e., areas where the Nyquist criterion is not satisfied).

The lower-right window shows the landmark outline superimposed on the enhanced image at the computed offset. The offset was computed using the Maximum Average (i.e., crosscorrelation) algorithm. By recalling that the lake is only approximately 12 km on a side, it can be seen that the fit is very accurate.

The overall objective of this study was to determine whether the GOES Landmark Positioning System (GLPS) is capable of subpixel accuracy. The approach described in Fig. 6 made it possible to control and know the correct offset of a simulated GOES image with an accuracy of 4 µrad. The estimated offset was computed to a fraction of 4 µrad using the GLPS software. The positioning error was found simply as the difference between the computed and correct positions.

The positioning errors given in Table 4 were evaluated for two different landmarks using both Natural and Derived upsampled images with three different matching algorithms. For each of the 12 combinations, error statistics were determined on the basis of eight trials (i.e., selected positions). The mean and standard deviation given in this table are measured in terms of upsampled pixels which are 4 µrad or 143 m. The results presented in this table support the following conclusions:

[7]The Nyquist criterion requires that the signal be sampled at a rate of at least twice the highest frequency present in the signal.

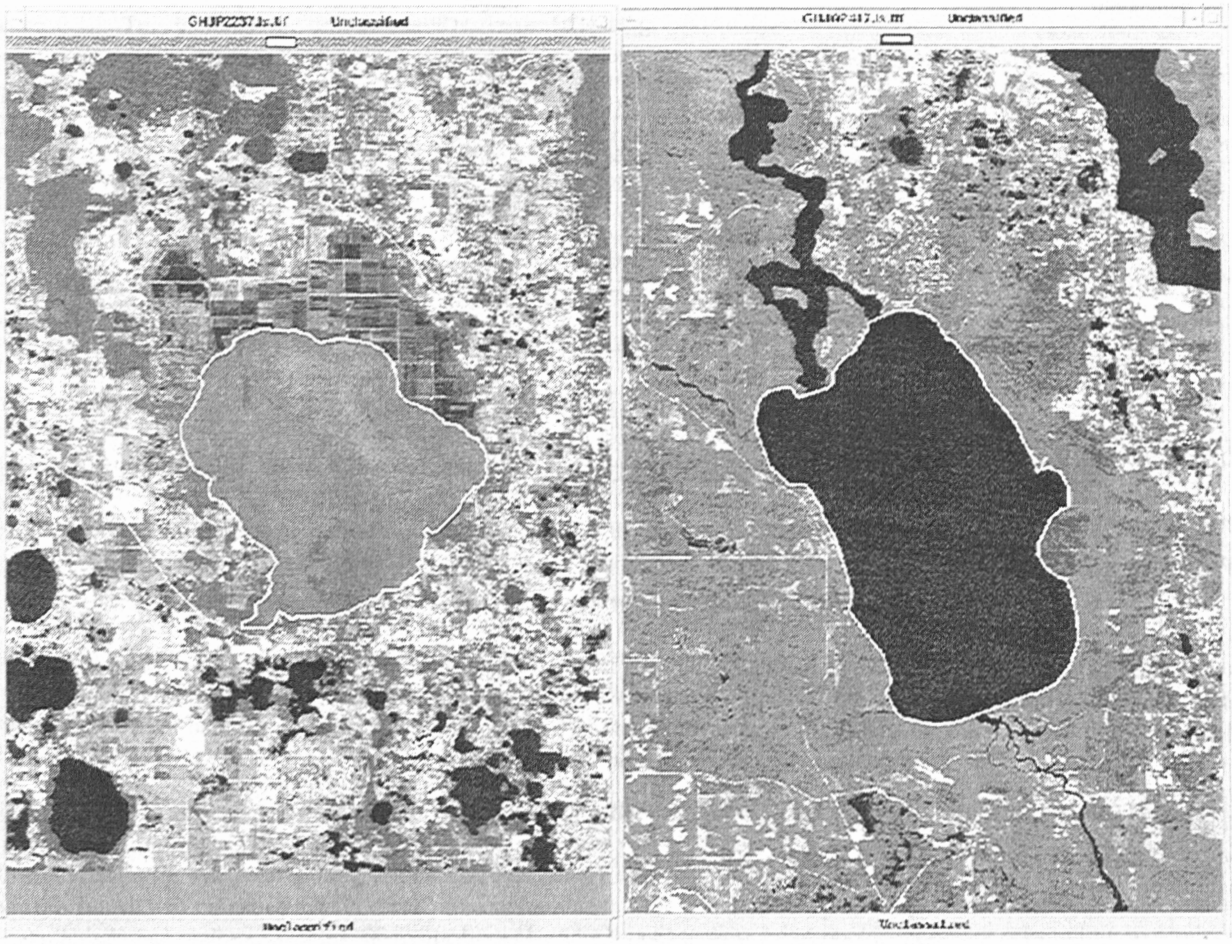

Figure 7. Sections of Landsat Image Used for Subpixel Accuracy Study

- The results obtained using Derived upsampled images (the ones used in GLPS) are only slightly less accurate than obtained using the ideal but unrealizable Natural upsampled images. The difference in standard deviations is always less than 2 μrad.
- As expected, the results using Crosscorrelation and Normalized Crosscorrelation (NCC) algorithms were almost exactly the same.
- The accuracy was slightly higher using either of the two Correlation algorithms than using Edge Matching.
- In all cases in which either correlation algorithm was used the mean and standard were always less than 4 μrad or 143 m in the visible channel.

It should be emphasized that these results apply to cases in which the landmark perimeters are almost perfect; i.e., these results do not include errors incurred in the real GLPS situation in which the landmark perimeters must be derived from cartographic source products.

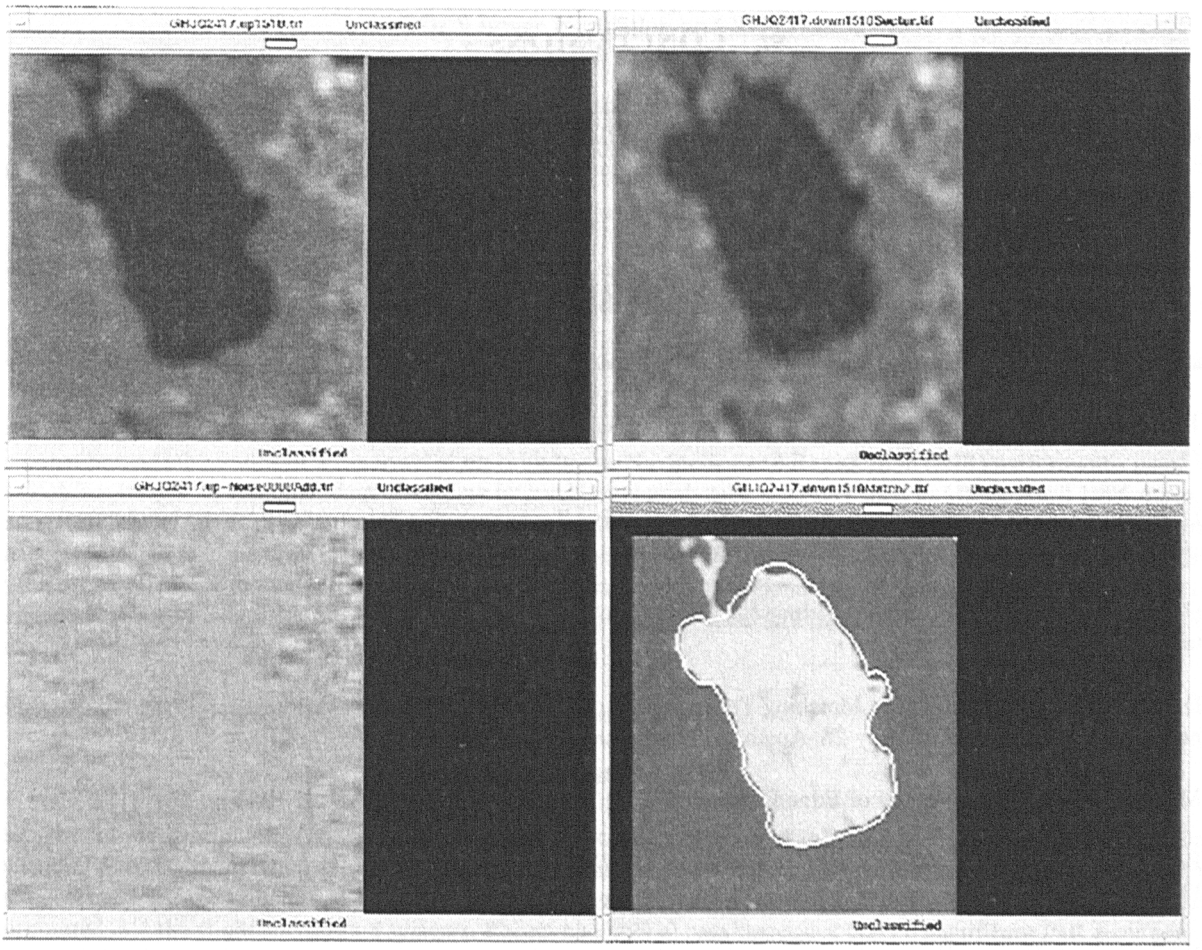

Figure 8. Results of Upsampling Analysis for Lake George

Table 4. Results of Subpixel Accuracy Study

Landmark	Upsampled Image	Statistic*	Matching Algorithm					
			Edge Matcher		Normalized Cross Correlation		Cross Correlation	
			Row	Column	Row	Column	Row	Column
GHJQ2417	Natural	μ	–1.77	–0.41	–0.04	0.08	–0.23	0.08
		σ	0.43	0.03	0.02	0.01	0.02	0.01
	Derived	μ	–1.08	–0.70	–0.24	0.10	–0.45	0.06
		σ	0.34	0.21	0.21	0.16	0.24	0.19
GHJP2237	Natural	μ	0.16	–0.80	–0.28	0.59	–0.45	0.01
		σ	0.23	0.60	0.16	0.11	0.14	0.03
	Derived	μ	–0.17	–0.18	–0.60	0.93	–0.81	0.13
		σ	0.64	0.13	0.36	0.33	0.40	0.30

*Errors are measured in units of 4 μrad or 143 m.

9. CONCLUSIONS

The overall conclusion of this study is that the position of a landmark in a GOES image can be determined automatically and reliably with subpixel accuracy. This is true for both visible and IR imagery under a wide range of acquisition conditions. The GOES Landmark Positioning System (GLPS) is well suited for operational use because a large number of landmarks are available worldwide.

10. REFERENCES

1. "Earth Location User's Guide," DRL504-11, Space Systems/Loral, September 30, 1994.

2. A. Kamel, "Image Navigation and Registration System," GOES-8 and beyond SPIE proceedings, Vol. 2812, August 1996.

3. C. D. Kuglin, A. F. Blumenthal, J. J. Pearson, "Map Matching Techniques for Terminal Guidance Using Fourier Phase Information," *SPIE*, vol. 186, Digital Processing of Aerial Images, 1979.

4. C. D. Kuglin, "Histogram-Based Algorithms for Scene Matching," *SPIE*, vol. 302, Infrared Technology for Target Detection and Classification (1981).

5. C. D. Kuglin, W. G. Eppler, "Map Matching Techniques for Use with Multispectral/Multitemporal Data," SPIE 24th Annual Technical Symposium, July 28–August 1, 1980, San Diego, California.

6. D. Marr and E. Hildreth, "Theory of Edge Detection," *Proc. Roy. Soc. Lon. B.*, vol. 207, 1980, p. 187-217.

7. G. Borgefors, "Distance Transformations in Digital Images," *Comput. Vision Graphics Image Process.*, vol. 34, 1986, p. 334-371.

8. D. Paglieroni, "A Unified Distance Transform Algorithm and Architecture," *Mach. Vision Appl.*, vol. 5, 1992, p. 47-55.

9. B. V. K. Vijaya Kumar, F. M. Dickey, J. M. DeLaurentis, "Correlation Filters Minimizing Peak Location Errors," *J. Opt. Soc. A.*, vol. 9, No. 5, May 1992.

10. R. Burnstein, "Digital Image Processing of Earth Observation Sensor Data," *IBM Journal of Research and Development*, January 1976.

GOES Image Navigation and Registration On-Orbit Performance

William C. Bryant, Jr.
Sanford Ashton
Gus Comeyne III
Douglas A. Ditillo

Swales & Associates, Inc.
Beltsville, MD 20705

ABSTRACT

This paper presents the results of an analysis of on-orbit Image Navigation and Registration (INR) performance using GOES-8 and GOES-9 Imager operational data. Two time intervals were analyzed: a 35-day span in March/April 1996 during eclipse season and a 35-day span in May/June 1996. These data were used to derive the performance of each specified INR parameter and then compared to its performance requirement. Significant sources of INR error discovered on-orbit and the methods adopted to reduce their effect are discussed. The study results confirm that the operational use of Short Span Attitude Adjusts (SSAAs) is critical to achieving acceptable INR performance. Also shown is that landmark measurement errors currently limit the ability to adequately assess INR performance.

Keywords: GOES, navigation, registration, orbit, attitude, landmarks

1. INTRODUCTION

After years of preparation, the GOES-8 spacecraft was launched in April 1994 followed by GOES-9 in May 1995. One of the challenging features of this new generation of GOES spacecraft was the stringent performance requirements of the INR system.[1] Three years of INR operations experience have been accumulated with two spacecraft and a host of improvements have been incorporated into the flight and ground systems. Recent operational results suggest that all significant INR error sources have been identified, the corrective measures adopted to date have been successful, and the system is currently providing stable INR performance within acceptable levels. The objective of this paper is to quantify the current status of INR performance with all existing improvements in place.

2. PERFORMANCE REQUIREMENTS

The Imager INR performance specifications are given in Table 2.0-1. Sounder INR performance is not addressed in this paper. The specifications are 3-sigma values and apply equally to the East-West (EW) and North-South (NS) scan directions. "Day" refers to the period ±8 hours about spacecraft local noon and "night" refers to ±4 hours about spacecraft local midnight (GOES-8 local midnight is 0500 UTC and GOES-9 is 0900 UTC). Note that these requirements were originally defined for GOES orbits maintained within 0.1° inclination. On-orbit, all GOES spacecraft are being maintained within 0.5° inclination to reduce the number of disruptive NS stationkeeping maneuvers from 6/year to 1/year. Operational experience has verified that the higher 0.5° inclination is not an important source of INR error. Consequently, the performance results presented here, which include data for inclinations well above 0.1°, are compared to the nominal 0.1° specification.

Following is a brief discussion of each specified parameter in Table 2.0-1.

Navigation. This requirement specifies absolute knowledge of the location of Imager pixels relative to the Earth. The requirements of 4 km (day) and 6 km (night) are defined at spacecraft nadir. This is equivalent to an angular requirement of 112 microradians (day) and 168 microradians (night). At Earth locations other than nadir, the equivalent navigation requirement in terms of kilometers increases with the angular distance from nadir. For reference, equivalent navigation requirements are summarized in Table 2.0-2.

TABLE 2.0-1 INR PERFORMANCE REQUIREMENTS

INR Parameter EW and NS	Specifications. (3σ)	
	Day	Night
Navigation Nadir (km)	4	6
Within Frame Registration (μrad)	42	42
15 Min Frame-Frame Registration (μrad)	42	70
90 Min Frame-Frame Registration (μrad)	84	105
24 Hr Frame-Frame Registration (μrad)	168	168
48 Hr Frame-Frame Registration (μrad)	210	210
Visible/IR Coregistration (μrad)	28	N/A
IR/IR Coregistration (μrad)	28	28

TABLE 2.0-2 NAVIGATION REQ'TS

Angle from Earth Nadir	Navigation (Km)	
	Day	Night
0°	4	6
30°	5	7.5
40°	6	9
50°	8	12
60°	11.8	17.6

Within Frame Registration (WIFR). The WIFR requirement limits the deviations from the nominal separation between any two pixels within the same image.

Frame-to-Frame Registration (FFR). The four FFR requirements limit the movement of the same pixel for repeated frames within 15 minutes, 90 minutes, 24 hours, and 48 hours. Of these, the 15 minute and 90 minute are the most critical to quantitative users, e.g., for the determination of wind velocities from frame-to-frame cloud motion. The 48 hour requirement is redundant to the navigation requirement and was not included in this analysis.

Coregistration. This requirement limits the relative separation between the visible channel and a reference IR channel and the relative separation between all IR channels. The IR/IR coregistration performance was measured during postlaunch testing for both spacecraft and found to be within specification. This parameter is not routinely trended and will not be discussed further in this paper. The visible/IR coregistration performance cited here is the error remaining after a correction is applied in the INR ground system. This ground correction does not, in actuality, adjust visible/IR alignment but rather provides a coregistration offset in the transmitted Imager data as information to the users.

3. ON-ORBIT EXPERIENCE

The launch of GOES-8 made possible the first accurate assessment of the INR system performance because a comprehensive, end-to-end test of all system elements was not possible on the ground. Most of the critical INR system elements, many unique to the GOES INR system, performed as expected. Principal among these were: use of the Image Motion Compensation (IMC) system, which applies compensation signals generated onboard to the instrument scan mirror gimbals, to correct GOES images for the apparent orbit and attitude motion; use of the Mirror Motion Compensation (MMC) system for pointing errors caused by rigid body coupling between the spacecraft body and the instrument scan mirrors; successful star detection by the Imager and Sounder instruments; diurnal repeatability of spacecraft/instrument system attitude and thermal profiles;[2] within allocation pointing performance of the instrument scan mirrors; spacecraft short term pointing within allocations; minimum structural

interactions between the instrument scan mirrors, momentum wheels, and Earth sensor scan mirror; and the ability to compute accurate orbit and attitude solutions on the ground using landmarks, stars, and range data.

A number of unexpected errors, however, became evident on-orbit, which adversely impacted initial INR performance. These errors are summarized in Table 3.0-1. Most involve spacecraft attitude stability in general and the Earth sensor in particular. Over the past 2 years, a number of corrective measures have been implemented to improve INR performance by removing or correcting for these unexpected errors. Critical to the success of this effort were several innovative flight software changes implemented by Space Systems/Loral (SS/L). These modifications provided the onboard capability to use the IMC system to compensate for several of the significant attitude errors and also improved spacecraft attitude pointing jitter and day-to-day repeatability performance.

TABLE 3.0-1: GOES INR ERROR SOURCES

Error Source	Correction Method	Uncompensated 0 - Peak (μrad)		After Compensation 0 - Peak (μrad)		Start Time	Duration	Frequency
		EW	NS	EW	NS	(SLT)	(Hrs)	(Days/Yr)
ES Non-Repeatability	SSAA	400	400	100	100	Continuous	Continuous	365
ES Batwing (GOES-8)	SMC	1300	650	200	150	22:30	3.0	160
ES Winglet (GOES-9)	N/A	100	50	N/A	N/A	22:30	3.0	160
ES Single Chord	SCC	800	600	100	200	Variable	3.0 - 4.0	250
ES Dual Chord Transition	N/A	100	800	N/A	N/A	Variable	0.3	250
ES Bevel (GOES-8)	Single Chord	100	50	0	0	22:30	3.5	120
ES Bevel (GOES-9)	Single Chord	200	100	0	0	22:30	3.5	120
Boom Shadowing	SMC	0	250	N/A	N/A	14:30	0.5	210
Eclipse Exit	N/A	200	200	N/A	N/A	01:00	0.3	90

FIGURE 3.0-1 GOES INR EVENTS TIMELINE

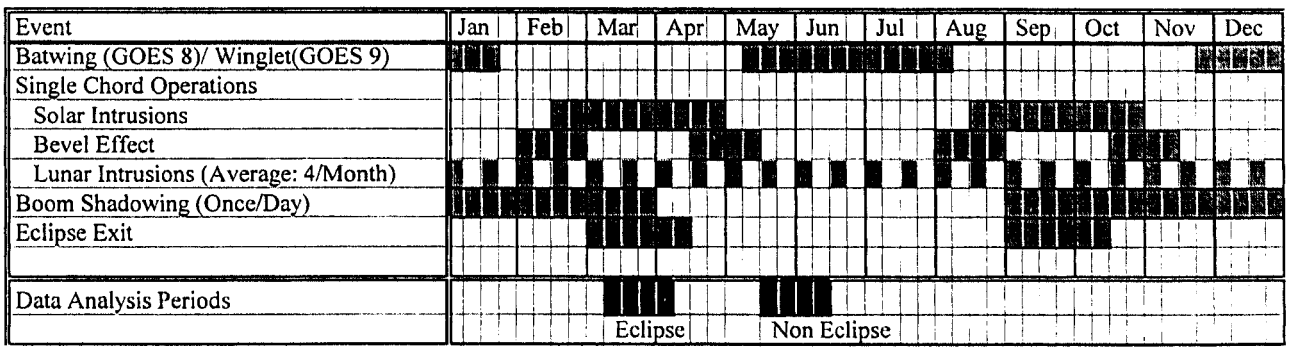

Figure 3.0-1 shows a timeline depicting when each of the various errors occurs. The data spans used in this analysis are also indicated. A brief discussion of each of the items in Table 3.0-1 follows:

ES Non-Repeatability. Non-repeatability of spacecraft nadir pointing performance is the most persistent source of large INR errors. The cause has been isolated to variations in the Earth's radiance near the limbs which result in roll and pitch pointing errors as seem by the IR horizon scanning ES.[3] As a result there are nearly continuous spacecraft pointing errors relative to nadir. This phenomenon was predicted prior to launch and design changes were made to the ES to reduce its effect. On-orbit experience, however, demonstrates that the magnitude of the effect is 5 times larger than predicted. Only continuous ground monitoring by the NOAA operators and constant use of the Short Span Attitude Adjust (SSAA) capability in the INR ground system has maintained INR performance within acceptable levels in the presence of this large, unpredictable disturbance.[4]

GOES-8 ES Batwing. GOES-8 experiences large attitude errors around spacecraft local midnight near the summer and winter solstices. This effect is caused by off axis solar energy inadvertently reaching the ES bolometers through an alignment hole in the ES telescope housing. The shape of the resulting disturbance led to its designation as "batwing." SS/L developed a correction scheme, Spacecraft Motion Compensation (SMC), which uses on-orbit data to characterize the batwing error as a function of solar declination and right ascension. SMC tables are uploaded daily and mirror compensation signals are generated in real-time and added to the IMC signal. This was the first of several correction schemes which use the IMC capability of the GOES spacecraft to correct for attitude variations. SMC has been successful in significantly reducing GOES-8 batwing errors.

GOES-9 ES Winglets. When the source of the GOES-8 batwing was isolated to the alignment holes, the GOES-9 ES alignment holes were potted prior to launch. It became apparent on-orbit, however, that the potting compound had not been totally successful in eliminating the stray solar energy. The resulting residual batwing, dubbed "winglet," also occurs near spacecraft local midnight but is much reduced in magnitude compared to the GOES-8 batwing. At the time of this paper, a correction scheme for the winglet effect has not been implemented.

ES Single Chord. To determine the roll and pitch signals needed by the spacecraft control system to maintain nadir pointing, the ES makes continuous north and south Earth chord measurements.[5] When the sun or moon intrudes into one of the two chords, that chord must be "inhibited" via ground command to prevent erroneous roll and pitch outputs. This is designated ES single chord mode (as opposed to the normal dual chord mode). On-orbit it was found that differential thermal distortions internal to the ES and the GOES orbit eccentricity produced systematic spacecraft attitude errors during single chord operations. Three compensation methods were developed. An autonomous onboard algorithm senses and corrects the random pitch error. A second algorithm corrects the deterministic orbit eccentricity effect. A third onboard algorithm uses Single Chord Compensation (SCC) coefficients, generated on the ground and uplinked periodically, to correct the roll thermal distortion error. All of these schemes have significantly improved INR performance during single chord events.

ES Dual Chord Transition. After a solar or lunar intrusion ends, the ES is commanded back to dual chord mode from single chord mode. This results in a step response to the spacecraft control system producing a roll transition error which persists for 10-15 minutes. Pending development of a compensation method, imaging is normally prohibited immediately following a return to dual chord.

ES Bevel. This effect is caused by a solar reflection off a beveled element internal to the ES. The effect lasts a few hours around midnight for a few weeks just prior to and following each eclipse season. This effect can be eliminated by inhibiting the proper ES chord. This approach has eliminated the ES bevel as a source of INR error, substituting compensated single chord errors.

Boom Shadowing. Another effect which occurs on both GOES-8 and GOES-9 is a large roll (NS) transient at the same time each day for about 7 months of the year. This error is the result of shadowing of the spacecraft solar sail boom by the magnetometer boom. The solar sail boom temporarily deforms causing a corresponding response in spacecraft roll/yaw attitude which persists until the magnetometer boom shadow has passed by the solar sail boom. A compensation method for this transient effect is still in development.

Eclipse Exit. Immediately following exit from eclipse, the pointing of both spacecraft undergoes rapid short term oscillations followed by more persistent long term disturbances. Both are apparently due to the rapid solar heating of the spacecraft and ES. It has not been possible to fully characterize post eclipse pointing of the instrument/spacecraft system due to the Imager solar keepout zones which preclude Imager operations for a period following exit from eclipse. No correction method for the post eclipse period has been defined to date.

The "after compensation" column in Table 3.0-1 contains representative residual errors when each effect is considered separately. On-orbit there are infrequent occasions when degraded INR performance is the result of two events occurring simultaneously. For example, lunar intrusions which occur during batwing degrade the SMC correction which is based on ES dual chord operation. Another example is a lunar intrusion during the ES bevel period which precludes inhibiting the appropriate chord to eliminate the bevel effect.

4. ANALYSIS

4.1 INR Data Processing

Measurements. Three types of observations are collected in support of routine INR operations for GOES - range, star, and landmark. Range and star observations are processed autonomously by the ground system to produce measurements suitable for subsequent orbit and attitude determination. Landmark measurements, however, require a human operator to identify geographic features in recorded images. Currently, the resolution of landmark measurements is limited to 1 pixel (visible channel - 28 μrads NS and 16 μrads EW and IR channel 2 - 112 μrads NS and 64 μrads EW).

Predictions. Figure 4.1-1 shows a representation of the INR prediction process. Each day a new orbit and attitude prediction is generated based upon all three types of measurements from the previous two days. The process begins by fitting an orbit and attitude estimate to the measurements. This fitting process produces residual errors which are called OAD (Orbit and Attitude Determination) fit residuals. The resulting orbit and attitude is then propagated forward for the next day. The resulting orbit and attitude prediction is called the parent set prediction. This parent set becomes the basis for all predictions for the next day as well as the basis for all IMC sets to be used for the next day. As real-time measurements are collected during routine operations throughout the day, the attitude prediction may be updated. These updates (SSAAs) modify the current IMC set on the spacecraft as well as the prediction resident in the ground system. Typically, the SSAA is a static bias to the roll, pitch, and yaw predictions.

FIGURE 4.1-1 : INR DATA FLOW

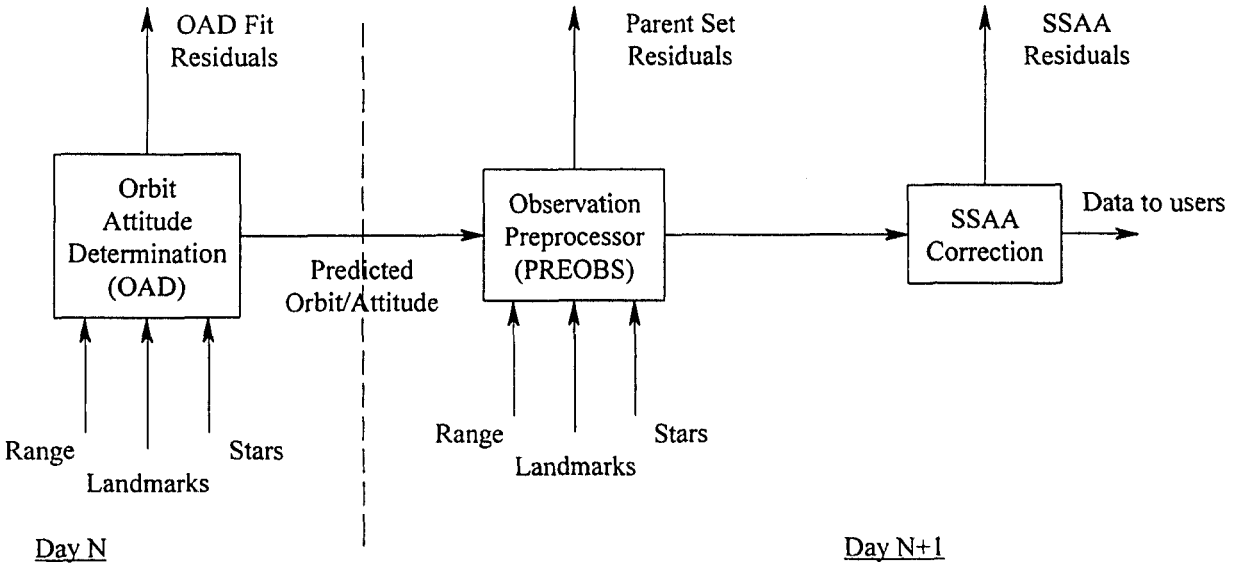

Residuals. As described here, measurement residuals are the difference between actual and expected measurements based on some orbit and attitude estimate. From each set of observations there are three types of residuals - SSAA residuals, parent set residuals, and OAD fit residuals. The first two types of residuals are predictive, based on an orbit and attitude estimate generated from an earlier set of measurements and applied to an ensuing set of measurements. In contrast, the third type is not predictive.

The OAD fit residuals indicate the ability of the orbit and attitude model to fit a given set of measurements.

The first type, SSAA residuals, are determined in real-time for all three observation types. These residuals consist of comparisons between the current measurements and the current prediction. Prior to enabling any SSAAs, the parent set is the current prediction. After an SSAA has been enabled, the SSAA replaces the parent set as the current prediction. (Typical SSAAs, which do not modify the orbit, have no effect on range residuals.)

The second type, parent set residuals, are always the difference between the current measurements and the parent set prediction. As stated before, prior to enabling any SSAAs, the parent set is the current prediction. As a result, prior to enabling any SSAAs, the SSAA residuals and the parent set residuals are the same. After an SSAA is enabled, however, the two sets of residuals calculations differ. The parent set residuals are always a reference back to the initial prediction.

The third type of residuals, OAD fit residuals, have already been described above. They describe the fitting error after completion of the orbit and attitude estimation process.

Each of the three types of residuals have a unique significance. The SSAA residuals are always based on the current prediction. As a result, they are representative of the quality of the products seen by the users. The parent set residuals capture the behavior of the system if there were no SSAA updates to the original parent set prediction. Consequently, they can be used for comparison purposes to evaluate the corrective effects of the SSAAs. Finally, the OAD fit residuals can be interpreted as the best possible performance which can be obtained with the current modeling and processing techniques because they involve no prediction errors.

4.2 Analysis Methodology

The INR performance assessment in this paper addresses four broad categories - navigation, frame-to-frame registration, within-frame registration, and channel-to-channel coregistration. In order to best characterize the performance seen by the users, SSAA residuals for landmarks are used for two main reasons. First, the SSAA residuals reflect the current prediction which is being used to earth locate the images. Second, landmark measurements are employed because they are extracted from the same data stream which delivers the image products to the users.

The performance assessment for all four categories listed above is derived from the SSAA residuals for landmarks. As applicable, the data are separated by spacecraft (8/9), by type (EW/ NS), by channel (visible/ IR), and by time of day (day/night). Assessment of navigation performance, a measure of the absolute accuracy of the system, proceeds directly from the landmark residuals with no supplemental processing required. Each landmark observation produces an EW and a NS navigation measurement.

Frame-to-frame registration, a measure of the precision of the system, has requirements for 4 different time periods - 15 minutes, 90 minutes, 24 hours, and 48 hours. For purposes of this analysis, a FFR measurement consists of a comparison between two observations of the same landmark separated by one of the specified time periods (with tolerances of ±5 minutes, 15 minutes, 1 hour, and 1 hour, respectively). The calculation is simply the difference between the navigation residuals for the same landmark in two different images. Therefore, every pair of observations of the same landmark which has the proper time spacing generates an EW and a NS FFR measurement. Each landmark may be used twice to evaluate each time period requirement - once as the first landmark in a pair and once as the second landmark in a different pair. Also, each landmark may be used to generate a measurement for any or all of the four time periods if appropriate observations exist.

For this analysis, determination of WIFR performance requires identifying which landmark observations occur in the same image. The WIFR measurements are then determined by taking all of the pair-wise combinations of landmarks within the frame. (Visible landmarks are not paired with IR landmarks, however.) Similar to the FFR measurements, the measurement is the difference between the navigation residuals for the pair of landmarks. Therefore, every pair of landmarks (in the same channel), within a single frame, produces an EW and a NS WIFR measurement. With this approach, individual landmark observations typically contribute to multiple WIFR measurements. Also, landmark observations which appear alone in a frame do not contribute to any WIFR measurements. Although there is a slight relaxation of the WIFR requirements for single chord periods, the analysis presented here combines single chord and normal mode performance into one statistic which is compared with the nominal ±42 microradian requirement.

The coregistration assessment is based on comparing aggregate navigation results for visible and IR landmarks. Specifically, the mean EW and NS navigation errors for the two groups of data were differenced.

4.3 Results

A summary of the results is presented in Table 4.3-1 for the non-eclipse time period. The eclipse results were similar and are not tabulated here. The summary includes both the standard deviation (STD) and the mean for each performance measurement. In several cases, particularly IR navigation, the bias in the data is large compared to the standard deviation. For this reason, both values have been included. As data are presented for each requirement, the statistical results in the table will be presented graphically to indicate the bias in the data and show its impact on compliance with the requirements.

TABLE 4.3-1: IMAGER INR ON-ORBIT PERFORMANCE SUMMARY

		On-Orbit Performance (non-eclipse period)							
		GOES-8				GOES-9			
		Day		Night		Day		Night	
		Mean	STD	Mean	STD	Mean	STD	Mean	STD
Navigation	EW	-0.2	1.3	-1.5	1.6	-0.6	1.2	-2.2	1.8
Nadir (Km)	NS	0.2	1.7	0.6	2.3	0.4	1.3	0.8	2.1
Within Frame	EW	-2	30	17	58	-8	29	-13	61
Registration (μrad)	NS	-5	55	17	78	-8	32	-14	71
15 Min Frame-Frame	EW	1	17	1	35	0.00	17	1	37
Registration (μrad)	NS	-1	23	0.00	44	0.00	20	0.00	49
90 Min Frame-Frame	EW	4	27	2	44	1	30	1	45
Registration (μrad)	NS	-1	29	2	57	-2	34	9	60
24 Hr Frame-Frame	EW	-8	47	0.00	54	-2	42	1	58
Registration (μrad)	NS	3	47	-4	79	-1	45	-4	72
48 Hr Frame-Frame	EW	-9	43	-3	58	-5	46	5	59
Registration (μrad)	NS	2	53	-11	78	-1	54	-3	82
Visible/IR	EW	-30	N/A	N/A	N/A	-43	N/A	N/A	N/A
Coregistration (μrad)	NS	16	N/A	N/A	N/A	15	N/A	N/A	N/A

Navigation. Navigation results for a five week period from 14 May 1996 until 18 June 1996 are shown in Figures 4.3-1 through 4.3-4. All of the SSAA residuals for landmarks are plotted versus time of day with the day/night specification included for reference. For clarity, each spacecraft is depicted separately with GOES-8 results appearing in Figures 4.3-1 and 4.3-2 and GOES-9 results in Figures 4.3-3 and 4.3-4. The data shown in Figures 4.3-5 and 4.3-6 are also for GOES-9, but cover an earlier five week period within the spring eclipse season (5 March 96 - 9 April 96).

FIGURE 4.3-1: GOES 8 EW

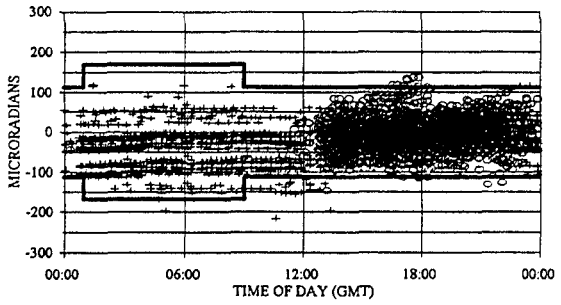

FIGURE 4.3-2: GOES 8 NS

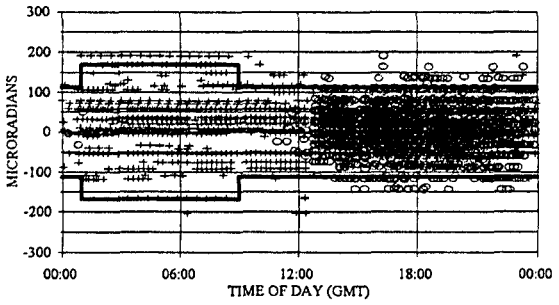

FIGURE 4.3-3: GOES 9 EW

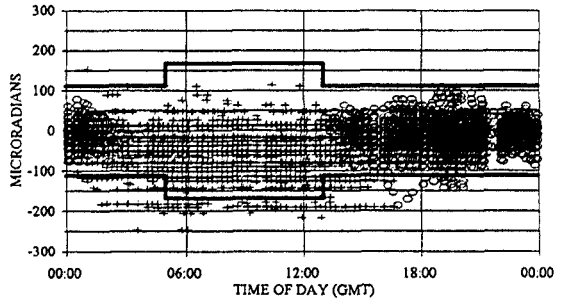

FIGURE 4.3-4: GOES 9 NS

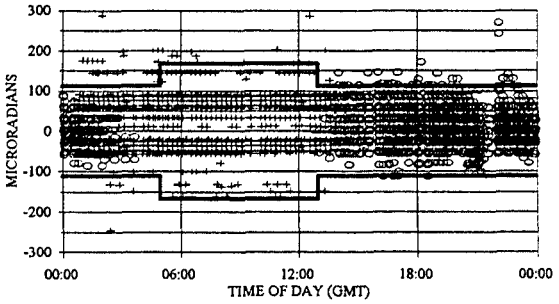

FIGURE 4.3-5: GOES 9 EW ECLIPSE

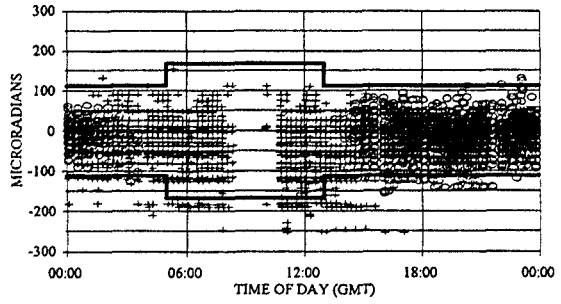

FIGURE 4.3-6: GOES 9 NS ECLIPSE

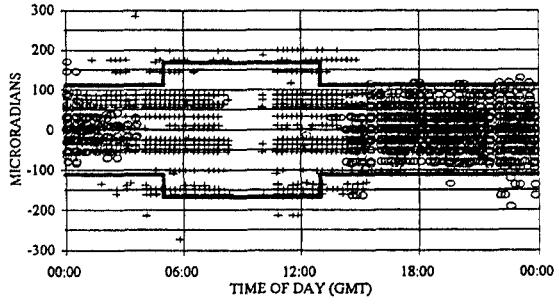

o VIS + IR _ SPEC

There are several features to note on these plots. The frequency of visible landmark observations is greater than that of IR landmarks by a factor of 1.5 - 2 due to the increased difficulty in identifying geographic features in the IR images. The transition from visible to IR landmarks is rather distinct, particularly for GOES-8. For both spacecraft, the IR landmarks extend into the day hours as defined by the specification. A brief data outage, associated with the IMC upload and enable, near 2130 UTC is seen in Figures 4.3-3 and 4.3-4. The corresponding gap for GOES-8, which occurs near 0030 UTC, is less noticeable because it coincides with the less frequent IR observations. Several of the plots exhibit obvious quantization effects. This is caused by the single pixel resolution of the landmark measurement system. The quantization is more obvious in the IR data because of the lower (by a factor of 4) resolution. Figures 4.3-5 and 4.3-6 clearly show the blackout period associated with eclipse operations centered around 0900 UTC for GOES-9 located at 135° W longitude. There is also an apparent EW shift between visible and IR data for both spacecraft. This will be discussed later as a coregistration issue. Otherwise, the performance during eclipse is indistinguishable from the non-eclipse period.

Figures 4.3-7 and 4.3-8 show a statistical summary of the data presented in Figures 4.3-1 through 4.3-6. Data for GOES-8 during eclipse is also summarized although a corresponding plot is not included. Each bar represents a data distribution with the height of the bar indicating ±3 standard deviations from the mean, indicated by a tick mark on the midpoint of the bar. Figure 4.3-7 shows all the visible data compared to the day specification. As noted before, there are many IR observations made during the hours corresponding to the day specification, but these have been excluded from the statistical summary to prevent the lower resolution IR observations from corrupting the statistics derived from the visible landmarks. Figure 4.3-8 shows the IR observations obtained during the night hours only, compared to the night specification.

FIGURE 4.3-7: NAVIGATION (VIS)

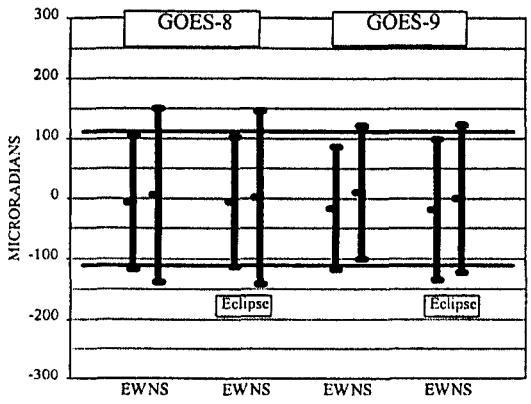

FIGURE 4.3-8: NAVIGATION (IR)

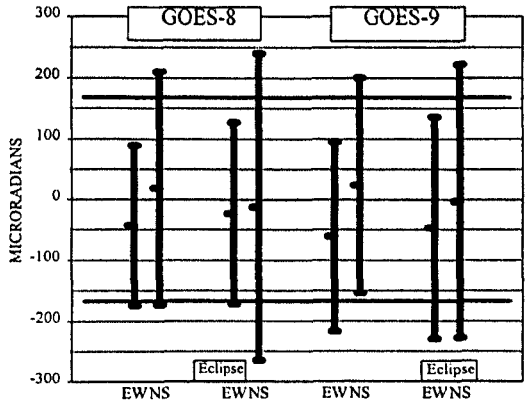

For the non-eclipse period, most of the visible results are very close to meeting specification, with the GOES-9 results somewhat better than the GOES-8 results. The GOES-8 NS results are the sole exception. The effect of the eclipse is expected to be most noticeable during the night hours closest to the actual eclipse event. In fact, no degradation can be detected for GOES-8. GOES-9 exhibits more sensitivity to the eclipse, however, its EW performance is still comparable to GOES-8 and the NS performance remains better.

For the non-eclipse period, the distribution of the EW IR results is narrow enough to satisfy the requirements, however, there is an apparent EW bias (see Coregistration section below) which distorts the results. Unlike the visible results, the EW results for GOES-8 are actually better than the GOES-9 results. More typically, the NS results for GOES-9 are better than GOES-8, although neither set of results satisfies the requirements. As expected, the effect of eclipse operations is more noticeable in the night IR data.

Within-Frame Registration (WIFR). WIFR results for the five week (non-eclipse) period 14 May through 18 June are shown in Figures 4.3-9 through 4.3-12. Statistical summaries, with eclipse results added, are provided in Figures 4.3-13 and 4.3-14. Although there is no change in the specification for day and night results, the convention of separating visible from IR data was followed. Both the raw data and the statistical summaries show that these measurements do not meet specification. However, it

WITHIN FRAME REGISTRATION

FIGURE 4.3 - 9: GOES-8 EW

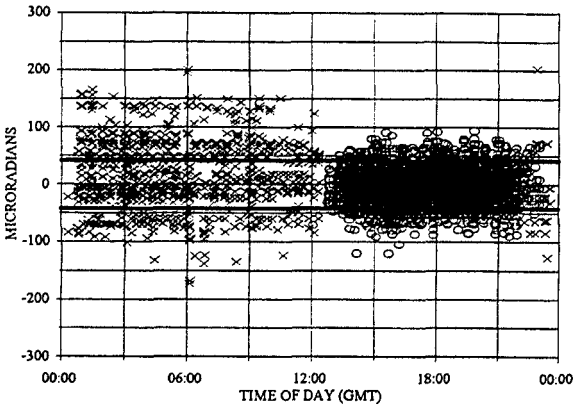

FIGURE 4.3 - 10: GOES-8 NS

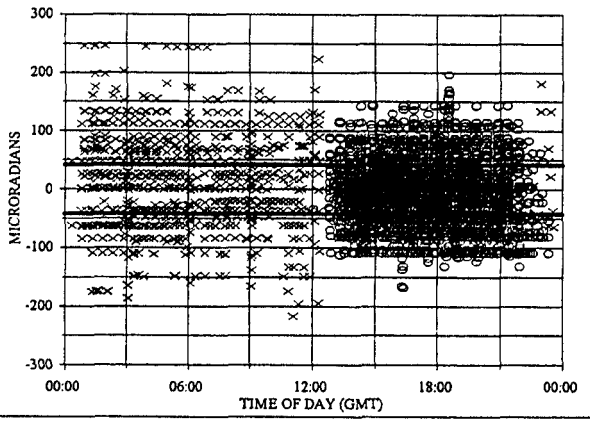

FIGURE 4.3 - 11: GOES-9 EW

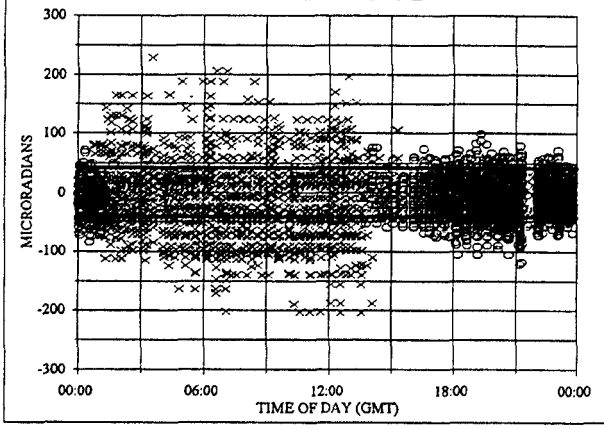

FIGURE 4.3 - 12: GOES-9 NS

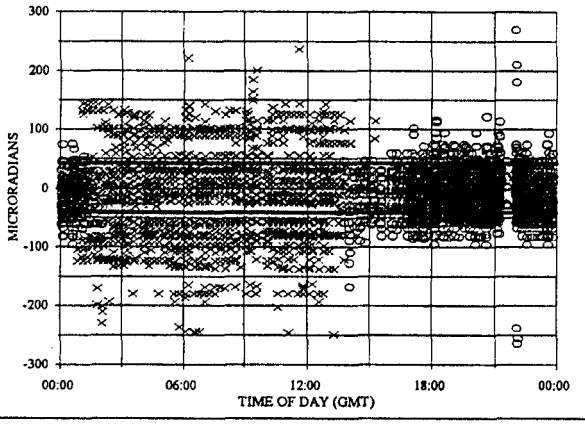

o VIS x IR _SPEC

FIGURE 4.3 - 13: VIS SUMMARY

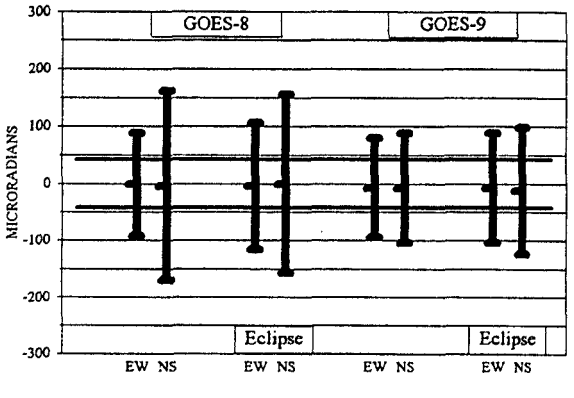

FIGURE 4.3 - 14: IR SUMMARY

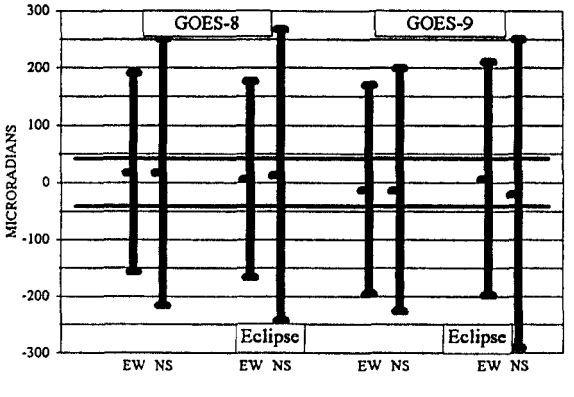

is expected that systematic biases associated with each landmark play a very significant role in degrading this particular performance measurement. The effect of systematic landmark biases is most significant in this analysis because WIFR measurements require pairing different landmarks which have their own unique systematic bias. Compared to the navigation analysis, the effect is worse because each measurement combines two navigation results. The FFR analysis is unaffected by these biases because FFR results compare the same landmark so that the systematic bias cancels. As discussed below, the 15 minute FFR results are a better indicator of the actual WIFR performance.

Frame-to-Frame Registration (FFR). As described earlier, there are four separate FFR specifications. The quantization is most pronounced in the FFR data. Although there is some quantization in the navigation data, it is not as distinct as in the FFR results. If navigation results for an individual landmark were plotted, they would show very distinct quantization with some nominal systematic bias. When many different landmarks are overlaid, each with its own bias, the results begin to show a more uniform distribution. The same argument applies to the WIFR measurements. However, the FFR measurements are generated by differencing observations of the same landmark so the bias always cancels. The result is that all of the FFR measurements clearly show the quantization effects.

The results for the 15 minute requirement are shown in Figures 4.3-15 through 4.3-18 followed by statistical summaries in Figures 4.3-19 and 4.3-20. The most striking feature in the results is that the NS IR quantization level exceeds the night specification. Also, both EW and NS IR quantization levels exceed the day specification which applies to many of the IR measurements. From this it is apparent that the quantization in the landmarking process is obscuring the true system performance. Notice also that there are several anomalous data points for GOES-8 NS near 1900 UTC. These points are associated with the boom shadowing effect.

The EW visible FFR results are close to meeting the 15 minute requirement, whereas the NS results are somewhat worse. As might be expected from the ratio of the IR quantization to the requirement, the IR results far exceed the requirements.

The 15 minute FFR results span a time period comparable to the span covered by the WIFR results. The only error contributors which differ between the two sets of performance measurements are those which are scan angle dependent. These include spacecraft yaw errors, instrument thermal misalignment errors and fixed pattern scan mirror pointing errors. The yaw and misalignment errors would have to be large to have a significant contribution on the landmark observations. The fixed pattern errors measured prior to launch are less than 10 μrads. (Another potential difference would be when an SSAA occurred between frames, but this impacts a small portion of the data.) The conclusion is that the vast difference between the WIFR results and the 15 minute FFR results is due to the systematic landmark biases. (A preliminary analysis involving individual pairs of WIFR results supports this conclusion.) Therefore, systematic biases are distorting the WIFR results. Consequently, the 15 minute FFR results are a better indicator of the true WIFR performance.

The 90 minute FFR results are shown in Figures 4.3-21 through 4.3-24 with statistical results shown in Figures 4.3-25 and 4.3-26. The non-eclipse visible results for both spacecraft are very close to satisfying the performance requirements. Again, the NS IR quantization levels exceed the requirement with the expected adverse effect on the statistics. The EW quantization level is still a very significant portion of the specification, so the EW IR results also exceed requirements.

The 24 hour results are shown in Figures 4.3-27 through 4.3-30 with statistical results shown in Figures 4.3-31 and 4.3-32. All of the visible data satisfies the requirements. The EW IR data satisfies the specification for GOES-8 and is very close for GOES-9. The NS IR data still exceeds the requirements, but again, the NS IR quantization is still a large portion of the requirement.

FRAME - FRAME REGISTRATION (15 MINS)

FIGURE 4.3-15: GOES-8 EW

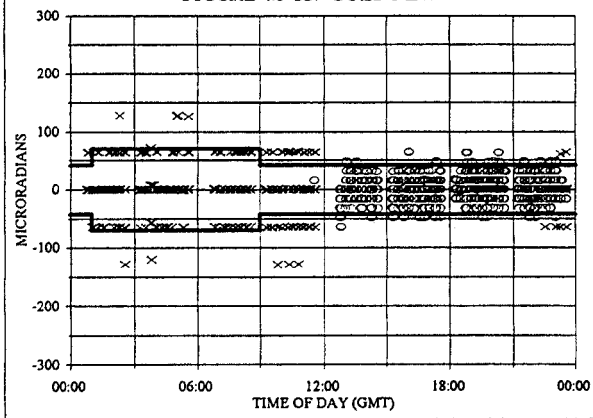

FIGURE 4.3-16: GOES-8 NS

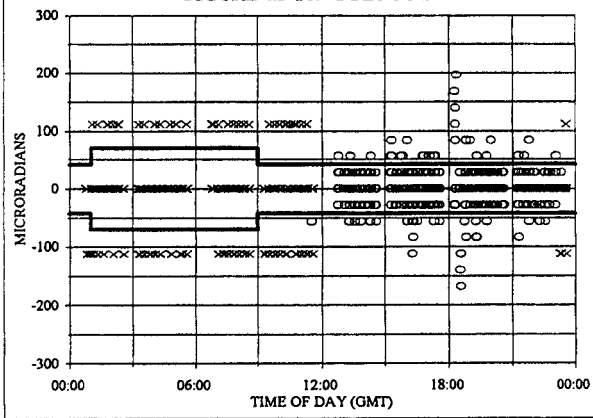

FIGURE 4.3-17: GOES-9 EW

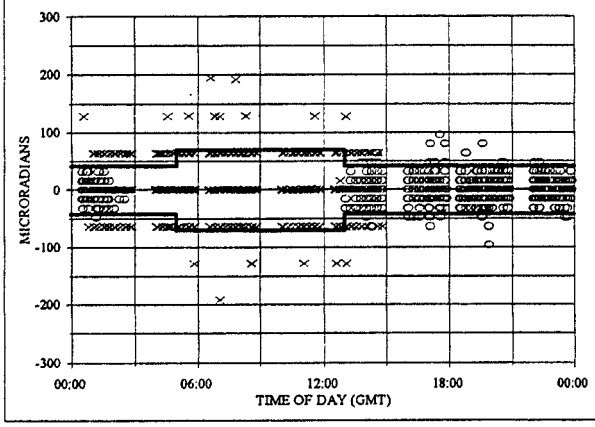

FIGURE 4.3-18: GOES-9 NS

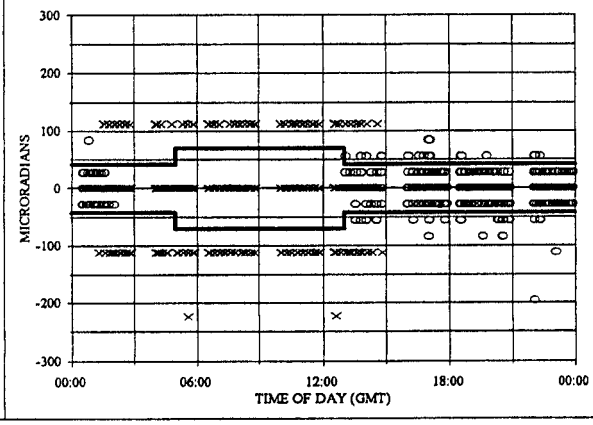

o VIS x IR _ SPEC

FIGURE 4.3-19: VIS SUMMARY

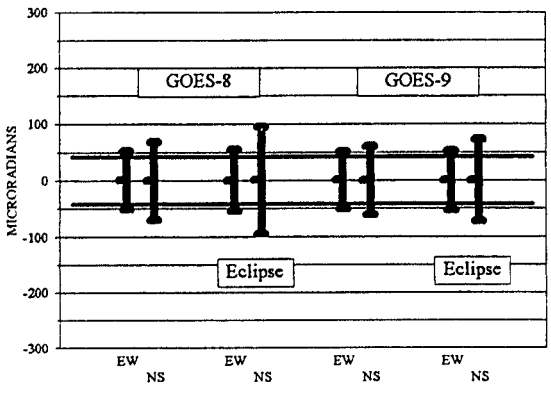

FIGURE 4.3-20: IR SUMMARY

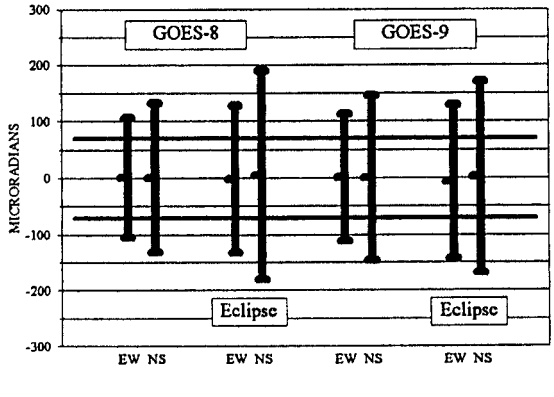

FRAME - FRAME REGISTRATION (90 MINS)

FIGURE 4.3-21: GOES-8 EW

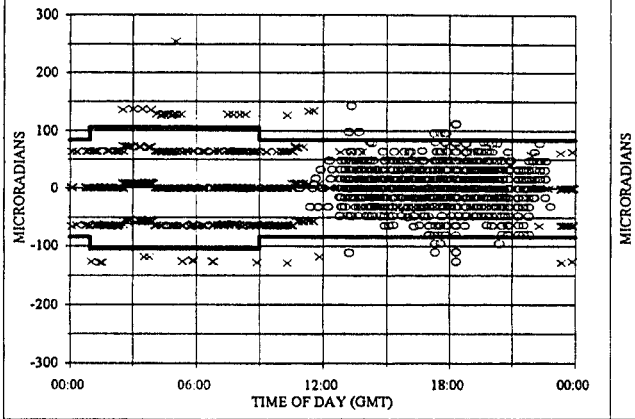

FIGURE 4.3-22: GOES-8 NS

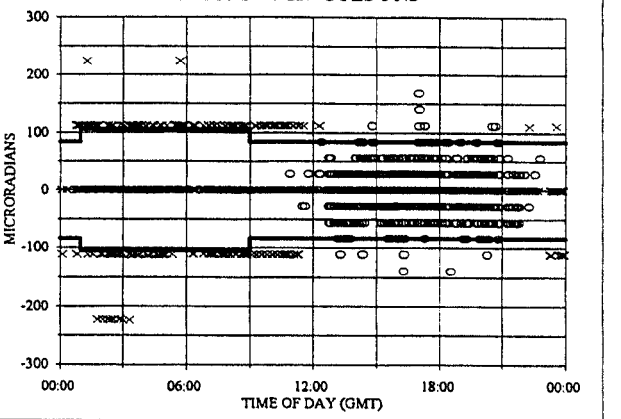

FIGURE 4.3-23: GOES-9 EW

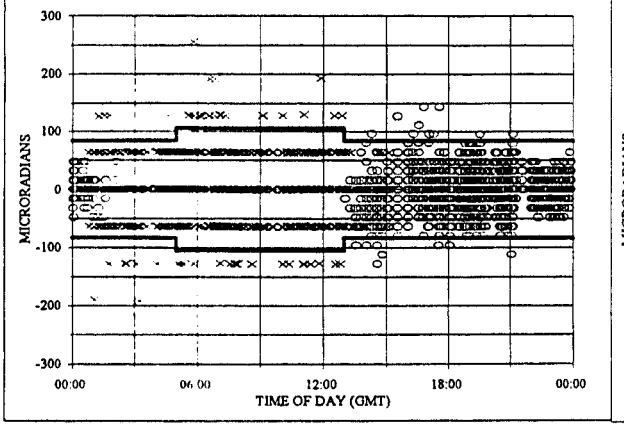

FIGURE 4.3-24: GOES-9 NS

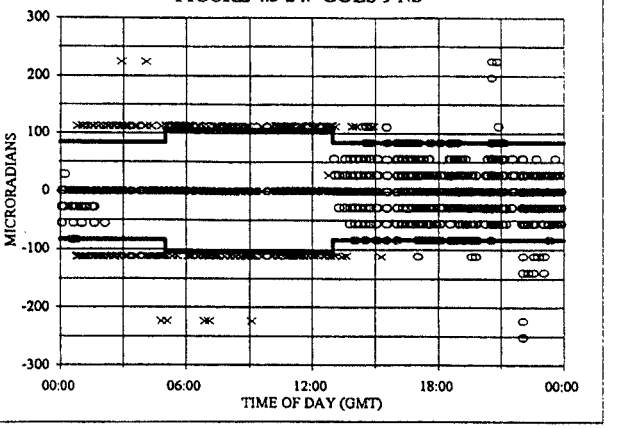

o VIS x VIS _SPEC

FIGURE 4.3-25: VIS SUMMARY

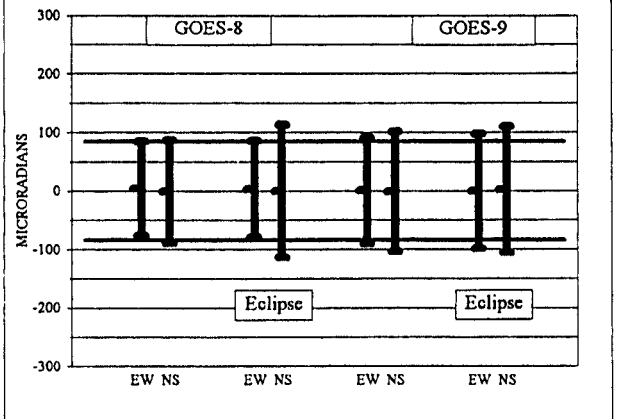

FIGURE 4.3-26: IR SUMMARY

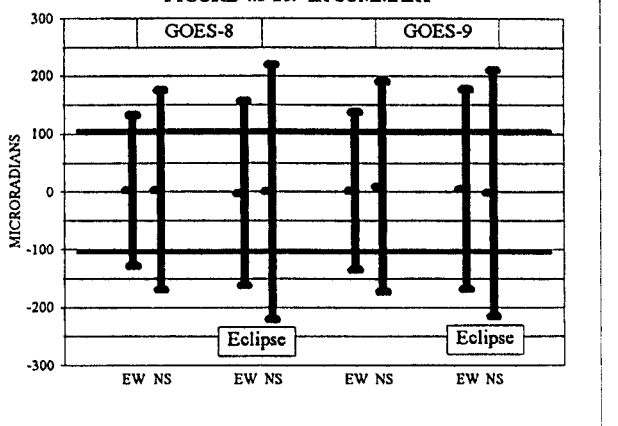

FRAME - FRAME REGISTRATION (24 HRS)

FIGURE 4.3-27: GOES-8 EW

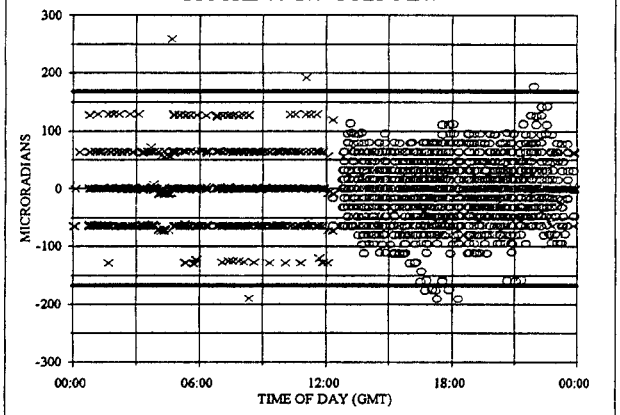

FIGURE 4.3-28: GOES-8 NS

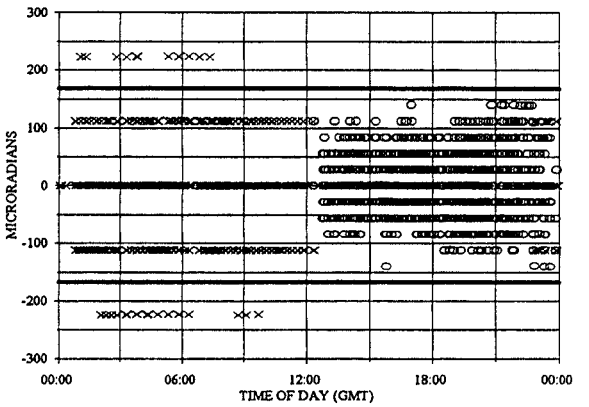

FIGURE 4.3-29: GOES-9 EW

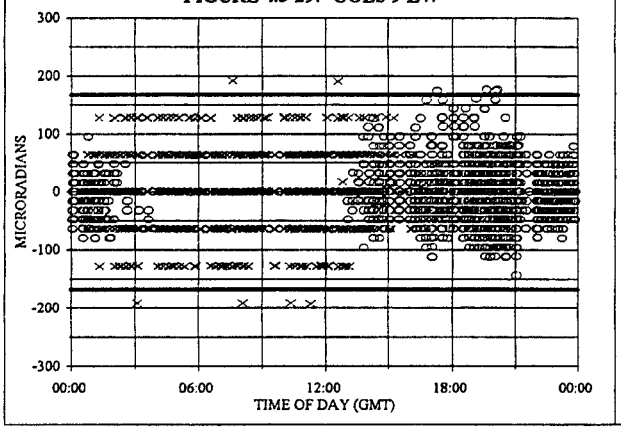

FIGURE 4.3-30: GOES-9 NS

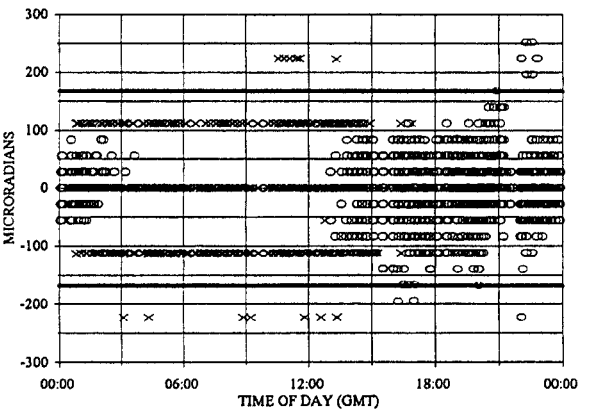

o VIS x IR _ SPEC

FIGURE 4.3-31: VIS SUMMARY

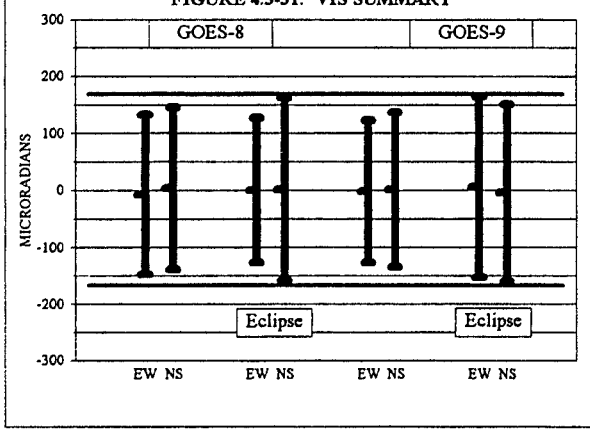

FIGURE 4.3-32: IR SUMMARY

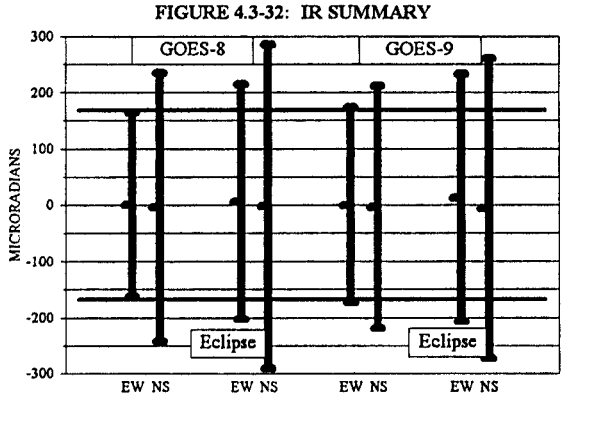

Coregistration. The coregistration results are summarized graphically in Figure 4.3-33. During the eclipse season, the coregistration results for both spacecraft fell within specification. The results from the non-eclipse period, however, indicated that both spacecraft had shifted outside the EW specification. Both spacecraft changed by roughly the same amount and in the same direction which may be attributable to seasonal variations in instrument temperature.

FIGURE 4.3-33: VIS/IR-2 COREGISTRATION

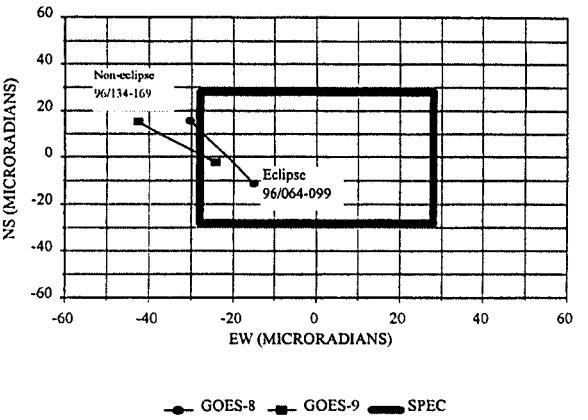

SSAA Performance. The statistical summaries shown in Figures 4.3-34 and 4.3-35 clearly illustrate the corrective abilities of the SSAAs. In each grouping of three bars, the parent set results are shown on the left, the SSAA results are shown in the middle, and the OAD results are shown on the right. As described earlier, each set of residuals has a unique interpretation. The parent set residuals and the OAD fit residuals represent opposing ends of the performance spectrum. With the current model, it is not possible to achieve pointing better than that obtained from the OAD fit after the measurements have all been collected. At the other extreme, the parent set residuals demonstrate the effect of never updating the prediction. The SSAA residuals as a whole more closely resemble the optimum performance represented by the OAD fit. All of the data summarized in Figures 4.3-34 and 4.3-35 are shown in Figures 4.3-36 through 4.3-41. The SSAAs are responsible for improving the performance from that seen in Figures 4.3-36 and 4.3-37 to that seen in Figures 4.3-38 and 4.3-39. The dramatic performance improvement due to SSAAs is particularly apparent in the visible channel.

FIGURE 4.3-34: SSAA PERFORMANCE (VIS)

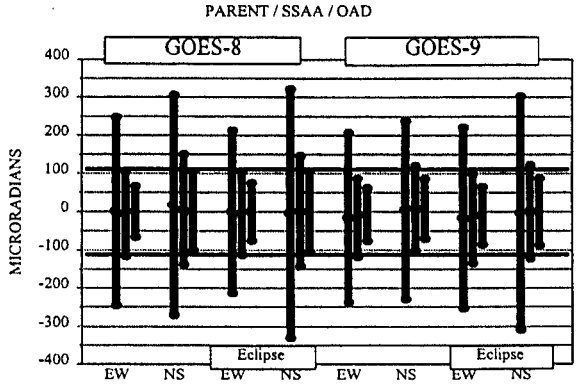

FIGURE 4.3-35: SSAA PERFORMANCE (IR)

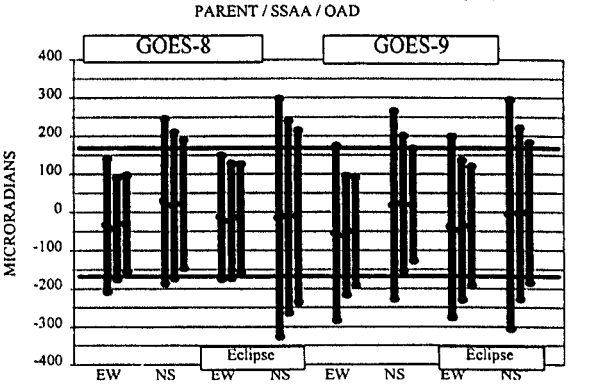

GOES-9 RESIDUALS

FIGURE 4.3-36: PARENT SET (EW)

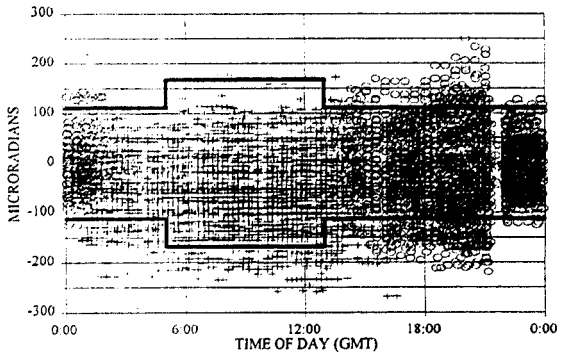

FIGURE 4.3-37: PARENT SET (NS)

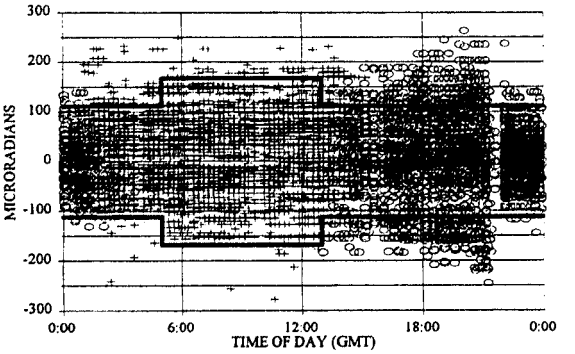

FIGURE 4.3-38: SSAA (EW)

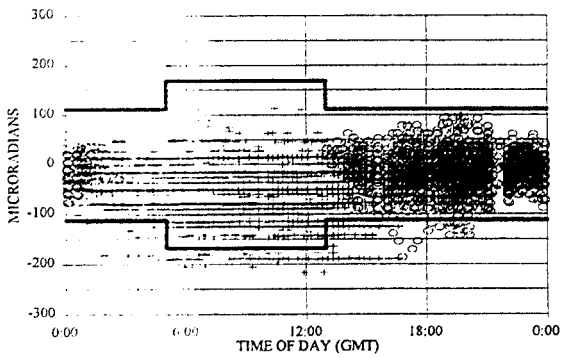

FIGURE 4.3-39: SSAA (NS)

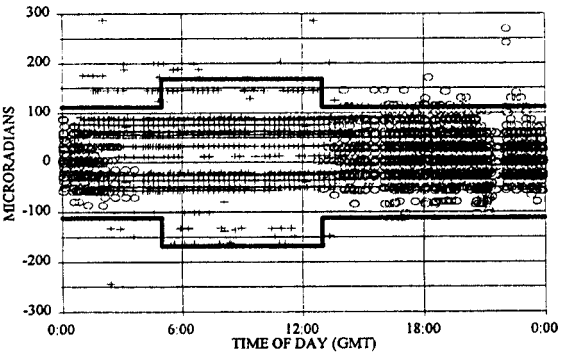

FIGURE 4.3-40: OAD FIT (EW)

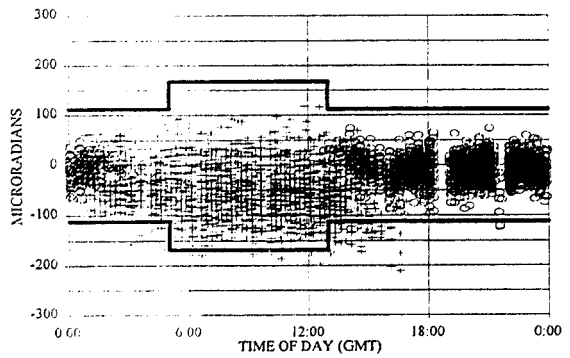

FIGURE 4.3-41: OAD FIT (NS)

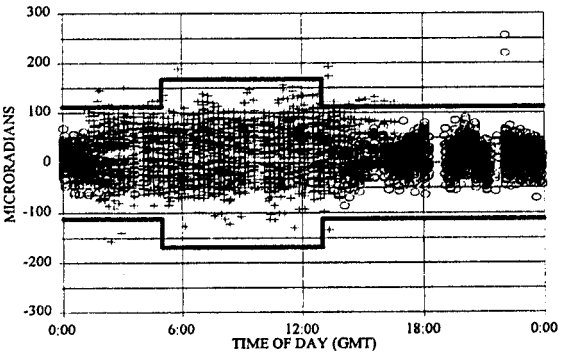

o VIS + IR _ SPEC

5. SUMMARY

This paper has shown that both the GOES-8 and -9 INR systems are performing at levels close to the specifications with the use of frequent SSAAs. It was also shown that the INR performance during eclipse season is not measurably different from non-eclipse performance. Further refinement of actual performance will require improved landmark measurement accuracy. Further improvements include more frequent adjustment of the visible/IR coregistration correction, compensation of the boom shadow and GOES-9 winglet effects, and further investigation into the post eclipse correction.

6. ACKNOWLEDGMENTS

The authors would like to acknowledge the efforts of Dave Noppenberger and Chetan Sayal, Swales & Associates, Inc., who were responsible for much of the data preparation. The authors would also like to thank Nick Pinkine, Lockheed Martin Corp., for his help with extracting the archived INR data files used in our analysis. Finally, we would like to acknowledge valuable discussions with Kathy Kelly and Tim Walsh, NOAA/NESDIS, and Keiko Chevray, Space Systems/Loral.

7. REFERENCES

1. Kamel, A., "Image Navigation and Registration System," SPIE Proceedings, Vol. 2812, (GOES-8 and Beyond Conference), August 1996.

2. Carr, J., "Long Term Stability of GOES-8 and -9 Attitude Control," SPIE Proceedings, Vol. 2812, (GOES-8 and Beyond Conference), August 1996.

3. Phenneger, M., Bryant, W., Baucom T., Woodham, K. "Evaluating the GOES-8 and -9 Earth IR Horizon Sensor Error Resposne Using the GOES-9 Sounder IR Channel 1-4 Data," SPIE Proceedings, Vol 2812 (GOES-8 and Beyond Conference), August 1996.

4. Kelly, K., Hudson, J., Pinkine, N., "GOES 8/9 Image Navigation and Registration Operations," SPIE Proceedings, Vol, 2812, (GOES-8 and Beyond Conference), August 1996.

5. Washwell, E., Chevray, K. Kamel, A., Dress, A., and Walsh, T., "Improved GOES Earth Sensor Performance," SPIE Proceedings, Vol. 2812 (GOES-8 and Beyond Conference), August 1996.

Blank page retained for pagination

SESSION 10

Star Trackers

Attitude determination designs for the GOES spacecraft

John L. Crassidis, F. Landis Markley, Arthur M. Kyle

Goddard Space Flight Center
Guidance and Control Branch, Code 712
Greenbelt, MD 20771

Kathie Blackman

Orbital Sciences Corporation
7500 Greenway Center Drive, Suite 700
Greenbelt, MD 20770

ABSTRACT

This paper presents a summary of the basic simulation parameters and results of a study for the Geostationary Operational Environmental Satellite (GOES). The study involves the simulation of minor modifications to the current spacecraft, so that the relative performance of these modifications can be analyzed. The first modification studied requires the placement of a baseline inertial reference unit, such as the Dry Rotor Inertia Reference Unit (DRIRU-II) or the Space Inertial Reference Unit (SIRU), onto the spacecraft. The second modification involves using the imager/sounder assembly for real-time on-board attitude determination information. The third modification studied is the addition of star trackers to provide precise attitude knowledge. Simulation results are presented for each modification.

KEYWORDS: Earth Sensor, Star Tracker, QUEST, Enhanced QUEST, Kalman Filter

1. INTRODUCTION

In this paper, a design study is shown for attitude determination of the Geostationary Operational Environmental Satellite (GOES). The current (GOES-8) spacecraft specification for the knowledge requirement is 112 μrad. This requirement is met through ground processing 99% of the time in the east/west direction and 95% of the time in the north/south direction. The spacecraft specification for the within-frame image registration is 42 μrad. This requirement is met through ground processing 90% of the time in the east/west direction and 70% of the time in the north/south direction. The current spacecraft uses an Earth Sensor Assembly (ESA) to provide roll and pitch information. A set of gyros, the Digital Integration Rate Assembly (DIRA), also is on the current spacecraft. However, the DIRA has an operational lifetime of 2000 hours. Therefore, the on-board gyros are not used for mission mode attitude determination and control.

A number of new attitude determination schemes and hardware modifications is presented. The first modification involves the addition of high precision gyros, such as the Dry Rotor Inertia Reference Unit (DRIRU-II) or Space Inertial Reference Unit (SIRU), onto the spacecraft with the existing ESA. Simulation results are presented using a Kalman filter for attitude determination.

The imager/sounder assembly is currently used to obtain landmark and/or star observations in order to compensate for spacecraft motions and external disturbances through ground processing. The second modification utilizes the imager/sounder assembly as another attitude sensor for on-board attitude determination. This provides a means to supplement the ESA determined attitude, as well as providing yaw information. Simulation results are also presented using a Kalman filter for attitude determination.

The final modification involves the addition of star trackers with or without high precision gyros to provide precise attitude knowledge. The proposed GOES attitude determination system includes one or two star trackers. A covariance analysis is first shown to determine the optimal orientations of the star trackers. Next, an actual star availability analysis is shown using the optimal tracker orientations and GOES orbit. The QUEST[1] algorithm is used for attitude determination without gyros. In order to further improve attitude knowledge an enhanced QUEST algorithm is also utilized. This involves a simple first-order Kalman filter type algorithm to filter noisy star measurements. Finally, simulation results for all case studies are presented.

0-8194-2200-2/96/$6.00

2. EARTH SENSOR, IMAGER/SOUNDER

In this section, a brief overview of the simulation parameters for the gyro model, the ESA model, and the imager/sounder model is shown. The true angular velocity is assumed to be modeled by[2]

$$\underline{\omega} = \underline{\tilde{\omega}}_g - \underline{b} - \underline{\eta}_1 \tag{1}$$

where $\underline{\omega}$ is the true angular velocity, $\underline{\tilde{\omega}}_g$ is the gyro-determined angular velocity, and $\underline{b}$ is the gyro drift vector,

$$\dot{\underline{b}} = \underline{\eta}_2 \tag{2}$$

The 3×1 vectors, $\underline{\eta}_1$ and $\underline{\eta}_2$, are assumed to be modeled by a Gaussian white-noise process with

$$E\left\{\underline{\eta}_i(t)\right\} = \underline{0} \qquad i = 1, 2 \tag{3}$$

$$E\left\{\underline{\eta}_i(t)\underline{\eta}_j^T(t')\right\} = Q_i\,\delta_{ij}\,\delta(t-t') \qquad i, j = 1, 2 \tag{4}$$

where

$$Q_1 = \sigma_v^2 I_{3\times3} \tag{5a}$$

$$Q_2 = \sigma_u^2 I_{3\times3} \tag{5b}$$

The DRIRU-II drift-rate noise and measurement noise characteristics are given by $\sigma_u = 2.15\times10^{-4}\ \mu\text{rad}/\text{sec}^{3/2}$ and $\sigma_v = 0.206\ \mu\text{rad}/\text{sec}^{1/2}$. The nominal motion of the spacecraft involves a rotation once per orbit about the spacecraft's y-axis. Therefore, the nominal angular velocity is given by

$$\underline{\omega} = \begin{bmatrix} 0 \\ \omega_n \\ 0 \end{bmatrix} \tag{6}$$

where ω_n is the orbit rotation rate $\left(7.27\times10^{-5}\ \text{rad}/\text{sec}\right)$.

The ESA measures the spacecraft's roll and pitch angles. These angles are measured with respect to a moving Earth frame. The gyros provide attitudes with respect to an inertially fixed frame (e.g., GCI). Since the body rotation axis is about the spacecraft's y-axis, the body measurement vector is given by[3]

$$\underline{B}_e = \begin{bmatrix} -\sin(p)\cos(r) \\ \sin(r) \\ \cos(p)\cos(r) \end{bmatrix} \tag{7}$$

where r and p are the scanner roll and pitch angles, respectively. The inertial reference vector is given by

$$\underline{I}_e = A^T(q)\underline{B}_e \tag{8}$$

where q is the true quaternion (obtained by kinematic propagation using the true angular velocity). The ESA "measurements" are obtained by using the following model

$$\tilde{p} = p + v_p + w_p \tag{9}$$

where v_p is a zero-mean Gaussian process with a 3σ value of 0.02 degrees, and w_p represents the non-repeatable errors due to Earth cloud and Earth radiance/gradients effects. The non-repeatable error is assumed to be modeled by the following discrete process

$$w_p(i+1) = A\,w_p(i) + L\left(1-A^2\right)^{1/2} g(i) \tag{10a}$$

$$A = \exp(-4\,\Delta t\,B) \tag{10b}$$

where Δt is the sampling interval (0.25 seconds for the ESA), B is the bandwidth (for weather purposes, this set to about 1/6 days), L is the 1σ amplitude (experience has shown that this is about 200 μrad), and g is a zero-mean normal Gaussian process. This same error model is applied to the Earth roll "measurement." Since the roll and pitch measurements from the Earth sensor are small, the body measurements can be approximated by

$$\underline{\tilde{B}}_B^e \approx \begin{bmatrix} -\tilde{p} \\ \tilde{r} \\ 1 \end{bmatrix} \tag{11}$$

The imager/sounder assembly can measure stars in a $23^\circ\mathrm{E/W} \times 21^\circ\mathrm{N/S}$ field of view, outside of the Earth limb. The orbit-attitude tracking system contains a catalog of bright stars visible by the imager/sounder which typically senses three stars at 45 second intervals. For simulation purposes these stars are assumed to be found in different quadrants in the field of view. Each instrument performs a star look every 30 minutes. The imager/sounder measures the tangent of two angles, β_1 and β_2, resulting in a body vector given by[3]

$$\underline{B}_{i/s} = \frac{1}{\sqrt{1+\tan^2\beta_1+\tan^2\beta_2}} \begin{bmatrix} \tan\beta_1 \\ \tan\beta_2 \\ 1 \end{bmatrix} \tag{12}$$

The imager/sounder "measurements" are obtained by using the following model

$$\tan\tilde{\beta}_i = \tan\beta_i + v_{bi} + w_{bi}, \qquad i = 1, 2 \tag{13}$$

where v_b is a zero-mean Gaussian process with a 3σ value of 28 μrad. The non-repeatable error in the imager/sounder is assumed to be modeled by the following process

$$\dot{\underline{x}} = \begin{bmatrix} 0 & 1 \\ -\omega_n^2 & 0 \end{bmatrix} \underline{x} + \begin{bmatrix} 0 \\ 1 \end{bmatrix} \eta \tag{14a}$$

$$w_b = \begin{bmatrix} 1 & 0 \end{bmatrix} \underline{x} \tag{14b}$$

where η is a zero-mean Gaussian process. The standard deviation of η is selected such that the output of w_b has a 3σ value of about 200 μrad.

2.1 Simulation Results

For this part of the study, an investigation of the relative performance between gyro-aided and gyroless attitude determination was examined. For the on-board gyro case, a standard Kalman filter with a gyro propagated model was used for attitude determination. The simulations were run for six cases: 1) ESA only with no non-repeatable (NR) errors, 2) ESA only with NR errors, 3) ESA and imager/sounder (I/S) with no NR ESA errors and no NR I/S errors, 4) ESA and I/S with no NR ESA errors and with NR I/S errors, 5) ESA and I/S with NR ESA errors and no NR I/S errors, and 6) ESA and I/S with both NR ESA errors and NR I/S errors.

The first two cases involve using the ESA only. A Monte Carlo type analysis shows that 200-250 μrad is about the 3σ range for this error. With no NR errors in the ESA, the attitude accuracy is within 60 μrad. With the NR errors in the ESA, this accuracy is degraded to about 200 μrad. Also, large errors in the yaw angle estimates are due to filter un-observability. The observability of using an ESA combined with gyro measurements in a Kalman filter can be shown by using the simplifying assumption of a constant coefficient system (see [4] for details). A summary of the results is shown in Table 1.

Table 1 Attitude Errors for Various Sensor Configurations and Error Sources

Case	Error Sources	Roll Errors	Pitch Errors	Yaw Errors
1	no NR ESA	60 μrad	60 μrad	1×10^5 μrad
2	NR ESA	200 μrad	200 μrad	1×10^5 μrad
3	no NR ESA, no NR I/S	60 μrad	60 μrad	200 μrad
4	no NR ESA, NR I/S	100μrad	100 μrad	200 μrad
5	NR ESA, no NR I/S	100 μrad	100 μrad	200 μrad
6	NR ESA, NR I/S	200 μrad	200 μrad	300 μrad

From Table 1, using the imager/sounder as another sensor significantly improves the yaw angle estimate. Also, since the magnitude of the non-repeatable errors is assumed to be approximately the same in the ESA and in the imager/sounder assembly, the attitude errors are also approximately equal when adding these errors to each sensor individually (i.e., case four and five). The sixth case involves using both the ESA and imager/sounder assembly with non-repeatable errors added to each sensor. A purely deterministic attitude found using QUEST yields errors which are approximately the same magnitude as case six. Therefore, the addition of gyros does not seem to significantly improve the attitude accuracy.

3. STAR TRACKER

In this section, the simulation results using a star tracker with and without gyros are presented. First, the star tracker model and parameters are shown. Then, a covariance analysis is presented in order to determine the optimal orientation of the star trackers. Next, the availability of actual stars for the GOES orbit is shown. Results are then presented using QUEST[1] to determine the spacecraft attitude. An Enhanced QUEST algorithm is also derived which filters sensor noise. Finally, simulation results are presented using gyros and a Kalman filter.

All results shown in this section include the dynamics and external disturbance on the spacecraft. The GOES Flight Software Dynamics Model implements a GOES Attitude and Orbit Control Electronics (AOCE) firmware emulation FORTRAN code, which uses a six degree-of-freedom dynamics model. The initial model was developed to examine the augmentation of the ESA with gyros, and the current capability was developed to compare with actual GOES performance using the ESA. A star tracker and star tracker/gyro were also added into the simulation. The simulation includes rotating solar array inertia effects with fully coupled inertia tensor dynamics, magnetic torquers with ideal torque response, and gravity gradient and solar pressure disturbances.

The star tracker can sense up to six stars in an $8^\circ \times 8^\circ$ field of view with a sampling interval of 0.1 seconds. The catalog contains stars ranging from +1.0 to +6.0 magnitude. The star tracker measures the tangent of two angles, β_1 and β_2, resulting in a body vector given by

$$\underline{B}_s = \frac{1}{\sqrt{1+\tan^2\beta_1+\tan^2\beta_2}}\begin{bmatrix}\tan\beta_1\\ \tan\beta_2\\ 1\end{bmatrix} \tag{15}$$

where the z-axis of the star tracker is along the boresight. The star tracker "measurements" are obtained by using

$$\tan\tilde{\beta}_i = \tan\beta_i + v_{s_i}, \qquad i=1,2 \tag{16}$$

where v_s is a zero-mean Gaussian process with a 3σ value of 87.2665 μrad (18 arc−sec).

Each star tracker must be positioned so that sun intrusions can be avoided at all times. For the GOES orbit, and available sun shade for the star tracker, the minimum exclusion area (allowing for a 3° safety margin) is from 55° North to

55° South of the Nadir vector. For the single star tracker case, the 55° orientation produces the following order for knowledge accuracy: (1) roll angle (i.e., about the spacecraft's x-axis) is known most accurately, then (2) yaw angle (i.e., about the spacecraft's y-axis), and (3) pitch angle (i.e., about the spacecraft's y-axis) being the least accurate. Roll is the most accurate since the star tracker is perpendicular to this spacecraft's x-axis. Pitch accuracy is least accurate since the 55° star tracker position leads to the y-axis being the least "orthogonal" axis with respect to the tracker boresight.

For the two tracker case, a covariance analysis was performed in order to determine the optimal orientation. Assuming that each star tracker measures one star for simplicity, the error covariance matrix is given by[5]

$$P = \frac{\sigma^2}{|b_1 \times b_2|^2}\left[b_1 b_1^T + b_2 b_2^T + \frac{1}{2}(b_1 \times b_2)(b_1 \times b_2)^T \right] \tag{17}$$

where σ is the measurement error standard deviation, and b_1 and b_2 are measurement vectors of each star. For a North-South configuration, these measurement vectors are given by

$$b_1 = \begin{bmatrix} 0 \\ \sin 55^\circ \\ \cos 55^\circ \end{bmatrix} \equiv \begin{bmatrix} 0 \\ s \\ c \end{bmatrix} \tag{18a}$$

$$b_2 = \begin{bmatrix} 0 \\ -\sin 55^\circ \\ \cos 55^\circ \end{bmatrix} \equiv \begin{bmatrix} 0 \\ -s \\ c \end{bmatrix} \tag{18b}$$

Using Equation (18), the covariance in Equation (17) becomes

$$P = \frac{\sigma^2}{2}\begin{bmatrix} 1 & 0 & 0 \\ 0 & \frac{1}{c^2} & 0 \\ 0 & 0 & \frac{1}{s^2} \end{bmatrix} \tag{19}$$

The next configuration studied was to place the both star trackers 55° North (or South) from Nadir and rotated by an angle ϑ, The measurement vectors for this case are given by

$$b_1 = \begin{bmatrix} c\tilde{s} \\ s \\ c\tilde{c} \end{bmatrix}, \qquad b_2 = \begin{bmatrix} -c\tilde{s} \\ s \\ c\tilde{c} \end{bmatrix} \tag{20}$$

where $\tilde{s} \equiv \sin\vartheta$, and $\tilde{c} \equiv \cos\vartheta$. The covariance matrix in Equation (17) for this case is given

$$P = \frac{\sigma^2}{2\left(c^4\tilde{s}^2\tilde{c}^2 + c^2\tilde{s}^2 s^2\right)}\begin{bmatrix} c^2\tilde{s}^2 & 0 & 0 \\ 0 & s^2 + c^4\tilde{s}^2\tilde{c}^2 & cs\tilde{c} - c^3\tilde{s}^2\tilde{c}\,s \\ 0 & cs\tilde{c} - c^3\tilde{s}^2\tilde{c}\,s & c^2\tilde{c}^2 + c^2\tilde{s}^2 s^2 \end{bmatrix} \tag{21}$$

In order to determine the optimal rotation angle, a cost function involving roll and pitch errors (i.e., allowing for relaxed yaw error conditions) is defined, given by the sum of the roll and pitch covariances,

$$J(\vartheta) = \frac{\sigma^2}{2\left(c^4\tilde{s}^2\tilde{c}^2 + c^2\tilde{s}^2 s^2\right)}\left(c^2\tilde{s}^2 + s^2 + c^4\tilde{s}^2\tilde{c}^2\right) \tag{22}$$

Minimizing this cost function with respect to ϑ leads to the optimal rotation given by $\vartheta = 90^\circ$. Therefore, the covariance matrix in Equation (21) becomes

$$P = \frac{\sigma^2}{2}\begin{bmatrix} \frac{1}{s^2} & 0 & 0 \\ 0 & \frac{1}{c^2} & 0 \\ 0 & 0 & 1 \end{bmatrix} \tag{23}$$

Equation (23) shows that the yaw angle contains the smallest error, even though yaw was relaxed for the optimal separation angle. Therefore, comparing Equation (19) and Equation (23) leads to the conclusion that the optimal location for the two tracker case is given by one tracker 55° North and one tracker 55° South from Nadir.

3.1 Simulation Results

Figure 1 shows the actual number of stars within the North pointing tracker field of view. There is always a minimum of 2 stars, except for the interval from 2.15 to 2.283 hours. A star with a magnitude of 6.256 was added in this interval for the QUEST solution. Figure 2 shows the number of stars within the South pointing tracker field of view. Stars can be added to the South tracker catalog in order to insure a minimum of two stars, but this was not done, since the North tracker was used for simulations involving one tracker. Figure 3 shows the combined number of stars for both trackers (without the addition of any stars). This shows that a minimum of 4 stars is available for the two tracker case. Also, the percentages of time in the orbit with the number of stars in the field of view are shown by Tables 2 and 3.

Table 2 North Pointing Star Catalog

Number of Stars	Percentage in FOV
0	0.0
1	0.625
2	10.972
3	15.625
4	27.709
5	23.958
6	21.111

Table 3 South Pointing Star Catalog

Number of Stars	Percentage in FOV
0	0.0
1	1.458
2	8.056
3	20.972
4	28.889
5	23.272
6	17.153

In this section simulation results using the QUEST and Enhanced QUEST algorithms without gyros are presented. The QUEST algorithm minimizes the following cost function

$$J(A) = \frac{1}{2}\sum_{k=1}^{n}\frac{1}{\sigma^2}\left|\underline{B}_{s_k} - A\,\underline{I}_{s_k}\right|^2 \tag{24}$$

where A is the attitude matrix, and n is the number of stars available. QUEST is a deterministic approach which utilizes a point-by-point solution. Therefore, previous measurements are not utilized in the attitude solution. This algorithm requires at least two star measurements to determine the attitude, so a star is added (as previously described) to the single star tracker case.

In general, the attitude knowledge is determined more accurately as the number of star measurements at one time increases and/or the separation distance between stars increases. This can be seen by the deterministic error covariance, given by[1]

$$P_{\tilde{q}\tilde{q}_k} = \sigma^2 \sum_{k=1}^{n} \left[I_{3\times 3} - \underline{B}_{s_k} \underline{B}_{s_k}^T \right]^{-1} \tag{25}$$

Figure 4 shows the attitude errors from QUEST determined attitude using a single (North) star tracker. Note the large errors about 2 hours into the simulation corresponds to the point where the star availability is primarily 2 stars with a small separation. Figure 4 also shows the 3σ bounds from Equation (25). This shows excellent agreement between theory and simulation. Figure 5 shows the attitude errors and 3σ bounds for the two star tracker case. This shows the significant improvement in attitude knowledge by using two trackers.

In order to further improve the attitude accuracy, an Enhanced QUEST algorithm (EQA) was developed. This is a simple first-order Kalman filter which combines a propagated model with the QUEST determined attitudes. Since gyros are not used for this case, the angular velocity is assumed to be perfect (i.e., given by Equation (6)). This assumption is a poor one, since external disturbances, and control and sensor errors are present in the actual system. Typical control errors using the ESA are shown in Figure 6. This shows the large errors and coupling in the roll/yaw axis. The EQA is given by

$$\underline{\hat{q}}_{k+1}(-) = \exp\left\{\frac{1}{2}\Omega(\underline{\omega})\Delta t\right\} \underline{\hat{q}}_k(+) \tag{26a}$$

$$\underline{\hat{q}}_k(+) = (1-\alpha)\underline{\hat{q}}_k(-) + \alpha\, \underline{\tilde{q}}_k \tag{26b}$$

where $\Delta t = 0.1$ seconds, $\underline{\tilde{q}}_k$ is the QUEST determined attitude at time t_k, and α is a scalar gain. This gain was determined by minimizing the attitude errors from the simulated runs. A value which is too small adds tends to neglect measurements, and emphasizes the inadequacy of the approximation in Equation (6). A value which is too large adds too much measurement noise, and tends to neglect model corrections. A value of $\alpha = 0.05$ was determined to be optimal. The EQA covariance is derived by re-writing Equation (26) as

$$\underline{\hat{q}}_{k+1} = \Phi_4\, \underline{\hat{q}}_k \otimes \left[\underline{I} + \alpha \left(\left\{ \Phi_4\, \underline{\hat{q}}_k \right\}^{-1} \otimes \underline{\tilde{q}}_{k+1} - \underline{I} \right) \right] \tag{27a}$$

$$\Phi_4 \equiv \exp\left\{\frac{1}{2}\Omega(\underline{\omega})\Delta t\right\} \tag{27b}$$

where $\otimes$ denotes quaternion multiplication (see [2]). The QUEST determined quaternion is written as

$$\underline{\tilde{q}}_{k+1} \approx \begin{bmatrix} \delta \underline{\tilde{q}}_{k+1} \\ 1 \end{bmatrix} \otimes \underline{q}_{k+1} \tag{28}$$

where $\underline{q}_{k+1}$ is the true quaternion, and $\delta \underline{\tilde{q}}_{k+1}$ is a three component error vector. Substituting Equation (28) into Equation (27a), and post-multiplying both sides of the resulting equation by $\underline{q}_{k+1}^{-1}$ yields

$$\underline{\hat{q}}_{k+1} \otimes \underline{q}_{k+1}^{-1} \approx \begin{bmatrix} \delta \underline{q}_{k+1} \\ 1 \end{bmatrix} = \Phi_4\, \underline{\hat{q}}_k \otimes \underline{q}_{k+1}^{-1} (1-\alpha) + \alpha \begin{bmatrix} \delta \underline{\tilde{q}}_{k+1} \\ 1 \end{bmatrix} \tag{29}$$

Using a first-order approximation yields the following covariance for the EQA

$$P_{\hat{q}\hat{q}_{k+1}} = (1-\alpha)^2 \Phi_3\, P_{\hat{q}\hat{q}_k}\, \Phi_3^T + \alpha^2 P_{\tilde{q}\tilde{q}_k} \tag{30}$$

where Φ_3 is the state transition matrix of $[\underline{\omega}\times]$. Since this matrix is constant and nearly the identity matrix, the diagonal elements of Equation (30) approach the following steady-state value

$$p_{\hat{q}\hat{q}_k} \approx \frac{\alpha}{2-\alpha} p_{\tilde{q}\tilde{q}_k} \tag{31}$$

Figure 7 shows the attitude errors and bounds from Equation (31) using one star tracker and the EQA. Comparing Figure 7 with Figure 4 shows a significant improvement using the EQA. Figure 8 shows the attitude errors using two trackers and the EQA. Comparing Figure 8 with Figure 5 again shows a significant improvement using the EQA.

In this section, the results using gyros and a Kalman filter are presented. Two gyro cases are simulated. The first case involves the use of a DRIRU-II. The second case involves the use of a SIRU. The parameters for both gyros are summarized in Table 4.

Table 4 Gyro Parameters

Parameters	DRIRU-II	SIRU
σ_u (white noise)	2.15×10^{-4} μrad/sec$^{3/2}$	1.55×10^{-4} μrad/sec$^{3/2}$
σ_v (random walk)	0.206 μrad/sec$^{1/2}$	1.6 μrad/sec$^{1/2}$

The gyro model is shown by Equations (1) and (2). The relative performance of the attitude estimation can be found by numerically iterating the Kalman filter equations to steady state. Farrenkopf[6] obtained an analytic solution for the case when the three attitude error angles are assumed decoupled. Farrenkopf's results for the preupdate and postupdate attitude error standard deviations, denoted by $\sigma(-)$ and $\sigma(+)$, respectively, can be written as

$$\sigma(-) = \sigma\left(\xi^2 - 1\right)^{\frac{1}{2}} \tag{32a}$$

$$\sigma(+) = \sigma(-)/\xi \tag{32b}$$

where

$$\xi = \frac{1}{2}\left[\gamma + \frac{1}{2}S_u + \left(\gamma S_u + S_v^2 + \frac{1}{3}S_u^2\right)^{\frac{1}{2}}\right], \quad \gamma = \left[4 + S_v^2 + (1/12)S_u^2\right]^{\frac{1}{2}} \tag{33a}$$

$$S_u = \sigma_u \Delta t^{\frac{3}{2}}/\sigma, \quad S_v = \sigma_v \Delta t^{\frac{1}{2}}/\sigma \tag{33b}$$

In the limiting case of very frequent updates, the preupdate and the postupdate attitude error standard deviations both approach the continuous-update limit, given by

$$\sigma_\infty = \Delta t^{\frac{1}{4}} \sigma^{\frac{1}{2}} \left(\sigma_v^2 + 2\sigma_u \sigma_v \Delta t^{\frac{1}{2}}\right)^{\frac{1}{4}} \tag{34}$$

Using the parameters in Table 4 in Equation (34), it was determined that the DRIRU-II steady-state error is approximately 2.8 times better (i.e., more accurate) than the SIRU. This is also shown in the simulations. Figures 9 and 10 show the attitude errors using the SIRU for the one tracker and two tracker cases, respectively. Figures 11 and 12 show the attitude errors using the DRIRU-II for the one tracker and two tracker cases, respectively. Comparing Figure 9 to Figure 11, and Figure 10 to Figure 12, it is seen that the DRIRU-II is approximately 2 to 3 more accurate for the attitude knowledge than using the SIRU. Results for the cases without gyros and cases with gyros are shown in Table 5 and Table 6, respectively.

Table 5 Attitude Error Results Without Gyros

Cases Simulated	Roll Error (μrad) 3σ	Pitch Error (μrad) 3σ	Yaw Error (μrad) 3σ
QUEST (1 Tracker)	60	1250	900
QUEST (2 Trackers)	35	70	50
EQA (1 Tracker)	12	225	175
EQA (2 Trackers)	6	10	8

Table 6 Attitude Error Results With Gyros

Cases Simulated	Roll Error (μrad) 3σ	Pitch Error (μrad) 3σ	Yaw Error (μrad) 3σ
KF. DRIRU-II (1 Tracker)	3	15	10
KF. DRIRU-II (2 Trackers)	2	3	2.5
KF, SIRU (1 Tracker)	7	30	12
KF. SIRU (2 Trackers)	5	9	7

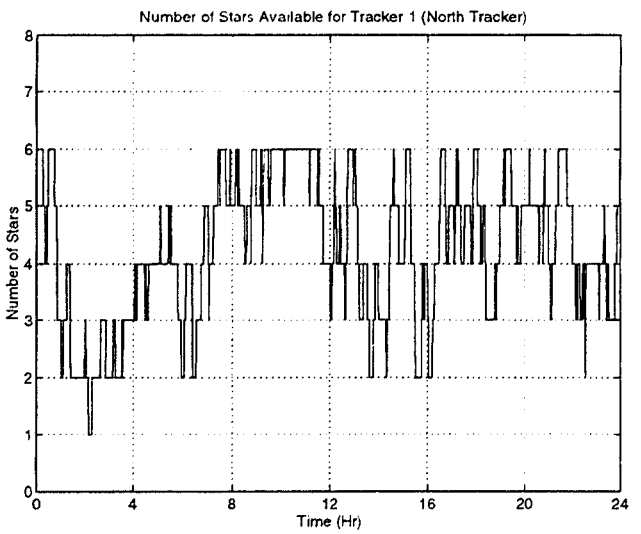

Figure 1 Availability of Stars for the North Tracker

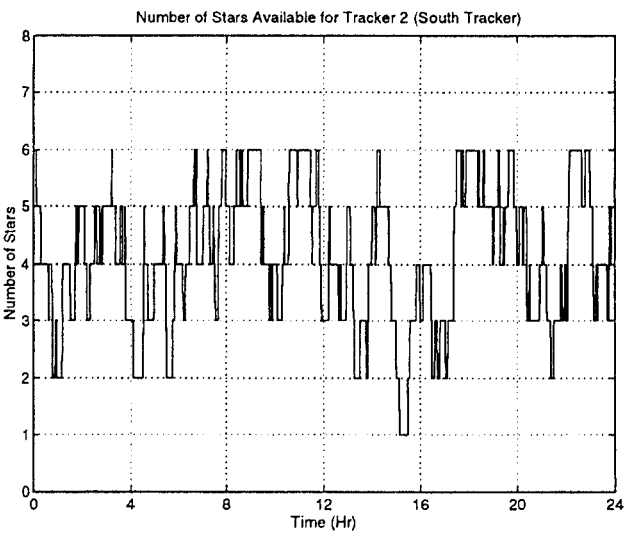

Figure 2 Availability of Stars for the South Tracker

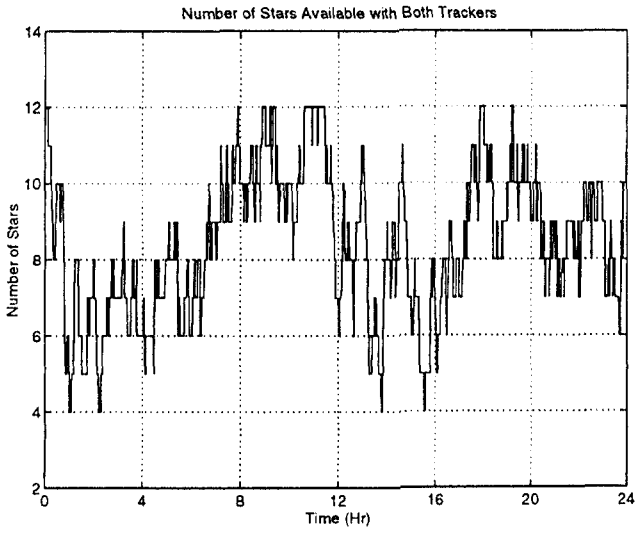

Figure 3 Availability of Stars for Both Trackers

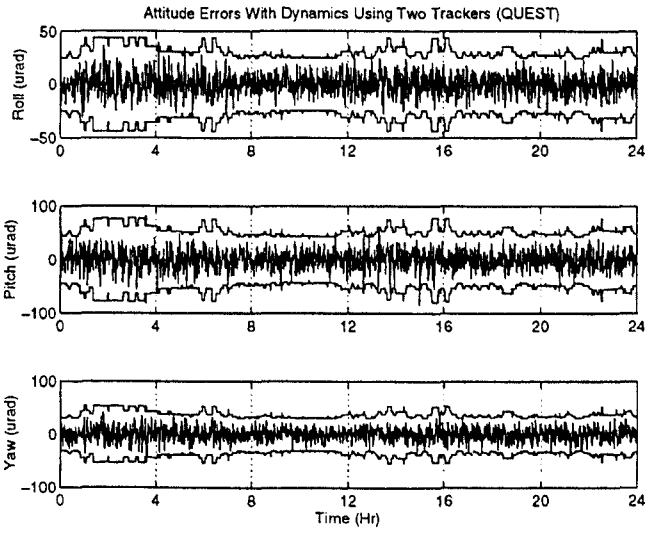

Figure 5 QUEST Errors and Bounds Using Two Trackers

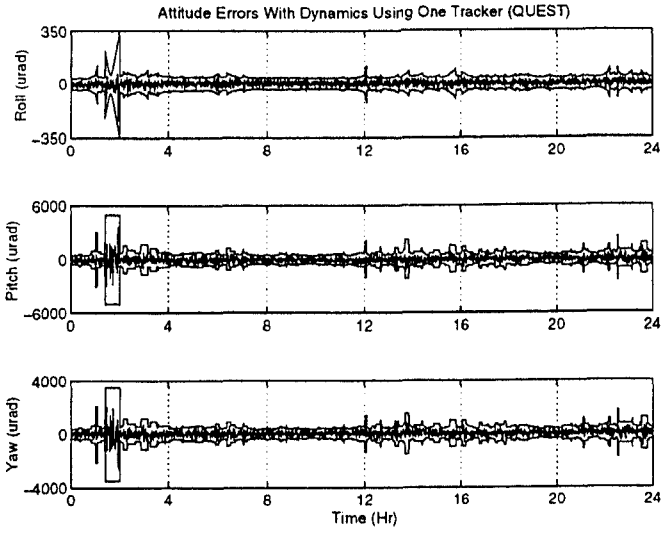

Figure 4 Attitude Errors and Bounds Using One Tracker (QUEST)

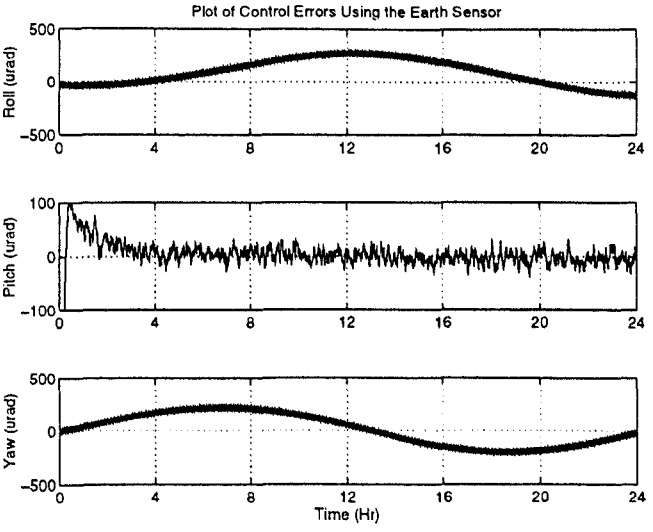

Figure 6 Control Errors

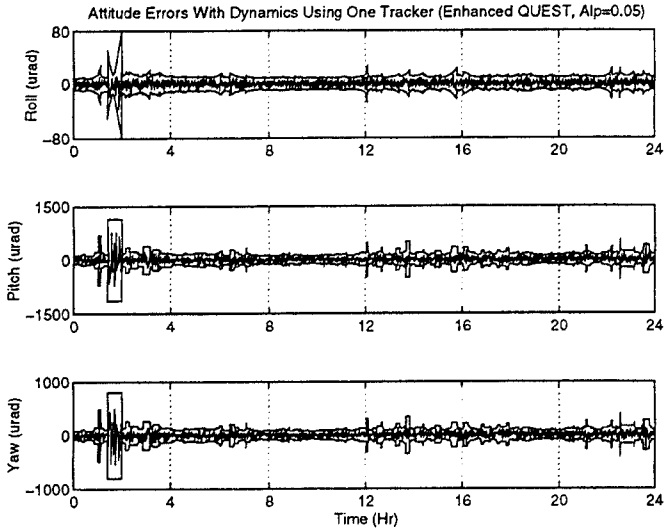

Figure 7 Attitude Errors and Bounds Using One Tracker (Enhanced QUEST)

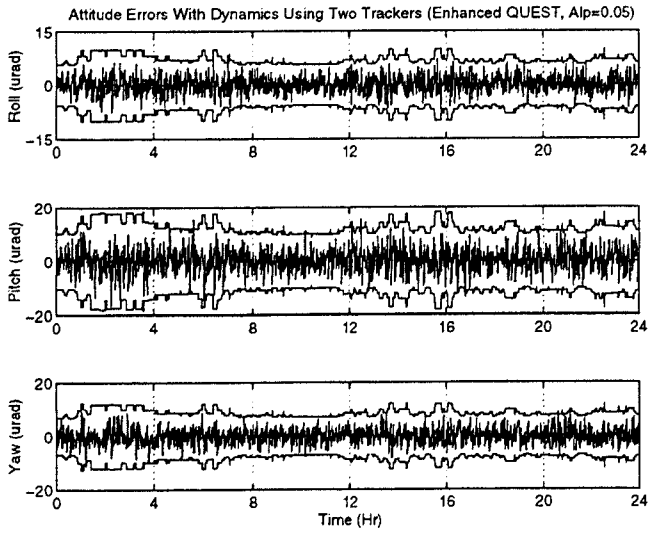

Figure 8 Attitude Errors Using Two Trackers (Enhanced QUEST)

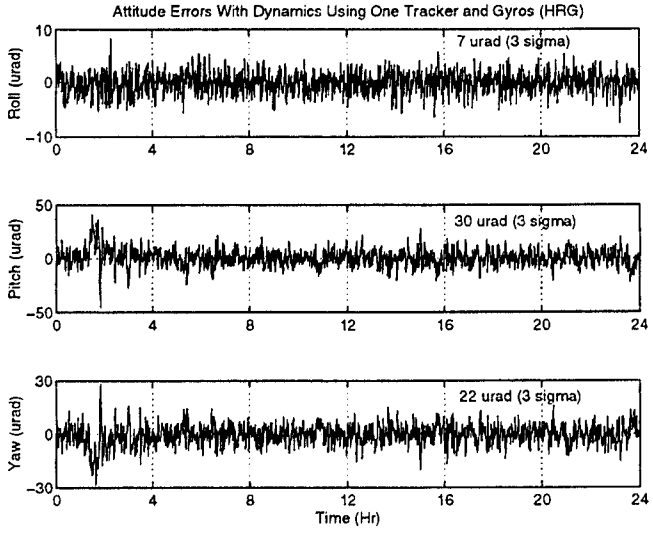

Figure 9 Attitude Errors Using One Tracker (Kalman Filter, SIRU)

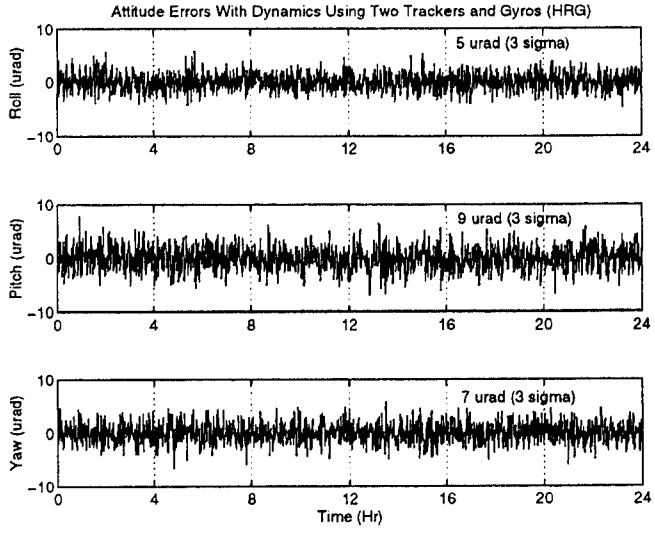

Figure 10 Attitude Errors Using Two Trackers (Kalman Filter, SIRU)

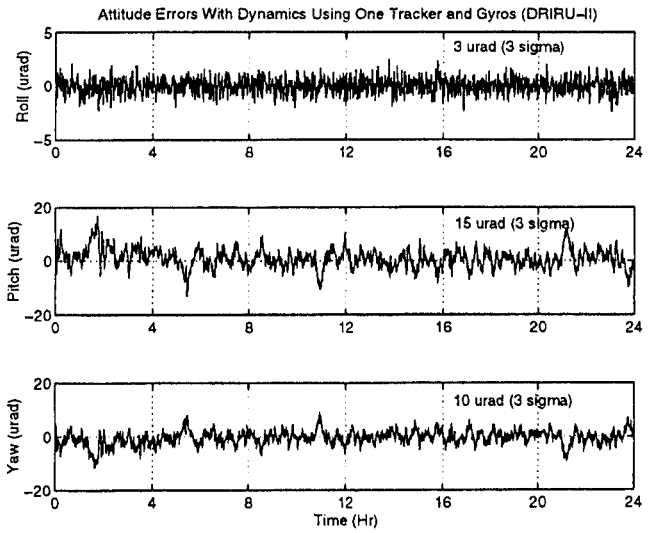

Figure 11 Attitude Errors Using One Tracker (Kalman Filter, DRIRU-II)

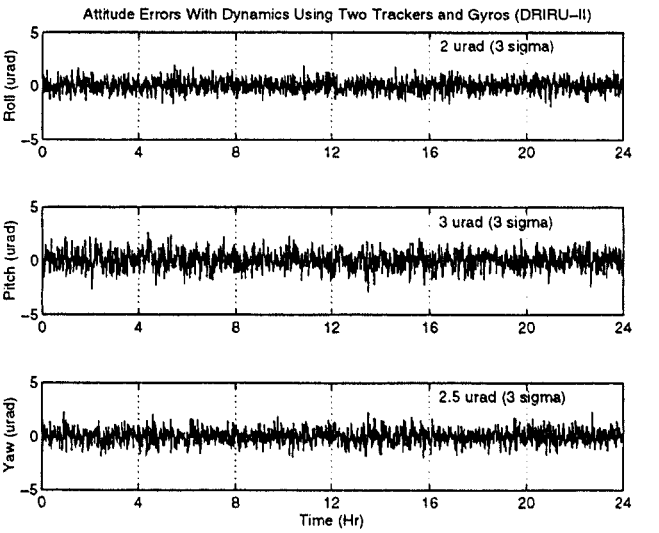

Figure 12 Attitude Errors Using Two Trackers (Kalman Filter, DRIRU-II)

4. CONCLUSIONS

This study provided some insights for using gyros and/or star trackers on the GOES spacecraft. It was determined that the gyros do not significantly reduce the non-repeatable errors with the ESA. Also, using gyros does not provide any observability in the yaw angle estimate, when using the ESA. The star tracker simulation results show a significant improvement over the ESA attitude knowledge errors. The greatest improvements were shown using either: (1) two trackers with the EQA, or (2) one tracker and a DRIRU-II type gyro, and (3) two trackers and either a SIRU type gyro or a higher quality gyro such as the DRIRU-II. Adding gyros to the spacecraft is the most ideal case, since the Kalman filter bandwidth is larger than the EQA filter bandwidth (i.e., the Kalman filter with gyros can sense higher frequency spacecraft motions than with the EQA). The utilization of on-board gyros may also improve the pointing accuracy, since the controller bandwidth may be increased.

5. ACKNOWLEDGMENTS

The first author's work was supported by a National Research Council Postdoctoral Fellowship tenured at NASA-Goddard Space Flight Center. The author greatly appreciates this support.

6. REFERENCES

1. M.D. Shuster and S.D. Oh, "Three-Axis Attitude Determination from Vector Observations," *Journal of Guidance and Control*, Vol. 4, No. 1, pp. 70-77, Jan.-Feb. 1981.

2. E.J. Lefferts, F.L. Markley, and M.D. Shuster, "Kalman Filtering for Spacecraft Attitude Estimation," *Journal of Guidance, Control and Dynamics*, Vol. 5, No. 5, pp. 417-429, Sept.-Oct. 1982.

3. Wertz, J.R., (editor) *Spacecraft Attitude Determination and Control*, Kluwer Academic Publishers, Dordrecht, 1978.

4. J.L. Crassidis, F.L. Markley, A.M. Kyle, and K. Kull, "Attitude Determination Improvements for GOES," Proceedings of the Flight/Mechanics/Estimation Symposium, NASA-Goddard Space Flight Center, Greenbelt, MD, pp. 151-165, 1996.

5. F.L. Markley, "Attitude Determination Using Vector Observations: A Fast Optimal Matrix Algorithm," *Journal of the Astronautical Sciences*, Vol. 41, No. 2, pp. 261-280, April-June 1993.

6. R.L. Farrenkopf, "Analytic Steady-State Accuracy Solutions for Two Common Spacecraft Attitude Estimators," *Journal of Guidance and Control*, Vol. 1, pp. 292-284, July-Aug. 1978.

Image navigation improvement using star trackers

Sun H. Hur-Diaz and Ahmed A. Kamel

Space Systems/Loral
3825 Fabian Way, Palo Alto, CA 94303

ABSTRACT

In this paper, the improvement in the Image Navigation and Registration (INR) obtained by using two star trackers onboard a GOES satellite is investigated. The star trackers would augment the current INR system to eliminate the nonrepeatable errors caused mainly by the Earth Sensor. The focus is on decreasing the spacecraft bus attitude error component in the total INR error budget with minimal changes to the current system.

Keywords: star trackers, image navigation, attitude determination, orbit determination

1 INTRODUCTION

The current GOES satellites (GOES-8 at 75° West longitude and GOES-9 at 135° West longitude) are three-axis, body-stabilized spacecraft that are capable of real-time coverage of the Earth's weather system.[1] The two main instruments, the Imager and the Sounder, operate independently and employ flexible scan controlled mirrors that can cover areas of different sizes. The instrument data are processed on the ground and retransmitted near real-time to the users via the spacecraft.

The instrument mirrors are compensated in real-time[2] for the orbital and attitude motions of the spacecraft via the Image Motion Compensation (IMC) and for the motions of the mirrors themselves via the Mirror Motion Compensation (MMC). The latter is autonomous compensation for the spacecraft response to large mirror motions and is provided by an onboard software representation of the closed-loop spacecraft response. IMC, on the other hand, relies on a 24-hour data fit on the ground of range measurements from a single ground station and measurements of landmark and stars by the instruments themselves. The underlying concept of the IMC system is based on the fact that the instrument line of sight attitude over the next 24 hours is identical to the current 24 hours, and the fact that nonrepeatable errors, mainly due to Earth Sensor (ES) radiance gradients and single-chord operations, can be significantly reduced by the Short Span Attitude Adjustments (SSAA) which update the IMC parameters using a more recent set of star and landmark measurements.

Star trackers can provide significant improvement to the pointing performance of the GOES satellites. The improvement in the image navigation accuracy comes from a more accurate knowledge of the spacecraft bus attitude to compensate the mirrors with. Since the star-tracker data is available real-time, its use is essentially an augmentation of the autonomous MMC system currently onboard. The implementation of the star trackers would not affect the current IMC procedure. The star trackers will also eliminate SSAAs and simplify ground operations.

0-8194-2200-2/96/$6.00

In the rest of this paper, the assumptions made in the current study and the nominal star tracker orientation are first discussed in Section 2. Then in Section 3, the design of the filter to reduce the random errors is presented followed by a discussion of the nonrandom errors in Section 4. Simulations conducted to evaluate the star tracker performance are presented in Section 5. Finally, summary and conclusions are given in Section 6.

2 STAR TRACKER ORIENTATION

Star trackers considered in this study have an 8° × 8° rectangular field-of-view (FOV). They are capable of tracking up to 5 or 6 stars each with a sensitivity to magnitude 6 stars at 10 Hz date rate or up to magnitude 7 at 4 Hz. The random component of the centroidal error of a single star is assumed to be 5.33 arcsec (25.8 μrad) RMS for the limiting magnitude stars at either data rate. The total centroidal error is a combination of the noise equivalent angle (NEA), spatially random errors, and boresight stability/misalignment errors. Other errors contribute to the estimate of the spacecraft attitude including thermal distortions and orbit knowledge errors. For onboard generation of orbit information, the onboard clock error can also be significant. For the GOES INR system, the repeatable portion of these errors is removable by the IMC.

The orientation of the star trackers is defined using three consecutive angles: azimuth (β) about $+y$-axis measured from the $+z$-axis, elevation (η) about the resulting $+x$-axis measured from the $+z$-axis, and a "roll" (γ) about the resulting $+z$-axis which is the star tracker boresight. These angles are illustrated in Fig. 1. The

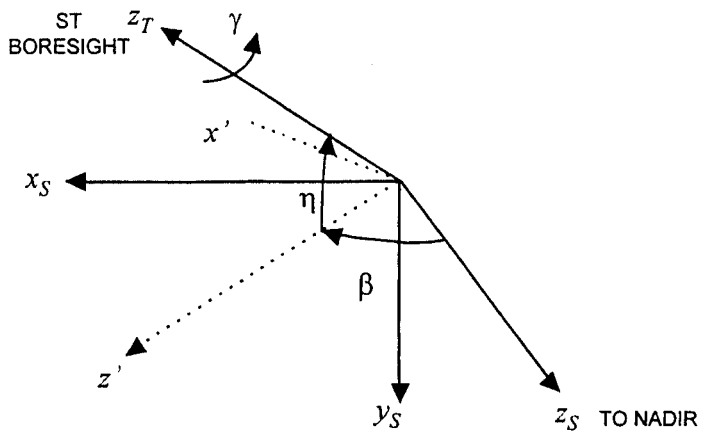

Figure 1: Star tracker alignment angles

nominal orientation angles of the two star trackers are

$$\beta_1 = -43°, \quad \beta_2 = 43°, \tag{1}$$

$$\eta_1 = 55°, \quad \eta_2 = 55°. \tag{2}$$

The nominal angles are shown in Fig. 2. This orientation is based on a Earth-face panel mount, a 30 deg Sun exclusion angle (SEA), and a 25 deg separation from the Earth panel to avoid reflections off of the panel. Both star trackers are northward pointing to avoid reflections off of the solar array on the South side. The elevation angle was primarily influenced by the SEA. The minimum elevation angle is given by:

$$\eta_{min} = \eta_{SUN} + \text{SEA} + \eta_{MARGIN}, \tag{3}$$

$$= 23.5° + 30° + 1.5°, \tag{4}$$

$$= 55°. \tag{5}$$

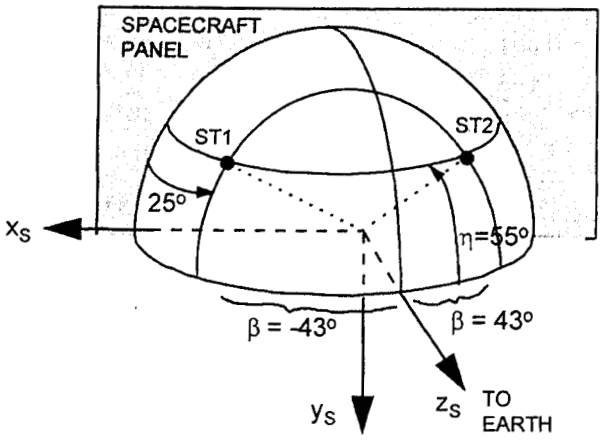

Figure 2: Nominal orientation of star trackers

The margin allocated is 5% of the SEA. For minimum error about the spacecraft pitch axis, the elevation angle of the star tracker should be as small as possible. This is seen from contour plots of spacecraft unfiltered attitude accuracy as a function of elevation and azimuth separation given in Fig. 3. The contour plots were generated

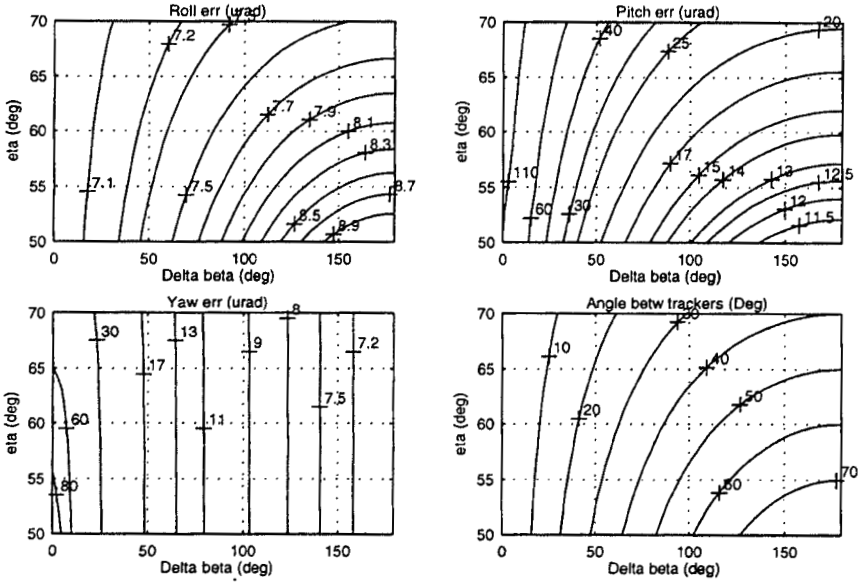

Figure 3: Unfiltered attitude accuracy (1σ) of two star trackers as a function of η and $\Delta\beta = \beta_2$-β_1

assuming symmetrical placement of the star trackers about the y-z plane of the spacecraft. The roll/pitch/yaw accuracies are derived from a nominal snapshot multi-star average of each star tracker of 10/10/200 μrad (1σ) in the star tracker axes. The plots also indicate that greater the azimuth separation between the two trackers, closer the enclosed angle is to 90° (*cf.* plot 4) and hence higher the accuracy. For the nominal orientation angles given in Eqns. 1 and 2, the roll/pitch/yaw accuracies are 8/16/10 μrad (1σ).

The azimuth orientations were selected primarily to avoid reflections from the spacecraft body into the star trackers mounted on the Earth panel. If the Earth-panel restriction is removed, then azimuth angles of 0° and 180° are more ideal. This latter set gives the maximum azimuth separation as well as the best and equivalent roll

performance in case one tracker fails. For the present analysis, we assume an Earth panel mount and the nominal orientation angles given in Eqns. 1 and 2.

Star availability is another consideration in determining the optimum orientation. However, it is not an issue for a 4 Hz data rate with sensitivity to magnitude 7 stars. The 4 Hz data rate was chosen for the current study. The orientation of the star trackers will also be affected by thermal and configuration constraints. These are ignored for the current performance analysis.

3 FILTERING OF RANDOM NOISE

The purpose of the filter is to reduce random star tracker-induced noise. Other nonrandom errors due to thermal variations and orbit error are not affected by the filter. The design of the filter is determined by the acceptable level of the noise floor and the types of disturbances that are to be detected by the star tracker.

One disturbance of particular interest is the black body calibration (and slew) of the instrument mirrors. During a black body calibration, the disturbance can be high as 150 μrad in roll. Currently, this disturbance is compensated by the MMC where the spacecraft response to the mirror motion is modeled and predicted onboard. MMC operates continuously without operator intervention. The frequency range in which MMC operates is roughly between 0.001 Hz and 1 Hz. To avoid "double-bookkeeping" of this disturbance by the star tracker, the bandwidth of the star tracker filter can be selected to be below 0.001 Hz or above 1 Hz. At the lower cutoff frequency, both the star trackers and the MMC can operate. However, since MMC corrects only for the mirror motions, the ability of the star trackers to detect other disturbances at higher frequencies is severely limited. At the higher cutoff frequency, on the other hand, the MMC may be eliminated, but the star tracker-induced noise remains high without much attenuation. In this case, the star tracker introduces more errors to the system than are currently present. At the cutoff frequency of 1 Hz, the attenuation at the 4 Hz data rate is only about:

$$\sqrt{\frac{1\ \text{Hz}}{4\ \text{Hz}/2}} = 0.7 \tag{6}$$

With the raw two-star tracker pitch error of 48 (=16×3) μrad, the filtered accuracy is only about 34 μrad (3σ). The MMC performance, on the other hand, is currently estimated to be 6 μrad (3σ).

Since the MMC operates very well, especially in correcting for the rigid body motion of the spacecraft due to mirror slew motions, it is not imperative to eliminate it. Rather, it can be used in a complementary filter to achieve both low background noise and good detection of the mirror slew response. This concept is illustrated in Fig. 4. The star tracker estimate of the spacecraft attitude is fed into the low-pass filter. The MMC signal is fed into the complementary high-pass filter. The sum of the two filtered signals is then the best estimate of

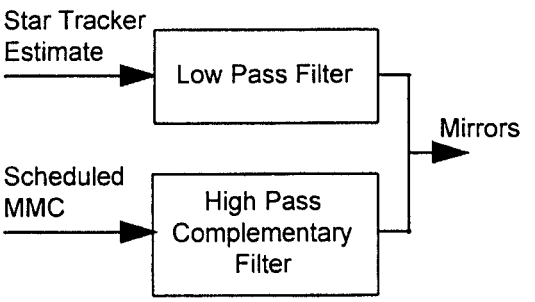

Figure 4: Complementary filter concept

the spacecraft attitude. The cutoff frequency of the low-pass filter is selected based on the trade between a low noise floor and the ability to detect disturbances other than the mirror motion, especially in the high frequency range. Some of these other disturbances include thermal snap, return from ES single chord, thruster unloads, and trim tab adjustments. For a preliminary performance assessment, a cutoff frequency of 0.1 Hz was selected for all three axes in a second-order Butterworth filter. Some simulation results of this filter are given in Section 5.

4 NONRANDOM ERRORS

In addition to the random errors discussed above, there are nonrandom errors associated with the use of the star trackers. These include constant and time-varying star tracker misalignments and onboard orbit knowledge error. The misalignments are variations from the nominal alignments as measured on the ground. Thermal variations mainly due to the orbital motion of the spacecraft can cause the misalignments to vary with time with a period of one sidereal day. These will vary from season to season but fairly repeatable from day to day. Because of the repeatability of the misalignments, it is expected that a significant portion of this error will be removed by the IMC.

Because star trackers are inertial sensors, orbit knowledge is required to determine the orbit-relative spacecraft attitude (roll, pitch, and yaw). The onboard orbit knowledge is obtained from a set of coefficients that are uploaded as part of the IMC set. The process involves a ground-based orbit determination (OD) using range, star, and landmark measurements. The OD solution is then propagated using an accurate ephemeris generator. A reduced set of orbital elements spanning at least a day is curve-fitted and the corresponding coefficients as well as the epoch time are generated. Currently, these coefficients are uploaded on a daily basis. An enhanced set of coefficients has been derived with a fit accuracy of less than 10 μrad over one week that would allow weekly updates instead of daily updates.

To determine the order of magnitude error of the onboard orbit knowledge, a covariance analysis of the recent flight data was performed. The results were then combined with worst case fit error to arrive at the total error. The results are summarized in Table 1. The orbit determination error is the dominant source of the error. Because

Table 1: Onboard orbit knowledge error, μrad (3σ)

	Propagated OD error	3 day fit error	RSS
E/W	15.6	4.5	16
N/S	20.7	7.0	22

of high correlation of the uncertainty in the OD solution, the OD error does not grow appreciably, even over one week. Therefore, with the improved set of orbital coefficients, comparable orbit knowledge error can be retained even over one week. A heuristic analysis of the star and landmark residuals resulted in similar numbers for the current total onboard orbit knowledge error. The orbit error will be "seen" by the instruments as attitude error. It is expected that part of this error will be removed from the attitude portion of the IMC.

5 SIMULATIONS

A star tracker simulator was built in Matlab to investigate the performance of the star trackers. A block diagram of the simulator is shown in Fig. 5. The true spacecraft attitude is provided by a separate simulation of the long term response, the short term response, and the response to black body calibrations. The long-

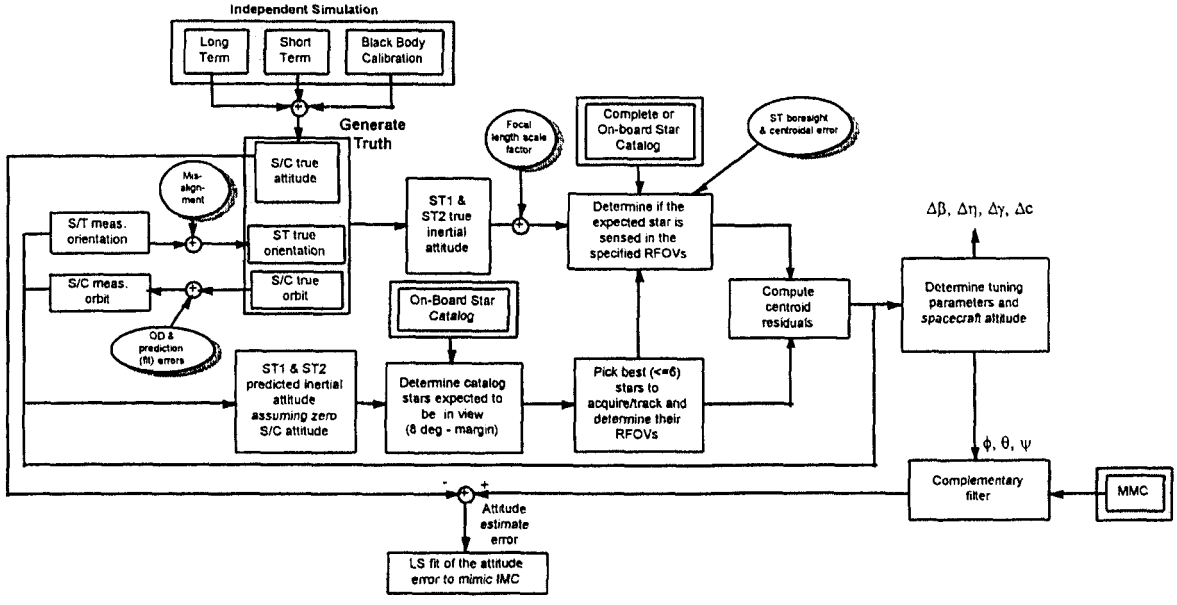

Figure 5: Simulation block diagram

term response contains responses to continuously changing solar torque, magnetic torques from measured B-field, radiance gradient model from measured data, ES thermal distortion as measured by the instruments, and daily trim tab adjustments. The short-term responses can be selected to be responses to ES noise or ES noise plus any one of the following: thermal snap, return from ES single chord, wheel unloads, or trim tab adjustments. The black body calibration response is an output of the MMC. Depending on the simulation, these responses can be turned on or off. Other true quantities that are generated are the star tracker orientation and the orbit. The star tracker true orientation is the sum of the measured orientation and the misalignments which can be time-varying. The spacecraft true orbit is provided by an accurate ephemeris generator and orbit determination and fit errors are added to simulate the measured orbit, *i.e.*, the onboard orbit knowledge.

The onboard star catalog for the simulations was built from Sky Catalog 2000. For the results shown, 5 or more stars of magnitude 7 and brighter were visible all the time (for a 4 Hz data rate). The star trackers are commanded to acquire and track stars that are expected to be in the field of view as predicted from the measured orientation and measured orbit assuming zero attitude. The actual positions of the stars seen by the star trackers are determined by the true attitude, true alignment, and true orbit and are modified by any focal length errors and star tracker boresight and random centroid errors. The star centroid residuals are computed as the difference between the predicted and the measured centroids. Star tracker tuning parameters as well as spacecraft attitude are then determined using least-squares from the centroid residuals. Different error sources can be turned off or on depending on the type of performance being evaluated.

Three sets of simulations were conducted: 1) short term performance during black body calibration, 2) short term performance during other spacecraft disturbances, and 3) long term performance with focal length variations and thermal misalignments. The single tracker performance is also briefly discussed. These simulations are discussed in the following subsections. Except as noted, the cutoff frequency of the star-tracker filter was set at 0.1 Hz for a nominal noise floor of about 10 μrad (3σ) in pitch.

5.1 Performance under black body calibration

For analysis of performance under black body calibration, the misalignments, focal length variations, and orbital errors were turned off in the simulation. The true attitude was the sum of the long-term, short-term, and black body calibration responses provided by an external simulation as described above. No time delays were modeled in this simulation. Fig. 6 shows the results of this simulation in four columns of plots. The first

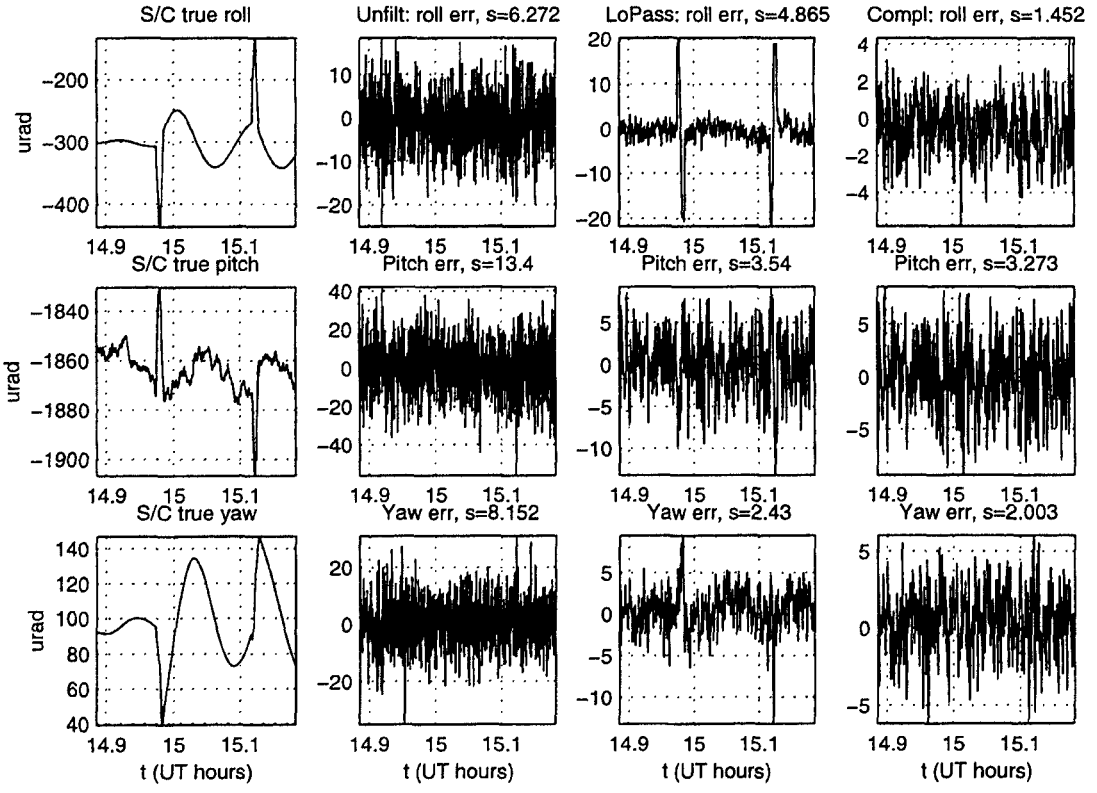

Figure 6: Star tracker performance under black body calibration

column shows roll, pitch, and yaw time-histories of the true spacecraft attitude. The second column is the error in the star tracker estimate of the spacecraft attitude without any filtering. The third column shows the estimate error with the low-pass filter only. The fourth column shows the estimate error with the complementary filter. In general, the pitch performance is the worst of the three axes because of the minimum elevation constraint on the star trackers. In roll, the background noise is significantly reduced with the low pass filter only, but the error during the rigid body motion can be higher than the error without filtering. The best performance is with the complementary filter. Here we get the best of both worlds: low background noise and good detection of the mirror slew response.

5.2 Performance under other short-term disturbances

Simulations were also conducted to analyze the performance of the 0.1 Hz filter on other short-term disturbances. These include ES noise only, thermal snap, return from ES single chord, pitch unload, yaw unload, and trim tab adjustment. The last five disturbances also include the ES noise. For the last four disturbances, imaging is inhibited during the initial 10-minute transient period; therefore, the star tracker performance is based on the post transient period. During the ES noise and thermal snap disturbances, imaging is not inhibited, so the star

Table 2: Short term spacecraft attitude estimate error with two star trackers, roll/pitch/yaw (μrad)

Disturbance	Without Star Tracker (Max)	With Star Tracker (1σ)	With Star Tracker (Max)
ES noise (20 min.)	10/16/5	1.3/3.0/1.9	5/10/7
Thermal snap (40 min.)	120/21/85	1.8/3.0/2.0	7/12/7
ES single chord*	145/22/85	2.3/2.9/2.3	6/9/8
Pitch unload*	9/16/33	1.3/2.9/1.8	4/8/5
Yaw unload*	450/21/390	6.8/2.9/6.6	17/10/14
Trim tab adjust*	50/15/27	1.5/3.1/1.7	5/10/6

*Numbers correspond to the second 10-minutes of simulation after the initial 10-minute transient

tracker performance during these disturbances is based on the entire period of the simulation. The simulation results are tabulated in Table 2. During nominal operation with ES noise only, the worst roll/pitch/yaw performance is 5/10/7 μrad. The worst overall performance is after the yaw unload of 17/10/14 μrad. The performance with the star tracker is significantly better than without. By having separately-tuned filters for each axis, the performance can be improved further.

5.3 Long term performance with misalignments and focal length error

In this simulation, the true attitude was the long-term response provided by the external simulation as described above. Orbit error was turned off but a constant bias in each of the star tracker's focal length scale factor as well as time-varying misalignments of each star tracker were included. The focal length scale factor is defined as

$$c \equiv \frac{f}{f_o}, \tag{7}$$

where f is the true focal length and f_o is the nominal value. The focal length scale factor variations were set in the simulations to be Δc_1=0.01 and Δc_2=0.02 for Star Tracker 1 and Star Tracker 2, respectively. The misalignments were modeled as a bias plus a simple sinusoid for each alignment angle of each star tracker.

The star tracker misalignments and the spacecraft attitude are not completely observable from the star centroid residual measurements. Either the misalignments or the attitude can be solved but not both. The resulting solution (from least-squares of multi-star measurements) contains errors due to the other unsolved quantity. For example, solving for attitude alone will result in the attitude solution containing errors due to the misalignments. This is unavoidable. However, when the mirrors are corrected with this attitude solution, the misalignment errors will be detected by the IMC. Since the misalignment errors are largely due to thermal variations during the orbit, they are expected to be repeatable from day to day. Therefore, most of the misalignments are removable by the IMC which is designed to remove repeatable errors in the INR system.

The misalignment errors will be "seen" by the instruments as repeatable, low frequency errors. Focal length errors, on the other hand, will appear as high frequency errors in the attitude solution. Therefore, it is desirable to calibrate out the focal length variations. Fortunately, this error is observable. Fig. 7 shows the scale factor solution from a simulation. The first column of plots shows the true focal length scale factor variation in solid line and the snapshot least-squares solution in circles for Star Tracker 1 and Star Tracker 2, respectively. The second column of plots shows the error in the solution of the scale factor variation to be less than 5×10^{-4}. With a curve-fit to remove the high frequency component, the error can be reduced to less than 2×10^{-5}.

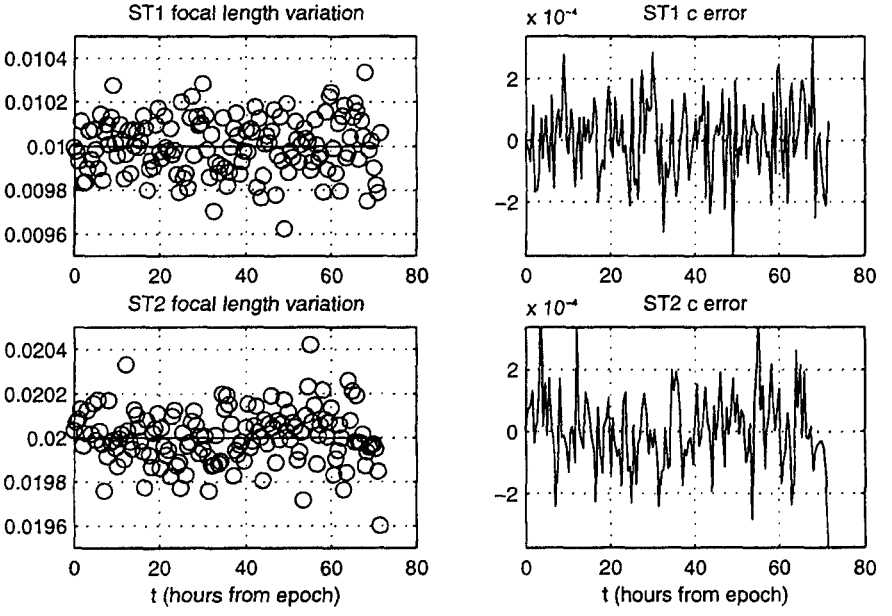

Figure 7: Solution of scale factor variation for Δc_1=0.01 and Δc_2=0.02

With the scale factor calibrated for each star tracker, the normal operation of the star trackers was simulated by solving for attitude (containing the misalignment errors) and then curve-fitting the resultant attitude error. The curve-fitting process is a very simplified simulation of the IMC process. Fig. 8 shows the results of this simulation. The first column of plots shows the actual error in the spacecraft roll, pitch, and yaw estimates (dashed line) mainly due to the star tracker misalignments. Overlayed on top are solid curves which are curve-fits of the attitude errors. The second column of plots shows the difference between the curve-fit and the actual attitude estimate error. What remains is the random star tracker noise with a standard deviation of 6/13/9 μrad in roll/pitch/yaw axes which would have been reduced by the onboard filter as described in Section 3.

5.4 Performance with a single star tracker

A fully redundant system requires three star trackers with two operating at any one time. Two trackers is not a fully redundant system in that the performance with one star tracker is not equivalent to two star trackers. However, one tracker failure is not a total system failure; it leads to degraded performance. The multi-star average accuracy of one star tracker as a function of orientation is shown in Fig. 9. As in Fig. 3, the snapshot multi-star average of 10/10/200 μrad (1σ) in the star tracker axes was assumed. For INR, roll accuracy is more important than yaw accuracy; therefore, a zero azimuth angle is preferred, if possible, over the nominal orientation given by Eqns. 1 and 2. Then with a little bit of averaging, the roll accuracy of the two trackers can be achieved. Pitch accuracy, on the other hand, is limited by the minimum elevation angle. At 55 degrees, the accuracy is 492 (=164×3) μrad (3σ). To bring this error down to the level of 10 μrad obtained with two trackers, the time constant of the filter has to be as high as 20 minutes (0.00083 Hz). For long term performance, this time constant is acceptable. Short term performance, on the other hand, is greatly compromised. To improve the short term performance, other sensors resident in the spacecraft may be employed.

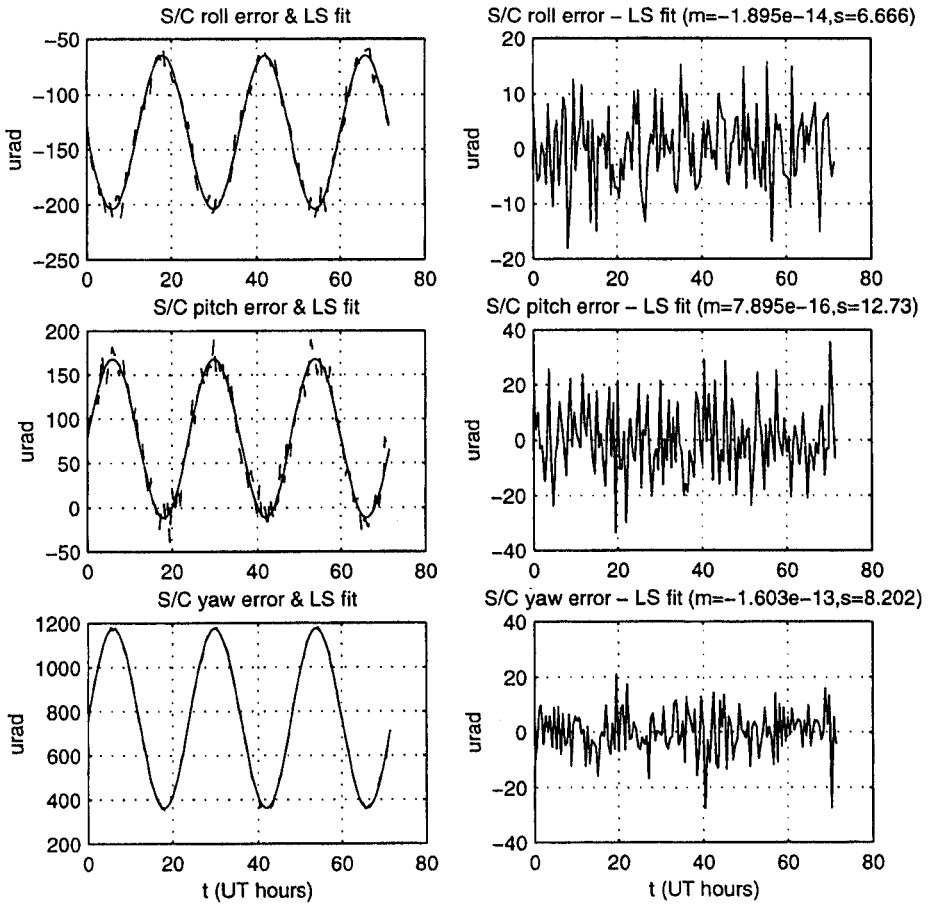

Figure 8: Spacecraft attitude estimate error due to misalignments and the IMC curve-fit

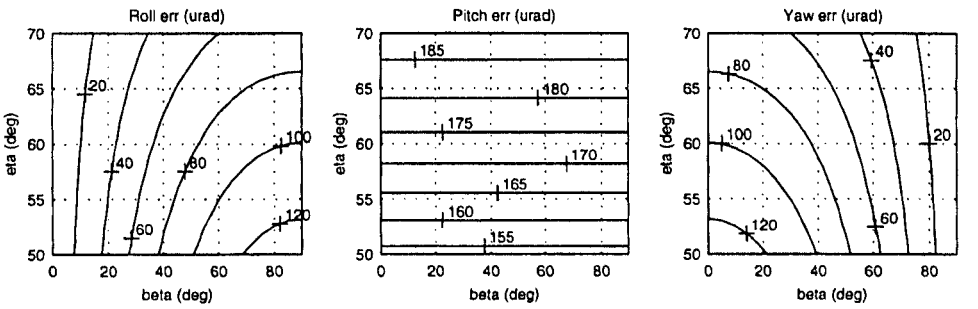

Figure 9: Unfiltered accuracy (1σ) of one star tracker

6 SUMMARY AND CONCLUSIONS

The performance of two typical narrow FOV star trackers on a GOES spacecraft was evaluated. The design and performance of a complementary filter that works with the MMC currently onboard was presented. Results of simulations show excellent improvement in short-term performance over the current system without star trackers during typical spacecraft disturbances. Long-term simulations have also shown how the focal length variations and the thermal misalignments can be removed through calibration and IMC, respectively.

Star trackers can significantly reduce the spacecraft bus error component of the total INR error budget by eliminating the nonrepeatable errors. With appropriately designed filters, the nonrepeatable errors are observed and compensated real-time. Then the errors that remain, most of which IMC can detect and correct, are primarily due to the thermal variations of the star trackers and the instruments. Hence, with star trackers, ground operations effort can be significantly reduced by eliminating SSAAs. The frequency of the IMC update can also be reduced from once a day to once a week with an enhanced set of orbital coefficients.

Further work is planned to investigate the performance and operations after an orbit adjustment when the onboard orbit knowledge provided by IMC is not very accurate. Also, the improvement of short-term single tracker performance using other sensors on the spacecraft is currently being studied. Further tuning of the filters is also planned to optimize performance about each axis.

7 ACKNOWLEDGMENTS

The work presented in this paper was performed under the Internal Research and Development at Space Systems/Loral. Some of the results of the simulation applicable to GOES were produced under a separate government contract.

8 REFERENCES

[1] *GOES I-M: Databook*, DRL 101-08, Space Systems/Loral.

[2] Kamel, A. A., *GOES Image Navigation and Registration System*, International Symposium on Optical Science, Engineering, and Instrumentation, SPIE's Annual Meeting, Denver, CO, 4-9 August 1996.

Autonomous star trackers for geostationary satellites

Roelof W. H. van Bezooijen

Lockheed Martin Advanced Technology Center
3251 Hanover Street, Palo Alto, California 94304

ABSTRACT

An autonomous star tracker (AST) is a "star field in, 3-axis attitude out" device capable of determining its attitude rapidly without requiring any a-priori attitude knowledge. Following attitude acquisition, the AST switches to a track mode where it outputs its attitude and rate at typically 5 Hz. The Lockheed Martin Advanced Technology Center has developed the first version of a line of reliable, highly accurate, low cost, ASTs. This "AST-201" is to be test flown on a sounding rocket and will function as a key attitude sensor aboard NASA's Small Spacecraft Technology Initiative (SSTI) "Clark" spacecraft scheduled for launch in 1996.

The AST is of modular construction and comprises athermalized, radiation hard refractive optics, a frame-transfer CCD with a sensitive area of 512 by 512 pixels, camera electronics, a single board computer, an all-sky guide star database and a highly effective sunshade that allows operation to within 25 degrees from the Sun. Initial star identification is performed by a memory-efficient algorithm that provides an attitude acquisition success rate of better than 99.85% anywhere in the sky. The AST achieves its high accuracy through use of a moderate 8.8 by 8.8 degree field of view and by tracking 27 stars on average.

On geostationary satellites a single AST can provide 3-axis attitude with greater precision, at lower cost, and with higher reliability than is possible with a combination of Earth sensors, fine Sun sensors, and a high performance gyro system. In addition, ASTs are devoid of angular range limitations, avoid Sun and Moon interference by proper orientation on the spacecraft, and enable rapid fault recovery, a capability especially important to geostationary missions where outages are usually costly. Two ASTs can provide a geostationary spacecraft with an attitude accuracy of 5 microradians (1 σ). The paper contains a description of the AST, a summary of the functions enabled or improved by the device, real-sky AST test results, and accuracy statistics for an AST on a geostationary spacecraft, as obtained through realistic simulations.

Keywords: star tracker, autonomy, attitude determination, pattern recognition, geostationary satellites, spacecraft attitude control.

1. INTRODUCTION

Lockheed Martin, in anticipation of the need for smart sensors capable of supporting autonomous, long duration space flight missions, has been developing a low cost, highly accurate, Autonomous Star Tracker (AST) on an IRAD program beginning in 1991. The AST, shown schematically in Fig.1, is basically a "starfield-in, attitude-out" device capable of determining its attitude in a few seconds without requiring any a-priori attitude knowledge. Following atttitude acquisition, the AST transitions to its track mode where it provides its 3-axis attitude at a 5 Hz rate. In addition, the device can be used to perform attitude updates autonomously. Besides providing the functionality needed for future advanced attitude control and navigation systems, ASTs can be used to increase the reliability of spacecraft while reducing their mass, power, cost, and operating expenses.

The AST comprises a-thermalized, refractive optics, a frame-transfer CCD, camera electronics, a compact single board computer with a 32 bit RISC processor, and an all-sky guide star database. Star identification is performed by a memory-efficient and highly robust algorithm that finds the largest group of observed stars matching a group of guide stars.[1,2] The sensitivity of the AST permits it to operate at all sky locations, while it tolerates bright objects in the FOV (e.g., due to Jupiter and space debris) because of the geometrical and brightness constraints imposed by the star identification algorithm. The AST is designed to survive sun pointing without the use of a shutter.

Functions enabled or enhanced by the AST include: rapid attitude acquisition; fast fault recovery; autonomous updating of gyro based attitude control and navigation systems; gyroless or low-cost gyro spacecraft attitude control; autonomous acquisition of celestial targets by orbiting, sub orbital, airborne, or ground-based astronomy telescopes; precision pointing to terrestrial targets from space (GPS assisted); autonomous optical navigation of planetary spacecraft; and autonomous position acquisition (longitude and latitude) of planetary rovers using a zenith pointed AST.

0-8194-2200-2/96/$6.00

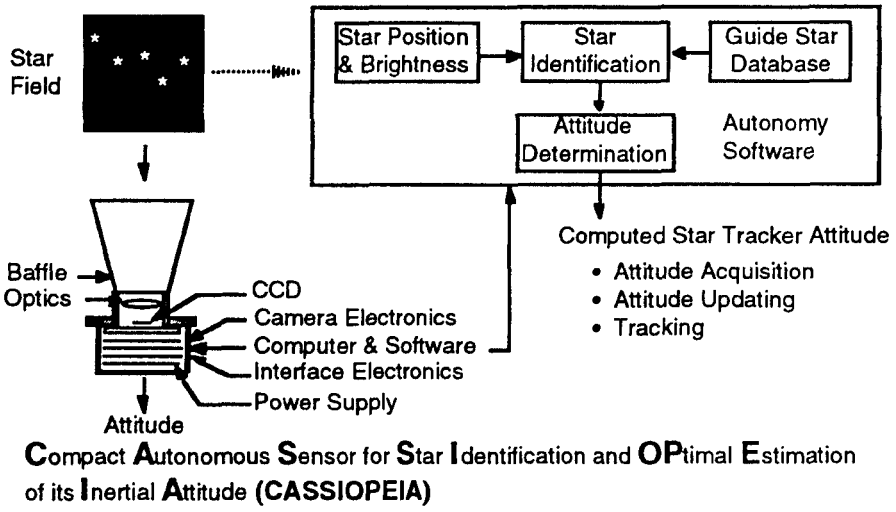

Fig. 1 Schematic of the autonomous star tracker

ASTs are particularly beneficial to geostationary satellites, where they can replace Earth Sensor Assemblies (ESA) and Fine Sun Sensors (FSS), allow the use of lower performance gyros, improve pointing precision, and enable rapid fault recovery, a capability especially important to geostationary missions where outages are costly. Replacement of the Earth and Sun sensors and use of lower performance gyros reduces spacecraft cost and improves reliability. The latter benefit, which is important for future long duration missions, is due primarily to the fact that ASTs are more reliable than ESAs because of the absence of moving parts and a lower number of electronic parts.

In 1991 and 1992 the IRAD program was used to develop software for generating the guide star database required for the AST. In addition, the star identification algorithm, originally developed for a different application while at Stanford University,[1] was refined and optimized for use with the AST. The SKYMAP[3] star catalog is used both for generating the guide star database and for describing the sky in the simulations. This catalog was compiled primarily for the purpose of satellite attitude determination and provides 622 bytes of information for each of its 248,563 stars.

The attitude acquisition capability of the AST was demonstrated early in 1994 through correct and rapid (less than 1 sec) identification of all 704 true-sky star fields obtained at the Lick Observatory with an uncalibrated proof-of-concept AST developed in 1993.[4] This device is equipped with a 512 by 1024 pixel frame-transfer CCD and a 50 mm f/1.2 lens that provides an effective 6.5 by 13.2 degree field of view. The overlapping fields covered 47% of the sky, including both rich and sparse areas. The engineering model (EM) of the AST has been used in 1995 and 1996 to successfully demonstrate attitude acquisition and track using both a star field simulator and the real sky. This EM is virtually identical to the ASTs that will be flown on two missions later in 1996.

The AST is described in section 2, a number of its applications are covered in section 3, and the acquisition and track operation and performance are reported on in sections 4 and 5. The performance of ASTs on geostationary satellites, as predicted by realistic simulations, is presented in section 6, while the conclusions are contained in section 7.

2. AST DESCRIPTION

The AST is of a modular design, comprising a baffle or sun shade, optics assembly, sense head, camera electronics, processor, and power supply. The AST version that will be used for the first deep space mission (DS-1) of JPL's New Millenium Program (NMP) is shown in Fig. 2. The baffle is adapted to meet customer defined Sun / Earth / Moon exclusion angles. For DS-1 the solar exclusion angle is 40 degrees, meaning that the AST has to function when the Sun is 40 or more degrees from the boresight. This can be achieved with a 12.6 cm long baffle. The AST for NASA's SSTI Clark spacecraft, being built by CTA Space Systems, has a 32 cm long baffle that provides a 20 degree solar exclusion angle.

The optical assembly consists of a fused silica window, radiation hard lens elements, an aluminum lens barrel, and a cylindrical thermal radiation shield that surrounds the barrel and minimizes radiative heat transfer to and from the barrel. Boresight stability is ensured by a thermal design that eliminates radial temperature gradients in the lens barrel. A stress-free

mounting method has been adopted for the lens elements in order to maintain centration stability over a large temperature range. The optical prescription for the 50 mm f/1.2 lens has very low distortion, low color sensitivity and an effective focal length that is highly stable versus temperature (changes less than 0.05% over a 50 degree temperature range). In addition, it provides a line spread function that allows accurate centroiding without the need for a lookup table. Special materials and geometry are used to athermalize the optical system, i.e., focus is maintained over a large temperature range. The optics are designed to accommodate a field of view (FOV) with a diameter up to 17 degrees.

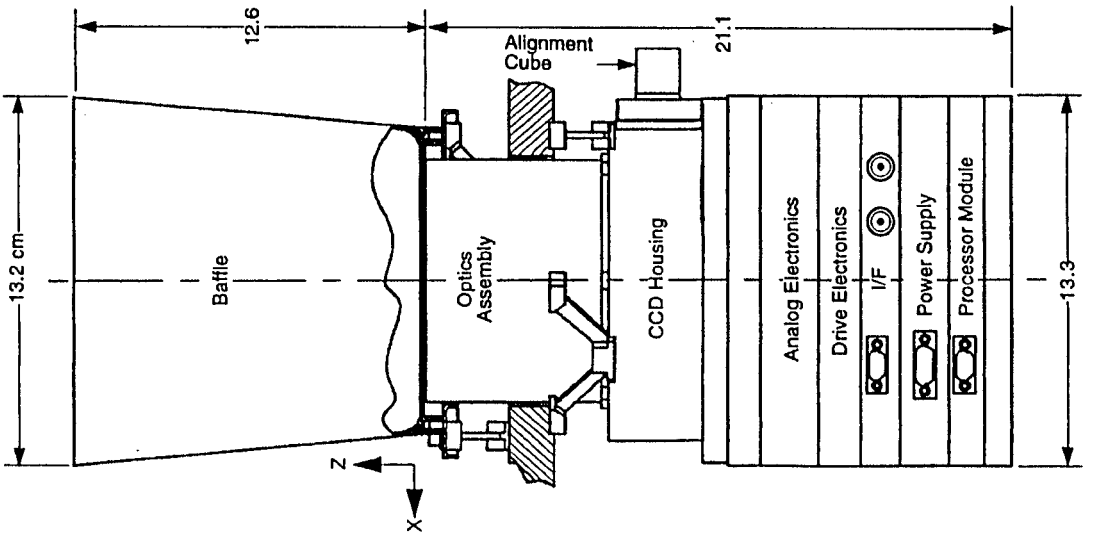

Fig. 2 AST for DS-1 Mission

The sense head consists of a cylindrical aluminum housing for the thermoelectrically cooled CCD. The CCD, which is operated in the MPP mode for low dark noise, is of a split, frame transfer architecture, has 512 by 512 imaging pixels and 4 output amplifiers. An alignment cube with 5 usable faces measuring 16 by 16 mm each is mounted to the CCD housing. The cylindrical section is connected to the sense head bottom plate which also serves as the heat sink for the thermoelectric cooler (TEC) and as the top plate for the electronics enclosure.

The camera electronics consists of analog electronics, drive electronics and interface electronics modules. It is configured as a state machine, which maximizes the amount of processing time available to the AST processor. The analog electronics module contains a signal chain for each CCD half, while the drive electronics hosts the circuitry for the CCD clock drivers. The interface electronics includes the circuitry for the dual 1553 B interface, as well as the circuitry for the communication interface with the AST processor. It has one connector for an optional redundant square wave synchronization signal input plus two 1553 connectors. The AST has partial redundancy because each CCD half has its own output amplifier, its own signal chain, comparator, and analog to digital converter. In addition to providing partial redundancy, the split frame implementation has the additional benefit of being less sensitive to Charge Transfer Efficiency (CTE) degradation because it reduces the number of charge transfers by approximately a factor of two.

A high performance, low power, R3000 based single board computer developed by Lockheed Martin Missiles and Space (LMMS) is employed as the AST processor. It includes 2 Mbyte of EDAC protected SRAM and 1 Mb of EEPROM. Its clock rate was reduced from 24 to 12 MHz to reduce its power consumption to less than 4 W. Its dimension of 13.3 by 15.3 cm defined the form factor of the AST electronics. An almost identical processor is used for the Lockheed Martin Launch Vehicle. The processor module has a connector for dual RS422 communication, implying that the AST can be used either with a 1553 B or an RS422 communication interface. The power supply module hosts the DC DC converters, the TEC controller, the watch dog timer, and the survival heater, if required. Eight bolts are used to attach an end cover plus the frames of all five electronics modules to the bottom plate of the CCD housing.

As may be seen from Fig. 2, three titanium bipod flexures, bolted to the top face of the CCD housing, connect the AST to the spacecraft. This solution was adopted for several reasons. First of all, the low thermal conductivity of the bipods minimizes the heat flow in the sense head, which contributes to the iso-thermal state of the top face of the CCD housing to

which both the lens barrel and the CCD assembly are attached. This iso-thermal state is needed to guarantee boresight stability. The bipod flexures also provide for a stress free mount of the AST, which further promotes boresight stability. Furthermore, the flexures allow for easy installation of the AST because their flexibility in the radial direction facilitates mounting even if the holes in the heads of the bipods do not line up perfectly with the holes in the top face of the CCD housing. The baffle, which, depending upon the sun angle variation, typically shows large temperature swings, is isolated from the AST and connected to the spacecraft using three identical titanium bipod flexures.

Instead of the bulkhead type of mounting shown in Fig.2, the AST is usually attached to either a spacecraft bracket or an internal AST bracket, which in turn is mounted to the spacecraft. For either solution, the attachment of the bracket to the spacecraft will be on the +X side of the AST. By properly sizing the bracket, three radiator plates, one on either side and one on top (- X side), can be mounted to the bottom plate of the sense head from which they extend forward to the baffle mount plate at the base of the baffle. If the AST is mounted external to the spacecraft bus, as is the case for the Clark AST, these radiators are used to passively cool the AST CCD to approximately zero degrees C, thus minimizing AST power consumption. If mounted internal to the spacecraft bus, as is the case for the ASTs used for the P59 program, the radiators are used to maximize radiative heat transfer between the AST and its cavity, which offsets the low conductive heat transfer through the bipods. The radiators of the externally mounted AST are covered with high emissivity, low absorptance fosar tape, while the emissivity of the internally mounted AST is maximized by using paint. By enclosing the cavity around the optics assembly and CCD housing at the +X side and by applying a low emissivity coating on all surfaces that can be seen by the CCD housing and the thermal radiation shield around the lens barrel, radiative heat transfer to the lens barrel and the CCD housing is minimized, which further promotes boresight stability.

The characteristics of the AST-201 are summarized in Fig. 3.

Characteristic	Value	Comment
Number of imaging pixels	512 x 512	AST uses a split, frame transfer CCD
Field of view (deg)	8.8 x 8.8	
Sensitivity (m_V)	7.5	Ensures all-sky tracking
Number of stars tracked		
Capability / Average	50 / 26.9	Av. number obtained with all-sky simulation
Accuracy at 0 / 0.2 deg/s rate (arcsec, 1 σ)		
Per star, per axis at magnitude limit	3.9 / 7.0	Does not include alignment uncertainty
Overall*, "pitch and yaw"	2.3 / 2.7	Includes 2 arcsec alignment uncertainty
Overall*, "roll"	20.3 / 28.3	Includes 10 arcsec alignment uncertainty
Track mode update rate (Hz)	5	Can be reduced, if desired
Track rate, at reduced performance (deg/s)	0.8	Loss of full sky coverage at rates > 0.8 deg/s
Attitude output format	Quaternion	Dir. cosine matrix and Euler angle are options
Communication interface	1553 B / RS422	Either interface can be accommodated
Power (W), 0 / 50 deg C	12 / 16.5	TEC usually not needed below 20 deg C; power can be reduced when lowering update rate
Mass, with radiators but without shade (kg)	4.0	3.25 kg lightweighted option is available
Operating temperature (deg C)	-30 to +50	
Solar exposure duration	No limit	
Number of acquisition guide stars in database	6,400	
Number of supplementary guide stars in database	10,000	
Mean time between failures (hr)	10^6	

*) Assumes use of 16 tracked stars (average number of stars tracked is 27)

Fig. 3 AST-201 Characteristics

In addition to the primary AST output, which includes the 3-axis attitude, the rate about each axis, the number of stars used for the attitude computation, and the rms value of the position error of the tracked stars, the AST also provides auxiliary output upon request. One of the auxiliary output packets that can be commanded contains the following information for each star tracked: star ID, star position about the X and Y axes, star brightness and brightness error, and the position error of the tracked star about both axes. The AST can be operated in its default free running mode where the exposure timing is

determined by the AST based on the commanded exposure time, or its exposure timing can be controlled by an external square wave synchronization input signal provided by e.g., the attitude control system (ACS). If free-running, the AST provides timing information from which the ACS can determine when each exposure started and ended. If operated in its synchronized mode, the end of each exposure occurs at the rising edge of the synchronization signal, thus minimizing the time uncertainty of each exposure.

3. APPLICATIONS

3.1 Attitude acquisition

Conventional attitude acquisition methods are complex, time consuming processes where typically a combination of the Sun, the Earth, and the Earth's magnetic field is employed to obtain an initial coarse attitude fix. Next, a star sensor (sometimes in combination with a fine Sun sensor) is used to determine the attitude accurately. By contrast, an AST can perform accurate attitude acquisition in a few seconds, following stabilization of the spacecraft.

The Assured Crew Return Vehicle (ACRV) is an example of a spacecraft that would benefit from an AST. Following separation from the Space Station, the ACRV must be placed in the correct attitude to perform a collision avoidance burn. This maneuver needs to be carried out within 15 minutes, which is hard to accomplish with conventional attitude acquisition methods that rely on use of the Earth's magnetic field. The latter method is time consuming because the magnetic field vector needs to rotate over an angle sufficiently large to allow adequate 3-axis attitude determination.

3.2 Fast fault recovery

The AST enables fast recovery from faults that result in a loss of attitude knowledge. This capability is important for spacecraft where outages either are unacceptable, are very costly, or would result in catastrophe if not remedied quickly. JPL's Cassini mission to Saturn is just one example of a project where an AST could be used to avert catastrophe.

For Cassini, the quick fault recovery enabled by an AST would reduce the length of the critical sequences associated with Saturn orbit insertion, Titan Probe release, and the Titan fly-by targeting burns needed for gravity assist. This reduction in critical sequence length translates directly into a reduced probability of catastrophic failure.

3.3 Celestial target acquisition

The observing efficiency of high-precision airborne and orbiting astronomy telescopes can be improved markedly by automating celestial target acquisition using an AST that is coboresighted with the telescope. After a slew to a new target, the AST identifies the stars in its FOV, determines its attitude and provides this information to the attitude control system. The telescope pointing error is then reduced to a level where the Fine Guidance Sensor (FGS) can acquire the guide star(s) used for pointing control.

Relative to an automated acquisition scheme that uses the FGS exclusively[1,5], the addition of an AST eliminates the need for ground selection and on-board storage of a significant number of guide stars around each target (in addition to the one(s) needed for pointing control).

SIRTF, SOFIA, and the Kuiper Airborne Observatory (KAO) are examples of programs that would benefit from the presence of an AST. Implementation of automated target acquisition would increase the KAO observing time by some 15%. The observation time for sounding rocket payloads could be increased by at least 25% when using an AST.

3.4 Attitude updating

When used to update the attitude of gyro-based attitude control systems, the AST eliminates ground selection and onboard storage of guide stars for each update. By operating in the update mode, the AST provides its attitude every time a request is received from the attitude control system. Since there is no penalty for performing frequent updates, the AST can be used either to improve accuracy, or to reduce cost by allowing the use of cheaper, lower performance gyros.

3.5 Gyroless spacecraft

ASTs can provide their attitude at rates high enough (e.g., up to 10 Hz) to eliminate the need for gyros on spacecraft in certain cases, thus improving reliability, mass, power, and cost.

3.6 Optical navigation

Optical navigation is employed by planetary spacecraft to determine their location relative to nearby bodies such as planets, satellites, comets, and asteroids. It involves establishing the inertial direction and rotation rate of the vector from the spacecraft to the solar system body of interest using multiple images of that body against the stellar background. Being performed on the ground, optical navigation is currently hampered by long delay times, making it unacceptable for future missions like Rosetta, a joint NASA/ESA effort for returning a comet nucleus sample. The AST software can be expanded to perform detection and inertial direction determination of the solar system bodies used for optical navigation.

3.7 Precision pointing to terrestrial targets

Combined with a Global Positioning System (GPS) receiver, the AST enables autonomous, high-precision pointing from space to terrestrial targets as required for e.g., secure laser communication and efficient, quick-response surveillance. The AST will make it possible to point to targets with better than 10 m accuracy from an altitude of 500 km.

3.8 Position determination

A zenith pointed AST can be used for autonomous position acquisition of planetary rovers. The AST would be used to determine the inertial direction of the local vertical. Given the time of the star field observation and the direction of the local vertical, the position of a vehicle on Mars can be computed to an accuracy of a few hundred meters.

3.9 Attitude determination for geostationary satellites

High precision geostationary satellites typically measure their attitude about their roll and pitch axes using an Earth Sensor Assembly (ESA). In parts of the orbit a Fine Sun Sensor (FSS) is used to determine the yaw angle. In order to obtain accurate 3-axis attitude information for the entire orbit, it is necessary to propagate the attitude using a high-performance gyro system. ASTs can measure the 3-axis attitude of the spacecraft throughout the orbit with increased precision, thus eliminating the need for ESAs, FSSs, and high performance gyro systems. In addition, ASTs enable rapid fault recovery, a capability especially important to geostationary missions where outages are typically costly. Replacement of the ESAs and FSSs and use of simpler, lower performance gyros not only reduces spacecraft cost but also improves reliability because a) the FSSs are eliminated, b) simpler gyros are typically more reliable, and c) ASTs are more reliable than ESAs due to the absence of moving parts plus a reduced electronics parts count. Also, ASTs are not hampered by angular range limitations, implying that offset pointing can be accomplished easily. Furthermore, ASTs can be oriented on the spacecraft such that, unlike ESAs, there is no interference problem with either the Sun or the Moon.

4. ATTITUDE ACQUISITION

4.1 Star identification

An efficient, highly robust star pattern recognition algorithm[1] was adapted and refined at the Lockheed Martin Advanced Technology Center for use with ASTs. The algorithm finds the largest group of observed stars that matches a group of guide stars and maximizes its success rate by exploiting the full information contents of a star pattern. The AST acquisition guide star database consists of the position and brightness of the acquisition guide stars plus a sorted list of all acquisition guide star pairs that fit in the FOV of the AST. The storage space required for this database is an order of magnitude smaller than that of an algorithm based on matching stored guide star triplets.[2] This memory efficiency makes it practical to build accurate, moderate-FOV ASTs.

Star identification is a five step process illustrated in Fig. 4. The brightest observed stars, typically from 8 up to 12, are used for this process. In step A it is determined which pairs of guide stars match each pair of observed stars, a process that results in the formation of "match groups." The example match group shown in Fig. 4 consists of a kernel and three members. It was created because first it was found that the pair consisting of guide stars 14 and 26 matched the pair made up

of observed stars 1 and 2. Then the pair consisting of guide stars 14 and 51 was found to match the pair made up of observed stars 1 and 4, while, finally, it was found that the pair consisting of guide stars 14 and 3 matched the pair comprising observed stars 1 and 7. In step B, small match groups are eliminated as they are likely to be spurious.

Validation of the remaining match groups is performed in step C where it is checked if the angular separation (dashed lines) between the members match. If the match group shown in Fig. 4 were validated, an additional 3 match groups with the same stars would have been found. The first one would have observed star 7 and guide star 3 as its kernel, the kernel of the second one would consist of observed star 4 and guide star 51, while observed star 2 and guide star 26 would form the kernel of the third group. Hence, there is a lot of redundancy which is eliminated in step D. Next, it is assumed that the largest remaining match group represents a correct match of the observed and guide stars involved. It there are a number of equally sized large match groups, the group with the highest match quality is selected as the correct one. If properly implemented, this non-iterative identification process provides highly reliable and very rapid star identification.

A. Generate Match Groups via Star Pair Matching

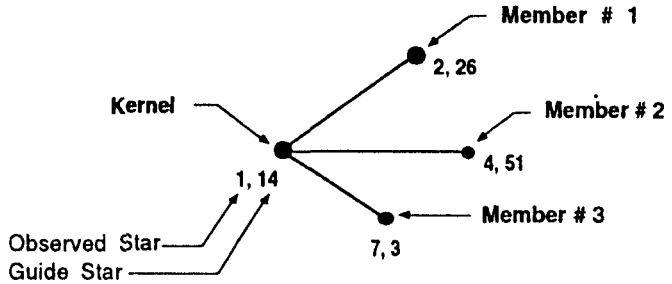

B. Eliminate Small Match Groups (Likely to be Spurious)
C. Validate Remaining Match Groups

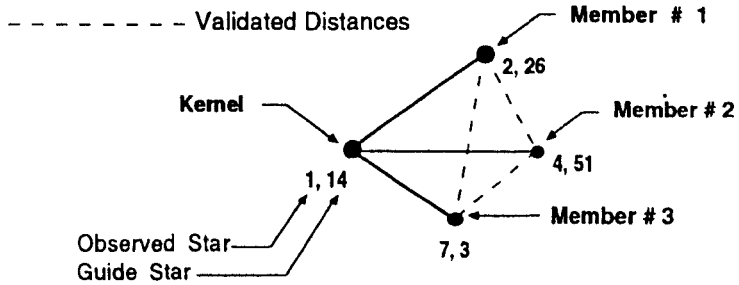

D. Eliminate Redundant Match Groups
E. Extract Largest Match Group (Select Highest Quality Match Group if Needed)

Fig. 4 Star identification process

4.2 Attitude acquisition simulation

A realistic simulation program was developed to test the attitude acquisition performance of the AST.[2] This program selects guide stars based on a specified density, brightness limit, and criteria for the absence of close neighboring stars. It then proceeds to generate the "observable sky," using catalog completeness, catalog reliability, and star brightness error inputs. It perturbs the position and brightness of the guide stars among the observable stars by taking into account: a) the position uncertainty of the stars as reported by the SKYMAP star catalog, b) the effect of uncompensated proper motion, and c) the effect of neighboring stars within a "precision guide star" radius. The latter effect is incorporated conservatively by

computing the combined centroid location. Additional close neighbors are generated around faint guide stars in a statistically correct manner in order to compensate for insufficient catalog depth. In addition, the brightness of all other stars is perturbed as well.

To obtain the predicted acquisition performance of the flight AST with its 6394 acquisition guide stars, the FOV was placed on 10,000 evenly spaced locations on the celestial sphere. For each position, the stars within the 8.8 by 8.8 degree FOV are extracted, the position of the guide stars among them is further perturbed to reflect the AST accuracy, and the 10 brightest observed stars are then used for identification.

Using a brightness error of 0.3 magnitude (1 σ), a per star per axis position error of 4.5 arcsec (1 σ), a 60 arcsec tolerance on guide star separation angle, a 1 magnitude tolerance on guide star brightness, a criterion of having to identify at least 4 stars for success, and solution ambiguity resolution through selection of the match group with the highest match quality, an acquisition success rate of 99.81% is found. The 19 failures included two cases with only 2 guide stars among the 10 stars used for the identification attempt, and eleven cases with only 3 guide stars among the stars used for identification. All of the remaining six failure cases had four guide stars among the brightest 10. Four of the six failure cases can be turned into successes through a slight modification of the identification algorithm, which would then raise the success rate to 99.85%. An AST rotation of 2 degrees about its X or Y axis is sufficient to achieve acquisition for all but one of the 19 failure cases where a 4 degree rotation is required. There were only two cases where the number of guide stars among the brightest 10 was reduced to less than four due to the 0.3 magnitude star brightness error assumed. As expected, there were no erroneous attitude acquisitions. At least 8 stars brighter than magnitude 7 were available for each of the 19 failed acquisition cases, implying that star availability is not a problem. Hence, the failure rate can be driven to zero by replacing the currently used simple guide star selection algorithm by a more sophisticated version.

The distribution of the number of identified stars was as follows: 51, 207, 469, 1144, 2166, 2891, and 3053 cases with 4, 5, 6, 7, 8, 9, and 10 identified stars respectively. Next, the star position error was increased to 15 arcsec, and, as expected, the acquisition success rate dropped slightly from 99.81 to 99.74%. The average time required for acquisition was 1.4 sec using a Mac Centris 650, with a maximum of 4.0 sec.

4.3 Real-sky acquisition demonstrations

In the beginning of 1994, true-sky demonstrations validated the robust and rapid attitude acquisition capability of the AST through correct identification of all 704 star fields obtained at the Lick Observatory with an uncalibrated proof-of-concept AST equipped with a 512 by 1024 pixel frame transfer CCD and a 50 mm f/1.2 lens that provided a 6.5 by 13.2 degree FOV.[4] The fields cover 47% of the sky, including both rich areas like the Milky Way, and sparse ones such as the region near the Galactic North Pole. Identification and attitude determination was performed using the brightest 10 stars in each frame, an all-sky database of 5126 guide stars, a 60 arcsec tolerance on star separation, and a 1 magnitude tolerance on star brightness. The FOV area was approximately 11% greater than that of the AST, implying that the guide star density was 12.5% lower than used for the flight AST (see section 4.2). Simulations predicted a 99.65% success rate versus the 100% achieved, which indicates that the simulations tend to be conservative.

A total of 132 of the 704 star fields were imaged again after removal of a 2 mm BG38 filter used to force an AST spectral response close to visual at the cost of a sensitivity reduction by a factor of two. The resulting increase in star brightness error caused some deterioration in the distribution of the number of identified stars and contributed to the failed identification of one of the fields. Based on this mild degradation, it is fully anticipated that the filter can be eliminated when a rather simple algorithm is employed to translate star visual magnitude into instrument magnitude using the star color index. The integration time of the proof-of-concept AST was reduced from 0.6 to 0.3 seconds following removal of the filter.

The AST tolerates the presence of bright objects as was demonstrated by a frame containing an image of Jupiter, in addition to just 4 identifiable guide stars. Jupiter was 1000 times brighter than one of the 4 identified stars located within 1 degree from the planet, while it was 2100 times brighter than the faintest identified star which had a magnitude of 6.2.

Starting in November, 1995, successful real-sky attitude acquisition has been demonstrated using the AST EM on the roof of one of the LMATC buildings in Palo Alto, California. This unit is fully self contained with all of the software loaded into its R3000 based flight computer. It communicates via its RS422 interface with a PC that simulates the ACS computer. It has been shown that the unit has sufficient sensitivity to operate at a 5 Hz update frequency. More extensive tests will be performed at the Lick Observatory where the viewing is much better.

5. TRACK MODE

5.1 Track operation

When performing attitude acquisition, the AST first identifies a subset of the 10 brightest stars in its FOV, then computes its attitude using the identified stars, and subsequently determines which guide stars should be located inside its FOV, an operation for which it considers both the acquisition guide stars and the supplementary guide stars. It then determines which of the observed stars match guide stars inside the FOV. Following this matching process, the attitude computation is refined using all matched observed stars, the attitude is reported to the ACS and propagation guide stars are selected. Next, the AST transitions to the track mode, takes its first track frame, extracts up to 50 stars and performs an identification operation to determine which of the observed stars match the propagation guide stars, and computes its attitude following identification. It then determines which guide stars should be in its FOV, repeats the match operation, refines its attitude using all matched stars, outputs its attitude and selects the propagation guide stars. This two step process, which has proven to be extremely robust, is repeated for every frame while in the track mode.

5.2 Track simulation

In addition to predicting attitude acquisition performance, the simulation program can also be used to predict the AST track performance. For the track simulation, the program selects supplementary guide stars, in addition to the guide stars used for acquisition. The track performance is evaluated by having the AST boresight scan along a great circle through both poles that is precessed at two degrees per AST revolution. In this way the complete celestial sphere can be scanned in 90 revolutions. The AST is stepped along the great circle in 0.2 degree intervals, implying a total of 1800 steps per revolution for a total of 162,000 positions. At the first of these positions, acquisition is to take place, after which the performance at the remaining points is evaluated while in the track mode. In case of a track failure, the AST switches to its acquisition mode and attempts acquisition in the next point along the trajectory and switches back to the track mode if acquisition is successful.

With the addition of 10,077 supplementary guide stars, no loss of track was experienced anywhere in the sky, while, on average, 26.87 stars were tracked with a minimum of 7 and a maximum of 48. Fig. 5 shows the percentage of cases that fall in each of nine number of tracked stars intervals.

	Number of Tracked Stars Range								
	7-9	10-14	15-19	20-24	25-29	30-34	34-39	40-44	45-48
% of Cases in Range:	0.11	1.47	5.06	23.64	40.36	23.48	5.19	0.66	0.03

Fig. 5 Distribution for the number of tracked stars

The AST attitude error for the entire sky was found to be 1.1, 1.1, and 18.0 arcsec (1 sigma) about the X, Y, and Z axes respectively. For the cases where 16 stars were tracked, the AST attitude error was found to be 1.4, 1.4, and 22.6 arcsec about the three axes. This is higher than the 1.1, 1.1, and 18.3 that would result from the 4.5 arcsec, 1 sigma error that was added per axis for each guide star. This implies that the per star per axis error due to the combined effect of the position uncertainty of the stars reported in the SKYMAP star catalog and the assumed effect of neighboring stars within a "precision guide star" radius of 310 arcsec is 3.3 arcsec, 1 sigma, a number that seems too large. When we add an alignment uncertainty of 2 arcsec about the X and Y axes and 10 arcsec about the Z axis, the attitude errors increase to 2.4, 2.4, and 24.7 arcsec.

There were only 42 cases out of the total of 162,000 (0.026%) where the attitude errors were found to be "excessive," defined as greater than 6 arcsec about the X and/or Y axis and 100 arcsec about the Z axis, which roughly corresponds to 4.4 sigma. The largest errors found about X, Y, and Z were 12.6, 8.0, and 134 arcsec.

5.3 Real-sky track demonstration

The EM AST has been used with the real sky to successfully demonstrate the track performance from a rooftop in Palo Alto. With the Moon nearly full, stars down to magnitude 7.3 were tracked. More extensive track tests will be executed at the Lick Observatory.

6. AST PERFORMANCE ON GEOSTATIONARY SATELLITES

Track simulations were executed to assess the performance of an AST on a geostationary satellite. It is assumed that the boresight of the AST points along a small circle at a fixed declination as the spacecraft moves along its orbit. The absolute value of the declination angle needs to be large enough to avoid the Sun, while it needs to be small enough to avoid interference with spacecraft appendages, such as the solar panels, that usually extend in the North South direction. The declination ranges of interest are assumed to extend from 46 to 70 degrees in the northern hemisphere and from -46 to -70 degrees in the southern hemisphere, implying that sun shades with a solar avoidance angle down to 46 - 23.5 = 22.5 degrees are being considered.

One full orbit simulation run was performed for each of 13 declination bands in the northern hemisphere and for each of 13 declination bands in the southern hemisphere. For each run, the AST FOV was positioned on 1800 equally spaced locations on the declination ring. A brightness error of 0.3 magnitude was assumed, while the guide star positions were corrupted by 4.5 arcsec per axis (1 σ), in addition to the error introduced to account for the position uncertainty reported in the SKYMAP star catalog and the effect of close neighbors within a 310 arcsec precision guide star radius. The simulation results are tabulated in Fig. 6

Declination (deg)	Number of Stars Tracked			Accuracy about X (arcsec)		Accuracy about Y (arcsec)		Accuracy about Z (arcsec)	
	Mean	Min	Max	rms	worst	rms	worst	rms	worst
70	26.66	15	36	1.1	4.2	1.1	3.8	17.5	63.0
68	27.69	18	37	1.1	4.9	1.2	4.6	17.8	67.3
66	28.36	18	40	1.1	4.6	1.2	5.0	18.4	68.0
64	28.41	17	42	1.2	4.5	1.2	3.9	18.2	61.9
62	29.02	18	42	1.1	4.7	1.1	4.4	17.5	57.9
60	29.05	15	41	1.2	4.1	1.1	4.3	18.1	69.4
58	27.92	17	42	1.2	**6.1**	1.1	4.2	17.3	71.0
56	27.85	17	43	1.3	5.6	1.1	4.5	18.0	68.9
54	26.45	15	38	1.3	4.5	1.1	3.8	18.3	78.8
52	25.74	14	41	1.3	5.1	1.1	4.7	19.0	**94.0**
50	26.53	17	40	1.2	4.3	1.1	3.8	18.2	68.6
48	25.60	14	38	1.2	4.2	1.1	4.3	18.8	71.2
46	25.54	15	39	1.2	4.8	1.2	4.6	17.6	59.1
-46	27.20	16	**45**	1.1	3.8	1.1	3.8	17.0	84.1
-48	26.91	16	41	1.1	3.7	1.1	4.5	17.1	64.9
-50	26.61	14	41	1.1	3.9	1.1	4.8	16.9	72.4
-52	25.50	13	36	1.2	5.4	1.1	4.5	18.0	80.7
-54	25.57	**12**	36	1.2	4.8	1.2	4.7	17.3	74.4
-56	25.35	14	38	1.3	5.7	1.1	4.3	17.7	69.3
-58	25.01	**12**	38	1.2	4.4	1.1	4.7	18.8	74.0
-60	26.80	14	41	1.1	4.9	1.1	4.5	**19.3**	77.0
-62	28.30	18	38	1.1	3.8	1.1	5.0	18.4	70.4
-64	28.70	19	42	1.1	4.0	1.1	4.7	18.7	79.3
-66	29.11	16	44	1.2	4.0	1.1	4.1	17.7	71.6
-68	27.91	13	44	1.1	4.1	1.1	4.0	17.9	71.6
-70	26.59	13	40	1.1	4.9	1.2	**5.8**	17.4	63.3

Fig. 6 Track simulation results for ASTs on geostationary satellites

From Fig. 6 it may be seen that the AST performance is very good for any declination value in the Northern and Southern declination bands. The minimum number of stars tracked ranges from 12 to 19, the maximum ranges from 36 to 45, while the average ranges from 25.01 to 29.11. The worst case rms or 1 sigma AST attitude errors about the X, Y and Z axes are 1.3, 1.2, and 19.3 arcsec respectively, while the corresponding peak values are 6.1, 5.8, and 94.0 arcsec. The alignment uncertainty, assumed at 2 arcsec about X and Y and 10 arcsec about Z (1 sigma), should be added to the errors in Fig. 6 to obtain the overall attitude accuracy. This raises the 1 sigma values for the AST attitude error about the X, Y, and Z axes to 2.4, 2.3, and 21.7 arcsec for the worst declination angles. Hence, the 3 sigma values are 0.002, 0.002, and 0.018 deg about the three axes. If the alignment uncertainty can be calibrated out, the 3 sigma values improve to 0.0014, 0.0014, and 0.016 deg about the three axes.

If we mount the AST such that it points toward a declination of 50 or -50 deg, which necessitates a sun shade with a 26.5 degree solar exclusion angle, the effect of the error about the AST boresight on the spacecraft pointing direction toward Earth is equal to 0.018 x sin 50 = 0.014 deg (3 σ), while its effect on the angle about the pointing direction toward Earth is less than 0.018 x cos 50 = 0.012 deg (3 σ). Or, said differently, a single AST is capable of providing a combined spacecraft roll / pitch accuracy of 0.014 deg per frame, while providing a spacecraft yaw accuracy of better than 0.012 deg per frame. This is superior to the accuracy that is traditionally achieved using ESAs, FSSs, and a high performance gyro system, and will satisfy the pointing requirements of most geostationary missions. If the alignment uncertainty can be removed through calibration, the spacecraft roll / pitch accuracy provided by the AST improves to 0.012 deg per freme, while its contribution to the spacecraft yaw error reduces to 0.010 deg per frame.

It should be noted that the above results were obtained with a standard AST not optimized for the geostationary mission. A significant improvement in accuracy can be obtained by increasing the number of tracked guide stars. This is achievable by increasing the number of supplementary guide stars in the declination band used by the AST. Doubling the guide star density in this band raises the number of supplementary guide stars by less than 1000, a number that can easily be accommodated. The larger guide star density may necessitate the use of guide stars fainter than magnitude 7.5, which can be accommodated by increasing the exposure time. This would not impact the accuracy because star motion due to orbital rate is limited to only 9.6 arcsec/s, or 0.16 pixel/s.

In the absence of alignment uncertainty, doubling of the number of tracked stars would improve the AST accuracy by a factor of approximately $2^{1/2}$, thus enabling a single AST to provide satellite pointing knowledge with an accuracy of 0.0085 deg (3 σ) in roll / pitch per frame, and better than 0.0071 deg (3 σ) in yaw per frame. If the alignment uncertainty is not calibrated out and amounts to 10 arcsec (1 σ) about the AST Z axis, the AST contribution to the S/C roll / pitch accuracy degrades to 0.011 deg (3 σ) per frame, while its contribution to the spacecraft yaw accuracy degrades to 0.009 deg (3 σ) per frame.

Use of two ASTs would reduce the AST contribution to the error in satellite pointing knowledge to less than 0.002 deg per frame (3 σ) , a number expected to decrease to 0.0018 deg per frame if the guide star density is doubled in the declination band swept by the AST. A further reduction to 0.00077 deg can be achieved if the AST alignment uncertainty can be calibrated out.

7. CONCLUSIONS

Used on geostationary satellites, a single AST-201 with an 8.8 by 8.8 deg FOV and a 7.5 magnitude sensitivity, can provide a combined (= vector sum) spacecraft roll / pitch accuracy of 0.014 deg (3 σ) per frame and a yaw accuracy better than 0.012 deg (3 σ) per frame, as was shown using realistic computer simulations. This per frame accuracy is expected to improve to 0.011 deg for spacecraft roll / pitch and 0.009 deg for spacecraft yaw when the number of guide stars in the declination band swept by the AST FOV is doubled. If the AST alignment uncertainty can be removed through calibration, the per frame accuracy in spacecraft roll / pitch provided by a single AST further improves to 0.0085 deg, while in spacecraft yaw it improves to 0.0071 deg.

Even without doubling the guide star density and without removal of the alignment uncertainty, the performance is superior to what is traditionally achieved with a combination of Earth Sensor Assemblies (ESAs), Fine Sun Sensors (FSSs) and a high performance gyro system. Hence, ASTs can replace ESAs and FSSs and allow the use of a lower performance gyro system. Replacement of the ESAs and FSSs and use of simpler, lower performance gyro system not only reduces spacecraft cost but also improves reliability because a) the FSSs are eliminated, b) simpler gyros are typically more reliable, and c) ASTs are more reliable than ESAs due to the absence of moving parts plus a reduced electronics parts count. In addition, ASTs are devoid of angular range limitations, avoid Sun and Moon interference by proper orientation on the spacecraft, and enable rapid fault recovery, a capability especially important to geostationary missions where outages are typically costly.

Use of two ASTs would increase the accuracy in spacecraft pitch, yaw, and roll to 0.002 deg (3 σ) per frame, a number expected to improve to 0.0018 deg when the guide star density in the declination band swept by the AST FOV is doubled. If the alignment uncertainty can be removed by calibration, a further improvement to 0.00077 deg (3 σ) per frame can be achieved.

The computer simulations were validated in 1994 by real-sky testing at the Lick Observatory with a proof-of-concept AST having a 6.5 by 13.2 deg FOV. The 704 star fields obtained during that test covered approximately 47% of the sky, and were all correctly identified. This represented a 100% success rate, which is higher than the 99.65% predicted by the computer simulations, indicating that the simulations tend to be conservative.

Computer simulations predict a 99.81% acquisition success rate for the AST-201. This number was obtained by placing the FOV on 10,000 evenly spaced sky locations. This rate can be improved to 99.85% through implementation of a minor modification to the identification algorithm. Since the failures can be attributed primarily to inadequate guide star coverage at certain sky locations, rather than star availability, the success rate can be improved significantly through adoption of a more sophisticated guide star selection algorithm.

The robustness of the track algorithm was demonstrated with an all-sky computer simulation where the boresight was moved in 0.2 deg steps along a great circle through the poles that was precessed by two degrees per AST revolution. No loss of track was experienced, the mean number of stars tracked was 26.87, with a minimum of 7 and a maximum of 48. Only 42 cases, out of a total of 162,000 FOV position cases, had "excessive" attitude errors, defined as greater than 6 arcsec about X and Y, and greater than 100 arcsec about the Z axis of the AST.

8. REFERENCES

1. R. W. H. van Bezooijen, *Automated Star Pattern Recognition,* Ph. D. Dissertation, Stanford University, Stanford, California, June 1989.

2. R. W. H. van Bezooijen, "Star sensors for autonomous attitude control and navigation," *Optical Technologies for Aerospace Sensing: Proceedings of a conference held 16 - 17 November 1992 in Boston, Massachusetts*, J. E. Pearson, Vol. CR47, pp. 153-180, SPIE Optical Engineering Press, Bellingham, WA 1993.

3. S. F. McLaughlin, "SKYMAP Star Catalog, version 3.5," National Space Science Data Center, Goddard Space Flight Center, Greenbelt, Maryland, 1989.

4. R. W. H. van Bezooijen, "True-sky demonstration of an autonomous star tracker," *SPIE's International Symposium on Optical Engineering in Aerospace Sensing, held 5-8 April 1994 in Orlando, Florida*, M. K. Masten, Vol. 2221 "Space Guidance, Control, and Tracking," pp. 156-168, SPIE Optical Engineering Press, Bellingham, WA 1994.

5. R. W. H. van Bezooijen, K. R. Lorell, and J. D. Powell, "Automated Star Pattern Recognition for use with the Space Infrared Telescope Facility (SIRTF)," *Preprints of 10th IFAC Symposium on Automated Control in Space*, pp. 59-67, Toulouse, France, June 1985.

Stellar attitude determination for geosynchronous missions

David J. Flynn and Lawrence W. Cassidy

Hughes Danbury Optical Systems, Inc.
100 Wooster Heights Road, Danbury, Connecticut, USA 06810-7589

ABSTRACT

The performance and functionality of star trackers has greatly improved over the past decade due to technological advances in charge-coupled devices (CCDs), microprocessors, and application-specific integrated circuits (ASICs). These technological advances have also lowered the cost of star trackers to the range of competing attitude sensors such as horizon sensors.

This study evaluates the attitude reference requirements of a three-axis stabilized geosynchronous satellite (GOES-NEXT) and addresses the use of star trackers to replace a traditional attitude determination sensor suite based on horizon sensors and digital fine sun sensors (DFSSs).

Although the GOES-NEXT satellite is used as a specific example in this study, the results are applicable to other geosynchronous remote sensing or communications satellites.

1. ATTITUDE REFERENCE REQUIREMENTS

In a nominal geosynchronous satellite orientation, the pitch axis is normal to the orbital plane (which is nominally zero inclination), the yaw axis is nadir pointing, and the roll axis is along the velocity vector (see Figure 1). At geosynchronous altitude, the line-of-sight (LOS) rate of an instrument with its boresight in the orbit plane is 0.25 deg/minute. During maneuvers, it is assumed that the LOS rate is less than 0.3 deg/second.

For the GOES-NEXT mission the single-frame attitude knowledge requirement during normal operation will be 0.03 degree, 3 sigma per axis. This is relatively tight, since a typical communications satellite knowledge requirement is 0.1 degree, 3 sigma per axis.

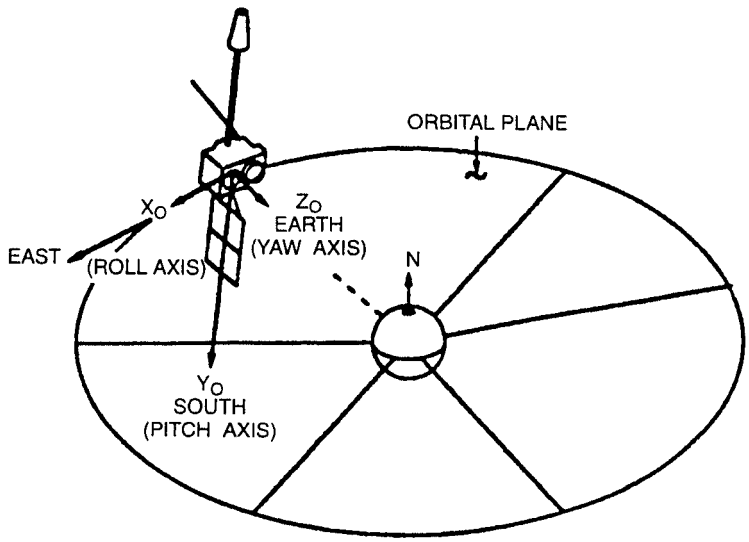

Figure 1. Nominal GOES I-M Orientation.

2. CURRENT SENSOR SUITE

2.1 Description

The primary instruments on the GOES-NEXT satellite will be an imager and a sounder that will be oriented along the yaw axis of the spacecraft, Earth pointing, as shown in Figure 2. The satellite's design currently uses six different attitude sensors. Figure 3 shows the orientation of these sensors (Ref. 1). Two sets of coarse analog sun sensors (CASSs) are used to orient the spacecraft with respect to the Sun during transfer orbit.

Redundant digital integrating rate assemblies (DIRAs) comprise a system of three mutually perpendicular rate integrating gyros. The DIRAs are used to monitor attitude drift throughout the transfer orbit and during station keeping maneuvers. Due to the limited life of the DIRAs, they are turned off during routine operation (Ref. 2).

Redundant digital sun sensors (DSSs) are oriented to measure pitch and yaw. The DSSs are used during transfer orbit to calibrate the DIRAs and during nominal operation to measure yaw. The encoded bits of the DSSs provide 0.125 degree quantization and the interpolation bits provide 0.012 degree, 3 sigma accuracy. The primary attitude sensors used during nominal operation are redundant horizon sensors that measure pitch and roll. At a geosynchronous altitude, the horizon sensors provide 0.03 deg, 3 sigma accuracy in pitch and roll. The orientation of the Sun relative to the solar arrays is monitored using two sun analog sensors that are located on the solar array yoke. Also, a magnetometer measures the direction and magnitude of the Earth's magnetic field.

For the GOES mission the imager is also used to calibrate and correct for systematic attitude errors. By using the imager to measure the position of landmarks on the Earth and by over-scanning above the horizon to measure the positions of stars, systematic attitude errors can be measured and corrections can be uplinked to the satellite. Reference 3 provides a more complete discussion on how the imager is used for image navigation and registration (INR) and image motion compensation (IMC).

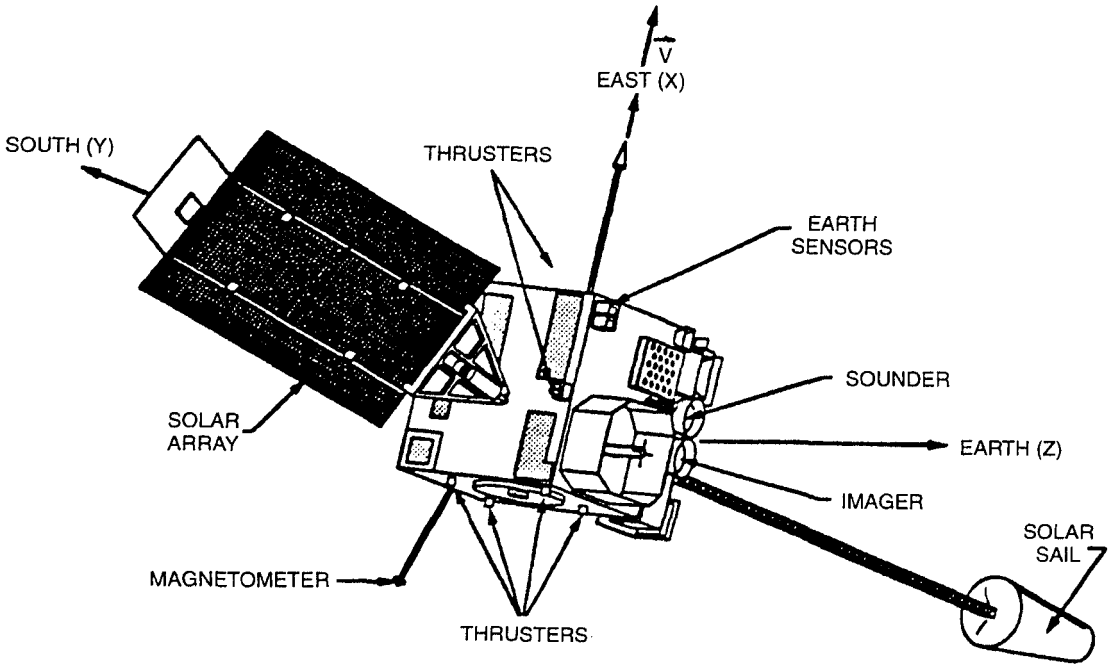

Figure 2. GOES Spacecraft Configuration.

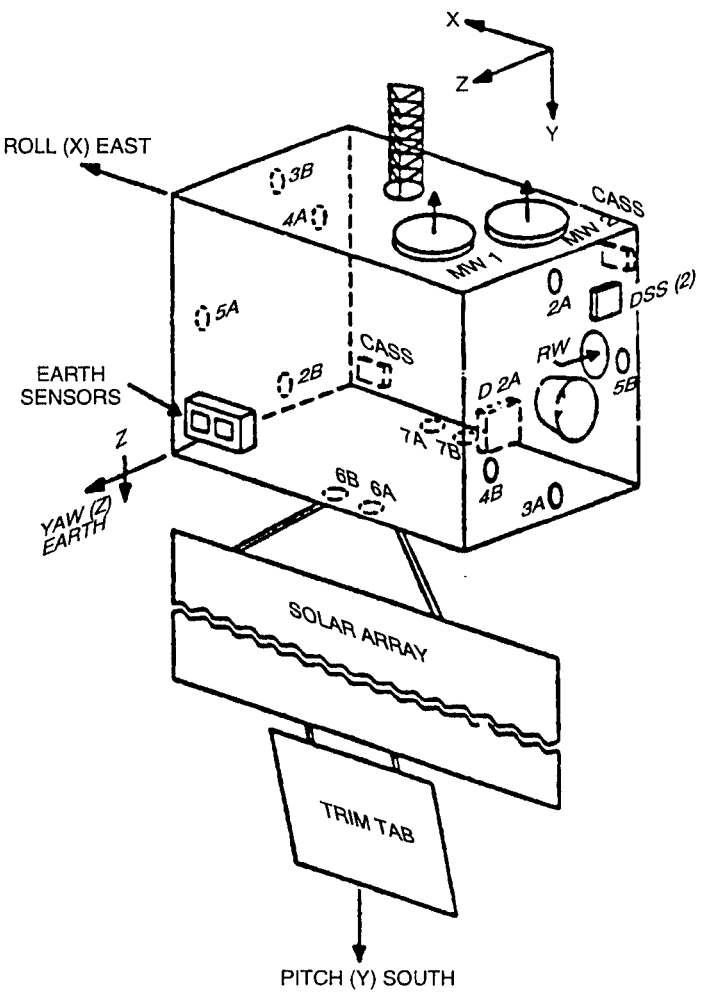

Figure 3. GOES-NEXT Attitude and Orbit Control System.

2.2 Limitations

The current attitude sensor configuration has several limitations:

- The Sun is only visible to the sun sensors during two thirds of the orbit
- Yaw cannot be directly measured during the 8-hour period around local midnight
- Attitude must be propagated without the benefit of gyro data during this period, because the DIRAs are not on during nominal operation (Ref. 2)
- Considerable ground support is required for the current GOES-NEXT attitude determination concept (Ref. 1).
- No single sensor measures attitude about all three axes simultaneously and continuously throughout the mission.

3. STAR TRACKER BENEFITS

A star tracker based attitude determination system provides continuous three-axis attitude estimates over the entire orbit and has several other benefits:

- Autonomy – An autonomous all-stellar attitude determination system is now possible, given the demonstrated improvements in star trackers and space qualified microprocessors (Ref. 4). The current GOES-NEXT concept requires considerable ground support.
- Higher Reliability and Lifetime – Star trackers have no moving parts, unlike scanning horizon sensors, which are subject to mechanical failures. Our HD-1003 tracker achieves a mean time between failures (MTBF) of 114 years.
- Lower Cost – DIRAs can be eliminated or replaced with lower cost, high reliability, solid-state gyros, because a star tracker based system can provide attitude and rate estimates every tenth of a second for LOS rates up to 1.0 deg/second. The potential also exists to eliminate horizon sensors and DSSs.

4. THE HD-1003 STAR TRACKER

4.1 Description

The HD-1003 star tracker, developed by Hughes Danbury Optical Systems (HDOS), has been designed to meet the requirements of a wide range of potential applications. The HD-1003 is now being produced for NASA's Small Satellite Technology Initiative and will be demonstrated in space in mid-1996. Based on our experience in developing CCD star sensors since 1973, and current CCD, microprocessor, and ASIC technology, reductions in size, weight, power, and cost have been achieved while maintaining high accuracy and reliability.

The HD-1003 star tracker uses a Loral frame transfer CCD array with a 512×512 pixel imaging area. The CCD incorporates a multiphase pinned (MPP) design to improve dark current and charge transfer efficiency (CTE) performance after exposure to radiation encountered in a space environment. A color corrected, 8×8 degree field of view lens is used to provide full performance over the range of star colors and thermal environments.

The HD-1003 is a highly autonomous, flexible, microprocessor-based system. Using flight-proven algorithms, the HD-1003 can acquire and track up to six stars in the presence of up to 150 proton-induced transient events per frame (Ref. 6). The ability to track up to six stars simultaneously greatly enhances the functional capability of this star tracker. By comparing the measured separation between stars and their intensity with data from an onboard star catalog, stars can autonomously be identified without prior knowledge of the spacecraft attitude (Ref. 7). Using the measured star orientations, the three-axis attitude of the spacecraft with respect to an inertial coordinate system can be estimated using data from a single HD-1003 star tracker (Ref. 8). If data from another star tracker or another sensor is available, the data can be combined to improve accuracy.

Given the high update rate (10 Hz) from the HD-1003, attitude rate about all three axes can be determined by comparing frame-to-frame star image location changes.

In-flight calibration of multi-star trackers is also easier than with a tracker capable of tracking only one star. Geometric distortions due to vibration and thermal environment can be estimated by comparing the measured star patterns with the known star patterns. Also, since the attitude of each star tracker with respect to inertial space can be measured independently of the other instruments, alignment to science instruments and other attitude sensors can be readily determined.

Table 1 provides a performance summary of the standard HD-1003 star tracker. The HD-1003 design is highly modular and adaptable. For special applications the field of view, sensitivity, and radiation hardening can be modified to meet customer requirements. The HD-1003 can also be adapted to output an attitude estimate (e.g., quaternion) using a pre-stored star catalog and attitude estimation algorithms. Such a capability is especially useful when the performance of the spacecraft guidance and control computer is limited.

4.2 Stellar attitude determination system

As discussed earlier, using the data from one or more multi-star trackers, the absolute three-axis attitude of the spacecraft with respect to inertial space can be determined. Based on the required accuracy, the permissible outage periods, and the required redundancy of the system, we can determine the number of star trackers required, the optimal orientation of the star trackers, and the required field of view of the star trackers.

For this study we have assumed the following:

- The system will use two standard HD-1003 star trackers
- No simultaneous outage of both trackers is permitted
- The system must meet full performance, 0.03 degree, 3 sigma per axis with two star trackers and reduced performance with a single tracker.

Table 1
HD-1003 Performance Specifications

Parameter	Requirement
Size (without light shade)	< 200 cubic inches
Weight	< 8 lb with radiation shielding
Power (at 28 V dc)	< 11 W
Update Rate	10 Hz
Number of Stars Tracked	6 stars simultaneously
Lifetime (GEO)	> 15 years
Reliability(MTBF)	$> 1 \times 10^6$ hours
Sensitivity	+ 6.0 (KOV spectral class)
Accuracy	6 arc-sec rms per axis per star
Field of View	8 × 8 deg
Bright Object Rejection (half angle) - Sun - Earth Limb - Moon	 > 35 deg > 30 deg > 25 deg

Figure 4 shows a top-level block diagram of the our stellar attitude determination system. The two HD-1003 star trackers autonomously acquire stars in their field of view and report the orientation and intensity of the tracked stars. Using this data, the stars can be identified and the attitude of the spacecraft estimated by the spacecraft guidance computer. For the best accuracy the data from both trackers should be used to estimate the spacecraft attitude. The host can also send commands to the HD-1003 trackers to break track on stars that cannot be identified or to limit the position and magnitude range in which a star can be acquired.

4.2.1 *Star identification*

To estimate the attitude of the spacecraft using data from the star trackers, the stars being tracked are first identified. During initialization, before an accurate attitude estimate is available, the separation between star pairs and magnitude can be used to identify stars. Since the HD-1003 star tracker can track up to six stars simultaneously, star identification can be performed without data from other sensors. Autonomous star identification algorithms have been developed to allow initialization without special spacecraft maneuvers (Ref. 7). Star identification can be performed either in the spacecraft or in the star tracker (with modification).

Once the system has been initialized, an accurate attitude estimate is available and a simple direct position and magnitude match can be used to identify new stars.

4.2.2 *Star tracker outage vs. orientation*

The Sun, Moon, and Earth can all "blind" the star tracker if they are too close to the sensor field of view. Since the z axis of the spacecraft is nadir pointing, the star trackers can be oriented to avoid the Earth. The y axis of the spacecraft nominally points normal to the equatorial plane. The ecliptic plane, in which the Sun and the Moon lie, is inclined about 23.5 deg to the equatorial plane. If the star sensors are oriented at least 58.5 degrees off the equatorial plane, then the Sun and Moon are always further than 35 degrees from the star tracker boresight and no Sun/Moon outage will occur.

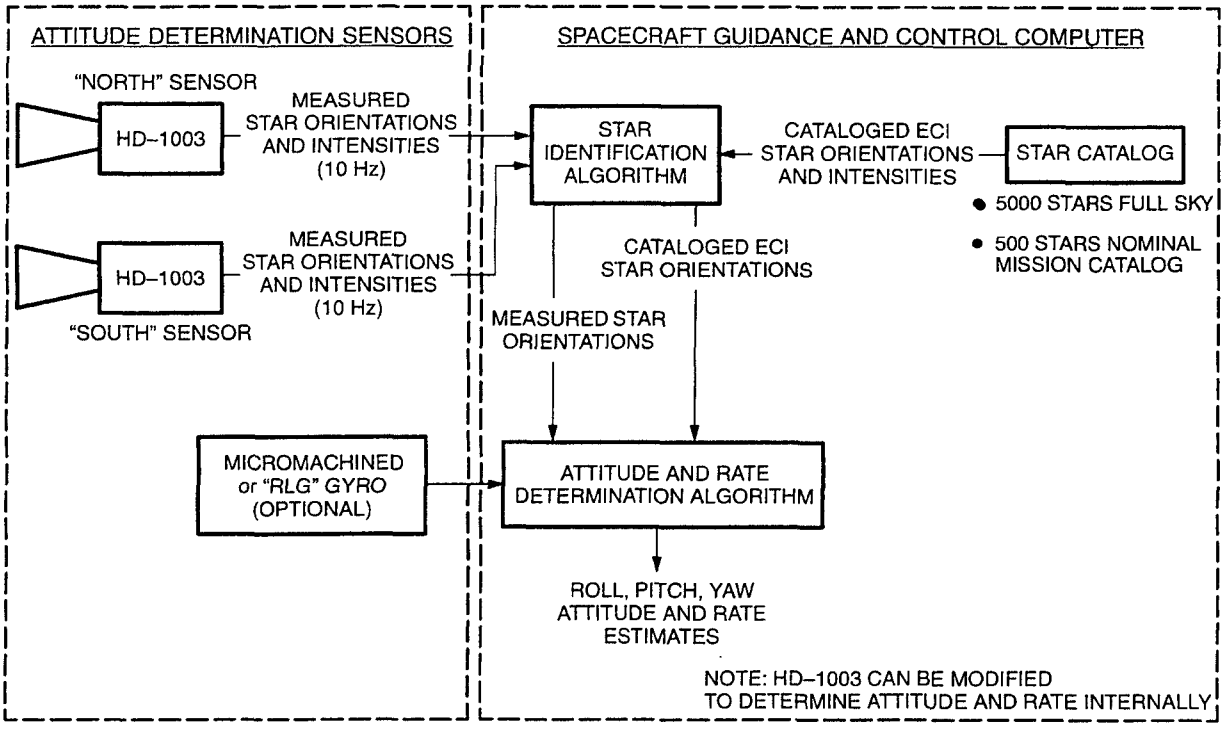

Figure 4. Star Tracker Based Attitude/Attitude Rate Architecture.

Depending on the field of view of the sensor and its sensitivity, there may also be outages due to "holes" in the sky, where no acceptable stars are in the sensor field of view. Figure 5 shows the swath of the sky seen by the "North" and "South" star trackers. The "North" sensor is pointed 58.5 degrees above the equatorial plane, the "South" sensor is 58.5 degrees below the equatorial plane. Figures 6 and 7 show the number of stars in the 8×8 degree field of view of the sensor as a function of azimuth angle over a complete 24-hour orbit. At least one star is in each sensor field of view for 98% of the orbit and in no case do both sensors lack stars at the same time. The mean number of stars in the sensor field of view is greater than six, the maximum number of stars HD-1003 can simultaneously track. If 100% star coverage is required for each tracker, then the field of view, or sensitivity, of the HD-1003 tracker can be increased. However, these modifications may impact the performance of the HD-1003 and are not addressed here.

4.2.3 *Attitude accuracy vs. orientation*

The accuracy of the estimated attitude about the spacecraft axes is determined by the orientation of the star trackers. Data from a single HD-1003 multi-star tracker can be used to estimate the spacecraft attitude in all three axes, however the accuracy about the boresight of the sensor is not as accurate as in the other two axes (Ref. 5). To meet the GOES attitude requirements, two HD-1003 star trackers are needed.

To increase accuracy about a given spacecraft axis, the star tracker boresights must be positioned normal to that axis, or as close to normal as possible. As discussed previously, Sun/Moon outage considerations drive the star tracker boresights to be oriented at least 58.5 degrees from the orbital plane. To maximize accuracy about the spacecraft pitch axis, the star tracker boresight must be oriented as close to the orbital plane as possible. Based on these two considerations, the two star trackers would be oriented 58.5 degrees off the orbital plane.

For optimal attitude accuracy in all three axes the star tracker boresights should be oriented 90 degrees apart from one another, or as close to 90 degrees as possible. Since we have constrained the boresights to lie on the cones 31.5 degrees from the orbit normal, the largest effective separation angle possible is 63 degrees, which occurs if both boresights are oriented to lie in a plane that passes through the orbit normal.

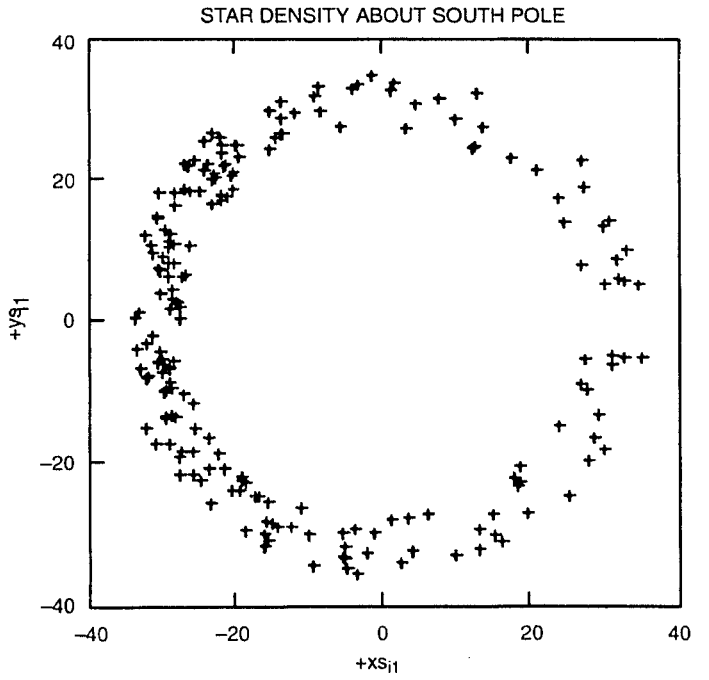

(a)

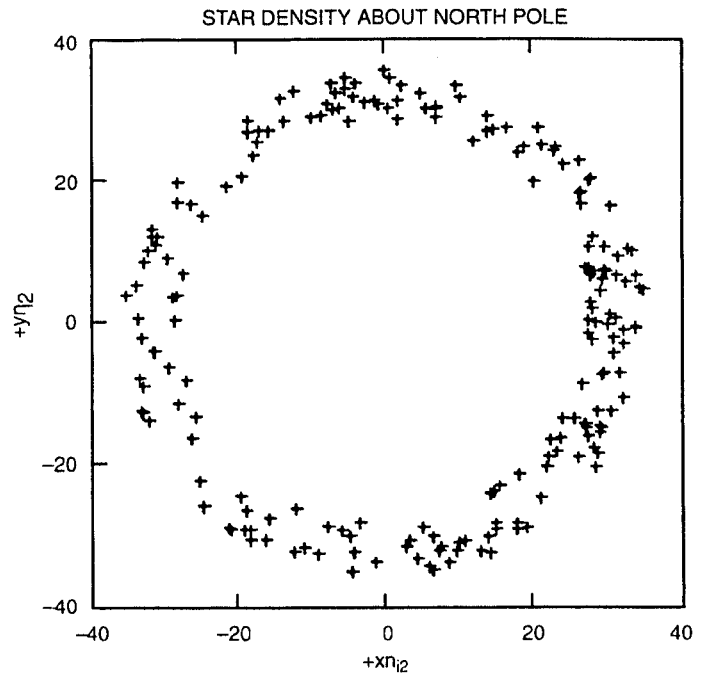

(b)

Figure 5. Star Density. (a) About South Pole, and (b) About North Pole.

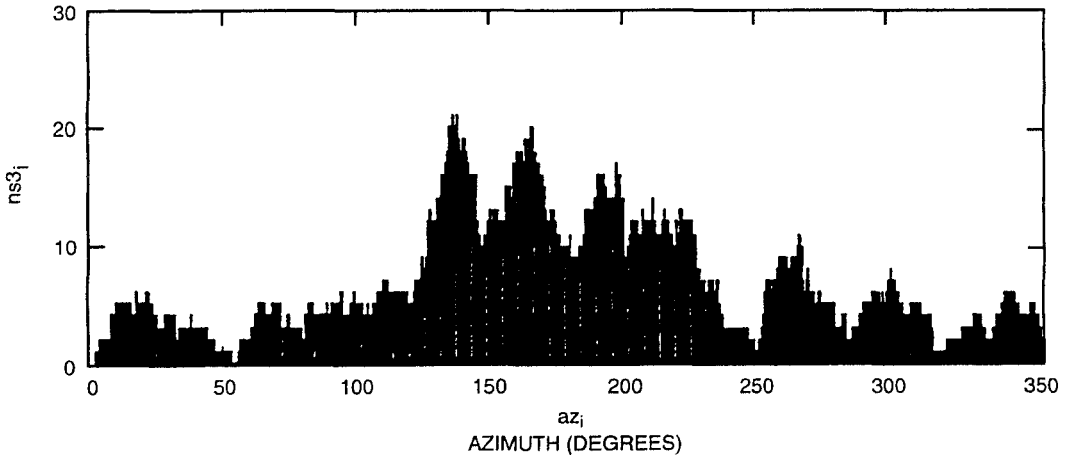

MEAN	(ns3)	=	6.89	MEAN NUMBER OF STARS IN FIELD OF VIEW
MAX	(ns3)	=	21	MAXIMUM NUMBER OF STARS IN FIELD OF VIEW
MIN	(ns3)	=	0	MINIMUM NUMBER OF STARS IN FIELD OF VIEW

d3 = 0.011 FRACTION OF ORBIT WITH < 1 STAR IN SENSOR FIELD OF VIEW

Figure 6. "South" Sensor: Number of Stars in Field vs Azimuth (Magnitude ≤ +6.0).

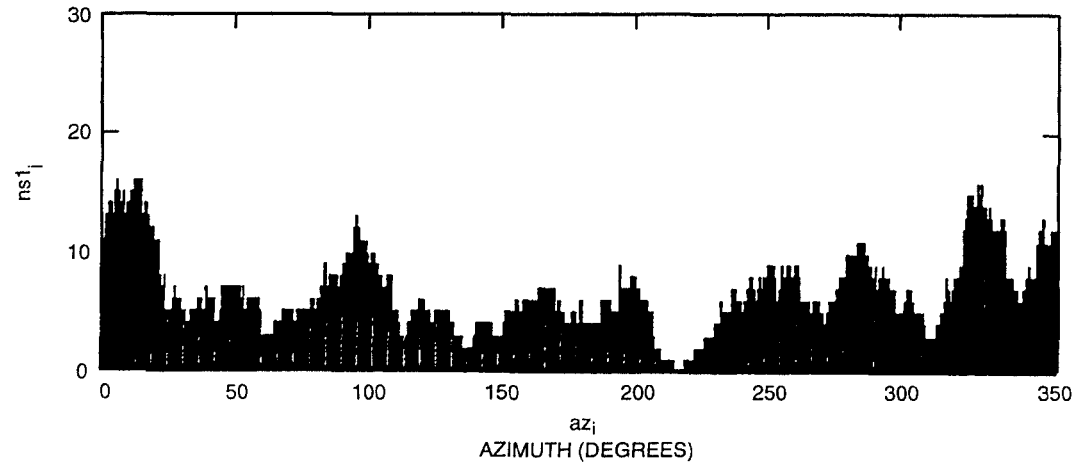

MEAN	(ns1)	=	6.707	MEAN NUMBER OF STARS IN FIELD OF VIEW
MAX	(ns1)	=	16	MAXIMUM NUMBER OF STARS IN FIELD OF VIEW
MIN	(ns1)	=	0	MINIMUM NUMBER OF STARS IN FIELD OF VIEW

d1 = 0.011 FRACTION OF ORBIT WITH < 1 STAR IN SENSOR FIELD OF VIEW

Figure 7. "North" Sensor: Number of Stars in Field vs Azimuth (Magnitude ≤ +6.0).

It is possible to choose how this plane is oriented to optimize either roll or yaw accuracy. Assuming that roll accuracy is more critical than yaw accuracy for the GOES mission, the tracker boresights would be oriented in the Y/Z plane, 58.5 degrees from the X/Z plane, both pointing away from the Earth, one nominally pointed South and the other pointed North, as shown in Figure 8.

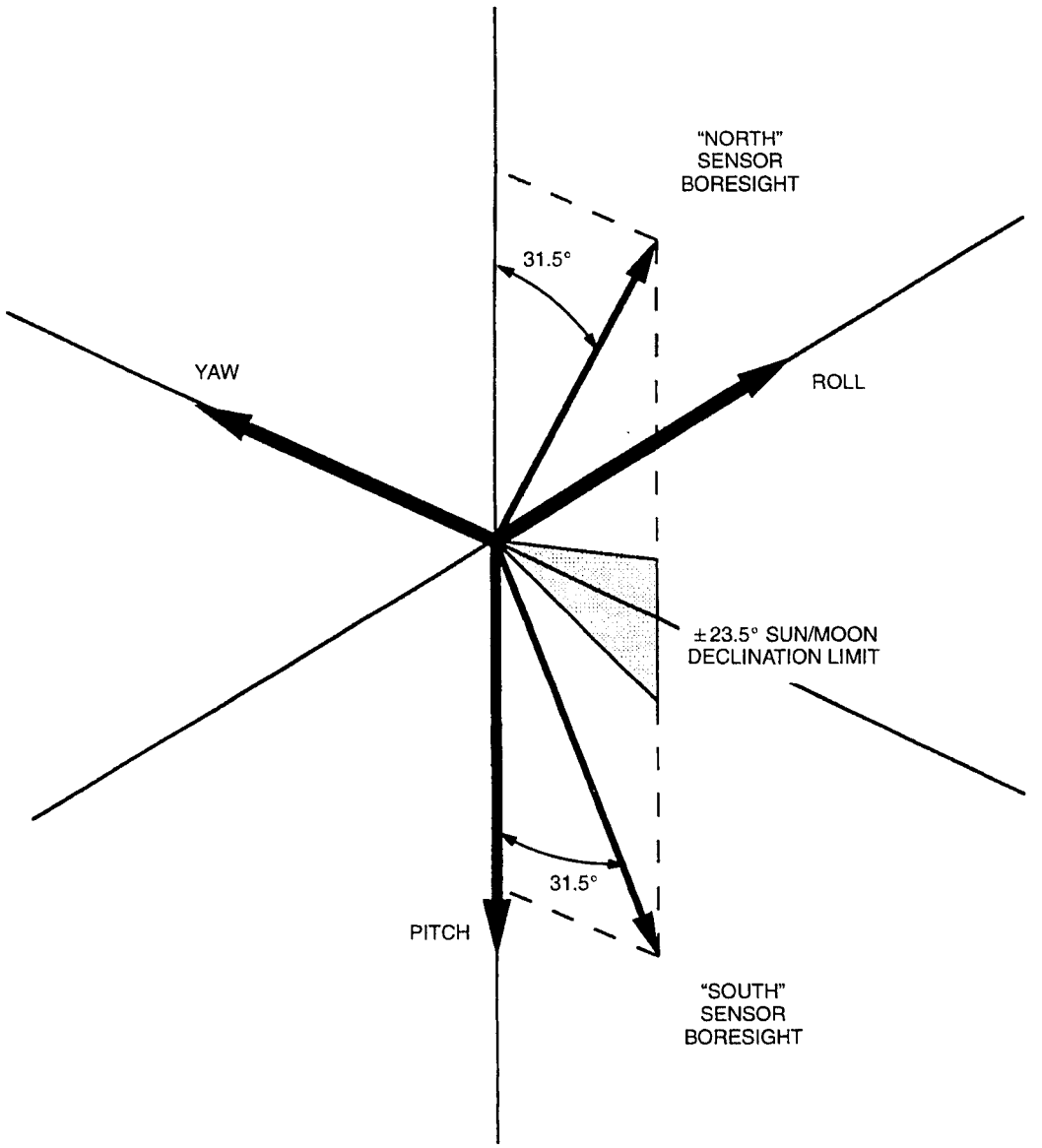

Figure 8. Star Tracker Orientation.

4.2.4 *Attitude accuracy*

Given the orientation of the star trackers and the error in star measurements (Figure 9), a covariance analysis was performed to determine the error in the single frame attitude estimate (Ref. 8). To bound the problem, two worst-case conditions were analyzed:

(1) In this case at least one star appears in each sensor field of view (this is true for 98% of the orbit). It was assumed that the stars are located at the sensor boresights and have a worst-case error of 6 arc-sec rms per axis. The accuracy for this case is as shown in Table 2. Even this worst case, accuracy is a factor of four better than required.

(2) For 2% of the orbit data will be available from only one sensor. Based on the star availability analysis, when one sensor lacks stars, the other will have at least five stars in its field of view. Again, assuming a centroid error of 6 arc-sec rms per axis, and assuming that the stars are uniformly distributed over the sensor field of view, the accuracy is as shown in Table 3. During the 2% of the orbit when data is available from only one sensor, our worst-case analysis predicts that the required roll and yaw accuracy are met. Pitch accuracy, however, is 44% larger than permissible.

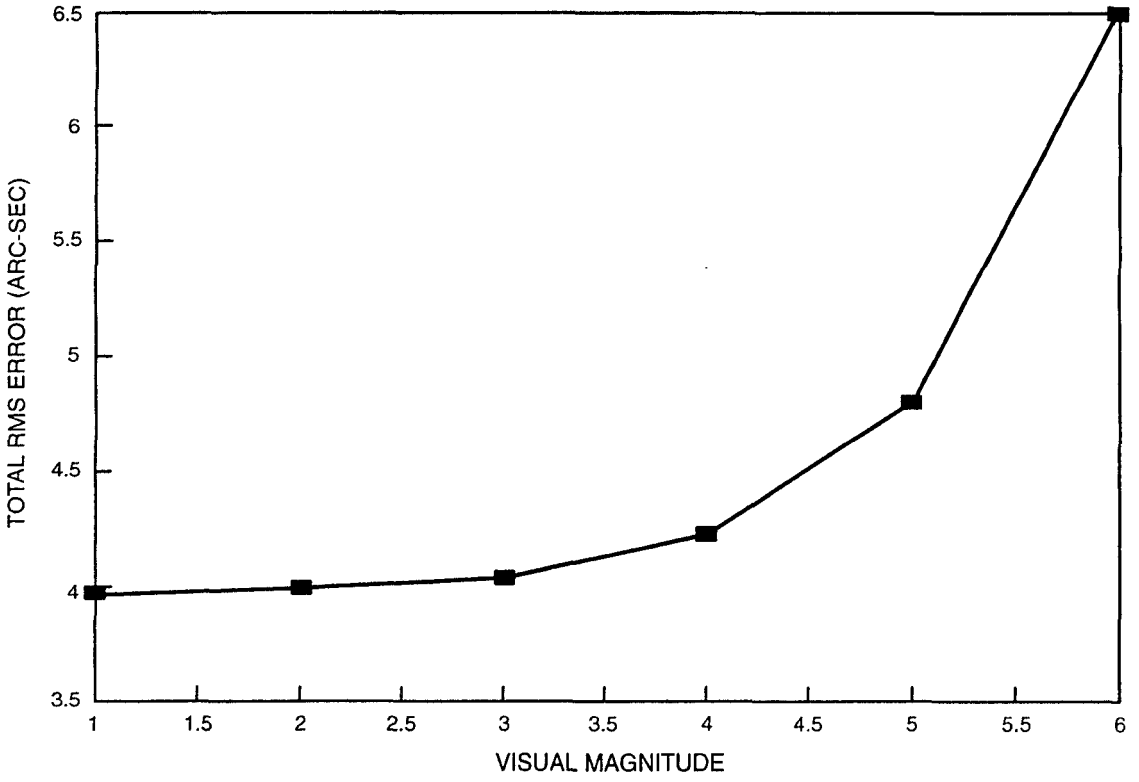

Figure 9. HD-1003 Accuracy vs Magnitude.

Table 2
Worst-Case Performance Estimate Assuming Two Sensors Operating

Axis	Worst Case Accuracy: 2 Sensors
Roll	< 0.0033 deg, 3 sigma
Pitch	< 0.0068 deg, 3 sigma
Yaw	< 0.0042 deg, 3 sigma

Table 3
Worst-Case Performance Estimate Assuming One Sensor Operating

Axis	Worst Case Accuracy: 1 Sensor
Roll	< 0.0022 deg, 3 sigma
Pitch	< 0.0443 deg, 3 sigma
Yaw	< 0.0265 deg, 3 sigma

To develop statistics on the expected performance of the operational system, a simulation was performed. For 720 samples over the orbit (a sample every 2 minutes) the orientation and expected error of the tracked stars for each sensor were determined. Using this data, a covariance analysis was performed and the error in the attitude estimate was determined for each of the 720 samples over the orbit. Figures 10 through 12 show the error for each spacecraft axis over the orbit. Figures 13 through 15 show the associated error histograms. As expected, during the 98% of the orbit, where data is available from both sensors, accuracy in all three axes meets the requirement with margin. During 2% of the orbit, where a star outage occurs in one of the sensors, error "spikes" can be seen in the yaw and pitch estimates. Roll accuracy is insensitive to a sensor outage and is more closely correlated to the total number of stars tracked by both sensors since both sensor boresights are normal to the roll axis. As predicted by the worst-case analysis, throughout the orbit, roll and yaw accuracy remains below the 0.03 arc-sec, 3 sigma requirement, and pitch accuracy exceeds this requirement by 20% during 1% of the orbit. Table 4 shows the results of the orbital simulation.

The accuracy numbers above are for a single frame attitude estimate. For GOES-NEXT, and other geosynchronous missions where the external torques and dynamics of the spacecraft are well behaved, Kalmen filtering can be used to improve attitude estimates by a factor of two or more (Ref. 4).

4.3 Rate estimation

In addition to providing high accuracy attitude estimates, the HD-1003 can also be used for rate estimation. The HD-1003 star tracker can track stars moving at up to 0.3 deg/second with full accuracy and up to 1.0 deg/second with degraded accuracy. Algorithms have been developed to determine rate from star tracker data prior to attitude initialization, without gyro inputs (Ref. 9). Since the HD-1003 based attitude determination system can meet the attitude accuracy requirements without gyro inputs and can provide rate estimates up to 1.0 deg/second, a high performance gyro may not be required. If rate estimation is required for rates greater than 1.0 deg/second, a low cost, high reliability, solid-state gyro may be used. Vendors such as Systron-Donner, Rockwell/Draper, Honeywell, Smith Industries, Delco, and Allied Signal, produce small, inexpensive, solid state, 3-axis gyros accurate to several degrees per hour.

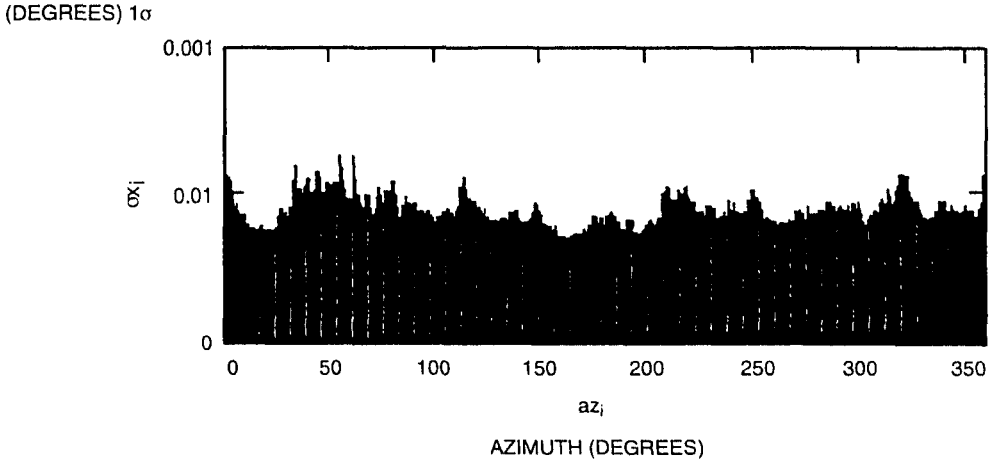

Figure 10. Roll Error vs Azimuth (GOES: Magnitude ≤ +6.0).

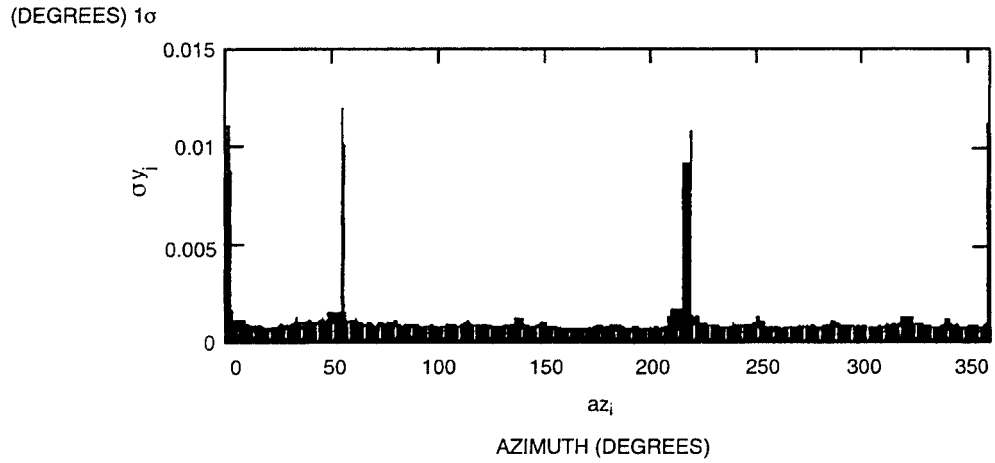

Figure 11. Pitch Error vs Azimuth (GOES: Magnitude ≤ +6.0).

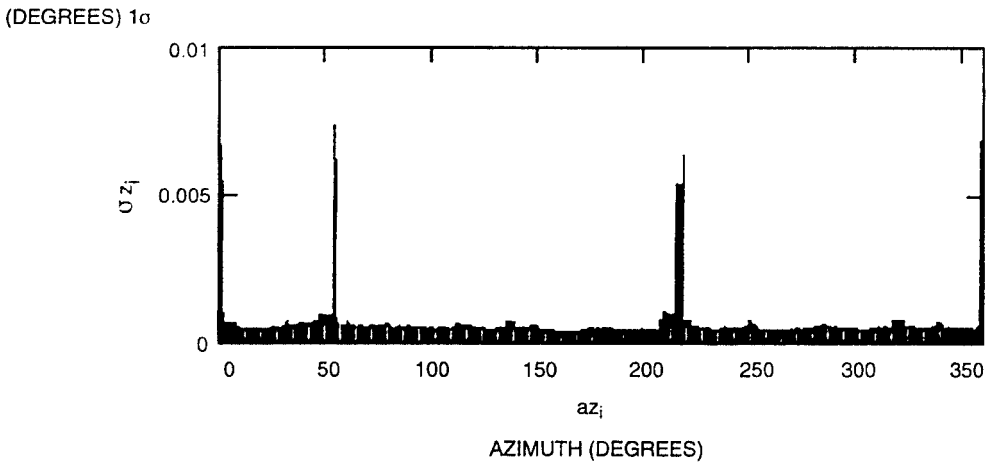

Figure 12. Yaw Error vs Azimuth (GOES: Magnitude ≤ +6.0).

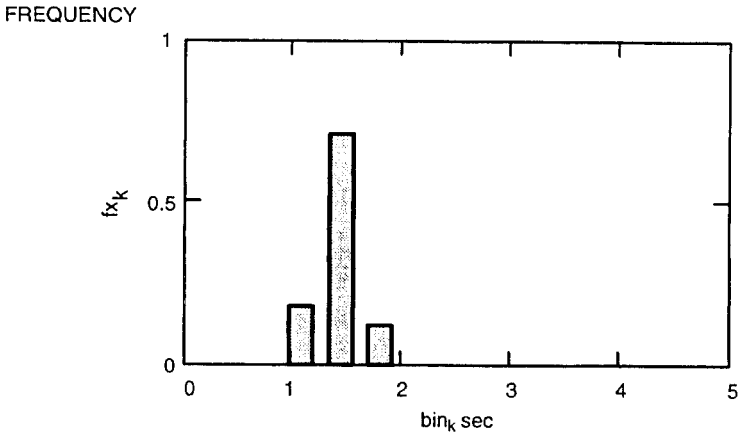

MAX	(σx)	=	0.000625	(DEGREES) 1σ MAXIMUM ROLL ERROR
MIN	(σx)	=	0.00035	(DEGREES) 1σ MINIMUM ROLL ERROR
MEAN	(σx)	=	0.00044	(DEGREES) 1σ MEAN ROLL ERROR
MEDIAN	(σx)	=	0.000435	(DEGREES) 1σ MEDIAN ROLL ERROR

Figure 13. Roll Error Histogram.

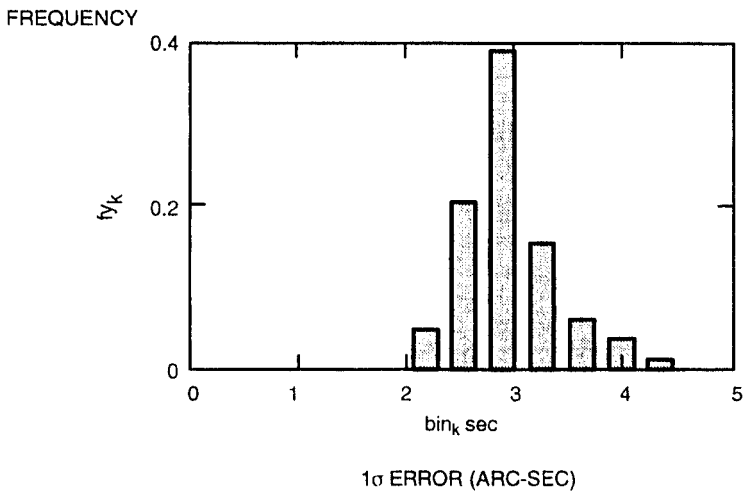

MAX	(σy)	=	0.011946	(DEGREES) 1σ MAXIMUM PITCH ERROR
MIN	(σy)	=	0.000676	(DEGREES) 1σ MINIMUM PITCH ERROR
MEAN	(σy)	=	0.001126	(DEGREES) 1σ MEAN PITCH ERROR
MEDIAN	(σy)	=	0.000859	(DEGREES) 1σ MEDIAN PITCH ERROR

Figure 14. Pitch Error Histogram.

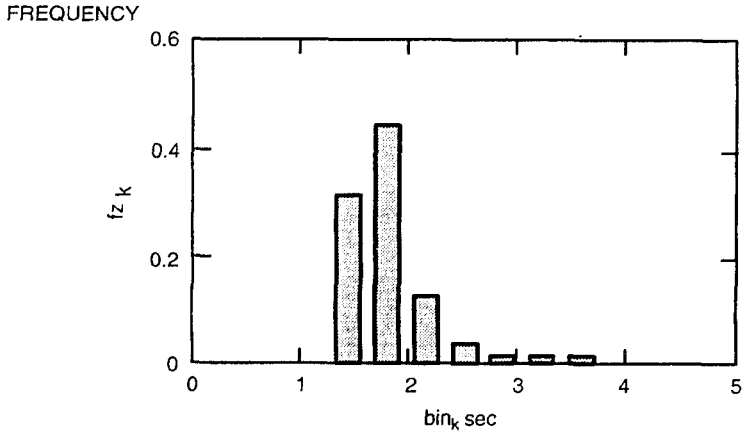

MAX	(σz)	=	0.007345	(DEGREES) 1σ MAXIMUM YAW ERROR
MIN	(σz)	=	0.000413	(DEGREES) 1σ MINIMUM YAW ERROR
MEAN	(σz)	=	0.000688	(DEGREES) 1σ MEAN YAW ERROR
MEDIAN	(σz)	=	0.000527	(DEGREES) 1σ MEDIAN YAW ERROR

Figure 15. Yaw Error Histogram.

Table 4
Result of Orbital Simulation

Axis	Mean 3 sigma	Median 3 sigma	Maximum 3 sigma	Minimum 3 sigma
Roll	0.0013 deg	0.0013 deg	0.0019 deg	0.0011 deg
Pitch	0.0034 deg	0.0026 deg	0.0358 deg	0.0020 deg
Yaw	0.0021 deg	0.0016 deg	0.0220 deg	0.0012 deg

5. SUMMARY

This paper describes how a stellar attitude determination system based on two HD-1003 multi-star trackers can be used in place of a traditional attitude sensor suite for GOES-NEXT and other geosynchronous missions. Improved performance, coverage, and reliability are achieved with reduced weight, power, and size. Cost savings accrue as well due to:

- Lower procurement costs versus a combined suite of analog and digital sun sensors, gyros, horizon sensors, and magnetometers.
- Lower integration, alignment, and system-level verification costs.
- Lower rework costs (higher reliability).

6. REFERENCES

1. J.L. Fiorello, Jr., I.H. Oh, and C.L. Ranne, "GOES-Next Navigation Operations," NASA/GSFC Flight Estimation Theory Symposium (May 11, 1988).
2. F.L. Markley, E. Seidewitz, D. Chu, and J.N. Rowe, "GOES Dynamic Propagation of Attitude," NASA/GSFC Flight Mechanics/Estimation Theory Symposium.
3. J.L. Fiorello, Jr., I.H. Oh, K.A. Kelly, and C.L. Ranne, "GOES I-M Image Navigation and Registration," NASA/GSFC Flight Mechanics/Estimation Theory Symposium (1989).
4. H.L. Fisher, T.E. Strickwerda, C.C. Kilgus, and L.J. Frank "Autonomous All-Stellar Attitude Determination Experiment: Ground Test Results," 14th Annual AAS Guidance and Control Conference, AAS 91-025 (2-6 February 1991).
5. R. Abreu, "Stellar Attitude Determination Accuracy with Multiple-Star Tracking Advanced Star Tracker," SPIE Space Guidance, Control, and Tracking, 1949 (April 1993).
6. K.J. Miklus, F. Kissh, and D.J. Flynn "Star Tracker Operation in a High Density Proton Field," NASA/GSFC Flight Mechanics Estimation Theory Symposium (1992).
7. L. DeAntonio, S. Udomkesmalee, J. Alexander, R. Blue, G. Sevaston, and M. Scholl "Star-Tracker Based, All-Sky, Autonomous Attitude Determination," SPIE Space Guidance, Control, and Tracking, 1949 (April 1993).
8. M.D. Shuster and S.D. Oh, "Three Axis Attitude Determination from Vector Measurements," Journal of Guidance and Control, AIAA 81-4003, 4 (1) (1981).
9. J. Weiss, "Rate Determination form Vector Observations," NASA/GSFC Flight Mechanics/ Estimation Theory Symposium (1992).

Addendum

The following papers were announced for publication in this proceedings but have been withdrawn or are unavailable.

[2812-39] **Lightning Mapper**
H. J. Christian, S. Goodman, NASA Marshall Space Flight Ctr.; E. Howard, NOAA

[2812-51] **Vicarious calibration of meteorological satellite sensors in the visible and near-infrared regions of the spectrum**
C. R. Rao, J. Chen, N. Zhang, NOAA

Author Index

Alley, Phillip W., 182
Ashton, Sanford, 805
Balch, C., 309
Baucom, Jeanette G., 587, 721
Bengston, Charlie, 40
Berthiaume, Gregory D., 552
Bicknell, William E., 389, 409
Blackman, Kathie, 824
Blackwell, William J., 472
Bornmann, Patricia L., 291, 309, 320, 552
Bouwer, S. David, 299
Bradley, Scott E., 182
Bremer, James C., 618
Briscoe, J., 638
Bryant, William C., Jr., 721, 805
Burgess, A. S., 490
Burke, Barry E., 552
Cafferty, Michael S., 376
Campbell, G. Garrett, 95
Candell, Lawrence M., 376, 446, 608
Carr, James L., 709
Cassidy, Lawrence W., 859
Cauffman, Sandra, 329, 697, 732
Chappell, Jon H., 638
Chen, Jianhua, Addendum
Chesters, Dennis, 30, 68, 80, 134, 146
Chevray, Keiko, 677, 685
Chipman, Eric G., 732
Christian, Hugh J., Addendum
Comeyne, Gustave J., III, 805
Corder, Eric L., 638
Cousins, Daniel, 376
Crassidis, John L., 824
Crosby, David S., 614
DeFoor, Thomas, 274
Dellinger, Wayne, 664
Ditillo, Douglas A., 805
Dittberner, Gerald J., 11, 20
Dress, Andre', 677, 685
Dunham, Warren D., 365
Ehlert, John C., 260, 559
Eppler, Walter G., 789
Farthing, Winfield H., 329, 732
Finkle, Harry R., 437
Flynn, David J., 859
Frederick, J. Ray, 528, 540
Friday, Elbert W., 2
Garcia, Howard A., 291
Ghaffarian, Benny, 251
Goodman, Steven, Addendum
Gregory, James A., 552
Grubb, Richard N., 281, 291, 299, 309, 320
Hagopian, Mike, 664
Hanser, Frederick A., 344, 353
Hanson, Jeffrey, 789
Hartley, Jeanne M., 518
Harvie, Edwin, III, 741
Hasler, A. Frederick, 80, 122, 134, 146
Hassler, Richard T., 518
Heaney, James B., 182
Hearn, David R., 426
Heckman, Gary, 274, 309, 320
Heymann, Roger, 20
Hillger, Donald W., 111
Hinkal, Sanford W., 174
Hirman, Joseph W., 274, 291, 309
Hooker, Ronald, 329
Howard, Edward, Addendum, 20
Hu, Kelley, 490
Hudson, James F., 777
Hur-Diaz, Sun H., 836
Hursen, Kathleen A., 160
Jenstrom, Del T., 30
Jentoft-Nilsen, Marit, 80, 134
Johnson, R., 490
Johnson, Rongrong X., 596
Kambhamettu, Chandra, 122
Kamel, Ahmed A., 685, 766, 836
Kelly, Kathleen A., 777
Kerekes, John P., 409, 437
Kimchi, Joseph, 376, 528, 540
Kirkner, Steven, 20
Knack, Jennifer L., 753
Kotecki, C. A., 490
Krebs, Danny J., 490
Krishna, Ramuhalli, 199
Krueger, Eric E., 501
Kunches, Joseph, 281
Kyle, Arthur M., 824
Lencioni, Donald E., 426
Lesondak, Edward P., 518
Louie, Marcus, 789
Lutz, Steven D., 652
Macintyre, Steven A., 365
Manthripragada, S., 490
Markley, F. Landis, 824
Martineau, Robert J., 490
Matheson, Lorne, 281, 291, 299
McCuistion, D., 40
McDonald, Peter, 231
Menzel, W. Paul, 50, 60, 84
Molnar, Gyula I., 68
Mott, David B., 490
Murphy, Jeanine E., 174
Newman, Ann, 299
Nielsen, Torben, 146
Nieman, Steven J., 60
O'Dette, P., 501
Ong, Kwok M., 652
Onsager, Terrance G., 281, 320
Paglieroni, David W., 789
Palaniappan, Kannappan, 80, 122, 134
Parker, Alexander C., 462
Peters, F. A., 490

Phenneger, Milton C., 721, 753
Pinkine, Nickalaus, 777
Pizzo, Victor J., 309
Plaut, Alan B., 462
Prins, Elaine M., 50
Purdom, James F. W., 95
Randou, Elena, 614
Rao, C. R., Addendum
Reine, Marion B., 501, 518
Ross, Robert W., 160
Rowe, John, 741
Russell, K., 638
Ryan-Howard, Danette P., 409, 453, 462
Sauer, Herb, 281
Schmit, Timothy J., 630
Sellers, Francis Bach, 344, 353
Sharma, Om, 146
Shea, James J., 210, 221
Shi, Jack, 490
Shu, Peter K., 490
Si, Guojun, 618
Singer, Howard J., 299, 320
Smith, William L., 84
Speich, David, 274, 281, 291, 309
Sprunger, Kent, 251
Staelin, David H., 472
Stewart, Kenneth P., 182
Sudey, John, Jr., 664
Tadikonda, Sivakumar S. K., 697
Terzis, C. L., 501, 518
Tsui, Yo-Kung J., 741
Upton, Charles R., 365
van Bezooijen, Roelof W. H., 847
Vaughn, Carol, 95
Velden, Christopher S., 60
Verrilli, Anthony J., 518
Viereck, R., 291, 320
Wack, Edward C., 608
Wallace, S., 638
Walsh, Tim, 685
Wanzong, Steve, 60
Washwell, Edward R., 685
Weidler, Darryl E., 479
Weinreb, Michael P., 572, 587, 596
Weitz, David M., 446, 462
Wickholm, David R., 260, 559
Williams, Frederick L., 260, 559
Wong, Theodore T. S., 528, 540
Woodham, Kurt, 721
Wu, Xiangqian, 84
Zhang, Nian, Addendum
Zimmermann, Frank, 329
Zwickl, Ron W., 281